VOLUME 24 NUMBER 1
JANUARY 1963

THE JOURNAL OF PHYSICS AND CHEMISTRY OF SOLIDS

AN
INTERNATIONAL
JOURNAL

Editor-in-Chief
HARVEY BROOKS
Cambridge, Mass.

Associate Editors

H. B. G. CASIMIR
Eindhoven

G. J. DIENES
Brookhaven

JACQUES FRIEDEL
Paris

E. M. LIFSHITZ
Moscow

PERGAMON PRESS
NEW YORK · LONDON · PARIS · LOS ANGELES

THE JOURNAL OF PHYSICS AND CHEMISTRY OF SOLIDS

Editors

Prof. Harvey Brooks (*Editor-in-Chief*), *217 Pierce Hall, Harvard University, Cambridge 38, Mass., U.S.A.*

Prof. Dr. H. B. G. Casimir, *N.V. Philips' Gloeilampenfabrieken, Eindhoven, The Netherlands*

Dr. G. J. Dienes, *Brookhaven National Laboratory, Upton, Long Island, New York, U.S.A.*

Prof. Jacques Friedel, *Service de Physique des Solides, Faculté des Sciences (Group II), B.P. No. 11, Orsay, (S. & O.) France*

Prof. E. M. Lifshitz, *Institute for Physical Problems, Vorobievskoye Chaussee, 2, Moscow, V-334, U.S.S.R.*

Editorial Advisory Board

U.S.A.

E. N. Adams, New York
D. Alpert, Illinois
L. Apker, Schenectady
J. Bardeen, Illinois
D. S. Billington, Oak Ridge
R. G. Breckenridge, Cleveland
Leo Brewer, Berkeley, Calif.
E. Burstein, Penn.
J. A. Burton, New Jersey
N. Cabrera, Virginia
G. C. Danielson, Iowa
J. C. Fisher, Schenectady
F. Herman, Palo Alto
Conyers Herring, New Jersey
A. R. von Hippel, Cambridge, Mass.
J. H. Hollomon, Schenectady
W. V. Houston, Houston
H. B. Huntington, Troy
H. M. James, Purdue
C. Kittel, Berkeley, Calif.
W. Kohn, La Jolla, Calif.
J. A. Krumhansl, Ithaca
A. W. Lawson, Riverside, Calif.
H. W. Leverenz, Princeton
O. T. Marzke, Pittsburgh
B. T. Matthias, New Jersey
L. R. Maxwell, Silver Spring
Joseph E. Mayer, La Jolla, Calif.
J. W. Mitchell, Charlottesville
E. W. Montroll, Yorktown Heights, N.Y.
David Pines, Princeton
George T. Rado, Washington, D.C.
H. Reiss, Canoga Park, Calif.
J. R. Reitz, Cleveland
A. Rose, Princeton
R. A. Smith, Cambridge, Mass.
R. Smoluchowski, Princeton
F. H. Spedding, Iowa
D. Turnbull, Schenectady
J. H. Van Vleck, Cambridge, Mass.
B. E. Warren, Cambridge, Mass.
Eugene P. Wigner, Princeton
B. H. Zimm, La Jolla, Calif.

Canada

R. E. Burgess, Vancouver
D. K. C. MacDonald, Ottawa
W. B. Pearson, Ottawa

United Kingdom

A. Charlesby, Shrivenham, Berks
W. J. Dunning, Bristol
I. Estermann, London
F. C. Frank, Bristol
H. K. Henisch, Reading
H. Jones, London
A. B. Pippard, Cambridge
M. H. L. Pryce, Bristol
O. C. Simpson, Baldock
K. W. H. Stevens, Nottingham
F. C. Tompkins, London

France

E. F. Bertaut, Grenoble
A. Guinier, Orsay
Louis Néel, Grenoble
Louis Weil, Grenoble

Germany

M. Born, Bad Pyrmont
Ulrich Dehlinger, Stuttgart
R. Hilsch, Göttingen
G. Leibfried, Aachen
E. Mollwo, Erlangen
H. Pick, Stuttgart
H. Welker, Erlangen

Italy

F. G. Fumi, Pavia

Czechoslovakia

J. Tauc, Praha

Japan

Toshinosuke Muto, Tokyo

The Netherlands

A. Michels, Amsterdam
G. W. Rathenau, Amsterdam

Sweden

J. O. Linde, Stockholm
Per-Olov Löwdin, Uppsala

Switzerland

G. Busch, Zurich
P. Scherrer, Zurich

U.S.S.R.

G. S. Zhdanov, Moscow

Publishing Offices

American Continent *Pergamon Press, Inc., 122 East 55th Street, New York 22, N.Y.*
Rest of the World *Pergamon Press Ltd., Headington Hill Hall, Oxford.*

Issued in parts. Annual Subscription (A) for libraries, £35 (U.S.A. $100.00); (B) for subscribers who write directly to the publisher certifying that the subscription is for their own personal use, £5 5s. (U.S.A. $15.00), including postage.

Surcharge for airmail subscriptions:

U.S.A. and South America	$28.00 (£10) per annum
Far East	$40.00 (£14) per annum
European countries	£5 ($14.00) per annum

Copyright © 1963 Pergamon Press Ltd.

PERGAMON PRESS, INC.
122 EAST 55th STREET, NEW YORK 22, N.Y. HEADINGTON HILL HALL, OXFORD

THE JOURNAL OF PHYSICS AND CHEMISTRY OF SOLIDS

AN INTERNATIONAL JOURNAL

VOLUME 24 1963

EDITORS

Editor-in-Chief: **HARVEY BROOKS** *Cambridge, Mass.*

Associate Editors:
H. B. G. CASIMIR *Eindhoven*
G. J. DIENES *Brookhaven*
JACQUES FRIEDEL *Paris*
E. M. LIFSHITZ *Moscow*

Supported by an International Advisory Editorial Board

Copyright © 1963
Pergamon

PERGAMON PRESS

OXFORD · NEW YORK · LONDON · PARIS

THE JOURNAL OF PHYSICS AND CHEMISTRY OF SOLIDS

Editors

Prof. Harvey Brooks (*Editor-in-Chief*), 217 *Pierce Hall, Harvard University, Cambridge* 38, *Mass., U.S.A.*

Prof. Dr. H. B. G. Casimir, *N.V. Philips' Gloeilampenfabrieken, Eindhoven, The Netherlands*

Dr. G. J. Dienes, *Brookhaven National Laboratory, Upton, Long Island, New York, U.S.A.*

Prof. Jacques Friedel, *Service de Physique des Solides, Faculté des Sciences* (*Group II*), *B.P. No.* 11, *Orsay,* (*S. & O.*) *France*

Prof. E. M. Lifshitz, *Institute for Physical Problems, Vorobievskoye Chaussee*, 2, *Moscow V*–334, *U.S.S.R.*

U.S.A.

E. N. Adams, New York
D. Alpert, Illinois
L. Apker, Schenectady
J. Bardeen, Illinois
D. S. Billington, Oak Ridge
R. G. Breckenridge, Cleveland
Leo Brewer, Berkeley, Calif.
E. Burstein, Penn.
J. A. Burton, New Jersey
N. Cabrera, Virginia
G. C. Danielson, Iowa
J. C. Fisher, Schenectady
H. K. Henisch, Penn.
F. Herman, Palo Alto
Conyers Herring, New Jersey
A. R. von Hippel, Cambridge, Mass.
J. H. Hollomon, Schenectady
W. V. Houston, Houston
H. B. Huntington, Troy
H. M. James, Purdue
C. Kittel, Berkeley, Calif.
W. Kohn, La Jolla, Calif.
J. A. Krumhansl, Ithaca
A. W. Lawson, Riverside, Calif
H. W. Leverenz, Princeton
O. T. Marzke, Pittsburgh
B. T. Matthias, New Jersey
L. R. Maxwell, Silver Spring
Joseph E. Mayer, La Jolla, Calif.
J. W. Mitchell, Charlottesville
E. W. Montroll, Yorktown Heights, N.Y.
David Pines, Princeton

Editorial Advisory Board

George T. Rado, Washington, D.C.
H. Reiss, Canoga Park, Calif.
J. R. Reitz, Cleveland
A. Rose, Princeton
R. A. Smith, Cambridge, Mass.
R. Smoluchowski, Princeton
F. H. Spedding, Iowa
D. Turnbull, Schenectady
J. H. Van Vleck, Cambridge, Mass.
B. E. Warren, Cambridge, Mass.
Eugene P. Wigner, Princeton
B. H. Zimm, La Jolla, Calif.

Canada

R. E. Burgess, Vancouver
D. K. C. MacDonald, Ottawa
W. B. Pearson, Ottawa

United Kingdom

A. Charlesby, Shrivenham, Berks.
W. J. Dunning, Bristol
I. Estermann, London
F. C. Frank, Bristol
H. Jones, London
A. B. Pippard, Cambridge
M. H. L. Pryce, Bristol
O. C. Simpson, Baldock
K. W. H. Stevens, Nottingham
F. C. Tompkins, London

France

E. F. Bertaut, Grenoble
A. Guinier, Orsay
Louis Néel, Grenoble
Louis Weil, Grenoble

Germany

M. Born, Bad Pyrmont
Ulrich Dehlinger, Stuttgart
R. Hilsch, Göttingen
G. Leibfried, Aachen
E. Mollwo, Erlangen
H. Pick, Stuttgart
H. Welker, Erlangen

Italy

F. G. Fumi, Pavia

Czechoslovakia

J. Tauc, Praha

Japan

Toshinosuke Muto, Tokyo

The Netherlands

A. Michels, Amsterdam
G. W Rathenau, Amsterdam

Sweden

J. O. Linde, Stockholm
Per-Olov Löwdin, Uppsala

Switzerland

G. Busch, Zurich
P. Scherrer, Zurich

U S.S.R.

G. S Zhdanov, Moscow

Publishing Offices

American Continent: Pergamon Press, Inc., 122 *East 55th Street, New York* 22, *N.Y.*
Rest of the World: Pergamon Press Ltd., Headington Hill Hall, Oxford.

Issued in parts. Annual Subscription (*A*) *for libraries*, £35 (*U.S.A.* $100.00); (*B*) *for subscribers who write directly to the publisher certifying that the subscription is for their own personal use*, £5 5*s*. (*U S.A.* $15.00), *including postage.*

Surcharge for airmail subscriptions:

U.S.A. and South America	$28.00 (£10) per annum
Far East	$40.00 (£14) per annum
European countries	£5 ($14.00) per annum

Copyright © 1963 Pergamon Press Ltd.

PERGAMON PRESS, INC.
122 EAST 55TH STREET, NEW YORK 22, N.Y. HEADINGTON HILL HALL, OXFORD

Author Index to Volume 24

References with (L) are to Letters to the Editor; (E) to Errata

Abrahams, S. C. Absence of antiferromagnetism in palladium. 589(L)

Adam, J. (see **Gergely, Gy.**). 687

Adams, L. H. (see **Davis, B. L.**). 787

Aharoni, A., H. Ditkovsky, E. H. Frei and A. Tzalmona. Transients in thermochromy of anils. 927

Albon, N. and A. E. Owen. The influence of twin structure on growth directions in dendritic ribbons of materials having the diamond or zinc-blende structures. 899

Alperin, H. A. (see **Will, G.**). 1679

Anderson, O. L. A simplified method for calculating the Debye temperature from elastic constants. 909

Andres, K. and B. Lüthi. Magnetostriction of yttrium iron garnet. 584(L)

Arajs, S. and R. V. Colvin. Paramagnetism of polycrystalline nickel. 1233
(see **Chessin, H.**). 261

Arnikar, H. J. and O. P. Mehta. Surface self-diffusion of iodide ions in thin films. 1633

Arnott, R. J. (see **Rogers, D. B.**). 347

Ballestracci, R., E. F. Bertaut et R. Pauthenet. Structure et propriétés magnétiques de l'oxysulfure d'uranium UOS. 487

Balluffi, R. W. (see **Minch, R. B.**). 443

Banks, E. (see **Robbins, M.**). 759

Barker, W. A. (see **Obermoeller, W. C.**). 641

Barrer, R. M., R. F. Bartholomew and L. V. C. Rees. Ion exchange in porous crystals—I. Self- and exchange-diffusion of ions in chabazites. 51
, R. F. Bartholomew and L. V. C. Rees. Ion exchange in porous crystals—II. The relationship between self- and exchange-diffusion coefficients. 309

Bartholomew, R. F. (see **Barrer, R. M.**). 51, 309

Bauer, Gy. T. (see **Gergely, Gy.**). 687

Bemski G., B. Szymanski and K. Wright. A new paramagnetic center in electron irradiated silicon. 1.

Benoit à la Guillaume, C. et J. Cernogora. Photoconductivité extrinsèque avec émission de phonons dans le germanium. 383

Beretka, J. Differential thermal analysis of yttrium iron garnet. 169(L)

Berghout, C. W. The uniaxial magnetic anisotropy of the f.c.c. cobalt precipitate in copper. 507

Bertaut, E. F. (see **Ballestracci, R.**). 487

Bienenstock, A. and G. Burley. Thermal expansion of silver iodide. 1271

Bir, G. L., E. I. Butikov and G. E. Pikus. Spin and combined resonance on acceptor centres in Ge and Si type crystals—I. Paramagnetic resonance in strained and unstrained crystals. 1467
II. The effect of the electrical field and relaxation time. 1475

Bis, R. F. Temperature-pressure projection of lead telluride phase diagram. 579

Blasse, G. (see **Schulkes J. A.**). 1653

Bleil, C. E. (see **Sturner, H. W.**) 735

Blinc, R., M. Schara and S. Poberaj. Paramagnetic resonance of irradiated ferroelectric $LiN_2H_5SO_4$. 559

Blinc, R. and I. Zupancic. Evidence for hindered rotation of the BeF_4 ions in ferroelectric (Glycine)$_3$ BeF_4. 1379(L)

Bok, J. and P. Nozieres. Instabilities of transverse waves in a drifted plasma. 709

Bokhout, H. and P. H. van Lent. Electric properties of gray tin single crystals grown in tin-mercury alloys. 704(L)

Boutin, H., B. C. Frazer and F. Jona. Structural effects of ionizing radiation in ferroelectric rochelle salt. 1341

(see **Brajovic, V.**). 617

(see **Safford, G.**). 771

Brajovic, V., H. Boutin, G. J. Safford and H. Palevsky. A study of rotational freedom in several ammonium salts by slow neutron inelastic scattering. 617

(see **Safford, G.**). 771

Braner, A. A. and R. Chen. Some optical properties of iodine single crystals. 135

Braun, T. (see **Maxim, I.**). 537

Brebrick, R. F. Deviations from stoichiometry and electrical properties in SnTE. 27

Brindley, G. W. (see **Schaefer, W. L.**). 919

Burgers W. G. (see **Geudeke, M.**) 667

Burley, G. (see **Bienenstock, A.**) 1271

Butikov, E. J. (see **Bir, G. L.**) 1467, 1475

Buyers, A. G. Calculation of work functions for surfaces composed of ionic crystals. 431

Cable, J. W. (see **Wollan, E. O.**). 1141

(see **Felcher, G. P.**). 1663

Callaway, J. Transition processes in semiconductors lasers. 1063(L)

Calvo, C. The crystal structure and luminescence of γ-zinc orthophosphate. 141

Campbell, E. S. Existence of a "well defined" specific energy for an ionic crystal; justification of Ewald's formulae and of their use to deduce equations for multipole lattices. 197

Cardona, M. Band parameters of semiconductors with zincblende, wurtzite, and germanium structure. 1543

Casella, R. C. On the possibility of observing a Bose-Einstein condensation of excitons in CdS and CdSe. 19

Casselman, T. N. and J. J. Markham. Some effects of a perturbation in a lattice on the normal modes. 669

Cernogora, J. (see **Benoit à la Guillaume, C.**). 383

Chadderton, L. T. Optical properties of the pthalocyanines. 751

, A. G. Fitzgerald and A. D. Yoffe. Pressure induced stacking faults in zinc sulphide crystals. 592(L)

Chen, J. H. (see **O'Connor, J. R.**). 1383(L)

Chen, R. (see **Braner, A. A.**). 135

Chessin, H., S. Arajs, R. V. Colvin and D. S. Miller. Paramagnetism and lattice parameters of iron-rich iron-germanium alloys. 261

Chibrikin, V. M. (see **Karimov, Yu. S.**). 1683.

Claiborne, L. T. Concentration dependence of the transition temperature in dilute superconducting alloys. 1363

Cochran, J. F. (see **Shiffman, C. A.**). 1369

Colvin, R. V. (see **Arajs, S.**). 1233
(see **Chessin, H.**). 261

Companion, A. L. and R. E. Wyatt. The diffuse reflectance spectra of some titanium oxides. 1025

Conway, J. M., D. A. Greenwood, J. A. Krumhansl and W. Martienssen. Oscillator strength for optical absorption by silver ions in alkali halide crystals. 239

Cornil, P. (see **Duchesne, J.**). 1333

Coulter, L. V., G. L. Stepakoff and G. C. Roper. The nature of the motion of N_2, CO and CH_4 in their β-quinol clathrates at low temperatures. 171(L)
(see **Stepakoff, G. L.**) 1435

Cox, D. E., W. J. Takei and G. Shirane. A magnetic and neutron diffraction study of the Cr_2O_3–Fe_2O_3 system. 405

Csavinszky, P. Corrections to the ground state energies of shallow donors in silicon and germanium. 1003

Cutler, M., R. L. Fitzpatrick and J. F. Leavy. The conduction band of cerium sulfide $Ce_{3-x}S_4$. 319

Daane, A. H. (see **Smidt, F. A.**). 361

Daniel, E. et J. Friedel. Sur la polarisation de spin des electrons de conductibilité dans les métaux ferromagnétiques 1601

Davies, R. G. An X-ray and dilatometric study of order and the "*K*-state" in iron–aluminum alloys. 985

Davis, B. L. and L. H. Adams. Transition rates of KNO_3 high-pressure polymorphs. 787

Delves, R. T. HgTe–MnTe alloys—II. Electrical properties. 885
and B. Lewis. Zinc blende type HgTe–MnTe solid solutions—I. 549

Didchenko, R. and F. P. Gortsema. Some electric and magnetic properties of rare earth monosulfides and nitrides. 863

Ditkovsky, H. (see **Aharoni, A.**). 927

Dougherty, J. E. (see **Johnson, V. J.**). 85

Douglass, R. M. (see **Johnson, V. J.**). 85

Drabble, J. R. Summary of Conference on the Physics of Semiconductors, Exeter, 1962. 161

Drain, L. E. Nuclear magnetic resonance in platinum. 379

Dreyfus, B., A. Lacaze, P. Thomas et L. Weil. Conduction thermique d'alliages or cobalt à basse temperature. 219

Duchesne, J., M. Read et P. Cornil. Effet stark en spectroscopie quadripolaire pure. 1333

Dutton, H. M. (see **Keys, J. D.**). 563

Elwell, D., R. Parker and A. Sharkey. The influence of manganese on the electrical conductivity of nickel ferrite. 1325

Englert, A. and H. Tompa. Energy and configuration of atoms in a simple model of an edge dislocation—II. Morse potential. 1145(L)

Felcher, G. P., J. W. Cable and M. K. Wilkinson. The magnetic moment distribution in Cu_2MnAl. 1663

Feller, H. G. und H. Wever. Thermodiffusion in den Hochtemperaturphasen von Zirkon und Titan. 969(L)

Fitzgerald, A. G. (see **Chadderton, L. T.**). 592(L)

Fitzpatrick, R. L. (see **Cutler, M.**). 319

Flores, J. M. (see **Messier, J.**). 1541
Franse, J. J. M. (see **Veerman, J.**). 947
Frazer, B. C. (see **Boutin, H.**). 1341
Fredkin, D. R. and H. Suhl. A note on the short-range order at the ferromagnetic Curie point. 217
Frei, E. H. (see **Aharoni, A.**). 927
Freymuth, P. und G. Sauerbrey. Ausheilung von Bestrahlungsschäden in Quarz-Schwingkristallen. 151
Friauf, R. J. (see **Pilcher, F.**). 1687
Friedel, J. (see **Daniel, E.**). 1601
Frindt, R. F. The optical properties of single crystals of WSe_2 and $MoTe_2$. 1107
Fromhold, A. T., Jr., Kinetics of oxide film growth on metal crystals—I. Formulation and numerical solutions. 1081
    Kinetics of oxide film growth on metal crystals—II. Homogeneous field approximations. 1309
Fukuda, Nobuyuki and M. Wortis. Bound states in the spin wave problem. 1675
Fukuta, N. and B. J. Mason. Epitaxial growth of ice on organic crystals. 715

Galleron, G. (see **Jerome, D.**). 1557
Garber, M. (see **Shiffman, C. A.**). 1369
Gardner, R. F. G., F. Sweett and D. W. Tanner. The electrical properties of alpha ferric oxide—I. The impure oxide. 1175
    The electrical properties of alpha ferric oxide—II. Ferric oxide of high purity. 1183
Gautier, F. Structure électronique des impuretés dans le nickel. 387
Geballe, T. H. (see **Raub, Ch. J.**). 1093
Geller, S., H. J. Williams and R. C. Sherwood. Comments on "A study of neodymium substituted yttrium iron garnet" by T. H. Ramsey, Jr., H. S. Steinfink and E. J. Weiss. 583(L)
George, A. M. and M. D. Karkhanavala. Studies of the electrical properties of uranium oxides—I. Electrical conductivity of α-U_3O_8. 1207
Gergely, Gy. Excitation spectra of ZnS phosphors—I. Theoretical analysis. 681
    , J. Adam and Gy. T. Bauer. Excitation spectra of ZnS phosphors—II. Experimental results. 687.
Gerson, R. and H. Jaffe. Electrical conductivity in lead titanate zirconate ceramics. 979
Geudeke, M. and W. G. Burgers. Origin of F-centers in X-ray irradiated NaCl crystals. 667
Gingerich, K. A. (see **Irani, K. S.**). 1153
Glarum, S. H. Electron mobilities in organic semiconductors. 1577
Gomes, W. The influence of vacancies on the reduction of silver ions in silver doped alkali halides. 1671
Goodenough, J. B. (see **Rogers, D. B.**). 347
Goodman, F. O. On the theory of accommodation coefficients—III. Classical perturbation theory for the thermal accommodation of light gases. 1451
Gortsema, F. P. (see **Didchenko, R.**). 863
Green, M., V. Jendrasic and J. McBreen. Surface states at the germanium-electrolyte cathode. 701(L)
Greenwood, D. A. (see **Conway, J. M.**). 239
Grover, N. B. and R. Oren. Majority-carrier mobility on germanium surfaces. 693, 1152(E)
Gschneidner, K. A., Jr., R. O. Elliott and R. R. McDonald. Effects of alloying additions on the $\gamma \rightleftharpoons \alpha$ transformation of cerium—I. Pure cerium. 785(E)

Halperin, A. (see **Nahum, J.**). 823

Halpern, V. Overlap functions in planar crystals. 1495

Ham, F. S. Anisotropic spin-orbit interaction in paramagnetic resonance. 1165

Hamilton, D. R. (see **Seidensticker, R. G.**). 1585

Harbeke, G. Absorption edge in ferroelectric SbSI under electric fields. 957

Hardeman, G. E. C. Electron and nuclear spin resonance in *n*-type silicon carbide. 1223

Harman, T. C., J. M. Honig and B. M. Tarmy. Galvano-thermomagnetic effects in semiconductors and semimetals—III. The standard and Kane band models. 835

Harvey, W. W. The thermodynamic activity of the semiconductor. 701(L)

Hasiguti, Ryukiti R. (see **Ishino, Shiori**). 1033

Hass, M. Infrared lattice reflection spectra of LiCl, LiBr, KF, RbF, and CsF. 1159

Hatcher, A. P. (see **Merton, U.**). 1064(L)

Hauser, J. J. and R. G. Treuting. Relation between structure anisotropy and superconducting anisotropy. 371

Heckman, R. C. and D. M. Mattox. Electrical properties of single crystal Bi_2S_3. 973(L)

Hegyi, I. J., E. E. Loebner, E. W. Poor, Jr., and J. G. White. Two crystal forms of ZnP_2, their preparation, structure, and optoelectronic properties. 333(L)

Herrmann, G. F. Resonance and high frequency susceptibility in canted antiferromagnetic substances. 597

Hirth, J. P. (see **Mullins, W. W.**). 1391.

Hoch, M. Order-disorder reactions in α-Ti(O) and TiO. 157

Hodgson, J. N. The optical effective mass and absorption edge of electrons in sodium. 1213

Hoesterey, D. C. and G. M. Letson. The trapping of photocarriers in anthracene by anthraquinone, anthrone and naphthacene. 1609

Holmes, P. J. A competitive adsorption model of steady-state growth of a crystal from a lightly-doped melt. 1239

Honig, J. M. (see **Harman, T. C.**). 835

Houska, C. R. A theoretical treatment of atomic configurations found in some iron-aluminum solid solutions. 95

Hughes, F. and H. Rabin. Investigation of optical absorption in irradiated CsF. 586(L)

Hulliger, F. and E. Mooser. Electrical properties of anomalously composed daltonides. 283

Iida, S. The difference between Gilbert's and Landau-Lifshitz's equations. 625

Illingworth, R. Diffusion of thallous ions in single crystals of KBr. 129

Irani, K. S. and K. A. Gingerich. Structural transformation of zirconium phosphide. 1153

Ishikawa, Yoshikazu and Yasuhiko Syono. Order-disorder transformation and reverse thermoremanent magnetism in the $FeTiO_3$-Fe_2O_3 system. 517

Ishino, Shiori, Fumiko Nakazawa and Ryukiti R. Hasiguti. Annealing of γ-ray irradiated *n*-type germanium. 1033

Ives, M. B. On kink kinetics in crystal dissolution. 275

Jach, J. The thermal decomposition of $NaBrO_3$—I. Unirradiated material. 63
  The thermal decomposition of $NaBrO_3$—II. Irradiated material. 75

Jackson, J. A. Detection of oxygen-17 n.m.r. in solid MgO. 591(L)

Jacobs, P. W. M. and J. N. Maycock. Conductance of strontium-doped potassium chloride crystals (L). 1693

Jaffe, H. (see **Gerson, R.**). 979

Jayaraman, A., W. Klement, Jr., R. C. Newton and G. C. Kennedy. Fusion curves and polymorphic transitions of the group III elements—aluminum, gallium, indium and thallium—at high pressures. 7

Jendrasic, V. (see **Green, M.**). 701(L)

Jerome, D. et G. Galleron. Polarisation dynamique du sodium métallique en champ faible à la température de l'helium liquide. 1557

Johnson, V. J., M. W. Valenta, J. E. Dougherty, R. M. Douglass and J. W. Meadows. $Pb(Sc_{0.5}N_{0.5})_x\Phi_{1-x}O_3$, Perovskite-type ferroelectric solid solutions possessing relatively large spontaneous polarizations. 85

Jona, F. (see **Boutin, H.**). 1341

Joseph, R. I. and B. D. Silverman. Optical modes of the perovskite structure. 1349

Kalvius, M. (see **Zinn, W.**). 993

Kankeleit, E. (see **Zinn, W.**). 993

Kaplan, H. Impurity states associated with subsidiary energy-band minima. 1593

Karimov, Yu. S., V. M. Chibrikin and I. F. Shchegolev. A study of hyperfine interaction in cations of dibenzenechromium and ditoluenechromium. 1683

Karkhanavala, M. D. (see **George, A. M.**). 1207

Kasper, J. S. (see **Kouvel, J. S.**). 529

Keating, P. N. Hole injection into CdS from Cu_2S. 1101

Keller, J. M. Resistivity of vacancy-impurity pairs. 1121

Kelley, P. L. Nonlinear effects in solids. 607
 Second harmonic generation in solids. 1113

Kemp, J. C. and V. I. Neeley. Optical and E.S.R. spectra of irradiated CaO crystals. 332(L)
 (see **Neeley, V. I.**). 1301

Kennedy, G. C. (see **Jayaraman, A.**). 7

Keys, J. D. and H. M. Dutton. Diffusion and solid solubility of silver in single-crystal bismuth telluride. 563

Khubchandani, P. G. and S. Sanatani. Scattering of cold neutrons in beryllium oxide. 782(L)

Kienle, P. (see **Zinn, W.**). 993

Kleefstra, M., Z-bands in KCl. 1567

Klement, W., Jr. (see **Jayaraman, A.**). 7

Knippenberg, W. F. (see **van Daaal, H. J.**). 109

Knof, H. and W. G. Maisch. Pressure effect on color centers in RbF, RbCl, RbBr and CsI. 1625

Koehler, W. C. (see **Wollan, E. O.**). 1141

Kohn, W. and M. Luming. Orbital susceptibility of dilute alloys. 851

Kouvel, J. S. A ferromagnetic antiferromagnetic model for copper–manganese and related alloys. 795
 and J. S. Kasper. Long-range antiferromagnetism in disordered Fe–Ni–Mn alloys. 529

Krause, B. H. X-ray induced particle size changes in thallous azide. 779(L)

Krumhansl, J. A. (see **Conway, J. M.**). 239

Kudman, I. and L Vieland. Absorption edge in degenerate *n*-type gallium arsenide. 967(L)
 (see **Vieland, L. J.**). 437

Kunnmann, W. D. B. Rogers and A. Wold. The use of $CO–CO_2$ atmospheres for the preparation and free energy determinations of several oxide systems. 1535

Lacaze, A. (see **Dreyfus, B.**). 219
La Force, R. C., L. E. Toth and S. F. Ravitz. The temperature dependence of the nuclear magnetic resonance of Co^{59}. 729
Lallement, R. Dilatation et pouvoir thermoélectrique du plutonium α à basse température. 1617
Langston, S. A. and B. Lewis. Compounds with the C33 tetradymite-type structure. 1387(L)
Leavy, J. F. (see **Cutler, M.**). 319
Lehovec, K. and A. Slobodskoy. Sub-eutectic solubilities of impurities in germanium and silicon. 593
Lerner, S. (see **Robbins, M.**). 759
Letson, G. M. (see **Hoesterey, D. C.**). 1609
Levengood, W. C. Systematics of defect structures in glasses with ionic substitutions. 1011
Lewis, B. (see **Delves, R. T.**). 549
(see **Langston, S. A.**). 1387(L)
Liu, S. H. Spin ordering in the superconducting state. 475
Loebner, E. E. (see **Hegyi, I. J.**). 333(L)
Loh, E. Spectral photoresponse of Si, GaAs and Ge shallow junction in the region 1–5 eV. 493(L)
and J. C. Phillips. Band structure effects in photoconductivity of semiconductors. 495(L)
Loiaono, G. M. (see **Nassau, K.**). 1503
Luming, M. (see **Kohn, W.**). 851
Lüscher, E. (see **von Goeler, E.**). 1217
Lüthi, B. (see **Andres, K.**). 584(L)

Mackintosh, A. R. and L. Sill. The thermoelectric power in chromium and vanadium. 501
Mackliet, C. A. and A. I. Schindler. Heat capacity of Ni–Pd Alloys. 1639
Maisch, W. G. (see **Knof, H.**). 1625
Manaila, R. (see **Rosenberg, M.**). 1419
March, N. H. (see **Worster, J.**). 1305
Markham, J. J. (see **Casselman, T. N.**). 669
Martienssen, W. (see **Conway, J. M.**). 239
Martin, J. E. (see **Owen, N. B.**). 1519
Mason, B. J. (see **Fukuta, N.**). 715
Mathur, S. C. (see **Mookherji, A.**). 1386(L)
Matossi, F. Atomic polarizabilities in III–V compounds. 706(L)
Matthias, B. T. (see **Raub, Ch. J.**). 1093
Mattox, D. M. (see **Heckman, R. C.**). 973(L)
Maxim, I. and T. Braun. Effects of reactor radiations on the chemisorption equilibrium of oxygen on nickel oxide. 537
Maycock, J. N. (see **Jacobs P. W. M.**). 1693 (L)
McBreen, J. (see **Green, M.**). 701(L)
McCaldin, J. O. and A. E. Widmer. Silicon heavily doped by energetic cesium ions. 1073
McClure, J. W. The electronic structure of rare earth monosulfides. 871
McGuire, T. R. and S. J. Pickart. Ferrimagnetism of manganese ferrite-chromite. 1531
McLellan, R. B. and R. Shuttleworth. The determination of the vibrational entropies of solute atoms in dilute copper solid solutions by the measurement of vapour pressures. 453
McNiff, E. J.,Jr., and S. Shapiro. Nuclear magnetic resonance in metal hexaborides. 939
Mead, S. W. (see Ramsey, W. J.). 1066(L)

Meadows, J. W. (see **Johnson, V. J.**). 85
Mehrotra, B. N. Lattice thermal conductivity of antiferromagnetic MnF_2 below its Néel temperature. 1053
Mehta, O. P. (see **Arnikar H. J.**). 1633
Merriam M. F. and D. S. Schreiber. Search for superconductivity in the hydrides of lanthanum. 1375
Merten, U. and A. P. Hatcher. The distribution of zinc between solid GaSb and Ga–Sb melts. 1064(L)
Messier, J. and J. M. Flores. Temperature dependence of Hall mobility and μ_H/μ_D for Si. 1539
Mikoshiba, Nobuo. Weak-field magnetoresistance of hopping conduction in simple semiconductors. 341
Miller, D. S. (see **Chessin, H.**). 261
Minch, R. B. and R. W. Balluffi. On the magnitude of vacancy supersaturations in silver during deformation at elevated temperatures. 443
Mitsui, Toshio (see **Shiozaki, Yōichi**). 1057
Mnyukh, Yu. V. Laws of phase transformation in a series of normal paraffins. 631
Montefinale, A. C. (see **Petriconi, G. L.**). 573
Mookherji, A. and S. C. Mathur. Two-dimensional antiferromagnetism in cupric formate tetrahydrate single crystal. 1386(L)
Mooser, E. (see **Hulliger, F.**). 283
Morehead, F. F. Luminescence in ZnS, Se:Cu, Cl. 37
  and R. S. Title. Correlation of e.p.r. and electro-optical measurements in ZnS. 719
Morgan, T. N. Application of the uncertainty principle to electron scattering by phonons in solids. 1657
Morton, J. R. A paramagnetic species in irradiated $(NH_4)_2HPO_4$. 209
Mullins, W. W. and J. P. Hirth. The microscopic kinetics of step motion in growth processes. 1391
Murphy, P. V. The formation and discharge of Carnauba wax electrets in nuclear radiation fields 329(L)
Murti, Y. V. G. S. (see **Ramasastry, C.**). 1385(L)
Musgrave, M. J. P. On the transition from white tin (β-Sn) to the body-centred cubic form under pressure. 557

Nagy, E. and J. Tóth. Ordering in alloy Cu_3Au—III. 1043
Nahum, J. and A. Halperin. Thermoluminescence and the relation between thermal and optical activation energies in diamond. 823
Nakajima, Seizo. The crystal structure of $Bi_2Te_{3-x}Se_x$. 479
Nakazawa, Fumiko (see **Ishino, Shiori**). 1033
Nassau, K. Calcium tungstate—IV. The theory of coupled substitution. 1511
  and G. M. Loiacono. Calcium tungstate—III. Trivalent rare earth substitution. 1503
Nathans, R. (see **Will, G.**). 1679
Neeley, V. I. and J. C. Kemp. Optical absorption in CaO single crystals. 1301
  (see **Kemp, J. C.**). 332(L)
Newman, P. C. Crystal structures of adamantine compounds. 45
Newton, R. C. (see Jayaraman, A.). 7
Nicholas, J. F. Rearrangement of a flat surface without altering the number of broken bonds. 1279.
Nicolau, P. (see **Rosenberg, M.**). 1421
Nozieres, P. (see **Bok, J.**). 709

Obermoeller, W. C. and W. A. Barker. Calculated specific heat contribution of F_2 centers in LiF. 641
O'Connor, J. R. and J. H. Chen. Optical spectra of several d^1-electron systems. 1383(L)

Ogilvie, G. J., J. V. Sanders and A. A. Thomson. The bombardment of gold films by inert gas ions. 247
Oguchi, Takenhiko. Antiferromagnetic ground state. 1049
Olsen, T. Attenuation of longitudinal soundwaves by conduction electrons. 187.
    Fermi surface of white tin from magnetoacoustic measurements. 649
Oren, R. (see **Grover, N. B.**). 693
Orr, J. C. Pressure and high current effects on a graphite contact. 1695
Otte, H. M. Faulting in sodium azide. 169(L)
Owen, A. E. (see **Albon, N.**). 899
Owen, N. B., P. L. Smith, J. E. Martin and A. J. Wright. X-ray diffraction at ultra-high pressures. 1519

Packard, J. R. and Swenson, C. A. An experimental equation of state for solid xenon. 1405
Palevsky, H. (see **Brajovic, V.**). 617
Papée, H. M. (see **Petriconi, G. L.**). 573
Parker, R. (see **Elwell, D.**). 1325
Pausescu, P. (see **Rosenberg, H.**). 1419
Pauthenet, R. (see **Ballestracci, R.**). 487
Petriconi, G. L., T. W. Zawidski, A. C. Montefinale and H. M. Papée. Change of sodium chloride surfaces in electric discharges. 573
Phillips, J. C. (see **Loh, E.**). 495(L)
Pick, R. Étude de la résistivité électrique des alliages binaires ordonnés. 741
Pickart, S. J. (see **McGuire, T. R.**). 1531
    (see **Will, G.**). 1681
Pikus, G. E. (see **Bir, G. L.**). 1467, 1475
Pilcher, F., D. Schinke and R. J. Friauf. Optical absorption of color centers in lithium fluoride containing magnesium additive. 1687
Piller, H. Electron effective mass in gallium antimonide determined by Faraday rotation measurements. 425
Poberaj, S. (see **Blinc, R.**). 559
Poole, C. P., Jr. A simple model for the Curie temperature of a small ferro-magnetic particle. 781(L)
Poor, E. W., Jr. (see **Hegyi, I. J.**). 333(L)

Quimby, S. L. (see **Weisberg, L. R.**). 1251
Quinn, J. J. The diamagnetic susceptibility of a quantum plasma. 933
    (see **Will, G.**). 1679

Rabin H. (see **Hughes, F.**). 586(L)
Ramachandran, P. N. and R. E. Salomon. High voltage photovoltaic effect at low temperatures. 583(L)
Ramasastry, C. and Y. V. G. S. Murti. Electrical conductivity of sodium bromate crystals. 1385(L)
Ramsey, W. J., D. E. Sands and S. W. Mead. Neutron diffraction by Li_2MgPb. 1066(L)
Rathenau, G. W. (see **Veerman, J.**). 947
Raub, Ch. J., W. H. Zachariasen, T. H. Geballe and B. T. Matthias. Superconductivity of some new Pt-metal compounds. 1093

Ravitz, S. F. (see **La Force, R. C.**). 729
(see **Toth, L. E.**). 1203
Read, M. (see **Duchesne, J.**). 1333
Rees, L. V. C. (see **Barrer, R. M.**). 51, 309
Richman, D. Dissociation pressures of GaAs, GaP and InP and the nature of III–V melts. 1131
Robbins, M., S. Lerner and E. Banks. Some effects of charge-compensating ions on cation site preferences in complex oxides. 759
Roberts, G. G. and R. H. Tredgold. Space charge injection into impurity semiconductors. 1263
Rogers, D. B., R. J. Arnott, A. Wold and J. B. Goodenough. The preparation and properties of some vanadium spinels. 347
(see **Kunnmann, W.**). 1535
Roper, G. C. (see **Coulter, L. V.** 171(L)
Rosenberg, M., P. Nicolau, R. Manaila and P. Pausescu. Preparation, electrical conductivity and tetragonal distortion of some manganite-systems. 1419

Sachs, M. Rotational properties of paramagnetic resonance spectra of non-cubic crystals. 500(E)
Safford, G., V. Brajovic and H. Boutin. An investigation of the energy levels in alkaline earth hydroxides by inelastic scattering of slow neutrons. 771
(see **Brajovic, V.**). 617
Salomon, R. E. (see **Ramachandran, P. N.**). 583(L)
Sanatani, S. (see **Khubchandani, P. G.**). 782(L)
Sanders, J. V. (see **Ogilvie, G. J.**). 247
Sands, D. E. (see **Ramsey, W. J.**). 1066(L)
Sarma, G. On the influence of a uniform exchange field acting on the spins of the conduction electrons in a superconductor. 1029
Sauerbrey, G. (see **Freymuth, P.**). 151
Schaefer, W. L. and G. W. Brindley. Oxidation of magnesiowustite single crystals—I. Optical and kinetic data. 919
Schara, M. (see **Blinc, R.**). 559
Schindler, A. I. (see **Mackliet, C. A.**). 1639
Schinke, D. (see **Pilcher, F.**). 1687
Schlosser, H. Symmetrized combinations of plane waves and matrix elements of the Hamiltonian for cubic lattices. 340
Schreiber, D. S. (see **Merriam, M. F.**). 1375
Schulkes, J. A. and G. Blasse. Crystallographic and magnetic properties of the systems lithium ferrite-aluminate and lithium ferrite-gallate. 1651
Schumacher, R. T. and W. E. Vehse. The paramagnetic susceptibility of sodium metal. 297
Secco, E. A. Thermal decomposition of sodium azide crystals. 469
Seidensticker, R. G. and D. R. Hamilton. The dendritic growth of InSb. 1585
Seki, Syûzô (see **Suga, Hiroshi**). 330(L)
Seltzer, M. S. and J. B. Wagner, Jr. Diffusion of lead in lead sulphide at 700°C. 1525
Shapiro, S. (see **McNiff E. J., Jr.**). 939
Sharkey, A. (see **Elwell, D.**). 1325
Shchegolev, I. F. (see **Karimov, Yu. S.**). 1685
Sherwood, R. C. (see **Geller, S.**). 583(L)
Shiffman, C. A., J. F. Cochran and M. Garber. The specific heat jump in superconducting lead. 1369

Shiozaki, Yōichi and Toshio Mitsui. Powder neutron diffraction study of $LiNbO_3$. 1057
Shuttleworth, R. (see **McLellan, R. B.**). 453
Sill, L. (see **Mackintosh, A. R.**). 501
Silverman, B. D. (see **Joseph, R. I.**). 1349
Simhony, M. Measurements on the dielectric constant of iodine single crystals in various crystallographic directions. 1297
Singer, J. Study of the bands of uniform birefringence in faulted ZnS. 1645
Simkovich, G. The nature of point defects in solid lead chloride. 213, 1071(E)
Sirtl, E. Die "Sandwich-Methode"—ein neues Verfahren zur Herstellung epitaktisch gewachsener Halbleiterschichten. 1285
Slobodskoy, A. (see **Lehovec, K.**). 593
Smidt, F. A., Jr. and A. H. Daane. Electrical resistivity of rare-earth alloys. 361
Smith, P. L. (see **Owen, N. B.**). 1519
Somorjai, G. A. Charge transfer controlled surface interactions between oxygen and CdSe films. 175
Spinar, L. H. (see **Wang, C. C.**). 953
Statz, H. Maximum solid solubility and distribution coefficient of impurities in germanium and silicon 699(L)
Stepakoff, G. L. and L. V. Coulter. The thermodynamics and hindered rotation of occluded CO in the β-quinol clathrate. 1435
    (see **Coulter, L.V.**). 171(L)
Stephens, D. R. The phase diagram of plutonium. 1197
Sturner, H. W. and C. E. Bleil. Induced conductivity in cadmium selenide by electron bombardment. 735
Suga, Hiroshi and Syûzô Seki. Availability of high-resolution n-m-r method for the study of molecular motion in the crystalline state. 330(L)
Suhl, H. (see **Fredkin, D. R.**). 217
Sweett, F. (see **Gardner, R. F. G.**). 1175, 1183
Swenson, C. A. (see **Packard, J. R.**), 1405
Syono, Yashuhiko (see **Ishikawa, Yoshikazu**). 517
Szigeti, B. Impurity activated infra-red absorption in valency crystals. 225
Szymanski, B. (see **Bemski, G.**). 1

Takei, W. J. (see **Cox, D. E.**). 405
Tannenwald, P. E. (see **Weber, R.**). 1357
Tanner, D. W. (see **Gardner, R. F. G.**). 1175, 1183
Tarmy, B. M. (see **Harman, T. C.**). 835
Teitler, S. Anisotropic free carrier Voigt effect in cubic semiconductors. 1487
Tharmalingam, K. Interstitial mobility in NaCl. 1380(L)
Thomas, P. (see **Dreyfus, B.**). 219
Thomson, A. A. (see **Ogilvie, G. J.**). 247
Title, R. S. (see **Morehead, F. F.**). 719
Tompa, H. (see **Englert, A.**). 1145(L)
Tosi, M. P. A comment on the Born model treatment of the polymorphic transitions of the alkali halides. 1067(L)
    Cohesive energy of the alkali halide crystals. 965(L)
Tóth, J. (see **Nagy, E.**). 1043

Toth, L. E. and S. F. Ravitz. Ferromagnetic nuclear resonance in cobalt nuclei in stacking faults and twins. 1203
(see **La Force, R. C.**). 729
Tredgold, R. H. (see **Roberts, G. G.**). 1263
Treuting, R. G. (see **Hauser, J. J.**). 371
Tzalmona, A. (see **Aharoni, A.**). 927

Valenta, M. W. (see **Johnson, V. J.**). 85
van Daal, H. J., W. F. Knippenberg and J. D. Wasscher. On the electronic conduction of α-SiC crystals between 300 and 1500 K. 109
van Lent, P. H. (see **Bokhout, H.**). 704(L)
Veerman, J., J. J. M. Franse and G. W. Rathenau. Dependence of magnetocrystalline anisotropy on field strength. 947
Vehse, W. E. (see **Schumacher, R. T.**). 297
Vieland, L. J. and I. Kudman. Behavior of selenium in gallium arsenide. 437
(see **Kudman, I.**). 967(L)
von Goeler, E. and E. Lüscher. Radiotracer studies of gold adsorption and desorption on clean molybdenum surfaces. 1217
Wagner, J. B., Jr. (see **Seltzer, M. S.**). 1525
Walker, W. C. *d*-band transitions in solids. 1667
Wang, C. C. and L. H. Spinar. Electron transfer in zinc-blende III–V compounds. 953
Wasscher, J. D. (see **van Daal, H. J.**). 109
Weber, R. and P. E. Tannenwald. Second-order exchange interactions from spin wave resonance. 1357
Weil, L. (see **Dreyfus, B.**). 219
Weisberg, L. R. and S. L. Quimby. Ordering and disordering processes in Cu_3Au—III. 1251
Wever, H. (see **Feller, H. G.**). 969(L)
White, J. G. (see **Hegyi, I. J.**). 333(L)
Widmer, A. E. (see **McCaldin, J. O.**). 1073
Wiedemann, W. (see **Zinn, W.**). 993
Wilkinson, M. K. (see **Felcher, G. P.**). 1663
Will, G., S. J. Pickart, H. A. Alperin and R. Nathans. Antiferromagnetic structure of EuTe. 1679
Williams, H. J. (**see Geller, S.**). 583(L)
Wise, H. Energy exchange between gases and solids. 1291
Wold, A. (see **Rogers, D. B.**). 347
(see **Kunnmann, W.**). 1535
Wollan, E. O., J. W. Cable and W. C. Koehler. The hydrogen atom positions in face centered cubic nickel hydride. 1141
Woodbury, H. H. Measurement of the Cd–CdS liquidus. 881
Worster, J. and N. H. March. Interaction energies between defects in metals. 1305
Wortis, M. (see **Fukuda, Nobuyuki**). 1675
Wright, A. J. (see **Owen, N. B.**) 1521
Wright, K. (see **Bemski, G.**). 1
Wyatt, R. E. (see **Companion, A. L.**). 1025

Yoffe, A. D. (see **Chadderton, L. T.**). 592(L)

Zachariasen, W. H. (see **Raub, Ch. J.**). 1093
Zawidzki, T. W. (see **Petriconi, G. L.**). 573
Zinn, W., M. Kalvius, E. Kankeleit, P. Kienle und W. Wiedemann. Untersuchung der Nahordnung in magnetisch Isotropen und Anisotropeneisen-Nickel-Legierungen mit der Mössbauer-Methode. 993
Zupancic, I. (see **Blinc, R.**). 1379(L)

BOOK REVIEWS

Bond, G. C. Catalysis by Metals (**G. Ehrlich**). 1149
Brown, W. F., Jr., Magnetostatic Principles in Ferromagnetism of Selected Topics in Solid State Physics. Vol. I., Series edited by E. P. Wohlfarth (**R. S. Tebble**). 498
Chalmers, B. (Editor) Progress in materials science (incorporating Progress in metal physics) Vol. 9 (**A. S. Nowick**). 174
de Sy, A. and J. Vidts. Metallurgie Structurale (**G. Saada**). 977
Gay, R. Cours de Cristallographie, Livre III (**M. J. Bruerger**). 337
Hellwege, K.-H. and A. M. Hellwege (Editors) Volume II: Eigenschaften der Materie in ihren Aggregatzuständen Part 9: Magnetische Eigenschaften I—Magnetic Properties I. in the Landolt-Börnstein Zahlenwerte und Funktionen aus Physik, Chemie, Astronomie, Geophysik und Technik series (W. P. Wolf). 1069
Hoff, N. J. (Editor) Creep in structures (**J. L. Sanders, Jr.**). 595
Lynton, E. A. Superconductivity, Methuen's monographs on physical subjects (**W. V. Houston**). 499
Michelson, A. A. Studies in optics (**W. Shurcliff**). 498
Preuss, L. E. (Editor) 1961 Transactions of the Eighth National Vacuum Symposium and the Second International Congress (**F. G. Allen**). 595
Semenchenko, V. K. Surface phenomena in metals and alloys (**H. H. Uhlig**). 977
Simpson, W. T. Theories of electrons in molecules (**R. G. Parr**). 1150
Wooster, W. A. Diffuse X-ray reflections from crystals (**B. L. Averbach**). 338
Young, D. M. and A. D. Crowell. Physical adsorption of gases (**G. Ehrlich**). 1150

J. Phys. Chem. Solids Pergamon Press 1963. Vol. 24, pp. 1–6. Printed in Great Britain.

A NEW PARAMAGNETIC CENTER IN ELECTRON IRRADIATED SILICON*

G. BEMSKI† **and B. SZYMANSKI**
Bell Telephone Laboratories, Murray Hill, N.J.
and
K. WRIGHT
Massachusetts Institute of Technology, Cambridge, Massachusetts

(*Received* 27 *April* 1961; *revised* 5 *September* 1962)

Abstract—Electron irradiation of silicon produces paramagnetic centers in *n*-type silicon. Experiments are described in which a new paramagnetic center is observed. In contrast to the two previously studied centers, electrons of 0·5 MeV energy do not produce the new center. The dependence of the rate of formation of this center on the energy of electrons makes it plausible that it represents a divacancy or a complex of vacancies and (or) interstitials. The symmetry of the *g* factor supports this idea.

INTRODUCTION

ELECTRON spin resonance has recently elucidated the structure of two paramagnetic centers in electron irradiated silicon.(1,2) These centers have been positively identified as in one case, a single vacancy in the immediate neighborhood of oxygen impurity (*A*-center)(3) and in the other case, a single vacancy next to phosphorus impurity (*E*-center).(4) In either case the vacancies were introduced as a result of displacement of silicon atoms in crystals irradiated with 0·5 to 1·5 MeV electrons. The vacancies diffuse to the neighborhood of oxygen, or phorphorus atoms producing stable (up to at least 150°C) paramagnetic centers. In the present work we would like to describe a third center, which does not directly involve impurities. From the dependence of its rate of formation on the energy of the electrons producing the damage it is argued that the center represents a divacancy or a more complex agglomerate of vacancies and (or) interstitials.

EXPERIMENTAL

All but two bombardments of the silicon samples have been performed at room temperatures (Table 1). The irradiations were done at 0·5, 1, 2, 3 and 6 MeV. The Bell Laboratories Van de Graaff accelerator operating at a current of 50 μA/cm^2 was used for the 0·5 and 1 MeV irradiations. The M.I.T. 3 MeV Van de Graaff covered the 1–3 MeV range at a current of 140 μA/cm^2. Finally Ethicon's High Voltage Linear Accelerator(5) provided 6 MeV electrons at 500 μA/cm^2. All the samples were 0·5 mm thick. Since the electrons lose about 250 keV in traversing the sample the irradiations were performed from one side only for energies of 1 MeV and higher, but equally from both sides at 0·5 MeV.

Water and air cooling were used to keep the samples' temperatures close to the room temperature. It was found by independent experiments that the defect of interest does not anneal below 250°C; therefore, the actual temperature was not very critical. The low temperature irradiations were performed by circulating liquid nitrogen

---

* The support of the National Science Foundation under Grant G7365 for the M.I.T. portion of the work is gratefully acknowledged. This work was supported in part by the Wright Air Development Center of the U.S. Air Force.

† Present address: Centro Brasileiro de Pesquisas Fisicas, Rio de Janeiro, Brazil.

Table 1. *Results of the irradiations*

Sample	Electron energy	Rate of formation of *C* centers (center/electron-cm)	Oxygen	Impurity present in Si (cm^{-3})	Temp. of irrad.
V-43	0·5 MeV	none observed	no*	P, 3×10^{16}	300°K
V-44	1 ,,	0·001	no*	P, 3×10^{16}	,,
V-46	1 ,,	0·001	no*	P, 3×10^{16}	100°K
V-47	1 ,,	none observed	yes*	P, 4×10^{15}	300°K
V-30	1 ,,	0·001	no*	P, 3×10^{16}	,,
V-40	1 ,,	none observed	yes*	B, 9×10^{16}	,,
V-31	2 ,,		no*	P, 3×10^{16}	,,
V-32	3 ,,	0·002	no*	P, 3×10^{16}	,,
V-41	3 ,,	0·009	yes*	As, 6×10^{16}	,,
V-39	3 ,,	none observed	yes*	B, 9×10^{16}	,,
V-49	6 ,,	0·005	no*	P, 3×10^{16}	,,

no*- oxygen concentration below $10^{16}/cm^3$ (vacuum floating zone).(8)
yes*—oxygen concentration above $10^{17}/cm^3$ (pulled crystals).(9)

through a copper holder to which the samples were fastened. Between irradiations and spin resonance runs the samples were kept at liquid nitrogen temperature.

The concentrations of the defects have been determined at all stages of experiments by comparing the amplitudes and widths of the resonance lines of interest with a conduction electron line of an independent silicon sample. This sample, phosphorus doped, and of resistivity 0·014 Ω-cm shows a line 0·6 Oe wide at 1·2°K. Its g value is 1·99875.(6) The number of the unknown (bombardment) defects can be obtained from the following formula:

$$\text{unknown spins} = \left(\frac{H_{MS}}{H_{MU}}\right)\left(\frac{\Delta H_U}{\Delta H_S}\right)^2 \left(\frac{A_U}{A_S}\right)\left(\frac{G_S}{G_U}\right)\left(\frac{H_{0S}}{H_{0U}}\right) \times \text{ silicon spins}$$

where: S refers to silicon

U refers to unknown spins
H_M = modulation amplitude
ΔH = line width
A = signal amplitude
G = gain of complete system
H_0 = d.c. magnetic field at center of line.

Precautions have been taken in order to observe the true, undiminished by relaxation effects, amplitude of the defects.

The spin resonance spectrometer operates at 24,000 mc/s using a superheterodyne detection system. A glass Dewar and slits in the copper cavity allow illumination of the samples during the experiment. The experiments were performed at liquid helium and liquid hydrogen temperatures.

RESULTS

a. *Condition for paramagnetism of the C center*

The new center (called hereafter the *C* center)(7) has been observed in n-type silicon only (Table I). Its structure was the same in both arsenic and phosphorus doped silicon. Figure 1 shows the rate of growth of this center with electron dose at different electron energies. From these data it is apparent that there is a strong dependence on the energy of the bombarding electrons. This dependence is different than in the case of formation of single vacancies (*E* center) (Table 2).

Table 2. Ratio of concentration of C to E centers as a function of electron energy

Energy (MeV)	C/E
0·5	0
1	0·1
2	0·3
3	1

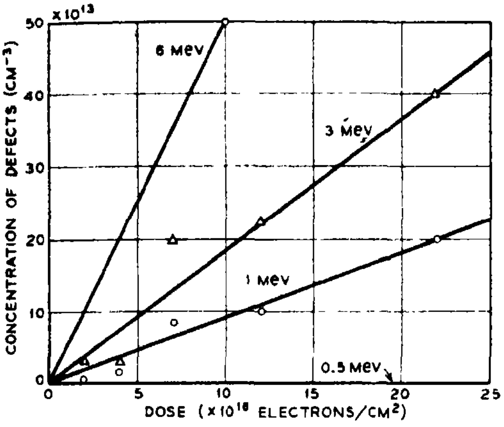

FIG. 1. Rate of formation of the C center in phosphorus doped silicon (3×10^{16} P/cm^3).

At the highest electron flux used ($5{\cdot}5 \times 10^{17}$ electrons/cm^2 at 1 MeV, not indicated on the figure) the concentration of the paramagnetic C centers dropped. We have been simultaneously observing the E center, the concentration of which also decreased after this maximum dose. From the known position of the energy level corresponding to the E center at 0·43 eV below the conduction band,(1) we can estimate that the C center is located further than 0·43 eV from the conduction band and that it is paramagnetic when filled with an electron (Fermi level above the level corresponding to this center). The absence of a spectrum in the high resistivity n-type sample V-47 and the decrease in concentration of paramagnetic centers in the heavily bombarded sample mentioned above indicate that the energy level of the C center lies close to the center of the gap.

In this connection it is important to add some observations concerning the behavior of the C and E centers under illumination with white light. In the absence of the C center, i.e. at low energy irradiation, the E center is paramagnetic with or without illumination. When the concentration of C centers exceeds that of E centers the situation changes drastically, as depicted in Fig. 2. The figure shows that when the sample is not exposed to light while cooling from room temperature to hydrogen temperature the E center is absent in the presence of the C center. Upon illumination the E center appears. This process is irreversible at low temperatures and indicates that the electron responsible for the resonance of E center may be drained by the C center in darkness. Upon illumination with white light electron-hole pairs are formed and the E center traps an electron. This process is not yet fully understood and the above interpretation is not unique.

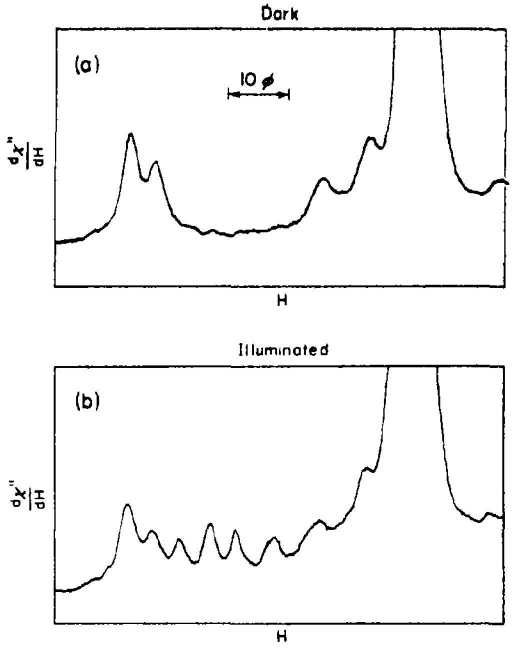

FIG. 2. Spin resonance spectrum of C and E centers at 10°K with the magnetic field along [110]. (a) Dark: C center alone, (b) Illuminated: E and C centers. The large line to the right of the spectrum is due to phosphorus resonance.

b. *Structure of the C center*

The paramagnetic spectrum of the C center is shown in Fig. 2a. It consists of several lines at any orientation of the external magnetic field with respect to the main crystalline axes. The applied field is contained in the (110) plane of the sample and can be rotated to point along [100], [111] and [110] and intermediate directions. The anisotropy of the spectrum is evident in Fig. 3 which shows the position of the individual lines as a function of the angle between H and [100]. The experiment is performed in a standard way, with constant oscillator frequency and variable magnetic field.

The anisotropy and splitting of the spectrum is due to the anisotropy of the g value. The simplest form of the spin Hamiltonian is:

$$\mathscr{H} = \mu_0 H \cdot g \cdot S \tag{1}$$

where μ_0 is the Bohr magneton, g the spectroscopic splitting factor and S the effective electronic spin. This leads to the simple relation

$$\nu = g\frac{\mu_0 H}{h} \tag{2}$$

where g is not necessarily a constant but in the presence of spin-orbit coupling varies with the orientation of the magnetic field.

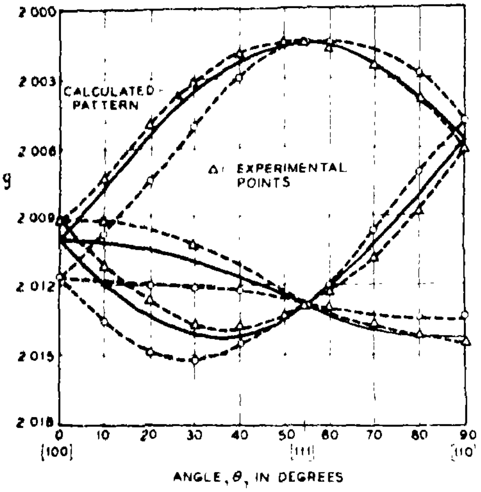

FIG. 3. Angular dependence of the C center spectrum. Calculated pattern for $g_{\parallel} = 2{\cdot}0014$ and $g_{\perp} = 2{\cdot}0145$ and axially symmetric g factor with [111] direction the axis of symmetry.

In the present case we try to interpret our data with an axially symmetric g factor, which can be expressed in the form:

$$g = \sqrt{[g_{\parallel}^2 \sin^2\theta + g_{\perp}^2 \cos^2\theta]} \tag{3}$$

where θ is the angle between the magnetic field and the axis of symmetry. The attempt to fit our data of Fig. 3 according to equations (1) and (3) with $g_{\parallel} = g_{[111]} = 2{\cdot}0014 \pm 0{\cdot}0002$ and $g_{\perp} = 2{\cdot}0145 \pm 0{\cdot}0002$ results in the solid line fit of Fig. 3. We notice that it does not account for splitting in data even though it gives the right form of anisotropy. We have, therefore, to inquire into the possible explanation of the observed splittings. There exist several possibilities:

1. The presence of nuclei of spin 1/2 with the resulting hyperfine interaction. In the present case different known impurities, P and As, make no difference to the spectrum even though the nuclear spin of P is 1/2 and that of As is 3/2 and their magnetic moments differ by more than 20 per cent. The possibility that an unknown impurity was present in all crystals is small because of different methods of crystal growing used in fabrication. Hydrogen could be the impurity in question but one would expect orders of magnitude difference in hydrogen concentration between crystals grown in vacuum and pulled in the presence of gaseous ambients. No large differences were, however, detected in the concentration of the C center.

2. Possibility that the electronic state is $S = 1$. This would lead to two transitions for each center which at low temperature should exhibit amplitude differences due to Boltzmann distribution of electrons among the three levels ($M_s = 1, 0, -1$). No changes in the ratios of amplitudes of the two lines as a function of temperature were observed between 1·2 and 35°K at which temperature the whole spectrum disappears.

3. Jahn–Teller distortion. No shifts in the position of lines and no broadening of the lines were observed between 1·2 and 35°K, making this possibility unlikely.

4. Nonequivalence of the different centers in the lattice. In the case in which the observed spectrum is due to a defect composed of two or more constituents (vacancies, interstitials, impurities) one can expect that the wave function, and in consequence the g tensor, will acquire a symmetry related to the symmetry of the defect. In the simplest case: two adjacent vacancies in the diamond lattice should exhibit axial symmetry, with the principal axes parallel to the [111] directions of the crystal. There exist four [111] directions, therefore at any orientation of the magnetic field a maximum of four lines can be observed since the energies and thus the resonance frequencies for axially symmetric centers discussed here go as $3\cos^2\theta_i - 1$ where θ_i are the angles between H and the different [111] directions. One can verify

that doubling of the number of the lines is then expected.

This situation can also arise without actual change of the symmetry of the defect, but due to a change in the immediate surrounding of the defect. A third member of the group could have such an influence on the wave function. We feel that (4) provides the correct explanation.

c. *Speculations*

The composition of the defect can only be speculated. Single vacancies have an unexpectedly high diffusion rate at room temperature and migrate to impurities.(1,2) It is unlikely that we are observing single vacancies particularly because of the dependence of the rate of formation of the centers on the electron energy which differs from that of single vacancies (Table 2). Similarly Frenkel pairs would not be stable at the temperatures of the experiments.

We believe that the center is due to a more complex group of vacancies or interstitials. We expect that multiple vacancies are formed preferentially at higher energies. The simplest of those, a double vacancy is shown in Fig. 4. Each group of three silicon atoms and the vacancy (ABCD and EFGH) can be expected to have one unpaired electron. The [111] symmetry would be due to silicon vacancy direction. The exact model has to await the observation of hyperfine interaction with Si^{29} (4·7 per cent abundant). We are unable to see any effect of such interaction, probably because of small amplitude of lines.

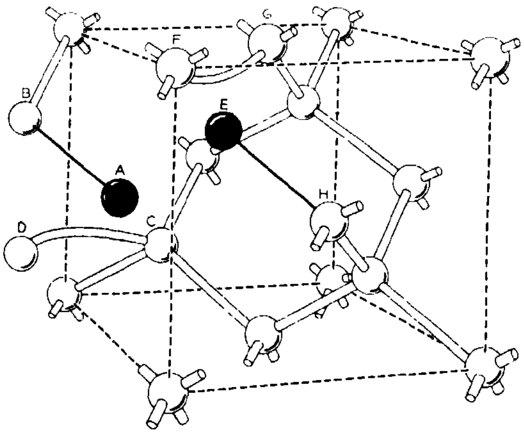

FIG. 4. Model of the *C* center. *A* and *E* are vacancies. This is only one of several models consistent with the observations.

d. *Role of impurities and temperature*

The *C* center formed at increased rate in low resistivity, As doped samples as compared with higher resistivity, P doped silicon (samples V-41 and V-32 respectively). The influence of impurity concentration on the rate of formation of the center may be due to competition between annihilation of interstitials and vacancies free to form complexes. Elucidation of this point requires more experiments.

The temperature of the bombardment did not influence the rate of formation of the center. This points to the fact that the diffusion of components of the *C* center is not important to the formation of the center.

Finally one should add that the *C* center is relatively stable up to 200–250°C, annealing at the latter temperature in periods of minutes.

DISCUSSION

Table 3 shows the calculated increase in the number of secondary displacements as a function of electron energy in silicon, calculated after SEITZ and KOEHLER.(10) One can also calculate that the silicon atoms displaced by 10 MeV electrons lose most of their energy within less than 100 Å. This indicates that the vacancies produced by a single initial collision of a primary electron

Table 3. *Calculated displacements in electron irradiated* Si

Electron energy (MeV)	(a) T_d(eV)	(b) K
0·5	24	1·1
1	32	1·3
3	50	1·8
6	64	2·1
10	79	2·7

(a) Mean energy transferred to silicon in those collisions transferring at least the threshold energy, assumed to be 13 eV.(11)

(b) Average number of secondary displacements.

can be expected to form in a relatively compact group and the density of these vacancies increases with electron energy. It is therefore quite likely that double vacancies and other complexes will form preferentially at higher bombardment energies. This belief is strengthened by the known mobility of vacancies$^{(1,2)}$ at room temperature. At higher energies ($\geqslant$ 1 MeV) one should expect that such complex formation competes favorably with vacancy-impurity production.

Acknowledgements--The authors would like to thank several of their colleagues for helpful discussions of this work. In particular thanks are due to W. L. BROWN, G. K. WERTHEIM and G. FEHER.

REFERENCES

1. WATKINS G., CORBETT J. and WALKER R. M., *J. appl. Phys* **30**, 1198 (1959)
2. BEMSKI G., *J. appl. Phys.* **30**, 1195 (1959).
3. WATKINS G. D., and CORBETT J. W., *Phys. Rev.* **121**, 1001 (1961).
4. WATKINS G. D., and CORBETT J. W., to be published.
5. The authors would like to acknowledge the kind cooperation of Drs. VAN WINKLE and ARKANDI, and Mr. INDECK of the staff of Ethicon in carrying out the 6 MeV irradiations.
6. FEHER G., *Phys. Rev.* **114**, 1219 (1959), also E. GERE, private communication.
7. This designation has been given because it is likely that the present center is the same as the *C* center observed by WATKINS. Note added in proof: see CORBETT J. W. and WATKINS G. D., *Phys. Rev. Letters* **7**, 314 (1961).
8. Vacuum floating zone crystals from Merck Chemical Co.
9. Pulled crystals.
10. SEITZ F. and KOEHLER J., *Solid State Physics*, Vol. **2**, p. 309 Academic Press, New York (1955).
11. LOFERSKI J. J. and RAPPAPORT P., *Phys. Rev.* **111**, 432 (1958).

J. Phys. Chem. Solids Pergamon Press 1963. Vol. 24, pp. 7–18. Printed in Great Britain.

FUSION CURVES AND POLYMORPHIC TRANSITIONS OF THE GROUP III ELEMENTS—ALUMINUM, GALLIUM, INDIUM AND THALLIUM—AT HIGH PRESSURES*

A. JAYARAMAN, W. KLEMENT JR., R. C. NEWTON and G. C. KENNEDY

Institute of Geophysics, University of California, Los Angeles

(*Received* 13 *August* 1962)

Abstract—The fusion curves of aluminum and thallium to 50 kbars, and of gallium to 70 kbars, were investigated by differential thermal analysis. Comparison is made with previous work and with the fusion curve of indium. A break in slope of the melting curve of gallium near 45°C and 30 kbars led to the discovery of a new polymorph. This phase—Ga III—is slightly less dense than Ga II, both persisting to 75 kbars. Solid–solid phase boundaries for gallium and thallium were determined by changes in volume and resistance as well as with DTA. The Ga II to Ga III transition is rapid and characterized by a substantial heat as well as a drop in resistance. From the investigation of the metastability phenomena, it is tentatively concluded that Ga III is identical with Bridgman's Ga II′ and that the metastable phase studied by Defrain at 1 atm. is closely related to Ga II. The existence of three polymorphs of thallium is definitely established, although the undercooling noted by Ponyatovskii for the b.c.c.–h.c.p. transition was verified. The triple point for the solid thallium phases is near 115°C and 39 kbars, with melting of the high pressure polymorph expected above 650°C and 90 kbars.

INTRODUCTION

THE ELEMENTS aluminum, gallium, indium, and thallium, although closely associated in the periodic classification, exhibit a variety of crystal structures. Aluminum crystallizes in the common face-centered cubic (f.c.c.) structure. Gallium, on the other hand, possesses a unique orthorhombic structure(1, 2) featuring closely associated pairs of atoms ("Ga_2 molecules"), with considerably weaker binding among the other atoms. The increase in density and the decrease in resistivity upon melting, the ease of undercooling, and the anomalously low melting point of 29·8°C are related to this complex structure. The face-centered tetragonal (f.c.t.) structure of indium can be considered as a distortion of a face-centered cubic closest packing. The hexagonal close-packed (h.c.p.) low temperature polymorph of thallium was first correctly described by SEKITO,(3) who also reported that, for liquids solidified with sufficient rapidity, a f.c.c. phase could be obtained; this f.c.c. structure was then attributed to the high temperature polymorph, which was known from thermal analysis to be stable from 230°C to the melting point. LIPSON and STOKES(4) later identified the high temperature form as body-centered cubic (b.c.c.) on the basis of X-ray diffraction work at 262°C.

Neither the fusion curve of aluminum to 20 kbars,(5) the fusion curve of indium to 75 kbars,(6) nor the electrical resistivities of these two elements to 70 kbars(7) give any hint of phase changes. BRIDGMAN(8) discovered a high pressure polymorph of gallium and located the triple point, Ga II–Ga I-liquid, near 2·4°C and 11·9 kbars. Another form of gallium sometimes "capriciously" appeared in place of Ga II, and was considered by Bridgman to be a "totally unstable" phase. For thallium, BRIDGMAN(8) proposed that a third polymorph appeared above 40 kbars. This has been questioned, though, by PONYATOVSKII.(9)

---

* Publication No. 253, Institute of Geophysics and Planetary Physics, University of California, Los Angeles 24, California.

The present investigation was undertaken to extend previous data on the melting of these Group III elements in order to compare their fusion curves and to resolve, if possible, the controversies concerning the sub-solidus phase relations of thallium and the appearance of metastable phases for gallium.

EXPERIMENTAL METHODS

An unsupported carboloy piston moving into a ½ in. dia. by 2 in. long supported carboloy pressure chamber was used to generate pressures up to 50 kbars. Talc was used as the pressure medium. Details of the apparatus have been published elsewhere.(10)

A double-stage apparatus, with a ½ in. carboloy piston supported by compressed solid bismuth, was used to generate sample pressures up to 75 kbars. A 1 in. dia. carboloy piston, moving into a supported steel core, compressed the bismuth and pushed the ½ in. piston into the high pressure chamber. Bismuth undergoes a phase change with a 7 per cent volume decrease at 25·4 kbars. The pressure applied by the ½ in. piston was computed from the ram load and the areas of the pistons, since the pressure in the bismuth (25·4 kbars) was known. The range of sample pressure desired was adjusted by varying the height of the bismuth column. The ram load for which the bismuth went into transition was determined precisely by plotting piston displacement vs. pressure on an x-y recorder. Fig. 1 is a diagrammatic sketch of the double-stage apparatus.

The frictional correction was estimated by determining points on the phase boundary being investigated, both on the increasing and the decreasing pressure cycle and was found to be about 7 kbars at 70 kbars sample pressure. Friction was also estimated by using the accurate single-stage results for the same boundary, previously determined, as an absolute pressure indicator. When the bismuth goes into transition, it is assumed that all further applied ram load directly increases the sample pressure. The friction correction thus estimated compared very well with the correction by the previous method. Pressures were measured to ± 0·5 kbar in the single-stage apparatus and ± 1 kbar in the double-stage apparatus.

The techniques of differential thermal analysis (DTA), piston displacement and resistance measurement were employed to detect phase changes.

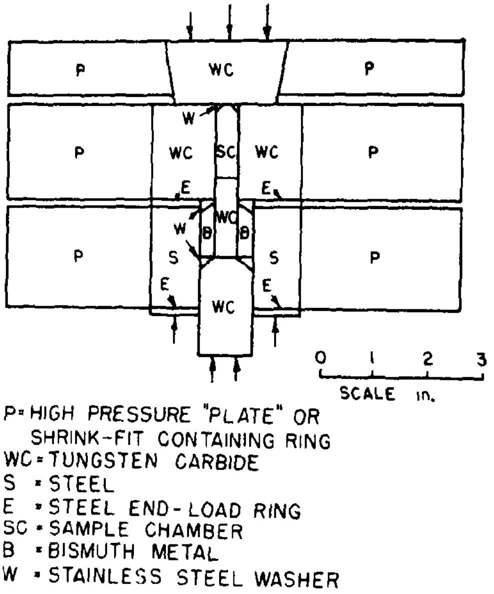

FIG. 1. Diagrammatic sketch of double-stage apparatus.

The DTA set-up consisted of a talc cylinder 1·25 in. long containing a graphite sleeve serving as a heating element. The sample, sealed in a suitable container, was placed in the middle of the heater and electrically insulated from it. Boron nitride or talc cylindrical pieces filled the rest of the graphite sleeve, except for a hole for the thermocouple assembly. This consisted of two chromel-alumel junctions, with one junction in intimate contact with the sample container and the other about a ¼ in. away. The output from the sample thermocouple was fed to a strip chart recorder with a calibrated temperature scale, and the difference in output between the two thermocouples to a sensitive 500 μV scale on the same recorder. Temperatures were determined to ± 2°C. KENNEDY and NEWTON(10) have described the procedure for detecting the thermal arrests with this technique. Signals are roughly proportional to the heat of the transformation and thus very strong signals were observed for the melting of aluminum, moderately strong for the melting of the other metals and only weak signals for the solid–solid transitions.

Molybdenum proved to be a satisfactory container for liquid aluminum. There appeared to be contamination in tantalum. Platinum was used as a container for liquid indium. Containers of iron, tantalum and molybdenum were used in gallium DTA measurements, all giving identical results. Platinum was found to alloy with thallium, lowering the normal melting point from 303°C to 294°C. The fusion curve reported in a platinum container and previously published by KENNEDY and NEWTON(10a) is thus in error and by an amount which increases steadily with pressure. The melting curve for thallium presented by KENNEDY and NEWTON falls fully 40°C below that given by BUTUZOV *et al.*(5) The melting curves for thallium redetermined in the present experiments in copper and iron containers are in agreement but fall 8–10°C lower than that of BUTUZOV *et al.*, at 30 kbars. It is not certain whether this discrepancy was due to contamination in the present work. Platinum was, however, found to be an excellent container for DTA work with solid thallium.

In the volume discontinuity method, the high-pressure chamber was packed with as much as 6 cm^3 of sample, which was separated from the core wall by very thin lead-foil to reduce wall friction. Ram pressure and displacement were converted into electrical signals by a pressure-resistance cell and a linear potentiometer, respectively. Piston displacement was plotted vs. ram load on an x–y recorder. In these experiments, a very hard $\frac{1}{16}$ in. steel liner separated the sample from the carboloy core. This step was taken because it has been found that some metals at high pressure, notably bismuth, thallium, and the alkalis, rupture the carboloy pressure chamber. In the present experiments it was found that thallium could be safely contained to 40 kbars but that solid gallium would rupture both steel liner and carboloy core at about 30 kbars. A heating tape was wound around the supporting rings of the pressure vessel in order to heat to 250°C. The pressure plate could also be cooled with dry ice down to -20°C and, by pouring liquid nitrogen over it, to -100°C.

For resistance measurements, a 10 mil dia. wire about $\frac{1}{2}$ in. long was embedded in a good hydrostatic pressure-transmitting medium. Silver chloride was used for thallium, but talc had to be used for gallium, since there was reaction with silver chloride. The voltage drop across the wire for a known current was plotted on an x–y recorder as a function of pressure. The pressure plate could be externally cooled or heated for resistivity measurements exactly as for volume measurements. The resistivity changes associated with all the phase changes in gallium and thallium were pronounced, even for those phase changes in which the DTA signal was just barely detectable.

The aluminum used to determine the fusion curve was C.P. grade, having a purity of 99·6 per cent. The indium and thallium were obtained from American Smelting and Refining Co., and had stated purities of 99·995 per cent. The measurements of indium melting points were made previously.(10) The gallium was from Chemical Commerce Co., and claimed to be of 99·99 per cent purity.

RESULTS AND DISCUSSION

Aluminum and Indium

The melting curve of Al is reproduced in Fig. 2 along with that of In. Melting points for Al as obtained by BUTUZOV *et al.*(5) up to 20 kbars are also plotted. The accurate work of MCDANIEL, BABB and SCOTT(11) is considered as definitive for the low pressure melting of indium. At somewhat higher pressures, the results of BUTUZOV and PONYATOVSKII(5) and of KENNEDY and NEWTON(10) are in good agreement. At the highest pressures, there are available the data of DUDLEY and HALL.(6) In replotting these, their pressure scale* has been revised downward in accordance with fixed points of solid–solid transitions obtained by KENNEDY and LA MORI.(12)

LEIGH's analysis(13) apparently accounts for the isotropy of the elastic constants in aluminum and can probably be directly extended to higher pressures until there is appreciable interaction among the relatively small ion cores. The contribution of the overlapping electrons to the elastic moduli will decrease as the Brillouin zones move outward at the higher pressures. The instability of the f.c.c. phase in the submegabar range is considered unlikely at the lower temperatures.

---

* Other pressures quoted in this paper have also been revised, as appropriate.

The f.c.t. structure of indium can be considered as a slight distortion from f.c.c.; the c/a ratio(1) decreases monotonically with temperature from 1·082 at −183°C to 1·065 at 135°C. WINDER and SMITH(14) have determined the elastic constants of indium at 25°C, finding a slightly smaller stiffness along the c-axis than along the a-axes. Pursuing the analogy with aluminum, they have given a discussion for "pseudo-cubic" f.c.c. indium in terms of LEIGH's model. It seems likely that the tetragonality for indium is closely related to the overlap of electrons across the several Brillouin zones, an effect expected to diminish for the metal under pressure. The smooth variation with pressure of the volume,(15) resistance(7) and the melting point thus suggest the possibility of a "continuous distortion" of the f.c.t. structure toward f.c.c., both with temperature and pressure. Although estimates based on the WINDER and SMITH data(14) are difficult, c/a may become unity at submegabar pressures near the melting point.

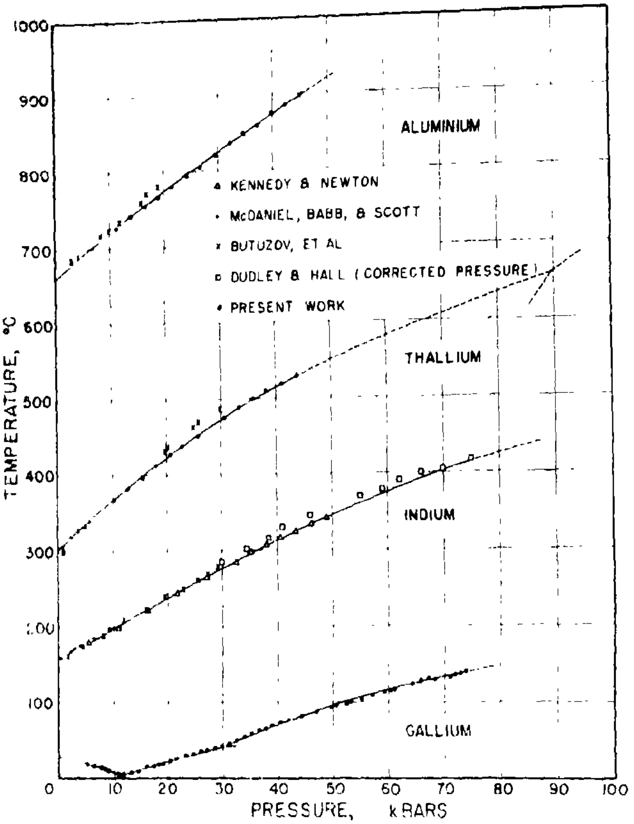

FIG. 2. Melting curves of aluminum, thallium, indium and gallium. Data for Ga are from present work (cf. Fig. 5); other data as cited.

Thallium

WERNER(16) first studied the effect of pressure to 3 kbars on the solid–solid transition in thallium, using a massive piece of the metal in an oil-filled bomb, and found that the transition temperature dropped with increasing pressure. His determination of the volume change, based on the indirect method of pressure change in the bomb, showed a surprisingly great two-fold increase at 3 kbars over the one atm. value. BRIDGMAN(8) discovered a volume discontinuity for thallium at 43 kbars and

−70°C, the pressure for this transition decreasing with rising temperature. However, the volume change found at 170°C was so small and at such a low pressure that he considered it to be associated with a different transition. Since this fell on the extension of WERNER's curve, BRIDGMAN proposed a phase diagram with three polymorphs and a triple-point at 153°C and 38·2 kbars.

PONYATOVSKII(9) followed the one atm. solid–solid transition in thallium up to pressures of 33 kbars. He found a large curvature for this boundary towards the pressure axis and an undercooling interval which increased with pressure to as much as 25°C. He proposed that the smooth continuation of his equilibrium boundary would successfully account for all of BRIDGMAN's experimental points without the necessity of a third form of thallium. KAUFMAN(17) produced thermodynamic arguments for the high pressure stability of an f.c.c. form. PIERMARINI (private communication) has tentatively identified the structure of thallium at 45 kbars and room temperature as f.c.c. by X-ray diffraction using a diamond anvil.

The results for the melting of thallium from all sources are plotted in Fig. 2. At lower pressures, the results from MCDANIEL *et al.*(11) are considered definitive. The points due to BUTUZOV and coworkers(5) lie too low in temperature at the lower pressures and lie above the results of the present experiments at higher pressures. However, the present results may have been somewhat affected by sample contamination in the containers.

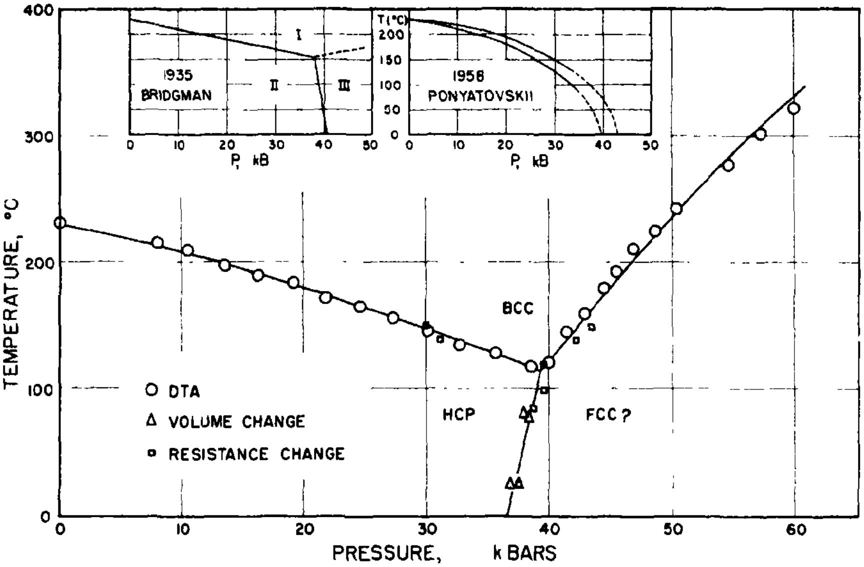

FIG. 3. Equilibrium subsolidus phase diagram of thallium. The insets indicate previous proposals.

The subsolidus phase diagram of thallium is presented in Fig. 3. Readable DTA signals were obtained on the h.c.p.–b.c.c. boundary. The undercooling of b.c.c. thallium at high pressures, reported by PONYATOVSKII,(9) was confirmed. A string of weak but readable signals were obtained along the Tl I–Tl III boundary postulated by Bridgman, thus establishing a triple-point. No undercooling effects, such as those for the b.c.c.–h.c.p. transition, were observed for the new transformation.

The pressure and volume change (Table I) of the Tl II–Tl III transition were measured at 25 and 85°C. The accuracy of the present measurements is again considered to be superior to the 1935 measurements of BRIDGMAN(8) because of large sample volume and continuous recording of displacement. The slope obtained for this transition is positive, in contrast to the result of Bridgman. Relative resistance data are shown for five temperatures in Fig. 4. Because of contact resistance at low pressures, it was necessary to standardize the resistance measurements according to BRIDGMAN's(7) determinations (i.e. 28 per cent resistance change in transition). The pressures obtained from resistance measurements confirm the positive slope for the Tl II–III boundary. The resistance change associated with the transition Tl I–Tl III is quite pronounced and proves beyond any doubt that Tl III is distinct from Tl I. The existence of three discrete polymorphs of thallium has thus been irrefutably established. If, as is probable, the highest pressure polymorph is f.c.c., this is the first example of a phase diagram with a triple point between the h.c.p., b.c.c. and f.c.c. phases, with expectations also for several other metals.

PONYATOVSKII's(9) observations of hysteresis in the b.c.c.–h.c.p. transformation are fully verified in the present experiments. Especially pronounced is the increase in undercooling interval with pressure, an effect apparently not due to impurities. The diffusionless nature of this transformation is clear(18) although the mechanism is not established. Due to the greater compressibility of the b.c.c. phase, there is an increasing volume change with pressure, which, it is suggested, may be intimately involved in the increasing hysteresis of the transition.

Also deserving of attention are the metastable f.c.c. structures apparently found for thallium at one atm. Besides that of SEKITO,(3) SCHNEIDER and HEYMER(19) have presented lattice spacings for the structures at 244°C and 284°C; these spacings can only be appropriate to a f.c.c. structure and are, within experimental error, compatible with the volume change at the transition as determined by the present experiments. KAUFMAN(17) has considered the f.c.c. spacings of Sekito and of Schneider and Heymer to be compatible with extrapolations from thallium-alloys and commented that the retention of such a metastable phase is not unusual. DUWEZ(18) was unable to quench the high temperature polymorph of thallium to lower temperatures with cooling rates to 10^4 °C/sec. Only the h.c.p. structure was ever observed upon cooling

Table 1. Slope, volume change, latent heat, and change of electrical resistance of the transitions of thallium at the triple-point

Triple-point	P (kb) Present work	T (°C)	P (kb) BRIDGMAN (1935)	T (°C)	Transition	dT/dP (°C/kb) Present work	BRIDGMAN (1935)	ΔV (cm³/gm) Present work	BRIDGMAN (1935)	ΔH (cal/gm) Present Work	BRIDGMAN (1935)	ΔR (per cent)
I–II–III	38·5	115	38·2	153	II → III	+2·0	−63·2	−0·00053	−0·000492	−0·119*	0·063*	−25
					II → I	−3·5	−1·9	−0·000092	−0·00024	0·249*	0·098*	−14
					→ III	11·2	2·4*	−0·00044*	−0·00029*	−0·368*	−0·091*	−11

* Calculated

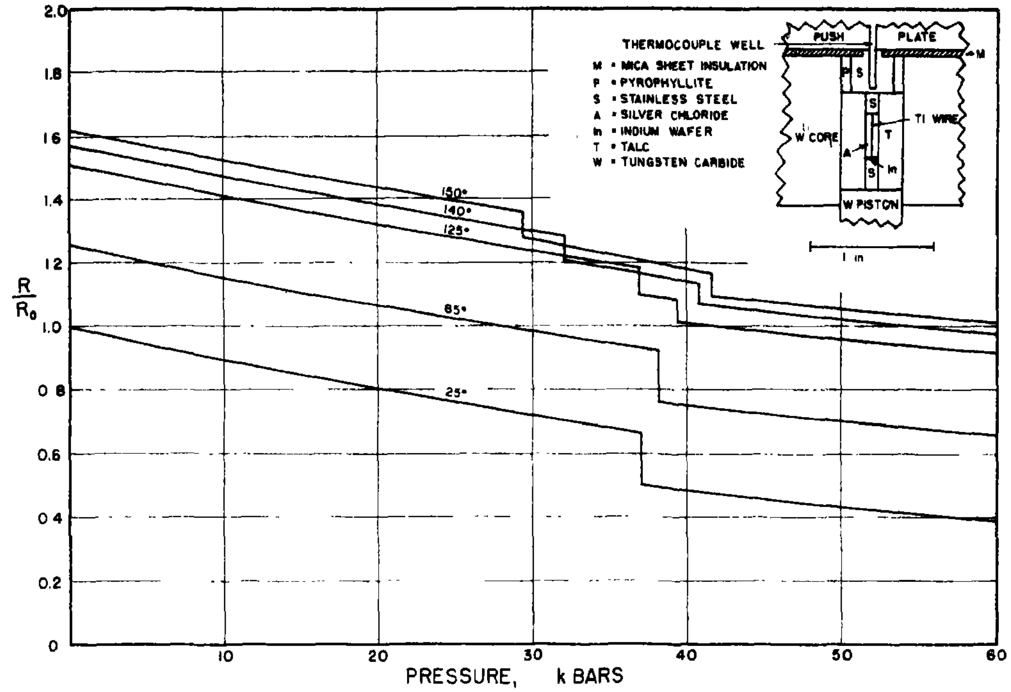

FIG. 4. Resistance of thallium relative to Tl II (h.c.p.) at 25°C. The inset shows the set-up for resistance measurements.

from the melt to room or liquid nitrogen temperatures at very high rates.(20) It seems clear that the most important factor controlling the reversion of a metastable form of a structurally simple element must be the diffusion rate. The data of SHIRN(21) indicate that diffusion in the high temperature polymorph of Tl is high, as is typical for a simple metal; it is difficult to understand how the metastable f.c.c. structure of SCHNEIDER and HEYMER(19) could then persist in the pure element at high temperatures. The f.c.c. phase obtained by SEKITO,(3) but not by KLEMENT,(20) is very likely associated with the presence of impurities.

Gallium

BRIDGMAN(8) discovered a solid–solid transition in gallium at about 20 kbars and −70°C, and located a triple-point among liquid, Ga I, and Ga II at 11·9 kbars and 2·4°C, without obtaining experimental points on the melting curve of Ga II. He found that yet a third form of gallium, Ga II′, whose properties are very similar to those of Ga II, sometimes "capriciously" appeared in place of Ga II upon compression just below the triple-point temperature. He located a triple-point, liquid-Ga I–Ga II′, at 0·4°C and 12·5 kbars.

Recently DEFRAIN *et al.*(22) have found a new, metastable form of gallium which crystallizes from the undercooled melt near −16·3°C at one atm. The transient phase has the space-group D_{2h}^{17} (identical with α-uranium), the structure(23) consisting of chains of atoms, each atom having two nearest neighbours. From measurements of the density and heat of fusion, and noting that the Ga II melting curve computed by Bridgman produces to −15·8°C at one atm., they suggested that their metastable form was the same as Bridgman's Ga II.

The melting curve of gallium is reproduced in Fig. 2, with the complete phase diagram shown in Fig. 5. At pressures above 30 kbars it was found that Ga II transforms to a new solid form which is

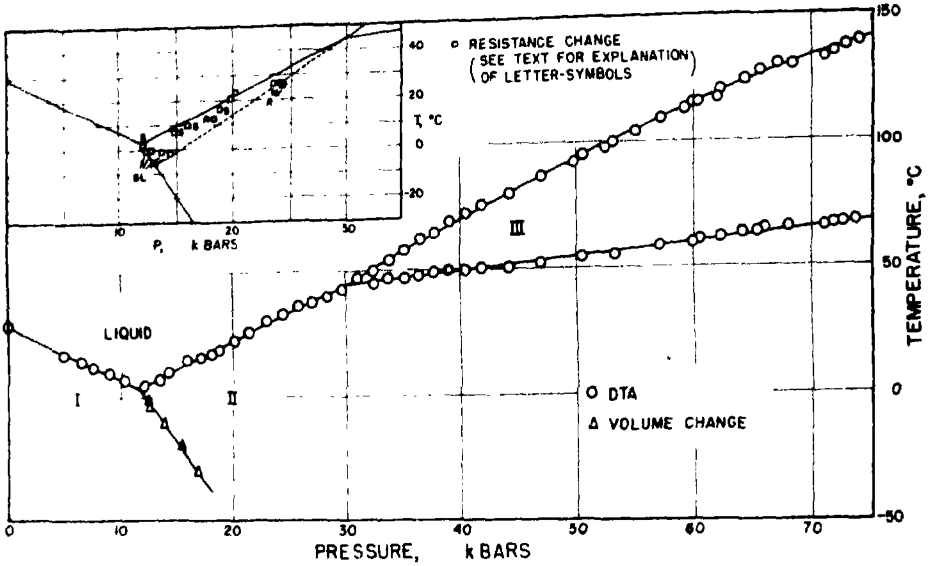

Fig. 5 Equilibrium phase diagram of gallium. The inset shows the nonequilibrium points from the present work (cf. text) relative to the equilibrium phase boundaries; the dotted line represents the metastable extrapolation of the Ga III melting curve.

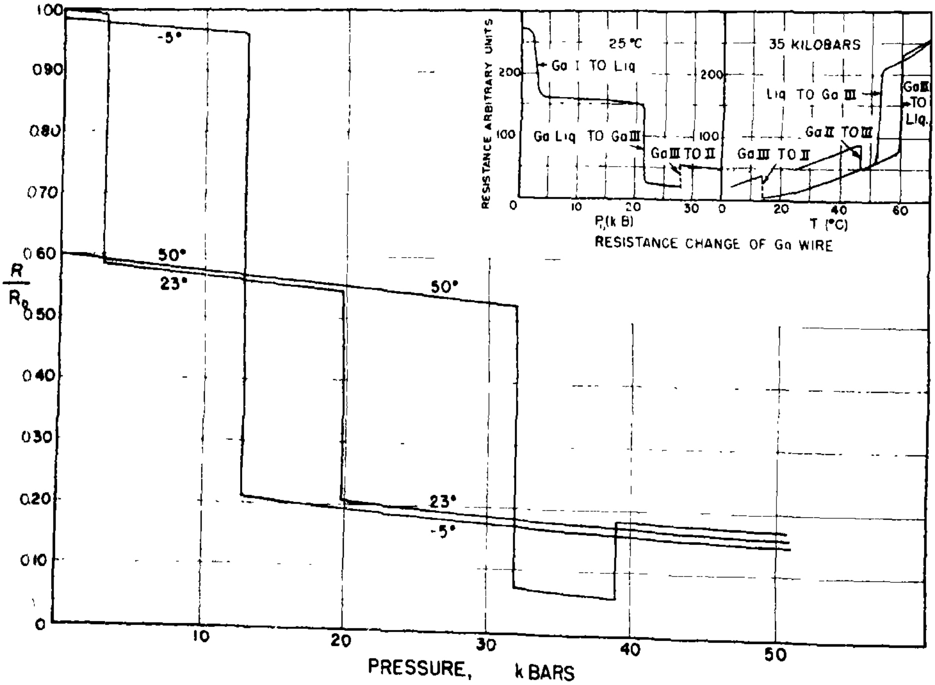

Fig. 6. Resistance of gallium relative to Ga I at 23°C and one atm. The insets show resistance experiments wherein metastable phenomena were encountered.

Table 2. Slope, volume change, latent heat, and change of electrical resistance for transitions in gallium at the two triple-points

Triple-point	P (kb) Present work	T (°C) Present work	P (kb) Bridgman (1935)	T (°C) Bridgman (1935)	Transition	dT/dP (°C/kb) Present work	dT/dP (°C/kb) Bridgman (1935)	ΔV(cm³/gm) Present work	ΔV(cm³/gm) Bridgman (1935)	ΔH(cal/gm) Present work	ΔH(cal/gm) Bridgman (1935)	ΔR (per cent)
L–I–II	11·7	3	11·9	2·4	I → L	−2·32	−2·70	−0·0078*	−0·0074	22·4*	18·3*	−42
					II → L	2·29	1·51*	0·0036*	0·0024*	10·6*	10·6*	35
					I → II	−6·46	−8·52	−0·0114	−0·0098	9·1*	7·4*	−77
L–II–III	30·0	45			II → L	2·29		0·0036*		12·2*		35
					III → L	2·75		0·0035*		9·75*		49
					II → III	0·49		0·00015*		2·46*		−14

* Calculated

labelled as Ga III. The Ga II–Ga III transition has sufficient heat associated with it to give a moderately strong DTA signal. It was found that the Ga III–Ga II transition undercools as much as 20–25°C at the highest pressures. Therefore the DTA signal obtained on heating was accepted. No further solid–solid changes were recorded in pursuing the melting curve to 75 kbars.

The Ga I–Ga II curve and the associated volume change were determined by the piston-displacement method. In these experiments, a very large amount of gallium (25 g) was used. Since the chamber diameter was much larger than that used by Bridgman(8) ($\frac{1}{4}$ in.) in making similar measurements, and since displacement was continuously recorded on the x–y recorder, it may be presumed that the present measurements are more accurate than those of Bridgman. The data for gallium, together with the Bridgman data, are given in Table 2.

In Fig. 6, the results of resistance measurements for gallium are presented. Relative resistance is plotted against pressure at −5°C, 23°C and 50°C. In plotting these curves, the experimental data were standardized in terms of the resistance change $R/R_0 = 0{\cdot}58$ associated with the melting of Ga I(24) and the resistance change, $R/R_0 = 0{\cdot}39$, for liquid to Ga II given by Defrain *et al.*(22) under the assumption that the metastable cooling product was Ga II. The large contact resistance at low pressure in the present experiments prevented the accurate measurement of the resistance change for the Ga I—liquid transition. The pressure coefficients of resistance at the higher pressure, and the temperature coefficients of resistance for the various forms of gallium were determinable however, as was the resistance change of Ga II to Ga III owing to the great reduction of contact resistance at the higher pressures.

Various metastability phenomena were revealed in the present resistance measurements. When the gallium wire was compressed at 25°C, the liquid crystallized at a pressure about 2 kbars higher than the equilibrium liquid—Ga II pressure as determined from DTA. A sudden 15 per cent rise in resistance often took place upon pumping to a higher pressure. Sometimes the sudden rise did not take place at all and sometimes it occurred as pressure was being released. In the cases where the sudden rise occurred, the wire melted on release of pressure at exactly the equilibrium Ga II melting boundary. The insert in Fig. 6 shows the resistance changes, plotted to an arbitrary scale, when gallium was compressed to 35 kbars and then heated, at pressure, to 70°C. At 48°C, Ga II reverted to Ga III, with a change of resistance equal in magnitude to the erratically occurring rise found on compression at 25°C mentioned above. When further heated, the solid melted upon intersecting the melting line. On cooling, the liquid first froze to Ga III and instead of reverting to Ga II at 48°C, undercooled to temperatures in the range 0–20°C and then suddenly reverted, as evidenced by an abrupt rise in resistance identical to the one previously detected in the work at 25°C. Release of pressure then caused the Ga II to melt on its equilibrium melting boundary.

The insert in Fig. 5 shows how Ga III may be prepared metastably below the liquid- Ga II–Ga III triple-point by compressing the liquid. The letter *R* beside a symbol indicates that the wire reverted at a higher pressure to Ga II. The letter *S* indicates that Ga II was prepared directly from the liquid, but with some superpressing beyond the Ga II melting line. The letters *SL* indicate a sluggish, rather than a crisp resistance change, with erratic drops in resistance through the solid–solid transitions Ga I–Ga II or Ga I–Ga III owing to contact effects which would have been ameliorated if the wire had passed through the liquid state.

It is clear from the above experiments that Bridgman's Ga II′ was prepared in the region bounded by the Ga II melting curve and the metastable extension of the Ga III melting curve and that Ga II′ is indeed Ga III.

The present experiments have established the equilibrium phase diagram for gallium and also yielded some insight into the difficulties encountered by BRIDGMAN.(8) The resistance measurements show especially clearly that, in the Ga II stability field, there may occur distinct undercooling of the melt with capricious crystallization of Ga II or Ga III. The similarity in volume makes it impossible to identify either Ga II or Ga III as the transient phase investigated by DEFRAIN *et al.*(22, 23) Moreover, ABU-SHUMAYS *et al.** could not verify the plateau temperature of crystallization, −16·3 ± 0·2°C, found by Defrain *et al.* The French workers also determined the heat of fusion, 9·09 ± 3 cal/g, for the transient phase, and the volume change on solidification, 0·0025 ± 6 cm^3/g—where the uncertainty has been estimated from the data presented in DEFRAIN's thesis.(22) The slope of the fusion curve, dT/dP, thus calculated, 1·65 ± 0·40°C/kbars, is more in agreement with BRIDGMAN's(8) computed value for the Ga II–liquid boundary than with that of the revised boundary from the present experiments. Capriciousness in the occurrence of the transient phase at 1 atm. is not inconsonant with the behavior discovered at higher pressures. It is thus perhaps illusory to attach much weight to the metastable extrapolation of the equilibrium melting boundaries.

Nevertheless, plausible explanations of the Ga II phenomena at high pressures can be made if the structure(23) determined for the transient phase or some close variant thereof is identified with Ga II. According to structural and diffusion(25) data, there is no preferential association of atoms in liquid gallium. Because of its complex structure, Ga I crystallizes with difficulty, and undercooling is easy. Likewise, it may be expected that Ga II, with its chain-like array of atoms, may also crystallize with difficulty, which is in accord with the present observations. The persistence of metastable structures in gallium, in contrast to thallium, would presumably be explained by low diffusion rates owing to "molecular" or "chain" bonding.

The occasional solidification of Ga III in the region of stability of Ga II infers that the structure of the former may be rather simple. A simple structure, common to high-temperature phases because of its larger entropy, is b.c.c., which is hereby suggested for Ga III. The observed ease in undercooling of the Ga III to Ga II transformation and the lower resistance of Ga III are also compatible with this view. Also to be rationalized is the rather extensive range of stability (to at least 75 kbars) of Ga II in spite of the complex structure herein attributed to it. If, however, the structure is viewed as analogous to that of α-uranium, a derivation from h.c.p., and if a continuous distortion toward h.c.p. with pressure is allowed, the above features may be plausibly explained. The features of ease of undercooling, suddenness of transformation, and large latent heat of the Ga II–Ga III transition are all reminiscent of the b.c.c. to h.c.p. transitions encountered for many elements.

---

* Unpublished work by A. ABU-SHUMAYS, W. KLEMENT, P. DUWEZ and R. VARANASI indicated that gallium of 99·99 per cent purity, prepared as in the French work,(22) and cooled in quartz at rates from 0·04 to 30°C/min crystallized at temperatures of −13°C to −22°C for various samples of 3 to 11 g. No correlation was found between initial temperature, degree of undercooling, crystallization temperature, temperature of reversion, etc., the experiments being much more capricious than those previously reported.(22)

DISCUSSION OF FUSION CURVES

Table 3 presents a comparison of available data on initial melting slopes of Al, Ga, In and Tl, together with the slopes calculated(26) from one atm. data.

Table 3. Collected data for initial slopes, dT/dP, *of fusion curves*

		(°C/kb)
Al	Butuzov *et al.*	6·4
	Present Work	5·9
	Calculated	5·5
Ga	Bridgman	−2·05
	Present Work	−2·0
	Calculated	−2·0
In	McDaniel *et al.*	5·0
	Butuzov	4·3
	Kennedy and Newton	4·1
	Dudley and Hall	4·3
	Calculated	4·3
Tl	McDaniel *et al.*	6·8
	Butuzov *et al.*	6·8
	Present Work	6·2
	Calculated	5·3

It has been observed that gallium, indium and, to a lesser degree, aluminum and thallium exhibit anomalously extensive liquid ranges at one atm.; this has been attributed to the relatively weak binding in the crystals.(27)

Bridgman's compression measurements(15) to 100 kbars at room temperature show that aluminum is about half as compressible as indium or thallium. Similar relations are perhaps valid at higher temperatures also for Al and In, although b.c.c. Tl is more readily compressed than the h.c.p. and, probably, f.c.c. form. There are no data for the compressibility of Ga or the liquid metals at higher pressures; however, the magnitude of compressibility may perhaps be inferred from the coordination. The metallic liquids with high coordination are thought to be relatively less compressible than those with a more open packing. The coordination(28) for liquid aluminum and gallium is about 11, and for indium and thallium, 4 nearest neighbors and 8 next nearest.

Under the foregoing hypothesis, the decreasing curvature, in order, of the In, Ga III, Tl, and Al fusion curves may be rationalized. The slight curvature of the Al curve is related to the high coordination number of the liquid, whereas the marked curvature for In, noted by all observers, can be correlated with the readily compressible liquid, which tends toward higher coordination. Liquid Tl should also be similarly compressible, but the ease in compressing the b.c.c. polymorph may be somewhat compensatory, with only a small curvature manifested in the fusion curve. More curvature is probable for the liquid-f.c.c. Tl boundary, which is expected above 90 kbars and 650°C.

Acknowledgements—Thanks are owing to S. E. Babb, Jr., D. T. Griggs, L. D. Jaffe, and L. Kaufman for reviewing this manuscript and making many valuable criticisms. T. J. Thomas kept the apparatus in excellent working order and S. Schutz machined most of the precise experimental assemblies. Financial support for this research was supplied in part by Livermore LRL 1138400 and ONR Nonr 233(53) contracts.

REFERENCES

1. Pearson W. B., *Handbook of Lattice Spacings and Structures of Metals and Alloys*, Pergamon Press, New York (1958).
2. Sharma B. D. and Donohue J., *Z. Kristallogr.* (in press).
3. Sekito S., *Z. Kristallogr.* **A74**, 189 (1930).
4. Lipson H. and Stokes A. R., *Nature, Lond.* **148**, 437 (1941).

5. Butuzov V. P., *Sov. Phys. Crystallogr.* **2,** 533 (1957) and references cited therein.
6. Dudley J. D. and Hall H. T., *Phys. Rev.* **118,** 1211 (1960).
7. Bridgman P. W., *Proc. Amer. Acad. Arts Sci.* **81,** 165 (1952).
8. Bridgman P. W., *Phys. Rev.* **48,** 893 (1935).
9. Ponyatovskii E. G., *Sov. Phys. Crystallogr.* **4,** 237 (1959).
10. Kennedy G. C. and Newton R. C., *Solids under Pressure*, McGraw-Hill, New York (1962); also Newton R. C., Jayaraman A. and Kennedy G. C., *J. Geophys. Res.* **67,** 2559 (1962) and Kennedy G. C., Jayaraman A. and Newton R. C., *Phys. Rev.* **126,** 1363 (1962).
10a. Kennedy G. C. and Newton R. C., *Quart. Progr. Rep.* N.O.N.R. 233 (53) (1960).
11. McDaniel M. L., Babb S. E. and Scott G. J., *J. chem. Phys.* **37,** 822 (1962).
12. Kennedy G. C. and La Mori P. N., *Progress in Very High Pressure Research*, Wiley, New York (1961).
13. Leigh R. S., *Phil. Mag.* **42,** 139 (1951); also Schmunk R. E. and Smith C. S., *J. Phys. Chem. Solids* **9,** 100 (1959).
14. Winder D. R. and Smith C. S., *J. Phys. Chem. Solids* **4,** 128 (1958).
15. Bridgman P. W., *Proc. Amer. Acad. Arts Sci.* **74,** 425 (1942); **76,** 55 (1948).
16. Werner M., *Z. anorg. Chem.* **83,** 275 (1913).
17. Kaufman L., *Acta Met.* **9,** 896 (1961).
18. Duwez P., *Trans. Amer. Inst. min. (metall.) Engrs.* **191,** 765 (1951).
19. Schneider A. and Heymer G., *Z. anorg. Chem.* **286,** 118 (1956).
20. Klement W., Ph.D. Thesis, California Institute of Technology (1962).
21. Shirn G. A., *Acta Met.* **3,** 87 (1955).
22. Defrain A., Thesis, Paris (1960); also published in *C.R. Acad. Sci. Paris* **248,** 1486 (1959); **249,** 50 (1959); **250,** 483 (1960); *J. Phys. Radium* **21,** 76 (1960).
23. Curien H., Rimsky A. and Defrain A., *Bull. Soc. Franc. Miner. Crist.* **84,** 260 (1961).
24. Bridgman P. W., *Proc. Amer. Acad. Arts Sci.* **56,** 61 (1921).
25. Petit J. and Nachtrieb N. H., *J. chem. Phys.* **24,** 1027 (1956).
26. Kaufman L., *Manufacturing Labs Report* (1961).
27. Hume-Rothery W., *J. phys. Chem.*, **44,** 808 (1940).
28. Vineyard G. H., *Liquid Metals and Solidification*, American Society of Metals, (1958).

J. Phys. Chem. Solids Pergamon Press 1963. Vol. 24, pp. 19–26. Printed in Great Britain.

ON THE POSSIBILITY OF OBSERVING A BOSE–EINSTEIN CONDENSATION OF EXCITONS IN CdS AND CdSe

R. C. CASELLA

International Business Machines Corporation, Thomas J. Watson Research Center,
Yorktown Heights, New York

(*Received* 18 *June* 1962; *revised* 20 *August* 1962)

Abstract—It is shown that ideally a Bose–Einstein condensation of excitons ought to be observable in CdSe as a narrowing of the fundamental emission line with increasing concentration above a critical concentration, $\sim 10^{16}/\text{cm}^3$, using available pulsed light sources. It is concluded (with less justification) that the effect ought also to be observable in CdS. Deviations from ideality and their expected effects on conditions required for observation of the condensation and on its existence are discussed.

1. INTRODUCTION

THE WANNIER(1)* model of an exciton in insulators consists of an electron and hole bound together by coulomb attraction. Since the exciton consists of two particles, each of which is a fermion, the composite exciton behaves like a boson under certain limiting conditions, to be discussed. As is known,(6) at a suitably low temperature, T_c and high concentration, N_c an ideal Bose gas undergoes a phase transition, the Bose–Einstein condensation. As T is lowered further keeping N fixed (or alternatively as N is increased further keeping T fixed) an increasingly larger fraction of the bosons occupies the single-particle ground state of zero momentum. This concept has been invoked by LONDON(7) to explain qualitatively the phase transition and other of the peculiar properties of liquid He^4. LANDAU(6) has noted that at densities appropriate for a liquid the interaction between the physical particles must be taken into account. As recently remarked by Blatt,† it is reasonable to inquire as to whether at sufficiently high light intensities incident on an insulator in the exciton band, the crystal may exhibit new properties which may be associated with a Bose–Einstein condensation of the excitons. It is the purpose of this note to investigate further this possibility. In particular, we shall consider the following:

1. Differences between the exciton system under external light excitation and an ideal Bose gas in thermal equilibrium.
2. Available crystals and light sources with which one might hope to achieve experimentally the conditions for the condensation (or a related phenomenon) to occur.
3. Methods of observing the effect.

2. THEORETICAL ESTIMATES

1. *Deviations from ideality and thermal equilibrium*

We begin with a brief review of the low temperature behavior of an ideal Bose gas of *indestructible* particles.(6,7) The average occupation number, N_p of particles with momentum p in thermal equilibrium is given by the familiar Bose formula,

$$N_p = (\exp\{(\epsilon_p-\mu)/kT\}-1)^{-1} \qquad (1)$$

---

* The Wannier model has enjoyed remarkable success in explaining optical data in a number of solids including Ge,(2) CdS,(3) (4) and CdSe.(5)

† The possibility was noted by Professor J. M. BLATT during a lecture series at the International Business Machines Corporation, Research Center, Yorktown, New York (December 1961–January 1962). The idea also occurred to us independently in connection with a proposed experiment involving the use of a ruby laser to excite a copious supply of excitons in CdSe at nitrogen temperature. See also Ref. (8). (Because absorption of the ruby light must be accompanied by phonon absorption, the laser does not appear to be a practicable source at the requisite temperatures for the Bose–Einstein condensation. In Section II, we shall consider incoherent pulsed sources.)

where the chemical potential, μ is determined by the relation,

$$\textstyle\sum_p N_p = N. \tag{2}$$

ϵ_p is the single particle energy and N is the total number of particles in the system. We shall assume unit volume throughout, unless otherwise noted. For bosons μ is either negative or zero. At fixed T a negative μ tends to zero as N increases. The maximum number of particles which can be accommodated in states other than $\boldsymbol{p} = 0$ is given by summing equation (1) over all $\boldsymbol{p} \neq 0$ with $\mu = 0$. The sum is bounded above, as can be shown by converting the sum to an integral. For N greater than this number the remaining particles must be in the ground state, $\epsilon_0 = 0$, which, as may be seen from equation (1), can accommodate an arbitrarily large number of particles since μ can be arbitrarily small in magnitude. The expression giving the critical volume per particle, v_c, below which condensation occurs is

$$v_c = \left(\frac{1}{2{\cdot}61}\right)(4\pi)^{3/2}\left(\frac{\hbar^2}{2MkT}\right)^{3/2} \tag{3}$$

where M is the mass of the boson. Equation (3) may be thought of as defining a critical temperature, T_c. If we now fix the number of particles and decrease T, the fraction (N_0/N) of particles in the ground state is given by the relation

$$(N_0/N) = 1-(T/T_c)^{3/2}. \tag{4}$$

For destructible bosons (e.g. photons, phonons) in thermal equilibrium, equation (2) need not hold, μ is always zero, and equation (1) reduces to the Planck law. Such systems may be thought of as being always in the condensed state, since the number of oscillators in the ground state is not observable. We may arrive at this result formally by setting $M = 0$ in equation (3).

Excitons are destructible. Moreover, in thermal equilibrium, the number of excitons in insulators with band gaps of the order of 1 eV is effectively zero for reasonable temperatures. High concentrations of excitons can be achieved only in the presence of an intense photon flux, i.e., under conditions which differ appreciably from equilibrium. The considerations involving equation (1) and equation (2) may be thought to apply only if the excitons are able to exchange kinetic energy with the lattice in a time interval which is short compared with their lifetime for radiative decay. We may then regard the average number of excitons as being fixed for a given light intensity and treat the excitons as being in quasi-equilibrium. To summarize, we assume relations (1) through (4) hold for an exciton gas and moreover that T is the lattice temperature. (Our assumptions are analogous to assuming that the velocity distribution in a dilute gas of excited atoms undergoing resonant fluorescence is maxwellian with a temperature characteristic of the walls of the container, not the effective black body temperature of the incident radiation.) The existence of the quasi-equilibrium state is an unproved assumption—to be tested by experiment.

The second aspect of deviations from ideality concerns the interactions between the excitons. The first type of interaction we consider is dynamical. The induced electric dipole interactions (i.e. Van der Waals forces) may be expected to alter the effective single particle energies (i.e. excitation spectrum). We compare the exciton gas to liquid helium, which has additional hard core interactions. In He^4 the interactions lead to a phonon part of the excitation spectrum as shown by LANDAU.(6) This aspect is omitted in the ideal Bose gas theory. Nevertheless, the latter suffices to predict the phase transition. We assume that provided the condensation occurs at concentrations such that, on the average, the hydrogenic exciton wave functions do not overlap appreciably, changes in the excitation spectrum will be small compared with the binding energy of the exciton. Clearly, at too high a density the entire picture breaks down. As the mean overlap becomes appreciable, the fermi nature of the constituent particles (i.e. statistical effects due to the exclusion principle) becomes important. Finally at sufficiently high densities the bound states cease to exist and the excited solid is better described in terms of an electron-hole plasma. The degree of overlap at the critical concentration for a suitably chosen temperature is one criterion for establishing which materials might be expected to exhibit a condensation. Because of collision ionization it is clear that the excitonic binding energy also plays an important role.

Let us define a critical radius, r_c, by the relation

$$\frac{4\pi}{3} r_c^3 = v_c \tag{5}$$

where the critical volume, v_c, is given by equation (3). Solving for r_c, we obtain

$$r_c = \left(\frac{3}{2\cdot 61}\sqrt{(4\pi)}\right)^{1/3}\left(\frac{\hbar^2}{2\mu a_h^2}\cdot\frac{\mu}{M}\cdot\frac{1}{kT}\right)^{1/2} a_h. \tag{6}$$

For convenience we have multiplied the result obtained from direct calculation of r_c by the quantity $(\mu/\mu a_h^2)^{1/2} a_h = 1$. Here, μ is the reduced mass of the exciton and a_h its first Bohr radius. For simplicity we shall neglect the anisotropy in the exciton envelope function caused by anisotropy in the electron and hole effective masses and in the dielectric constant. (The approximation is quite good for the two systems, CdS and CdSe which we shall consider mainly. For these materials the electron mass is nearly isotropic and dominates the reduced mass. We shall however account for the appreciable hole-mass anisotropy in the total mass, M which is a density-of-states mass as it appears in equation (3).) By application of the relative kinetic energy operator, $(-\hbar^2/2\mu)\nabla^2$ to the hydrogenic ground state, $[\propto \exp(-r/a_h)]$, one sees that the first factor in the radicand of equation (6) is the mean kinetic energy of relative motion, which, by the virial theorem, equals the binding energy, B of the exciton. Thus, evaluating the prefactor, we obtain

$$\left(\frac{r_c}{a_h}\right) = 1\cdot 6\left(\frac{\mu}{M}\cdot\frac{B}{kT}\right)^{1/2}. \tag{7a}$$

For future reference we note that for electrons and holes with ellipsoidal energy surfaces, centered at the origin of the Brillouin zone, and having a common axis of revolution.

$$\begin{aligned} M &= (M_\perp^2 M_\parallel)^{1/3} \\ M_\perp &= m_{e\perp} + m_{h\perp} \\ M_\parallel &= m_{e\parallel} + m_{h\parallel}. \end{aligned} \tag{7b}$$

m_e and m_h with suitable additional subscripts denote the components of the electron and hole masses perpendicular and parallel to the common axis of revolution.

$(r_c/a_h)^{-1}$ is a measure of the degree of overlap and hence, of the deviation from ideality at any given temperature.

Before considering specific systems, we shall remark on two additional points, the applicability of which to the exciton problem has not yet been carefully assessed: (a) BOGOLUBOV(9) has given an approximate theory of weakly interacting bosons. He finds an energy spectrum for elementary (non-interacting) excitations which is of the form

$$\epsilon(p) = \{\text{const.} \times \phi(p) \times p^2/2m + (p^2/2m)^2\}^{1/2}$$

where p is the momentum of the excitation and $\phi(p)$ the fourier transform of the interaction potential $\Phi(r_i - r_j)$. For attractive interactions $\phi(p)$ is negative, as $p \to 0$, yielding positive imaginary values for $\epsilon(p)$. He interprets the result as indicating that the condensed state for bosons with dominant attractive interactions is unstable and attributes the condensation in He^4 to the repulsive hardcore forces. Applied to the exciton problem, his result implies that a condensation may not occur. (b) The attractive interactions can lead to bound states, i.e., exciton molecules, analogous to hydrogen molecules. Molecular states will be important if the mean time for molecular formation is short compared with the radiative lifetime of an exciton. Should this condition be satisfied, the resulting molecules can undergo a Bose–Einstein condensation. Because of the saturation of the covalent bond the interaction between the molecules may be expected to contain a sizeable repulsive component. If the foregoing argument (a) is correct, molecular formation is probably a necessary condition for the achievement of a condensation. We remark that whereas the exciton molecule system more closely resembles molecular hydrogen than atomic helium, the factor preventing H_2 from remaining a quantum liquid at $T = 0°K$ (solidification) is not relevant here because of the much lighter mass of the exciton molecules and the subsequent greater extent of their zero-point motion.

In what follows we shall ignore the two points just discussed. We believe that should bound states be important, the results obtained in Section 2 will remain substantially correct. We expect that the main modification introduced by the molecular states is that the results for the critical concentration of excitons ought to be multiplied by a factor of order 2.

2. *Possible experimental systems and requirements on light sources*

To minimize interactions between the excitons we seek systems for which the quantity (r_c/a_h) is maximal at a given temperature, say 2°K. From equation (72) we see that crystals with large exciton binding energies and not too great a disparity between electron and hole masses are desirable. In Table 1, we give values for the ratio r_c/a_h as computed from equations (7) with $T = 2$°K for excitons in Ge, CdS, and CdSe. is a particularly convenient choice. For $T_c > 2$°K, (r_c/a_h) diminishes. By considering $T_c < 2$°K we may increase the ratio, but we must remember that we wish to obtain a considerable fraction of the excitons in the condensed state if we are to observe the effect. We see from equation (4), that if we consider the light intensity to be adjusted such that $T_c = 2$°K, then by operating at say $T = 1{\cdot}3$°K, approximately one-half of the excitons will be in the condensed state and the ratio r_c/a_h is that given in Table 1. We have

Table 1. *Ratio of the radius, r_c, of a sphere having the critical volume, v_c to the exciton radius a_h at $T = 2$°K. All masses are given in units of the free-electron mass. μ is the reduced mass, $M_\perp$, $M_\parallel$ and the density-of-states mass, M are defined by equation* (7b), *B is the excitonic binding energy, and N_c, the critical concentration of excitons at $T = 2$°K.*

	$\mu_{(\perp)}$	$M_\perp$	$M_\parallel$	M	B (eV)	r_c/a_h at 2°K	a_h (Å)	$N_c = v_c^{-1}$ (cm^{-3}) at 2°K
Ge[a]	0·08[b]	—	—	0·27	0·005	4·7	97[e]	2×10^{15}
CdS[a]	0·16	0·89[c]	5·2[c]	1·6[c]	0·027	6·3	29	$3{\cdot}9 \times 10^{16}$
CdSe[a]	0·10	0·58[c]	3·4[d]	1·0[c]	0·013	4·4	54	$1{\cdot}8 \times 10^{16}$

a. See Refs. (2), (4) and (5).
b. We use the light transverse electron mass, Ref. (13).
c. Computed from equations (7b).
d. Estimated (known to be $\gtrsim 1$. [Ref. 5]).
e. Computed from B and μ assuming spherical symmetry, a poor approximation for Ge.

For these materials considerable experimental data concerning the excitons is available. It is interesting to compare the results with the value of a similar quantity, r_c/r_0 for He^4 at the transition temperature $T_\lambda = 2{\cdot}2$°K. Here r_c is given by equation (5) using the experimentally determined value of the density* to obtain v_c, and r_0 is the distance from the helium nucleus at which the radial charge density is maximal in atomic He, as determined by Hartree–Fock calculation.† We find $(r_c/r_0) = (2{\cdot}2\ \text{Å}/0{\cdot}3\ \text{Å}) = 7{\cdot}3$ which is approximately equal to the values obtained for (r_c/a_h) for all three solids considered. Because of the weaker binding of the Ge exciton, it appears to us less suitable. Somewhat arbitrarily we henceforth restrict attention to CdS and CdSe. We remark that whereas T_λ is prescribed by nature for He^4, T_c is dependent upon the applied light intensity for the excitons. Therefore our choice of $T_c = 2$°K is somewhat arbitrary. Nevertheless it assumed that the coolant is He^4 and have neglected heating effects due to the light. While we are unable to draw rigid conclusions concerning the effects of interactions, we believe the results obtained to be sufficiently encouraging to warrant further investigation.

To establish approximate requirements on light sources we must estimate the average number of excitons, N^e present under a given intensity of illumination in the exciton band. We first consider a simpler problem, to which the answer is well known:

Given a dilute gas of N atoms in the presence of radiation appropriate for resonant fluorescence from the first excited state, what is the average number of excited atoms, N^e? Let p_e = probability that a given atom is excited, p_0 = probability it is in the ground state, τ = natural lifetime of the excited state, and $\langle n_{q\epsilon}\rangle$, the average occupation number of the radiation mode q, ϵ where q and ϵ denote wave vector and polarization. In steady state

$$\frac{p_0\langle n_{q\epsilon}\rangle}{\tau} = p_e\frac{\langle n_{q\epsilon}\rangle + 1}{\tau} \qquad (8)$$

---

* We use the value, 0·146 g/cm^3 given by KAMERLINGH ONNES and BOKS, as reported in Ref. (7).

† See, for example, Table 6.4.2 of Ref. (10).

For low excitations, i.e., $\langle n_{q\epsilon}\rangle \ll 1$, it follows that $p_e \ll 1$, $p_0 \approx 1$ and we obtain the desired result

$$N^e/N = p_e = \langle n_{q\epsilon}\rangle. \tag{9}$$

We recall that if I_0 is the number of photons per second in the incident beam crossing unit area in the line width $\Delta\nu$,

$$\langle n_{q\epsilon}\rangle = I_0/(c\mathscr{N}) \tag{10}$$

where c is the velocity of light, $\nu = cq/2\pi$ and $\mathscr{N}$ is the number of modes in the line width $\Delta\nu$.

$$\mathscr{N} = \frac{2(4\pi)}{(2\pi)^3}q^2\Delta q = \frac{8\pi}{c^3}\nu^2\Delta\nu. \tag{11}$$

For simplicity a square line shape has been assumed.

To estimate the number of excitons present we assume that within the experimental line width there exists a number, N_{eff}, of exciton oscillators coupled to each other via the phonons* and undergoing resonant fluorescence. To minimize heating effects we shall wish to filter out all radiation except that in the linewidth of the 1*s* exciton which is $\lesssim 40$ Å for CdSe.[11] We assume further that (a) N_{eff} is equal to the number of molecules, N, times the (experimentally determined) oscillator strength per molecule, $f1_s$ of the line, (b) a radiative lifetime τ_R exists† and is constant within the line width, and (c) each oscillator is either in the ground state (no exciton) or first excited state (1 exciton). The last assumption, which formally restricts the analysis to concentrations below the critical concentration, has been made only for convenience. A more extended analysis, elminating this requirement, has been carried out,[15] but, in view of the vagueness underlying assumption (a), there seems to be no point in reproducing it here. Letting τ_{ij} be the lifetime for decay of the ith oscillator accompanied by excitation of the jth oscillator (phonon scattering of the exciton), p_i^e be the probability that the ith oscillator is excited and p_i^0, the probability that it is in the ground state, we obtain in steady state

$$p_i^0\left\{\frac{\langle n_{q\epsilon}\rangle}{\tau_R} + \sum_{j=1}^{N_{\text{eff}}}\frac{p_j^e}{\tau_{ji}}\right\} = p_i^e\left\{\frac{\langle n_{q\epsilon}\rangle + 1}{\tau_R} + \sum_{j=1}^{N_{\text{eff}}}\frac{1}{\tau_{ij}}\right\} \tag{12}$$

Because $\langle n_{q\epsilon}\rangle \ll 1$ (see Table 2) we may take $p_i^0 \approx 1$. Summing equation (12) on i, we obtain, with a little manipulation,

$$N_{\text{eff}}\langle n_{q\epsilon}\rangle = \sum_{i=1}^{N_{\text{eff}}} p_i^e = N^e. \tag{13}$$

Setting $N^e = N_c$ and recalling the definition of N_{eff}, we obtain the desired result

$$\langle n_{q\epsilon}\rangle_c = (N_c/f_{1s}N). \tag{14}$$

Values for $\langle n_{q\epsilon}\rangle_c$ at $T_c = 2$°K are given in Table 2 along with the related quantity, I_0 (see equation (10)) for CdS and CdSe. The related light intensities per unit wavelength interval are respectively 0·4 W/cm^2 Å at 4855 Å and 0·1 W/cm^2-Å at 6790-Å. The upper limit obtainable from present pulsed light sources‡ is ~ 5 W/cm^2-Å at the desired wavelengths. By the way of comparison a monochrometer and standard lamp can supply typically ~ 1 mW/cm^2 Å continuously over an area ~ 0·1 cm^2. Thus, the analysis implies that conditions for the Bose-Einstein condensation can be achieved experimentally for CdSe and CdS, although not without considerable practical difficulty in filtering out unwanted radiation.

A possible difficulty with the above treatment is that it does not include the possibility of recombination via Auger processes. Quite apart from the formation of the molecular state discussed in the previous section, it may happen that two excitons collide, one recombines non-radiatively, and the excess energy is carried off by the dissociated electron and hole of the other. Let $\mathscr{R}_c$ equal the rate of Auger recombination at the critical concentration, N_c. The rate of exciton production is αI_0, where α is the absorption coefficient. Recently CHOI and RICE(16) have given a formula for estimating the Auger rate. Their analysis is based upon a hypothetical lattice of hydrogen atoms. Setting the distance parameter, R, which appears in their equation (9) equal to the lattice constant, a and using values for α and I_0 given in Table 2, we obtain $\mathscr{R}_c/I_0 \alpha \sim 1$ per cent for both CdS and CdSe indicating that the Auger recombination is negligible at the critical concentration. However, the applicability of results based upon the hydrogen lattice to CdS and CdSe (for which the Wannier model is appropriate) is clearly subject to question.

---

* Note that if it were not for this coupling the earlier assumption of quasi-equilibrium would be untenable.

† HOPFIELD[12] has noted that there exist difficulties in discussing the interaction of light with excitons in the way we have just treated the dilute gas. He points out that in the absence of phonon interaction the radiative lifetime cannot be defined. For atomic decay the nuclear recoil allows a spread in the allowed values of photon momentum and, hence, in the energy of the final state. The continuum of final states allows a finite transition probability. For exciton decay the photon momentum is prescribed by the exciton momentum before decay, there being no exciton after the event. He finds exciton-photon stationary states with no absorption. Therefore, absorption is attributed to interaction with phonons or other imperfections. The very strong absorption observed for the 1*s*-exciton line ($\epsilon_\perp$ *c*-axis) in CdSe and CdS (see Table 2) indicates that the excitons are not too weakly coupled to the imperfections. With the relaxation of the momentum selection rule, it appears reasonable to define a lifetime τ_R for radiative decay.

‡ We thank Dr. P. P. SOROKIN and Dr. M. NATHAN for information concerning available light sources (private communications).

Table 2. Critical light intensity, I_0, and other parameters. $h\nu$ (λ) is the resonant photon energy (wave length) associated with the creation of the 1s exciton using light polarized perpendicular to the crystalline c-axis; α is the peak absorption coefficient of the 1s line; $\Delta h\nu$ ($\Delta\lambda$) is the line width in $\mathbf{q}\epsilon$. (Å); f_{1s} is the oscillator strength; $\langle n_{q\epsilon}\rangle_c$ is the critical mean occupation number of the photons in the mode, $\mathbf{q}$, ϵ; s is the sound velocity associated with the longitudinal accoustic mode; ΔE is the estimated line width of the emission line associated with the condensed state

	$h\nu$ (eV) λ (Å)	α (cm^{-1})	$\Delta h\nu$ (eV) $\Delta\lambda$ (Å)	f_{1s}	$\langle n_{q\epsilon}\rangle$	I_0 (photons sec-cm^2) (W/cm^2)	s (cm/sec)	ΔE (eV) (Å)
CdS[a]	2·55 4855	$1{\cdot}0\times10^{6}$[d]	$3{\cdot}5\times10^{-3}$ 6·7	$2{\cdot}6\times10^{-3}$[c]	$7{\cdot}5\times10^{-4}$	$6{\cdot}8\times10^{18}$ 2·8	$4{\cdot}3\times10^{5}$[e]	$2{\cdot}8\times10^{-4}$ 0·54
CdSe[a]	1·83 6790	$1{\cdot}3\times10^{5}$[b]	10^{-2}[b] 40	$1{\cdot}0\times10^{-3}$[d]	$1{\cdot}0\times10^{-3}$	$1{\cdot}3\times10^{19}$ 3·9	$3{\cdot}7\times10^{5}$[f]	$3{\cdot}2\times10^{-5}$ 0·12

a. See Refs. (4) and (5).
b. Estimated from Fig. 10, Ref. (11).
c. See Ref. (3).
d. Calculated using the approximate relation, $\alpha\Delta h\nu = 2hNf_{1s}e^2/mc$, which follows by Kramers–Kronig inversion of the expression giving the dielectric constant as a function of f [footnote 14 in Ref. (3)] assuming a Lorentzian line shape.
e. Ref. (14).
f. Estimated by a method due to R. W. KEYES (private communication).

3. *Methods of observation*

Two properties of the condensed system which come to mind are superfluidity and an intense, narrow emission line. We consider the latter method first. Ideally, under conditions leading to a 50 per cent condensation, one-half of the absorbed light is re-emitted in a narrow line associated with what we have previously referred to as the $\boldsymbol{k} = 0$ oscillator. Since wave vector is not strictly conserved we shall henceforth refer to this state simply as the "lowest" oscillator. It is necessary to distinguish between two senses in which the term, non-conservation of wave vector is used here. Earlier we noted that the exciton wave vector is only an approximate quantum number because of the interaction with phonons, but tacitly assumed conservation of wave vector for the system exciton + phonon + photon. Because of the relatively small penetration depth, Δx, of the light into the crystal for the ls exciton line, wave vector is not conserved in the wider sense, but obeys the uncertainty relation,

$$\Delta k \Delta x \sim 1. \tag{15}$$

We shall employ the uncertainty, Δk to estimate an upper bound for the width of the emission line of the lowest oscillator. To establish the existence of a condensed state, it is essential that the radiative line width of the lowest oscillator be discernably less than that due to the recombination of the uncondensed excitons. The latter width, $\sim kT$ is due ideally to the kinetic energy of the excitons in quasi-equilibrium. (It should perhaps be emphasized that we are concerned here with the *intrinsic* exciton emission line.* The lines associated with exciton recombination at impurities have much narrower line widths. The latter transitions dominate at low exciton densities. We have assumed that at concentrations appropriate for condensation the impurity recombination has saturated for sufficiently pure crystals and that the intrinsic decay mode dominates. In any event, the narrow intrinsic emission expected to result upon condensation ought to be distinguishable from the impurity transitions because of the higher photon energy of the intrinsic peak.) The uncertainty, ΔE in the energy of the emitted phonon accompanying photon emission from the lowest oscillator is given approximately by the relation

---

* In Ref. (3) this line is referred to as "peak A" in association with Figs. 3 and 4.

$$\Delta E = \hbar s \Delta k \tag{16}$$

where s is the sound velocity for the longitudinal acoustic mode. Setting the penetration depth, Δx equal to α^{-1} where α is the absorption constant, we obtain from equations (15) and (16)

$$\Delta E = \hbar s \alpha. \tag{17}$$

We assume ΔE is the major source of line width for the lowest oscillator. Values for s and α for CdS and CdSe are given in Table 2. Thus, for CdSe, equation (17) yields, $\Delta E = 3 \times 10^{-5}$ eV, whereas, $kT = 10^{-4}$ eV at $T = 1{\cdot}3$°K. The Bose–Einstein condensation ought to be observable as a narrowing in the emission line with increasing light intensity at fixed sample temperature. For CdS, we obtain $\Delta E = 3 \times 10^{-4}$ eV, which is greater than kT at $T = 1{\cdot}3^{\circ}$ but somewhat less than the observed emission line width which is about 10^{-3} eV at $T = 4{\cdot}2$°K.(3) By operating slightly off resonance (thereby decreasing α) at somewhat higher temperature the narrowing might be observable. Moreover, we note that the quantity $\hbar s \alpha$ is probably an overestimate for the emission line width ΔE. In the foregoing we have neglected the effects of exciton diffusion or super-fluid flow away from the surface. Such flow will improve the line width ratio by increasing the penetration depth Δx, but will impose stronger requirements on the light source than those calculated previously (cf. Table 2).

We now consider briefly the property of superfluidity. Using Galilean relatively LANDAU(6) has shown that friction with the walls of a container cannot occur for a Bose liquid at $T = 0$°K until a critical minimum velocity, $\epsilon(p)/p$ is attained, where $\epsilon(p)$ is the excitation energy with momentum, p. In order that $\epsilon(p)/p$ remain finite as $p \rightarrow 0$ (assuming $\epsilon(0) = 0$) it is necessary that the interactions alter the single-particle excitation energy from the quadratic form appropriate for excitons at low densities. Since the critical velocity cannot be ascertained without more detailed knowledge of the effect of interactions on the excitation spectrum, we can say very little about the possibility of observing a superfluidity of the excitons. We simply note that whereas a Bose–Einstein condensation and concomitant narrowing of the fundamental emission line occurs in the limit of zero interaction, superfluidity cannot. For non-negligible interaction, the requirement that the interaction be dominantly repulsive probably renders molecular formation a necessary condition for condensation to occur. In order to attain a sizeable probability for an exciton to combine with another exciton rather than with an impurity, it appears necessary that the impurity concentration be much smaller than the critical concentration N_c, which is $\sim 10^{16}$ cm^{-3} for the materials considered. Thus, the impurity content of the crystals is a limiting factor for achieving superfluidity in the exciton system.

Finally, we remark that LASHER(17) has noted that the lowest oscillator, which is highly excited, can be regarded as a classical polarization wave. In the absence of phonon interaction the radiation emitted by the lowest oscillator has coherence properties which could be of aid in identifying the condensation.

3. SUMMARY

As it stands, the analysis contains many imponderables. We have not attempted a systematic search for optimal materials, but have focused our attention, more or less arbitrarily, on two crystals, CdS and CdSe. Our main result, based upon the simplest and most idealistic set of assumptions, is that conditions for observing the condensation, (if one exists) ought to be achievable with CdSe and, with less certainty, in CdS as well. The effect is to be observed as a narrowing of the intrinsic exciton emission line with increasing light intensity above the critical concentration.

We have assumed that at the high light intensities required for condensation the intrinsic exciton recombination process dominates and have omitted the effects of impurity-assisted recombination in deriving equation (14) from which we obtained the critical light intensities. In this sense we have underestimated the actual intensities required. On the other hand, our assumption that quasi-equilibrium can be obtained only if all the exciting light lies within the narrow 1*s* exciton line width, is probably unduly restrictive. Given that excitons created at higher energies and those formed from free electron-hole pairs can equilibrate, one could employ broader-band sources with considerably lower intensities per wavelength interval than those obtained in the analysis. To what extent these effects tend to cancel in presently available crystals is not known. It would appear desirable to reduce the content of the impurities interacting with the excitons below the critical concentration.

Note added in proof: Contrary to what we have assumed in Section 2, Blatt[18] reports that the effects of the exclusion principle on the constituent particles aid the establishment of a Bose-Einstein condensation. However, we believe his definition of this term is somewhat broader than the usual simple picture of statistical effects on *localized* (weakly interacting) bosons which we adopt here.

Acknowledgements—I have benefited from stimulating discussions with my associates. I am particularly indebted to Dr. Gordon Lasher for helpful comments and suggestions.

REFERENCES

1. Wannier G. H., *Phys. Rev.* **52,** 191 (1937).
2. MacFarlane G., McLean T., Quarrington J. and Roberts V., *Phys. Rev.* **108,** 1377 (1957).
3. Thomas D. G. and Hopfield J. J., *Phys. Rev.* **116,** 573 (1959).
4. Hopfield J. J. and Thomas D. G., *Phys. Rev.* **122,** 35 (1961).
5. Dimmock J. O. and Wheeler R. G., *J. appl. Phys.* **32,** Suppl. 2271 (1961).
6. Landau L. D. and Lifshitz E. M., *Stastistical Physics*, Addison-Wesley, Reading, Massachusetts (1958).
7. London F., *Superfluids II*, John Wiley, New York (1954).
8. Blatt J. M., Boer K. W. and Brandt W., *Phys. Rev.* **126,** 169 (1962).
9. Bogolubov N., *Zh. fiz. Mosk.* **11,** 23 (1947).
10. Slater J. C., *Quantum Theory of Matter*, McGraw-Hill, New York (1951).
11. Parsons R., Wardzynski W. and Yoffe A., *Proc. Roy. Soc.* **262A,** 120 (1961).
12. Hopfield J. J., *Phys. Rev.* **112,** 1555 (1958).
13. Lax B., Zeiger H. J., Dexter R. N. and Rosenblum E. S., *Phys. Rev.* **93,** 1418 (1954).
14. Hutson A. R., *J. appl. Phys.* **32,** Suppl. 2287 (1961).
15. Casella R. C., *I.B.M. Res. Rep.* No. RC-692 (unpublished).
16. Choi S. and Rice S., *Phys. Rev. Letters* **8,** 410 (1962).
17. Lasher G. J. (private communication).
18. Blatt J. M., *Progr. Theor. Phys. (Kyoto)* **27,** 1137 (1962).

J. Phys. Chem. Solids Pergamon Press 1963. Vol. 24, pp. 27-36. Printed in Great Britain.

DEVIATIONS FROM STOICHIOMETRY AND ELECTRICAL PROPERTIES IN SnTe

R. F. BREBRICK

Lincoln Laboratory,† Massachusetts Institute of Technology, Lexington 73, Massachusetts

(*Received* 26 *July* 1962)

Abstract—The maximum melting point of SnTe has been found to be 805·9 ± 0·3°C near 50·4 at. per cent Te by thermal analysis. The apparent hole concentration, $p^* = 1/eR$, at 300° and 77°K has been measured for single crystals saturated with Sn or Te between 550° and 797°C and quenched. For saturation at 700°C, the apparent hole concentration at 300°K (p^*_{300}) is 2×10^{20} cm^{-3} for Sn-saturated SnTe and $1{\cdot}5 \times 10^{21}$ cm^{-3} for Te-saturated SnTe. The corresponding concentrations for saturation at 775°C are 5×10^{20} and $1{\cdot}1 \times 10^{21}$ cm^{-3}, respectively. The maximum melting composition corresponds to about 8×10^{20} holes/cm^3. The relationships between apparent hole concentration at 300° or 77°K and at. per cent Te have been determined by equilibrating small crystals of SnTe at 750°C with large ingots having known compositions within the SnTe solidus field. In both cases, it is linear and for p^*_{300} is given by

$$\frac{p^*_{300}}{10^{20}} = 16{\cdot}94\,(\text{at. per cent Te} - 50{\cdot}00) + 0{\cdot}51$$

On the basis of the above, the solidus field of SnTe lies entirely on the Te-rich side of 50 at. per cent Te above 600°C and has its maximum width near 600° where the limits of stability are 50·1 and 51·1 at. per cent Te. The density determined by weighing is 6·445 ± 0·010 gm/cm^3 at 25°C for all samples. The lattice parameter varies linearly with at. per cent Te from 6·318 Å at 50·17 at. per cent Te to 6·306 Å at 51·06 at. per cent Te. Comparison of the ideal and observed densities indicates that Sn-vacancies are the predominant atomic point defects.

The ratio of the apparent hole concentration to the Sn-vacancy concentration varies between 3·4 and 3·2 for p^*_{300} and between 4·5 and 3·2 for p^*_{77}. Cu is a fast diffusing donor in SnTe crystals which have values of p^*_{300} between 2 and $2{\cdot}5 \times 10^{20}$ cm^{-3}. Hall measurements on SnTe crystals grown from Bi-doped melts indicate Bi is a donor and/or the SnTe solidus surface in the Sn–Bi–Te system is not symmetric about the SnTe solidus lines. The Hall mobility at 300° and 77°K and the absolute thermoelectric power at 300°K are given as a function of the apparent hole concentration.

INTRODUCTION

THE PUBLISHED phase diagram(1) for the Sn–Te system shows a single compound, SnTe, with the NaCl structure. Although the broad features of the diagram are believed to be correct, there is considerable discrepancy among the various determinations of the maximum melting point and lattice parameter of SnTe. Moreover, careful investigation of the range of compositions over which this compound is stable and the control of composition necessary for a fuller understanding of its electrical properties have been attempted only recently.(2,3) In order to better characterize SnTe, we have (a) determined the liquidus line near 50 at. per cent, (b) measured the Hall constant and resistivity at 300° and 77°K and thermoelectric power at 300°K of single crystals saturated with either Sn or Te between 550° and 797°C and then quenched, (c) determined the relationship between composition in at. per cent and $1/eR$, where R is the Hall constant at 300° or 77°K, (d) measured the lattice parameter and density as a function of composition, and (e) investigated the behavior of Bi and Cu impurities. As a consequence, we have been able to construct the solidus lines for SnTe,

---

† Operated with support from the U. S. Army, Navy, and Air Force

and to identify the predominant atomic point defects present in non-stoichiometric SnTe as Sn vacancies.

For many semiconductor compounds, the existence of a range of composition stability has been inferred from changes in electrical properties produced by techniques expected to produce changes in composition. These include the following compounds closely related to SnTe: GeTe,(4) PbTe,(5) SnSe,(6) PbSe,(7) SnS,(8) and PbS.(9) Except for SnTe and possibly GeTe, however, the range of stability and the relationship between composition and electrical properties cannot be determined experimentally, since the stable compositions do not differ from 50 at. per cent by more than the limits of experimental error of present methods. In the present investigation, crystals of known composition have been prepared by weighing out Sn and Te to prepare relatively large ingots with compositions inside the SnTe solidus field and equilibrating these with small single crystals of known weight and Hall constant. At equilibrium, the composition of both crystals and ingot is just the average composition of the system excluding the vapor phase. This technique is a straightforward extension of the method used to saturate a binary compound with one of its components(5) and depends upon the same application of the Gibbs' phase rule.

On the basis of its electrical properties, SnTe has been postulated to be a semi-metal(10) or a semiconductor with a complicated valence band structure.(11,12) Since the relationship between Hall constant and actual carrier concentrations is therefore unsettled, $1/eR$ will be referred to as the apparent carrier concentration, p^*.

EXPERIMENTAL

SnTe *crystals*

The crystals were grown occasionally by the Czochralski technique or more commonly by a modified Bridgman technique.(13) In the former case, a fused silica crucible, induction heating, 1/3 atm. argon atmosphere, pull rate of 1/4 in/hr and rotation rate of 10 rev/min were used. In the latter case, a fused silica boat containing the elements was sealed inside an evacuated silica tube and placed inside a horizontal resistance furnace. A temperature gradient of 50°C was established across the 6 in. length of the boat. The power to the furnace was decreased automatically so that 72 hr were required to freeze the entire ingot. In both cases, about 200 g of 99·999 per cent pure Sn (Cominco Products, Spokane, Wash.) and 99·999 per cent pure Te (American Smelting and Refining Co., New Jersey) in stoichiometric proportions were first heated to 850°C. The ingots obtained were examined visually for grain boundaries, and slices 1–2 mm thick were cut from the best portions. The samples were then ground to rectangular form and rinsed successively in distilled water and acetone. In general, the samples used showed no grain boundaries, or only a few as revealed by a polishing etch.(14) The last portions of the ingots to freeze in horizontal boats showed a honeycomb structure associated with constitutional supercooling and occasionally showed small exterior portions of metallic Sn. These portions were avoided in taking samples. Bismuth-doped crystals were grown by the Bridgman technique described. The melts had compositions of Bi_xSnTe where $100x$ was 5, 3, or 1·5. Cu-doped samples were prepared by electroplating Cu from a 1M $CuSO_4$, 0·5N H_2SO_4 solution onto sandblasted SnTe crystals. These were then annealed for 3 hr at 500°C under 1/4 atm.H_2.

Thermal analysis

About 100 g of the high purity Sn and Te cited were sealed in an evacuated, 33 mm o.d., 6 in. long fused silica tube. The Sn and Te were weighed to the nearest 0·1 mg. The tube had a 1 in. long, 3 mm i.d. re-entrant thermocouple well through its flat bottom. The tube had previously been rinsed in 37 per cent HF, then distilled water, then acetone, and outgassed at 950°C for 17 hr. The final pressure was below 10^{-6} mm Hg. After loading, the tube was outgassed near 180°C for 4 hr and then sealed off at about 10^{-6} mm Hg. After initiation of the reaction with a hand torch, the tube was placed inside a 7 in. long, 2 in. o.d., 1¼ in. i.d. stainless steel liner and placed in a box furnace at about a 45° angle. The Pt:Pt, 13 per cent Rh thermocouple was placed ¾ in. into the well, its ceramic insulation fitting snugly, and the whole assembly was wrapped in alundum blanket insulation. The material was heated to 850°C (being above the melting point of 806°C for some 2 hr), and the furnace power was turned off. The cooling rate was 3°C min^{-1}. Within a few degrees below the clearly visible freezing temperature, the material was reheated to 850°C. This procedure was repeated to obtain two more cooling curves. On the third freeze, the temperature was followed about 30°C below the freezing point.

Some of the freezing point samples were annealed for 24 hr at 750°C and cooled rapidly to below the eutectic temperatures. Melting curves with heating rates of approximately 7°C min^{-1} were used to establish the temperatures of the eutectic halts.

Thermocouple e.m.f.s were recorded with an accuracy of $\pm$ 0·25 μV and a time resolution of $\pm$ 1 sec. The difference between the thermocouple e.m.f. and the bucking voltage from a Leeds and Northrup K-3 potentiometer was amplified by a Leeds and Northrup d.c. μV amplifier and recorded with a Sargent multirange recording potentiometer. The thermocouple was provided with an ice junction and was calibrated against the freezing points of 100 g of 99·999 per cent pure Sb and 140 g of 99·999 per cent pure Ag (both from Cominco Products, Spokane, Wash.) using the same procedure as for the Sn–Te samples. The freezing points obtained for Sb and Ag were respectively 630·50 $\pm$ 0·04°C and 960·9 $\pm$ 0·1°C. Since these values agree within $\pm$ 0·1°C or better with those accepted,(15) subsequent temperatures were not corrected.

Limits of stability: Apparent carrier concentrations for Sn- *or* Te-*saturated* SnTe

SnTe crystals were saturated with either Sn or Te using a technique previously described for PbTe(5) and used for PbSe.(7) Small single crystals were heated in vapor contact with a Sn–Te ingot that was partly liquid and partly solid at the heat-treatment temperature. At equilibrium, the crystals were therefore either Sn-saturated or Te-saturated depending upon whether the average composition of the condensed phases was outside the SnTe solidus field on the Sn-rich or on the Te-rich side. The silica tube containing the crystals was then quenched in brine, and the thermoelectric power at 300°K and the Hall coefficient and resistivity at 300° and 77°K were measured. Apparent carrier concentrations were calculated according to the equation $p^* = 1/eR$, where R is the Hall coefficient.

The Sn–Te ingots were synthesized by fusing weighed quantities of the elements totalling 10 g in a sealed, evacuated silica tube at 850°C. After 10 min at 850°C with occasional shaking, the tubes were quickly immersed vertically in water to the height of the melt. The quenched ingot was then broken on ashless filter paper into pieces 1 to 10 mm in diameter.

The ingot and three SnTe crystals 7 to 15 mm long, 4 to 6 mm wide and 1 to 1·5 mm thick were loaded into 22 mm o.d. silica tube 3½ in. long after seal-off. The tube had previously been outgassed for 17 hr at 1050°C after cleaning as described above. After loading, the tube was again outgassed at 180° to 220°C and sealed off at or below 10^{-6} mm Hg. Direct contact between the crystals and ingot was prevented by placing the crystals either on a silica shelf or in a 12 mm o.d. silica test tube inside the larger tube. In the latter case, the ingot separated the crystals from the outside walls and as a result the quench rate was less rapid than with a shelf tube.

The tube containing the crystals and ingot was put into a 6 in. long steel liner with ½ in. thick walls already at temperature inside a box furnace. Temperatures were recorded using a Pt:Pt, 10 per cent Rh thermocouple and were held constant to better than $\pm$ 2½°C during runs that lasted as long as 400 hr. In Table 1 are given the temperature, ingot composition, and the equilibration period for the various saturation runs.

The thermoelectric power was measured near 30°C against Fe using a vise-like device that provided pressure contacts between the thermocouples and the SnTe crystal. The gradient across a typically 10 mm long samplew as 3° to 5°C. A value of + 11·0 $\mu V/°C$ for the absolute thermoelectric power of iron was used to calculate the absolute thermoelectric power of SnTe. Voltages were measured to within $\pm$ 0·25 μV using the apparatus for measuring temperature described in the last section. The Hall constant was measured at 6000 G using either pressure or indium solder contacts. The conventional d.c. method was used, but the small Hall voltages were measured with the amplifier and recorder used for temperature measurements.

Table 1. *Temperatures, ingot compositions, and equilibration times used for saturation of* SnTe *crystals*

Run	T(°C)	Ingot (at. per cent Te)	(Hr)
24	550	38·3	433
8	707	38·3	162
10	706	38·3	338
13	745	47·3	28
15	772	49·7	18
37	788·5	50·00	18
23	550	53·2	433
6	710	53·2	114
9	706	53·2	166
12	706	56·0	166
14	747	53·2	17
16	771	53·2	18
38	797	50·8	21

Relation between apparent carrier concentration and composition

The relationship between the apparent carrier concentration, p^* and the composition of SnTe in at. per cent Te was obtained by a simple extension of the technique used to saturate SnTe with Sn or Te. Whereas both liquid and solid phases are present in the saturation runs, in these experiments the ingot composition is chosen so that only solid SnTe and a vapor phase are present at the equilibrium temperature. In the presence of only two phases, the intensive thermodynamic variables are a function of average composition as well as temperature, according to Gibbs' phase rule.

Twenty-gram ingots with average compositions between 50·10 and 50·82 at. per cent Te were synthesized as described in the last section. These were broken on ashless filter paper into pieces about 4 mm dia. and less. Each ingot was then sealed off in an evacuated silica tube along with three SnTe crystals whose dimensions and Hall constants had previously been measured. The degassing procedure was the same as in the saturation runs. The tubes were heated for 66 hr at 750°C and quenched in brine. The Hall constants and resistivities of the crystals were then measured at 300°C and 77°K and apparent carrier concentrations calculated.

Density and lattice parameter

The densities of a number of samples of SnTe were determined by weighings in air and in Baker's Reagent Grade toluene near 25°C.

The calculated density of SnTe in air was converted to that in vacuo by a correction of -1 part in 1000 for the effect of air buoyancy.(16)

Samples were prepared for the lattice parameter(17) measurement by grinding to pass through a 325 mesh screen, annealing for 24 hr at 350°C in a sealed, evacuated silica tube, furnace cooling, and selecting the portion of the powder retained between 325 and 400 mesh screens. The anneal was found necessary to obtain sharp lines. To minimize errors due to absorption, a small sample held within a 0·02 mm i.d. glass vial was taken. A 114·6 mm radius Debye-Scherrer powder camera and a point source target operated at 35 kV and 20 mA were used. The Cu λ radiation was passed through a Ni filter and the film was exposed for 5 hr. The temperature of the sample was 29°C. The calculated values of the lattice parameter were plotted against $\sin^2\theta$, the largest angle at which a point was obtained being about 78°. A line of constant lattice parameter was drawn through the five points at the highest angles and the largest deviation taken as the error.

RESULTS AND DISCUSSION

Thermal analysis

The results for Sn–Te are given in Table 2 where the composition, liquidus temperature, and eutectic temperature are listed. The errors in temperature are the root mean square deviations for three determinations. The compositions are believed to be accurate to better than $\pm$ 0·02 at. per cent. Loss of material on seal-off was negligible, amounting to 2 to 4 mg out of the 100 g total. The maximum error due to loss of material to the vapor phase at 805°C was calculated knowing: (i) the partial pressure of gaseous SnTe over solid SnTe(18) to be 1 mm Hg, (ii) the vapor pressures of pure Te(19) and Sn to be 110 and below 10^{-3} mm Hg respectively, (iii) the volume of the vapor phase to be 0·1 l and (iv) assuming diatomic tellurium and SnTe are the predominant species in an ideal gas phase. The maximum possible change in the composition of the condensed phases was found to be $-0·02$ at. per cent Te.

Generally, the Sn–Te melts supercooled from 2° to 20°C. There was no correlation between the amount of supercooling and the maximum temperature (freezing temperature) reached after freezing started. The duration of the halt in the freezing curve was calculated using a zero of time obtained by extrapolation of maximum freezing temperature back to the cooling curve where supercooling started and a final time taken when the temperature dropped 0·04°C below the maximum freezing temperature. These halts were between 8 and 10 min long for all the compositions listed.

Table 2. *Liquidus and eutectic temperatures for* Sn–Te

at. per cent Te	Liquidus temperature, T(°C)	Eutectic, T(°C)
49·60	805·0 ± 0·2	232·0 ± 0·1
50·01	806·0 ± 0·2	232·0 ± 0·1
50·40	805·8 ± 0·1	—
50·80	805·9 ± 0·1	—
51·20	805·2 ± 0·1	401·3 ± 0·1

The liquidus line is roughly symmetric about a composition of 50·40 at. per cent Te. The maximum liquidus temperature is 805·9 ± 0·3°C, in comparison with earlier values ranging from 769° to about 796°C.(1) Within the limits of experimental error, this maximum temperature was observed for compositions of 50·01, 50·40, and 50·80 at. per cent Te. Complete cooling curves for comparable supercooling show, however, that the duration of the freezing plateau is slightly shorter for 50·01 or 50·80 at. per cent Te than for 50·40 at. per cent Te, indicating that the latter composition is closest to the value at the maximum melting point.

Occurrence of the maximum melting point at a composition greater than 50 at. per cent Te is consistent with the appearance of Sn-eutectic in the last-to-freeze portions of crystals grown from stoichiometric melts. It is also consistent with the eutectic data given in Table 2, since the Sn-eutectic point is observed for 50·01 at. per cent Te, whereas the Te-eutectic was observed only for compositions of at least 51·20 at. per cent Te. The temperature of the Sn-eutectic agrees with that of earlier investigators, among whom there is exact agreement.(1) The temperature of the Te-eutectic is intermediate among those reported earlier.(1)

Limits of stability: apparent carrier concentrations for Sn- *or* Te-*saturated* SnTe

Generally the SnTe crystals appeared unchanged after saturation with one of the components, although occasionally the edges of Te-saturated crystals were somewhat rounded. The yellow-green vapor of Te_2 could be seen in tubes containing Te-rich ingots upon removal from the furnace.

The results of the saturation experiments are shown in Fig. 1, where the reciprocal equilibration temperature is plotted against p^*_{300}. For a given value of $1/T$, the points at lower values of p^*_{300} are for Sn-saturated crystals. The points at 600°C are taken from HOUSTON, BIS and GUBNER,(2) who used a similar technique with single crystals grown by the Czochralski technique. The reliability of these results is contingent upon the assertions that equilibrium was established and that the quench rate was rapid enough to freeze in the high temperature net acceptor concentration. The evidence for these assertions is given in the Appendix.

The value of p^*_{300} at the maximum melting point is taken as 8×10^{20} cm^{-3}, based on the composition of 50·4 at. per cent Te at this point

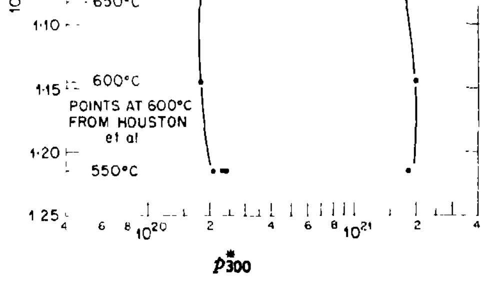

FIG. 1. Reciprocal equilibration temperature vs. $p^*_{300} = 1/eR$ for Sn- and Te-saturated SnTe. Lower values of p^*_{300} are for Sn-saturation.

obtained in the thermal analysis studies and the relationship between p^*_{300} and composition described in the following section. Consistent with this value, the first portions of crystals grown from stoichiometric melts generally had values of p^*_{300} between 6 and 8×10^{20} cm^{-3}. It is seen that p^*_{300} varies over a large range from about 2×10^{20} to 2×10^{21} cm^{-3}. Most probably these apparent concentrations do not differ significantly from the actual hole concentrations, at least for values above about 10^{21} cm^{-3}. Thus, a large portion of the carriers in undoped SnTe result from large deviations from stoichiometry with the atomic point defects behaving as acceptors.

Relation between apparent carrier concentration and composition

In Fig. 2 are plotted the values of p^* at 300° and 77°K as a function of composition in at. per cent Te for SnTe crystals annealed at 750°C for 66 hr. in the presence of nearly stoichiometric ingots. The composition is the average calculated by an iteration process, from the weight and composition of the ingot and the weights and initial values of p^* for the SnTe single crystals. This calculated average differs most from the composition of the ingot itself for the run at 50·35 at. per cent Te, where the difference is 0·035 at. per cent. Since the composition of the SnTe solid phase is the desired variable, the calculated average is in error due to loss of material to the vapor phase. However, an estimate for the maximum loss, similar to that made in the discussion of the maximum melting point, corresponds to an error of only $-0{\cdot}05$ at. per cent Te. As can be seen in Fig. 2, the data for both 300° and 77°K are represented fairly well by straight lines, that for p^*_{300} being represented by the equation

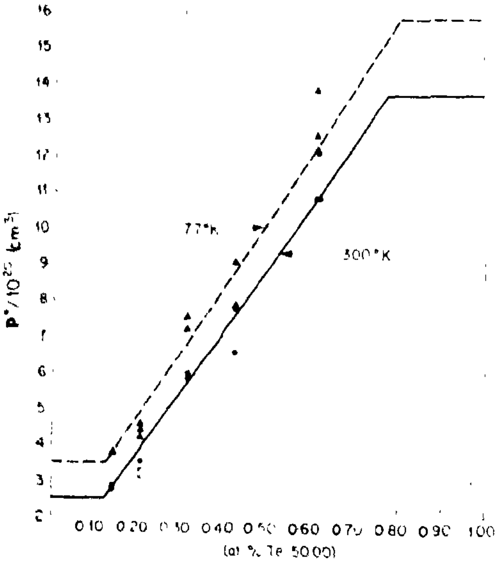

FIG. 2. p^*_{300} and p^*_{77} vs. composition in at. per cent Te for SnTe equilibrated for 66 hr at 750°C with ingots whose compositions are within the SnTe solidus field.

$$p^*_{300}/10^{20} = 16{\cdot}94\,(\text{at. per cent Te} - 50{\cdot}00) + 0{\cdot}51$$

The p^*_{77} line is only slightly steeper and extrapolates to a value of $p^*_{77} = 1{\cdot}25\times10^{20}$ at 50 at. per cent Te. Thus the ratio p^*_{77}/p^*_{300} decreases towards unity at the higher apparent carrier concentrations as is generally observed for SnTe. The intersections of these straight lines with horizontal lines at the values of p^* obtained from the saturation experiments (with 47·3 and 53·2 at. per cent Te ingots, as given in Table 1 and Fig. 1) give the limits of stability of SnTe at 750°C as 50·1 and 50·8 at. per cent Te.

The results shown in Fig. 2 are in fair agreement with those of MAZELSKY and LUBELL[3] for SnTe samples prepared by a powder metallurgy technique and sintered at 500°C for 16 hr. For a given value of p^*_{300} in the overlapping range between $2{\cdot}5\times10^{20}$ and 11×10^{20} cm^{-3}, the compositions agree to 0·10 at. per cent or better. The agreement is good enough to show there is no strong temperature dependence of the linear relationships of Fig. 2. Therefore this relationship can be used to convert Fig. 1 into a conventional solidus line plot with at. per cent as the composition variable. Accordingly, the field of stability of SnTe is entirely on the Te-rich side of 50 at. per cent and is a maximum at 600°C where the limits are 50·1 and 51·1 at. per cent Te. The limits of stability at 500°C obtained by Mazelsky and Lubell are based upon the variation of lattice parameter with composition and are 50·00 at. per cent Te or less and 50·8 at. per cent Te. This would indicate a sharp curvature of the SnTe solidus lines towards 50 at. per cent between 500 and 600°C.

The linear relation between p^* and at. per cent Te implies a linear relation between p^* and D, the net concentration of atomic point defects defined by $D/4S$ = (at. per cent Te $-50{\cdot}00)/100$, where S is $1{\cdot}6\times10^{22}$ cm^{-3}, the concentration of normal Sn or Te lattice sites per cm^3. Between 50·1 and 50·7 at. per cent Te, the ratio p^*/D calculated from the above equation and Fig. 2 varies from 3·4 to 3·2 for p^*_{300} and from 4·5 to 3·2 for p^*_{77}. One would expect no more than two carriers per native atomic point defect, e.g. Sn-vacancy, in SnTe. Whether this intuitive notion is incorrect or whether the actual hole concentration is actually smaller than p^*_{300} and p^*_{77} depends upon further elucidation of the band structure.

Density and lattice parameter

The densities of SnTe samples with p^*_{300} ranging from 2×10^{20} to $18{\cdot}4\times10^{20}$ cm^{-3}, were all found to be within ± 0·01 g cm^{-3} of 6·445 g cm^{-3} at 25°C. Assuming a linear coefficient of expansion of 2×10^{-5}, the same as for PbS(20) the density of SnTe changes by only about 0·004 g cm^{-3} over a 10°C interval. Since the density values were determined between 23 and 25°C, they are all given uncorrected for temperature. Samples from five as-grown crystals, including one crystal pulled by the Czochralski technique, gave densities between 6·450 and 6·442 g cm^{-3}. Values for the individual samples were reproducible to within ± 0·004 g cm^{-3} or better. The average for all five samples was 6·445 g cm^{-3}. Samples with p^*_{300} between 2 and $3{\cdot}4\times10^{20}$ cm^{-3} had the same density of 6·450 g cm^{-3} whether Sn-saturated at 772°C or at 550°C indicating that the effect of intrinsic point defects is either insignificant or constant over this temperature range.

Lattice parameters for four samples with p^*_{300} between 3·4 to $18{\cdot}4\times10^{20}$ cm^{-3} are given in Table 3. The lattice parameter decreases linearly with p^*_{300} and therefore with at. per cent Te. Mazelsky and Lubell(3) have also determined the lattice parameter of SnTe as a function of composition. Compared to our values, theirs are high by 0·005 Å at 50·1 at. per cent Te, in exact agreement at 50·4 at. per cent Te, and low by 0·006 Å at 50·8 at. per cent Te.

In addition to the lattice parameter, Table 3 gives the sample treatment, p^*_{300}, and weighing density. The net concentration of atomic point defects D obtained from p^*_{300} and Fig. 2 is given in column 6. For the last two samples, the straight line between p^*_{300} and at. per cent Te in Fig. 2 had to be extrapolated to higher carrier concentrations as can be seen. This leads to some uncertainty in the following discussion, at least for the last sample for which the necessary extrapolation is the longest. The difference between the ideal density calculated from the lattice parameter and that obtained by weighing is listed in column 7. Finally, column 8 gives the value calculated for this difference if the atomic point defects are all tin vacancies. Although the differences between the last two columns are outside experimental error for three of the four samples, it is seen that the assumption that Sn-vacancies are the predominant point defects is substantially correct. Exact agreement between columns 7 and 8 for the last two samples can be obtained without greatly

Table 3. *Treatment, apparent hole concentration at* 300°K, *lattice parameter, weighing density, net defect concentration, D, from composition in* at. per cent Te, *difference between ideal and observed densities, and calculated value for this difference assuming* Sn-*vacancies in concentration, D*

1 Sample	2 Treatment		3 $p^*_{300}/10^{20}$ (cm^{-3})	4 a(Å)	5 d_w (gm/cm^3)	6 $D/10^{20}$ (cm^{-3})	7 $-\Delta d$ (gm/cm^3)	8 $-\Delta d$ (gm/cm^3)
15-2	Sn-satd.	772°C	3·38	6·318 ± ·002	6·450 ± ·005	1·0	0·038	0·020
III-H	As grown		6·48	6·314 ± ·001	6·445 ± ·004	2·0	0·052	0·039
9	Te-satd.	706°C	15·1	6·308 ± ·001	6·443 ± ·005	4·7	0·073	0·093
23-2	Te-satd.	550°C	18·4	6·306 ± ·001	6·446 ± ·002	6·0	0·086	0·120

increasing the discrepancy for the first two by assuming the presence of Te-interstitials whose concentration is 0·15 that of the Sn-vacancies (the sum of the Sn-vacancy and Te-interstitial concentrations being equal to D). If the lattice parameters given by MAZELSKY and LUBELL(3) are used, the difference between the ideal and weighing densities agrees with that calculated assuming only Sn-vacancies to within 0·01 g cm^{-3} for all four samples in Table 3.

Bi *and* Cu *impurities*

Even the best samples from Bi-doped melts contained about 10 crystallites per cm^3. However, their mobilities and thermoelectric powers agree well with those for higher quality undoped samples as shown in the next section. Values of p^*_{300} for as-grown samples were positive and near 2×10^{20} cm^{-3} for all three melt compositions, $x = 0{\cdot}15$, $0{\cdot}30$, $0{\cdot}50$ in Bi$_x$SnTe. Spectrographic analysis of dissolved samples indicated that the distribution coefficient is about 0·6 for all three melt compositions.(21) Since nothing is known about the concentration of Sn-vacancies in the doped crystals, the decrease in apparent hole concentration per Bi atom cannot be calculated from the above.

When SnTe containing about 3×10^{20} Bi atoms cm^{-3} (as determined by spectroscopic analysis) was Sn-saturated at 750°C by vapor equilibration with a 47 at. per cent Te Sn-Te ingot, the resulting value of p^*_{300} was the same as for undoped crystals saturated in the same manner. Making the assumption that Bi is a donor in SnTe, this indicates that the free energy of SnTe is lowest when enough Sn-vacancy acceptors are introduced to compensate the Bi donors. Thus the chemical potential of Sn in SnTe depends more strongly on composition through its dependence on the Fermi level than through its dependence on the concentration of ionized Sn-vacancies.(22) This is confirmed by the behavior of Cu cited below.

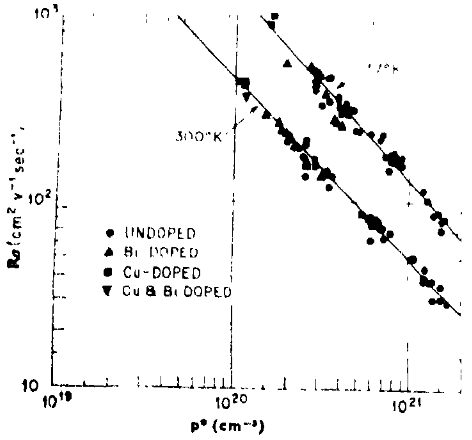

FIG. 3. Hall mobility $R\sigma$ as a function of p^* at both 300 and 77°K for pure and doped SnTe.

Sn-saturated SnTe crystals with values of p^*_{300} at 300°K between 2 and $2{\cdot}5 \times 10^{20}$ cm^{-3} showed a decrease of $1{\cdot}3 \times 10^{20}$ cm^{-3} in p^*_{300} and $1{\cdot}6 \times 10^{20}$ cm^{-3} in p^*_{77} when doped by diffusion with 2×10^{20} Cu atoms cm^{-3}. The fast diffusion and donor behavior are suggestive of interstitial Cu. Similar to the case for Bi-doped SnTe, these crystals attain a value of p^*_{300} typical of undoped crystals after Sn-saturation at 750°C.

Electrical properties of SnTe

Some of the electrical properties of SnTe are given here in order to characterize the material used in this study and for their own interest. No attempt is made to analyze the data. The Hall mobility, $R\sigma$ is shown as a function of p^* in Fig. 3. The mobilities agree well with the few values quoted(11) for single crystal SnTe grown by the Czochralski method, saturated with Sn or Te at 600°C or below, and then quenched. It is to be noted that the mobilities of the polycrystalline Bi-doped samples and those of the Cu-doped samples at the lowest values of p^* fall close to the straight line extrapolated from data for undoped SnTe.

The ratio of Hall coefficients $R_{300°\mathrm{K}}/R_{77°\mathrm{K}}$ decreases from values near 1·5 at $p^*_{300} = 1 \times 10^{20}$ cm^{-3} to near 1·0 near $p^*_{300} = 1{\cdot}3 \times 10^{21}$ cm^{-3}. Similar behavior has been reported by ALLGAIER for SnTe(11) and for p-type PbTe(23) and attributed by him to a complex valence band.

The absolute thermoelectric power at 300°K is shown as a function of p^*_{300} in Fig. 4. The curve agrees to within a few $\mu V/°$C or better with the data of SAGAR and MILLER(10) on single crystals between about 2×10^{20} and $1{\cdot}8 \times 10^{21}$ cm^{-3}, and is close to that obtained for sintered samples by Mazelsky and Lubell. The few values quoted by HASHIMOTO and HIRAKAWA(24) also fall close to the curve. Of particular interest is the fact that the thermoelectric power between 1 and 2×10^{20} cm^{-3} appears to be nearly flat. This might be interpreted as evidence for the presence of two phases. However, the mobilities for these samples, obtained by Cu-doping, appear normal as pointed out above.

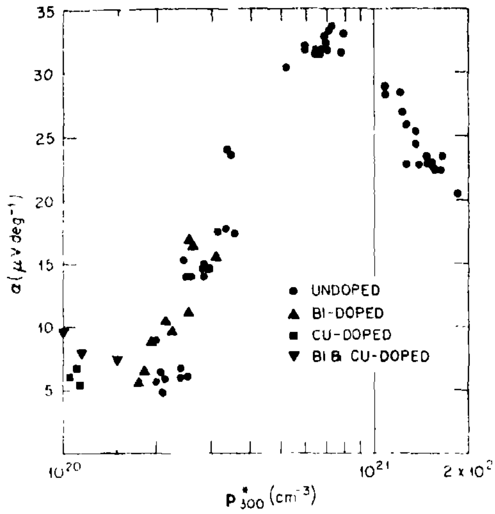

FIG. 4. Absolute thermoelectric power of SnTe at 300°K as a function of apparent hole concentration, p^*_{300}.

Acknowledgements—The author wishes to acknowledge the capable technical assistance of Mrs. D. DIBLEY in all phases of the experimental work. He is also grateful to Dr. A. J. STRAUSS for aid in obtaining the electrical measurements and for helpful discussions. Finally, he wishes to thank Dr. R. MAZELSKY and Dr. M. S. LUBELL for communicating their results prior to publication.

APPENDIX

EVIDENCE FOR EQUILIBRATION AND EFFECTIVENESS OF QUENCH IN EXPERIMENTS ON THE LIMITS OF STABILITY

For Sn-saturation at 707°C, runs of 163 and 338 hr gave the same results. After 28 hr at 745°C, as-grown crystals and previously treated crystals with initial values of p^*_{300} of $7\times 10^{20}/\text{cm}^3$ and $2\times 10^{20}/\text{cm}^3$ respectively, both had values of $2{\cdot}5\times 10^{20}/\text{cm}^3$. A similar test in which equilibrium was again attained from both higher and lower apparent hole concentrations showed that 18 hr at 772°C and *a fortiori* 18 hr at 788·5°C, was sufficient for Sn-saturation. For the Te-saturation runs at 706°C, crystals run for 114 or 166 hr had nearly identical electrical properties. At 771°C, 17 hr was sufficient to convert crystals with initial values of p^*_{300} of 7 and 12×10^{20} cm^{-3} to a final value of $13{\cdot}5\times 10^{20}$ cm^{-3}. Although the 433 hr runs at 550°C were preceded by heat treatment at 700°C for 92 hr, the fact that equilibrium was attained was not established.

The effectiveness of the quench rate was checked using crystals previously saturated with Sn or Te near 700°C in "double tubes" and quenched. As described in the experimental section, in a double tube the crystals are surrounded by the 10 g ingot and are therefore cooled less slowly upon quenching than if they were in direct contact with the outside walls of the silica tube. These crystals were sealed in evacuated silica tubes, heated for 12 to 15 min at 700°C, and quenched in brine. The Hall constants were found to have changed by less than 10 per cent. From Fig. 1, it is seen that SnTe saturated with Sn at a high temperature remains within the field of stability at least to about 600°C when cooled. Thus, down to this temperature, a major thermodynamic driving force for composition change by internal precipitation, is not encountered. It has been observed elsewhere$^{(12)}$ in an investigation of the thermoelectric power of SnTe that samples of the same size and apparent hole concentrations as used here can be heated for hours near 200°C and minutes near 500°C with no significant change in the thermoelectric power either at temperature or upon cooling. We therefore conclude that the quench rates used here were adequate in freezing in the high temperature net acceptor concentrations.

REFERENCES

1. HANSEN M., *Constitution of Binary Alloys* 2nd. ed. McGraw-Hill, New York (1958).
2. HOUSTON B. B., BIS R. F. and GUBNER E., *Bull. Amer. phys. Soc.* Series II, **6**, 436 (1961).
3. MAZELSKY R. and LUBELL M. S., to be published under the *Symposium on Non-Stoichiometry* in *J. inorg. Chem.*
4. MCHUGH J. P. and TILLER W. A., *Trans. met. Soc. AIME* **218**, 187 (1960); HEIKES R. R., MILLER R. C. and URE R. W., JR. *Thermoelectricity* p. 405. Interscience Publishers, New York (1961).
5. BREBRICK R. F. and ALLGAIER R. S., *J. chem. Phys.* **32**, 1826 (1960). BREBRICK R. F. and GUBNER E., *ibid.* **36**, 1283 (1962).
6. ALBERS W., HAAS C., OBER H., SCHODDER G. R. and WASSCHER J. D., *J. Phys. Chem. Solids* **23**, 215 (1962).
7. BREBRICK R. F. and GUBNER E., *J. chem. Phys.* **36**, 170 (1962).
8. ALBERS W., HAAS C., VINK H. J. and WASSCHER J. D., *J. appl. Phys.* **32**, 220 (1961).
9. BLOEM J. and KROGER F. A., *Z. phys. Chem.* **7**, 1 (1956).
10. SAGAR A. and MILLER R. C., *Bull. Amer. phys. Soc.* Series II, **7**, 203 (1962).
11. ALLGAIER R. S. and SCHEIE P. O., *Bull. Amer. phys. Soc.* Series II, **6**, 436 (1961).
12. BREBRICK R. F. and STRAUSS A. J., *Bull. Amer. phys. Soc.* Series II, **7**, 203 (1962).
13. The author is indebted to Dr. A. J. STRAUSS and Mr. R. MCLEAN of this Laboratory for growing the SnTe crystals used in this investigation.

14. The author is indebted to Miss M. FINN for developing the etch. The crystals are immersed at room temperature for 15 min in 20 ml of 15 per cent NaOH plus 20 ml of saturated sodium persulfate solution, then rinsed successively in 10 per cent H_2O_2 and distilled water.
15. ROSSER W. F. and LONBERGER S. T., *Nat. Bur. Stand. Wash.* Circular **590** (1958).
16. SMAKULA A. *Methods of Experimental Physics*, (edited by LARK-HOROVITZ K. and JOHNSON V. A. Vol. **6**, Part A, Chap. 4.1, Academic Press (1959).
17. The author is indebted to Mr. A. MARIANO of this Laboratory for determining the lattice constants.
18. NESTEROVA YA. M., PASHINKIN A. S. and NOVOSELOVA A. V., *Zh. neorgan, khim.* **6**, 2014 (1961).
19. BROOKS L. S., *J. Amer. chem. Soc.* **74**, 227 (1952).
20. *Handbook of Chemistry and Physics, 42nd ed.* p. 2247. Chemical Rubber Publishing Co., Cleveland (1960).
21. The author is indebted to Dr. E. B. OWENS and Mr. F. DUNNINGTON of this Laboratory for performing the spectroscopic analyses. The SnTe samples were dissolved and compared against a series of synthetic standard solutions.
22. BREBRICK R. F., *J. Phys. Chem. Solids* **18**, 116 (1961).
23. ALLGAIER R. S., *Proceedings of the International Conference of Semiconductor Physics* p. 1037. Czechoslovak Academy of Sciences, Prague (1961).
24. HASHIMOTO K. and HIRAKAWA K., *J. phys. Soc. Japan* **11**, 716 (1951).

J. Phys. Chem. Solids Pergamon Press 1963. Vol. 24, pp. 37–44. Printed in Great Britain.

LUMINESCENCE IN ZnS, Se:Cu, Cl

F. F. MOREHEAD

International Business Machines Corporation, Thomas J. Watson Research Center,
Yorktown Heights, New York

(*Received* 18 *June* 1962)

Abstract—A series of ZnS, Se phosphor alloys activated with $1 \cdot 5 \times 10^{-3}$ Cu and 10^{-3} Cl was investigated for the wavelength dependence of the excitation and quenching of photoluminescence and the photoluminescence emission. Glow curves and the temperature dependence of the photoluminescence were also studied. The objective of this work is simply to show the position of the recombination and trapping levels that exist in these materials as a function of the varying base lattice composition and band edge. A modified SCHÖN–KLASENS(1,2) model is shown to accommodate the data with a satisfactory degree of consistency. The chemical nature of the centers that are actually responsible for the levels is not deduced.

INTRODUCTION

SEVERAL recent studies(2, 3, 4, 5, 6, 7) of optical effects in ZnS have shown that the simple, one-level model for activator centers is inadequate. Further, attempts have been made to assign the well-known "blue" and "green" emissions of ZnS:Cu to the same doubly ionizable center.(7, 4) The most successful effort to assign the transitions responsible for absorption, excitation, quenching, etc. with this model is that of BROSER and SCHULZ.(4) A schematic modification of this model is shown in Fig. 1 with the appropriate transitions involving this center in its un-ionized, singly ionized, and doubly ionized states. The transition for the optical stimulation of phosphorescence is shown in a separate center (T), although both MEIJER(2) and (more tentatively) BROSER(4) suggest that transitions within (C) are responsible for the spectral dependence of stimulation as well as quenching. It is a major purpose of the present work to show the variation of the activator levels with composition in the ZnS, ZnSe series and to account for the simulation data.

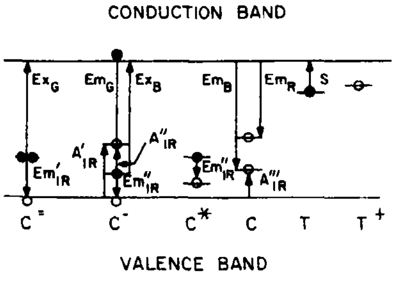

FIG. 1. The doubly ionizable center in ZnS:Cu.

MATERIALS

Alloys of ZnS and ZnSe containing 0, 20, 40, 60, 80 and 100 per cent at. per cent ZnSe were prepared by firing the luminescent grade materials in sealed quartz capsules at 950°C. for 2·5 hr with 0·0015 Cu and 0·001 Cl as CuS and CuCl. The products were quenched in air and given a cyanide wash.

APPARATUS

The source of high energy radiation was a high-pressure Xe lamp with a 250 mm Bausch and Lomb grating monochromator, the slit widths of which were set at each wavelength to give a constant photon intensity. The longer wavelength radiation used in the quenching and stimulation measurements came from a Sylvania type DXL movie lamp and a Perkin Elmer 98 monochromator with a quartz prism, where again the slit widths were set for constant photons at each wavelength. The emission spectra (visible only) were measured with the Perkin Elmer monochromator and a 1P22 photomultiplier detector. The samples were mounted on a Cu block within a metal Dewar with a quartz window to allow measurements at nitrogen temperatures. With the insertion of a heater, we could measure the thermal glow and the temperature dependence of the visible luminescence. A 1P21 photomultiplier with the appropriate Corning filters was used to measure the quenching and stimulation of the visible luminescence as well as the thermoluminescence and temperature dependence of the photoluminescence. Provision was also made for electrical contact to a conducting silica disc so that electric fields could be applied to the phosphor powders as required for measurements of photoconductivity, electroluminescence, and electrophotoluminescence. The electrical contact also made possible the measurement of pulsed and continuous Dember effect currents. This latter technique was described previously.[8]

MEASUREMENTS

Emission and excitation

Figure 2 shows four of the visible emission spectra obtained at 80°K, at which temperature the separation of the two emission bands present in each case is readily determined. At room temperature the resolution is poorer and the contribution of the high energy band much weaker. The exciting radiation was extrinsic in each case, but quite close to the gap. The energy of the forbidden gap was determined from pulsed Dember measurements.[8] (The wavelength at which the Dember current pulse falls most rapidly with increasing wavelength is taken to be that corresponding to the width of the forbidden energy band.)

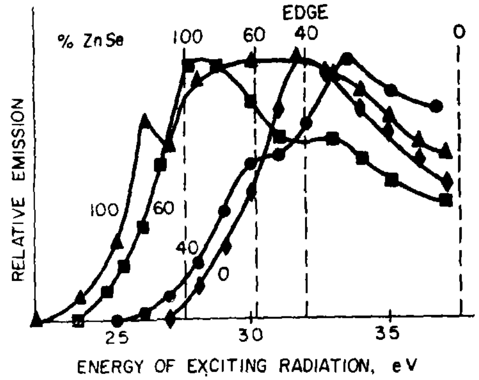

Fig. 3. Excitation spectra of ZnS, Se:Cu, Cl at 80°K. The number indicate the percentage (atomic) ZnSe. The vertical lines indicate the position of the band edge.

Figure 3 shows four of the excitation spectra for visible luminescence measured at 80°K. The relative heights are not intended to be significant in determining comparative quantum efficiencies from one phosphor to another. Equal photon intensities were used at each wavelength. Figure 4 shows the excitation spectra for the same four phosphors at room temperature. One should note that for 60 per cent ZnSe and above, no exciting radiation less energetic than the edge is effective in producing visible luminescence. The strong thermal quenching of these phosphors (> 60 per cent ZnSe), to be described below, is undoubtedly

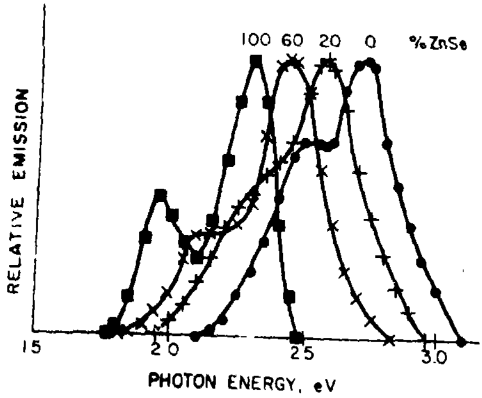

Fig. 2. Emission spectra of ZnS, Se:Cu, Cl at 80°K.

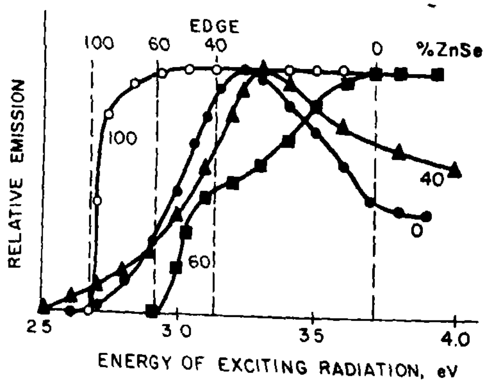

Fig. 4. Excitation spectra of ZnS, Se:Cu, Cl at 300°K. The vertical lines indicate the position of the edge.

responsible for this fact. Only the high excitation densities produced at the phosphor surfaces by strongly absorbed band gap light can overcome the thermal release of holes into the valence band and the consequent decreases in radiative transitions.

Quenching and stimulation

Figure 5 shows the relative effect of low energy radiation in decreasing the room temperature fluorescence excited by extrinsic radiation. No infra-red quenching was observed at room temperature for 80 and 100 per cent ZnSe. Equal photon intensities of the infra-red were used (about ten times the photon intensity of the exciting radiation). Figure 6 shows the spectral dependence of infra-red radiation in quenching the visible fluorescence at 80°K, which was obtained for all samples. In the case of ZnS:Cu, Cl, a region of continuous enhancement of the fluorescence was obtained which peaks near 1 eV.

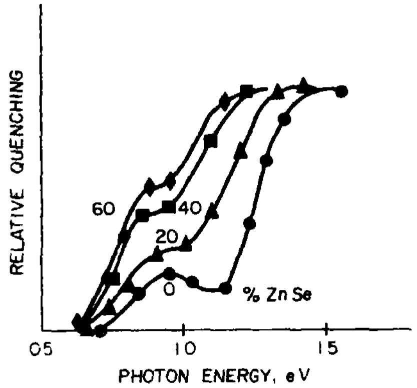

FIG. 5. Quenching of the visible fluorescence at 300°K for ZnS, Se:Cu, Cl.

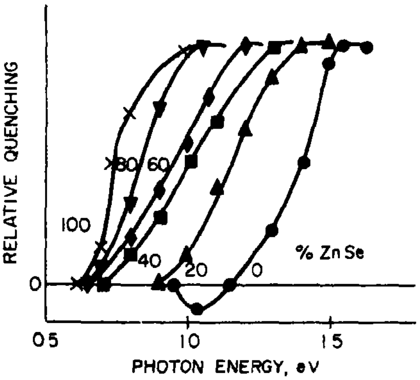

FIG. 6. Quenching of the visible fluorescence at 80°K for ZnS, Se:Cu, Cl.

The spectral dependence of the infra-red stimulation of phosphorescence at 80°K is shown in Fig. 7 for the ZnS, Se:Cu, Cl phosphors. When the extrinsic exciting radiation was removed, the phosphorescence was allowed to decay to a negligible value, and the sample was then exposed to the stimulating infra-red light. A burst of visible phosphorescence occurred, followed by a roughly exponential decay. The peak value of the stimulated burst is plotted in Fig. 7 as the relative stimulation. (A momentary burst of emission, similar in shape and spectral dependence, also occurs when the exciting, extrinsic light is on and the infra-red light is applied, followed, of course, in most cases, by a continuous quenching of the fluorescence.)

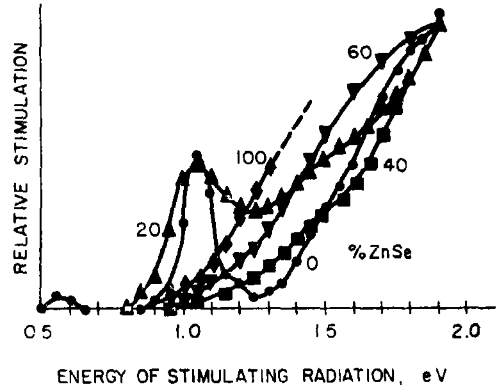

FIG. 7. Stimulation of the visible phosphorescence in ZnS, Se:Cu, Cl at 80°K.

Thermoluminescence and the temperature dependence of the photoluminescence

Figure 8 shows both the thermoluminescence (TL) glow curves and plots of the temperature dependence of the photoluminescence efficiency (TPL). Extrinsic radiation was used in each case to fill the traps for TL or to excite the phosphors for TPL. For the latter measurements, the same photon intensity was used on each phosphor. The results of an analysis of these data are shown in Table 1. The activation energies E_a for the TL were computed from the slope of the logarithm of

Table 1. Analysis of thermoluminescence and temperature dependence of luminescence efficiency data

per cent ZnSe	T_m, glow	E_a, glow	$T_{1/2}$PL	E'_a, PL
0	133, 191°K	0·15-0·32, 0·31 eV	412°K	1·05 eV
20	120	0·3-0·4	278	1·0
40	106	0·2	315	0·6
60	106, 165	0·2, 0·3 eV	263	0·5
80	—	—	243	0·45
100	—	—	238	0·4

the light intensity vs. the reciprocal absolute temperature at the leading edge of the glow curves. To obtain E_a for the last traps to be emptied during the TL as well as the first, the glowing phosphor is quickly cooled to 80°K before the glow curve has been completed and the linear heating (0·3°K/sec) begun again. A leading edge is produced which is suitable for the above activation energy analysis and which corresponds to the deeper traps. The shift in the temperature of the glow peak with composition is smaller than that reported by HOOGENSTRAATEN;(9) the changes in the values of E_a are neither large nor particularly consistent with any trend.

The column headed $T_{1/2}$, PL indicates the temperature at which the photoluminescence has dropped to half its maximum. The activation energies E'_a for the thermal escape of holes from radiative recombination centers were computed from the usual relation

$$I = I_0/[1+b\exp(-E'_a/kT)],$$

where I is the emitted luminescence at temperature T, I_0 is the maximum value of I, and b is a constant which is independent of T.

Electrophotoluminescence

In the case of ZnS:Cu, Cl, the application of a small positive field (about 10^3 V/cm) to the surface of the phosphor which is illuminated with intrinsic (strongly absorbed) radiation produces a momentary increase in photoluminescence, while the removal of this field, or the application of a negative field produces a momentary decrease in the luminescence. This behavior is consistent with the radiative recombination of trapped holes and free electrons.(8, 10) The latter are drawn toward the narrow excitation region at the illuminated surface by a positive field, increasing the luminescence, and are repelled from this region by a negative field, diminishing the luminescence. ZnSe:Cu, Cl shows only decreases in luminescence for applied fields of either sign. This behavior may be due to the low activation energy for the escape of holes from the recombination centers (Cf. Table 1), so that, at room temperature, both holes and electrons can be displaced by the field. The 20 and 40 per cent ZnSe phosphors behaved similarly to ZnS. The 60 per cent ZnSe sample showed only momentary decreases in luminescence for fields of either sign, but the decrease was smaller for the positive field. While a more extensive series of experiments and a more complicated analysis than that described here are required to produce completely unambiguous results, the present experiments are at least not inconsistent with the radiative recombination of free electrons and trapped holes.

DISCUSSION

Figure 1 shows the possible states of the doubly ionizable center (C), plus those of the trapping level (T) involved in stimulation (S). Filled levels in the forbidden and conduction bands are indicated by solid circles (electrons), while empty levels in the forbidden and valence bands are represented by empty circles (holes). The chemical identity of the center is not shown since the evidence (magnetic susceptibility) on this point is ambiguous.(11) Ex_G is the ionization of C^{2-} which leads to green emission (Em_G) when a conduction electron recombines with C^-. The recombination of a free hole with C^{2-} results in an infra-red emission (Em_{IR}). Ionization of C^-(Ex_B) leads to blue enission Em_B when a free electron recombines with C (or possibly to red emission (Em_R) in some cases

82554
30.11.62

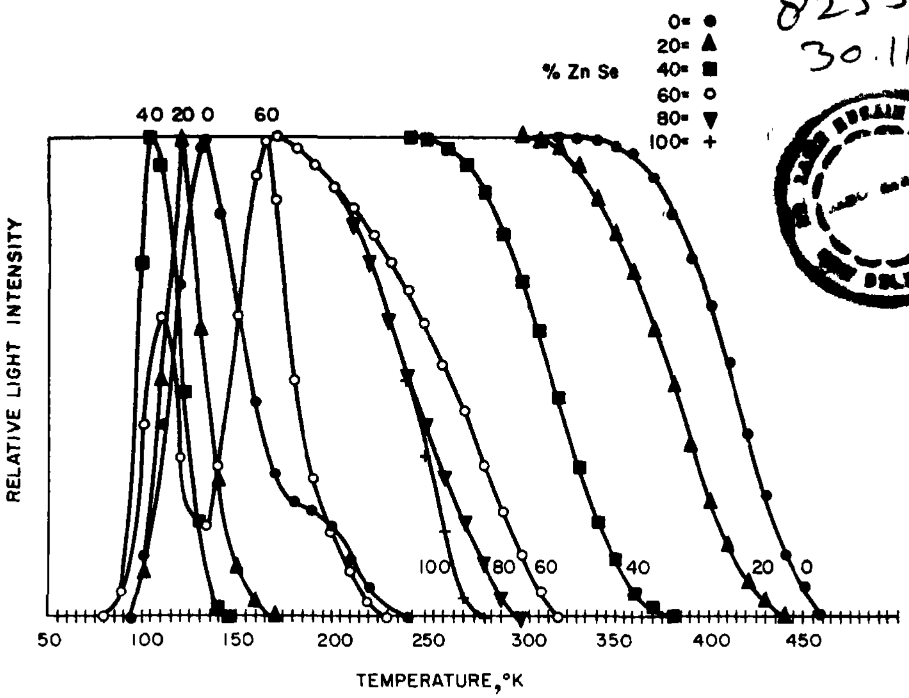

Fig. 8. Thermoluminescence and the temperature dependence of the photoluminescence efficiency for ZnS, Se:Cu, Cl.

as suggested by Broser[(4)]). The excitation of a valence electron into $C^-(A'_R)$ quenches the green emission Em_G, or it may lead to infra-red emission Em'_{IR}. The excitation of a valence electron into $C(A'''_{IR})$ leads to a quenching of the blue emission Em_R or possibly to an infra-red emission Em''. Excitation within $C^-(A''_{IR})$ leads to an excited state C^{-*}, which may be followed either by (a) infra-red emission Em'''_R on relaxation or (b) a thermal equilibration with the valence band. During this latter process, (b), an electron has been raised from the valence band to C^{-*}, which then relaxes into the ground state of C^{2-}; as a result there is quenching of the green emission. This thermal equilibration occurs at room temperature but not at that of liquid nitrogen.

A tabulation of the above transition energies for ZnS, taken from this work and from other publications is given in Table 2. Although $\mathrm{Em}_G + A_R$ $\mathrm{Ex}_G + \mathrm{Em}'_{IR}$, $\mathrm{Em}_B + A'''_{IR}$ and $\mathrm{Ex}_B + \mathrm{Em}''_{IR}$ need not, necessarily exactly equal the band gap (or greater, to allow for Frank–Condon shifts) the reasonably close agreement (3·85, 3·83, 3·9 and 3·95 eV) is comforting.

Table 2. Transition energies for ZnS :Cu, Ce

Transition	Optical	Thermal
Ex_G	3·0 eV	
Ex_B	3·2	
Em_G	2·5	
Em_B	2·7	
Em_R	1·85[(4)]	
A'_{IR}	1·35	1·1 eV
A''_{IR}	0·95	
A'''_{IR}	1·20	
Em'_{IR}	0·83[(2, 4, 7)]	
Em''_{IR}	0·75[(2, 4, 7)]	
Em'''_{IR}	0·69[(2, 4, 7)]	
S	1·1	0·3
Gap	3·7	

Figure 9 shows the experimentally determined energies of most of the transitions indicated in

Fig. 1 for the ZnS, Se:Cu, Cl phosphors as a function of composition. First, it will be noted that the sum of Em_G and A'_{IR} is only slightly greater than the gap in each case. Further, the total shift in A'_{IR} is nearly 2/3 of the decrease in band gap, while that of Em_G is only 1/3. The position of the empty level in Cl remains nearly constant with respect to its distance from the conduction or Zn^{2+} band.

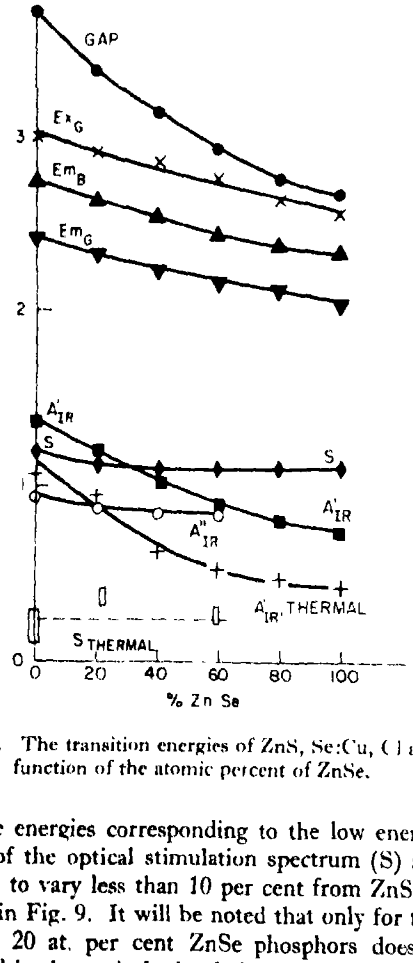

FIG. 9. The transition energies of ZnS, Se:Cu, Cl as a function of the atomic percent of ZnSe.

The energies corresponding to the low energy edge of the optical stimulation spectrum (S) are shown to vary less than 10 per cent from ZnS to ZnSe in Fig. 9. It will be noted that only for the 0 and 20 at. per cent ZnSe phosphors does a "peak" in the optical stimulation spectrum occur, at around 1·2 microns. (Figure 7.) For these two cases only, the optical stimulation of the phosphorescence extends to longer wavelengths than that of the optical quenching of the fluorescence. For all the other samples, quenching occurs for all wavelengths which produce stimulation. If the same wavelength produces both stimulation of the phosphorescence and quenching of the fluorescence, then the observed stimulation is less than that which would occur in the absence of the quenching. Thus an increase in the observed stimulation with increasing wavelength would be expected at a particular wavelength if at that wavelength the quenching effect cuts off. It is reasonable then to conclude that the peaked structure in the optical stimulation edge for the ZnS and $ZnS_{0\cdot8}Se_{0\cdot2}$ is due to the occurrence of the quenching edge at shorter wavelengths and not to a narrow transition energy band.

The energies corresponding to the thermal transitions S and A'_{IR} are also shown in Fig. 9. These energies were obtained from thermoluminescence and temperature dependence of photoluminescence studies described in the Measurements section. (Cf. Fig. 8 and Table 1.) The optical transition in ZnS that is usually associated with the 0·3 eV glow curve is the small stimulation peak at around 2·5 microns.(2, 4) This latter light is relatively ineffective in either stimulating phosphorescence or in reducing the amount of thermoluminescence, when compared to, say 1·1 eV light. Also, heating to 200°K (approximately the highest temperature at which glow was observed in the ZnS sample) completely eliminated all optical stimulability measured at 80°K. One therefore, associates the optical stimulation at 1·1 eV and the 0·3 eV glow peak.

The energy corresponding to the peaks in the optical quenching spectra measured at room temperature are plotted in Fig. 9 as A'_{IR} (cf. Fig. 5). As would be expected from this model, no quenching corresponding to A''_{IR} occurs at liquid nitrogen temperature. (Figure 6.) The value of A''_{IR} was unobtainable in this way from 80 and 100 per cent ZnSe since there was no measurable quenching of the visible luminescence in these samples at room temperature. The strong thermal quenching of those phosphors (ZnSe and $ZnS_{0\cdot2}Se_{0\cdot8}$) is such so as to make the optical effect negligible at room temperature (cf. Fig. 8).

It should also be mentioned that when an effort was made to distinguish between the quenching edge for the blue emission A_{IR} and that for the green A'_{IR} at 80°K in ZnS, a difference of 0·15 eV was obtained; that is A'''_{IR} = 1·20 eV, as indicated in Table 2. As would be predicted from the model, the stimulation spectra were identical for both blue and green emission.

The small variation of the stimulation edge S with composition in going from ZnS to ZnSe shows that the T level also maintains its constant separation from the conduction or Zn^{2+} band, as one expects from an ionic picture of the II–VI compounds.(12) This expectation follows from the identification of the T levels with conduction or Zn^{+} states perturbed into the forbidden band by the added impurities. A similar view of the C^{-} level as a perturbed S^{2-} or valence band level predicts a drastic change in the transition A'_{IR} in going from ZnS to ZnSe, which prediction accords with the present observations.

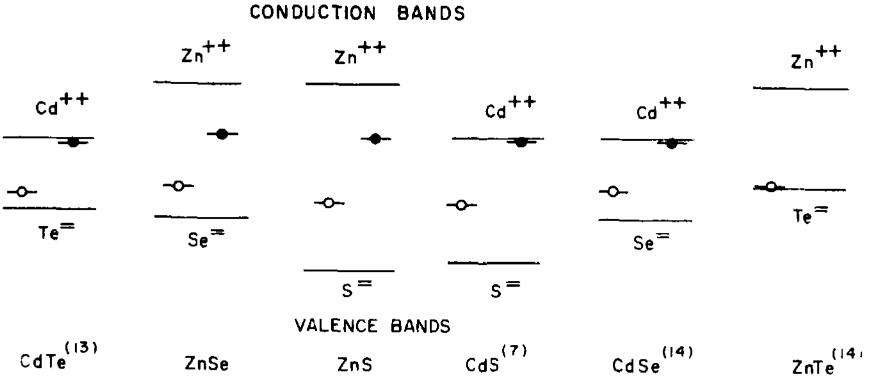

FIG. 10. A schematic presentation of C^{-} and T levels in the forbidden gap of several II–VI compounds.

Figure 10 shows the experimentally determined positions of the C^{-} and T levels in several II–VI compunds,(7, 13, 14) including the present data on ZnS and ZnSe. In each case, for all compounds containing the same anion the separation of the C^{-} level from the valence band is the same; for all compounds containing the same cation the energy separation of the T level from the conduction band is constant. The agreement of the data with the ionic model of the II–VI's, in which the conduction band is associated with the cation and the valence band with the anion,(12) is surprisingly good. Further it is interesting to note that the separation of both levels from the valence band is nearly the same for compounds having the same anion; and that the energy difference of both levels is also nearly constant for the common cation compounds. That is, the energy separation between the C^{-} and the T levels themselves is approximately a constant.

To sum up, the present data from ZnS, Se:Cu, Cl agree with the energy level diagram in Fig. 1, which is essentially a modification of the Schön–Klasens model. The "blue" and "green" recombination centers are represented as two of the three possible states of a single doubly ionizable center. It has also been shown that the optical stimulation edges in these materials agree with a rather deep T level and that the 1·2 micron stimulation "peak" in ZnS (and in $ZnS_{0.8}Se_{0.2}$) is not due to a definite narrow band transition but to the overlap of the stimulation and quenching edges at that point.

Acknowledgement—The author wishes to express his thanks to Dr. S. P. KELLER for helpful discussion and support, to Dr. L. SUCHOW for the sample preparation, and to Mr. W. N. HAMMER for assistance in making the measurements.

REFERENCES

1. SCHÖN M., *Halbleiter Probleme* **4**, 282 (1958).
2. KLASENS H. A., *J. Phys. Chem. Solids* **7**, 175 (1958).
3. APPLE E. F. and PRENER J. S., *J. Phys. Chem. Solids* **13**, 81 (1960).
4. BROSER I. and SCHULTZ H. J., *J. electrochem. Soc.* **108**, 545 (1961).

5. MELAMED N. T., *J. electrochem. Soc.* **97**, 33 (1950).
6. BUBE R. H., *Phys. Rev.* **99**, 1105 (1955).
7. BROWNE P. F., *J. Electron.* **1**, 1, 95 (1956); ibid. **1**, 154 (1956).
8. MOREHEAD F. F. and FOWLER A. B., *J. electrochem. Soc.* **109**, 688 (1962).
9. HOOGENSTRAATEN W., *Philips Res. Rep.* **13**, 515 (1958).
10. HALSTED R. E., *Phys. Rev.* **99**, 1897 (1955).
11. BOWERS R. and MELAMED N. T., *Phys. Rev.* **99**, 1781 (1955).
12. KLASENS H. A., *J. electrochem. Soc.* **100**, 72 (1953).
13. JENNY D. A. and BUBE R. H., *Phys. Rev.* **96**, 1190 (1954).
14. BUBE R. H. and LINDS, E. L., *Phys. Rev.* **110**, 1040 (1958).

J. Phys. Chem. Solids Pergamon Press 1963. Vol. 24, pp. 45–50. Printed in Great Britain.

CRYSTAL STRUCTURES OF ADAMANTINE COMPOUNDS

P. C. NEWMAN
Mullard Research Laboratories, Redhill, Surrey

(*Received* 26 *July* 1962)

Abstract—A method is given for deriving the crystal structures of adamantine compounds by the stacking of hexagonal nets. This leads to a series of structures for compounds of the formulae ABC_2, A_2BC_3, and A_3BC_4, many of which have been observed in actual compounds. This method of deriving crystal structures is also useful in the case where only part of the crystallographic information has been obtained from X-rays.

1. INTRODUCTION

SEVERAL elements and many compounds crystallize with a fourfold tetrahedral co-ordination of atoms. These are generally known as adamantine materials; typical compounds are GaAs, ZnO, SiC. The crystal structures of adamantine materials may be depicted by two interlocking sub-lattices, with equal numbers of sites on each sub-lattice. In GaAs, these sub-lattices are geometrically similar to cubic close-packed atoms of one element only, in ZnO to hexagonal close-packed atoms, and in SiC to a mixed close-packing. However, adamantine materials also exist with unequal distributions of atoms on each sub-lattice, and the structure of these compounds will be considered in this paper.

When the structures of adamantine compounds are considered in the form of two sub-lattices, it is found that each lattice site is surrounded by four sites on the other sub-lattice. However, it is also possible to consider the structures to be built up from nearly plane nets with hexagonal symmetry. Three of the bonds from one atom to its neighbours lie in the net, while the fourth is perpendicular to the mean plane of the net. The structure of such a net is shown in Fig. 1.

The different crystal structures can then be built up by the stacking of such nets, each net being itself stoichiometric. It must be assumed that the stacking is arranged so that consecutive nets are connected by bonds between atoms of the two different types. Then the zincblende structure will be built up by consistent cubic stacking, the wurtzite structure by consistent hexagonal stacking and the various polytypes of SiC by a mixed, but repetitive, stacking. All these stacking sequences obey the conditions that each atom on the A sub-lattice is surrounded by 4 nearest neighbours on the B sub-lattice and 12 next-nearest neighbours on the A sub-lattice.

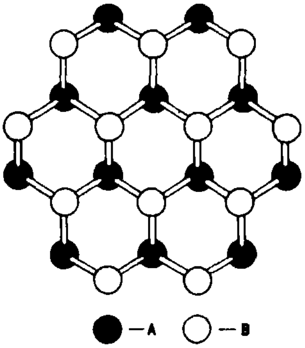

FIG. 1. Hexagonal net, AB compounds.

2. HEXAGONAL NETS AND SETS OF NEIGHBOURS

The compounds to be considered in this paper have the formulae A_2BC_3, ABC_2, or A_3BC_4. These are the three simplest deviations from the typical formula AB. The hexagonal nets for these compounds are shown in Figs. 2–4. It is also quite easy to calculate the simplest arrangement of neighbours and next-nearest neighbours for all types of atoms in the compounds (see Ref. (1) for the case of A_2BC_3 compounds). The arrangements of neighbours will control the possible stacking sequences for the nets, and also the structure of the nets themselves.

For the compounds of the type A_2BC_3, the table of neighbours is shown in Table 1.

Table 1. *A_2BC_3 compounds*

Atom	Neighbours	Next-nearest neighbours
A	1 $C(X)$ and 3 $C(Y)$	7 A and 5 B
B	2 $C(X)$ and 2 $C(Y)$	10 A and 2 B
$C(X)$	2 A and 2 B	2 $C(X)$ and 10 $C(Y)$
$C(Y)$	3 A and 1 B	5 $C(X)$ and 7 $C(Y)$

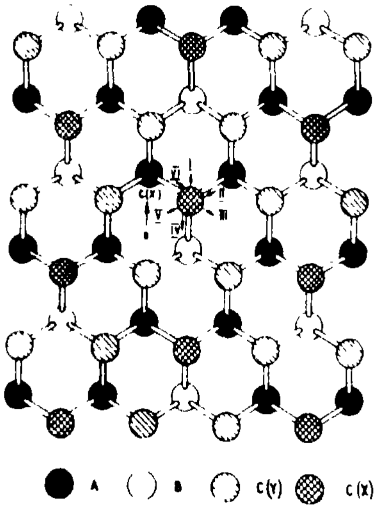

FIG. 2. Hexagonal net, A_2BC_3 compounds.

It can be seen that there must be two types of C atom, which are defined by their nearest neighbours.(1)

The hexagonal net for A_2BC_3 compounds is shown in Fig. 2; this contains a unique direction, shown by the arrow $B \rightarrow C(X)$. The B atoms (and also the $C(X)$ atoms) are arranged in a hexagonal pattern in the net. It is possible to construct other nets, but these do not appear to lead to any fresh structures.

For compounds of the type ABC_2, the table of neighbours is shown in Table 2.

Table 2. *ABC_2 compounds*

Atom	Neighbours	Next-nearest neighbours
A	4 C	4 A and 8 B
B	4 C	8 A and 4 B
C	2 A and 2 B	12 C

Here, it is only necessary to use one type of C atom.

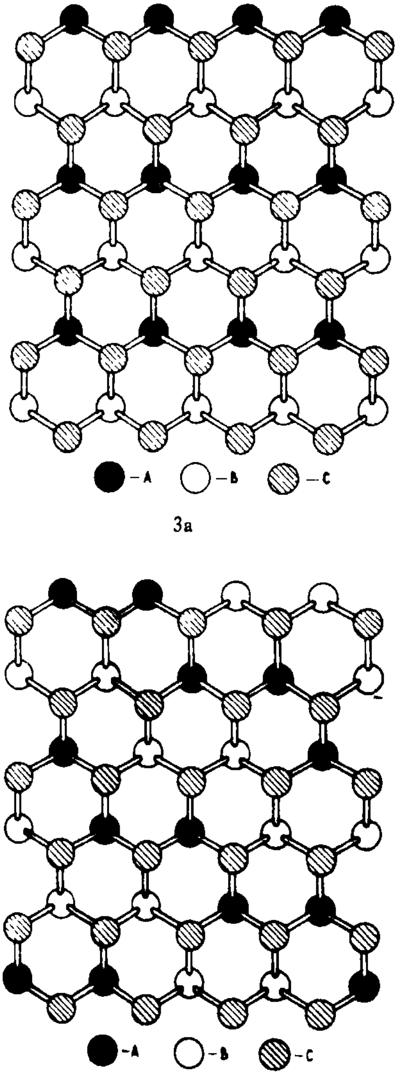

3a

3b

FIG. 3. Hexagonal nets, ABC_2 compounds.

The hexagonal nets for ABC_2 compounds must contain alternate lines of A and B atoms. The two simplest cases are shown in Fig. 3; in Fig. 3a, the lines are straight, but in Fig. 3b the lines are zig-zag (with the shortest possible repeat distances). More complicated zig-zags are, of course, possible, but will not be considered here.

For compounds of the type A_3BC_4, the table of neighbours is shown in Table 3.

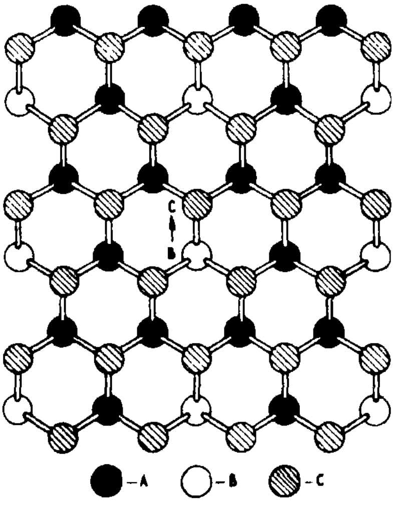

4a

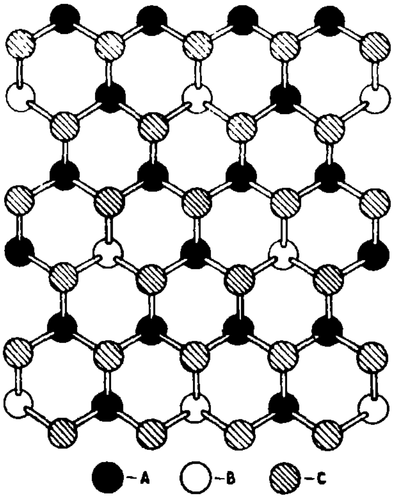

4b

FIG. 4. Hexagonal nets, A_3BC_4 compounds.

Table 3. *A_3BC_4 compounds*

Atom	Neighbours	Next-nearest neighbours
A	4 C	8 A and 4 B
B	4 C	12 A
C	3 A and 1 B	12 C

There are only two possible types of hexagonal net for A_3BC_4 compounds. That shown in Fig. 4a has a rectangular pattern of B atoms with a unique direction $B \rightarrow C$ while that in Fig. 4b has a hexagonal pattern of B atoms, but with no unique direction. There do not appear to be any other forms of net, which will allow stacking.

3. CRYSTAL STRUCTURES

3.1 A_2BC_3 *compounds*

These are built up by stacking the nets shown in Fig. 2 one above the other. Because of the conditions laid down by the neighbours, they must be stacked with a B in one net above a $C(X)$ in the net below. When this is done, there are six ways of setting the unique direction in the upper net relative to that in the lower net. If this setting is maintained for all layers, the six structures shown in Table 4 are obtained. These structures have been deduced previously(1) by a less rigorous method. However, it is always possible to have a mixed form of stacking, as will be discussed below.

Several of these crystal structures have been observed in III–VI compounds, where the B atom represents a vacant site. The structure I has been found for In_2Te_3(2) and the structures II and VI (an enantiomorphous pair) for Ga_2S_3,(3) β-In_2Se_3.(4)

Table 4. *A_2BC_3 structures*

Type	Space Group	Z	Unit cell dimensions a_0 for disordered zincblende		
			a	b	c
I	C_{2v}^{20}–$Imm2$	2	$a_0/\sqrt{2}$	$3a_0/\sqrt{2}$	a_0
II	C_6^3–$P6_5$	6	$\sqrt{\frac{3}{2}}\,.\,a_0$		$2\sqrt{3}\,.\,a_0$
III	C_3^3–$P3_2$	3	$\sqrt{\frac{3}{2}}\,.\,a_0$		$\sqrt{3}\,.\,a_0$
IV	C_{2v}^{12}–$Cmc2_1$	4	$3a_0/\sqrt{2}$	$\sqrt{\frac{3}{2}}\,.\,a_0$	$2a_0/\sqrt{3}$
V	C_3^2–$P3_1$	3	$\sqrt{\frac{3}{2}}\,.\,a_0$		$\sqrt{3}\,.\,a_0$
VI	C_6^2–$P6_1$	6	$\sqrt{\frac{3}{2}}\,.\,a_0$		$2\sqrt{3}\,.\,a_0$

(Z = number of formula units in unit cell.)

The case of Ga_2S_3 is of particular interest. HAHN and FRANK⁽³⁾ originally obtained a unit cell for Ga_2S_3 consisting of types II or VI stacking. Recently, GOODYEAR *et al.*⁽⁵⁾ have published results giving a monoclinic unit cell for Ga_2S_3 and proposing one of the space groups C2, C2/*m*, or *Cm*. If the *a* and *c* axes of this unit cell are transformed as shown in Fig. 5 then the close-packed *S* planes become (001) planes. The only way of obtaining this unit cell from the hexagonal net of Fig. 2 is by the stacking sequence –II–VI–II–VI–.

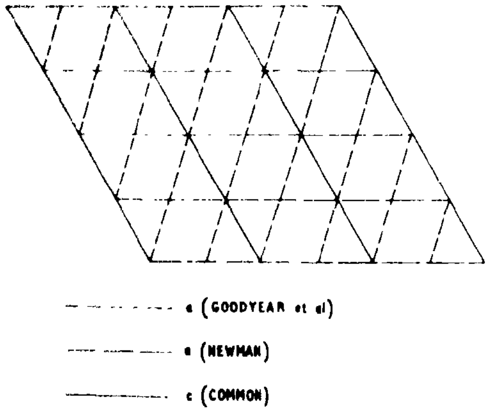

FIG. 5. Relation between *a*, *c* in the two monoclinic unit cells for Ga_2S_3.

This would give a side-centred monoclinic cell with the space group C_s^4–*Cc*. The shape of this cell agrees well with the experimental result of Goodyear *et al.* as shown below and GOODYEAR has more recently confirmed⁽⁶⁾ that the space group *Cc* is indeed consistent with his results.

Ga_2S_3 *Unit cell*

	a: *b*	*b*: *c*	*β*
Calc.	1·732	0·9045	121·48°
Obs.	1·738	0·9109	121·85°

The two structures are compared in Figs. 6 and 7.

It seems likely that the crystal structures of Al_2S_3⁽⁷, ⁸⁾ and Tl_2Te_3,⁽⁹⁾ which are not yet completely resolved, may be determined by thinking along the same lines.

3.2 *ABC_2 compounds*

Taking the two hexagonal nets shown in Fig. 3, four crystal structures may be built, by using either cubic or hexagonal stacking consistently with each net. It is not possible to mix the types of net, or have more than the two ways of stacking. The structures obtained are detailed in Table 5.

Table 5. ABC_2 structures

Type	Net	Space Group	*Z*	Unit cell dimensions a_0 for disordered zincblende *a*	*b*	*c*
I	*A*	D_{2d}^5–$P\bar{4}m2$	1	$a_0/\sqrt{2}$		a_0
II	*A*	C_{2v}^2–$Pmc2_1$	2	$a_0/\sqrt{2}$	$\sqrt{\frac{3}{2}}\,.\,a_0$	$2a_0/\sqrt{3}$
III	*B*	D_{2d}^{12}–$I\bar{4}2d$	4	a_0		$2a_0$
IV	*B*	C_{2v}^9–$Pna2_1$	4	$\sqrt{\frac{3}{2}}\,.\,a_0$	$\sqrt{2}\,.\,a_0$	$2a_0/\sqrt{3}$

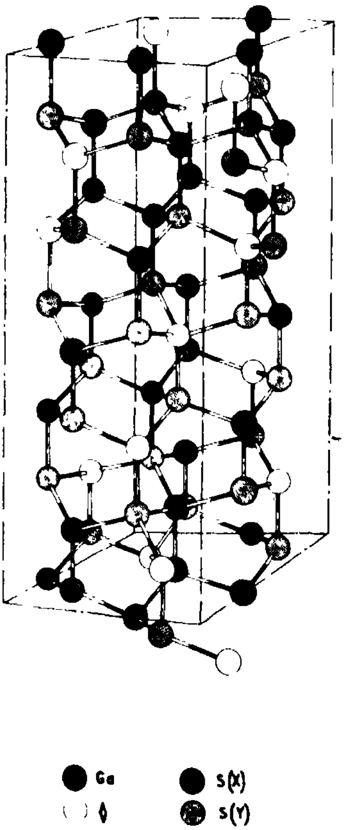

FIG. 6. Crystal structure of Ga_2S_3 according to HAHN and FRANK.⁽³⁾

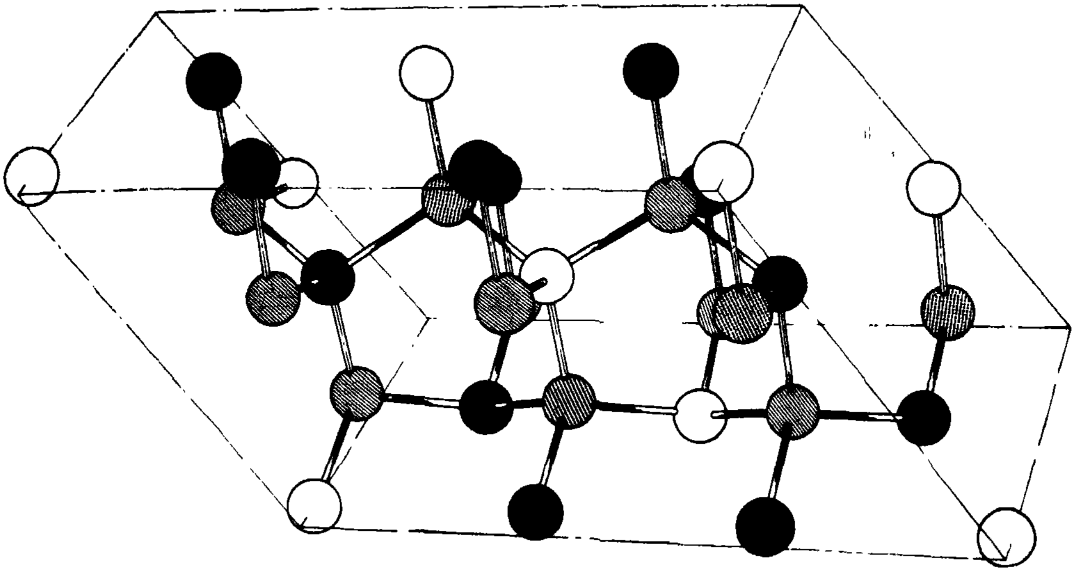

FIG. 7. Crystal structure of Ga_2S_3 from data of GOODYEAR *et al.*(5)

Structure III is the well known structure of chalcopyrite, $CuFeS_2$.(10) Recently, many other compounds have been found to have the same structure.(11, 12) However, HAHN *et al.*(11) found that ABC_2 compounds containing either Cu and Ga together or Ag and In together could not be indexed very convincingly on the basis of the chalcopyrite structure. All the lines found in the powder patterns can however be indexed on the basis of the structure I (but with the condition $h+k+l = 2n$). Because of the very similar scattering factors for the Cu and Ga atoms (or the Ag and In atoms) in their surroundings in these crystals, it is extremely difficult to distinguish by X-rays between this structure and the statistically distributed arrangement of metal atoms suggested by HAHN *et al.* Structure I, however, should give rise to some very weak extra lines with $h+k+l \neq 2n$. It also seems more likely that the structure will be distorted from exact tetrahedral bonding when the two types of metal atom are arranged in alternate layers than when they are randomly mixed.

3.3 A_3BC_4 *compounds*

There are four types of crystal structures which may be built by consistent cubic or hexagonal stacking with the two hexagonal nets shown in Fig. 4. It is not possible to mix the two types of net or have more than the two ways of stacking. The four structures are shown in Table 6.

Table 6. A_3BC_4 *structures*

Type	Net	Space Group	Z	Unit cell dimensions a_0 for disordered zincblende		
				a	*b*	*c*
I	*A*	D_{2d}^{11}–$I\bar{4}2m$	2	a_0		$2a_0$
II	*A*	C_{2v}^{7}–$Pmn2_1$	2	$\sqrt{2}\,.\,a_0$	$\sqrt{\frac{3}{2}}\,.\,a_0$	$2a_0/\sqrt{3}$
III	*B*	T_d^{5}–$F\bar{4}3c$	8	$2a_0$		
IV	*B*	C_{6v}^{4}–$P6_3mc$	2	$\sqrt{2}\,.\,a_0$		$2a_0/\sqrt{3}$

Structure I is the structure of the Luzonite–Famatinite series $Cu_3As_xSb_{1-x}S_4$,(13) and also of the compound Cu_3SbSe_4.(14) Structure II is the structure of Enargite Cu_3AsS_4(15) and of the compound Cu_3PS_4.(16) It is interesting to see that the compound Cu_3AsS_4 which occurs in two forms contains the same type of hexagonal net in both forms.

Recently, a new compound In_3Te_4 has been proposed in the In–Te system,[17] and it seems likely that this compound has tetrahedral bonding. If the existence of In_3Te_4 is confirmed, it may be expected to have a structure based on those detailed in Table 6.

4. CONCLUSIONS

A range of possible crystal structures has been derived for admantine compounds containing more than two differently situated atoms. These crystal structures are obtained by varying the stacking of hexagonal nets of atoms, which are themselves stoichiometric. Only very simple arrangements within the net have been considered. Many of the crystal structures so derived have been found to occur in actual compounds. Moreover, this recipe for the building up of crystal structures is very helpful in situations where insufficient X-ray data are available for a complete structure determination (for instance, only the unit cell may be known). However, it can not claim to be entirely exhaustive, without extension to more complicated hexagonal nets.

REFERENCES

1. Newman P. C., *J. Phys. Chem. Solids* **23,** 19 (1962).
2. Woolley J. C., Pamplin B. R. and Holmes P. J., *J. Less-Common Metals* **1,** 362 (1959).
3. Hahn H. and Frank G., *Z. anorg. Chem.* **278,** 333 (1955).
4. Semiletov S. A., *Sov. Phys. Crystallogr.* **5,** 673 (1961); *Krystallogr.* **5,** 704 (1960).
5. Goodyear J., Duffin W. J. and Steigmann G. A., *Acta Cryst.* **14,** 1168 (1961).
6. Goodyear J., unpublished.
7. Flahaut J., *Ann. Chim.* **7,** 632 (1952).
8. Geiersberger K. and Galster H., *Angew Chem.* **64,** 81 (1952).
9. Rabenau A., *Z. Metallk.*, **51,** 295 (1960).
10. Pauling L. and Brockway L. O., *Z. Kristallogr.* **82,** 188 (1932).
11. Hahn H. *et al.*, *Z. anorg. Chem.* **271,** 153 (1953).
12. Zhuze V. M., Sergeeva V. M. and Shtrum E. L., *J. Tech. Phys. Moscow* **28,** 2093 (1958). *Sov. Phys. Tech. Phys.* **3,** 1925 (1958).
13. Gaines R. V., *Amer. Min.* **37,** 291 (1952).
14. Wernick J. H. and Benson K. E., *J. Phys. Chem. Solids* **3,** 157 (1957).
15. Pauling L., and Weinbaum S., *Z. Kristallogr.* **88,** 48 (1934).
16. Ferrari A. and Cavalca L., *Gazz. Chim. Italia* **78,** 783 (1948).
17. Mason D. R., unpublished.

J. Phys. Chem. Solids Pergamon Press 1963. Vol. 24, pp. 51–62. Printed in Great Britain.

ION EXCHANGE IN POROUS CRYSTALS
PART I. SELF- AND EXCHANGE-DIFFUSION OF IONS IN CHABAZITES

R. M. BARRER, R. F. BARTHOLOMEW and L. V. C. REES

The Physical Chemistry Laboratories, The Chemistry Department,
Imperial College, London, S.W.7

(*Received* 18 *June* 1962)

Abstract—Self-diffusion and exchange diffusion kinetics have been studied for a number of ions in hydrated chabazites, and the corresponding diffusion coefficients have been determined. Values of the self-diffusion coefficients follow the Arrhenius equation [$D^* = D_0 \exp(E/RT)$]. The energy barriers, E, associated with each unit self-diffusion process are about 7 kcal for all the ions Na^+, K^+, Rb^+ and Cs^+; for Ca^{2+} and Sr^{2+} the barriers are approximately twice this magnitude, but for Ba^{2+} they are $8{\cdot}7_5$ kcal. The results have been considered in terms of the structure of the crystals and of the possibility that the periodic variation in the intracrystalline electrostatic field determines E. Entropies of activation, and also comparison with other rate processes in chabazite (self-diffusion of water, electrical conductivity and dielectric relaxation) suggest that ions and water molecules may participate together in each unit diffusion process. In mixed (Ca, Sr)-chabazites the self-diffusion coefficients D^* of Ca^{2+} and of Sr^{2+} each decrease strongly with the exchangeable cation fraction of Ca^{2+} and of Sr^{2+} respectively. Values obtained for exchange diffusion coefficients of Ca–Sr, Ca–Ba and Sr–Ba pairs are integral values over a range of cation fractions. Their relation with the self-diffusion coefficients is considered in the following paper (Part II).

1. INTRODUCTION

THE random walk of ions in solids may conveniently be studied as self-diffusion processes using radioactive tracers. In many silicates, and particularly aluminosilicates, a second kinetic process of interest is exchange diffusion. Both processes may be studied in glasses and in crystals, and although in silicates kinetic measurements of either kind are not as yet extensive, such media provide a very suitable range in the degrees of openness of the immobile anionic frameworks within which cations migrate. This should allow the inter-play between dispersion, repulsion and direct coulombic interactions to be studied. In very compact silicates ion jumps could be dominated by repulsion energies at squeeze points; in very open frameworks such squeeze points do not arise and the migration barriers may be largely influenced by periodicity in the intracrystalline electrostatic fields.

In the present paper we report on exchange diffusion and self-diffusion of ions in hydrated chabazite crystals. In this open structure the narrowest apertures through which diffusion would have to occur are rings of eight (Al, Si)O_4 tetrahedra. These rings have free diameters of about 3·9 Å so that repulsion energy barriers associated with squeeze points need hardly be considered. It is still possible that some ions are located within the hexagonal prisms composed of 12 (Al, Si)O_4 tetrahedra which are to be found as important structural units in the chabazite group of zeolites,(1) in which case migration through 6-rings could also be involved. Particular interest attaches to ion-diffusion in chabazite not only on account of its open structure, but also because movements of ions and water molecules have been studied by n.m.r.,(2) dielectric relaxation,(2) electrical conductivity(3) and (in the case of water) by measurements of self- and intrinsic diffusion.(4)

2. EXPERIMENTAL

2.1. *Preparation of homoionic exchanged forms*

The hand-picked mineral of Nova Scotian origin was broken down in an agate mortar until it could be sieved between an 18 and 32 mesh sieve, except for the material from which the "pure" calcium and strontium exchange forms were prepared. For these two samples the mineral passing through a 200 mesh sieve was used. The sodium and calcium ions present in the natural mineral were replaced by the various cations required for the self-diffusion experiments by heating the mineral on a water bath with a solution containing a twenty fold excess of the exchanging ion. In the preparation of rubidium, calcium, and strontium chabazite, chabazite enriched as far as possible in Na (Table I, column 2) and laced with some ^{22}Na tracer was used as the starting material and the progress of the exchange followed radiochemically. With the natural material the exchange was followed by determining the calcium content of the liquid phase. Exchanges usually required 3–4 weeks before no further replacement could be detected and during this time the supernatant liquid was replaced five times with fresh solution. The chemical analyses of the seven different ionic forms are given in Table I. The results refer to samples obtained from different rock materials and give the limits of exchange obtainable under the experimental conditions. For example, there appears in the Ca- and Sr-chabazites to be a residue of 0·08 moles of very difficultly exchangeable Na_2O.

Table 1. *Molar proportions of some oxide constituents of crystals*

Moles of	Exchange Form						
	Na	K	Rb	Cs	Ca	Sr	Ba
SiO_2	6·74	6·13	4·68	6·31	5·88	5·53	6·05
Al_2O_3	1·00	1·00	1·00	1·00	1·00	1·00	1·00
Na_2O	0·88		0·13		0·08	0·08	
K_2O		0·91					0·12
Rb_2O			0·82				
Cs_2O				0·81			
CaO	0·051	0·02$_0$		0·13	0·88		
SrO						0·88	
BaO							0·85
H_2O	6·46	5·37	4·60	4·52	6·67	6·79	6·3

In what follows it is assumed that the small amounts of residual Na^+ take no part in the subsequent exchanges of Ca for Sr, or the converse. The difficulty in exchanging the residual sodium could arise if, for example, a few Na^+ ions were embedded in the hexagonal prism units (1) but Ca^{2+} and Sr^{2+} ions were for reasons of local charge balance confined to the large cavities only. Whatever the reason for this difficulty, it is possible to define an exchangeable cation fraction, N, for Ca and Sr as

$$N_{Ca} = \frac{[Ca]}{[Ca]+[Sr]}; \quad N_{Sr} = \frac{[Sr]}{[Ca]+[Sr]} \qquad (1)$$

where [Ca] and [Sr] denote the concentrations of Ca and Sr within the crystal. This convention will be employed both in this paper and in Part II.

2.2. *Preparation of* Ca, Sr *chabazite*

Chabazites containing various ratios of Ca to Sr were prepared by equilibrating either calcium or strontium chabazite with solutions containing various ratios of calcium and strontium nitrates. For the calcium rich samples the solution was tagged with $^{(85+89)}Sr$ tracer and the exchange followed by radiochemical analysis of the solution phase. From this analysis the amount of Sr tracer in the chabazite was readily obtainable. For the strontium rich samples the solution was tagged with ^{45}Ca and the same procedure followed.

Except where large amounts of exchange occurred, equilibrium was attained in a few days.

The densities of the samples were measured using a specific gravity bottle. The water content of each exchange form was obtained from the loss in weight on heating to a dull red heat.

2.3. *Surface area measurements*

The surface area of the samples were determined by the krypton adsorption method.(5) As only the external surface area of the chabazites was required, precautions had to be taken to avoid or at least to minimize krypton sorption in the interstitial channels. It was necessary, therefore, to ensure that no zeolitic water was removed when air was being evacuated. The surface area was calculated by application of the B.E.T. theory using a value of 19·5 Å^2 for the cross-sectional area of the krypton atom.

The surface areas of the sodium and rubidium chabazites were determined also by projecting the image of a known weight of material onto photographic paper using a photographic enlarger. From the known degree of enlargement the true cross-sectional area of the sample was calculated. Multiplying this area by a factor of four(6) gave the total surface area. The B.E.T. and visual areas are shown in Table 2. They differ substantially, as expected, since surface detail down to molecular magnitudes is contained in the krypton areas, but no such detail can be given by projected areas. The significance of these areas in evaluating diffusion coefficients is considered later.

2.4 *Self-diffusion measurements*

The tracer ions used were ^{22}Na, ^{42}K, ^{86}Rb, ^{134}Cs, ^{45}Ca, $^{(85+89)}$Sr, ^{133}Ba. A similar experimental technique to that described by BARRER and REES(7) for the self-diffusion of Rb in Rb-analcite was employed throughout this work. However, the sample size was reduced to 0·2 or 0·25g and in some runs the solution and exchanger phases did not contain exactly the same equivalent amount of the cation whose self-diffusion was being measured. The radiochemical technique was changed for ^{45}Ca tracer, because the weak β-radiation was incapable of penetrating the walls of the liquid counter. This tracer was counted as a solid using a Geiger Muller counter type MX123 with window thickness of 2·3 mg cm^{-2}. 0·5 ml of the calcium sample was pipetted from a micro syringe pipette on to a ½ in. diameter glass fibre disc (Whatman GF/B) which was fused on to a 1 in. diameter aluminium planchet through a ½ in. diameter disc of polythene. The calcium sample on evaporation to dryness with an infra-red lamp, was distributed evenly throughout the glass fibre disc and errors due to variations in the self-adsorption of the deposit were eliminated. To obtain consistent count rates the original deliquescent calcium chloride deposit was converted to calcium oxalate by pipetting 0·5 ml of solution containing a slight excess of oxalic acid on to the glass fibre disc followed by evaporation to dryness.

2.5 *Self- and exchange-diffusion measurements in heteroionic exchanger*

The preparation of the heteroionic forms of known calcium and strontium contents in equilibrium with a solution containing these ions was described previously. By this method one obtained a sample of exchanger containing a known amount of radioactive tracer of one of the two cation types present. In order to measure the two self-diffusion coefficients simultaneously, the solution containing inactive *A* ions and active *B* ions was replaced with a solution containing exactly the same equivalent ratio of ions *A* and *B* with type *A* active and type *B* inactive. As *A* and *B* represent either calcium or strontium in these experiments, it was possible to measure the changes in radioactivity of each ion species in the solution phase as diffusion proceeded by the following method.

The solution phase was separated from the solid phase by centrifuging and a sample of the solution prepared for solid counting in the same way as described for pure ^{45}Ca samples. The total activity of this solid source was determined and then redetermined through an aluminium filter of 87·5 mg cm^{-2}. This filter absorbed the ^{45}Ca radiation and allowed a known fraction of the $^{(85+89)}$Sr activity through. The total activity of the strontium sample was obtained by adjusting this figure with the previously determined factor for the filter, and the ^{45}Ca count obtained by difference between the original count without filter and this total strontium count.

Although this method allowed activities to be measured simultaneously, a more accurate

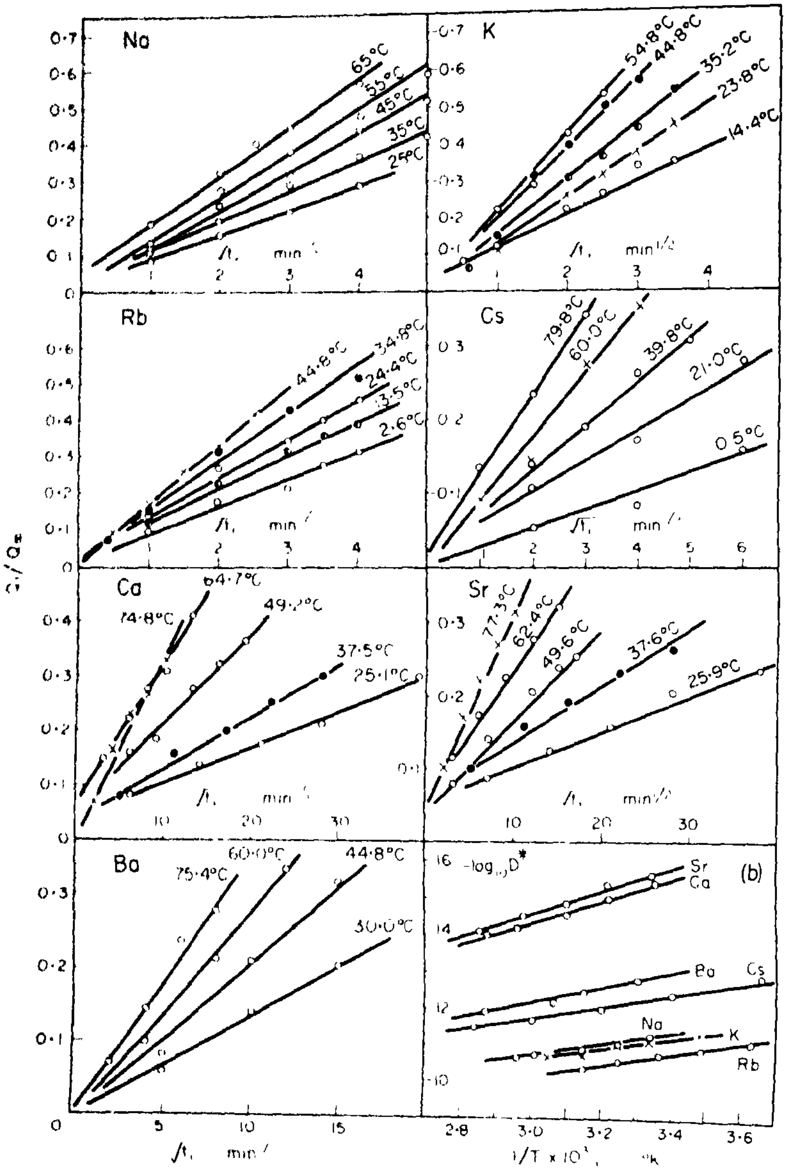

FIG. 1. (a) Rates of exchange of ^{22}Na, ^{42}K, ^{86}Rb, ^{134}Cs, ^{45}Ca, $^{(85+89)}$Sr and ^{133}Ba in their respective cationic forms of chabazite. The values of the factor $Q_0/(Q_0-Q_\infty)$ involved in these experiments were

Ion	Na	K	Rb	Cs	Ca	Sr	Ba
$\frac{Q_0}{Q_0-Q_\infty}$	2·000	2·254 for 14·4°C, 23·8°C and 35·2°C 2·110 for 44·5°C and 54·8°C	2·304	2·408	2·000	2·056	2·038

(b) Plots of $-\log D^*$ (D^* in cm^2 sec^{-1}) against $1/T$.

determination of the strontium activity could be obtained by liquid counting making only a slight correction for the very small increase in the background count due to the ^{45}Ca present in the sample. In the ion-exchange experiments the solution contained initially a twenty fold excess of the entering ion. The ion present in the exchanger was always tagged with radioactive tracer and the exchange followed radiochemically from the increase in activity of the solution phase.

3. RESULTS

3.1 *Self-diffusion in nearly homoionic chabazites*

Rates of exchange between radioactive and non-radioactive isotopic cations are shown for various chabazites in Fig. 1. The $\sqrt{t}$ law is well obeyed, the appropriate version of this law for the experimental boundary conditions being:$^{(8)}$

$$\frac{Q_t}{Q_\infty} = \frac{Q_0}{Q_0 - Q_\infty} \cdot \frac{2S}{V} \sqrt{\left(\frac{D^* t}{\pi}\right)} \tag{2}$$

Q_t and Q_∞ are the amounts of exchange after time t and at equilibrium respectively in a volume V of crystals of surface area S. Q_0 is the amount of radioactive cation initially in solution and D^* is the self-diffusion coefficient in the crystals. Reference to Table 1 will show that in no case was self-diffusion measured in completely homoionic chabazites, although usually there was at least 90 per cent exchange of the ion being studied. Rubidium chabazite with 82 per cent and caesium chabazite with 80 per cent exchange are exceptions.

In all cases, except that of Ba–chabazite, curves of Q_t/Q_∞ vs. $\sqrt{t}$ give intercepts on the axis of Q_t/Q_∞. The intercepts are about 0·02 for the samples with small surface area (i.e. Na-, K-, Rb- and Cs-forms) and 0·06 for Ca- and Sr-chabazites, which have krypton surface areas about ten-fold greater. If these intercepts are associated with adsorption of ions, and if the krypton areas are used, then in a monolayer of adsorbed ions only about 0·5 Å^2 would be available per cation for the Na-, K-, Rb- and Cs-forms and only about 3·3 Å^2 for the Ca- and Sr-forms. However, the behaviour is compatible with very rapid distribution in depth throughout a layer on the surface of the crystals. If the distribution of cations corresponds to the same cation density as in the parent crystal the extremely rapid "sorption" responsible for the intercepts would be equivalent to a film thickness of some thirty to fifty layers of cations in the crystals.

The krypton areas must be regarded as upper limits to the areas, S, appropriate to equation (2). On the other hand, the projected areas, which ignore all surface roughness, will be too small and will constitute lower limits to these areas. Accordingly, in Table 2 lower limits have been calculated from equation (2) for D^* using the krypton areas (column 4), and where projection areas were available, upper limits were also calculated (column 6). Provided the same method is used to measure the surface area of each sample of a series the true values of D^* are likely to be reasonably nearly related to those measured, through a single proportionality constant. However, anomalous results may arise such as those for Rb-chabazite. These crystals were visually smaller than those of Na-chabazite, and thus have a larger projected area. On the other hand despite their smaller size they have a smaller krypton area. The photomicrograph of Rb-chabazite showed these crystals to be smooth in appearance. The Na-chabazite and the other large crystals used for studying self-diffusion of the monovalent cations on the other hand looked considerably less smooth. As a result, if the krypton area is used D^*_{Rb} exceeds D^*_{Na}, while if the projection areas are used the converse is true (Table 2). The general importance of the area is seen by comparing the actual magnitudes of D^*, which for Na-chabazite differ by a factor of ~ 500 and for Rb-chabazite by one of ~ 600.

In all the self-diffusion studies the solution was 10^{-2} to 5×10^{-2} molar with respect to the ion being studied. At these concentrations diffusion was never solution controlled, the values of D^* being independent of the aqueous concentrations. The shortest half-life, $t_{1/2}$, among the radioisotopes was 12·5 hr for ^{42}K. However, the rates of exchange were sufficiently rapid to make unnecessary any correction for $t_{1/2}$ even for ^{42}K, for which self-exchange the $\sqrt{t}$ law is still valid (Fig. 1).

3.2 *Self-diffusion of* Ca *and* Sr *ions in* (Ca, Sr)-*chabazites*

The (Ca, Sr)-chabazites were selected to study the relations between D^*_{Ca} and D^*_{Sr} and the

Table 2. Lower and upper limits to self-diffusion coefficients

Exchange Form	Temp (°C)	Krypton areas (cm^2 g^{-1})	D^* (cm^2 sec^{-1}) (krypton area)	Projected areas (cm^2 g^{-1})	D^* (cm^2 sec^{-1}) (projected area)	D^* at 25°C (smoothed value, krypton area)
Na	25·0	750	$6{\cdot}0_3 \times 10^{-12}$	32·6	$3{\cdot}1_8 \times 10^{-9}$	$6{\cdot}1_7 \times 10^{-12}$
	35·0		$9{\cdot}1_6$		$4{\cdot}8_4$	
	45·0		$12{\cdot}8_3$		$6{\cdot}7_7$	
	55·0		17·2		9·1	
	65·0		22·5		11·9	
K	14·4	1,120	$4{\cdot}5_2 \times 10^{-12}$			$6{\cdot}9_2 \times 10^{-12}$
	23·8		$6{\cdot}7_6$			
	35·2		$9{\cdot}3_7$			
	44·8		15·5			
	54·8		19·4			
Rb	2·6	503	$7{\cdot}8_3 \times 10^{-12}$	67·8	$0{\cdot}43 \times 10^{-9}$	$19{\cdot}5 \times 10^{-12}$
	13·4		12·7		0·70	
	24·4		17·7		0·97	
	34·8		28·4		1·45	
	44·8		42·6		2·34	
Cs	0·5	1,170	$0{\cdot}15 \times 10^{-12}$			$0{\cdot}49 \times 10^{-12}$
	21·0		0·45			
	39·8		0·94			
	60·0		$2{\cdot}0_0$			
	79·8		$3{\cdot}2_3$			
Ca	25·1	8,100	$0{\cdot}40 \times 10^{-15}$			$4{\cdot}1_7 \times 10^{-16}$
	37·5		0·97			
	49·2		$2{\cdot}9_1$			
	64·7		$6{\cdot}9_3$			
	74·8		10·2			
Sr	25·9	7,690	$0{\cdot}26 \times 10^{-15}$			$1{\cdot}3_2 \times 10^{-16}$
	37·6		0·54			
	49·6		$1{\cdot}4_7$			
	62·4		$3{\cdot}1_7$			
	77·3		$8{\cdot}3_2$			
Ba	30·0	817	$1{\cdot}5_9 \times 10^{-13}$			$1{\cdot}3_2 \times 10^{-13}$
	44·8		$3{\cdot}6_7$			
	60·0		$6{\cdot}3_8$			
	75·4		11·7			

cationic composition of the chabazites. This choice of diffusion media was guided by the virtually equal water contents of Ca-chabazite and of Sr-chabazite (Table 1) so that changes in water content with cationic composition will not be significant, and by the comparable self-diffusion coefficients of Sr^{2+} in Sr-chabazite and of Ca^{2+} in Ca-chabazite, so that two conditions for the validity of the HELFFERICH and PLESSET(9) treatment are satisfied. Moreover, because of the very great differences in the energies of the β-particles emitted by ^{45}Ca and by $^{(85+89)}$Sr it was relatively easy to follow the self-diffusion both of Ca and of Sr ions simultaneously.

Three different samples of chabazite were used. Those designated *A* and *B* were initially Ca-rich of compositions given in Table 3; while sample *C* was initially Sr-chabazite and had the composition given in Table 1. As noted in Section 2.1 in all samples the sums of the exchangeable cation fractions of the bivalent ions as defined by equation (1) were taken as equivalent to one, i.e. the residual sodium content was neglected.

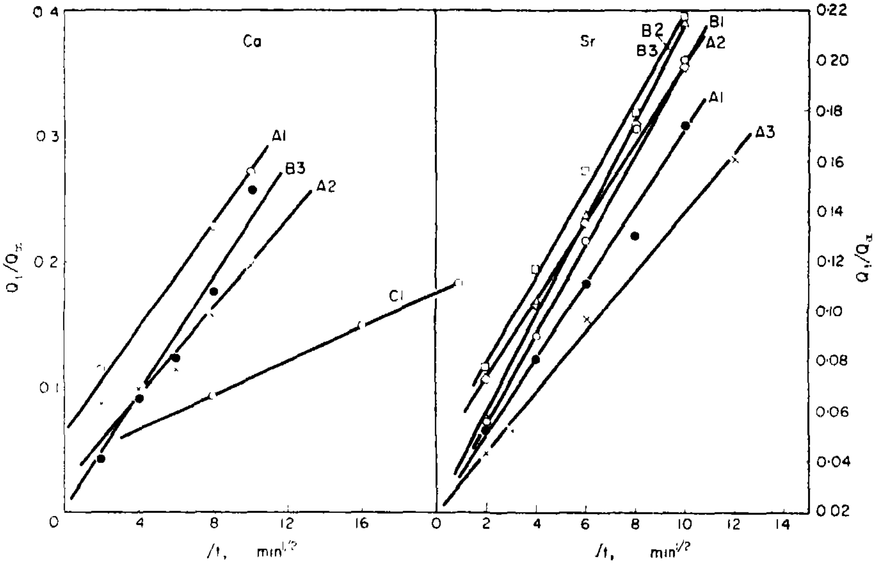

FIG. 2. Self-diffusion of Ca^{2+} and Sr^{2+} ions in (Ca, Sr)-chabazites. See Table 4 for the composition of samples designated *A*, *B* and *C*.

Table 3. *Initial compositions of chabazites A and B (molar proportions)*

	Chabazite *A*	Chabazite *B*
SiO_2	5·46	5·09
Al_2O_3	1·00	1·00
CaO	0·97	0·90
Na_2O	—	0·11
H_2O	7·53	6·91

The linear plots of amount of self-exchange vs. $\sqrt{t}$ are shown in Fig. 2. The liquid phases were made of such compositions with respect to Ca and Sr that the liquids were always in exchange equilibrium with the solid exchanger. Because of this necessity the factor $Q_0/(Q_0 - Q_\infty)$ (see equation 1) was often far from the most convenient value of about two (Table 4), and the experimental scatter therefore tended to be greater than for self-diffusion in the homoionic forms. In these solutions, however, the concentrations of both ions were always greater than 10^{-2}M to eliminate any possibility of liquid controlled diffusion (Section 3.1). Table 4 contains the values of D^* derived from the linear plots in Fig. 2, using the krypton surface areas. Evidently the self-diffusion coefficients depend very much upon the cationic composition of the crystals.

3.3 *Kinetics of exchange diffusion*

The rates of exchange of the ion pairs Ca–Sr, Ca–Ba, Sr–Ba and Na–Ba were followed radiochemically for both forward and reverse exchanges. The Sr-, Ba- and Na-chabazites were from the same batches as were used in the self-diffusion runs, while the Ca-sample was that designated *B* in Table 3. The amounts of exchange plotted against $\sqrt{t}$ are shown in Fig. 3. For the Ca–Sr exchanges the results have been adjusted by means of the factor *Sp* (Table 4) in order to compare samples at constant surface area per cm^3 of sample. A most noticeable feature of exchange diffusion

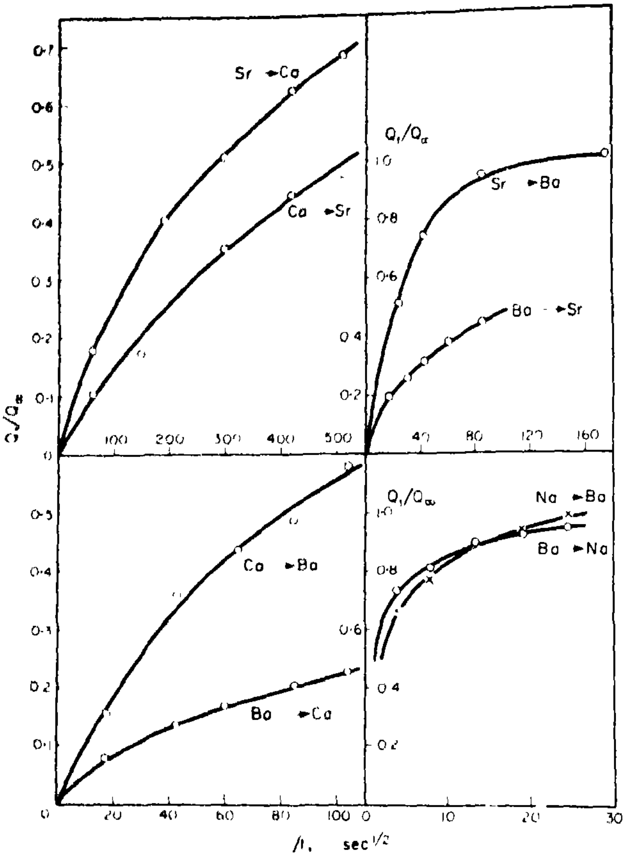

FIG. 3. Rates of ion-exchange.

Table 4. Self-diffusion coefficients in (Ca, Sr)*-chabazites*

Sample	Cation Fractions in Solid $\frac{Ca}{Ca+Sr}$	$\frac{Sr}{Ca+Sr}$	Krypton Surface Area, S (cm² g⁻¹)	Density ρ, (g cm⁻³)	D^* (cm² sec⁻¹ × 10¹⁵) Ca	Sr	$\frac{Q_0}{Q_0-Q_\infty}$ Ca	Sr
***A*1**	0·742	0·258	11,100	2·14	$8{\cdot}2_9$	0·43	1·13	3·55
***A*2**	0·555	0·445	8,250	2·16	$3{\cdot}8_4$	0·55	1·42	4·14
***A*3**	0·803	0·197	9,250	2·12	—	0·095	—	7·50
***B*1**	0·905	0·095	7,920	2·10	—	0·090	—	12·24
***B*2**	0·596	0·404	9,050	2·16	—	1·03	—	3·52
***B*3**	0·276	0·724	6,550	2·18	1·74	1·63	2·00	4·02
***C*1**	0·043	0·957	6,750	2·22	0·019	—	16·45	—

is the much earlier deviation of the curves of Q_t/Q_∞ vs. $\sqrt{t}$ from linearity than is the case for self-diffusion.

This deviation introduces some extra uncertainty into exchange diffusion coefficients. Another interesting observation is the extremely rapid exchange in both forward and reverse directions for the Na–Ba system.

4. DISCUSSION

4.1 *Self-diffusion in almost fully exchanged chabazites*

When $-\log D^*$ was plotted against $1/T$ satisfactory straight lines were obtained (Fig. 1). Thus the Arrhenius equation, $D^* = D_0 \exp(-E/RT)$, is valid, and the energies of activation E and pre-exponential constants, D_0, are recorded in Table 5. The uncertainty regarding the appropriate area appears in D_0 but not in E. For this reason values of D_0 for self-diffusion of Na^+ and Rb^+ calculated from the projection surface areas are also included in Table 5. The activation energies approach 7 kcal/g ion for monovalent ions and 14 kcal/g ion for Ca^{2+} and Sr^{2+}. Ba^{2+} is exceptional among the three bivalent ions as regards both the values of E (Table 5) and of D^* (Table 2). At 25°C the self-diffusion coefficients of all the monovalent ions (based on krypton areas) lie in the range $19{\cdot}5 \times 10^{-12}(Rb^+)$ to $4{\cdot}9 \times 10^{-13}(Cs^+)$ cm² sec⁻¹. Those of Ca^{2+} and Sr^{2+} respectively are $4{\cdot}2 \times 10^{-16}$ and $1{\cdot}3 \times 10^{-16}$ cm² sec⁻¹, being considerably smaller.

Table 5. *Self-diffusion in chabazite.* $T = 298{\cdot}3$°K

Cation	Energy of activation, E (kcal/mole)	Krypton surface area, S			Projected surface area, S		
		D_0(cm² sec⁻¹) × 10⁷)	ΔS^+ (cal/mole-deg)	ΔG^+ (kcal/mole)	D_0(cm² sec⁻¹) × 10⁴	ΔS^+ (cal/mole-deg)	ΔG^+ (kcal/mole)
Na	$6{\cdot}5_5 \pm 0{\cdot}13$	$3{\cdot}9_6$	−23	12·8	$2{\cdot}0_1$	−10·6	9·1
K	$7{\cdot}0_1 \pm 0{\cdot}14$	$9{\cdot}4_2$	−21	12·8			
Rb	$6{\cdot}7_5 \pm 0{\cdot}13$	$17{\cdot}_3$	−20	12·1	$0{\cdot}8_8$	−12·3	9·8
Cs	$7{\cdot}5_5 \pm 0{\cdot}14$	$1{\cdot}6_8$	−25	14·3			
Ca	$13{\cdot}8_1 \pm 0{\cdot}40$	$55{\cdot}_1$	−18	18·5			
Sr	$14{\cdot}5_9 \pm 0{\cdot}44$	101	−17	18·9			
Ba	$8{\cdot}8_3 \pm 0{\cdot}27$	$3{\cdot}9_7$	−23	15·1			

4.2 *Self-diffusion in heteroionic* (Ca, Sr)-*chabazites*

In Table 4 values of D^*_{Ca} and D^*_{Sr} are given for exchangeable cation fractions in the range 0·043 to 0·905. All measurements were made at 75·8°C. As explained in Section 3·2 these self-diffusion coefficients are less accurate than those obtained in the nearly homoionic Ca–chabazite and Sr–chabazite. However, their self-diffusion coefficients decrease very rapidly with decreasing exchangeable cation fraction, and may be represented very approximately by the relation

$$D^*_A = D^0_A N^2_A \tag{5}$$

where A represents either Sr or Ca. Giving most weight to the value of D^*_A at $N_A = 1$, straight lines of slope 2 have been drawn passing through the values of D^* at $N_A = 1$. The concentration dependence of D^*_{Sr} might be better represented by a higher power of N_{Sr}, but equation (5) will be used to approximate to the strong concentration dependence for both ions. $D^0_{Ca} = 1{\cdot}15 \times 10^{-14}$ cm² sec⁻¹ and $D^0_{Sr} = 7{\cdot}4 \times 10^{-15}$ cm² sec⁻¹, in equation (5). The equation predicts that $D^*_A = 0$ at $N_A = 0$, but this is merely a measure of its limitations at this end of the concentration scale.

Boyd and Soldano(10) measured the self-diffusion coefficients of various cations in heteroionic ion-exchange resins when equilibrium existed between external aqueous solution and resin. The diffusion coefficient of the more mobile ion was lowered and that of the less mobile ion increased when the cation fraction of the relevant ion was reduced to a small value within the exchanger. The maximum change in diffusion rate was however only about two-fold. There is no counterpart to the behaviour observed in chabazite.

4.3 *Ion exchange diffusion*

In polymer-penetrant systems where concentration dependent diffusion coefficients arise, an integral inter-diffusion coefficient may be defined as(11)

$$D_{AB} = \frac{1}{C_2 - C_1} \int_{C_1}^{C_2} D_{AB} \, dC \qquad (6)$$

where D_{AB} is the value of the interdiffusion coefficient at a particular concentration C of penetrant. D_{AB} may with sufficient accuracy be obtained by measuring both sorption and desorption kinetics expressed in terms of the $\sqrt{t}$ diffusion law:

$$\frac{Q_t}{Q_\infty} = 2S_p \sqrt{\left(\frac{D_{AB} t}{\pi}\right)} \qquad (7)$$

If D_f denotes the value of the integral diffusion coefficient from the sorption run and D_b is this value from the desorption run, then the best value is

$$D_{AB} = \tfrac{1}{2}(D_f + D_b) \qquad (8)$$

Sorption and desorption of penetrant in a polymer has its counterpart in the forward and reverse ion exchanges.

$$A\text{-zeolite} \underset{\text{XS } A^+ \text{ in soln.}}{\overset{\text{XS } B^+ \text{ in soln.}}{\rightleftharpoons}} B\text{-zeolite}$$

and D_f and D_b are now the integral interdiffusion coefficients for A-chabazite → B-chabazite and the reverse, respectively. These exchanges, as in polymer-penetrant systems, occur at different rates (Fig. 3). In the Ca–Sr, Ca–Ba and Sr–Ba exchanges the diffusion coefficients D_{AB} (based on the krypton areas of the powders and using equations (7) and (8)) are respectively $1{\cdot}7 \times 10^{-14}$, $1{\cdot}2 \times 10^{-13}$ and $1{\cdot}1 \times 10^{-12}$ cm^2 sec^{-1} at 75·8°C. The theoretical basis of relations between exchange and self-diffusion coefficients is considered in Part II.

4.4 *Diffusion and relaxation processes in chabazite*

The pattern of the results for self-diffusion of monovalent ions in analcite(7) and in chabazite is strikingly different, and can be related to the structures of the two crystals. During ion migration through analcite, cations must pass through rings of six and eight (Si, Al)O_4 tetrahedra, having maximum free diameters of 2·3 and 2·4 Å respectively. The ionic diameters of the diffusing ions Na^+, K^+, Rb^+ and Cs^+ are 1·90, 2·66, 2·96 and 3·38 Å respectively, and the Arrhenius energies of activation are in turn 11·5, 16·4, 20·1 and 26·0 kcal/g ion. These energies are a linear function of the cation polarizabilities, a property which has been interpreted as due to the dispersion–repulsion interactions between the ions moving through the six and eight-membered rings.(12) In this case, the interaction resulting from dispersion-repulsion forces should be negligible for sodium and a maximum for caesium. Thus the barrier of 11·5 kcal/g ion for sodium should reflect primarily the periodic variation of the coulombic energy along the diffusion path through the rings.

In chabazite, ion migration will result in movement through the important eight-membered rings of free diameter ~ 3·9 Å.(13) If this step is rate determining and is free of steric hindrance by water molecules, the barrier for all monovalent ions should be governed by the variation in coulombic energy in moving through the ring, and should thus, as observed, be approximately the same for all these ions. The coulombic energy barrier should then be twice as large for divalent ions as for monovalent ones. Ca^{2+} and Sr^{2+} ions conform with this picture but Ba^{2+} is out of line, and behaves more nearly as though it were monovalent.

For self-diffusion of water in a (Ca, Na)-chabazite, the Arrhenius energy is 8·7 ± 0·3 kcal/mole, and for intrinsic diffusion the barrier is 6·7 ± 0·3 kcal/mole.(4) These values are sufficiently close to values of E for self-diffusion of monovalent ions to suggest as an alternative possibility that diffusion whether of ions or of water is a co-operative process involving cations, water molecules, and possibly some framework oxygens. This time, however, Ca^{2+} and Sr^{2+} ions are out of line, so that the full interpretation is more complex than either of those advanced in this or the preceding paragraph.

In the hope of obtaining further information on the nature of the diffusion process, entropies of activation, ΔS^+, and free energies of activation, ΔG^+ were obtained from the relations*

$$D_0 = \exp\left(\frac{\Delta S^+}{R}\right)\frac{2\cdot72kTd^2}{h} \qquad (9)$$

and

$$D^* = \frac{kT}{h}d^2\exp\left(-\frac{\Delta G^+}{RT}\right) \qquad (10)$$

T was taken as 298·3°K, and d, the mean jump distance, was taken as 5 Å. The results are shown in Table 5. Whether the krypton or the projected areas are employed to calculate D^*, ΔS^+ is negative. This is compatible with co-operative movements between more than one particle. If, for a successful unit diffusion process, each of n particles must move in one out of m directions, the chance of this is $(1/m)^n$, constituting in terms of equation (9), a negative entropy contribution to ΔS^+. When $m = n = 6$, this contribution is $-22\cdot3$ cal/mole deg.

The energy barriers associated with cation migration in dehydrated chabazite(3) are much increased as compared with the hydrated zeolite. For Na^+ and Ca^{2+} the values of E are $\sim$ 15 and $\sim$ 19 kcal/g ion. Removal of water must result in cation shifts in which the cations adhere more closely to the rings of anionic oxygens constituting the walls of each cavity, so that the coulombic energy barriers increase. The energy barriers in certain Linde Sieves are also higher in the dehydrated than in the hydrated crystals,(15) but in the dehydrated crystals which have been fully investigated E decreases with increasing radius of monovalent cations, and increases with radius of divalent cations. No simple 1:2 ratio exists between the magnitudes of E for mono-and divalent ions.

Two dielectric loss peaks have been observed by DUCROS(2) in hydrated (Ca, Na)-chabazite, corresponding to relaxation processes with energy barriers of about 8 and 16·1 kcal/Avogadro number of unit processes. The largest barrier has been ascribed to Ca^{2+} migration, and it seems likely that the smaller barrier is attributable to Na^+ migration, since both barriers are rather close to those we have measured for self-diffusion of these two ions. On the other hand, another relaxation process which can now refer only to the zeolitic water (e.g. rotation) has been observed using n.m.r. spectroscopy.(2)

5. CONCLUSION

It has been found in this paper, and earlier(7) that projected surface areas and areas measured by adsorption methods may differ considerably. In these circumstances the $\sqrt{t}$ diffusion law is likely to give respectively lower and upper limits to the diffusion coefficient. One might anticipate that initially the adsorption area will give values of D^* nearer the correct magnitude, but to prove this methods of evaluating D^* must be used which are independent of the surface area. Two such methods for self-diffusion may be the measurement of d.c. conductivity or of dielectric relaxation times. In the latter case one must be sure that the relaxation measured is indeed that for cation jumps, and in the former, one must be sure that pure d.c. conductivity in the interior of the crystal particles is measured, free of polarization and of surface conductivity effects. Energy barriers obtained from self-diffusion studies are of course independent of the surface area measurements.

Acknowledgement—One of us (R.F.B.) wishes to acknowledge the award of a D.S.I.R. maintenance grant which enabled him to take part in this research.

REFERENCES

1. DENT L. S. and SMITH J. V., *Nature, Lond.* **181,** 1794 (1958).
2. DUCROS P., *Bull. Soc. franç. Minér.* **83,** 85 (1960).
3. BEATTIE I. R., *Trans. Faraday Soc.* **50,** 581 (1954).
4. BARRER R. M. and FENDER B., *J. Phys. Chem. Solids* **21,** 12 (1961).
5. ROSENBERG A. J., *J. Amer. chem. Soc.* **78,** 2929 (1956).
6. KENRICKS F. B., *J. Amer. chem. Soc.* **62,** 2838 (1940).
7. BARRER R. M. and REES L. V. C., *Trans. Faraday Soc.* **56,** 709 (1960).
8. BARRER R. M., *Trans. Faraday Soc.* **45,** 358 (1949).
9. HELFFERICH F. and PLESSET M. S., *J. chem. Phys.* **28,** 418 (1958).

---

[*] Equation (9) as quoted in Refs. 7 and 14 needs correction; in particular ΔS^+ given in Ref. 7 as -11 and -19 cal/mole deg. should be -15 and -23 cal/mole deg.

10. Boyd G. E. and Soldano B. A., *J. Amer. chem. Soc.* **75**, 6091 and 6107 (1953).
11. Crank J. and Park G. S., *Trans. Faraday Soc.* **45**, 240 (1949).
12. Barrer R. M. and Rees L. V. C., *Nature, Lond.* **187**, 768 (1960).
13. Barrer R. M. and Kerr I., *Trans. Faraday Soc.* **55**, 1915 (1959).
14. Barrer R. M., *Proc. phys. Soc. Lond.* **52**, 58 (1940).
15. Freeman D. C. and Stamires D. N., *J. chem. Phys.* **35**, 799 (1961).

J. Phys. Chem. Solids Pergamon Press 1963. Vol. 24, pp. 63–73. Printed in Great Britain.

THE THERMAL DECOMPOSITION OF $NaBrO_3$*
PART I—UNIRRADIATED MATERIAL

JOSEPH JACH†

Picatinny Arsenal, Dover, New Jersey, U.S.A.

(*Received* 6 *July* 1962; *revised* 23 *August* 1962)

Abstract—The thermal decomposition of polycrystalline $NaBrO_3$ has been studied in the temperature range 323–430°C. The only products are NaBr and Oxygen. Like $KBrO_3$, the reaction begins essentially on surfaces by the rapid formation of an interface and is followed by the penetration of this interface into the crystallite. The melting of a eutectic formed between the product NaBr and the parent material causes a marked increase in rate over certain temperature ranges. This is evident as a very sharp discontinuity on the Arrhenius plot. Evidence also exists for reaction along other routes such as at dislocations and other defects. Some of these conclusions are borne out by results with finely ground material.

INTRODUCTION

In recent years interest has been revived in thermal decomposition studies in the solid state. This interest has been paralleled by and is probably a result of the enormous strides made during the post-war period in the field of solid state physics. In an attempt to study one of the most simple chemical species undergoing such decompositions, a program was recently initiated with bromates. The results with the first compound studied, $KBrO_3$ are published$^{(1)}$ and include an examination of the effect of various irradiations on the decomposition. The present study also includes irradiation effects but the decomposition of unirradiated $NaBrO_3$ has proved interesting in its own right and these results are separately published now. The irradiation effects are reported in Part II.

$NaBrO_3$ falls into that class of decomposition in which surfaces become completely covered with a layer of product (NaBr) right from the beginning of the reaction which then proceeds by an advance into the crystal of the interface created between the undecomposed bromate and the product bromide. At certain temperatures, the simultaneous presence of these two species allows a type of eutectic formation and melting occurs. The presence of the resulting liquid phase then plays a dominant role in the decomposition.

EXPERIMENTAL

Preparation of crystals

A. R. grade $NaBrO_3$ was purified by evaporation of warm aqueous saturated solutions. The crystals used were those which passed through a number 30 but were retained by a number 40 sieve. Spectroscope examination for impurities revealed only Fe, Si and Mg in the range 0·001 per cent to 0·0001 per cent. About 5 mg portions (~ 20 crystals) were dried for 3 hr at 120°C and encapsulated in quartz ampoules, and each portion used for one run.

Apparatus and procedure

The course of the reaction was followed by automatic pressure measurements in a closed system of the evolved oxygen. The apparatus and procedure have been previously described.$^{(1)}$ Basically, the reaction takes place in a quartz tube on a surface of NaBr, being reproducible with respect to a bare quartz surface. The temperature

---

* Work performed primarily at Brookhaven National Laboratory and supported jointly by Picatinny Arsenal and the U.S. Atomic Energy Commission.

† Guest Scientist, Brookhaven National Laboratory, Upton, N.Y.

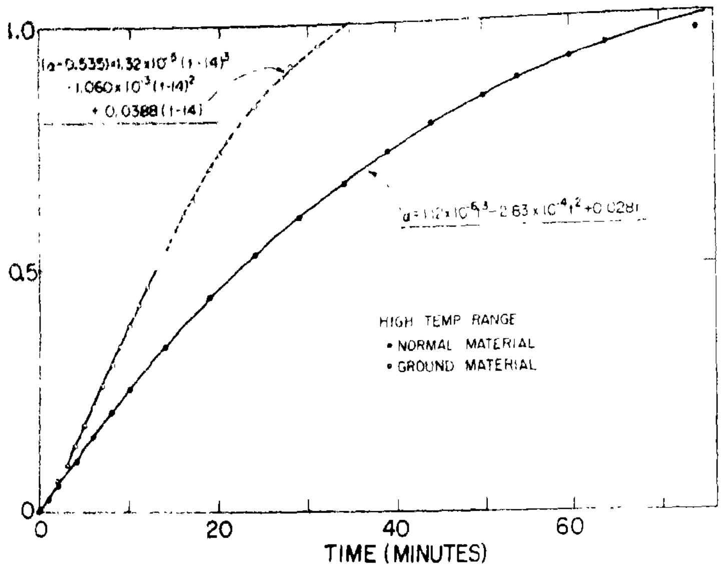

FIG. 1. Fractional decomposition α vs. time in the higher temperature range.
Run for normal material at 373·0°C.
Run for ground material at 370·6°C.

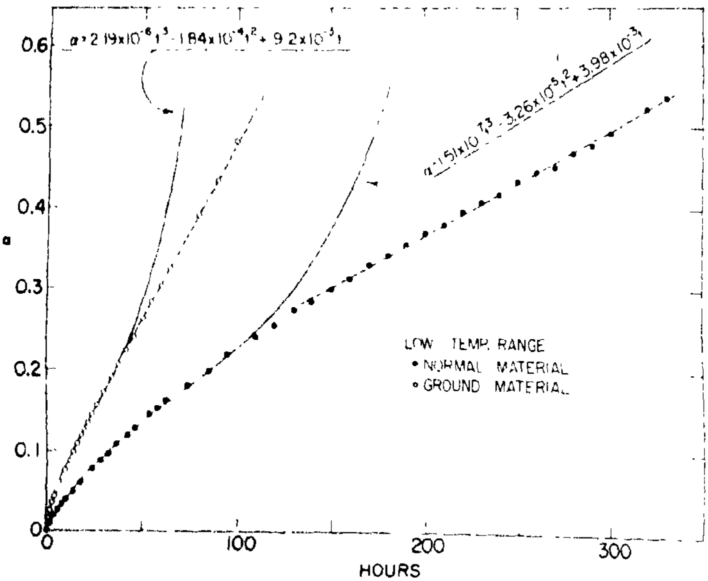

FIG. 2. Fractional decomposition α vs. time in the low temperature range.
Run for normal material at 330·0°C.
Run for ground material at 330·0°C.

is controlled electronically to ± 0·1°C and warm up times are negligible. Final pressures never exceed 150 μ and reproducibility is better than 3 per cent.

RESULTS

The shape of the decomposition curve

The reaction which is represented by $NaBrO_3 \rightarrow NaBr + 3/2\ O_2$ was studied in the temperature range 323–430°C and within experimental error was found to go to completion. Over the greater part of this temperature range, the form of the decomposition curve was constant, but at the very lowest temperatures studied, a marked change occurred. Figure 1 shows α, the fraction of the total decomposition as a function of time for a temperature typical of the higher range. The full circles represent experimental points. Figure 2 shows corresponding results typical of the lowest temperatures. Both indicate the type of behavior where surfaces become nucleated instantaneously followed by some form of contracting envelope mechanism. The reaction, therefore, begins at its maximum rate and as the product-reactant interface advances into the crystal, the rate gradually falls off. The absence of an acceleratory period is also typical of this behavior. Various attempts to fit the curves with a mathematical expression failed except for the cubic expression

$$\alpha = at^3 - bt^2 + ct \qquad (1)$$

where a, b, c are positive numbers. This fit is shown as the unbroken line in Fig. 1. In the low temperature range (Fig. 2) only the initial part can be fitted to equation (1) and the parameters are therefore, less accurate. Following this initial part is a region of constant reaction rate maintained to unusually high values of α. Such "linear" behavior is not unknown but its interpretation always presents a perplexing problem.

A few runs were carried out on material which had been finely ground. The effect was to enhance the rates somewhat as well as alter the form of the α, t curve. In the higher temperature range the open circles (Fig. 1) represent experimental points for ground material. The rate begins with its maximum value but does not begin to fall off until an abnormally high α. This "linear" behavior is maintained from $\alpha = 0$ to about $\alpha = 0{\cdot}5$. The rate then falls off and the curve once again fits equation (1) after a judicious choice of a starting point (somewhere around $\alpha = 0{\cdot}5$). is made. Using this starting point (α_0, t_0) the upper part of the curve is fitted to equation (1). This behavior is very similar to normal unground material which has been subjected to heavy irradiation, but this will be discussed in Part II of this paper. In the very low temperature region, grinding appears to lengthen the "linear" region at the expense of the initial region. In other words the linear region extends over a longer range of α. This is shown as open circles in Fig. 3. The initial part can be fitted to equation (1).

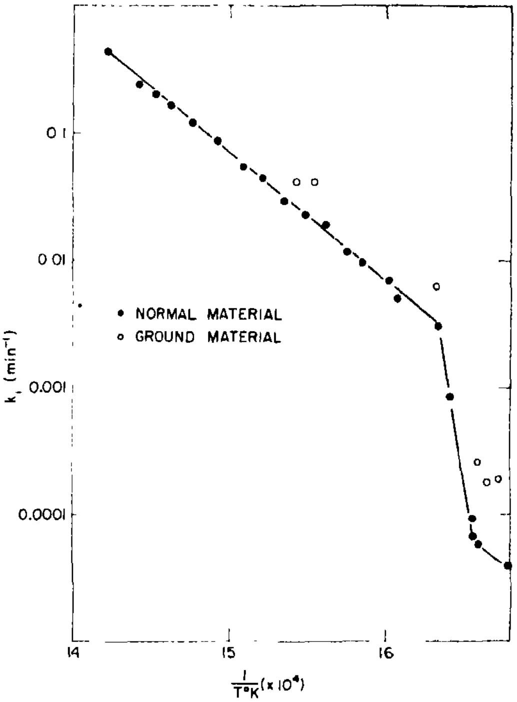

FIG. 3. Arrhenius plot of k_i.

Arrhenius plots

The change in kinetics with temperature makes it obvious that a choice of parameter for an Arrhenius plot over the entire temperature range is a difficult if not impossible one. It was decided to use k_i, the initial rate $(d\alpha/dt)_{t=0}$. For a curve obeying equation (1), k_i should be equal to the constant "c", so that in practice where it was sometimes difficult to get these initial slopes from the curves (especially at the lower temperatures), the quantity "c" was used. In view of the changed shapes of the curves at low temperatues, one may question the physical integrity of an Arrhenius plot of k_i over the whole temperature range. It does however, give some idea of the gross variations with temperature. This is shown in Fig. 3. It is immediately apparent that over the greater part of the temperature range (corresponding to the behavior represented by Fig. 1) the parameter k_i exhibits a classical straight line plot corresponding to an activation energy of 45·3 kcal/m. However, at about 339°C, an abrupt drop in rate occurs. At the lower end of this discontinuity a levelling off appears to set in. Not many points are available here because of the experimental difficulty of obtaining them at these low temperatures. The rate drops over the discontinuity by about a factor of 40. This resembles the behavior with $KBrO_3$,⁽¹⁾ except that the discontinuity is "sharper" and "deeper" here.

The values of k_i for ground material are also shown in Fig. 2. (open circles). An enhancement in rate occurs (about a factor of 2 in the upper range and about 3 at the lower temperatures). In the upper range, k_i for ground material is the slope of the initial "linear" region. The physical meaning of such a comparison is discussed later.

TOPOCHEMISTRY OF THE REACTION

1. *The discontinuity*

The cause of the discontinuity is almost undoubtedly the onset of melting. The product of the reaction, NaBr, probably forms a eutectic with $NaBrO_3$ and the result is melting below the thermodynamic melting point. This has also been detected visually under a hot-stage vacuum microscope. Exactly the same phenomenon was observed in $KBrO_3$.⁽¹⁾ It must be emphasized that this is different to ordinary melting of a pure substance. The melting here is dependent on the presence of a "foreign" substance (NaBr) the quantity of which is determined by decomposition. Two rate processes are therefore involved, the melting of a eutectic mixture and decomposition and the two are linked to each other in a complex way. Melting cannot proceed without the decomposition and decomposition (at the elevated rates in the higher temperature region) cannot proceed without melting.

The discontinuity occurs in the temperature range 330·9–339·4°C, while the m.p. quoted in a standard reference book⁽²⁾ is 381°C. It is consistent that the melting of a eutectic mixture begins before the normal melting point, but the absence of another discontinuity at 381°C is strange. An equivalent absence was found with $KBrO_3$. In the standard reference texts, no mention is made as to how these melting points were obtained. In some instances the standard references are in disagreement even about the melting point. For example, with $KBrO_3$, one source quotes the m.p. as 370°C with decomposition⁽³⁾ while another⁽²⁾ quotes 434°C with decomposition at 370°C. It is very difficult to obtain an accurate melting point with compounds decomposing in this way, except at very high external pressures. This problem was also reported by GLASNER and WEIDENFELD⁽⁴⁾ who studied the decomposition of perchlorates. They found the m.p. of $KClO_4$ to be about 536°C after partial decomposition while the m.p. is quoted as 610°C. This substance begins decomposing at 500°C.

2. *The upper temperature range*

An attempt was made to seek further information about this region from the parameters a, b and c of equation (1). Simple topochemical reasoning gives the fraction of decomposition, α, as a function of time t for a cube, side A, which is instantly nucleated over the whole surface and then follows a contracting envelope mechanism. It is

$$\alpha = 8r^3t^3 - 12r^2t^2 + 6rt \qquad (2)$$

where $r = k/A$, t = time, k = velocity of advance of the interface (see Appendix I). Clearly, the same equation applies to a batch of similar cubes as well as just one.

Provided the build up of liquid is not large, occurrence of melting will not alter equation (2). The only difference would be that k represents the velocity of advance of the interface through melting and decomposition instead of just decomposition.

The material consisted of batches of crystals approximately similar in size and almost cubic. However, decomposition begins from all surfaces whether visible or not. The absence of any dramatic effect of grinding on the rate bears this out. This is, incidentally, typical of $KBrO_3$(1) and many other decompositions.(5) The visible shape or size of the crystal is, therefore, relatively unimportant. The shapes of the ultimate units of decomposition determine the topochemical equation. If these are very different from cubic, the numbers 8, 12 and 6 in equation (2) will be altered, but not its cubic form (or the negative coefficient of the square term). Assuming that the ultimate units are cubic, the experimental curves were fitted to equation (2) and the values of r obtained. The experimental value of r derived from the coefficient of t^3 is denoted as r_c, that for the square term r_s and for the linear term r_l. Thus,

$$r_c = \left(\frac{a}{8}\right)^{1/3}, \quad r_s = \left(\frac{b}{12}\right)^{1/2} \text{ and } r_l = \left(\frac{c}{6}\right)$$

Equality of these three values of "r" would tend to confirm the correctness of the contracting envelope mechanism. For this reason, these 3 values for each run were obtained and plotted as an Arrhenius plot. This is shown in Fig. 4. For comparison the values in the low temperature region are included. The following features are worth noting:

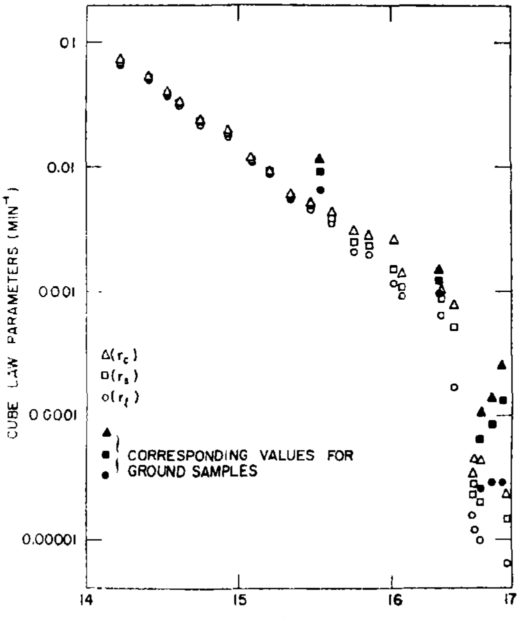

FIG. 4. Arrhenius plot of cube law parameters.

(a) At higher temperatures, the three values of "r" for any given run are sensibly equal.

(b) At lower temperatures (but still above the discontinuity) they begin to diverge somewhat and below the discontinuity, they are very widely separated.

(c) The "activation energy" for "r_l" i.e. for the lowest set of points on the graph corresponds exactly to the value obtained from Fig. 3. This is correct since $k_t = 6r$.

The results for one run on ground material are also shown. However, as mentioned previously, the cubic expression fitted the *upper* portion of the curves for ground material and the 3 "r" values refer to that portion. The effect of grinding (if the points have any significance in view of the above) is thus to increase the "r" divergence.

One other point must be clarified now. The model used for obtaining the cube law parameters was a simple cube. This was chosen for simplicity. One might just as well have chosen a sphere or any other 3-dimensional shape. Applying the arguments used in Appendix I, the equation for a sphere corresponding to equation (2) is

$$\alpha = r^3t^3 - 3r^2t^2 + 3rt$$

where $r = k/A$, and k is the same as before. A is now the initial radius of the sphere. Using this equation, the same form of Arrhenius plots are obtained for r (with slightly different numerical values of course). In other words, at high temperatures, the three values of r essentially are the same but diverge at lower temperatures. One may safely conclude that the shapes of the ultimate units are of not too great significance and that the same phenomena regarding the 3 values of r apply for any shape. The choice of any one is arbitrary, but necessary for an analysis to be made.

It is now shown that the divergence of the "r" values and its temperature dependence is of considerable importance and supplies much useful topochemical information. The divergence can be explained in terms of certain reactions which are considered "abnormal" in the sense that they are not fast surface nucleation followed by a contracting envelope behaviour. These reactions may include the following:

(a) Decomposition at sites such as sub-grain boundaries.

(b) Reaction at point defects close to internal or external surfaces. This may be followed by a radial growth so that one defect could be responsible for the final decomposition of many molecules.

(c) Reaction along dislocation lines possibly followed by expanding cylinders. Some or all of these reactions may have a temperature dependence different from the "normal" reaction. Alternatively, the temperature dependence of their growth may be the same as the "normal" type but that of their rate of initiation may be different. In both cases the variation with temperature of the "r" divergence can be explained.

It is not possible to determine which or to what extent any or all of the above mentioned processes are operative. The analysis which follows is designed merely to show that these "abnormal" processes, when considered in conjunction with the main process, will lead to an equation describing in a qualitative way the divergence of the 3 "r" values and its temperature effect. The main decomposition, which is the penetration of an interface from a fully and rapidly nucleated surface will be referred to as the "normal" process while the "abnormal" processes referred to above will be labelled "internal".

Consider a cubic crystal of side "A" and that within the crystal there are on the average effectively "m" distinct smaller cubes each with an effective side "L" which can independently undergo decomposition in a manner identical to the parent crystal. Then it can be shown (Appendix II) that the final expression for α is given by

$$\alpha = 8r^3t^3(1+m)-12r^2t^2(1+m\theta)+6rt(1+\theta^2m) \quad (3)$$

where $\theta = L/A$, $r = k/A$ (having the same significance as before). The values of r_c, r_s and r_1 predicted by the above mechanism are, therefore,

$$r_c = r(1+m)^{1/3}$$
$$r_s = r(1+\theta m)^{1/2}$$
$$r_1 = r(1+\theta^2 m)$$

It is possible to solve for r, θ and m for any run. In a typical case, $T = 373°C$, the values are $r_c = 0{\cdot}00519\ m^{-1}$, $r_s = 0{\cdot}00486\ m^{-1}$ and $r_1 = 0{\cdot}00470\ m^{-1}$. The corresponding values of r, θ, m are

$$r = 0{\cdot}00107\ m^{-1}, \quad \theta = 0{\cdot}17, \quad m = 114$$

At higher temperatures, when the separation of r_c, r_s and r_1 becomes smaller, the values of r, θ and m naturally have larger error. However, it is possible to obtain crude values and thus also get an idea of their temperature dependence. The latter, quoted as activation energies, are

$$E_r = 29 \text{ kcal/m}$$
$$E_m = 42 \text{ kcal/m}$$
$$E_\theta = -12 \text{ kcal/m}$$

Note that θ has a small but negative "activation energy" (See Appendix III). The observed "activation energies" for r_c, r_s and r_1 are given by

$$r_c = 41 \text{ kcal/m}, \quad r_s = 42 \text{ kcal/m}, \quad r_1 = 44 \text{ kcal/m}$$

Since $m \gg 1$, and $\theta m > 1$ and over most of the temperature range studied $\theta^2 m > 1$,

Act. energy for $r_c = 29+42/3 = 43$ kcal/m
Act. energy for $r_s = 29+42/2-12/2 = 44$ kcal/m
Act. energy for $r_1 = 29+42-2\times 12 = 47$ kcal/m

Considering the errors involved in obtaining r, θ and m the agreement is good. These analyses may be further pursued but no useful purpose would be served because the above is intended as a guide to the topochemistry rather than a model. As mentioned above, numerous other schemes involving "internal" reactions also lead to equations for α which can justifiably give the changes in the "r" separations of Fig. 4. Some other examples will now be given.

(a) It can be assumed that the velocity of penetration of the "internal" type of reaction is k_1, and is different from k, the normal velocity of penetration. If $f = k_1/k$ then

$$\alpha = 8r^3t^3(1+f^3m) - 12r^2t^2(1+f^2\,\Theta m) + 6rt(1+f\,\Theta^2 m)$$

(b) The "internal" reaction can be considered to be merely a reaction at N_0 internal sites (perhaps point defects) which react with a velocity constant k' assumed quite small compared to the constants of the normal reaction such that $k't < 1$ for all t during the run. The number of bromate ions decomposed by this mechanism is then given by

$$n = N_0\,[1-\exp(-k't)]$$

$$\therefore\ \mathrm{d}n/\mathrm{d}t = N_0 k' \exp(-k't) \doteqdot k'N_0 - k'^2N_0t + \frac{k'^3N_0t^2}{2}$$

By the same arguments as used in Appendix II, the result is then

$$\alpha = 6rt\left(1+\frac{\sigma\Phi A}{6}\right) - 12r^2t^2\left(1+\frac{\sigma^2\Phi A^2}{24}\right) + 8r^3t^3\left(1+\frac{\sigma^3\Phi A^3}{48}\right)$$

where

$$\sigma = k'/k, \quad \Phi = N_0/aA^3$$

$$= N_0/(\text{Total No. of molecules in the cube})$$

It can be shown that $r_c > r_s > r_l$ in this case too.

(c) Reaction at dislocations can be expected to give terms within the cubic, square and linear coefficients. Thus, reaction along a dislocation line yields product molecules proportional to time. If reaction proceeds very quickly along a dislocation line and then the whole length of the line grows radially, the number of product molecules will be proportional to t^2 (c.f. YOUNG's work on reaction around a fission track).(6) Reaction along the line and radially at about similar rates yields reaction products proportional to t^3.

It is clear that many different types of "internal" reactions can yield the same type of α/t dependence. There are many variations even on the few examples mentioned above. For instance, in the example (b), the number of internal sites could be very small, yet each could give rise to the decomposition of many molecules. Their reaction law could be linear rather than exponential, but their growth law cubic or even square, etc. etc. The models are outlined merely to show that "internal" reactions can account for the behavior of the cube law parameters. The reason for the introduction of the cube law analysis is that it tends to demonstrate quite vividly that irradiation enhances these "internal" processes, but this discussion will be left to Part II of this paper.

3. *The low temperature region*

It is not possible to draw too many rigid conclusions about the topochemistry in the low temperature region. The α/t plots are necessarily less accurate and it was impossible to obtain any activation energy values. However, some interesting features exist and some inferences of a qualitative kind can be made. Two salient features emerge:

(a) The cube law parameters "r" where they are feasibly obtained, show very large divergence.

(b) The middle part of the reaction consists of an unusually large "linear" region, i.e. where $\mathrm{d}\alpha/\mathrm{d}t$ is constant.

With a contracting envelope mechanism the maximum rate occurs initially and then the rate decays. However, reaction along a dislocation line is at a constant rate. This type of decomposition is discussed later. If it should assume a significant role at any temperature, the rate would drop at first due to the dominance of the contracting envelope mechanism and when it reached a low enough point, the constant "linear" region would begin to dominate. The author believes that the appearance of the "linear" region is due specifically to decomposition along dislocation lines. It is interesting to note that the "linear" region becomes more pronounced the lower the temperature. Figure 5 shows a plot of α_B vs. temp., where α_B is the approximate value of α at which the linear region becomes noticeable. The full circles are for normal unground material and the values clearly drop with decreasing temperature. Thus the process causing the "linearity" is more in evidence at lower temperatures and at the same temperature is more pronounced upon grinding (open circles). If the values of r_c, r_s and r_l can be trusted at low temperatures, it may also be supposed that all of the "internal" type of reactions are relatively enhanced here—this is not an unreasonable suggestion since these processes will probably have lower activation energies than the "normal" ones.

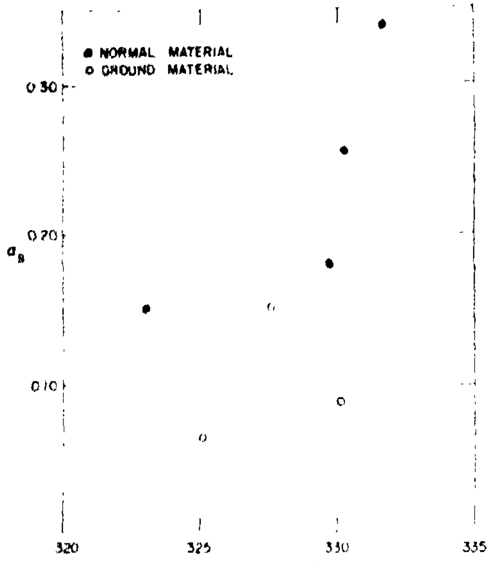

FIG. 5. α_B vs. temperature

4. *The effect of grinding*

The appearance in the high temperature range of the initial "linear" region on grinding is probably indicative of processes which occur at constant rate superimposed on the main reaction. The early stages of the latter are in any case "linear" since $(d\alpha/dt)_{t=0} = c$. The superimposed reaction, therefore, need not be as relatively important as the α/t curves would suggest. They can be identified with reaction along dislocation lines or even reaction at isolated point defects (the number decomposed at time t is $n = N_0 [1-\exp(-kt)]$ which becomes $(N_0k)t$ at low times). The "r" separations (after this initial region) are larger and if they can be trusted, one might again conclude a relatively larger contribution from "internal" reactions—a reasonable supposition with ground material.

In the low temperature region, the effect of grinding is to lower α_B (see Fig. 5) relative to unground material. This suggests an enhanced influence of decomposition along dislocations. The reason for the appearance of a linear region before the cubic at high temperature and vice versa at low temperatures is probably related in some subtle way to relative activation energies. At very low temperatures decomposition along dislocations are very pronounced. As the temperature increases, they become less so. However, below the discontinuity one is still dealing with reaction of a solid. In the absence of incipient melting, the "linear" region would probably disappear at higher temperatures. Since melting does occur, a whole new set of activation energies come into play. Now it is possible again for *melting* at a dislocation to be faster than at a surface. However, these ideas are speculative and should be treated as such.

DISCUSSION

The decomposition appears to belong to the same general class as $KBrO_3$, i.e. those decompositions in which nucleation is rapid over all surfaces. The nuclei are not discreet but form in large numbers and constitute an interface which, as decomposition proceeds, moves progressively into the interior of the crystal. The implication is that the activation energy for nucleus formation is of the same magnitude as that for interface penetration. Both processes may be simple molecular decompositions of single bromate ions.

Of more interest is the large discontinuity in the Arrhenius plot. It is of larger magnitude than that observed for $KBrO_3$ and is sharper, i.e. occurs over a smaller temperature range. There is very little doubt that the discontinuity is associated with the onset of melting. This is confirmed by visual observations. The following consideration shows also that the increase in rate by a factor of about forty over the discontinuity is consistent with melting. A decomposing bromate ion in the liquid phase will need to overcome an energy barrier which is smaller than the corresponding value for the solid by an amount equal to the latent heat of fusion. Assuming the same activated complexes and approximately the same frequency factors, then the ratio of reaction rate in the two phases is given by

$$k_L/k_s = 40 = \exp(\Delta E/RT)$$

The temperature at the discontinuity is ~ 330°C, therefore $\Delta E \sim 4{\cdot}4$ kcal/m which is probably of the right order of magnitude for melting (the actual quantity is not known). The latent heat of fusion of $NaClO_3$ for example is 5·2 kcal/m. This argument could not have been used had true melting occurred, i.e. for total liquifaction, for then one would be comparing the homogeneous decomposition of *all* the molecules in the system (in the case of the liquid) with the decomposition of only the surface molecules in the solid. However, in the present system the melting is of the eutectic type and occurs at surfaces where the product and reactant can mix. Hence, in the above analysis, the same number of molecules are being compared.

The most interesting conclusion of this work concerns the possibility of reactions on a large scale at places other than the surface. Decomposition at point defects, dislocations and in general any type of imperfection can occur concurrently with the main reaction. This possibility has hitherto been ignored in treating reactions of the type which proceed through rapid surface nucleation and subsequent interface penetration. However, these reactions have from time to time been postulated in solid state reactions where the activation energy for nucleus formation is high, so that preferential nucleus formation at "irregular" sites become noticeable.(5)

The assertion of decomposition along dislocation lines must be clarified. The question is raised as to how large a cross-section is involved (with the dislocation line as center). If one only considers the immediate vicinity of a dislocation, where the strains are excessive, one may not have sufficient dislocations, as a general rule, to account for the sizeable effect observed here. However, certain mechanisms can be envisaged which allow for the decomposition of considerably more molecules than the above consideration predicts. One such mechanism is the preferential decomposition at a step which is present when a screw dislocation meets a surface. This would proceed by decomposition at the same step which is never eliminated, so that layer upon layer of crystals perpendicular to the screw dislocation are decomposed. This in a sense is the reverse of FRANK's theory of crystal growth from slightly supersaturated solutions.(11) It is very likely that such mechanisms would involve activation energies lower than "normal" and would therefore become noticeable only at lower temperatures. The "linear" rates at low temperatures have been previously observed and are discussed in a separate paper.(10) It might be mentioned here that a similar phenomenon was found in the oxydation of graphite.(12)

One might, in passing, mention the possible connection between the "internal" reactions and some recent findings in the field of radiation chemistry.(8, 9) In the latter strong evidence has been found for a "cage" effect in radiation decomposition. Thus, in the radiation decomposition of say, NO_3^- ions, an enhancement of rate is suspected in regions where an unusually large "free space" exists into which the reaction $NO_3^- \rightarrow NO_2^- + O$ may proceed. This preferential decomposition is suspected at defect structure such as vacancies or dislocations (which also possess additional "free space"). In principle, the thermal decomposition of BrO_3^- ions may experience a similar influence. This is especially true if the mechanism of the decomposition is a simple unimolecular splitting not involving electron transfers of any kind (since the decomposition might conceivably occur through electronic excitation to unstable excited species).

As with the $KBrO_3$ decomposition,(1) there is little light thrown on the fundamental molecular step which leads to decomposition. The present experiments can describe some of the topochemical behavior but not the final chemical act leading to decomposition. However, there is no evidence that this final act is not a simple unimolecular disruption of a bromate ion to yield a bromide ion and oxygen, the latter in the form of either three atoms or one molecule and one atom. It might be added here that the Br–O bond strength is about 50 kcal/m which is quite close to the value of the activation energy. There is the possibility that this decomposition is catalysed by bromide ions as was mentioned in the discussion of the $KBrO_3$ reaction.(1) The bromide ions may act as electron donors to the oxygen atoms on an undisrupted bromate ion and so facilitate the decomposition.

It was not possible to get an activation energy in the low temperature range and the kinetic behavior appeared markedly changed here. It is interesting to compare this aspect of the reaction with $KBrO_3$. In the latter case, the kinetic behavior below the discontinuity was not too different from above it. Also, it was possible to obtain activation energies in the low temperature range because the rates were measurable over a long enough temperature span. The essential difference between the high and low temperature decomposition was the melting. With $NaBrO_3$, however, there is the qualitative change at low temperature. The "abnormal" reactions at imperfections may now be dominant at lower temperatures. The melting temperature is somewhat lower than $KBrO_3$ but it is quite likely that if it were higher, a region within the low temperature range would be visible where the normal type of reaction would become dominant. One probably need not go further than this for an explanation of the different behavior between $NaBrO_3$ and $KBrO_3$.

SUMMARY

Sodium bromate decomposes completely into sodium bromide and oxygen. The bromide can form a eutectic mixture with the bromate and incipient melting occurs above a certain temperature which is accompanied by a greatly enhanced reaction rate. The normal tendency is for rapid nucleation at surfaces, but other reactions such as decomposition along dislocation lines (and maybe at defects) occur as well, particularly at lower temperatures.

Acknowledgements The author wishes to thank Drs. G. J. Dienes, T. B. Flanagan and D. Rosenblatt for many useful discussions. The continued interest of Dr. J. V. R. Kaufman is appreciated.

REFERENCES

1. Jach J., *Proc. 4th International Symposium on the Reactivity of Solids.* (Edited by de Boer J. H.) p. 334. Elsevier, Amsterdam (1960).
2. *Handbook of Chemistry and Physics*, 40th ed. Chemical Rubber Publishing Co.
3. *Lange's Handbook of Chemistry.*
4. Glasner A. and Weidenfeld L., *J. Amer. Chem. Soc.*, **74**, 2467 (1952)
5. Garner W. E., *Chemistry of the Solid State*, Chap. 7 and 9. Butterworths, London (1955).
6. Young D. A., *J. Chem. Soc.* **877**, 4533 (1960).
7. *International Critical Tables.*
8. Cunningham J., *J. phys. Chem.* **65**, 628 (1961).
9. Johnson E. R., *J. Amer. chem. Soc.* **80**, 4460 (1958).
10. Jach J. (to be published).
11. Frank F. C., *Dislocations and Plastic Flow in Crystals*, Cottrell, Oxford (1953).
12. Hennig G. R., Dienes G. J. and Kosiba W. *International Conference on the peaceful uses of atomic energy. Geneva* (1958). *Proceedings of the Second*, Paper No. 1778.

APPENDIX I

Consider a cube, side A, all of whose surfaces nucleate instantly. The decomposition then follows a contracting envelope mechanism in which the sides advance into the crystal at a velocity k. After time t, the virgin crystal remaining is still a cube, but of side $(A-2kt)$ and the volume of crystal decomposed at time t, i.e. V_t is given by

$$V_t = A^3-(A-2kt)^3 \tag{4}$$

and

$$\begin{aligned}\alpha = \frac{V_t}{A^3} &= \frac{A^3-(A-2kt)^3}{A^3}\\ &= 8\left(\frac{k}{A}\right)^3 t^3-12\left(\frac{k}{A}\right)^2 t^2+6\left(\frac{k}{A}\right)t\\ &= 8r^3t^3-12r^2t^2+6rt\end{aligned} \tag{5}$$

where

$$r = k/A$$

APPENDIX II

The number of molten bromate ions at time t resulting from the normal process is given by

$$n = a[A^3-(A-2kt)^3]$$

(See Appendix I), where "a" is a conversion factor from volume to number of molecules. The rate of production of these due to the normal process is then

$$(\mathrm{d}n/\mathrm{d}t)\text{ normal} = 6ka(A-2kt)^2$$

and that due to the "internal" process is

$$(\mathrm{d}n/\mathrm{d}t)\text{ internal} = m[6ka(L-2kt)^2]$$

The net rate of production of molten bromate ions is then

$$\mathrm{d}n/\mathrm{d}t = 6ka(A-2kt)^2+6kam(L-2kt)^2$$

If it is now assumed that the rate of decomposition of bromate ions equals their rate of appearance as molten ions, then

$$\mathrm{d}/\mathrm{d}t\ (O_2) = \tfrac{3}{2}\cdot \mathrm{d}n/\mathrm{d}t$$

where (O_2) = number of molecules oxygen evolved.

$$\therefore\ (O_2) = \tfrac{3}{2}\int (\mathrm{d}n/\mathrm{d}t)\,\mathrm{d}t + \text{constant}$$

and $\alpha = (O_2)/$total number of oxygen molecules which can be evolved.

$$= \frac{\frac{3}{2}\int\left(\frac{\mathrm{d}n}{\mathrm{d}t}\right)\mathrm{d}t}{\frac{3}{2}\,aA^3} + \text{constant}$$

$$\therefore\ \alpha = 1/aA^3\int[6ka(A-2kt)^2 + 6kam(L-2kt)^2]\,\mathrm{d}t + \text{constant}$$

$$= 8r^3t^3(1+m) - 12r^2t^2(1+\theta m) + 6rt(1+\theta^2 m)$$

Note:

$$\alpha = 0\ at,\quad t = 0$$

$$\theta = L/A,\quad r = k/A$$

APPENDIX III

The fact that the experimental data yields a negative value for the "activation energy" of Θ is consistent with the definition of Θ. Thus $\Theta = L/A$ and since there are on average m smaller cubes of average size L per large cube of size A, $mL^3 = A^3$ and $m\Theta^3 = 1$.
Hence

$$\frac{\partial \ln m}{\partial(1/T)} = -3\frac{\partial \ln \Theta}{\partial(1/T)} \quad \therefore\ E_m = -3E_\Theta$$

Substituting the value $E_m = 42$ kcal/m and $E_\Theta = -12$ kcal/m, it is seen that the consistency is good.

J. Phys. Chem. Solids Pergamon Press 1963. Vol. 24, pp. 75–84. Printed in Great Britain.

THE THERMAL DECOMPOSITION OF $NaBrO_3$* PART II–IRRADIATED MATERIAL

JOSEPH JACH†

Picatinny Arsenal, Dover, New Jersey, U.S.A.

(*Received* 6 *July* 1962; *revised* 23 *August* 1962)

Abstract—Studies of the thermal decomposition of $NaBrO_3$ reported in Part I have been extended to include material pre-irradiated with Co^{60} γ-ray and reactor irradiations. The primary effect of the irradiation appears to be an enhancement of the melting rate of the eutectic formed between $NaBrO_3$ and the product NaBr, and is accompanied by an enhanced decomposition rate. The conclusion reached with unirradiated material that alternate decomposition routes exist such as at dislocations and other defects is strengthened.

INTRODUCTION

THE THERMAL decomposition of unirradiated polycrystalline $NaBrO_3$ in the temperature range 323–430°C was described in Part I of this paper. The reaction appears to follow a contracting envelope mechanism on the whole, but an attempt was made to demonstrate that decomposition at internal defects such as dislocations, etc. play an important role. Over the larger part of the temperature range studied, the α/t plots fitted very well a cubic equation of the form

$$\alpha = at^3 - bt^2 + ct \qquad (1)$$

where a, b, c are positive numbers. From these numbers it is possible to extract a certain parameter, r, the ratio of the interface penetration rate to a quantity related to the size of the ultimate unit undergoing decomposition. The equality of r derived from each coefficient was shown to be a measure of the truth of the contracting envelope mechanism, while their divergence indicated the apparent importance of reaction at defects already mentioned. The expected increase in the number of such defects upon irradiation might, therefore, be readily detectable.

Towards the lower temperatures, a sharp decrease in overall rate occurs. An exactly similar discontinuity occurred in another bromate, $KBrO_3$(1) and the effect of irradiation on this substance was, in essence, to nullify the discontinuity. It was shown in both bromate studies, that the onset of melting was the cause of the discontinuity and in $KBrO_3$ that irradiation enhances the melting rate and thus inhibits the appearance of the discontinuity. A similar effect was sought in this study.

The original search was directed towards finding any possible changes in activation energies upon irradiation. No big changes of this sort were observed here. However, many runs at different temperatures for one irradiation dose were conducted in order to obtain these activation energies. It turned out that the time available for these experiments would have been more profitably spent had attention been paid to the effect of irradiation *dose* at constant temperature. However, enough information is available for an analysis of the primary irradiation effects. There is one compensation, namely that the many runs at constant dose demonstrate a temperature effect of great interest.

EXPERIMENTAL

The experimental procedures have been outlined in Part I of this paper. The ampoules containing the $NaBrO_3$ were divided into batches of 15 and each batch simultaneously irradiated. Two separate ^{60}Co gamma-ray irradiation doses and three reactor irradiation doses were performed. The details of these irradiations are given below:

---

* Work performed primarily at Brookhaven National Laboratory and supported jointly by Picatinny Arsenal and the U.S. Atomic Energy Commission.

† Guest Scientist, Brookhaven National Laboratory, Upton, N.Y.

Batch 1—^{60}Co gamma-ray irradiation, $3{\cdot}8 \times 10^5$ r/hr at room temperature for 847 hr. Total dose, $3{\cdot}2 \times 10^8$r. The irradiated crystals were a yellow-brown color.

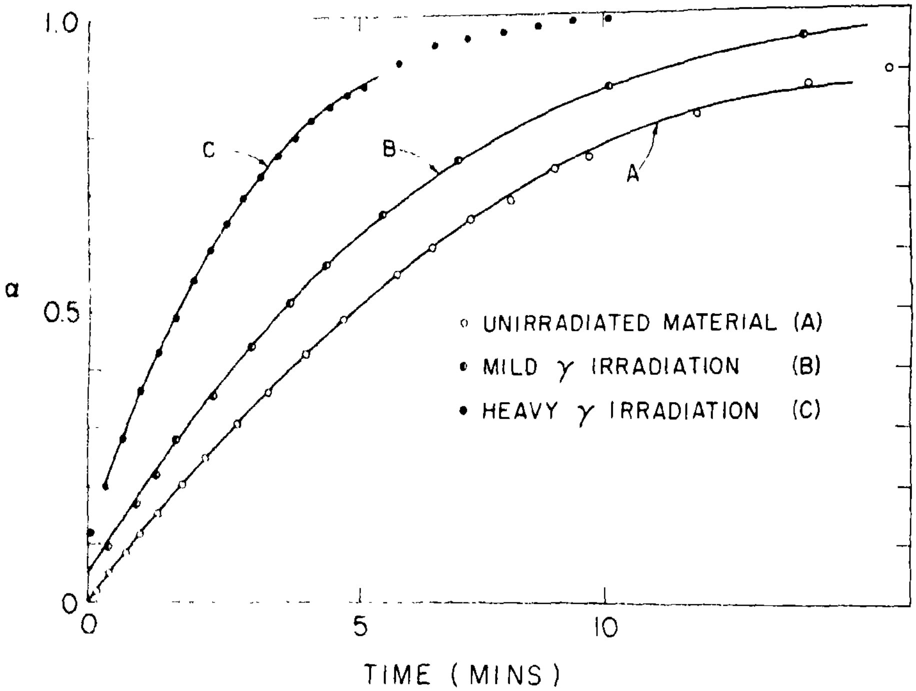

FIG. 1. Fractional decomposition α vs. time (higher temperature range) "Unirradiated" run (404·7°C) fitted to $\alpha = 1{\cdot}33 \times 10^{-5} t^3 - 4{\cdot}56 \times 10^{-3} t^2 + 1{\cdot}234 \times 10^{-1} t$.
"Mild γ" run (408·8°C) fitted to $(\alpha - 0{\cdot}047) = 1{\cdot}95 \times 10^{-4} t^3 - 9{\cdot}30 \times 10^{-3} t^2 + 1{\cdot}576 \times 10^{-1} t$. "Heavy γ" run (395·8°C) fitted to $(\alpha - 0{\cdot}20) = 8{\cdot}95 \times 10^{-4} (t - 0{\cdot}32)^3 - 2{\cdot}86 \times 10^{-2} (t - 0{\cdot}32)^2 + 2{\cdot}604 \times 10^{-1} (t - 0{\cdot}32)$. All runs reduced to common temperature (404·7°C).

Batch 2—Same facility, for 2,496 hr. Total dose, $9{\cdot}5 \times 10^8$r—deep brown crystals.

Batch 3—Brookhaven Research Reactor, 8 hr at a flux 5×10^{12} neutrons/cm² per sec (of which approximately 2×10^{11} were epi-cd). Total dose $1{\cdot}44 \times 10^{17}$ nvt. Temperature of the facility was 50–70°C. Crystals were brownish yellow.

Batch 4—Flux 1×10^{13} neutrons/cm² per sec. 48 hr, total dose $1{\cdot}7 \times 10^{18}$ nvt. Temperature, 50–70°C. Bright yellow crystals.

Batch 5—Same facility as batch 4, total dose $2{\cdot}3 \times 10^{19}$ nvt. Crystals were white and tended to be crumbly with respect to the unirradiated.

These five series will be referred to as follows:

Batch 1—mild γ irradiation.
Batch 2—heavy γ irradiation.
Batch 3—mild reactor irradiation.
Batch 4—intermediate reactor irradiation.
Batch 5—heavy reactor irradiation.

Note: only 4 of the fifteen samples of Batch 4 were successfully irradiated, but the results of the available four are presented.

RESULTS

Shapes of the α/t curves

The effect of irradiation on the α/t plots at constant temperature are described in terms of two temperature regions. The region above the discontinuity (see Fig. 3, Part I) which comprises the

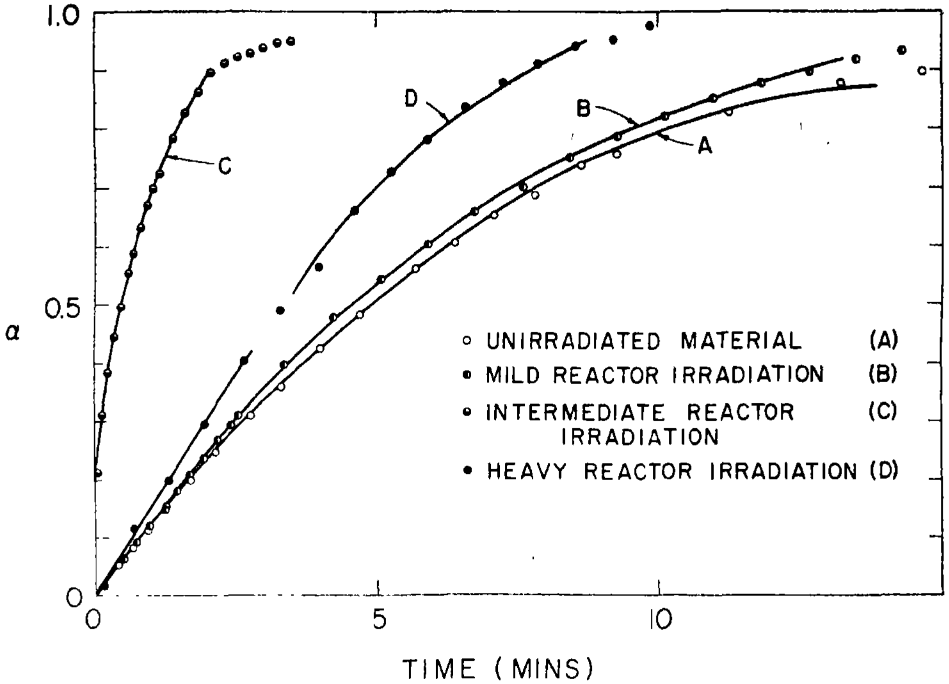

FIG. 2. Fractional decomposition α vs. time (higher temperature range).
"Unirradiated" run (404·7°C) fitted to $\alpha = 1{\cdot}33 \times 10^{-5}t^3 - 4{\cdot}56 \times 10^{-3}t^2 + 1{\cdot}234 \times 10^{-1}t$.
"Mild reactor" run (401·3°C) fitted to $(\alpha - 0{\cdot}15) = 1{\cdot}93 \times 10^{-4}\,(t-1{\cdot}2)^3 - 7{\cdot}83 \times 10^{-3}\,(t-1{\cdot}2)^2 + 1{\cdot}299 \times 10^{-1}\,(t-1{\cdot}2)$
"Intermediate reactor" run (400·5°C) fitted to $(\alpha - 0{\cdot}2) = 0{\cdot}06t^3 - 0{\cdot}32t^2 + 0{\cdot}747t$
"Heavy reactor" run (413·7°C) fitted to $(\alpha - 0{\cdot}51) = 2{\cdot}13 \times 10^{-3}\,(t-3{\cdot}5)^3 - 2{\cdot}54 \times 10^{-2}\,(t-3{\cdot}5)^2 + 1{\cdot}588 \times 10^{-1}\,(t-3{\cdot}5)$
All runs reduced to common temperature (404·7°C).

greater part of the temperature range, is described in Fig. 1. The lower curve is typical of an unirradiated sample, the open circles being experimental points and the solid line a plot of equation (1). The numerical values of the equation appear in the legend. The half closed circles are experimental points for the "mild γ" irradiation and the full circles the "heavy γ" irradiation. Again, equation (1) is represented by the solid lines and the fit is excellent. Two points should be noted:

1. Both irradiations enhance the decomposition rate, the heavier dose having the larger effect.

2. A very rapid gas evolution occurs prior to the main part of the decomposition of irradiated samples which is almost certainly the release of occluded gases when the crystals are placed in the furnace. This is supported by the fact that the amount released is virtually temperature independent.

3. A better fit to the cubic equation is obtained if an origin t_0, α_0 is chosen rather than $t = 0$, $\alpha = 0$. The initial gas evolution is responsible for this.

The corresponding results for neutron irradiation (in the higher temperature range) are shown in Fig. 2. The same run for unirradiated crystals lower line) is shown for reference. Again the points are experimental points and the curved lines represent equation (1) the numerical values being shown in the legend. The following features are of interest here.

1. An overall increase in rate occurs for all the doses.

2. The heaviest dose does *not* result in the

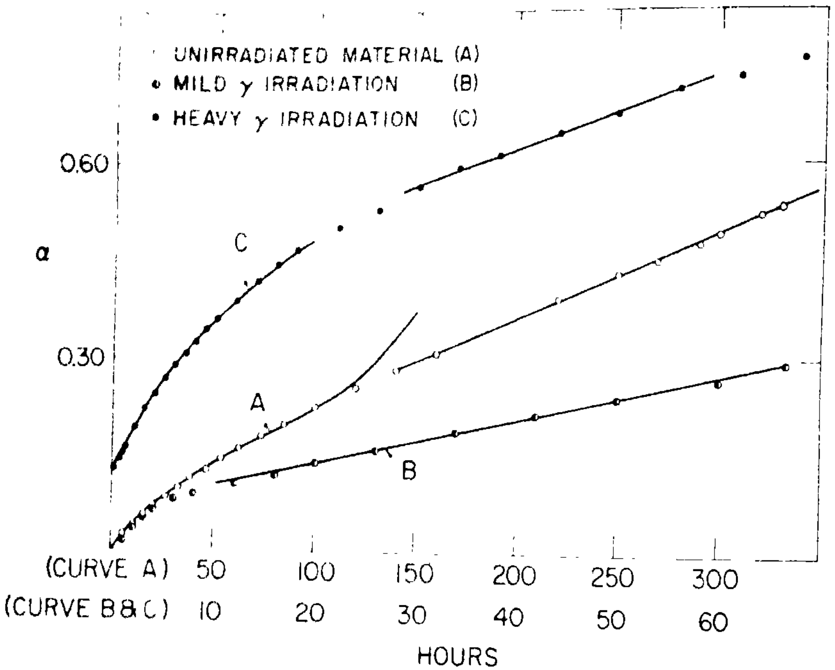

Fig. 3. Fractional decomposition α vs. time (lower temperature range).
"Unirradiated" run (330·0°C) fitted to $\alpha = 1{\cdot}51\times10^{-7}\,t^3 - 3{\cdot}26\times10^{-5}\,t^2 + 3{\cdot}98\times10^{-3}\,t$.
"Mild γ" run (329·3°C) no fit possible.
"Heavy γ" run (331·0°C) fitted to $(\alpha - 0{\cdot}13) = 2{\cdot}17\times10^{-5}\,t^3 - 1{\cdot}18\times10^{-3}\,t^2 + 0{\cdot}0327\,t$

biggest effect. The "intermediate dose" increases the rate far more than either the low or high dose.

3. Curves for the "mild dose" and the "intermediate dose" adequately fit equation (1). The "heavy dose" however, has a specific effect. The points fit a *straight line* to a quite high value of $\alpha(\sim 0{\cdot}45)$. After this equation (1) is fitted by using a judicious α_0, t_0 value. (c.f. ground material in Part I).

The temperatures of the "irradiated" runs in Figs. 1 and 2 are close to but not equal to that for the unirradiated case shown. However, the time scales for the "irradiated" runs are all modified slightly (using an activation energy of 45·3 kcal/m) to correspond to the same temperature as the "unirradiated" run. Since the Arrhenius plot is a straight line, this procedure is justified. The procedure is not justified for runs below or on the discontinuity which are described next. The Arrhenius plot is not a straight line here and, therefore, for purposes of comparison one has to be satisfied with choosing runs as close in temperature as possible.

The behavior of γ-ray irradiated material for temperatures "below" the discontinuity are shown in Fig. 3. Note the time scale change for irradiated material. The details of interest are:

1. The rates are increased upon irradiation including the linear region.

2. The initial stages are complex. With unirradiated material, it is possible to fit equation (1) over a limited region (0–0·2). With "mild γ" the linear region begins at lower α so that the initial range is too small to meaningfully fit equation (1). With "heavy γ" it is again possible to fit the equation (from 0·13–0·50).

3. The "heavy γ" shows an initial gas evolution

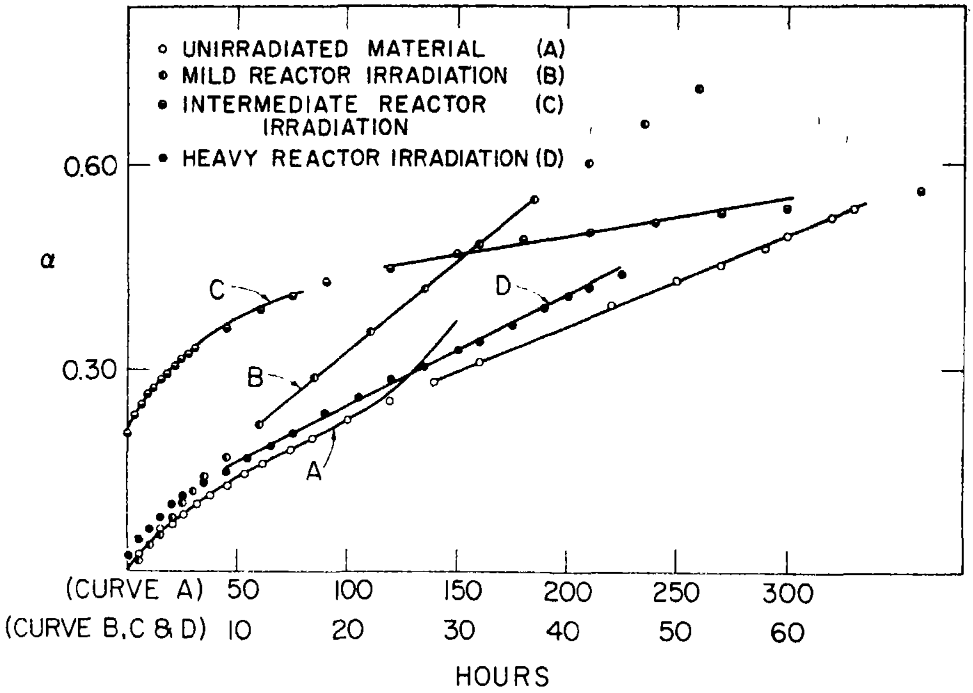

FIG. 4. Fractional decomposition α vs. time (lower temperature range)
"Unirradiated" run (330·0°C) fitted to $\alpha = 1{\cdot}51 \times 10^{-7}\, t^3 - 3{\cdot}26 \times 10^{-5} t^2 + 3{\cdot}98 \times 10^{-3} t$.
"Mild reactor" run (333·4°C) no fit possible.
"Intermediate reactor" run (332·6°C) fitted to $(\alpha - 0{\cdot}21) = 3{\cdot}73 \times 10^{-5} t^3 - 1{\cdot}67 \times 10^{-3} t^2 + 2{\cdot}980 \times 10^{-2} t$
"Heavy reactor" run (330·0°C) no fit possible.

of about the same magnitude as at higher temperatures.

The low temperature decomposition curves of reactor irradiated material are shown in Fig. 4. Again, the salient features are:

1. Irradiation accelerates the rates including those of the linear regions.

2. Complexities again occur at low α. The "mild" and "heavy" runs cannot be fitted with any accuracy to the cubic equation in the initial stages of reaction, since the "linear" regions begin at too low values of α. However, the curve for the "intermediate" dose can be well fitted.

3. An initial gas evolution of about the same magnitude as the high temperature case (0·20) occurs with "intermediate" dose material. A slight evolution occurs with the "mild" dose (0·02) and again no evolution at all for a very long irradiation.

Activation energies

The parameter $k_i = (d\alpha/dt)_{t=0}$ was again chosen to show up the gross variations with temperature. In those cases where the initial slopes were difficult to obtain, k_i was taken from the coefficient of the linear term of the fit to equation (1). The solid line in Fig. 5 represents unirradiated material and the points various irradiations. Irradiation always increases k_i especially at lower temperatures. The longer doses cause bigger increases except for the "heavy reactor" dose which has only a very slight effect.

The activation energy for unirradiated material (above the discontinuity) = 45·3 kcal/m. The corresponding values for irradiated material as determined from a least squares fit to the points above the discontinuity are the following:

"mild γ" 45·1 ± 1·5 kcal/m
"heavy γ" 45·1 ± 1·3 kcal/m
"mild reactor" 42·1 ± 1·3 kcal/m
"heavy reactor" 42·6 ± 1·2 kcal/m

It was, of course, impossible to derive a value for the "intermediate reactor irradiation".

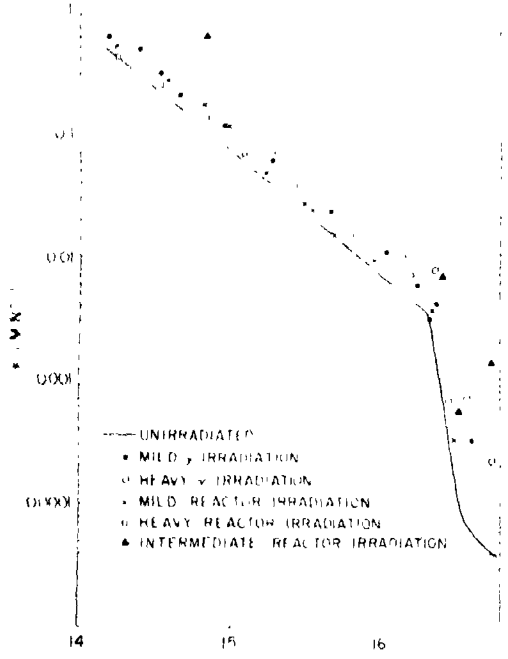

FIG. 5. Arrhenius plot of k_l.

Cube law parameters. The values of r_c, r_s and r_l were obtained from the fits to equation (1) in the same manner as for the "unirradiated" decompositions.

These values are represented by

$$r_c = (a/8)^{1/3}, \quad r_s = (b/12)^{1/2}, \quad r_1 = (c/6).$$

As explained in Part I, for a cube of side A undergoing decomposition by a simple contracting envelope mechanism, the interface penetration velocity being k, the theoretical dependence of α on t, is given by

$$\alpha = 8(k/A)^3t^3-12(k/A)^2t^2+6(k/A)t \quad (2)$$

Equality of r_c, r_s and r_l is then a measure of the correctness of this topochemical scheme and gives (k/A). Departure from equality was interpreted as due to the influence of "internal" type reactions such as those along dislocation lines or at defects, superimposed on the normal contracting envelope reaction.

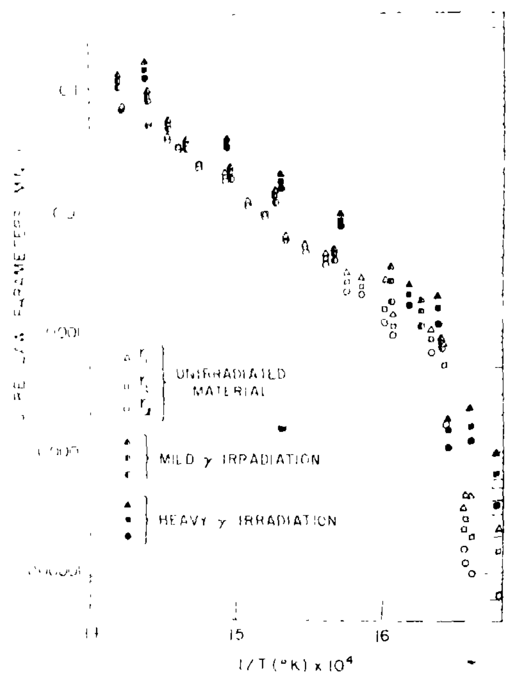

FIG. 6. Arrhenius plot of cube law parameters (showing γ-ray effects).

The values of r_c, r_s and r_l for the γ-ray irradiations are shown in Fig. 6. The triangles represent r_c, the squares r_s and the circles r_l. The open symbols are for unirradiated crystals, the half-full symbols for the "mild γ" case and the full symbols for the "heavy γ" runs. One result from this plot must be emphasized. Irradiation tends to destroy such equality of the r values as exists for the unirradiated material and where there is only a slight spread for the latter, it is enhanced. At very low temperatures, where only the "heavy γ" case can be represented with any accuracy, the "r"

values are higher than the corresponding "unirradiated" ones, but there are insufficient points to conclude an increased spreading.

The corresponding plot for neutron irradiations are shown in Fig. 7. The same general enhanced spreading of the cube law parameters is the rule. (The α/t plot for "heavy reactor" irradiation showed an initial linear region which persisted to high values of $\alpha(0{\cdot}5)$. Equation (1) could only be fitted after this point. For this reason, no emphasis will be placed on their values of r, only two sets being shown for reference.) The "mild reactor" points behave in a very similar way to the "mild γ" ones except that there is a little more scatter here. The "intermediate reactor" values exhibit an even greater spread both at the high and low temperatures.

A summary is given in Table I of the magnitudes of some of the enhancements in rate accompanying irradiation. Also given are the percent decomposition caused by the irradiation prior to the thermal decomposition denoted by "pre-thermal decomposition" and the initial gas evolution at the beginning of the thermal decomposition. The symbol R_{th} is the average ratio of k_t (irradiated) to k_t (unirradiated) considered at the

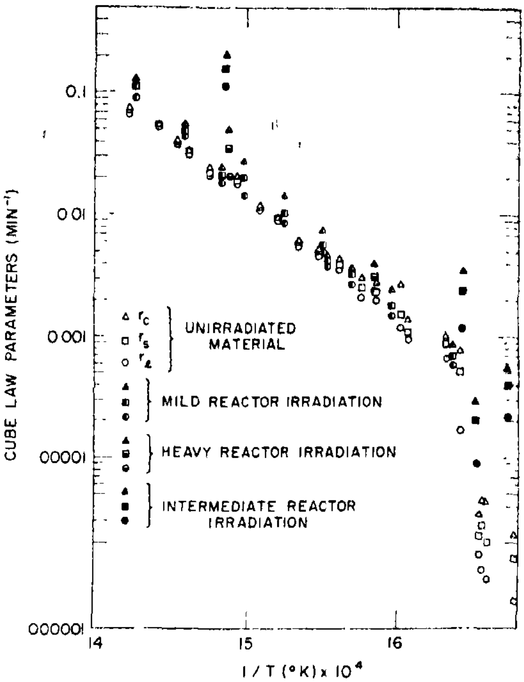

FIG. 7. Arrhenius plot of cube law parameters (showing reactor irradiation effects).

Table 1.

Type of irradiation	Pre-thermal decomposition per cent	Initial gas evolution per cent	R_{th}	R_{tl}	L
Unirradiated	—	0	1	1	1
Mild γ ($3{\cdot}2\times10^8$R)	7	0–5	1·5	5	5
Heavy γ ($9{\cdot}5\times10^8$R)	26	12	2·2	10	4
Mild Reactor ($1{\cdot}4\times10^{17}$ nvt)	3	0	1·4	2	10
Intermediate Reactor ($1{\cdot}7\times10^{18}$ nvt)	51	20	6·0	25	2
Heavy Reactor ($2{\cdot}3\times10^{19}$ nvt)	70	0–2	1·3	—	6

higher temperatures (i.e. above the discontinuity) while R_{ll} represents the same quantity at temperatures "below" the discontinuity. The symbol L refers to the irradiation enhancement ratio of the rate of the "linear" region (found at the low temperatures). The "pre-thermal decomposition" values are obtained from the average decrease accompanying irradiation of the values of $P\infty/w$, the final pressure/weight ratios of the samples. After each run the temperature was raised to about 450°C to ensure complete decomposition. With unirradiated material this corresponded to theoretical 100 per cent decomposition. Where the unirradiated material was taken to apparent completion in a run, i.e. at the higher temperatures there was no further gas evolution at 450°C. The reaction therefore normally goes to completion within experimental error.

DISCUSSION

Topochemical effects of the irradiation

The results in Part I were interpreted in terms of a contracting envelope which is modified, especially at low temperatures, by reactions at defects, dislocations, etc. The general increase in spread of the cube law parameters for all the irradiations is regarded as strengthening this conclusion since an increase in the number of such imperfections is expected on irradiation. However, account must also be taken of the melting occurring above the discontinuity and the effect of irradiation on it.

(a) *Upper temperature range.* For all irradiations the overall rates are increased and the cube-law parameters more spread out. The shape of the α/t plots remain the same, except for an initial gas evolution in some cases. The probable origin of these enhanced rates is twofold. An increase in the number of imperfections from which reaction can propagate and an enhanced melting rate. The latter is almost certainly the main influence for the following reasons. Nucleation consists of a rapid decomposition of surface molecules with the formation of an interface which then penetrates the crystal through further decomposition. In many other decompositions a different situation exists in that a relatively small number of nuclei form which grow to relatively large sizes and are even visible as distinct units sometimes.(3, 4) With this latter type irradiation is expected to enhance the decomposition rate through increased numbers of nuclei. Clearly the same enhancement mechanism cannot apply with $NaBrO_3$ since in this case nucleation is rapid and complete even without irradiation. Thus the enhanced rates upon irradiation must arise from an increased penetration (or growth) rate. Melting precedes decomposition and since irradiation will not affect the liquid state it is safe to assume an enhanced melting rate. This conclusion is strengthened by the fact that, except for "heavy reactor" dose which is discussed separately below, the cube law is maintained upon irradiation suggesting an essentially quantitative change only. Another supporting feature is that the temperature at the upper end of the discontinuity in the Arrhenius plot (see Fig. 5) is somewhat lowered by irradiation In other words, irradiation maintains melting to slightly lower temperatures.

The mechanism of the irradiation enhanced melting rate is probably associated with strain brought about by the irradiation decomposition products NaBr and O_2. The replacement of BrO_3^- ions by Br^- must result in large localized strains for the percentage decomposition brought about by the irradiation doses used here. This replacement is not confined to any specific location but occurs more or less homogeneously throughout the bulk. An irradiation decomposition of say 3·7 per cent (which is very low compared to the samples considered here) means on average one foreign body in a cage $3\times3\times3$ lattice units, a situation which must result in considerable strain. The radius of the BrO_3^- ion is more than double that of the Br^- ion.

The other contribution to enhanced rates is the superimposition upon the main reaction of decomposition along and at defects. The increased "r" separation is evidence for this In essence this means that melting and decomposition have found routes in addition to those on surfaces. These exist in unirradiated material but are multiplied upon irradiation.

The result for a very heavy reactor irradiation is a perplexing one. The much enhanced rate of the "intermediate" dose almost entirely disappears. The author believes that a full and correct answer cannot be given without a thorough X-ray examination of this material prior to and during decomposition. What follows is merely a speculation. A possible clue is the strange correlation between the initial gas evolution and the enhanced reaction rate. (See Table 1.) The evolutions are most probably derived from pockets of gas collected during irradiation which leave the crystallites in a highly strained state. The absence of the evolution for the "heavy" dose suggests a partial relaxation of this strain which might then supposedly result in a reduced melting rate and thus decomposition rate. In view of the high percentage pre-thermal irradiation decomposition for this material, it seems appropriate to regard it in a somewhat different light compared to the milder doses. The author feels that the principles outlined in Part I regarding reaction at "abnormal" sites be invoked only in an explanation of the behavior of material irradiated at the milder doses.

(b) *Low temperature range.* In Part I, the "linear" region of the α/t plot for unirradiated material was explained in terms of reaction along dislocation lines which are supposedly of lower activation energy and hence more noticeable at lower temperatures. The meaning of decomposition along a dislocation was examined in Part I. The linear region is preceded by one which more or less fits equation (1). The main reaction begins at its maximum rate which decays to a point where the "dislocation" reaction becomes a significant contributor. With more dislocations initially present, the "linear" region is expected to begin at lower α's. This does occur for ground material. Figures 3 and 4 show the same phenomenon true for "mild γ", "mild reactor" and "heavy reactor" irradiations. However, the two irradiations which caused the biggest overall rate increase, i.e. "heavy γ" and "intermediate reactor" do not conform to this behavior. Instead they begin with a large gas evolution which is followed immediately by a region well fitted to equation (1), after which a "linear" region is observed at high α. It seems reasonable to now assume that the state of the crystal, which is probably highly strained after the latter two irradiations leads to an onset of melting either non-existent or small with lower irradiation doses. The "main" reaction is thus once more enhanced, leaving the "linear" region observable only at high α. At this point some of the reactions leading to "linear" kinetics have probably terminated and for this reason the values of L (see Table 1) for the two irradiations which showed such big increases in k_t now show only a poor acceleration of the "linear" region.

In passing, it may be noted that R_{tl} (see Table 1) is in general bigger than R_{th}, i.e. the initial stages of the reaction are accelerated by irradiation by larger factors at low than at high temperatures. On the basis of what has already been postulated this makes good sense. Above the discontinuity, the irradiation enhances melting already present. Below the discontinuity, incipient melting is actually brought on by the irradiation. This certainly represents a bigger reaction rate increase.

Activation energy

One further point is worth noting on the overall topochemical behavior and this concerns the slight drop in activation energy (above the discontinuity) observed with reactor irradiation. (Only a very slight drop occurs with γ-ray irradiation and this is within the experimental and statistical probable error.) The true meaning of the activation energy when melting is present is a complex question. Melting and decomposition are both rate processes and are in this case mutually dependent on each other. However, if melting is easier along a dislocation line than on a normal surface, this "dislocation decomposition" will have a lower overall activation energy. If this is accepted, the drop in activation energy on neutron but not on γ-ray irradiation is interesting. It suggests that possibly the damage with neutrons is a more severe but more localized affair, occurring in tracks from which melting and decomposition occur at the beginning of the reaction. The damage from γ-rays, if more homogeneously spread, would not show up in so definite a way in the activation energy. A difference of this kind between γ-ray and pile irradiation damage of NaN_3 has recently been reported.(2)

The results described in this paper do not point to any mechanism for the ultimate molecular decomposition. In Part I it was suggested that a direct molecular split is not inconsistent with any of the results so far obtained with either $NaBrO_3$ or $KBrO_3$. For a further discussion of this the reader is referred to Part I and to the paper dealing with the $KBrO_3$ decomposition.(1) Some aspects of melting are discussed in Part I of the paper.

SUMMARY

There is a two-fold effect on this decomposition of neutron and γ-ray irradiation. Firstly, the melting rates of a eutectic formed between $NaBrO_3$ and the product NaBr are enhanced by both types of irradiation. It is believed that this acceleration is caused by strain imposed by radiation decomposition products. Secondly, the irradiations increase the number of imperfections already present in unirradiated material and that these provide further routes by which the reaction may proceed.

Acknowledgements—The author wishes to thank Drs. G. J. Dienes, T. B. Flanagan and D. Rosenblatt for many useful discussions. The continued interest of Dr. J. V. R. Kaufman is appreciated.

REFERENCES

1. Jach J., *Proc. 4th Int. Sym. Reactivity of Solids.* (Edited by de Boer J. H.), p. 334. Elsevier, Amsterdam (1960).
2. Keating D. and Krasner S., *J. Phys. Chem. Solids* **20,** 150 (1961).
3. Flanagan T. B., *Nature, Lond.* **181,** 43 (1958).
4. Garner W. E., *Chemistry of the Solid State* Chap. 7 Butterworths, London (1955) and others.
5. Sawkill J., *Proc. Roy. Soc.* **A229,** 135 (1955).

J. Phys. Chem. Solids Pergamon Press 1963. Vol. 24. pp. 85–93. Printed in Great Britain.

$Pb(Sc_{0\cdot5}Nb_{0\cdot5})_x\Phi_{1-x}O_3$, PEROVSKITE-TYPE FERROELECTRIC SOLID SOLUTIONS POSSESSING RELATIVELY LARGE SPONTANEOUS POLARIZATIONS*

V. J. JOHNSON, M. W. VALENTA, J. E. DOUGHERTY, R. M. DOUGLASS and J. W. MEADOWS

Los Alamos Scientific Laboratory, University of California, Los Alamos, New Mexico

(*Received* 26 *October* 1961; *revised* 14 *August* 1962)

Abstract—The spontaneous polarization and Curie temperature were measured for various compositions of the perovskite-type ferroelectric solid solution systems $Pb(Sc_{0\cdot5}Nb_{0\cdot5})_x\Phi_{1-x}O_3$, where Φ is either Ti, Zr, or Hf; ceramic samples were used in all the measurements. The maximum value for the spontaneous polarization of a particular system is found to decrease as Ti is replaced by Zr and Zr by Hf, although the corresponding concentration of the four-valent Φ ion and the temperature at which the spontaneous polarization is measured are not necessarily the same for the three different compositions exhibiting the maximum spontaneous polarization; 30 $\mu C/cm^2$ was the largest value that was observed for the spontaneous polarization. An increase in the concentration of Φ increases the Curie temperature of the respective solid solution system. Curie points decrease in value, correspondingly, as Ti is replaced by Zr and Zr by Hf. For perovskite-type ferroelectric solid solutions having the general stoichiometric formula $Pb[(B_{I}^{a+})_x(B_{II}^{b+})_y \ldots]O_3$, it is found that the maximum room temperature spontaneous polarization is obtained when the average ionic radius for all the *B*-ions (of the metal–oxygen octahedra) is approximately 0·75 Å.

INTRODUCTION

APPARENTLY one of the important features of the perovskite-type ferroelectrics having the general formula ABO_3 is the BO_6 octahedron.(1) Perovskite-type compounds in which more than one kind of metal ion is in the *B*-position have been reported.(2,3) A general example of these latter compounds for specific *A* and *B* valences is $A^{2+}[(B_{I}^{3+})_{0\cdot5}(B_{II}^{5+})_{0\cdot5}]O_3$. Ferroelectric, perovskite-type compounds with the formula

$$Pb[(B_{I}^{3+})_{0\cdot5}(B_{II}^{5+})_{0\cdot5}]O_3,$$

where B_I is either Fe or Sc and B_{II} is either Nb or Ta, have also been reported in the literature.(4–6) Matthias' empirical rule(7–9) that for perovskite-type ferroelectrics the *B*-ion(s) within the oxygen octahedra be of a noble gas configuration formed by the removal of the *s* and *d* electrons from the *B*-atom(s) is usually found to be obeyed [with the possible exception of Sn solid solutions such as $Pb(Ti, Sn)O_3$ and $(Ba, Pb)SnO_3$(10,11)].

The purpose of the present investigation was to observe the change in the spontaneous polarization, Curie point, and lattice dimensions with change in composition of some of the more complex perovskite-type ferroelectrics. In compounds (solid solutions) of the type

$$Pb[(B_{I})_x(B_{II})_y(B_{III})_z \ldots]O_3,$$

one would expect qualitatively that the effective *B*-ion would have essentially the average radius and valence of all the different *B*-position ions provided that B_I, B_{II}, B_{III}, ... are each randomly distributed and of similar electron configuration. We have begun an investigation of the solid solution systems

$$Pb[(B_{I}^{3+})_{0\cdot5}(B_{II}^{5+})_{0\cdot5}]O_3\text{–}Pb\Phi O_3,$$

where the randomly distributed B_I and B_{II} ions are both replaced by a four-valent Φ ion. We are reporting in this paper the results obtained on the

---

* Work performed under the auspices of the U.S. Atomic Energy Commission.

solid solution systems $Pb(Sc_{0.5}Nb_{0.5})_x\Phi_{1-x}O_3$, where Φ is either Ti, Zr, or Hf.

EXPERIMENTAL

Solid solution samples were prepared by the usual ceramic techniques. Metallic oxides were ball-milled together, prefired at 800°C, and finally fired as 1 cm diameter discs at a temperature in the range 1200-1400°C.

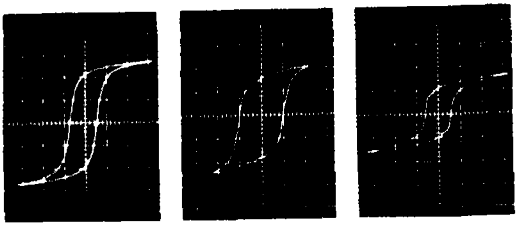
(a) (b) (c)

FIG. 1. Several of the better dielectric hysteresis loops obtained from ceramic solid solution samples. Given are the spontaneous polarization, P_s, coercive field, E_c, and maximum applied electric field, E_a. Samples H, D2, and D3 broke down electrically (as did most of the other samples used in the present investigation) at applied electric fields somewhat greater than values of E_a reported in this paper. Samples D2 and D3 had room temperature values of P_s (about 8 $\mu C/cm^2$) comparable to sample D. (a) $Pb(Sc_{0.5}Nb_{0.5})_{2/3}Zr_{1/3}O_3$ (sample H); $P_s = 22\ \mu C/cm^2$, $E_c = 2{\cdot}7$ kV/cm, and $E_a = 15$ kV/cm at 25°C. (b) $Pb(Sc_{0.5}Nb_{0.5})_{0.5}Ti_{0.5}O_3$ (sample D2); $P_s = 27\ \mu C/cm^2$, $E_c = 8$ kV/cm, and $E_a = 20$ kV/cm at 50°C. (c) $Pb(Sc_{0.5}Nb_{0.5})_{0.5}Ti_{0.5}O_3$ (sample D3); $P_s = 30\ \mu C/cm^2$, $E_c = 5{\cdot}5$ kV/cm, and $E_a = 36$ kV/cm at 150°C. 30 $\mu C/cm^2$ is the largest value of P_s observed in the present work. Some of the samples demonstrated kinks in their hysteresis loops as is clearly seen in this Fig.; the kinks may possibly arise from internal strains causing a partial alignment of domains.

Spontaneous polarizations were obtained from hysteresis loops observed at 60 c/s with the aid of a Sawyer-Tower circuit.(12) Figure 1 shows several of the hysteresis loops.

The Curie temperature is determined from the peak in the value of the relative dielectric constant when measured as a function of temperature. Figure 2 shows the typical behavior of the relative dielectric constant as a function of temperature and composition.

The precision of the spontaneous polarization is estimated to be ± 10 per cent of the values reported in this work, and the precision of the Curie temperatures is estimated to be ±10°C. In the preparation of certain solid solution compositions, the firing procedures proved to be very critical in that relatively small changes in the firing temperature and time could produce a change of a factor of two in the value of the spontaneous polarization and a 50°C change in the observed Curie temperature. A qualitative rule is that the best samples usually had the most square hysteresis loops, the largest value of the spontaneous polarization, and the sharpest peak at the Curie point. The above quoted values for the precision in the spontaneous polarization values and Curie temperatures were estimated from measurements made on several different samples, of a particular composition, prepared under previously determined optimum firing conditions.

In this work the coercive field is considered to be only a measurement of the half-width of a particular hysteresis loop for a given applied electric field.

X-ray powder diffraction photographs were employed in analyzing the reacted samples.

RESULTS

Table 1 contains values of the spontaneous polarization measured at room temperature. With increasing temperature, the spontaneous polarization decreases

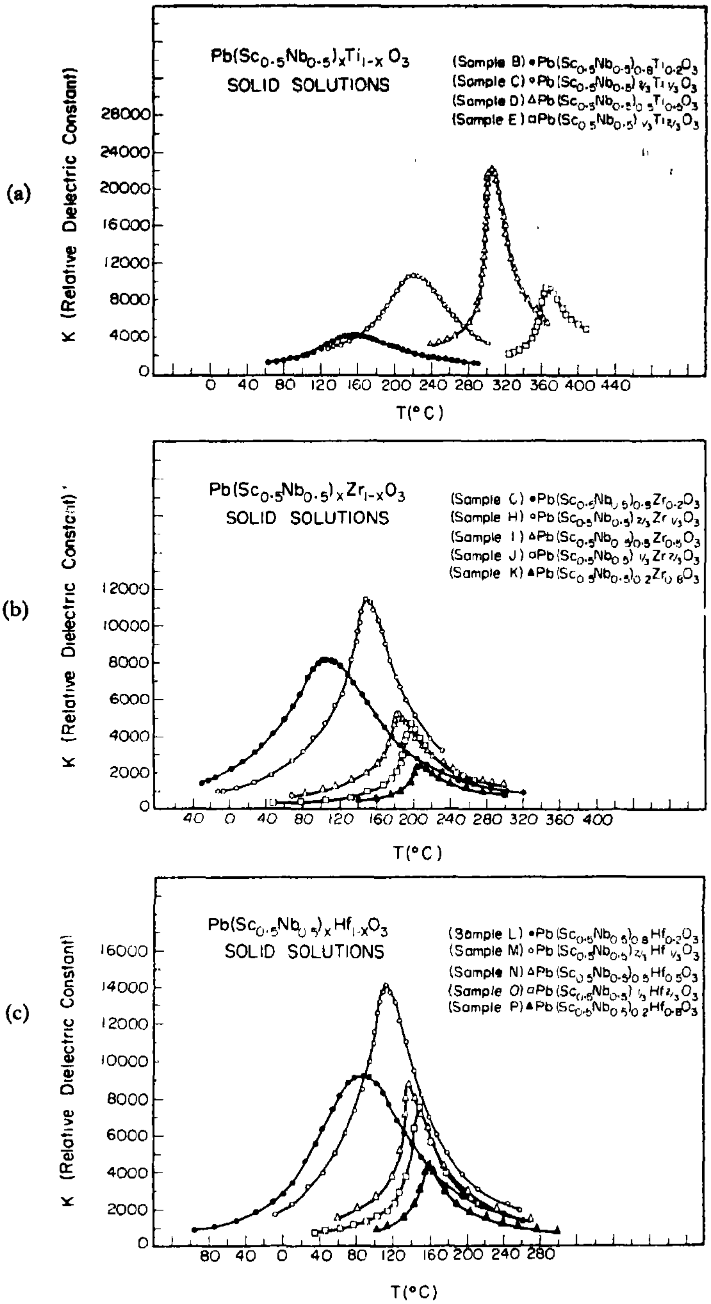

FIG. 2. The relative dielectric constant, *K*, as a function of temperature and composition. (a) The system $Pb(Sc_{0.5}Nb_{0.5})_xTi_{1-x}O_3$. Due to the relatively large electrical conductivity at elevated temperatures, it was not possible to measure *K* in the vicinity of the Curie point of $Pb(Sc_{0.5}Nb_{0.5})_{0.2}Ti_{0.8}O_3$. (b) The system $Pb(Sc_{0.5}Nb_{0.5})_xZr_{1-x}O_3$. (c) The system $Pb(Sc_{0.5}Nb_{0.5})_xHf_{1-x}O_3$.

below the room temperature value [the typical behavior shown in Fig. 3(a)] in all cases except for $Pb(Sc_{0.5}Nb_{0.5})_{0.5}Ti_{0.5}O_3$; in the latter case the spontaneous polarization initially increases with increasing temperature then decreases in the usual manner [Fig. 3(b)].

Table 1. *Values of the spontaneous polarization, P_s, at* 25°C *for a maximum applied electric field, E_a, on ceramic, solid solution samples of the systems* $Pb(Sc_{0.5}Nb_{0.5})_x\Phi_{1-x}O_3$

Solid Φ	Solution x	P_s ($\mu C/cm^2$)	E_A (kV/cm)	Sample
–	1	13	20	A
Ti	0·8	7	26	B
Ti	2/3	14	28	C
Ti	0·5	8	20	D
Ti	1/3	2	30	E
Ti	0·2	0·6	30	F
Zr	0·8	13	28	G
Zr	2/3	22	15	H
Zr	0·5	14	30	I
Zr	1/3	11	28	J
Zr	0·2	5	28	K
Hf	0·8	8	20	L
Hf	2/3	14	20	M
Hf	0·5	7	20	N
Hf	1/3	8	20	O
Hf	0·2	5	20	P

For a particular solid solution system, the composition with the greatest value of the spontaneous polarization also has the sharpest peak in the dielectric constant vs. temperature curve (compare Figs. 1 and 2 and Table 1).

Figures 4 and 5 show the variation of the unit cell dimensions and unit cell volume, respectively, with composition. Generally the X-ray diffraction photographs showed one perovskite-type phase as the principal or only phase detected. In some samples a second, minor phase of uncertain composition having a face-centered-cubic lattice was detected; the cell dimensions used in Figs. 4 and 5 are for the principal phase. No superstructure was found in any of the solid solution samples fabricated by the present experimental techniques; possibly annealing, particularly the solid solutions having the sharpest Curie points, would promote some ordering.

Figure 6 gives a plot of the axial ratio vs. Curie temperature, and a plot of the Curie temperature as a function of composition for the three solid solution systems in question is given in Fig. 7.

Our values of the Curie temperature and spontaneous polarization for $Pb(Sc_{0.5}Nb_{0.5})O_3$ are 81°C and 13 $\mu C/cm^2$, respectively. SMOLENSKII *et al.* have reported(4) 90°C and 3·6 $\mu C/cm^2$; the Curie temperatures agree within our precision. ISMAILZADE reported superstructure(13) which was not detected in our samples.

DISCUSSION

It is seen that the Curie temperature is decreased, correspondingly, as Ti is replaced by Zr and Zr by Hf and that the Curie temperature of a particular solid solution system increases as the concentration of either Ti, Zr, or Hf is increased (see Figure 7). Qualitatively this is a reasonable behavior, since the transition temperature of $PbTiO_3$ is greater than $PbZrO_3$, and $PbZrO_3$ is greater than $PbHfO_3$; also $PbTiO_3$, $PbZrO_3$, and $PbHfO_3$ all have higher transition temperatures than $Pb(Sc_{0.5}Nb_{0.5})O_3$. Considering that the ionic radii of Ti^{4+}, Zr^{4+}, and Hf^{4+} are 0·68 0·79, and 0·78 Å, respectively, and that the average radius for Sc^{3+} and Nb^{5+} is 0·75 Å,(17) it is seen that the general behavior of the unit cell volume with composition is reasonable (Fig. 5). Comparing the general behaviors shown in Figs. 5 and 7, one can conclude that the change in the Curie temperature due to the substitutional replacement of Ti by Zr and Zr by Hf is not only a size effect. Further, niobium ferroelectrics tend to have higher Curie points than tantalum ferroelectrics, e.g. $Pb(Sc_{0.5}Nb_{0.5})O_3$ (80–90°C),(4) $Pb(Sc_{0.5}Ta_{0.5})O_3$ (26°C);(4) $Pb(Fe_{0.5}Nb_{0.5})O_3$ (112°C),(5) $Pb(Fe_{0.5}Ta_{0.5})O_3$ (−30°C);(6) $KNbO_3$ (434°C),(18) and $KTaO_3$ (−260°C).(19) Consequently, a systematic trend is for the Curie temperature to decrease on replacing a *B*-ion (within the oxygen octahedron) by another metal ion positioned lower in a column of the periodic table, e.g. the Curie temperature decreases on going down column IVB from Ti to Zr to Hf or down column VB from Nb to Ta. At present the reason for this trend is not known.

In Fig. 8 a plot is made of the room temperature spontaneous polarization as a function of the average radius for the *B*-position ions. Many different solid solution samples having the stoichiometric formula

$$Pb[(B_{I}^{a+})_x(B_{II}^{b+})_y(B_{III}^{c+})_z\ldots]O_3$$

were prepared in ceramic form. Both the ferroelectric and non-ferroelectric (no observable hysteresis loop) solid solutions are included in the Fig. One notes that the average radius of the metal ions within the oxygen octahedra must be between 0·69 and 0·80 Å for ferroelectricity to occur in a perovskite-type structure having Pb in the *A*-position; a peak in the spontaneous polarization occurs at about 0·75 Å.

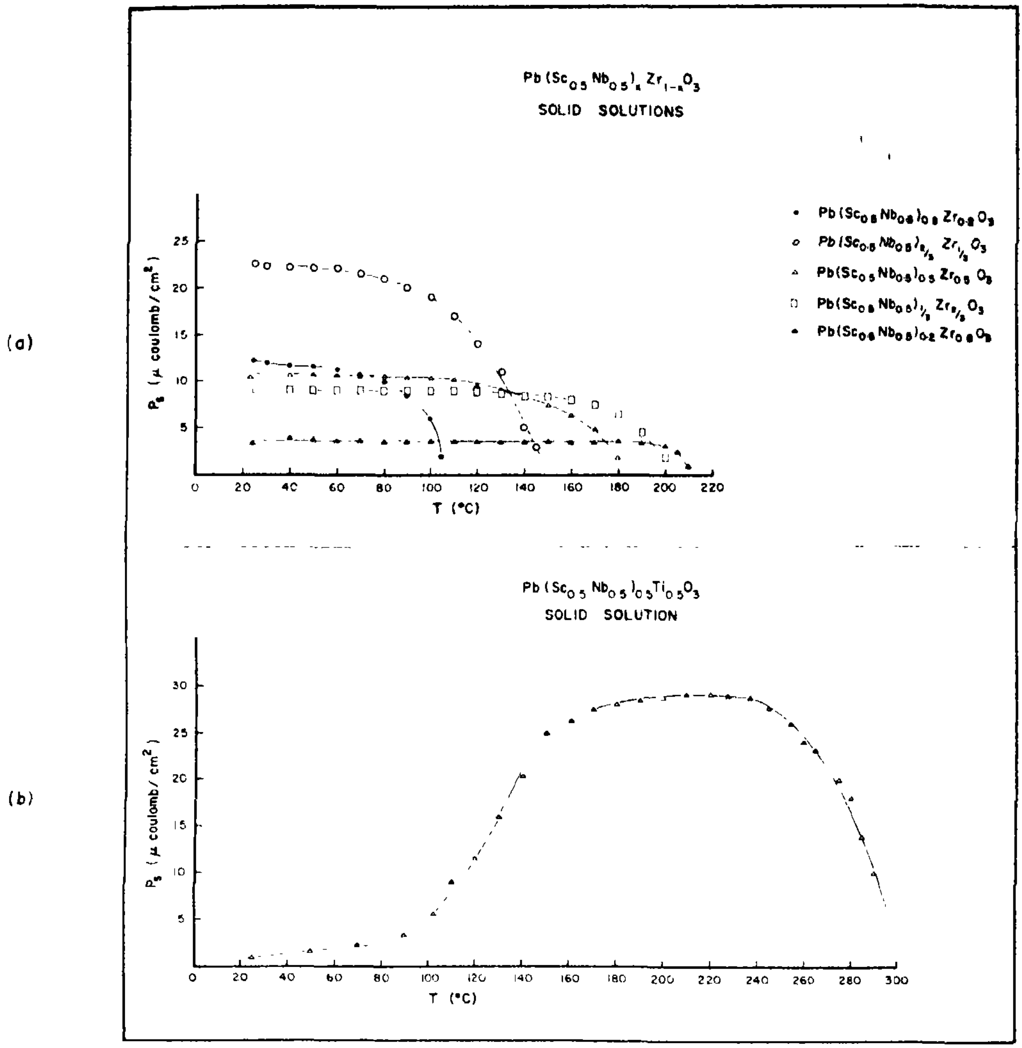

FIG. 3. The spontaneous polarization, P_s, plotted as a function of temperature T. (a) Typical behavior of P_s vs. T shown by five samples of the system $Pb(Sc_{0.5}Nb_{0.5})_xZr_{1-x}O_3$. (b) $Pb(Sc_{0.5}Nb_{0.5})_{0.5}Ti_{0.5}O_3$ samples behaved differently in that P_s initially increases with increasing temperature. Sample D4, used to obtain these data, has an unusually low value of P_s (being appreciably outside our quoted precision) at 25°C; however, this sample gives the most striking increase in P_s with increasing temperature.

These results are in essential agreement with MATTHIAS' empirical rule(20) that the metal ion within the oxygen octahedron must have a radius between 0·6 and 0·7 Å.

The ferroelectric systems

$$Pb(Sc_{0.5}Ta_{0.5})_x\Phi_{1-x}O_3$$

(Φ = Ti, Zr, or Hf) have been studied and the results will be reported shortly in this journal. Also under investigation at present are the ferroelectric systems $Pb[Fe_{0.5}(B_{II})_{0.5}]_x\Phi_{1-x}O_3$, where B_{II} is Nb or Ta. Some of the data from these nine systems have already been included in Fig. 8.

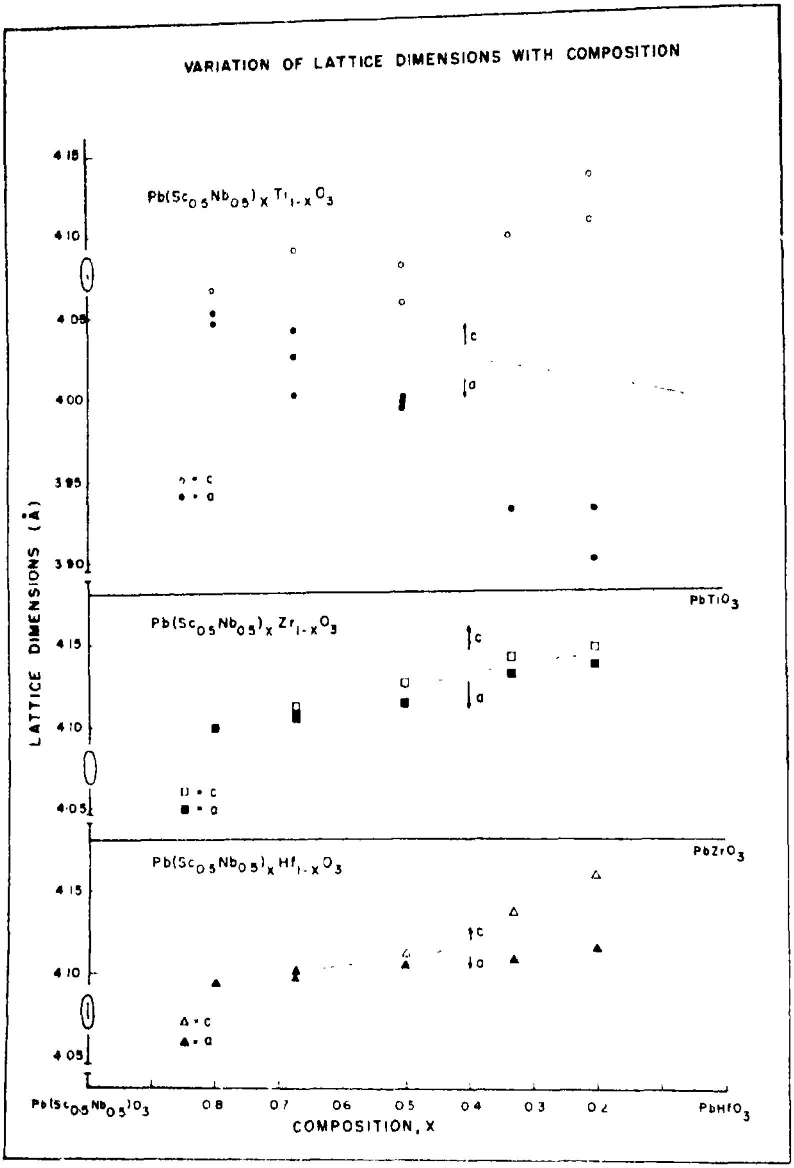

FIG. 4. The variation of the lattice dimensions with composition for the systems $Pb(Sc_{0 \cdot 5}Nb_{0 \cdot 5})_x\Phi_{1-x}O_3$. Several of the data for cubic $Pb(Sc_{0 \cdot 5}Nb_{0 \cdot 5})O_3$ have been included in the Fig. For $x < 0 \cdot 2$, the apparent symmetry changes from tetragonal to orthorhombic in the cases Φ = Zr or Hf.

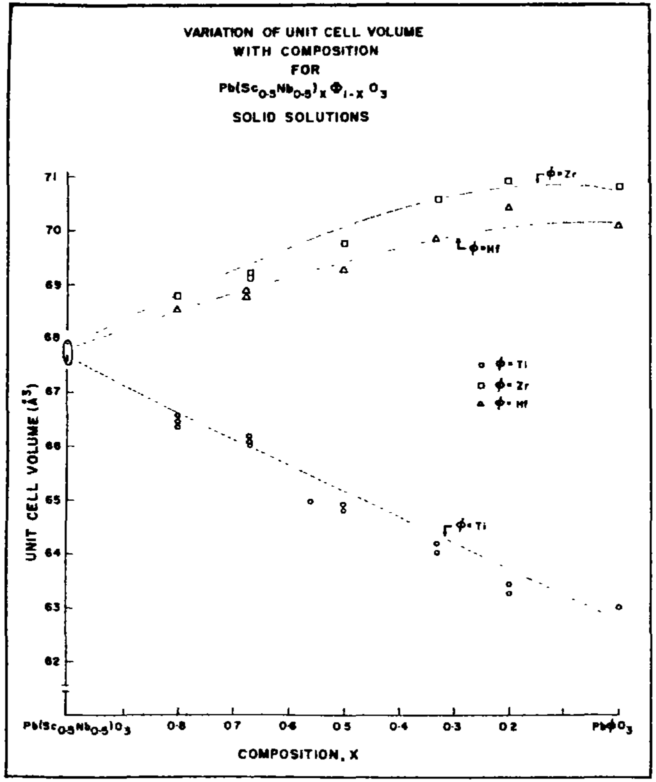

FIG. 5. Variation of the unit cell volume with composition. The unit cell volumes of $PbΦO_3$ ($Φ$ = Ti, Zr, or Hf) are in good agreement with published values.(14-16)

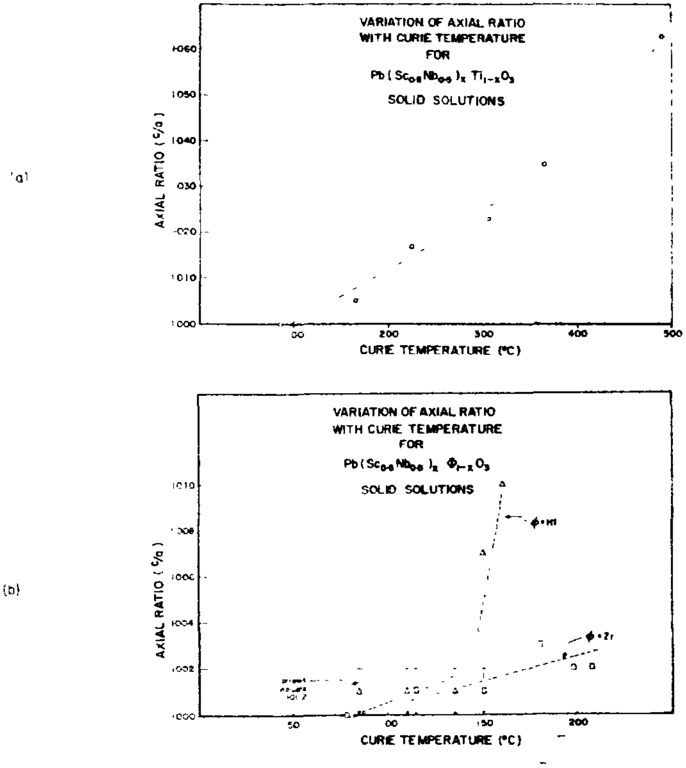

FIG. 6. (a) Dependence of the c/a ratio on the Curie point of the system $Pb(Sc_{0\cdot5}Nb_{0\cdot5})_xTi_{1-x}O_3$. (b) The change in the c/a ratio with Curie point of the systems $Pb(Sc_{0\cdot5}Nb_{0\cdot5})_xΦ_{1-x}O_3$, where $Φ$ is either Zr or Hf.

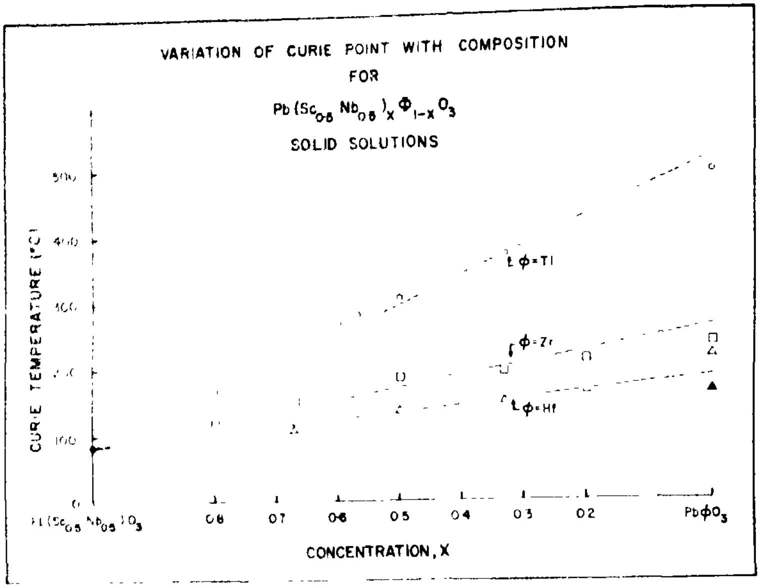

FIG. 7. Dependence of the Curie temperature on the composition of the systems $Pb(Sc_{0.5}Nb_{0.5})_x\Phi_{1-x}O_3$ Published values(14-16) of the end point transition temperatures have been included: 490°C for $PbTiO_3$ and 230°C for $PbZrO_3$, both transition temperatures, 163°C (solid triangle) and 215°C (open triangle), of $PbHfO_3$ have been included for comparison. Dashed straight lines have been drawn through the experimental points only to allow easy differentiation between the three systems.

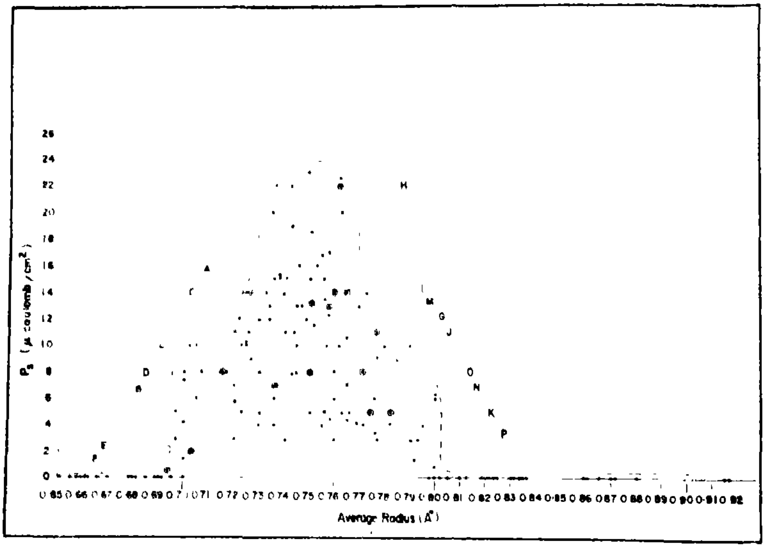

FIG. 8. Dependence of the spontaneous polarization on the average radius for all the metal ions within the oxygen octahedra of Pb perovskite-type ferroelectrics. The labeled points refer to samples listed in Table 1 and Fig. 2. The dashed envelope covering the points serves only to aid easy visual estimation of the ferroelectric ($P_s \neq 0$) and non-ferroelectric ranges ($P_s = 0$).

Acknowledgements—The authors are deeply grateful to B. T. Matthias for his careful reading of the manuscript and constructive criticism. Also, the authors are indebted to J. P. Remeika for many helpful suggestions and stimulating discussions. We would further like to express our appreciation to John A. Gjevre, a temporary staff member at Los Alamos from the University of North Dakota, for his assistance in the early stages of the experimental work.

REERENCES

1. See e.g. Megaw Helen D., *Ferroelectricity in Crystals*. Methuen, London (1957) or Kanzig W., *Solid State Physics*, Vol. 4 (edited by Seitz F. and Turnbull D.) Academic Press, New York (1957).
2. Galasso F., Katz L. and Ward R., *J. Amer. chem. Soc.* **81,** 820 (1959).
3. Brixner L. H., *J. phys. Chem.* **64,** 165 (1960).
4. Smolenskii G. A., Isupov V. A. and Agranovskaya A. I., *Sov. Phys. Solid State* **1,** 150 (1959).
5. Smolenskii G. A., Agranovskaya A., Popov S. and Isupov V., *Sov. Phys. tech. Phys.* **3,** 1981 (1958).
6. Smolenskii G. A., Agranovskaya A. and Isupov V., *Sov. Phys. Solid State* **1,** 907 (1959).
7. Matthias B. T., *Phys. Rev.* **75,** 1771 (1949).
8. Smolenskii G. A. and Kozhevnikova N. V., *Dokl. akad. nauk S.S.S.R.* **76,** 519 (1951).
9. Matthias B. T., *Science* **113,** 591 (1951).
10. Nomura S., *J. phys. Soc. Japan* **10,** 112 (1955).
11. Smolenskii G. A., Agranovskaya A., Kalinina and Fedotova, *Zh. tekh. fiz.* **25,** 2134 (1955).
12. Sawyer C. B. and Tower C. H., *Phys. Rev.* **35,** 269 (1930).
13. Ismailzade I. G., *Sov. Phys. Cryst.* **4,** 389 (1960).
14. Shirane G., Hoshino S. and Suzuki K., *Phys. Rev.* **80,** 1105 (1950).
15. Shirane G., Sawaguchi E. and Takagi Y., *Phys. Rev.* **84,** 476 (1951).
16. Shirane G. and Pepinsky R., *Phys. Rev.* **91,** 812 (1953).
17. Ahrens L. H., *Geochim. Cosmochim. Acta* **2,** 155 (1952).
18. Matthias B. T. and Remeika J. P., *Phys. Rev.* **82,** 727 (1951).
19. Hulm J. K., Matthias B. T. and Long E. A., *Phys. Rev.* **79,** 885 (1950).
20. Matthias B., *Helv. Phys. Acta.* **23,** 167 (1950).

J. Phys. Chem. Solids Pergamon Press 1963. Vol. 24, pp. 95–107. Printed in Great Britain.

A THEORETICAL TREATMENT OF ATOMIC CONFIGURATIONS FOUND IN SOME IRON–ALUMINUM SOLID SOLUTIONS*

C. R. HOUSKA

Union Carbide Research Institute, P. O. Box 278, Tarrytown, New York

(*Received* 23 *July* 1962)

Abstract—Theoretical calculations have been carried out for the two ordering phases which occur in the FeAl system. The statistical treatment involves first and second neighbor interaction parameters as well as a magnetic interaction between first neighbor iron atoms. The phase diagram, and the amount and type of long range order for slowly cooled alloys are calculated. Further calculations include short range order for the disordered phase at three compositions and two temperatures. As expected, short range order increases as a critical temperature is approached either in composition or in temperature.

In each case, a comparison is made with experiment. The magnetic interaction gives a closer approach to experimental results. However, the three-constant-model does not give complete agreement. To quantitatively describe the asymmetry of the Fe_3Al loop, the rapid rise in the FeAl boundary, the rapid decline in Curie temperature, and the short range order coefficients, it was necessary to postulate rapid changes in the first neighbor interaction parameters within the range 20–30 at. per cent aluminum. These effects are concurrent with the rapid decline in magnetic saturation.

I. INTRODUCTION

CONSIDERABLE experimental information has become available on the FeAl system within the past 5 years. Much of the effort has been expended in establishing the details of the phase diagram. The disagreement between workers points out the difficulty in obtaining conclusive data in this system. Three solid phases are known to exist up to 50 at. per cent Al and each is complicated by the possibility of becoming ferromagnetic. A part of the difficulties might also be attributed to sluggish kinetics and the fact that the phenomena are interdependent. In addition, observable changes are most often small and continuous.

The system is equally difficult to describe theoretically. Early theoretical work on the diagram(1) did not have the benefit of the present mass of data and tended to complicate the problem. Recent work capable of describing the general shape of the diagram,(2) considerably simplified theory by neglecting magnetic effects. The present work tends to simplify the long range order (LRO) problem and still treat it in its more complete form; i.e. with magnetic effects. To the author's knowledge, it also contains the only calculations of short range order (SRO) for the FeAl system. Again, magnetic effects are included. By comparing the present theory with experiment, it is possible to strengthen both forms of information and obtain a more coherent and detailed picture of the system.

II. EXPERIMENTAL RESULTS

The phase diagram

In the composition range extending from pure Fe to 50 at. per cent Al, three solid phases have been confirmed on a sound experimental basis.(3) These are designated as FeAl, Fe_3Al, and the disordered solid solution.† Other phases have been proposed, however, their existence is based upon indirect evidence which makes them somewhat hypothetical. Emphasis will be placed upon the simplest diagram consisting of three phases representing different states of atomic order. It has been found that magnetization decreases with the sequence: Disordered, Fe_3Al, and FeAl type structures.(4) Each exhibits a different dependence upon temperature and composition.

---

* This work was performed in the Department of Metallurgy at the Massachusetts Institute of Technology, Cambridge, Massachusetts.

† The γ phase is not considered in the following discussions.

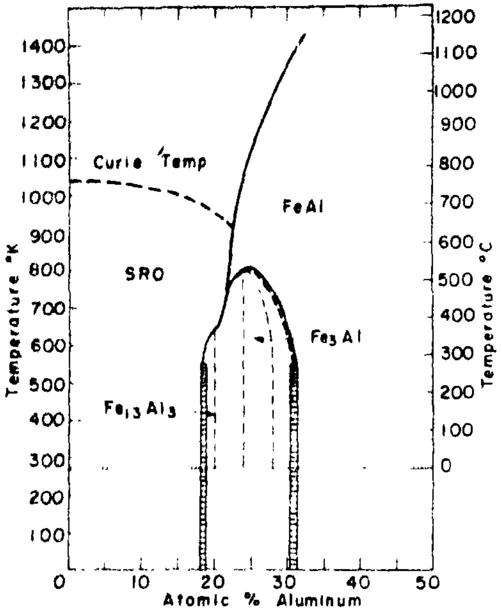

FIG. 1. The Fe–Al phase diagram obtained from X-ray lattice parameter measurements.

The diagram of Fig. 1 obtained from lattice parameter data,(5) shows a further subdivision of the Fe_3Al field into $Fe_{13}Al_3$, Fe_3Al, and adjacent two phase fields. These subdivisions, however, might also be considered collectively as one phase of the Fe_3Al type.(5) The latter point of view is preferred. Figure 2 illustrates a diagram obtained from a differential dilatometer.(6) In this case, the Fe_3Al phase spans a somewhat larger range of composition. More recent data,(7) obtained from X-ray line intensities are in better agreement with the broadened version of the Fe_3Al loop.

Figure 3 illustrates at temperature X-ray intensities obtained from a specimen containing 25·6 per cent Al. The specimen was held at the indicated temperature until consecutive runs indicated that equilibrium had been established. Intensity from the (200) line vanishes with the disappearance of the FeAl type structure, while the (111) vanishes with the Fe_3Al type.

These results clearly illustrate that both structures disorder at two distinct temperatures for the 25·6 per cent Al composition. Similar measurements made on a 22·2 per cent Al alloy give coincident critical temperatures in agreement with

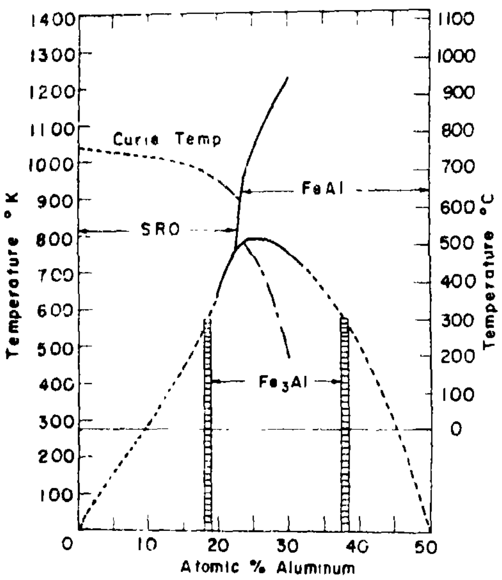

FIG. 2. The Fe–Al phase diagram obtained from differential dilatometer data.

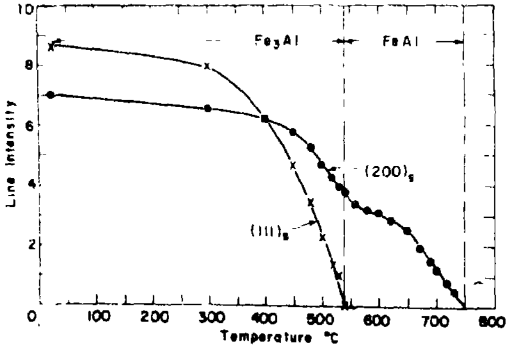

FIG. 3. X-ray integrated intensities for the (111) Fe_3Al, and (200) FeAl superlattice lines measured at temperature.

McQueen and Kuczynski. These results and others$^{(7)}$ show a continuous decrease in line intensity with increasing temperature. Changes in lattice parameter are also found to be continuous through the critical temperatures,$^{(5)}$ however, one does observe sudden changes in the expansion coefficient.$^{(6)}$ Each of these measurements is in agreement with a transformation of the second order or higher.

Curie temperatures presented in the various phase diagrams are similar in shape but show quantitative differences within the Fe$_3$Al field. Increasing Al content gives a nearly linear decrease within the disordered field, no ferromagnetism for FeAl, and a rapid decrease of the Curie temperature within the Fe$_3$Al field. Magnetic behavior therefore, appears to differ greatly with structure.

Measurements of atomic order and related phenomena

The degree of atomic order in FeAl alloys was found to be sensitive to composition and thermal treatment. LRO was first obtained from a series of slowly cooled alloys* using X-ray powder patterns.$^{(3)}$ Occupation preferences are illustrated in Fig. 4 and refer to the site designations of Fig. 5. From 25, to 50 per cent Al, the atomic fraction of Al in α sites slowly increases to a maximum at roughly 30 per cent Al where almost all α sites are rightly occupied. Concurrently, the amount of Al in β sites increases rapidly. This increase continues up to point 3 (37 per cent Al) where the FeAl phase first appears. Beyond 30 per cent Al, the α sublattice substitutionally accepts Fe atoms until point 3 is reached. Further increases in Al concentration enrich α and β sites without preference, and the Al in γ sites slowly goes to zero. At stoichiometric FeAl all cube centers are occupied by Al and all corner positions are occupied by Fe. Reducing the Al composition from stoichiometric Fe$_3$Al results in a rapid decrease of Al in α sites and a slower rise in Al enrichment for β sites. The Al concentration found in γ sites rises in a similar way. At point 2, α and β lattices contain the same concentrations. Further reductions in Al content results in an identical decrease in occupation for α and β sites while γ sites continue to show an increasing Al concentration, until point 1 is reached. Bradley and Jay, interpreted points 1 and 2 to be coincident at 1. On heating to the critical temperature, LRO is continuously lost.

Below about 20 per cent Al, one finds SRO for slowly cooled specimens.$^{(9)}$ SRO becomes most pronounced as a phase boundary is approached and decreases continuously with increasing temperature. This is contrary to findings which postulate a critical temperature for SRO.$^{(7)}$ A slowly cooled alloy of 20·0 per cent Al exhibits very strong SRO. In this case, the distinction between SRO

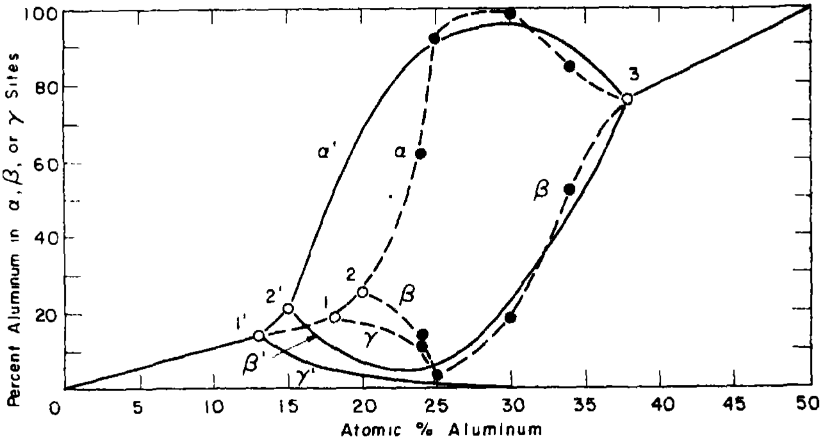

FIG. 4. Sub-lattice occupation as a function of composition. The dashed line is drawn through experimental points while the solid line has been calculated from theory.

---

* From 750°C to 600°C the cooling rate was 50°C/hr and from 600°C to 450°C it was reduced to 30°C/hr.

and LRO becomes confused. The diffuse scattering results of Lawley and Cahn also show increasingly strong modulations for slowly cooled alloys of 21·2, 22·2, and 22·9 per cent Al. In these cases, it is reasonable to interpret the modulations as broadened superlattice lines.

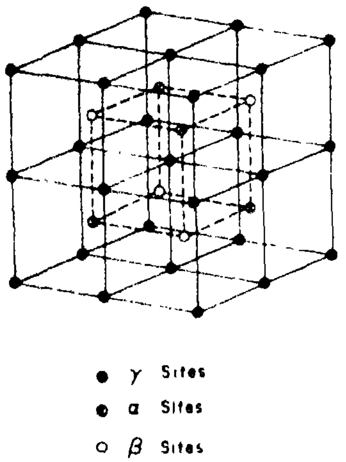

FIG. 5. Site designations for Fe_3Al and FeAl type superlattices.

It was found that static displacements,(8) arising from atomic size differences, increase to a maximum near the phase boundaries.(9) The largest maximum is found between the disordered state and Fe_3Al. A somewhat smaller maximum is found between Fe_3Al and FeAl. No static disturbances were observed for pure Fe, and fully ordered Fe_3Al. Stoichiometric FeAl should also be free of static displacements. As Al is added to pure Fe, the static displacements increase with a decreasing slope. At and above 15 per cent Al some relaxation appears to take place in conjunction with enhanced SRO.

III. THEORETICAL CALCULATIONS

The phase diagram and long range order

Certain approximate calculations were carried out in an attempt to explain the experimental results of the preceding section. The following subsections focus mainly upon results rather than upon mathematical detail which is given in the Appendix. Theoretical considerations include critical and Curie temperatures, the LRO to be expected from slowly cooled alloys, and the SRO coefficients.

The Fe_3Al type structure can be represented by four interpenetrating FCC sub-lattices having the relative translations (see Fig. 5):

$$\begin{aligned} &\gamma(\text{Fe rich})\text{—}0(a_1+a_2+a_3)\\ &\alpha(\text{Al rich})\text{—}\tfrac{1}{4}(a_1+a_2+a_3)\\ &\gamma(\text{Fe rich})\text{—}\tfrac{1}{2}(a_1+a_2+a_3)\\ &\beta(\text{Fe rich})\text{—}\tfrac{3}{4}(a_1+a_2+a_3)\end{aligned} \qquad (1)$$

The axes a_1, a_2, and a_3 are the cell edges for the Fe_3Al type structure which encompass eight body centered cubes. FeAl can be described by the same set of translations provided the sub-lattices α and β are indistinguishable and show a preference for Al atoms. This is more compactly given by a β brass structure having Fe atoms at cube corners and an Al preference at the centers. For convenience, a common set is chosen for both structures. The various atomic transformations, can be given schematically in terms of the sub-lattices.

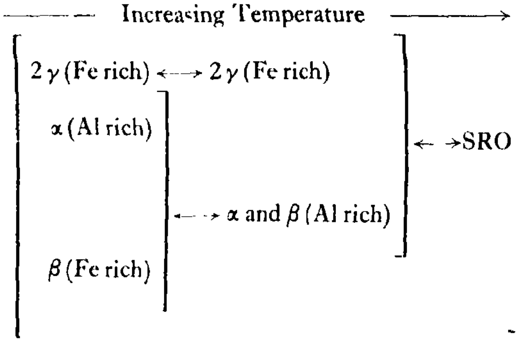

It was found that the mathematics could be most simply written in terms of the following order parameters:

$$\begin{aligned} X_\alpha &= r_\alpha - m_{\text{Al}}\\ X_\beta &= -(r_\beta - m_{\text{Fe}})\\ X &= r_\gamma - m_{\text{Fe}}\end{aligned} \qquad (2)$$

which are related by

$$r_\gamma = m_{\text{Fe}} + \tfrac{1}{2}(X_\alpha + X_\beta) \qquad (3)$$

The quantities r_α, r_β, and r_γ signify the probability for Al, Fe, and Fe occupation on α, β and γ

sub-lattices and m_{Al}, m_{Fe} are the atom fractions. The number of Al–Al, Fe–Al, and Fe–Fe pairs are readily calculated from equations (2) and (3) and the sub-lattice designation given by (1). We define $V(\text{Al}-i)$, $V(\text{FeAl}-i)$, and $V(\text{Al}-i)$ to represent ith neighbor energy interactions between Al–Al, Fe–Al, and Fe–Fe pairs. Only a first neighbor interaction is necessary for the stability of the FeAl type lattice. The Fe_3Al structure type requires, in addition, a second neighbor interaction to give ordering in the second neighbor sites. Consequently both are used throughout the calculations.

Magnetic first neighbor interaction is introduced by altering the energy between first neighbor Fe–Fe pairs. Like and unlike spin pairs are distinguished energetically by: $V(\text{Fe}-1)+V$, and $V(\text{Fe}-1)-V$ respectively. The occurrence of each can be computed from the spin probabilities designated as "p", and $(1-p)$. Parallel Fe–Fe pair probabilities are given by p^2, or $(1-p)^2$ and antiparallel pairs by $2p(1-p)$.

The Helmholtz free energy is readily calculated by using a Bragg–Williams approach, and parameters giving a minimum are obtained by solving equations (13A), (14A), and (15A) of the Appendix. This leads to a set of order parameters (including spin) for each temperature and composition. One obtains equations (18A), (20A), and (21A) by taking limits which give both Curie and critical temperatures. Solutions are plotted as a function of temperature in Fig. 6. As an illustration of the interplay between ferromagnetism and order, two diagrams are plotted: The dotted and dashed curves ignore the interplay while the solid curves were calculated with both present. The required energy parameters (16A) were obtained by fitting theory to experiment at three points. A value of $V = -130k$ was obtained by fitting the Curie temperature to the value for pure Fe, while $V_1^S(p = \frac{1}{2}) = 564k$ and $V_2 = 265k$ were obtained from the critical temperatures for FeAl and Fe_3Al at the 25 per cent Al composition. In each case, the data given in Fig. 1 was used.

Figure 6 illustrates the magnetic lowering of the FeAl critical temperature below the composition $m_{Al} = 0{\cdot}18$. Above this value, the Curie temperature is lowered by FeAl type order. For these two cases, the co-operative phenomena occurring at the higher temperature reduces the stability of that found at the lower temperature. The dashed Fe_3Al critical temperature was calculated under the assumption that FeAl type order is complete; i.e. $r_\gamma = 1$, and $X = m_{Al}$; exact solutions show that this assumption becomes increasingly poor for compositions below $m_{Al} \doteq 0{\cdot}25$, and rather $r_\gamma < 1$ giving $X < m_{Al}$. In this manner, the FeAl critical temperature is reduced magnetically and the Fe_3Al temperatures by a loss of FeAl type order. The assymetry displayed by the solid Fe_3Al loop of Fig. 6 results from such a sequence of interactions.

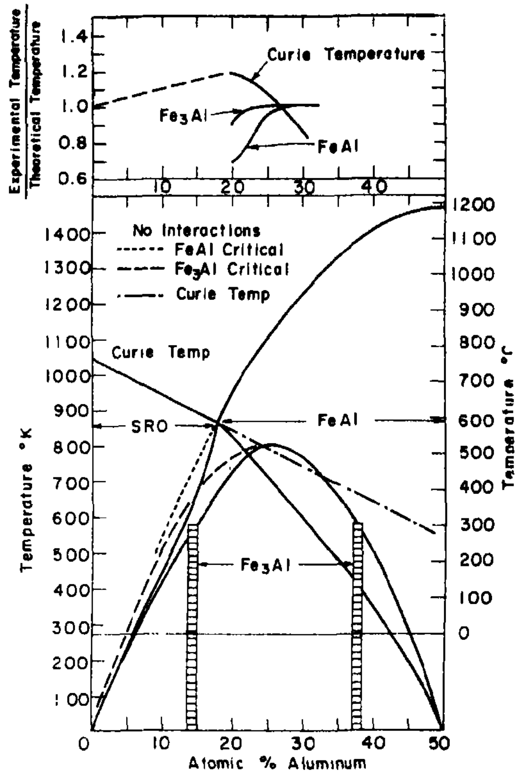

FIG. 6. Theoretical phase diagrams showing results with and without interactions. The upper curves give experimental to theoretical ratios for the various critical temperatures.

It is possible, by using equations (13A), (14A), and (15A), to calculate the LRO expected from slowly cooled alloys. Such calculations can be compared with experiment (Fig. 4), only if a prior knowledge of the ordering kinetics exists. It was found[9] that ordering kinetics became sluggish below about 300°C. Consequently, this will be assumed to be a practical lower limit within each of the diagrams and is illustrated by the dashed columns. Theoretical values of order for slowly cooled alloys are plotted as solid lines in Fig. 4. Agreement with experiment is good for $m_{\text{Al}} > 0{\cdot}25$. Below this value, theory becomes quantitatively inadequate. It is evident that the basic problem results mainly from the location of the theoretical boundary points 1′ and 2′. If these points could be made to coincide with the experimental points 1 and 2, theory and experiment would be in quantitative agreement. This difficulty will be considered in a later section.

Short range order

The following results are based upon a COWLEY(10) approach to SRO modified to include a first neighbor spin interaction. Instead of referring to sub-lattice occupation, one considers a series of concentric shells having specified either an Fe or an Al center. A given shell "i" of radius r_i has an atomic occupation preference specified by the SRO coefficient, α_i, and a coordination number given by C_i. With these preferences, occupation of the lattice sites within a shell is assumed random. In this approximation, the shell is comparable to the sub-lattice. Occupation probabilities are defined in terms of the SRO coefficients in the usual way:

$$\begin{aligned} P(\text{Al}, \text{Fe}-i) &= m_{\text{Fe}}(1-\alpha_i) \\ P(\text{Al}, \text{Al}-i) &= m_{\text{Al}}+m_{\text{Fe}}\alpha_i \\ P(\text{Fe}, \text{Fe}-i) &= m_{\text{Fe}}+m_{\text{Al}}\alpha_i \\ P(\text{Fe}, \text{Al}-i) &= m_{\text{Al}}(1-\alpha_i) \end{aligned} \tag{4}$$

The quantities, $P(A, B-i)$, represent the probability of "B" atom occupancy in the ith shell about an "A" atom origin. Spin probabilities are defined as before, i.e. "p" represents the probability for alignment in the predominant direction and $1-p$ is the probability for an opposing spin.

The internal energy was calculated by using pairwise interactions between first and second neighbors of the ith shell and summing over all shells:

$$U = \tfrac{1}{2}\sum_{i}^{\text{All shells}} U_i \tag{5}$$

Two partial energies are required for the total energy: one represents the energy for shells containing an Fe center and the other is for shells having an Al center. According to COWLEY(10) the total shell energy is written in terms of its partial energies as follows:

$$U_i = m_{\text{Fe}}U(\text{Fe}-i)+m_{\text{Al}}U(\text{Al}-i) \tag{6}$$

Similar equations can be written for the entropy. In calculating $S(\text{Fe}-i)$ and $S(\text{Al}-i)$, the partial entropies, each specie (Fe(+spin), Fe(−spin), and Al) is assumed to be randomly located within shell "i", and for simplicity, arrangements in $i-1$ and $i+1$ are not directly considered. In this way, the total entropy

$$S = \sum_{i}^{\text{All shells}} S_i \tag{7}$$

is written in terms of the weighted, partial entropies

$$S_i = m_{\text{Fe}}S(\text{Fe}-i)+m_{\text{Al}}S(\text{Al}-i) \tag{8}$$

A minimum free energy is obtained by taking a self consistant minimum for each shell. Equation (28A), and (29A) of the Appendix were obtained on this basis. In principle, one can obtain the distribution of order parameters for a given alloy composition and temperature or instead the energy parameters (25A) V_1, V_2, and V. The preceding LRO theory gave critical temperatures and order parameters for both FeAl, and Fe_3Al superlattices from the energy parameters. By using the same energy parameters, and the present SRO theory, calculations of order can be extended into the region above the critical temperature.

SRO coefficients up to the fourth neighbor were calculated by using (28A) and (30A) for 300°C and 400°C at 14·8, 18·2, and 20·0 per cent Al. Each of these points is well under the Curie temperature. The theoretical results are given in Table 1 in terms of the SRO coefficients. For comparison, calculations were also made without a magnetic interaction ($V = 0$). Table 2 gives a listing of the number of Fe atoms surrounding an Al atom using the coefficients of Table 1 which contain the magnetic interaction. As a comparison, shell occupation for the random solution is also listed. One finds a strong preference for unlike neighbors in the first coordination shell and nearly random occupation

Table 1. *Short range order for three* Fe–Al *alloys calculated by using* $V_1^S(p = \frac{1}{2}) = 564k$, $V_2 = 265k$, *and* $V = -130k$. *Calculations were also made without the magnetic interaction using the same parameters but with* $V = 0$

With Magnetic interaction

Specimen	Temperature	α_1	α_2	α_3	α_4
Fe 14·8 at. per cent Al	300	$\overline{0{\cdot}139}$	$\overline{0{\cdot}015}$	0·111	$\overline{0{\cdot}025}$
	400	$\overline{0{\cdot}126}$	$\overline{0{\cdot}019}$	0·074	$\overline{0{\cdot}012}$
Fe 18·2 at. per cent Al	300	$\overline{0{\cdot}194}$	0·026	0·201	$\overline{0{\cdot}066}$
	400	$\overline{0{\cdot}171}$	0·014	0·128	$\overline{0{\cdot}036}$
Fe 20·0 at. per cent Al	300	$\overline{0{\cdot}217}$	0·057	0·230	$\overline{0{\cdot}081}$
	400	$\overline{0{\cdot}194}$	0·043	0·150	$\overline{0{\cdot}045}$

Without magnetic interaction

Specimen	Temperature	α_1	α_2	α_3	α_4
Fe 14·8 at. per cent Al	300	$\overline{0{\cdot}152}$	0·011	0·127	$\overline{0{\cdot}033}$
Fe 18·2 at. per cent Al	300	$\overline{0{\cdot}210}$	0·097	0·260	$\overline{0{\cdot}099}$
Fe 20·0 at. per cent Al	300	$\overline{0{\cdot}240}$	0·146	0·336	$\overline{0{\cdot}139}$

for the second. As expected, the SRO increases with decreasing temperature. And, increasing the Al concentration results in a closer approach to the ordered phases and enhanced SRO. The same general trend was found in the diffuse scattering data.⁽⁹⁾ A quantitative comparison between theory and experiment is difficult in the present case since both results are susceptible to errors. Agreement appears to be best between first and third neighbor SRO coefficients and, in general, theoretical values tend to be somewhat higher than those given by experiment.

Table 2. *The number of* Fe *atoms in the first four shells surrounding an* Al *center as calculated from the theoretical SRO coefficients of Table* 2

Atomic Shell i		1	2	3	4
Coordination number C_i		8	6	12	24
Fe 14·8 at. per cent Al					
Random solution		6·8	5·1	10·2	20·4
From SRO coefficients	300°C	7·8	5·2	9·1	20·9
	400°C	7·7	5·2	9·4	20·6
Fe 18·2 at. per cent Al					
Random solution		6·5	4·9	9·8	19·6
From SRO coefficients	300°C	7·8	4·8	7·8	20·9
	400°C	7·6	4·8	8·5	20·3
Fe 20·0 at. per cent Al					
Random solution		6·4	4·8	9·6	19·2
From SRO coefficients	300°C	7·8	4·5	7·4	20·8
	400°C	7·6	4·6	8·2	20·1

IV. QUANTITATIVE CORRELATIONS AND THE EXTENDED THEORY

A comparison between the theoretical diagram of Fig. 6 and the experimental curves of Figs. 1 and 2 demonstrates that theory predicts the general shape of the phase diagram. However, quantitative differences are evident. For instance, FeAl critical temperatures do not drop off rapidly enough with temperature as the Fe_3Al loop is approached, and the two are never coincident. Under these conditions slow cooling from the disordered state into the region of LRO first results in a sorting of Fe atoms to cube corners and Al atoms to cube centers. Further cooling through the Fe_3Al critical temperature leads to a re-arrangement of cube centers. Coincidence of both FeAl and Fe_3Al critical temperatures does not lead to a prior assortment of Fe and Al to corner and center positions. Rather this re-arrangement coincides with the positioning of center atoms. The combined effect being an enrichment of Al and α sites and Fe on both β and γ sites. If one postulates that the FeAl critical temperature can never fall below that of Fe_3Al, then lowering the FeAl boundary must eventually result in a lowering of the Fe_3Al boundary. Such an effect is possible if the energy parameter V_1^S is a function of composition. In particular V_1^S must decrease below 564k in the region $m_{\mathrm{Al}} < 0{\cdot}25$.

Such a variation is already contained in the theory as a result of spin interactions, however, this was found to be insufficient.

Figure 6 illustrates the ratio of experimental critical temperature(6) to theoretical FeAl in the region of interest. A similar ratio is taken for the critical temperature of Fe_3Al and for the Curie temperature. One observes that the ratio involving Curie temperatures decreases rapidly in the range 20–30 at. per cent Al. Magnetic saturation was also found to decrease in the same composition range.(11, 12) It has been suggested that these magnetic properties might result from electronic transfer between Al and Fe atoms.(5, 13) One would expect to find corresponding adjustments in the interaction energies. Taking the Curie temperature to be proportional to $-V$ (equation (21A)), requires a 20 per cent decrease relative to pure Fe. A maximum change of about 40 per cent is found within the range 20–30 per cent Al.

The ratio of experimental to theoretical critical temperature for the FeAl phase shows an increase with Al content. In this case, the critical temperature is proportional to V_1^S and $-V_2$. A theoretical fitting to experiment requires either an increasing V_1^S or a decreasing V_2 as Al is added. A changing V_2 can be ruled out since generally good theoretical agreement is found for the Fe_3Al critical temperatures which depend directly upon V_2. Consequently, the observed theoretical discrepancy probably results mainly from variations in V_1^S. The possibility of electron transfer must again be considered as a possible reason for rapid changes in the energy parameter. Several interdependent phenomena have been ignored in the theory: thermal vibrations, strain energy resulting from static displacements, and superexchange interactions.(4) A more rigorous theory would include these effects. However, the simplified theory of LRO, making use of the more dominant interactions, offers considerable insight towards the behavior of the Fe–Al system.

The theoretical calculations for SRO assumed the energy parameters to be constant over an interval of 5 at. per cent Al and over at 100°C. It was also assumed that the energy parameters obtained from critical temperature data and Bragg–Williams calculations are equivalent to those found in the Cowley theory. Previous considerations indicate that the parameters are interchangeable for a β brass type structure.(14, 10) From Table 1, it was seen that magnetic interaction reduces the magnitudes of the SRO coefficients. The second neighbor coefficient, α_2, shows a particularly large percentage change between calculations containing magnetic interaction and those without it. If the 20 per cent rise in experimental Curie temperature above that calculated from theory results from an increase in $|V|$, a further reduction in the coefficients will result. This change should, in general, be considerably smaller than that indicated in Table 1. A reduction in $V_1^S(p = \frac{1}{2})$ would also reduce the SRO. The latter cannot be ruled out since this parameter was obtained by matching to the data at 25·0 per cent Al. Each of these possible changes in the energy parameters would lead to improved agreement with experiment.

V. CONCLUSIONS

1. Three solid phases (excluding the γ loop) are found in the range extending from pure Fe to Fe 50 at. per cent Al. They are designated as FeAl, Fe_3Al, and a disordered phase which exhibits strong SRO.

2. The available data, i.e. X-ray intensities, lattice parameters, and thermoelectric power,(15) all show LRO transformations of the second order or higher. Under these conditions two phase regions can be eliminated from the diagram.(14)

3. The Fe_3Al loop is contained within the FeAl envelope and at certain compositions the two critical temperatures are coincident. The lowering of the FeAl boundary, the assymetry displayed by the Fe_3Al loop, and the SRO coefficients cannot be completely accounted for by magnetic interaction. It was necessary to consider further changes in the first neighbor energy parameter. These changes correlate with the rapid decrease in magnetic saturation in the composition range 20–30 per cent Al and suggests that electron transfer between solute and solvent plays an important role in shaping the phase diagram.

4. Within the disordered phase, SRO increases as the LRO fields are approached either in temperature or in composition.

5. Static atomic displacements are at a maximum within the disordered region and adjacent to the ordered loops. In general, fully ordered materials do not exhibit such disturbances.

Acknowledgement—The author is grateful to Mrs. M. F. Houska, for her helpful criticism and to the Atomic Energy Commission for partial sponsorship of this work.

REFERENCES

1. Sato H., *Sci. Rep. Tohoku Univ.* **A3,** 13 (1951).
2. Rudman P. S., *Acta Met.* **8,** 321 (1960).
3. Bradley A. J. and Jay A. H., *Proc. Roy. Soc.* **A136,** 210 (1932).
4. Sato H. and Arrott A., *J. appl. Phys.* **29,** 515 (1958).
5. Taylor A. and Jones R. M., *J. Phys. Chem. Solids* **6,** 16 (1958).
6. McQueen H. J. and Kuczynski G. C., *Trans. Amer. Inst. min. (metall.) Engrs.* **215,** 619 (1959).
7. Lawley A. and Cahn R. W., *J. Phys. Chem. Solids* **20,** 204 (1961).
8. Herbstein F. S., Borie B. and Averbach B. L., *Acta Cryst.* **9,** 466 (1956).
9. Houska C. R. and Averbach B. L., To be published.
10. Cowley J. M., *Phys. Rev.* **77,** 669 (1950).
11. Sucksmith W., *Proc. Roy. Soc.* **A171,** 525 (1939).
12. Nathans R., Pigott M. T. and Shull C. G., *J. Phys. Chem. Solids* **6,** 38 (1958).
13. Radcliffe S. V., Averbach B. L. and Cohen M., *Acta Met.* **9,** 169 (1961).
14. Guttman L., *Solid State Physics* **3,** 145 (1956).
15. Eroz G. and Rudman P. S., *J. Phys. Chem. Solids* **18,** 307 (1961).

APPENDIX

Long range order

The entropy can readily be calculated for a given energy, by using the definitions given by (2) and (3) in terms of the sub-lattices defined by (1). The number of distinguishable arrangements of three species (Fe(+), Fe(−), and Al) on α, β, and γ lattices is defined by $\omega_\alpha(=\omega_\alpha^c\omega_\alpha^M)$, $\omega_\beta(=\omega_\beta^c\omega_\beta^M)$, and $\omega_\gamma(=\omega_\gamma^c\omega_\gamma^M)$. Each represents a product of configurational and spin terms. Writing the entropy in terms of the usual expression

$$S = k\ln\omega_\alpha^c\omega_\beta^c\omega_\gamma^c\omega_\alpha^M\omega_\beta^M\omega_\gamma^M \tag{1A}$$

The configuration terms were calculated by assuming random occupation on each sub-lattice and are given by:

$$\begin{aligned}\omega_\alpha^c &= \frac{\frac{N}{4}!}{\left[\frac{N}{4}r_\alpha\right]!\left[\frac{N}{4}(1-r_\alpha)\right]!}\\ \omega_\beta^c &= \frac{\frac{N}{4}!}{\left[\frac{N}{4}r_\beta\right]!\left[\frac{N}{4}(1-r_\beta)\right]!}\\ \omega_\gamma^c &= \frac{\frac{N}{2}!}{\left[\frac{N}{2}r_\gamma\right]!\left[\frac{N}{2}(1-r_\gamma)\right]!}\end{aligned} \tag{2A}$$

and the spin terms by

$$\begin{aligned}\omega_\alpha^M &= \frac{\left[\frac{N}{4}(1-r_\alpha)\right]!}{\left[\frac{N}{4}p(1-r_\alpha)\right]!\left[\frac{N}{4}(1-p)(1-r_\alpha)\right]!}\\ \omega_\beta^M &= \frac{\left[\frac{N}{4}r_\beta\right]!}{\left[\frac{N}{4}pr_\beta\right]!\left[\frac{N}{4}(1-p)r_\beta\right]!}\\ \omega_\gamma^M &= \frac{\left[\frac{N}{2}r_\gamma\right]!}{\left[\frac{N}{2}pr_\gamma\right]!\left[\frac{N}{2}(1-p)r_\gamma\right]!}\end{aligned} \tag{3A}$$

The total entropy is the sum of configurational and spin terms:

$$\begin{aligned}S &= S^c+S^M\\ S^c &= k\{\ln\omega_\alpha^c+\ln\omega_\beta^c+\ln\omega_\gamma^c\}\\ S^M &= k\{\ln\omega_\alpha^M+\ln\omega_\beta^M+\ln\omega_\beta^M\}\end{aligned} \tag{4A}$$

Substituting the quantities (2A and 3A), and applying Stirling's formula leads to

$$\begin{aligned}S^c = -\frac{N}{4}\{&r_\alpha\ln r_\alpha+(1-r_\alpha)\ln(1-r_\alpha)\\ &+r_\beta\ln r_\beta+(1-r_\beta)\ln(1-r_\beta)\\ &+2r_\gamma\ln r_\gamma+2(1-r_\gamma)\ln(1-r_\gamma)\}\end{aligned}$$

and

$$S^M = -km_{\mathrm{Fe}}N\{p\ln p+(1-p)\ln(1-p)\} \tag{5A}$$

The internal energy consists of the following additive terms:

$$U = U_1^c+U_2^c+U^M \tag{6A}$$

where

$$U_1^c = \frac{N}{4}C_1\{V(\mathrm{Fe}-1)[(1-r_\alpha)r_\gamma+r_\beta r_\gamma]+V(\mathrm{Al}-1)[r_\alpha(1-r_\gamma)+(1-r_\beta)(1-r_\gamma)] + V(\mathrm{FeAl}-1)[1+r_\beta-r_\alpha+2r_\alpha r_\gamma-2r_\beta r_\gamma]\}$$

$$U_2^c = \frac{N}{4}C_2\{V(\mathrm{Fe}-2)[r_\beta(1-r_\alpha)+r_\gamma^2]+V(\mathrm{Al}-2)[r_\alpha(1-r_\beta)+(1-r_\gamma)^2] + V(\mathrm{FeAl}-2)[r_\alpha r_\beta+(1-r_\beta)(1-r_\alpha)+2(1-r_\gamma)r_\gamma]\}$$

$$U^M = \frac{N}{4}C_1[(1-r_\alpha)r_\gamma+r_\beta r_\gamma][1-4p+4p^2]V \tag{7A}$$

These expressions can be written in terms of the parameters X_α and X_β

$$\begin{aligned} S^c = -\frac{N}{4}k\{&(m_{\mathrm{Al}}+X_\alpha)\ln(m_{\mathrm{Al}}+X_\alpha)+(m_{\mathrm{Fe}}-X_\alpha)\ln(m_{\mathrm{Fe}}-X_\alpha)\\ &+(m_{\mathrm{Al}}+X_\beta)\ln(m_{\mathrm{Al}}+X_\beta)+(m_{\mathrm{Fe}}-X_\beta)\ln(m_{\mathrm{Fe}}-X_\beta)\\ &+2[m_{\mathrm{Al}}-\tfrac{1}{2}(X_\alpha+X_\beta)]\ln[m_{\mathrm{Al}}-\tfrac{1}{2}(X_\alpha+X_\beta)]\\ &+2[m_{\mathrm{Fe}}-\tfrac{1}{2}(X_\alpha+X_\beta)]\ln[m_{\mathrm{Fe}}-\tfrac{1}{2}(X_\alpha+X_\beta)]\}\end{aligned} \tag{8A}$$

$$\begin{aligned} U_1^c = \frac{N}{4}C_1\{&[2m_{\mathrm{Fe}}^2-\tfrac{1}{2}(X_\alpha+X_\beta)^2]V(\mathrm{Fe}-1)+[2m_{\mathrm{Al}}^2-\tfrac{1}{2}(X_\alpha+X_\beta)^2]V(\mathrm{Al}-1)\\ &+[4m_{\mathrm{Al}}m_{\mathrm{Fe}}+(X_\alpha+X_\beta)^2]V(\mathrm{FeAl}-1)\}\end{aligned} \tag{9A}$$

$$\begin{aligned} U_2^c = \frac{N}{4}C_2\{&[2m_{\mathrm{Fe}}^2+X_\alpha X_\beta+\tfrac{1}{4}(X_\alpha+X_\beta)^2]V(\mathrm{Fe}-2)+[2m_{\mathrm{Al}}^2+X_\alpha X_\beta+\tfrac{1}{4}(X_\alpha+X_\beta)^2]V(\mathrm{Al}-2)\\ &+[4m_{\mathrm{Al}}m_{\mathrm{Fe}}-2X_\alpha X_\beta-\tfrac{1}{2}(X_\alpha+X_\beta)^2]V(\mathrm{FeAl}-2)\}\end{aligned} \tag{10A}$$

$$U^M = \frac{N}{4}C_1[2m_{\mathrm{Fe}}^2-\tfrac{1}{2}(X_\alpha+X_\beta)^2][1-4p+4p^2]V \tag{11A}$$

at a given T, m_{Al}, the equilibrium set of X_α, X_β, and p are solutions to

$$\delta F = \frac{\partial F}{\partial X_\alpha}\,\delta X_\alpha+\frac{\partial F}{\partial X_\beta}\,\delta X_\beta+\frac{\partial F}{\partial p}\,\delta p = 0$$

or

$$\frac{\partial F}{\partial X_\alpha} = \frac{\partial F}{\partial X_\beta} = \frac{\partial F}{\partial p} = 0 \tag{12A}$$

Substituting the entropy and internal energy expressions into (12A) gives the following equilibrium equations:

$$-16(X_\alpha+X_\beta)(V_1^s-\tfrac{3}{8}V_2)+12X_\beta V_2 + kT\ln\frac{(m_{\mathrm{Al}}+X_\alpha)[m_{\mathrm{Fe}}+\tfrac{1}{2}(X_\alpha+X_\beta)]}{(m_{\mathrm{Fe}}-X_\alpha)[m_{\mathrm{Al}}-\tfrac{1}{2}(X_\alpha+X_\beta)]} = 0 \tag{13A}$$

$$-16(X_\alpha+X_\beta)(V_1^s-\tfrac{3}{8}V_2)+12X_\alpha V_2 + kT\ln\frac{(m_{\mathrm{Al}}+X_\beta)[m_{\mathrm{Fe}}+\tfrac{1}{2}(X_\alpha+X_\beta)]}{(m_{\mathrm{Fe}}-X_\beta)[m_{\mathrm{Al}}-\tfrac{1}{2}(X_\alpha+X_\beta)]} = 0 \tag{14A}$$

$$-16(1-2p)[m_{\mathrm{Fe}}^2-\tfrac{1}{4}(X_\alpha+X_\beta)^2]V + kTm_{\mathrm{Fe}}\ln\frac{p}{1-p} = 0 \tag{15A}$$

with

$$\begin{aligned} 2V_1^s &= V(\mathrm{Fe}-1)+[1-4p(1-p)]V+V(\mathrm{Al}-1) -2V(\mathrm{FeAl}-1) \end{aligned} \tag{16A}$$

$$2V_2 = V(\mathrm{Fe}-2)+V(\mathrm{Al}-2)-2V(\mathrm{FeAl}-2)$$

Solutions for X_α, X_β, and X are given in Fig. 7 for 25 per cent Al and clearly illustrate a transformation of the second order. On heating Fe_3Al, the parameters X_α and X_β approach the limit X at T_{c1} without a discontinuity. Further heating again results in a continuous decrease in X or FeAl type order. Finally at T_{c2}, FeAl type order disappears giving way to SRO. Each of the critical temperatures were fitted to those of Fig. 1. Solutions for X_α and X_β were obtained by taking $X = \frac{1}{2}(X_\alpha + X_\beta)$ to be continuous through the temperature T_{c1}. In other words, the occupation within the γ sub-lattices continues to be governed by the FeAl order parameter below T_{c1}. The essential features of the Fe_3Al superlattice are derived entirely from the sorting of Al atoms to α sites and Fe atoms to β sites with the fraction of Al atoms available to $\alpha+\beta$ sites determined by X. Exact solutions for $X(T)$, and $X_\alpha(T)$, and $X_\beta(T)$ are tedious to obtain. An example, however, serves to illustrate the details of the transformation.

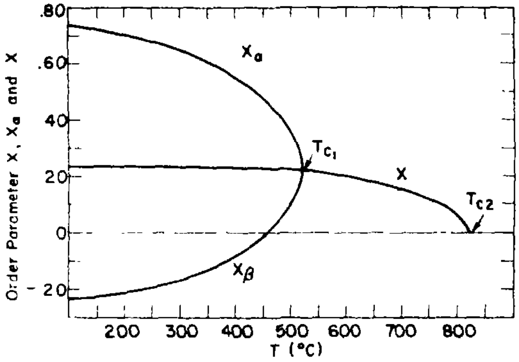

FIG. 7. Calculated order parameters for Fe 25 per cent Al.

To calculate the FeAl–Fe_3Al—magnetic phase diagram, expressions must be obtained which give the corresponding critical temperatures for these phenomena. For FeAl, $X = X_\alpha = X_\beta$, using (13A).

$$32X\left(V_1^s - \tfrac{3}{4}V_2\right) = kT \ln \frac{(m_{Al}+X)(m_{Fe}+X)}{(m_{Al}-X)(m_{Fe}-X)} \tag{17A}$$

As $X \to 0$

$$V_1^s - \tfrac{3}{4}V_2 = \frac{kT_{c1}}{16 m_{Al} m_{Fe}} \tag{18A}$$

To obtain T_{c2} for the transformation $Fe_3Al \to FeAl$, subtract (14A) from (13A)

$$-12(X_\beta - X_\alpha)V_2 = kT \ln \frac{(m_{Al}+X_\alpha)(m_{Fe}-X_\beta)}{(m_{Al}+X_\beta)(m_{Fe}-X_\alpha)} \tag{19A}$$

and with $X_\alpha = X+a$ and $X_\beta = X+b$ let $a \to 0$, and $b \to 0$ giving

$$V_2 = \frac{kT_{c2}}{12(m_{Al}+X)(m_{Fe}-X)} \tag{20A}$$

The magnetic critical temperature is obtained from (15A) by letting $p = \frac{1}{2}+m$, and $m \to 0$

$$-V = \frac{m_{Fe} k T_{c3}}{8(m_{Fe}^2 - X^2)} \tag{21A}$$

Short range order

The SRO coefficients, α_i, are given by (4). A spin probability is defined for each shell and is designated by p_i, the probability of finding alignment in the predominant direction. No distinction is made with respect to the atom type at the center. The energy for the *i*th shell with an Fe center is calculated on the basis of a pairwise interaction and given by:

$$\begin{aligned}\frac{1}{C_i}U(\mathrm{Fe}-i) = {} & P(\mathrm{Fe}, \mathrm{Fe}-i)p_i[V(\mathrm{Fe}-1)+V]\sum_j^f p_j P(\mathrm{Fe}, \mathrm{Fe}-j) \\ & + P(\mathrm{Fe}, \mathrm{Fe}-i)(1-p_i)[V(\mathrm{Fe}-1)+V]\sum_j^f (1-p_j)P(\mathrm{Fe}, \mathrm{Fe}-j) \\ & + P(\mathrm{Fe}, \mathrm{Fe}-i)p_i[V(\mathrm{Fe}-1)-V]\sum_j^f (1-p_j)P(\mathrm{Fe}, \mathrm{Fe}-j) \\ & + P(\mathrm{Fe}, \mathrm{Fe}-i)(1-p_i)[V(\mathrm{Fe}-1)-V]\sum_j^f p_j P(\mathrm{Fe}, \mathrm{Fe}-j) \\ & + P(\mathrm{Fe}, \mathrm{Fe}-i)V(\mathrm{Fe}-2)\sum_j^8 P(\mathrm{Fe}, \mathrm{Fe}-j)\end{aligned}$$

$$+P(\mathrm{Fe,\ Al}-i)V(\mathrm{Al}-1)\sum_j^f P(\mathrm{Fe,\ Al}-j)$$

$$+P(\mathrm{Fe,\ Al}-i)V(\mathrm{Al}-2)\sum_j^s P(\mathrm{Fe,\ Al}-j)$$

$$+P(\mathrm{Fe,\ Al}-i)V(\mathrm{FeAl}-1)\sum_j^f P(\mathrm{Fe,\ Fe}-j)$$

$$+P(\mathrm{Fe,\ Fe}-i)V(\mathrm{FeAl}-1)\sum_j^f P(\mathrm{Fe,\ Al}-j)$$

$$+P(\mathrm{Fe,\ Al}-i)V(\mathrm{FeAl}-2)\sum_j^s P(\mathrm{Fe,\ Fe}-j)$$

$$+P(\mathrm{Fe,\ Fe}-i)V(\mathrm{FeAl}-2)\sum_j^s P(\mathrm{Fe,\ Al}-j)$$

A similar sum can be obtained with an Al atom center. Combining these results with equation (5) and summing (6) gives the shell energy.

The number of arrangements of atomic species and spin in the ith shell with energy $U(\mathrm{Fe}-i)$ and $U(\mathrm{Al}-i)$ are:

$$\omega(\mathrm{Fe}-i) = \frac{C_i!}{[p_iC_iP(\mathrm{Fe,\ Fe}-i)]![(1-p_i)C_iP(\mathrm{Fe,\ Fe}-i)]![C_iP(\mathrm{Fe,\ Al}-i)]!}$$

$$\omega(\mathrm{Al}-i) = \frac{C_i!}{[p_iC_iP(\mathrm{Al,\ Fe}-i)]![(1-p_i)C_iP(\mathrm{Al,\ Fe}-i)]![C_iP(\mathrm{Al,\ Al}-i)]!}$$

Corresponding entropies are given by

$$S(\mathrm{Fe}-i) = k\ln\omega(\mathrm{Fe}-i)$$

$$S(\mathrm{Al}-i) = k\ln\omega(\mathrm{Al}-i)$$

and logarithmic forms are obtained from Stirling's formula.

The equilibrium set of $\alpha_i'^s$ and $p_i'^s$ for a given temperature and composition are determined by minimizing the free energy.

$$\delta U - T\delta S = 0$$

Using (5) and (7)

$$\sum_i \{\delta(\tfrac{1}{2}U_i) - T\delta S_i\} = 0$$

Where

$$\delta(\tfrac{1}{2}U_i) = \left(\frac{\partial U_i}{\partial\alpha_i}\right)\delta\alpha_i + \left(\frac{\partial U_i}{\partial p_i}\right)\delta p_i$$

$$\delta S_i = \left(\frac{\partial S_i}{\partial\alpha_i}\right)\delta\alpha_i + \left(\frac{\partial S_i}{\partial p_i}\right)\delta p_i$$

For each shell "i"

$$\frac{\partial U_i}{\partial\alpha_i} - T\frac{\partial S_i}{\partial\alpha_i} = 0 \tag{22A}$$

and

$$\frac{\partial U_i}{\partial p_i} - T\frac{\partial S_i}{\partial p_i} = 0 \tag{23A}$$

or

$$\frac{1}{2}\frac{\partial U_i}{\partial\alpha_i} = m_{\mathrm{Al}}m_{\mathrm{Fe}}C_i(FV_i + SV_2)$$

or

$$\frac{\partial U_i}{\partial p_i} = -2C_iV\left\{m_{\mathrm{Fe}}^2C_1\left(1-2\frac{P}{C_1}\right) + m_{\mathrm{Al}}m_{\mathrm{Fe}}\alpha_iF\left(1-2\frac{M}{F}\right)\right\} \tag{24A}$$

Where

$$F = \sum_{j}^{f} \alpha_j, \quad S = \sum_{j}^{s} \alpha_j, \quad P = \sum_{j}^{f} p_j,$$

and $M = \sum_{j}^{f} p_j \alpha_j$

represent first neighbor, "f", and second, "s", neighbor summations with respect to atoms in the "i" shell.

$$\frac{\partial S_i}{\partial p_i} = kC_i m_{\mathrm{Fe}} \ln \frac{1-p_i}{p_i} \tag{27A}$$

Combining energy and entropy terms,

$$kT \ln \frac{m_{\mathrm{Al}} m_{\mathrm{Fe}} (1-\alpha_i)^2}{(m_{\mathrm{Al}} + m_{\mathrm{Fe}} \alpha_i)(m_{\mathrm{Fe}} + m_{\mathrm{Al}} \alpha_i)} = 2(FV_i + SV_2) \tag{28A}$$

$$\boxed{kT \ln \frac{1-p_i}{p_i} = -2V\left\{m_{\mathrm{Fe}} C_1 \left(1 - 2\frac{P}{C}\right) + m_{\mathrm{Al}} \alpha_i F \left(1 - 2\frac{M}{F}\right)\right\}} \tag{29A}$$

$$2V_i = V(\mathrm{Fe}-1) + (1-2p_i)\left(1-2\frac{M}{F}\right)V + V(\mathrm{Al}-1) - 2V(\mathrm{FeAl}-1) \tag{25A}$$

$$2V_2 = V(\mathrm{Fe}-2) + V(\mathrm{Al}-2) - 2V(\mathrm{FeAl}-2)$$

and

$$\frac{\partial S_i}{\partial \alpha_i} = kC_i m_{\mathrm{Al}} m_{\mathrm{Fe}} \ln \frac{m_{\mathrm{Al}} m_{\mathrm{Fe}} (1-\alpha_i)^2}{(m_{\mathrm{Fe}} + m_{\mathrm{Al}} \alpha_i)(m_{\mathrm{Al}} + m_{\mathrm{Fe}} \alpha_i)} \tag{26A}$$

Numerical calculations have been limited to the temperatures and compositions were p_i can be taken as a constant over the first four shells. This occurs below the Curie temperature. With this restriction, equation (29A) can be written as

$$kT \frac{1-p}{p} = -2V m_{\mathrm{Fe}} C_1 (1-2p) \tag{30A}$$

The influence of SRO has been taken to be small and neglected. These approximations have little effect upon the value of the SRO coefficients for those points given in Table 1.

J. Phys. Chem. Solids Pergamon Press 1963. Vol. 24, pp. 109–127. Printed in Great Britain.

ON THE ELECTRONIC CONDUCTION OF α-SiC CRYSTALS BETWEEN 300 AND 1500°K

H. J. VAN DAAL, W. F. KNIPPENBERG and J. D. WASSCHER

Philips Research Laboratories, N.V. Philips' Gloeilampenfabrieken, Eindhoven, The Netherlands

(*Received* 19 *July* 1962)

Abstract—The Hall constant and the conductivity of lamellar hexagonal SiC crystals were measured in a temperature range from 77 to 1500°K. The measurements were performed in a plane perpendicular to the hexagonal *c*-axis using van der Pauw's method. Besides being experimentally advantageous this method also may reveal inhomogeneities.

Most crystals were *p*-type conducting. They were grown by the Lely method and purposely doped during growth. The amount of impurities present was investigated by chemical and spectrochemical procedures. Dominating impurities determined by these methods are respectively Al, B and Cl. As to Boron a check by paramagnetic resonance methods was made.

The Hall data in the temperature range from 300 to 1300°K were analysed using a schablone technique in terms of donor and acceptor concentrations. The latter results were compared with those from chemical analysis. An acceptor level of 0·27 eV above the valence band could be related to aluminium. Another level at 0·39 eV was found. This level could not be identified. A ratio of four was found for the multiplicity factors of the two levels, from which it was concluded that the unknown acceptor has paired electrons in the non-ionized state.

It appeared that chlorine has no effect on the electric conduction. The ionization energy of the majority centres was found to be a function of the minority centre concentration. The density of states of the valence band could be determined, from which a provisional value for the density-of-states effective mass of 1·0 m_0 could be deduced for the holes.

An analysis of the dependence of the mobility of holes and electrons is given in terms of optical, acoustical, piezoelectric and impurity scattering. For the electrons it follows from the polar scattering that the effective mass equals 0·72 m_0, from the acoustical scattering that the deformation potential of the conduction band amounts to 11·5 eV and from piezoelectric scattering that the piezoelectric-mobility-constant lies in between those of CdS and ZnS.

A similar description of the hole mobility gives an effective mass of 3·5 m_0 for the holes. This high value probably indicates that another scattering mechanism is present. For this a scattering of holes between two subbands of a split valence band by optical phonons is proposed.

A rough analysis of the impurity scattering in the *p*-type samples has been made.

1. INTRODUCTION

UNTIL 1954 all data reported in the literature concerning hexagonal SiC referred to measurements on samples prepared from single crystals occasionally found in the technical process of preparing silicon carbide. These crystals were sometimes colourless, but mostly green, blue or black.

Temperature-dependent resistivity measurements were made by WEIGEL,(1) SEEMANN(2) and HENNINGER(3) establishing an ohmic behaviour and a negative temperature coefficient of the resistivity. Non-ohmic behaviour could be accounted for by rectifying properties of the contacts used. These investigations were not extensive and the material used was only specified as to colour.

HOCHBERG and SOMINSKI(4) found by measuring the Seebeck coefficient that the green material was *n*-type and the black *p*-type. That deepening of the colour was correlated with an increase of the conductivity was remarked by BRAUN and BUSCH.(5)

The first more extensive study was made by BUSCH(6) and by BUSCH and LABHART.(7) Their measurements were made on ten transparent yellow and green, and ten black opaque bars. The ohmic behaviour and homogeneity of the samples were checked. The conductivity and the Hall effect were measured over a temperature range from 100 to 1100°K. At high temperatures a maximum in the conductivity was found which was attributed to degeneration of the electron gas. Below the maximum the dependence of the conductivity (σ) on temperature could be represented by the formula

$$\sigma(T) = A_1 \exp(-E_1/2kT)+A_2 \exp(-E_2/2kT). \tag{1}$$

For yellow and green crystals the values of E_1 varied from 1·57 to 0·157 eV and E_2 from 0·191 to 0·057 eV. For black crystals E_1 values were found between 0·282 and 0·226 eV and E_2 values between 0·052 and 0·038 eV. E_2 was taken as the activation energy of an impurity conduction band, whereas E_1 was attributed to the ionization energy of impurities. As chemical analyses were not made identification of the impurities was not obtained.

In 1954 LELY published his method for preparing pure SiC crystals on a laboratory scale.[(8)] Pure colourless crystals were prepared and impurities were deliberately introduced during growth. It was seen that incorporation of nitrogen resulted in green crystals that were n-type and that incorporation of aluminium gave blue, p-type crystals. In both cases the heavily doped material appeared almost black. From electrical measurements on these crystals LELY and KRÖGER[(9)] obtained the following results:

(1) The depth of the N-donor level below the conduction band E_D lies in between 0·06 and 0·085 eV for the samples investigated.
(2) The separation of Al and B acceptor levels from the valence band amounts to E_A = 0·275 eV.
(3) Lattice scattering causes the mobility to decrease with temperature according to $\mu_H = aT^{-b}$ with b = 1·5 to 1·8 for electrons and b = 2·2 to 3·0 for holes.
(4) The effective mass of electrons was estimated from the onset of degeneracy to be 0·6 m_0.

An estimate based on the mobility ratio for electrons and holes, assuming acoustical scattering to be dominant, then leads to an effective mass for the holes of $m^* = 1{\cdot}2\, m_0$.

(5) The maximum in the conductivity was interpreted as being effected by exhaustion of the levels combined with the decrease of the mobility.

The p-type crystals were not measured up to the onset of saturation and no complete chemical analysis of the crystals was made.

Continuing the work of LELY and KRÖGER it was thought necessary to extend the electrical measurements to higher temperatures, especially for p-type material, so that a correct analysis of the Hall data could be made. These high temperatures required the development of appropriate experimental techniques and imposed higher demands on the contacting methods. Further it was necessary to make a total chemical analysis of the crystals grown under varying doping conditions so that a more general correlation could be given between the results of chemical analysis and electrical measurements.

In the following the results of this work are reported. In addition a new method of analysing the electrical measurements and the behaviour of the mobility in SiC are treated. Part of this work was presented at the Schenectady Conference of July 1961.[(10)]

2. MATERIAL

The crystals grown as proposed by LELY[(8)] were lamellar with average dimensions of 5×5×0·5 mm³. They were hexagonal with the normal to the platelet parallel to the crystallographic c-axis. Some were strict plane-parallel while others had only one very well developed base plane, the second base plane showing a poor development. X-ray analysis indicated that they were predominantly SiC II (6H), with more or less stacking faults.

According to the different conditions of growth they were labeled:

(1) "*Argon crystals*" (A) grown in an argon atmosphere without deliberate doping. The impurities present originated from the starting material, the furnace used for the growth and from the ambient.
(2) "*Aluminium crystals*" (Al) grown while adding to the argon atmosphere vapours containing $AlCl_3$ or Al coming off dissociating Al_4C_3.
(3) "*Chlorine crystals*" (Cl) grown adding chlorine to the argon atmosphere.
(4) "*Oxygen crystals*" (O) grown adding CO to the argon atmosphere.

The colour of these crystals varied from light to dark greyish. The highly doped "aluminium crystals" were dark blue to black. As the nitrogen content of the argon was at least 1 ppm, all crystals are expected to have a nitrogen concentration of at least 10^{17} cm^{-3}.⁽⁹⁾

3. CONTACTS AND EXPERIMENTAL PROCEDURE

The alloys Au–Ta ($\approx$ 1 per cent tantalum) and Ni–Mo ($\approx$ 5 per cent molybdenum) were used for making contacts by alloying techniques. The contacts are mechanically strong and show an ohmic behaviour on *n*-type material over the temperature range from liquid nitrogen up to 1500°K. The same is obtained for *p*-type material if a small amount of aluminium is added. Especially the Au–Ta alloy has extraordinary favourable properties. It can be rolled into very thin foils or drawn into wires. It wets the SiC perfectly and gives mechanically very strong contacts. There is almost no penetration into the crystal.

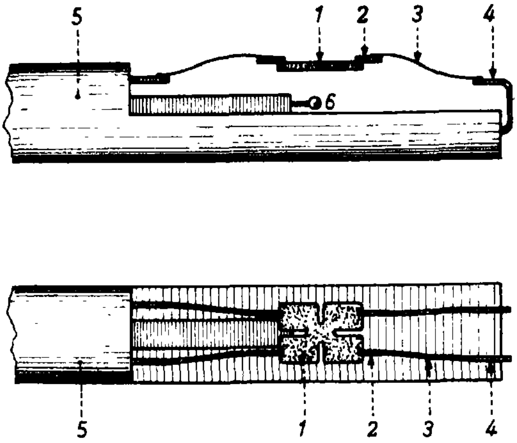

FIG. 1. Mounted crystal. 1. Sample 2. Molybdenum strips. 3. Platinum strips. 4. Platinum measuring leads. 5. Alumina rod. 6. Thermocouple (Pt–Pt/Rh).

An alumina rod with six small holes and one large hole in the centre was fashioned into a crystal holder by removing a certain part at one end (Fig. 1). In the large central hole a thermocouple is placed. Through the other holes platinum wires are passed which are used as measuring leads.

In a favourite mounting procedure molybdenum strips spotwelded to thin platinum strips at one end are alloyed at the other end to the crystal using nickel (V–aluminium) contact alloy. The free ends of the Pt strips are spotwelded to the platinum wires of the crystal holder. In this way a very flexible connection between the measuring leads and the crystal is obtained. After mounting, the crystal is very carefully sandblasted to remove metal particles deposited on the surface during the alloying procedures.

The alumina rod is clamped into a metal cylinder provided with two flanges (Fig. 2). The measuring leads pass to the outside through the wall of the metal cylinder by means of glass seals. A lid containing two glass seals through which the thermocouple threads pass is attached to the upper flange. The other flange fits to a metal flange which is connected to a glass cone by means of a glass to metal seal. This glass cone fits to the ground top of an alumina furnace tube. All connections are made vacuum tight.

Part of the alumina tube is heated by a bifilarly wound Pt furnace. The temperature is kept constant within 0·3 per cent by taking the resistance of the Pt wire in a bridge circuit regulating the power input. To avoid chimney effects the furnace is placed horizontally. The measurements are made in a pure argon atmosphere. The sample is surrounded by a tantalum cylinder which flattens the temperature gradient of the furnace, acts as a getter and screens the crystal electrically. The total arrangement is shown in Fig. 2.

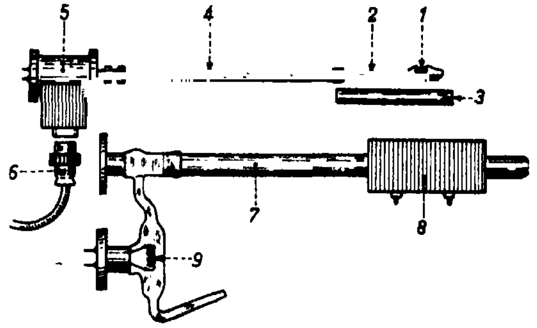

FIG. 2. Sample holder and furnace. 1. Position of the sample. 2. Alumina rod. 3. Tantalum cylinder. 4. Copper screening. 5. Metal cylinder with flanges. 6. Plug for measuring leads. 7. Alumina furnace tube. 8. Bifilar platinum furnace. 9. Tantalum spiral.

The furnace is placed in an electromagnet with a field strength of 5000 G. The electrical measurements were performed using carefully screened d.c. circuits. The current source was a stabilized d.c. power supply. Potential differences between contacts were measured by compensation using an electronic Voltmeter (Philips GM 6010) or a galvanometer (Kipp C 6160) as a zero-instrument.

The current of the electromagnet was stabilized to within 2 per cent, resulting in a constancy of 0·2 per cent of the magnetic field.* The absolute accuracy of the measured Hall resistance was ±3 per cent.

4. VAN DER PAUW'S THEOREM

We decided to use VAN DER PAUW's theorem$^{(11)}$ for measuring the resistivity. Its use requires plane-parallel samples of arbitrary shape with four small contacts on its circumference. Especially where our crystals are lamellar, a minimum of shaping is required and full use can be made of the available surface area.

A current is passed between two adjacent contacts while the potential difference between the other two is measured. By cyclic permutation two independent pseudo-resistances R_1 and R_2 are obtained as voltage-current ratios. It has been shown by VAN DER PAUW that between R_1 and R_2, the resistivity ρ and the thickness of the platelet d the following relation exists

$$\rho = \{\pi d/(2 \ln 2)\}(R_1+R_2)f(R_1/R_2). \qquad (2)$$

The function $f(R_1/R_2)$ is given by VAN DER PAUW in graphical form.

The Hall constant R_H is determined, using the same contacts, by passing the current through two non-adjacent contacts. The change in voltage is measured across the two other contacts when a magnetic field is applied perpendicular to the sample.

The theorem strictly requires that the contacts be infinitesimally small. To reduce the error introduced by the use of contacts of finite size, four incisions were made into the samples (as indicated by VAN DER PAUW) giving the sample the shape of a four-leaf clover. Care was taken that the samples were really plane-parallel. For this purpose the crystals with a badly developed base plane had to be polished.

5. QUALITATIVE INTERPRETATION OF THE MEASUREMENTS

The Hall constant R_H and the conductivity σ were used for evaluating the free hole concentration p and the mobility μ, taking:

$$p = r/(R_H ec) \qquad (3)$$

$$\mu = R_H \sigma / r. \qquad (4)$$

Throughout this work we have assumed that the Hall factor r in these equations is $3\pi/8$, though according to the analysis of the mobility, given in Section 10, it may change from 1·0 at high temperatures (polar scattering) to about 2 at low temperatures in extreme cases of strong ionized impurity scattering. In view of the strong temperature dependence of R_H and μ on T, changes of r with T may, however, in the first instance be neglected. We have also neglected the influence of a possible anisotropic effective mass. This would give an additional but constant factor in both equations.

In Fig. 3 various $\log p$ vs. $1/T$ curves are plotted and Fig. 4 gives a plot of $\log \mu$ vs. $\log T$ for the same samples. The curves of $\log p$ vs. $1/T$ are interpreted as follows: The straight part at intermediate temperatures is due to the changing degree of ionization of partly compensated acceptor levels, which makes the free hole concentration change approximately exponentially with $1/T$. The fact that compensation has to be taken into account is due to the expected presence in all crystals of a

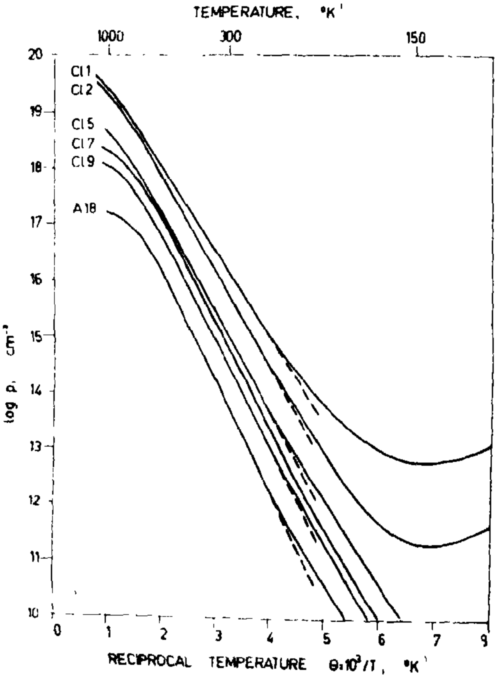

FIG. 3. Examples of p vs. $1000/T$ curves. The symbols marking the curves refer to Table 1.

---

* The apparatus for stabilizing the magnet-current was devised by Mr. H. RADSTAKE.

minimum concentration of 10^{17} cm^{-3} nitrogen donors. In this respect our interpretation differs from that of Busch and Labhart. Lely and Kröger also took compensation into account. The bending of the curves at high temperatures is caused by the exhaustion of the acceptors. These parts of the curves are analysed in more detail in Section 7.

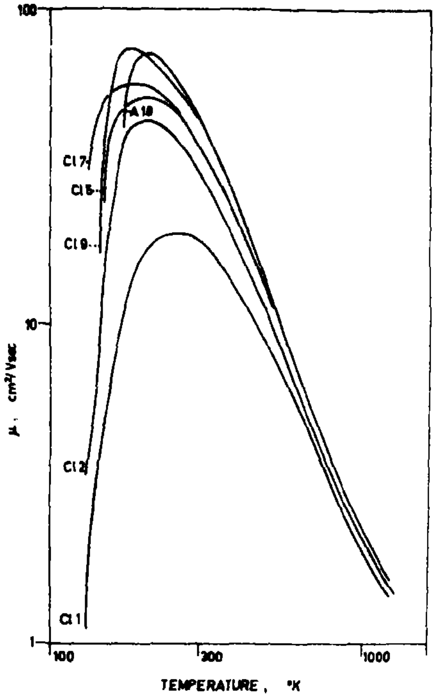

FIG. 4. Examples of μ vs. T curves for the same samples as in Fig. 3.

In Fig. 3 the curves for samples Cl 1 and Cl 2 show a pronounced bend at low temperatures. The other curves change slope between 200 and 250°K, as indicated by the dotted lines representing the extrapolation of the straight part of the curves at intermediate temperatures. In all cases the bends are accompanied by a very sharp decrease in the mobility calculated from equation (4); see Fig. 4. This decrease is very much steeper than $T^{3/2}$ expected for ionized impurity scattering. These facts can only be explained on the assumption that a different conduction mechanism is present at these temperatures, e.g. surface conduction or impurity conduction. Busch and Labhart, who found a similar low temperature behaviour, assumed only impurity conduction. In this temperature region p and μ calculated according to equations (3) and (4) of course have to be considered as effective quantities.

We have not yet investigated this part of the curves and we shall not discuss it further in this paper. When referring to this temperature region in the following, we shall call it the impurity conduction region.

6. HOMOGENEITY OF THE SAMPLES

The ratio R_1/R_2 which appears in equation (2), depends only on the geometry of sample and contacts. This means that it should be independent of the temperature. When, nevertheless, R_1/R_2 for a sample is found to change with temperature, the sample must be inhomogeneous, the resistivity of different parts of the sample having a different temperature-dependence. Although the crystals had no visible inhomogeneities, this phenomenon was found to occur in several samples.

A striking example is shown by curve 1 in Fig. 5(a). This curve was obtained from a lamellar

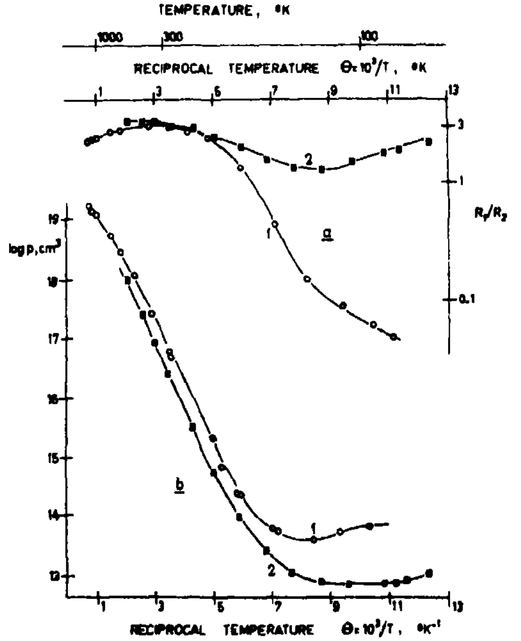

FIG. 5(a). The ratio R_1/R_2 plotted vs. $1000/T$ for a sample before (1) and after (2) incisions were made.
(b). p vs. $1000/T$ curve for the same sample before (1) and after (2) incisions were made.

crystal as grown. Curve 2 was obtained from the same crystal after four incisions as described in Section 4 had been made into it. Clearly the making of the incisions results in a more constant ratio R_1/R_2. This may be understood by realizing that then, as it were, only a small part of the sample is measured, which may be more homogeneous than the whole sample. This is another advantage of the four-leaf clover shape. Figures 5(b) and 6 show the results for p and μ before and after making these incisions.

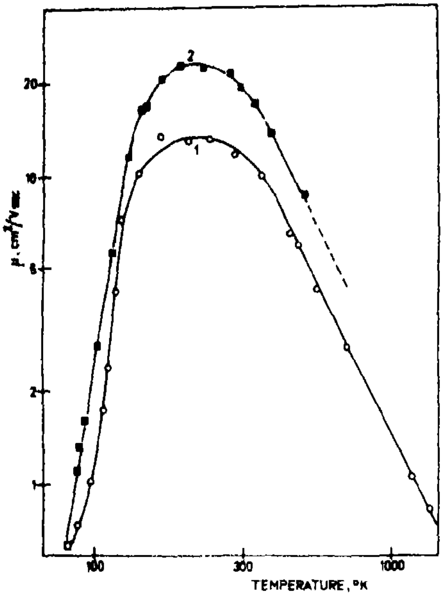

FIG. 6. μ vs. T curve for the sample in Fig. 5 before (1) and after (2) incisions were made.

More curves of R_1/R_2 obtained from incised samples are shown in Fig. 7. Apparently the largest variations of R_1/R_2 occur in the low temperature region. This may be connected with the possible occurrence of impurity conduction at these temperatures. Because the resistivity in the impurity conduction range may depend very strongly indeed on the concentration of impurities, small variations in the dope may provoke marked inhomogeneity in the resistivity in this temperature region. This would mean that, although strictly any change in R_1/R_2 with temperature indicates that the sample is inhomogeneous in composition, this inhomogeneity is small when the change only occurs in the region of impurity conduction.

Although a change of R_1/R_2 with temperature indicates that the sample is not homogeneous, it must be borne in mind that constancy of R_1/R_2 does not necessarily mean that the sample is homogeneous. It may still be composed of homogeneous layers of different composition parallel to the plane of the sample, or it may be composed of parts with different resistivities having the same temperature-dependence.

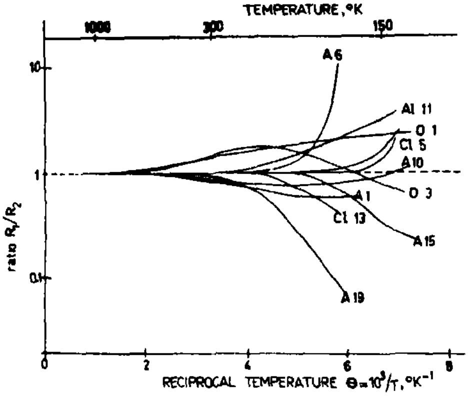

FIG. 7. Examples of R_1/R_2 vs. $1000/T$ curves. The symbols marking the curves refer to Table 1. The measured ratios were normalized to the value 1 at high temperatures.

7. ANALYSIS OF THE HALL CURVES

If the qualitative interpretation of the Hall curves presented in Section 5 is right, the curves should quantitatively be described by

$$p(p+N_D)/(N_A-N_D-p) = (N_v/g)\exp(-E/kT). \qquad (5$$

This equation[12] gives the temperature dependence of the free hole concentration p in a valence band with an effective density of states

$$N_v = 2(2\pi m^* kT/h^2)^{3/2} \qquad (6)$$

for a semiconductor with a concentration of N_A acceptors having the ionization energy E, partly compensated by donors with a concentration N_D. The multiplicity factor g takes account of the number of ways a hole can be exchanged between valence band and acceptor level.[13, 14]

To simplify the equations we shall use the following abbreviations:

$$\theta = 1000/T\,(°\mathrm{K})^{-1} \tag{7}$$

$$N = (N_v/g)\theta^{3/2}\ \mathrm{cm}^{-3} \tag{8}$$

$$\beta = 5{\cdot}04\ E \text{ with } E \text{ in eV.} \tag{9}$$

N is temperature-independent. β has the dimension of a temperature. With these abbreviations equation (5) becomes:

$$p(p+N_D)/(N_A-N_D-p) = N\theta^{-3/2}10^{-\beta\theta}. \tag{10}$$

It contains four adjustable parameters N_A, N_D, N and β. At low temperatures only a small number of acceptors will have accepted an electron from the valence band. Then $p \ll N_A-N_D$ and also $p \ll N_D$, which means that for those temperatures equation (10) becomes

$$p = \{(N_A-N_D)/N_D\}N\theta^{-3/2}10^{-\beta\theta}. \tag{11}$$

In our interpretation this equation corresponds to the intermediate part of the curves (Section 5).

Another explanation of this straight part would be that in this temperature region $N_D \ll p \ll N_A-N_D$. This is, however, highly improbable as all crystals are expected to contain at least a concentration of 10^{17} nitrogen donors (Sections 2 and 5) and the straight parts of the curves mostly extend to much lower free hole concentrations. This interpretation also leads to much too high values for N.

Because of the presence of the $\theta^{-3/2}$ factor in the R.H.S. of equation (11), plots of $\log p\theta^{3/2}$ versus θ were made to evaluate β and $N(N_A-N_D)/N_D$ (Fig. 8).

If N_A-N_D can be obtained from the value of p in the exhaustion region and N is known—as is the case, e.g. for shallow levels in germanium—N_D can be calculated. In our case N was not known. Furthermore the acceptor levels turned out to have rather high ionization energies, owing to which the exhaustion was not completed even at 1500°K, which was the highest temperature at which measurements of the Hall effect were taken. We were able, however, to obtain these quantities from the behaviour of the Hall coefficient near the onset of exhaustion.

For this region we can calculate a quantity α defined by

$$\alpha = p\theta^{3/2}\left[\frac{N_A-N_D}{N_D}N10^{-\beta\theta}\right]^{-1}. \tag{12}$$

This is readily done using the $\log p\theta^{3/2}$ versus θ plot already made to obtain β and $N(N_A-N_D)/N_D$. In Fig. 8 the values of $\log\alpha$ are represented by the lengths of the vertical lines. By substitution of equation (10) into equation (12) we also have

$$\alpha = \left(1-\frac{p}{N_A-N_D}\right)\left(1+\frac{N_A-N_D}{N_D}\,\frac{p}{N_A-N_D}\right)^{-1}. \tag{13}$$

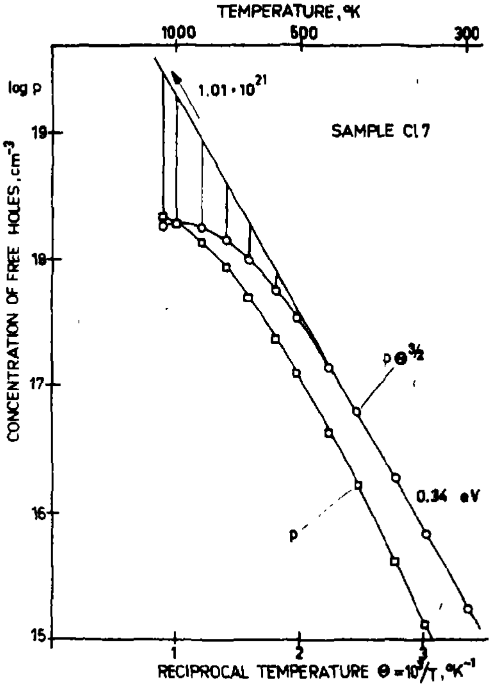

FIG. 8. A p vs. θ plot and $p\theta^{3/2}$ vs. θ plot, used for the analysis.

According to this equation, α may be looked upon as a function of the variable $p/(N_A-N_D)$ in which $(N_A-N_D)/N_D$ occurs as a parameter. Denoting $p/(N_A-N_D)$ by x and $(N_A-N_D)/N_D$ by γ, this means that a plot of $\log p$ versus α must be identical with a curve $\log x$ versus α satisfying

$$\alpha = (1-x)(1+\gamma x)^{-1} \tag{14}$$

except for a vertical shift by $\log(N_A-N_D)$ along the $\log p$ axis.

Therefore a standard set of auxiliary curves $\log x$ versus α satisfying equation (14) is made for various values of γ on transparent paper. This paper is shifted over the experimental log p versus α plot to select the best fitting auxiliary curve, taking care that the log p axis coincides with the log x axis (Fig. 9). The γ value of this curve is the value of $(N_A-N_D)/N_D$ for the sample and the line $\log x = 0$, i.e. $x = 1$, covers the value of N_A-N_D. From the values of $N(N_A-N_D)/N_D$, N_A-N_D and $(N_A-N_D)/N_D$ which now have been obtained, N_A, N_D and N may be calculated separately.

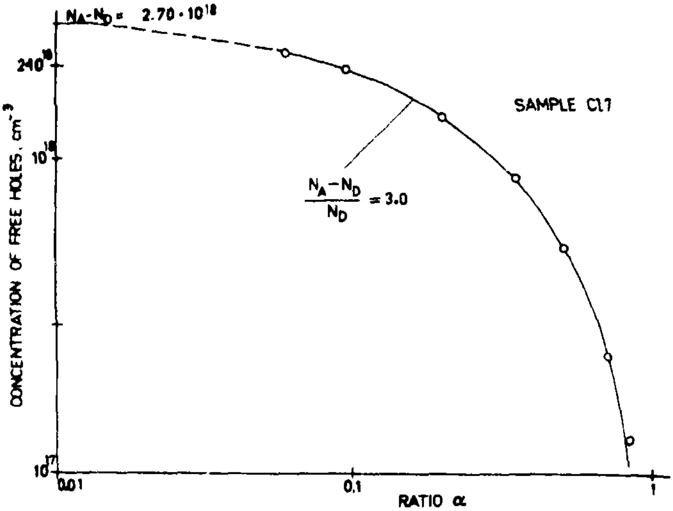

FIG. 9. p vs. α plot for the same sample as in Fig. 8.

Effectively this method extrapolates the measured curves to the region of complete exhaustion, and at the same time gives information concerning the degree of compensation. This schablone method proved to work more satisfactorily than the technique proposed by WEDEPOHL, quoted by MITCHELL.(15) It must be said that the results are very sensitive to the choice of position and slope of the straight line in the log $p\theta^{3/2}$ vs. θ plot. This is not due to the choice of the analysing technique but to the problem itself. Furthermore in most cases the straight line could be drawn quite accurately because the straight part of the log $p\theta^{3/2}$ vs. θ curves mostly extended over several decades (Figs. 11, 12 and 13).

Instead of the set of curves according to equation (14) we also used a set of curves log y versus α satisfying

$$\alpha = \{1-y/(1+\gamma)\}\{1+\gamma y/(1+\gamma)\}^{-1}. \quad (15)$$

This makes no essential difference, but the advantage over the other set is that these curves all coincide for low values of y and that they show more clearly the relative accuracy of the γ-values which are obtained. In the final version α too was plotted on a logarithmic scale. In this way a shift of the auxiliary set over the experimental log p vs. α curve in the direction of the log α axis corresponds to a vertical shift of the straight line representing equation (11). This is useful in cases where the slope of this line is known already, but it is difficult to ascertain where its exact position is.

Figure 10 shows the set of auxiliary curves log y vs. log α (equation 15). The N_D/N_A value for each curve is indicated. Also shown are the log p vs. log α-values derived from the measurements on the chlorine and oxygen samples after these had been shifted in the direction of the log p axis to coincide with one of the auxiliary curves. This figure shows that the measured Hall curves can be described accurately by equation (5).

Figures 11, 12 and 13 show the Hall effect measurements for the different groups of samples in the high temperature range, i.e. from room temperature up to about 1300°K. The results for these samples, obtained with the method of analysis presented, are given in Table 1.

In view of the considerations given in Section 6, only those samples have been included for which the ratio R_1/R_2 was constant over the temperature range used for the analysis, though in several cases where low temperature measurements were carried out, R_1/R_2 changed considerably in the region of impurity conduction. Following the arguments given in Section 6 we have, however, assumed that these samples could nevertheless be considered homogeneous in the region of normal conduction.

8. LEVEL DEPTH AND DENSITY OF STATES

As is seen from Table 1, a wide continuous range of values for the activation energy is found. This may be due to the presence of different centres but also to the fact that the level depth of one and the same centre can be influenced by the concentration of all impurities present. If we plot the activation energy as a function of the majority centre concentration (acceptors) no relation is found. Plotting the level depth, however, as a function of the minority centre concentration (donors) a definite relation is found. Theoretical considerations have been published concerning the dependence of the majority centre level depth on the minority centre concentration.

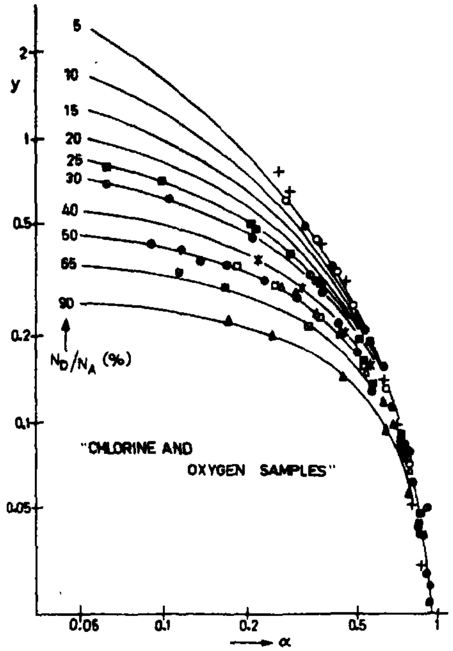

FIG. 10. Auxiliary set of log y vs. log α curves. The markings indicate experimental values for the chlorine and oxygen samples.

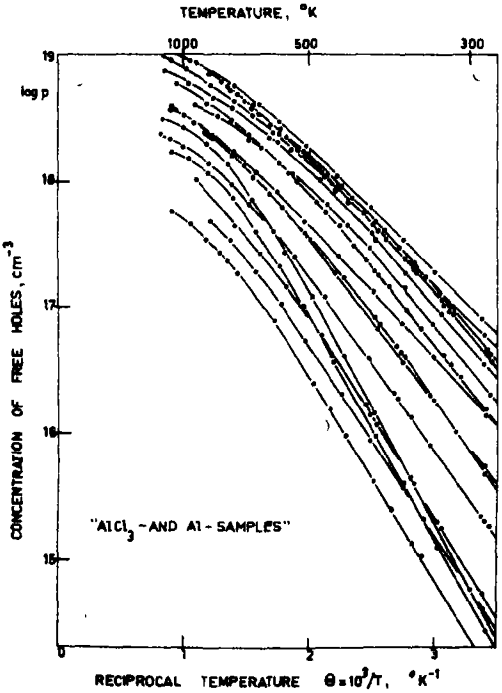

FIG. 11. p vs. θ plots for the aluminium samples.

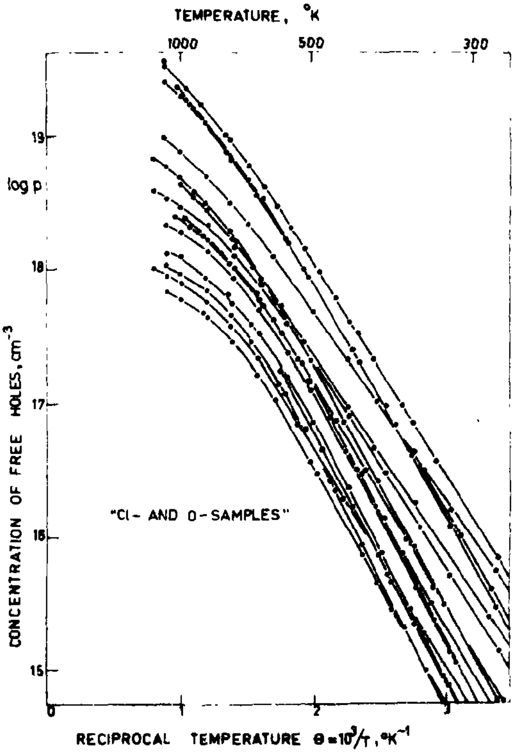

FIG. 12. p vs. θ plots for the chlorine and oxygen samples.

Table 1. *Numerical results obtained from analysing the Hall curves, measured on p-type samples of hexagonal* SiC, *in the temperature range from* 300 *to* 1300°K

Sample	E Ionization energy (meV)	N_A Acceptor concentration ($\times 10^{17}$ cm^{-3})	N_D Donor concentration ($\times 10^{17}$ cm^{-3})	N_D/N_A Compensation degree (per cent)	N ($\times 10^{17}$ cm^{-3})
		"Aluminium Samples"			
Al 1	310	45	16	35	1,750
Al 2	315	79	24	30	2,600
Al 3	220	99	25	25	630
Al 4	225	140	14	10	820
Al 5	165	240	73	30	1,400
Al 6	270	17	9·4	55	560
Al 7	245	23	15	65	800
Al 8	230	55	25	45	1,000
Al 9	190	170	34	20	960
Al 10	160	230	81	35	1,000
Al 11	170	110	57	50	850
Al 12	240	110	9·6	9	400
Al 13	220	140	10	7·5	670
Al 14	180	430	43	10	460
Al 15	200	280	28	10	810
Al 16	190	230	29	12·5	1,000
Al 17	200	320	29	9	700
		"Chlorine and Oxygen Samples"			
Cl 1	275	3,600	120	3·0	750
Cl 2	290	850	140	20	3,250
Cl 3	305	900	82	9	3,200
Cl 4	290	70	35	50	3,400
Cl 5	310	120	30	25	2,550
Cl 6	280	66	55	80	4,150
Cl 7	340	36	9·0	25	3,400
Cl 8	260	93	47	50	2,700
Cl 9	345	23	7·6	30	3,250
Cl 10	355	43	4·8	9	2,100
Cl 11	305	34	26	80	4,000
Cl 12	330	31	14	45	3,400
Cl 13	340	25	12	50	3,650
O 1	230	320	160	50	3,200
O 2	310	70	28	40	3,500
O 3	230	340	230	70	2,900
		"Argon Samples"			
A 1	270	200	90	45	3,600
A 2	285	140	50	35	2,800
A 4	265	290	36	13	880
A 5	285	180	54	30	2,600
A 6	350	11	7·4	70	3,000
A 7	310	390	22	5	800
A 8	315	68	23	30	3,000
A 10	280	88	44	50	3,100
A 11	200	320	190	60	2,900
A 12	265	230	120	50	3,900
A 13	305	170	59	35	4,000
A 14	315	70	19	25	1,600
A 15	345	28	12	45	3,200
A 17	365	3·2	1·1	30	1,800
A 18	355	3·7	1·9	50	2,000

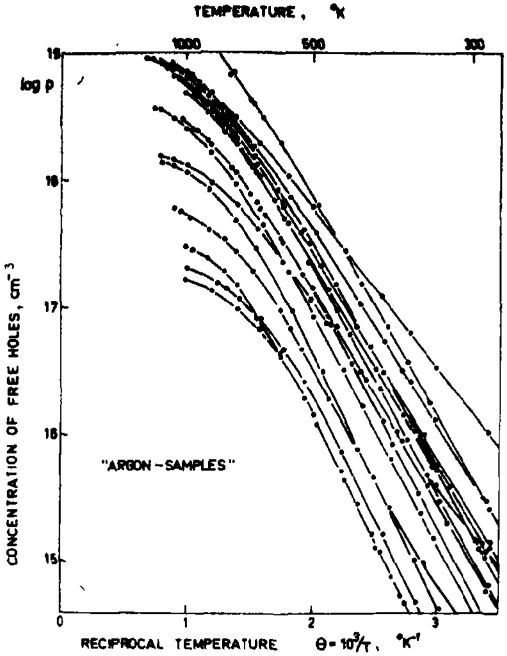

FIG. 13. p vs. θ plots for the argon samples.

According to CONWELL and DEBYE(16) the level depth should decrease from its zero concentration limit in inverse proportion to the mean distance between the ionized majority centres. Below the region of exhaustion the concentration of the ionized majority centres is equal to the concentration of the compensating minority centres, so that we should have

$$E = E_0 - CN_D^{1/3} \tag{16}$$

where

$$C = 2{\cdot}66\, e^2/\epsilon_0 \tag{17}$$

as calculated by PEARSON and BARDEEN,(17) and ϵ_0 is the static dielectric constant.

The existence of such a relationship is shown in Fig. 14, from which it appears, however, that two different groups of p-type crystals have to be distinguished. The two upper straight solid lines drawn represent activation energies:

$$E_1 = 0{\cdot}27 - 4(e^2/\epsilon_0)N_D^{1/3}\ \text{eV} \tag{18}$$

and

$$E_2 = 0{\cdot}39 - 4(e^2/\epsilon_0)N_D^{1/3}\ \text{eV} \tag{19}$$

with

$$\epsilon_0 = 10{\cdot}2.^{(18)}$$

The factor 4 in these equations is higher than the factor derived by Pearson and Bardeen, possibly because other mechanisms also play a rôle.(19–22) The fact that it agrees with the value derived by CHETKAROV,(23) who used an oversimplified model, seems to be a coincidence. The third line in Fig. 14 is drawn for n-type samples with nitrogen as the dominating impurity, assuming that the same relation holds as for the p-type samples. The indicated points are taken from the measurements of LELY and KRÖGER.(9)

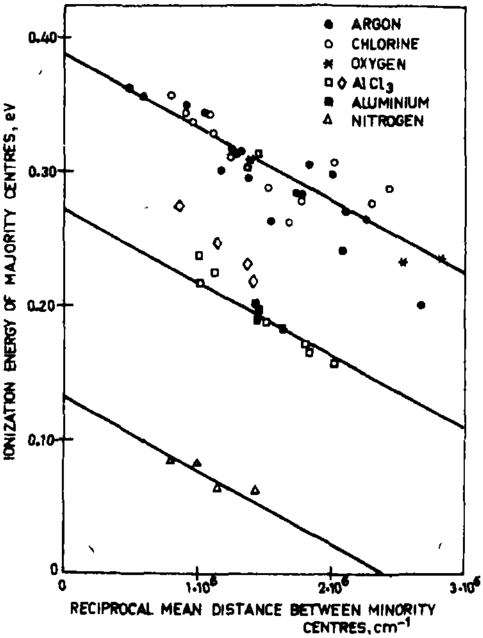

FIG. 14. Ionization energy of the majority centres vs. the reciprocal distance of the minority centres. The two upper lines refer to p-type samples, the lower line to n-type samples (LELY and KRÖGER(9)).

For the p-type samples again a division into two groups is found when looking at the values of N (see equation (8)) as shown in Fig. 15. Averaged over each group we find

$$N_1 = 0{\cdot}77 \times 10^{20}\ \text{cm}^{-3} \text{ and}$$
$$N_2 = 3{\cdot}00 \times 10^{20}\ \text{cm}^{-3}.$$

The group with E_1 and N_1 solely consists of crystals grown in the presence of aluminium. Besides, as shown in the next section, chemical analysis has revealed that these crystals contained Al in quantities comparable with their acceptor concentration. This means that E_1 and N_1 are characteristic of the aluminium level. We have not been able to identify the nature of the impurity responsible for the level characterized by E_2 and N_2.

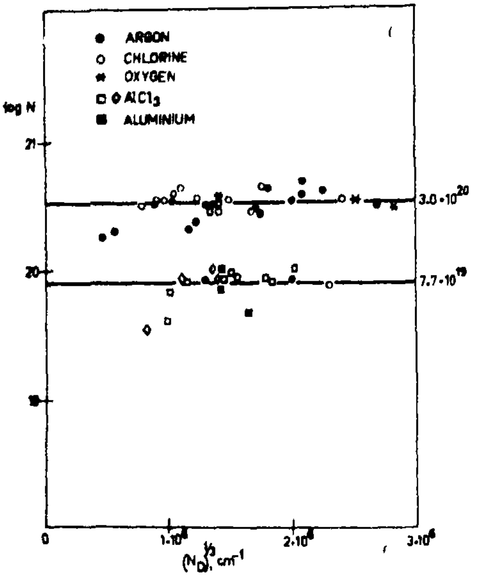

Fig. 15. The quantity N arbitrarily plotted vs. the reciprocal distance of the minority centres.

In some cases the presence of both levels in the same crystal was revealed by a small shoulder in the Hall curve, such as shown in Fig. 16. In two instances of lightly doped AlCl$_3$ crystals the unknown acceptors completely dominated the Al acceptors. It is quite possible that in other Al-doped crystals the deeper acceptors were also present, which could seriously affect the results from the analysis of their Hall curves. We believe that this is the reason for the scattering of the points of the Al group being greater at the left hand (i.e. the purer) side of Fig. 14 than at the right-hand side.

The fact that the ratio N_2/N_1 is almost exactly 4 (it is 3·91) strongly suggests that the difference in N_1 and N_2 is due to a difference in the multiplicity factors g of the levels. Woodbury and Ludwig[24] concluded from their paramagnetic resonance studies that boron in SiC has an orbitally non-degenerate ground level. This probably will then also be the case for Al. Furthermore it is expected that an Al level exchanges holes of either spin with the valence band. On these grounds g should be taken equal to 2 for the Al level. From N_2/N_1 being 4 it then follows that $g = \frac{1}{2}$ for the unknown level, suggesting that it can only exchange holes of a definite spin orientation with the valence band (i.e. that it has paired electrons when it has not accepted an electron from the valence band). With these values of g, N_1 and N_2 yield for the density-of-states effective mass a value of $m^*_{dh} = 1{\cdot}0\, m_0$.

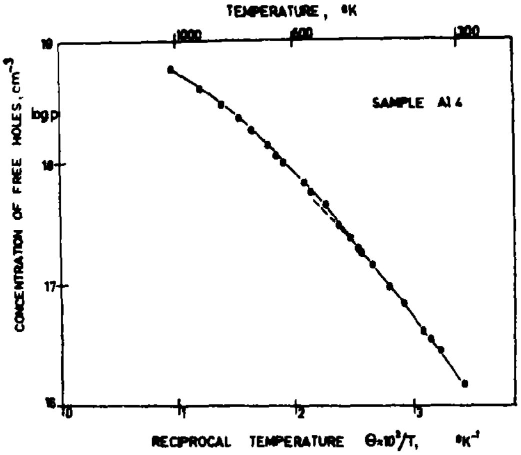

Fig. 16. p vs. θ plot showing shoulder due to presence of two levels.

A characterization of the blue technical grade material investigated by Busch[6] can now be given. When comparing the results of Busch with our results it should be borne in mind that the high temperature activation energies for the conductivity should be divided by 2 because compensation was not taken into account. His results therefore indicate ionization energies between 0·14 and 0·11 eV. The fact that these values are derived from the conductivity instead of $p\theta^{3/2}$ plots is of little importance. As aluminium is the dominant impurity in blue technical material these levels should correspond to a high concentration of aluminium acceptors ($>2\times10^{19}$) partly compensated by 1–2×10^{19} donors cm^{-3} according to Fig. 14.

9. CORRELATION BETWEEN ACCEPTOR AND IMPURITY CONCENTRATION

In many cases spectrochemical analyses were performed on crystals originating from batches from which crystals had also been taken for the electrical measurements. Boron, aluminium and chlorine were also determined by normal wet analysis. The boron content was checked in a number of cases by paramagnetic resonance.(24, 25) The spread in the results obtained on different crystals out of one batch can be as large as a factor of 2. The agreement between the electrical and chemical analysis cannot therefore be expected to be better than this.

In Fig. 17 the impurity content is plotted for the three main impurities, i.e. for Al, B and Cl, vs. the acceptor concentration for the crystals showing the lower level in Fig. 14. All other impurities detectable by spectrochemical methods like Ti or V were present in a smaller concentration.

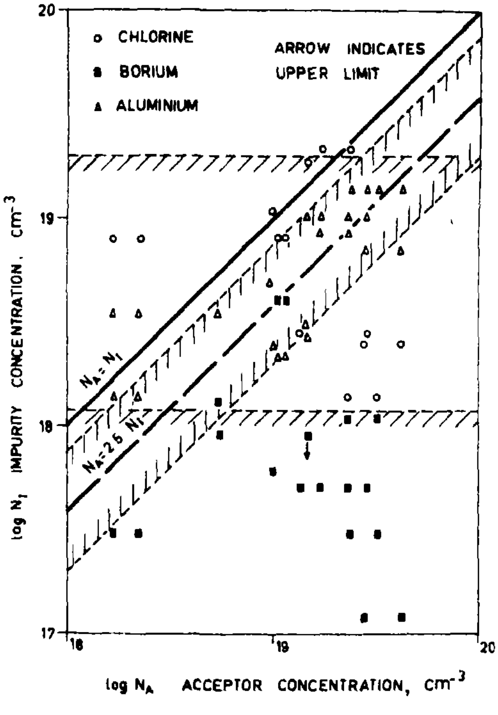

Fig. 17. Comparison of the impurity content and acceptor concentrations for the samples showing the lower level in Fig. 14.

It is striking that the Cl content in the samples doped with $AlCl_3$ is quite high. There does not seem to be, however, any relation between this Cl content and the electrically active centres. The B concentration in these crystals is in general much smaller than the Al concentration. The Al concentrations form a band that lies below but parallel to the line for $N_A = N_{imp}$, except for two samples having low acceptor concentrations. Taking into account the uncertainties involved, it is reasonable to assume from Fig. 17 a one to one relation between the Al atoms and the acceptors. We thus conclude that the level characterized by a multiplicity factor of 2 and a level depth for zero minority centre concentration of 0·27 eV (Fig. 14) is due to Al. The systematic difference between the acceptor and Al concentrations found is probably due to an over-simplification of the model assumed (see Section 11).

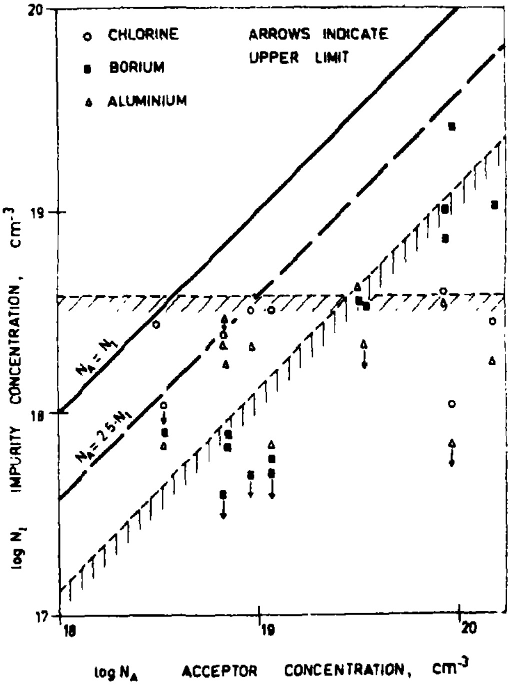

Fig. 18. Comparison of the impurity content and acceptor concentrations for the chlorine and oxygen samples.

In Fig. 18 the concentration of the three main impurities in the Cl and O crystals is plotted against the number of acceptors. The chlorine concentration is seen to be lower than 4×10^{18} cm^{-3}. The boron concentration lies below a line $N_{imp} = 0{\cdot}1\,N_A$ with only one exception. The other impurities detectable by spectrochemical methods were still less than this. Even when a systematic error of a factor 2 is admitted, the acceptor levels cannot be attributed to any of the elements mentioned. Thus the level lying at 0·39 eV for zero minority centre concentration and characterized by a multiplicity factor of $\frac{1}{2}$ can not yet be ascribed to a specific impurity.

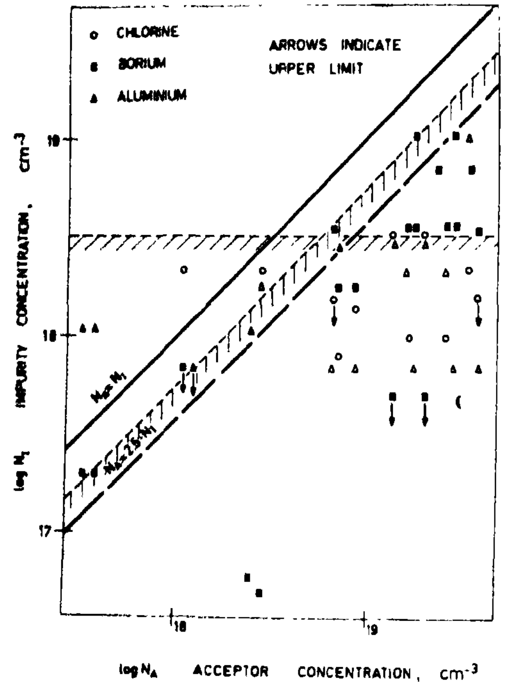

FIG. 19. Comparison of the impurity content and acceptor concentrations for the argon samples.

In Fig. 19 for the argon samples the concentration of the three main impurities is plotted versus the acceptor concentration. In a number of cases the concentration of acceptors equals 2·5 times the boron or aluminium concentration. This was also about the systematic error admitted for the aluminium samples (Fig. 17). But in view of the fact that these samples show the level depth and g value found for chlorine samples—the higher level in Fig. 14—we are inclined to assume that in these crystals the dominating centre is the same unknown centre that dominates in the chlorine and oxygen samples.

10. ANALYSIS OF THE MOBILITY

In Fig. 20 a representative set of μ vs. T curves, calculated according to equation (4), is shown. For comparison two curves obtained on n-type samples are included.

The mobility increases rather steeply from high to low temperatures. At about 250°K a maximum is reached except for curve 1. For lower temperatures there is a very fast decrease characteristic for the impurity conduction already mentioned in Section 5. μ-values obtained at these low temperatures, using equation (4), must be regarded as effective quantities. We have not yet analysed this low-temperature behaviour. From the $p\theta^{3/2}$ vs. θ curves it may be concluded that above 250°K the impurity conduction may be neglected. In the impure samples impurity scattering takes place, causing the divergence of the curves when going from high to lower temperatures. Only in the

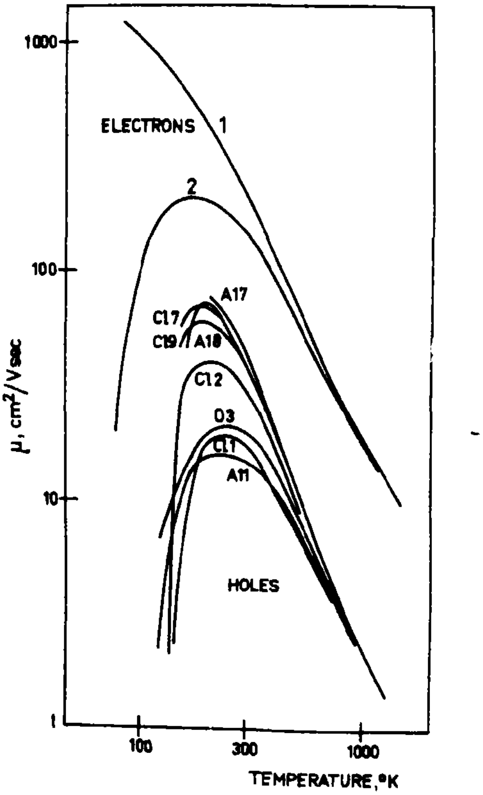

FIG. 20. Examples of μ vs. T curves for electrons and holes.

purest samples is the mobility solely determined by lattice scattering down to at least room temperature. Sample 1 is an example of a pure n-type crystal. From the low temperature part of its Hall curve it is estimated that N_A in this sample is less than $10^{15}\,\mathrm{cm}^{-3}$.* This sample probably exhibits the lattice mobility down to 77°K. As is seen from Fig. 20 the lattice mobilities show approximately the same behaviour for electrons as for holes. At room-temperature the lattice mobility is 220 $\mathrm{cm}^2/\mathrm{Vsec}$ for the electrons and 48 $\mathrm{cm}^2/\mathrm{Vsec}$ for the holes.

The bonding in SiC is partly ionic(26, 27) and the crystallographic modification investigated has no centre of inversion. According to theory the lattice vibrations of such crystals are expected to scatter the free charge carriers in three different ways. Longitudinal optical as well as both types of acoustical modes give rise to polarization waves. The corresponding interactions with the free charge carriers are called respectively polar(28) and piezoelectric scattering.(29)

The acoustical modes introduce periodic changes in the energy band boundaries, resulting in a scattering described as deformation potential or acoustical scattering.(30) A similar interaction exists between optical modes and free charge carriers, but it is negligible compared to the polar interaction which in polar crystals is involved at the same time.

The equation for the polar mobility is given(31, 32) by

$$\mu_{\mathrm{pol}} = (8/3\pi^{1/2})A\epsilon^*(m^*/m_0)^{-3/2}z^{-1/2}\chi(z)(e^z-1) \tag{20}$$

where

$$A = e\hbar^2/\{(2kT_c m_0)^{1/2}m_0e^2\}$$
$$\epsilon^* = \epsilon_0\epsilon_\infty/(\epsilon_0-\epsilon_\infty)$$
$$z = T_c/T.$$

T_c is the temperature characteristic for the longitudinal optical phonons. $\chi(z)$ is given by HOWARTH and SONDHEIMER.(31) Using $\epsilon_0 = 10{\cdot}2$(18) and $\epsilon_\infty = 6{\cdot}7$(27) equation (20) reduces to

$$\mu_{\mathrm{pol}} = 13{\cdot}3(m^*/m_0)^{-3/2}z^{-1/2}\chi(z)(e^z-1)\ \mathrm{cm}^2/\mathrm{V\,sec}. \tag{21}$$

From the Reststrahl wavelength 12·6 μ(27) follows that $T_c = 1410$°K. The only adjustable parameter in this equation is the effective mass m^*.

The mobility due to piezoelectric scattering(29) has the form

$$\mu_{\mathrm{piez}} = P(m^*/m_0)^{-3/2}T^{-1/2} \tag{22}$$

where P contains the macroscopic piezoelectric constants of the material. These, however, are not known for SiC, but P should be equal in p and n-type material.

The equation for the mobility due to acoustical scattering(30) is given by

$$\mu_{\mathrm{ac}} = BE_d^{-2}(m^*/m_0)^{-5/2}T^{-3/2} \tag{23}$$

in which

$$B = (2/3)(2\pi)^{1/2}e\hbar^4m_0^{-5/2}k^{3/2}u^2\rho.$$

E_d is the deformation potential of the appropriate band, ρ the density of the material and u is the velocity of sound. Taking $\rho = 3{\cdot}22\,\mathrm{g\,cm}^{-3}$ and estimating u, $1\times10^6\,\mathrm{cm\,sec}^{-1}$(33), equation (23) reduces for SiC to

$$\mu_{\mathrm{ac}} = 1{\cdot}05\times10^8E_d^{-2}(m^*/m_0)^{-5/2}T^{-3/2}\ \mathrm{cm}^2/\mathrm{V\,sec}. \tag{24}$$

In equation (24) E_d has to be expressed in eV. The only adjustable parameters are E_d and m^*.

For simplicity we have assumed that reciprocal mobilities are additive, disregarding the fact that the relaxation times for the different scattering processes depend differently on the energy of the charge carriers. This is believed to be a good first approximation because for the three scattering mechanisms mentioned the Hall factor r to be used in equations (3) and (4) lies in between 1 and 1·18. In Figs. 21 and 22 the experimentally found values for μ^{-1} are plotted vs. T. As far as lattice mobilities are concerned these values can be represented by addition of the reciprocal mobilities according to equations (21), (22) and (24) by adjusting the values of the unknown parameters.

For the electrons (Fig. 21) we find in this way from the polar contribution $m^* = 0{\cdot}72\,m_0$. A (density-of-states) effective mass of $0{\cdot}6\,m_0$ was estimated by LELY and KRÖGER.(9)

From the acoustical contribution we find

$$E_{dc}^2(m^*/m_0)^{5/2} = 57(\mathrm{eV})^2$$

---

* The Hall curves of the n-type samples were more complicated than those of the p-type samples and they could not be analysed in the manner described in Section 7.

which, using $m^* = 0{\cdot}72\,m_0$, gives $E_{d0} = 11{\cdot}5$ eV for the deformation potential of the conduction band. The small contribution of piezoelectric scattering yields

$$P(m^*/m_0)^{-3/2} = 2{\cdot}1\times10^4\ {}^\circ\mathrm{K}^{1/2}\ \mathrm{cm}^2(\mathrm{Vsec})^{-1}$$

or $P = 1{\cdot}3\times10^4$. This value cannot be checked, as other experiments determining this quantity are lacking. For ZnO, CdS and ZnS one finds P values of $2{\cdot}8\times10^3$, 7×10^3 and 5×10^4 respectively.(29, 35, 36) Our value of $1{\cdot}3\times10^4$ for SiC does not appear unreasonable. The deviation at the highest temperatures between the theoretical curve and the experimental points is due to the onset of intrinsic conduction.

The hole lattice mobility seems to be due solely to polar and piezoelectric scattering, as shown in Fig. 22. The polar part yields $m^* = 3{\cdot}5\,m_0$. From the piezoelectric part the same high value for the effective mass is found using

$$P = 1{\cdot}3\times10^4\ {}^\circ\mathrm{K}^{1/2}\ \mathrm{cm}^2(\mathrm{Vsec})^{-1}.$$

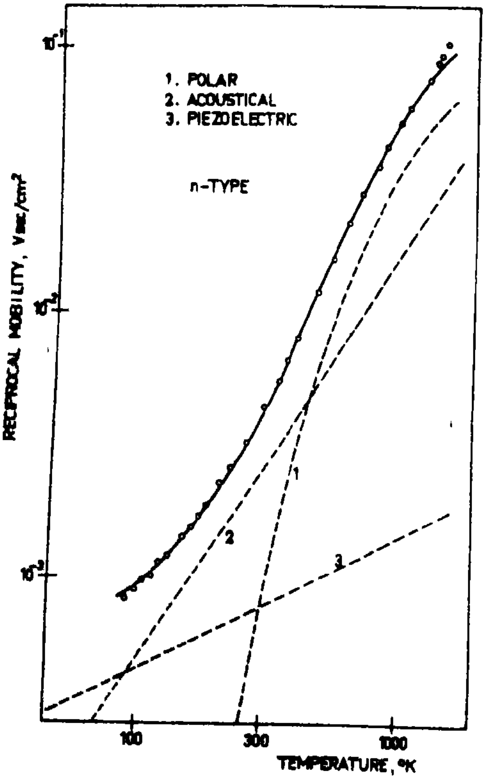

FIG. 21. Reciprocal mobility for the electrons. Dashed lines: 1. for polar, 2. for acoustical, 3. for piezoelectric scattering. Solid line: sum of the three contributions. Dots represent the experimental points.

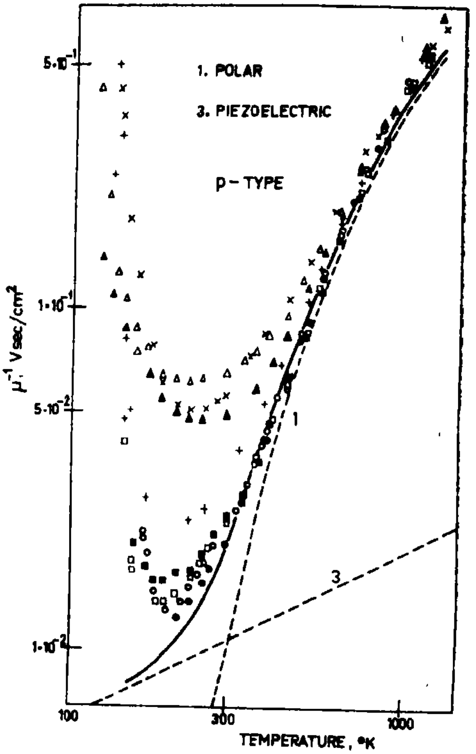

FIG. 22. Reciprocal mobility for the holes. Dashed lines: 1. for polar, 3. for piezoelectric scattering. Solid line: sum of the two contributions. Dots represent the experimental points.

This value of $3{\cdot}5\,m_0$ for the effective mass of the holes is very large compared to the density-of-states effective mass, which in Section 8 was found to be about $1{\cdot}0\,m_0$. Furthermore the effective mass derived from the Al acceptor level depth, using a simple hydrogen model,(37) is calculated to be $1{\cdot}5\,\mathrm{m}_0$. In view of the assumptions underlying the hydrogen model, even this certainly represents a too high value of the effective mass of the holes.

As the mobility measured represents the mobility perpendicular to the c-axis, the conduction effective mass of 3·5 m_0 also refers to this direction. A possible explanation of the difference between this conduction effective mass and density-of-states effective mass is that the latter is obtained by averaging processes. As a consequence the effective mass of the holes in the direction of the c-axis must then be very small.

It can also be that the scattering is not simply polar and piezoelectric. There is evidence for the valence band being completely split up.(24, 38) Assuming the distance between the two highest sub-bands to be about 0·1 eV, i.e. somewhat smaller than the energy of an optical phonon, an interband scattering is possible, produced by optical phonons scattering the holes from the upper band into the lower band. The temperature dependence of the resulting mobility would be essentially the same as for normal polar scattering, both being mainly determined by the concentration of optical phonons present. The small value of the mobility could indicate that the density-of-states effective mass in the lower sub-band is large. The density-of-states effective mass of 1·0 m_0 would in any case be characteristic of the highest of the sub-bands.

Piezoelectric interaction cannot give rise to such interband transitions and should be characterized by the smaller effective mass and should give a much higher mobility than shown in Fig. 22. Here it must be remarked that both for electrons and holes, the evidence for piezoelectric scattering from Figs. 21 and 22 is questionable. It would be desirable to obtain the lattice mobility, in n-type as well as p-type samples, at lower temperatures.

The bending of the lattice mobility below 400°K can also be due to acoustical mode scattering, for which we find

$$E_{dv}^2(m^*/m_0)^{5/2} = 170(\text{eV})^2$$

or with $m^* = 1{\cdot}0\, m_0$, $E_{dv} = 13$ eV. This in any case is an upper limit for this quantity. It should be remarked that the combination of polar and acoustical scattering does not represent the experimental points at high temperatures as well as the combination of polar and piezoelectric scattering.

A rough analysis as to the ionized impurity scattering has been made for a number of p-type samples. We have plotted the differences between the reciprocal value of the measured mobility and the lattice mobility at a temperature of 330°K versus the donor concentration (Fig. 23). At this temperature impurity conduction is still absent for all samples. For SiC the Brooks–Herring formula(34) for impurity scattering reads:

$$\mu_{\text{imp}} = 9{\cdot}6\times 10^{17}(m^*/m_0)^{-1/2} \times N_{\text{I}}^{-1}T^{3/2}f(x)\ \text{cm}^2/\text{Vsec} \qquad (25)$$

where

$$f(x) = \{\ln(1+x)-x(1+x)^{-1}\}^{-1}$$

$$x = 6{\cdot}05\times 10^{14}(1-N_D/N_A)^{-1}N_D^{-1}(m^*/m_0)T^2.$$

The concentration of charged impurities N_I is taken as $2N_D$. The solid lines in Fig. 23 represent the theoretical dependence according to formula (25) for several mass-values and $N_D/N_A = 0{\cdot}5$. Although no definite conclusion as to the appropriate mass-value can be drawn from this figure, it seems to favour the density-of-states effective mass $m^* = 1{\cdot}0\, m_0$ more than the polar mass $m^* = 3{\cdot}5\, m_0$.

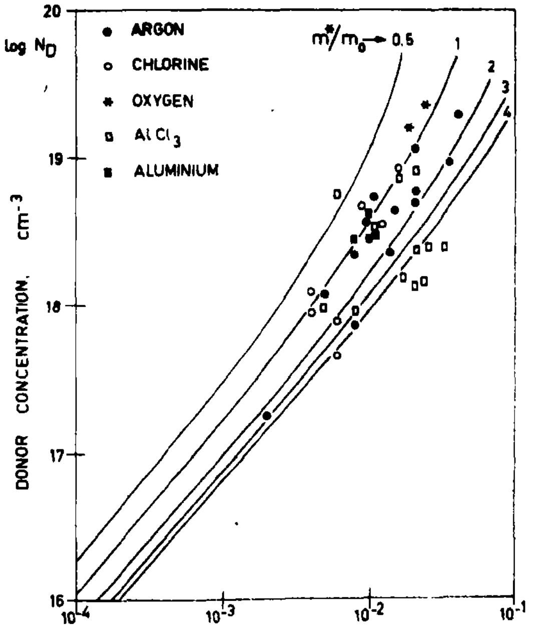

Fig. 23. Reciprocal mobility minus the reciprocal lattice mobility at $T = 330$°K versus the donor concentrations in the p-type samples. The lines have been drawn according to the Brooks–Herring formula for different effective masses as indicated. For all curves the same compensation degree of 50 per cent has been taken.

11. CONCLUDING REMARKS

The present investigation shows that a careful analysis of the Hall curves measured on *p*-type SiC samples not only yields the ionization energy of the acceptors but also their concentration as well as the concentration of the donors and the density-of-states effective mass. In this way it was established that there are two kinds of acceptors dominant in these samples with different ionization energy and different multiplicity factor. One of these acceptors could not be identified but the other one was found to be due to aluminium.

In the Al-doped crystals, however, the concentration of the acceptors is on the average 2·5 times the concentration of Al found by chemical analysis. The qualitative consistency of the results shows that the methods employed are essentially correct but the quantitative discrepancy indicates that some corrections have still to be applied. For these the following complications could be considered.

(1) The relative contributions of the different scattering mechanisms to the total scattering change with temperature. This implies a changing Hall factor contrary to the assumed constant value.

(2) If the ionization energy of the majority centres depends on the concentration of the ionized majority centres, as is stated in Section 8, it should also decrease with increasing concentration of free charge carriers.

In calculating the effective mass of 0·59 m_0 quoted in Ref. (10) this effect was taken into account by re-analysing the Hall curves after substituting in equation (5):

$$E = E' - C(N_D + p)^{1/3} \qquad (26)$$

in which E' and N_D were the activation energy and donor concentration found from the first analysis and $C = 4e^3/\epsilon_0$. It was also supposed that the level depth depended linearly on the temperature and a term $-aT$ with $a = 3\times 10^{-5}$ eV/°K (i.e. about 1/10 of the temperature coefficient of the bandgap) was added to the r.h.s. of equation (26). These procedures appear, however, to be thermodynamically uncorrect (see e.g. Refs. 39 and 40).

(3) The presence of excited states and of different ionization energies for impurities on unequivalent lattice sites has not been accounted for.

(4) If again the valence band is split, as mentioned in Section 10, it will depend on the distance between the sub-bands whether our assumption of a single valence band, which underlies equation (5) as well as equations (3) and (4), is seriously wrong.

Application of these corrections will of course also affect the value of the density-of-states effective mass of 1·0 m_0 calculated in Section 8.

The lack of information on the structure of the valence band is also the reason why no conclusive statement can be given concerning the effective mass of the free holes. In a complicated band structure it is to be expected that evaluating the effective mass from measurements of different effects will lead to different values. An attempt will be made to obtain more information from measurements of the Seebeck coefficient and of Faraday rotation. To obtain the utmost information from Hall effect and resistivity measurements we shall try to measure these quantities in other crystallographic directions, e.g. parallel to the *c*-axis. Also measurements on the other polytypes of SiC, e.g. the cubic modification, could yield valuable material for comparison and for constructing a more definite picture.

With regard to the hole mobility, we remark that it is so low that the question may be raised whether it is still permissible to use a broad-band model and to use the equations for describing the mobility which have been derived using perturbation theory. Although we were aware of this, we hoped that in our case too the well-known fact would be true that many theories still describe the phenomena well even in cases where the theoretical limit of their applicability is somewhat exceeded.

Acknowledgements—The authors are pleased to thank Dr. D. HAMILTON of Westinghouse Research Laboratories for supplying the pure *n*-type sample labelled 1 in Fig. 23, Mr. J. VISSER for providing the wet chemical analysis and many colleagues for fruitful discussions and suggestions.

They are also indebted to Messrs. G. VERSPUI and J. G. VAN LIEROP for much appreciated assistance in the preparation of the crystals and to Mr. G. KNUVERS for reliable performance of the greater part of the measurements.

REFERENCES

1. WEIGEL O., *Göttinger Nachr., Math. Phys. Kl.* p. 299 (1915).
2. SEEMANN H. J., *Phys. Z.* **30**, 143 (1929).
3. HENNINGER F., *Ann. Phys., Paris* **28**, 245 (1937)

4. Hochberg B. M. and Sominski M. J., *Phys. Z. U.S.S.R.* **13**, 198 (1938).
5. Braun A. and Busch G., *Helv. Phys. Acta* **15**, 571 (1942).
6. Busch G., *Helv. Phys. Acta* **19**, 167 (1946).
7. Busch G. and Labhart H., *Helv. Phys. Acta* **19**, 463 (1946).
8. Lely J. A., *Ber. Dtsch. keram. Ges.* **32**, 229 (1955).
9. Lely J. A. and Kröger F. A., *Halbleiter und Phosphore*, Vorträge des internationalen Kolloquiums 1956 in Garmisch-Partenkirchen. p. 525. Vieweg, Braunschweig (1958).
10. Daal H. J. van, Greebe C. A. A. J., Knippenberg W. F. and Vink H. J., *J. appl. Phys.* **32**, 2225 (1961).
11. Pauw L. J. van der, *Philips Res. Rep.* **13**, 1 (1958).
12. Boer J. H. de and Geel W. C. van, *Physica* **2**, 186 (1935)
13. Landsberg P. T., *Proc. phys. Soc. Lond.* **A65**, 604 (1952).
14. Rose F. W. G., *Proc. phys. Soc. Lond.* **B70**, 801 (1957).
15. Mitchell E. W. J., *J. Phys. Chem. Solids* **8**, 444 (1959).
16. Debye P. P. and Conwell E. M., *Phys. Rev.* **93**, 693 (1954).
17. Pearson G. L. and Bardeen J., *Phys. Rev.* **75**, 865 (1949).
18. Hofman D., Lely J. and Volger J., *Physica* **23**, 236 (1957).
19. Pincherle L., *Proc. phys. Soc. Lond.* **A64**, 663 (1951).
20. Castellan G. W. and Seitz F., *Semiconducting Materials*, p. 8. Butterworths, London (1951).
21. Lehman G. W. and James H. M., *Phys. Rev.* **100**, 1698 (1955).
22. Barnes J. F. and Tredgold R. H., *Proc. phys. Soc. Lond.* **78**, 716 (1961).
23. Chetkarov M. L., *Sov. Phys. Tech. Phys.* **3**, 895 (1958).
24. Woodbury H. H. and Ludwig G. W., *Phys. Rev.* **124**, 1083 (1961).
25. Wieringen J. S. van, *Halbleiter und Phosphore*, Vorträge des internationalen Kolloquiums 1956 in Garmisch-Partenkirchen. p. 367. Vieweg, Braunschweig (1958).
26. Pauling L., *The Nature of the Chemical Bond.* p. 58. Cornell University Press, Ithaca (1940).
27. Lely J. A. and Kröger F. A., *Halbleiter und Phosphore* Vorträge des internationalen Kolloquiums 1956 in Garmisch-Partenkirchen. p. 514. Vieweg, Braunschweig, (1958).
28. Fröhlich H. and Mott N. F., *Proc. Roy. Soc.* **A171**, 496 (1939).
29. Meyer H. J. G. and Polder D., *Physica* **19**, 255 (1953).
30. Shockley W. and Bardeen J., *Phys. Rev.* **77**, 407 (1949).
31. Howarth D. and Sondheimer E., *Proc. Roy. Soc.* **A219**, 53 (1953).
32. Petritz R. L. and Scanlon W. W., *Phys. Rev.* **97**, 1620 (1955).
33. Tolpygo K. B., *Sov. Phys. Solid State* **2**, 2367 (1961).
34. Brooks H., *Advanc. Electron. Electron Phys.* **VII**, 157 (1955).
35. Hutson A. R., *J. appl. Phys.* **32**, 2287 (1961).
36. Piper W. W. and Halsted R. E., *Proceedings of the International Conference on Semiconductor Physics, Prague* 1960. p. 1046. Czechoslovak Academy of Sciences, Prague (1961).
37. Hoogenstraaten W. Philips Res. Rep. **13**, 515 (1958); see especially p. 654.
38. Birman J. L., *Proceedings of the Conference on Silicon Carbide, Boston, Mass.* 1959, p. 257. Pergamon Press, London (1960).
39. Harvey W. W., *Phys. Rev.* **123**, 1666 (1961).
40. Haven Y. and Santen, J. H. van, *Philips Res. Rep.* **7**, 474 (1952).

J. Phys. Chem. Solids Pergamon Press 1963. Vol. 24, pp. 129–133. Printed in Great Britain.

DIFFUSION OF THALLOUS IONS IN SINGLE CRYSTALS OF KBr*

R. ILLINGWORTH

The Institute of Optics, University of Rochester, Rochester 20, New York

(*Received* 30 *July* 1962)

Abstract—Diffusion of thallous ions in single crystals of KBr has been investigated within the temperature range 350–700°C. After heating pure KBr crystals in TlBr vapour, the distribution of Tl^+ in the crystals was found by measuring the absorption spectrum as successive layers were removed from the crystals by polishing. The activation energy for diffusion is 1·03 eV. The temperature dependence of the diffusion coefficient confirms the substitutional nature of the luminescence centre in KBr(Tl).

INTRODUCTION

THE following pages will describe measurement of the rate of diffusion of thallium in single crystals of potassium bromide as a function of temperature. In work on the luminescence of the thallium-activated alkali halide phosphors, it is usually assumed that the luminescence centre consists of a monovalent Tl^+ ion occupying a substitutional cation site. This view has been confirmed theoretically(1) and experimentally(2) for KCl(Tl). The present work was undertaken to give further confirmation of the substitutional nature of the luminescence centre in KBr(Tl). In addition, from an experimental point of view, knowledge of the diffusion coefficient as a function of temperature would be useful in connection with experiments involving the annealing and cooling of the phosphor and, under certain circumstances, might enable crystals of the phosphor to be prepared from the pure alkali halide by controlled diffusion from the vapour phase.

THEORY AND PREVIOUS WORK

If the Tl^+ ion in KBr(Tl) occupies a substitutional K^+ site, simple theory(3) shows that diffusion can only occur if the K^+ site adjacent to a particular Tl^+ site is vacant. Then the diffusion coefficient may be written

$$D = D'n_v \exp(-\phi/kT), \tag{1}$$

where D' = constant, n_v = fraction of cation sites which are unoccupied, ϕ = activation energy required to move a Tl^+ ion into a neighbouring positive ion vacancy, k = Boltzmann's constant, T = absolute temperature. In the pure crystal, n_v is equal to the concentration of Schottky defects. If the crystal contains, in addition to the Schottky defects, a small amount of some divalent cation impurity, an equal number of positive ion vacancies are required to compensate for the additional charge on the impurity. Thus equation (1) may be written

$$D = D'(n_+ + \gamma \exp(-W/2kT)) \exp(-\phi/kT), \tag{2}$$

where n_+ = mol. fraction of divalent impurities, W = energy required to create a Schottky defect at temperature T°K, γ is the constant which enters into the well-known expression for the concentration of Schottky defects.(4) Substituting $D_1 = D'\gamma$ and $D_2 = D'n_+$, equation (2) becomes

$$D = D_1 \exp(-(\tfrac{1}{2}W+\phi)/kT) + D_2 \exp(-\phi/kT). \tag{3}$$

TAMAI(4) has measured the diffusion coefficient

---

[*] Research supported by the National Aeronautics and Space Administration, Goddard Space Flight Center, under Contract NASW-107.

for Tl^+ in single crystals of KBr in the temperature region 520–700°C where the second term in equation (3) is assumed to be negligible. He finds that D is of the form $D = 47 \exp(-1{\cdot}98/kT)$ cm^2/sec where Boltzmann's constant is expressed in electron volts. Glasner *et al.*[5] using a different technique, have investigated diffusion of Tl^+ into powdered KBr, and find that, in the temperature range 140–205°C, $D = 0{\cdot}23 \exp(-1{\cdot}02/kT)$ cm^2/sec. In the present work, by means of an improved technique similar in principle to that used by Tamai,[4] measurement of the diffusion coefficient of Tl^+ in single crystals of KBr has been extended to lower temperatures where the second term on the right-hand side of equation (3) may be expected to predominate.

EXPERIMENTAL PROCEDURE

Crystals of KBr measuring about 10 × 5 × 3 mm were cut from a single ingot, grown by the writer, using the Kyropoulos technique. The diffusion treatment was carried out in a horizontal tube furnace with temperature control accurate to about ± 3°C. Each crystal was heated in a pyrex tube to a diffusion temperature in the range 350–700°C. Thallous bromide was placed in another part of the tube and held at a lower temperature to provide a convenient vapour pressure of TlBr. To avoid reaction between the thallous bromide and oxygen, the pyrex tube was flushed out with nitrogen, evacuated to forepump pressure, and sealed prior to the diffusion treatment. After heating for a time which varied from 1 hr to 2 days (depending on the rate of diffusion) and cooling quickly to room temperature, the crystals were cleaved in half and the absorption spectrum due to the Tl^+ impurity measured with a Cary Recording Spectrophotometer. The distribution of Tl^+ in the crystal was then found by polishing layers of known thickness from the surface and measuring the optical absorption spectrum after each polish. Assuming that the maximum optical density in the A band in KBr(Tl) is proportional to the number of Tl^+ ions in the crystal, the diffusion coefficient could be calculated from the dependence of the optical density on the thickness of the layer removed by polishing.

Polishing was carried out with a silk cloth, using a paste of alumina powder and alcohol. Usually, each layer measured from 2 to 3 microns in thickness. The thickness of the removed layers was measured with a simple optical comparator consisting of a fixed glass plate A with the upper surface polished to an optical flat, on one edge of which was pivoted another optical flat B. The crystal was cemented into a holder which was placed on a third optical flat C fixed in position with respect to A. One end of B rested on a steel ball, which in turn rested on the surface of the crystal. Thus there was a wedge-shaped air film between A and B, the wedge angle being determined by the height of the crystal surface above C. The initial wedge angle before polishing was measured by recording the separation of interference fringes set up between A and B with parallel monochromatic light. The crystal (cemented in its holder was removed, the absorption spectrum measured, a, layer polished from the surface, the crystal replaced in the comparator, and the new fringe separation measured. From the change in fringe separation, the change in total thickness of the crystal was calculated. This simple device gave the thickness of the layer removed by polishing accurate to better than ±0·8 microns in the range 5–50 microns.

If the dimensions of the KBr crystal are large compared with the depth of penetration of the Tl^+ ions, the impurity concentration $C(x, t)$ after heating the crystal for time t sec at some steady temperature is given by the diffusion equation

$$\frac{\partial C(x,t)}{\partial t} = D\frac{\partial^2 C(x,t)}{\partial x^2}, \tag{4}$$

where it is assumed that the diffusion coefficient D is independent of the impurity concentration, and x is the distance into the crystal measured from the surface.

With the boundary conditions

$$C(0, t) = C_0 = \text{constant}, \tag{5}$$

and

$$C(\infty, t) = 0, \tag{6}$$

the solution to (4) is

$$C(x, t) = C_0(1 - \operatorname{erf} X), \tag{7}$$

where $X = x\,.\,(4Dt)^{-1/2}$ and erf signifies Gauss's error function.

The magnitudes of C_0 and D were found from the experimental data by the following procedure. The maximum optical density in the A band due to absorption by Tl^+ ions for which $x > \delta x$ is given by

$$d_{\delta x} = K \int_{\delta x}^{\infty} C(x, t)\, dx, \tag{8}$$

where K is a constant, the value of which will be calculated below, and $d_{\delta x}$ is the optical density of a crystal when a layer of thickness δx has been removed from the surface by polishing. Substituting (7) into (8), equation (8) becomes

$$d_{\delta x} = KC_0 \int_{\delta x}^{\infty} (1-\operatorname{erf} X)\,dx. \tag{9}$$

Then, making the substitutions

$$F(\beta) = (KC_0(4Dt)^{1/2})^{-1}\, d_{\delta x} \tag{10}$$

and

$$\beta = \delta x\,.\,(4Dt)^{-1/2}, \tag{11}$$

(9) may be written in the form

$$f(\beta) = \int_{\beta}^{\infty} (1-\operatorname{erf} X)\,dX. \tag{12}$$

In practice, the function $f(\beta)$ was obtained from tables(6) and plotted against β. Then the experimental values for $d_{\delta x}$ were plotted against δx on a different sheet of paper. For convenience, logarithmic graph paper was used. Then, as shown in Fig. 2, the theoretical curve (plotted with respect to the $f(\beta)$ and β axes) was fitted to the experimental points (plotted with respect to the $d_{\delta x}$ and δx axes) by adjusting the relative positions of the two sets of axes. Since the experimental points in Fig. 2 now fitted a curve of the form of equation (12), equations (10) and (11) were valid. Then, as indicated in Fig. 2, when β and $f(\beta)$ were equal to unity, the corresponding values of δx and $d_{\delta x}$ could be read directly from the superimposed graphs and substituted into equations (10) and (11) to give the magnitudes of $KC_0(4Dt)^{1/2}$ and $(4Dt)^{1/2}$.

The constant K was evaluated in the following way. From (8) the optical density d' of a crystal of KBr(Tl) of thickness h cms in which the Tl^+ impurity concentration C' is uniform throughout the crystal is

$$d' = K\int_{0}^{h} C'\,dx = KC'h. \tag{13}$$

Using TAMAI's value(8) of 0·073 for the oscillator strength of the A band in KBr(Tl) and applying SMAKULA's formula(7) it was found that

$$K = 1{\cdot}50\times 10^{-4}\,(\text{cms})^{-1}\,(\text{mol. per cent})^{-1}.$$

RESULTS AND DISCUSSION

Figure 1 shows the ultraviolet absorption spectrum of a typical crystal of KBr which had been heated for $1{\cdot}5\times 10^5$ sec at 389°C in thallous bromide vapour and then polished. Figure 2 shows the maximum optical density of the A band, plotted against δx. The spectrum in Fig. 1 is identical to that obtained from crystals of the phosphor prepared by adding the impurity during growth from the melt,(8) except that, in addition to the A, B and C thallium bands, a very small unidentified band is present at 3000 Å. Absorption in this band, which did not occur in the undoped crystals, was uniform throughout the crystals, whereas absorption in the thallium bands was confined to regions of the crystals within 50 microns of the surface. Since the magnitude of the 3000 Å band bore no apparent relation to the quantity of thallium in the crystal, and since the absorption coefficient at 3000 Å was never greater than 0·01 cms^{-1}, its presence has been ignored.

In Fig. 2, the theoretical curve fits the experimental points for $(4Dt)^{1/2} = 5{\cdot}75\times 10^{-4}$ cms and $KC_0(4Dt)^{1/2} = 7{\cdot}6$. Thus, for this particular crystal, $D = 5{\cdot}5\times 10^{-13}\,\text{cm}^2/\text{sec}$ and $C_0 = 0{\cdot}88$ mol. per cent. Figure 3 shows the concentration profile for this crystal, calculated using these values for D and C_0.

The magnitude of C_0 in the various crystals normally lay within the limits of 0·4 mol. per cent to 1 mol. per cent. The theoretical curve $f(\beta)$ could always be fitted accurately to the experimental points, indicating that D was independent of the impurity concentration, and that boundary conditions (5) and (6) were obeyed. The accuracy of the individual measurements of D was estimated in several crystals by measuring the diffusion coefficient at the opposite faces of each crystal. The two values for D obtained in this way for each crystal, agreed to within 5 per cent.

In Fig. 4, log D is plotted against the reciprocal of the absolute temperature. The line drawn through the experimental points satisfies a relation of the form of equation (3),

$$D = 50\exp(-2{\cdot}01/kT) + 4{\cdot}1\times 10^{-5}\exp(-1{\cdot}03/kT) \tag{14}$$

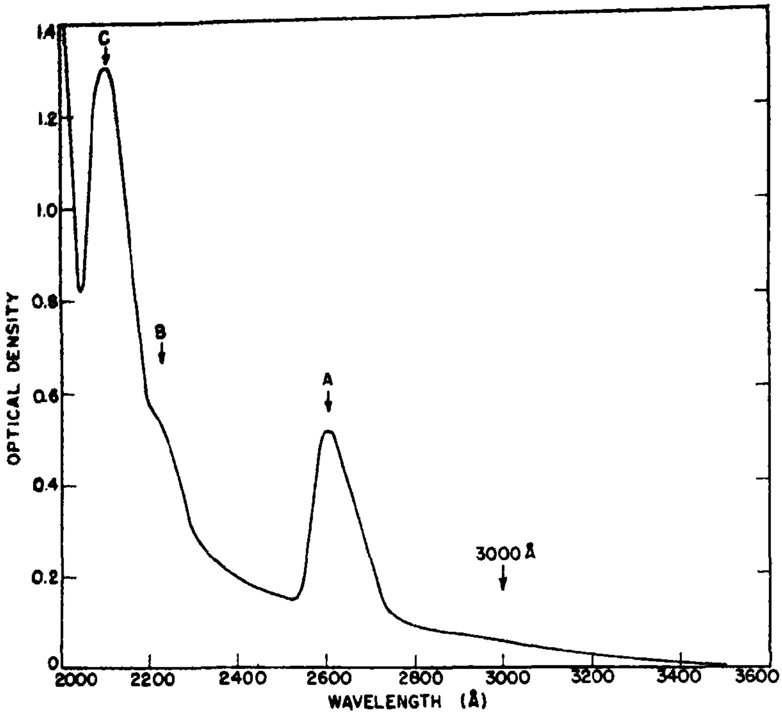

FIG. 1. Absorption spectrum of a crystal of KBr previously heated for $1{\cdot}5 \times 10^5$ sec at 389°C in TlBr vapour. A layer of thickness $6{\cdot}3 \times 10^{-4}$ cm has been removed from the surface of the crystal.

where D is expressed in cm²/sec, and k is Boltzmann's constant expressed in eV. In fitting a curve of the form of equation (3) to the experimental points, there is an uncertainty of about ± 3 per cent in the gradients of the high and low temperature regions (proportional to $(\frac{1}{2}W+\phi)$ and ϕ respectively). This relatively small uncertainty in the gradients leads to large errors of about ± 80 per cent in the values for D_1 and D_2 which are obtained by extrapolation to $1/T = 0$.

It is apparent that the experimental results confirm the simple model for the diffusion of a substitutional Tl^+ impurity. Comparison of (3) with (14) gives a value of 1·96 eV for W in the temperature range of the experiment. This value for W may be compared with the theoretical value of 1·92 eV calculated by MOTT and LITTLETON(9) for zero degrees Kelvin. In addition, from equations (2), (3), and (14), assuming(4) that γ is of the order of 50, the concentration of divalent impurities is of the order of 5×10^{-5} mol. fraction, a reasonable concentration for crystals grown from the melt without previous recrystallization.

Examination of Fig. 4 shows that the scatter of the experimental points about the solid line is considerably greater in the low-temperature region than in the high-temperature region, and, at low temperatures, is somewhat larger than expected from random errors in the measurement of the temperature and diffusion coefficient. It is thought that these deviations of the diffusion coefficient from the mean value are caused by variations in the concentration of positive ion vacancies throughout the ingot of KBr, presumably arising during growth from the melt.

The results given above are in agreement with TAMAI's data(4) in the temperature range 520–700°C, and the magnitude of the activation energy ϕ agrees well with the value obtained in the temperature range 140°C to 30°C by GLASNER *et al.*,(5) using powdered KBr instead of single crystals. Thus, for the single crystals used in the present experiment, it is probable that the diffusion coefficient may be represented by equation (14) for all temperatures at which significant diffusion occurs.

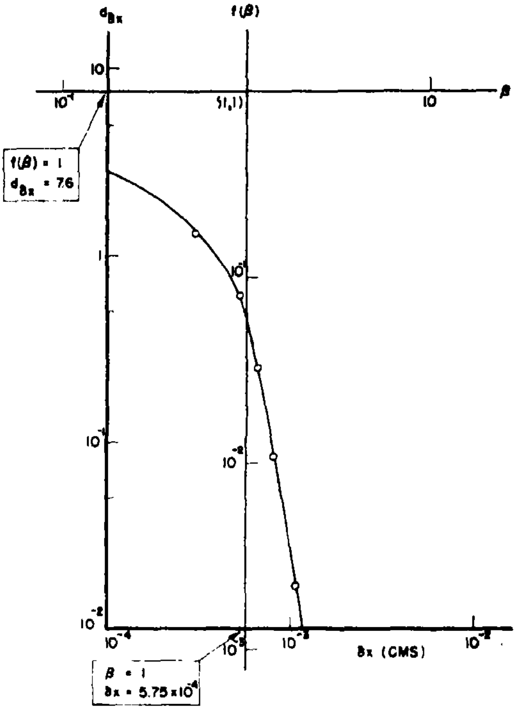

FIG. 2. The experimental values for $d_{\delta x}$ are plotted against δx. The solid line is the theoretical function $f(\beta)$ plotted against β and is fitted to the experimental points by adjusting the relative positions of the two sets of axes. Since $f(\beta) = 1$ when $d_{\delta x} = 7{\cdot}6$, and $\beta = 1$ when $\delta x = 5{\cdot}75\times10^{-4}$ cm, the values of $(4Dt)^{1/2}$ and $(KC_0(4Dt)^{1/2}$ can be found immediately from equations (10) and (11).

REFERENCES

1. BRAUER P. *Z. Naturf.* **6a**, 560 (1951); *ibid* **7a**, 372 (1952).
2. RUNCIEMAN W. A. and STEWARD E. G., *Proc. phys. Soc. Lond.* **A66**, 484 (1953).
3. MOTT N. F. and GURNEY R. W., *Electronic Processes in Ionic Crystals*, p. 30. University Press, Oxford (1957).
4. TAMAI T., *J. phys. Soc. Japan* **16**, 2459 (1961).
5. GLASNER A., REJOAN A. and REISFELD R., *J. Phys. Chem. Solids* **19**, 332 (1961).
6. cf. JOST W., *Diffusion in solids, liquids, and gases.* Academic Press, New York (1960).
7. SMAKULA A., *Z. Phys.* **59**, 603 (1930).
8. TAMAI T., *J. phys. Soc. Japan* **15**, 2116 (1960).
9. MOTT N. F. and LITTLETON M. J., *Trans. Faraday Soc.* **34**, 685 (1938).

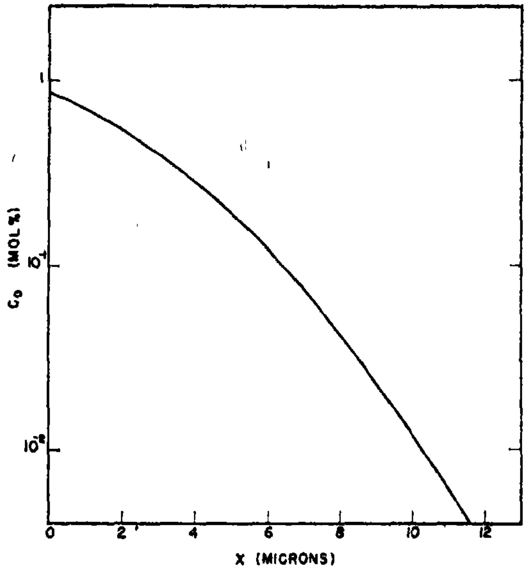

FIG. 3. Concentration profile calculated from the data given by Fig. 2. C is the Tl$^+$ concentration in mol. per cent and x is the distance into the crystal measured from the surface.

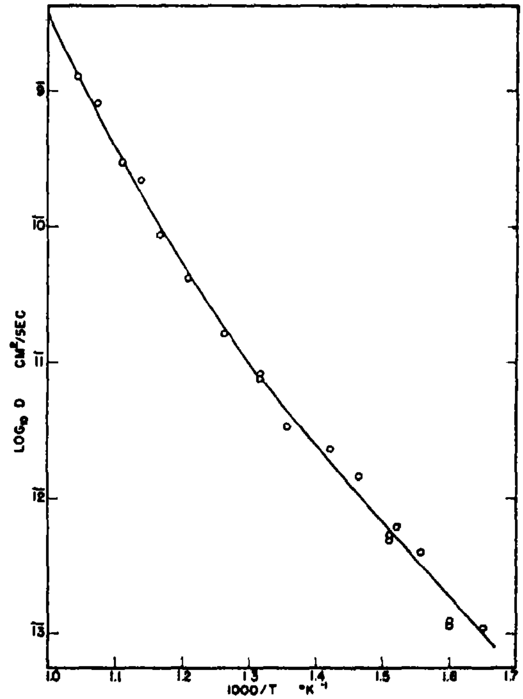

FIG. 4. Log$_{10}D$ plotted against the reciprocal of the absolute temperature.

J. Phys. Chem. Solids Pergamon Press 1963. Vol. 24, pp. 135–139. Printed in Great Britain.

SOME OPTICAL PROPERTIES OF IODINE SINGLE CRYSTALS

A. A. BRANER* and **R. CHEN**
Department of Physics, The Hebrew University of Jerusalem, Israel

(*Received* 29 *June* 1962)

Abstract—The absorption edge of iodine single crystals shifts in the direction of longer wavelengths with increasing temperature: $-8{\cdot}3 \times 10^{-4}$ eV/degree between liquid air (L.A.T.) and room temperatures (R.T.). Specular reflectivity in the region of strong absorption shows a structure similar to the photoconductivity response curve. The refractive index is about 2 as calculated from the reflectivity in the infrared. Weak thermoluminescence glow peaks in the visible were obtained after irradiation with X-rays at L.A.T. The peaks at 105°K and 172°K have thermal activation energies of about 0·11 and 0·13 eV.

INTRODUCTION

IODINE single crystals were the subject of intense research in this department during the past few years.(1, 2) These crystals, although molecular, show interesting semiconducting properties and it was found that the phenomenological behaviour of iodine is not fundamentally different from that of other covalent or ionic crystals. The results of the photoconductivity measurements(1) stimulated this study of the optical properties of iodine, as the information found in the literature is very scant.(3) Optical work with iodine involves severe experimental difficulties because of the peculiar physical and chemical properties of iodine. The present work reports the results of absorption, specular reflectivity, and thermoluminescence measurements on iodine single crystals.

EXPERIMENTAL

Single crystals were grown from the vapor phase of resublimated iodine (A.C.S. specifications), and are obtained in the form of thin (≈ 0·1 mm), lustrous plates from which larger samples of 5 × 10 mm dimensions are selected.

The absorption and thermoluminescence measurements were performed on crystals placed in a vacuum cryostat(4) where they could be cooled to L.A.T. and warmed up to higher temperatures. A Beckman DK spectrophotometer was used for absorption measurements and the thermoluminescence detection system was composed of an EMI 6256B photomultiplier, a Keithley 410 micro-microammeter, and a Brown recorder.

Reflectivity spectra were taken with a special attachment designed to fit the sample compartment of the Beckman DK spectrophotometer (Fig. 1). The "sample beam" from the monochromator is deflected by an evaporated aluminum surface mirror *a* to nearly normal incidence on the crystal *c*. The reflected beam is brought back into the optical path by mirror *b*. A similar arrangement with a freshly evaporated aluminum mirror or other reference material at *c* in the "reference beam" of the spectrophotometer is not shown in

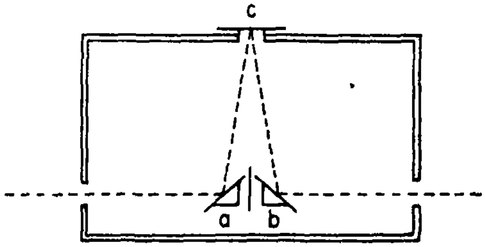

FIG. 1. Reflectance attachment diagram.

---

* Present address: The Technological Institute Department of Materials Science, Northwestern University, Evanston, Illinois.

Fig. 1. It was found more reliable, however, to compare two successive measurements of reflectance, one with the investigated crystal in the "sample beam" and the other after replacing the crystal by a reference material. The reported reflectivity spectra were calculated from such measurements. Freshly evaporated aluminum films and a polished and etched germanium crystal served as reference materials.(5, 6)

Thermoluminescence was measured in crystals after irradiation with X-rays or u.v. light at L.N.T. as described for other crystals(4,7).

RESULTS

Absorption

Iodine has a broad maximum of absorption in the ultra-violet but is transparent in the infrared.(3) The absorption of crystals was measured from the absorption edge (if we may call it so in a molecular crystal) up to 2·5 μ between L.A.T. and room temperature. An allowance was made for the reflectance. Figure 2 represents the absorption spectra at various temperatures up to 1·0 μ, as the absorption is constant at longer wavelengths. The absorption edge is shifted with increasing temperature

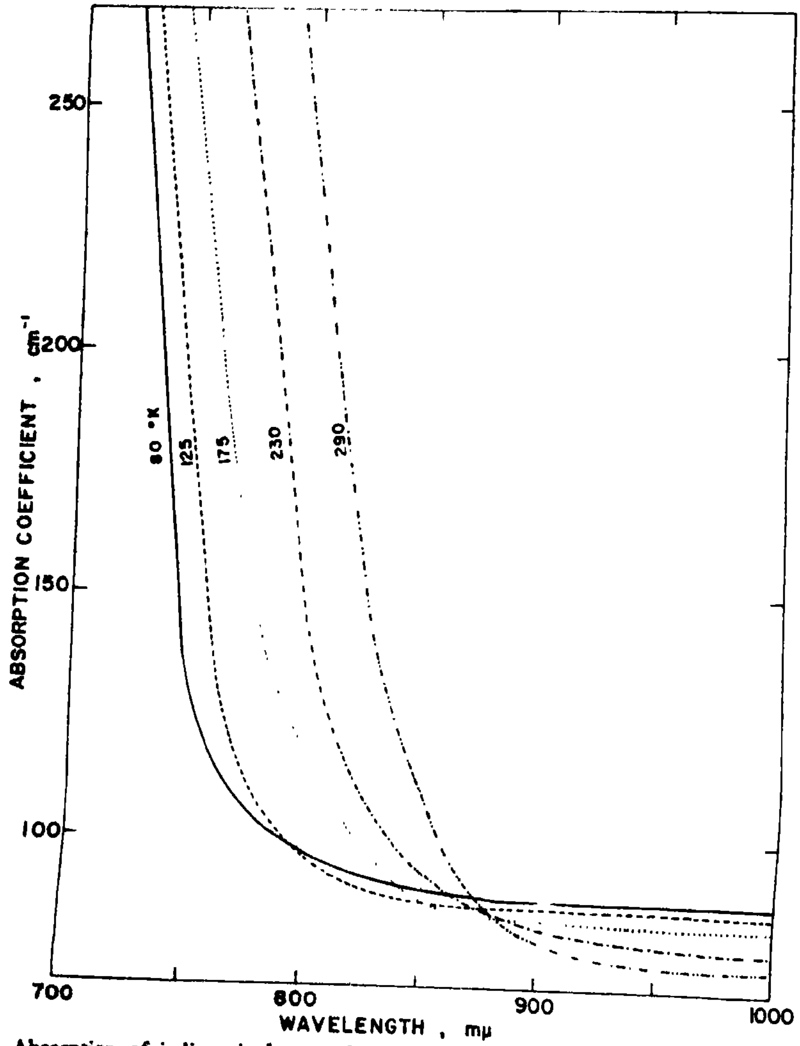

FIG. 2. Absorption of iodine single crystals near the absorption edge at various temperatures.

to longer wavelengths. This shift is illustrated by Fig. 3 for an arbitrarily chosen absorption (170 cm^{-1}). The shift parameter as derived from the straight part of Fig. 3 is $-8{\cdot}3\times10^{-4}$ eV/deg.

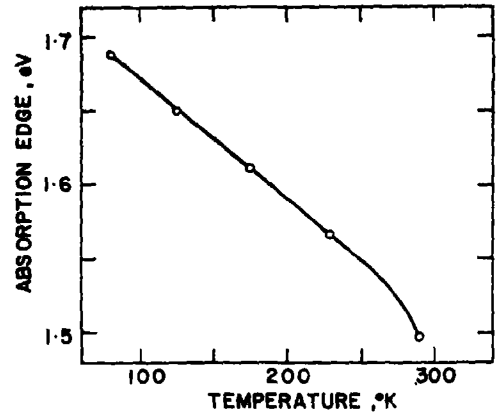

FIG. 3. Shift of the absorption edge with temperature.

Reflectivity

The spectrum of reflectivity was measured at R.T. only and the results are given in Fig. 4. After a steep rise between 220 and 300 mμ there are two maxima in the region of strong absorption at 320 and 460 mμ and a lower maximum near the absorption edge at 900 mμ. Between 1·0 μ and 2·6 μ the reflectivity was constant at 11 per cent. No correction was made for the reflection from the back surface of the crystal as this is not expected to influence the result appreciably and in addition the back surface was generally not parallel to the front one.

In the transmitting region we can obtain the refractive index from reflectance data by using the expression $n = (1+R^{1/2})/(1-R^{1/2}) \approx 2$.

The relative spectral photosensitivity as obtained by MANY *et al.*(1) was replotted in Fig. 4 for purposes of comparison.

Thermoluminescence

The thermoluminescence glow curve, as given in Fig. 5a, was obtained after irradiation of the crystal at L.A.T. with X-rays (35 kVp, 14 mA, Cu-target) for 20 min in the dark. The heating rate was kept constant at 10°/min. The glow was detected with a blue sensitive photomultiplier and was found to be extremely weak; no thermoluminescence was detectable with a red-sensitive photomultiplier. The spectral composition of the glow can be estimated by the use of Wratten Light Filters. The glow measured through Filter No. 4 ($\lambda > 460$ mμ) is given by curve *b* and that through Filter No. 23A ($\lambda > 570$ mμ) by curve *c*. Filter No. 0 ($\lambda > 300$ mμ) transmits most of the glow.

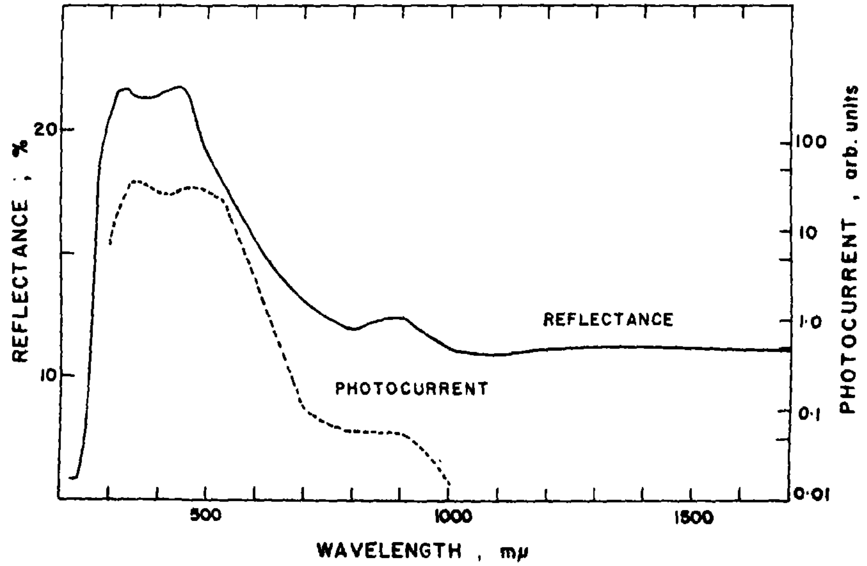

FIG. 4. Specular reflectivity spectrum (solid curve) and relative spectral photosensitivity (dashed curve) in iodine at room temperature.

Comparing the three curves we conclude that the thermoluminescence is composed of one or two spectral bands centered at about 500 mμ.

The rise in the glow curve near R.T. continued up to 320°K when the measurement was discontinued because of the sublimation of the crystal. A very weak thermoluminescence peak was also detected at about 110°K after the irradiation of the crystal with ultra-violet light from a high-pressure mercury vapor lamp.

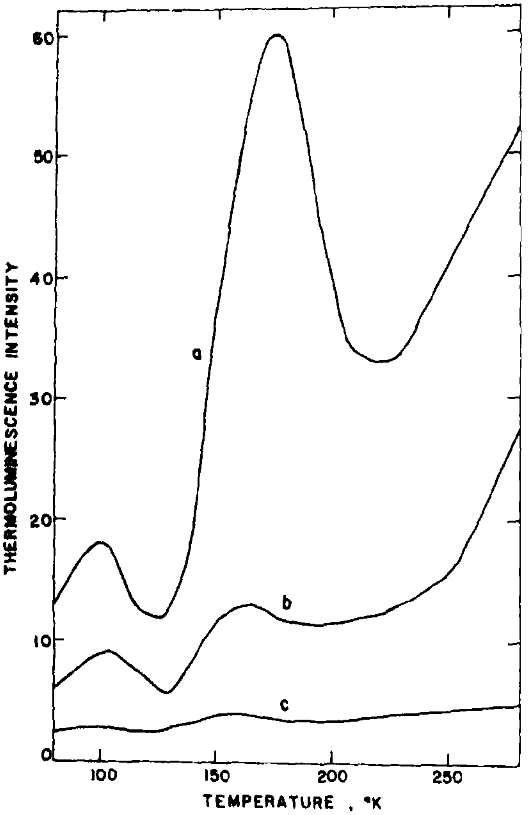

Fig. 5. Thermoluminescence glow curve of an iodine single crystal excited by 20 min of X-irradiation (Cu target, 35 kVp, 14 mA) at liquid air temperature,

a—without filter,

b—transmitted by a Wratten Light Filter No. 4 ($\lambda > 460$ mμ),

c—transmitted by a Wratten Filter No. 23A ($\lambda > 570$ mμ).

No color centers were observed by absorption measurements between the absorption edge and 2·6 μ after X-irradiation at L.A.T.

The thermal activation energies for the two major glow peaks at 105°K and 172°K were evaluated[8] to be about 0·11 and 0·13 eV.

DISCUSSION OF RESULTS

The equipment used in the absorption measurements was insufficient for the study of the detailed structure of the region of high absorption. Both the reflectivity and photoresponse curves (Fig. 4) indicate that structure should be expected.

The shift of the absorption edge as given in Fig. 3 is similar to curves obtained for other semiconducting materials. The shift of $-8{\cdot}0 \times 10^{-4}$ eV/deg differs from the result quoted by Moss[3] -15×10^{-4} eV/deg. The latter result was obtained from different measurements by various investigators, so that the results presented here are expected to be more reliable.

The curves of reflectivity and spectral photoresponse in Fig. 4 are strikingly similar. It seems worthwhile to investigate the interrelation of these curves and to check whether the small apparent shift in the position of the two corresponding maxima is due to experimental error or has a physical meaning. The small increase in reflectivity at 850 mμ and the similar behavior of the photocurrent cannot be related only to the penetration of the light beam near the absorption edge into the bulk of the crystal and to the reflectance from its back surface.

In the studies of photoconductivity$^{(1, 2)}$ hole traps were found lying 0·4–0·5 eV above the valence band edge. The shallow traps responsible for the glow peaks in Fig. 5 have an even smaller thermal activation energy and probably differ from those investigated in photoconductivity.

Acknowledgements—The authors wish to thank Professor A. Many and Dr. M. Simhony for stimulating advice and helpful discussions. We are also indebted to Dr. Y. Brada for the use of the reflectance attachment.

REFERENCES

1. Many A., Simhony M., Weisz S. Z. and Levinson J. *J. Phys. Chem. Solids* **22**, 285 (1961).
2. Many A., Weisz S. Z. and Simhony M., *Phys. Rev.* **126**, 1989 (1962).
3. Moss T. S., *Photoconductivity in the Elements*, Butterworths, London (1952), references therein and West D. C., *Canad. J. Phys.* **31**, 691 (1953).
4. Braner, A. A. and Halperin A., *Phys. Rev.* **108**, 932 (1957).
5. Hass G., *J. opt. Soc. Amer.* **45**, 945 (1955).
6. Philip H. R. and Taft E. A., *Phys. Rev.* **113**, 1002 (1959).
7. Halperin A., Braner A. A. and Alexander E., *Phys. Rev.* **108**, 928 (1957).
8. Halperin A. and Braner A. A., *Phys. Rev.* **117**, 408 (1960); Halperin A., Braner A. A., Ben-Zvi A. and Kristianpoller N., *Phys. Rev.* **117**, 416 (1960).

J. Phys. Chem. Solids Pergamon Press 1963. Vol. 24, pp. 141–149. Printed in Great Britain.

THE CRYSTAL STRUCTURE AND LUMINESCENCE OF γ-ZINC ORTHOPHOSPHATE

C. CALVO

Radio Corporation of America Laboratory, Princeton, New Jersey

and

McMaster University, Hamilton, Ontario

(*Received* 17 *May*, 1962; *revised* 18 *July* 1962)

Abstract—γ-$Zn_3(PO_4)_2$ crystallizes in the monoclinic space group P^2_1/c with the lattice parameters: $a = 5{\cdot}074 \pm 0{\cdot}008$ Å, $b = 8{\cdot}469 \pm 0{\cdot}01$ Å, $c = 8{\cdot}766 \pm 0{\cdot}015$ Å, and $\beta = 120°51' \pm 10'$. One-third of the cations lie on centers of symmetry and are coordinated octahedrally, while the remaining cations are tetrahedrally coordinated in general positions. The γ-phase is stabilized by the addition of divalent cations with a strong preference for the octahedral-cation site of this structure. This research supports the empirical generalization that the emission wavelength increase as the coordination number of Mn^{2+} increases.

INTRODUCTION

IT IS WELL known that Mn^{2+}, when incorporated into a large variety of solid environments, can be induced to luminesce. The characteristics of this emission have been extensively studied and found to depend upon the host lattice, the Mn^{2+} concentration, the temperature, the quality and quantity of other impurities and some other preparation variables. Considerable interest has arisen in the past regarding the effects of the structural characteristics of the host lattice on the emission wavelengths. LINWOOD and WEYL(1) concluded that in glasses the relationship was simply one between the coordination number of the Mn^{2+} and the emission color. The green emission was attributed to Mn^{2+} in tetrahedral coordination and the red emission to Mn^{2+} in octahedral coordination. SCHULMAN(2) extended these thoughts to crystalline solid systems, such as Zn_2SiO_4, $(Zn, Be)_2SiO_4$ and Mg_2SiO_4, by assuming various patterns of lattice substitution which were restricted primarily by considerations of ionic radius ratios and electrical change compensation. For example, the green emission of $(Zn, Be)_2SiO_4$:Mn was attributed to Mn^{2+} substituted directly for the cation in a tetrahedral site whereas the red emission is attributed to interstitial Mn^{2+} with an equivalent amount of Zn^{2+} or Be^{2+} replacing Si^{4+}. This latter substitution scheme is invoked to provide the necessary charge compensation. KROEGER and ZALM(3) have indicated that the concentration dependence of the ratio of the intensity of the red to green band in Zn_2SiO_4 is not properly predicted by this theory. They suggested that the appearance of the red band is due to a clustering of Mn^{2+} as near neighbors to a given tetrahedrally coordinated Mn^{2+}.

An obvious difficulty arises because of one's ignorance of the site that Mn^{2+} assumes upon substitution in the lattice. In some cases such as Mg_2SiO_4 it is quite clear that Mn^{2+} substitutes directly for the Mg^{2+} since Mg_2SiO_4 and Mn_2SiO_4 are isomorphic. In most cases this isomorphism either does not exist or has not been proven. Additionally, from a chemical standpoint, the assumption of divalent cations replacing Si^{4+} in SiO_4 group seems unreasonable as attested to by the stability of silicate structure in nature. Lastly, the electrical potential at an interstitial site, computed on an ionic model, is in general too small to stabilize Mn^{2+} in preference to Mn^0.

A theoretical framework exists within which one can discuss the correlation between the crystal environment and the emission wavelength. The electronic states of transition-metal ions in crystalline solids have been amenable to attack by ligand field methods[4] which, in one approximation, considers the electric field due to the near neighbor ions as a perturbation on the free ion states. If we make the reasonable assumption that the electric field strength increases as the coordination number increases, we would expect the absorption energy of Mn^{2+} for the $^6S \rightarrow {}^4G$ transition to decrease as the coordination number increases. This follows from the fact that the energy difference between the two states has a negative slope with increasing electric field. In general a sufficient time elapses between the absorption and the emission to permit the nuclei to redistribute in presence of the excited state. The relaxed excited state is at a considerably lower energy relative to the ground state, so that the absorption wavelength is much smaller than the emission wavelength. If the parameters describing the energy surfaces of the ground and excited states are comparable for Mn^{2+} as an impurity in the tetrahedral and octahedral sites then the correlation which exists between the coordination number and the absorption energy should also hold for the emission process. It is not at all clear that the two cases are sufficiently identical. They differ not only in the distribution of bonding orbitals which effects the polarizability but also in the number of near neighbors which through repulsive energy terms must balance at equilibrium, the electrical forces introduced by the added Mn^{2+}.

In lieu of a detailed theoretical study of the relaxed electronic levels of Mn^{2+} in crystalline environments we must seek an empirical correlation between the knowledge of the Mn^{2+} site and the emission color. In this regard the $ZnO:P_2O_5$ system seems ripe for study. Three orthophosphate, two pyrophosphate and two metaphosphate phases have been reported.[5,6,7] Each compound has a high and low temperature form and the third orthophosphate phase (γ) occurs only upon the addition of five or more mole per cent of Mg^{2+}, Mn^{2+} or Ca^{2+}. In this latter phase Mn^{2+} must substitute directly into some of the Zn^{2+} sites since the γ-phase is a solid solution of $Zn_3(PO_4)_2$ and $Mn_3(PO_4)_2$ within a defined range of compositions and temperatures. The site of Mn^{2+} in the high temperature form of $Zn_2P_2O_7$ is also determined because an isomorphism exists between β-$Zn_2P_2O_7$ and $Mn_2P_2O_7$.[8]

The luminescence of Mn^{2+} under cathode-ray bombardment in these orthophosphates changes from green in α-phase (low temperature form) to primarily red in the γ-phase, to entirely red in the β-phase (high temperature form). The α-phase of zinc metaphosphate emits red while the β-phase (high temperature form) emits green. Mn^{2+} in both forms of $Zn_2P_2O_7$ emits in the red portion of the spectrum. Thus without making any chemical substitution but by varying the ratio of the substituents and the temperature we generate a wide range of behavior that we can attempt to correlate with the cation environment.

In this paper we will study the crystallography of the γ-$Zn_3(PO_4)_2$ phase and indicate its influence upon the Mn^{2+} luminescence. We will show that Mg^{2+}, and by implication Mn^{2+}, preferentially dissolves in the centrosymmetric cation site and indicate the order of magnitude of this site preference.

EXPERIMENTAL

Crystals of γ-$Zn_3(PO_4)_2$ were grown in a sealed quartz tube with molten $ZnCl_2$ as the solvent. A 7 to 1 molar ratio of $Zn_3(PO_4)_2$ to $Mn_3(PO_4)_2$ was mixed in a 10-fold excess of $ZnCl_2$. The sealed quartz tube containing this mix was heated to 900°C and then slowly cooled to room temperature γ-$Zn_3(PO_4)_2$ crystals were recovered from the slurry of hydrated $ZnCl_2$ formed when excess water was added. These crystals were small but with extremely well developed faces. Morphological studies indicated that the crystals belonged to the point group $2/m$ with a β angle near 120°. The lattice parameters reported here were obtained from films calibrated by superimposing NaCl lines upon oscillation photographs of γ-$Zn_3(PO_4)_2$. These parameters are

$$a = 5{\cdot}074 \pm 0{\cdot}008\ \text{Å}$$
$$b = 8{\cdot}469 \pm 0{\cdot}01$$
$$c = 8{\cdot}766 \pm 0{\cdot}015$$
$$\beta = 120°51' \pm 10'$$
$$\text{volume} = 323{\cdot}1\ \text{Å}^3.$$

These parameters are expected to be sensitive to the exact Mn to Zn ratio, and since this ratio is not known for the crystals studied the system is not completely defined.

A consideration of the systematic extinctions resulted in assigning this crystal to the space group P^{2}_{1}/c. The number of molecules per unit cell was determined by comparing the volume of the α-phase with that of the γ-phase. Since the former was found to have four molecules per 666·1 Å^3(9) it is reasonable to assume that the latter will have two molecules per unit cell. Since the general position is a four-fold one in this space group, at least one-third of the six cations must be located in the special positions. At least two Zn^{2+} per unit cell are located in centered positions; thus this structure differs from α-$Zn_3(PO_4)_2$ where all the cations are tetrahedrally coordinated.

The intensities of reflections recorded with both Cu and MoK$_\alpha$ radiations diffracted from three different crystals were visually estimated and corrected for Lorentz and polarization effects but not for absorption. The data consisted of the *hk*O, *h*O*l*, O*kl* and *hkh̄* type reflections within the range of the Weissenberg technique with CuK$_\alpha$ radiation and the precession technique with MoK$_\alpha$ radiation. Only the *hk*O and O*kl* reflections were recorded with both types of radiation. The overall agreement between the data taken by the use of both Mo and Cu radiations was seven per cent (comparing F_H's). However, some serious disagreements did occur among the strong reflections when the data obtained with Mo radiation diffracted from the smallest crystal were compared to data obtained with Cu radiation diffracted from the largest crystal. The former crystal measured about 0·08 × 0·08 × 0·16 mm while the latter measured approximately 0·3 × 0·3 × 0·5 mm. It should be remarked that the anomalous dispersion of Zn^{2+} for CuK$_\alpha$ radiation was accounted for in this comparison.

Approximate Zn and P parameters were determined from Patterson functions projected on the $x = 0$ and $y = 0$ planes. The patterns were readily interpreted for the position of these atoms since a strong scatterer was located at the origin. From these trial positions the signs of the larger structure factors were computed and these signs used in preparing electron density projections on the x, z and x, y planes. Three out of the four oxygen atoms in the asymmetric zone resolved readily in the x, z projection while overlap with the phosphorus atom prevented the resolution of the last oxygen atom. The overlap in the x, y projection was more serious. It prevented the early resolution of the y parameters of three of the four oxygen atoms. However these y parameters were estimated from the atom positions already determined by assuming a tetrahedral distribution of the four oxygen atoms about the phosphorus atom with a P–O bond length of about 1·5 Å. Continued refinement by the use of difference Fourier techniques led to the parameters shown in Table 1.

In the final stages of refinement a disparity was noted between the values of the scale constants of those reflections to which the special positions made no contribution ($k+l$ = odd) and the value of the scale constant for all other reflections ($k+l$ = even). This disparity was attributed to the fact that a significant fraction of the special site ions were Mn^{2+} rather than Zn^{2+}. The disparity in scale constants was removed by assuming that twenty per cent of the total number of special site cations were Mn^{2+}. This amount of Mn^{2+} corresponds to an overall 6·7 mole per cent and exceeds but is near the minimum amount of Mn^{2+} found

Table 1. *Atomic parameters and standard deviations*

	x	y	z	(x)(Å)	(y)(Å)	(z)(Å)
Zn^{2+}, Mn^{2+} (I)	0·000	0·000	0·000			
Zn^{2+} (II)	0·037	0·365	0·118	0·001	0·0005	0·001
P	0·333	0·690	0·306	0·007	0·007	0·001
O(I)	0·256	0·638	0·451	0·050	0·012	0·042
O(II)	0·694	0·700	0·400	0·050	0·036	0·040
O(III)	0·254	0·589	0·136	0·034	0·014	0·103
O(IV)	0·170	0·850	0·238	0·030	0·013	0·021

necessary to stabilize the γ-phase.[7] Further evidence for this non-homogenous distribution of Mn^{2+} among the cation sites is discussed below.

Table 2. Reliability indices

zone	R	number of reflections	R_{k+l-2n}	$R_{k+l-2n+1}$
$hk0$	0·10	50	0·08	0·15
$0kl$	0·12	82	0·10	0·13
$h0l$	0·10	47	0·13	
$hk\bar{h}$	0·17	54	0·17	0·17

The final values of the reliability indices are found in Table 2. These values are separated by zone designation and according to the criterion $k+l$ = odd or even. Since reflections of the former type contain no contribution from the special site, their reliability might be a more adequate indication of the strength of the proposed structure. The overall reliability index for all the data stands at 0·13. The observed and calculated structure factors are compared in Table 3.

In Fig. 1 the structure is seen projected on to the x, z plane and in Fig. 2 projected perpendicular to the y, z plane. The cation at the origin, designated by Zn_I, shares one oxygen atom with each of the

Table 3. Observed and calculated structure factors

hkl	$\|F_0\|$	F_c	hkl	$\|F_0\|$	F_c	hkl	$\|F_0\|$	F_c
020	20·0	−21·4	110	54·7	52·3	40$\bar{2}$	79·0	82·5
040	80·1	−81·9	130	23·9	23·6	50$\bar{2}$	100·1	104·2
060	96·8	89·5	150	9·0	−16·1	60$\bar{2}$	38·8	37·1
080	48·1	52·8	170	14·9	17·6	004	41·7	48·4
0·10·0	16·0	13·1	190	−27·9	−23·8	104	40·1	−51·0
100	121·7	122·0	210	−30·5	−39·2	204	< 8·7	5·8
120	47·9	46·0	230	8·6	−12·5	304	36·5	42·5
140	52·6	49·0	250	34·4	29·7	404	33·1	52·0
160	52·6	52·2	270	11·2	−5·3	10$\bar{4}$	33·0	18·6
180	80·2	96·0	290	10·6	1·3	20$\bar{4}$	63·2	65·2
1·10·0	32·7	−23·5	310	57·1	−50·6	30$\bar{4}$	< 8·9	−21·2
200	37·1	36·7	330	52·0	−51·3	40$\bar{4}$	32·9	19·1
220	48·7	52·7	350	38·7	46·4	50$\bar{4}$	< 8·7	1·0
240	8·6	−5·2	370	21·5	24·5	604	48·4	36·5
260	39·9	39·2	390	34·5	−40·1	006	19·8	11·1
280	86·9	84·7	410	31·5	−31·4	106	62·9	64·0
2·10·0	−16·6	15·7	430	40·5	−35·7	206	< 8·9	−11·8
300	115·2	−123·5	450	36·6	42·4	306	21·2	18·8
320	17·8	1·2	470	26·0	−27·1	10$\bar{6}$	62·4	−64·2
340	8·6	4·8	510	57·1	56·6	20$\bar{6}$	29·0	30·6
360	61·4	55·6	530	14·5	−8·3	30$\bar{6}$	8·9	24·2
380	17·8	25·8	002	20·9	21·5	40$\bar{6}$	74·1	−76·6
400	62·3	69·5	102	21·3	25·4	50$\bar{6}$	20·0	−36·8
420	36·0	35·0	202	< 8·7	2·4	008	58·4	59·4
440	8·6	−12·4	302	21·4	−15·9	108	81·4	96·8
460	27·8	−20·3	402	24·1	13·5	208	93·5	94·1
500	26·0	26·0	10$\bar{2}$	90·5	106·3	10$\bar{8}$	73·8	76·6
520	32·7	36·0	202	116·0	126·2	20$\bar{8}$	23·6	37·2
540	5·0	−1·3	30$\bar{2}$	116·5	114·2	30$\bar{8}$	65·8	65·3
408	38·9	42·7	062	24·9	17·2	043	21·8	−11·9
00·10	53·6	58·8	064	26·3	25·9	045	15·0	10·1
10·10	78·2	61·7	066	21·2	14·5	047	43·2	33·8
10·$\overline{10}$	106·2	98·9	068	19·5	18·9	049	37·5	−39·0
20·$\overline{10}$	58·5	60·1	071	15·5	−6·9	052	93·0	90·0
30·$\overline{10}$	43·9	50·1	073	78·2	71·8	054	14·9	14·7

Table 3.—continued

hkl	$\|F_0\|$	F_c	*hkl*	$\|F_0\|$	F_c	*hkl*	$\|F_0\|$	F_c
011	17·5	16·3	075	60·5	59·2	056	43·4	−43·8
013	88·7	88·5	077	< 14·6	1·8	058	7·7	−6·2
015	91·2	90·9	082	55·4	50·4	061	83·1	81·4
017	11·4	−12·9	084	14·0	−14·0	063	34·2	−34·8
019	8·1	8·5	086	< 16·0	−0·1	065	46·0	36·0
022	66·4	67·0	091	30·6	11·7	067	42·9	42·4
024	37·1	41·6	093	34·6	35·9	072	< 15·5	−6·0
026	33·6	35·1	095	18·8	19·7	074	34·2	25·8
028	32·8	34·1	0·10·2	16·2	20·3	076	24·7	25·7
031	56·7	59·0	012	109·9	131·0	081	45·2	41·0
033	30·4	23·0	014	11·2	−8·5	083	24·3	16·0
035	40·5	−33·6	016	18·2	22·2	085	19·0	−18·9
037	67·5	73·5	018	23·3	23·2	092	37·9	−39·9
039	47·9	49·6	021	30·5	32·7	094	37·7	34·6
042	35·9	34·9	023	27·0	30·7	0·10·1	38·0	42·8
044	87·5	94·6	025	25·1	−28·1	0·10·3	23·2	23·8
046	41·8	46·6	027	78·2	−73·5	$11\bar{1}$	46·0	−32·3
048	21·6	25·3	029	35·2	33·6	$13\bar{1}$	113·1	134·7
051	84·3	92·1	032	12·4	−15·7	$15\bar{1}$	47·8	59·9
053	36·9	−28·5	034	32·8	−29·8	$17\bar{1}$	< 8·6	1·4
055	29·0	17·1	036	36·6	29·5	$19\bar{1}$	28·1	17·5
057	33·2	24·3	041	13·6	10·1	$22\bar{2}$	32·6	32·7
$24\bar{2}$	17·4	−2·0	$21\bar{2}$	49·2	47·7			
$26\bar{2}$	57·8	61·6	$23\bar{2}$	38·2	47·6			
$28\bar{2}$	29·9	28·8	$25\bar{2}$	36·1	−35·4			
$2{\cdot}10{\cdot}\bar{2}$	19·3	19·0	$27\bar{2}$	13·7	−20·7			
$31\bar{3}$	22·5	45·5	$29\bar{2}$	20·3	20·1			
$33\bar{3}$	57·8	57·2	$32\bar{3}$	101·6	−110·3			
$35\bar{3}$	8·6	−11·0	$34\bar{3}$	31·3	25·7			
$37\bar{3}$	54·7	52·7	$36\bar{3}$	51·0	65·1			
$39\bar{3}$	26·8	30·6	$38\bar{3}$	35·0	−28·2			
$42\bar{4}$	31·1	15·2	$3{\cdot}10{\cdot}\bar{3}$	26·8	−30·8			
$44\bar{4}$	19·9	12·2	$41\bar{4}$	70·3	72·1			
$46\bar{4}$	54·9	68·6	$43\bar{4}$	35·2	25·7			
$48\bar{4}$	29·7	38·2	$45\bar{4}$	61·7	−50·7			
$4{\cdot}10{\cdot}\bar{4}$	19·4	−15·8	$47\bar{4}$	< 8·6	0·7			
$12\bar{1}$	62·5	−70·0	$53\bar{5}$	72·9	50·6			
$14\bar{1}$	36·3	22·1	$54\bar{5}$	34·4	−29·6			
$16\bar{1}$	8·6	11·9	$61\bar{6}$	26·2	11·6			
$18\bar{1}$	< 8·0	−0·3	$63\bar{6}$	< 8·6	−12·0			
$1{\cdot}10{\cdot}\bar{1}$	8·4	−9·3						

six neighboring phosphorus atoms. These oxygen atoms occupy a distorted octahedron about the origin. The cation in the general position, designated $\mathrm{Zn_{II}}$, has a distorted tetrahedral environment of oxygen atoms. The oxygen atoms labelled II and IV are shared between a $\mathrm{Zn_{I}}$ and a $\mathrm{Zn_{II}}$, while $\mathrm{O_{I}}$ is bonded only to $\mathrm{Zn_{I}}$, and $\mathrm{O_{III}}$ is shared between two $\mathrm{Zn_{II}}$ atoms but not with $\mathrm{Zn_{I}}$. The average $\mathrm{Zn_{I}}$–O bond distance is 2·10 ± 0·10 Å while the average $\mathrm{Zn_{II}}$–O bond distance is 2·04 ± 0·06 Å. The individual values for the bond distances are listed in Table 4. The distance between $\mathrm{O_{I}}$ and $\mathrm{Zn_{I}}$ is particularly small ($\mathrm{Zn_{I}}$–$\mathrm{O_{I}}$ = 1·95 Å) and the distances of the $\mathrm{Zn_{II}}$ to the pair of $\mathrm{O_{III}}$ atoms are surprisingly dissymmetric. These values together with the large $\mathrm{O_{I}}$–$\mathrm{O_{III}}$ distance in the P–$\mathrm{O_4}$ group seems to be indicative of small errors in *x* parameters of the

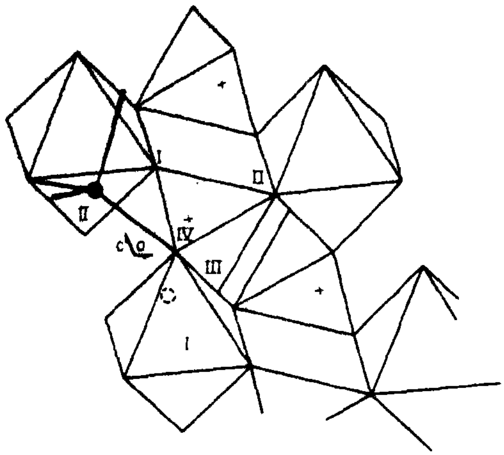

FIG. 1. The γ-$Zn_3(PO_4)_2$ structure is projected onto the $y = 0$ plane. Zn_I is located at the center of the octahedron while Zn_{II} is represented by the circles. The phosphorus position, enclosed within the tetrahedron; is represented by a cross. The oxygen atoms are labelled I through IV.

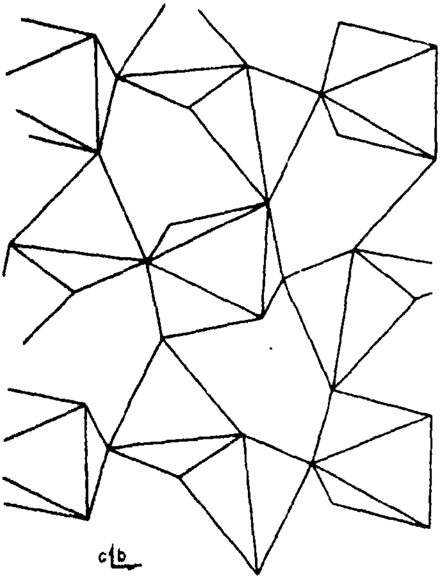

FIG. 2. The cation coordination about the b–c plane is shown. Zn_I is located at the center of the octahedron while Zn_{II} lies in the center of each of the tetrahedron shown. The oxygen atoms lie at the corners of each of the polyhedron shown.

Table 4. Bond distances

A.	PO_4 group			
	P–O_I	1·57 Å	O_I–O_{II}	2·52 Å
	P–O_{II}	1·58	O_I–O_{III}	2·79
	P–O_{III}	1·58	O_I–O_{IV}	2·48
	P–O_{IV}	1·54	O_{II}–O_{III}	2·42
			O_{II}–O_{IV}	2·61
			O_{III}–O_{IV}	2·52
B.	Zn_6–O_0 group			
	Zn_I–O_{IV}	2·20 Å		
	Zn_I–O_{II}	2·16		
	Zn_I–O_I	1·95		
C.	Zn_{II}–O_4 group			
	Zn_{II}–O_{II}	2·00 Å		
	Zn_{II}–O_{IV}	2·02		
	Zn_{II}–O_{III}	2·16		
	Zn_{II}–O_{III}	1·98		

oxygen atoms involved. Efforts to refine the structure such that it would appear more esthetic were unsuccessful.

The PO_4 group is found to exist as an independent irregular tetrahedron. The average P–O bond distance is $1{\cdot}568 \pm 0{\cdot}015$ Å while the average oxygen-oxygen atom distance around the tetrahedron is $2{\cdot}56 \pm 0{\cdot}10$ Å. Both these values are about one per cent higher than the values found for similar distances on extensively refined orthophosphate structures.

UPPER PHASE BOUNDARY

The non-equivalence of the cation sites in γ-$Zn_3(PO_4)_2$, one-third six-fold coordinated and two-thirds four-fold coordinated, suggests that a generalized representation for this phase should be $A_2B(PO_4)_2$. A limited amount of evidence supports this implied solubility difference of the divalent cations in the two types of sites. Hummel and Katnack found that the γ-phase was unstable for Mn^{2+} additions above 25 mole per cent and suggested that this might be due either to oxidation of Mn^{2+} or a phase boundary. The present crystal structure would suggest a phase boundary could exist near thirty-three per cent Mn^{2+} corresponding to a saturation of the special cation site with Mn^{2+}.

Of course this phase limit will vary somewhat with temperature due to the entropy difference between the γ-phase and the phase beyond the upper limit.

In contrast SARVER, KATNACK and HUMMEL[10] found that Mg^{2+} could completely replace Zn^{2+} while maintaining the γ structure in the temperature range around 900°C and, as with Mn^{2+}, a minimum of around 5 mole per cent Mg^{2+} in $Zn_3(PO_4)_2$ is needed to stabilize the γ-phase with respect to the α-phase. The major difference between α and γ structures is the change of the special site cations from tetrahedral to octahedral coordination. Thus these γ-phases appear to be stabilized by the great preference of "impurity" cations for an octahedral site and its disappearance at high "impurity" concentrations by the relative dislike for the tetrahedral site. It then appears that Zn ions in these orthophosphate systems greatly prefer the tetrahedral coordination relative to octahedral coordination while the inverse appears true of Mn^{2+}. Since the γ-phase remains stable beyond the thirty-three per cent limit for the

$$(Zn, Mg)_3(PO_4)_2$$

system, Mg^{2+} seems to be an intermediate case.

Although a direct measurement of this preferred Mn^{2+} distribution into the higher coordinated sites is difficult by direct X-ray means due to the small difference in scattering power between Zn^{2+} and Mn^{2+}, such is not the case for Mg^{2+} in γ-$Zn_3(PO_4)_2$. If a sufficiently non-random distribution can be shown to exist for $(Zn, Mg)_3(PO_4)_2$ by X-ray means then by implication such an ordering also exists in $(Zn, Mn)_3(PO_4)_2$. Conveniently SARVER, KATNACK and HUMMEL have recorded powder data for the

$$Mg_3(PO_4)_2\text{–}Zn_3(PO_4)_2$$

solid solution system prepared in a temperature range near 900°C. This data has been analyzed for an indication of a preferred Mg^{2+} distribution in the octahedral site. First the data reported here was compared with that reported by SARVER *et al.* for $(Zn_{2\cdot95}Mn_{0\cdot05})(PO_4)_2$. The first seventeen powder lines were indexed and corrected for Lorentz, polarization and multiplicity effects. These data showed an average deviation of nine per cent (based on F_H's) when compared with present data. Next a sample of $Mg_3(PO_4)_2$ was prepared and a diffractometer trace recorded. This confirmed the reported homomorphism[11] of the γ-$Zn_3(PO_4)_2$ solid solution with $Mg_3(PO_4)_2$ and yielded the following lattice parameters.

$$a = 5{\cdot}07\ \text{Å}$$
$$b = 8{\cdot}31$$
$$c = 8{\cdot}80$$
$$\beta = 120{\cdot}7°$$

The first eight powder lines intensities reported by Sarver *et al.* on six $Zn_3(PO_4)_2$–$Mg_3(PO_4)_2$ compositions were indexed, corrected and converted to structure factors. Structure factors were calculated based upon two extreme assumptions, i.e. a completely random distribution of Mg^{2+} and an infinite preference of Mg^{2+} for the octahedral site. The reliability index for the two models are compared in Table 5. A significantly better agreement is obtained for the ordered model for four out of the five $(Mg, Zn)_3(PO_4)_2$ compositions. In addition for all of these compositions the (011) reflection was reported as unobserved and predicted to be below the lowest observed intensity for the ordered structure. The random structure in each case, on the other hand, predicted that this reflection should be observed. It should be remarked that the intensity data used in this calculation probably was only peak height rather than integrated intensity and that the atom parameters used were those determined by the refinement of the γ-$(Zn, Mn)_3(PO_4)_2$ structure. The effect of both errors was suppressed by taking data from a narrow range of diffraction angle near

Table 5. Reliability indices for order and disordered cation arrangements

Composition	Reliability Index	
	Random	Ordered
$Zn_3(PO_4)_2$	0·11	0·11
0·95 $Zn_3(PO_4)_2$–0·05 $Mg_3(PO_4)_2$	0·21	0·12
0·80 $Zn_3(PO_4)_2$–0·20 $Mg_3(PO_4)_2$	0·25	0·14
0·60 $Zn_3(PO_4)_2$–0·40 $Mg_3(PO_4)_2$	0·29	0·10
0·40 $Zn_3(PO_4)_2$–0·60 $Mg_3(PO_4)_2$	0·21	0·18
0·20 $Zn_3(PO_4)_2$–0·80 $Mg_3(PO_4)_2$	0·24	0·19
$Mg_3(PO_4)_2$	0·17	0·17

$\theta = 0$. This restricted the structure factors to the low frequency components of the electron density and as such they are not sensitive to small errors in the atom positions.

The emission characteristics of

$$\gamma\text{-}Zn_3(PO_4)_2\text{:Mn}$$

under cathode ray bombardment can be interpreted in a manner such as to give additional support to the proposed ordered distribution of Mn^{2+}. For Mn^{2+} concentrations near eleven per cent two emission peaks are noted (see Fig. 2 footnote 7). The predominant one is at 6300 Å and the weak one has a maximum near 5500 Å. Thus for high Mn^{2+} concentrations it appears that two emission centers are seen and these can be accounted for by assuming direct substitution of Mn^{2+} for Zn^{2+}. The red band can be attributed to Mn^{2+} in the octahedral site and the green band to Mn^{2+} in the tetrahedral site. Since the green emission of the α-structure, where all the cations are tetrahedrally coordinated, coincides with the green band γ-phase the model appears to be consistent.

The fraction of Mn^{2+} in each type of site can be used as a measure of the average energy involved in the exchange reaction

$$Mn_O^{2+} + Zn_T^{2+} \rightarrow Mn_T^{2+} + Zn_O^{2+} \qquad (1)$$

where the subscript indicate either an octahedral (O) or a tetrahedral (T) site. In the quasi-chemical approximation[12] the exchange energy is related to the concentration of species by the pseudo-equilibrium constant relationship,

$$\frac{[Mn_T^{2+}][Zn_O^{2+}]}{[Mn_O^{2+}][Zn_T^{2+}]} = \exp\left(\frac{\Omega}{kT}\right) \qquad (2)$$

where kT is the thermal energy, and Z_S is the concentration of species Z in a site of type S and Ω is the average energy expended in exchanging an octahedral Mn^{2+} for a tetrahedral Zn^{2+}. If for a total of N cation sites ξN are occupied by Mn^{2+} and further a fraction, σ, of these Mn^{2+} are on tetrahedral sites we can obtain,

$$\frac{\sigma}{1-\xi\sigma}\,\frac{(1-\xi)-2/3(1-\xi\sigma)}{(1-2/3\sigma)} = \exp\left(-\frac{\Omega}{kT}\right) \qquad (3)$$

In evaluating the concentrations we have made use of the fact that 2/3 of the sites are tetrahedrally coordinated. For the case at hand $\xi = 0{\cdot}11$ and T is near 1200°K.

Either σ or ξ must be determined from the experimental data. The ratio of the area under the green peak to that under the red peaks together with the relative efficiency for emission of each type of site can be used to determine σ. The peak ratio is of the order of 1 to 30. The efficiency however is not known. One expects however that the emission of tetrahedral Mn^{2+} should exceed that for the octahedral Mn^{2+}, because the emission of the latter, by symmetry consideration requires the aid of lattice vibrations. McClure[4] states that this efficiency ratio upon absorption seems to be of the order of 100 to 1 and favors of the emission of tetrahedral Mn^{2+}. We ignore consideration regarding the validity of the use of this ratio for the emission transition, and are led to an exchange energy of 0·9 eV. It is of interest that Miller[13] has computed a preference energy in spinels for a formally analogous reaction to that indicated by equation (1) and has obtained the value 0·7 eV.

The composition dependence of the lower phase boundary will be discussed in a future publication of the α-$Zn_3(PO_4)_2$ structure.

DISCUSSION

This structure can be described in terms of sheets of closely coordinated cation polyhedra extended along the y, z plane. The Zn_{II}^{2+} occur in pairs of ZnO_4 tetrahedra sharing a common edge. These Zn_2O_6 groups are separated by ZnO_6 octahedra with which they share four corners. The P atoms bridge from one sheet to the next along a by sharing three oxygen atoms with five Zn^{2+} in one sheet and one oxygen atom with two Zn^{2+} in the next sheet. A short zinc oxygen distance (2·32 Å) is found beyond the first coordination shell and it may be through this oxygen that the γ-structure transforms into the β-structure. The structure of phosphophyllite,

$$Zn_2Fe(PO_4)_2 \cdot 4H_2O,^{(14)}$$

shows some features similar to those found in γ-$Zn_3(PO_4)_2$. The Zn ions in the former structure are found as a pair of edge sharing tetrahedra and the FeO_6 groups are centered with octahedral coordinaton. The distribution of cations among the available sites should be similar to that found in γ-$Zn_3(PO_4)_2$.

One of the interesting aspects of the γ-$Zn_3(PO_4)_2$ structure is the existence of two types of cation sites and the apparent relationship of the Mn^{2+} emission to the crystallography of these sites. NEUHAUS(15) has proposed the use of the optical absorption transition between the 3*d* electronic levels as a guide to the crystallographic environment of the transition metal ion in the parent structure. It appears that despite theoretical weaknesses such crystallographic information is available in the emission spectra.

The fact that Ca^{2+}, Mn^{2+} and Mg^{2+} all promote the appearance of the γ-phase can be correlated with the known empirical tendencies of these cations for sites of six-fold coordination. We can conclude from the existence of the γ-phase in $(Zn, Mg)_3(PO_4)_2$ for all compositions above thirty-three per cent Mg that Mn^{2+} has a stronger preference for the octahedral site in these phosphates than does Mg^{2+}. Apparently after the added cation has saturated the octahedral site additional amounts must substitute into the tetrahedral site or find a new crystal structure of preferred stability. The Mg^{2+} substitutes into the tetrahedral site while Mn^{2+} apparently chooses a new phase. The conclusion that Mn^{2+} has a greater octahedral-to-tetrahedral site preference than does Mg^{2+} seems contrary to experience and parenthetically disagrees with the results of the calculations of Miller. Our conclusion however seems to be verified by the results of the luminescence of Mn^{2+} in $(Mg, Mn)_3(PO_4)_2$. SARVER *et al.*(10) found that the emission was red and thus we would conclude that Mn^{2+} preferred the octahedral site in the presence of Mg^{2+}. The anomaly may arise in this case because of the special nature of the tetrahedral site consisting of edge sharing ZnO_4 groups across a center of symmetry. Both Mg^{2+} and Zn^{2+} as free ions have completed inner shells whereas Mn^{2+} has a half filled 3*d* shell. As a result a Mg^{2+} substitution for Zn^{2+} will present a smaller perturbation than a Mn^{2+} substitution. However the sign of this perturbation remains to be determined.

Some comment seems in order with regards to the accuracy of the crystal structure reported here. Errors no doubt arise because (1) the composition of the crystal is not exactly known, (2) the effects of absorption have not been considered and (3) only an overall temperature factor has been applied. However the internal consistency of the structure proposed and the luminescence data strongly supports the structure proposed. In the light of the nature of errors involved it seems advisable to change to a study of $Mg_3(PO_4)_2$ if a further refinement of this structure is desired.

Acknowledgements—The author wishes to thank Dr. A. L. SMITH for suggesting this problem, Dr. P. N. YOCUM and Dr. M. KESTIGIAN for their aid in growing the crystals and the National Research Council of Canada for their support throughout the final stages of this work.

REFERENCES

1. LINWOOD S. H. and WEYL W. A., *J. opt. Soc. Amer.*, **32**, 443 (1942).
2. SCHULMAN J. H., *J. appl. Phys.* **17**, 902 (1947).
3. KROEGER F. A. and ZALM P., *J. electrochem. Soc.* **98**, 177 (1951).
4. MCCLURE D. S., *Solid State Physics* (edited by SEITZ F. and TURNBULL D.), Vol. **9**, Academic Press, New York (1959).
5. SMITH A. L., *J. electrochem. Soc.* **98**, 363 (1951).
6. KATNACK F. L. and HUMMEL F. A., *J. electrochem. Soc.* **105**, 125 (1958).
7. HUMMEL F. A. and KATNACK F. L., *J. electrochem. Soc.* **105**, 528 (1958).
8. CALVO C., to be published.
9. CALVO C., to be published.
10. SARVER J. F., KATNACK F. L. and HUMMEL F. A., *J. electrochem. Soc.* **106**, 960 (1958).
11. Homomorphism is used here in preference to isomorphism in its mathematical sense of a relationship of many elements of a set to one element of a second set.
12. FOWLER R. and GUGGENHEIM E. A., *Statistical Thermodynamics*, University Press, Cambridge (1952).
13. MILLER A., *J. appl. Phys.* **30**, 24S (1959).
14. KLEBER W., LIEBAU F. and PRATKOURAK E., *Acta Cryst.* **14**, 795 (1961).
15. NEUHAUS A. VON, *Z. Kristalogr.* **113**, 13 (1960).

J. Phys. Chem. Solids Pergamon Press 1963. Vol. 24, pp. 151–155. Printed in Great Britain.

AUSHEILUNG VON BESTRAHLUNGSSCHÄDEN IN QUARZ-SCHWINGKRISTALLEN

P. FREYMUTH und G. SAUERBREY

I. Physikalisches Institut, Technische Universität Berlin

(*Received* 29 *March* 1962)

Zusammenfassung—Schwingquarzplatten vom *AT*-Schnitt wurden mit Röntgenstrahlen mit Dosen bis $6 \cdot 10^6$ rad bestrahlt. Dabei zeigte sich die bereits bekannte Erniedrigung der Eigenfrequenz mit Sättigungscharakter. Diese durch Strahlungsschädigung der mechanischen Konstanten des Kristalls hervorgerufene Änderung der Eigenfrequenz wurde durch Tempern bei Temperaturen zwischen 150°C und 250°C wieder ausgeheilt. Aus der Temperaturabhängigkeit der Ausheilkurven kann die Aktivierungsenergie der für mechanische Veränderungen verantwortlichen Störstellen berechnet. werden Die experimentellen Werte lassen sich durch zwei Störstellenarten mit den Aktivierungsenergien $E_1 = 0{,}3 \pm 0{,}1$ eV und $E_2 = 1{,}3 \pm 0{,}3$ eV wiedergeben.

Abstract—Quartz crystal plates (*AT*-cut) were irradiated by X-rays up to $6 \cdot 10^6$ rad absorbed dose and showed the frequency decrease with saturation character already known. This decrease of the resonance frequency induced by radiation damage in the crystal was annealed at temperatures in the range from 150°C to 250°C. The activation energy of the traps responsible for the change of frequency can be computed from the temperature dependence of the annealing curves. The experimental values are reproduced by two forms of traps with activation energies of $E_1 = 0{\cdot}3 \pm 0{\cdot}1$ eV and $E_2 = 1{\cdot}3 \pm 0{\cdot}3$ eV.

1. EINLEITUNG

NACH FRONDEL(1) ändert ein Schwingquarz, der energiereicher Strahlung ausgesetzt wird, seine mechanische Eigenfrequenz (vergleiche auch BECHMANN(2)). Diese Veränderungen, die im Kristall bei Bestrahlung auftreten, sind bei γ- und β-Strahlung von Energien unter 1 MeV allein die Folge von Ionisationsprozessen, während schwere Teilchen zusätzlich auch Frenkeldefekte erzeugen (vergleiche DIENES und VINEYARD(3)).

Werden durch Ionisation abgetrennte Elektronen in Elektronenfallen im Kristall eingefangen, so kommt es zu bleibenden Veränderungen. In erster Linie werden davon die optischen und magnetischen Eigenschaften betroffen. Aber auch die elastischen Konstanten und die Dichte werden beeinflusst, da durch Ionisation von Gitteratomen die Bindungskräfte geändert werden. Die Änderungen der mechanischen Eigenschaften sind jedoch so gering, dass sie sich nur mit empfindlichen Untersuchungsmethoden nachweisen lassen. Die Eigenfrequenz eines piezoelektrisch angeregten Schwingquarzes lässt sich mit grosser Genauigkeit messen und bietet daher eine einfache Möglichkeit, die durch ionisierende Strahlung hervorgerufene Beeinflussung mechanischer Eigenschaften eines Kristalls zu untersuchen.

Durch Zufuhr von Wärmeenergie werden die eingefangenen Elektronen wieder beweglich gemacht, so dass es zur Ausheilung der Strahlungsschäden kommt. Die Ausheilung der Strahlungsschädigung in Schwingquarzen ist bisher noch nicht näher untersucht worden. FRONDEL(1) gibt lediglich an, dass bei Temperaturen über 180°C die Bestrahlungsschäden ausheilen und bei 300°C die Ausheilung nahezu plötzlich erfolgt.

In der vorliegenden Arbeit war die Temperaturabhängigkeit des Ausheilvorganges zu messen und daraus die Aktivierungsenergie der strahlungsinduzierten Fehlstellen zu berechnen. Dazu war es zunächst notwendig, die Erzeugung von Fehlstellen durch Röntgenstrahlung an Hand der

Erniedrigung der Eigenfrequenz des Schwingquarzes festzustellen.

2. MESSUNG DER STRAHLUNGSINDUZIERTEN FREQUENZÄNDERUNG

Die Verringerung der Eigenfrequenz eines mit 46 kV_{eff}-Röntgenstrahlung bestrahlten Schwingquarzes ist in Fig. 1 wiedergegeben. Ähnliche Bestrahlungskurven sind zuerst von Frondel veröffentlicht worden. Die strahlungsinduzierte Frequenzerniedrigung besitzt einen Sättigungswert. Vollständige Sättigung war experimentell nur zu erhalten, wenn sich die bestrahlten Quarzscheiben in evakuierten Glaskolben befanden, sonst trat infolge ungeklärter Einflüsse ein geringer konstanter Restanstieg auf. Die relative Sättigungsfrequenzänderung betrug bei dem Quarzexemplar nach Fig. 1 $\Delta f/f = -10^{-6}$ (f: Eigenfrequenz der Quarzplatte, Δf: Frequenzänderung). Der Absolutwert der Frequenzänderung ist für das Material nicht charakteristisch, da er von Form, Grösse und Schwingungsform des Schwingquarzes und wegen der Anisotropie der Strahlungsschädigung auch von der Orientierung des Schwingquarzes zu den Kristallachsen abhängt.

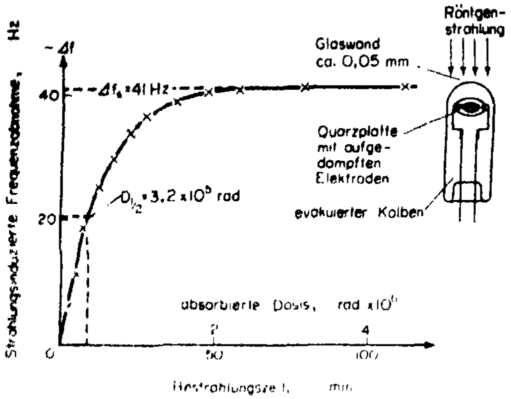

FIG. 1. Frequenzänderung eines Schwingquarzes bei Bestrahlung mit 46 keV_{eff}-Röntgenstrahlung (4 MHz-*AT*-Quarz, Durchmesser 13 mm mit 1,5 mm Facette; Goldelektroden 10^{-6} cm dick, 5 mm Durchmesser).

Für unsere Experimente wurden 0,17 und 0,4 mm dicke Quarzplatten vom *AT*-Schnitt (Dickenscherungsschwinger mit Frequenzen $f = 4$ MHz bzw. $f = 10$ MHz, Scheibendurchmesser 13 mm) verwendet.

Die Dosis, bei der die Hälfte der Sättigungsfrequenzänderung erreicht ist, beträgt nach unseren Messungen $D_{1/2} = 3 \cdot 10^5$ bis $10 \cdot 10^5$ rad.* Der Anfangsanstieg der Frequenzänderung betrug im Mittel sowohl bei Röntgen- wie auch bei β-Bestrahlung† $(\Delta f/f) : D = 10^{-11}$ rad^{-1}.

3. MESSUNG DER AUSHEILGESCHWINDIGKEIT DER STRAHLUNGSINDUZIERTEN FREQUENZÄNDERUNG

Um die Aktivierungsenergie der für die mechanischen Strahlungsschäden verantwortlichen Fehlstellen zu bestimmen, war die Ausheilung der Frequenzänderung zeitlich zu verfolgen. Messtechnisch gut erfassbare Ausheilzeiten zwischen 20 Minuten und 5 Stunden ergaben sich bei Ausheiltemperaturen $T = 150$–250°C. Die Ausheilung wurde mit einer direkten (a) und einer inversen (b) Methode gemessen (Fig. 2).

(a) *Direkte Ausheilmessung*

Der Quarz wird zunächst bei Zimmertemperatur bis zur Sättigung bestrahlt (Intervall *AB*). Dann wird der Quarz in einem Thermostaten auf die Ausheiltemperatur T gebracht, während einer Zeit Δt_a getempert und danach wieder auf Zimmertemperatur abgekühlt.

Die Eigenfrequenz wird im Punkt B und im Punkt C bei Zimmertemperatur gemessen. Durch die Temperung bei der Temperatur T während der Zeit Δt_a tritt die Frequenzänderung Δf_a (Frequenzausheilung) auf. Die so erhaltenen Werte $\Delta f_a(\Delta t_a, T)$ waren jedoch nur schlecht reproduzierbar und gaben keinen glatten Kurvenverlauf. Vermutlich traten während des Temperns oder bei der Aufheizung oder Abkühlung des

---

* Die angegebene Dosis wird immer auf die Mittelebene der Platte bezogen, da dort die grösste elastische Beanspruchung auftritt. Änderungen der elastischen Konstanten haben deshalb in der Mittelebene der Platte den grössten Einfluss auf die Eigenfrequenz. Da die Platten sehr dünn waren und höchstens die Hälfte der auftreffenden Strahlung absorbierten, war auch die Dosis an den Oberflächen der Platte nicht wesentlich anders als in der Mittelebene.

† Die Aktivität der β-Quelle (T^{204}, β-Energie 760 keV) war für Bestrahlungen bis zur Sättigung zu klein. Deshalb wurde nur der Anfangsanstieg der Frequenzänderung bis 10^5 rad gemessen.

Quarzes Frequenzänderungen auf (bei S angedeutet), die nichts mit dem Ausheilvorgang zu tun haben*). Die nach der Ausheilzeit Δt_a gemessene Frequenzänderung Δf_a ist dann verschieden von der eigentlichen Frequenzausheilung Δf_a.

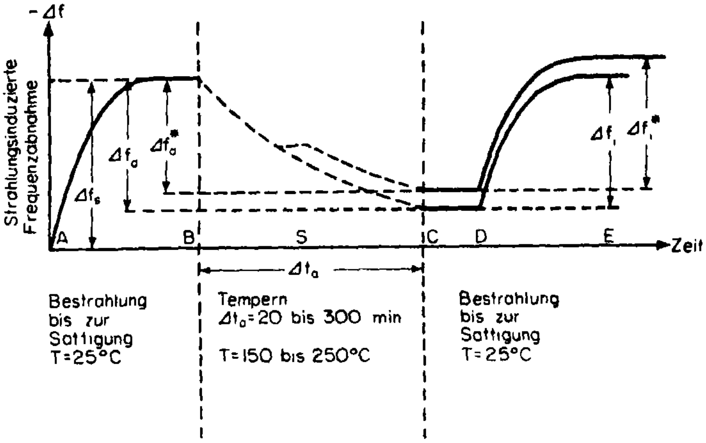
- Δf
Strahlungsinduzierte Frequenzabnahme
Δfs
Δfa
Δfa*
Δfi
Δfi*
A
B
S
C
D
E
Zeit
Δta
Bestrahlung bis zur Sattigung T=25°C
Tempern Δta=20 bis 300 min
T=150 bis 250°C
Bestrahlung bis zur Sattigung T=25°C

FIG. 2. Messung der Ausheilung der strahlungsinduzierten Frequenzänderung nach der direkten Methode (Δf_a) und nach der inversen Methode (Δf_i); Δf_a^*, Δf_i: Ausheilraten bei Störungen im Temperintervall BC.

Bei der hohen Temperatur während der Temperung war es wegen der starken Temperaturabhängigkeit der Eigenfrequenz der Schwingquarze nicht möglich, den Ausheilvorgang laufend zu verfolgen. Bei genügend guter Temperaturstabilisierung und bei Verwendung geeigneter Plattenschnitte muss es jedoch möglich sein, bereits die Bestrahlung (Intervall AB) bei der Ausheiltemperatur T vorzunehmen und von dem sich dabei einstellenden Gleichgewicht aus die Ausheilung zu messen.

(b) *Inverse Ausheilmessung*

Um die bei hoher Temperatur und beim Temperaturwechsel auftretenden Störungen zu vermeiden, wurde zur Messung der Ausheilung eine inverse Methode angewendet. Der Bestrahlungs- und Temperprozess wird bis zum Punkt C wie bei der direkten Methode durchgeführt. Nach der Abkühlung wird der Quarz jedoch wieder bis zur Sättigung der Strahlungsschädigung bestrahlt (Intervall DE). Dabei erniedrigt sich die Eigenfrequenz um den Betrag Δf_i bzw. Δf_i^*. Da die neue Bestrahlung (Intervall DE) bei Zimmertemperatur vorgenommen wird, kann der Kurvenverlauf während der Messung verfolgt werden. Aus der geringen Streuung der Messwerte ergibt sich, dass die Frequenzänderung von den beim Tempern aufgetretenen Störungen frei ist ($\Delta f_i = \Delta f_i^*$).

Bisweilen waren auch die nach der direkten Methode gemessenen Ausheilraten Δf_a reproduzierbar. Diese Werte stimmten mit den nach der inversen Methode gewonnenen Werten gut überein, so dass die Gleichsetzung von Δf_a und Δf_i allgemein zulässig ist.

4. ERGEBNISSE DER AUSHEILMESSUNGEN

Ausheilkurven $\Delta f_i(\Delta t_a) = \Delta f_a(\Delta t_a)$ für verschiedene Ausheiltemperaturen T sind in Fig. 3 dargestellt. Diese Kurven wurden mit der inversen Methode an einer 4 MHz-AT-Quarzscheibe gewonnen. Ähnliche Kurven ergaben sich an 10 MHz-AT-Scheiben. Die vollständige Ausheilung des Bestrahlungseffektes war innerhalb der Messzeit von 5 Stunden erst bei Temperaturen

---

* Als Ursache der Frequenzsprünge kommen z.B. Adsorption bzw. Desorption von Gasen auf den Quarzelektroden oder elastische Spannungen im Quarz infolge der Abkühlung in Frage.

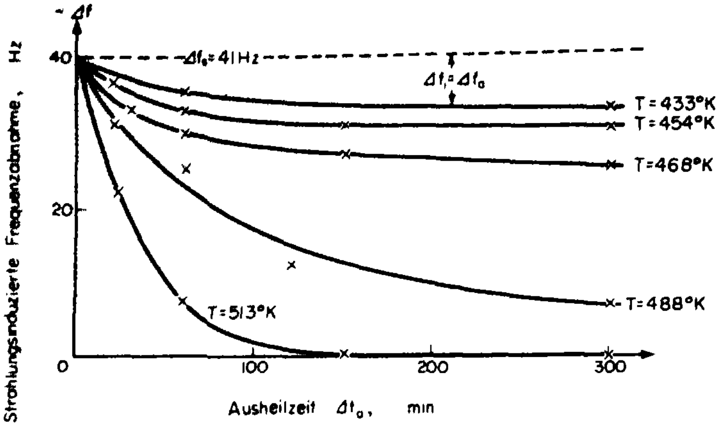

FIG. 3. Ausheilung der strahlungsinduzierten Frequenzänderung einer 4-MHz-Quarzplatte. Δf_l : ausgeheilte Frequenzänderung, Δf_s : Sättigungsfrequenzänderung, T : Ausheiltemperatur.

über 500°K zu erreichen, während bei tieferer Temperatur die Ausheilung nur unvollständig verläuft.

Dieser Kurvenverlauf lässt sich durch eine einzige Störstellenart konstanter Aktivierungsenergie nicht erklären. Versucht man trotzdem, aus dem Anfangsanstieg benachbarter Kurven unter der Annahme einer einzigen Störstellenart die Aktivierungsenerige für die Ausheilung der mechanischen Strahlungsschäden zu berechnen,* so ergibt sich im Mittel $E = 0{,}6 \pm 0{,}3$ eV. (Für die Ausheilung der strahlungsinduzierten optischen Absorption in Quarz ermittelten MITCHELL und PAIGE[4] eine Aktivierungsenergie $e = 0{,}75$ eV.).

Eine gute Annäherung an die experimentellen Kurven ergibt bereits die Annahme von zwei Störstellenarten verschiedener Aktivierungsenergie. Diesen beiden Störstellenarten werden die Sättigungsfrequenzänderungen Δf_{s1} und Δf_{s2} zugeordnet. Unter der Annahme, dass die Ausheilgeschwindigkeit der Zahl der noch nicht ausgeheilten Störstellen proportional ist (Reaktion 1. Ordnung), ergibt sich für die Frequenzausheilung Δf_a :

$$\Delta f_a = \Delta f_s - \{\Delta f_{s1} \exp(-\kappa_1 \Delta t_a) + \Delta f_{s2} \cdot \exp(-\kappa_2 \Delta t_a)\} \tag{1}$$

Δf_a : ausgeheilte Frequenzänderung
Δf_s : Sättigungsfrequenzänderung
Δf_{s1}; Δf_{s2} : Sättigungsfrequenzänderung, die von den Störstellen 1 bzw. 2 herrührt (1)
Δt_a : Ausheilzeit

mit :

$$\kappa_1 = K_1 \cdot \exp[-(E_1/kT)]$$
$$\kappa_2 = K_2 \cdot \exp[-(E_2/kT)] \tag{2}$$

T : Ausheiltemperatur
K_1, K_2 : Frequenzfaktoren
E_1, E_2 : Aktivierungsenergie der Störstellen 1 bzw. 2 (2)
k : Boltzmannkonstante

---

* Über Theorie der Ausheilung von Bestrahlungsschäden siehe DIENES und VINEYARD.[3]

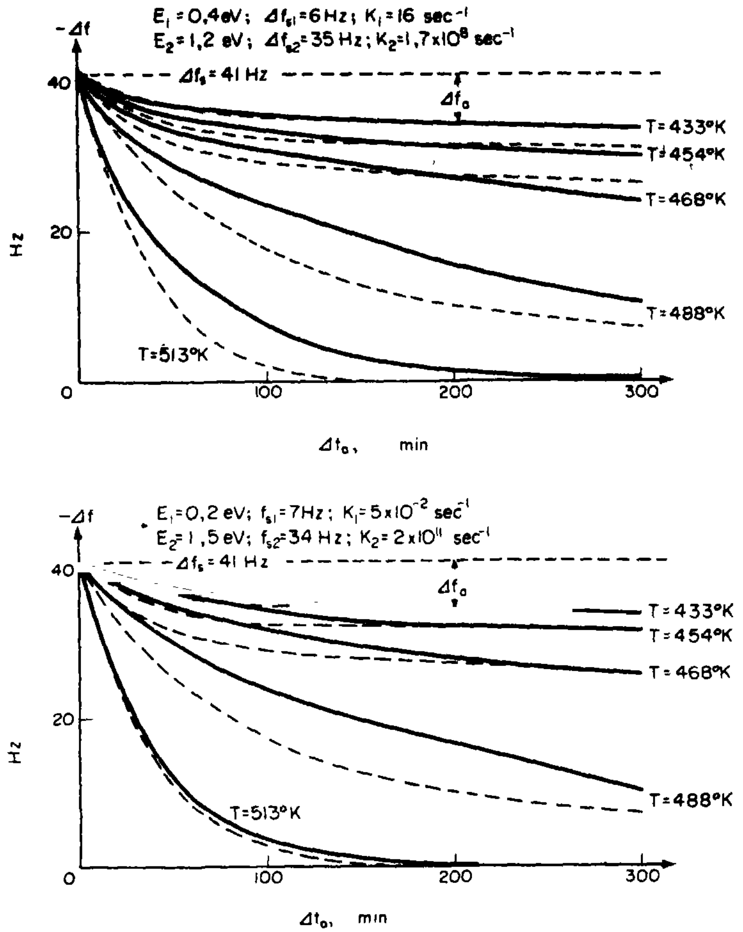

FIG. 4. Für zwei Störstellenarten unter Aktivierungsenergie E_1 bzw. E_2 nach Gl. (1) berechnete Ausheilkurven (ausgezogen). Die experimentellen Kurven nach Fig. 3 sind zum Vergleich eingezeichnet (gestrichelt).

Figur 4 zeigt zwei nach Gl. (1) berechnete Scharen von Ausheilkurven für unterschiedliche Werte der Konstanten E_1, E_2, K_1, K_2, Δf_{s1} und $\Delta f_{s2} = \Delta f_s - \Delta f_{s1}$ im Vergleich mit den experimentellen Kurven. Die beste Übereinstimmung zwischen der Rechnung und den experimentellen Kurven ergibt sich für die Aktivierungsenergien $E_1 = 0{,}3 \pm 0{,}1$ eV und $E_2 = 1{,}3 \pm 0{,}3$ eV.

Vollständige Übereinstimmung zwischen experimentellen und berechneten Kurven liess sich nicht erzielen. Es kann nicht entschieden werden, ob die aus Fig. 4 erkennbaren Unterschiede von Rechnung und Experiment auf die Unsicherheit der experimentellen Kurven oder die Beschränkung auf zur zwei Störstellenarten nach G.l (1) zurückzuführen sind.

Anerkennung — Die Verfasser danken Herrn Prof. Dr. H. BOERSCH für die Förderung dieser Arbeit und für wertvolle Anregungen. Die Arbeit wurde durch den Bundesminister für Atomkernenergie finanziell unterstützt.

LITERATUR

1. FRONDEL C., *Amer. Mineral.* **30**, 432 (1945).
2. BECHMANN R., *Nucleonics*, **16**, 122 (1958).
3. DIENES G. und G. VINEYARD, *Radiation Effects in Solids*, McGraw Hill, New York (1957).
4. MITCHEL E. und PAIGE E., *Phil. Mag.* **1**, 1085 (1956).

J. Phys. Chem. Solids Pergamon Press 1963. Vol. 24, pp. 157–159. Printed in Great Britain.

ORDER–DISORDER REACTIONS IN α-Ti(O) AND TiO*

MICHAEL HOCH

Materials Science Program, Graduate School, University of Cincinnati, Cincinnati, Ohio

(*Received* 11 *July* 1962)

Abstract—The appearance of a superstructure at low temperatures in hexagonal α-Ti containing oxygen and in TiO has been related to the properties of unoccupied lattice sites, i.e. vacancies. From the interaction energy between vacancy pairs the critical temperature for ordering has been calculated and found to be in agreement with experimental data.

INTRODUCTION

α-Ti CAN dissolve a fairly large amount of oxygen and the close relationship between the hexagonal α-Ti containing oxygen [called α-Ti(O)] and TiO has been pointed out by BUMPS *et al.*(1) and by ROSTOCKER.(2) To summarize, the Ti–Ti distance in TiO is 2·955 Å and in the oxygen-saturated α-Ti(O), 2·960 Å. KAUFMAN(2) explains the structural relationship between α-Ti(O) and TiO as a stacking fault.

MAGNELI *et al.*(4) point out that when TiO is heated at 800°C for 14 days, a superstructure forms. The strong X-ray diffraction lines of the low-temperature structure are at the same place as those of the high-temperature form and additional weak lines appear.

Similar ordering(4) occurs in α-Ti(O) where superstructure lines appear if the samples are heated at 700–800°C. The structure is of the anti-$Cd(OH)_2$ type, oxygen atoms occupying only every second layer. At lower oxygen concentration ordered vacancies appear in the occupied oxygen layers.

In treating the palladium–hydrogen system, FOWLER and GUGGENHEIM(5) point out that if the vacancy interaction energy is negative, a critical mixing temperature exists, above which one phase is present and below which two phases are coexistent. As the statistical treatment of order–disorder phenomena and of the appearance of a miscibility gap is quite similar,(8) a critical temperature for vacancy ordering must exist when the vacancy interaction energy is positive. The aim of the present work is to explain the ordering of vacancies (and therefore oxygen atoms) in α-Ti(O) and the ordering of vacancies (thus also titanium and oxygen atoms) in TiO through the use of vacancy interaction energies.

THEORY

TiO: The statistical treatment of vacancies in TiO has been given(6) earlier.

α-Ti(O): The grand partition function (GPF) of a compound which contains vacancies in the sites of one of the components can be written as follows:(5)

$$GPF = \sum_{V_1} \frac{N!}{V_1!(N-V_1)!}[a_1\cdot K_1(T)]^{N-V_1} \times [a_2\cdot K_2(T)]^N \exp - \left[V_1E_1 + \frac{z}{2}\frac{V_1^2}{N}E_{11}\right]\Big/kT \qquad (1)$$

where the subscript 1 refers to oxygen and the subscript 2 to titanium, N is the number of titanium atoms and also of oxygen lattice sites, V_1 is the number of vacancies in the oxygen lattice, E_1 is the energy necessary to create an oxygen vacancy, E_{11} is the interaction energy of oxygen vacancies per pair, a_1 and a_2 are the absolute activities of oxygen and titanium in the crystal phase, $K_1(T)$ and $K_2(T)$ are contributions of an added atom of oxygen and titanium, respectively, to the partition function for the normal vibrational modes of the crystal, k is the Boltzmann constant, T is the absolute temperature, and z is the number of nearest neighbor oxygen sites around each oxygen site. Furthermore, the assumption is made that the interaction energy E_{11} does not influence the random distribution of vacancies and that $K_1(T)$ and $K_2(T)$ are independent of composition. The equilibrium condition can be obtained⁽⁵⁾ by replacing the sum by its largest term and by partial differentiation of the logarithm of the grand partition function with respect to the concentration of vacancies V_1.

---

* This research was supported in part by the Aeronautical Research Laboratory, Office of Aerospace Research, United States Air Force, under Contract AF 33(616)–6299.

During the differentiation the number of titanium atoms and the number of available oxygen sites, N, is kept constant. Carrying out the differentiation of equaton (1),

$$-\ln V_1 + \ln(N-V_1) - \ln a_1 \cdot K_1(T) - \frac{E_1}{kT} - z\cdot\frac{E_{11}}{kT}\frac{V_1}{N} = 0 \qquad (2)$$

The oxygen concentration is given by

$$n_1 = \frac{N-V_1}{2N-V_1} \qquad (3)$$

from which the vacancy concentration is

$$V_1 = N\frac{1-2n_1}{1-n_1} \qquad (4)$$

Considering the reaction at another composition (denoted by ′), subtracting the two equations, and replacing the V's by n's results in

$$-\ln a_1\frac{(1-2n_1)}{n_1} + \ln a_1'\frac{(1-2n_1')}{n_1'} = \frac{z\cdot E_{11}}{kT}\left[-\frac{n_1}{1-n_1}+\frac{n_1'}{1-n_1'}\right] \qquad (5)$$

Plotting

$$\ln a_1\frac{1-2n_1}{n_1} \text{ vs. } \frac{n_1}{1-n_1}$$

gives the vacancy interaction energy.

The critical mixing temperature, T_c, can be calculated from the vacancy interaction energies E_w,⁽⁵,⁸⁾

$$\frac{z}{2}E_w = 2RT_c$$

EXPERIMENTAL RESULTS AND DISCUSSION OF DATA

TiO

In the case of TiO,⁽⁶⁾ the vacancy interaction energy between similar charges is $E_{11} = E_{22} = 2{\cdot}10 \pm 0{\cdot}03$ kcal/mole; for charges with opposite sign, $E_{12} = -2{\cdot}97 \pm 0{\cdot}04$ kcal/mole. The total interaction energy is $z \times E_{11} + z' \times E_{12}$ where z and z' are the number of next nearest sites of similar and opposite charge, respectively, around each site ($z = 12$, $z' = 6$). The total interaction energy thus is 7·38 ± 0·6 kcal/mole which corresponds to a critical temperature of 923 ± 75°K. This temperature is somewhat lower than the 800°C obtained by MAGNELI *et al.*⁽⁴⁾ but the agreement is good, considering the use of the zeroth order approximation.⁽⁸⁾

α-Ti(O)

HEPWORTH⁽⁷⁾ made measurements of hydrogen activity in Ti–O–H alloys. From these measurements he extracted the activity of oxygen as a function of composition at 800°C. These data are given in Table 1. The composition is given in column 1, the oxygen activity in column 2. Columns 3 and 4 contain

$$\frac{n_1}{1-n_1} \text{ and } \log a_1\frac{(1-2n_1)}{n_1}$$

needed in the evaluation of equation (5).

Least square treatment of the data in Table 1 according to equation (5) gives

$$zE_{11} = 8{\cdot}592 \pm 0{\cdot}343 \text{ kcal/mole} \qquad (6)$$

Application of the criterion for ordering results in a critical temperature of 1074 ± 43°K which is in very good agreement with the data of MAGNELI *et al.*⁽⁴⁾ (800°C, for $TiO_{0{\cdot}35}$) As can be seen from equation (6), the oxygen vacancies repel each other; this explains why the oxygen vacancies and thus also the oxygen atoms, line themselves up in every second layer. Each oxygen

Table 1. *Oxygen activity in* α-Ti(O) *alloys at* 800°C(7)

n_1	a_1	$\frac{n_1}{1-n_1}$	$\log \frac{a_1(1-2n_1)}{n_1}$
0·0212	0·9916	0·0217	+1·6512
0·0405	1·8677	0·0421	+1·6272
0·0580	2·9190	0·0616	+1·6483
0·0738	4·0485	0·0797	+1·6699
0·0872	5·2480	0·0955	+1·6963
0·0986	6·5072	0·1094	+1·7241
0·1088	7·8176	0·1221	+1·7499
0·1173	9·1633	0·1329	+1·7766
0·1253	10·498	0·1432	+1·7979
0·1327	11·751	0·1530	+1·8133
0·1396	12·862	0·1623	+1·8222

site is surrounded by 6 oxygen sites in the *a* plane (perpendicular to the *c* axis) at a distance of *a*, and by 2 oxygen sites in the *c* direction at a distance of $c/2$. As $c/2 < a$, the first tendency will be to avoid having vacancy neighbors along the *c* axis and therefore the alternate ordering. At lower oxygen concentration, the vacancies, again repelling each other, will settle in the *a* layers in an ordered fashion.

REFERENCES

1. BUMPS E. S., KESSLER H. D. and HANSEN M., *Trans. Amer. Soc. Metals* **45**, 1008 (1953).
2. ROSTOCKER W., *Trans. Amer. Inst. min. (metall.) Engrs.* **194**, 981 (1952).
3. KAUFMAN L., *ASD Tech. Rep.* 61-445 (1961).
4. MAGNELI AL., ANDERSSON S., WESTMAN S., ASBRINK S. and HOLMBERG B., *ASTIA* 157156 (1958).
5. FOWLER R. and GUGGENHEIM E. H., *Statistical Thermodynamics*, pp. 552, 431, 559. University Press, Cambridge (1949).
6. HOCH M., IYER A. S. and NELKEN J., *J. Phys. Chem. Solids* **23**, 1463 (1962).
7. HEPWORTH M., Doctoral Dissertation, Purdue University (1958).
8. GUGGENHEIM F. H., *Mixtures*, Clarendon Press, Oxford (1952).

J. Phys. Chem. Solids Pergamon Press 1963. Vol. 24, pp. 161–168. Printed in Great Britain.

SUMMARY OF CONFERENCE ON THE PHYSICS OF SEMICONDUCTORS, EXETER, 1962

THE Sixth International Conference on Semiconductor Physics was held at the University of Exeter, England, from July 16 to July 20, 1962. It was attended by some 400 delegates representing 27 different countries. The scientific programme was organized under the Chairmanship of Professor R. A. SMITH, F.R.S., with Dr. C. A. HOGARTH as Technical Secretary. The local organization was directed by Professor G. K. T. CONN, Professor of Physics at Exeter.

OPENING SESSION

Professor Sir NEVILL MOTT (University of Cambridge) looked back over the last few years and forward into the future. Good progress in our general understanding of solids had been made using the one-electron approach. Recently, the many-electron approach, necessary in metal theory, had been applied to semiconductors. He picked out, as current problems of special interest, highly degenerate semiconductors, the transition from non-metallic to metallic conduction (e.g. under pressure) and the hopping, or localized electron state, type of transport process. He concluded by expressing the view that, by about 1970, the present surge of interest in semiconductor fundamental physics would have spent its force and the main problems would by then be of a technical nature.

TRANSPORT (EXPERIMENTAL)

S. H. KOENIG (I.B.M. Zurich), gave the review paper. He concentrated on five topics, namely, the sonic amplification experiments of Hutson in Cadmium Sulphide, degenerate semiconductors, measurements involving the use of uniaxial strain (this being a way to measure tensor components of quantities which otherwise average out to a scalar), hot electrons and plasma effects.

The use of uniaxial strain was very much in evidence in the subsequent papers. J. J. HALL (I.B.M., New York), reported on the use of this technique to determine the shear deformation potential of the germanium valence band. H. FRITZSHE (University of Chicago) used the technique to determine intra- and inter-valley scattering relaxation times (by effectively reducing *n*-type germanium to a single valley semiconductor) and R. J. SLADEK (Purdue University) measured the piezo-thermal conductivity of doped germanium and hence investigated the scattering of phonons by bound impurity centres.

I. M. TSIDILKOVSKI (Sverdlovsk, U.S.S.R.) discussed the scattering of electrons in indium antimonide and came to the conclusion that, in intrinsic material, scattering by the optical lattice vibrations was dominant, in support of the theory of Ehrenreich.

B. ABELES (R.C.A.) presented a very thorough and accurate study of the high temperature thermal conductivity of germanium, silicon, germanium–silicon alloys and some III–V compounds. Various contributions to this were discussed, definite evidence being found for a radiation contribution in some cases.

TRANSPORT (EXPERIMENTAL—HOT ELECTRONS)

M. BROWN (R.R.E.) *et al.* attempted to measure the energy distribution of hot holes in germanium by comparing the optical absorption as a function of the electric field and independently, as a function of the lattice temperature. J. B. GUNN (I.B.M., New York) deduced the energy distribution of electrons in germanium from measurements of noise as a function of electric field. Both of these papers arrived at the conclusion that the distribution was Maxwellian only in very limited regions of field and temperature.

Three papers on impact ionization phenomena were submitted to the Conference. The one by S. M. RYVKIN (Leningrad) was not read, but will be available in the proceedings. It dealt with "induced intensity breakdown"—an impurity breakdown in a compensated specimen illuminated by light, due to impact ionization of non-equilibrium electrons trapped by shallow donor levels during illumination. B. M. VUL *et al.* (Moscow) described critical field measurements as a function of thickness of specimens of p-type germanium. The critical voltage was found to be independent of thickness below a certain value. D. J. OLIVER (S.E.R.L. England), presented a study of impact ionization and non-ohmic effects generally in gallium arsenide at low temperatures.

B. ANCKER-JOHNSON (Boeing, Washington) described the electric and magnetic field conditions required to observe plasma oscillations in indium antimonide. Her results indicated either pinch instabilities or hydromagnetic screw instabilities depending on the field conditions.

A. LIBCHABER (Paris) discussed experimental observations of the propagation of circularly polarized electromagnetic waves (helicons) in indium antimonide. Y. K. POZHELA (Vibryus, U.S.S.R.) gave a general paper on hot electron phenomena including some measurements of hot electron emission.

TRANSPORT AND MISCELLANEOUS

K. HUBNER (Shockley Transistor) reported on the use of the transmitted phonon-drag technique to study the interaction of phonons with dislocations as a function of the phonon wavelength and showed that decoration of the dislocations with copper reduced their effectiveness as phonon scatterers.

O. V. EMELYANENKO (Leningrad) presented data on the conductivity, Hall effect and magnetoresistance in gallium arsenide at low temperatures and interpreted these in terms of impurity band conduction.

W. RINDER (Raytheon) described work on the current-voltage characteristics of plastically deformed p–n junctions and found evidence for the existence of stress dependent generation and recombination levels.

Two papers on lead telluride were presented from the U.S. Naval Ordnance Laboratory. R. S. ALLGAIER reported on mobility studies in p-type material with carried densities in the range 5×10^{17} to 2×10^{21} cm^{-3}. Ionized impurity scattering was found to be very weak at low concentrations and lattice scattering was found to increase with increasing concentration almost as fast as impurity scattering. J. R. DIXON studied the optical properties, finding evidence for changes in the effective mass of holes with increasing concentration and with increasing temperature.

S. VAN HOUTEN (Philips, Eindhoven) described measurements of the internal friction in Lithium doped Nickel Oxide, associated with the mechanical relaxation of Li^+-Ni^{3+} dipoles and correlated his results with the conduction mechanism and mobility of holes in this material.

K. J. SCHMIDT-TIEDEMAN (Philips, Hamburg) discussed the theory of the infra-red birefringence in germanium subjected to uniaxial strain. Measurements of this effect led to an estimate of the shear deformation potential constant.

L. E. GUREVICH (Leningrad) discussed the absorption mechanism in homopolar crystals.

TRANSPORT (THEORETICAL)

J. R. DRABBLE (University of Exeter) gave the review paper. He concentrated on recent developments of theoretical techniques, with special reference to the density matrix method of Kohn and Luttinger and to the relation between hopping and band transport mechanisms in mixed valence and impurity band semiconductors.

P. N. ARGYRES (Lincoln Laboratory) developed a very general theory of transport effects to finish up with a transport equation for the elements of the one-electron density matrix for electrons in the presence of electric, magnetic and phonon fields.

J. APPEL (General Atomic, California) dealt with the theory of carrier-carrier scattering in semiconductors and arrived at conclusions regarding the effect of hole-hole scattering on the mobility of holes in p-type germanium.

J. J. HOPFIELD (University of California) emphasized the use of optical studies in transport theory, using the fine structure of the impurity level spectra to investigate the nature of the coupling between free carriers and the lattice.

R. STRATTON (Texas Instruments, Dallas) discussed the theory of dipole scattering in nearly compensated semiconductors.

M. POLLAK (Westinghouse, Pittsburgh) in his paper, reasoned that hopping and band conduction

FIG. 1. *Left to right:* Dr. H. Nelkowski, Mrs. Gobrecht, Professor Dr. H. Gobrecht, Mrs. Nikitine, Professor Dr. S. Nikitine, Mrs. Broser and Dr. I. Broser.

FIG. 2 *Left to right:* Mrs. Conn, Professor F. Barlow (Deputy Vice-Chancellor), Mrs. Smith and Professor R. A. Smith.

could be distinguished by the behaviour of the real part of the electrical conductivity as a function of frequency. L. SOSNOWSKI (Warsaw) presented a theory of thermoelectric and thermomagnetic effects for nonparabolic bands.

P. J. PRICE (I.B.M., New York) dealt with the theory of the transmission of electrons through epitaxial interfaces.

Y. TOYOZAWA (University of Tokyo) proposed that, in impurity band conduction at high concentrations of impurities, some of the impurity band states have localized spin and an associated large magnetic moment and used this idea to explain the negative magnetoresistance in *n*-type germanium in this region of concentration.

DISORDERED SEMICONDUCTORS

The first half of this session was given over to the problem of the determination of the density of states distribution for highly doped semiconductors. L. V. KELDYSH (Moscow) gave a paper of his own and also read one submitted by V. L. BONCH-BRUEVICH (Moscow). Papers were also given by P. A. WOLFF (Bell Laboratories), E. O. KANE (Bell) and E. M. CONWELL (General Telephones, New York). A variety of techniques were used to solve the problem, most of them fortunately leading to similar results. The conclusion was that in such highly doped materials, the impurity band and the conduction band, which are separate at low concentrations, merge together and a continuous density of states is obtained. The form of this at high energies (near the Fermi surface) is similar to that of a degenerate electron gas but, at low energies, near the unperturbed band edge and below, there is a large effect due to the carrier-impurity interaction. This produces an exponentially decreasing tail on the density of states. Formulae for the shape of this and the conditions for formation were given for a number of cases.

Various other problems were considered in the remaining part of the session. P. AIGRAN (University of Paris) discussed the influence of electron–phonon interaction on the melting process, G. BUSCH (Zurich) described the electrical properties of liquid tellurium, H. C. WRIGHT (Mullards, England) presented electrical and optical properties of Gallium Telluride and P. M. SPENCER (University of Durham) discussed the properties of some complex solid solution systems between mercury and cadmium telluride on the one hand and indium and gallium telluride on the other.

SURFACE EFFECTS

W. H. BRATTAIN (Bell Telephone Labs.) described an electrochemical technique which produced a "perfect" germanium surface, i.e. one that had a zero surface recombination velocity and no capacity associated with surface states. By suitable modifications of the technique, controlled surface physical characteristics could be produced.

A number of surface conductance measurements under various conditions yielding information about the density and properties of surface states were reported. YU V. PLESKOV (Moscow) considered a germanium-electrolyte surface. A. MANY (Israel) discussed transient changes following the application of high electric fields normal to the surface. P. C. BANBURY (University of Reading) reported studies on cleaved germanium surfaces under high vacuum and under controlled oxygen contamination.

Some very careful and extensive measurements of the photoelectric emission from clean silicon (111) surfaces over a range of doping were reported by F. G. ALLEN (Bell Telephone Labs.) and by J. VAN LAAR (Philips, Eindhoven). These yielded considerable information about the band and surface state densities.

H. E. FARNWORTH (Brown University) presented low energy electron diffraction studies of cleaned diamond surfaces and cleaved germanium surfaces showing that, in the former case, a displacement of the surface atoms took place which was similar, though smaller, to that on comparable germanium surfaces, previously reported.

EFFECTIVE MASS DETERMINATION

B. LAX (Lincoln Laboratory) gave the review paper. He summarized the various techniques including the original, but by no means outdated, galvanomagnetic and thermoelectric measurements, and high magnetic field oscillatory transport effects. These suffer from the disadvantage of having to make some assumptions about the scattering and Lax showed how the new techniques of cyclotron resonance, when they can be applied, are free from this restriction. The same is true of various optical and magneto-optical techniques which have proved most rewarding, particularly in measuring the parameters of higher bands which are not otherwise accessible.

In subsequent papers there was considerable concentration on the Faraday and Voigt effects. E. D. **Palik** (U.S. Naval Research) reported measurements on *n*-type indium antimonide T. S. **Moss** (Royal Aircraft Establishment) gave results for *n*-type gallium phosphide and aluminium antimonide and S. D. **Smith** (University of Reading) described results bearing on the shape of the conduction band in indium antimonide as a function of temperature.

I. M. **Boswarva** (U.K.A.E.A.) presented a very general theoretical paper which took into account the Faraday rotation due to direct band to band transitions, to forbidden direct transitions and to phonon assisted transitions.

C. J. **Rauch** (Lincoln Laboratories) described millimetre cyclotron resonance work on semiconducting diamond. This showed that the valence band structure is similar to that of germanium and silicon and yielded values of the effective masses of the various bands and of the spin orbit splitting.

J. C. **Hensel** (Bell Telephone Laboratories) presented a very detailed study of cyclotron resonance effects in germanium and silicon, which showed up some new quantum effects in the valence band and confirmed previous theoretical predictions regarding the Landau levels in this band. G. C. **Dousmanis** (R.C.A. Laboratories) reported further work on negative mass cyclotron resonance, in particular on the effect of various deep impurity levels.

K. F. **Cuff** (Lockhead Research) discussed measurements of the oscillatory magnetoresistance and other transport effects in *n*- and *p*-type lead telluride at low temperatures. The results indicated [1,1,1] prolate ellipsoids at the zone edge for the structure of both the valence and conduction bands. The valence band was particularly non-parabolic in the direction of the minor axes of the ellipsoids.

MATERIALS

III–V *Compounds*

M. **Gershenzon** (Bell Telephone Laboratories) presented a study of radiative absorption and emission in the region of the band gap of gallium phosphide, arising from phonon and exciton effects. H. Y. **Fan** (Purdue University) described the transport properties of *n*-type gallium arsenide at low temperatures, using these to deduce the band structure and scattering mechanisms. C. S. **Fuller** (Bell Telephone Laboratories) discussed the reaction kinetics of lithium in gallium arsenide as a function of doping.

II–VI *Compounds*

A. C. **Aten** (Philips, Eindhoven) studied the absorption edge in zinc telluride and deduced that the value of the direct band gap was about 0·10 eV larger than the indirect gap. A. J. **Strauss** *et al.* (Lincoln Laboratory) reported on the optical and electrical properties of cadmium telluride–mercury telluride alloys over a wide range of compositions. At zero and low cadmium concentrations these are probably semi-metals but a transition to semiconducting behaviour occurs at cadmium concentrations of about 20 per cent. The effective masses at the bottom of the conduction band are always very low. A. **Quilliet** (C.N.R.S., France) studied high purity mercury telluride. E. **Cruceanu** (Bucharest) reported on electrical and optical properties of solid solutions of zinc selenide–mercury selenide.

Other Materials

R. **Wolfe** (Bell Telephone Laboratories) described the properties of bismuth–antimony alloys as did also H. J. **Goldsmid** (G.E.C., England). In the range between 5 and 40 per cent antimony, these alloys are high mobility intrinsic semiconductors with high thermoelectric figures of merit which increase by up to 50 per cent in a suitably orientated magnetic field.

A. **Averkin** (Leningrad) and W. **Paul** (Harvard) both described the effects of pressure on the electrical properties of lead salts and interpreted their measurements in terms of the band structure.

A. **Sagar** (Westinghouse) discussed experimental investigations of the band structure of Tin Telluride showing that this is probably a semimetal. R. W. **Ure** (Westinghouse) reported measurements on Bismuth Telluride containing excess tellurium, this material having a very much higher mobility at low temperatures than had been previously reported for material with other donor centres. D. L. GREENAWAY (R.C.A. Zurich) presented optical data on alloys of indium arsenide–indium telluride. The physical chemistry of these alloys was discussed by D. B. GASSON (A.E.I. Aldermaston) and correlated with the electron concentration. T. NIEMSYSKI (Warsaw) reported on the preparation of pure boron single crystals, G. BUSCH (Zurich) on the electromagnetic properties of rare earth selenides and tellurides, G. FISCHER (N.R.C., Ottawa) on optical properties of gallium sulphide, selenide and telluride, V. FREI (Prague) on the band structure of Cadmium Antimonide, as deduced from magneto resistance and optical data and H. J. VAN DAAL (Philips, Eindhoven) on the mobility of electrons and holes in hexagonal silicon carbide over the temperature range 77°K to 1400°K.

OPTICAL PROPERTIES

J. TAUC (Prague) in his review paper summarized existing methods and data and concluded by remarking that with the advent of lasers, we can look forward to the detailed investigation of a number of new optical phenomena.

E. BURSTEIN *et al.* (University of Pennsylvania) followed with a paper on free carrier magneto-optical phenomena at optical and microwave frequencies, showing the relation between Azbel-Kaner cyclotron resonance, ordinary cyclotron resonance and magneto-plasma resonance.

B. LAX *et al.* (Lincoln Laboratory) extended the Kramers-Heisenberg dispersion theory to obtain tensor components for inter-band transitions in the presence of a magnetic field and used these to obtain formulae for magneto-absorption and inter-band Faraday and Voigt effects.

S. M. DE VEER (Philips, Eindhoven) discussed measurements of infra-red absorption by free carriers in germanium and used these to estimate the sum of the acoustic and optical deformation potentials and to estimate band parameters.

H. EHRENREICH (G.E.C. Schenectady) presented a very detailed study of the reflectance, between 1 and 26 eV, of several elemental and compound semiconductors. The data led to information about the band structure several volts away from the normal band edges. In particular, transitions from d-band states were identified in several materials. A comparison with characteristic high energy electron losses showed that optical measurements could be used to infer plasma oscillation properties.

H. Y. FAN *et al.* (Purdue University) reported on a study of exciton and impurity spectra and the Zeeman splitting of these in the region of the band edge in Gallium Antimonide.

J. W. ALLEN (S.E.R.L. Baldock, England) described work on the optical spectra associated with excited states of copper in a number of semiconductors and showed that these led to information about the crystal fields. F. LUKES (Purkyre University, Czechoslovakia) reported reflectance measurements on semiconducting compounds and interpreted these in terms of band theory. M. LAX (Clarendon Laboratory, Oxford) discussed the influence of time reversal on the selection rules governing optical transitions between various points in the Brillouin zone.

In the second session, D. G. THOMAS (Bell Telephone Laboratories) presented a study of the Zeeman splitting of the intrinsic exciton spectrum of Cadmium Sulphide and obtained the effective mass and g values of holes and electrons, in this material. Evidence was also found for excitons being bound to ionized impurities.

Several papers on exciton phenomena were submitted. The one by E. F. GROSS *et al.* (Moscow) (not read at the meeting) described the effect of magnetic and electric fields and of uniaxial strain on the exciton spectrum in Copper Oxide. S. NIKITINE *et al.* (University of Strasbourg) also reported on similar effects. S. I. PEKAR (Kiev), discussed some interesting effects on the optical properties in the exciton absorption region, involving the existence of extra light waves in addition to those due to double refraction. H. HAKEN (Stuttgart) discussed the theory of the selection rules governing exciton absorption.

T. P. MCLEAN (R.R.E., Malvern, England) discussed the shape of the direct, indirect and split-off band conduction band edges in germanium in terms of a carrier lifetime limited by high energy phonon scattering.

S. ZWERDLING *et al.* (Lincoln Laboratory) reported on oscillatory magneto-absorption effects in indium antimonide. These established, in particular, the non-parabolicity of the electron and light hole bands, the effects of degeneracy on the valence band magnetic levels and the structure of excitons in high magnetic fields.

LATTICE VIBRATIONS

W. **Cochran** (Cavendish Laboratory, Cambridge) in his review paper emphasized the impetus which had been given to the subject by the experimental technique of neutron diffraction. This had provided a new stimulus to the theoretical aspects, which had been met by taking the polarizability and the long-range dipole interactions into account as well as the short range interatomic forces. The so-called shell model, in which the electrons and the core oscillate somewhat independently of each other, although not physically realistic, had led to good agreement between theory and experiment.

M. G. **Holland** (Raytheon) presented a study of the effect of a wide range of impurities on the lattice thermal conductivity of silicon. Some disagreement between the results and existing theories was found and presented in terms of the behaviour of a relaxation time associated with an unknown factor.

W. B. **Daniels** (Princeton University), in a paper on the anomalous thermal expansion of germanium, silicon and some zinc blende structure compounds, pointed out that some of the γ's (variation of frequency with compression) of individual transverse acoustic modes must be negative and that this presented a problem in the theory of lattice thermal conductivity.

Several papers on the relation between optical effects and lattice vibrations were presented. R. F. **Wallis** (U.S. Naval Research, Washington) developed a theory of optical absorption taking into account electric dipole moments and cubic anharmonic terms in the potential energy. Lattice absorption spectra were studied by T. **Deutsch** (Raytheon) in zinc sulphide and by D. L. **Stierwalt** (U.S. Naval Ordnance, California) in silicon, germanium and cadmium sulphide.

J. R. **Hardy** *et al.* (University of Reading) reported studies on semiconducting diamond which showed fine structure in the spectrum associated with bound holes. These were interpreted in terms of the carrier-optical mode interactions. Such effects are too weak to be observed except in the specially favourable case of diamond.

S. D. **Smith** *et al.* (University of Reading) discussed the interpretation of infra-red absorption spectra in diamond and obtained phonon energies at various symmetry points in the Brillouin zone for this material. Defects, introduced by irradiation, relaxed the selection rules, permitting normally forbidden one-phonon processes.

BAND THEORY

L. **Pincherle** (Bedford College, University of London) gave the review paper. He considered the problem of the sensitivity of band calculations to the assumed crystal potential for non-self-consistent calculations. There are some "sensitive" levels which change independently of the main group. He also considered (optimistically) the possibility of self-consistent calculations using the pseudo-potential approach. Correlation effects and various methods of band calculations were discussed and finally, some calculations for bismuth telluride, using the augmented plane wave method, were presented.

L. **Kleinman** (University of Pennsylvania) compared the crystal charge density obtained from a "directed valence orbital" model with that obtained from detailed band calculations and discussed the concept of the covalent bond.

J. C. **Phillips** (University of Chicago) presented the results of calculations of the energy bands of germanium at a large number of points in the Brillouin zone, using the pseudo potential approach, and used these in the interpretation of u.v. interband transitions.

G. **Della Riccia** (University of Naples) described the application of the electron network model of C. A. Coulson to the calculation of the band structure of complex crystals.

P. J. **Stiles** *et al.* (University of Pennsylvania) presented a study of Azbel-Kaner cyclotron resonance and De Haas–Van Alphen oscillations in *p*-type lead telluride. The valence band was found to consist of four [1,1,1] ellipsoids of revolution with a subsidiary degenerate minima at the centre of the zone. Effective mass values at these points were given.

J. **Callaway** (University of California) considered the transition between metallic and insulating states of an anti-ferromagnet, using the energy band theory of anti-ferromagnetism proposed by Slater. V. **Evtuhov** (Hughes, Malibu, California) analyzed the Landau levels in the valence bands of diamond type semiconductors and computed the cyclotron resonance quantum effects numerically for germanium subject to a magnetic field in the (001) direction.

D. HANEMAN (University of New South Wales) extended previous studies of free-surface dangling bonds to include such bonds at dislocations on diamond type semiconductors.

MAGNETIC PROPERTIES

G. A. BUSCH (Zurich) gave the review paper on magnetic susceptibility measurements on semiconductors. There were a number of contributions to the magnetic susceptibility, including the lattice contribution, impurity contribution and free carrier contribution. It was sometimes difficult to distinguish between these.

L. ESAKI (I.B.M., New York) discussed the effect, recently discovered by him, of the non-linear behaviour of the transverse magneto resistance at low temperatures in bismuth and bismuth–antimony alloys. There is a sudden change in the slope of the current-voltage characteristic at a certain high electric field. The effect is associated with the electron-phonon interaction, a large phonon emission taking place when the drift velocity of electrons and holes reaches a critical value and resulting in a drastic decrease in the scattering time.

G. LANDWEHR (Braunschweig, Germany) reported on the magneto-resistance of the narrow *p*-type space charge region adjacent to the grain boundary in a germanium bicrystal. The effect was found to be widely variable in magnitude and sign depending on temperature and the orientation of the magnetic field.

L. J. NEURINGER (Raytheon), measured the longitudinal magneto-resistance of *n*-type silicon in d.c. magnetic fields up to 90,000 G. Saturation above 40,000 G was observed for $\langle 110 \rangle$ and $\langle 111 \rangle$ directions but not for $\langle 100 \rangle$. Some size effects were found. Values of the mobility anisotropy parameter for the conduction band valleys were given.

C. YAMANOUCHI *et al.* (Electrotechnical Laboratory, Tokyo), presented results of the low field magneto-resistance in the impurity conduction region of *n*-type germanium. A theory, assuming that the effect is caused by a change in overlap integrals in the presence of a magnetic field, could explain only a part of the observed effect.

H. KAWAMURA *et al.* (University of Tokyo) discussed the broadening of the cyclotron resonance lines in *n*-type germanium due to carrier heating by r.f. and d.c. fields. For high carrier temperatures (the lattice being at helium temperature) there was a redistribution of electrons from hot valleys to cooler valleys due to intervalley scattering.

D. GEIST (University of Cologne, Germany) reported on electron spin resonance in boron. The *g* value was nearly equal to the free electron value.

H. MIYAZAWA (Toshiba Electric Co., Kawasaki) presented a series of very accurate measurements of the anisotropy of the Hall effect and of the magneto-resistance in *p*-type germanium over a wide range of temperature and magnetic fields. The results give information about the anisotropy of relaxation time in the valence band and should be useful in the development of transport theory for this band.

B. DONOVAN (Westfield College, London), discussed the anisotropic Faraday effect in *n*-type germanium as a function of frequency, magnetic field strength and specimen thickness.

RECOMBINATION

J. ZUCKER (General Telephone and Electronics, New York), reported on a study of the recombination of hot carriers generated by a microwave field. The cross section for electron capture was found to vary in a different way with speed for different recombination centres.

P. T. LANDSBERG (University College, Cardiff) discussed the non-equilibrium distributions of electrons in a non-degenerate semiconductor subject to optical excitation and radiative recombination. Corrections to the usually assumed quasi-Fermi distribution were obtained.

A. TORUN (Warsaw University) in his study of light emission from a reverse biased *p–n* junction, proposed a new hypothesis for the source, namely from the bremstrahlung of hot carriers in a Coulomb field of charge centres.

C. CONSTANTINESCU (Bucharest) investigated the temperature dependence of the recombination cross sections of copper and nickel centres in germanium. P. LAVALLARD (Ecole Normale

Superieure, Paris), presented high resolution measurements of recombination radiation from pure and doped indium antimonide. Effects associated with direct, phonon assisted and carrier tunnelling were observed.

S. G. KALASHNIKOV (Moscow) studied the lifetime of excess charge carriers in p- and n-type germanium as a function of the majority carrier concentration. The lifetime was found to vary in a non-monotonic way in both cases.

J. R. FASSETT (University of Minnesota) discussed the noise in semiconductors as a function of the lifetime, trapping time and dielectric relaxation time. In particular, certain "giant" fluctuations in the noise, observed in cadmium sulphide and selenide were accounted for.

CLOSING SESSION

Summaries of the experimental aspects of the Conference and of the theoretical were given by Dr. A. F. GIBSON (R.R.E. Malvern, England) and by Dr. R. J. ELLIOT (Clarendon Laboratory, Oxford), respectively.

The Washington Singer Laboratories,
The University,
Exeter,
Devon

J. R. DRABBLE

LETTERS TO THE EDITOR

Faulting in sodium azide

(*Received* 25 *October*, 1962)

In a recent paper Keating and Krasner(1) reported measurements of X-ray powder pattern diffraction line shapes and positions from sodium azide (NaN_3) after various treatments. In particular, they noted that after deformation, the line broadening was consistent with that expected from the formation of deformation stacking faults, but that the anticipated shifts in the peak positions could not be detected. The purpose of this communication is to suggest a possible explanation.

Sodium azide is rhombohedral, but the structure may also be described as hexagonal with *ABCABC* ... stacking, as in f.c.c. close-packed metals. The analysis of the diffraction effects due to stacking faults was given by Keating and Krasner, and is similar to that for f.c.c. structures.(2) Since there is a unique slip plane in sodium axide, no correction is needed for a multiplicity of slip planes and the powder pattern analysis is thus simpler than for the f.c.c. case.

If only intrinsic (or deformation) stacking faults are formed upon deformation or irradiation, then the application of the analysis by Keating and Krasner would be valid. However, if extrinsic (or double-deformation) faults are also produced, then the expected diffraction effects would have to be re-examined. Published work to-date indicates that in metals, intrinsic faults predominate. However, in other materials, the stacking fault energy of intrinsic and extrinsic faults may be of about equal magnitude (and possibly even less for the extrinsic faults). Such a situation appears to prevail in Si,(3) where intrinsic and extrinsic faults form in about equal amounts when the material is deformed in a suitable manner. Since sodium azide has a unique slip plane, the mode of deformation would not be too important in producing both types of faults if their energies were approximately equal.

The diffraction effects from extrinsic faults in f.c.c. structures have recently been calculated by Johnson.(4) He found that although the same reflections were shifted and broadened as for intrinsic faulting, the shift produced by a low density of extrinsic faults was in the opposite direction to that produced by intrinsic faults. If α' is the probability of an intrinsic fault and α'' is that of an extrinsic fault, then for small α the peak shift depends upon the difference $\alpha'-\alpha''$ and the broadening depends upon the sum $\alpha'+\alpha''$.(5) Consequently, for $\alpha' = \alpha''$, no net peak shift will be observed and the broadening will be double that from intrinsic faults only.

Thus on the basis of the supposition that (i) extrinsic stacking faults are at least as likely to form in sodium azide as intrinsic stacking faults and that (ii) the X-ray diffraction analysis for extrinsic stacking faults is applicable, one can explain qualitatively the results of Keating and Krasner.

Acknowledgement—I would like to thank the Office of Naval Research for financial support.

RIAS, Div. of Martin Marietta, Henry M. Otte
Baltimore, 12,
Maryland

References

1. Keating D. T. and Krasner S., *J. Phys. Chem. Solids* **20**, 150 (1961).
2. Warren B. E., *Progr. Met. Phys.* **8**, 147 (1959).
3. Aerts E., Delavignette P., Siems R. and Amelinckx S., *Electron Microscopy*, Academic Press, New York and London (1962), paper **B-3** (5th *International Congress for Electron Microscopy, Philadelphia* (1962); also *J. Appl. Phys.*, **33**, 3078 (1962).
4. Johnson C. A., *Acta Cryst.* (In press).
5. Warren B. E., personal communication.

Differential thermal analysis of yttrium iron garnet

(*Received* 7 *September* 1962)

The use of differential thermal analysis (DTA) techniques for the investigation of ferrites has been reported by other workers(1) but very little information is available about work carried out on ferrimagnetic garnet materials(2) especially in the temperature range above 1200°C. Technical difficulties, e.g. reactions of the sample with the thermocouple, electrical leakages, radiation effects, etc., have discouraged many investigators from applying the DTA method.

A simple DTA apparatus which overcomes these difficulties has been designed for measurements up to 1500°C, using platinum crucible sample holders.

A characteristic DTA curve obtained for yttrium iron garnet (*YIG, 37·5 mole per cent* Y_2O_3 and 62·5 mole per cent Fe_2O_3) is shown in Fig. 1.

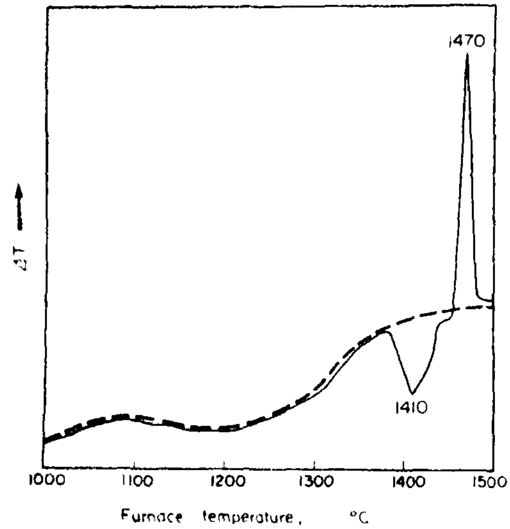

FIG. 1. Differential thermal analysis of yttrium iron garnet (37·5 mole per cent Y_2O_3, 62·5 mole per cent Fe_2O_3); heating rate 10°C/min; air 4 l/min; sensitivity 1/5; inert material Y_2O_3; dotted line, estimated base line.

In YIG no thermal reactions were expected or observed below 1100°C. Certain irregularities shown in the DTA curves between 1100°C and 1380°C were more probably due to base line drift than to thermal reactions. The first endothermic peak commencing at 1381°C with a minimum at 1410°C, corresponds rather closely to the phase change of haematite-garnet into magnetite-garnet observed by VAN HOOK[3] at 1387°C. The second peak, commencing at 1450°C, with a maximum at 1470°C coincides with the transformation of magnetite-garnet into garnet-liquid phase. VAN HOOK[3] reported the temperature of this phase change as 1467°C.

Samples of Y_2O_3 and Fe_2O_3 of varying molecular percentages were also made up not unlike those used for the construction of the phase diagram of Fe_2O_3–$YFeO_3$ by VAN HOOK[3] and DTA measurements carried out in an air atmosphere. The nature of the thermal reactions occurring throughout the series of experiments is shown in a simplified manner in Fig. 2.

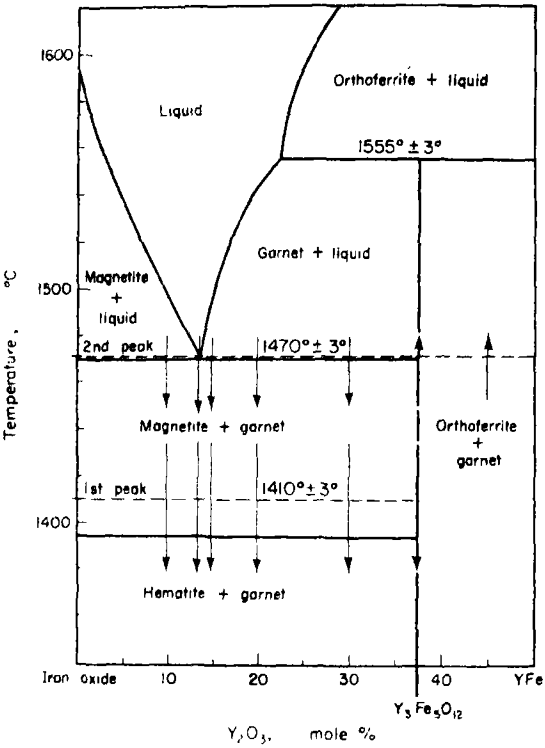

FIG. 2. Simplified diagram of DTA reactions in mixtures of yttrium oxide and iron oxide of various percentages; (superimposed on the original phase diagram of Fe_2O_3–$YFeO_3$ reproduced from Ref. 3;) ↑ exothermic reactions; ↓ endothermic reactions; the magnitude of arrows are indicating the commencement and the end of peaks; dotted line, peak temperatures in °C.

The first peaks with minima at 1410°C were endothermic up to the composition of YIG (37·5 mole per cent Y_2O_3) but not observed at 45 mole per cent Y_2O_3. This was found to be in agreement with the phase diagram of Fe_2O_3–$YFeO_3$[3] since only the orthoferrite-garnet phase was present.

The second peaks, commencing at 1450°C with minima at 1470°C were endothermic for composition below 37·5 mole per cent Y_2O_3, but exothermic for YIG. The same exothermic phase change was also found at 45 mole per cent Y_2O_3. This was not reported previously and probably indicates a certain transition of orthoferrite-garnet into the garnet-liquid phase.

According to the phase diagram of Fe_2O_3–$YFeO_3$^(3)^ at 13·5 mole per cent Y_2O_3 the magnetite-garnet phase transfers into liquid phase at 1467°C. This was also observed by DTA and shown in Fig. 2 with an extended arrow.

It is obvious from these measurements that quick information is yielded by the DTA method about the phase transition temperatures of YIG. With sufficient variation of the oxide ratios, it is possible to construct part of the phase diagram with considerable accuracy. The somewhat high temperature readings (especially in the case of the transition of haematite-garnet into magnetite-garnet) are caused by the prevailing dynamic conditions due to the standard heating rate of 10°C/min.

Further investigations of other rare earth and substituted garnets are in progress. A detailed study of this investigation as well as a description of the apparatus will be published at a later date.

R. G. Menzies Research Laboratory, J. BERETKA
Philips Electrical Industries,
Hendon, South Australia

References

1. JEFFERSON C. F., *U.S. Govt. Res. Rep.* **32,** 256 (1959); BERGSTEIN A. and CERVINKA L., *J. Phys. Chem. Solids* **18,** 264 (1961).
2. AHARONI A., FREI E. H., SCHIEBER M., *J. appl. Phys.* **32,** 1851 (1961).
3. VAN HOOK H. J., *J. Amer. ceram. Soc.* **44,** 208 (1961); **45,** 162 (1962).

The nature of the motion of N_2, CO and CH_4 in their β-quinol clathrates at low temperatures*

(*Received* 13 *August* 1962; *revised* 3 *October* 1962)

THE β-QUINOL clathrates provide convenient systems for the study of the rotational motion of the simpler polyatomic molecules in a fixed potential well which is presumably independent of temperature. COOKE and collaborators(1) found the magnetic susceptibility of O_2 in its β-quinol clathrate to be consistent with a free rotation model except at very low temperatures. Accordingly, VAN DER WAALS(2) included as a reasonable assumption in his statistical mechanical development of the thermodynamic equations for clathrates the feature of free rotation for the smaller guest molecules in the β-quinol cavities. MEYER, O'BRIEN and VAN VLECK(3) accounted for the magnetic susceptibility of clathrated oxygen below 4°K with a hindered rotator model having a barrier of 127 cal mole^{-1} which has been confirmed by paramagnetic resonance measurements.(4) Restricted rotation of N_2 in its clathrate has also been indicated by the temperature dependence of the pure quadrupole resonance spectrum measured by MEYER and SCOTT(5) who report a frequency of 52 cm^{-1} for the librational motion of N_2 below 25°K. In qualitative agreement with these results, PARSONAGE and STAVELEY(6) have observed a decreased rotational heat capacity at low temperatures for CH_4 in the β-quinol clathrate relative to gaseous CH_4, but conclude that "the methane molecules virtually rotate freely in their cells above ~150°K.(6)

We have recently completed the measurement of the heat capacities of several clathrates of N_2 and CO by which we have been able to corroborate the conclusions of MEYER and SCOTT(5) and, in addition, to obtain evidence for similar behavior for clathrated CO. This preliminary note communicates our results for the heat capacities at low temperatures and employs the restricted rotator model to account for the heat capacities of clathrated N_2 and CO, and the heat capacity of clathrated CH_4 reported by PARSONAGE and STAVELEY.(6)

We have found that the total heat capacities of the clathrates of N_2 and CO are linearly dependent on composition for yN_2 (or CO) · $(\beta\text{-quinol})_3$ where $0 < y < 1$. As a consequence, the molar heat capacities of each of the guest species are readily obtained from the heat capacity-composition isotherms at selected temperatures and have been plotted in Fig. 1 for the 15–100°K range.

To account for the dependence of these heat

---

* Supported in part by a grant from the National Science Foundation.

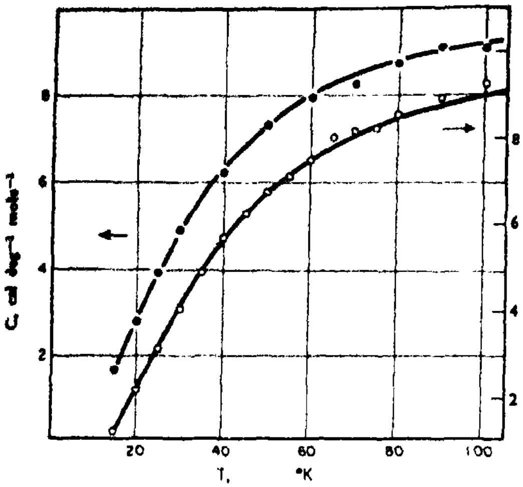

FIG. 1. Heat Capacities of N_2 and CO in β-quinol clathrates:

● —Experimental molar hear capacity for N_2 (left scale; ○—for CO (right scale)

Upper curve—$C_{(\mathrm{calc})} = C_{(3^\circ\ \mathrm{H.O.};\ \nu = 83\cdot4\ \mathrm{cm}^{-1})} + C_{(2^\circ\ \mathrm{H.O.};\ \nu = 37\cdot9\ \mathrm{cm}^{-1})}$

Lower curve—$C_{(\mathrm{calc})} = C_{(3^\circ\ \mathrm{H.O.};\ \nu = 97\cdot3\ \mathrm{cm}^{-1})} + C_{(2\ \mathrm{H.O.};\ \nu = 43\cdot1\ \mathrm{cm}^{-1})}$

capacities on temperature, we have assumed that the motion of the guest molecules in the approximately spherically symmetrical potential wells of the cavities consists of a rattling vibration characteristic of a three dimensional harmonic oscillator, and a librational motion as described by a two dimensional harmonic oscillator which approximates the restricted rotational behavior of N_2 and CO for the barriers and temperatures involved. In the case of clathrated N_2, the calculated heat capacity based on $\nu = 83\cdot4\ \mathrm{cm}^{-1}$ and $37\cdot9\ \mathrm{cm}^{-1}$ for the rattling and librational frequencies, respectively, is given by the upper curve in Fig. 1 and agrees well with the experimental data. For CO, the calculated heat capacity based on $\nu = 97\cdot3\ \mathrm{cm}^{-1}$ and $43\cdot1\ \mathrm{cm}^{-1}$ for the rattling and librational vibrations, respectively, also agrees with the experimental data up to 80°K as is demonstrated by the lower curve in Fig. 1.

For the barriers restricting rotation we obtain from $\nu_{(\mathrm{IIb})} = (V_0/2\pi^2 I)^{1/2}\ \mathrm{sec}^{-1}$, $V_0 = 511$ cal and 691 cal for N_2 and CO, respectively. Although the librational frequency for N_2, $37\cdot9\ \mathrm{cm}^{-1}$, based on the heat capacity data is only in fair agreement with the frequency, $\nu = 52\ \mathrm{cm}^{-1}$, found by MEYER,⁽⁵⁾ the relative magnitudes of the barriers for N_2 and CO are in accord with the larger collision diameter⁽⁸, ¹¹⁾ quadrupole and dipole moments of CO, which may be contributing factors.

Indication of the restricted rotation of CO in its quinol clathrate has also been obtained from the infrared absorption spectrum⁽⁹,¹⁰⁾ of the clathrate. BALL and MCKEAN⁽¹⁰⁾ have found an absorption at $2133\ \mathrm{cm}^{-1}$, $10\ \mathrm{cm}^{-1}$ below the band center of gaseous CO, which has been assigned to CO in restricted rotational states. In addition, at ~ 130°K several weaker absorptions have been noted including two at 2180 and $2195\ \mathrm{cm}^{-1}$ which have been tentatively interpreted⁽¹⁰⁾ as combinations of the fundamental with torsional and translational modes for which $\nu = 47$ and $62\ \mathrm{cm}^{-1}$.

We suggest that the former is to be associated with the librational (torsional) mode in view of the agreement with $\nu_{(\mathrm{IIb})} = 43\cdot1\ \mathrm{cm}^{-1}$ based on heat capacity data, and that the latter is to be identified with the rattling frequency for which the heat capacity data give $\nu = 97\cdot3\ \mathrm{cm}^{-1}$.

It is to be noted that exact agreement is not to be expected since the frequencies based on the heat capacity data hold only below 80°K, whereas the spectroscopic measurements were made at 130°K and above. With increasing temperatures it is to be expected that the librational frequency will be larger,⁽¹¹⁾ and it is also plausible that at higher temperatures increasing anharmonicity may modify to some extent the rattling frequencies as well.

The heat capacity of clathrated CH_4 reported by PARSONAGE and STAVELEY⁽⁶,⁷⁾ may also be analyzed in a similar manner as the sum of the heat capacities of a three dimensional harmonic oscillator with $\nu = 160\ \mathrm{cm}^{-1}$, presumably the rattling frequency, and a second three dimensional harmonic oscillator with $\nu = 56\cdot5\ \mathrm{cm}^{-1}$, tentatively associated with the librational motion. Although it is likely that the frequencies of two of the modes of libration differ from the third for reasons of symmetry, and this may also be the case for the rattling motion in all clathrates as well, it appears that the approximations involved are sufficiently accurate to account for the heat capacity of CH_4 up to 50°K in a satisfactory manner as is indicated in Fig. 2. For the barrier restricting rotation we obtain $V_0 = 193$ cal mole^{-1}.

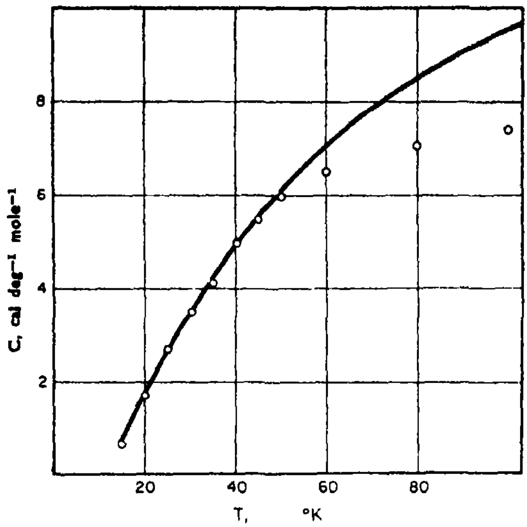

FIG. 2. Heat Capacity of CH_4 in the β-quinol clathrate: ○—Experimental molar heat capacity, PARSONAGE and STAVELEY.(6)

Solid curve—$C_{(calc)} = C_{(3^\circ\ H.O.;\ \nu = 160\ cm^{-1})} + C_{(3^\circ\ H.O.;\ \nu = 56{\cdot}5\ cm^{-1})}$,

As is to be expected for this low barrier the divergence between the calculated and experimental heat capacities occurs at a lower temperature than is found to be the case with N_2 and CO.

Department of Chemistry, L. V. COULTER
Boston University, G. L. STEPAKOFF
Boston, Massachusetts G. C. ROPER

References

1. COOKE A. H., MEYER H., WOLF W. P., EVANS D. F. and RICHARDS R. E., *Proc. Roy. Soc.* **A225,** 112 (1954).
2. WAALS J. H. VAN DER, *Trans. Faraday Soc.* **52,** 184 (1956); WAALS J. H. VAN DER, and PLATTEEUW J. C., *Advanc. chem. Phys.* **2,** 1 (1959).
3. MEYER H., O'BRIEN M. C. M. and VAN VLECK J. H., *Proc. Roy. Soc.* **A243,** 414 (1957).
4. FONER S., MEYER H. and KLEINER W. H., *J. Phys. Chem. Solids* **18,** 215 (1961).
5. MEYER H. and SCOTT T. A., *J. Phys. Chem. Solids* **11,** 215 (1959).
6. PARSONAGE N. G. and STAVELEY L. A. K., *Mol. Phys.* **3,** 59 (1960). Also see GREY N. R., PARSONAGE N. G. and STAVELEY L. A. K., *ibid.* **4,** 153 (1961).
7. PARSONAGE N. G. and STAVELEY L. A. K., *Mol. Phys.* **2,** 212 (1959).
8. HIRSCHFELDER J. O., CURTIS C. F. and BIRD R. B., *Molecular Theory of Gases and Liquids,* p. 1111. Wiley, New York (1954).
9. ROCK P., Unpublished observation, this laboratory. The fundamental at 2130 cm^{-1} has been observed at ~ 100°K.
10. BALL D. F. and MCKEAN D. C., *Spectrochim. Acta,* **18,** 933 (1962).
11. WAALS J. H. VAN DER, *J. Phys. Chem. Solids,* **18,** 82 (1961).

BOOK REVIEW

Progress in Materials Science (incorporating **Progress in Metal Physics**), Vol. 9. (Edited by Bruce Chalmers), Pergamon Press, New York, 1961. 386 pp., $20.00.

WITH this appearance of the ninth volume, the well-known series "Progress in Metal Physics" has undergone a change of title to "Progress in Materials Science", probably attempting to reflect the trend at many universities toward broadening the Metallurgy curriculum into a Materials Science program. Furthermore, according to a new procedure, articles will also be sold individually, in paper backing.

The present volume does not yet reflect any broadening of subject matter to match the new title; all of the articles still fall into the category of "Metal Physics". A perusal of this volume shows that publication was held up for some time, since most articles cover the literature fully only up to 1959. Articles in the more active fields, such as nuclear magnetic resonance and plastic deformation, were therefore somewhat out of date at the time of publication.

The first article, called "Nuclear Magnetic Resonance in Metals", is an excellent review by T. J. ROWLAND, a leading contributor to that field. The topic is completely new to the series, and is a most welcome one in view of the important contributions that resonance techniques have made to the study of metals and alloys. The second article, "Effect of Temperature and Alloying Additions on the Deformation of Metal Crystals", by R. W. K. HONEYCOMB, is a fine review emphasizing experimental observations. Unfortunately, the article was written too early to cover recent developments, particularly on the use of transmission electron microscopy. For example, the current conflict between the Cambridge and Stuttgart groups on the nature of work hardening is not covered.

The next two articles become involved in more specialized topics in the field of mechanical properties of metals. The article by I. R. KRAMER and L. J. DEMER reviews the "Effects of Environment on Mechanical Properties of Metals" in a comprehensive manner. The article could have been even more valuable if the topic were broadened to include the related work on environmental effects on nonmetallic crystals, in the spirit of the new title for the series. Following this article, P. COTTERILL reviews the complex field of "Hydrogen Embrittlement of Metals". He sorts out the principle experimental observations on a wide range of materials. Finally, he attempts to develop a general theory of hydrogen embrittlement by considering conditions under which micro-cracks can arise and be propagated.

In the last article, J. M. SIVERTSEN and M. E. NICHOLSON take a comprehensive look at the subject of solid solutions from the classical point of view. Emphasis is placed on what can be learned from lattice parameters, heats of solution, X-ray diffuse scattering, and electrical resistivity. There is almost no mention of the newer techniques, in particular those now being used to study the Fermi surface.

In all, this book continues the tradition of the earlier "Progress in Metal Physics" series in providing coverage of the important and active fields in metal physics and physical metallurgy. This reviewer cannot help, however, in commenting upon the price of $20.00 for a 386-page volume. Such a price is quite inconsistent with the cost of similar books by other major publishers. It is not inconsistent, however, with the past performance of this particular publisher, who has always evinced a callous disregard for the needs of the scientific community. Particularly because of the value of this series to students, the price of future volumes should be brought more into line.*

A. S. NOWICK

---

* Sub-Editors footnote:

As the reviewer points out in the first paragraph of his review, under new publishing procedure for this series, separate articles are available in paperback form precisely so as to make them easily accessible to students.

J. Phys. Chem. Solids Pergamon Press 1963. Vol. 24, pp. 175–186. Printed in Great Britain.

CHARGE TRANSFER CONTROLLED SURFACE INTERACTIONS BETWEEN OXYGEN AND CdSe FILMS

G. A. SOMORJAI
IBM Research Center, Yorktown Heights, N.Y.

(*Received* 10 *July* 1962; *revised* 1 *October* 1962)

Abstract—The interaction of oxygen with CdSe surfaces has been studied with thin films of CdSe evaporated in ultra high vacuum in the temperature range 0–360°C and pressure range 10^{-4}–10 mm Hg. The effect was monitored via conductivity measurements, carried out *in situ*. When oxygen is introduced, the initially "clean" film undergoes an instantaneous irreversible chemisorption followed by a slow uptake which is also irreversible in the studied temperature range. This interaction brings about a 3–5 orders of magnitude decrease in the conductivity of the *n*-type film, i.e. oxygen exhibits acceptor-like properties. The rate of the slow irreversible oxygen uptake can be expressed as $dN/dt = kP_{O_2}^{1/4}\exp(-bN)$ and the activation energy for the process has been measured. Donor type weakly adsorbed oxygen was also found to be present on CdSe films which could be reversibly removed from the surface; this reaction was also accompanied by charge transfer and was strongly pressure dependent. The heat of reaction for this process is 12 kcal/mole. The boundary layer theory was evoked to explain the kinetics of the slow uptake of the acceptor-like oxygen. Attempts have been made to explain the mechanism of the different surface reactions.

INTRODUCTION

THE electrical properties of semiconductor surfaces are sensitive to changes in the composition and pressure of the ambient atmosphere. The interaction which takes place between the semiconductor and the adsorbed gas atoms or molecules can induce permanent chemical changes of the semiconductor surface and can drastically change the distribution of charge carriers in the solid.

It has been known(1) for sometime that oxygen has a large effect on the surface properties of germanium. This effect has been studied rather extensively(2, 3) and it was concluded that oxygen which adsorbs on the germanium surface dissociates,(4) can act either as an acceptor(5) or as a donor(6) depending on the pressure of the gas and on certain physical properties of the studied material. Since oxygen changes the electron density of the solid at the surface by adsorption, electrical resistance measurements prove to be(7) very effective in the study of the mechanism of gas uptake on semiconductors.

Compound semiconductor surfaces have been studied(8, 9) to a lesser extent since the chemistry of a two component system is more complex. The stoichiometry of the semiconductor compounds may also vary and therefore alter electrical properties which are known to be sensitive to minute impurities or deviations from stoichiometry. In these materials, preparation of well defined surfaces may be more difficult. This has been demonstrated clearly by studies of ZnO(10) and CdS,(11) etc. However, little is known about the surface properties of II–VI compounds or about their oxidation kinetics which is of great importance in determining their electrical(12) and photoelectrical(13, 14) properties. Only ZnO(15) has been studied to a greater extent. The purpose of this paper is to report on the surface properties and oxidation mechanism of one representative of the II–VI compounds, cadmium selenide.

It is apparent that the higher the surface to bulk ratio of a studied semiconductor the more sensitive it becomes to changes due to interactions on its surface. Therefore, it is of advantage to use evaporated thin films for investigations of this kind. Another important factor in surface studies is the cleaning of the exposed surface. This may be done by ion bombardment(16) or, heating the sample in vacuum(17) just below its melting point to drive off the adsorbed gases by evaporating a few monolayers of the solid itself. These methods, although giving the expected result, may drastically change the surface structure. Crushing of single crystals in vacuum(2) and the measurement of gas adsorption on the freshly created surfaces has been another important technique to study surface interactions; unfortunately, the nature of this latter method makes sensitive electrical measurements on the sample very difficult to perform.

The experimental technique used to study the surface reactions of CdSe has been to evaporate thin films of CdSe in ultra-high vacuum (10^{-8}–10^{-9} mm Hg) and to measure the electrical resistance of the films *in situ*. At these pressures the surface stays monolayer-free for a few minutes and allows one to study the surface interactions on initially clean samples with large surface to bulk ratio. In this way, surface properties are enhanced and easily separated from bulk interactions which might also take place in the studied temperature and pressure range.

In this work the reactions of oxygen with CdSe surfaces were studied in the temperature range of 0–360°C and O_2-pressure range of 10^{-4} mm Hg to 10 mm Hg. The reactions were monitored by electrical conductivity measurements in the dark. The kinetics of oxygen chemisorption and weak adsorption were derived from the experiments since it was found that both processes involved charge transfer between the solid and the adsorbed species.

EXPERIMENTAL PROCEDURE

The experimental apparatus and the magnified reaction vessel is shown in Fig. 1. Heating of the quartz crucible was done from the outside by a ring-like roll of platinum wire coated with alundum for good insulation. This small heater was pulled onto the finger shaped quartz crucible and

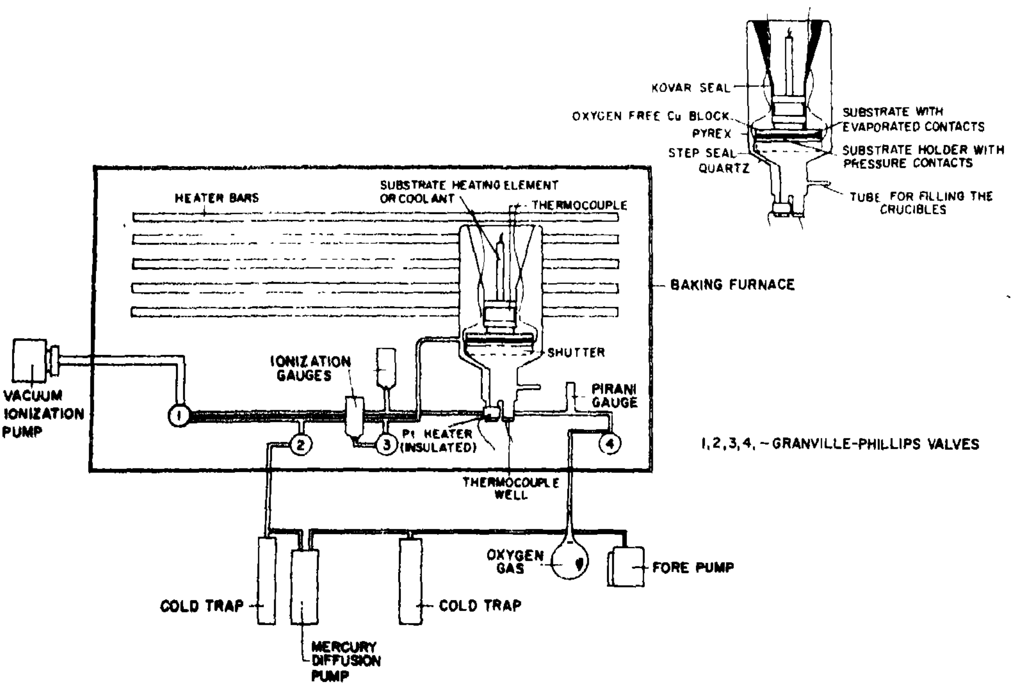

FIG. 1. High vacuum system and reaction vessel.

was resistance heated. By external heating of the CdSe power, the vapor pressure of the heating element which is generally a source of film contamination during evaporation was not introduced into the experiment at all. Evaporating the CdSe from the quartz crucible was possible only because of the high vapor pressure(18) of the material at relatively low temperatures. Evaporation temperature was generally between 600–700°C at which CdSe has a vapor pressure(18) 10^{-2}–10^{-1}mm. Since the softening point of quartz is over 1300°C and it does not react with CdSe in vacuum, it has proven to be a practical container for evaporation of CdSe.

As can be seen from Fig. 1, the substrate can be heated or cooled easily through the copper block by a small resistance heater or by pouring liquid N_2 (or liquid He) onto the block. A stainless steel shutter blocks the substrate from the source and prevents condensation on the substrate while the source is being degassed.

The source temperature was monitored by a thermocouple placed in a small pit in the middle of the quartz crucible from the outside. Initial calibration showed a 3° difference in temperature reading by placing the thermocouple outside instead of inside the crucible. Substrate temperature was measured by placing the thermocouple against the Cu-block from the outside and/or by substituting two leads from the four which made pressure contacts to the sample by thermocouples to measure directly the substrate temperature. There was no detectable difference in temperature reading between the two arrangements after the Cu-block has achieved equilibrium; therefore, in most cases, the former arrangement was used, which is more convenient experimentally. The source and substrate temperatures were monitored continuously. Prior to evaporation of the purified CdSe the system was baked out at 350°C for 6–18 hr. After cooling the ambient pressure was generally in the 10^{-9}–10^{-8} mm range. Substrate temperature was kept at 25°C for all the evaporations. Evaporation rate was generally in the order of 10 Å/sec.

Electrical resistance measurements were made in the dark by either two or four probe techniques. The two types of measurements gave identical results in trial runs, hence the two probe technique was used mostly throughout the experiments since it can be assembled with less difficulty. The circuit consists of a highly filtered d.c. power supply (ripple less than 20μV) with a reversing switch whose purpose was to check for rectifying contacts. The voltage can be varied from 0·1 to 100 V. The current was monitored by an electrometer (Keithley 610 A). Measurements were generally made at $V = 1$ V.

Since the direction of the applied voltage is parallel to that of the surface on which oxygen uptake occurs it should have minimal influence on the surface reactions.

Film characteristics

The film thickness varied between 2000–8500 Å from film to film and each had a thickness uniformity within 80 Å. Thickness measurements were made after each experiment by multiple beam interferometric technique.(19) The thickness could be controlled accurately by monitoring the conductivity change of the condensing film during the evaporation. X-ray data showed that the deposited film has a highly oriented hexagonal structure with the *c*-axis normal to the substrate plane, since the strongest line corresponds to the 002 face.

CdSe has been reported as dissociating in the vapor phase(18) like many other II–VI compounds.(20) However, only stoichiometric CdSe could be detected by standard spectroscopic and chemical analytical tools as the film constituent. An important experimental problem is the reproducibility of the film stoichiometry. In order to make the film stoichiometric, the source material must also be stoichiometric. It was found that vacuum baking of CdSe containing either large excesses of Cd or of Se improves the stoichiometry of the compound. The CdSe source material bake-out and evaporation temperature were identical.(21)

The evaporated films show high conductivity in the order of 1–10 $(\Omega\ \text{cm})^{-1}$ which is interpreted as indicative of high vacancy concentration of the film. The CdSe films are weakly photoconductive. The light to dark conductivity ratio was about 2–3 throughout the experiments. It is also known(22) that photodesorption or adsorption of gases also occurs on such films, hence, for the sake of reproducibility of the measurements, light should be excluded. The samples were observed to rectify only after successive oxygen treatments at the highest temperatures (360°C).

The film mobility was determined by Hall coefficient measurement. Samples which had been exposed to oxygen only at room temperature gave mobilities of 50 cm^2/V sec; films heat treated in oxygen at the highest experimental temperatures gave values of 10 cm^2/V sec. This variation is presumably due to increased impurity scattering of electrons; in order to calculate the concentration of electrically active oxygen atoms as a function of temperature and heat treatment, the corresponding mobilities were used.

The sign of the charge carrier was determined by Dember measurements.[23] This method was found to give a rapid and very accurate check on the studied films.[24] In all cases the CdSe films were reproducibly *n*-type and remained *n*-type throughout the experiments.

It should be noted that neither chemical analysis nor X-ray studies detected oxide formation or change of the film stoichiometry; it was therefore concluded that the amount of oxide which was formed by the reactions of CdSe film with oxygen is below the detection level of these analytical methods.

Reaction with oxygen

The ultra-high vacuum evaporated films were brought in contact immediately with oxygen at room temperature since it takes minutes at the applied ambient pressure (10^{-9}–10^{-8} mm) to produce a monolayer coverage of a gas other than oxygen on the surface. Absorption was followed by monitoring the change in the film resistance. The reaction bulb was then evacuated and the film heated to a desired temperature between 0–360°C. Thermal equilibrium was established and O_2 gas of known pressure was admitted to the reaction vessel. The film resistivity and pressure changes were observed as a function of time. After the reaction was complete the oxygen gas was pumped off to test the reversibility of the solid–gas interaction at the experimental temperature. The same procedure was repeated at different gas pressures and/or film temperatures.

In order to make sure that oxygen alone is responsible for the changes in the sample resistance, after the uptake of an O_2 monolayer at room temperature, the film was heated and cooled several times in ultra-high vacuum. These heat cycles followed the pattern of the experiments performed generally with oxygen gas in the bulb. No change in the initial conductivity was observed after the heating cycles were completed. This was accepted as an indication that the effect of possible electrode diffusion into the film is negligible in the studied temperature range and particle sintering does not effect the film electrical characteristics.

EXPERIMENTAL RESULTS

By "irreversible" oxygen effect, we mean that the oxygen which has reacted with the CdSe film at a given temperature and pressure and has markedly changed the sample resistance cannot be removed *at the same temperature* by continued pumping in ultra-high vacuum. Hence, its effect on the sample resistance cannot be reversed. On the other hand, in the case of a "reversible" oxygen effect, all changes caused by the interactions between the CdSe film and oxygen gas at a temperature, T, can be fully reversed at the same temperature.

Furthermore, if the number of oxygen atoms reacting with the film are of the same order of magnitude as the number of electrons in the conduction band of CdSe, large changes in the film conductivity are expected. This seems to be the case for the system under study.

Figure 2 shows the experimental observations in sequence. One can divide the observed oxygen effects tentatively into two parts to make their discussion easier: One part relates to the irreversible acceptor action of oxygen, the other relates to the reversible donor action. In turn the irreversible acceptor action can be divided into two parts as follows:

I(a) Rapid and irreversible oxygen uptake at room temperature—and pressures 10^{-2}–10 mm*—acceptor action*

The freshly evaporated films had conductivities of the order of 1–10 (Ω cm)$^{-1}$. When oxygen gas was admitted at room temperature the conductivity decreased extremely rapidly by approximately one order of magnitude. This effect is so fast at room temperature that the kinetics of this reaction cannot be followed.

I(b) *Slow irreversible uptake of oxygen between* 50–360°C *and pressures of* 10^{-4}–10 mm—*acceptor action*

After the initial oxygen uptake at room temperature was completed as indicated by 1a on Figure 2, the system was evacuated and the CdSe film was heated to a temperature between 50–360°C in high vacuum. After equilibrium was reached, oxygen gas of known pressure was admitted. Figure 3 and the middle section of Fig. 2 show the type of conductance changes which take place. The conductance diminishes irreversibly by several orders of magnitude during the uptake. The actual magnitude of the conductance decrease is a function of the temperature; a higher film temperature effects a larger conductance change. For the first 5 min the conductance change is rapid, then it slows down and the reaction goes to completion in less than an hour, except at lower temperatures where it may take somewhat longer. The initial rate of oxygen uptake is also pressure dependent; the higher the oxygen pressure the faster the CdSe film reaches its new, lower conductance equilibrium value.

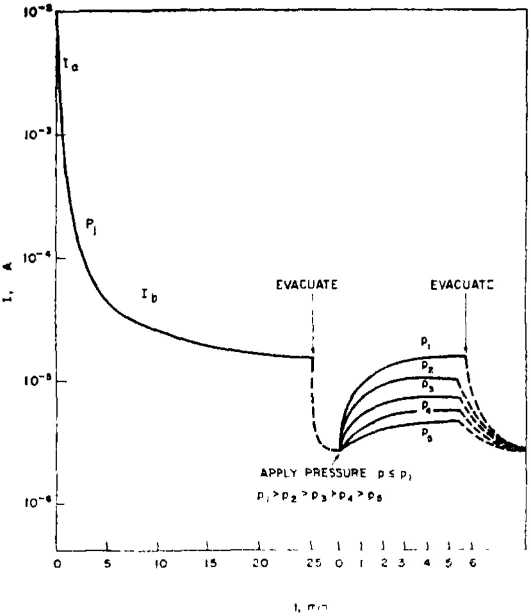

FIG. 2. Reversible and irreversible conductance changes on clean CdSe film saturated initially at $P_{O_2} = p_1$. $V = 1$ V, $d' = 2{\cdot}7 \times 10^{-5}$ cm.

This irreversible conductance change appears to be the dominant effect in the interaction of oxygen with the CdSe film. This irreversible change can be further increased by an increase in oxygen pressure. The reversible effect discussed below is superimposed upon this. CdSe films which have undergone the irreversible change resulting in a permanent decrease of the film conductivity will be called oxygen "saturated" films. It was also found that upon heating the oxygen saturated CdSe films to above 630°C fast desorption of the adsorbed oxygen takes place which is indicated by a large pressure and conductivity increase. Unfortunately, these measurements can give only qualitative results because the observed magnitudes of the conductivity changes were irreproducible due to the probable partial evaporation of the CdSe film, electrode diffusion or oxidation reactions which could all become appreciable above 600°C.

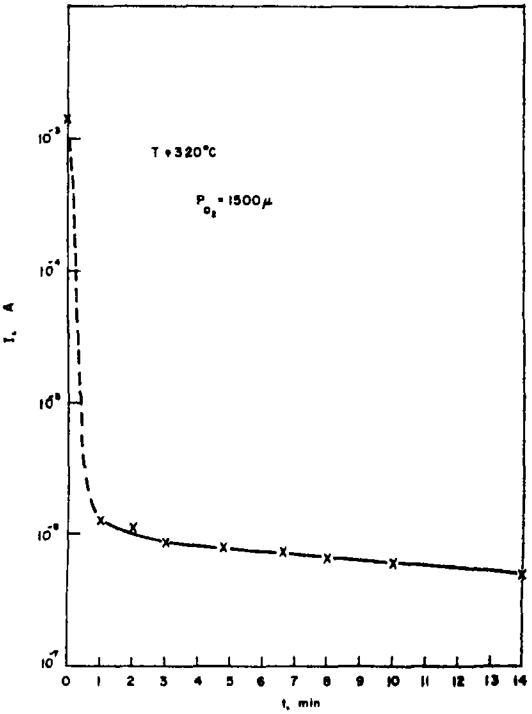

FIG. 3. Conductance change of CdSe "clean" film upon introduction of oxygen gas ($T = 320$°C; $p_{O_2} = 1{\cdot}5$ mm, $V = 1$ V, $d' = 3{\cdot}2 \times 10^{-5}$ cm).

Below 50°C, this slow irreversible effect cannot be observed. The CdSe film conductance remains unchanged for weeks at these temperatures.

II(a) Reversible uptake of oxygen between 100–360°C *and pressures of* 10^{-8}–10 mm—*donor action*

If one saturates a CdSe film with oxygen at a certain temperature and oxygen pressure and then evacuates the reaction vessel, the conductivity decreases by about one order of magnitude (Fig. 2). If oxygen is admitted again at pressures less than or equal to the saturation pressure one gets a conductivity increase proportional to the pressure. By pumping out the admitted oxygen again, the CdSe film returns to its lower vacuum conductivity value. This effect is also illustrated by Fig. 2.

This reaction can be repeated many times and it remains reversible as long as the pressure does not exceed the oxygen saturation pressure. Since oxygen increases the conductivity of the film, it appears to be acting as a donor. By contributing electrons, it increases the electron density of the film. Figures 4 and 5 show the reversible conductivity changes as a function of pressure. If one applied an oxygen pressure larger than the saturation pressure ($P \geqslant 1600\,\mu$, $T = 360$°C in Fig. 4), the dashed curves in Fig. 4 result. A distinct maximum appears on the conductivity curve, and then the conductivity drops slowly below the initial vacuum conductivity and obtains a new lower equilibrium conductivity in about 1 hr. This effect is irreversible again; the new vacuum conductivity value is the one that would be obtained by initially applying this pressure to an unsaturated film. Similar effects can be observed if one interrupts the irreversible saturation of the CdSe film at a pressure P_1, by suddenly introducing a larger oxygen pressure P_2. Figure 6 shows the effect. A small conductivity increase takes place first and then a further, somewhat accelerated, conductivity decrease continues. The hump is due to the increased concentration of donor type oxygen which is then mostly converted to acceptor type species. The final conductivity value obtained by increasing the saturation oxygen pressure from P_1 to a larger P_2 during saturation is the same as one would obtain by starting out the saturation at an oxygen pressure P_2. This is illustrated in Fig. 6 by the dotted line.

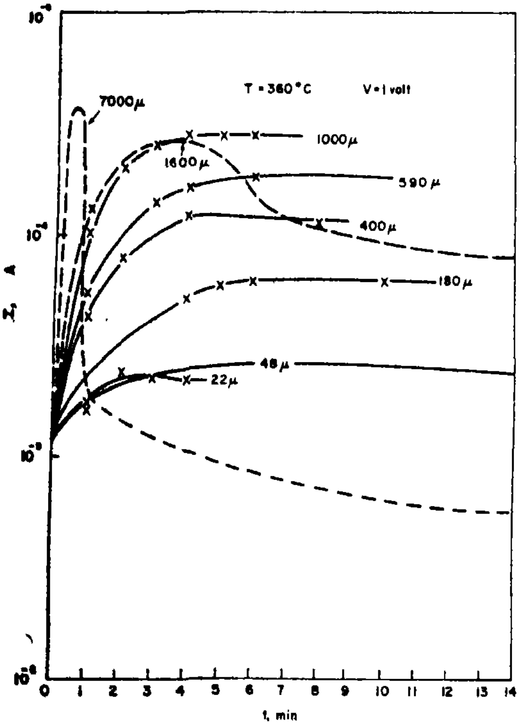

FIG. 4. Donor type oxygen interaction on oxygen saturated CdSe films.

Over $T = 100$ C at a given pressure, the oxygen reaction is virtually completed after 30 min. However, the irreversible conductivity decrease was still observable at $T = 50$°C to produce marked changes in the CdSe film resistance, although it may take days to reach equilibrium.

DISCUSSION

(a) *Irreversible oxygen uptake*

The relatively rapid change in conductivity due to the presence of oxygen, its pressure dependence, and the observed desorption of the gas above 630°C suggest that the chemisorption of oxygen on the CdSe lattice takes place. It should be emphasized that there may be several reactions taking place simultaneously which are either fast or do not result in charge transfer and hence, cannot be detected by our dark conductivity measurements.

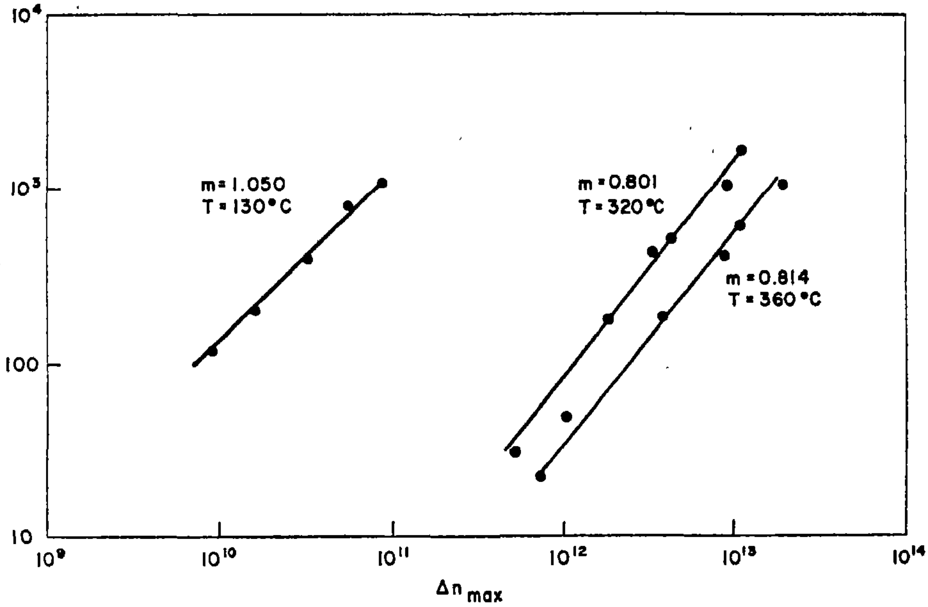

FIG. 5. The pressure dependence of the reversible O_1 uptake rate on oxygen treated CdSe film. *m* is the slope.

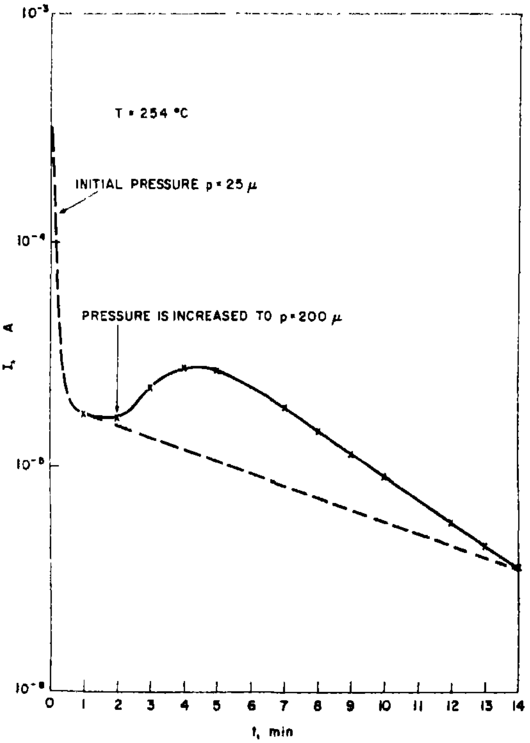

FIG. 6. Conductance change of CdSe "clean" film interrupted by increase of the ambient pressure ($T = 254$°C, $V = 1$ V).

Plots of the current versus the logarithm of time for the slow irreversible uptake gave straight lines indicating that a relationship

$$-bI = \log t + c \qquad (1)$$

holds, where b and c are constants at a given temperature and pressure, and t is the time in minutes. Figures 7 and 8 show the experimental results for two different temperatures. The data were corrected for film geometry variations. The rate of conductivity change and hence, the adsorption rate of oxygen is pressure and temperature dedependent. It was found that the rate of additional oxygen adsorption on CdSe films which had previously been saturated with oxygen at a lower pressure is less than the rate of oxygen adsorption on unsaturated films. Therefore, in order to compare rates and to find the pressure dependence of the process only those experimental data were plotted in Figs. 7 and 8 which were taken on

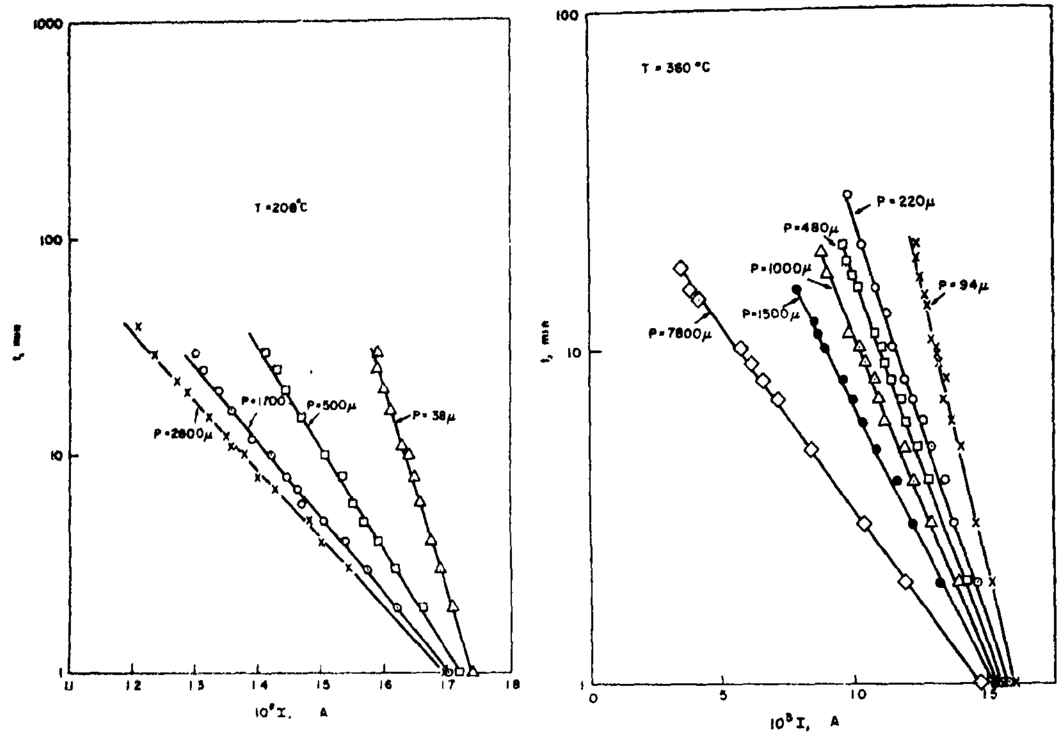

FIGS. 7 and 8. Irreversible conductance change at several oxygen pressures at $T = 208°C$ and $360°C$ on a log t vs. I plot.

nitially unsaturated, "clean" films. From equation (1):

$$-\frac{dI}{dt} = \frac{1}{bt}. \qquad (2)$$

b, the slope in equation (1), is pressure dependent as can be seen in Figs. 7 and 8. The pressure dependence of the rate can be found by plotting the logarithm of the pressure as a function of the logarith of the rate, $-\frac{dI}{dt}$, as is shown in Fig. 9. Hence, the pressure dependence can be expressed as

$$-\frac{dI}{dt} = P_{O_2}^{1/4} \qquad (2')$$

in the temperature and pressure range studied. From Fig. 9 one can obtain ΔH for the irreversible oxygen uptake at a given pressure by using the

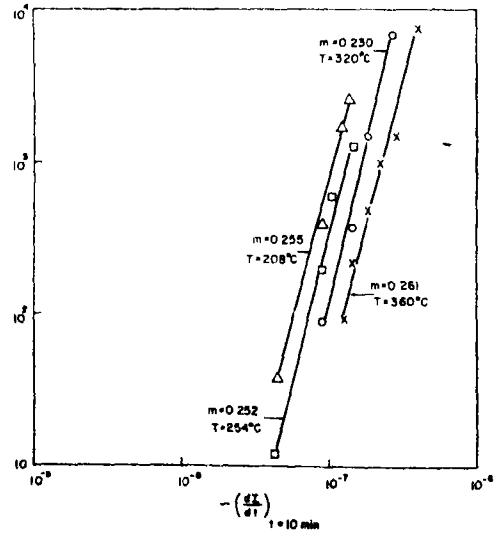

FIG. 9. The pressure dependence of the irreversible oxygen uptake rate on CdSe film. m is the slope.

Arrhenius equation; the results are given in Table 1. ΔH increases somewhat with increasing temperature which might be an indication that the surface coverage increases at elevated temperatures.(4) The lack of gas adsorption measurements does not permit one to find a relationship between the surface coverage and the change in ΔH.

Table 1. *Heat of activation for the slow irreversible oxygen uptake calculated by Arrhenius equation*

T°C	ΔH (kcal/mole)
208–254	2·10
254–320	2·46
320–360	5·06

In order to express equation (1) in terms of changes in the surface charge concentration I should be converted into σ, the conductivity. [$-L = 0\cdot32$ cm, $A = 1\cdot5\times10^{-4}$ cm^2 for $d' = 2\cdot8\times10^{-5}$ cm and $V = 1$ V]. Then, $\sigma_{\text{surface}} = \sigma\cdot d'$ where d' is the film thickness. Since $\sigma_{\text{surface}} = n_s e\mu_s$, where n_s and μ_s are the surface charge carrier density and surface mobility, respectively, then $n_s = \dfrac{\sigma\cdot d'}{e\mu_s}$. If one makes the assumption that the mobility change during the irreversible oxygen uptake is small, equation (1) can then be expressed as

$$-B'n_s = \log t + c \qquad \text{and}$$

the rate of depletion of charge carriers at the surface due to oxygen uptake is

$$-\frac{dn_s}{dt} = ke^{B'n_s} \tag{3}$$

where $k = e^c/B'$.

Table 2 gives the values of B' for different pressures and temperatures. Charge concentration changes in the film were calculated from the difference of the conductivities in *vacuum* before and after oxygen uptake.

The type of rate law given by equation (3) seems to describe many adsorption processes(25) especially those which take place on semiconductor surfaces.(26) Oxygen on germanium(2) and on zinc oxide(3) show similar adsorption characteristics to CdSe and have been studied extensively. In order to explain the experimental dependence of the adsorption rate on the concentration of adsorbed species, HAUFFE(27) and WEISZ(28) formulated the "boundary layer" theory according to which any reaction where electron transfer through a potential barrier is the rate determining step, one expects the rate to be exponentially dependent on the concentration to give the type of rate law which was obtained in equation (3). In the case of oxygen adsorption electrons are transferred from the solid to the adsorbate because of the difference in chemical potential. As a consequence a potential is induced at the surface(29) in such a manner as to oppose further electron transfer from the bulk to the surface. The potential energy associated with this barrier is higher for a large charge concentration at the surface.*

Table 2. *Values of* B' *as a function of pressure and temperature*

P_μ	T°C	$B'\times10^{+11}$ (cm^2)
38	208	9·22
500	208	4·44
1700	208	3·36
2600	208	2·98
12	254	9·60
200	254	4·56
600	254	3·86
1300	254	2·78
90	320	1·51
380	320	0·941
1500	320	0·762
7000	320	0·521
94	360	1·08
220	360	0·957
480	360	0·763
1000	360	0·624
1500	360	0·500
7800	360	0·354

It is apparent that the freshly evaporated high conductivity CdSe films have an accumulation layer present at the surface although one cannot measure this in the given experimental conditions. This accumulation layer is produced by the high vacancy concentration of the film which has been created during evaporation. In the fast irreversible process these donors react with the oxygen atoms and upward band bending occurs at the surface of the n-type CdSe. If adsorption stops at the flat band condition the slow rate of the slow irreversible oxygen adsorption cannot be explained unless one postulates electron relaxation times of the order of 30 min at 300°C, a condition which is not likely to exist. Therefore, it is suggested that as oxygen adsorption proceeds, band bending upward at the surface of the film continues and gives rise to the formation of a depletion layer. The potential barrier thus created, controls further electron transfer and accounts for the decelerated rate of irreversible gas uptake to give the rate law of equation (3).

---

* It has been called to our attention recently that KRUSEMEYER and THOMAS (*J. Phys. Chem. Solids* **4**, 78 (1958)) have presented a general treatment of the charge transfer assuming the Langmuir adsorption model.

One can calculate the excess charge concentration at the surface, i.e. in the so called boundary layer by integrating the Poisson equation with suitable boundary conditions. Without presenting the detailed integration which has been given elsewhere,(29) one finds good agreement between the B' calculated from the theory for reasonable values of the physical constants of the system and the experimental B' values listed in Table 2. The experimental results are insensitive to changes in k, hence, direct comparison with that calculated from the theory is of little value.

If a full layer of unreacted oxygen has adsorbed, the concentration of oxygen at the surface is much larger than the free electron concentration in the boundary layer and one would expect the electron transfer process to be pressure independent. However, we have found pressure dependence for the slow irreversible oxygen uptake (Fig. 9 notes that the rate $\sim P_0^{1/4}$). It was noted before that the fast irreversible uptake involves approximately 99 per cent of the available current carriers. One would expect that subsequent oxygen uptake would result in multilayer adsorption. The low activation energy of 4–5 kcal/mole that was found supports this model. If this is the case, the sticking coefficient would be expected to be lower(30, 31, etc.) than 10^{-3} which essentially makes the effective pressure much lower than the operating pressure. As a result, a pressure dependence of the rate for the working pressure ranges is not surprising. A further note should be added that multilayer adsorption has been observed(2, 4) on other semiconductor–oxygen systems.

CdSe film is about $n_s \sim 5 \times 10^{13}\,\mathrm{cm}^{-2}$. After the fast irreversible oxygen uptake $n_s \sim 10^{12}\,\mathrm{cm}^{-2}$ and it decreases an additional two orders of magnitude during the slow irreversible uptake depending on the oxygen pressure. The number of surface sites which are available for adsorption is of the order of $\sim 10^{15}\,\mathrm{cm}^{-2}$. Since the total concentration of adsorbed ions is $\sim 5 \times 10^{13}\,\mathrm{cm}^{-2}$; approximately five out of 100 adsorbed atoms are ionized if one assumes that all the electrons are localized. What the exact distribution of electrons over the surface is has yet to be determined. It may be that the charge is evenly distributed(32) among the chemisorbed oxygen atoms.

The following statements present a summary of the results for the irreversible processes:

(1). Fast irreversible electron transfer from the semiconductor film to the oxygen takes place when oxygen is introduced into the reaction vessel at all experimental temperatures. This is interpreted as the formation of chemisorbed oxygen of the acceptor type in the monolayer of adsorbed atoms.

(2). Slow irreversible charge transfer follows (1), the rate of which can be expressed as

$$\frac{-\mathrm{d}n_s}{\mathrm{d}t} = kP_0^{1/4}\,e^{B'n_s}$$

from (2′) and (3).

The rate equation can be derived if one assumes that electron transfer over a potential barrier is the rate determining process. This reaction has a low activation energy which is accepted as an indication that completion of the first monolayer of oxygen or multilayer adsorption of acceptor type oxygen takes place. These processes would require an activation energy of the same order of magnitude(2) as observed for this reaction.

(3). At high enough temperatures, above 630°C, fast desorption of the oxygen takes place accompanied by large increase of the film conductivity. The conductivity approaches the value of that of the "clean" CdSe film.

(4). The experimentally obtained activation energy for the slow process (ΔH = 4–5 kcal/mole) is much too low to permit one to explain the slow irreversible oxygen uptake by diffusion of oxygen into the CdSe lattice. The fastest interstitial diffusion known for solids(33) requires more than double the activation energy obtained for this reaction. Calculations based on a number of diffusion models invariably gave negative entropy values for diffusion which were taken as proof that oxygen uptake is not diffusion controlled.

(5). Electron transfer via tunneling through the potential barrier at the surface is judged to be improbable because the thickness of the boundary layer makes electron tunneling unlikely. It should be noted however, that tunneling would give rise to rate equations of similar form as equation (13) which was derived for adsorption due to electron transfer over the barrier.*

(6). The experimental values of B', the slope of the log t vs. n plots listed in Table 2, agree well with that, calculated from the boundary layer theory for reasonable values of the physical constants of the system.

$$[\epsilon = 10 \ N_D = 10^{19} \text{ cm}^{-3} \ n_s = 10^{13} \text{ cm}^{-2}]$$

(7). Exponential concentration dependence of the rate has been found for the CdSe–O_2 system. Chemisorption on semiconductors obeys this kind of rate dependence frequently. Oxygen on germanium,$^{(2)}$ silicon$^{(26)}$ and ZnO$^{(13)}$ surfaces show similar behavior. The observed rate equation can be derived from the "boundary layer" theory.

(8). A pressure dependence of the rate ($R \sim P^{1/}_{O}$) was found for slow oxygen uptake. Although the pressure dependence is expected for multilayer adsorption as was indicated before, attempts to explain the observed power dependence of the oxygen pressure by some satisfactory mechanism were unsuccessful.

(b) *Reversible, donor type oxygen effect*

It is easily seen from Fig. 2 that after the termination of the irreversible oxygen adsorption at a given ambient pressure, evacuation of the reaction vessel results in a further, relatively small decrease in the CdSe film conductivity. By applying again the same pressure, the conductivity increases by the same amount. Figures. 2 and 4 show how the conductivity increases with increasing pressure. The conductivity pressure dependence can be expressed as

$$\Delta n \approx P_{O_2}^{m}$$

where m is unity at lower temperatures and becomes less than unity at higher temperatures as it is seen from Fig. 5 where m is the slope of the log p vs. log Δn plot. This proportionality reflects the experimental observation that these surface adsorbed oxygen molecules donate charge carriers to the solid. The interaction takes place in about 5 min and it is easily reversible. One can conclude from the experimental observations that the donor type oxygen molecules are weakly held species, adsorbed on the semiconductor film. Higher temperature or pressure increases their concentration on the surface.

If one interrupts the slow saturation of the semiconductor film at a given oxygen pressure by applying a larger pressure, a small temporary increase in conductivity results. The saturation then continues to give further diminishing conductivities. Figure 6 shows this effect.

A similar maximum is found by applying oxygen pressures larger than the pressure which has already saturated the CdSe film as it is shown by dashed curves in Fig. 4.

The two reactions, i.e. the irreversible slow oxygen uptake and the reversible reaction takes place simultaneously. It is fortunate that the reversible uptake can be isolated and studied on oxygen saturated films since they show no irreversible effects as long as the applied pressure is lower than the initial saturation pressure at a given temperature. Since the presence of donor type oxygen, it is concluded that acceptor type adsorbants must already be present in order to form donor type species on the surface.

Once acceptor type species exist on the surface due to a saturation pressure, then the pressure is raised above the saturation value, oxygen molecules will first sit in a multilayer structure and effect donor action. This will be followed by conversion to acceptor type species. Due to the large difference between electron affinities of oxygen, selenium and cadmium, it is more likely that this donor action results from an oxygen–oxygen or oxygen–selenium rather than oxygen–cadmium interaction.$^{(34)}$

---

* Kinetics of reactions where electron tunneling is the rate determining process will be dealt with in a future publication.

The heat of reaction for this reversible oxygen uptake was calculated from the temperature dependence of Δn to be $\Delta H \sim 12$ kcal per mole. It was found that there is no unique way to explain the pressure dependence of the donor action by a single mechanism. However, all the reaction schemes postulated had to involve molecular oxygen as a reactant.

The experimental results would indicate that charge transfer can take place not only due to monolayer adsorption but successive multilayer adsorption as well. Furthermore, there are at least two types of adsorbed oxygen species present on the surface of CdSe and there is strong experimental evidence that the conversion of one type to the other can take place.

It should be noted that although the charge concentration changes orders of magnitudes, the CdSe films remain *n*-type throughout the experiment.

It is of importance to determine the direct correlation between electron transfer and adsorption of oxygen since if one assumes a one to one correlation, only a fraction of the adsorbed species can be accounted for by charge transfer. Simultaneous adsorption and conductivity measurements may give an answer to this question.

Hall mobility measurements in high vacuum would help to verify the mechanism of electron transport and the band structure at the surface. The use of epitaxially grown single crystal thin films for the experiments described above can verify the effect of grain boundaries on the kinetics of processes reported in this paper.

Acknowledgements—I am indebted to E. H. STUPP and S. P. KELLER for valuable discussions on the present paper, to A. B. FOWLER who also carried out the mobility measurements and to F. MOREHEAD for the Dember measurements on the CdSe films.

REFERENCES

1. BRATTAIN W. H. and BARDEEN J., *Bell Syst. tech. J.* **32,** 1 (1953).
2. GREEN M., KAFALAS J. A. and ROBINSON P. H., *Semiconductor Surface Physics*, p. 349. University Press, Pennsylvania, Philadelphia (1957).
3. MORRISON S. R., *J. phys. Chem.* **57,** 860 (1953).
4. BENNETT M. I. and TOMPKINS F. C., *Proc. Roy. Soc.* **259A,** 28 (1961).
5. HANDLER P., *Semiconductor Surface Physics*, p. 23 University Press, Pennsylvania, Philadelphia (1957).
6. PALMER D. R., MORRISON S. R. and DAVENBOUGH C. E., *2nd Conference on Semiconductor Surfaces*, Maryland (1959).
7. LAW J. T. and GARRETT C. G. B., *J. appl. Phys.* **27,** 656 (1956).
8. HEILAND G. and MOLLWO E., *Solid State Physics.* (Edited by SEITZ F. and TURNBULL D.) **8,** 191 Academic Press, New York (1959).
9. FRITZSHE H., *Z. Phys.* **133,** 422 (1952).
10. THOMAS D. G. and LANDER J. J., *J. Phys. Chem. Solids* **2,** 318 (1957).
11. KRÖGER F. A., VINK H. J. and VAN DEN BOOMGAARD J., *Z. phys. Chem.* **203,** 1 (1954).
12. BEVAN D. J. M. and ANDERSON J. S., *Disc. Faraday Soc.* **8,** 246 (1950).
13. MELNICK D. A., *J. chem. Phys.* **26,** 1136 (1957).
14. BUBE R. H., *J. chem. Phys.* **27,** 496 (1958).
15. MORRISON S. R., *Advances in Catalysis*, **VII**, p. 259. Academic Press, New York (1955).
16. FARNSWORTH H. E., SCHLIER R. E., GEORGE T. H. and BURGER R. N., *J. appl. Phys.* **26,** 252 (1955).
17. LAW J. T., *J. phys. Chem.* **59,** 543 (1955).
18. SOMORJAI G. A., *J. phys. Chem.* **65,** 1059 (1961).
19. TOLANSKY S., *Multiple Beam Interferometry*, Clarendon Press, Oxford (1948).
20. GOLDFINGER P., *Final Rep. U.S. Air Force* AF 61(052)-19.
21. MANDEL G., *IBM Res. Rep.* RC-433.
22. TERENIN A. and SOLONITZIN Y. U., *Disc. Faraday Soc.* **28,** 28 (1959).
23. BUBE R. H., *Photoconductivity of Solids*, p. 384. Wiley, New York (1960).
24. MOREHEAD F. and FOWLER A., *IBM Res. Labs.*, to be published.
25. ELOVICH S. YU. and ZHABROVA J., *J. phys. Chem. U S S R* **13,** 1761 (1939).
26. LAW J. T., *J. Phys. Chem. Solids* **4,** 91 (1958).
27. HAUFFE K. and ENGELL H. J., *Z. Elektrochem.* **56,** 366 (1952).
28. WEISZ P. B., *J. chem. Phys.* **21,** 1531 (1953).
29. SPENKE E., *Electronic Semiconductors*, para. 82. McGraw-Hill, New York (1958).
30. WHITE P., *IBM Res. Labs.*, to be published.
31. RHODIN T. N., *Structure and Properties of Thin Films*, p. 87. Wiley, New York (1959).
32. VOLKENSTEIN F., *J. Chim. phys.* **54,** 175 (1957).
33. HANNAY N. B., *Semiconductors*, p. 244. Reinhold, New York (1958).
34. VOLKENSTEIN F. F., *Usp. khim* **27,** 1304 (1958).

J. Phys. Chem. Solids Pergamon Press 1963, Vol. 24, pp. 187–196. Printed in Great Britain.

ATTENUATION OF LONGITUDINAL SOUNDWAVES BY CONDUCTION ELECTRONS

TORE OLSEN

Department of Physics, Brown University, Providence, Rhode Island
and
Fysisk Institutt, Universitetet i Oslo, Blindern, Norway*

(*Received* 18 *September* 1962)

Abstract—The attenuation of longitudinal soundwaves in high purity tin has been measured in a large, perpendicular magnetic field as well as in the absence of a field. It is shown that such measurements make it possible to investigate the magnitude of the electron–phonon interaction, the electronic mean free path, and the temperature dependence of the mean free path.

1. INTRODUCTION

ULTRASONIC attenuation by electron interaction has since it was first observed by BÖMMEL,(1) proved to be a most powerful tool in the study of the properties of the conduction electrons in metals. So far the experimental emphasis has been put on the magnetoacoustic effect that was first studied in any detail by MORSE and co-workers.(2) Several authors have reported interesting findings relating to the structure of the Fermi surface in a number of metals.(3–11) It is now obvious that the magnetoacoustic method has a prominent place among the more established methods in the study of the electron distribution in metals. A main advantage of the method is that results can be interpreted in terms of a few basic properties.

Because of the success of the magnetoacoustic method, the fact that the ultrasonic attenuation represents a very direct way to investigate electron–phonon interactions, is too often overlooked. The electronic part of the attenuation should directly be a measure of such interactions. But electron–phonon interactions have so far mainly been studied by means of the transport effects like the electric and thermal conductivities. These effects include the whole thermal spectrum and the entire electron distribution and most details about the interactions will be obscured. Thus, the information from ultrasonic attenuation of well defined waves has shown to be valauable in the interpretation of transport properties in metals.(12, 13)

In spite of the great difference in the frequency-range for ultrasonic waves and the main part of the thermal spectrum, they have, being of identical nature, the same theoretical description. However, one cannot, as is often done for thermal waves, ignore the mean free path (l_e) of the conduction electrons. Two extreme possibilities will be at hand. Firstly, the mean free path may be longer than the ultrasonic wavelength (λ). This is generally the case for thermal waves because of their short wavelength, but this condition can only be obtained for ultrasonic waves at high frequencies in very pure metals at low temperatures. Secondly, the mean free path can be shorter than the wavelength. For a large part of the thermal spectrum this condition should be fulfilled at high temperatures and in impure metals even at low temperatures.

The former case was described theoretically long before the interaction of ultrasound with electrons was discovered since it is part of the general problem of electron scattering by elastic waves. The quantum mechanical treatment of free electrons scattered by longitudinal waves is now part of most textbooks in the field. The latter case, $ql_e < 1$ ($q = 2\pi/\lambda$), has so far been described by semi-classical methods mostly, and it can be called the region of relaxation. The most remarkable work starting from this point of view is given by Pippard(14) who develops a formula for the attenuation that covers all values of the parameter ql_e. This is interesting because it was previously thought that quantum physics alone could explain the attenuation in the long mean free path case.

---

* Present address.

Tsuneto(15) has given a treatment of the attenuation, valid for an arbitrary mean free path, based on the quantum mechanical derivation of the conductivity from the density matrix formalism and his result agrees with Pippard's. A quantum mechanical theory has also been given by Nagaoka.(16)

Introduction of an external magnetic field complicates the theoretical description considerably. But it can be solved by semiclassical techniques. This was done independently by Kjeldaas and Holstein(17) and by Cohen *et al.*(18) Several authors have treated this problem by similar techniques.(19, 20, 21) Quantum theoretical treatments have been attempted by Skobov,(22) Zyryanov(23) and Stolz.(24)

The purpose of this paper is to report some measurements of the attenuation of longitudinal ultrasonic waves caused by the interaction with the conduction electrons. We will compare our data with some of the above mentioned theoretical works and show that ultrasonic attenuation measurements make it possible to study several fundamental parameters in the electron–phonon interaction, namely the strength of the interaction, the mean free path of groups of electrons, and the temperature dependence of the mean free path.

To do such experiments one needs a sample where the mean free path of the electrons is so large that $ql_e \sim 1$. This can be achieved in high purity metals at liquid helium temperatures. Furthermore, separation of the electronic attenuation from the total attenuation is best done with a superconductor. Here the electronic part of the attenuation is removed as $T \to 0$. However, we will show that a superconductor is not a necessity for this kind of measurement. In the present investigation high purity white tin was used.

In Section 2 we shall briefly review some important theoretical findings for longitudinal waves, and in the case of $ql_e \gg 1$ we shall extend the usual quantum mechanical perturbation method to a general Fermi surface. In Section 3 we shall report the experiments, and the discussion of the results will be found in Section 4.

2. THEORY

Absence of a magnetic field

Pippard(21) has given a thorough treatment of the ultrasonic attenuation both in the absence of a magnetic field and in a transverse magnetic field for general Fermi surfaces. In the former case the attenuation for longitudinal waves takes the form

$$\alpha = \frac{\hbar q}{4\pi^3 \rho_0 u_q}\left\{\int \frac{\mathscr{D}^2 q l_e \,\mathrm{d}S}{1+(ql_e)^2\cos^2\phi} + \left[\int \frac{\mathscr{D}\,\mathrm{d}S}{1+(ql_e)^2\cos^2\phi}\right]^2 \Big/ \int \frac{ql_e \cos^2\phi\,\mathrm{d}S}{1+(ql_e)^2\cos^2\phi}\right\} \tag{1}$$

where ρ_0 and u_q is the mass density and sound velocity respectively and $\mathscr{D} = K_x + k_x \cos\phi$. Here K_x is a component of the deformation coefficient K and k_x is the x-coordinate of the element $\mathrm{d}S$ of the Fermi surface, and ϕ the angle between the x-axis and the normal to $\mathrm{d}S$.

Since the second term in (1) is only important when $ql_e \sim 1$, one can write

$$\alpha \approx \frac{\hbar q^2}{4\pi^3 \rho_0 u_q}\int \mathscr{D}^2 l_e\,\mathrm{d}S \tag{2}$$

when $ql_e \ll 1$ and

$$\alpha' \approx \frac{\hbar q}{4\pi^2 \rho_0 u_q}\oint R^2 K_x l_e\,\mathrm{d}\psi \tag{3}$$

when $ql_e \gg 1$. Here R is the reciprocal of the Gaussian curvature of the Fermi surface, and the integral in (3) is taken over those electrons that stay in phase with the sound wave.

Assuming free electrons (1) can be reduced to(14)

$$\alpha = \alpha' \frac{6}{\pi}\left[\frac{ql_e}{3}\frac{a}{1-a} - \frac{1}{ql_e}\right] \tag{4}$$

where $a = \mathrm{arctg}\; ql_e/ql_e$, and α' is the limiting attenuation when $ql_e \gg 1$. This limiting attenuation can then be written

$$\alpha' = \frac{\pi}{6}\frac{nmv_F}{\rho_0 u_q} q \tag{5}$$

where n is the number of free electrons, m their mass, and v_F the Fermi velocity. The free electron form of (2) was first derived by MORSE:(25)

$$\alpha = \frac{4}{15}\frac{nmv_F}{\rho_0 u_q}q^2 l_e \qquad (6)$$

MORSE(26) and MIKOSHIBA(27) have shown that (5) can be derived quantum mechanically by a simple perturbation calculation of the phonon-electron scattering. Below we shall attempt a similar approach with no restrictions on the shape of the Fermi surface.

We shall adopt the view that an ultrasonic wave can be represented by one of the normal modes of the crystalline lattice. This is a reasonable assumption as the experimental radiation field approximates a plane harmonic wave. We shall calculate the energy loss from (that is the attenuation of) a longitudinal mode with the wave vector $\mathbf{q}$ as caused by the collision with the electrons. According to ordinary first order time-dependent perturbation theory the scattering probability will depend on the square of the matrix element between the initial and final states. The matrix element describing the scattering of an electron from the state $\mathbf{k}$ to $\mathbf{k}'$, with the simultaneous absorption of a phonon from the mode $\mathbf{q}$ will be:

$$M(\mathbf{k},n_q;\mathbf{k}',n_q-1) = \left[\frac{n_q\hbar}{2\rho_0 V\omega_q}\right]^{1/2}\delta_{\mathbf{k}'-\mathbf{k}-\mathbf{q}}\cdot I_q(\mathbf{k}',\mathbf{k}) \qquad (7)$$

where ω_q is the frequency of the lattice mode $\mathbf{q}$ being in the phonon state n_q, and V is the volume. The Kronecker delta tells that the momentum is conserved. The last factor is more explicitly

$$I_q(\mathbf{k}',\mathbf{k}) = \int \psi_{\mathbf{k}}^*\left(\mathbf{e}_q\cdot\frac{\partial U}{\partial\eta}\right)\psi_{\mathbf{k}'}\,\mathrm{d}\mathbf{r} \qquad (8)$$

where $\mathbf{e}_q$ is the polarization vector and $\psi_{\mathbf{k}}$ is the electronic wavefunction. One arrives at (7) and (8) through the assumption that the perturbing potential δU resulting from the movement of the ions, can be written as a linear function of the ion displacements (η_b)

$$\delta U = \sum_b \eta_b \frac{\partial U}{\partial \eta_b} \qquad (9)$$

Several methods to evaluate the integral in (8) have been presented. The best is probably based on the self-consistent method first used by BARDEEN.(28) However, this is of lesser importance because all methods yield the same result in the limit of acoustic waves.(29) We obtain, as $q \rightarrow 0$

$$I_q(\mathbf{k}',\mathbf{k}) \rightarrow i\mathbf{q}\cdot\mathbf{e}_q\frac{n}{N(E_F)} \qquad (10)$$

Here $n/N(E_F)$ is the ratio of the total number of electrons to the density of electrons at the Fermi surface. This ratio is equal to $2/3\ E_F$ in the case of a parabolic band.

For a longitudinal acoustic oscillation, our matrix element takes the form

$$M(\mathbf{k},n_q;\mathbf{k}',n_q-1) = \left[\frac{n_q\hbar}{2\rho_0 V\omega_q}\right]^{1/2} iq\frac{n}{N(E_F)}\delta_{\mathbf{k}'-\mathbf{k}-\mathbf{q}} \qquad (11)$$

The inverse process, in which a phonon is emitted, is described by a similar expression where n_q is replaced by (n_q+1). We are interested in the net rate between the process described by (11) and the process where a phonon is emitted, when $n_q \gg 1$.

The transition probability per unit time will be given as

$$P_f^i(\mathbf{k},\mathbf{k}') = \frac{2\pi}{\hbar}|M|^2\frac{\sin[(E_f-E_i)t/\hbar]}{\pi(E_f-E_i)} \qquad (12)$$

where t is the time, and E_f and E_i denote the final and initial energy respectively.

The energy attenuation α is the intensity loss per unit distance travelled, thus

$$\alpha = -\frac{1}{u_q n_q}\frac{\partial n_q}{\partial t} \qquad (13)$$

where u_q is the velocity of the wave. Summing over all electrons we obtain

$$\frac{\partial n_q}{\partial t} = \sum_{\mathbf{k},\mathbf{k}'} P_f^i(\mathbf{k},\mathbf{k}')\cdot f_{\mathbf{k}}(1-f_{\mathbf{k}'}) \qquad (14)$$

where $f_{\mathbf{k}}$ is the Fermi–Dirac function describing the probability of finding the state $\mathbf{k}$ initially occupied.

We can now write for the attenuation

$$\alpha = -\frac{\pi[n/N(E_F)]^2q^2}{\rho_0 V u_q\omega_q}\sum_{\mathbf{k}}(f_{\mathbf{k}'}-f_{\mathbf{k}})\frac{\sin[(E_f-E_i)t/\hbar]}{\pi(E_f-E_i)} \qquad (15)$$

where we have used the δ-function to simplify the summation.

Transforming the sum in (15) to an integral we obtain

$$\alpha = -\frac{[n/N(E_F)]^2 q^2}{4\pi^2 \rho_0 u_q \omega_q} \int (f_{k'} - f_k) \times \frac{\sin[(E_f - E_i)t/\hbar]}{\pi(E_f - E_i)} \, d\boldsymbol{k} \qquad (16)$$

At this point we shall restrict ourselves to the case where the mean free life time (τ) for the electrons due to scattering with impurities and thermal phonons is long ($ql_e \gg 1$). In this limit t in (16) can be made large and the last factor in the integrand becomes the delta function $\delta(E_f - E_i)$.

The argument is

$$E_f - E_i = (E_{k'} - E_k) - \hbar\omega_q \qquad (17)$$

and since the energy of the phonon is small compared to E_k we can write

$$\delta[(E_{k'} - E_k) - \hbar\omega_q] = \delta\left[\frac{\partial E}{\partial \boldsymbol{k}} \cdot \boldsymbol{q} - \hbar\omega_q\right] = \delta[\xi] \qquad (18)$$

Let us define a coordinate system so as to make $\boldsymbol{q} = q\boldsymbol{i}$ Then (18) says that only the electrons satisfying $\frac{\partial E}{\partial k_x} q - \hbar\omega_q = 0$ will contribute to the integral in (16). Furthermore, they have to be located on the Fermi surface because as long as the energy of the acoustic phonon is small compared to the thermal phonons, we can write

$$f_{k'} - f_k = \hbar\omega_q \frac{\partial f}{\partial E} \qquad (19)$$

and the factor $\frac{\partial f}{\partial E}$ also has the character of a delta-function.

An easy way to find the contributing areas on the Fermi surface is to use the approximation $E_f \sim E_i \sim E_F$ and draw the Fermi surface also around a point $\boldsymbol{q}$ away *from the origin* in the reciprocal space. Then the contributing areas will, roughly speaking, be narrow ribbons along the curves of intercepts. This has been illustrated in Fig. 1 for the undulating cylinder type of a Fermi surface where $\boldsymbol{q}$ has an arbitrary direction.

We can now simplify the integral in (16) by writing the volume element

$$d\boldsymbol{k} = dk_n dS = dk_n dk_\xi dk_\eta \qquad (20)$$

where k_n is normal to the energy surfaces and where dk_ξ and dk_η is taken along and normal to curves with ξ = const. respectively. But, when $\xi = 0$ as required by (18), we can replace dk_ξ with dk_x, and we find

$$\alpha = \frac{[n/N(E_F)]^2 q}{4\pi^2 \rho_0 u_q} \oint \frac{1}{\partial^2 E/\partial k_x^2} \cdot \frac{dk_\eta}{v_k} \qquad (21)$$

where v_k is the group velocity.

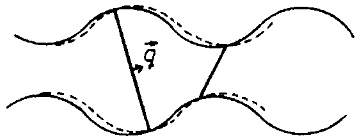

FIG. 1. The areas on an undulating cylinder type of a Fermi surface that will contribute to the interaction with a phonon of momentum $\boldsymbol{q}$ when $ql_e \gg 1$.

The integral in (21) says that we sum up all the states on the Fermi surface where $\xi = 0$ and that each state should be weighed according to the inverse of the curvature in the x-direction. In the free electron case (21) reduces to (5) as to be expected, and compared with (3) it has the advantage of not containing the deformation coefficient K_x. However, the above method applies only to longitudinal waves as it would yield no attenuation for a shear wave in the case of free electrons.

Transverse magnetic field

In this paper we will not be interested in the oscillatory part of the magnetoacoustic effect but only in the behaviour of the attenuation of longitudinal waves in a strong magnetic field perpendicular to the direction of sound propagation. Both KANER(20) and PIPPARD(21) have treated this case for a general Fermi surface, but their treatments differ essentially on some points.

Kaner found that both open and closed electron orbits lead to the same kind of attenuation in high fields, i.e. a saturation proportional to $q^2 l_e$. On the other hand, according to Pippard open orbits should cause the attenuation to increase with H^2 at high fields, except when the open orbits are directed along the propagation direction. As we will show later, the experiments seem to favour Kaner's approach. Unfortunately, the exact expression is extremely cumbersome to write out, but it will have the form

$$\alpha(H) = B_q^H q^2 l_e \tag{22}$$

when $H \to \infty$. Here B_q^H is a constant depending on the direction of the field and the direction of the sound propagation as denoted by the superscripts and subscripts respectively. We note that the form of (22) is the same as the expression for the attenuation in the absence of a magnetic field when $ql_e \ll 1$. According to KANER(20) one should find pronounced anisotropy of the saturation when open orbits are present. Whenever the angle between q and a direction of open orbits is of the order $1/ql_e$, large changes in $\alpha(H)$ should occur with a small change in the angle.

3. EXPERIMENTS

The sample

The high purity single crystal of tin used in these experiments was grown from 99·9999 per cent pure tin by the Virginia Institute for Scientific Research, Virginia. The sample was oriented by the Laue back-reflection X-ray method and at first two sets of parallel faces were cut, perpendicular the [001]-axis and the [110]-axis. To obtain a set of faces perpendicular the [100]-axis the sample was later reshaped. Ordinary machine tools were used in the cutting of the sample, but care was taken to make the cuts as fine as possible. The faces were later lapped by hand with No. 600 carborundum lapping compound until they were flat and parallel within 0·00003 cm across the faces (1–2 cm in diameter). Finally the damaged surface layers were removed by etching, and the faces checked to be within one degree of being perpendicular to the crystalline axis.

Experimental method

The ultrasonic attenuation was measured by a pulse method employing pulses of one microsecond duration in the frequency range 5–100 Mc/s. A detailed account of this method and the apparatus has been given elsewhere.(11, 26, 30)

The observed ultrasonic attenuation stems from many different sources, firstly the electron interaction, but also reflection losses at the different interfaces and from diffraction of the sound beam. Hence one cannot determine very accurately the total absolute attenuation using the pulse technique. However, we are not interested in the total attenuation, but the variation of the electronic part as function of the external parameters T and H. This part of the attenuation can most accurately be studied by observation of the relative attenuation of one of the echoes. Furthermore, this method is the only one possible when the electronic attenuation becomes so large that only the first echo is observable. The validity of the relative method rests upon the fact that none of the other effects contributing to the attenuation will change with H or with T in the liquid helium temperature range. This has been shown by MORSE and BOHM.(26)

Experimental results

To compare the measurements with the theory one needs to know the electronic part of the observed attenuation for a set of different ql_e-values. In a superconductor we can easily find this by reducing the Temperature below the transition temperature (T_c) where the electronic attenuation will decrease toward zero. In tin the decrease will be exponential around 1°K and the electronic part of the attenuation can be found within 1 per cent by extrapolating to $T = 0$°K.(31) We have done this in our sample for q along the three principal axes [100], [001], and [110] and in each case for several frequencies between 10 and 100 Mc/s. The results at 4·2°K are shown in Table 1.

Table 1 shows that the attenuation increases with increasing frequency approaching a linear dependence. This is in agreement with (1). However, a closer comparison is not possible without a detailed knowledge of the Fermi surface. We can avoid this difficulty if we take advantage of (4) and assume that a similar expression can be found in real metals. PIPPARD(32) argues that, contrary to α', the last factor in (4) is not fundamentally related to the strength of the phonon–electron interaction, but only expresses the dependence on ql_e and that this dependence will not differ essentially in a real metal.

Our data can be compared with (4) if we normalize the frequencies, i.e. the ql_e-values, divide the measured attenuation by the frequency, and

Table 1. The measured electronic attenuation at 4·2° K in tin in the absence of a magnetic field with q along the three principal directions

Direction of q	Frequency (Mc/s) ν	Norm.	Attenuation (db/cm.) α	α/ν	Best fit to Pippard's theory ql_e	α/α'
[001]	12·0	1	1·90	0·159	1·5	0·54
	31·5	2·62	7·42	0·236	4·0	0·79
	51	4·3	12·9	0·254	6·4	0·85
	72	6·0	19·5	0·264	9·0	0·89
[100]	11·0	1	3·44	0·313	2·2	0·65
	26·2	2·38	10·5	0·400	5·3	0·83
	28·0	2·54	11·5	0·411	5·6	0·85
[110]	12·0	1	1·35	0·112	3·0	0·73
	11·7	0·97	1·29	0·110	2·9	0·72
	28·0	2·34	3·70	0·132	6·5	0·86
	76	6·3	11·2	0·148	18·9	0·96

fit the outcoming set of data to α/α'. This is done in Table 1. The fit is good as is shown in Figs. 2, 3 and 4 and within the experimental error. The uncertainty is estimated to be 3 per cent both in ql_e and α/α'.

Writing (21) as $\alpha' = A_q \cdot q$, we can, using the Figs. 2, 3 and 4, calculate the A_q's for different directions of q. From Table 2 we see that this quantity varies considerably. It should be noted that the magnitude of A_q is not very sensitive to the shape of the α/α' vs. ql_e-curve because the attenuation at the higher frequencies is near proportional to q. In the limit $ql_e \to \infty$ the only electrons contributing to the attenuation are those having a velocity component along the direction of sound propagation equal to the sound velocity as expressed by (18). This means that the variation in A_q reflects a large anisotropy of the Fermi surface. This information can serve as a valuable guide in interpreting the complicated electron distribution in tin.

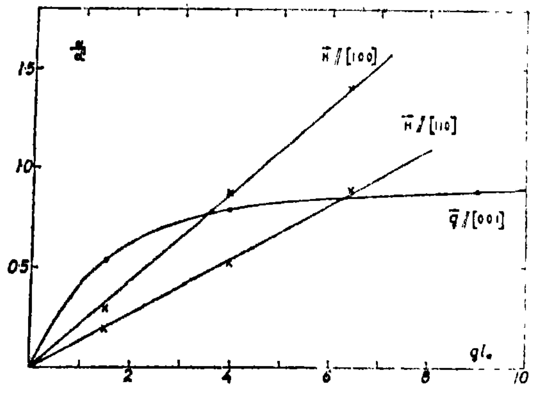

FIG. 2. Attenuation of a longitudinal wave in tin vs. ql_e with q// [001]. Circles represent the attenuation measured in the absence of a magnetic field, and the crosses the attenuation measured in a magnetic field of 6500 Oe.

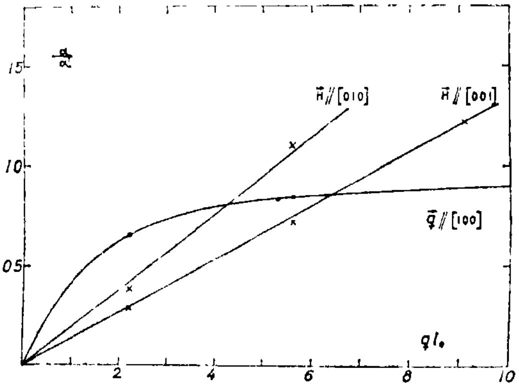

FIG. 3. Attenuation of a longitudinal wave in tin vs. ql_e with q // [100]. Circles represent the attenuation measured in the absence of a magnetic field, and the crosses the attenuation measured in a magnetic field of 6500 Oe.

Knowing q one can from Figs. 2, 3 and 4 calculate the parameter l_e. It is interesting to note the

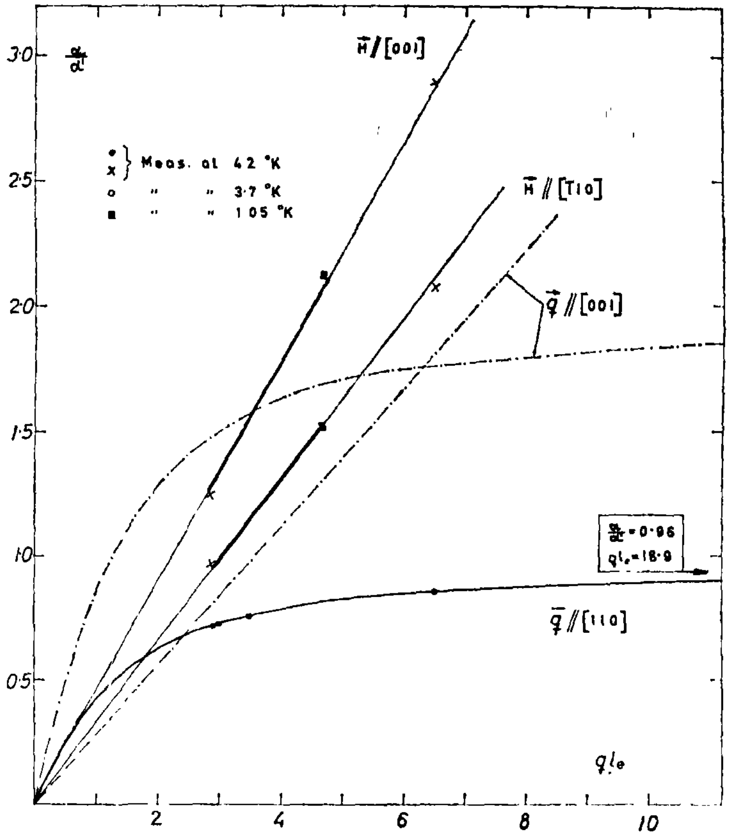

FIG. 4. Attenuation of a longitudinal wave in tin vs. ql_e with q//[110]. filled and open circles represent the attenuation measured in the absence of a magnetic field, and crosses and filled squares the attenuation measured in a magnetic field of 6500 Oe. The dashed curves show α/α' observed with q//[001] multiplied by A_{001}/A_{110}.

Table 2. The longitudinal sound velocities at 4·2°K *along the three principal directions, and the calculated mean free path of the electrons. The* A_q*'s are defined by* $\alpha' = A_q q$*, and the* B_q^H*'s by* $\alpha(H) = B_q^H \cdot q^2 l_e$

Direction of q	Velocity (longitudinal) cm/sec	$\alpha' = A_q q$	Mean free path (T = 4·2°K) (cm)	$\alpha(H) = B_q^H q^2 l_e$		
		A_q		B_q^{100}	B_q^{001}	B_q^{110}
[100]	$3{\cdot}19 \cdot 10^5$	$2{\cdot}58 \cdot 10^{-3}$	$1{\cdot}02 \cdot 10^{-2}$	$5{\cdot}0 \cdot 10^{-4}$	$3{\cdot}5 \cdot 10^{-4}$	
[001]	$3{\cdot}78 \cdot 10^5$	$2{\cdot}10 \cdot 10^{-3}$	$0{\cdot}75 \cdot 10^{-2}$	$4{\cdot}6 \cdot 10^{-4}$		$2{\cdot}8 \cdot 10^{-4}$
[110]	$3{\cdot}61 \cdot 10^5$	$1{\cdot}02 \cdot 10^{-3}$	$1{\cdot}44 \cdot 10^{-2}$		$4{\cdot}4 \cdot 10^{-4}$	$3{\cdot}3 \cdot 10^{-4}$

variations in l_e found with different $\boldsymbol{q}$-directions. The l_e found at 4·2°K is written down in Table 2. Since the three sets of measurements were done on one sample (the sound beam travelled through the same part of the sample), the differences cannot be attributed to differences in the impurity contents.

The attenuation was also measured at 4·2°K in perpendicular fields up to 6500 Oe with $\boldsymbol{q}$ along the three principal directions and for a set of different frequencies in each case. A typical behaviour in increasing fields is at first a number of oscillations in the attenuation and then a levelling off at high fields. Usually the attenuation at high fields is larger than in the absence of the field, and in some cases, especially for large ql_e's, it increases out of the measurable range. However, for the smallest values of ql_e the attenuation when $\boldsymbol{H} \to \infty$ could be lower than in zero field. This has also been observed by GALKIN *et al.*[9]

These observations are easily understood if one plots $\alpha(\boldsymbol{H})/\alpha'$ vs. ql_e. Here $\alpha(\boldsymbol{H})$ is the total electronic attenuation when $\boldsymbol{H} \to \infty$. The results are plotted in Figs. 2, 3 and 4 for the field along the three principal axes. The observed points fall on straight lines through the origin proving that $\alpha(\boldsymbol{H})$ is proportional to $q^2 l_e$ in this region. This is in agreement with (22). These measurements are more uncertain than the ones taken in the absence of a magnetic field, especially at large ql_e's where 6500 Oe is not enough to remove all traces of the magnetoacoustic oscillations. It is estimated that this will render an uncertainty on the slope of the $\alpha(\boldsymbol{H})/\alpha'$-curves of approximately 10 per cent. All the investigated directions of the field give straight lines in the $\alpha(\boldsymbol{H})/\alpha'$-plot, but the slope varies drastically with the direction of the field.

It is also of interest to see to what extent B_q^H in (22) varies with the direction of $\boldsymbol{q}$. Three pairs of $\alpha(\boldsymbol{H})/\alpha'$-curves with common field directions and different directions of $\boldsymbol{q}$ were investigated as can be seen from Figs. 2, 3 and 4. Since the slopes of these lines will be B/A_q^H we can calculate the B's. Table 2 shows that B probably depends less upon the direction of $\boldsymbol{q}$ than the direction of $\boldsymbol{H}$. Another way to illustrate this is indicated in Fig. 4 where the $\alpha(\boldsymbol{H})/\alpha'$-curve found when $\boldsymbol{q}//[001]$ and $\boldsymbol{H}//[110]$ has been multiplied by A_{001}/A_{110}. Such a plot also illustrates the relative magnitudes of the attenuation found with different $\boldsymbol{q}$-directions and, therefore, we have scaled the Pippard curve similarly.

The high purity of the sample made it possible to investigate the temperature dependence of l_e. Most directly this can be done by measuring $\alpha(\boldsymbol{H})$ at different temperatures as this attenuation is proportional to l_e. The attenuation in a large field was measured for all directions of the field with $\boldsymbol{q}//[001]$ at four temperatures below 4·2°K. A decrease in the temperature led to an increase in $\alpha(\boldsymbol{H})$, but the relative increase was the same for all directions of $\boldsymbol{H}$. In Fig. 5 we have plotted $\alpha(\boldsymbol{H})_{4\cdot 2^\circ\mathrm{K}}/\alpha(\boldsymbol{H})_T$ vs. T. The experimental points can best be fitted to

$$\alpha(\boldsymbol{H})_{4\cdot 2^\circ\mathrm{K}}/\alpha(\boldsymbol{H})_T = 0{\cdot}610+0{\cdot}125 \cdot 10^{-2}\, T^4 \quad (23)$$

choosing an integer power in T. A similar set of data was taken for $\boldsymbol{q}//[110]$ at $T = 1{\cdot}05$°K yielding the same attenuation ratio as given by (23).

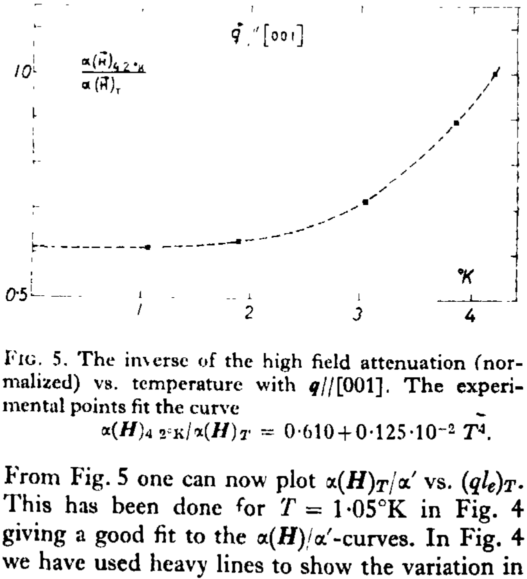

FIG. 5. The inverse of the high field attenuation (normalized) vs. temperature with $\boldsymbol{q}//[001]$. The experimental points fit the curve

$$\alpha(\boldsymbol{H})_{4\cdot 2^\circ\mathrm{K}}/\alpha(\boldsymbol{H})_T = 0{\cdot}610+0{\cdot}125\cdot 10^{-2}\, T^4.$$

From Fig. 5 one can now plot $\alpha(\boldsymbol{H})_T/\alpha'$ vs. $(ql_e)_T$. This has been done for $T = 1{\cdot}05$°K in Fig. 4 giving a good fit to the $\alpha(\boldsymbol{H})/\alpha'$-curves. In Fig. 4 we have used heavy lines to show the variation in $\alpha(\boldsymbol{H})/\alpha'$ with a temperature reduction from 4·2 to 1·05°K. In turn, Fig. 4 together with Fig. 5 can be used to deduce the attenuation in the absence of a field as a function of temperature. This deduced attenuation can be compared with the measured α above T_c. One should expect these two quantities to be identical if the temperature dependence of l_e is the same in a large magnetic field as in the absence of a field. No systematic study along this line has been done, but the result of a preliminary investigation is shown in Fig. 6. Within the experimental error the observed α, in the normal state, is equal to the attenuation one can deduce from $\alpha(\boldsymbol{H})$. However, tin is not well suited for this kind of investigation because of the high T_c. Therefore, one should not put too much emphasis on this observation.

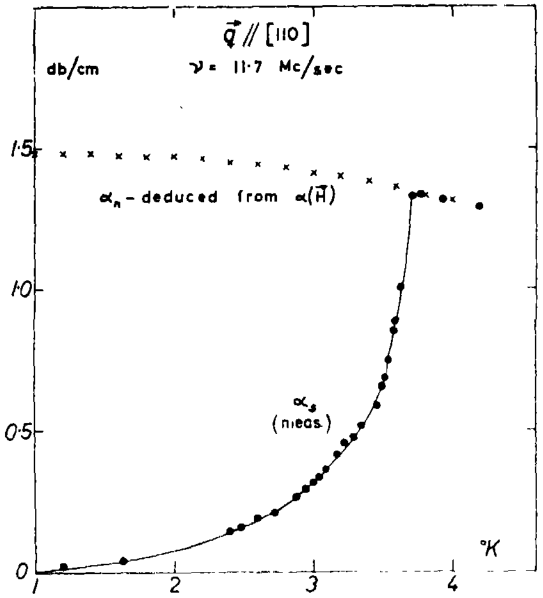

FIG. 6. The attenuation in the normal state deduced from $\alpha(\boldsymbol{H})$ compared with the measured attenuation above T_c.

4. DISCUSSION

The comparison between the measured electronic attenuation in tin and Pippard's theory for an ideal metal, was based on the assumption that the ql_e-dependence was not sensitive to the strength of the phonon–electron interaction. The good agreement between the α/α' vs. ql_e-curve and the measurements justifies this assumption. Attenuation measurements of longitudinal waves represent a simple way to measure the magnitude of the phonon–electron interaction and from (21) we see that this parameter also yields information about the Fermi surface. Furthermore, such measurements are of importance in the understanding of phonon–electron interaction in the transport effects.(12, 13) It is important to note that a superconductor is not a necessity for finding the electronic part of the total attenuation and hence to measure the phonon–electron interaction. It is possible to deduce α' for non-superconductors by observing $[\alpha(\boldsymbol{H})-\alpha']$ at different ql_e's and fit the results to plots like Figs. 2, 3 and 4. This should be possible as long as the attenuation in large fields follows (22). However, some results in indium indicate that this is not always possible.(9)

The magnitude of the attenuation of longitudinal waves in a strong, perpendicular magnetic field follows a q^2l_e-law and from the measurements in tin it seems to depend less on the direction of $\boldsymbol{q}$ than on the field direction. This points to the possibility of studying the topological features of the Fermi surface by comparing high field polar plots of the attenuation for different directions of sound propagation. This has been used together with the magnetoacoustic oscillations to investigate possible open orbits in tin.(11)

Another interesting parameter that comes out of the above measurements is the electron mean free path. We see from (21) that the attenuation in the absence of a field does not depend upon the mean free path if $ql_e \to \infty$. This means that the ultrasonic attenuation method will not be very useful to investigate the anisotropy of the relaxation time (τ). A large variation in l_e was observed with the three different directions of $\boldsymbol{q}$, but whether the differences are caused by the relaxation time being a function of $\boldsymbol{k}$, or a different average over the contributing Fermi velocities. or both, is difficult to determine.

But the relatively large l_e and small A_q found when $\boldsymbol{q}$//[110] could both tentatively be interpreted as resulting from large electron velocities in view of (21) when it is remembered that $l_e = \langle v_F \cdot \tau \rangle$.

In the literature one can find estimates of the mean free path based on the number of oscillations in the magnetoacoustic effect. GALKIN *et al.*(9) claim that $l_e \sim n\lambda/2\pi$, where n is the number of clearly observable oscillations. RAYNE and CHANDRASEKHAR(10) use the relation $l_e \sim n\lambda\pi$. We have studied the magnetoacoustic oscillations in the same sample(11) as the one used in this investigation and found that the latter relation yields l_e-values that are larger than those listed in Table 2. However, several momenta contribute and each momentum leads to a set of oscillations and since the number of oscillations varies drastically from set to set, a measurement of l_e this way can be no more than a very crude estimate. It seems that the values in Table 2 should be considered more reliable. It is also interesting to note that within the experimental error l_e is the same in a strong, perpendicular field as in the absence of a magnetic field. This is not obvious and should be investigated more closely.

The ratio between the resistances at helium and room temperature respectively was not measured in our sample. Therefore, no comparison can be made between our estimate of the mean free path and a similar estimate from electrical data. Galkin *et al.*(9) have measured the resistance ratio in their sample and deduced a mean free path that agrees with the one they get from the number of oscillations. Their high field saturation values of the attenuation seems, on the other hand, to indicate a much smaller mean free path.

We see from (23) that the temperature dependent part of the mean free path varies as T^{-4}, contrary to the T^{-5} dependence observed electrically just above T_c.(33) This could be another indication that the mean free path is different in the two types of processes. However, more data are needed before any conclusions can be made concerning the relationship between the mean free path deduced from electrical and from ultrasonic measurements. Only very few investigations have been done along this line so far.(34, 35)

In Fig. 6 we have illustrated the possibility of deducing the attenuation in the normal state (α_n) from $\alpha(H)$ below T_c. When one investigates the superconducting energy gap ultrasonically, one needs α_s/α_n. If the parameter ql_e is large, one can safely assume α_n to be a constant below T_c as was done by Morse *et al.*(31) But the possibility of finding α_n even when ql_e is small means that the ultrasonic method might be used to study super conductors over a wide range in the parameter ql_e.

Acknowledgements—The author would like to express his thanks to the members of the low-temperature group at Brown University, and especially Professor R. W. Morse and Dr. J. D. Gavenda. The author is also indebted to J. Lothe for valuable discussions.

REFERENCES

1. Bömmel H. E., *Phys. Rev.* **100**, 758 (1955).
2. Morse R. W., Bohm H. V. and Gavenda J. D., *Phys. Rev.* **109**, 1394 (1958).
3. Reneker D. H., *Phys. Rev.* **115**, 303 (1959).
4. Morse R. W. and Gavenda J. D., *Phys. Rev. Letters* **2**, 250 (1959).
5. Galkin A. A. and Korolyuk A. P., *Zh. eksp. teor. Fiz. S.S.S.R.* **38**, 1688 (1960); English translation *Sov. Phys. JEPT* **11**, 1218 (1960).
6. Roberts B. W., *Phys. Rev.* **119**, 1889 (1960).
7. Morse R. W., Myers A. and Walker C. T., *Phys. Rev. Letters* **4**, 605 (1960).
8. *The Fermi Surface*, (edited by Harrison W. A. and Webb M. B.) Wiley, New York (1960).
9. Galkin A. A., Kaner E. A. and Korolyuk A. P., *Zh. eksp. teor. Fiz. S.S.S.R.* **39**, 1517 (1960); English translation *Sov. Phys. JETP* **12**, 1055 (1961).
10. Rayne J. A. and Chandrasekhar B. S., *Phys. Rev.* **125**, 1952 (1962).
11. Olsen T., *J. Phys. Chem. Solids* **24**, (1963). In press.
12. Olsen T., *J. Phys. Chem. Solids* **12**, 167 (1960).
13. Lindenfeld P. and Pennebaker W. B., *Phys. Rev.* **127**, 1881 (1962).
14. Pippard A. B., *Phil. Mag.* **46**, 1104 (1955).
15. Tsuneto T., *Phys. Rev.* **121**, 402 (1961).
16. Nagaoka Y., *Progr. theor. Phys.* **26**, 589 (1961).
17. Kjeldaas T. and Holstein T., *Phys. Rev. Letters* **2**, 340 (1959).
18. Cohen M. H., Harrison M. J. and Harrison W. A. *Phys. Rev.* **117**, 937 (1960).
19. Gurevich V. L., *Zh. eksp. teor. Fiz. S.S.S.R.* **37**, 71 (1959); English translation *Sov. Phys. JEPT* **10**, 51 (1960); *Zh. eksp. teor. Fiz. S.S.S.R.* **37**, 1680 (1959); English translation *Sov. Phys. JEPT* **10**, 1190 (1960).
20. Kaner E. A., *Zh. eksp. teor. Fiz. S.S.S.R.* **38**, 212 (1960); English translation *Sov. Phys. JETP* **11**, 154 (1960); *Zh. eksp. teor. Fiz. S.S.S.R.* **39**, 1071 (1960); English translation *Sov. Phys. JETP* **12**, 747 (1961).
21. Pippard A. B., *Proc. Roy. Soc.* **A257**, 165 (1960).
22. Skobov V. G., *Zh. eksp. teor. Fiz. S.S.S.R.* **40**, 1446 (1961); English translation *Sov. Phys. JETP* **13**, 1014 (1961).
23. Zyryanov P. S., *Zh. eksp. teor. Fiz. S.S.S.R.* **40**, 1353 (1961); English translation *Sov. Phys. JETP* **13**, 953 (1961).
24. Stolz H., *Phys. Status solidi* **1**, 328 (1961).
25. Morse R. W., *Phys. Rev.* **97**, 557 (1955).
26. Morse R. W., *Progr. in Cryogenics* **I**, Heywood, London (1959).
27. Mikoshiba N., *J. phys. Soc. Japan* **14**, 22 (1959).
28. Bardeen J., *Phys. Rev.* **52**, 688 (1937).
29. Ziman J. M., *Electrons and Phonons*, University Press, Oxford (1960).
30. Chick B., Anderson G. and Truell R., *J. acoust. Soc. Amer.* **32**, 186 (1960).
31. Morse R. W., Olsen T. and Gavenda J. D., *Phys. Rev. Letters* **3**, 15 (1959); *ibid.* **3**, 193 (1959).
32. Pippard A. B., *J. Phys. Chem. Solids* **3**, 175 (1957).
33. Zernov V. B. and Sharvin Yu V., *Zh. eksp. teor. Fiz. S.S.S.R.* **36**, 1038 (1959); English translation *Sov. Phys.* **9**, 737 (1959).
34. Filson D. H., *Phys. Rev.* **115**, 1516 (1959).
35. Lax E., *Phys. Rev.* **115**, 1591 (1959).

J. Phys. Chem. Solids Pergamon Press 1963. Vol. 24 pp. 197–208. Printed in Great Britain.

EXISTENCE OF A "WELL DEFINED" SPECIFIC ENERGY FOR AN IONIC CRYSTAL; JUSTIFICATION OF EWALD'S FORMULAE AND OF THEIR USE TO DEDUCE EQUATIONS FOR MULTIPOLE LATTICES*

E. S. CAMPBELL

Department of Chemistry, New York University, New York

(*Received* 2 *January* 1962; *revised* 19 *September* 1962)

Abstract—The EWALD[1] calculation of the potential defined by an ionic lattice is shown to be justified under simple general conditions which are given for the existence of a "well-defined" specific energy for an ionic crystal. The significance of the Ewald calculation and of these conditions is clarified by a prior discussion of the connection between the specific energy for finite and infinite lattices. It is shown that the original argument given[2] to justify the deduction of formulae for multipole lattices from Ewald's equations contains a logical error which led to misleading statements about the potential defined by a lattice of dipoles. Conditions for the validity of these formulae are given and proved. Advantages of these formulae are discussed.

1. EXISTENCE OF A "WELL-DEFINED" SPECIFIC ENERGY FOR AN IONIC LATTICE

TO DISCUSS the validity of the EWALD[1] calculation, it will be necessary to consider briefly the problems which arise because the potential of each lattice site varies as r^{-1}. The infinite series are at most conditionally (i.e. simply) convergent.† Any series which fails to converge absolutely possesses the well known property that it can be made to diverge or to converge to any arbitrary value by an appropriate choice of order of summation. This property has a different implication in one dimension than it has in two or more dimensions. A one dimensional series,

$$\sum a_n \tag{1}$$

has a "natural" order of summation, the order of increasing n. This order for the infinite series corresponds to computing the limit for finite lattices of increasing size.

For a P dimensional series, $P \geqslant 2$, the analogue of a sum for all $n \leqslant N$ would be a sum over all $\langle n_1, \ldots, n_P \rangle$ such that

$$0 \leqslant f(\langle n_1, \ldots, n_P \rangle) \leqslant \text{constant} \tag{2}$$

where $f(\langle n_1, \ldots, n_P \rangle)$ is an arbitrary monotone increasing function of each n_i. This order for the infinite series corresponds to computing the limit for finite lattices of increasing size and the *fixed shape* defined by the function $f(\langle n_1, \ldots, n_P \rangle)$. Thus it is only in one dimension that the model for increasing the size of a finite lattice imposes a unique order of summation. Conversely, in two or more dimensions, it is necessary to specify the function $f(\langle n_1, \ldots, n_P \rangle)$. In other words, the concepts of potential and of specific energy are defined for an infinite lattice *only* if the order of summation is specified.‡ In physical terms, this

---

* This research was supported by the Directorate of Chemical Sciences, Air Force Office of Scientific Research.

† EMERSLEBEN[3a] gives a simple proof that the series for NaCl converges only conditionally.

‡ Frequently the Madelung constant is supposed to be defined as the limiting value of the work per ion required to remove it from the lattice. This definition suffers from the defect that the work depends upon the shape assumed for the crystals for which the limit is to be computed. Both mathematically and physically, the term "infinite lattice" can only mean a suitably defined limiting process on finite lattices.

order can be specified by *defining* the specific energy to be the limit (if it exists) obtained by increasing the size of finite lattices of a fixed shape.

Thus the absence of absolute convergence gives rise to two practically important questions:*

(1) Consider a particular crystal structure and finite electrically neutral specimens of fixed shape. If the specimen size is increased without changing the shape does the specific energy approach a limiting value and, if so, what is the limit? If the limit exists, macroscopic specimens of this shape will have a specific energy which will be constant within experimental error and can, therefore, be said to be "well-defined".

(2) If the series converges, does it converge to the minimum specific energy, i.e. is the shape in the class of one or more most stable crystal forms? Finally, do actual specimens attain one of these most stable forms under the conditions in which they are grown? In this case the observed macroscopic specimens can be said to have a "well-defined" specific energy.

Therefore, to investigate the validity of Ewald's calculation, it is necessary to consider the order of summation which Ewald's calculation implicitly assumes and to determine whether this order defines a convergent series. If it does, then the limit will be the specific energy obtained by increasing the size of finite crystals of the shape corresponding to the assumed order of summation. Simple general conditions will be given which ensure the conditional convergence of the lattice sums. First one, and then two and three dimensional lattices will be considered. Then it will be shown that whenever these conditions are satisfied, the series converge for the Ewald order of summation. The practical need for careful attention to the question of summation order is illustrated by the fact that even in the case of the simple NaCl lattice, divergent orders have been assumed to be convergent.†

The standard theorem on alternating series states: A (real) alternating series of which the absolute values of the terms form a monotonic null sequence is invariably convergent . . . Its value lies between any two successive partial sums.(5) It follows at once that the series for the potential of any simple one-dimensional lattice of alternating equal plus and minus charges converges conditionally.

Whereas this model is too restrictive, the theorem has a simple generalization of wider applicability.

Theorem 1. Generalized alternating series theorem

1. Let $I = \sum_{p} a_p$ where the a_p are real and $|a_p|$ form a monotone non-increasing null sequence.

2. Suppose there is a positive integer n such that for each j, a_j and a_{n+j} have opposite signs.

Then, the series I converges conditionally and for each positive integer k, its limit lies between the successive partial sums,

$$\sum_{p=1}^{kn} a_p, \quad \sum_{p=1}^{(k+1)n} a_p. \tag{3}$$

This theorem generalizes the requirement of an alternation of sign for successive terms to a requirement that if the terms are divided into a sequence of ordered n-tuples,

$$X_1 = \langle a_1, \ldots, a_n \rangle, \quad X_2 = \langle a_{n+1}, \ldots, a_{2n} \rangle, \ldots, \tag{4}$$

then the i-th element of X_i and X_{i+1} have opposite signs. The proof, which parallels that for the standard theorem, is a consequence of the generalized alternation in sign and non-increasing conditions. It follows that the series converges if it is summed in the order of increasing n. Since this is the order specified by increasing the size of a finite specimen, it follows that any one-dimensional lattice which satisfies this generalized sign alternation has a "well-defined" specific energy.

---

* EMERSLEBEN(3b) has pointed out that the problem of convergence for the infinite series is directly related to the effects of boundary regions of finite crystals. He did not develop this observation as it is done here. BOUMAN(4a) (in his discussion of Ewald's and Kornfeld's formulae) observes that the absolute convergence "signifie que cette force dans un cristal infini ne depend pas de la forme sous laquelle on fait croître le crystal a l'infini". However, he did not develop this observation to show what shape their work implicitly assumes. Instead, he chose to discuss their work in terms of charge distributions which would have the same potental.

† EMERSLEBEN(3c) gives an example from the recent literature.

To generalize the result to two dimensions it is only necessary to suppose that two axes (x,y) can be found for which generalized alternating sign conditions hold. To describe these conditions, let:

$\langle L_1, L_2\rangle$: the set of pairs of integers which order the lattice sites in the (x,y) coordinate system; (5)

$\mathscr{L}j$: the array of lattice points parallel to the y axis for which $x = x_j$ (i.e. the set of lattice points designated by the set of ordered pairs, $\{\langle j,L_2\rangle\}$). (6)

The conditions are:

Condition A. The alternating sign condition for an array parallel to the y axis

Suppose that for each $\mathscr{L}_j$, the set of lattice points of $\mathscr{L}_j$ give a series which satisfies the generalized alternating sign condition of Theorem I. Then the series necessarily converges conditionally to a value which will be denoted by U_j.

Condition B. The alternating sign condition for an array parallel to the x axis

If arrays parallel to the x axis also follow the generalized alternating sign condition, then there will be a positive integer m such that for each j and each L_2, the charges at the lattice site $\langle j,L_2\rangle$ and $\langle j+m,L_2\rangle$ are of opposite sign.

It can be seen that in this case the series of the U_j obeys a generalized alternating sign condition and that, therefore, the series for the potential of the two-dimensional array converges conditionally. Finally, consider the order of summation defined by including all points contained within an increasing sequence of parallelopipeds whose edges are parallel to the axes. The argument given above can be completed to show that this order defines a convergent series. The extension to three dimensions is obvious.

2. JUSTIFICATION OF EWALD'S FORMULAE FOR IONIC LATTICES

Ewald[(1)] conceived of an elegant approach to the problem of calculating the potential of a general ionic crystal. By an ingenious device, he was able to construct two absolutely convergent series which in some cases converge far more rapidly and whose limit is just the desired limit of the one more slowly conditionally convergent series. However, only heuristic arguments were given to establish the basis for his approach.[(1a)] Recognizing this, Kornfeld[(2)] later remarked that his work (based upon Ewald's equations) had at least the justification of Ewald's. The argument of Section 1 has shown that whenever a generalized sign alternation holds for each of three independent axes (x_1, x_2, x_3), then the series converge when they are summed for points contained within an increasing sequence of parallelopipeds whose edges are parallel to the axes. Equivalently, finite specimens of such a shape can be said to possess a "well-defined" specific energy. The proof of Ewald's formula as given below will show that they yield the limiting specific energy for crystals of this shape.

Let $\boldsymbol{r}$: vector from some lattice point which is taken as the origin to some point, P, at which the potential is to be computed, where P is not a lattice point;

$U(\boldsymbol{r})$: the potential at P defined by an electrically neutral crystal;

$\boldsymbol{\rho}$: a vector from the origin to an arbitrary lattice point;

$\boldsymbol{R} = \boldsymbol{r}-\boldsymbol{\rho}$: a vector of magnitude, R. (7)

The potential of a point charge at the endpoint of $\boldsymbol{\rho}$ is replaced by an approximating function, $\varphi(R,k_0)$, which satisfies the following conditions:

Condition 1: k_0 is an imaginary number,

$$k_0 = u+iw.^* \tag{8a}$$

$\varphi(R,k_0)$ is continuous at the origin and has the limit:

$$\lim_{k_0\to 0} \varphi(R,k_0) = 1/R. \tag{8b}$$

Condition 2: Consider an electrically neutral ionic lattice and a summation order which gives a series converging to $U(\boldsymbol{r})$ [cf. equation (7)]. Form a corresponding series by multiplying $\varphi(R,k_0)$ by the charge of the lattice site. Suppose $\varphi(R,k_0)$ is chosen so that:

---

* For the purpose of this argument, u can be taken to be zero. However, k_0 is used as a complex number to maintain agreement with Ewald's notation.

(a) The series converges absolutely to $U(r,k_0)$ whenever $w > 0$ (This will permit interchange of order of algebraic operations.)

(b) For each u, the series converges uniformly for $w \geqslant 0$. Then it follows from the continuity of $\varphi(R,k_0)$ that

$$U(r) = \lim_{\substack{k_0 \to 0 \\ w \geqslant 0}} U(r,k_0). \tag{9}$$

Thus if $\varphi(R,k_0)$ can be chosen to give a convenient equation for $U(r,k_0)$, the desired potential can be computed as $U(r,0)$. Ewald derived a convenient equation in the study of optical potentials of the form:*

$$\sum_{p'} \{P(p') \exp[ik_0 R_{pp'} + i(\xi \cdot R_{(p')})]\}/R_{pp'} \tag{10}$$

$R_{pp'}$: the distance between p and p'.

To examine the validity of his equations for the electrostatic potential, we can replace $P(p')$ by the charge at p', set $\xi = 0$, choose k_0 to be a pure imaginary, $k_0 = iw, w > 0$, so that the approximating potential for a unit charge is:

$$\varphi(R,k_0) = [\exp(-wR)]/R. \tag{11}$$

Clearly, this choice satisfies condition (1). To see that it satisfies the uniformity requirement of condition (2), it is sufficient to use the simple alternating sign condition of Section 1. (The argument for the general condition is essentially the same and merely has more complicated notation.)

Along any of the three axes for which the alternating sign condition holds, select two successive sites, R_1 and R_2. Then $(1/R_1) > (1/R_2)$ and the convergence will be uniform if

$$(1/R_1) - (1/R_2) > [\exp(-wR_1)]/R_1 - [\exp(-wR_2)]/R_2. \tag{12}$$

To establish the inequality, define

$$f(R_1,R_2) \equiv (R_2/R_1) - [1-\exp(-wR_2)]/[1-\exp(-wR_1)]. \tag{13a}$$

Then rearrangement of (12) shows that the inequality will hold if

$$(R_2 > R_1) \to (f(R_1,R_2) > 0). \tag{13b}$$

Now $f(R_1, R_2)$ vanishes when $R_2 = R_1$. The partial derivative satisfies the inequality:

$$\begin{aligned} \partial f/\partial R_2 &= [1-\exp(-wR_1) \\ &\quad - wR_1 \exp(-wR_2)]/[R_1\{1-\exp(-wR_1)\}] \qquad (14) \\ &\geqslant [1-(1+wR_1)\exp(-wR_1)]/[R_1\{1-\exp(-wR_1)\}]. \end{aligned}$$

Since $(1+wR_1)\exp(-wR_1) < 1$ for $wR_1 > 0$, both numerator and denominator are positive. This proves (13b) and, therefore, establishes that the convergence is uniform when the series is summed over lattice sites contained in an increasing sequence of parallelopipeds whose edges are parallel to the axes.† It follows that whenever the alternating sign conditions hold, the Ewald equation for $U(r,0)$ gives the limiting value for the potential of an increasing sequence of parallelopipeds whose edges are parallel to the three axes.‡

3. RELATION OF CONDITIONS TO SOME PREVIOUS STUDIES OF CRYSTAL SHAPE

Emersleben(6a) treated rigorously the one-dimensional ionic crystal which satisfies the more restrictive simple alternating sign condition of Section 1. He showed that for a finite crystal the total energy, E, could be written as the sum:

$$E = e_1 n + e_0 + Z(n) \tag{15a}$$

e_1, e_0: constants, independent of n

n: number of ion pairs

$Z(n)$: a remainder term such that $\lim_{n\to\infty} Z(n) = 0$.

The value of this subdivision lay in the following facts: (1) he was able to develop an interpretation of $e_0/2$ as the energy per end of the finite chain; (2) e_1 is just the limit of the specific energy defined uniquely by the order of summation corresponding to a one-dimensional crystal of increasing size.(7a) Therefore, he viewed $e_1 n$ as a "bulk" energy and $Z(n)$ as a correction term.

---

* See Ewald(1), equation (6), p. 256.

† Bouman(4b) gives the analogue of equation (9) [cf. equation (23), p. 4]. However, he does not establish the uniform convergence, nor does he note that the uniformity is relative to the presumed order of summation. Neglect of this would lead to the immediate contradiction of the valid equation (9): $\lim_{k_0\to 0} U(r,k_0)$ is unique, but the value of $U(r)$ depends upon the order of summation.

‡ This same conclusion can also be reached independently by the argument developed for multiple formulae in the next section.

Since he was not able to extend his treatment rigorously to any two or three dimensional lattices, he made many numerical studies. Upon the basis of these results he postulated that the total coulombic energy for finite parallelopipeds could be written as a sum analogous to (15a):

$$E = e_3 n^3 + e_2 n^2 + e_1 n + e_0 + Z(n) \qquad (15b)$$

e_3, e_2, e_1, e_0: constants independent of n

n: number of ion-pairs along a crystal edge

$Z(n)$: a remainder term such that $\lim_{n\to\infty} Z(n) = 0$.

The total number of pairs in the parallelopiped is proportional to n^3, where the proportionality factor depends upon the crystal structure. Therefore, dividing by n^3 and passing to the limit as $n \to \infty$ shows that e_3 is proportional to the limiting specific energy/ion pair. At first he did not realize that the criterion that a finite crystal be electrically neutral is not sufficient to define a unique limiting value for the specific energy as $n \to \infty$. Subsequently, he studied different parallelopipeds for two and three dimensional electrically neutral crystals which could be divided into two groups:

Class I. All boundaries electrically neutral;

Class II. Some boundaries electrically charged.

The different classes gave different values for e_3 for the same crystal structure. It is interesting that the stable shapes of Class I are those for which the axes satisfy the alternating sign conditions of Section 1.*

Such studies of specific shapes represent a step towards the answer to question (2) of Section 1. Whereas Emersleben deals only with the point charge contribution, it is necessary to consider other terms as well. Some of the more general problems are discussed briefly by EWALD and JURETSCHKE.(9) They also offer an alternative attempt to calculate the surface energy for a perfect bounded lattice.†

4. DEDUCTION OF EQUATIONS FOR MULTIPOLE LATTICES FROM EWALD'S EQUATIONS

The potential at a point P_β produced by a multipole of the n-th order of moment $p^{(n)}$, and characteristic directions $s_1, \ldots, s_n$ is defined as

$$\frac{(-1)^n p^{(n)}}{n!}(s_n \cdot \nabla_\beta) \ldots (s_1 \cdot \nabla_\beta)(1/r\langle A,\beta\rangle);$$

$$s_1, \ldots, s_n\text{: unit vectors} \qquad (16)$$

$$r\langle A,\beta\rangle = \{\sum_{i=1}^{3} (X^i_\beta - X^i_A)^2\}^{1/2};$$

$$\nabla_\beta = \langle \partial/\partial X^1_\beta,\ \partial/\partial X^2_\beta,\ \partial/\partial X^3_\beta\rangle.$$

Similarly the energy of interaction between multipoles of order m and q is a scalar multipole of an $(m+q)$-th order directional derivative.‡ This led KORNFELD(2) to suggest that the formulae for multipole lattices could be deduced by taking directional derivatives of Ewald's equations for an ionic lattice. Kornfeld's discussion of the justification for his work does not establish the validity of interchanging the order of the limiting processes involved in Ewald's transformation and of differentiation. Furthermore, it contains a logical error which led to misleading statements.

To understand the problem, it will be necessary to consider some details of Ewald's derivation. The exact formulae will be given here to connect the argument to a subsequent extension of KORNFELD's work.(10)

The entire crystal lattice is decomposed into sublattices, each of which is a simple translation lattice in the sense that the entire sub-lattice can be reproduced from a single point by a combination of unit translations along three independent axes. Let:

---

* It seems that EMERSLEBEN thought of a surface contribution to the energy in two distinct senses. In the first sense, the specific surface energy was proportional to e_2 of equation (15b).(7) In the second sense, the surface contribution was a change in e_3 (i.e. in the "bulk" energy, $e_3 n^3$)(8) as the order of summation (i.e. the shape of the finite specimen) was changed. It would be desirable to use different terms for these two distinct interpretations.

† As the authors carefully note, their formulae depend upon the validity of interchanging the order of certain limiting operations. This interchange must still be investigated.

‡ For further discussion of the use of multipoles, see CAMPBELL.(10)

e_T: charge at each site of the simple translation lattice, T;

$(\boldsymbol{a}_1, \boldsymbol{a}_2, \boldsymbol{a}_3)$: vectors which define a unit cell for the crystal;

$L = \langle L_1, L_2, L_3 \rangle$, an arbitrary ordered triple of integers;

$$\boldsymbol{r}_L = \sum_{i=1}^{3} L_i \boldsymbol{a}_i; \qquad (17)$$

$\boldsymbol{b}_i$: the vector reciprocal to $\boldsymbol{a}_i$, $i = 1,2,3$, [i.e. $\boldsymbol{b}_i = (\boldsymbol{a}_j \times \boldsymbol{a}_k)/(\boldsymbol{a}_i \cdot \boldsymbol{a}_j \times \boldsymbol{a}_k)$, where $\langle i, j, k \rangle$ may undergo any cyclic permutation];

$$\boldsymbol{q}_L = 2\pi \sum_{i=1}^{3} L_i \boldsymbol{b}_i,$$

a vector of magnitude q_L.

By applying a transformation on a theta function of three variables, Ewald was able to deduce an alternative representation for $U(\boldsymbol{r},k_0)$, the potential at the endpoint of $\boldsymbol{r} = \langle r^1,r^2,r^3 \rangle$, defined by a crystal of singularities, $\varphi(R,k_0)$. This representation is a sum over the set of translation lattices:

$$U(\boldsymbol{r},k_0) = \sum_{T} e_T U_T(\boldsymbol{r},k_0). \qquad (18a)$$

e_T: the charge at each site of the simple translation lattice T.

For each translation lattice, $U_T(\boldsymbol{r},k_0)$ is itself a sum of two functions:*

$$U_T(\boldsymbol{r},k_0) = U_{T,1}(\boldsymbol{r},k_0,\epsilon) + U_{T,2}(\boldsymbol{r},k_0,\epsilon). \qquad (18b)$$

Subsequently, it will be seen to be convenient to decompose the first term, $U_{T,1}(\boldsymbol{r},k_0,\epsilon)$, into two terms, one of which is independent of $\boldsymbol{r}$ and of L:

$$U_{T,1}(\boldsymbol{r},k_0) = U'_{T,1}(\boldsymbol{r},k_0,\epsilon) + U''_{T,1}(k_0,\epsilon); \qquad (19a)$$

$$U'_{T,1}(\boldsymbol{r},k_0,\epsilon) = \frac{4\pi}{(\boldsymbol{a}_1 \cdot \boldsymbol{a}_2 \times \boldsymbol{a}_3)} \sum{}' \{(q_L)^2 + k_0^2\}^{-1}$$
$$\times \exp\left\{\frac{-[(q_L)^2 - k_0^2]}{4\epsilon^2} + i(\boldsymbol{q}_L \cdot \boldsymbol{r} - \boldsymbol{r}_T)\right\}; \qquad (19b)$$

where

$\sum{}'$ Summation over all L Such that $q_L \neq 0$; (19c)

$$U''_{T,1}(k_0,\epsilon) = \frac{4\pi}{(\boldsymbol{a}_1 \cdot \boldsymbol{a}_2 \times \boldsymbol{a}_3)} k_0^{-2} \exp(k_0^2/4\epsilon^2); \qquad (19d)$$

$$U_{T,2}(\boldsymbol{r},k_0,\epsilon) = \sum_{\{L\}} \left\{\frac{\cos(k_0 R_{L,T})}{R_{L,T}}\right.$$
$$-1/2R_{L,T}[\exp(ik_0 R_{L,T})\phi(\epsilon R_{L,T} + ik_0/2\epsilon)$$
$$\left.+\exp(-ik_0 R_{L,T})\phi(\epsilon R_{L,T} - ik_0/2\epsilon)]\right\}; \qquad (19e)$$

$$\boldsymbol{R}_{L,T} = \boldsymbol{r} - (\boldsymbol{r}_L + \boldsymbol{r}_T); \qquad (19f)$$

$$R_{L,T} = \{\sum_{i=1}^{3} [r^i - r_L^i - r_T^i]^2\}^{1/2} \qquad (19g)$$

$$\phi(X) = \frac{2}{\sqrt{\pi}} \int_0^X \exp(-\alpha^2)\, d\alpha; \qquad (19h)$$

ϵ: an arbitrary parameter (vide infra). (19i)

Whenever the lattice is neutral so that,

$$\sum_{\{T\}} e_T = 0, \qquad (20)$$

then, [since $U''_{T,1}(k_0,\epsilon)$ is the same for each lattice T],

$$\sum_{\{T\}} e_T U''_{T,1}(k_0,\epsilon) = 0 \qquad (21)$$

In this case, equation (18) can be written in the form:

$$U(\boldsymbol{r},k_0) = \sum_{\{T\}} e_T U'_T(\boldsymbol{r},k_0); \qquad (22a)$$

$$U'_T(\boldsymbol{r},k_0) = U'_{T,1}(\boldsymbol{r},k_0,\epsilon) + U_{T,2}(\boldsymbol{r},k_0,\epsilon). \qquad (22b)$$

Ewald's transformation which gives equation (18) is valid only for $w > 0$. However, for neutral lattices, this equation can be replaced by (22) which converges uniformly for $w \geqslant 0$ and is continuous at $k_0 = 0$. Thus the original conditionally convergent series for an ionic lattice has been replaced by a sum of absolutely convergent series, two for each translation lattice. Obviously, the finite sum,

---

* These are essentially EWALD's equations (33,4), p. 273,(1) specialized for an ionic lattice. In terms of the symbols of equation (10), this means that $\xi = 0$ and $P(p')$ is replaced by the charge at p'. Note that there is a misprint in EWALD's equation (33). The magnitude χ_L should read χ_L^2. [Compare with his equation (30), p. 272.] In agreement with KORNFELD's notation(2) $\boldsymbol{\chi}_L$ has been replaced by $\boldsymbol{q}_L$ and E by ϵ.

$$U'_T(\mathbf{r},0) = U'_{T,1}(\mathbf{r},0,\epsilon)+U_{T,2}(\mathbf{r},0,\epsilon)$$

is *not* the infinite potential defined by a simple translation lattice [the infinite potential is, of course, $\lim_{k_0\to 0} U_T(\mathbf{r},k_0)$];

$$U'_T(\mathbf{r},0)$$

is merely the contribution of a simple translation lattice to the sum (22a) for the potential of a neutral ionic lattice. KORNFELD(2) made the logical error of equating the potential of a simple translation lattice of dipoles to the contribution the simple lattice makes to a sum for the potential. This can be seen by citing the steps he used to deduce equations for the potential of a simple translation lattice of dipoles:

Step I: Take the directional derivative of Ewald's equation for a *neutral* ionic lattice composed of two simple translation lattices and multiply by minus one [cf. equation (16)].

Step II: Determine the contribution of each simple translation lattice to the directional derivative.

Step III: Infer that the contribution of each simple translation lattice to the directional derivative of the equation for a neutral lattice is the negative of the potential defined by a simple lattice of unit dipoles.

Unfortunately, it is well known that the series for the potential of a simple lattice of dipoles fails to converge absolutely. Thus, just as in the case of the ionic lattice, two conclusions follow immediately: (1) The convergence of the series must be established for the particular order of summation which is assumed; (2) The question of whether the summation order prescribed by crystal growth for this shape will give a "well-defined" specific energy is equivalent to the question of whether the summation order prescribed by crystal growth for this shape gives a convergent series. As previously seen, the Ewald formulae are for summation along the axes of the translation lattice and it is shown in Appendix B* that the series for this order of summation does not converge. It is, therefore, inappropriate to speak of the potential of a simple translation lattice of dipoles as computed by the Kornfeld formulae.†

Conditions under which the equations derived from Ewald's formulae will be valid can be established by the following steps.

Step I: Convergence of lattice sums for multipoles for the Ewald order of summation

In Appendix C it is shown that (at least in the case of the general orthogonal crystal), the necessary and sufficient condition under which the potential for a dipole crystal converges for the Ewald order of summation is that the crystal has a zero net dipole moment [cf. equation (C.11):

$$\sum_{\{T\}} p_T s_T = 0].‡$$

Furthermore, the argument of Appendix D shows that the interaction energy between a dipole and a simple translation lattice of dipoles always converges for this order of summation (at least in the case of the general orthogonal crystal). The series for all higher order interactions decrease as $1/r^n$, $n \geqslant 4$ and necessarily converge.

Step II: Use of the Ewald equations; Inversion of order of limiting operations

Consider an n-th order directional derivative of $\varphi(R,k_0)$. For each $w \geqslant 0$, it can be shown that the lattice sum for $\varphi(R,k_0)$ and the lattice sum for such a directional derivative converge uniformly over the exterior of any sphere containing the endpoint of $\mathbf{r}$. Since the derivatives of φ are continuous, it follows that the series for the lattice sum of $\varphi(\mathbf{R},\mathbf{k}_0)$ can be differentiated termwise to obtain:

---

* Conversely, as is well-known, it is a simple consequence of the symmetry of the dipole potential that leading terms in any sum over a spherically symmetric set of lattice sites must vanish [cf. equation (C.6) of Appendix C]. For this order, the series does converge.

† BOUMAN(4) also discusses the Kornfeld formulae. As noted under the discussion of ionic lattices, he does not include a proof of the uniform convergence which he asserts. Furthermore, since he discusses the calculation in terms of equivalent distributions, it is worthwhile to present a simple justification of the Kornfeld formulae which shows clearly their relation to the order of summation.

‡ This condition is often used. Since, as has been observed, the series does converge conditionally (e.g. when summed over spherically symmetric arrays of lattice sites) it is desirable to include a careful proof for the Ewald summation order.

$$\sum_{\{L\}}\prod_{j=1}^{n}(\mathbf{s}_{j,T}\cdot\nabla)\varphi(\mathbf{R}_{L,T},\mathbf{k}_0)$$

$$=\prod_{j=1}^{n}(\mathbf{s}_{j,T}\cdot\nabla)U_T(\mathbf{r},\mathbf{k}_0); \qquad (23)$$

$$\nabla=(\partial/\partial r^1,\ \partial/\partial r^2,\ \partial/\partial r^3).$$

It should be possible to assume suitable conditions (e.g. those of Appendix C) under which equation (23) could be shown to converge uniformly for the Ewald summation order for $w \geqslant 0$. Then it would be justified to pass to the limit $\mathbf{k}_0 = 0$. Since a careful and general argument would involve complicated notation, it is better to proceed by the following steps:

Step IIA: Termwise differentiation of $U'_{T,1}$ and $U_{T,2}$; Formation of the lattice sum

Consider the series,

$$U'_T(\mathbf{r},0) = U'_{T,1}(\mathbf{r},0,\epsilon)+U_{T,2}(\mathbf{r},0,\epsilon); \qquad (24)$$

$$U'_{T,1}(\mathbf{r},0,\epsilon) = \frac{4\pi}{(\mathbf{a}_1\cdot\mathbf{a}_2\times\mathbf{a}_3)}\sum{}'(q_L)^{-2}$$

$$\times\exp[-(q_L)^2/4\epsilon^2+i(\mathbf{q}_L\cdot\mathbf{r}-\mathbf{r}_T)]; \qquad (25a)$$

$$U_{T,2}(\mathbf{r},0,\epsilon) = \sum_{\{L\}} G(\epsilon R_{L,T})/R_{L,T};\ G(x) = 1-\phi(x) \qquad (25b)$$

Since for each $\epsilon > 0$ the derived series for $U'_{T,1}$ and $U_{T,2}$ converge uniformly over the exterior domain of any sphere centered at $\mathbf{r}$, and since the derivatives of the terms of the series are continuous, they can be differentiated termwise. Multiplication by the magnitude of the multipole of the T-th translation lattice and summation over $\{T\}$ gives:

$$\sum_{\{T\}}p_T\prod_{j=1}^{n}(\mathbf{s}_{j,T}\cdot\nabla)U'_T(\mathbf{r},0)$$

$$=\sum_{\{T\}}p_T\prod_{j=1}^{n}(\mathbf{s}_{j,T}\cdot\nabla)U'_{T,1}(\mathbf{r},0,\epsilon) \qquad (26)$$

$$+\sum_{\{T\}}p_T\prod_{j=1}^{n}(\mathbf{s}_{j,T}\cdot\nabla)U_{T,2}(\mathbf{r},0,\epsilon).$$

Step IIB: Reordering of the derived series for $U_{T,2}$ and introduction of the multipole series

Since the derived series for $U_{T,2}$ converges absolutely, it can be reordered to give [cf.(25b)],

$$\sum_{\{T\}}p_T\prod_{j=1}^{n}(\mathbf{s}_{j,T}\cdot\nabla)U_{T,2}(\mathbf{r},0,\epsilon)$$

$$=\sum_{\{L\}}\sum_{\{T\}}p_T\prod_{j=1}^{n}(\mathbf{s}_{j,T}\cdot\nabla)\,[G(\epsilon R_{L,T})/R_{L,T}]. \qquad (27)$$

According to equation (25b), $G(x) = 1-\phi(x)$. If the multipole lattice sum,

$$U(\mathbf{r},\{\mathbf{s}_j\}) = \sum_{\{L\}}\sum_{\{T\}}p_T\prod_{j=1}^{n}(\mathbf{s}_{j,T}\cdot\nabla)\,(1/R_{L,T}), \qquad (28)$$

converges for the Ewald order of summation (cf. Step 1), then the right side of equation (27) must be the sum of two convergent series:

$$\sum_{\{T\}}p_T\prod_{j=1}^{n}(\mathbf{s}_{j,T}\cdot\nabla)U_{T,2}(\mathbf{r},0,\epsilon) = U(\mathbf{r},\{\mathbf{s}_j\})$$

$$+U_2(\mathbf{r},\{\mathbf{s}_j\},\epsilon); \qquad (29)$$

$$U_2(\mathbf{r},\{\mathbf{s}_j\},\epsilon) = \sum_{\{L\}}\sum_{\{T\}}p_T\prod_{j=1}^{n}(\mathbf{s}_{j,T}\cdot\nabla)\cdot$$

$$\times\ [\phi(\epsilon R_{L,T})/R_{L,T}].$$

Substitution of (29) into (26) gives the absolutely convergent series on the left of (26) as a sum of 3 convergent series, one of which is the multipole summation:

$$\sum_{\{T\}}p_T\prod_{j=1}^{n}(\mathbf{s}_{j,T}\cdot\nabla)U'_T(\mathbf{r},0)$$

$$=\sum_{\{T\}}p_T\prod_{j=1}^{n}(\mathbf{s}_{j,T}\cdot\nabla)U'_{T,1}(\mathbf{r},0,\epsilon) \qquad (30)$$

$$+U(\mathbf{r},\{\mathbf{s}_j\})+U_2(\mathbf{r},\{\mathbf{s}_j\},\epsilon).$$

The sum of the second and third terms on the right side of (30) can be shown to vanish by the following argument. Since Ewald's work implies that $U'_T(r,0)$ is independent of ϵ, therefore, the right side of (30) must be independent of ϵ so that:

$$\sum_{\{T\}} p_T \prod_{j=1}^{n} (s_{j,T} \cdot \nabla) U'_{T,1}(r,0,\epsilon) + U_2(r,\{s_j\},\epsilon) = C; \tag{31}$$

C: a constant.

Now examination of (25a) shows that,

$$\lim_{\epsilon \to 0} \prod_{j=1}^{n} (s_{j,T} \cdot \nabla)\, U'_{T,1}(r,0,\epsilon) = 0. \tag{32}$$

Therefore, $\lim\limits_{\epsilon\to 0} U_2(r,\{s_j\},\epsilon) = C$. But since the form of $\phi(x)$, [cf.(19h)] shows that $\lim\limits_{\epsilon\to 0}$ of any partial sum for U_2 vanishes, $C = 0$. Thus, whenever $U(r,\{s_j\})$ converges for the Ewald order of summation, its limit (for this order) can be computed as the sum of absolutely convergent series:

$$U(r,\{s_j\}) = \sum_{\{T\}} p_T \prod_{j=1}^{n} (s_{j,T} \cdot \nabla) U'_{T\,1}(r,0,\epsilon)$$

$$+ \prod_{j=1}^{n} (s_{j,T} \cdot \nabla)\, U_{T,2}(r,0,\epsilon). \tag{33}$$

The general equations for the right side of equation (33) have been obtained in a form convenient for calculation on an electronic computer.(10) These equations have two marked advantages over the direct use of equation (28):

(1) *Convenient check for error.* The functions $U'_{T,1}$ and $U_{T,2}$ (and their derivatives) depend upon the arbitrary parameter ϵ, but their sum, U'_T (and its derivatives) do not. This provides a simple independent check of the calculation by performing the computation for two different values of ϵ. It is imperative to note that approximate agreement is meaningless. Two values for a given $U'_T(r,0)$ which agreed to a few per cent were found to be in error by one hundred per cent.

(2) *Rapidity of convergence.* In general, the series given by (33) should converge more rapidly than those given by (28). Since a decrease [increase] in ϵ will cause $U'_{T,1}(r,0,\epsilon)$ $[U_{T,2}(r,0,\epsilon)]$ to converge more rapidly, values should be chosen in a range to minimize the total work.

REFERENCES

1. Ewald P. P., *Ann. Phys. Lpz.* **64**, 253; (a) 265–6 (1921).
2. Kornfeld H., *Z. Phys.* **22**, 27–43 (1924).
3. Emersleben Otto, *Math. Nachr.* **4**, 468–80; (a) 473; (b) 474; (c) 472 (1951).
4. Bouman J., *Archives néerl. Sci.* (IIIA), **13**, 1–28; (a) 3 (1931).
5. Knopp K., *Infinite Sequences and Series*, Theorem 2, 68. Dover, New York (1956).
6. Emersleben Otto, *Math. Nachr.* **9**, 221–34; (a) 227–30 (1953).
7. Emersleben Otto, *Z. phys. Chem.* **199**, 170–90; (a) 183–4 (1952).
8. Emersleben Otto, *Z. phys. Chem.* **204**, 121–30 (1955).
9. Ewald P. P. and Juretschke H., *Structure and Properties of Solid Surfaces* (Edited by Gomer R. and Smith C. S.). 82–119. University Press, Chicago (1953).
10. Campbell E. S., submitted for publication.
11. Pierce B. O., *A Short Table of Integrals*, 25. Ginn, New York (1929).

APPENDIX A

Generalized integral tests for the convergence of multiple series

The first theorem is a simple extension of the ordinary theorem for series in one index whose terms are all either positive or negative.[*]

Theorem 1. Suppose:

(1) $f(\{x_i\})$ is a non-negative function defined over the set of $\{x_i\}$, $1 \leqslant x_i$, $i = 1,\ldots, n$.

(2) For any fixed choice of $(n-1)$ variables, $f(\{x_i\})$ is a monotone non-increasing function of the n-th variable.

(3) For each ordered n-tuple of positive integers, $\langle p_1,\ldots, p_n\rangle$, define

$$F(\langle p_1,\ldots,p_n\rangle) = f(\{p_i\}).$$

Then,

$$\int_2^{q_n+1} \cdots \int_2^{q_1+1} f(\{x_i\}) \prod_{i=1}^{n} \mathrm{d}x_i \leqslant \sum_{p_n=2}^{q_n} \sum_{p_1=2}^{q_1} F(\langle p_1,\ldots,p_n\rangle)$$

$$\leqslant \int_1^{q_n} \cdots \int_1^{q_1} f(\{x_i\}) \prod_{i=1}^{n} \mathrm{d}x_i.$$

---

[*] See Knopp,(5) p. 64.

The proof parallels that for the standard theorem.*

A second theorem is a test for the convergence of the difference of two series, each of which satisfies the condition of Theorem 1.

Theorem 2. Suppose

(1) $f(\{x_i\}) = g(\{x_i\}) - h(\{x_i\})$ where g and h satisfy the conditions of Theorem 1.

(2) For each ordered n-tuple of positive integers, $\langle p_1,\dots,p_n\rangle$, define

$$F(\langle p_1,\dots,p_n\rangle) = f(\{p_i\});\ G(\langle p_1,\dots,p_n\rangle) = g(\{p_i\});\ H(\langle p_1,\dots,p_n\rangle) = h(\{p_i\}).$$

Then:

$$-\int_1^{q_n}\cdots\int_1^{q_1} h(\{x_i\})\prod_{i=1}^{n}\mathrm{d}x_i + \int_2^{q_n+1}\cdots\int_2^{q_1+1} g(\{x_i\})\prod_{i=1}^{n}\mathrm{d}x_i$$

$$\leqslant \sum_{p_n=2}^{q_n}\cdots\sum_{p_1=2}^{q_1} F(\langle p_1,\dots,p_n\rangle) \leqslant \int_1^{q_n}\cdots\int_1^{q_1} g(\{x_i\})$$

$$\times\prod_{i=1}^{n}\mathrm{d}x_i - \int_2^{q_n+1}\cdots\int_2^{q_1+1} h(\{x_i\})\prod_{i=1}^{n}\mathrm{d}x_i.$$

This follows immediately from the inequalities of Theorem 1 for g and h.

APPENDIX B

Potential of a simple translation lattice of dipoles

Since the equations of the next Appendix could be used to establish the well-known result that the series for the potential would converge when summed over a spherically symmetric set of lattice points, a careful proof has been included to show that they do not converge for the Ewald summation order. In other words, a sequence of finite specimens in the shape of parallelopipeds whose edges are parallel to the axes of the translation lattice will *not give* a "well-defined" *potential* in the sense of Section 1.

For simplicity, consider a simple cubic lattice whose unit cell has unit length along each axis. Suppose that the potential is to be computed at a point, P, which is not a lattice point. Place the origin at the nearest lattice site and let $\boldsymbol{\rho} = \langle \rho^1, \rho^2, \rho^3\rangle$ be the vector from the origin to P. Then each $|\rho^i| < 1$. The potential at P defined by a lattice of unit dipoles of characteristic direction, $\boldsymbol{s} = \langle s^1, s^2, s^3\rangle$, is

$$U(P) = -\sum_{\{L^3\}}\sum_{\{L^2\}}\sum_{\{L^1\}} \frac{(\boldsymbol{s}\cdot\boldsymbol{\rho} - \boldsymbol{r}_L)}{\|\boldsymbol{r}_L - \boldsymbol{\rho}\|^3}; \qquad \text{(B.1)}$$

$$\boldsymbol{r}_L = \langle L^1, L^2, L^3\rangle, \text{ each } L^i \text{ an integer.}$$

Consider the coefficient of s^1 in the equation for $U(P)$. The terms in the coefficient for a fixed L^1 satisfy the conditions of Theorem 1 of Appendix A so that for $L^1 > |\rho^1|$:

$$I \equiv (x^1-\rho^1)\int_2^{\infty}\int_2^{\infty}[\mathrm{d}x^2\mathrm{d}x^3/\{\sum_{i=1}^{3}(x^i-\rho^i)^2\}^{-3/2}]$$

$$\leqslant (L^1-\rho^1)\sum_2^{\infty}\sum_2^{\infty}\{\sum_{i=1}^{3}(L^i-\rho^i)^2\}^{3/2} \qquad \text{(B.2)}$$

$$x^1 = L^1.$$

To obtain a simple bound for I, first translate the origin and then transform to plane polar coordinates to obtain:

$$I = (x^1-\rho^1)\int_{2-\rho^2}^{\infty}\int_{2-\rho^3}^{\infty}\frac{\mathrm{d}y^2\mathrm{d}y^3}{\{(x^1-\rho^1)^2+(y^2)^2+(y^3)^2\}^{3/2}}$$

$$\geqq 2\pi(x^1-\rho^1)\int_3^{\infty}\frac{r\,\mathrm{d}r}{\{(x^1-\rho^1)^2+r^2\}^{3/2}} \qquad \text{(B.3)}$$

$$= \frac{2\pi(x^1-\rho^1)}{\{9+(x^1-\rho^1)^2\}^{1/2}}.$$

Thus, for each $\epsilon > 0$, for sufficiently large $x^1 = L^1$ $I \geqslant 2\pi - \epsilon$. That is, although the contribution to the coefficient of s^1 in the potential by lattice sites in the plane $\langle L^1, x^2, x^3\rangle$ approaches asymptotically minus one times the contribution by sites in the plane $\langle -L^1, x^2, x^3\rangle$, it approaches a finite non-zero value as $L^1 \to \infty$. Physically, this would mean that in a finite crystal of this shape, the potential would depend upon the number of planes to either side of the point at which the potential is to be computed.

APPENDIX C

Sufficient conditions for the existence of a "well-defined potential" of a finite lattice of dipoles for the shape corresponding to the Ewald summation order

This Appendix derives sufficient conditions to ensure that a dipolar crystal of this shape will possess a "well-defined" potential. Let:

$\boldsymbol{r}_T$: a vector from the origin to a site of the simple translation lattice T of dipoles;

$p_T, \boldsymbol{s}_T$: the moment and characteristic direction of the dipoles of translation lattice T;

$\boldsymbol{r}$: a vector whose end point does not lie at any lattice site;

$\boldsymbol{r}_L$: a vector defining sites of a simple translation lattice [see equation (17)].

---

* See KNOPP,[5] p. 64.

Then the potential defined at the endpoint of $\boldsymbol{r}$ by the entire lattice is given by the following sum over the sets $\{L\}$ and $\{T\}$:

$$U = -\sum_{\{L\}}\sum_{\{T\}} p_T \frac{(\boldsymbol{s}_T \cdot \boldsymbol{r} - [\boldsymbol{r}_L + \boldsymbol{r}_T])}{\|\boldsymbol{r} - [\boldsymbol{r}_L + \boldsymbol{r}_T]\|^3}. \tag{C.2}$$

In order to derive conditions for the convergence of U, we shall expand each term for which $\boldsymbol{r}_L \neq \langle 0,0,0\rangle$ in a Taylor Series about $\boldsymbol{r} - \boldsymbol{r}_T = \boldsymbol{0}$.
This gives:

$$\begin{aligned} U = &-\sum_{\{T\}} \frac{p_T(\boldsymbol{s}_T \cdot \boldsymbol{r} - \boldsymbol{r}_T)}{\|\boldsymbol{r} - \boldsymbol{r}_T\|^3} \\ &+ \sum{}' \sum_{\{T\}} p_T \frac{(\boldsymbol{s}_T \cdot \boldsymbol{r}_L)}{\|\boldsymbol{r}_L\|^3} \\ &\quad - \left[\frac{(\boldsymbol{s}_T \cdot \boldsymbol{r})}{\|\boldsymbol{r}_L\|^3} - 3\frac{(\boldsymbol{s}_T \cdot \boldsymbol{r}_L)(\boldsymbol{r} \cdot \boldsymbol{r}_L)}{\|\boldsymbol{r}_L\|^5}\right] \\ &\quad + \left[\frac{(\boldsymbol{s}_T \cdot \boldsymbol{r}_T)}{\|\boldsymbol{r}_L\|^3} - 3\frac{(\boldsymbol{s}_T \cdot \boldsymbol{r}_L)(\boldsymbol{r}_T \cdot \boldsymbol{r}_L)}{\|\boldsymbol{r}_L\|^5}\right] \\ &\quad + 0(1/\|\boldsymbol{r}_L\|^4); \end{aligned} \tag{C.3}$$

Σ': a summation over all $\boldsymbol{r}_L \neq \langle 0,0,0\rangle$.

Since any term of the order of $1/\|\boldsymbol{r}_L\|^4$ will surely give a convergent series, the Taylor Series Expansion will be valid whenever the three [ ] under Σ' give convergent series. The argument of Appendix B shows that the series from the first term of the double sum does not converge in general for this summation order. Since it will be shown below that the second and third terms give convergent series,* it follows that U will converge if and only if a condition is imposed which will ensure the convergence of the series from the first term. This will occur if and only if,

$$\sum_{\{T\}} p_T \boldsymbol{s}_T = \boldsymbol{0}, \tag{C.4}$$

i.e. the crystal has no net dipole moment.

The convergence of the series from the third term will now be established rigorously for the case when the simple translation lattice is orthogonal with arbitrary unit lengths $\langle a^1, a^2, a^3\rangle$ along the three axes. Thus $\boldsymbol{r}_L$ is of the form,

$$\boldsymbol{r}_L = \langle L^1a^1, L^2a^2, L^3a^3\rangle;\ L^1, L^2, L^3 \text{ integers.} \tag{C.5}$$

Since $(\boldsymbol{s}_T \cdot \boldsymbol{r}_L)(\boldsymbol{r}_T \cdot \boldsymbol{r}_L)/\|\boldsymbol{r}_L\|^5$ varies as $1/\|\boldsymbol{r}_L\|^3$, the symmetry of the summation ensures that the series for terms which are odd functions of the components, r_L^i must converge to zero. Therefore:

$$\begin{aligned} &\sum{}' \frac{(\boldsymbol{s}_T \cdot \boldsymbol{r}_L)}{\|\boldsymbol{r}_L\|^3} - 3\frac{(\boldsymbol{s}_T \cdot \boldsymbol{r}_L)(\boldsymbol{r}_T \cdot \boldsymbol{r}_L)}{\|\boldsymbol{r}_L\|^5} \\ &= \sum{}' \left\{\sum_{i=1}^{3} s_T^i r_T^i \left[\frac{1}{\|\boldsymbol{r}_L\|^3} - \frac{3(r_L^i)^2}{\|\boldsymbol{r}_L\|^5}\right]\right\}. \end{aligned} \tag{C.6}$$

Since the coefficients of $s_T^i r_T^i$ are of the same form for each i, it is necessary to consider only the case $i = 1$. This series satisfies the conditions of Theorem 2 of Appendix A so that the integral test can be applied. Since the argument is similar for the integrals of both sides of the inequality, we shall consider only the integrals of the right side. These integrals can be rewritten as a sum:

$$\int_1^{q_3}\int_1^{q_2}\int_1^{q_1} \frac{dx^1dx^2dx^3}{\|\boldsymbol{r}_L\|^3} - \int_2^{q_3+1}\int_2^{q_2+1}\int_2^{q_1+1} \frac{3(a^1x^1)^2}{\|\boldsymbol{r}_L\|^5} \times dx^1dx^2dx^3 \tag{C.7a}$$

$$\equiv I + S;$$

$$I = \int_2^{q_3}\int_2^{q_2}\int_2^{q_1} \left\{\frac{1}{\|\boldsymbol{r}_L\|^3} - \frac{3(a^1x^1)^2}{\|\boldsymbol{r}_L\|^5}\right\} dx^1dx^2dx^3; \tag{C.7b}$$

S: a sum of triple integrals (*vide infra*).

For each triple integral of the sum S, the range of integration for at least one coordinate x^i, remains finite as $q_i \to \infty$. Since the integrand varies as $1/\|\boldsymbol{r}_L\|^3$, each triple integral of S converges. It remains to show that I converges. To cast the integral in a standard form, let $y^i = a^ix^i$, to obtain:

$$|I| = \frac{1}{a^1a^2a^3}\left|\int_{2a^3}^{q_3a^3}\int_{2a^2}^{q_2a^2}\int_{2a^1}^{q_1a^1} \left\{\frac{1}{Y\sqrt{Y}} - \frac{3(y^1)^2}{Y^2\sqrt{Y}}\right\} \times dy^1dy^2dy^3\right|; \tag{C.8a}$$

$$Y = \sum_{i=1}^{3}(y^i)^2. \tag{C.8b}$$

---

[*] The proof is given only for the case in which each simple translation lattice is orthogonal.

Integration over y^1 gives*

$$|I| = \frac{1}{a^1a^2a^3}\left|\int_{2a^3}^{q_3a^3}\int_{2a^2}^{q_2a^2}\left\{\frac{q^1a_1}{[(y^2)^2+(y^3)^2+(q^1a^1)^2]^{3/2}}\right.\right. \tag{C.9}$$

$$\left.\left.-\frac{2a^1}{[(y^2)^2+(y^3)^2+(2a^1)^2]^{3/2}}\right\}\mathrm{d}y^2\mathrm{d}y^3\right|.$$

Since the absolute value of the integral is less than or equal to the integral of the absolute values, and since $a^2+b^2 \geqslant 2|a|\,|b|$ (or $(a^2+b^2)^{-3/2} \leqslant [2|a|\,|b|]^{-3/2}$), it follows that

$$|I| \leqslant \frac{1}{2^{3/2}a^1a^2a^3}\int_{2a^3}^{q_3a^3}\int_{2a^2}^{q_2a^2}\left\{\frac{1}{(2a^1)^2}+\frac{1}{(q_1a^1)^2}\right\} \tag{C.10}$$

$$\times\left\{\frac{1}{(y^2)^2+(y^3)^2}\right\}^{3/2}\mathrm{d}y^2\mathrm{d}y^3.$$

Since the last two dimensional integral clearly converges, the series converges by the integral test. The convergence of the series from the second [ ] can be established by the same argument.†

Thus for the general orthogonal crystal, the series for the dipole potential converges if it is summed for points contained within an increasing sequence of parallelopipeds whose edges are parallel to the axes if and only if the crystal has zero net dipole moment:

$$\sum_{\{T\}} p_T s_T = 0. \tag{C.11}$$

Equivalently, finite specimens of such a shape will give a "well-defined" potential in the sense of Section 1.

APPENDIX D

Energy of interaction between a dipole and a simple translation lattice of dipoles

Consider a dipole of moment p and characteristic direction s. If the dipole is located at the endpoint of r, then using the notation of equations (C.1,2) the interaction energy with a simple translation lattice of dipoles is:

$$E = -p\,p_T\sum_{\{L\}}\left\{\frac{(s\cdot s_T)}{\|r-[r_L+r_T]\|^3}-3\right.$$

$$\left.\times\frac{(s\cdot r-[r_L+r_T])\,(s_T\cdot r-[r_L+r_T])}{\|r-[r_L+r_T]\|^5}\right\}. \tag{D.1}$$

In a Taylor Series Expansion [cf. Appendix C, especially equation (C.3)] the only terms of order $\leqslant 3$ in reciprocal distance are:

$$-p\,p_T\sum_{\{L\}}{}'\left\{\frac{(s\cdot s_T)}{\|r_L\|^3}-3\,\frac{(s\cdot r_L)\,(s_T\cdot r_L)}{\|r_L\|^5}\right\}. \tag{D.2}$$

The argument of Appendix C shows that this series converges when summed for points contained within an increasing sequence of parallelopipeds whose edges are parallel to the axes. Equivalently, finite specimens of such a shape always give "well-defined" specific interaction energies.

---

* cf. equation (174), p. 25 of PIERCE.(11)

† Whenever (C.11) holds, after summation over $\{T\}$ each term in the Σ' vanishes identically. It is not convenient to use this argument since the same series occurs in Appendix D where (C.11) is not assumed, and Appendix D relies upon the arguments of Appendix C.

J. Phys. Chem. Solids Pergamon Press 1963. Vol. 24 pp. 209–212. Printed in Great Britain.

A PARAMAGNETIC SPECIES IN IRRADIATED $(NH_4)_2HPO_4$

J. R. MORTON

Applied Chemistry Division, National Research Council, Ottawa, Canada

(*Received* 10 *October* 1962)

Abstract—An oriented paramagnetic fragment has been detected in single crystals of $(NH_4)_2HPO_4$ γ-irradiated at 300°K. The E.P.R. spectra of the species are characteristic of a π-electron radical centred on a nitrogen atom. The fragment is of the form $\mathrm{H{-}\overset{+}{N}<}$, its orientation in the lattice probably being determined by very weak hydrogen bonds to a phosphate ion.

1. INTRODUCTION

IN RECENT years considerable interest has been shown in the E.P.R. spectra of oriented π-electron radicals. The isotropic(1) and anisotropic(2) hyperfine interactions of a proton attached to the radical centre were estimated by McCONNELL and CHESNUT, and McCONNELL and STRATHDEE respectively. The conclusions of these authors were substantiated by observations on the fragment $CH(CO_2H)_2$ formed by irradiation of a single crystal of malonic acid.(3) GHOSH and WHIFFEN(4) also gave a semi-quantitative interpretation of the anisotropy in the α-proton hyperfine interaction of the radical $CHNH_3^+CO_2^-$ formed in irradiated glycine. Recent examples have corroborated the earlier work on π-electron radicals centred on carbon, and radical geometry has been inferred(5,6) from the anisotropic α-proton hyperfine interaction.

Anisotropic ^{13}C hyperfine interactions have been measured for the radicals $^{13}CH(CO_2H)_2$ in irradiated malonic acid(7,8) and $^{13}CH(SO_3)_2^{2-}$, in irradiated potassium methane disulphonate.(9) Relatively few nitrogen centred π-radicals are known. Examples are $N(SO_3)_2^{2-}$ in potassium amine disulphonate,(9) $NHSO_3^-$ in potassium sulphonate(10) and NH_2SO_3 in a single crystal of sulphamic acid.(10)

The present work describes a nitrogen centred π-radical $\mathrm{H{-}\overset{+}{N}<}$ which is formed as an oriented paramagnetic centre in $(NH_4)_2HPO_4$ γ-irradiated at 300°K. The species was discovered in the course of an investigation of radiation damage to various phosphorus oxy-salts.(11,12)

2. EXPERIMENTAL

Crystals of $(NH_4)_2HPO_4$ were grown by slow evaporation of aqueous solutions. The unit cell is monoclinic,(13) containing four molecules of $(NH_4)_2HPO_4$, and the space group is $P2_1/a$. The unit cell dimensions are $a = 8{\cdot}03$ Å, $b = 6{\cdot}68$ Å

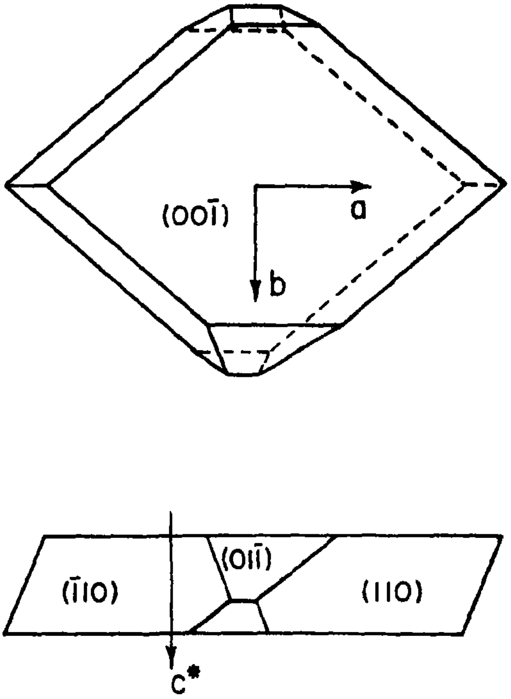

FIG. 1. Morphology of $(NH_4)_2HPO_4$ crystal, showing unit-cell directions.

and $c = 11{\cdot}02$ Å; $\beta = 113°\ 38'$. Most of the crystals had the form indicated in Fig. 1, which also shows the directions of the orthogonal axes a, b, c^* to which all direction cosines relate. Deuterated crystals were also tabular on (001) and were grown after several recrystallizations from D_2O.

Suitably sized crystals were irradiated at room temperature with 1·3 MeV ^{60}Co γ-rays, dosages of up to 5 Mrads being given. The E.P.R. spectra of the irradiated crystals were recorded with a Varian V-4500 X-band spectrometer having 100 kc/s modulation. A small one circle goniometer was attached to the outside of the cavity, enabling a crystal mounted on a perspex post to be rotated about one of the axes a, b or c^*. The axis of rotation was perpendicular to the main magnetic field of the spectrometer, and the spectra were recorded at intervals of 10°.

The magnetic field sweep was calibrated with an automatic proton magnetometer.(14)

3. INTERPRETATION OF THE SPECTRA

The E.P.R. spectrum of an irradiated crystal of $(NH_4)_2HPO_4$ for the magnetic field parallel to the c^*-axis of the crystal is shown in Fig. 2(a) The spectrum is seen to consist of a pair of triplets, evidence of hyperfine interaction with a ^{14}N nucleus ($I = 1$) and a nucleus having $I = \frac{1}{2}$ (^{1}H or ^{31}P). The change in the spectrum on deuteration proved the nucleus having $I = \frac{1}{2}$ to be a proton. Figure 2(b) shows the spectrum of an irradiated, deuterated crystal also for the direction H_0 parallel to c^*. This spectrum, which is a triplet of triplets, is consistent both with the spin of the deuteron ($I = 1$) and its lower magnetogyric ratio, as compared to the proton.

The spectra were interpreted in terms of the Hamiltonian

$$\mathcal{H} = -\beta S \cdot g \cdot H_0 + S \cdot T_N \cdot I_N + S \cdot T_H \cdot I_H$$

where β is the Bohr magneton and H_0 the applied magnetic field. The first term represents the interaction of the electron spin S with the magnetic field H_0, described by the symmetric, second-rank tensor g. The second and third terms represent the interaction of the electron spin with ^{14}N and ^{1}H nuclear spins respectively. These interactions are described by the hyperfine tensors T_N and T_H. This Hamiltonian neglects terms involving the interaction of the nuclei with the magnetic field, the ^{14}N quadrupole interaction, and the interaction between the nuclei. The spectrum for a particular crystal orientation gave the value of $(H_0 \cdot T_N^2 \cdot H_0)^{1/2}$ and $(H_0 \cdot T_H^2 \cdot H_0)^{1/2}$ where H_0 is a unit vector in the direction of the applied field,(15) and T_N^2 and T_H^2 are symmetric, second-rank tensors. The data enabled the elements of T_N^2 and T_H^2 to be deduced, and their principal values and directions obtained by diagonalization. Since the principal values of T are the square roots of the principal values of T^2 the elements of T_N and T_H could be computed. The tensors T_N and T_H are given in Table 1, together with their principal values and principal direction cosines (referred to the abc^* axis system). The relative signs of the principal values of the hyperfine tensors could not be determined experimentally. The signs of the principal values of T_N have been assumed all positive, but principal values of T_H have been given negative signs in accordance with the theory(2) which requires that the spin density on the α-proton be negative.

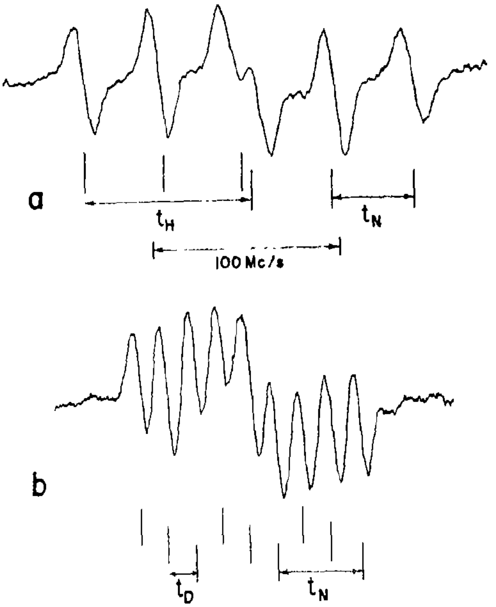

FIG. 2. First derivative E.P.R. spectrum of irradiated crystal for H_0 parallel to c^* (a) $(NH_4)_2HPO_4$, (b) $(ND_4)_2DPO_4$.

Table 1. *Hyperfine and g-tensors, their principal values and the corresponding direction cosines in the* abc* *system*

	Tensor			Principal values	Direction cosines
T_N	18·5	0·0	6·3	(+) 22·6 ± 5·0 Mc/s	(0·810, ∓0·257, 0·528)
	0·0	87·3	±31·5	(+)101·0	(0·030, ±0·916, 0·399)
	6·3	±31·5	28·3	(+) 10·4	(0·586, ±0·307, −0·750)
T_H	31·6	0·0	0·0	(−) 31·6 ± 5·0 Mc/s	(1·000, 0·000, 0·000)
	0·0	70·6	∓14·8	(−) 63·4	(0·000, ±0·893, 0·437)
	0·0	∓14·8	93·9	(−)101·1	(0·000, ∓0·437, 0·899)
g	2·0066	0·0000	−0·0023	2·0089 ± 0·0008	(0·688, ±0·169, −0·706)
	0·0000	2·0033	∓0·0013	2·0026	(0·253, ±0·856, 0·451)
	−0·0023	∓0·0013	2·0064	2·0048	(0·680, ∓0·489, 0·546)

The **g**-tensor was assembled by remeasuring the spectra using a crystal smeared with a speck of αα-diphenyl β-picryl hydrazyl, assumed to have a g-value of 2·0036.

4. DISCUSSION OF THE RESULTS

4.1 *General features*

There seems no doubt that the spectra discussed in the previous Section* are due to an oriented π-electron radical centered on a nitrogen atom. The unpaired electron in such a fragment essentially occupies a central-atom $2p$-orbital directed perpendicular to the radical plane. The ^{14}N hyperfine tensor T_N has the expected axial symmetry, and the directions (0·030, ± 0·916, 0·399) may be taken to be perpendicular to the planes of the two magnetically distinguishable sites observed. In spite of the considerable experimental error in determining the principal directions of the **g**-tensor, the direction of minimum g (0·253, ± 0·856, 0·451) was approximately parallel (angle 14·9°) to the axial direction of T_N. This is in accord with observations on other π-electron radicals.(3,6)

It is apparent that the radical contains an α-proton, i.e. a hydrogen atom bonded to the free-radical centre. The principal values of T_H are similar to those obtained for α-protons in many carbon-centred π-radicals.(3,4,5,6) It is not unreasonable to expect similar anisotropy from protons α to nitrogen centred π-radicals, and quantitative estimates(16) based on the equations of McConnell and Strathdee(2) confirm this view.

The direction corresponding to the intermediate principal value of T_H is expected(3,4) to be perpendicular to the π-electron radical plane, and from Table 1 it may be calculated that this direction is only 3·0° from the unique direction of T_N. This confirms that the perpendicular to the radical plane lies in bc^* and ± 24·8° ± 1·5° from b. The direction corresponding to the smallest, or least negative, principal value of T_H is parallel to the N—H bond, and this implies that the N—H bond of both radical sites is parallel to the a-axis of the crystal.

4.2 *Quantitative features*

The hyperfine-tensor of the central atom of a π-electron radical is expected to exhibit axial symmetry about the direction perpendicular to the radical plane, i.e. the p-orbital density direction. Resolving the tensor into its isotropic component A and an anisotropic component B, the hyperfine interaction expected for the magnetic field parallel to the p-orbital density direction is $A+2B$, and for the magnetic field in the plane perpendicular to this direction $A-B$. Assuming all principal values of T_N to be positive in sign the isotropic parameter A is 45 ± 5 Mc/s and is a measure of the unpaired spin density in the ^{14}N $2s$-orbital, this being A/A_{atom} if $1s$ polarization can be neglected. A_{atom} is the hyperfine interaction to be expected for an electron in the ^{14}N 2s-orbital, and may be estimated from $2s\psi^2(0) = 4{\cdot}770$ a.u.(9) to be $(8\pi g\beta\gamma/3h)\psi^2(0) = 1540$ Mc/s. The ratio A/A_{atom} thus indicates a N^{14} 2s spin population of 0·03.

---

* The fragment PO_3^{2-} was also detected.(11) The ^{31}P hyperfine splitting was 739 ± 5 G along (0·928, ± 0·257, −0·268) and 573 ± 5 G perpendicular to this direction.

The anisotropy parameter B is a measure of the unpaired spin-density in the ^{14}N 2p-orbital, which is given by the ratio B/B_{atom}. The quantity B_{atom} is equal to $(2g\beta\gamma/5h)\langle r^{-3}\rangle_{\text{Av}}$ Mc/s. The value of $\langle r^{-3}\rangle_{\text{Av}}$ has been estimated(9) to be 3·10 a.u. for the ^{14}N 2p-orbital, leading to $B_{\text{atom}} = 48$ Mc/s. The value of B depends on the sign choice for the principal values of T_N. The largest principal value of T_N is certainly positive, but the two smaller principal values could be of either sign. Since the two smaller principal values of T_N are nearly equal, the directions to which they correspond are not accurately determined. However, the direction corresponding to the 22 Mc/s principal value of T_N is more nearly parallel to the N—H bond than is the direction corresponding to the 10 Mc/s principal value. Provided both smaller principal values of T_N are positive in sign, this observation is consistent with polarization of the N—H bond in the sense which gives rise to negative spin density at the proton. With this sign choice, the value of B is 28 Mc/s, corresponding to an ^{14}N 2p spin population of 0·58.

5. THE NATURE OF THE RADICAL

In the absence of atomic coordinates for the unit cell of $(NH_4)_2HPO_4$ the exact nature of the radical formed by γ-irradiation of this material remains the subject of some conjecture. Since $H{-}N^+$ would be expected to migrate through the crystal at 300°K, the precisely oriented nature of the fragment may be due to very weak hydrogen bonds, as in structure I. This formulation (I) has the advantage that

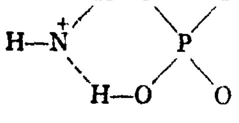

I

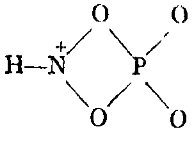

II

only one N—H bond need be broken to form this fragment. On the other hand it is difficult to see why the weakly bound hydrogen atoms do not contribute to the hyperfine pattern if the (dotted) hydrogen bonds are strong enough to orient the radical. Structure II does not raise this difficulty, but in this case the ^{31}P nucleus would be expected to contribute to the hyperfine pattern.

If the structure of the radical can be represented by I or II, then one would expect that the perpendiculars to the radical planes, which lie in bc^* at ± 24·8° ± 1·5° from b, would also be perpendicular to OPO planes in the undamaged crystal, provided that the phosphate ion retains its original orientation.

Acknowledgements—The author is grateful to Dr. L. D. Calvert for discussions on the possible crystal structure of $(NH_4)_2HPO_4$, and also to Dr. J. R. Rowlands for information on the radical $NHSO_3^-$ prior to its publication.

REFERENCES

1. McConnell H. M. and Chesnut D. B., *J. chem. Phys.* **28**, 107 (1958).
2. McConnell H. M. and Strathdee J., *Molec. Phys.* **2**, 129 (1959).
3. McConnell H. M., Heller C., Cole T. and Fessenden R. W., *J. Amer. chem. Soc.*, **82**, 766 (1960).
4. Ghosh D. K. and Whiffen D. H., *Molec. Phys.* **2**, 285 (1959).
5. Morton J. R. and Horsfield A., *J. chem. Phys.* **35**, 1142 (1961).
6. Horsfield A., Morton J. R. and Whiffen D. H., *Molec. Phys.* **4**, 327 (1961).
7. McConnell H. M. and Fessenden R. W., *J. chem. Phys.* **31**, 1688 (1959).
8. Cole T. and Heller C., *J. chem. Phys.* **34**, 1085 (1961).
9. Horsfield A., Morton J. R., Rowlands J. R. and Whiffen D. H., *Molec. Phys.* **5**, 241 (1962).
10. Rowlands J. R. and Whiffen D. H., *Nature, Lond.* **193**, 61 (1962).
11. Horsfield A., Morton J. R. and Whiffen D. H., *Molec. Phys.* **4**, 475 (1961).
12. Morton J. R., *Molec. Phys.* **5**, 217 (1962).
13. Smith J. P., Lehr J. R. and Brown W. E., *Acta. Cryst.* **10**, 709 (1957).
14. Horsfield A., Morton J. R. and Moss D. G., *J. sci. Instrum.* **38**, 322 (1961).
15. Holmberg R. W., Livingston R. and Smith W. T., *J. chem. Phys.* **33**, 541 (1960).
16. Rowlands J. R., private communication.

J. Phys. Chem. Solids Pergamon Press 1963. Vol. 24 pp. 213–216. **Printed in Great Britain.**

THE NATURE OF POINT DEFECTS IN SOLID LEAD CHLORIDE

GEORGE SIMKOVICH*

Max-Planck-Institut für physikalische Chemie, Göttingen, Germany

(*Received* 7 *September* 1962)

Abstract—The electrical conductivity of pure solid $PbCl_2$ and $PbCl_2$ doped with KCl and $LaCl_3$ has been measured between 175 and 350°C. Results indicate that anion vacancies and associates involving an anion vacancy and a cation vacancy are the prevailing point defects in pure $PbCl_2$ at 250 and 300°C.

LEAD chloride is known to be an anionic conductor.[1] In principle, one may assume that lead chloride contains essentially interstitial chlorine ions and anion vacancies in equal concentrations. However, in view of the large size of the chlorine ions and the narrow free space around interstitial sites, this assumption is highly objectionable. Instead, one may assume the SCHOTTKY disorder type[2] with cation and anion vacancies in equivalent concentrations. Then, one must assume that the mobility of anion vacancies is much greater than the mobility of cation vacancies in order to account for the prevalence of anionic conduction. The latter assumption may be justified on account of the higher effective charge of cation vacancies corresponding to a saddle point energy much higher for cations than for anions. To test this assumption one may evaluate conductivity measurements on lead chloride doped with KCl or $LaCl_3$.

In the first place, one may disregard the presence of associated defects. Then, using symbols suggested previously by SCHOTTKY,[3] cation vacancies $Pb\square''$ and anion vacancies $Cl\square^{\bullet}$ are formed from an ideal crystal according to the equation

$$\text{null} = Pb\,\square'' + 2\,Cl\,\square^{\bullet} \tag{1}$$

with the equilibrium condition

$$K = x_{Pb\square''}\, x^{2}_{Cl\square^{\bullet}} \tag{2}$$

where concentrations in mole fractions are denoted by x with the appropriate subscript and K is the equilibrium constant.

The equation of electrical neutrality reads

$$x_{Cl\square^{\bullet}} + x_{La\bullet^{\bullet}} = 2x_{Pb\square''} + x_{K\bullet'} \tag{3}$$

where $x_{K\bullet'}$ and $x_{La\bullet^{\bullet}}$, respectively, are the mole fractions of K^+ and La^{3+} ions substituted for Pb^{2+} ions, which in turn are equal to the mole fractions y_{KCl} and y_{LaCl_3} of KCl and $LaCl_3$ used as dopes. Introducing the net anion deficit Δy given by

$$\Delta y = y_{KCl} - y_{LaCl_3} = x_{K\bullet'} - x_{La\bullet^{\bullet}} \tag{4}$$

one obtains from equations (3) and (4)

$$x_{Cl\square^{\bullet}} = \Delta y + 2x_{Pb\square''} \tag{5}$$

Denoting quantities referring to pure $PbCl_2$ ($\Delta y = 0$) by a degree superscript, one has in view of equation (5)

$$x^{0}_{Cl\square^{\bullet}} = 2x^{0}_{Pb\square} \tag{6}$$

Dividing through equation (5) by $x^{0}_{Cl\square^{\bullet}}$ and using equation (6), one has

$$\frac{x_{Cl\square^{\bullet}}}{x^{0}_{Cl\square^{\bullet}}} = \frac{\Delta y}{x^{0}_{Cl\square^{\bullet}}} + \frac{x_{Pb\square''}}{x^{0}_{Pb\square''}} \tag{7}$$

From equation (2) it follows that

$$\frac{x_{Pb\square''}}{x^{0}_{Pb\square''}} = \left(\frac{x^{0}_{Cl\square^{\bullet}}}{x^{0}_{Cl\square^{\bullet}}}\right)^{-2} \tag{8}$$

Since conduction in pure $PbCl_2$ and also in $PbCl_2$ doped with KCl is due only to anions, the electrical conductivity κ is

$$\kappa = -x_{Cl\square^{\bullet}}\, u_{Cl\square^{\bullet}}\, \frac{F}{V} \tag{9}$$

where $u_{\mathrm{Cl}\square^\bullet}$ is the mobility of anion vacancies, F is the Faraday constant, and V is the molar volume of $\mathrm{PbCl_2}$.

In view of equation (9) one may write

$$\frac{x_{\mathrm{Cl}\square^\bullet}}{x^0_{\mathrm{Cl}\square^\bullet}} = \frac{\kappa}{\kappa^0} \qquad (10)$$

where κ^0 is the conductivity of undoped $\mathrm{PbCl_2}$.

Substituting equations (8) and (10) in equation (7) and regrouping terms, one obtains

$$\frac{\kappa}{\kappa^0} - \frac{1}{(\kappa/\kappa^0)^2} = \frac{\Delta y}{x^0_{\mathrm{Cl}\square^\bullet}} \qquad (11)$$

Thus plotting the left-hand member of equation (11) vs. $\Delta y = y_{\mathrm{KCl}} = y_{\mathrm{LaCl_3}}$, one may expect a straight line whose slope is supposed to be equal to the reciprocal of the mole fraction $x^0_{\mathrm{Cl}\square^\bullet}$ of anion vacancies in pure $\mathrm{PbCl_2}$.

On the other hand, if one assumes that virtually each cation vacancy is associated with an anion vacancy and the associate is denoted by a′, one has instead of equation (1)

$$\text{null} = a' + \mathrm{Cl}\square^\bullet \qquad (12)$$

with the equilibrium condition

$$K' = x_{a'}\, x^0_{\mathrm{Cl}\square^\bullet} \qquad (13)$$

The equation of electrical neutrality reads

$$x_{\mathrm{Cl}\square^\bullet} = \Delta y + x_{a'} \qquad (14)$$

Dividing through equation (14) by $x^0_{\mathrm{Cl}\square^\bullet}$ and letting ${}^0_{\mathrm{Cl}\square^\bullet} = x^0_{a'\square^\bullet}$ for $\Delta y = 0$, one obtains

$$\frac{x_{\mathrm{Cl}\square^\bullet}}{x^0_{\mathrm{Cl}\square^\bullet}} = \frac{\Delta y}{x^0_{\mathrm{Cl}\square^\bullet}} + \frac{x_{a'}}{x^0_{a'}} \qquad (15)$$

According to equation (13) one has

$$\frac{x_{a'}}{x^0_{a'}} = \left(\frac{x_{\mathrm{Cl}\square^\bullet}}{x^0_{\mathrm{Cl}\square^\bullet}}\right)^{-1} \qquad (16)$$

Substituting equations (10) and (16) in equation (15) and regrouping terms, one has

$$\frac{\kappa}{\kappa^0} - \frac{1}{\kappa/\kappa^0} = \frac{\Delta y}{x^0_{\mathrm{Cl}\square^\bullet}} \qquad (17)$$

Thus, plotting the left-hand member of equation (17) vs. $\Delta y = y_{\mathrm{KCl}} - y_{\mathrm{LaCl_3}}$ one may expect a straight line whose slope is again equal to the reciprocal of the mole fraction $x^0_{\mathrm{Cl}\square^\bullet}$ of anion vacancies in pure $\mathrm{PbCl_2}$.

EXPERIMENTAL

In order to test the aforementioned models, electrical conductivities of pure and doped $\mathrm{PbCl_2}$ were made.

Lead chloride was prepared in the following manner. Pure $\mathrm{Pb(NO_3)_2}$ (analytical grade) was dissolved in doubly distilled water. The solution was filtered through a fine glass frit to remove carbonaceous matter. $\mathrm{PbCl_2}$ was precipitated by adding HCl (analytical grade) and the liquid was separated from the crystals by filtration. After washing the $\mathrm{PbCl_2}$ with doubly distilled water and a dilute solution of HCl, the $\mathrm{PbCl_2}$ was dryed at 110°C in air. Weighed portions of $\mathrm{PbCl_2}$ and doping material were melted at about 525°C under an atmosphere of cleaned HCl gas for approximately 24 hr. After quenching these melts tablets of approximately 6 mm dia and 4 mm height were pressed in a stainless steel mold.

Conductivities were measured between about 175 and 350°C with the help of an a.c. philoscop in a slight variation of a Wheatstone bridge while the samples were enclosed in a tube through which flowed a gentle stream of purified $\mathrm{N_2}$ gas.

Figure 1 shows representative values of the conductivities of various samples vs. the reciprocal of absolute temperature. From Fig. 1 and analogous plots for samples not included in Fig. 1, values of κ for 250° and 300°C were obtained by interpolation. Figures 2 and 3 show plots of the left-hand members of equations (11) and (17) for 250 and 300°C in order to test the two models considered for the derivation of equations (11) and (17). The plot in Fig. 2 does not give a straight line, whereas points in Fig. 3 may be fitted by a straight line as a reasonable approximation, in spite of a great scatter of points for $\Delta y < 0$ corresponding to $\mathrm{PbCl_2}$ doped with $\mathrm{LaCl_3}$ with very low conductivities. Thus the model involving no associated vacancies appears to be much less likely than the model involving anion vacancies and associates of an anion vacancy and a cation vacancy. This type of disorder may be considered as a modified Schottky disorder type.

Evaluation of the slope of the lines shown in Fig. 3 according to equation (17) yields the values of defect concentrations in pure $\mathrm{PbCl_2}$ compiled

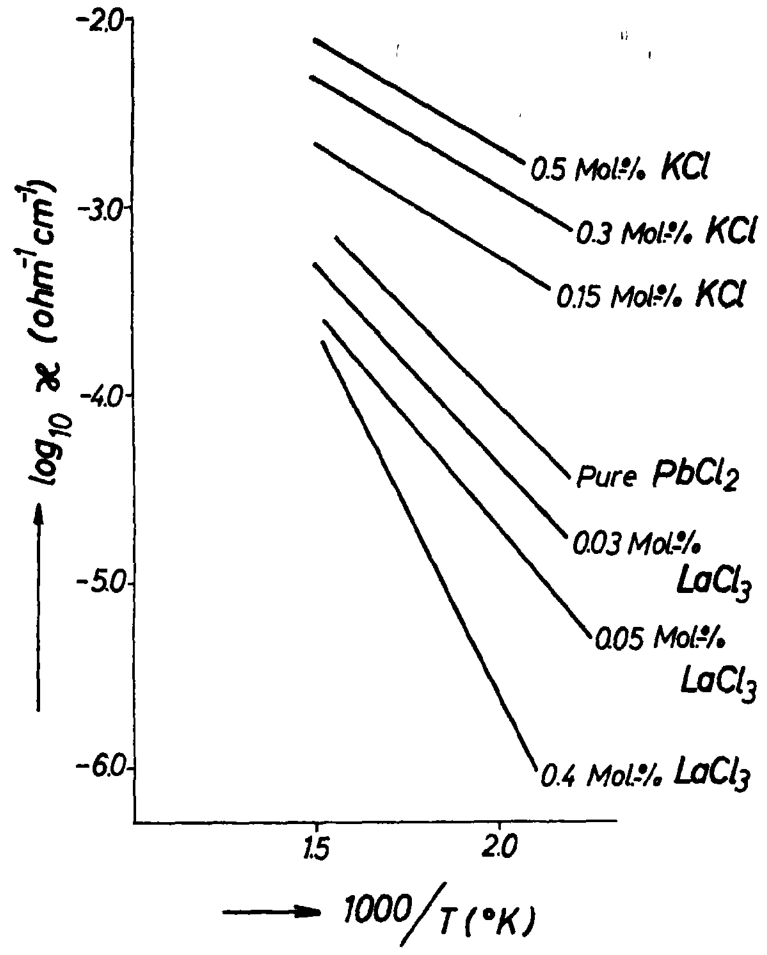

FIG. 1. Log$_{10}$ κ vs. the reciprocal absolute temperature for various $PbCl_2$ samples.

Table 1. *Mole fraction of defects in pure* $PbCl_2$ *and mobilities of anion vacancies*

Temp. (°C)	$x^0_{Cl\square^\cdot} = x_a$	$u_{Cl\square^\cdot}$ (cm^2 V^{-1} sec^{-1})
250	$2{\cdot}6 \times 10^{-4}$	$2{\cdot}50 \times 10^{-4}$
300	$3{\cdot}6 \times 10^{-4}$	$3{\cdot}86 \times 10^{-4}$

in Table 1 which also contains values of the mobility of anion vacancies as calculated from equation (9) for $\Delta y = 0$,

$$u_{Cl\square^\cdot} = \kappa^0 V / x_{Cl\square^\cdot} F \qquad (18)$$

Acknowledgements—Sincere thanks are extended to Professor C. WAGNER who derived the various equations, directed the experimental work, and discussed the results with the writer. Thanks are also extended to the National Science Foundation and the Max-Planck-Institut für physikalische Chemie for financial support.

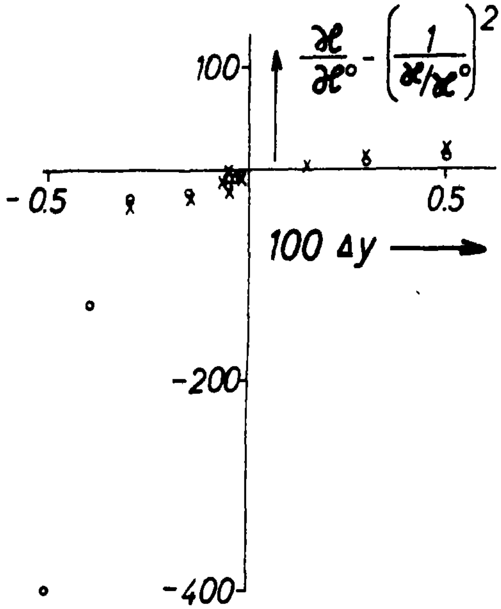

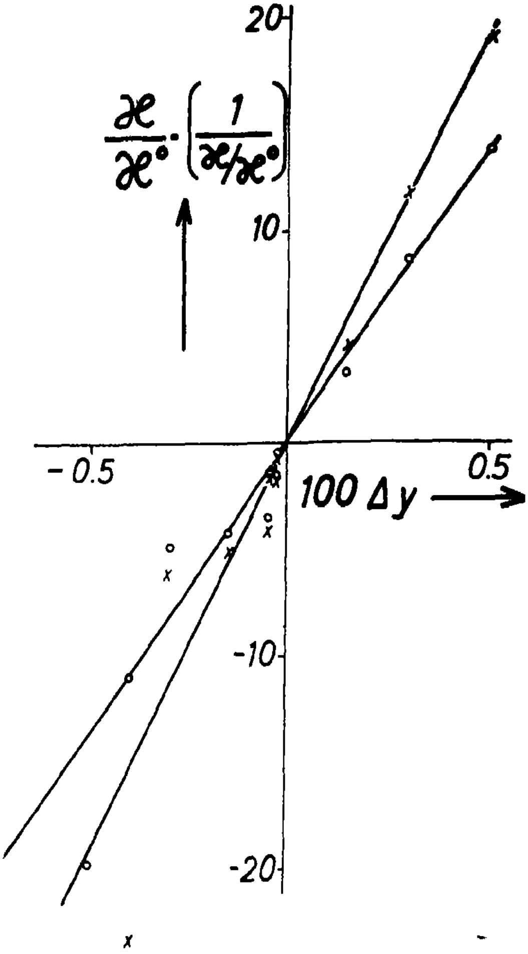

FIG. 2. $\frac{\kappa}{\kappa^0}\left(\frac{1}{\kappa/\kappa^0}\right)^2$ vs. Δy at 250°C (x) and 300°C (0).

FIG. 3. $\frac{\kappa}{\kappa^0}\left(\frac{1}{\kappa/\kappa^0}\right)$ vs. Δy at 250°C (x) and 300°C (0).

REFERENCES

1. TUBANDT C. and EGGERT S., *Z. anorg. Chem.* **110**, 196 (1920); TUBANDT C., *Z. anorg. Chem.* **115**, 105 (1921); TUBANDT C. and REINHOLD H., *Z. Elektrochem.* **29**, 313 (1923); TUBANDT C., REINHOLD H. and LIEBOLD G., *Z. anorg. Chem.* **197**, 225 (1931).
2. SCHOTTKY W., *Z. phys. Chem.* **B29**, 335 (1935).
3. SCHOTTKY W., *Z. Elektrochem.* **45**, 33 (1939); SCHOTTKY W. and STÖCKMANN F., *Halbleiterprobleme*, Vol. **1**, pp. 80–106, Vieweg, Braunschweig (1954); HAUFFE K., *Reaktionen in und an festen Stoffen*. Springer, Berlin (1955).

J. Phys. Chem. Solids Pergamon Press 1963. Vol. 24 pp. 217–218. Printed in Great Britain.

A NOTE ON THE SHORT-RANGE ORDER AT THE FERROMAGNETIC CURIE POINT*

D. R. FREDKIN and H. SUHL

University of California, La Jolla, California

(*Received* 4 *September* 1962)

Abstract—Ordinary thermodynamic fluctuation theory, which assumes a Gaussian fluctuation ensemble, leads to complete ordering of a Heisenberg ferromagnet at the Curie point. We show that a simple extension of the usual theory, utilizing Landau's phenomenological theory of second-order phase transitions, remedies this difficulty. The relation of this approach to molecular field theory is discussed.

THE purpose of this note is to discuss the application of thermodynamic fluctuation theory to the short-range order of an ionic ferromagnetic spin system in the immediate vicinity of the Curie point. The treatment of critical fluctuations starting from (1), and the nonlinear equation (4), is applicable to any critical point or second-order phase transition. FIXMAN has given a discussion of density fluctuations at the critical point which is essentially identical with the present approach.⁽¹⁾ We shall first show that the usual (Ornstein-Zernicke type) theory as developed by VAN HOVE⁽²⁾ fails at temperatures in the range

$$T_c < T < T_c + \mathrm{O}(l^2/L^2),$$

where l is the lattice spacing, and L is a typical linear dimension of the sample. We then demonstrate that going beyond the usual Gaussian fluctuation theory by utilizing the LANDAU hypothesis⁽³⁾ concerning second-order phase transitions remedies these difficulties. In the Landau theory, the free energy F is expanded as a functional power series in the magnetization field $\boldsymbol{M}$

$$F = \int \left\{ aM^2 + b \sum_{\alpha\beta} \left(\frac{\partial M_\alpha}{\partial x_\beta} \right)^2 l^2 + c(M^2)^2 + \dots \right\} \frac{\mathrm{d}^3 r}{l^3} \tag{1}$$

where a is zero at the Curie point, negative below and positive above, while b and c are positive and practically constant near T_c. The differential equation for the conditional average $\langle \boldsymbol{M} \rangle_{\boldsymbol{M}_0}$ of $\boldsymbol{M}$ is the Euler-Lagrange equation for the extrema of F. When the fourth- and higher-order terms are neglected, Van Hove's equation results:

$$l^2 \nabla^2 \langle \boldsymbol{M}(r) \rangle_{\boldsymbol{M}_0} - \frac{a}{b} \langle \boldsymbol{M}(r) \rangle_{\boldsymbol{M}_0} = 0 \tag{2}$$

The usual source solution

$$C \exp - \left(\sqrt{\left[\frac{a}{b}\right]} \frac{r}{l} \right) \Big/ r$$

of this equation holds if T is sufficiently greater than T_c (a/b sufficiently large), so that boundary conditions are unimportant. When T is very close to T_c, the growing solution must be added to satisfy some boundary condition, such as that of RADO and HERRING⁽⁴⁾ ($\partial \boldsymbol{M}/\partial n = 0$, where $\partial/\partial n$ denotes the derivative along the normal to the surface of the sample). It is then found that if α goes to zero like $(T/T_c - 1)^n$, then, for

$$T_c < T < T_c + \mathrm{O}[(l/L)^{2/n}],$$

the solution becomes independent of r, i.e. the spin system "locks". Such a rapid, essentially discontinuous, change of the solution from the source type to that corresponding to the absolute

---

* Supported in part by the Office of Scientific Research, U.S. Air Force.

zero of temperature is due to the neglect of higher terms in the free energy (1).

When the fourth-order term is included, the differential equation (which now describes the most probable rather than the average course of $\mathbf{M}$) takes the form

$$l^2\nabla^2\mathbf{M} - \frac{a}{b}\mathbf{M} - \frac{2c}{b}M^2\mathbf{M} = 0 \qquad (3)$$

Above T_c, the appropriate solution of (3) has all components of $\mathbf{M}$ equal to zero except that along the prescribed $\mathbf{M}_0$. Thus (3) may be replaced by the scalar equation

$$l^2\nabla^2 M - \frac{a}{b}M - \frac{2c}{b}M^3 = 0 \qquad (4)$$

At the Curie point it is easy to see that equation (4) has an asymptotic solution of the form $1/r\sqrt{(lnr)}$.

The following simple circuit analog can be used to demonstrate the failure of the usual theory and the crucial role of the nonlinear term: Interpreting all integrals as sums over lattice sites and all differential operators as difference operators, we can make in equation (4), the identification

$$l^2\nabla^2 M \to \frac{6}{z}\sum_{\delta}(M_{i+\delta} - M_i)$$

where z is the number of nearest neighbors, and, identifying M_i with the voltage at lattice site i, we see that (4) corresponds to a network with resistors of value $z/6$ connecting adjacent lattice sites, an additional linear resistor of value b/a from each lattice site to ground, and, finally, a nonlinear resistor with current-voltage characteristic: (current) $= 2c/b$ (voltage)^3, also to ground. When the nonlinear resistor is omitted, the network "floats" at the Curie point ($a = 0$) and M is everywhere equal to its imposed value at the origin. The nonlinear resistance corrects this peculiarity.

It is possible to derive equation (4) from molecular field theory. In exchange for the loss of generality, we gain definite values for a/b and c/b. Molecular field theory is contained in the relations

$$M_i = \gamma B_S(\gamma H_i/kT) \qquad (5)$$

and

$$H_i = \frac{J}{\gamma^2}\sum_{\delta} M_{i+\delta} = \frac{zJ}{\gamma^2}\left(M_i + \frac{l^2}{b}\nabla^2 M_i\right) \qquad (6)$$

where γ is the gyromagnetic ratio, S is the magnitude of a single spin, H_i is the exchange field at site i, J is the usual exchange integral, and $B_S(x)$ is the Brillouin function

$$B_S(x) = (S+\tfrac{1}{2})\coth(S+\tfrac{1}{2})x - \tfrac{1}{2}\coth\frac{x}{2}$$

Substituting (6) in (5), and letting B_S^{-1} be the inverse of the Brillouin function, we obtain

$$l^2\nabla^2 M + 6M - \frac{6\gamma kT}{zJ}B_S^{-1}\left(\frac{M}{\gamma}\right) = 0 \qquad (7)$$

Above the Curie temperature we may expand $B_S^{-1}(M/\gamma)$ in a power series, and, neglecting terms of order M^5 and higher we recover (4) with

$$\frac{a}{b} = \frac{18kT}{zJS(S+1)} - 6 = 6\left(\frac{T}{T_c} - 1\right)$$

$$\frac{c}{b} = \frac{27kT(S^2+S+\frac{1}{2})}{5zJS^3(S+1)^3\gamma^2}$$

The present theory is, clearly, subject to the same limitations as molecular field theory. Any theory which expresses the magnetic moment M_i at a site i in terms of the magnetic moments at nearby sites will lead to an equation similar to (7). If a theory replaced B_S^{-1} by a function which is nonanalytic at zero, (4) would be incorrect, as would the Landau theory of the second-order phase transition.

REFERENCES

1. Fixman M., *J. Chem. Phys.* **36**, 1965 (1962).
2. van Hove L., *Phys. Rev.* **95**, 1374 (1954).
3. Landau L. and Lifschitz E., *Statistical Physics*, Chap. XIV, Addison-Wesley, Cambridge, Mass. (1958).
4. Ament W. S. and Rado G. T., *Phys. Rev.* **97**, 1558 (1955).

J. Phys. Chem. Solids Pergamon Press 1963. Vol. 24, pp. 219–224. Printed in Great Britain.

CONDUCTION THERMIQUE D'ALLIAGES OR COBALT À BASSE TEMPERATURE

BERNARD DREYFUS, ALBERT LACAZE, PIERRE THOMAS et LOUIS WEIL

Institut Fourier, Grenoble (Isère), France

(*Received* 17 *August* 1962)

Résumé—Des mesures de conduction thermique entre 3 et 35°K sur quatre échantillons d'or–cobalt à 0,34; 1; 2 et 4 pour cent at. de cobalt ont permis de déterminer la densité relative de dislocations dans les alliages et l'influence de divers traitements sur celle-ci. L'analyse des résultats à plus haute température a permis de déterminer la section efficace du cobalt pour les phonons. Celle-ci a été trouvée anormalement élevée.

Abstract—The thermal conductivities of four gold–cobalt alloys with 0·34; 1, 2 and 4 at. per cent cobalt have been measured between 3 and 35°K. The relative densities of dislocations in the alloys and their variation with heat treatment have been deduced from the results. The cross-section of cobalt for phonons has been calculated through an analysis of the conductivities. This cross section is rather high.

INTRODUCTION

Les alliages des métaux de transition (Mn, Co, Fe etc. . . .) avec les métaux nobles (Cu, Ag, Au) font actuellement l'objet de nombreuses études tant théoriques qu'expérimentales. Deux séries de problèmes sont particulièrement étudiées. La première est relative à l'état électronique et magnétique des impuretés supposées dispersées et à leurs interactions.(1,2,3) Les limites de solubilitié étant parfois assez faibles, la deuxième série concerne la dissolution et sa modification par les divers traitements mécaniques ou thermiques.(4)

L'étude de la conduction thermique peut apporter des informations utiles pour ces deux catégories de problèmes. Nous présentons ici le résultat de quelques mesures relatives à des alliages Au–Co.

DÉTAILS EXPÉRIMENTAUX

Nos mesures ont été effectuées entre 3 et 35°K par une méthode classique de régime permanent.

Une extrémité de l'échantillon (Fig. 1) est mise en contact avec le bain d'hélium ou d'hydrogène par l'intermédiaire d'une résistance thermique. L'autre extrémité reçoit de la chaleur. Deux colliers de prise de température sont fixés sur l'échantillon.

La température est mesurée à l'aide de deux thermomètres à gaz dont les bulbes, d'un volume de 16 cm^3 sont soudés aux colliers. Des capillaires en constantan (diamétre inérieur 0,4 mm) relient les réservoirs aux manometres de mesure. La

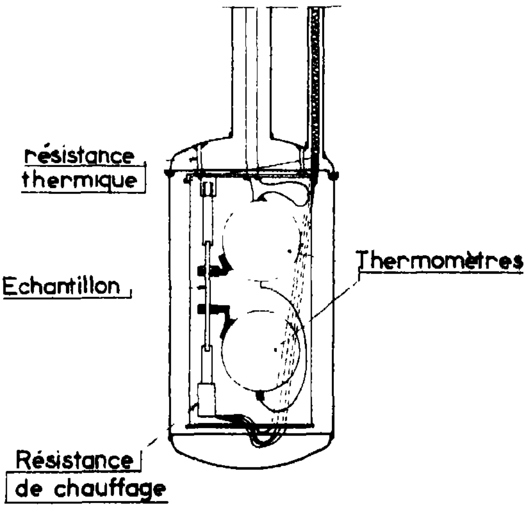

FIG. 1. Schéma de l'enceinte de mesure

pression absolue dans l'un des bulbes est lue sur un manomètre à mercure à volume constant. La différence de pression entre les deux réservoirs est lue sur un manomètre différentiel à huile de silicone. Cette différence est en première approximation proportionnelle à l'écart de température entre les deux colliers: ceci suppose que les deux thermomètres sont identiques et ont été remplis à la même pression à la température d'étalonnage.

La résistance thermique intercalée entre l'échantillon et le bain de liquide cryogénique permet, grâce á un chauffage auxiliaire de faire des mesures à des températures supérieures à celle du bain.

Le système que nous avons utilisé permet de réduire les corrections, dues aux volumes morts du thermomètre, rapportées à la température, à environ 1 pour cent.

Sur l'écart de température, les corrections augmentent rapidement avec la température (elles varient comme T^2) mais sont toujours inférieures à 8 pour cent dans notre zone de mesure. Elles peuvent se calculer avec une precision de 10 pour cent; on peut donc s'attendre pour un échantillon donné à une dispersion des valeurs de la conduction de l'ordre de 1 pour cent.

Pour chaque échantillon s'ajoutent les erreurs sur les dimensions géométriques, ce qui porte l'erreur totale sur la valeur absolue de la conductivité à 4 pour cent.

La température est connue à 0,5 pour cent près.

PRÉPARATION DES ÉCHANTILLONS

L'échantillon de 0,34 pour cent at. de cobalt a été fourni par Johnson Matthey et Cie et ceux de 1, 2 et 4 pour cent at. ont été préparés au laboratoire.

L'alliage a été fondu pendant 1 hr à 1200°C sous hydrogène pur contenant mois de 4 p.p.m. d'impuretés. Le lingot a été étiré jusqu'au diamètre de 3 mm.

Avant les mesures nous avons recuit tous les échantillons à 800°C pendant 24 hr pour éliminer les dislocations apparues dans le travail à froid.

Pour éviter la précipitation du cobalt pendant le refroidisement nous avons trempé les échantillons à partir de 800°C, température à laquelle le cobalt était dissous pour tous nos alliages.(5) La trempe est obtenue par refroidissement dans un courant h'hydrogène à grande vitesse qui peut être caractérisé par son nombre de Reynolds de 70.000. La constante de temps de la trempe peut être estimée à 0,1s. Elle est déterminée en grande partie par la diffusivité thermique et les dimensions de l'échantillon.

RÉSULTATS

Nous avons reporté Fig. 2 les résultats obtenus pour nos quatre alliages trempés dans les conditions précédemment décrites. Sur la Fig. 3 nous avons tracé les résultats obtenus pour l'alliage à 1 pour cent après divers traitements : brut d'étirage (E); recuit 24 hr à 800°C et trempé (T); recuit 4 hr à 800°C puis 24 hr à 300°C, pour précipiter le cobalt, et refroidi lentement (R). Nous avons également incorporé à la Fig. 3 les résultats de Powell(6) sur un fil à 2,1 pour cent étiré à froid. L'allure de cette courbe est analogue à nos mesures sur le 1 pour cent (E).

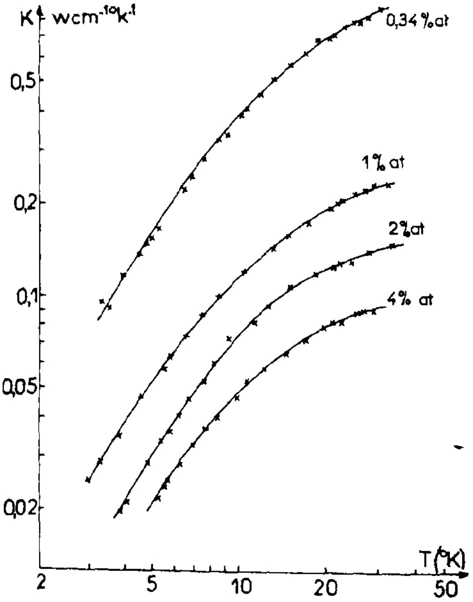

Fig. 2. Conductivité thermique des alliages Au–CoT.

L'analyse des diverses contributions à la conductivité thermique peut se faire en utilisant d'une part les lois connues de variation de chacun des termes en fonction de la température et d'autre part le fait que l'addition d'impuretés, si elle modifie fortement quelques uns d'entre eux, est par contre, en principe, sans effets sur certains autres.

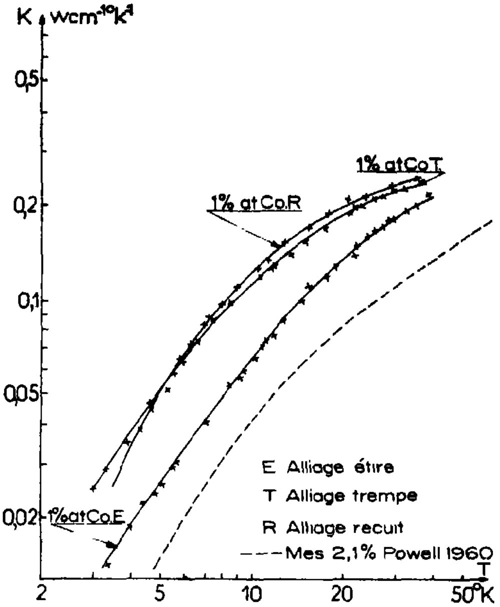

FIG. 3. Conductivité thermique des alliages Au–Co 1 pour cent at.

L'énergie étant transportée par les électrons et les phonons nous écrivons :

$$K = K_e + K_{ph} \tag{1}$$

Les mesures de WHITE(7) sur l'or pur ont montré que la contribution électronique K_e masquait complètement celle du réseau K_{ph} Il n'en est évidemment pas de même pour les alliages où la contribution électronique est fortement réduite. (A titre d'indication à 5°K la conduction thermique du plus mauvais des échantillons de White est environ dix fois supérieure à celle de notre alliage à 0,34 pour cent.)

La conduction par les électrons est essentiellement limitée par leur diffusion par les phonons et les impuretés. En admettant les processus de relaxation additifs,

$$\frac{1}{K_e} = W_e = W_e^{ph} + W_e^i \tag{2}$$

Dans l'or pur recuit le premier therme l'emporte nettement; WHITE(7) a montré qu'à basses températures et jusqu'à 30°K environ on peut le représenter par la formule :

$$W_e^{ph} = 3{,}78\left(\frac{T}{\theta}\right)^2 (W^{-1}\,\text{cm}\,^\circ\text{K}) \tag{3}$$

(θ, température de Debye = 170°K)

Pour $T = \theta/2$, W_e^{ph} devient indépendant de T et vaut 0,290 (W^{-1} cm °K). Pour les alliages le terme W_e^{ph} est bien plus faible que W_e^i; il n'intervient que comme correction. Par ailleurs il n'y a pas de raison de supposer que les interactions électron-phonons sont radicalement modifiées par la présence d'impuretés et nous admettrons que ce terme correctif a la même valeur que pour l'or pur, c'est à dire qu'il est donné par (3).

W_e^i est dû à la diffsion des électrons par les imperfections (atomes de cobalt, dislocations, joints de grains, etc. . . .). Ce terme est lié à la résistivité résiduelle par la loi de Wiedemann-Franz.

$$W_e^i = \frac{\rho_0}{L}\frac{1}{T} \tag{4}$$

L = nombre de Lorenz

De même la résistance thermique due aux phonons est donnée par une somme de termes.(8)

$$\frac{1}{K_{ph}} = W_{ph} = W_{ph}^e + W_{ph}^d + W_{ph}^{ph} + W_{ph}^i \tag{5}$$

Ceux-ci sont dus respectivement à la diffusion des phonons sur les électrons (e), les dislocations (d) les phonons (ph) et les impuretés (i).

Ces divers termes ont des lois de variation thermique différente W_{ph}^i et W_{ph}^{ph} varient en T et prédominent à haute température; par contre W_{ph}^e et W_{ph}^d varient en T^{-2} et donc l'emportent vers les basses températures.

Ainsi combinant (1) (4) et (5) on trouve qu'à basse température la loi de variation de K doit être de la forme :

$$K = \frac{1}{A}T + \frac{1}{B}T^2 \tag{6}$$

Figure 4 nous avons reporté les résultats expérimentaux dans le diagramme K/T fonction de T. En dessous de 8°K on obtient des droites conformément à (6) et il est possible d'en déduire graphiquement A et B. La précision de cette détermination est cependant limitée par le fait que nous n'ayons pas de résultats en dessous d'environ 4°K.

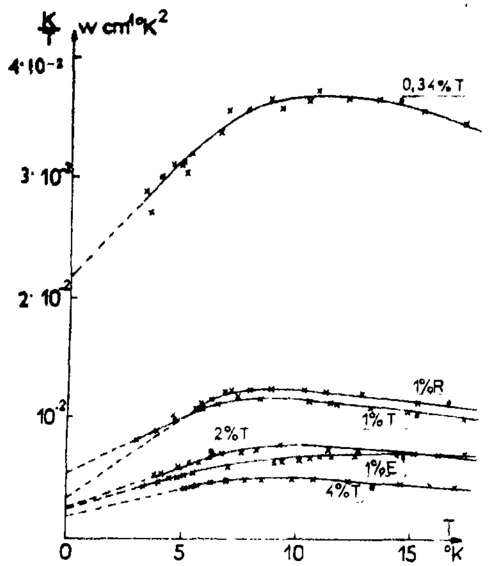

FIG. 4. Diagramme K/T en fonction de T.

A partir de la valeur de A et de mesures électriques que nous avons effectuées à 4,2°K nous pouvons estimer $\rho_0/W_e^i T = \rho_0/A$ qui devrait être égal à L.

On peut constater que A/c est constant à 50 pour cent près dans les alliages trempés alors que c varie d'un facteur 10. Par contre les échantillons étirés (E) et recuits (R) ont une valeur de A/c nettement plus élevée comme si dans un cas (E) l'accroissement du nombre de dislocations et dans l'autre (R) la précipitation du cobalt avaient pour conséquence d'augmenter la section efficace des impuretés pour la diffusion des électrons. Cependent les valeurs de ρ_0/A sont loin d'être égales entre elles et à la valeur $L = 2{,}45 \cdot 10^{-8}$ (W °K^{-2}). Il est possible que ce comportement soit lié à des phénomènes magnétiques, en particulier à l'existence probable d'un minimum de résistivité électrique.

Figure 5 nous avons reporté les valeurs de B.

$$W^e_{ph} + W^l_{ph} = CT^{-2} \qquad (7)$$

Pour les échantillons (T) nos valeurs s'extrapolent assez bien vers la valeur donnée par KEMP⁽⁹⁾ (350 W^{-1} cm deg^3) qui a été également reportée sur le graphique.

On constate que B coît nettement avec c. Il est possible qu'une partie de cette augmentation soit due à W^e_{ph}. FRIEDEL et BLANDIN⁽¹⁾ prévoient une augmentation de la densité électronique à la surface de Fermi consécutive à l'existence de

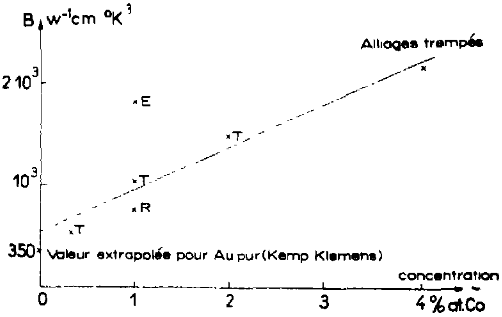

FIG. 5. Variation de B = WphT^2 avec la concentration de Co.

Echantillon	A(W^{-1} cm °K^2)	$\rho_0 10^{+6}$ (Ω cm)	ρ_0/c	A/c	$\rho_0/A \cdot 10^8$(W°K)
0,34 % T	45,8	1,72	5,05	135	3,75
1 % T	187			187	
2 % T	392	12,65	6,3	196	3,23
4 % T	564	23,34	5,83	141	4,1
1 % T	187			187	
1 % E	413			413	
1 % R	290	6,99	6,99	290	2,41

c = concentration atomique.

niveaux d virtuels localisés et effectivement des mesures de chaleurs spécifiques de CRANE *et al.*(2,3) et TOURNIER *et al.*(4) semblent avoir mis cet effet en évidence. Une telle variation de W^e_{ph} devrait être linéaire en c et assez faible : dans ces conditions on ne fait par une grosse erreur en admettant que W^e_{ph} est constant et que la variation avec c est due exclusivement à W^d_{ph}. Qualitativement cette hypothèse est cohérente avec l'influence des traitements sur l'échantillon 1 pour cent. Après étirage (E) on a augmenté le nombre de dislocations et B croît (Fig. 5). Après un recuit à 300°C (R) on a certainement diminué le nombre de dislocations, à la fois par rapport à l'échantillon étiré (E) et par rapport à échantillon trempé depuis 800°C (T). On constate sur la Fig. 5 que la valeur correspondante de B est effectivement la plus faible mesurée sur les échantillons à 1 pour cent.

Des valeurs de B nous pouvons déduire, la densité de dislocations en appliquant la formule.(9)

$$W^d_{ph}T^2 = B = 0,17\frac{vh^2}{k^3}b^2N \qquad (8)$$

W exprimé en (W^{-1} cm °K)

v = vitesse du son

h = constante de Planck

k = constante de Boltzmann

b = vecteur de Bürgers

N = densité de dislocations en lignes par cm^2

Pour l'or, ce calcul donne $B = 4{,}0\,10^{-9}\ N$ avec les unités précédentes. Différents auteurs(10) pensent que (8) surestime la densité par un facteur de l'ordre de 5.

Nous donnons dans le tableau suivant, les valeurs de N tirées de (8), étant bien entendu que les valeurs absolues constituent au plus un ordre de grandeur.

Les valeurs de N ainsi obtenues ont une grandeur raisonnable. On constate que sur la série trempée T la variation de N avec C est approximativement linéaire. L'étirage de l'échantillons 1 pour cent fait plus que doubler le nombre de dislocations et le recuit (R) en laisse subsister un nombre assez important. Ce dernier fait a déjà été observé.(9)

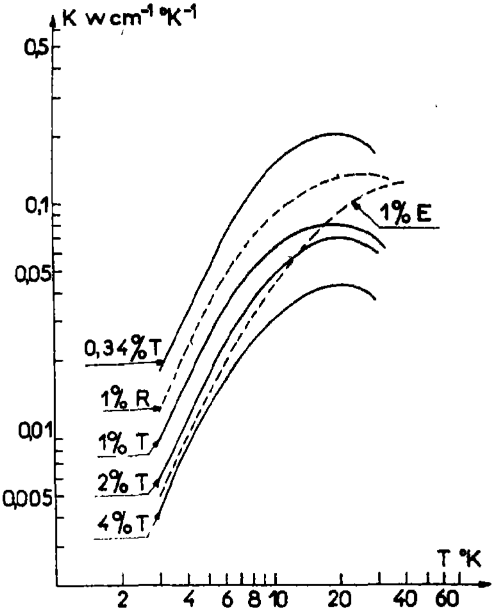

FIG. 6. Conductivité du réseau des alliages Au–Co.

Quand la température est supérieure à 8°K la formule (6) devient insiffisante. En particulier la conductivité due aux phonons K_{ph} doit passer par un maximum et à plus haute température décroître comme $1/T$. A partir des résultats précédents les formules (3) (4) et (6) nous permettent de soustraire la conductivité électronique. Nous avons porté Fig. 6 la conductivité restante due au réseau K_{ph}. On voit apparaître nettement le maximum à des températures de l'ordre de 20 à 30°K. Pour obtenir avec certitude les termes

Echantillon	0,34% T	1% T	2% T	4% T	1% E	1% T	1% R
$W_{ph}T^2 = B$ (W^{-1} cm °K^3)	527	1030	1483	2140	1820	1030	765
$W^d_{ph}T^2 = B-350$	177	680	1133	1790	1470	680	415
N tire de (8) (10^{10} lignes/cm^2)	4,42	17	28	45	37	17	10,5

W_{ph}^{ph} et W_{ph}^{i} il aurait fallu poursuivre les mesures à plus haute température. Nous avons essayé cependant de les estimer en posant

$$W_{ph} = \frac{B}{T^2} + DT \qquad (9)$$

Le terme DT est dû aux *interactions* anharmoniques phonons–phonons et aux interactions phonons–impuretés. La formule (9) est très approximative en particulier dans la région du maximum de conductivité où l'on ne peut utiliser l'additivité des divers procesus. Les valeurs de D que nous tirons de nos résultats sont donc certainement imprécises.

En supposant W_{ph}^{ph} indépendant de D et ayant *la même valeur* que pour l'or pur ($W_{ph}^{ph}/T =$ 0,125 W^{-1} cm) nous pouvons estimer le terme dû aux imperfections ponctuelles. Les valeurs sont reportées dans le tableau suivant :

Echantillons	0,34% *T*	1% *T*	2% *T*	4% *T*	1% *E*	1% *T*	1% *R*
D(W^{-1} cm)	0,16	0,45	0,47	0,79		0,45	0,21
$W_{ph}^{i}/T = \mathrm{D}-0{,}125$	0,035	0,33	0,35	0,67		0,33	0,09

Les valeurs les plus précises sont celles des fortes concentrations, et on trouve d'ailleurs qu'approximativement le terme W_{ph}^{i} pour 4 pour cent est double de celui pour 2 pour cent. On peut essayer de confronter ces valeurs de la section efficace des impuretés avec celles données par KLEMENS⁽⁸⁾ et WHITE⁽¹¹⁾ dans le cas où l'impureté agit surtout par la différence de masse.

$$W_{ph}^{i}/T = 3{,}3\ 10^{11} \cdot \frac{C}{v^2} \cdot \frac{M}{\rho} \cdot \frac{1}{12}\left(\frac{\Delta M}{M}\right)^2 \qquad (10)$$

C = Concentration atomique d'impuretés
v = vitesse du son
M = masse moyenne dans l'alliage
ΔM = différence de masse due aux
ρ = masse spécifique

La comparaison pour le 2 pour cent donne une valeur expérimentale vingt fois plus élevée que la valeur tirée de (10). En fait il semble bien que la section efficace du cobalt dans l'or pour les phonons est bien plus élevée que pour d'autres impuretés déjà mesurées.⁽¹¹⁾ Il est à signaler que nos résultats sont en concordance avec ceux mesurés par POWELL⁽⁶⁾ sur un alliage à 2,1 pour cent étiré [D = 0,4 (W^{-1} cm).]

CONCLUSION

L'analyse de nos mesures de conduction thermique entre 3°K et 35°K sur des alliages Au–Co nous a permis de déterminer la densité relative des dislocations et l'influence d'un traitement sur celle-ci. Nous avons pu également déterminer au moins approximativement la section efficace du cobalt pour les phonons et l'avons trouvé anormalement élevée.

En étendant le domaine des températures et en mesurant plus systematiquement la résistance électrique, en particulier dans la région du minimum de résistance, on pourrait accroître la précision sur chaçun des termes, ce qui permettrait d'étudier l'influence de divers traitements mécaniques et thermiques sur la dissolution du cobalt.

BIBLIOGRAPHIE

1. BLANDIN A. et FRIEDEL J., *J. Phys. Radium* **20,** 160 (1959).
2. CRANE L. T. et ZIMMERMAN J. E., *Phys. Rev.* **123,** 113 (1961).
3. CRANE L. T., *Phys. Rev.* **125,** 1902 (1962).
4. TOURNIER R., VEYSSIE J. J. et WEIL L. à paraître. *J. Phys. Radium.*
5. HANSEN M., *Constitution of binary alloys* (1958).
6. POWELL R. L., BUNCH M. D. et GIBSON E. F., *J. appl. Phys.* **31,** 504 (1960).
7. WHITE G. K., *Proc. phys. Soc.* **A46,** 559 (1953).
8. KLEMENS P. G., *Handb. Phys.* **14,** 198–281 (1956).
9. KEMP W. R. G. et KLEMENS P. G., *Austr. J. Phys.* **13,** 247 (1960).
10. LOMER J. N. et ROSENBERG H. M., *Phil. Mag.* **4,** 467 (1959). KEMP W. R. G., KLEMENS P. G. et TAINSH R. J. *Phil. Mag.* **4,** 485 (1959).
11. WHITE G. K., *Austr. J. Phys.* **13,** 255 (1960).

J. Phys. Chem. Solids Pergamon Press 1963. Vol. 24, pp. 225–237. Printed in Great Britain.

IMPURITY ACTIVATED INFRA-RED ABSORPTION IN VALENCY CRYSTALS*

B. SZIGETI

Department of Theoretical Physics, University of Liverpool†

(*Received* 18 *June* 1962)

Abstract—The frequency-dependence of the infra-red absorption due to impurities or lattice defects in valency crystals is investigated. Exact solutions are obtained for simplified one-dimensional models; the results allow certain conclusions for real three-dimensional crystals. For isolated impurity atoms or for point defects, the absorption spectrum is very similar to the density spectrum of the lattice frequencies, although the maxima of the two need not coincide. Entirely different spectra occur if the impurity atoms are not isolated from each other or if the defects are not point defects. The results provide a qualitative explanation for both the similarities and the differences between the infra-red spectra of various samples of type I diamond.

1. INTRODUCTION

VALENCY crystals like diamond, silicon or germanium frequently exhibit absorption bands in the region of the lattice frequencies. Following the suggestion of BLACKWELL and SUTHERLAND(1) it is now generally accepted that this absorption is due to impurities or lattice defects. Various important features of this impurity activated absorption are however not yet understood.

The behaviour of diamond, in particular, has aroused interest for a considerable time. Samples of diamond are usually divided into type I and type II; type II is the purest, but all the clear and well grown crystals are of type I. Type II does not absorb in the region of the lattice frequencies, while type I exhibits a number of weak but well defined absorption bands in this region. There is much similarity but also a great deal of variation in the absorption of various samples of diamond I: certain bands, if they occur, always occur at the same frequency; but the shapes and relative intensities of some of the bands, and even the number of the bands, may vary for stones of different origin (cf. SUTHERLAND *et al.*(2)).

If ϵ'' denotes the imaginary part of the dielectric constant and ω the circular frequency, then for any given frequency $\omega\epsilon''$ measures the absorption per sec. Assuming, in a first approximation, that a lattice wave with frequency ω only absorbs light with a frequency very similar to ω, we can write

$$\epsilon''\omega = \alpha_\omega d(\omega) \tag{1}$$

where $d(\omega)$ is the density of lattice frequencies and α_ω measures the absorption of a lattice vibration with frequency ω. If different types of lattice waves have the same ω then α_ω represents an average value.

In previous papers it was usually assumed that α_ω is either the same for all the lattice vibrations or, at any rate, varies only slowly with ω, and that the absorption peaks therefore coincide with the maxima of $d(\omega)$. But this clearly cannot be true, because in that case all impurities and lattice defects would produce the same absorption spectrum, and the spectra of various diamond samples would only differ in absolute intensity.

It is therefore of interest to investigate the frequency dependence of α_ω. This involves a consideration of the mechanism by which the impurity or defect activates the lattice vibrations. We shall have principally the diamond structure in mind, although most of the results will be of general validity.

---

* A short account of the results has been given at the Diamond Conference in Reading in July 1961.

† Present address: Department of Physics, University of Reading.

Some of the recent work on the vibrations of crystal lattices containing a few impurity atoms is summarized in the review articles by LIFSHITZ[(3)] and MONTROLL *et al.*[(4)] It is known that an impurity atom takes part in the lattice vibrations, although it only alters the lattice frequencies by a negligible amount. In addition, under certain conditions there may be a few vibrations localized near the impurity atom. A vibration can only be localized if its frequency is outside the frequency bands of the lattice. Since the lattice frequencies in the diamond structure extend continuously from zero up to a maximum frequency, localized frequencies can only occur above the highest lattice frequency. In this paper we shall therefore not be interested in localized vibrations.

The problem of the absorption produced by a foreign atom was considered by the author[(5)] in connection with long chain molecules. It was then found that α_ω may vary a great deal from one frequency to another because the amplitudes of the displacements are changed in the neighbourhood of the foreign atom, and this effect is frequency dependent. For several simplified models α_ω will now be calculated exactly; the results will allow some general conclusions concerning the behaviour of α_ω in an actual crystal. For the reasons given, only the non-localized vibrations will be taken into account.

We shall choose two types of one-dimensional models. The first will be the "atomic" chain, where in the absence of an impurity all the atoms are equal and equally spaced. The second model will be the "molecular" chain, illustrated in Fig. 1.

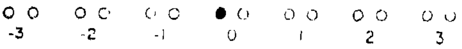

FIG. 1. The "molecular" chain with one impurity atom.

In this model all the atoms are still equal but they are arranged in pairs. The "atomic" chain bears a resemblance to the conditions for waves in the diamond lattice propagated in the (100) direction, as the atomic planes perpendicular to that direction are equally spaced; while the "molecular" chain bears an analogy to lattice waves propagated in the (111) direction in the diamond lattice, as the atomic planes perpendicular to that direction are arranged in pairs. The molecular chain is also of interest because it has several branches of vibration and several maxima in the density of frequencies.

We shall also consider quantitatively a particular three-dimensional model, representing a very special arrangement of impurities.

2. EXPRESSION FOR $\omega\epsilon''$

Let ϵ_{st} and ϵ_{op} denote the static and the optical dielectric constants, and ϵ'' the frequency dependent loss factor. It follows from the Kramers-Kronig dispersion relations that these quantities satisfy the relation

$$\epsilon_{st}-\epsilon_{op} = \frac{2}{\pi}\int\limits_{\text{i.r.}} \frac{\epsilon''}{\omega}\,d\omega \tag{2a}$$

(cf. for instance equation (7) in Ref. 6). The integral extends over infra-red frequencies only, so the right-hand-side represents the absorption due to the lattice vibrations; similarly the left-hand-side represents the lattice contribution to the static dielectric constant.

If M is the dipole moment arising from the lattice displacements and Q_i is one of the normal coordinates, in first order we may write

$$M = \sum_i (dM/dQ_i)Q_i$$

where the sum goes over all the normal coordinates. In the present case the dipolar field connected with the lattice vibrations is negligible, and the expression for M therefore does not depend on the shape of the crystal. If v denotes the volume, it follows from straightforward arguments (cf. SZIGETI[(7)]) that the contribution of the i'th vibration to the static dielectric constant is $4\pi(dM/dQ_i)^2/v\omega_i^2$. The contribution of the i'th vibration to ϵ'' will be denoted by ϵ_i''. In any frequency region, ϵ'' is the sum of all the ϵ_i''.

In the harmonic approximation the normal vibrations are independent of each other. The contributions of any particular vibration to the two sides of equation (2a) must therefore be equal, and we may write

$$\frac{2}{\pi}\int \frac{\epsilon_i''}{\omega}\,d\omega = 4\pi\frac{(dM/dQ_i)^2}{v\omega_i^2}. \tag{2}$$

In a first approximation we may assume that each vibration only absorbs in the immediate neighbourhood of its frequency. The integral in equation (2) is then very narrow, so we can take $1/\omega$ outside the integral; moreover, if the distribution of the lattice frequencies is very dense, the shape of this narrow integral does not matter. Therefore

$$\omega\epsilon'' = \frac{2\pi^2}{v}\frac{1}{\delta\omega}\sum_{\omega,\delta\omega}(\mathrm{d}M/\mathrm{d}Q_i)^2 \tag{3}$$

where the sum goes over the vibrations with frequencies between ω and $\delta\omega$.

In the cases to be considered, the normal coordinate of a vibration is a unique function of its frequency. The suffix i can then be replaced by the suffix ω, and the summation consists in multiplying the contribution of one term by $d(\omega)$ i.e. by the density of vibrational frequencies. The right-hand-side of equation (3) thus becomes $(2\pi^2/v)(\mathrm{d}M/\mathrm{d}Q_\omega)^2 d(\omega)$. If the concentration of the impurity atoms is low and they are isolated from each other, we may write

$$\omega\epsilon'' = \frac{2\pi^2 N'}{v}\left(\frac{\mathrm{d}M}{\mathrm{d}Q_\omega}\right)_1^2 d(\omega) \tag{4}$$

where N' is the number of the impurity atoms in the crystal and $(\mathrm{d}M/\mathrm{d}Q_\omega)_1$ represents the effect of one impurity atom. The last equation is clearly equivalent to equation (1).

3. THE ONE-DIMENSIONAL "ATOMIC" CHAIN

In this Section we consider a linear chain of evenly spaced atoms. All the atoms are equal and have the mass m, except for one impurity atom whose mass is m'. The interaction is restricted to nearest neighbours; the force constant between the normal atoms will be denoted by f, and between the impurity atom and its two neighbours by f'. The impurity atom will be labelled by the suffix 0, the atoms on its right by 1, 2, 3, ... etc. and on its left by -1, -2, -3, etc.

The equation of motion for the impurity atom is:

$$m'\ddot{x}_0 = -f'(2x_0-x_1-x_{-1}) \tag{5}$$

For its two neighbours:

$$\begin{aligned} m\ddot{x}_1 &= -f(x_1-x_2)-f'(x_1-x_0) \\ m\ddot{x}_{-1} &= -f(x_{-1}-x_{-2})-f'(x_{-1}-x_0) \end{aligned} \tag{6}$$

and for all other atoms:

$$m\ddot{x}_n = -f[(x_n-x_{n+1})+(x_n-x_{n-1})] \tag{7}$$

We shall assume that the chain satisfies the periodic boundary conditions, whose implementation will be discussed below.

Since different atoms cannot have the same electron affinity, the impurity will either take up or give some electronic charge to the lattice atoms and will therefore remain charged with respect to the latter. If this charge exchange is restricted to the impurity and its nearest neighbours, then M, the dipole moment of the whole chain, for an arbitrary displacement can be written

$$M = e[x_0-\tfrac{1}{2}(x_1+x_{-1})] \tag{8a}$$

where e is an effective charge.

In the other extreme, we could assume that all the lattice atoms take part equally in the charge exchange with the impurity. This is an unrealistic assumption, but is of interest as a limiting case. Since the centre of gravity of the chain is at rest during the internal vibrations, in this second case M is approximately given by

$$M = ex_0 \tag{8b}$$

The actual situation is usually between equation (8a) and (8b) but much nearer to (8a).

In addition to the static charge, there is also a polarization due to the fact that the electron clouds get distorted in a displacement, and in the case of unequal atoms the distortion polarizations do not cancel. In a first approximation, the distortion polarization is linear in the displacements and both in equations (8a) and (8b) it is included in e.

In the case of periodic boundary conditions, the solutions of the equations of motion (5–7) can always be chosen so that half of them are symmetrical and the other half antisymmetrical with respect to the impurity atom. The antisymmetrical modes can have no dipole moment and are therefore of no interest for the present problem.

The symmetrical solutions can be written

$$x_n = A\cos\omega t\cdot\cos(|n|\sigma+\delta)\quad\text{for } n\neq 0 \tag{9}$$

$$x_0 = B\cos\omega t \tag{10}$$

where $|n|$ denotes the absolute value of n. Inserting equation (9) into equation (7) gives

$$\omega^2 = (4f/m)\sin^2(\sigma/2) \tag{11}$$

And inserting the last three equations into equation (5), one obtains

$$\frac{B}{A} = \frac{\cos(\sigma+\delta)}{1-2(fm'/f'm)\sin^2(\sigma/2)} \tag{12}$$

Next we may insert the last four equations into either of the equations (6) and solve for $\tan\delta$. Using straightforward trigonometric formulae, after some calculation one obtains

$$\tan\delta = \left\{-1+\left[\frac{m}{m'}+\left(1-\frac{f}{f'}\right)2\sin^2\frac{\sigma}{2}\right]^{-1}\right\}\tan\frac{\sigma}{2} \tag{13}$$

Alternatively, instead of solving for $\tan\delta$ we may solve equation (6) for $\cos^2(\sigma+\delta)$ and get

$$\cos^2(\sigma+\delta) = \frac{(1-U)^2\cos^2(\sigma/2)}{(1-U)^2\cos^2(\sigma/2)+[1-U+(m'/m)]^2\sin^2(\sigma/2)}$$

where $$U = 2\frac{fm'}{f'm}\sin^2\frac{\sigma}{2} \tag{14}$$

Comparing equation (14) with equation (12) shows that B/A can never become infinite. In view of the usual arguments, all physically independent solutions are contained in the range

$$0 < \sigma < \pi \tag{15}$$

It is also seen that changing the value of δ by $\pi/2$ has the only effect of multiplying all the displacements by -1. Therefore we can restrict δ to the range

$$-\frac{\pi}{2} < \delta < \frac{\pi}{2} \tag{16}$$

This same problem has been solved in a previous paper by the author (Ref. 5) for the case when $f' = f$. It is easily seen that if we put $f' = f$ in the present solutions (9–13), these reduce to the solutions in Ref. (5). As in Ref. (5), the present solutions represent standing waves that are strongly modified at the position of the impurity.

In Ref. (5) the total number of atoms N was relatively small and hence the exact boundary conditions were of some importance. In the present case N is very large and we can therefore impose periodic boundary conditions. To do this, we imagine that at either end of our chain of N atoms there is an infinite number of further atoms; in order to insure periodicity, at every N'th position there is an impurity atom. The displacements of all the additional normal atoms are still given by equation (9), and if these satisfy the periodic boundary condition it follows automatically that the displacements of all the additional impurity atoms are equal to x_0.

The periodic boundary condition can be written $x_{-n} = x_{N-n}$. In view of equation (9) this means

$$\cos(n\sigma+\delta) = \cos(N\sigma-n\sigma+\delta)$$

This gives the allowed values of σ:

$$\sigma = l\frac{2\pi}{N}-\frac{2\delta}{N},\quad l = 1, 2, 3, \ldots \tag{17}$$

where δ is given by equations (13) and (16). In the absence of an impurity δ would be zero; it is thus seen that the shift in σ, and therefore in ω, produced by the impurity is negligibly small. But the change of the displacements in the neighbourhood of the impurity atom can be large, and this will affect the dipole moment.

In addition to the non-localized vibrations discussed so far, under certain conditions a vibration localized near the impurity can also occur. This localized vibration is of no interest to us, as its frequency is always above the highest non-localized frequency, but as a matter of interest we point out that this vibration is also given by the solutions (9–13) if we allow σ to be of the complex form $\sigma = \pi+i\alpha$. It can be shown that a symmetric localized vibration occurs if

$$\frac{m'}{m}-1 < 2\left(\frac{f}{f'}-1\right)$$

Returning to the non-localized symmetric vibrations, $d(\omega)$ the number of frequencies in unit range of ω is given by the usual relation

$$d(\omega) = \frac{\mathrm{d}l}{d\omega} = \frac{dl}{\mathrm{d}\sigma}\frac{\mathrm{d}\sigma}{\mathrm{d}\omega} \tag{18}$$

since there is one symmetric vibration for each integer value of l. Using equations (11) and (17) and neglecting quantities of order unity next to N, this leads to the same result as in the chain without impurity, namely

$$d(\omega) = \frac{N}{2\pi}\sqrt{\left(\frac{m}{f}\right)}\frac{1}{\cos\frac{1}{2}\sigma} \tag{19}$$

The normalization condition of normal co-ordinates requires that for any single normal vibration

$$Q^2 = \sum_n m_n x_n^2$$

where Q is the normal coordinate of the vibration considered, and the sum goes over the N atoms of the chain. In the sum we may neglect the fact that one of the atoms is different and assume therefore that all the x are given by equation (9). Inserting the solution (9) and summing over n we obtain

$$A_\omega \cos\omega t = \sqrt{\left(\frac{2}{Nm}\right)}Q_\omega \tag{20}$$

which again is the same as for the chain without the impurity. In equation (20), as well as in the equations which follow, quantities referring to a particular vibration are labelled by the frequency ω.

Absorption

With the use of equations (9), (10) and (12), equation (8a) can be written

$$M = e\sum_\omega A_\omega \cos\omega t\left[\frac{1}{1-2(fm'/f'm)\sin^2\frac{1}{2}\sigma_\omega} - 1\right] \times \cos(\sigma_\omega + \delta_\omega) \tag{21a}$$

where the sum goes over all the normal modes. On the other hand, if M is given by equation (8b), in a similar way we obtain

$$M = e\sum_\omega A_\omega \cos\omega t\frac{\cos(\sigma_\omega+\delta_\omega)}{1-2(fm'/f'm)\sin^2\frac{1}{2}\sigma_\omega} \tag{21b}$$

Introducing equation (20) into equation (21a) and differentiating with respect to Q_ω leads to

$$\left(\frac{\mathrm{d}M}{\mathrm{d}Q_\omega}\right)^2 = \frac{2e^2}{Nm}\left[\frac{1}{1-2(fm'/f'm)\sin^2\frac{1}{2}\sigma_\omega} - 1\right]^2 \times \cos^2(\sigma_\omega+\delta_\omega)$$

Introducing this equation and equation (19) into (4) and making use of (14) we obtain the required expression for the absorption due to N' impurity atoms, namely

$$\omega\epsilon'' = \frac{N'2\pi e^2}{v}\sqrt{\left(\frac{1}{fm}\right)}\left(2\frac{fm'}{f'm}\sin^2\frac{\sigma}{2}\right)^2\frac{\cos(\sigma/2)}{D} \tag{22a}$$

where D is the denominator of equation (14) and the relation between ω and σ is determined by (11). In a similar way, when M is given by (8b) and (21b) we get

$$\omega\epsilon'' = \frac{N'2\pi e^2}{v}\sqrt{\left(\frac{1}{fm}\right)}\frac{\cos(\sigma/2)}{D} \tag{22b}$$

Although our model is a linear chain of atoms, the last two equations contain the volume v. This is because the absorption is essentially a volume effect. This apparent difficulty is easily overcome by assuming that our linear chain consists of three-dimensional atoms.

After a simple transformation D can be written

$$D = \cos^2\frac{\sigma}{2} + \left(\frac{m'}{m} - 1\right)^2\sin^2\frac{\sigma}{2} + 4\frac{m'}{m}\left(\frac{f}{f'} - 1\right)\sin^2\frac{\sigma}{2}\left(\frac{m'f}{mf'}\sin^2\frac{\sigma}{2} - 1\right)$$

It is seen that D vanishes for $\sigma = \pi$ only if simultaneously $f' = f$ and $m' = m$. For an impurity these two conditions cannot hold exactly and therefore D never vanishes.

According to equation (19), the maximum of $d(\omega)$ is at $\sigma = \pi$, where it becomes infinite. On the other hand, since D remains finite, the right hand sides of both equations (22a) and (22b) vanish at that point. The absorption maximum can thus never coincide with the maximum of $d(\omega)$. This must clearly be true not only if the dipole moment is given by equation (8a) or (8b) but also it is given by an intermediate expression.

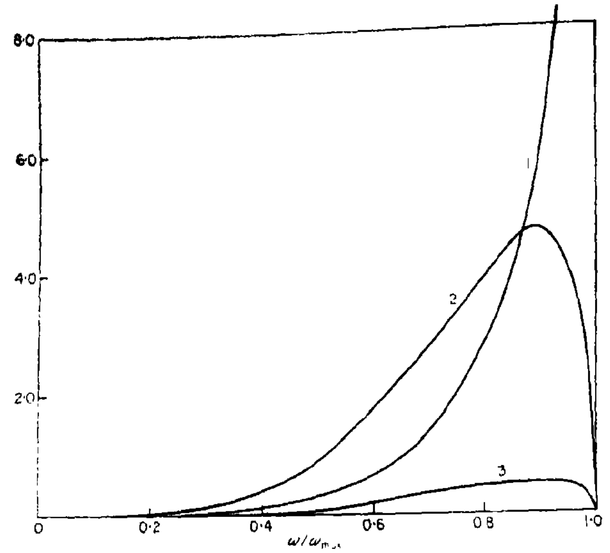

FIG. 2

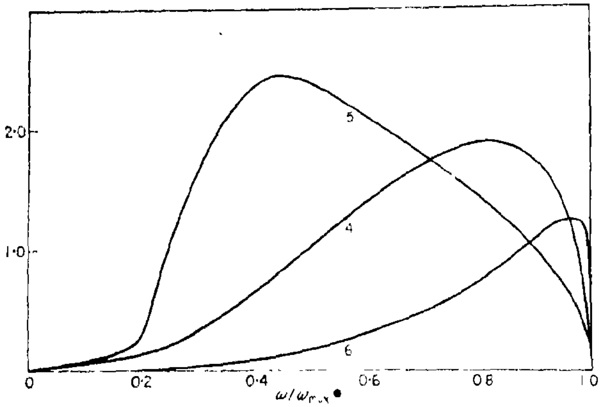

FIG. 3

FIGS 2 and 3. Absorption due to various impurities in the "atomic" chain according to equation (22a). The ordinate is $[(2fm'/f'm)\sin^2(\sigma/2)]^2\cos(\sigma/2)/D$, representing the frequency dependent part of the absorption. $\omega_{\max}$ is the highest frequency of the chain.

Curve 1: $m'/m = 1$, $f/f' = 1$.
Curve 2: $m'/m = 2$, $f/f' = 1$.
Curve 3: $m'/m = 0{\cdot}5$, $f/f' = 1$.
Curve 4: $m'/m = 10{\cdot}0$, $f/f' = 1$.
Curve 5: $m'/m = 3$, $f/f' = 2$.
Curve 6: $m'/m = 3$, $f/f' = 0{\cdot}5$.

m and f denote mass and force constant for the pure lattice; m' and f' denote corresponding quantities for the impurity.

Having proved this, we shall now discard (22b) and only consider (22a) further, as the equation (8a) on which it is based represents a much more realistic situation than equation (8b).

The absorption as given by equation (22a) is plotted in Figs. 2 and 3 for several cases. If both $f' = f$ and $m' = m$, the absorption behaves in a similar way as $d(\omega)$ and has a sharp narrow peak at the highest lattice frequency $\omega_{\max}$. For all other values of f'/f and m'/m, the absorption peak is shifted away from $\omega_{\max}$. Obviously the shift must always occur towards lower frequencies as the absorption is restricted to the region of the lattice frequencies.

Curve 1 actually becomes infinite at $\omega_{\max}$, while beyond $\omega_{\max}$ it is zero. This discontinuous behaviour is a consequence of the approximation inherent in equation (3) according to which the absorption due to any single lattice vibration is infinitely narrow.

It is seen that the integrals under the absorption curves differ considerably from each other, but this is of little interest for our present problem. This variation occurs partly because the total absorption depends on f', and partly because for some values of f'/f and m'/m a significant part of the absorption is contributed by the localized vibration whose effect is not included in our result.

4. THE "MOLECULAR" LINEAR LATTICE

In the "molecular" linear lattice illustrated in Fig. 1 each suffix refers to a pair of atoms. The displacements of the two atoms in the n'th pair will be denoted by x_n and ξ_n, respectively; x_n refers to the atom on the left and ξ_n to the atom on the right. We assume that the impurity atom is the left-hand atom in the 0'th pair, i.e. the one whose displacement is denoted by x_0.

For the pure lattice, there are two force constants because the two nearest neighbour distances for any particular atom are unequal. These two force constants will be denoted by f_1 and f_2. The mass of a lattice atom is denoted by m, that of the impurity atom by m'. It will be assumed that the force constants for the impurity atom are the same as for the pure lattice, since the results of the previous Section showed that all the essential features can be obtained by varying m'/m only.

The equations of motion then are:

$$m'\ddot{x}_0 = -f_1(x_0-\xi_0)-f_2(x_0-\xi_{-1}) \qquad (23)$$

$$m\ddot{x}_n = -f_1(x_n-\xi_n)-f_2(x_n-\xi_{n-1}) \text{ for } n \neq 0 \qquad (24)$$

$$m\ddot{\xi}_n = -f_1(\xi_n-x_n)-f_2(\xi_n-x_{n+1}) \qquad (25)$$

In view of the results of the previous Section, it will be sufficient to consider the case when the dipole moment M is given by an expression of the type (8a). However, because of the unequal nearest neighbour distances we must now have two effective charges e_1 and e_2. We therefore put

$$M = \tfrac{1}{2}e_1(x_0-\xi_0)+\tfrac{1}{2}e_2(x_0-\xi_{-1}) \qquad (26)$$

As the impurity is not a centre of symmetry, the solutions of the equations of motion cannot be divided into symmetrical and antisymmetrical vibrations. However, for about half the solutions the impurity atom is stationary; these solutions are the same as for the pure lattice, and can be written

$$\begin{aligned} x_n &= A\cos\omega t\sin n\sigma \\ \xi_n &= A\cos\omega t\sin(n\sigma+\epsilon) \end{aligned} \qquad (27)$$

The other half of the solutions is altered by the presence of the impurity atom. These can be written

$$\left.\begin{aligned} x_n &= A\cos\omega t\cos(|n|\sigma+\delta) \\ \xi_n &= A\cos\omega t\cos(n\sigma+\delta+\epsilon) \quad \text{if } n \geqslant 0 \\ \xi_n &= A\cos\omega t\cos(|n|\sigma+\delta-\epsilon) \quad \text{if } n < 0 \end{aligned}\right\} \qquad (28)$$

Inserting either the solutions (28) or (27) into (24) and (25), we obtain the same expressions for ϵ and ω as in the case of the pure lattice, namely

$$\begin{aligned} \sin\epsilon &= \frac{f_2\sin\sigma}{f_1+f_2-m\omega^2} \\ \cos\epsilon &= \frac{f_2\cos\sigma+f_1}{f_1+f_2-m\omega^2} \end{aligned} \qquad (29)$$

$$\omega^2 m = f_1+f_2 \pm \sqrt{[(f_1+f_2)^2-4f_1f_2\sin^2(\sigma/2)]} \qquad (30)$$

where the positive sign results in the "optical" and the negative in the "acoustical" branch. δ is obtained if the solutions (28) are inserted into equation (23). One obtains

$$\tan\delta = F/G \tag{31}$$

where

$$F = f_1+f_2-m'\omega^2-f_1\cos\epsilon-f_2\cos(\sigma-\epsilon)$$

$$G = -f_2\sin(\sigma-\epsilon)-f_1\sin\epsilon$$

With the help of equations (29) and (30), the last two expressions can be written

$$F = (m-m')\omega^2$$

$$G = \frac{2f_1f_2\sin\sigma}{\pm\sqrt{[(f_1+f_2)^2-4f_1f_2\sin^2(\sigma/2)]}}$$

In view of the relation between cosine and tangent, it follows from equation (31) that

$$\cos^2\delta = \frac{G^2}{F^2+G^2} \tag{32}$$

For the same reason as in the previous section, σ and δ can again be restricted to the range given by equations (15) and (16). It is seen that if $m' = m$, then $G = 0$, hence $\delta = 0$. The solutions (28) then reduce to the solutions for the pure lattice.

If N is the total number of atom pairs in the chain, then the periodic boundary condition implies that $x_{N+n} = x_n$ and $\xi_{N+n} = \xi_n$. For the sine-solutions (27) the allowed values of σ are the same as for the pure lattice, namely

$$\sigma = l2\pi/N, \quad l = 1, 2, 3, \ldots \tag{33}$$

while for the cosine solutions (28) it is found that the allowed values are again given by equation (17), except that in the present case N is the number of atom pairs and δ is now given by (31). Thus the impurity causes again only a negligibly small change in σ, and therefore in ω.

In addition to the non-localized vibrations represented by equations (27) and (28), there is also one localized vibration if $m' > m$ and two if $m' < m$ (cf. Ref. 4). As stated before, these are of no interest for the present problem and therefore they will not be considered here.

The relation between amplitude A and normal coordinate Q can be derived in the same way as in Section 1. Instead of equation (20) we now find, for both the sine and the cosine modes,

$$A_\omega\cos\omega t = \sqrt{\left(\frac{1}{Nm}\right)}Q_\omega \tag{34}$$

since the number of atoms is now $2N$.

Within each of the two branches each integer value of l corresponds to one sine and one cosine mode. Hence, for either the sine or the cosine modes separately, $d(\omega)$ is again given by

$$d(\omega) = \mathrm{d}l/\mathrm{d}\omega = \frac{\mathrm{d}l}{d\sigma}\left|\frac{d\sigma}{d\omega}\right|$$

We have to take the absolute value, as $d(\omega)$ is obviously always positive. $d\sigma/d\omega$ is obtained from equation (30) and $\mathrm{d}l/d\sigma$ from equation (33), for both sine and cosine modes, since similarly to the "atomic" chain, the effect of the impurity on $\mathrm{d}l/d\sigma$ is again negligibly small. The result may be written

$$d(\omega) = \frac{Nm}{\pi f_1f_2}\frac{\omega}{\sin\sigma}\sqrt{[(f_1+f_2)^2-4f_1f_2\sin^2(\sigma/2)]} \tag{35}$$

This expression represents the density of frequencies for either the sine or the cosine modes. Since $f_1 \neq f_2$, the square root can never vanish. The infinities of $d(\omega)$ are therefore determined by $\omega/\sin\sigma$. This quantity becomes infinite as $1/\sin\sigma$ at three points, namely for $\sigma = \pi$ in the acoustical branch and for both $\sigma = \pi$ and $\sigma = 0$ in the optical branch.

Absorption

In the "molecular" lattice, the impurity is not a centre of symmetry, hence the sine modes (27) are not antisymmetric with respect to it. In general, therefore, both the sine modes (27) and the cosine modes (28) contribute to the absorption.

Inserting a sine-solution with frequency ω into equation (26), with the use of equation (34) we get

$$\frac{\mathrm{d}M}{\mathrm{d}Q_\omega}(\sin) = \frac{1}{2}\sqrt{\left(\frac{1}{Nm}\right)}$$

$$\times[e_2(\sin\sigma\cdot\cos\epsilon-\cos\sigma\sin\epsilon)-e_1\sin\epsilon] \tag{36}$$

In a similar way, for a cosine solution of frequency ω we obtain

$$\frac{\mathrm{d}M}{\mathrm{d}Q_\omega}(\cos) = \frac{1}{2}\sqrt{\left(\frac{1}{Nm}\right)}$$
$$\times \{e_1[\cos\delta - \cos\epsilon\cos\delta + \sin\epsilon\sin\delta]$$
$$+e_2[\cos\delta - (\cos\sigma\cos\epsilon + \sin\sigma\sin\epsilon)\cos\delta$$
$$+(\sin\sigma\cos\epsilon - \cos\sigma\sin\epsilon)\sin\delta]\} \tag{37}$$

$d(\omega)$ is infinite at the three points where $\sin\sigma = 0$ but $\omega \neq 0$. Equations (29) and (32) show that at these points $\sin\epsilon$ vanishes as $\sin\sigma$ and, if $m' \neq m$, so does $\cos\delta$. Therefore, if $m' \neq m$ at these three points both (36) and (37) vanish at least as strongly as $\sin\sigma$, while $d(\omega)$ becomes infinite as $1/\sin\sigma$. Since the absorption, given by equation (4), is proportional to $(\mathrm{d}M/\mathrm{d}Q)^2 d(\omega)$, it follows that the absorption vanishes at the three points where $d(\omega)$ is infinite.

Thus, as in the case of the atomic lattice, we again find that the maxima of the absorption cannot coincide with the maxima of $d(\omega)$. Details of the actual absorption curve depend on the values of the various parameters, e.g. on e_1/e_2, f_1/f_2 and m'/m.

Numerical calculations

A few curves have been calculated for the special case when

$$e_1/e_2 = f_1/f_2 \tag{38}$$

With the use of equations (38) and (29), it is readily found that the right-hand-side of equation (36) vanishes for all σ. Thus in this special case the absorption arises from the cosine modes alone.

Considering the cosine modes, inserting equation (38) into (37) and making use of equation (31) and of the definition of F and G, we find that the curly bracket in equation (37) reduces to $[(e_1+e_2)/(f_1+f_2)]m'\omega^2\cos\delta$. When this simplified form of (37), together with (32) and (35), is introduced into equation (4), it is convenient to express the result in terms of $\omega_{\max}$, the highest optical frequency. It is seen from equation (30) that $m\omega_{\max} = 2(f_1+f_2)$. It is then found that for the case considered, equation (4) may be written in the form

$$\omega\epsilon'' = \frac{16\pi N'(e_1+e_2)^2}{v\sqrt{[2m(f_1+f_2)]}}\eta \tag{39}$$

where

$$\eta = \left(\frac{m'}{m}\right)^2$$
$$\times \frac{\gamma(\omega/\omega_{\max})^5 \sin\sigma\sqrt{[1-\gamma\sin^2(\sigma/2)]}}{\left(\frac{m'-m}{m}\right)^2 16\frac{\omega^4}{\omega_{\max}^4}(1-\gamma\sin^2(\sigma/2)) + \gamma^2\sin^2\sigma}$$
$$\gamma = 4f_1f_2/(f_1+f_2)^2$$

and the connection between $\omega/\omega_{\max}$ and σ is determined by equation (30). The meaning of the volume v is interpreted in the same way as for the atomic chain in Section 2. Since $f_1 \neq f_2$, γ is always less than unity and equation (39) therefore shows clearly that ϵ'' vanishes for $\sin\sigma = 0$, as long as $m' \neq m$.

For the case when $f_1/f_2 = 3$, η has been plotted on Fig. 4 for four values of m'/m. The curve for $m'/m = 1$ is not shown; this curve has peaks at ω_a, ω_b and $\omega_{\max}$, i.e. at the three points where $d(\omega)$ is infinite. But for all other values of m'/m the maxima are shifted away from these frequencies. It is also of some interest to note that as m'/m increases, the absorption is reduced in the optical and increased in the acoustical branch.

5. ABSORPTION DUE TO ISOLATED IMPURITY ATOMS OR TO POINT DEFECTS IN A REAL THREE-DIMENSIONAL CRYSTAL

The last two Sections dealt with linear chains containing isolated impurity atoms, i.e. impurity atoms well separated from each other. Concerning the absorption of the non-localized lattice vibrations in such chains, we may reach the following conclusions:

(a) The absorption has approximately as many maxima as the density of lattice frequencies $d(\omega)$; but the absorption maxima do not coincide exactly with the maxima of $d(\omega)$.

(b) The shift between the maxima of the absorption and of $d(\omega)$ usually amounts to only a few parts per cent on the frequency scale, although in some cases it can be much larger (cf. curve 5 on Fig. 3).

(c) The number of maxima in the absorption spectrum is not always exactly the same as in $d(\omega)$. If $d(\omega)$ has two maxima near to each other, the absorption spectrum may only exhibit one broad maximum corresponding to these two (cf. curve 3 on Fig. 4).

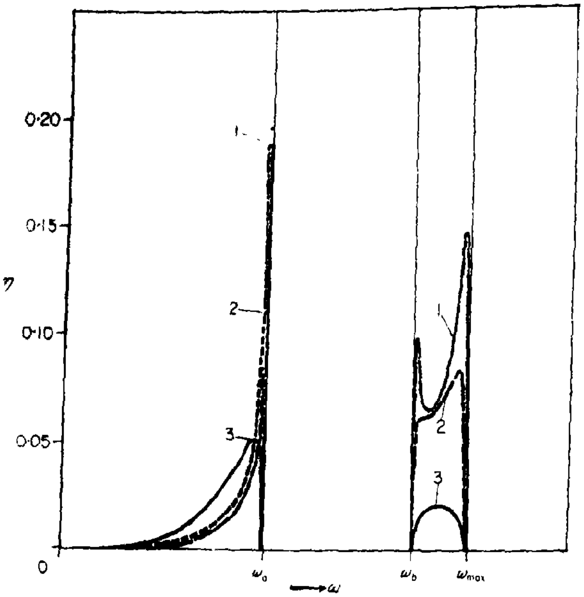

FIG. 4. Absorption due to various impurities in the molecular chain as given by equation (39), if $e_1/e_2 = f_1/f_2 = 3$. The acoustical frequencies extend from 0 to ω_a, the optical frequencies from ω_b to ω_{max}. $\omega_a/\omega_{max} = 0\cdot5$; $\omega_b/_{max} = 0\cdot5 \times \sqrt{3}$.
Curve 1: $m'/m = 1\cdot1$
Curve 2: $m'/m = 1\cdot2$
Curve 3: $m'/m = 2\cdot0$.
m = mass of lattice atom; m' = mass of impurity atom. The force constants for the impurity are assumed to be the same as for the pure lattice.

(d) Two very different impurities may produce absorption peaks at almost the same frequency, even though this frequency does not coincide with the maximum in $d(\omega)$ (cf. curve 2 on Fig. 2 and curve 4 on Fig. 3).

The solutions in the last two sections for both the "atomic" and the "molecular" lattice, show that the displacements of the impurity and of its neighbours vanish at the points where the reduced wave number σ is either 0 or π, i.e. at the points where $d(\omega)$ has its maxima. This is essentially the reason for the shift between the maxima of the absorption and of $d(\omega)$.

We may note that the vibrations with $\sigma = 0$ and $\sigma = \pi$ are not waves at all. For $\sigma = 0$ the displacements are the same in each unit cell, while for $\sigma = \pi$ they have opposite sign in alternate unit cells, but in both cases the magnitudes of the displacements are the same throughout the lattice. It seems that these vibrations are characteristic of the pure lattice only and in these vibrations the impurity cannot take part.

It seems reasonable to conclude that this behaviour is quite general. If this is so, then in a three dimensional crystal the displacement of the impurity vanishes if the wave number is either zero or if it corresponds to the zone boundaries. On the other hand, as far as is known, the maxima of $d(\omega)$, or at least most of the maxima, are very near to the frequencies corresponding to zero wave number or to the zone boundaries, although they are not exactly at those positions. Even in three dimensions, therefore, the impurity displacement almost vanishes at the maxima of $d(\omega)$, or at least at most of the maxima.

It seems therefore reasonable to assume that the validity of the above four conclusions (*a*)–(*d*) can be extended to isolated impurities in a three-dimensional crystal. Similar conclusions hold also for point defects, i.e. interstitial atoms or vacant lattice points.*

Obviously the conclusions (*a*)–(*d*) are only valid for the absorption arising from the non-localized vibrations. However, as explained earlier, in the diamond lattice a localized vibration can only occur at frequencies above the highest lattice frequency.

Our results suggest, therefore, that in a diamond lattice various point impurities or point defects give rise to absorption spectra which are similar to each other and to the density distribution of the lattice frequencies $d(\omega)$. Some of these spectra may be very similar to each other, while others may differ in important details.

6. ABSORPTION DUE TO A PLANE OF IMPURITY ATOMS

Entirely different absorption spectra occur if the impurity atoms are not isolated from each other, or if the defects are not point defects. As an extreme example, we shall discuss the case when in the diamond lattice a (100) plane is entirely occupied by impurity atoms, all the impurity atoms being of the same type. This case bears a close resemblance to an impurity arrangement that may actually occur in diamond.

The absorption is connected with the displacements of the impurity atoms relative to the lattice atoms. We are again interested in the non-localized lattice vibrations only. We may take these to be plane waves, distorted in some way in the neighbourhood of the impurity plane. The symmetry of the distortion is determined by the symmetry of the interaction between the impurity plane and the wave. It is clear, therefore, that for waves propagated perpendicularly to the impurity plane all the atoms of the plane vibrate in phase. For all other waves, however, the displacements in various parts of the impurity plane have opposite sign and the total dipole moment cancels. Hence only waves propagated in the (100) direction, perpendicular to the (100) planes, can be infra-red active.

We consider first the longitudinal waves propagated in this direction. We note that in a diamond lattice all the atoms of a (100) plane are crystallographically equivalent. Therefore, for the waves considered, all the atoms of a (100) plane vibrate with the same amplitude and phase, and the displacement of each (100) plane may be described by a single coordinate. Moreover, all the (100) planes are identical with each other, except the one plane containing the impurity atoms.

Thus, if the interaction is restricted to nearest neighbours, the situation is formally the same as for the "atomic" linear chain treated in Section 3. In the equations of motion (5)–(7), each x_n now represents the displacement of a whole atomic plane. The solutions, the density of frequencies and the absorption spectra are exactly the same as derived in Section 3.

In the actual case the interaction is not restricted to nearest neighbours, but this can hardly affect the major features of the absorption. Thus if we restrict ourselves to cases where m'/m and f/f' differ from unity by less than a factor $\simeq 1{\cdot}5$, then the curves in Figs. 2 and 3 suggest that the absorption peak due to longitudinal waves should differ from the maximum frequency $\omega_{\max}$ by only a few per cent.

Moreover, in the region of long optical waves the transverse and longitudinal vibrations are almost identical, and the highest longitudinal and highest transverse frequencies coincide with each other and with the Raman frequency. For the case considered, where m'/m and f/f' are not very different from unity, we may expect, therefore, that the absorption bands due to the longitudinal and the transverse vibrations coincide, and that the resulting single peak is only a few per cent below the Raman frequency.

On the basis of papers by HOERNI and WOOSTER,(9) FRANK,(10) KAISER and BOND,(11) ELLIOTT(12) and others, it is now generally believed that type I diamonds contain a few (100), (010) and (001) planes where large portions are entirely occupied by nitrogen atoms. In such a plane, the portion occupied by nitrogen is about 100 Å in diameter. This is very large compared with the lattice distance and the absorption should therefore be governed by practically the same selection rules as when the entire plane is occupied by impurity atoms. Assuming that the regions occupied by nitrogen are well separated from each other, the absorption due to each of them should superpose independently; moreover, the (100), (010) and (001) planes produce identical absorption as they are crystallographically identical.

---

* In a recent paper, WALLIS and MARADUDIN(8) examined the effect of impurity atoms in *ionic* lattices and derived absorption curves that are very different from those obtained for valency crystals here. It is therefore worth stressing that the two cases are very different. In particular, the ionic lattice can obviously absorb even if the displacement of the impurity atom is zero, and in an ionic chain the absorption at $\omega_{\max}$ is therefore always a maximum.

For nitrogen, m'/m is near unity and f/f' is probably also much nearer to 1 than to 2. Therefore, if the nitrogen atoms are arranged in such planes they should produce a single absorption peak just below the Raman frequency.

Similar spectra should result if lattice defects were arranged in such planes. These spectra are thus completely different from those produced by point impurities or point defects. If the impurities or defects are neither isolated nor situated in special planes, but follow some other arrangement, then we may expect a different type of spectrum again.

7. DISCUSSION

Our results throw some light on the infra-red absorption of valency crystals in the region of the lattice frequencies. They show that different types of impurities or lattice defects may in some cases produce similar absorption spectra, while in other cases entirely different spectra may result. Bearing in mind that the spectra observed in diamond I presumably represent the superposed effect of various impurities and defects, we may conclude that our results are in qualitative agreement both with the variations and also with the similarities observed between various samples of diamond.

In this paper we shall not attempt to explain individually the origin of the various absorption bands observed in diamond I. We may note, however, that if the nitrogens are arranged in (100) planes as assumed, then according to our results these planes are probably responsible for the band nearest to the Raman frequency. This would be the band at 1282 cm^{-1} (0·159 eV, 7·8 μ) which only differs by 4 per cent from the Raman frequency.

The intensity of this band is known to be proportional to the nitrogen concentration (cf. KAISER and BOND(11)). Moreover, this assignment is also in good agreement with the spectra obtained by SMITH and HARDY(13) and SMITH.(14) By irradiating diamond II with neutrons and electrons, these authors produced spectra whose peaks coincide with several of the important infra-red peaks of diamond I; but the peak at 0·159 eV is completely absent in the irradiated samples. Since the absorption in these samples is believed to arise from the lattice defects produced by the irradiation, it is clear that they cannot exhibit an absorption band connected with impurities or defects arranged in particular planes.

Nevertheless, this assignment of the peak at 0·159 eV is only of tentative character, since it is based on the assumption that macroscopic portions of a few atomic planes are occupied exclusively by nitrogen. Actually, the X-ray results do not rule out the possibility that in the impurity planes only a part of the lattice sites is occupied by nitrogen, while other sites may be occupied by carbon. If this is the case then lattice waves whose propagation vectors are not perpendicular to the impurity planes can also absorb and the selection rules discussed in Section 6 either do not apply at all or only apply partially, depending on how the carbon and nitrogen atoms are mixed. In this case there may be no basis for assigning the 0·159 eV band to the nitrogen planes.

Finally, our calculations show that the measurement of the absorption spectra of impurity activated lattice vibrations provide some clues to the distribution of the lattice frequencies, but the connection is not straightforward and each case has to be judged according to the circumstances.

Acknowledgements—A part of this work was done at the National Physical Laboratory in 1960 during a month spent there by the author as vacation consultant. He is grateful to the Director of N.P.L., Sir GORDON SUTHERLAND, for drawing his attention to the problem and for very helpful discussions on the infra-red properties of diamond. He also very much appreciates the assistance provided by N.P.L. in the way of carrying out the numerical calculations and drawing the figures.

REFERENCES

1. BLACKWELL D. E. and SUTHERLAND G. B. B. M., *J. Chim. Phys.* **46**, 9 (1949).
2. SUTHERLAND G. B. B. M., BLACKWELL D. E. and SIMERAL W. G., *Nature, Lond.* **174**, 901 (1954).
3. LIFSHITZ M., *Nuovo Cim.* Ser. X, Vol. 3, Suppl., p. 716 (1956).

4. MARADUDIN A. A., MAZUR P., MONTROLL E. W. and WEISS G. H., *Rev. mod. Phys.* **30,** 175 (1958).
5. SZIGETI B., *Proc. phys. Soc. Lond.* **B65,** 19 (1952).
6. SZIGETI B., *Proc. Roy. Soc.* **A252,** 217 (1959).
7. SZIGETI B., *Trans. Faraday Soc.* **45,** 155 (1949).
8. WALLIS R. F. and MARADUDIN A. A., *Progr. theor. Phys.* **24,** 1055 (1960).
9. HOERNI J. A. and WOOSTER W. A., *Acta Cryst.* **8,** 187 (1955).
10. FRANK F. C., *Proc. Roy. Soc.* **A, 237,** 168 (1956).
11. KAISER W. and BOND W. L., *Phys. Rev.* **115,** 857 (1959).
12. ELLIOTT R. J., *Clarendon Laboratory (Oxford) Report,* Ref. **23/60** (1960).
13. SMITH S. D. and HARDY J. R., *Phil. Mag.* **5,** 1311 (1960).
14. SMITH S. D., *Disc. Faraday Soc.* **31,** 254 (1961).

J. Phys. Chem. Solids Pergamon Press 1963. Vol. 24, pp. 239–245. Printed in Great Britain.

OSCILLATOR STRENGTH FOR OPTICAL ABSORPTION BY SILVER IONS IN ALKALI HALIDE CRYSTALS*

J. M. CONWAY, D. A. GREENWOOD,† J. A. KRUMHANSL and W. MARTIENSSEN‡

Laboratory of Atomic and Solid State Physics, Cornell University, Ithaca, New York

(*Received* 6 *August* 1962)

Abstract—The optical absorption oscillator strength for excitation of a silver ion dissolved in an alkali halide crystal is analyzed. The transitions involved are unallowed for the free ion; however, in a lattice the fluctuating coulomb potential due to the motion of the ions is assumed to polarize the free ion states to make such transitions possible. The zero temperature oscillator strength for Ag^+ ion in NaCl is calculated to be $f = 0{\cdot}0014$. The experimental value as found by Martienssen is $f = 0{\cdot}0016$. The temperature dependence is found to agree satisfactorily with experiment. Quadrupole transitions cannot account for this magnitude of oscillator strength.

1. INTRODUCTION

A NaCl CRYSTAL doped with a small percentage of AgCl shows a weak u.v. absorption in the wavelength region 180–230 mμ where pure NaCl does not absorb. This was first studied by SMAKULA(1) in 1930. At low temperatures MARTIENSSEN(2) has shown that there are four absorption peaks whose oscillator strength has a strong temperature dependence. The experiments show peaks at energies which correspond to the $4d^{10}$ to $4d^{9}5s$ levels. In the free ion, dipole transitions between these levels are forbidden; the oscillator strength and the temperature dependence of the absorption in the doped crystal cannot be explained on the basis of quadrupole transitions, as is shown in Appendix I. It is the purpose of this paper to show that the interaction between the Ag^+ ions and the ions of the host lattice make dipole transitions partially allowed, and to show, using a simple model that the measured values of the absorption are consistent with this interpretation.

The problem of the interaction between a crystal lattice and electrons making optical transitions is a well known one, but numerical estimates appear to be scanty—HUANG and RHYS,(3) PEKAR,(4) KUBO *et al.*,(5) DEXTER(6) and MARKHAM.(7) We couple the electron to the NaCl lattice by making a Born Oppenheimer type of calculation for the dependence of the Ag^+ ion electron wave functions on the positions of the six nearest neighbors. These positions are expressed in terms of the normal modes assuming a Debye phonon spectrum; this is recognized as an approximation to a situation which may involve localized modes in an important way. By admitting $5p$ components to the ground and the excited states, dipole transitions become possible between these modified states.

2. DETAILS OF THE MODEL

The potential due to a Cl^- ion, approximated by a point charge $-e$, at its equilibrium distance $\boldsymbol{a}$ from a silver ion at the origin, is $\dfrac{-e}{|\boldsymbol{a}-\boldsymbol{r}|}$ where $\boldsymbol{r}$ is the vector from the silver ion nucleus to the A^+ ion electron. If the Ag^+ ion and the Cl^- ion are displaced from equilibrium, $\boldsymbol{U}_1$ and $\boldsymbol{U}_2$ respectively (see Fig. 1), the change in potential is

$$\frac{-e}{|\boldsymbol{a}+\boldsymbol{U}_1-\boldsymbol{r}-\boldsymbol{U}_2|}+\frac{e}{|\boldsymbol{a}-\boldsymbol{r}|}$$

---

[*] This work was supported by the Office of Naval Research.

[†] Present Address: Birkbeck College, (University of London) England.

[‡] Present Address: University of Frankfurt, Germany.

Now expanding; letting

$$\boldsymbol{d} = \boldsymbol{U}_2 - \boldsymbol{U}_1, \quad |\boldsymbol{a}| = a$$

$$\frac{-e}{|\boldsymbol{a}-(\boldsymbol{r}+\boldsymbol{d})|}+\frac{e}{|\boldsymbol{a}-\boldsymbol{r}|} = -e\left[\frac{\boldsymbol{a}\cdot\boldsymbol{d}}{a^3}+\frac{3}{2}\frac{(\boldsymbol{a}\cdot\boldsymbol{d})^2}{a^5}-\frac{d^2}{a^3}\right]$$

$$+-e\left[\frac{3(\boldsymbol{a}\cdot\boldsymbol{r})(\boldsymbol{a}\cdot\boldsymbol{d})}{a^5}-\frac{(\boldsymbol{d}\cdot\boldsymbol{r})}{a^3}\right]+O\left(\frac{dr^2}{a^4},\frac{rd^2}{a^4},\dots\right)$$

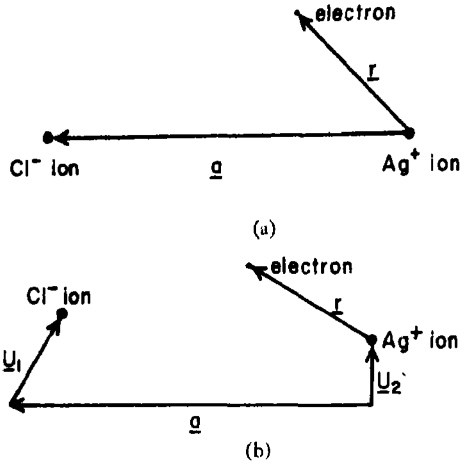

FIG. 1. (a) Positions of ions and electron in equilibrium. (b) Positions of ions and electron displaced from equilibrium.

The first term concerns phonon–phonon interactions which play no role in the distortion of the electron wave functions, but the second term which we shall use here arises from electron phonon interactions. The contributions of the other terms will be considered in Appendix II. The principal perturbation potential acting on the Ag⁺ ion due to the lattice is taken as the above expression evaluated for the six nearest neighbors of the Ag⁺ ion. We treat the lattice as simple cubic with one atom per unit cell (i.e. we regard the optical modes as continuations of the acoustical modes). We also simplify by neglecting localized phonon modes although the formulation of the problem to include these has been considered, but not solved by us as yet. The term used for our perturbation calculations is then

$$-e\left[\frac{3(\boldsymbol{a}\cdot\boldsymbol{r})(\boldsymbol{a}\cdot\boldsymbol{d})}{a^5}-\frac{(\boldsymbol{d}\cdot\boldsymbol{r})}{a^3}\right] \tag{1}$$

The displacement U_n of an ion at $\boldsymbol{a}_n$ is then

$$U_n = \sum_{f,s} q(f,s)\exp(if\cdot\boldsymbol{a}_n)\,V(f,s) \tag{2}$$

where the notation follows PEIERLS.⁽⁹⁾

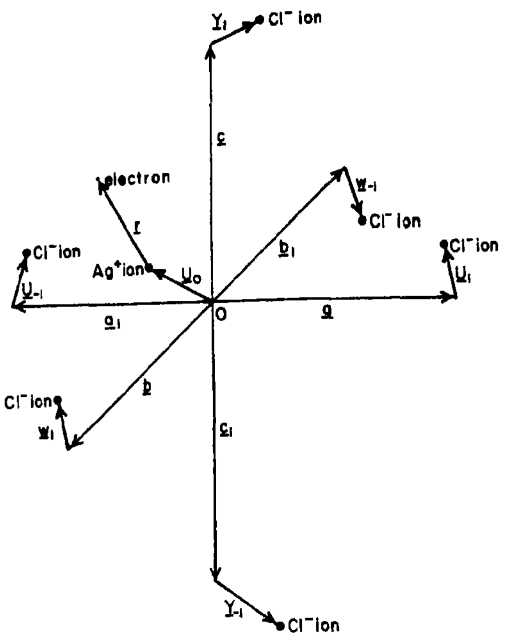

FIG. 2. Positions of 6 nearest neighbor Cl⁻ ions, Ag⁺ ion and electron.

Now considering the perturbation due to the six nearest neighbors (see Fig. 2) we get

$$\frac{V_{\text{pert.}}}{e^2} = \left[\frac{3(\boldsymbol{a}\cdot\boldsymbol{r})\boldsymbol{a}\cdot(U_1+U_{-1})}{a^5}-\frac{\boldsymbol{r}\cdot(U_1+U_{-1})}{a^3}\right.$$

$$+\frac{3(\boldsymbol{b}\cdot\boldsymbol{r})\boldsymbol{b}\cdot(W_1+W_{-1})}{a^5}-\frac{\boldsymbol{r}\cdot(W_1+W_{-1})}{a^3}$$

$$\left.+\frac{3(\boldsymbol{c}\cdot\boldsymbol{r})\boldsymbol{c}\cdot(Y_1+Y_{-1})}{a^5}-\frac{\boldsymbol{r}\cdot(Y_1+Y_{-1})}{a^3}\right]$$

substituting (2) we find

$$V_{\text{pert.}} = -eF_1x-eF_2y-eF_3z \tag{3}$$

where

$$F_i = \frac{2e}{a^3} \sum_{f,s} q(f,s) \exp(i\boldsymbol{f} \cdot \boldsymbol{a}_0) V_i(f,s) \times [2 \cos f_i a - \cos f_j a - \cos f_k a] \qquad i \neq j \neq k \tag{4}$$

In the ground state the Ag$^+$ ion is assumed to have a $4d^{10}$ configuration, and in the excited state a $4d^9 5s$ configuration. The potential (3) can mix $5p$ states with the d and the s orbitals and it is this admixture which we calculate, using atomic orbitals given by the Slater–Zener rules. For the radial parts of the orbitals (in atomic units). (KAUZMANN$^{(10)}$)

$$\begin{aligned} \chi_{4d}(r) &= r^{2\cdot 7} \exp(-2\cdot 1r) \\ \chi_{5s}(r) &= \chi_{5p}(r) = r^3 \exp(-1\cdot 14r) \end{aligned} \tag{5}$$

In the energy denominators of the perturbation theory we used the experimental values for the separation between $4d^{10}$–$4d^9 5s$ and $4d^9 5s$–$4d^9 5p$ configurations of the free ion which are about 5 eV. With this model the dependence of the electron wave function $\Psi(\boldsymbol{r}X)$ on the lattice configuration $\boldsymbol{X}$ (specified by equation (2)) is obtained as

$$\Psi(\boldsymbol{r}\boldsymbol{X}) = \left[\psi_{5s}(\boldsymbol{r}) - \sum\nolimits_{i,j} \frac{eF_j \langle p_i | r_j | s \rangle \psi_{5pi}(\boldsymbol{r})}{E_{5s} - E_{5p}}\right] \psi_\alpha(\boldsymbol{X}) \tag{6}$$

with similar expressions for the $4d$ orbitals.

3. CALCULATION OF THE OSCILLATOR STRENGTH

For the definition of the oscillator strength we use the expression (DEXTER$^{(6)}$)

$$f_{ab\alpha\beta} = \frac{2m^*}{\hbar^2} \int E |r_{ab\alpha\beta}|^2 S_{ab\alpha\beta}(E)\, \mathrm{d}E \tag{7}$$

where m^* refers to the effective mass of the electron,

a to the initial ion state,
α to the initial lattice state,
b to the final ion state and
β to the final lattice state.

It is to be noticed that in the excited lattice state we must use a different set of normal modes.

$S_{ab\alpha\beta}(E)$ refers to the line shape which is approximated here by

$$\delta(E_{b\beta} - E_{a\alpha} - E)$$

and

$$r_{ab\alpha\beta} = \int \mathrm{d}\boldsymbol{r} \int \mathrm{d}\boldsymbol{X} \chi^*_{a\alpha}(\boldsymbol{X}) \Phi_{a\boldsymbol{X}}(\boldsymbol{r}) \boldsymbol{r} \chi_{b\beta}(\boldsymbol{X}) \Phi_{b\boldsymbol{X}}\ (\boldsymbol{r})$$

where $\chi_{a\alpha}(\boldsymbol{X})$ refers to the lattice wave functions, $\boldsymbol{X}$ refers to the position of the nuclei, $\Phi_{a\boldsymbol{X}}(\boldsymbol{r})$ refers to the ion wavefunction, $\boldsymbol{r}$ refers to the position of the electron.

Sum over the final lattice states and average over the initial states, then

$$f_{ab} = \frac{2m^*}{3\hbar^2} Av_\alpha \sum\nolimits_\beta (E_{b\beta} - E_{a\alpha}) |r_{ab\alpha\beta}|^2$$

It is convenient and reasonable to choose an average $E_{b\beta} - E_{a\alpha}$ and factor it out. The justification for this is that the final lattice configuration differs from the initial configuration by an energy of 20–50 phonons. Now $E_{\text{phonon}} \leqslant \hbar\omega_{\max}$ which is $\simeq 0\cdot 01$ eV; therefore, the total energy due to the change in lattice configuration is small in comparison with the energy of the electronic transition ($E_{b\beta} - E_{a\alpha} = 5$ eV). Thus we rewrite

$$F_{ab} = \frac{2m^*}{3\hbar^2} (E_b - E_a) Av_\alpha \sum\nolimits_\beta |r_{ab\alpha\beta}|^2 \tag{8}$$

In the case of the transition d'_{xy} to s', where the prime refers to the modified state,

$$\begin{aligned} \sum\nolimits_\beta |r_{ab\alpha\beta}|^2 = \sum\nolimits_\beta \Bigg| \int \mathrm{d}\boldsymbol{X} \int \mathrm{d}\boldsymbol{r} \Bigg[d_{xy}(\boldsymbol{r}) - \frac{e}{E_{4d} - E_{5p}} \sum_{ij} \langle p_i | r_j |\ d_{xy} \rangle \\ \times\ p_i(\boldsymbol{r}) F_j \Bigg]^* \chi^*_\alpha(\boldsymbol{X}) \cdot \boldsymbol{r} \cdot \Bigg[S(\boldsymbol{r}) - \frac{e}{E_{5s} - E_{5p}} \sum_{i,j} \langle p_i | r_j | s \rangle p_i(\boldsymbol{r}) F_j \chi_\beta(\boldsymbol{X}) \Bigg] \Bigg|^2 \end{aligned} \tag{9a}$$

Using the relation

$$\int d_{xy}(r)\cdot r\cdot s(r)\,\mathrm{d}r = \int p_i(r)\cdot r\cdot p_j(r)\,\mathrm{d}r = 0$$

this becomes

$$\sum_\beta |r_{ab_{\alpha\beta}}|^2 = \sum_\beta \Bigg| \int \mathrm{d}X\,\frac{(-e)}{E_{4d}-E_{5p}} \sum_{i,j} \langle p_i|r_j|d_{xy}\rangle$$

$$\times \langle p_i|r|s\rangle (F_j\chi_\alpha(X))^*\chi_\beta(X) + \int \mathrm{d}X\,\frac{(-e)}{E_{5s}-E_{5p}}$$

$$\sum_{i,j} \langle p_i|r_j|s\rangle\langle d_{xy}|r|p_i\rangle\chi_\alpha^*(X)F_j\chi_\beta(X)\Bigg|^2 \qquad (9b)$$

Defining the quantities A_j and B_j by

$$\sum_i \frac{(-e)}{E_{4d}-E_{5p}}\langle p_i|r_j|d_{xy}\rangle\langle p_i|r|s\rangle \equiv A_j$$

$$\sum_i \frac{(-e)}{E_{5s}-E_{5p}}\langle p_i|r_j|s\rangle\langle d_{xy}|r|p_i\rangle \equiv B_j$$

and using notation such that

$$\chi_\beta(X) = |\beta\rangle,\quad \chi_\alpha(X) = |\alpha\rangle$$

then

$$\sum_\beta |r_{ab_{\alpha\beta}}|^2 = \sum_{\beta,j} |(A_jF_j|\alpha\rangle)^*|\beta\rangle + \langle\alpha|B_jF_j|\beta\rangle|^2 \qquad (9c)$$

From equation (4)

$$F_i = \sum_{f,s} C_i(f,s)q(f,s) = \sum_{f,s} C_i(f,s)[Q(f,s) + Q^*(-f,s)] \qquad (10)$$

again following the phonon notation of Peierls. Therefore

$$\sum_\beta |r_{ab_{\alpha\beta}}|^2 = \sum_{\beta,jf,s,\alpha'} |A_jC_j(f,s)\{[Q(f,s) + Q^*(-f,s)]|\alpha\rangle\}^*$$

$$|\alpha'\rangle\langle\alpha'|\beta\rangle + \langle\alpha|B_jC_j(f,s)[Q(f,s) + Q^*(-f,s)]|\alpha'\rangle\langle\alpha'|\beta\rangle|^2 \qquad (11)$$

In order to take account of the fact that the excited lattice state is expressed in a different set of normal coordinates than the ground state, we have expanded $|\beta\rangle$ in terms of the "α" set of normal coordinates, i.e.

$$|\beta\rangle = \sum_{\alpha'} \langle\alpha'|\beta\rangle|\alpha'\rangle$$

When all the matrix elements of Q and Q^* are evaluated, and with some algebra we finally obtain a usable expression to employ in (7):

$$\sum_\beta |r_{ab_{\alpha\beta}}|^2 = \sum_{f,s,j} |A_jC_j(f,s)+B_jC_j(f,s)|^2 \times \frac{\hbar(2N_\alpha(f,s)+1)}{2M^Nw(f,s)} \qquad (12)$$

where we have set $N_\alpha(-f,s) = N_\alpha(f,s)$ due to thermal equilibrium. In thermal equilibrium $2N_\alpha(E,s)+1 = \coth\frac{\hbar w(f,s)}{2kT}$. If a single frequency approximation is used the temperature dependence of the oscillator strength would be of the form $\coth\frac{hw}{2kT}$. KNOX[(8)] has fit Martienssen's data quite well with a single frequency of $1{\cdot}18\times10^{12}$ sec^{-1}. This is to be compared with the reststrahl frequency of NaCl which is $4{\cdot}92\times10^{12}$ sec^{-1}.

We now apply the foregoing to calculate the oscillator strength in the limit of zero temperature by taking the initial state to be the equilibrium ground state of the lattice. Because the density of modes is large for the higher frequency lattice modes, these make the major contribution but essentially are in their zero point state for typical measurements at low temperatures.

4. NUMERICAL EVALUATION

The radial and angular parts of the Slater–Zener orbitals are normalized separately so that (KAUZMANN[10])

$$\int f^2(r)r^2\,\mathrm{d}r = 1;\quad \int g^2(\theta,\phi)\,\mathrm{d}w = 1$$

The $5p$ radial = $5s$ radial

$$= \frac{r^3\exp(-1{\cdot}14r)}{\left(\dfrac{\Gamma(9)}{(2{\cdot}28)^9}\right)^{1/2}}$$

and the $4d$ radial

$$= \frac{r^{8\cdot 7}\exp(-2\cdot 12r)}{\left(\dfrac{\Gamma(8\cdot 7)}{(4\cdot 24)^{8\cdot 7}}\right)^{1/2}}$$

The angular wave functions are

$$s = \left(\frac{1}{4\pi}\right)^{1/2} \quad p_x = \left(\frac{3}{4\pi}\right)^{1/2}\sin\theta\cos\phi$$

$$p_y = \left(\frac{3}{4\pi}\right)^{1/2}\sin\theta\sin\phi$$

$$p_z = \left(\frac{3}{4\pi}\right)^{1/2}\cos\theta$$

$$d_{zx} = \left(\frac{15}{4\pi}\right)^{1/2}\sin\theta\cos\theta\cos\phi$$

$$dx^2-y^2 = \left(\frac{15}{16\pi}\right)^{1/2}\sin^2\theta\cos 2\phi$$

$$d_{xy} = \left(\frac{15}{4\pi}\right)^{1/2}\sin^2\theta\cos\phi\sin\phi$$

$$d3z^2-1 = \left(\frac{5}{16\pi}\right)^{1/2}(3\cos^2\theta-1)$$

$$d_{yz} = \left(\frac{15}{4\pi}\right)^{1/2}\sin\theta\cos\theta\sin\phi$$

Numerical matrix elements are:

$$\langle p_x|y|d_{xy}\rangle = 0\cdot 65$$

$$\langle p_x|x|s\rangle = 2\cdot 28$$

We can evaluate equation (12) for the "mixed" states d'_{xy} and S' in the zero temperature limit:

$$\sum_{f,s,j}|A_jC_j(f,s)+B_jC_j(f,s)|^2\frac{\hbar w(f,s)}{2M^N}$$

$$= \sum_j |A_j\mathscr{F}_j+B_jM_j|^2 \qquad (13)$$

where

$$\mathscr{F}_j = \sum_{f,s}\frac{2e}{a^3}\sqrt{\{\hbar/[2M^N w(f,s)]\}}\exp(i\boldsymbol{f}\cdot\boldsymbol{a}_0)$$

$$\times\ V_j(f,s)[2\cos\cdot f_ja-\cos\cdot f_ka-\cos\cdot f_la]$$

$$j\neq k\neq l$$

Substituting for A_j and B_j from equation (9) the above expression becomes

$$\sum_j|A_j\mathscr{F}_j+B_j\mathscr{F}_j|^2 = \sum_{i,j}\left|\frac{-e}{E_{4d}-E_{5p}}\right.$$

$$\times\ \langle d_{xy}|r_j|p_i\rangle\langle p_i|r|s\rangle\mathscr{F}_j$$

$$\left.\frac{-e}{E_{5s}-E_{5p}}\langle d_{xy}|r|p_i\rangle\langle p_i|r_j|s\rangle\mathscr{F}_j\right|^2$$

$$= 2\left(\frac{e}{E_{5d}-E_{5p}}+\frac{e}{E_{5s}-E_{5p}}\right)^2|\langle p_x|r_1|s\rangle|^2$$

$$\times\ |\langle d_{xy}|r_1|p_y\rangle|^2|\mathscr{F}_1|^2 \text{ as } |\mathscr{F}_i|^2 = |\mathscr{F}_j|^2$$

Evaluating for d'_{xz} and s' we find we can transform it, by a suitable rotation of the coordinate axes into an evaluation of equation (10) for d'_{xy} and s', since $\Sigma_j\mathscr{F}_jr_j$ is a scalar. The quantity

$$\langle d_{xz}|\mathscr{F}_jr_j|p_i\rangle\langle p_i|r|s\rangle$$

can be transformed by a rotation, $x\to x$, $y\to z$, $z\to -y$ into

$$\langle d_{xy}|\mathscr{F}_jr_j|p_i\rangle\langle p_i|r|s\rangle$$

Thus, the evaluation of equation (10) for d'_{xz} and s' is the same as for d'_{xy} and s' and similarly for the other d' states. The total oscillator strength is found by summing over all lattice modes and over the d electrons.

$$F_{\text{total}} = 2\cdot\frac{2}{3}\frac{m}{\hbar^2}(E_{5s'}-E_{4d'})\textstyle\sum_{d\text{ states}}|\langle d'|r|s'\rangle|^2$$

$$= \frac{4}{3}\frac{m}{\hbar^2}(E_{5s'}-E_{4d'})(5)(290)|\mathscr{F}_{r1}|^2 \qquad (14)$$

Denoting r_1, r_2, r_3, by x, y, z:

$$|\mathscr{F}_x|^2 = \left|\sum_{f,s}\frac{2e}{a^3}\sqrt{\{\hbar/[2M^N w(f,s)]\}}\right.$$

$$\times\ \exp(i\boldsymbol{f}\cdot\boldsymbol{a}_0)\,V_x(f,s)$$

$$\left.\times\ [2\cos f_xa-\cos f_ya-\cos f_za]\right|^2$$

$$= \frac{4e^2}{a^6}\frac{\hbar}{2M^N}\sum_{f,s}\frac{1}{w(f,s)}V^2(f,s)$$

$$\times\ (2\cos f_xa-\cos f_ya-\cos f_za)^2 \qquad (15a)$$

Using a Debye approximation for the spectrum

$$|\mathscr{F}_x|^2 = \frac{4e^2}{a^6}\frac{\hbar}{2M^N}\frac{1}{3}\cdot 3\left(\frac{V}{2\pi}\right)^3\iiint_{-\pi/a}^{\pi/a} \mathrm{d}^3f\,\frac{1}{c|f|}$$

$$\times\,(2\cos f_x a-\cos f_y a-\cos f_z a)^2$$

$$=\frac{1}{4\pi^2}\frac{e^2\hbar^2}{Ma^6k\theta_D}6I \tag{15b}$$

Where

$$I=\iiint_{-\pi}^{\pi}\frac{\cos^2 x-\cos x\cos y}{r}\,\mathrm{d}x\mathrm{d}y\mathrm{d}z$$

M = mass of chlorine atom.

Numerical integration yields $I \simeq 35$; thus, $M \simeq 35\times 1{\cdot}8\times 10^{-3}$ atomic units.

Assuming $\theta_D = 300$°K, a reasonable choice for NaCl, we obtain finally

$$f_{ab} = 0{\cdot}0014$$

This is the total theoretical oscillator strength due to all ten electrons in the $4d$ configuration.

Experimentally the oscillator strength can be determined by measuring first the integrated absorption $\int k\,\mathrm{d}(\hbar w)$ due to the transitions $4d^{10}$–$4d^9 5s$ of the Ag^+ ions per volume N in the crystal. To evaluate the experimental oscillator strength f we use the formula (DEXTER[6])

$$Nf_{ab} = \frac{nm_e}{2\pi^2e^2\hbar}\left(\frac{\epsilon_0}{\epsilon_{eff}}\right)\int k\,\mathrm{d}(\hbar w)$$

where n is the refractive index of NaCl at $\lambda =$ 2100 Å. For m_e use the vacuum mass of the electron and for the effective field determination, the Lorentz field correction.

Up to a concentration of 10^{-1} mole percent of AgCl in NaCl the experimental determination of the oscillator strength at 20°K yields $f_{exp} =$ 0·0016.

Considering the approximations which have been made in the calculation, the experimental and the theoretical values are in fortuitously good agreement; certainly no more than the correct order of magnitude need be claimed *a priori*, as indicative of the reasonableness of our suggested mechanism.

The theoretical quadrupole oscillator strength is estimated (Appendix I) to be 2×10^{-6}.

5. SUMMARY

We have considered a simple model to estimate the magnitude of the optical absorption cross section (oscillator strength) for excitation of a silver ion dissolved in an alkali halide crystal. The transitions involved would not be "allowed" for the free silver ion; in a lattice the fluctuating coulomb potential due to the motion of the ions is assumed to polarize the free ion states to make such transitions possible. We have calculated the magnitude of the absorption to be expected and its dependence on temperature. The agreement with experiment is better than the assumptions made might have suggested. It is clear that quadrupole transitions cannot be the cause of the transition since calculation shows the probability to be small by three orders of magnitude.

Acknowledgement—We would like to acknowledge informative discussions with R. KNOX.

REFERENCES

1. SMAKULA A., *Z. Phys.* **59**, 603 (1930).
2. MARTIENSSEN W., *Proceedings of the International Conference on Semiconductor Physics* p. 760. Czechoslovak Academy of Science, Prague (1960).
3. HUANG K. and RHYS A., *Proc. Roy. Soc. Lond.*
4. PEKAR S. I., *Zh. eksp. teor. Fiz. S.S.S.R.* **20**, 510 (1950), translated by Professor B. GOODMAN.
5. KUBO R. and TOYOZAMA Y., *Progr. theor. Phys. Kyoto* **13**, 160 (1955).
6. DEXTER D. L., *Solid State Physics* (edited by SEITZ F. and TURNBULL D.) Academic Press, New York (1958). Vol. 6.
7. MARKHAM J. J., *Rev. mod. Phys.* **31**, 956 (1959).
8. KNOX R. (private communication)
9. PEIERLS R. E., *Quantum Theory of Solids*, Clarendon Press, Oxford (1955).
10. KAUZMANN W., *Quantum Chemistry*, Academic Press New York (1957).

APPENDIX I

Quadrupole transition

The matrix element for radiative transition is:

$$M = \langle\phi_{5s}(\boldsymbol{r})|(1+i\boldsymbol{k}\cdot\boldsymbol{r}+\ldots)\hat{\boldsymbol{A}}\cdot\nabla|\phi_{4d}(\boldsymbol{r})\rangle$$

where $\hat{\boldsymbol{A}}$ is a unit vector in the direction of $\boldsymbol{A}$

$$M = \langle\phi_{5s}(\boldsymbol{r})|\hat{\boldsymbol{A}}\cdot\nabla|\phi_{4d}(\boldsymbol{r})\rangle+i\langle\phi_{5s}(\boldsymbol{r})|(\boldsymbol{k}\cdot\boldsymbol{r})\times(\hat{\boldsymbol{A}}-\nabla)|\phi_{4d}(\boldsymbol{r})\rangle$$

$$M = -\frac{im}{\hbar}\cdot w_{5s-4d}\langle\phi_{5s}|\hat{A}\cdot r|\phi_{4d}\rangle\frac{im}{2\hbar^2}$$

$$\times(E_{5s}-E_{4d})\langle\phi_{5s}|(k\cdot r)(\hat{A}\cdot r)|\phi_{4d}\rangle$$

$$-\frac{1}{2\hbar}\langle\phi_{5s}|(k\times\hat{A})\cdot \mathrm{L}|\phi_{4d}\rangle$$

$$M = -\frac{im}{2\hbar^2}(E_{5s}-E_{4d})\langle\phi_{5s}|(k\cdot r)(A\cdot r)|\phi_{4d}\rangle$$

$$f_{mk} = \frac{2m}{3\hbar}w_{5s-4d}\left|\frac{\langle\phi_{5s}|k\cdot r)(\hat{A}\cdot r)|\phi_{4d}\rangle}{2}\right|^2 \approx \frac{2}{3}\frac{m}{\hbar^2}$$

$$\times(E_{5s}-E_{4d})\frac{a^4k^2}{4}$$

where a is approximately the atom's radius

$$f_{mk} \sim \frac{2}{3}\frac{1}{1^2}\frac{5}{27}\frac{1}{4}\frac{5^4}{(1000)^2} \sim 2\times 10^{-6}$$

which is to be compared with the experimental value of 0·0016. Thus the quadrupole terms are not sufficient to account for the oscillator strength.

APPENDIX II

Other terms in the perturbation

In the expansion of the perturbing potential there were terms which appeared to be of similar magnitude to the terms we used in the calculation. We will consider these terms now. The terms we used were of order $\frac{rd}{a^3}$ but we neglected terms of order $\frac{dr^2}{a^4}$. The r^2 terms cannot mix in any p state with the d or the s state as

$$\langle d|r^2|p\rangle = \langle s|r^2|p\rangle = 0$$

We also neglected terms quadratic in the normal coordinates, terms of order $\frac{rd^2}{a^4}$. The linear and quadratic coefficients are of relative order of magnitude:

$$\sum_{f,s}\alpha(f,s)q(f,s)\exp(if\cdot a_0)$$

and

$$\frac{1}{a}\sum_{f,f',s,s'}\beta(f,f',s,s')q(f,s)q(f',s)\exp(ifa_0)\exp(if'a_0)$$

where α and β are numerical coefficients of order unity. We see the linear term is

$$\sim\sum_{f,s}\frac{\hbar w(f,s)}{M^N}$$

the quadratic term is

$$\sim\frac{1}{a^2}\sum_{f,s,f',s'}\frac{\hbar w(f,s)}{M^N}\frac{\hbar w(f',s')}{M^N}$$

where again we have used the zero temperature limit. Hence, the contribution of the quadratic part is, relative to the linear term, of order

$$\frac{1}{a^2}\sum_{f,s}\frac{\hbar w(f,s)}{M^N}\sim\frac{1}{a^2}\frac{\hbar}{M^N}\left(\frac{V}{2\pi}\right)^3\int_0^{f_{\max}}\frac{d^3f}{c|f|}$$

$$\sim\frac{1}{(2\pi)^3}\frac{\hbar^2k\theta_D}{Ma^2}$$

which is approximately 10^{-4} for an NaCl lattice. Despite the ruthless approximations we have made, it seems clear that at low temperatures our neglect of higher terms is justified. At higher temperatures corrections will be more important.

J. Phys. Chem. Solids Pergamon Press 1963. Vol. 24, pp. 247-259. Printed in Great Britain.

THE BOMBARDMENT OF GOLD FILMS BY INERT GAS IONS

G. J. OGILVIE, J. V. SANDERS and A. A. THOMSON
Division of Tribophysics, C.S.I.R.O., University of Melbourne, Australia

(*Received* 16 *July* 1962)

Abstract—Films of gold have been bombarded by nearly mono-energetic ions of helium, neon, argon or xenon in the energy range 15–250 eV, and then examined in an electron microscope. The damage caused by the bombardment is found to depend markedly on the energy of the ions and the gas, and to a lesser extent on the orientation of the crystal and the ion flux density. There is a threshold energy for the ions below which no damage is detectable, and its values for neon, argon, and xenon but not helium, are consistent with a model in which a simple collision at the surface may create an interstitial gold atom below the surface. The annealing characteristics depend upon the gas producing the damage. Sputtering yields were measured; at low energies argon sputters {100} surfaces more rapidly than {111}.

1. INTRODUCTION

EXAMINATION by electron diffraction of metal specimens bombarded with ions of inert gases has shown that they have been damaged in that dislocations and sometimes disoriented crystallites have been formed near the bombarded surface.(1–6) The electron microscope has revealed dislocation lines and loops probably formed by the aggregation of point defects produced by collisions of the ions with atoms at the surfaces of the specimens.(7–11) Since this damage has been observed for a number of different metals (Ag, Au, Pt, Al), for ions of a variety of gases (Ar, He, H, or O), and for ion energies between 75 eV and several keV, it appears to be a general effect associated with ion bombardment.

In this paper we are concerned with the lowest range of ion energies, where with decreasing energy of bombarding ions we have succeeded in detecting a threshold energy (E_T) for the ions below which no damage could be seen in an electron microscope. We imagine that a simple collision occurs at the surface of the crystal, and that the bombarding ion transfers a certain proportion of its energy to a gold atom, the maximum proportion depending upon the relative masses of the ion and a gold atom. Then if an atom on the surface behaves like one in the interior, the energy imparted to the gold atom at this threshold should be E_d, the threshold energy needed to permanently displace an atom from a lattice site in a crystal. This parameter E_d has been the subject of theory and experiment for some time, and the theoretical estimate due to SEITZ(12) of $E_d = 25$ eV has been widely used. For copper HUNTINGTON(13) calculated that E_d lay between 17 and 34 eV, and a recent computation by GIBSON, GOLAND, MILGRAM and VINEYARD(14) gave thresholds of 25 eV in ⟨100⟩, 25–30 in ⟨110⟩ and 85 eV in ⟨111⟩, which agree reasonably with experimental values of 22 eV(15) and 25 eV.(16)

All experimental determinations of E_d for metals have been obtained from specimens bombarded by electrons, and the only value for gold is 42 eV(17) obtained from measurements of resistance. The acceleration of ordering in Cu_3Au indicated a value of about 10 eV for this alloy.(19) For other metals experimental determinations give 30 eV for silver(15) and 27 eV for iron.(18)

In the experiments to be described here we have used an electron microscope to examine films of gold after they have been bombarded by monoenergetic (within ± 0·5 eV) ions of helium, neon, argon or xenon with energies in the range 15–250 eV. We shall describe the nature of the damage produced by the bombardment and how it varies with ion energy, the gas, and several other factors. We have deduced energy thresholds for damage for ions of the four different gases and also, because we could measure changes of thickness of many of the films, determined sputtering yields at the lower energies.

2. EXPERIMENTAL TECHNIQUE

2.1 *Method*

Specimens were bombarded in plasmas of non self-sustaining arc discharges in inert gases at pressures in the range 0·15–0·03 torr. The energy of the ions attracted to a specimen was controlled by adjusting its potential with respect to that of the plasma. This method has been used by a number of workers studying sputtering(20–27) and has important advantages. These are:

(a) Only singly charged ions will bombard the specimen if the arc voltage is less than the potential needed by electrons to produce doubly charged ions from singly charged ions. This condition has not been met in any of the investigations referred to in the Introduction. Nearly all other ion sources produce important numbers of multiply charged ions and consequently for the determination of sputtering or damage thresholds their use is most unsatisfactory.

(b) The potential which accelerates the ions can be measured to within 0·5 eV if the arc is operated in a quiet mode. A Langmuir probe can be used to measure the plasma potential and to establish that the discharge is not noisy or oscillating. Most sources give ions with a large energy spread (e.g. 10 eV(28)) because the potential of the region from which the ions are extracted is fluctuating.

(c) Provided the sheath surrounding the specimen is thin, charge exchange is a rare process and consequently very few neutral atoms reach the specimen with appreciable energies. Sputtering due to neutral atoms has been shown to be important in experimenting using ion beams.(29, 30)

(d) It is believed that the range of energies of ions from the type of arc discharge under consideration is small (e.g. 0·2 eV,(31) 1 eV(32)), although this is not well established by direct experiments.

(e) Large current densities of ions can be drawn to the specimen at low energies.

2.2 *Apparatus*

The specimens were small pieces of evaporated films mounted on gold grids and then enclosed in discharge tubes, separate tubes being used for each experiment. Since many tubes were therefore necessary, a commercial diode (Phillips 6X2) was used as the basic structure to which extra elements were added. A perspective drawing of an experimental tube is given in Fig. 1. The specimen (S) and the tip of the Langmuir probe (P) are placed in the annular space between the anode (A) and the oxide-coated nickel cathode (K). An auxiliary chamber (G), connected to the tube by a side arm, contains barium pellets in two perforated nickel containers spot welded to two leads. In order to maintain the cathode coating in good condition(33) while the tube was open to the air its filament was kept hot by connecting it to a 3V battery.

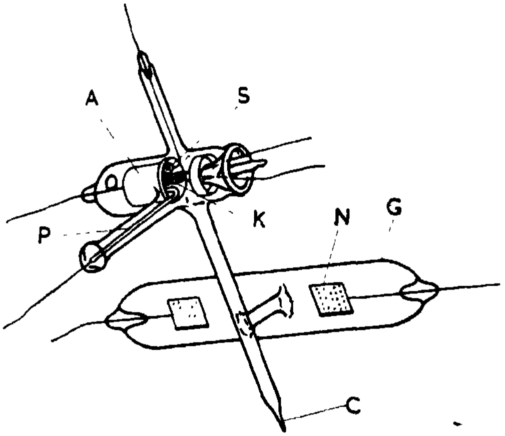

FIG. 1. Sketch of experimental discharge tube. A, anode; K, cathode; S, specimen; P, Langmuir probe; C, constriction for sealing off; G, gettering chamber; N, getter pellets.

2.3 *Specimen preparation*

Films 400, 800, or 1200 Å thick, were made by evaporating gold at about 100 Å per sec from a tantalum filament on to a freshly cleaved NaCl crystal maintained at 300°C. During the evaporation the pressure rose from 3×10^{-6} torr to 7×10^{-5} torr. The films were then annealed *in situ* for 10 min at 400°C. The evaporator was similar to small commercial units but had a stainless steel mercury diffusion pump and liquid-air trap.

Pieces of film about 2 mm square were obtained by cleaving the crystal and then stripping the film on to the surface of distilled water. The pieces of film were washed, picked up on a cleaned gold grid, and enclosed in a gold capsule (Fig. 2), which was then sealed into a discharge tube attached to the pumping line.

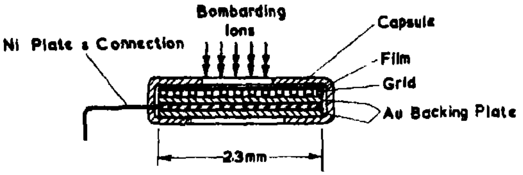

FIG. 2. Section through gold capsule for holding specimen in a discharge tube.

2.4 *Processing of tubes*

The tubes with specimens in place were evacuated by a conventional pumping line containing liquid-air traps, and baked at 410–420°C until the pressure fell to $1\text{–}2\times10^{-6}$ torr, usually in about 2 hr. The filament of the tube was then heated until the cathode was evolving very little gas. Next the tube was isolated from the pumps and spectroscopically pure gas was admitted through the cold traps to the pressures listed in Table 1. The getter pellets were then fired by setting up a glow discharge in the getter chamber. The gas pressure was finally adjusted to the seal-off pressure given in Table 1, and the tube sealed. The rated voltage was applied to the filament of the tube until the discharge could be run continuously; usually this took about 48 hr. With the specimen at about 6V negative with respect to the anode, the discharge was maintained until the arc voltage had dropped to a stable value less than the second ionization potential (see Table 1). This process usually took 1–5 min for xenon and argon, 0·5–2 hr for neon, and 1–25 hr for helium. The arc was then switched off and the filament left running for 24 hr. The arc voltage was then re-applied and if the arc re-started and ran at the same voltage as before, the tube was considered to be ready for use.

Two checks were made to see if the gas in the tubes was pure at the end of processing. Firstly, the optical spectrum of a tube filled with neon was examined and only neon was detected. Secondly, an analysis of the contents of some of the tubes with a mass spectrometer showed no contaminant beyond the limit of detection of about 1 part in 400.

2.5 *Operation of the tubes*

The method of operation of the discharge tubes can be seen from the circuit diagram in Fig. 3 and the normal operating conditions are given in Table 1. Since small ripples in voltages supplied to the tubes caused the arc to become noisy or oscillate, batteries were used as sources of potential except for heating the filament, where a.c. was satisfactory. The potential of the arc plasma was found by displaying the derivative of the probe characteristic on a cathode ray oscilloscope, when the change of slope in the characteristic appears as a peak.

Table 1. *Discharge conditions*

	Ionization potentials[34]		Gas pressures		Normal operating conditions		
Gas	First (V)	Second (V)	Firing of getter (torr)	Seal off (torr)	Arc potential (V)	Arc current (mA)	Specimen current (μA)
He	24·6	54·4	0·8	0·15	50	40	200
Ne	21·6	41·1	0·4	0·13	35	40	100
Ar	15·8	27·6	0·23	0·08	22	90	200
Xe	12·1	21·2	0·3	0·03	15	90	250

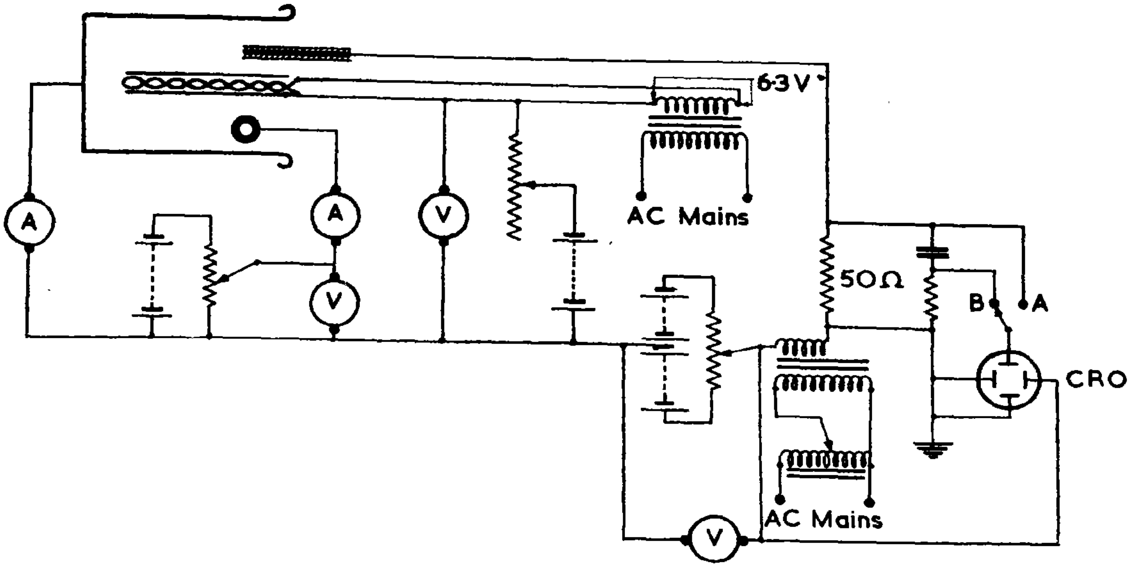

FIG. 3. Circuit diagram for the operation of the discharge tubes. The C.R.O. and circuits on the right hand side are associated with the Langmuir probe, the switch positions A and B applying a direct or differentiated signal to the C.R.O.

Most tubes were immersed in liquid air during the bombardment in order to retard the annealing of any damage. Since xenon condenses at the temperature of liquid air, such tubes were immersed in solid CO_2-acetone mixture. Some tubes were operated at ambient temperature.

The number of positive ions incident on a specimen is assumed to comprise the total current drawn by the specimen. No correction has been made for any secondary electrons contained in the current, and consequently all values quoted for ion densities or doses will be too large, the error being estimated to be at most 20 per cent. The energy of the ions was inferred from the potential difference between the anode and the specimen, any correction being obtained from the results of probe determinations of the plasma potential. These corrections were significant only in the case of the xenon-filled tubes where the potential of the plasma was found to be 2·5 eV above that of the anode when the arc current was 0·090 A.

2.6 *Electron microscopy*

When a bombardment had been completed, the tube was cracked open to remove the specimen, the capsule opened and the grid extracted for examination in a Siemens Elmiskop I operated at 75 or 100 keV. Both bright and dark field techniques were used with diffraction patterns being taken from selected areas when necessary. The tilts of the specimens were adjusted frequently to obtain suitable contrast, and to determine the effect of changes of contrast.

2.7 *Thickness of films*

The projected widths of stacking faults (assumed to lie in {111} planes) were used to measure the film thickness. Because the films were extensively buckled, it was necessary to select the few relatively small areas where the film was perpendicular to the electron beam by observing the diffraction pattern while the specimen was scanned, and adjusting the tilt if necessary. Faulted areas and their diffraction patterns were then photographed. With thinner films the contrast within the fault can be seen with sufficient clarity to determine whether the fault is single or multiple, and the thickness can be estimated to within about ± 7 per cent. In thicker films overlapping faults predominate, and it is difficult to interpret their contrast sufficiently well to obtain the same reliability. All thickness measurements were made on areas well away from the margin of the bombarded area.

3. RESULTS

Two types of films were produced, which we shall subsequently call {111} or {100}:

(a) Polycrystals, in which the grains, usually more than 1μ wide, had a strongly preferred orientation with {111} parallel to the surface. Our observations, being restricted to indvidual crystals within these specimens, are effectively made on single crystals with {111} parallel to the surface. No curious effects such as increased or diminished damage occurred at or near the boundaries. These films sometimes contained small {100} areas.

(b) Single crystal matrices with {100} parallel to the surface containing a few large grains, mostly oriented with {111} parallel to the surface.

Both {111} and {100} crystals contained stacking faults but few perfect dislocations. Since the {111} polycrystals were the more common specimen, most of our observations refer to this orientation; however there were sufficient {100} specimens to enable us to make significant observations on the orientation dependence of damage and sputtering.

Since an annular area of each specimen is protected from bombardment by the mounting capsule (Fig. 2), bombarded and unbombarded areas could be compared on every specimen. When sputtering is appreciable (e.g. for Ne^+ and Ar^+), the bombarded area is thinner and can then be readily detected in the microscope. This is illustrated in Fig. 4 which shows a {111} film having a bombarded and thinned region on the left, an unbombarded region on the right and a marginal zone between. When sputtering is negligible (e.g. He^+ and low energy Xe^+ ions), the bombarded area was distinguishable solely by the presence of damage. At the lowest energies, it was difficult to identify the bombarded area by looking at the image on the screen of the microscope. In this case fields were selected and photographed near the centre of the grid, and round the outside, and the photographs compared subsequently.

Several blank tests were made. In one set the specimens were examined at the end of the normal process for activation of the cathode (Section 2.4): in the other set no potential was applied to the specimens during the activation. No difference could be detected in the protected and unprotected areas of these films. The damage which we see, therefore, comes from the ion bombardment alone.

Pashley and Presland(35) found damage similar to ours being produced during examination of gold films in their electron microscope. To ensure that some of our damage was not similarly produced, we put an unbombarded film in the cold specimen holder to reduce contamination of the surface, and examined the same field for up to 15 min. The pressure inside the microscope was varied by leaking in argon, and the illuminating conditions were changed, but no detectable damage was ever produced.

3.1 *Description of the damage*

The exact form which the damage takes depends primarily on the ion energy and the gas, though the orientation of the crystal, the ion flux density, and the specimen temperature may also affect it. We shall first describe in detail the damage in {111} crystals bombarded by ions of the four gases, and then discuss the differences caused by a variation in the other factors. Unless otherwise specified the observations refer to experiments in which (i) the ion flux density was about 10^{16} ions cm^{-2} sec^{-1}; (ii) the total number of ions incident on 1 cm^2 was about 10^{20} when sputtering was inappreciable, or, when sputtering was important, was adjusted so that the specimen was thinned but not punctured; and (iii) the discharge tubes were run at sub zero temperatures.

The damage can be classified into three forms, which we shall call spots, loops or lines. The spots (Fig. 5a) are round, less than 50 Å diameter, have no resolved structure, and change contrast with specimen tilt. At present we cannot associate these with any particular type of defect in the crystal. The loops (Fig. 5b) consist of two closely-separated round or elongated spots which are usually less than 150 Å in diameter; their contrast is typical of that of dislocation loops. The lines (Fig. 5c) can be identified as lengths of dislocation line, since their contrast is typical of dislocations and they have been seen to move while the specimen is in the electron beam.

In {111} crystals, because the contrast is usually due to one or more 220 reflections, the images om the lines are broad and commonly multiple (Fig. 6). Their appearance is usually unlike that of a simple dislocation line; they are jagged and composed of sections about 100 Å long, so that they diffract inhomogeneously along their length. This irregular diffraction along the line is quite different from the dot contrast associated with a dislocation running at an angle to a surface. It is difficult to investigate this contrast because the lines are short and, the specimens being thin, there are usually a number of equally strong reflections occurring. Thus we have not established unambiguously the Burgers vector (b) of the lines, but we have examined the same areas with three adjacent 220 reflections; because of the complexity of detail in the images, it is not easy to locate and trace all dislocation lines in a small area, but where it has been possible they appear in all three images. It seems likely therefore that $b = \frac{1}{2}\langle 110\rangle$ rather than $\frac{1}{3}\langle 111\rangle$ or $\frac{1}{6}\langle 112\rangle$.

For all gases it has been possible to find an energy sufficiently low that no damage can be detected, but appears when the energy is increased by a few eV. The threshold energy for damage therefore lies within this interval, and it has been determined to a precision of ± 1 eV for xenon, and rather less for the other gases; the values are given in Section 4.3. As the energy is increased above this value, damage appears and the form which it takes at any energy depends upon the gas.

3.1.1 {111} *Crystals.* When {111} crystals are bombarded by Ne$^+$ or Ar$^+$ ions the abundance of the three forms of damage changes with ion energy. At low energies only spots appear, their concentration increasing with energy up to about 5×10^{10} per cm^2. This energy range for argon is 40–60 eV, and for neon it is larger, 60–110 eV. Above these energies loops are produced in addition to spots and their concentration also increases with energy to about 10^{11} per cm^2. For argon, at 60 eV short lines can be distinguished, initially about 100 Å long; their length and number increase with energy until a maximum length of about 3000 Å is reached at about 70 eV. The lines do not intersect, but tend to form into arrays in which the lines are nearly parallel (Fig. 5c). Ne$^+$ ions produce similar lines, but the energy must be increased to at least 150 eV before the long lines are formed. At the highest energies which we have used (250 eV), the lines are long, irregular

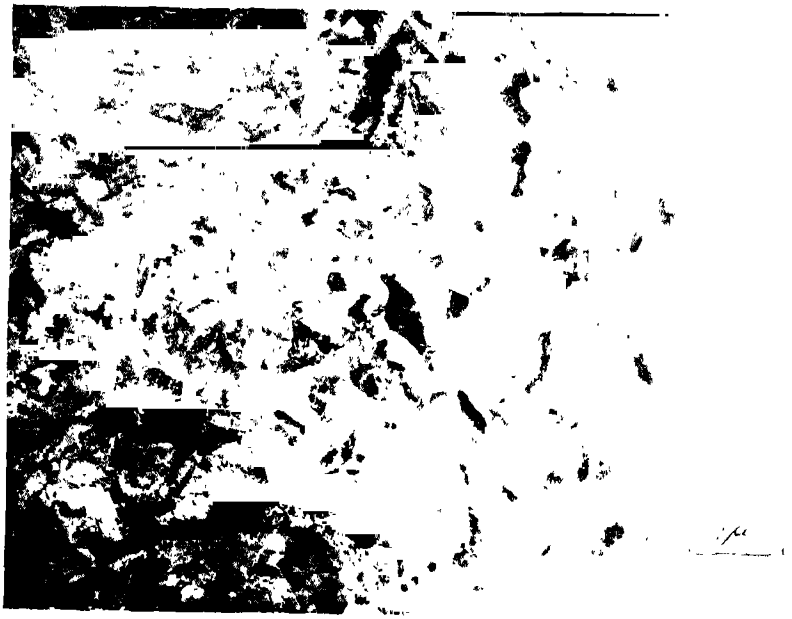

FIG. 4. Marginal area between bombarded (left) and unbombarded (right) regions {111} film, 92 eV Ar^+ ions (× 14,000).

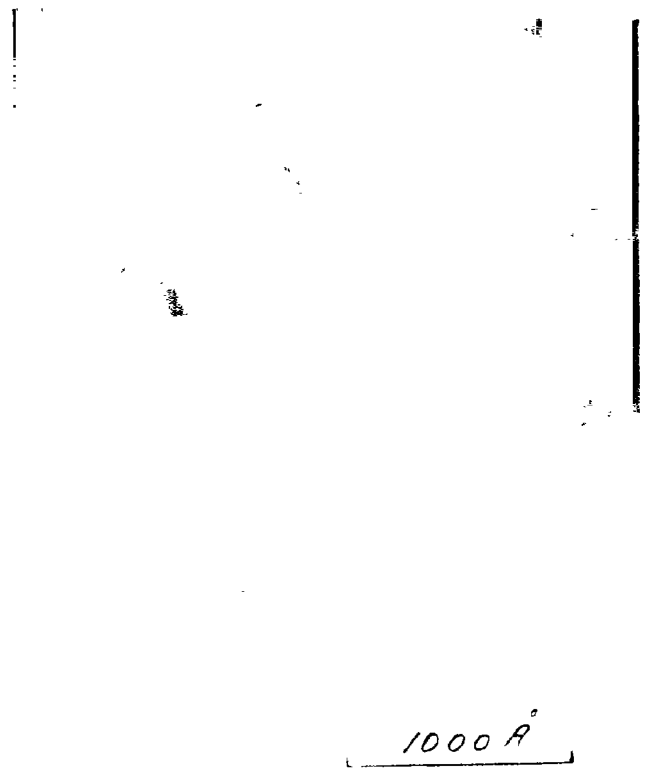

FIG. 5. (a) Spots in a film bombarded by 57·5 eV Ar^+ ions (× 300,000).

FIG. 5. (b) Loops in a film bombarded by 60 eV Ar^+ ions (× 300,000).

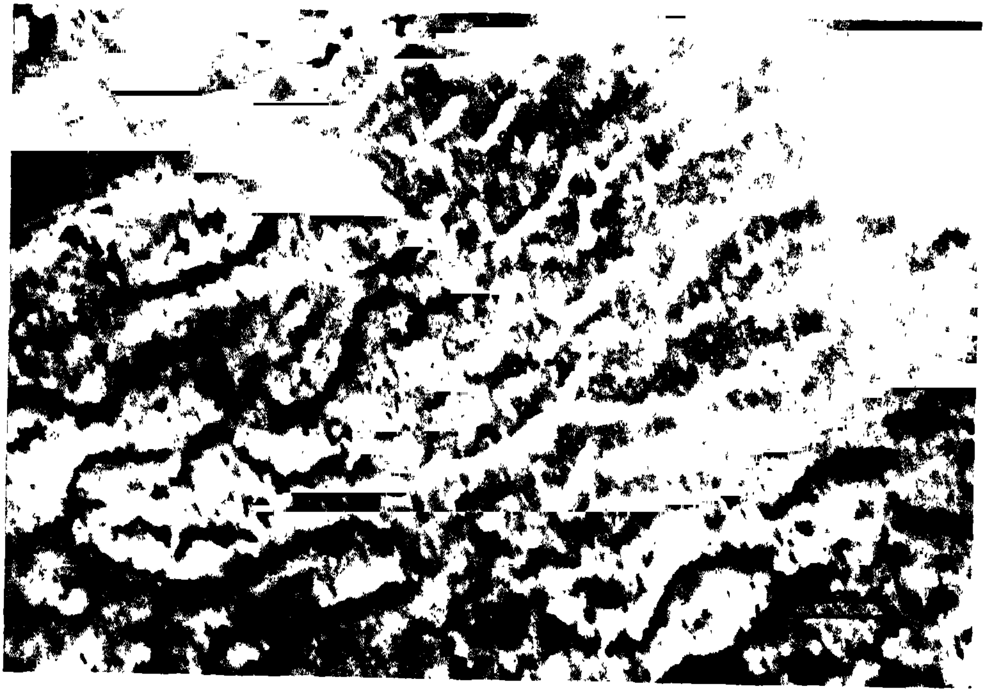

FIG. 5. (c) Dislocation lines from bombardment by 70 eV Ar+ ions (× 210,000).

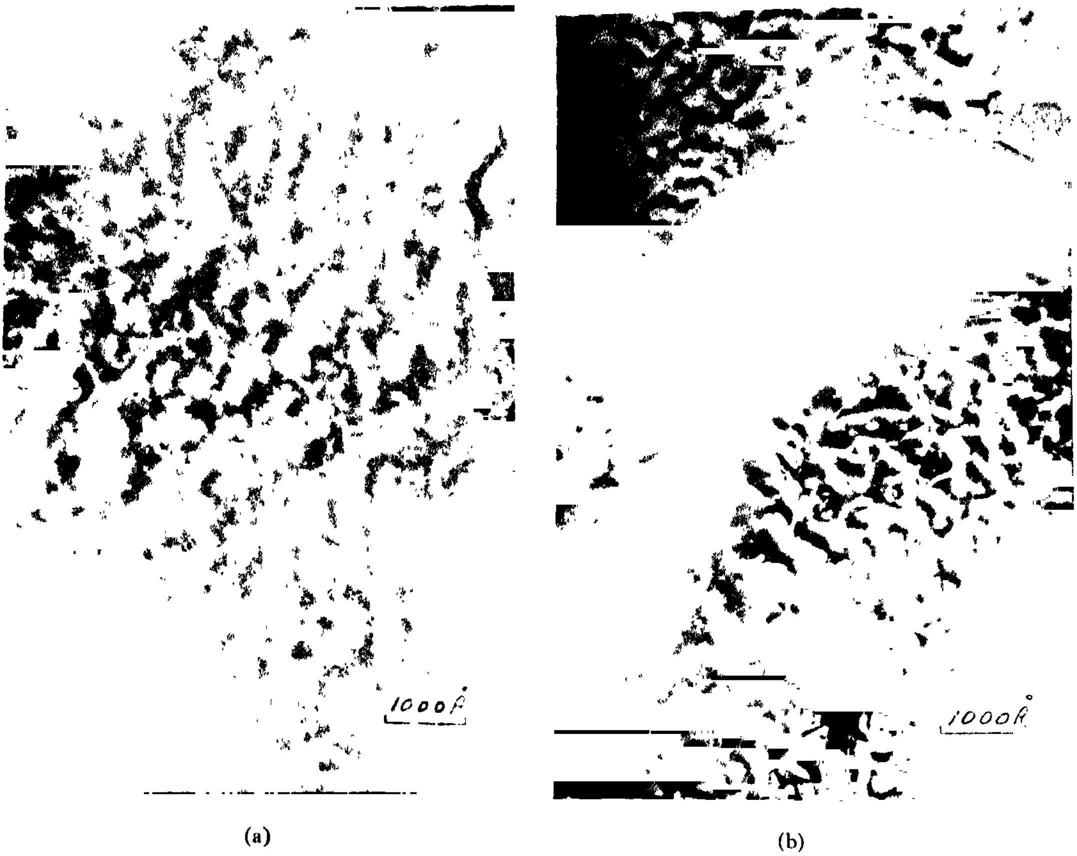

FIG. 6. The similarity of damage produced in {111} gold films by different gases at appropriate energies (× 112,000). (a) He⁺ ions, 120 eV. (b) Ne⁺ ions, 250 eV.

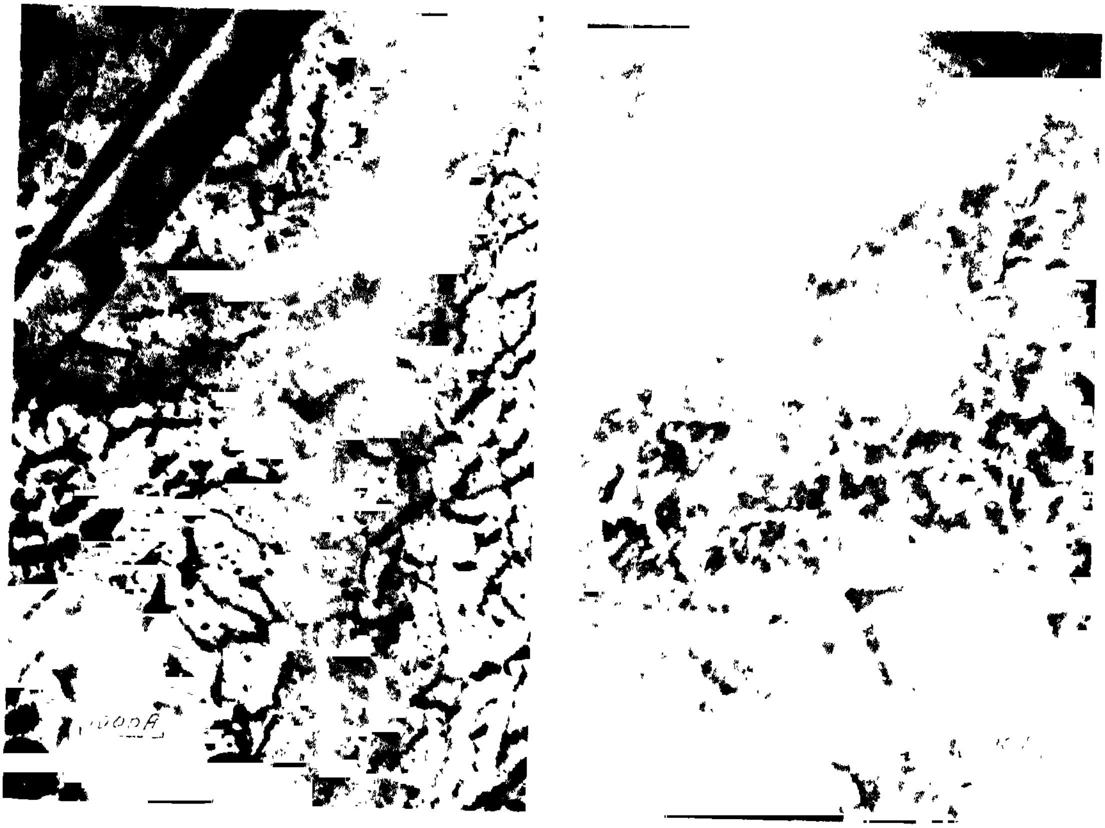

(c)

(d)

FIG. 6. The similarity of damage produced in {111} gold films by different gases at appropriate energies (× 112,000). (c) Ar^+ ions, 80 eV. (d) Xe^+ ions, 30 eV.

Fig. 7. Comparison of damage in adjacent {100} (right) and {111} (left) areas in a film bombarded by 77 eV Ar^+ ions (× 130,000)

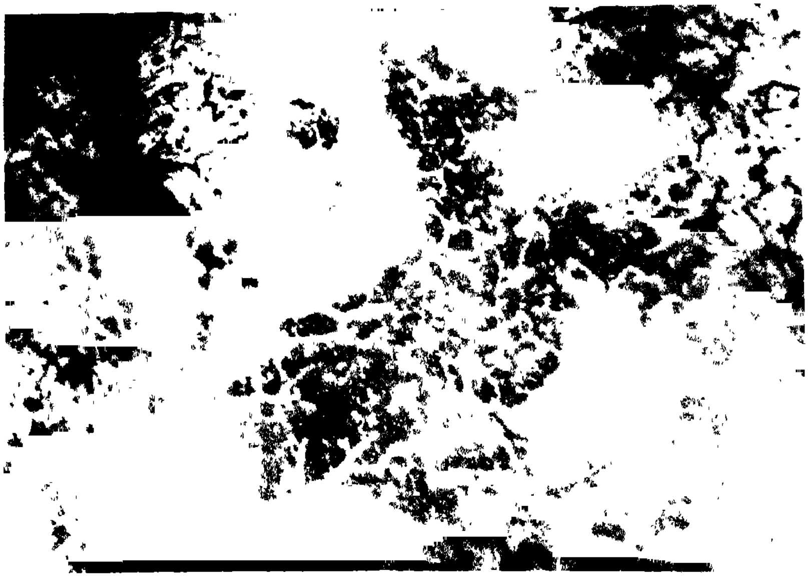

Fig. 8. {100} film bombarded by 50 eV Xe^+ ions (×100,000) to be compared with {111} film in Fig. 6(d).

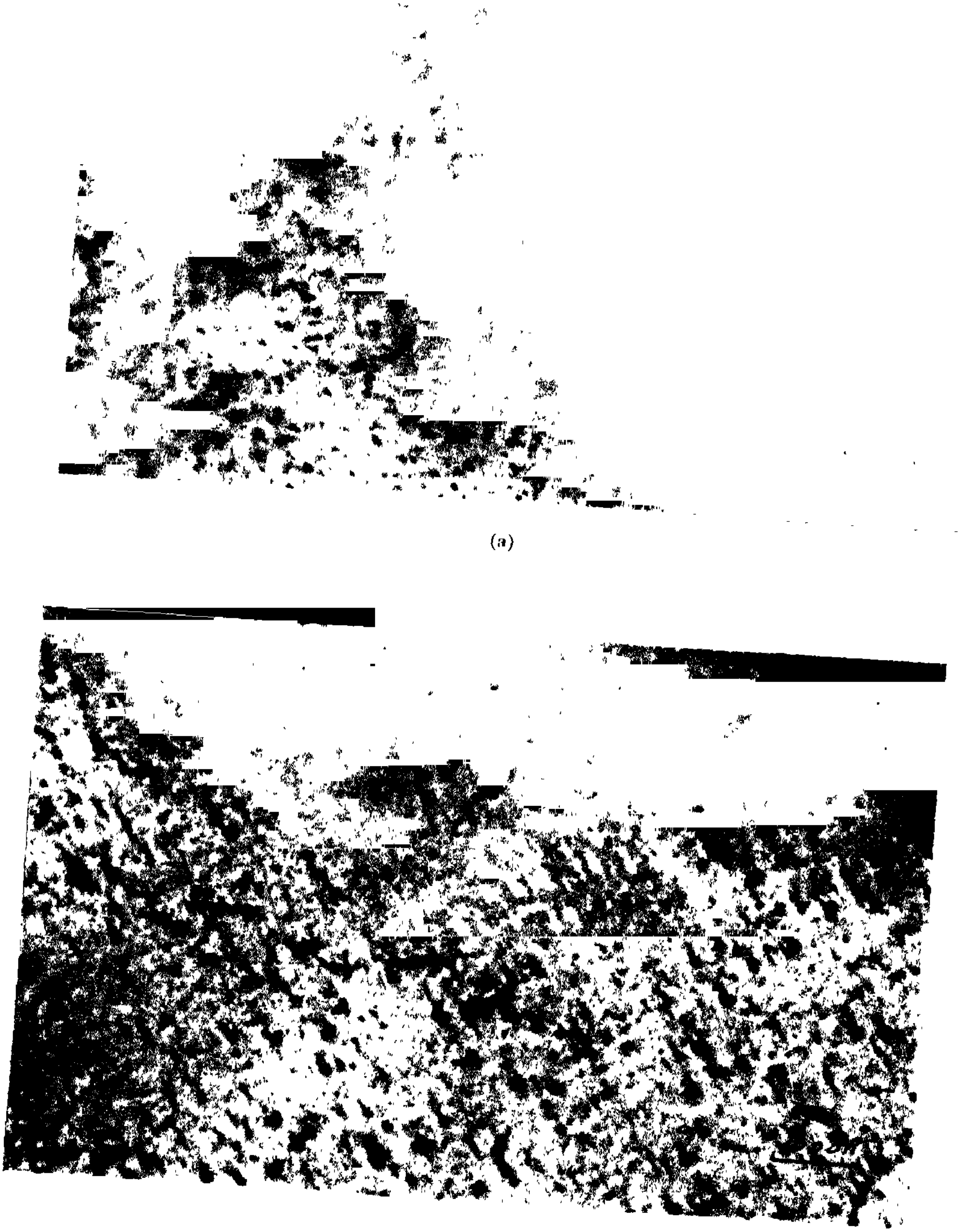

(a)

(b)

FIG. 9. Effect of variation of ion flux density on damage in a {111} film bombarded by 150 eV Ne$^+$ ions (× 170,000). (a) 5×10^{15} ions cm^{-2} sec^{-1} for 5 min. (b) 5×10^{14} ions cm^{-2} sec^{-1} for 90 min.

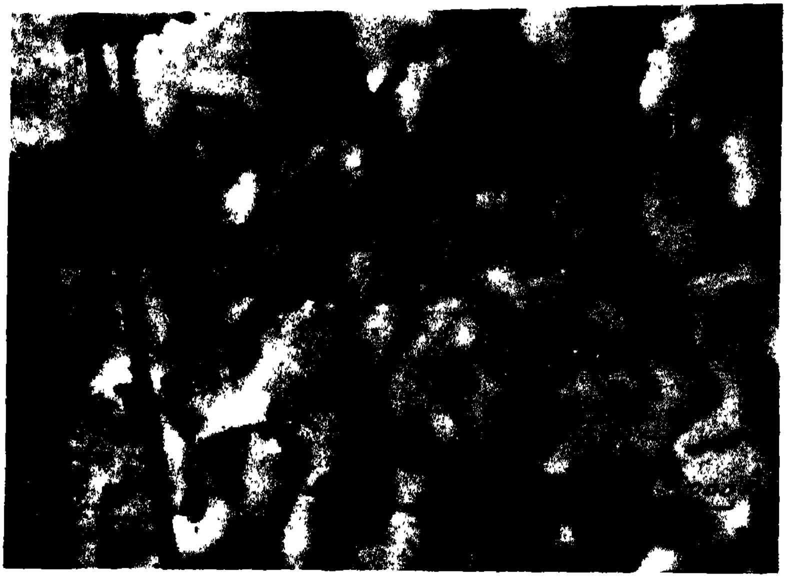

FIG. 10. Partially annealed damage in {111} film bombarded by 77 eV Ar^+ ions, subsequently heated to 280°C for 5 min (× 63,000).

and may be forked, but never cross; spots and loops can be seen between the lines.

With He^+ or Xe^+ ions, all forms of damage are produced together at all energies above the threshold (see Section 4.3). For xenon the lines are short and of low density just above the threshold energy, but with an increase of 10 eV the length increases to about 3000 Å; they are similar in appearance to the lines produced by argon and neon. Spots and loops between the lines attain a concentration of about 10^{11} per cm^2.

Thus the energies at which the different forms of damage predominate depend upon the gas, and Table 2 summarizes the energies at which each of the forms first appears. By appropriate choice of ion energy, specimens bombarded by each of the four gases can look very similar. Figures 6, a–d showing long lines, loops and spots, although similar in appearance, are from specimens bombarded by 120 eV He^+, 250 eV Ne^+, 80 eV Ar^+, and 30 eV Xe^+ ions respectively.

Table 2. *Ion energies for first appearance of the forms of damage in* {111} *crystals*

Gas	Spots	Loops	Short Lines	Long Lines
He	40	40	40	40
Ne	60	110	111–150	150–250
Ar	40	59	60	70–80
Xe	21	21	21	30

3.1.2 {100} *Crystals.* For Ne^+ and Ar^+ ions, the damage in the matrix of {100} crystals is much less than in any {111} grains included in the same specimen, or in {111} polycrystals. This is clearly shown in Fig. 7 where the boundary separates {100} matrix (containing many stacking faults, which appear as sets of fringes, arranged perpendicularly) from a {111} grain (no stacking faults). Damage in the {100} area consists almost entirely of spots, in contrast to the many lines in the {111} grain.

For He^+ and Xe^+ ions on the other hand, damage in {100} crystals is very similar to that in {111} crystals. A typical field from a {100} crystal bombarded by Xe^+ ions is shown in Fig. 8; there are many lines up to 3000 Å long with shorter lines and spots distributed between them. In some areas the dislocations are aligned into arrays which are roughly rectangular in projection.

3.1.3 *Penetration of damage.* Frequently, loops and lines can be seen interacting with stacking faults and the interaction occurs with an outer part of the fault only, assumed to be that part closer to the bombarded surface. The depth can be assessed by measuring the thickness of the film and the proportion of the width of the stacking fault over which interaction occurs. The maximum depth we have noticed is about 500 Å for specimens heavily damaged by xenon, or helium. The depth appears to be less than half this amount for neon or argon.

In some cases both {100} and {111} films have been thinned to such an extent that holes were produced. Under these conditions the film between the holes was extremely thin; some parts have been found to be less than 50 Å thick over areas of a few grid squares. In these very thin areas, there are no long lines; small loops can be detected, and there are spots which move in the electron beam which we suppose are dislocation lines running through the film, perpendicularly from top to bottom. These dislocations frequently extend into partials in the electron beam, so that lengths of stacking fault appear while the specimen is being viewed.

Two {111} specimens bombarded by Ar^+ ions (92 and 250 eV, doses $9{\cdot}1\times10^{18}$ and $4{\cdot}7\times10^{18}$ ions cm^{-2} respectively) were thinned in this way, but tapered slightly from the edge of the bombarded zone. In areas 300 Å thick, the lines were still visible, but they no longer appeared in areas 60 Å thick. The transition thickness was found to be about 150 Å in both specimens. We therefore agree with BRANDON *et al.*(8, 9) that the damage is restricted to a layer close to the bombarded surface.

3.1.4 *Variation of damage with ion flux density.* Some {111} crystals were bombarded by neon or argon at several selected energies, with the ion flux density being varied by factors of 10 and 100; the time of bombardment was adjusted to keep the dose the same. Reducing the flux of Ne^+ ions increased the amount of damage for bombardments at both 150 eV and 90 eV. A flux density of 5×10^{15} ions cm^{-2} sec^{-1} (Fig. 9a) results in damage predominantly in the form of dots and very short lines, while a flux density of 5×10^{14} ions cm^{-2} sec^{-1} (Fig. 9b) results in roughly the same concentration of dots and short lines, but in addition there are many lines up to 800 Å long.

With 60 eV Ar^+ ions, the behaviour was different. At the smallest flux density (5×10^{14} ions cm^{-2} sec^{-1}) only spots were visible. For flux densities of 5×10^{15} and 5×10^{16} ions cm^{-2} sec^{-1} the specimens looked almost identical showing mainly short lines and spots.

In every specimen at the margin of the unbombarded area, the flux density decreased to zero over a distance of about 10μ, and the dose decreased correspondingly. With all gases the damage decreased across this margin; that is, if a heavily damaged specimen were examined, as one scanned across this band from bombarded to shielded areas, the lines became shorter and fewer until only spots and loops could be seen at the edge of the undamaged area the shielded area always being free of any damage.

3.1.5 *Effect of temperature of film during bombardment.* Two {111} specimens were bombarded with 60 eV Ar^+ ions under conditions which were similar except that one tube was immersed in liquid air, and the other held at room temperature (20°C). The damage in the two specimens was indistinguishable. The experiment was repeated with 90 eV He^+ ions, and again the damage was similar in the two specimens.

Measurements by SCOTT(36) of the temperature of gold films on glass during bombardment in a larger but generally similar apparatus have shown that if the walls of the apparatus are not cooled the specimen temperatures can rise as high as 300°C. In our apparatus, heat in the specimen is much more efficiently conducted away, and with the apparatus immersed in a cold bath, we think that it is unlikely that the specimen temperature during bombardment is above 0°C. The experiments described above show that the temperature of the specimen during bombardment is not high enough to cause appreciable annealing of the visible damage.

3.2 *Annealing*

Some specimens were annealed by being kept for 5 min at a sequence of temperatures, increasing from 100°C to 340°C in 30°C intervals, and from 350°C to 700°C in 50°C intervals. Up to 340°C the specimen was heated in a glass tube immersed in an oil bath; above 340°C a small vacuum furnace was used. The specimens were examined after each annealing interval.

For all specimens it was possible to remove all the damage by annealing, and the temperatures at which changes occurred are summarized in Table 3. The spots and loops disappeared within one 30°C interval for all gases, whereas the behaviour of the lines depended upon the bombarding gas. For xenon the lines disappeared sharply between 250–280°C; for argon there was a rearrangement and reduction in number for similar annealing (Fig. 10); for helium no change occurred until the temperature was very much higher, and then the lines rearranged and straightened before disappearing.

Thus the stability of the lines depends markedly upon the nature of the bombarding gas; helium produced the most stable lines, and xenon the least stable. Loops and spots are essentially equally stable for the four gases.

3.3 *Surface roughening*

Sometimes the changes of contrast in transmission micrographs suggested that the surface was systematically roughened. Confirmation was obtained by shadowing a suitable specimen with a thin granular film of Au–Pd at a small angle of incidence. The small Au–Pd crystals can be readily seen and have a higher concentration on any parts of the surface more nearly normal to the direction of incidence.

We have detected systematic roughening only at very low bombarding energies. It takes the form of long undulations (in ⟨110⟩ on {100}) with a wave length of about 1000 Å and an amplitude of about 50–100 Å. This has been observed for Ar^+ ions up to 50 eV for {100} crystals and for {111}

Table 3. *Annealing characteristics*

Bombarding ions		Spots and loops disappeared	Lines	
He^+	92 eV	220–250°C	disappear	420–500°C
	180 eV	250–280°C	rearrange disappear	600–650°C 650–700°C
Ne^+	150 eV	220–250°C		—
Ar^+	57·5 eV	220–250°C		—
	77 eV	220–250°C	rearrange	250–280°C
Xe^+	22, 30 eV	250–280°C	disappear	250–280°C
	25 eV*	160–190°C	disappear	160–190°C

* We have no explanation for this anomaly.

crystals bombarded by 19 or 23 eV Xe^+; no roughening by He^+ or Ne^+ ions has been observed.

3.4 *Sputtering yield and its orientation dependence*

The thickness of the layer sputtered from the surface was determined from the difference in thickness between bombarded and unbombarded areas on the specimens. The ion current and time of bombardment were measured, giving the total apparent number of ions hitting the cathode surfaces. These surfaces comprise a short section of connecting wire, and the capsule holding the film; by assessing this area the flux density has been calculated to an accuracy of about ± 10 per cent. A simple calculation then gives the apparent sputtering yield (atoms sputtered for each bombarding ion, assuming the measured current to be made up of positive, singly-charged ions only). Graphs of apparent sputtering yield with changing ion energy are given in Fig. 11 for {100} and {111} crystals bombarded by Ar^+ ions, and {111} crystals bombarded by Ne^+ ions, the estimated accuracy of the yield being about ± 25 per cent, while the estimated relative accuracy is about ± 10 per cent. Erosion by He^+ and Xe^+ ions was so slight that thinning was inappreciable for doses up to ten times those used for argon and neon. At 50 eV, our maximum energy for Xe^+ ions, the thinning was just detectable and the yield was 0·003 atoms per ion. Measurements of the thickness of films bombarded at 250 eV were unreliable, and so have been excluded.

The curves for argon show that as the ion energy decreases the ratio yield {100}/yield {111} increases from nearly 1 at 100 eV to about 3 at 40 eV. For ion energies up to about 70 eV this orientation dependence of sputtering yield is sufficiently marked to give the bombarded area of those specimens containing both {100} and {111} crystals a characteristic appearance in the electron microscope when they are very thin, because the {111} crystals are much thicker than {100} areas.

4. DISCUSSION

4.1 *Damage*

We believe that the damage which we observe in the microscope is due solely to the intended bombardment, and is not modified by any bombardment or annealing process occurring either in the microscope or as the temperature of the specimen rises to room temperature after the bombardment. Our justification is that (i) the specimens bombarded in the tubes at ambient temperature were indistinguishable from those bombarded in a liquid air bath under otherwise similar conditions (Section 3.1.5); (ii) with one exception, no changes were detected until specimens had been heated subsequently to at least 220°C (Section 3.2); (iii) we have shown that the damage is due to the specified bombardment and is not produced accidentally in the microscope or discharge tubes (Section 3).

It is very significant that with increasing energy or dose of ions (Section 3.1.4) the dominant form

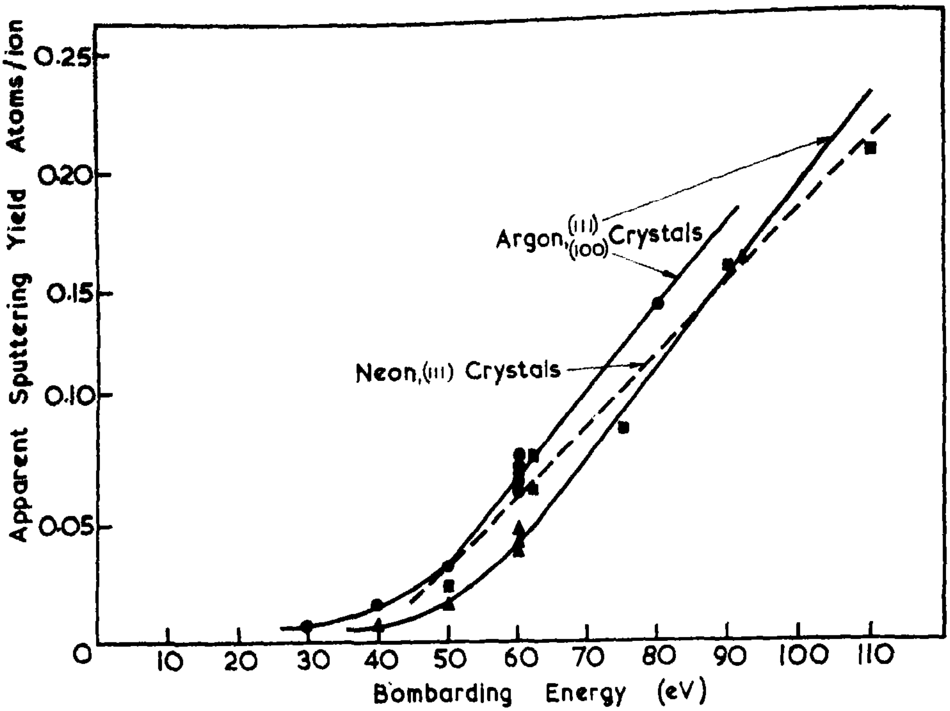

FIG. 11. Apparent sputtering yields for gold:
● {100} crystals bombarded by Ar^+ ions.
▲ {111} crystals bombarded by Ar^+ ions.
■ {111} crystals bombarded by Ne^+ ions.

of damage is at first dots, then loops and finally lines, and that these are concentrated near the surface. The formation of the dislocation loops confirms the suggestion that many point defects are generated near the surface of the crystal during bombardment. THOMPSON and NELSON,(37) and GIBSON *et al.*(14) have made calculations about two ways in which point defects might be generated—the focussed collision and the replacement sequences. If these events are initiated inside a crystal, then one or more Frenkel pairs may be generated, with the vacant site at or close to the initiating site and the interstitial appearing anywhere up to 150 or more interatomic distances away (but usually between 10 and 50 interatomic distances). If the initiation point is at the surface of a crystal, the vacant site will be at or near the surface, and the interstitial will appear inside the crystal. Then, in the absence of diffusion, we would expect vacancies to be concentrated just below the surface, whereas the concentration of interstitials should increase steadily from the surface inwards and then fall off from a peak value, at say, 30 interatomic distances below the surface. However, GILLAM(6) has shown that bombardment promotes diffusion within the surface layer, so that we can expect the point defects to diffuse freely. We expect therefore that vacancies will be lost at the surface or disappear when they meet a diffusing interstitial, so that the surface layer will contain primarily interstitials diffusing to the surface where many are lost. The concentration of interstitials should therefore rise from the surface inwards to its peak at a depth of say 30 interatomic distances and then fall off towards the interior.

This picture predicts that an increasing concentration of interstitials can aggregate into dislocation loops, all nucleated within about 100 Å from the surface. Experimentally we have seen that the Burgers vector of the lines is of the type $\frac{1}{2}\langle 110\rangle$, i.e. the dislocations are perfect. Since the loops are sufficiently close to the surface to be attracted to it by strong image forces, those loops whose ***b*** is inclined to the surface should glide out of the crystal. Thus the remaining loops should be inclined to the surface with ***b*** parallel to the surface, and indeed loops parallel to the surface are rarely observed.

As the loops grow by the accumulation of more interstitials they will intersect the surface and become U-shaped lengths of dislocation line, with each end terminating at the bombarded surface. The sides of the U will continue to grow through a roughly constant concentration of interstitials, but the base of the U will grow away from the surface into a decreasing concentration of interstitials. Consequently the line will elongate parallel to the surface rather than bulge into the interior. Micrographs such as Fig. 9(b) suggest that, at an early stage in their growth, these U loops are attracted and may join together to give longer cusped dislocation lines. These models agree with our observations that dislocation lines may be several thousand Å long in a film only a few hundred Å thick, and that the lines commonly appear jagged or discontinuous. When it was possible to observe specimens annealed so that the dislocation lines had rearranged they no longer appeared cusped, but had the contrast usually associated with dislocations except that the lines consisted of segments, sometimes with a different *b*, about 1000 Å long (Fig. 10). This arrangement suggests that each segment comes from a single loop, or group of loops with the same *b* which have initially been attracted together.

4.2 *Sputtering*

Sputtering sometimes occurs simultaneously with the production of the damage, but gold can be sputtered without being damaged (Ar^+ at less than 30 eV, Ne^+ at less than 60 eV), and vice versa (He^+ or Xe^+ at low energies). When the sputtering rate is appreciable (e.g. 250 Å min^{-1} as found for 90 eV Ar^+ ions with a flux density of $1{\cdot}5\times10^{16}$ ions cm^{-2} sec^{-1}) some of the damaged layer is sputtered away. Consequently a smaller number of point defects accumulate in the remaining damaged layer. Since the rate of climb of the dislocations depends upon the density of point defects, a dislocation line will take up an equilibrium position closer to the surface when sputtering occurs. For Ne^+ ions in the range 70–110 eV, sputtering is so efficient that the density of interstitials is just sufficient to nucleate small loops, but does not allow the dislocation lines to extend appreciably. On the other hand, when sputtering is slight, the damage tends to be in long lines rather than aligned lengths of short line or loops, to penetrate more deeply into the crystals, and to show a less marked dependence on orientation.

When sputtering occurs the damage depends upon orientation in the energy range where the rate of sputtering depends upon orientation; thus {100} crystals are sputtered faster than {111} crystals (Fig. 11), and when dislocation lines are observed in {111} crystals, the same bombardment may produce only dots and loops in {100} areas (Section 3.1.2). One possible explanation is that the number of point defects produced for each incident positive ion varies with the orientation of the crystal but this implies that orientation effects should be found after a bombardment by xenon ions which is contrary to the experimental finding. We infer, therefore, that the damage depends upon orientation and type of bombarding ions primarily because the sputtering rate depends upon these factors.

The measurements of sputtering yield confirm and amplify some of the results obtained by SCOTT(36) who measured sputtering yields for gold using He^+, Ne^+ or Ar^+ ions in a similar energy range. The curves show that for neon and argon the sputtering thresholds are below 50 and 30 eV respectively, and for argon the yield curve assumes a smaller slope below about 50 eV, an effect first found by MORGULIS and TISHCHENKO.(26, 27) The yield curves for neon and argon ({111} crystals) cross at about 80 eV, which is close to the value obtained by SCOTT(36) for polycrystals. The small sputtering yield which we have found for xenon fits in with the trend of measurements by WEIJSENFELD *et al.*(38) for some metals other than gold, bombarded at energies greater than ours. They find that although xenon sputters more efficiently than argon or neon at high energies, the yield curves for xenon cross those for argon and neon at a few hundred volts, and consequently the yield for xenon at low energies is less than that for argon or neon.

We have no explanation for the dependence of sputtering on orientation. The present result is the reverse of those obtained for copper by Rol, Fluit, Viehböck and de Jong[41] and for silver by Wehner[22] and Ogilvie and Ridge[39] (using 20 keV Ar+, 150 eV Hg+, 3 keV Ar+ respectively), when {111} planes were found to be eroded most rapidly. Nevertheless the present results were obtained in such a direct manner that we are sure that they are correct, and it is clear that more work is needed before we can understand the orientation dependence of sputtering yield.

4.3 *Threshold for damage*

We postulate that up to the threshold energy (E_T) the bombarding ions cannot impart sufficient energy to the struck atoms to create stable point defects, and that when the energy is just greater than E_T, the numbers created and their lifetimes are sufficiently great to produce visible damage. If we assume that there is a simple two-bodied collision between an incident ion and a surface atom, the maximum energy ($T_{\max}$) which can be transferred to the struck atom is given by

$$T_{\max} = 4Em_1m_2(m_1+m_2)^{-2} = \rho E$$

where E is the energy of the incident ion of mass m_1, m_2 is the mass of the struck atom, and ρ the energy transfer ratio. At the threshold, if $T_{\max}$ is just sufficient to create an interstitial-vacancy pair, the product ρE_T should be a constant for the four gases. Values for ρ, E_T and ρE_T are given in Table 4. The precision of the determination is very much less for argon than for the other gases, because in the range 30–58 eV, no loops are distinguishable as such, but the number of dots gradually increases from a small background value. We have therefore assumed that E_T lies somewhere in this range. This effect is probably associated with the relatively high sputtering rate of argon at these low energies. For the other gases sputtering does not complicate the measurement of E_T.

Table 4. Energies for damage threshold

Gas	He	Ne	Ar	Xe
ρ	0·0781	0·338	0·560	0·960
E_T eV	37·5 ± 3	64 ± 4	44 ± 14	20·5 ± 1
ρE_T eV	2·9 ± 0·2	21·6 ± 1·3	25 ± 8	19·7 ± 1

It can be seen that neon, argon and xenon give similar values for ρE_T, and that these values are comparable with the lowest estimate by Gibson *et al.*[14] of 25 eV for E_d in copper. However, the value of ρE_T for helium is quite different, but can be brought into agreement by using an energy transfer ratio of rather more than one half. This suggests that the damage created by helium does not arise from simple collisions at the surface; a different mechanism could arise from the presence of helium in the surface layers of the crystal.

Further evidence for the penetration of helium into the crystal, and its accumulation below the surface is given by the annealing characteristics. We find that gold bombarded by helium anneals in a manner similar to that of copper containing helium, where dislocations are much more stable than spots and loops.[40] We believe that the dislocations are stabilized by the gas which is forced into the crystal, and consequently the annealing experiments show that the concentrations retained decrease in the order helium, neon, argon, xenon, i.e. inversely with ionic size.

REFERENCES

1. Trillat J. J., *J. Chim. phys.* **53**, 570 (1956).
2. Trillat J. J., Tertis L. and Terao N., *J. Rech. Cent. Nat. Rech. Sci.* No. 43 156 (1958).
3. Ogilvie G. J., *J. Phys. Chem. Solids* **10**, 222 (1959).
4. Ogilvie G. J., *Aust. J. Phys.* **13**, 402 (1960).
5. Ogilvie G. J. and Thomson A. A., *J. Phys. Chem. Solids* **17**, 203 (1961).
6. Gillam E., *J. Phys. Chem. Solids* **11**, 55 (1959).
7. Castaing R. and Jouffrey B., *C.R. Acad. Sci., Paris* **252**, 2696 (1961).
8. Brandon D. G. and Bowden P., *Phil. Mag.* **6**, 707 (1961).

9. Brandon D. G., Bowden P and Baker A. J., *International Conference on the Properties of Reactor Materials, and the Effects of Radiation Damage*, C.E.G.B. Berkeley (1961).
10. Beevers C. J. and Nelson R. S., *International Conference on the Properties of Reactor Materials, and the Effects of Radiation Damage*, C.E.G.B. Berkeley (1961).
11. Menter J. W., Pashley D. W. and Presland A. E. B., *International Conference on the Properties of Reactor Materials, and the Effects of Radiation Damage*, C.E.G.B. Berkeley (1961).
12. Seitz F., *Disc. Faraday Soc.* **5**, 271 (1949).
13. Huntington H. B., *Phys. Rev.* **91**, 1092 (1953).
14. Gibson J. B., Goland A. N., Milgram M. and Vineyard G. H., *Phys. Rev.* **120**, 1229 (1960).
15. Corbett J. W. and Walker R. M., *Phys. Rev.* **117**, 970 (1960).
16. Eggen D. T. and Laubenstein M. J., *Phys. Rev.* **97**, 238 (1955).
17. Lucasson P. G. and Walker R. M., *Faraday Soc. Disc. on Radiation Damage, Saclay* (1961).
18. Denney J. M. *Phys. Rev.* **92**, 531 (1953).
19. Dugdale R. A. *Report on the Conference on Defects in Crystalline Solids, Phys. Soc. Lond.* 246 (1954).
20. Guentherschulze A. and Meyer K., *Z. Phys.* **62**, 607 (1930).
21. Fetz H., *Z. Phys.* **119**, 590 (1942).
22. Wehner G. K., *Phys. Rev.* **102**, 690 (1956).
23. Strachan J. F. and Harris N. L., *Proc. phys. Soc.* **B69**, 1148 (1956).
24. Laegreid N., Wehner G. and Meckel B., *J. appl. Phys.* **30**, 374 (1959).
25. Laegreid N. and Wehner G. K., *J. appl. Phys.* **32**, 365 (1961).
26. Morgulis N. D. and Tishchenko V. D., *Zh. eksp. teor. fiz. S.S.S.R.* **30**, 54 (1956); English translation *Sov. Phys. JETP* **3**, 52 (1956).
27. Morgulis N. D. and Tishchenko V. D., *Izv. akad. nauk. S.S.S.R. ser. fiz.* **20**, 1190 (1956).
28. Bradley R. C., *Phys. Rev.* **93**, 719 (1954).
29. O'Briain C., Lindner A. and Moore W. J., *J. chem. Phys.* **29**, 3 (1958).
30. Weiss A., Heldt L. and Moore W. J., *J. chem. Phys.* **29**, 7 (1958).
31. Koch J. and Bendt-Nielsen B., *K. danske vidensk. Selsk. Mat. fys. Medd.* **21**, No. 8, 22 (1944).
32. Boyd R. L. F., *Proc. Roy. Soc.* **A201**, 330 (1950).
33. Haas G. A. and Jensen J. T., *Rev. sci. Instrum.* **28**, 1007 (1957).
34. *American Institute of Physics Handbook* McGraw-Hill, New York (1957).
35. Pashley D. W. and Presland A. E. B., *Phil. Mag.* **6**, 1003 (1961).
36. Scott H. G., *J. appl. Phys.* **33**, 2011 (1962).
37. Nelson R. S. and Thompson M. W., *Proc. Roy. Soc.* **A259**, 458 (1961).
38. Weijsenfeld C. H., Hoogendorn A. and Koedam M., *Physica* **27**, 763 (1961).
39. Ogilvie G. J. and Ridge M. J., *J. Phys. Chem. Solids* **10**, 217 (1959).
40. Barnes R. S. and Mazey D. J., *Phil. Mag.* **5**, 1247 (1960).
41. Rol P. K., Fluit J. M., Viehböck F. P. and de Jong M., *Proceedings of the Fourth International Conference on Ionization Phenomena in Gases*, Uppsala (1959), North Holland, Amsterdam (1960).

J. Phys. Chem. Solids Pergamon Press 1963. Vol. 24, pp. 261–273. Printed in Great Britain.

PARAMAGNETISM AND LATTICE PARAMETERS OF IRON-RICH IRON-GERMANIUM ALLOYS

HENRY CHESSIN, SIGURDS ARAJS, R. V. COLVIN and D. S. MILLER

Edgar C. Bain Laboratory for Fundamental Research, United States Steel Corporation Research Center,
Monroeville, Pennsylvania

(*Received* 17 *September* 1962)

Abstract—Paramagnetic and X-ray studies have been made on iron-rich iron–germanium alloys. The lower boundaries of the γ-loop have been determined from magnetic susceptibility measurements. The γ-loop extends to about 5·5 w/o germanium. At high temperatures the paramagnetic behavior of iron–germanium solid solutions follows the Curie–Weiss law. These measurements show that germanium in solution in iron produces quantitatively different behavior in Curie point, Bohr magneton number, and lattice parameter than does silicon. Simple theoretical descriptions based on the Heisenberg model do not correctly describe the paramagnetism of binary iron alloys. The lattice spacings of solid solutions of germanium in iron, quenched from about 600°C, have been determined accurately as a function of atomic percentage of germanium. The plot of lattice constant vs. composition is a straight line to 10·45 a/o germanium. The abrupt change to zero in the slope of this line establishes the α-phase boundary at that composition, at approximately 600°C. A new scheme is proposed for relating lattice parameter changes to atomic volume of the solute. Under the proposed assumptions, a linear relation of lattice parameter to atomic volumes of solvent and solute is found. They also serve equally well as a basis for the lattice dilation of the nickel lattice with germanium as the solute. Furthermore, the changes in volume per atom as a function of composition for the systems iron–germanium and nickel–germanium agree very well up to 5 a/o germanium. The behavior of germanium as a solute in iron and nickel is in contrast to its behavior in the group 1B metals where the effect of valence difference is marked.

1. INTRODUCTION

WE HAVE recently begun extensive investigations of various ferromagnetic iron-base binary solid solutions above their ferromagnetic Curie temperatures to gain a better understanding of the origin of magnetism in these materials. Our studies on iron–silicon(1) and iron–vanadium(2) have already been reported. In this report we present the results of paramagnetic measurements and X-ray studies on iron–germanium solid solutions, and discuss their significance.

2. EXPERIMENTAL CONSIDERATIONS

The iron–germanium alloys (22 different compositions) used in this investigation were prepared either by vacuum melting in a crucible or levitation melting techniques. The alloy compositions, melt designations, sources of iron and germanium, and the physical properties of alloys studied are summarized in Table 1. Analyses of starting materials [except germanium (99·99+ per cent) obtained from Eagle–Picher Company, for which detailed analysis was not available] are given in Table 2.

The alloys designated by IVM were prepared by melting in vacuum (about 10^{-4} mm Hg) selected amounts of iron and germanium in a zirconium oxide crucible. They were kept in a molten state for about 10 min, then cast in a copper mold whose dia. was ⅝ in. and length 6 in. Following this, the alloys were sealed into silica tubes and homogenized at 1480°K for 48 hr.

The alloys designated by LM were made by the levitation melting technique. The molten metal was cast into a cooled copper mold whose inside diameter was ½ in. and depth 2½ in. These alloys were homogenized in the same manner as the vacuum melts. Chemical analysis of each

Table 1. Compositions of iron–germanium alloys used in this investigation

Alloy designation	Ge Concentration [w/o]	Ge Concentration [a/o]	Fe	Ge	Properties studied
LM 194	$0{\cdot}90$	$0{\cdot}69$	JM 849	EP	α
LM 195	$1{\cdot}8_{0}$	$1{\cdot}3_{9}$	JM 849	EP	α
IVM 534	$1{\cdot}8_{5}$	$1{\cdot}4_{3}$	PI 104–A	JM 510	α,γ
IVM 535	$2{\cdot}6_{5}$	$2{\cdot}0_{5}$	PI 104–A	JM 510	α,γ
LM 196	$2{\cdot}7_{0}$	$2{\cdot}0_{9}$	JM 849	EP	α
LM 197	$3{\cdot}4_{0}$	$2{\cdot}6_{4}$	JM 849	EP	α
IVM 536	$3{\cdot}7_{0}$	$2{\cdot}8_{6}$	PI 104–A	JM 510	α,γ
IVM 540	$4{\cdot}2_{5}$	$3{\cdot}3_{1}$	PI 104–A	JM 510	α,γ
LM 198	$4{\cdot}8_{0}$	$3{\cdot}7_{3}$	JM 849	EP	α
IVM 538	$4{\cdot}9_{5}$	$3{\cdot}8_{4}$	PI 104–A	JM 510	α,γ
LM 199	$6{\cdot}7_{0}$	$5{\cdot}2_{4}$	JM 849	EP	α
IVM 361	$6{\cdot}9_{0}$	$5{\cdot}3_{9}$	PI 104–A	EP	α
LM 200	$7{\cdot}3_{5}$	$5{\cdot}7_{5}$	JM 849	EP	α
IVM 365	$7{\cdot}8_{5}$	$6{\cdot}1_{5}$	PI 104–A	EP	α
IVM 360	$8{\cdot}7_{0}$	$6{\cdot}8_{3}$	PI 104–A	EP	α
LM 201	$8{\cdot}9_{0}$	$6{\cdot}9_{9}$	JM 849	EP	α
IVM 539	$9{\cdot}2_{0}$	$7{\cdot}2_{3}$	PI 104–A	JM 510	χ
LM 202	$10{\cdot}8_{0}$	$8{\cdot}5_{2}$	JM 849	EP	α
LM 203	$12{\cdot}8_{0}$	$10{\cdot}1_{8}$	JM 849	EP	α
IVM 362	$14{\cdot}9_{0}$	$11{\cdot}8_{7}$	PI 104–A	EP	α,χ
IVM 363	$16{\cdot}3_{0}$	$13{\cdot}0_{3}$	PI 104–A	EP	α,χ
IVM 364	$20{\cdot}0_{0}$	$16{\cdot}1_{3}$	PI 104–A	EP	α,χ

α = Lattice spacing measured.
γ = Used to determine the boundaries of γ-loop by magnetic susceptibility measurements.
χ = Magnetic susceptibility measured.
JM 849 = Iron obtained from Johnson, Matthey and Company, Cat. No. 849.
JM 510 = Germanium obtained from Johnson, Matthey and Company, Cat. No. 510.
PI 104–A = Plastiron 104–A, obtained from Glidden Company.
EP = Germanium (99·99+per cent) obtained from Eagle-Picher Company.

homogenized sample prepared by either method were made. The results are given in Table 1.

Before magnetic and X-ray diffraction studies, several of the alloys were polished and etched in suitable etchants and examined with the microscope. No evidence of second phases or segregations could be detected in those alloys assumed single phase. The surfaces of the ingots were subsequently ground to remove about 1 mm of depth so as to insure no contamination from the oxides or other sources.

The magnetic susceptibility of selected compositions of the iron–germanium alloys was measured using the Faraday method. The apparatus has been described elsewhere.(1) The samples were enclosed in silica capsules evacuated to 10^{-5} mm Hg and then filled with argon (15 cm Hg at room temperature).

For the X-ray studies, filings were prepared in a filing machine described by HUME-ROTHERY *et al.*(3) in an atmosphere of purified argon. Filings were made using either a machinist's high-speed file or a tungsten carbide file depending on the hardness of the alloy and each file was carefully examined under the microscope for any obvious signs of wear after each alloy was filed.

To avoid contamination of the filings from the preceding alloys, a new file was employed for the preparation of the powders for each alloy or, in the case of the tungsten carbide file, it was cleaned carefully after each sample preparation with a wire brush. There is no evidence either from the above

Table 2. *Analyses of iron and germanium used for preparing iron–germanium alloys*

Iron, JM 849 (99·9+ per cent)

Impurities [*ppm*]: Mn 3; Ni 3; Si 2; Cu < 1; Mg < 1; Ag < 1; Al, As, Au, B, Ba, Be, Bi, Ca, Cd, Co, Cr, Cs, Ga, Ge, Hf, Hg, In, Ir, K, Li, Mo, Na, Nb, Os, P, Pb, Pt, Rb, Re, Rh, Ru, Sb, Se, Sn, St, Ta, Te, Ti, Tl, V, W, Zn, Zr (not detected).

Plastiron 104–*A* (99·9+per cent)

Impurities [*w/o*]: O 0·004; H 0·010; Cu 0·004; N 0·004; Mo < 0·004; S 0·003; Si 0·003; C 0·002; P 0·002; Sn < 0·002; Mn 0·0015; Co 0·001; Cr 0·001; Ni 0·001; Pb 0·001; Al < 0·001; Ca < 0·001; Ta < 0·001; W < 0·001; V < 0·001; Zn < 0·001; Zr < 0·001; Mg 0·0005; Be < 0·0005.

Germanium, JM 510 (99·999 per cent)

Impurities [*ppm*]: Au < 1; Al, As, Au, B, B, Ba, Be, Bi, Ca, Cd, Co, Cr, Cs, Cu, Fe, Ga, Hf, Hg, In, Ir, K, Li, Mg, Mn, Mo, Na, Nb, Ni, Os, P, Pb, Pd, Pt, Rb, Re, Rh, Ru, Sb, Se, Si, Sn, Sr, Ta, Te, Ti, Tl, V, W, Zn, Zr, (not detected).

examination, by overexposing the X-ray diagrams or from the heat treatments to be discussed, that the filings suffered contamination from any second phase.

In order to determine whether or not the method of annealing would have any effect on the observed lattice parameters, the following heat treatments were carried out with several alloys. An alloy of given composition was divided into three parts, two parts sealed separately in evacuated silica capsules. One capsule was annealed for 10 min and the other for 24 hr at 600°C and then air quenched. The third portion was placed in an alumina sleeve in a silica capsule, baked out at 125°C and pumped on continuously for 24 hr, sealed in a vacuum of 10^{-5} mm Hg and then annealed at 600°C for 28 hr. The lattice parameters determined by these three different anneals did not vary more than 0·007 per cent indicating there was no significant reaction with the silica tubing or the formation of a second phase at these temperatures. It should be mentioned that KAISER and THURMOND⁽⁴⁾ found by observing the infrared absorption bands that SiO_2 is much more stable than GeO or GeO_2 which agrees with thermodynamic considerations, and, therefore, the probability that the alloy reacted with the silica capsule during the anneal appears very remote.

In the light of the above investigations, all subsequent sample preparation for X-ray analysis consisted of the following. The filings were passed through a 400 mesh screen, placed in a silica capsule, evacuated to about 10^{-5} mm of Hg and then filled with argon, to a pressure of 15 cm Hg at room temperature, prior to being sealed in the capsule. All samples were annealed at 600°C for 10 min and then air quenched. The powders were then mixed in equal proportion with 400 mesh high-purity silicon and sealed in a 0·3 mm diameter thin-walled silica capillary. The X-ray diagrams were taken with a 114·59 mm diameter camera, with exposure time of 3 hr, using iron-filtered radiation from a cobalt tube operated at 45 kV and 10 mA. With this radiation the lines farthest out in the back-reflection region for all alloys occurred between $2\theta = 158°$ and $2\theta = 164°$. The temperature of the specimens during exposure was 298°K controlled to ± 1·0°K. All X-ray diagrams were of the highest quality in that the film background was very low and all diffraction lines were sharp. The absence of retained cold work or second phase may be surmised from the observation that all diffraction lines showed no broadening or fuzziness and that the $K\alpha$ doublets were well resolved at Bragg angles of 33 to 35°.

The lattice parameters were determined using the wave lengths, $\lambda K\alpha_1 = 1{\cdot}78890$ Å and $\lambda K\alpha_2 = 1{\cdot}79279$ Å. The corrections applied to the diffraction data to take into account systematic errors were made in three ways and the average value determined by the three methods was chosen as the best value. In the first method the data were plotted against the NELSON–RILEY function[5] and the value of the lattice parameter obtained by extrapolation to $2\theta = 180°$. The second method employed a constant correction applied to the observed Bragg angle using silicon as an internal standard, as described by ANDREWS.[6] The third method consisted of a least squares determination, first suggested by COHEN.[7] All such determinations were concordant within 0·006 per cent and thus permits an estimated precision or reproducibility of lattice parameter determination of ± 0·0001 Å although no greater accuracy than one part in 10,000 can be claimed. A measure of the accuracy of this investigation may be had from the values of the parameter for the high-purity silicon internal standard used with each alloy where the average value of 5·4305 Å agrees well with that determined by the International Union of Crystallography[8] which is 5·43054 ± 0·00017 Å.

It is of interest to mention some observations made during the course of these studies which are of metallurgical importance. Abnormally large grains (circa 2 to 3 mm in dia.) were visible on the free surface of the ingots in a fine-grained matrix even though the ingots were cast from the levitation melt into a water-cooled copper mold. The alloys appear to be very ductile up to 10 at. per cent Ge and efforts to grind the alloys in mortar and pestle resulted in thin flat sheets.

3. RESULTS AND DISCUSSION

A. Magnetic studies

The iron–germanium system has received little attention in the past. We have found no record of magnetic susceptibility or lattice spacing measurements. Since we are primarily interested in the paramagnetism in single phases of alloys, in general we have purposely avoided compositions which undergo phase changes in the temperature range of interest. In the present instance, finding in HANSEN[9] that the boundaries of the γ-loop are relatively uncertain, we decided to study alloys of low germanium content for the purpose of making new determinations of these. The lower portions of γ-boundaries, according to our magnetic susceptibility measurements, are shown in Fig. 1 and summarized in Table 3.

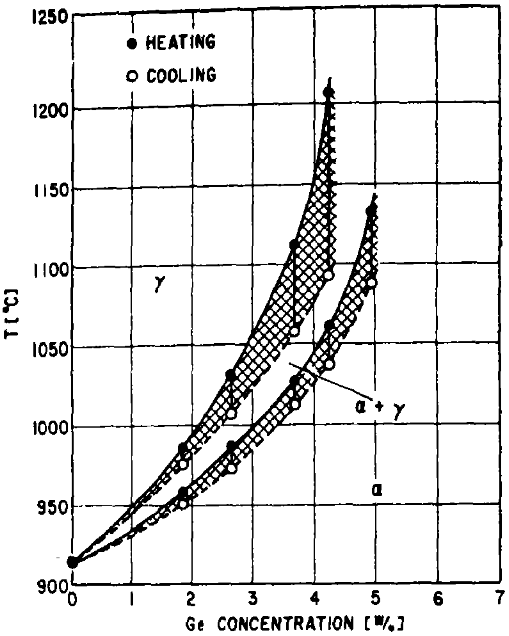

FIG. 1. Lower part of γ-loop boundaries in Fe–Ge systems (from magnetic susceptibility measurements).

We find, as indicated in Fig. 1, that the crystal structure changes in iron–germanium alloys are very sluggish, especially for larger concentrations of germanium. The transition temperatures were estimated within ± 5°C from the inverse magnetic susceptibility vs. temperature plots. Each sample, enclosed in a silica capsule, was gradually heated from room temperature to about 850°C in 4 hr. After this, the magnetic susceptibility of the sample was measured as a function of temperature, first, with increasing temperatures and then with decreasing temperatures using approximately 1·5°C per min. temperature change. A typical run from 850 to 1225°C required about 8 hr giving about 25 susceptibility values. We find these results consistent with X-ray studies made by L. ZWELL and B. F. OLIVER.[10] Figure 1 clearly shows that the γ-loop is more extended with

Table 3. Temperature of α–γ transformation in iron–germanium system

Ge concentration [w/o]	$T_{1,h}$[°C]	$T_{1,c}$[°C]	$T_{2,h}$[°C]	$T_{2,c}$[°C]
$1\cdot8_5$	957	950	985	977
$2\cdot6_5$	987	972	1032	1007
$3\cdot7_0$	1027	1012	1112	1057
$4\cdot2_5$	1062	1037	1207	1092
$4\cdot9_5$	1132	1087	1217	1177

$T_{1,h}$ = α to α+γ transformation obtained with increasing temperatures.
$T_{1,c}$ = α+γ to α transformation obtained with decreasing temperatures.
$T_{2,h}$ = α+γ to γ transformation obtained with increasing temperatures.
$T_{2,c}$ = γ to α+γ transformation obtained with increasing temperatures.

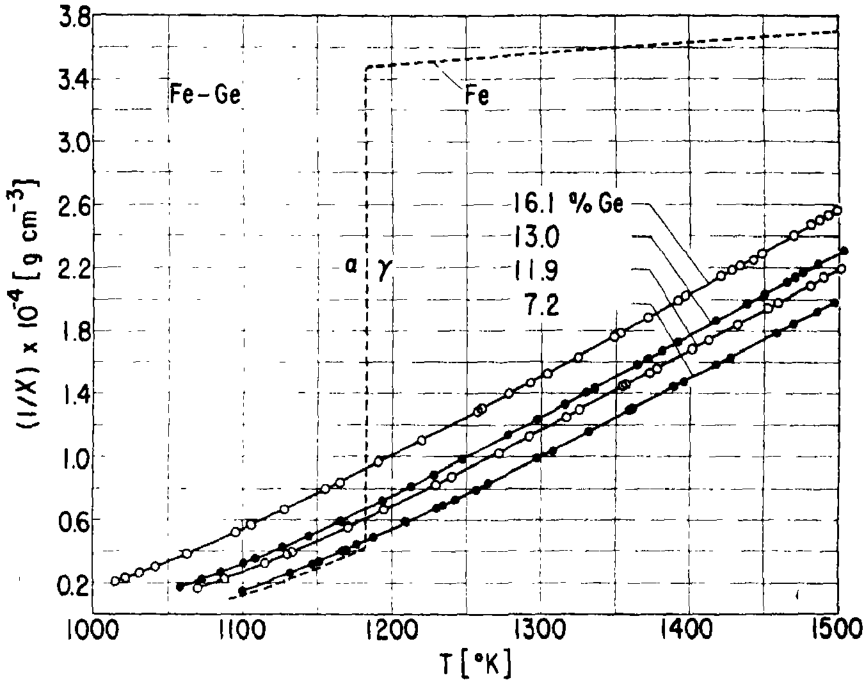

FIG. 2. Inverse magnetic susceptibility of Fe–Ge alloys as a function of temperature.

Table 4. Carbon analysis of some iron–germanium alloys

Alloy designation	Ge concentration [w/o]	Carbon concentration [w/o]
IVM 534	$1\cdot8_5$	0·0012
535	$2\cdot6_5$	0·0025
536	$3\cdot7_0$	0·0016
540	$4\cdot2_5$	0·0015
538	$4\cdot9_5$	0·0019

respect to the germanium concentration than shown in Ref. 9. Since it is known that some additional solutes such as carbon can strongly influence the γ-loop boundaries of iron–silicon systems,(11) the iron–germanium samples used for this particular study were analyzed for carbon. The results of the analysis are presented in Table 4. It appears that our results represent an intrinsic property of iron–germanium system and are not due to impurities. With the present equipment, which requires us to seal the samples into silica capsules, we cannot go much beyond 1500°K and, thus, we have been able only to determine the lower part of the γ-loop region.

Parenthetically, we wish to remark that the magnetic method is a particularly good way to study such metallurgical problems because of the very different magnetic susceptibilities of iron in the α- and γ-form. The measurements are done at the temperatures of interest, and the time dependence of the transformations can be explored.

The inverse susceptibility as a function of temperature ($1/\chi$ vs. T curves) is shown in Fig. 2. This plot also presents the inverse paramagnetic susceptibility of pure iron in the body-centered cubic and face-centered cubic states.(1) In all these alloys, above the ferromagnetic Curie temperatures, the usual deviation from the Curie–Weiss law occurs mainly due to the existence of short range magnetic ordering. At higher temperature the Curie–Weiss law seems to be obeyed. These iron–germanium alloys do not show the deviations from the Curie–Weiss behavior which would imply an additional positive contribution to the total

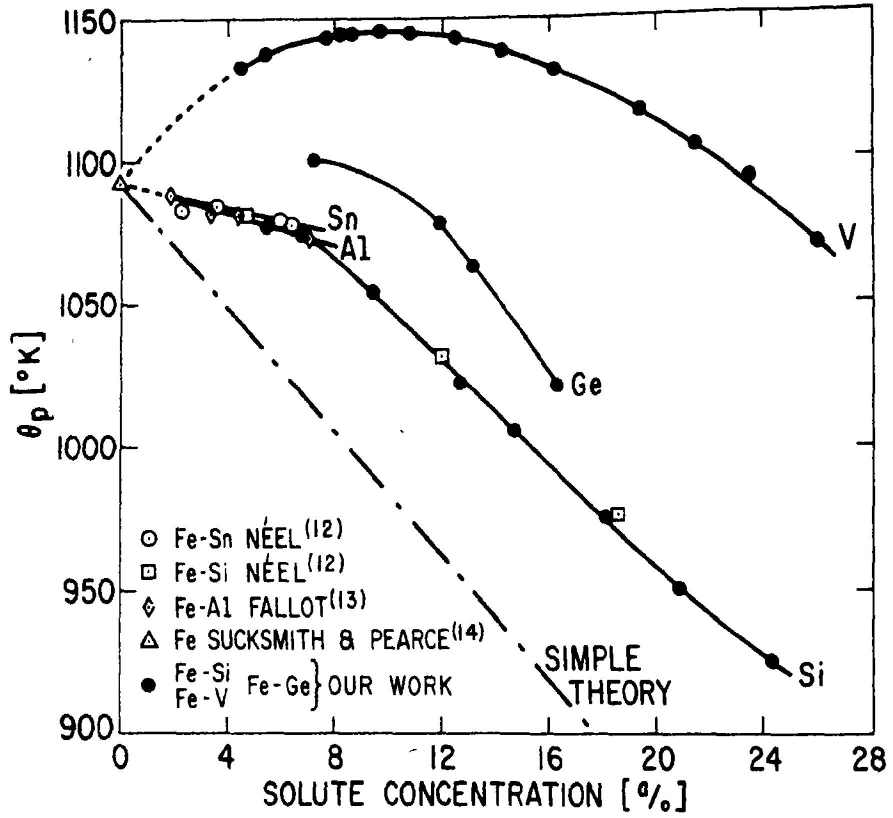

FIG. 3. Paramagnetic Curie temperatures of various binary iron alloys.

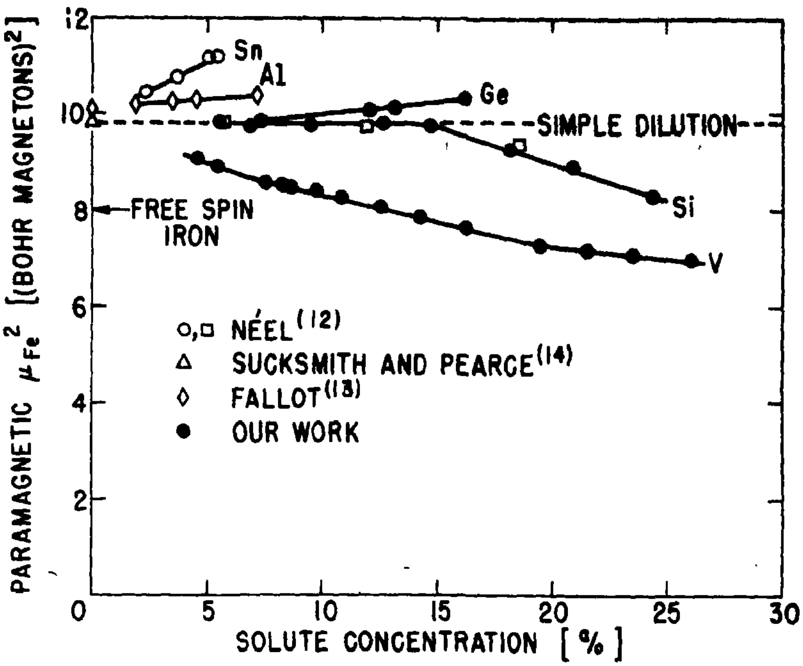

FIG. 4. Paramagnetic moments per iron atom of various binary iron alloys.

susceptibility as, for example, observed in the iron–vanadium system for large amounts of vanadium.[(2)]

The paramagnetic Curie temperature (θ_p), Curie constants (C) determined from the high temperature data, and the paramagnetic moments per iron atom (μ_{Fe}) of iron–germanium alloys are summarized in Table 5. Figure 3 shows the presently available information[(1, 2, 12, 13)] on the behavior of θ_p with the concentration of various solutes which themselves in a pure state do not show any co-operative magnetic effects. Figure 3 also includes the results on iron–germanium of this study. The quantity θ_p for pure iron was taken from the work by SUCKSMITH and PEARCE.[(14)] It is seen that germanium in solution with iron does not behave the same way as silicon. This is also observable from Fig. 4, which presents the square of the paramagnetic moment per iron atom as a function of solute concentration. One can see various types of behavior due to the alloying. Simple dilution occurs in iron–silicon systems up to about 14 a/o silicon while the other solutes show more complicated influence on the paramagnetic moment of iron.

Paramagnetic Curie temperatures of iron-rich

Table 5. Paramagnetic Curie temperatures, Curie constants, and paramagnetic moment per iron atom of iron–germanium alloys

Germanium concentration [a/o]	θ_p [°K]	$C \times 10^2$ [cm^3 °K g^{-1}]	μ_{Fe} [Bohr magnetons]	Temperature range [°K]
7·2	1100	$2{\cdot}00_5$	3·14	1300–1500
11·9	1078	$1{\cdot}92_3$	3·18	1350–1500
13·0	1063	$1{\cdot}90_4$	3·19	1350–1500
16·1	1021	$1{\cdot}86_0$	3·22	1350–1500

binary iron alloys indicate that the simple dilution theories(15–18) do not give quantitative agreement with the experimental results. The theoretical line in Fig. 3 is the consequence of simple molecular field approximation using the Heisenberg model. According to this approach, the paramagnetic Curie temperature of an alloy made up of atoms with and without magnetic moments should be proportional to the concentration of the magnetic atoms. The same conclusion about the Curie temperature variation has also been obtained by SMART(17) using the Bethe–Peirls–Weiss approximation. Although the more refined dilution theories give slightly different results for high concentrations of the magnetic atoms than the simple molecular field method, the deviations from the latter are not large enough to account for the experimental behavior of the quantity θ_p with the concentration of various solutes. It appears that the paramagnetic behavior of binary iron alloys is more complicated than originally expected. Definitely more experimental information is needed before one can get new realistic insight into this problem. Additional studies on other dilute iron systems are being planned for the near future.

B. X-ray studies

The lattice parameters ($a_{\mathrm{Fe-Ge}}$) and the atomic volumes ($V_{\mathrm{Fe-Ge}}$) of iron–germanium alloys at 298°K are given in Table 6. This table also presents the lattice parameters of silicon (a_{Si}) used as an internal standard with each alloy and the electron-atom ratio (ϵ) of the alloys. The quantity ϵ was calculated assuming zero for the valency of iron and four for the valency of germanium.

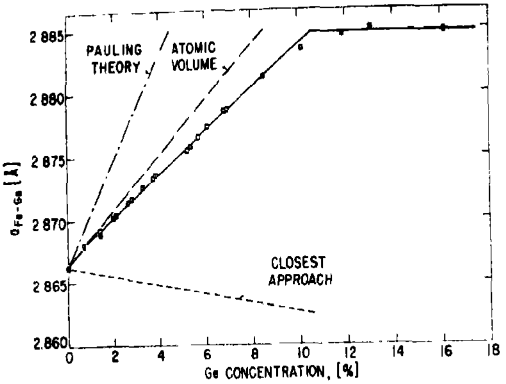

FIG. 5. Lattice parameters of Fe–Ge solid solutions at 298°K.

Table 6. Lattice constants and atomic values of iron–germanium alloys at 298°K

Ce concentration [a/o]	$a_{\mathrm{Fe-Ge}}$[Å]	a_{Si}[Å]	ϵ	$V_{\mathrm{Fe-Ge}}$[Å^3]
0	2·8663	5·4307	0	11·7743
0·69	2·8680	5·4304	0·0276	11·7953
$1{\cdot}3_9$	2·8690	5·4304	0·0556	11·8101
$1{\cdot}4_3$	2·8688	5·4304	0·0572	11·8039
$2{\cdot}0_5$	2·8702	5·4304	0·0821	11·8224
$2{\cdot}0_9$	2·8704	5·4305	0·0836	11·8249
$2{\cdot}6_4$	2·8714	5·4306	0·1058	11·8373
$2{\cdot}8_6$	2·8718	5·4305	0·1145	11·8422
$3{\cdot}3_1$	2·8726	5·4306	0·1325	11·8521
$3{\cdot}7_3$	2·8733	5·4304	0·1491	11·8608
$3{\cdot}8_4$	2·8735	5·4307	0·1537	11·8632
$5{\cdot}2_4$	2·8755	5·4306	0·2094	11·8880
$5{\cdot}3_9$	2·8758	5·4305	0·2156	11·8918
$5{\cdot}7_5$	2·8765	5·4305	0·2304	11·9004
$6{\cdot}1_5$	2·8722	5·4307	0·2460	11·9091
$6{\cdot}8_3$	2·8786	5·4307	0·2728	11·9265
$6{\cdot}9_9$	2·8787	5·4307	0·2796	11·9278
$8{\cdot}5_8$	2·8812	5·4304	0·3412	11·9589
$10{\cdot}1_8$	2·8834	5·4306	0·4060	11·9863
$11{\cdot}8_7$	2·8846	5·4304	0·4452	12·0013
$13{\cdot}0_3$	2·8850	5·4308	0·5224	12·0053
$16{\cdot}1_3$	2·8848	5·4304	0·6460	12·0038

A plot of lattice spacing vs. composition is shown in Fig. 5 and of volume per atom vs. electron–atom ratio, calculated on the basis of observed lattice parameters, is shown in Fig. 6.

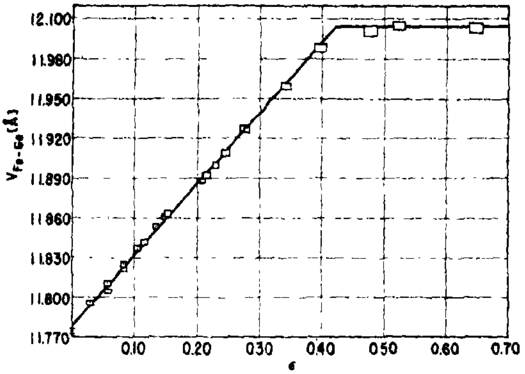

FIG. 6. Atomic volumes of Fe–Ge alloys at 298°K as a function of electron–atom ratio.

The uncertainties in the parameter determinations are represented by the vertical extent of the rectangles and in the composition by the horizontal extent. There is a suggestion of a slight inflection of the curves in both figures leading to a very small departure from the straight-line relationship between lattice constant and composition or volume per atom and electron per atom but in our estimation this reflects the inherent uncertainty of chemical analysis.

In the present discussion we shall take an analog of Vegard's rule,

$$R_{\text{alloy}} = R_A\left[1+n\frac{d_B-d_A}{d_A}\right],$$

where R_{alloy} = parameter of alloy,

R_A = parameter of solvent (the nature of this parameter to be defined later),

d_B = atomic diameter of solute,

d_A = atomic diameter of solvent,

n = atom fraction of solute.

The question arises, how are d_A, d_B to be defined? For purposes of discussion we present the relations obtained using d_A and d_B as obtained from

(1) distance of closest approach in the elemental structure,

(2) Pauling's calculation of radii,

(3) a new method presented here, based on atomic volume.

This last part will be discussed in greater detail and forms the major portion of the discussion of lattice parameter relations in this investigation. The curves resulting from these three hypotheses are shown in Fig. 5. In plotting the curve representing PAULING's theory we have employed for Ge, following PAULING,(19) a coordination number 8 and a valence of 2·56.

The curve in Fig. 6 was obtained assuming a valency for iron of zero, a matter about which there has been no general agreement (HUME-ROTHERY, IRVING and WILLIAMS,(20) PAULING,(21) JONES,(22) HAWORTH and HUME-ROTHERY,(23) and COLES(24)). The exact meaning of the term, valency of a transition metal, is not always clear. In the PAULING(19) sense it is used to denote the number of electrons regarded as present in bonding (*spd*) orbitals, and Pauling assumes group valency of 6 for all elements in Groups VI A, VII A and VIII A, B, and C. On the other hand, the experimental discovery that certain intermediate phases appear in alloy systems at definite compositions corresponding to three values of electron concentration, defined as the ratio of number of valence electrons to number of atoms in the unit cell, led to a systemization of many alloy phases. This scheme depends upon the assumption that the elements of Group VIII of the Periodic Table contribute no electrons to the crystal structure and thus permitted the recognition of the established values of electron concentration for analogous phases of copper and silver alloys, (*see*, for example, Refs. 25, 26). Since the electron concentration is a function of the difference in valency only of the alloy constituents, the valence assumed for iron will merely shift the origin along the electron concentration axis as given in Fig. 6. The discontinuous change in the lattice constant-composition curve at 10·45 atomic per cent germanium establishes the solid solubility limit of the alpha phase at approximately 600°C, and concomitant formation of the β-phase which is the NiAs type structure.(27, 28) The nomenclature here corresponds to that of HANSEN and ANDERKO.(9) The similarities between the phase diagrams, as reported by Hansen and Anderko of iron–germanium and nickel–germanium, are most pronounced. In the nickel–germanium system the boundary between the α and $\alpha+\beta$ phase fields occurs at about 10·4 atomic per cent germanium, where α is the terminal (face-centered cubic) solid solution and β has the structure of Cu_3Au. The similarity in the terminal solid solutions will be discussed in greater detail later in this paper.

Extensive systematic investigations of lattice spacing relationships in terminal solid solutions and intermediate alloy phases have shown that three main factors are important in controlling the total lattice distortions which may be additive or operative independently. These are: (1) size factor, (2) relative valency factor, and (3) electrochemical factor.

Several efforts have been made to explain the effect on the lattice constants of weak solutions of germanium in silver and copper.(29–31) In these studies it was found that equal atomic percentages of zinc, gallium, and germanium expand the copper lattice by amounts proportional to 3:4:4·48, and this relationship was confirmed for silver alloys even at high temperatures. RAYNOR(32) has observed that since an increase in the valency of the solute leads to an increased lattice expansion at equal solute concentrations, the distortion produced must depend to a marked extent on the valence of the solute. However, there is not yet agreement on the interpretation of the data since recently MASSALSKI and KING(33) showed that, for the lattice spacings of intermediate phases of the noble metals as well as terminal solid solutions, a different interpretation may be made invoking a concept proposed by JONES.(34) As will be shown in the discussion below, it is not necessary to invoke either the valency difference or the band theory considerations in discussing the effect of germanium on the iron lattice constant even though these ideas have met with success in explaining its behavior in the noble metals, nor is there any reason to suspect that such parallels can be drawn.(35) We suggest, rather, that the lattice distortion of germanium in the terminal (α) solid solution in iron is solely a size effect provided suitable provisions are made for compressibility of germanium.

The only apparently successful quantitative analysis of lattice spacing variation in terminal solid solutions of the first long period transition elements in each other, in copper and in nickel, is that given by PEARSON(36) and PEARSON and THOMPSON.(37) The relative variations in lattice distortion, defined as the change in lattice constant, follow very closely the relative variation of solute atom size and it is perhaps remarkable from these qualitative observations to note that the factors which control the size of the atoms in their elemental state also appear to play a large part in determining their apparent sizes when dissolved in nickel or each other. It is significant that the above workers show that the observed lattice distortion of the nickel lattice with germanium as the solute is opposite in sense to that expected from the relative sizes of the elemental atoms. In what follows, we shall show that it is possible to explain this anomaly as well as the lattice spacing relationship in this investigation solely on the basis of the size effect by taking into consideration the compressibility of the outer shell of the atoms. It should be noted that a relationship between atomic volumes and distance of closest approach of the solute in the solvent-type lattice was proposed by AXON and HUME-ROTHERY(38) though the relationship is expressed in terms of relative volume per valency electron in crystals of the solvent and solutes.

We envision the crystalline lattice as a packing of atoms in their usual characteristic ways in a metal (i.e. body-centered cubic, close-packed hexagonal or cubic, etc.) and regard these spheres as hard incompressible cores, each of volume V_h, in contact with each other as defined by the unit cell. In such a structure a considerable amount of space in the unit cell is not occupied by the spheres and we assume that this space is not empty but rather occupied by the compressible parts of the atoms, that is, a portion of volume V_s of each atom is smeared out through the space not filled by the hard spherical cores. It is necessary, then, to calculate the maximum proportion of the available volume in the unit cell which may be filled by hard spheres arranged on various structures. These volume fractions are

$w_{\text{fcc}} = \pi\sqrt{2}/6$ for face-centered structure,
$w_{\text{bcc}} = \pi\sqrt{3}/8$ for body-centered structure,
$w_{\text{dia.}} = \pi\sqrt{3}/8$ for diamond structure.

The lattice parameter for germanium in the diamond lattice is $a_{\text{Ge}} = 5{\cdot}6575$ Å(39, 40) at 298°K. The unit cell of this structure contains 8 atoms (spheres). The total volume ($V_{\mathrm{Ge,dia.}}$) of a germanium atom in the diamond structure consists of a hard incompressible volume ($V_{h,\mathrm{Ge}}$) and a smeared out volume ($V_{s,\mathrm{Ge}}$). These volumes are:

$$V_{h,\mathrm{Ge,dia.}} = \tfrac{1}{8}\, a_{\mathrm{Ge}}^{3}\, w_{\mathrm{dia.}} = 7{\cdot}6978\ \text{Å}^3 \tag{2}$$

and

$$V_{s,\mathrm{Ge,dia.}} = \tfrac{1}{8}\, a_{\mathrm{Ge}}^{3}\, (1-w_{\mathrm{dia.}}) = 14{\cdot}9374\ \text{Å}^3. \tag{3}$$

In the case of a dilute solution of germanium in iron, this volume must be compressed into a hypothetical body-centered cubic lattice with an accessible volume 0·32 of the unit cell volume as compared to an accessible 0·66 of the unit cell volume in the diamond structure. Thus, the volume $V_{s,\mathrm{Ge,bcc.}}$ of a germanium atom smeared out in the body-centered unit cell is

$$V_{s,\mathrm{Ge,bcc}} = \frac{1-w_{\mathrm{bcc}}}{1-w_{\mathrm{dia.}}}\, V_{3,\mathrm{Ge,dia.}} = 7{\cdot}2393\ \text{Å}^3. \tag{4}$$

The above argument appears to be plausible in view of the relatively large compressibility of germanium ($1{\cdot}44\times10^{-12}$ cm^2 dyne at room temperature).(41) Hence, the volume of a germanium atom in the body-centered cubic structure is

$$V_{\mathrm{Ge,bcc}} = V_{h,\mathrm{Ge,dia.}} + V_{s,\mathrm{Ge,bcc}} = 14{\cdot}9371\ \text{Å}^3. \tag{5}$$

The volume of an iron atom in the body-centered structure with $a_{\mathrm{Fe}} = 2{\cdot}8663$ Å at 298°K is

$$V_{\mathrm{Fe,bcc}} = \tfrac{1}{2}\, a_{\mathrm{Fe}}^{3} = 11{\cdot}7743\ \text{Å}^3. \tag{6}$$

Now, we can apply the analog of Vegard's law to calculate the atomic volume of iron–germanium solid solutions of the body-centered cubic structure

$$V_{\mathrm{Fe\text{-}Ge,bcc}} = (1-x)\, V_{\mathrm{Fe,bcc}} + x V_{\mathrm{Ge,bcc}}, \tag{7}$$

where x is the atomic fraction of germanium. For 1 a/o germanium this method gives the volume of 11·8060 Å^3 and the lattice constant, taken as a cube root of the unit cell, is 2·8689 Å. This value should be compared with the observed value 2·8684 Å obtained from Fig. 5. We believe, in view of the agreement between observed and calculated values, that the above discussion satisfactorily explains the lattice distortion of the dilute solid solution of germanium in iron.

It can be shown that the same type of analysis leads to an explanation of the lattice dilation of the dilute solution of germanium in nickel and thus resolves this apparent discrepancy between the observed change in lattice constant and that expected from the relative distances of closest approach in the nickel–germanium system.(42) The volume smeared out in the diamond structure occupies 0·66 of the unit cell volume and this must be compressed into the face-centered cubic structure where the available "empty space" is 0·26 of the unit cell. Hence, at room temperature

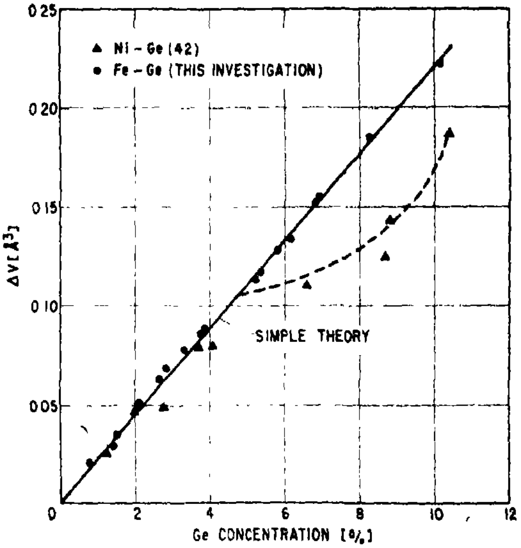

FIG. 7. Change in atomic volume per atom as a function of Ge concentration in Fe–Ge and Ni–Ge alloys.

$$V_{s,\mathrm{Ge,fcc}} = \frac{1-w_{\mathrm{fcc}}}{1-w_{\mathrm{dia.}}}\, V_{s,\mathrm{Ge,dia.}} = 5{\cdot}8850\ \text{Å}^3 \tag{8}$$

and

$$V_{\mathrm{Ge,fcc}} = V_{h,\mathrm{Ge,dia.}} + V_{s,\mathrm{Ge,fcc}} = 13{\cdot}5890\ \text{Å}^3. \tag{9}$$

The volume of a nickel atom in the face-centered unit cell is $V_{\mathrm{Ni,fcc}} = 10{\cdot}9333$ Å^3. Applying equation (6) to this alloy system gives $V_{\mathrm{Ni\text{-}Ge,fcc}} = 10{\cdot}9598$ Å for 1 a/o germanium in nickel. Thus, the calculated lattice constant is 3·5261 Å which should be compared with the observed value of 3·5258 Å.

A further demonstration that the terminal solid solutions of iron–germanium and nickel–germanium exhibit similar behavior may be had from an examination of the lattice distortions in the two systems. Figure 7 shows a plot of the change in volume per atom (ΔV) against composition of the alloys, where the change in volume per atom is defined relative to the volume per atom in the pure solvents. The equality of the initial slopes is striking. The large deviation in the slope of the curve for the nickel–germanium system is not understood except that PEARSON⁽³⁷⁾ implies that the experimental results for this system suffer particularly from factors involving the metallurgical preparation and chemical analysis which may explain his estimate of low accuracy. It should be mentioned that further calculations are promising in that agreement between observed lattice distortions and those calculated from volume of the atom, taking into account that the atom may be regarded as a hard core, surrounded by a compressible shell, show good agreement where the compressibility of the solute element is relatively large. This investigation is being pursued further in the expectation that further light may be shed on role of the size effect in terminal solid solutions of the transition metals. A refinement of the simple approach may be made on the basis of the model proposed by FRIEDEL.⁽⁴³⁾ Deviations from Vegard's law are discussed by Friedel in terms of the elemental compressibilities, but the discrepancies between Friedel's computed and observed deviations of the lattice constants are significant. Recently, we have examined the approximations made by Friedel and we are investigating the role of compressibilities in Vegard's law under more rigorous assumptions and more accurate data. It is expected that the results of this study will be made available soon.

Acknowledgements—The authors have profited greatly from discussions with Professor C. S. BARRETT of the Institute for the Study of Metals, Chicago, Professor P. A. BECK of the University of Illinois and Dr. O. RICHMOND of this Laboratory. They acknowledge with gratitude the technical assistance of Mr. G. R. DUNMYRE, Mr. R. C. PECK and Mr. J. M. PECK, the analytical work of Mr. G. W. MOMEYER and Mr. B. W. CONROY, and the preparation of the high-purity alloys by Dr. B. F. OLIVER and Mr. E. W. TROY; all staff members of this Laboratory.

REFERENCES

1. ARAJS S. and MILLER D. S., *J. appl. Phys.* **31**, 986 (1960).
2. ARAJS S., COLVIN R. V., CHESSIN H. and PECK J. M., *J. appl. Phys.* **33**, 1353 (1962).
3. HUME-ROTHERY W., CHRISTIAN J. W. and PEARSON W. B., *Metallurgical Equilibrium Diagrams* Institute of Physics, London (1952).
4. KAISER W. and THURMOND C. D., *J. appl. Phys.* **32**, 115 (1961).
5. NELSON J. B. and RILEY D. R., *Proc. Phys. Soc. Lond.* **57**, 160 (1945).
6. ANDREWS K. W. and ROGERS E. R., *Phil. Mag.* **35**, 544 (1944).
7. COHEN M. U., *Rev. sci. Instrum.* **6**, 68 (1935); **7**, 155 (1936).
8. PARRISH W., *Acta Cryst.* **13**, 838 (1960).
9. HANSEN M. and ANDERKO K., *Constitution of Binary Alloys*, p. 729. McGraw-Hill, New York (1958).
10. ZWELL L. and OLIVER B. F. (private communication).
11. BOZORTH R. M., *Ferromagnetism*, p. 72. Van Nostrand, New York (1951).
12. NÉEL L., *Ann. Phys., Lpz.* **17**, 5 (1932).
13. FALLOT M., *J. Phys. Radium* **5**, 153 (1944).
14. SUCKSMITH W. and PEARCE R. R., *Proc. Roy. Soc.* **A167**, 189 (1938).
15. SATO M., ARROTT A. and KIKUCHI R., *J. Phys. Chem. Solids* **10**, 19 (1959).
16. ELLIOTT R. J., *J. Phys. Chem. Solids* **16**, 165 (1960).
17. SMART J. S., *J. Phys. Chem. Solids* **16**, 169 (1960).
18. BELL G. M. and FAIRBAIRN W. M., *Phil. Mag.* **6**, 907 (1961).
19. PAULING L., *Theory of Alloy Phases*, p. 220. American Society for Metals, Cleveland, Ohio (1956).
20. HUME-ROTHERY W., IRVING H. M. and WILLIAMS R. J., *Proc. Roy. Soc.* **A208**, 431 (1951).
21. PAULING L., *Phys. Rev.* **54**, 899 (1938).
22. JONES H., *Phil. Mag.* **44**, 907 (1953).
23. HAWORTH J. B. and HUME-ROTHERY W., *Phil. Mag.* **43**, 613 (1952).
24. COLES B. R., *Phil. Mag.* **44**, 915 (1953).
25. HUME-ROTHERY W. and COLES B. R., *Advanc. Phys.* **3**, 149 (1954).
26. MASSALSKI T. B., in *Theory of Alloy Phases*, p. 63. American Society for Metals, Cleveland, Ohio (1956).
27. LAVES F. and WALLBAUM J. H., *Z. angew. miner.* **4**, 17 (1941–42).
28. CASTELLIZ L., *Mh. Chem.* **84**, 765 (1953).
29. HUME-ROTHERY W., LEWIN G. F. and REYNOLDS P. W., *Proc. Roy. Soc.* **A157**, 167 (1936).
30. OWEN E. A. and ROBERTS E. W., *Phil. Mag.* **27**, 294 (1939).
31. OWEN E. A., *J. Inst. Met.* **73**, 471 (1947).
32. RAYNOR G. V., *Trans. Faraday Soc.* **45**, 698 (1949).
33. MASSALSKI T. B. and KING H. W., *Prog. Materials Sci.* **10**, No. 1 (1962).
34. JONES H., *Proc. Roy. Soc.* **A147**, 396 (1934).
35. MOTT H. F. and JONES H., *Theory of the Properties of Metals and Alloys*. Clarendon Press, Oxford (1936).

36. Pearson W. B., *Canad. J. Phys.* **35**, 358 (1957).
37. Pearson W. B. and Thompson L. T., *Canad. J. Phys.* **35**, 349 (1957).
38. Axon H. J. and Hume-Rothery W., *Proc. Roy. Soc.* **A193**, 1 (1948).
39. Swanson H. E. and Tatge E., *Nat. Bur. Stand, Circ.* 539, **1**, 18 (1953).
40. Straumanis M. E. and Aka E. Z., *J. appl. Phys.* **23**, 330 (1952).
41. Köster W. and Franz H., *Metal. Rev.* **6**, 1 (1961).
42. Pearson W. B., *A Handbook of Lattice Spacings and Structures of Metals and Alloys* Pergamon Press, New York (1958).
43. Friedel J., *Phil. Mag.* **46**, 514 (1955).

J. Phys. Chem. Solids Pergamon Press 1963. Vol. 24 pp. 275–281. Printed in Great Britain.

ON KINK KINETICS IN CRYSTAL DISSOLUTION

M. B. IVES

Department of Metallurgy and Metallurgical Engineering,
McMaster University, Hamilton, Ontario, Canada

(*Received* 20 *July* 1962)

Abstract—A new acidic etchant, consisting of hydrofluoric acid and ferric fluoride, is described for producing dislocation etch pits on lithium fluoride. The geometry of pits produced by solutions containing concentrated hydrofluoric acid, ferric fluoride and water has been investigated by interference microscopy. These observations, with others of independent investigators, substantiate basic postulates concerning the effect of the etchant properties, undersaturation and inhibitive power, on the nucleation and subsequent motion of kinks in crystal ledges. At the present time, the interdependence of the environmental parameters allows only a qualitative description of their effect on crystal dissolution.

1. INTRODUCTION

It is now well-established that the surfaces which form crystallographically defined dislocation etch pits on crystals are extremely high-index surfaces. The etch pits produced, for example, on single crystal lithium fluoride with recently developed etchants[1, 2, 3] are pyramidal and have sides inclined to a {100} etched surface at angles varying between 5 and 12°, depending on etching conditions.[4] Indeed, much of the difficulty once experienced in developing etchants to reveal the emergence of dislocations at crystal surfaces was probably due to the difficulty of producing suitable surface illumination for microscopic examination. The studies to be described here have been aided principally by the use of interference microscopy, which enables the accurate measurement of pit face inclinations down to one degree of arc, and the detection of any dissolution involving depressions as shallow as $0{\cdot}03\,\mu$. Furthermore, the interference patterns show deviations in etch pit geometry much more readily than orthodox microscopy.

That such high-index faces should be so stable under etching conditions was first considered by Frank,[5] and investigated by Ives and Hirth,[4] who showed that dissolution at dislocation etch pits does not follow the same kinetics as dissolution of bulk crystal.[6] To understand the problem we will invoke Kossel's[7] concept of a crystal surface structure of low-index facets separated by ledges of monomolecular height. If we also idealize the model to overlook surface irregularities due to thermal motion of ions, and treat the nett structure as a perfect crystal surface (positive and negative ledges and kinks being considered to cancel themselves out after finite dissolution), then the close-packed {100} cleavage faces of lithium fluoride will be perfectly flat. Also, orientations differing from (100) in the [001] and [010] zones will be "ledge-surfaces" containing no nett density of kinks—a consequence of the cubic structure of the alkali halides. Further, crystallographic orientations differing from (100) in the [011] and [0$\bar{1}$1] zones will be "kink-surfaces". Using a cubic-block model of a crystal,* these two types of surface, {0*kl*} and {*hhl*,} are illustrated in Fig. 1. The {*hhl*} surfaces have, in fact, maximum possible kink density. The total ledge-plus-kink length on equal macroscopic areas of {0*kl*} and {*hhl*} surfaces differs by a factor of two.

When such surfaces dissolve, we treat the action in terms of the motion of the kinks in the ledges. By travelling the length of a ledge, a kink can produce an overall motion of that ledge by an amount

---

* In this way we may ignore the presence of both positive and negative ions.

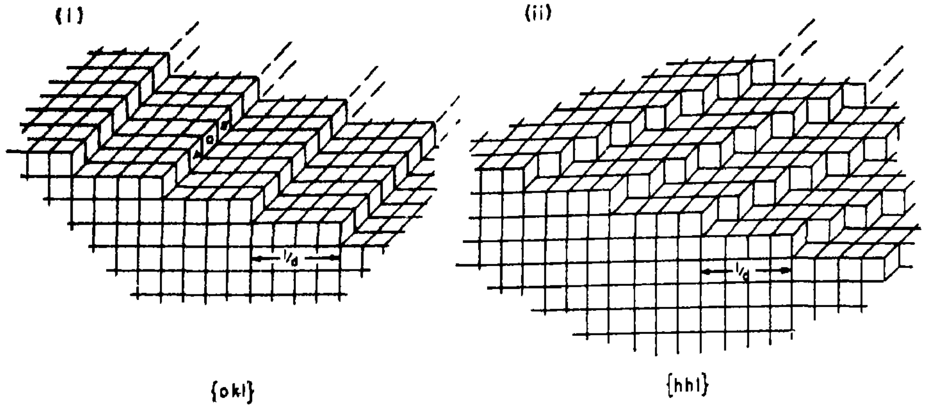

FIG. 1. Building block model of (i) a ledge-surface, {0*kl*}, and (ii) a kink-surface, {*hhl*}, on an alkali halide crystal, using Kossel's concept.

equal to the depth of the kink (henceforth considered monatomic). Continuous dissolution of ledge-surfaces therefore requires the continuous nucleation of kinks and their subsequent traversal of the length of the ledge.* To understand the stability of the high-index pit faces we must postulate how the various factors of etching environment affect kink nucleation and motion.

We shall show that the nucleation of kinks is influenced principally by the undersaturation of the dissolving specie in the etching medium, and that their subsequent motion is controlled primarily by the inhibitor that all crystallographic etchants must necessarily contain.

2. ETCH PITS IN LITHIUM FLUORIDE

The principal etchants developed to date for lithium fluoride(1, 2, 3) are a modified CP–4, consisting of equal parts by volume of concentrated hydrofluoric acid and glacial acetic acid saturated with ferric ions, usually as ferric fluoride (designated "A" etchant(2)), and a simpler one consisting of 2·5 p.p.m. ferric ions in aqueous solution ("W", for water, etchant(2)). It has been shown(1, 2, 3) that "A" etchant attacks the sites of both "fresh" and "aged" dislocations with equal vigour, but that "W" etchant distinguishes between the two, etching fresh dislocations more deeply. Further, and of more immediate interest, the "A" etchant pits are pyramidal with {*hhl*} faces, and "W" etchant pits are totally composed of {0*kl*} surfaces. This is demonstrated in the photomicrographs of Fig. 2.

The author has now established that the "A" etchant may be further simplified to provide a good fast selective etchant for lithium fluoride. If excess ferric fluoride is added to reagent grade (48 per cent) hydrofluoric acid, the solution at first attacks the crystal surface extremely roughly. However, if it is allowed to age its etching characteristics improve. This improvement, manifest by the eventual production of good pyramidal pits of the {*hhl*} type, is evidently dependent on the concentration of ferric ions in solution. For instance, two solutions were taken in which 0·27 g. anhydrous ferric fluoride was added to 50 ml of hydrofluoric acid. One solution was frequently stirred while the other was only disturbed by the stirring produced by the etching specimens. The stirred solution produced good etch pits on a smooth surface only $\frac{1}{2}$ hr after preparation. No solid residue could be seen remaining in the beaker after this time, suggesting a concentration of approximately 8×10^{-4} M fraction ferric fluoride (1000 times the concentration necessary in

---

* Correctly, we should consider the kink nucleation as the removal of a block such as '*a*' in Fig. 1, and the consequent production of two kinks which run in opposite directions to strip the ledge. The mean time for stripping will always be a simple function of the ledge length, however. We define the end of a ledge as the point at which kinks pile-up to form a kink-surface. If only ledge-surfaces are present, as in pits due to "W" etch on LiF, kinks moving together on adjacent surfaces are annihilated at the intersection.

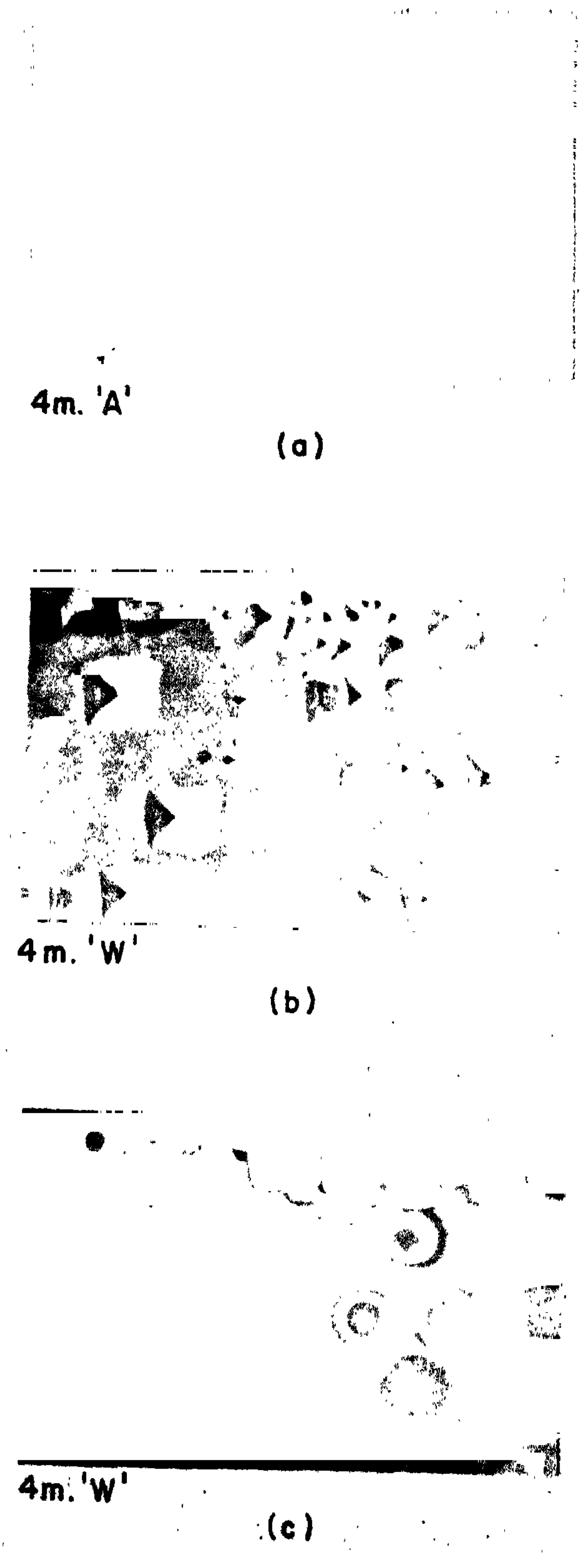

FIG. 2. Dislocation etch pits on lithium fluoride produced after 4 min of hand-stirring at 20°C in (a) "A" etch, and (b) "W" etch, (c) an interference micrograph of the field of (b). A crystal edge is seen across the top of these prints, and hence ⟨100⟩ directions are parallel to the page edges.

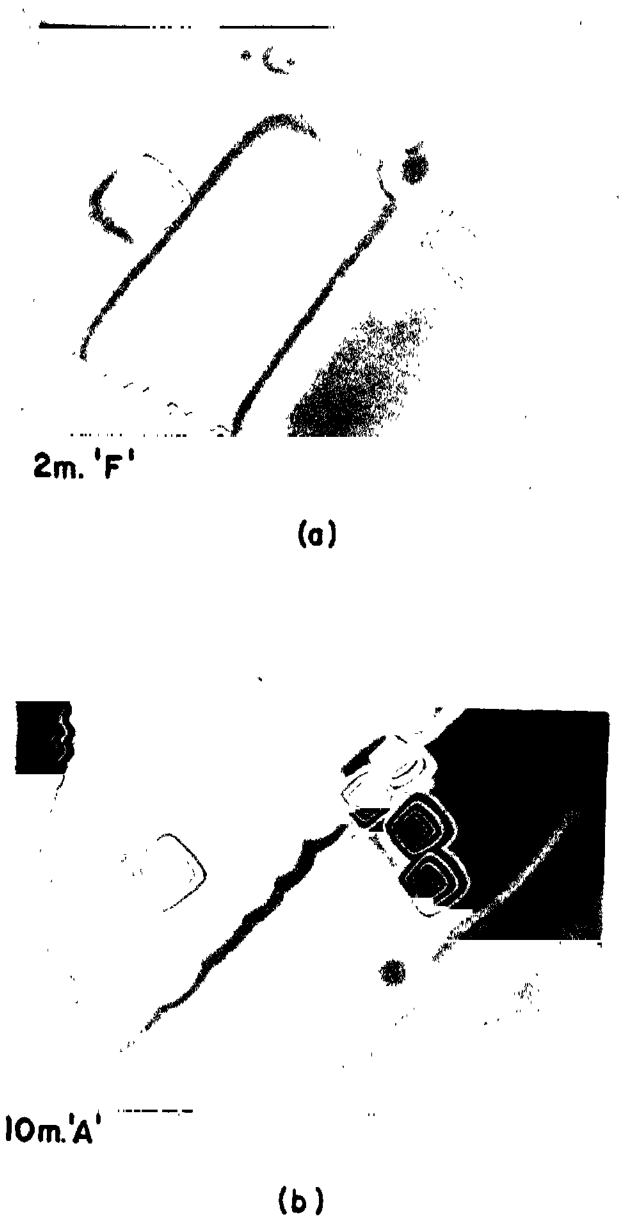

Fig. 3. Matching cleavage areas of lithium fluoride etched under identical conditions in (a) the new "F" etch, and (b) the original "A" etch (print reversed).

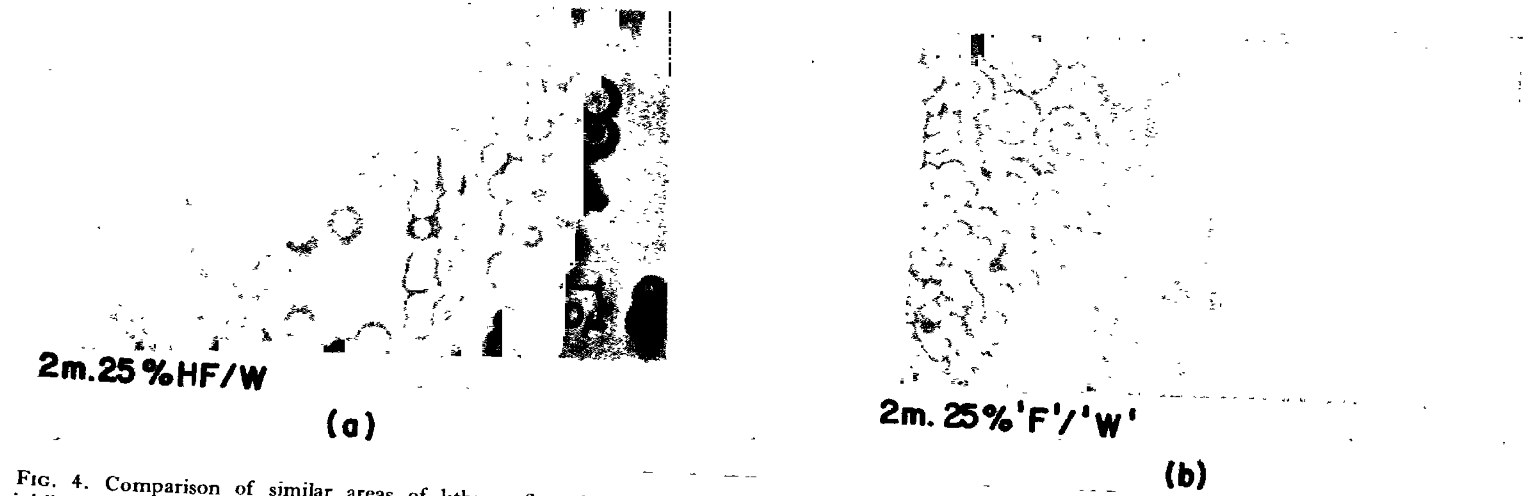

FIG. 4. Comparison of similar areas of lithium fluoride produced by etchants of the same acidity but with differing amounts of ferric fluoride inhibitor. (a) 25 vol per cent HF in "W" etch and (b) 25 vol per cent "F" etch in "W" etch. The crystal edge to extreme left verifies the ⟨100⟩ directions parallel to page edges.

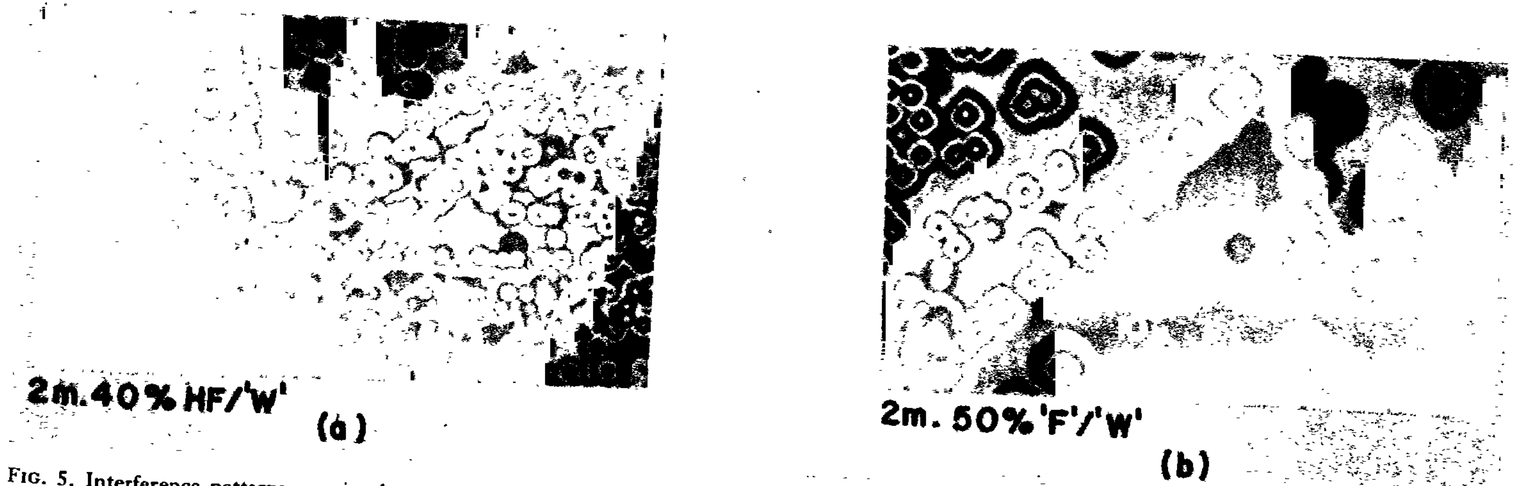

FIG. 5. Interference patterns on pits due to etching 2 min in (a) 40 vol per cent HF in "W" etch, and (b) 50 vol per cent "F" etch in "W" etch. ⟨100⟩ directions parallel to page edges.

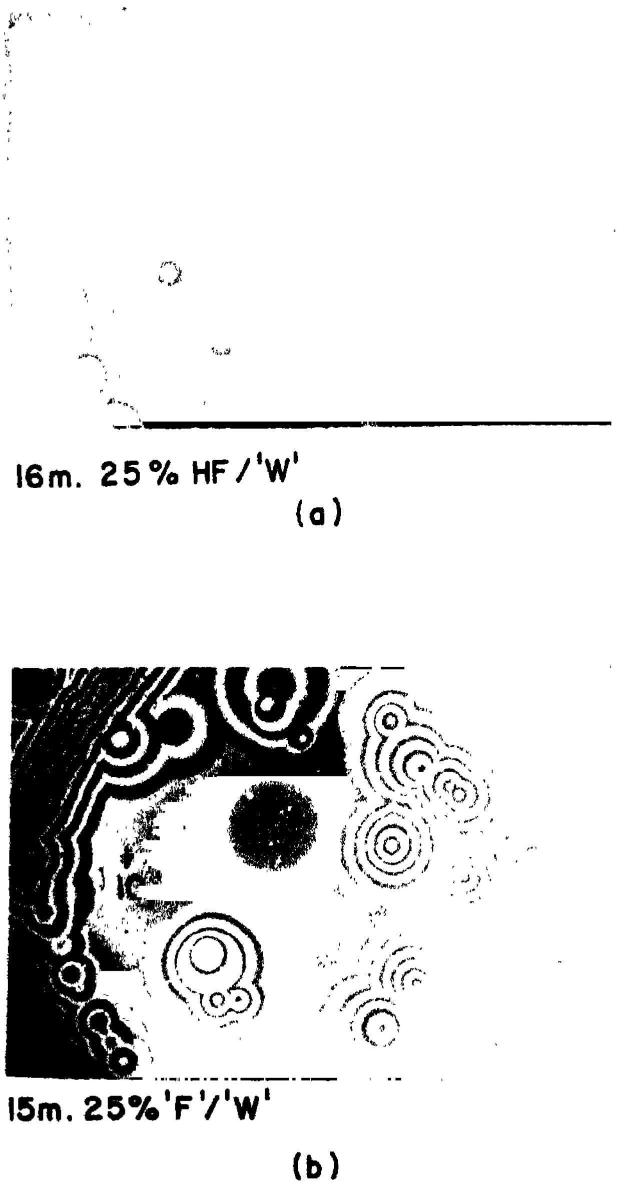

FIG. 6. Pits on matching cleavage faces of lithium fluoride, produced by (a) 16 min 25 vol per cent HF in "W" etch, and (b) 15 min 25 vol per cent "F" etch in "W" etch (print reversed). ⟨100⟩ directions parallel to page edges.

"W" etch). The unstirred solution did not become a good etch until 3 hr after preparation. The final interfering features appear to be hillocks which clear as time increases. Gravimetric analysis of this new etchant (henceforth denoted "F" etchant) has substantiated the above value for ferric ion content, although the optimum concentration does not appear to be critical.

The etch pits due to "F" etchant are similar to those produced with "A" etchant (Fig. 3), which has acetic acid added. They are of similar slope but grow in width at a rate approximately five times that in "A" etchant. Moreover as glacial acetic acid is added to "F" etchant, the rate of pit widening is steadily reduced, and the time for good pitting after preparation quickly shortens. Reduction of undersaturation appears to be the principal action of acetic acid, in which lithium fluoride is relatively insoluble. The reduction also necessitates less ferric ions for good etching.

The discovery of this simple acid etchant, "F", has led the author to investigate the two etchants in terms of the pits they produce.

A series of etchants were prepared by combining measured volumes of, first, "W" and "F" etchants, and secondly, "W" etchant and concentrated hydrofluoric acid. The geometry of the dislocation etch pits produced in freshly-cleaved {100} surfaces of lithium fluoride by these mixtures at temperatures between 18 and 23°C was investigated by means of a Zeiss interference microscope. By suitable arrangement of the optics of this instrument, the interference fringes become "geographic contours" with a vertical interval of 0·27 micron.

The observations may be summarized as follows:

1. Solutions of acid and "W" etchant produce pits which widen at uniformly increasing rates with increase of acid content, and independently of ferric ion concentration in excess of the optimum for "W" etchant. The rate in "W" etchant is only one-quarter the widening rate in "F" etchant, but the mean slope ($\approx 10°$) of pit sides remains relatively constant throughout the range of mixtures.

2. The addition of small quantities (< 10 vol per cent) of "F" etchant to "W" etchant produces etch pits which are partially rounded, in the manner typical of pits produced in conditions of excess inhibition.(3)

3. The addition of larger quantities (15 to 20 vol per cent) of "F" in "W" etchant produces the smaller "fresh" dislocation etch pits which are observed to be in the acidic orientation, constructed of $\{hhl\}$ faces. The more rounded "aged" dislocation pits also exhibit this tendency by a flattening of their faces in the region of $\{hhl\}$. At 25 vol per cent "F" in "W" etchant, the pits more clearly demonstrate this tendency, as exemplified by Figs. 4(b) and 6(b).

4. A 25 vol per cent solution of hydrofluoric acid in "W" etchant produces pits which still show preference for $\{0kl\}$ faces (Figs. 4(a) and 6(a), as they do at all lower concentrations. It is not until mixtures of between 30 and 40 vol per cent hydrofluoric acid are prepared that they tend to produce pits oriented in the "F" attitude. This tendency is only noticeable in the earlier stages of pit development (Fig. 5(a)). At longer times the etch pits are usually quite circular in section.

6. Excess hydrofluoric acid in the "W" etchant eventually causes uncontrolled general surface attack. Solutions of "W" etchant dominant in "F" etchant form pits which are well-defined (Fig. 5(b)) and increase in rate of widening as the composition of 100 per cent "F" etchant is approached.

The interference micrographs of Figs. 4 and 5 have been selected to demonstrate the appearance of typical pits formed by "W" etchant with additions of hydrofluoric acid and of "F" etchant at a common etching time of two minutes at 20°C, using hand stirring. Figure 6 illustrates the striking difference in etch pit morphologies produced by 25 vol per cent addition of (a) pure hydrofluoric acid, and (b) "F" etchant, after prolonged etching times, on matching areas produced by the same cleavage. One of the photomicrographs has been reversed in printing to allow easier comparison of pits produced by the two mixtures at the segments of what were the same dislocations prior to cleavage. The tendencies towards the two types of square pit is well demonstrated.

3. DISCUSSION

The observation that $\{hhl\}$-surfaces are stable at lower undersaturation (acid) content in the presence of a high concentration of ferric ions than they are with only a few p.p.m. of those ions in solution provides a basis upon which two postulates may be made. These are: (1) kink nucleation is primarily controlled by the effective undersaturation of the dissolving specie in the solvent, and (2) the principal effect of etchant inhibitor is in the retardation of kink motion. Unfortunately, these two effects are in no way independent. Whereas an uninhibited solvent attacks crystal surfaces very roughly, etchant containing inhibitors produce pits in an otherwise relatively smooth surface. It appears therefore that the inhibitor produces some modification in kink nucleation rate, in addition to its effect on kink motion. Another aspect of interdependence is expected when the effective undersaturation of an etchant is reduced. The direct effect is to produce a retardation of kink motion, which in turn allows for easier inhibition and a consequent secondary impedance to dissolution.(4)

In spite of these complications it is possible to distinguish between two basic categories of kink kinetics, which give rise to distinctive etch morphologies.

Type (*i*). Little inhibition;* if the mean time for kinks to sweep a length of ledge† is less than the time between successive kink nucleation in that length, unkinked ledges are stable. Their motion is then only dependent on the kink nucleation rate. Ledge-surface results, which corresponds to {0*kl*} in the alkali halides.

Type (*ii*). Greater inhibition;* when kinks are nucleated at a rate greater than they can clear the ledges, they will tend to pile-up. Kink-surface is produced, and in the limit maximum kink density will result in {*hhl*} surfaces for the alkali halides.

The interdependent effect of the principal etchant properties, undersaturation and inhibitive power, clearly makes the above classification an extremely simplified one. Under type (i) conditions, for instance, the amount of inhibitor must also modify the kink nucleation rate in order for pits to be composed of ledge-surface but to vary in slope and smoothness of surface, as has been demonstrated for lithium fluoride etched in aqueous solutions varying in ferric ion content.(3) Most of the observed etch pit morphologies produced on {100} surfaces of alkali halides are described by type (ii), since only in the case of pure {0*kl*} pits is kink-surface not produced. Figure 7 summarizes the conditions imposed on kink kinetics that could account for the various etch pit shapes observed in the present study. Case (a) belongs to type (*i*), but the remainder must be considered as varying degrees of type (ii). This new classification underlines the complex interrelated effects which are possible in an etchant system.

The kink distribution in a composite pit exhibiting both {0*kl*} and {*hhl*} in addition to intermediate surfaces is demonstrated by the model of an etch pit illustrated in Fig. 8. This model has been built to aid visualization of the deployment of kinks in an idealized block model which is necessary to form various macroscopic surfaces. It is seen that kink density is relatively high in all surfaces that are not oriented very closely to

	(a)	(b)	(c)	(d)	(e)
INTERFERENCE PATTERN	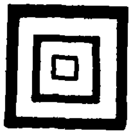	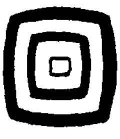	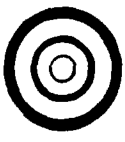	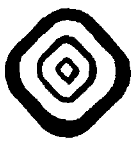	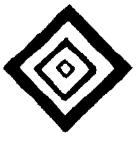
KINK NUCLEATION	LOW	LOW	HIGH	HIGH	HIGH
INHIBITION	LOW	MEDIUM	LOW	MEDIUM	HIGH
EXAMPLE	Fig 2b		Fig 4a	Fig 4b	Fig 3b
ETCHANT TYPE FOR LiF	"W"	"W"(excess Fe^{+++})	"W"+ HF	"W" + "F"	"F"

FIG. 7. Tabulation of the relative effects of kink nucleation rate and inhibition of kink motion on the geometry of dislocation etch pits.

---

* Relative term—used only for comparison between the respective stages. Absolute inhibitive power will depend on the particular etchant-crystal system.

† See footnote to p. 276.

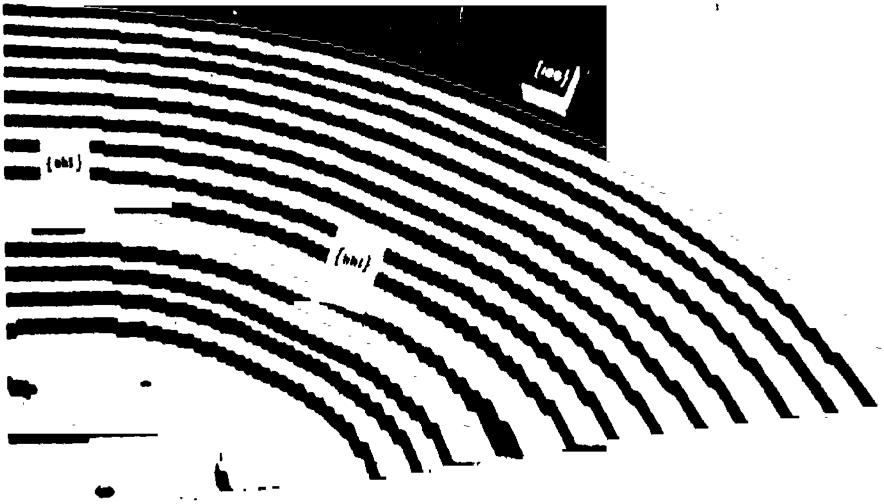

FIG. 8. Model of an etch pit exhibiting some {0*kl*} and some {*hhl*} surface and demonstrating the array of kinks and ledges which produce it.

{0*kl*}. Stable kink configurations are therefore very common on etching surfaces, and their application to a consistent theory is of great importance.

When acid content is equated to nucleation rate and ferric ion content identified with inhibition, the predictions of Fig. 7 satisfactorily fit the present results. Since lithium fluoride is only sparingly soluble in water (0·13 g per 100 ml., according to PAYNE(8)) we expect the kink nucleation rate in "W" etchant to be relatively slow. The low ferric ion content present in this etchant is consistent with the placing of the case (a) {0*kl*} pits in the type (i) classification. The addition of small amounts of "F" etchant, with its higher ferric ion content,* produces the characteristically over-inhibited pits of case (b). Addition of acid without additional inhibitor produces the rounded pits of case (c), wherein the increased kink nucleation rate without further inhibition produces diffusion-controlled motion, and the tendency to conical pits. When both undersaturation and inhibition are increased the additional kinks that are nucleated may now be effectively inhibited and the tendency to stable kink-surfaces increased by inhibitor-control, as in case (d). In the limit, nucleation rate and inhibition are increased to the extent that kink motion is a concept no longer applicable, as on {*hhl*} surfaces, case (e). Here the only process for dissolution is the successive loss of "blocks" at the salient corners of the kink-surface—there being no length of ledge between kinks, along which they can move. That the two factors producing case (e) must only be *relatively* high is substantiated by the observation that as glacial acetic acid is added to "F" etch to lower the undersaturation, the quantity of ferric fluoride required for optimum inhibition and production of {*hhl*} pits also decreases. The reduced undersaturation allows for easier inhibition.

It may now be understood why the change-over from {0*kl*}–{*hhl*}-faced pits occurs at lower undersaturation when there is more inhibitor present. The additional inhibition is able to stabilize the kinks and produce case (d) pits. Without the additional inhibition, the kink-surfaces of (d) are produced only when undersaturation is increased such that the profusion of kinks inhibit themselves by diffusion-control (Fig. 5(a)). However, such control, even in these conditions, is limited to early stages in pit growth when "ledge density" of nucleation sites is at its highest.

---

* The chemistry of hydrofluoric acid attack on lithium fluoride is probably quite complex, and it is likely that complex ion formation does not free all the added ferric ions for inhibitive action. If this were not so, it would be difficult to justify the need for 1000 times more ferric ions to successfully produce type (e) pits than to form type (a). The solubilities of lithium fluoride in the two etchants employed differ by a factor of only 50. So, although the absolute quantity of ferric ion added is not necessarily meaningful, the relative amounts are sufficient for the present correlation.

4. OTHER SYSTEMS

The conclusions of the previous section are substantiated by the recent results of Rozhanskii *et al.*[9] on the etching of sodium chloride with acetic acid-based solvents. Their observations are summarized in Fig. 9.* The addition of inhibitor ($CaCl_2$) is seen to introduce stable kink-surface {*hhl*} planes, after the manner of ferric fluoride in acidified etch on lithium fluoride. Etching under the conditions of a reduced undersaturation (Fig. 9(b)), where kink motion is retarded is explained in terms of a mechanism described by Ives and Hirth.[4] A decrease of dissolution rate allows a greater inhibition of the more slowly-moving kinks, and further emphasizes the interdependence of undersaturation and inhibition.

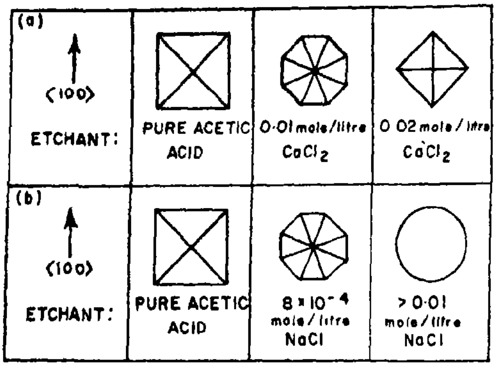

(after ROZHANSKII et al.)

Fig. 9. Summary of studies on the etching of sodium chloride in acetic acid-based solvents (after Rozhanskii *et al.*).

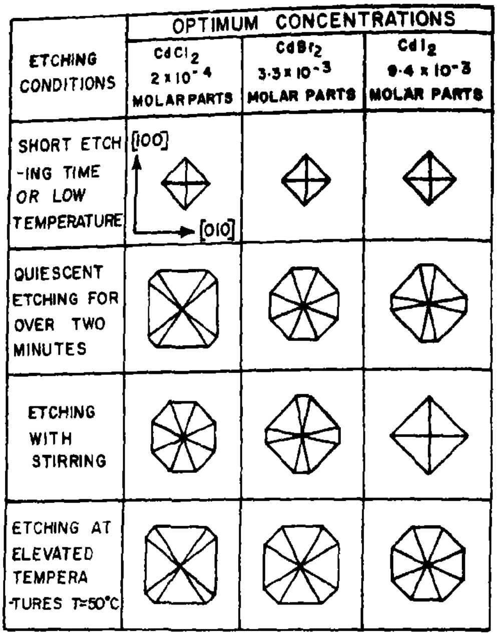
OPTIMUM CONCENTRATIONS
ETCHING CONDITIONS
CdCl2 2×10⁻⁴ MOLAR PARTS
CdBr2 3·3×10⁻³ MOLAR PARTS
CdI2 9·4×10⁻³ MOLAR PARTS
SHORT ETCHING TIME OR LOW TEMPERATURE
[100]
[010]
QUIESCENT ETCHING FOR OVER TWO MINUTES
ETCHING WITH STIRRING
ETCHING AT ELEVATED TEMPERATURES T=50°C

(after KOSTIN et al.)

Fig. 10. Summary of studies on the etching of sodium chloride in ethyl alcohol-based etchants (after Kostin *et al.*).

Other etching studies on sodium chloride, by Kostin *et al.*,[12] with ethyl alcohol as solvent, have used cadmium halides as inhibitors. A summary of etch pit geometries obtained is reproduced in Fig. 10. These results are also consistent with the conclusions of this paper. It may be seen that more cadmium iodide is required for optimum etching conditions than is required of the other halide inhibitors, and under all conditions there is more {*hhl*} face in the pits inhibited by the iodide. It has been suggested[12] that more iodide is required because it is less dissociated in solution, and that in fact the cadmium ion concentration is in each case similar. However, free cadmium ions need not be the only inhibiting specie here, as larger complexes are undoubtedly present. This is verified by the fact that different pit morphologies are produced by different halide additions but with identical etching conditions (Fig. 10). A direct correlation between inhibitive power and addition of solid halide is therefore consistent. That larger complexes must be active is born out by experiments(12) using optimum inhibitor concentration, but with the addition of ions which are known to bind cadmium ions into larger complexes. As the amount of complexing agent (alkalis KOH, KBr, or salts NH_4Cl, KI, BaI_2) added to a cadmium chloride—ethyl alcohol etchant was increased, so the proportion of {*hhl*} surface within the pits also increased. If the new complexed ions inhibit more effectively than the free cadmium ions,* such an observation is consistent with the present ideas.

---

* The maximum concentration here quoted for pitting by acetic acid is almost the solubility limit of NaCl in absolute glacial acetic acid. This suggests a critical undersaturation ratio, C_n/C_0,[4,10,11] for pit nucleation of close to unity. It is possible that the "less than 0·3 per cent" water content of the acid in these experiments is sufficient to increase the effective undersaturation and reduce the critical ratio consistent with observations on lithium fluoride.[6] The occurrence of additional corners to the pits of this study is also worthy of note, and suggests a modification of dissolution kinetics from those which produce the usual rounding effects and which merit further consideration.

Figure 10 also shows that more {0*kl*} surface is produced when quiescent etching rather than stirred etching is employed, and also when the etching temperature is raised. In the first case, the increased stagnant layer would decrease the kink nucleation rate, and in the second case, a higher temperature would allow less inhibition—both effects favouring the stability of ledge surface.

5. CONCLUSIONS

It has been seen that the basic postulates concerning the effects of etchant environment on kink nucleation and motion are consistent with dislocation etch pit geometries observed under widely varying conditions on lithium fluoride surfaces. The interdependence of the two primary parameters, under saturation and inhibitive power, does not allow at this time a direct quantitative analysis of the kinetics, but qualitatively the model appears consistent both with the results presented on lithium fluoride and with the independent experiments on sodium chloride. It should be noted that no claim is made for a specific mechanism for kink inhibition.

The conclusions of this paper should hold for kink kinetics on crystal surfaces in general. Dislocation etch pits are used for these kinetic studies only because dislocations are assumed to provide a steady source of ledges, the subsequent progress of which may then be studied in terms of environmental conditions. Investigations to this time have not demonstrated the validity of such an assumption.

The extension of the study of dissolution kinetics to the treatment of kink motion on crystal surfaces attacks the subject at its heart, and has permitted a consistent qualitative three-dimensional approach. It is to be hoped that the application of these ideas is a general one and that they may be successfully applied to the dislocation etch pitting of metals, once simpler etchants are available.

Acknowledgement—This work was performed with the support of a Research Grant awarded by the National Research Council of Canada, which is gratefully acknowledged.

REFERENCES

1. GILMAN J. J. and JOHNSTON W. G., *J. appl. Phys* **27,** 1018 (1956).
2. GILMAN J. J. and JOHNSTON W. G. *Dislocations and Mechanical Properties of Crystals* p. 116. Wiley, New York (1957).
3. GILMAN J. J., JOHNSTON W. G. and SEARS G. W., *J. appl. Phys.* **29,** 747 (1958).
4. IVES M. B. and HIRTH J. P., *J. chem. Phys.* **33** 517, (1960).
5. FRANK F. C., private communication (1957).
6. IVES M. B., *J. appl. Phys.* **32,** 1534 (1961).
7. KOSSEL W., *Nachr. Ges. Wiss. Göttingen* 135 (1927).
8. PAYNE J. H., *J. Amer. chem. Soc.* **56,** 947 (1937).
9. ROZHANSKII V. N., PARVOVA E. V., STEPANOVA V. M. and PREDVODITELEV A. A. *Kristallogr.* **6,** 704 (1961); English translation in *Sov. Phys.—Crystallogr.* **6,** 564 (1962).
10. CABRERA N., *The Surface Chemistry of Metals and Semiconductors* p. 71. Wiley, New York (1960).
11. CABRERA N. and LEVINE M. M., *Phil. Mag.* **1,** 450 (1956).
12. KOSTIN N. F., LUBENETS S. V. and ALEKSANDROV K. S., *Kristallogr.* **6,** 737 (1961); English translation in *Sov. Phys.—Crystallogr.* **6,** 588 (1962).
13. WESTWOOD A. R. C., OPPERHAUSER H. Jr. and GOLDHEIM D. L., *Phil. Mag.* **6,** 1475 (1961).

---

* We are presently investigating the effect of large polar molecules of the long-chain fatty acids on the etching behaviour of lithium fluoride, following the observations of WESTWOOD *et al.*(13) These appear to inhibit dissolution very effectively, and presumably the complexed ions present here could also be more active.

J. Phys. Chem. Solids Pergamon Press 1963. Vol. 24 pp. 283–295. Printed in Great Britain.

ELECTRICAL PROPERTIES OF ANOMALOUSLY COMPOSED DALTONIDES

F. HULLIGER and E. MOOSER
Cyanamid European Research Institute, Cologny-Geneva, Switzerland

(*Received* 7 *September* 1962)

Abstract—Criteria are given for the prediction of the character of the electrical conductivity in "anomalously composed" daltonides. To test the criteria, compounds of this type whose electrical properties are known are discussed in some detail. Moreover, the criteria are used to predict semiconductivity in a series of compounds such as, e.g. BaS_2, BaS_3, CsS_3, Hg_3P_4, KAs_2, ZnP_2, SnP_3, BaP_3, CdP_4, Na_2P_5, SiAs, GeAs, $SiAs_2$, etc., whose electrical properties have not so far been investigated. In compounds whose electrical properties are known, inversion of the arguments contained in some of the criteria permits predictions to be made of atomic coordination and structure.

1. INTRODUCTION

SEMICONDUCTORS are valence compounds, i.e. their chemical compositions adhere to the valence rules. There is, therefore, no fundamental difference between a semiconducting compound and an inorganic salt; in both the valences of the constituents are saturated. In fact, all intermediates between the extremely covalent semiconductor and the purely ionic salt are found in nature, so that the chemical bonding in a semiconductor can be described as arising from the resonance between one or more ionic and covalent valence structures. It is not surprising, therefore, that to most semiconducting compounds a simple ionic formula can be attributed.(1) However, the possibility of writing such a formula is not a sufficient condition for the occurrence of semiconductivity. Thus, there exists a series of metallic phases like InBi, TlBi... for which one can readily give ionic formulae, whose crystal structures do, however, immediately reveal that the component atoms cannot have the valences suggested by such formulae. Nor would the "ionic formula criterion" seem to be necessary, since a number of semiconducting compounds like CdSb and GaTe are known whose compositions differ from those expected from the normal valence rules. We propose in the present paper to discuss and/or predict the electrical properties of such "anomalously composed" phases which do not contain transition elements and rare earths. Since the saturation of the valences cannot immediately be recognized from the composition of these compounds, it is obviously difficult to make accurate predictions. Nevertheless, the criteria outlined in Section 2 will serve as a guide, so that in Sections 3 and 4 in which a survey is given of the known semiconductors of anomalous composition we will be able to venture some educated guesses as to the character of conductivity of a series of compounds whose electrical properties have not so far been investigated.

2. CRITERIA FOR THE PREDICTION OF THE ELECTRICAL PROPERTIES OF COMPOUNDS

Criteria with which to predict the character of, conduction or, more specifically, semiconductivity in families of compounds, have been proposed by various authors.(1,2) We therefore need only consider those which pertain to the anomalously composed phases discussed here. These criteria are of considerable interest, because they open the way to the search for new semiconducting materials among compounds which hitherto have only scarcely been investigated. Thus in many a case only the chemical composition is known. Sometimes data on crystal structure and perhaps magnetic properties are available, but only very rarely has a compound been prepared with sufficient perfection to allow unequivocal electrical measurements to be made. In surveying phases of anomalous composition it is, therefore, of importance to be guided by some criteria, even though these criteria are qualitative only and not as rigorous as one might wish them to be.

Every criterion with which to predict the electrical properties of a solid is either another formulation or a consequence of the one stating that the valences of the component atoms of a metal are unsaturated while those of a non-metal are saturated.(2) It follows immediately from this criterion that a non-metallic compound must contain an anion-forming element, i.e. an element with at least half-filled valence shells or subshells. The anion formers lie to the right of the Zintl border, i.e. in groups IVB to VIIB of the Periodic Table and they also include the elements H, Au and Pt. All these elements have high electronegativities and experience shows that the higher the electronegativity of the anion of a compound, the more likely it is that the compound is non-metallic.

Let $X^{(\chi)}$ be an anion with valence χ and $M^{(\mu)}$ a cation with valence μ. If then $M^{(\mu)}_{m}X^{(\chi)}_{x}$ is to represent the chemical formula of a normal valence compound, then the valence rules demand that $m\mu = x\chi$. However, these rules implicitly assume that bonding occurs between cations and anions only. If we drop this assumption, we can very well have $m\mu \neq x\chi$ without violating the saturation criterion. Thus if $m\mu = x(\chi - b_a)$, the formation by each anion of an average number b_a of bonds with neighbouring anions will still result in a complete saturation of the valences and hence in non-metallic properties. If on the other hand $m(\mu - b_c) = x\chi$, then it is only necessary that each cation forms an average of b_c cation–cation bonds to make the corresponding phase non-metallic. These conditions have been expressed by MOOSER and PEARSON(2) in terms of the number n_e of valence electrons per formula unit (not counting any unshared electrons on the cations), the number N_a and N_c of anions and cations per formula unit and the numbers b_a and b_c defined above:

$$\frac{n_e}{N_a} - \frac{N_c}{N_a} \cdot b_c + b_a = 8^*$$

For hydrides, aurides and platinides this formula is replaced by $n_e/N_a = 2$, because on the one hand, no anion–anion and cation–cation bonds are known to form in these compounds ($b_a = b_c = 0$) and on the other hand only the two *s*-states of the valence shells of H, Au and Pt are involved in the bond formation.

These formulae can be applied for the prediction of the electrical properties of a compound only if the values of n_e and b_a or b_c are known and this usually involves knowledge of the crystal structure or at least the short range order (i.e. the atomic coordination). If the structure of a compound is unknown, but its non-metallic nature has been established, then the formula affords the determination of b_a or b_c and thus gives valuable information about the coordination configurations met in the compound. The formula thus establishes a relationship between the crystal chemistry of a compound and its electrical properties. It should, however, be pointed out that this relationship is too complex to permit a clear-cut distinction to be made between metallic and non-metallic structures. In fact, many a metallic conductor crystallizes in a structure which is also found in semiconductors and insulators.

The relation between crystal chemistry and electrical properties is reflected also in the following rule: In series of chemically analogous compounds such as, e.g. InP, InAs, InSb and InBi, those with the heaviest anions—if they exist at all—normally have high coordinated structures and metallic properties, while in the lighter representatives low coordination numbers and semiconducting or insulating properties are observed. This rule is based on the fact that in the heavier anions the *d* levels of the valence shell become available for the valence electrons. Since in this case the number of available states exceeds that of the electrons, it becomes energetically favourable to form many unsaturated, i.e. metallic bonds, rather than a restricted number of saturated bonds. As seen, e.g. from the transition from semiconducting to metallic properties in the fourth group of the Periodic Table, this rule does not only hold for compounds, but for the anion-formers themselves.

---

*In the original paper the term $-N_c/N_a \cdot b_c$ was omitted because at that time no semiconductor was known for which $b_c \neq 0$. Later the formula was amended to include cases for which $b_c \neq 0$ and $N_a = N_c = 1$. The present formulation is completely general.

Since the valences of the constituents of a semiconducting compound are saturated, these compounds usually have a very narrow region of homogeneity, i.e. they appear as line phases in the phase diagram. Exceptions to this rule are found only among compounds containing transition elements which, as mentioned earlier, will not be considered here. This rule is not reversible. In fact, many metallic line phases—they usually contain B elements—are known. As examples we list BaAl, $CaAl_2$, LiTl, Li_2Al, Mg_2Ba, $CaCd_2$ Mg_2Ca, $NaCd_2$, $CsHg_2$, $MgGa_2$, etc.

The magnetic susceptibility of a great number of solids is known, because susceptibility measurements are relatively simple to perform, even though a material may be available in powder form only. It seems useful, therefore, to discuss briefly how magnetic data can give an indication of the electrical properties of a solid. The susceptibility of a solid containing no transition elements and/or rare earths is essentially made up of three terms, namely (1) of the Larmor–Langevin diamagnetism of the electrons in the filled shells, (2) of the Van Vleck term which arises from virtual transitions of the electrons into unoccupied levels and (3) of the susceptibility of any free charge carriers which might be present in the solid. The first term normally is very nearly equal to the diamagnetism of the ions composing the solid. The second term can be positive or negative, but in solids whose constituents do not contain unfilled inner shells it is usually small, so that we need not consider it here. The charge carrier susceptibility finally is made up of two terms, i.e. the Pauli–Landau spin paramagnetism and the Landau–Peierls orbital diamagnetism. Both these terms are proportional to the number of free charge carriers and the sign of their sum depends on the effective mass of the carriers. If the effective mass is of the order of, or larger than the electron mass, the spin paramagnetism predominates and this is the reason why metals normally show a weak, temperature independent paramagnetism. However, in some semimetals, such as Bi, the effective masses may be small enough for the orbital diamagnetism to predominate. The total susceptibility will then be negative. In semiconductors and insulators the diamagnetism of the filled shells is by far the largest term, so that they too are diamagnetic. However, since in semiconductors the number of free charge carriers changes with temperature, the resulting temperature dependence of the charge carrier susceptibility which is superimposed upon the ion diamagnetism may still permit to distinguish between a semiconductor and a diamagnetic semimetal.

3. COMPOUNDS FOR WHICH $m\mu < xX$

Let us first consider the phases of composition $M_m^{(\mu)}X_x^{(x)}$ for which $m\mu < xX$. Since saturation of the valences can only be achieved in these phases by the formation of anion molecules, it is easy to predict their electrical properties, if the crystal structure is known: If a sufficient number of X–X bonds form, the phase will be non-metallic and if no X–X bonds form, it will be metallic. The non-metallic representatives of these phases are called polycompounds. Their cations usually are heavy elements. Moreover, the cation–anion bonds in polycompounds containing K, Rb, Cs, Ca, Sr or Ba are predominantly ionic. They are predominantly covalent, however, in the polycompounds containing Cu, Ag, Zn or Cd.

a. *Polychalcogenides*

In Table 1 a survey is given of the polychalcogenides which are known at present. Only very few data are available on these compounds and in some cases their existence has not been established beyond all doubt. Thus compounds like Tl_2S_5(3) and PbS_3(4) seem to exist, but fail to show up on thermal analysis.(5) Moreover, the polychalcogenides of the alkali metals and probably those of Ca, Sr, Ba and Ra can be prepared by reacting the elements or their salts in liquid ammonia, but some of them exist only in the solvent. Finally, we add that compounds such as CaS_4, CaS_5, etc., which are prepared from water solution have been omitted in Table 1, since they may exist only as hydrates.

Because S, Se and Te all have comparatively high electronegativities, we expect the phases

Table 1. *Polychalcogenides*

$\mathrm{LiS}^{(12)}$	$\mathrm{NaS}^{(13,14)}$	$\mathrm{KS}^{(13,14)}$	$\mathrm{RbS}^{(14,15)}$	$\mathrm{CsS}^{(14,15)}$	$\mathrm{BaS_2}^{(5)}$				$\mathrm{PbS_2}^{(4)}$
	$\mathrm{NaSe}^{(14)}$	$\mathrm{KSe}^{(14)}$	$\mathrm{RbSe}^{(14)}$	$\mathrm{CsSe}^{(14)}$					
	$\mathrm{NaTe}^{(11,14)}$	$\mathrm{KTe}^{(14)}$	$\mathrm{RbTe}^{(14)}$			$\mathrm{GaTe_3}^{(16)}$	$\mathrm{InTe_3}^{(9,17)}$		
		$\mathrm{K_2S_3}^{(13)}$	$\mathrm{Rb_2S_3}^{(14,15)}$	$\mathrm{Cs_2S_3}^{(14,15)}$	$\mathrm{BaS_3}^{(5)}$			$\mathrm{Tl_2S_3}$	$\mathrm{PbS_3}^{(4)}$
	$\mathrm{Na_2Se_3}^{(14)}$	$\mathrm{K_2Se_3}^{(14)}$	$\mathrm{Rb_2Se_3}^{(14)}$	$\mathrm{Cs_2Se_3}^{(14)}$	$\mathrm{BaSe_3}$?			$\mathrm{Tl_2Se_3}^{(8)}$	
		$\mathrm{K_2Te_3}^{(14)}$	$\mathrm{Rb_2Te_3}^{(14)}$					$\mathrm{Tl_2Te_3}^{(18)}$	
$\mathrm{LiS_2}$?	$\mathrm{NaS_2}^{(13,14)}$	$\mathrm{KS_2}^{(13,14)}$	$\mathrm{RbS_2}^{(14)}$	$\mathrm{CsS_2}^{(14)}$				$\mathrm{TlS_2}^{(5)}$	
	$\mathrm{NaCuS_4}^{(19)}$	$\mathrm{KCuS_4}^{(19)}$	$\mathrm{RbCuS_4}^{(19)}$	$\mathrm{CsCuS_4}^{(19)}$					
	$\mathrm{NaSe_2}^{(14)}$	$\mathrm{KSe_2}^{(20)}$	$\mathrm{RbSe_2}^{(14)}$	$\mathrm{CsSe_2}^{(14)}$					
	$\mathrm{Na_2S_5}^{(13)}$	$\mathrm{K_2S_5}^{(13)}$	$\mathrm{Rb_2S_5}^{(15)}$	$\mathrm{Cs_2S_5}^{(15)}$				$\mathrm{Tl_2S_5}^{(3)}$	
	$\mathrm{Na_2Se_5}?^{(20)}$	$\mathrm{K_2Se_5}^{(20)}$							
		$\mathrm{KS_3}^{(13)}$	$\mathrm{RbS_3}^{(14)}$	$\mathrm{CsS_3}^{(14,15)}$					
	$\mathrm{NaSe_3}^{(14)}$								
	$\mathrm{NaTe_3}^{(11)}$								

listed in Table 1 to be true polycompounds, so that in spite of the lack of structural data we can expect them to be non-metallic. This expectation is corroborated by magnetic measurements which invariably show that the compounds are diamagnetic. Moreover, the semiconducting character of a few compounds has been established directly by electrical measurements.

In $\mathrm{Cs_2S_5}^{(6)}$ $\mathrm{CsS_3}^{(7)}$ and $\mathrm{BaS_3}^{(5)}$ whose structures are known, the sulfur atoms form zig-zag chain molecules which again are indicative for non-metallic behaviour and it is interesting to note that the longer the S-molecules, the smaller is the gap between valence- and conduction band. It does, however, never fall below about 1·5 eV in the sulfides. As indicated by the change of colour on going from $\mathrm{Na_2S_2}$ to $\mathrm{Na_2SSe}$ the energy gap decreases also if some of the S atoms in the chains are substituted by Se atoms. A similar decrease is observed if in the alkali polysulfides half the cations are replaced by copper.

Because the structures of the compound $\mathrm{Tl_2S_3}$, $\mathrm{Tl_2Se_3}$ and $\mathrm{Tl_2Te_3}$ have not been fully determined, we do not know whether these non-metallic phases are polycompounds of univalent Tl or normal valence compounds of trivalent Tl. In any case, the non-metallic $\mathrm{TlS_3}$ as well as $\mathrm{Tl_2S_5}$, which is known to crystallize in two modifications, must be true polycompounds. BUBYREVA and OBUKHOV$^{(8)}$ reported on the semiconducting properties of mixed crystals of the type $\mathrm{Tl(Se, Te)_2}$, and $\mathrm{InTe_3}^{(9)}$ and $\mathrm{GaTe_3}^{(10)}$ are known to be semiconductors with predominantly covalent bonding.

Even though the structures of most polychalcogenides have not been determined in detail, we know that they are normally built up of chain molecules of the type mentioned earlier. The melting point of these molecular crystals therefore marks the temperature at which the weak Van der Waals forces holding the molecules together break up. The intramolecular bonds remain unaffected, so that in the liquid state the compounds retain their non-metallic properties. However, the energy gaps and the charge carrier mobilities will change on melting. Thus it is possible from the electrical measurement of Kraus and Glass(11) to deduce an energy gap of 1·3 eV for liquid $NaTe_3$, while a gap of 0·9 eV is found in solid $NaTe_3$.

b. *Polycompounds with group* VB *anions*

In addition to the azides which will not be considered here, polycompounds of phosphorus, arsenic and antimony are known. Most of the bismuth phases of similar composition, however, are not true polycompounds, but rather metallic alloy phases. In view of what was said in Section 2 about phases containing heavy anion formers, this is perhaps not surprising. It is surprising, however, that many among these metallic Bi phases are superconductors and we should add that their structures are completely different from those of the corresponding phosphorus, arsenic and antimony compounds.

In Table 2, possible Group VB phases $M^{(\mu)}_m X^{(\chi)}_x$ ($\chi = 3$) for which $m\mu = x(\chi-1)$ have been listed. This Table, as well as those given below, are arranged as follows: The crossed fields correspond to non-existing phases. A question mark indicates that the corresponding phase is likely to exist. Among the known phases those set in standard type are presumed to be nonmetallic, while the nonmetallic character of those in bold type has been established experimentally. Similarly, the phases marked in italics are likely to be metallic conductors, and the phases set in bold italics are known to have metallic properties.

Among the compounds of composition $M_2^{(1)}X^{(3)}$ only Cs_2Sb(21) has known electrical properties: From the temperature dependence of its resistivity this compound was found to be a semiconductor with an energy gap of 0·62 eV.

ZnSb and CdSb are the only representatives of the $M^{(2)}X^{(3)}$ compounds, whose properties have been investigated to any extent. Their semiconducting character was discovered by Boltaks(22) and by Justi and Lautz(23) and it was explained in terms of the formation of anion–anion bonds by Mooser and Pearson.(2) The corresponding Bi-compounds do not exist, but it is possible that the arsenides and phosphides form peritectically. If they are found, we expect them to be nonmetallic like MgP and MgAs. The alkaline earth bismuthides SrBi and BaBi reported by Shchukarev *et al.*(24,25) will most likely prove to be metallic.

Only two compounds are known for which $m\mu = x(\chi-1)$ and which contain cations of Group IVB, namely $SiAs_2$ and $GeAs_2$. Preliminary measurements at our laboratory(10) show that they are both semiconductors. We therefore expect the cations to be tetrahedrally surrounded by four arsenic atoms, while each arsenic atom should have an average of one arsenic and two germanium neighbours forming the basis of a trigonal pyramid. Recently these expectations were substantiated for $GeAs_2$ by Bryden(26) who in addition to a tetrahedral coordination of the Ge atoms by four As atoms found that half the As atoms have 3 Ge neighbours while the rest have one Ge and two As neighbours.

A number of Group VB phases are known for which $x(\chi-1) > m\mu > x(\chi-2)$. Thus Gnutzmann and Klemm(33) reported on the existence of K_3Bi_2, Rb_3Bi_2 and Cs_3Bi_2. Like all other Bi compounds these phases are expected to be metallic conductors. Moreover, Hg_3P_4(5) has been known for some time and from its non-metallic character—its colour is indicative of an energy gap of about 2 eV—we conclude that in this compound the P atoms form an average number $b_a = \frac{3}{2}$ of bonds with neighbouring P atoms. Such non-integral numbers of anion–anion bonds

Table 2. Group V *compounds for which* $m\mu = x(\chi-1)$

Li_2P?(27)	Na_2P?(27)	K_2P?			MgP(28)			ZnP?	CdP?	SiP_2?	GeP_2?
	Na_2As?	——			MgAs(29)			ZnAs?	CdAs?	**$SiAs_2$**(5)	**$GeAs_2$**(26,3
	——	——	Rb_2Sb?	**Cs_2Sb**(21)	——	SrSb(31)		**ZnSb**(22)	**CdSb**(23)	——	——
	——	——	***Rb_2Bi***(32)	***Cs_2Bi***(32)	——	***SrBi***(24)	***BaBi***(25)	——	——	——	——

are always brought about by the presence in a compound of structurally non-equivalent anions, rather than by resonating bonds. We therefore expect that in Hg_3P_4 half the P atoms have two Hg and one P neighbours each and that each of the remaining P atoms has one Hg and two P neighbours.

Finally we should mention here a series of compounds which have recently been prepared by KLEMM *et al.*, namely K_5As_4,(34) K_5Sb_4, Rb_5Sb_4, Cs_5Sb_4(35), K_5Bi_4, Rb_5Bi_4 and Cs_5Bi_4.(33) Since neither structural nor physical data on these phases are available, we can only guess that with the possible exception of the arsenide they will probably all prove to be metallic.

Table 3. Group V *compounds for which* $m\mu = x(\chi-2)$

LiP(44)	NaP?	KP?	RbP?	CsP?	BaP_2(5)	ZnP_2(43)	CdP_2(43)
LiAs(36)	**NaAs**(10)	**KAs**(35)	RbAs?	CsAs?	$BaAs_2$?	**$ZnAs_2$**(41,42,45)	**$CdAs_2$**(42)
LiSb(10)	**NaSb**(36,38)	**KSb**(37,39)	RbSb(32,34)	CsSb(21,34)		——	——
LiBi(40)	***NaBi***(40)	——	——	——	——	——	——

In Table 3 we have listed Group VB phases for which $m\mu = x(\chi-2)$. The saturation criterion requires that in the non-metallic representatives of these compounds each anion has two anion neighbours. We therefore expect to find in the $M^{(1)}X^{(3)}$ polycompounds ring and/or chain molecules of the type:

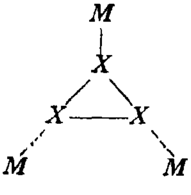

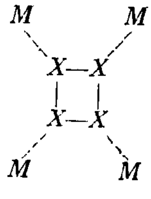

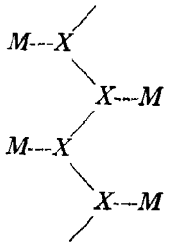

In LiAs,(36) NaSb,(36) and KSb(37) the anions do indeed form spiral chains similar to those observed in Se and Te. The cations are distributed between the chains in such a way that a rather dense packing results in which each atom has six neighbours of the other kind located at the corners of a distorted octahedron. This coordination is indicative of a strongly ionic component in the M–X bonding. So far semiconducting properties were found experimentally in NaSb,(38) KSb(39) and CsSb,(23) but without doubt all the other P, As and Sb compounds of this type will also prove to be semiconductors. This has since been verified for LiSb and NaAs.(10) The corresponding Bi compounds crystallize in the CuAu type of structure in which the two components occupy in ordered fashion the sites of a somewhat distorted cubic close packing. Saturated bonds cannot therefore form in these materials: They are known to be metallic and at low temperatures they actually become superconducting.(40)

Among the $M^{(2)}X_2^{(3)}$ type of compounds $ZnAs_2$(41) and $CdAs_2$(42) are known to be semiconductors. Moreover, the colour of the corresponding phosphides(43) indicates that they too are non-metallic with an energy gap of the order of 2 eV. The crystal structures of these compounds have not been fully determined, but we expect that the component atoms form sp^3 bonds. If this is indeed the case, then the saturation criterion requires that the unit cell must contain an even number Z of formula units and that the co-ordination of the atoms is as follows:

Number per unit cell	Atom	Neighbours
Z	Zn	4 P
2 Z	P	2 Zn
		2 P

Since BaP_2 and $BaAs_2$ are considerably more heteropolar than the above compounds, we expect to find an octahedral coordination here. However, we cannot *a priori* rule out the possibility of an eight-fold cubic coordination of Ba, such as is observed in the structure of BaS_3. To characterize the coordination configuration in these Ba compounds, we therefore define the bond number n, i.e. the ratio between the number of cation valence electrons and the cation coordination number and obtain, e.g. for BaP_2:

Number per unit cell	Atom	Neighbours
Z	Ba	$\frac{2}{n}$ P $n = \frac{1}{3}, \frac{1}{4}$
2 Z	P	$\frac{1}{n}$ Ba
		2 P

Very little is known about compounds with even higher anion excess. Among the phases of type $M_2^{(1)}X_3^{(3)}$ we know that Au_2P_3 is a semiconductor.(46) The $M^{(2)}X_3^{(3)}$ type of compounds $CaBi_3$,(40) $SrBi_3$(47) and $BaBi_3$(47) are all superconductors. They crystallize in the Cu_3Au type of structure which like the CuAu structure we met in LiBi and NaBi is characteristic of many alloy phases. The similarly composed BaP_3, however, is expected to be non-metallic, because of the high electronegativity of phosphorus. If this is indeed the case, then its unit cell will contain an even number of formula units and the coordination configurations of the components will be of the form:

Number per unit cell	Atom	Neighbours
Z	Ba	$\frac{2}{n}$ P_I $n = 1, \frac{1}{2}, \frac{1}{3}$
2 Z	P_I	$\frac{1}{n}$ Ba
		1 P_I
		1 P_{II}
Z	P_{II}	2 P_I
		1 P_{II}

Whether the semiconducting(10) SnP_3 contains bivalent tin, so that it belongs to the $M^{(2)}X_3^{(3)}$ type of compounds discussed here, or whether it contains quadrivalent tin will be known only when its structure has been determined.

Proceeding to the discussion of the phases for which $m\mu = x(X - \frac{5}{2})$—they are listed in Table 4—we note first of all that the $M^{(1)}X_2^{(3)}$ type of bismuthides are metallic. Indeed KBi_2, $RbBi_2$ and $CsBi_2$ which are isomorphous with Cu_2Mg

Table 4. Group V compounds for which $m\mu = x(X - \frac{5}{2})$

NaP_2?	KP_2?			CuP_2(46,49)	AgP_2(46,49)	MgP_4?	CaP_4?	ZnP_4?	CdP_4(48)
$NaAs_2$?	**KAs_2**(35)	$RbAs_2$?	$CsAs_2$?	$CuAs_2$?	$AgAs_2$?	$MgAs_4$(50)	$CaAs_4$(50)	$ZnAs_4$?	$CdAs_4$?
—	**KSb_2**(34)	$RbSb_2$(34)	$CsSb_2$(34)	—	—	—	—	—	—
—	***KBi_2***(40)	***$RbBi_2$***(32)	***$CsBi_2$***(32)	—	—	—	—	—	—

become superconducting at low temperatures.(40) They thus represent yet another example of an interesting, but not fully understood phenomenon: Many a bismuthide whose chemical composition corresponds to that of a polycompound of a lighter Group VB element is superconducting.

The semiconducting character of CuP_2 and AgP_2 has been corroborated(46) by measurements of electrical resistivity. In thin layers KAs_2 is transparent and its red colour indicates an energy gap of the order of 2 eV.(10)

The structure of the non-metallic $M^{(2)}X_4^{(3)}$ type of compound CdP_4 was determined by KREBS *et al.*(48) According to their findings each Cd atom is surrounded by six P atoms which lie at the corners of a distorted octahedron. Three different Cd–P distances were observed, namely $\text{Cd–P}_\text{I}' = 2{\cdot}64$ Å, $\text{Cd–P}_\text{I}'' = 2{\cdot}74$ Å and $\text{Cd–P}_\text{II} = 2{\cdot}94$ Å. They can be explained in terms of a resonance among the structures $Cd^{4-}P_4^{+}$, $Cd^{2-}P_2P_2^{+}$, $Cd^0P_4^0$ and $Cd^{2+}P_2P_2^{-}$. The P atoms have a distorted tetrahedral neighbourhood, so that the complete coordination configurations in CdP_4 can be characterized as follows:

Number per unit cell	Atoms	Neighbours
2	Cd	4 P_I 2 P_II
4	P_I	2 Cd 2 P_II
4	P_II	1 Cd 2 P_I 1 P_II

The somewhat unexpected six-fold coordination of Cd in this compound clearly illustrates how difficult it is to make reliable predictions about coordination by invoking the saturation criterion. In fact, this criterion can serve as a guide only and the actual coordination configurations will always have to be determined by other means.

Of the remaining phases listed in Table 4 probably all the phosphides, arsenides and antimonides are non-metallic. In the case of KSb_2 we were able to verify this by resistance measurements.(10)

The more the anion content of a phase exceeds that of the corresponding normal valence compound, the more likely it is that this phase is non-metallic. All the following phosphides therefore are non-metallic: Na_2P_5, K_2P_5, Rb_2P_5, Cs_2P_5(51) BaP_5, SnP_5, PbP_5, NaP_3(5), CuP_3, AgP_3, AuP_3,(49) $ZnPbP_{14}$, $CdPbP_{14}$ and $HgPbP_{14}$.(52) The diamagnetic susceptibility(49) observed in AgP_3 and AuP_3 would seem to support this view. Moreover, the colours of all the other compounds (except that of CuP_3) are indicative for their non-metallic character.

c. *Polycompounds with Group* IVB *anions*

In Tables 5 and 6 we have listed compounds containing Group IVB elements for which $m\mu = x(X-2)$ and $m\mu = x(X-3)$ respectively. The crystal chemistry of some of these compounds is of interest, because it illustrates rather clearly a phenomenon which is frequently met in phases whose electronegative components lie in Groups IIIB–VIB. The composition of these phases is such that if all the valence electrons of the electropositive partners were transferred to the electronegative ones, the latter would acquire the electron-configurations corresponding to the next or the one but next higher Group. As a consequence, the sublattices of the electronegative components

Table 5. *Group* IV *compounds for which* $m\mu = x(X-2)$

Li_2Si(5)			$CaSi$(5)	$SrSi$(56)	$BaSi$(5)
Li_2Ge?			$CaGe$(55)		
Li_2Sn(5)	Na_2Sn(5)	K_2Sn(5)	$CaSn$(55)		
—	Na_2Pb(5)	K_2Pb(5)	$CaPb$(55)	$SrPb$?	$BaPb$(5)

Table 6. *Group* IV *compounds for which* $m\mu = x(X-3)$

—	NaSi(59)	KSi(53)	RbSi(53)	CsSi(53)	*CaSi*$_2$(5)	*SrSi*$_2$(56)	**BaSi**$_2$(57)
	NaGe(59)	KGe(53)	RbGe(53)	CsGe(53)	*CaGe*$_2$(5)		
LiSn(5)	*NaSn*(5)				—		
LiPb(56)	*NaPb*(5)	*KPb*(60)	*RbPb?*	*CsPb?*	—		

in these phases correspond to or are closely related to the structures of the elements in the next or one but next higher Group (see also BUSMANN(53)).

The first compounds found to exhibit this phenomenon are the NaTl type of phases in which the Group III atoms occupy the sites of a diamond structure which is normally found only among the Group IV semiconductors. From the experimentally established metallic properties(54) of these compounds it follows that the bonding cannot be saturated and the charge transfer towards the IIIB atom therefore remains incomplete. Saturated bonds are, however, found in the semiconducting Group VB compounds LiAs, NaSb and KSb which were discussed earlier. The chain molecules found in these compounds which are reminiscent of the chains in Se and Te, are again met in the Group IVB phases CaSi,(5) CaGe,(55) CaSn,(55) and SrSi.(56) However, instead of spiraling the chains here are planar, so that the coordination of the atoms in these calcium and strontium compounds differs considerably from that in the LiAs type of phases. In particular, each Ca has not only seven Si, but also six Ca neighbours, which nearly touch each other. Such a coordination is possible only if the component atoms remain nearly neutral. It is likely therefore that the charge transfer which would be necessary to make the compounds semiconductors does not in fact occur: We expect CaSi, CaGe, CaSn and SrSi to be metallic.

Resemblences of the anion sublattices to the structures of the VB elements are found in KSi, RbSi, CsSi, KGe, RbGe and CsGe(53) on the one hand, and in CaSi$_2$ and CaGe$_2$ on the other hand. In the first family the Group IVB atoms form tetrahedra similar to the P_4 tetrahedra met in the white modification of phosphorus. Each tetrahedron is surrounded by a shell of alkali metal atoms, so that one can describe the KSi type of structure as being built up of isolated $(X_4)^{4-}$ tetrahedra, which are screened from one another by interstitially located A^+ ions. As was to be expected from this structure, preliminary measurements of the electrical resistivity of KGe(10) showed that this compound is non-metallic. It should be added here that while the structure of NaPb(5) is not isomorphous with that of KSi, its anions nevertheless form similar tetrahedra. The electrical properties of NaPb are, however, not known.

In the *C*12 type of structure of CaSi$_2$ and CaGe$_2$ the Si and Ge atoms are arranged in puckered layers similar to the double layers found in the structure of As, Sb and Bi. The Ca atoms form close packed layers which separate successive Si and Ge layers. In addition to seven Si or Ge neighbours each Ca atom therefore acquires six Ca neighbours. This coordination of the Ca atoms which is reminiscent of that found in the CaSi type of phases and the relatively short Ca–Ca distances (3·88 Å in CaSi$_2$, 3·91 Å in GaGe$_2$, single bond diameter of Ca: 3·48 Å) would seem to indicate metallic or semimetallic behaviour. It is not surprising, therefore, that we have found metallic conduction in polycrystalline samples cut from a technical grade CaSi$_2$ ingot.* We should, however, point out that BaSi$_2$ was reported to be a semiconductor by SAMSONOV and NESHPOR.(57)

The structural phenomenon discussed above seems to provide the only mechanism by which Group IVB elements can form polyanions. However, we have seen that even some of the phases exhibiting this phenomenon are metallic and hence not true polycompounds. The number of Group IVB polycompounds is therefore rather small. Indeed it seems likely that all the other materials listed in Tables 5 and 6 are alloy phases. Thus Li_2Sn, BaPb and LiSn have been shown experimentally to have metallic conductivities.(5) The metallic character of LiPb follows immediately from its structure in which no polyanion formation is observed. In fact, at low temperature LiPb crystallizes in a rhombohedrally distorted CaCl type of structure.(58) Above 214°C the distortion disappears. Each component thus obtains eight neighbours of the other kind, i.e. a coordination which is frequently met in alloys. Finally we add that in view of the metallic character of CaSi, CaGe and CaSn it is very probable that CaPb too will prove to be metallic even though it has a different structure.(55)

---

* Several large ingots of CaSi$_2$ were generously put at our disposal by the Lonza-Werke in Bodio, Switzerland.

We should also mention here a number of Group IVB compounds which are not listed in Tables 5 and 6. Among the $M^{(1)}X_2^{(4)}$ phases $LiSn_2$, $NaSi_2$, $NaSn_2$, $NaPb_2$, KSn_2 and KPb_2 only $NaSi_2$ might prove to be non-metallic (it was reported to be soluble in water!). However, its existence has not been established unequivocally. $LiSn_2$ on the other hand has been shown by conductivity measurements(5) to be metallic and the $MgZn_2$ type of structure of KPb_2 leaves no doubt about the metallic character of this phase. The $M^{(1)}X_3^{(4)}$ phases $CaSn_3$, $NaPb_3$, $CaPb_3$ and $SrPb_3$ all crystallize in the Cu_3Au type of structure in which no polyanions form. The bonding in these phases remains unsaturated and they must be metallic. It is likely that $NaSn_3$, $SrSn_3$, $BaSn_3$ and $BaPb_3$ have the same structure. In any case, it is virtually certain that they are metallic. Li_3Pb is of some interest, because it is isomorphous with the semiconducting Li_3Bi.(5,9) Since Li_3Pb contains one valence electron less than Li_3Bi, it must be metallic. However, if one of the Li atoms is replaced by Mg, then a normal valence compound results: Li_2MgPb is indeed a semiconductor.

4. COMPOUNDS FOR WHICH $m\mu > x\chi$

We have seen in Section II that complete saturation of the valences is possible in compounds of composition $M_m^{(\mu)}X_x^{(x)}$ for which $m\mu > x\chi$ only if bonds form between neighbouring cations. The non-metallic representatives of these compounds therefore must contain cation molecules. Moreover, it should be noted that if the valence shells of the cations contain unoccupied orbitals, then the cation molecules must be finite if non-metallic properties are to result (see, e.g. MOOSER and PEARSON(2)). This last condition is of particular importance in the case of compounds containing transition elements,(61) since in these compounds the *d* shells of the transition elements frequently remain unfilled.

The bonding between the like atoms within the cation molecules can obviously not be very ionic. Only elements with a strong tendency to form covalent bonds can therefore act as cations They are the transition elements whose compounds will be discussed in a later paper and the B elements. Within the B elements the tendency to form covalent bonds increases towards the right of the Periodic Table. It is not surprising therefore that only a few compounds are known in which atoms lying to the left of the Zintl border form cation molecules. In all the other compounds containing cation molecules, these molecules are made up of the anion formers of Groups IVB and VB. In view of this, as well as of the fact that the M–M and M–X bonding in all these compounds is predominantly covalent, it might be better to distinguish between the more and the less electronegative partners, rather than between anions and cations.

The number of orbitals available for bond formation in the Group VB and VIB elements is so small that the lighter compounds formed between them usually crystallize in molecular structures. Such structures have indeed been reported for the non-metallic phases P_4S_5,(62) P_4S_3 and P_4Se_3,(63) and similar structures are expected to be met in P_4S_2Se, P_4SSe_2 and P_4Te_3. The mineral "Realgar" of composition AsS is non-metallic and has an energy gap of the order of 2 eV. It contains puckered rings similar to those found in As_4S_4 vapour in which As and S atoms alternate and the As atoms on opposite sides of the rings are linked by bonds. The corresponding AsSe(64) is a vitreous semiconductor, but AsTe is unknown.

As the atomic weight of the components increases, the *d* orbitals of their valence shells become available for bond formation (see Section II). Instead of saturated bonds, metallic bonds will form: The heavier V–VI compounds show metallic properties and their structures are characterized by relatively high coordination numbers. Thus BiTe is known to crystallize in a rocksalt structure.(65) Its metallic properties, as well as those of SbTe, have been established experimentally by electrical(60,66,67) and magnetic measurements(67) carried out on the systems Bi–Te and Sb–Te. Above 422°C BiSe also crystallizes in the rocksalt structure.(65) Unfortunately, the structure of its low temperature modification is not known. While MOOSER and PEARSON(9) reported metallic conduction in this compound, HASHIMOTO(69) found it to be a semiconductor with an energy gap of 0·4 eV. It seems likely therefore that the different authors did not look at the same modification. If so, we expect the rocksalt type of phase to be metallic and the low temperature modification semiconducting. Moreover, in the semiconducting modification the saturation of the bonds should be the result of the formation of Bi_2 molecules.

Table 7. Chalcogenides for which $m(\chi-1) = x \cdot \chi$

AsS(5)	——	——
AsSe(64)	SbSe?	BiSe(65,70)
	SbTe(71)	***BiTe***(65)

The Si and Ge compounds listed in Table 8 are all semiconductors. In these compounds each Group IV atom therefore must have one neighbour of the same kind and the unit cells must contain an even number of formula units. Moreover, the tendency of Si and Ge to form tetrahedral bonds suggests that in addition to the like neighbour each Si and Ge atom should have three neighbours of the other kind. Each Group V atom must then acquire three Si or Ge neighbours. The recent determination of the crystal structure of GeAs by BRYDEN(26) has in fact confirmed these expectations.

Table 8. Group V compounds for which $m(\mu-1) = x \cdot \chi$

SiP(5)	GeP(5)	SnP(27)
SiAs(30)	**GeAs**(26,30)	*SnAs*(5)
——	——	*SnSb*(5)
——	——	*SnBi*(73)

Of the Sn compounds listed in Table 8 only SnP might prove to be semiconducting. All the others are metallic which in view of the rocksalt structure of SnAs and the slightly deformed rocksalt structure of SnSb is not surprising.

The non-metallic III–VI compounds listed in Table 9 are of some interest, because two different mechanisms of valence saturation are operative in these materials. Thus in the Ga compounds and in InS and InSe a charge transfer of the type Ga^-S^+ occurs which results in electron configurations similar to those found in GeAs. It is not surprising therefore, that the structures of these compounds are very similar to that of GeAs: The Group III atoms have one neighbour of the same kind and three neighbours of the other kind which together form a slightly distorted tetrahedron. The chalcogenes, on the other hand, each have three Group III neighbours. (For a more detailed discussion of the structures of GaS and GaSe see, e.g. BASINSKI *et al.*(74).) While one can thus clearly observe M_2 molecules in these materials, this is no longer the case in InTe and the Tl compounds. In fact, the *C*37 type of structure of these compounds reveals that here the Group III atoms are present in two different valence states. Their formulae should therefore correctly be written in the form $Tl^+(Tl^{III}S_2)^-$.

Table 9. Group III *chalcogenides for which* $m(\mu-1) = x \cdot \chi$

GaS(74)	**InS**(59)	**(TlS)**(5)
GaSe(74)	**InSe**(17,30)	(TlSe)(5)
GaTe(30)	(InTe)(17)	(TlTe)(5)

Localized cation–cation bonds of the type found in the above Ga and In compounds are met also in HgCl, HgBr and HgI. These diamagnetic compounds crystallize in non-metallic structures which are built up of linear molecules of the type halogen–Hg–Hg–halogen.

In phases containing good metals, i.e. alkali metals, rare earths and Cu, Ag or Au localized M–M bonds do not form so that the inequality $m\mu > x\chi$ here always indicates metallic properties. However, only few compounds between anion formers and good metals are known in which the metal content exceeds that corresponding to the normal valence compound. Ag_2F which crystallizes in the CdI_2 type of structure is an example. As indicated by measurements of electrical conductivity(75) and Hall coefficient(76) the (non localized) bonds between the silver atoms of adjacent Ag_2F layers do indeed lead to metallic properties in this compound.

5. CONCLUSION

In this paper an attempt was made to review the data available at present on compounds which do not obey normal valence rules and, starting from these data, to make predictions about their electrical properties. The inhomogeneity of this review clearly reflects the lack of knowledge of this interesting family of compounds. Thus we are far from any comprehensive understanding of conditions which lead to the formation of anomalously composed phases. Moreover, their crystal chemistry is only just emerging, even though (or perhaps because) some of the most extraordinary structures are met here. And finally, their physical properties, rather than being based on experimental investigation, still largely form the subject of speculation. Anomalously composed phases therefore represent a large and challenging field to the solid state physicist and if our review should succeed in stimulating interest in this field, it will have reached its goal.

REFERENCES

1. Goodman C. H. L., *J. Phys. Chem. Solids* **6**, 305 (1958).
2. Mooser E. and Pearson W. B., *J. Electron.* **1**, 629 (1956); *Progr. Semicond.* 5, 103 (1959).
3. Frasson E. and Scatturin V., *Chem. Abstr.* **52**, 9706a (1958).
4. Riolo C. B. and Soldi T., *Gazz. chim. ital.* **86**, 1162 (1956).
5. For reference see Hansen M., *Constitution of Binary Alloys*, McGraw-Hill New York (1958); or *Gmelins Handbuch der anorganischen Chemie*, 8 Auflage, Verlag Chemie, Weinheim (1926).
6. Abrahams S. C., Grison E. and Kalnajs J., *J. Amer. chem. Soc.* **74**, 3761 (1951).
7. Abrahams S. C. and Grison E., *Acta Cryst.* **6**, 206 (1953).
8. Bubyreva N. S. and Obukhov A. P., *Russ. J. inorg. Chem.* **4**, 53 (1959).
9. Mooser E. and Pearson W. B., *Phys. Rev.* **101**, 492 (1956).
10. Hulliger F., unpublished.
11. Kraus C. A. and Glass S. W., *J. phys. Chem.* **33**, 984 (1929).
12. Pearson T. G. and Robinson P. L., *J. chem. Soc.* **1931**, 413.
13. Fehér F. and Berthold J. J., *Z. anorg. Chem.* **275**, 241 (1954).
14. Klemm W., Sodomann H. and Langmesser P., *Z. anorg. Chem.* **241**, 281 (1939).
15. Fehér F. and Naused K., *Z. anorg. Chem.* **283**, 79 (1956).
16. Newmann P. C., Brice J. C. and Wright H. C., *Philips Res. Rep.* **16**, 41 (1961).
17. Sugaike S., *Miner. J.* (*Sapporo*) **2**, 63 (1957).
18. Rabenau A., Stegherr A. and Eckerlin P., *Z. Metallk.* **51**, 295 (1960).
19. Peyronel G. and Pacilli E., *Gazz. chim. ital.* **76**, 265 (1946).
20. Bergstrom F. W., *J. Amer. chem. Soc.* **48**, 146 (1926).
21. Miyake K., *J. appl. Phys.* **31**, 76 (1960).
22. Boltaks B. I. and Zhuse V. P., *Izv. akad. nauk S.S.S.R., Ser. Fiz.* **16**, 155 (1952).
23. Justi E. and Lautz G., *Z. Naturf.* **7a**, 602 (1952).
24. Shchukarev S. A., Morozova M. P., Kan K.-Y. and Kokosh G. V., *J. gen. Chem. U.S.S.R.* **26**, 1705 (1956).
25. Shchukarev S. A., Morozova M. P., Kan K.-Y. and Sharov V. T., *J. gen. Chem. U.S.S.R.* **27**, 321 (1957).
26. Bryden J. H., *Acta Cryst.* **15**, 167 (1962) and private communication.
27. Evers E. C., *J. Amer. chem. Soc.* **73**, 2038 (1951).
28. Levina M. E. and Safonova S. A., *Chem. Abstr.* **51**, 1753g (1957).
29. Klemm W., *Angew. Chem.* **62**, 133 (1950).
30. Schubert K., Dörre E. and Günzel E., *Naturwissenschaften* **41**, 448 (1954).
31. Shchukarev S. A., Morozova M. P. and Kan K.-Y., *J. gen. Chem. U.S.S.R.* **27**, 1803 (1957).
32. Zhuravlev N. N., Zhdanov G. S. and Kuzmin R. N., *Sov. Krist.* **5**, 532 (1961).
33. Gnutzmann G. and Klemm W., *Z. anorg. Chem.* **309**, 181 (1961).
34. Dorn F. W. and Klemm W., *Z. anorg. Chem.* **309**, 189 (1961).
35. Dorn F. W., Klemm W. and Lohmeyer S., *Z. anorg. Chem.* **309**, 204 (1961).
36. Cromer D. T., *Acta Cryst.* **12**, 36, 41 (1959).
37. Busmann E. and Lohmeyer S., *Z. anorg. Chem.* **312**, 53 (1961).
38. Ugai Ya A. and Vigutova T. N., *Sov. Phys. Solid State* **1**, 1635 (1960).

39. Suhrmann R. and Kangro C., *Naturwissenschaften* **40**, 137 (1953).
40. Alekseevskii N. E., Brandt N. B. and Kostina T. I., *Izv. Akad. Nauk S.S.S.R. Ser. Fiz.* **16**, 233 (1952).
41. Fritsche C., *Ann. Phys. Lpz.* **17**, 94 (1955).
42. Turner W. J., Fischler A. S. and Reese W. E., *Phys. Rev.* **121**, 759 (1961).
43. Stackelberg M. V. and Paulus R., *Z. phys. Chem.* **B28**, 427 (1935).
44. Maak I. and Rabenau A., *Angew. Chem.* **72**, 268 (1960).
45. Senko M. E., Dunn H. M., Weidenborner J. and Cole H., *Acta Cryst.* **12**, 76 (1959).
46. Juza R. and Bär K., *Z. anorg. Chem.* **283**, 230 (1956).
47. Matthias B. T. and Hulm J. K., *Phys. Rev.* **87**, 799 (1952).
48. Krebs H., Müller K. H. and Zürn G., *Z. anorg. Chem.* **285**, 15 (1956).
49. Haraldsen H., *Z. anorg. Chem.* **240**, 337 (1939).
50. Pigon K., *Helv. Chim. Acta* **44**, 30 (1961).
51. Hackspill L. and Bossuet R., *C.R. Acad. Sci. Paris* **154**, 209 (1912).
52. Krebs H. and Ludwig T., *Z. anorg. Chem.* **294**, 257 (1958).
53. Busmann E., *Naturwissenschaften* **47**, 82 (1960); *Z. anorg. Chem.* **313**, 90 (1961).
54. Junod P. and Mooser E., *Helv. Phys. Acta* **29**, 195 (1956).
55. Eckerlin P., Meyer H. J. and Wölfel W., *Z. anorg. Chem.* **281**, 322 (1955).
56. Weiss A. and Rocktäschel G., *Z. anorg. Chem.* **316**, 231 (1962).
57. Neshpor V. S. and Samsonov G. V., *Sov. Phys.-Solid State* **2**, 1966 (1961).
58. Zalkin A. and Ramsey J., *J. Phys. Chem.* **61**, 1413 (1957).
59. Schäfer R. and Klemm W., *Z. anorg. Chem.* **312**, 214 (1961).
60. Shoikhet D. N., Morachevskii A. G. and Alabyshev A. F., *Russ. J. inorg. Chem.* **4**, 728 (1959).
61. Hulliger F., *Helv. Phys. Acta* **32**, 615 (1959).
62. Van Houten S. and Wiebenga E. H., *Acta Cryst.* **10**, 156 (1957).
63. Keulen E. and Vos A., *Acta Cryst.* **12**, 323 (1959).
64. Krebs H. and Schultze-Gebhardt F., *Acta Cryst.* **8**, 412 (1955).
65. Semiletov S. A., *Trud. inst. krist., akad. nauk S.S.S.R.* **10**, 76 (1954); *Chem. Abstr.* **50**, 1403H (1956).
66. Haken W., *Ann Phys. Lpz.* **32**, 291 (1910).
67. Trabacchi G. C., *Nuovo Chim.* **9**, 95 (1915).
68. Honda K. and Endo H., *J. Inst. Met.* **37**, 29 (1927).
69. Hashimoto K., *Mem. Fac. Sci. Kyûsyû Univ.* Ser. B, **2**, 141 (1958).
70. Abrikosov N. Kh., Bankina V. F. and Kharitonovich K. F., *Russ. J. inorg. Chem.* **5**, 978 (1960).
71. Abrikosov N. Kh., Poretskaya L. V. and Ivanova I. P., *Russ. J. inorg. Chem.* **4**, 1163 (1959).
72. Katz G., Kohn J. A. and Broder J. D., *Acta Cryst.* **10**, 607 (1957).
73. Bridgman P. N., *Proc. Amer. Acad. Arts Sci.* **82**, 101 (1953).
74. Basinski Z. S., Dove D. B. and Mooser E., *Helv. Phys. Acta* **34**, 373 (1961).
75. Hilsch R., Minnigerode G. V. and Wartenberg H. V., *Naturwissenschaften* **44**, 463 (1957).
76. Trzebiatowski W. and Rozyczka J., *Roczn. Chem.* **32**, 183 (1958).

J. Phys. Chem. Solids Pergamon Press 1963. Vol. 24 pp. 297–307. **Printed in Great Britain.**

THE PARAMAGNETIC SUSCEPTIBILITY OF SODIUM METAL*

R. T. SCHUMACHER† **and W. E. VEHSE**‡

Department of Physics, Carnegie Institute of Technology,
Pittsburgh 13, Pennsylvania

(*Received* 20 *August* 1962)

Abstract—The remeasurement of the conduction electron spin susceptibility in sodium metal is reported. The result, $\chi_p = (1{\cdot}13 \pm 0{\cdot}05) \times 10^{-6}$ cgs volume units at 20°K, represents a substantial increase over the previously reported value. One major consequence of the remeasured value is that the conduction electron diamagnetism inferred from the present results combined with measurements of the total susceptibility is in substantial agreement with theoretical expectations. The present results, combined with the Knight shift, imply $\xi = P_A/P_F = 0{\cdot}60$, which is somewhat smaller than calculated values. Measurements were also made at 77°K and 4·2°K, and the results are temperature independent within experimental error.

1. INTRODUCTION

THE contribution of the conduction paramagnetism to the total magnetic susceptibility of a metal may be isolated and measured by comparing the intensity of the spin resonance of the conduction electron system with the intensity of the nuclear resonance in the same sample in the same apparatus. The first measurement of χ_p for sodium using this technique was reported by SCHUMACHER and SLICHTER.(1) The reader is referred to that paper for a detailed discussion of the principle of the method, and for the rigorous derivation of the working relation

$$\chi_p = \chi_n \frac{A_e}{A_n} \frac{\gamma_e}{\gamma_n} \tag{1}$$

In (1) χ_p is the conduction electron paramagnetic susceptibility, γ_e and γ_n the electron and nuclear gyromagnetic ratios, and A_e and A_n are respectively the areas under the electron and nuclear resonance absorptions at constant frequency. χ_n, the nuclear susceptibility, is given by the Langevin–Debye formula:

$$\chi_n = N \frac{\gamma_n^2 \hbar^2 I(I+1)}{3kT} \tag{2}$$

The value of χ_p reported in (1) was in approximate agreement with the calculation of χ_p by PINES.(2) However, when χ_p was combined with measurements of the total susceptibility, χ_t, and with reasonable estimates of the ion core diamagnetism, χ_{ion}, the best value of the conduction electron diamagnetism, χ_D, seemed to be zero. This result seemed strange and physically unjustifiable, and consequently the present remeasurement of χ_p was undertaken. In addition, measurements by FELDMAN and KNIGHT(3) of the temperature dependence of the Knight shift in sodium revealed an anomalous decrease in the Knight shift of about 3 per cent between 77°K and 20°K. It was originally hoped the precision of the present measurement of χ_p would be sufficient to detect a comparable variation, if it occurred, in χ_p. Although we have not been able to perform our measurement with the precision required to reveal or reject conclusively a similar temperature

---

[*] Supported by the National Science Foundation. Taken from a thesis submitted by W. E. Vehse in partial fulfillment of the requirements for the Ph.D. degree. The results have been reported at the International Conference on Magnetism and Crystallography (*J. phys. Soc. Japan*, to be published).

[†] Alfred P. Sloan Foundation Fellow.

[‡] Now at Physics Department, West Virginia University, Morgantown, W. Va.

dependence in χ_p, we will describe some measurements of the temperature dependence of χ_p between 77 and 20°K in this paper.

Since the principal result of our investigation has been to revise the first value⁽¹⁾ of χ_p, we will describe in some detail our measurement technique and particularly the analysis of the data, since it is in the treatment of the experimental data that the present measurement most differs from the one previously reported. We will also describe sample preparation, and some experimental anomalies associated with different preparation techniques.

2. EXPERIMENTAL DETAILS

A. The apparatus

The measurements were performed at approximately 10 Mc/s on electronic apparatus nearly identical to that described in Ref. 1. The applied field for the nuclear resonance, about 10,000 G, was supplied by a Varian 12 in. electromagnet system. The low field (~ 3 G) for the conduction electron resonance was supplied by a 15 in. diameter Helmholtz pair. The oscillator, sample coil, and dewar assembly were moved on a simple track between the magnet and the Helmholtz coils without disturbing the operating conditions of the electronic circuits. The only innovations over the apparatus previously described⁽¹⁾ was to place the receiver well away from the magnetic fields. The signal was coupled to the receiver by a quarter wavelength 75 Ω cable tapped down on the sample coil to maximize the signal-to-noise ratio. A detailed analysis of the "Q-meter" circuitry used in this experiment is given by ESTLE, HART and WHEATLEY.⁽⁴⁾

The resonances were photographed directly from the oscilloscope as was done for the first measurements of the lithium susceptibility.⁽⁵⁾ For the nuclear resonance a triangular wave modulation field of 10 G peak-to-peak at frequencies between 5 c/s and 15 c/s was superimposed on the d.c. field H_0. A sweep of the same shape and frequency going from −20 to +20 G was applied by the Helmholtz pair for observation of the electron resonance.

Fastened to each side of the tail of the outer dewar were two pickup coils consisting each of 2200 turns of No. 40 copper wire. The signal from these coils, *proportional to* dH_0/dt, was integrated by a transistorized Miller integrating circuit followed by a single stage amplifier which applied the signal to a helipot. The voltage derived from one end and the center tap of the helipot was applied to the horizontal axis of the oscilloscope, thus providing a drive proportional to the time-varying part of H_0, as required. The relative compressions of the horizontal scales for the electron and nuclear resonances could be read directly from the helipot readings.

The integrator was designed so that the error angle at 1 c/s was 0·1°. Checks on the integration were performed by comparing the integrated output of the pickup coils with the current through the Helmholtz pair over a wide range of frequencies. Linearity of the helipot was also carefully checked. The output of the integration where the pickup coils were between the magnet pole faces was checked against the output in the field of the Helmholtz pair through calibration of the field sweep by means of the narrow proton resonance in liquid H_2 in a high field and by means of the narrow electron resonances in the low field. No disagreement was observed.

In order to assure the resonance line shapes were being faithfully represented on the oscilloscope it is necessary to choose the field sweep rate so that transient effects do not distort the displayed signal. A safe criterion is that the length of time spent scanning the resonance must be long compared to the decay time of the transverse component of magnetization. This requirement may be expressed $dH_0/dt \ll \gamma_n(\delta H)^2$ for the nuclear resonance where δH is the half width of the nuclear resonance at half maximum. We chose dH_0/dt to be less than 2 per cent of the right hand side of the inequality. No transient effects were observed below field sweep rates four times those actually employed. A similar requirement must be satisfied for the electron resonance, except γ_e replaces γ_n in the inequality. Since $\gamma_e/\gamma_n \cong 2500$ for sodium, it turns out in practice to be much easier to satisfy the inequality for the electron resonance.

B. Sample preparation

The samples must satisfy three general requirements. The individual pieces of metal making up the sample must have at least one dimension small compared to some effective skin depth. The samples must be free of impurities which would either contribute to the strength of the observed resonances or which would appreciably broaden the electron resonance lines by shortening the electron spin-lattice relaxation time T_{1e}. Finally there must be sufficient metallic density to give a measurable signal.

The first requirement is in order to insure the r.f. field throughout the sample is uniform. In practice we used spherical particles. Particle sizes sufficient to guarantee a uniform r.f. field were determined empirically. Below 20°K our samples are in the anomalous skin effect region. The problem of the resonance line shape has not been solved, to our knowledge, for the case that all three dimensions of the sample are less than the mean free path. We found that our resonances were undistorted by size effects as long as the size of the particles was much less than the mean free path, which is 20μ at 20°K. Thus our acceptable samples had particles from 2μ to 4μ in diameter. At 77° the classical skin depth is 14μ, and it proved to be an easy matter to make particles of diameter less than 14μ.

The requirement that resonances from impurities do not contribute to the measured areas is obvious. A serious problem at 4°K was found to originate in pyrex glass sample holders, necessitating the use of quartz tubes for this purpose. More serious can be the effect of impurities on the electron resonance relaxation time T_{1e}. Although the area under the resonance is independent of T_{1e}, better signal-to-noise and more reliable treatment of the data can be achieved with narrow lines.

More important in practice than impurities is the effect of the surface of the metal particles on T_{1e}. Since a conduction electron with the Fermi velocity makes $\sim 10^{12}$ collisions/sec with the surface of a 1μ particle, one spin flip each 10^4 collisions would have a determining effect on the width of the electron resonance at 20°K and below. Indeed, we found it quite easy to prepare samples which showed a normal nuclear resonance clearly characteristic of the metal, and no observable conduction electron resonance at 10 Mc/s at all. We found the use of oleic acid in sample preparation as described below gave sufficiently narrow electron spin resonance, prevented coagulation of the small particles into large clumps, and aided in making the particles small in the first place.

Samples which satisfied these criteria were made by the following recipe. A mixture of 10 per cent sodium,(6) $\frac{1}{4}$ per cent to $\frac{1}{2}$ per cent oleic acid,(7) and 90 per cent sodium-dried paraffin oil(8) or paraffin wax(9) comprising a total volume of $\sim$ 5cm^3 was heated in a glass vial at 120°C under vacuum to remove the dissolved gases. While pumping was continued the mixture was agitated by ultrasonic power from an 18 kc/s ultrasonic "soldering gun". Since particle sizes under vacuum ranged up to an unacceptable 50μ in diameter, dispersion was completed under a $\frac{1}{2}$ atmosphere of helium gas while the temperature of the mixture was increased to 200°C. After the dispersion was complete, the mixture was transferred to sample tubes which were made of quartz to avoid the spurious resonances often seen in pyrex at low temperatures.

Whereas the exact pressure of helium was immaterial, the quantity of oleic acid was critical. Above $\frac{1}{2}$ per cent concentration of oleic acid the mixture became "soapy" and the length of time to break up the sodium prohibitive. For concentrations less than $\frac{1}{4}$ per cent one could not prepare samples which did not have a large number of particles in the 10–20μ range. Silicone oil and carbon black were also tried as anti-coagulants with less success.

Over fifty samples were prepared. Of these, all but ten were rejected because of reasons to be described below. Five of these with the best signal-to-noise ratio were eventually chosen for the 20°K runs and three others were used at 77°K. A description of the samples used is presented in Table 1.

C. *Miscellaneous experimental observations*

Upon cooling the samples to 20°K we observed several sample dependent effects. Since these effects were often the determining factors in the selection or rejection of a particular sample, and since some of them have not, to our knowledge, been previously reported in the literature, we describe them in some detail here.

1. *A decrease in the Q of the coil due to the presence of the metallic sodium.* This effect was expected and depended on the amount of metal present.

Table 1. *Sample description*

Sample No.	Dispersing medium	$\Delta Q/Q$ (per cent at 10 kG at 20°K)	T_{1s} at 20°K (sec × 10^7)	Dia. of largest particles (μ)	Volume of sample (cm^3)
1	oil	0·75	0·79	4	0·5
2	oil	0·1	0·65	2	0·5
3	wax	0·1	0·68	2	0·5
4	wax	0·1	0·86	2	0·5
5	oil	0·5	1·14	3	0·5
6	oil	4·5	0·42 (77°K)	10	0·6
7	oil	—	0·24 (77°K)	10	1·2
8	oil	—	0·37 (77°K)	10	1·2

All sodium was supplied by BAKER(8) except sample No. 5 which was from FISHER.(9)
Particle size was determined by examination with a microscope.

2. *A decrease in the inductance of the coil.* This decrease was always small (< 2 per cent) and in most cases < 0·2 per cent. We attribute this to an exclusion of the r.f. field from a portion of the sample. For an estimated filling factor of $\frac{1}{10}$, a 0·2 per cent decrease implies the field was excluded from 2 per cent of the sodium. Any samples showing changes in inductance greater than 0·1 per cent were rejected. This effect was invariably connected with samples which contained many particles in the 10–20μ range.

3. *A change in Q as a function of the applied magnetic field.* This effect seemed to be correlated with (2) although much more sensitive to particle size. In most cases the Q-factor increased quadratically with increasing field. It may possibly be associated with the transverse magneto-resistive effect observed in sodium wires whose radius is comparable to the radius of a cyclotron orbit. All samples with particles larger than 3μ showed this effect to some extent. Those samples with 10μ particles showed an increase in Q of ~ 5 per cent in a field of 10 kG. In three of the five samples on which 20 K measurements were made the effect was less than 0·1 per cent at 10 kG. In the other two there was a 0·75 per cent and a 0·5 per cent effect. Appropriate corrections were applied to the data obtained from these two samples. We also observed a quadratic decrease in Q with field for two samples, in both of which investigation revealed the presence of ~ 100μ "chunks" of metal.

4. *Asymmetry of the electron resonance.* This effect was associated with the presence of particles larger than 5μ. This asymmetry was characterized by a much steeper slope on the low field side than on the high field side (Fig. 1c), and to a first approximation could be reproduced by an admixture of χ' and χ''.

5. *Broad nuclear resonance.* The samples labeled 3 and 4 in Table 1 were dispersed in paraffin wax, a term we use to distinguish it from paraffin oil, which unlike the wax is liquid at room temperature. These two samples showed a much broader line than did the oil dispersions. For the latter the measured second moments were in agreement within experimental error with the second moments measured by GUTOWSKY and McGARVEY,(10) and with the calculations using the formula of VAN VLECK.(11) The wax dispersions showed measured moments twice as large as the oil dispersions, and a distinctly different line shape (contrast 1(d) and 1(e)). A dispersion in paraffin jelly gave a second moment intermediate between the two. A dispersion in a lighter hydrocarbon than paraffin oil showed the same width as in the oil. The effect is not associated with the Martensitic transformation reported by BARRETT(12) since the anomalous line shape was observed for the wax dispersion cooled from room temperature to 77°K. Since measurements of χ_p in both wax and oil dispersions gave the same results, the problem has not been investigated further. It would be interesting to measure the low field

rela
for

D

FIG. 1. Resonance Absorption Curves. [(a) through (e) top to bottom] (a) Typical electron resonance at 77°K, $\alpha = 2{\cdot}8$. Applied field is zero in center of figure; (b) Narrowest small particle electron resonance seen at 20°K, $\alpha = 7{\cdot}2$; (c) Electron resonance in large (10μ) particles at 20°K. Field increases to the right in the picture. Note that the resonance rises more steeply on the low field side. (d) Nuclear resonance in an oil dispersion. (e) Nuclear resonance in a wax dispersion with the same horizontal scale as (d).

relaxation rate (*à la* ANDERSON and REDFIELD(13)) for these samples.

D. Experimental procedure and treatment of the data

The following general procedure was followed in making a measurement. After allowing sufficient time for the electronics to stabilize, five pictures of the nuclear resonance were taken with a Polaroid oscilloscope camera. These were $\frac{1}{2}$ sec exposures, so one picture represented about ten passes through the resonance. The large field was then turned off and the apparatus rolled into the field of the Helmholtz pair in order to observe the electron resonance. The helipot on the integrator was adjusted so that the electron resonance now covered roughly the same portion of the oscilloscope face that the nuclear resonance had. Five pictures of the electron resonance were taken. Then the sample tank was retuned and the above procedure repeated, reversing the order in which the pictures were taken. These twenty pictures constitute a "run".

The pictures were projected with a carefully aligned opaque projector and traced on graph paper. A base line for the curves was determined and the experimental integration performed by counting squares.

Determination of the base line is no problem for the nuclear resonance. As can be observed from Fig. 1(d), the curve falls rapidly in the wings. (Figure 1(e) showing the nuclear resonance in a wax dispersion is displayed with a horizontal scale comparable to that of the oil dispersions. A wider sweep was used for making the measurements.)

The electron resonances have broad Lorentzian tails. To integrate the curve experimentally to an accuracy of 1 per cent requires displaying the entire curve from -150 to $+150$ G for $\omega T_{1e} = 2{\cdot}8$ (a typical 77°K, 10 Mc/s curve), and from -40 to $+40$ G for $\omega T_{1e} = 11$ (a curve one would conceivably find at 20°K). This procedure is impractical when using the photographic technique, since the gain in accuracy is entirely overshadowed by the loss in precision resulting from the compression of the main part of the electron resonances into a small fraction of the picture. The following analytical procedure was therefore devised.

An experimental base line is drawn through two points in the wings of the resonance curves. This line is higher than the true baseline, so that in measuring the area above this line we have neglected some of the total area. In Fig. 2 we show a stylized resonance curve at 77°K and 10 M/cs

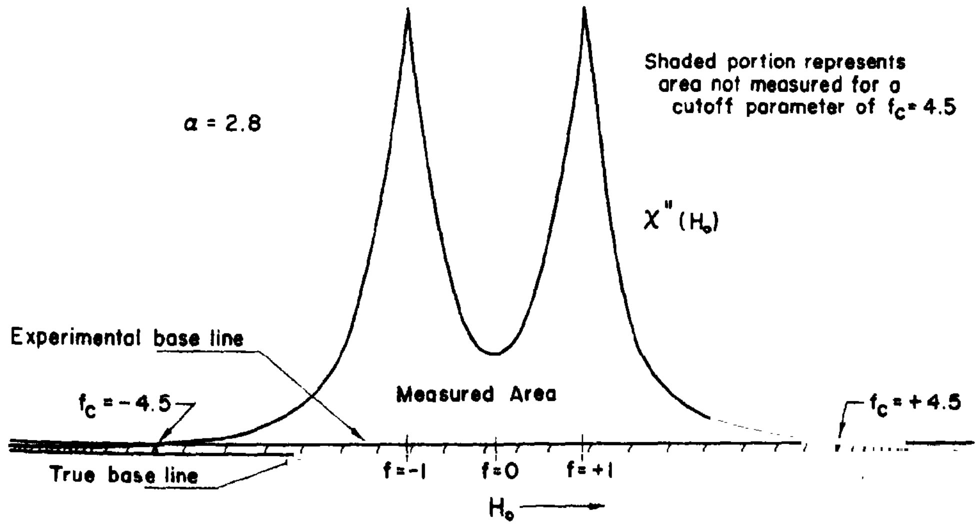

FIG. 2. Diagram of 77°K resonance showing area neglected by drawing an experimental baseline above the true baseline. Symbols are explained in the text.

with appropriate features labeled. Figure 2 represents a plot of

$$\chi_e'' = \tfrac{1}{2}\chi_p\alpha\left[\frac{c+f^2d}{(c-f^2d)^2-\psi f^2d}\right], \tag{3}$$

where
$\alpha = \omega T_{le}$, $c = 1+(\omega T_{le})^2$, $d = (\gamma_c H_r T_{le})^2$, and $f = H_0/H_r$ where H_r is the value of H_0 for which $\chi_e''(H_0)$ is a maximum. Equation (3), the line shape of the electron spin resonance, is derived in Ref. (1) and elsewhere. Referring to Fig. 2 we see that the "neglected area" consists of two parts:

1. All of those portions of the tails beyond the truncation points f_c and $-f_c$.
2. The rectangular portion bounded by f_c, $-f_c$, the line labeled "experimental base line", and the true baseline.

The contributions from these two portions are equal in the limit of large f_c and were nearly so for the values of f_c actually employed.

To obtain the "true" area from the experimental area we proceed as follows:

1. From each set of ten electron resonances per run we determine the average peak-to-peak distance. One-half this distance is one unit of f.
2. The $H_0 = 0$ point is determined by bisecting the peak-to-peak distance, the cutoff points f_c and $-f_c$ are chosen, and the experimental base line is drawn through these points. The experimental area is measured.
3. From the experimental curves the line shape parameter α is determined by reading α from normalized curves of $\chi_e''(f)$ plotted with α as a parameter. This procedure had to be applied self-consistently since α is sensitive to the true position of the baseline, the determination of which depends on α.
4. Using values of α and f_c we compute from equation (3) the fractional error one expects to make in the experimental integration due to the displacement of the experimental base line from its true value, and correct the measured value accordingly.

E. *Discussion of errors*

We will list and to some degree discuss the possible systematic and random errors which we have considered in the course of this experiment. Some of these have been discussed in detail in the previous measurement(1) and all of them are discussed in detail in the thesis of one of us (WEV).(14)

1. *Errors in experimental integration.* Most of the 20°K measurements were made with a cutoff parameter, f_c, chosen so that the wing correction was on the order of 6 per cent. The nitrogen measurements were made with the widest available field sweep and required a correction of 12 per cent. We checked the consistency of the correction procedure in the following manner. Using the scale factors determined by the peak height and peak-to-peak distance, and using α determined from the curve shape, we integrated the electron resonance analytically using equation (3). This result was compared to the result of the corrected integration by "square counting". In nearly every case the results agreed to within 5 per cent. An additional check was provided by comparing various runs with widely differing corrections. Except for some 77°K runs with a 20 per cent correction, no alarming differences were noted. The 77°K runs gave values of χ_p about 5 per cent lower than the quoted results.

Because of the more rapidly diminishing signals in the wings of the nuclear resonances, the problem of choosing the true base line was not serious.

2. *Sample dependent field effects.* The effect of the increase of Q with increasing H_0 was discussed above. In the two samples in which the Q did change, the change was less than 1 per cent. The measurements on these samples, corrected by the factor $\left(1+\frac{\Delta Q}{Q_0}\right)^2 = 1+\frac{2\Delta Q}{Q_0}$, were in good agreement with those in which no such effect was observed.

3. *Mixture of χ'.* The effect of a mixture of χ' into the signal because of mistuning of the sample coil was discussed in detail in Ref. 1.

4. *The earth's magnetic field.* Since the electron resonances are observed at low fields, it is important to consider the effect of a small static field on the order of ½ G with arbitrary direction on the measurement. Only components in the plane perpendicular to H_0 are important. The problem may further be subdivided into the two problems of obtaining solutions to the low field Bloch

equations in presence of a small field H_x parallel to H_1 and H_y perpendicular to H_1. It has been shown(14) that the important parameters are $(H_x/H_r)^2$ and $(H_y/H_r)^2$. These were both found to give corrections less than ½ per cent.

5. *Saturation.* The nuclear resonance may be saturated before the electron resonance. The susceptibility determined from a run in which the nuclear resonance is being saturated would be higher than the true value by the factor $(1+aV^2)$, where a is a constant and V the r.f. voltage across the sample coil. To make sure aV^2 is less than 1 per cent two major checks were made. Saturation runs were deliberately made to check the factor $(1+aV^2)$ in order to be sure the upper allowed value of V had been properly determined. In addition the data for which aV^2 was believed less than 0·01 was analyzed in groups determined by the value of V. No systematic trend of χ_p as a function of V in the accepted data was found.

6. *Impurities.* Impurities most likely to cause erroneous results are those containing unpaired electron spins with g-values near 2 and line widths less than 10 G. Particularly troublesome would be organic free radicals which might be formed in the process of dispersing the sodium.(15) Signals from such impurities presumably would obey a Curie Weiss $1/T$ law, and would reveal themselves out of the background of the temperature independent metal resonance. The temperature dependence of χ_p was carefully studied, and no $1/T$ component was detected within experimental error. Dummy samples (oil plus oleic acid, but no sodium), were checked for spurious resonances at 20°K, with negative results.

In some of the subsidiary experiments described below the presence of (paramagnetic) oxygen was detected on the signal. This resonance was extremely broad and distorted the line, especially at zero field. The strength of the resonance showed a sharp drop at 43°K and again at 23°K. The oxygen resonance, plus a $g = 4$ resonance in pyrex, were the only spurious resonances detected in our experiments.

7. *Distortion in the optical system.* We have checked the distortion of the entire optical system by displaying ellipses on various portions of the oscilloscope face, taking pictures of them, and projecting the pictures in the same manner as the resonance curves were projected. Rather large distortions were noted on some portions of the oscilloscope face. These portions were avoided in displaying the curves. In addition we were careful to display the electron and nuclear resonances so that the large portions of the curves covered nearly the same area of the oscilloscope face. We believe the error from this source is less than 1 per cent.

3. EXPERIMENTAL RESULTS

A. *The susceptibility measurements*

1. 77°K *measurements.* The average of thirteen runs (as defined above) is $\chi_p = (1{\cdot}12 \pm 0{\cdot}05)\times 10^{-6}$ c.g.s. volume units.* The standard deviation is 0·03, the standard error of the mean 0·01. The quoted uncertainty of 0·05 reflects our estimate of the maximum size of undetected systematic errors.

2. 20°K *measurements.* The average of thirty runs is 1·14. One standard deviation is 0·04, and the standard error of the mean 0·01. The average of the last eleven runs taken with the receiver far removed from the magnetic fields (as described above) was 1·13. We report $\chi_p = 1{\cdot}13 \pm 0{\cdot}05$ at this temperature.

3. 4·2°K *measurements.* Only three runs at 4·2°K were made on the one sample in which particle size effects were reasonably small. Because of the long nuclear T_1, small r.f. fields had to be used to avoid saturation. We were unable to prepare samples whose electron resonance narrowed below 20°K, so the signal-to-noise for the electron resonance was substantially worse than at 20°K. In addition, a 3 per cent field correction due to a change of Q was required. With peak signal-to-noise of only 4:1, we felt it would be unrewarding to make many measurements at this temperature, particularly since the interesting temperature effects all occur between 77 and 20°K.(8, 12) We quote as the result of three runs $\chi_p = 1{\cdot}09 \pm 0{\cdot}08$. We feel that under the circumstances this number is in agreement with the values at 77 and 20°K.

B. *Temperature dependence*

In addition to the absolute χ_p measurements made at 20 and 77°K, reported above, we have also made an effort to make relative measurements over this temperature range. The sample was allowed to warm up slowly while pictures of the electron resonance were taken. These pictures were not calibrated by the nuclear resonance, so the measurements demanded much more stability against drifts than the absolute measurements. Within the error of these observations, which is perhaps as large as ± 10 per cent, no temperature dependence of the electron resonance intensity was found.

---

* The factor of 10^{-6} and the units will be understood in the following.

The relative measurements described above were designed to investigate the effect of the phase change(12) of sodium on the susceptibility. To this end we also performed the following experiment. We measured χ_p at 20°K, warmed the sample to 80°K, then cooled to 20°K again and remeasured χ_p. We expect such a cycle to inhibit the phase change,(16) if it is occurring in our samples. These two measurements at 20°K agreed to within ½ per cent. We conclude that either there is no phase change in our samples or that such a cycling process does not inhibit the phase change in small particles as it does in bulk material, or that the phase change has little effect on χ_p.

Table 2. Direct comparison of experimental and theoretical values of χ_p

	χ_p(× 10^6 c.g.s. vol. units)
Sampson and Seitz(18)	1·24
Pines(2)	0·85
Shimizu(19)	0·97
Pauli(17)	0·64
This Research	1·13

4. CONCLUSIONS

A. Comparison with the previous measurement

The result of the first measurement of χ_p, reported by Schumacher and Slichter,(1) was $\chi_p = 0{\cdot}95 \pm 0{\cdot}1$. The difference between the present value of 1·13 and the previous one is almost certainly due to the more careful consideration given here to the problem of determining the area under a Lorentz-shaped line. The raw data of Schumacher and Slichter may be reanalyzed by assigning a value to the cutoff parameter f_0 of 4·3 to the resonance curve published in their paper.(1) Using $\alpha = 2{\cdot}1$, we find by the method described above an 18 per cent correction to the previous value is required, bringing it to 1·13, in perfect, if perhaps fortuitious, agreement with the present measurement.

B. Comparison with direct calculations

In addition to the famous independent electron calculation by Pauli,(17) calculations of χ_p including coulomb interactions between electrons have been published by Sampson and Seitz,(18) Pines,(2) and Shimizu.(19) In Table 2 we list the values of χ_p as calculated by the above authors. We have taken the liberty of recalculating the Sampson and Seitz value using the same value of m^*/m (0·98) as Pines, and the value of the correlation energy $E_{\text{corr}} = [-0{\cdot}88/(r_s+7{\cdot}8)]$ Rydbergs as given by Wigner.(20)

It is also interesting to compare the susceptibility to the electron specific heat in the manner formulated by Falicov and Heine.(21) In the free electron model the ratio of χ_p to the electronic specific heat $\gamma_{\text{S.H.}}$ is given by

$$\chi_p^{\text{free}}/\gamma_{\text{S.H.}}^{\text{free}} = 3\mu_e^2/\pi^2k^2, \tag{4}$$

where μ_e is the electron Bohr magneton, and k is Boltzmann's constant. Since the interactions which cause real metals to depart in their properties from the free electron model are spin dependent, $\gamma_{\text{S.H.}}$ and χ_p will be affected differently and the ratio (4) will not be preserved. Falicov and Heine have formulated their treatment of real metals such that one may express χ_p as follows:

$$\chi_p = \rho(E_0)\mu_e^2/(1-\nu), \tag{5}$$

where $\rho(E_0)$ is the density of states at the Fermi surface and $(1-\nu)^{-1}$ involves integrals over the Fermi surface of the interactions between electrons of parallel and antiparallel spin. Since $\gamma_{\text{S.H.}}$ =

$(\frac{1}{3})\pi k^2\rho(E_0)$, the factor $(1-\nu)^{-1}$ is a measure of the departure of real metals from those models in which the dominant effect of electron-electron interaction is a spin independent change in the density of states at the Fermi surface. We may solve for $(1-\nu)^{-1}$ by using the real specific heat data:

$$(\chi_p/\chi_p^{\text{free}})(\gamma_{\text{S.H.}}^{\text{free}}/\gamma_{\text{S.H.}}) = (1-\nu)^{-1} \qquad (6)$$

In Table 3 we present $(1-\nu)^{-1}$ as deduced from our data and several recent specific heat results. For comparison, note that FALICOV and HEINE(21) estimate $(1-\nu)^{-1}$ to be 1·24.

Table 3. *Values of* $(1\,\nu)^{-1}$ *from* $\gamma_{\text{S.H.}}$ a*and* χ_p *data*

	$\gamma_{\text{S.H.}}/\gamma_{\text{S.H.}}^{\text{free}}$	$\chi_p/\chi_p^{\text{free}}$	$(1-\nu)^{-1}$
GAUMER and HEER(a)	1·21	—	1·42
LIEN and PHILLIPS(b)	1·33	—	1·30
MARTIN(c)	1·27	—	1·36
This research	—	1·73	—

(a) GAUMER R. E. and HEER C. V., *Phys. Rev.* **118**, 955 (1960).
(b) LIEN W. H. and PHILLIPS N. E., *Phys. Rev.* **118**, 958 (1960).
(c) MARTIN D. L., *Phys. Rev.* **124**, 438 (1961).

C. Diamagnetic susceptibility

As we pointed out in the introduction, the major motivation for repeating these measurements was provided by the fact that the earlier measurements seemed to imply a surprisingly small diamagnetic susceptibility χ_D^{cond} for the conduction electrons. We obtain an experimental measure of χ_D^{cond} from the relation

$$\chi_D^{\text{cond}} = \chi_t - \chi_p - \chi_D^{\text{ion}} \qquad (7)$$

where χ_D^{ion} is the diamagnetic susceptibility of the ion core electrons and χ_t is the total susceptibility of metallic sodium. Using a value of 0·65(22) for χ_t and χ_p from this research, we find $\chi_D^{\text{cond}} + \chi_D^{\text{ion}} = -0{\cdot}47$.

The value of χ_D^{cond} obtained from the LANDAU–PEIERLS(23) formula with $r_0 = 3{\cdot}96$ a.u. and $m^*/m = 0{\cdot}98$ is $\chi_D^{\text{cond}} = -0{\cdot}22$. Calculations by PINES(24) and KJELDAAS and KOHN(25) yield $-0{\cdot}24$ and $-0{\cdot}23$ respectively. χ_D^{ion} may be estimated by assuming that the diamagnetism is the same for the metallic ions as for free ions. Numerous semi-empirical estimates have been made. A review of results prior to 1952 is given by MYERS.(26) Quoted values range from $-0{\cdot}16$ to $-0{\cdot}54$, with the most popular range between $-0{\cdot}18$ and $-0{\cdot}26$. A recent theoretical calculation for neon-like ions yields $-0{\cdot}22$ for sodium.(27) If we assume $-0{\cdot}18 > \chi_D^{\text{ion}} > -0{\cdot}26$, we find $-0{\cdot}21 > \chi_D^{\text{ion}} > -0{\cdot}29$, a range of χ_D^{cond} which is in agreement with existing theoretical calculations.

D. Comparison with Knight shift measurements

The fractional Knight shift $K = \Delta H_0/H_0$ is given by(28)

$$K = \frac{a(s)\chi_p}{N}\frac{P_F}{P_A}\frac{I}{2\mu_e\mu_n} \qquad (8)$$

ΔH_0 is the shift in the field-for-resonance at constant frequency for metallic nuclei from the field-for-resonance in the absence of conduction electron paramagnetism. $a(s)$ is the hyperfine coupling constant for electrons in the free atom and $P_F/P_A \equiv \xi$ is a factor which corrects for the fact that the probability density P_A of unpaired spins in free atoms is different from the probability density P_F in the metal averaged over the Fermi surface. Using $a(s) = 0{\cdot}0296\ \text{cm}^{-1}$ as determined from atomic beam measurements,(28) $\Delta H_0/H_0 = 1{\cdot}10\times10^{-3}$ from GUTOWSKY and McGARVEY(28) corrected to 77°K, and using χ_p from this research we find $\xi = 0{\cdot}60$. This value is 30 per cent lower than $\xi = 0{\cdot}80$ calculated by KJELDAAS and KOHN,(29) and 0·81 calculated by TOWNES, HERRING and KNIGHT.(30)

The dominant mechanism for spin-lattice relaxation of the nuclei below room temperature is via the conduction electrons. The same interaction which is responsible for the Knight shift is also responsible for this relaxation. The relationship between K and T_{1n} was derived for free electrons by KORRINGA(31) and modified by PINES(2) to include results from experiments which depend on electron-electron interactions. Pines gives

$$T_{1n}TK^2 = \frac{\hbar}{4\pi k}\,\frac{\gamma_e^2}{\gamma_n^2}\left[\frac{\chi_p}{\chi_p^{\text{free}}}\right]^2\left[\frac{\rho_{\text{free}}(E_0)}{\rho(E_0)}\right]^2 \tag{9}$$

Since T_{1n}, K, and $[\rho_{\text{free}}(E_0)/\rho(E_0)]$ have all been independently measured (the last term is the ratio of the specific heat to the free electron value) we may use the modified Korringa relation to compute χ_p^s and compare it with our value. Table 4 gives the results of this computation for the three most recent specific heat results. Considering three experiments are required to obtain χ_p in this manner, the value so obtained seems quite satisfactorily in agreement with our measurement.

Table 4. Comparison of χ_p with the Knight shift through the Korringa relation

$T_{1n}T$	$\gamma_{\text{S.H.}}/\gamma_{\text{S.H.}}^{\text{free}}$	$\Delta H/H_0 \times 10^3$	χ_p
5·1(13)	1·21(a)	1·10(d)	1·01
5·1	1·33(b)	1·10	1·11
5·1	1·27(c)	1·10	1·06
This research	—	—	1·13

(a) GAUMER R. E. and HEER C. V., *Phys. Rev.* **118**, 955 (1960).
(b) LIEN W. H. and PHILLIPS N. E., *Phys. Rev.* **118**, 958 (1960).
(c) MARTIN D. L., *Phys. Rev.* **124**, 438 (1961).
(d) McGARVEY B. R. and GUTOWSKY H. S., *J. chem. Phys.* **21**, 2114 (1953).

In connection with the Korringa relation it is interesting to note we might alternatively have chosen to write it in terms of the quantity introduced by FALICOV and HEINE,(21) $(1-\nu)^{-1}$. We may write

$$T_{1n}TK^2 = \frac{\hbar}{4\pi k}\left(\frac{\gamma_e}{\gamma_n}\right)^2(1-\nu)^{-2} \tag{10}$$

We find from this $(1-\nu)^{-1} = 1{\cdot}26$.

E. *Temperature dependence of χ_p*

There has been some theoretical speculation on a temperature dependence of χ_p, mainly via the effect of the electron–phonon interaction on the density of states.(32, 33) However, the theoretical situation seems somewhat hazy at this time. Another type temperature dependence would occur through a volume change, which is on the order of ½ per cent between 0 and 77°K, a negligible change for experiments of the accuracy obtained here.

Two experiments exist which have reported unexplained temperature dependences in sodium between 77 and 20°K. HEDGECOCK(34) observed an 8 per cent decrease in the total susceptibility. FELDMAN and KNIGHT(3) reported a 2·6 decrease in the Knight shift between 77 and 20°K. The precision of our experiments is such that we cannot rule out the possibility that the Knight shift anomaly may be explained by a corresponding anomaly in χ_p^s.

Acknowledgements—We wish to express our appreciation to Dr. J. L. Hall for his assistance in solving many electronic problems. Dr. ALARICH WEISS participated in some of the early sample making efforts. The low temperature laboratory of Professor S. A. FRIEDBERG provided its usual generous assistance in cryogenic matters.

REFERENCES

1. SCHUMACHER R. T. and SLICHTER C. P., *Phys. Rev.* **101**, 58 (1956).
2. PINES D., *Solid State Physics* (edited by SEITZ F. and TURNBULL D.) Vol. **I**, p. 367 Academic Press, New York (1956).
3. FELDMAN D. W. and KNIGHT W. D., Private Communication to R. T. SCHUMACHER.
4. ESTLE T. L., HART H. R. and WHEATLEY J. C., *Phys. Rev.* **112**, 1576 (1958).
5. SCHUMACHER R. T., CARVER T. R. and SLICHTER C. P., *Phys. Rev.* **95**, 1089 (L) (1954).
6. J. T. Baker Chemical Corp.
   Fisher Scientific Co., Certified 99·99 per cent Pure.
7. Fisher Scientific Co., Purified.
8. Fisher Scientific Co., U.S.P., Viscosity 335/350.
9. Esso Household Wax.

10. GUTOWSKY H. S. and MCGARVEY B. R., *J. chem. Phys.* **20**, 1472 (1952).
11. VAN VLECK J. H., *Phys. Rev.* **74**, 1168 (1948).
12. BARRETT C. S., *Acta Cryst.* **9**, 671 (1956).
13. ANDERSON A. G. and REDFIELD A. G., *Phys. Rev.* **116**, 583 (1959).
14. VEHSE W. E., Thesis, Carnegie Institute of Technology, (1961).
15. FEHER G. and KIP A. F., *Phys. Rev.* **98**, 337 (1955).
16. DUGDALE J. S. and DUGAN D., *Proc. Roy. Soc.* **A254**, 184 (1960).
17. PAULI W., *Ann. Phys. Lpz.* **41**, 81 (1927).
18. SAMPSON J. B. and SEITZ F., *Phys. Rev.* **58**, 633 (1940).
19. MASAO SHIMIZU, *J. phys. Soc. Japan* **15**, 2220 (1960).
20. WIGNER E. P., *Trans. Faraday Soc.* **34**, 678 (1938), footnote.
21. FALICOV L. M. and HEINE V., *Advanc. Phys.* **10**, 56 (1961).
22. The two most recent and, presumably, most accurate measurements of χ_t are by BOWERS R., *Phys. Rev.* **100**, 1141 (1955), ($\chi_t = 0{\cdot}70$) and VENKATESWARLU K. and SRIRAMAN S., *Z. Naturf.* **13a**, 451 (1958), ($\chi_t = 0{\cdot}60$). The average of these, as well as BOWERS' "guess" as to the correct value (private communication to R. T. SCHUMACHER) is 0·65, the number we have used.
23. LANDAU L., *Z. Phys.* **64**, 629 (1930); PEIERLS R., *ibid.* **80**, 763 (1933).
24. PINES D., *Proceedings of the* 10th *Congress* (*Brussels*, 1954) *of the Institute International de Physique Solvay*, edited by R. STOOPS, p. 38 (1954).
25. KJELDAAS T. JR. and KOHN W., *Phys. Rev.* **105**, 806 (1957).
26. MYERS W. R., *Rev. Mod. Phys.* **24**, 15 (1952).
27. TANI S., *Progr. Theor. Phys., Kyoto* **23**, 1157 (1960).
28. KNIGHT W. D., *Solid State Physics* (edited by SEITZ F. and TURNBULL D.) Vol. **II**, p. 105. Academic Press, New York (1956).
29. KJELDAAS T., JR., and KOHN W., *Phys. Rev.* **99**, 622A (1955).
30. TOWNES C. H., HERRING C. and KNIGHT W. D., *Phys. Rev.* **77**, 852 (1950).
31. KORRINGA J., *Physica* **16**, 601 (1950).
32. BUCKINGHAM M. J. and SCHAFROTH R., *Proc. phys. Soc., Lond.* **67A**, 828 (1954).
33. CHESTER G. V. and HOUGHTON A., *Proc. phys. Soc., Lond.* **73**, 609 (1959).
34. HEDGECOCK F. T., *Proceedings of the* 5th *International Conference on Low Temperature Physics and Chemistry* (edited by DILLINGER J. R.) p. 545. University of Wisconsin Press, Madison (1958).

.Phys. Chem. Solids Pergamon Press 1963. Vol. 24 pp. 309–317. Printed in Great Britain.

ION EXCHANGE IN POROUS CRYSTALS

PART II. THE RELATIONSHIP BETWEEN SELF- AND EXCHANGE-DIFFUSION COEFFICIENTS

R. M. BARRER, R. F. BARTHOLOMEW and L. V. C. REES

Physical Chemistry Laboratories, Chemistry Department, Imperial College, London, S.W.7

(*Received* 16 *July* 1962)

Abstract—It has been shown that, using chabazite as exchanger, no previous(1, 2) theoretical treatment allows one to calculate integral (and therefore differential) inter-diffusion coefficients, D_{AB}, from the self-diffusion coefficients, D_A^* and D_B^*, for the ion-pairs $Ca^{2+} \rightleftharpoons Sr^{2+}$, $Ca^{2+} \rightleftharpoons Ba^{2+}$ and $Sr^{2+} \rightleftharpoons Ba^{2+}$. In part the failure of the previous treatments arises from a strong dependence of the self-diffusion coefficients upon the cationic composition of the chabazites, as shown for Sr^{2+} and Ca^{2+}. However, correction for this concentration dependence still left a substantial discrepancy between theoretical and experimental values of D_{AB}. A second important factor is that the previously developed(1) expression relating the differential inter-diffusion coefficient D_{AB} and D_A^* and D_B^*,

$$\left(\text{i.e. } D_{AB} = \frac{D_A^* D_B^*(C_A Z_A^2 + C_B Z_B^2)}{D_A^* C_A Z_A^2 + D_B^* C_B Z_B^2}\right)$$

is over-simplified. The correct relationship has been derived, and a special case of this relationship has been used to recalculate the integral inter-diffusion coefficients for the $Sr^{2+} \rightleftharpoons Ca^{2+}$ exchange. Although this improved the correspondence between measured and calculated inter-diffusion coefficients, the discrepancy remained considerable. Some possible reasons for this were discussed.

1. INTRODUCTION

In Part I(3) measurements were reported of exchange diffusion of Ca–Sr, Ca–Ba, Ba–Sr, and Na–Ba, and of self-diffusion of Na, K, Rb, Cs, Ca, Sr, and Ba, each in its nearly homo-ionic form of chabazite, and of Ca and Sr in a series of (Ca,Sr)-chabazites. Attempts made to apply existing treatments of the relations between self- and exchange-diffusion coefficients, reported in this paper, revealed limitations in the theory and have led to the treatment to be described.

Two theoretical studies have been made, respectively by Helfferich and Plesset(1) and by Beattie and Davies(2) of the connection between exchange diffusion and self-diffusion coefficients. In the work of the first of these authors a relation was derived between differential exchange diffusion coefficients D_{AB} and self-diffusion coefficients D_A^* and D_B^*:

$$D_{AB} = \frac{D_A^* D_B^*(C_A Z_A^2 + C_B Z_B^2)}{D_A^* C_A Z_A^2 + D_B^* C_B Z_B^2} \qquad (1)$$

where C_A and C_B are the numbers of the exchanging ions of valencies Z_A and Z_B per unit volume of the crystal. The exchange diffusion kinetics for ion A are then governed by the non-linear equation

$$\frac{\partial C_A}{\partial t} = \operatorname{div}(D_{AB} \operatorname{grad} C_A) \qquad (2)$$

This equation was solved numerically for the appropriate boundary conditions (with D_{AB} as given by equation (1), assuming D_A^* and D_B^* to be independent of C_A or C_B) and the solution was then represented analytically to give Q_t/Q_∞ as a function of time, where Q_t is the amount of exchange at time t and Q_∞ is this amount at equilibrium. Helfferich(4) has tested these calculations for the exchange between Na^+ and H^+ ions in phenolsulphonic acid cation resin. Good agreement was obtained between experimental and theoretical results for certain resin beads when the solution concentration was 0·25 molar but when the concentration was increased to 1 molar the agreement was poor.

Beattie and Davis also used equation (1) for the case where $Z_A = Z_B$. They then solved equation (2) by a method due to FUJITA(5) which gave them an expression for Q_t/Q_∞. It will be noticed that in both these treatments equations for Q_t/Q_∞ stand or fall on the validity of equation (1), with D_A^* and D_B^* constants independent of C_A or C_B.

2. TEST OF EQUATION (1) RELATING D_{AB}, D_A^*, AND D_B^*

The concentration dependencies of D_A^* and D_B^* reported in Part I for Ca^{2+} and Sr^{2+} in (Ca,Sr)-chabazites at 75·8°C were, approximately,

$$\left.\begin{aligned} Ca^{2+}&: D_A^* \simeq 1{\cdot}15\times 10^{-14}\,N_A^2\ (\text{cm}^2\,\text{sec}^{-1})\\ Sr^{2+}&: D_B^* \simeq 7{\cdot}4\times 10^{-15}\,N_B^2 (\text{cm}^2\,\text{sec}^{-1})\end{aligned}\right\} \quad (3)$$

where

$$N_A = \frac{[\text{Ca}]}{[\text{Ca}]+[\text{Sr}]} \text{ and } N_B = \frac{[\text{Sr}]}{[\text{Sr}]+[\text{Ca}]}$$

are the exchangeable cation fractions of Ca and Sr respectively. [Ca] and [Sr] are the numbers of each of these ions per unit volume of crystal. In addition there is a small residue of Na^+ ions in the crystals (Part I) which are assumed not to be involved in the Ca ⇋ Sr exchanges.

The integral interdiffusion coefficients, D_{AB}, are defined by

$$\left.\begin{aligned} D_{AB} &= \frac{1}{(N_1-N_2)}\int_{N_2}^{N_1} D_{AB}\,\mathrm{d}N_A\\ &\text{or}\\ D_{AB} &= \frac{1}{(N_1'-N_2')}\int_{N_2'}^{N_1'} D_{AB}\,\mathrm{d}N_B\end{aligned}\right\} \quad (4)$$

over the accessible ranges of exchangeable cation fractions N_1 to N_2 for ion A, and N_1' to N_2' for ion B. These coefficients should then be given, according to equation (1), by

$$D_{AB} = \frac{1}{(N_1-N_2)}\int_{N_2}^{N_1} \frac{D_A^* D_B^*(N_A Z_A^2 + N_B Z_B^2)}{D_A^* N_A Z_A^2 + D_B^* N_B Z_B^2}\,\mathrm{d}N_A \quad (5a)$$

or

$$D_{AB} = \frac{1}{(N_1'-N_2')}\int_{N_2'}^{N_1'} \frac{D_A^* D_B^*(N_A Z_A^2 + N_B Z_B^2)}{D_A^* N_A Z_A^2 + D_B^* N_B Z_B^2}\,\mathrm{d}N_B \quad (5b)$$

With the aid of equation (3), equations (5a) and (5b) were integrated, the limits of exchangeable cation fractions being

for Ca^{2+}, $N_1 = 0$; $N_2 = 0{\cdot}84$

and for Sr^{2+}, $N_1' = 0$; $N_2' = 0{\cdot}90$

Table 1. *Comparisons of values of integral inter-diffusion coefficients in chabazites* ($\times 10^{15}$ cm² sec⁻¹), $T = 75{\cdot}8$°C

Exchange system	D_f B entering	D_b A entering	$D_{AB} = \frac{1}{2}(D_f+D_b)$	D_{AB}		D_{AB}	
				D_A^*, D_B^* depend on N_A, N_B (equation 3)		D_A^*,D_B^* do not depend on N_A and N_B and given largest values	
				A entering	B entering	A entering	B entering
A = Ca B = Sr	(a) 7·3 (b) 3·1	27·0 12·0	17·2 7·5	$1{\cdot}0_2$	$0{\cdot}9_5$	9·6	9·0
A = Ca B = Ba			(a) 120				52
A = Sr B = Ba			(a) 1100				37

The results are shown in Table 1, columns 5 and 6 respectively.

As indicated in Part I, D_{AB} may be independently estimated from the experimental exchange kinetics. The $\sqrt{t}$ equations appropriate to the boundary conditions (a large excess in the aqueous phase of the ion entering the crystal) are

$$\left.\begin{aligned}\left(\frac{Q_t}{Q_\infty}\right)_{A\ \text{entering}} &= 2S\rho\sqrt{\left(\frac{D_f t}{\pi}\right)};\\ \left(\frac{Q_t}{Q_\infty}\right)_{B\ \text{entering}} &= 2S\rho\sqrt{\left(\frac{D_b t}{\pi}\right)}\end{aligned}\right\} \quad (6)$$

and then[7]

$$D_{AB} = \tfrac{1}{2}(D_f + D_b) \quad (7)$$

In equation 6, S is the surface area of the crystals of density ρ, and D_f and D_b are integral interdiffusion coefficients for A entering and for B entering the crystals respectively. The results for D_{AB} from equations (6) and (7), over the same range of exchangeable cation fractions as for equations (5a) and (5b), are given in Table 1, columns 2a, 3a, and 4a. The values of D_{AB} thus determined differ substantially from those calculated on the basis of the Helfferich and Plesset equation (1) by means of equations (5a) and (5b).

For diffusion into spheres from infinite volume of solution phase,[6]

$$\left(\frac{Dt}{r^2}\right)^{1/2} = 0{\cdot}175 \text{ when } \frac{Q_t}{Q_\infty} = 0{\cdot}5.$$

Crank[7] suggests that the values of D_f and D_b obtained from this relationship when substituted into equation (7) give a better representation of D_{AB} in some cases. The results obtained by this method are also given in Table 1, columns 2b, 3b, and 4b (taking $r = 1{\cdot}74\times10^{-4}$ cm (see p. 312)) but, as before, the experimental and theoretical figures differ substantially.

As an empirical procedure the integrations of equations (5a) and (5b) were also carried out assuming D_A^* and D_B^* to be constant at their maximum values (i.e. when $N_A = N_B = 1$ in equation 3). Better agreement was now obtained between these values of D_{AB} (Table 1, columns 7 and 8) and those in column 4b. However, no *a priori* justification of this procedure is possible.

3. TEST OF EQUATIONS FOR Q_t/Q_∞ vs. t

Even if equation (1) had represented correctly the relation between D_{AB} and D_A^* and D_B^*, the expressions for Q_t/Q_∞ given by Helfferich and Plesset or by Beattie and Davies cannot be quantitatively correct in the present situation, because their equations relating Q_t/Q_∞ to D_A^* and D_B^* were derived assuming D_A^* and D_B^* to be independent of N_A and N_B. Nevertheless it is of considerable interest to examine the two expressions to determine the extent and direction of their quantitative failure. The respective expressions are[1]

$$\frac{Q_t}{Q_\infty} = [1-\exp\{\pi^2(f_1(\alpha)\tau+f_2(\alpha)\tau^2+f_3(\alpha)\tau^3)\}]^{1/2} \quad (8)$$

and,[2] when Ca is the entering ion,

$$\boxed{\frac{Q_t}{Q_\infty} = \frac{2^{3/2}S\rho[\{[\text{Ca}]+[\text{Sr}]\}D_A^*D_B^*\{([\text{Ca}]+[\text{Sr}])D_B^*+(D_A^*-D_B^*)[\text{Ca}]_0\}]^{1/2}}{\mu^{1/2}(D_A^*-D_B^*)}\times t^{1/2}} \quad (9)$$

In equation (8), $\alpha = \dfrac{D_A^*}{D_B^*}$, $\tau = \dfrac{D_A^* t}{r^2}$ where r denotes the radius of the exchanger particles considered as equal spheres, and $f_1(\alpha)$, $f_2(\alpha)$, and $f_3(\alpha)$ are constants dependent upon α. In equation 9 the total concentration of $[\text{Ca}]+[\text{Sr}]$ is constant at all points. $[\text{Ca}]_0$ is the concentration of the entering ion, Ca^{2+}, at $x = 0$ for $t > 0$, and μ is a parameter dependent on α. If the concentrations are expressed as exchangeable cation fractions, and when, as in the experiments here considered, the entering ion is in large excess in the solution phase, the second equation gives

$$\text{or}\quad \left.\begin{aligned}(Q_t/Q_\infty)_{\text{Ca entering}} &= k(D_A^* t)^{1/2}\\ (Q_t/Q_\infty)_{\text{Sr entering}} &= k(D_B^* t)^{1/2}\end{aligned}\right\} \quad (9a)$$

Moreover the coefficient k is the same in both equations (9a) if we take exchanger samples such that the product $S\rho$ is the same for each.

Helfferich and Plesset's equation (equation 8) was first applied to the Ca–Sr exchange in

chabazite taking as a mean particle radius, $r = \frac{3}{S\rho} = 1{\cdot}74 \times 10^{-4}$ cm, S being the krypton area of Part 1. In Fig. 1(a) the considerable divergences between calculated and observed rates of exchange for forward and reverse reactions are apparent.

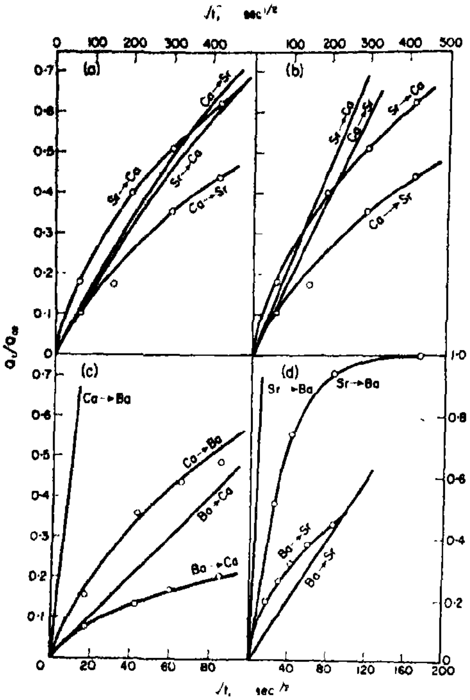

FIG. 1. Observed and calculated rates of ion-exchange at 75·8°C. The experimental points are shown as open circles. It was assumed in (c) and (d) that complete exchange occurred at infinite time.

The values of D_A^* and D_B^* used in the theoretical equation were the maximum measured values pertaining to the nearly pure homoionic exchange forms and which led to the values of D_{AB} in Table 1, columns 7 and 8.

According to the Helfferich and Plesset expression for Q_t/Q_∞, if the faster ion is initially present in the exchanger then the rate of exchange should be faster than with the reverse situation. This prediction has been confirmed recently for H^+–Na^+ exchange in phenol sulphonic acid cation resin.(4) However, Fig. 1 shows not only that for Ca^{2+}–Sr^{2+} exchanges in chabazite is exchange faster when Sr^{2+} (the slower ion) is initially in the exchanger but also that this type of behaviour is typical of all the other exchanges using chabazite.

When the comparison is made between observed exchange kinetics and those based on equation (9) (Beattie and Davies) there are still large discrepancies (Fig. 1, b, c, d). Equations (9a) do, however, predict correctly that, as observed in chabazite, when the faster diffusing ion is initially in the crystal, exchange proceeds more slowly than when this ion is in the aqueous phase.

From the (Ca–Ba)- and (Sr–Ba)-exchange rates shown in Fig. 1, D_{AB} was calculated using equations (6) and (7), and values are tabulated in column 4, Table 1. These can only be compared with the theoretical rates given by equations (5a) and (5b) (assuming the maximum values D_A^* and D_B^*) which are presented in column 8, Table 1.

4. RE-DEVELOPMENT OF RELATION BETWEEN D_{AB} AND D_A^*, D_B^*

The preceding analysis has shown, for the Sr ⇋ Ca and other exchanges in chabazite, that equation (1) relating D_{AB} with D_A^* and D_B^*, and hence the equations for Q_t/Q_∞ derived by Helfferich and Plesset and by Beattie and Davies are inadequate. The situation will therefore be re-examined with a view to obtaining relationships appropriate for the zeolites and for strong electrolytes.

When the mobilities of the counter-diffusing pair of ions are different a space charge tends to build up which accelerates the slower moving ion and decelerates the faster moving ion, so that the two rates become equal and exchange at any point is characterized by the single inter-diffusion coefficient, D_{AB}. It is possible that the water content of the exchanger is also modified during the exchange. For example, in the $H^+ \leftrightharpoons Na^+$ exchange in phenolsulphonic acid cation resin(4) when the Na^+ ion was diffusing into the resin, there was a transient increase in the water content; while the flow of water was reversed when Na^+ was diffusing out of the resin.

If we consider that ions 1 and 2 and water molecules 3 are flowing, then according to Fick's law for diffusion in the x-direction across unit area of a plane normal to x within the crystal, for ion 1 this flux is

$$J_1 = -D_{AB}\frac{\partial C_1}{\partial x} \tag{10}$$

while, according to the Nernst–Planck formulation of the flux,

$$J_1 = -D_1\left(\frac{\partial C_1}{\partial x}+\frac{C_1FZ_1}{RT}\frac{\partial V}{\partial x}\right) \tag{11}$$

with similar equations for ion 2. $\frac{\partial V}{\partial x}$ is the potential gradient across the plane. For water the flux is

$$J_3 = -D_{\mathrm{H_2O}}\frac{\partial C_3}{\partial x} \tag{12}$$

Also per unit volume of crystal, for electrical neutrality,

$$Z_1C_1+Z_2C_2 = \text{constant} \tag{13}$$

from which

$$Z_1\frac{\partial C_1}{\partial x}+Z_2\frac{\partial C_2}{\partial x} = 0 \tag{14}$$

Likewise through any plane the electrical neutrality condition requires that

$$Z_1J_1+Z_2J_2 = 0 \tag{15}$$

From these relationships we obtain

$$D_{AB} = \frac{D_1D_2(C_1Z_1^2+C_2Z_2^2)}{D_1C_1Z_1^2+D_2C_2Z_2^2} \tag{16}$$

In order to determine the significance of the Nernst–Planck diffusion coefficients D_1 and D_2 we next consider the irreversible thermodynamic formulation. In terms of the total chemical potentials, μ_1', μ_2' and μ_3'

$$J_1 = -C_1\left(L_{11}\frac{\partial\mu_1'}{\partial x}+L_{12}\frac{\partial\mu_2'}{\partial x}+L_{13}\frac{\partial\mu_3'}{\partial x}\right) \tag{17}$$

where the L's are the phenomenological coefficients. Similar expressions may be written for J_2 and J_3 in the cases of ion 2 and water respectively. For any charged particle we have for the total chemical potential, μ_1', as a function of temperature T, pressure P, the concentrations C, and the potential V:

$$\begin{aligned}\mathrm{d}\mu_1' = {} & \left(\frac{\partial\mu_1'}{\partial P}\right)_{T,C_1,C_2,C_3,V}\mathrm{d}P+\left(\frac{\partial\mu_1'}{\partial T}\right)_{P,C_1,C_2,C_3,V}\mathrm{d}T \\ & +\left(\frac{\partial\mu_1'}{\partial C_1}\right)_{P,T,C_2,C_3,V}\mathrm{d}C_1+\left(\frac{\partial\mu_1'}{\partial C_2}\right)_{P,T,C_1,C_3,V}\mathrm{d}C_2 \\ & +\left(\frac{\partial\mu_1'}{\partial C_3}\right)_{P,T,C_1,C_2,V}\mathrm{d}C_3+\left(\frac{\partial\mu_1'}{\partial V}\right)_{P,T,C_1,C_2,C_3}\mathrm{d}V\end{aligned} \tag{18}$$

As the present system is maintained at constant P and T, the first two terms are zero. Also

$$\left(\frac{\partial\mu_1'}{\partial V}\right)_{P,T,C_1,C_2,C_3,} = Z_1F$$

and so

$$\mathrm{d}\mu_1' = \mathrm{d}\mu_1+Z_1F\cdot\mathrm{d}V \tag{19}$$

where $\mathrm{d}\mu_1$ is that part of the total chemical potential which depends on P, T, C_1, C_2 and C_3 only. Then

$$J_1 = -C_1\left[L_{11}\frac{\partial\mu_1}{\partial x}+L_{12}\frac{\partial\mu_2}{\partial x}+L_{13}\frac{\partial\mu_3}{\partial x}+L_{14}Z_1\frac{\partial V}{\partial x}\right] \tag{20}$$

where

$$L_{14} = \left(L_{11}+L_{12}\frac{Z_2}{Z_1}\right)F \tag{21}$$

Comparison of equation (11) and (20) gives

$$D_1 = C_1\left(L_{11}\frac{\partial\mu_1}{\partial C_1}+L_{12}\frac{\partial\mu_2}{\partial C_1}+L_{13}\frac{\partial\mu_3}{\partial C_1}\right) \tag{22}$$

$$D_1 = L_{14}\frac{RT}{F} \tag{23}$$

Similarly, we obtain

$$D_2 = C_2\left(L_{22}\frac{\partial\mu_2}{\partial C_2}+L_{21}\frac{\partial\mu_1}{\partial C_2}+L_{23}\frac{\partial\mu_3}{\partial C_2}\right) \quad (24)$$

$$D_2 = L_{24}\frac{RT}{F} \quad (25)$$

$$D_3 = C_3\left(L_{33}\frac{\partial\mu_3}{\partial C_3}+L_{31}\frac{\partial\mu_1}{\partial C_3}+L_{32}\frac{\partial\mu_2}{\partial C_3}\right) \quad (26)$$

If the Onsager relations between the cross-coefficients in these equations are correct, then

$$L_{12} = L_{21};\quad L_{13} = L_{31};\quad L_{23} = L_{32} \quad (27)$$

For self-diffusion, using tracer elements of concentration C_1^*, one has

$$J_1^* = -C_1^*\left[L_{TT}\frac{\partial\mu_1^*}{\partial x}+L_{1T}\frac{\partial\mu_1}{\partial x}\right] \quad (28)$$

where the subscript "T" denotes the tracer element. In this case, $d\mu_2$ and $d\mu_3$ are zero, and so at constant P and T we have

$$C_1^*\,d\mu_1^*+C_1\,d\mu_1 = 0 \quad (29)$$

Combining these relations with the Fick equation

$$J_1^* = -D_A^*\frac{\partial C_1^*}{\partial x}$$

we find

$$D_A^* = C_1^*\left[L_{TT}-L_{1T}\frac{C_1^*}{C_1}\right]\frac{d\mu_1^*}{dC^*}$$

$$= RT\left[L_{TT}-L_{1T}\frac{C_1^*}{C_1}\right]\frac{d\ln a_1^*}{d\ln C_1^*} \quad (30)$$

Since, however, the mixture of isotopes represents an ideal solution, $\dfrac{d\ln a_1^*}{d\ln C_1^*} = 1$. Also because $C_1^* \ll C_1$ the second term in the square bracket may be omitted. Thus finally

$$D_A^* = RTL_{TT} = RTL_{11} \quad (31)$$

because for two isotopes of the same element the phenomenological coefficients should be the same. Similarly, $D_B^* = RT\,L_{22}$.

By combining the above expressions for D_A^* and D_B^* with equations (22) and (24), and substituting $d\mu = RTd\ln a$, we find that

$$D_1 = D_A^*\left(\frac{d\ln a_1}{d\ln C_1}+\frac{L_{12}d\ln a_2}{L_{11}d\ln C_1}+\frac{L_{13}d\ln a_3}{L_{11}d\ln C_1}\right) \quad (32)$$

and

$$D_2 = D_B^*\left(\frac{d\ln a_2}{d\ln C_2}+\frac{L_{12}d\ln a_1}{L_{22}d\ln C_2}+\frac{L_{23}d\ln a_3}{L_{22}d\ln C_2}\right) \quad (33)$$

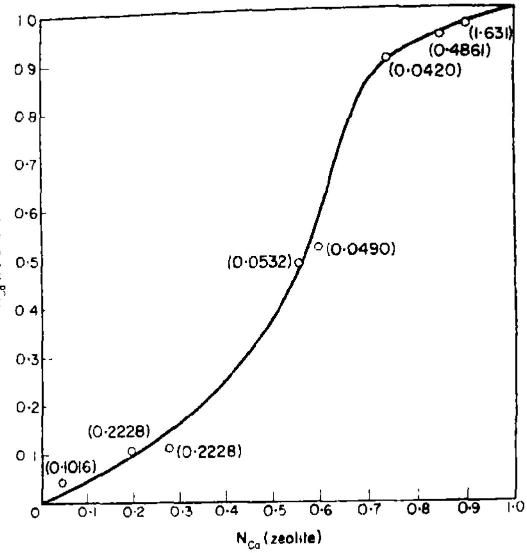

FIG. 2. (Ca/Sr)-chabazite exchange isotherm. Molalities of initial solutions are shown in brackets.

When equations (32) and (33) are inserted in equation (16), an expression relating D_{AB} with the self-diffusion coefficients is obtained and it is obvious that equation (1), considered appropriate by Helfferich and Plesset and by Beattie and Davies, must be significantly in error for crystalline zeolite exchangers, which correspond to very strong electrolyte solutions.

5. THE Ca-Sr EXCHANGE IN CHABAZITE

We may now consider the application of equations (32) and (33), somewhat simplified, to the problem of exchange diffusion in chabazite. Because for this exchange there was no measurable change in water content the last terms in equations

(32) and (33) may be omitted. If in addition we neglect the cross-coefficient L_{12}, then

$$D_1 \simeq D_A^*\left(1+\frac{\mathrm{d}\ln f_1}{\mathrm{d}\ln C_1}\right)$$
$$D_2 \simeq D_B^*\left(1+\frac{\mathrm{d}\ln f_2}{\mathrm{d}\ln C_2}\right) \tag{34}$$

To evaluate D_1 and D_2 for insertion into equation (16), we thus require the activity coefficients f_1 and f_2 of the ions A and B in the exchanger as functions of its composition. These activity coefficients were obtained as follows.

The exchange isotherm for $Sr^{2+} \leftrightharpoons Ca^{2+}$ in chabazite is shown in Fig. 2. On analysis it was found that KIELLAND's equation(8) did not apply. The thermodynamic equilibrium constant for this exchange is given by

$$K_a = \frac{N_1^2 f_1^2 \cdot m_2^2[\gamma_2^3]^2}{N_2^2 f_2^2 \cdot m_1^2[\gamma_1^3]^2} \tag{35}$$

where m_1, m_2, γ_1 and γ_2 are the molalities and mean activity coefficients of the calcium and strontium chloride solutions existing in equilibrium with the mixed exchanger. By using GLUECKAUF's expression(9) to calculate the γ's it is possible to evaluate K_e, where

$$K_e = \frac{N_1^2 m_2^2[\gamma_2^3]^2}{N_2^2 m_1^2[\gamma_1^3]^2} \tag{36}$$

EKEDAHL *et al.*(10) and ARGERSINGER *et al.*(11) have shown that the activity coefficients of the Ca^{2+} and Sr^{2+} ions in the exchanger, f_1 and f_2 respectively, may be obtained by integration as follows

$$2\ln f_1 = -\int_{K_{e_1}}^{K_e} N_2 \mathrm{d}\ln K_e \tag{37}$$

$$2\ln f_2 = +\int_{K_{e_2}}^{K_e} N_1 \mathrm{d}\ln K_e \tag{38}$$

where K_{e_1} and K_{e_2} are the values of K_e for "pure" calcium and strontium-chabazite respectively. The variation of these activity coefficients with composition is shown in Fig. 3.

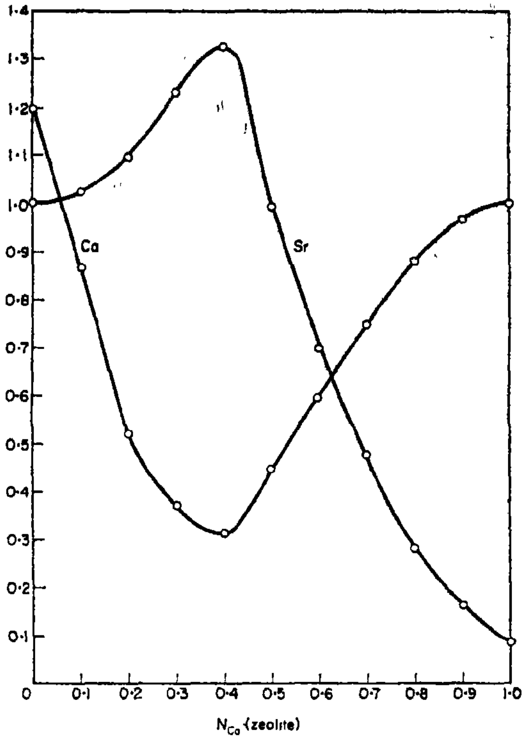

FIG. 3. Variation of the activity coefficients of Ca and Sr ions with the mole fraction of these ions in chabazite.

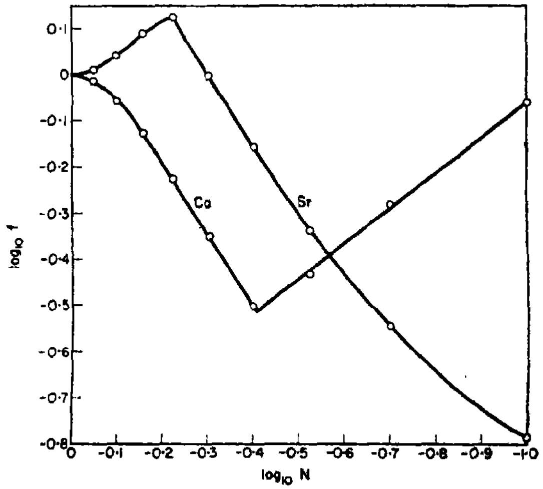

FIG. 4. Log–log plot of Fig. 3.

For this exchange system

$$\ln K_a = \int_0^1 \ln K_e \, dN_1 \tag{39}$$

from which a value of $K_a = 0{\cdot}9059$ is obtained. Since

$$\Delta G_0 = -\frac{RT}{4} \ln K_a \tag{40}$$

ΔG_0, the standard free energy of exchange per equivalent, is 15 cal.

The values of $\dfrac{d \ln f}{d \ln C}$ were obtained from Fig. 4 as functions of the concentrations, C. Then from equations (34), (3) and (16), D_{AB} was calculated at various concentrations over the accessible range in cation fractions of Ca and Sr in the chabazite. By integrating D_{AB} graphically over the same limits of exchangeable cation fractions as used in equation (5), the integral interdiffusion coefficient D_{AB} corrected for the activities of the ions in the exchanger can be obtained. These values of $1{\cdot}81 \times 10^{-15}$ cm²/sec and $1{\cdot}71 \times 10^{-15}$ cm²/sec are to be compared with the values of D_{AB} quoted for Ca and Sr in columns 5 and 6 of Table 1 respectively. The activity corrections improve the values of D_{AB} but they are still considerably different from the experimental figures quoted in column 4 of Table 1.

6. DISCUSSION

The analysis of ion-exchange diffusion presented in this paper has revealed for a zeolite exchanger substantial deviations from all previously existing theories which purported to relate exchange diffusion and self-diffusion coefficients and kinetics. In the present paper a fundamental improvement in the theory has been made but even in this treatment the calculated and observed values of the integral diffusion coefficients differ by a considerable factor. It is of interest to consider one or two of several factors which may contribute to the discrepancy.

The calculation of D_{AB} from experimental data depends on a treatment valid for polymer-penetrant systems. If D_{AB} is a function of concentration only there is no reason to doubt the applicability of the method. However, there is surprisingly early departure of exchange diffusion from the $\sqrt{t}$ diffusion law which is on the other hand very satisfactorily valid for self-diffusion (Part I). This introduces some experimental uncertainty in obtaining D_{AB} (see column 4, Table 1). Nevertheless this is not sufficient fully to explain the observed discrepancy.

A second factor which may affect the exchange kinetics arises from the space charge, which may cause forced flow of other ions, so that transiently the ion flows are not only of the main exchanging pair, *A* and *B*, but also of the residual sodium, and of H_3O^+ or of OH^-, supplied from the water of the aqueous phase or that within the crystals. HELFFERICH found (4) that transient changes in the anion and water concentrations in the resin accompanied the movement of the cations. Similarly, BARRER and FALCONER(12) showed that ion-exchange in crystalline exchangers was more complicated than the simple concepts assumed by Helfferich and Plesset in their theory. Thus the transient state equations governing exchange may be even more complex than those given in Section 4.

From the analysis of the experiments and from the theoretical developments given in this paper it may be concluded that, although exchange diffusion and self-diffusion coefficients can be related in principle, the evaluation of integral exchange diffusion coefficients from experimental data is uncertain for zeolites such as chabazite.

APPENDIX

Several special cases of equations (32) and (33) are of interest. In the absence of water flow, and since $\dfrac{dC_1}{dC_2} = -\dfrac{Z_2}{Z_1}$ (from equations 13), equations (32) and (33) become

$$\left.\begin{aligned} D_1 &= D_A^* \left[1 - \frac{C_1 Z_1}{C_2 Z_2}\left(\frac{d \ln f_1}{d \ln C_2} + \frac{L_{12}}{L_{11}}\right) + \frac{L_{12}}{L_{11}} \frac{d \ln f_2}{d \ln C_1}\right] \\ D_2 &= D_B^* \left[1 - \frac{C_2 Z_2}{C_1 Z_1}\left(\frac{d \ln f_2}{d \ln C_1} + \frac{L_{12}}{L_{22}}\right) + \frac{L_{12}}{L_{22}} \frac{d \ln f_1}{d \ln C_2}\right] \end{aligned}\right\} \tag{41}$$

It has been established(12, 13) that KIELLAND's equation(8) is sometimes valid for the activity coefficients of the exchanging ions within the crystal. Expressing concentrations C_1 and C_2 in terms of cation fractions N_1 and N_2 Kielland's equation is

$$\ln f_1 = KN_2^2;\ \ln f_2 = KN_1^2$$

and thus

$$\left.\begin{aligned} D_1 &= D_A^* \left[1 - \frac{N_1 Z_1}{N_2 Z_2}\left\{2KN_2^2 + \frac{L_{12}}{L_{11}}\right\} + \frac{L_{12}}{L_{11}}\{2KN_1^2\}\right] \\ D_2 &= D_B^* \left[1 - \frac{N_2 Z_2}{N_1 Z_1}\left\{2KN_1^2 + \frac{L_{12}}{L_{22}}\right\} + \frac{L_{12}}{L_{22}}\{2KN_2^2\}\right] \end{aligned}\right\} \tag{42}$$

When the cross-coefficients are small, these equations approach

$$\left.\begin{aligned} D_1 &= D_A^* \left[1 - 2KN_1N_2\frac{Z_1}{Z_2}\right] \\ D_2 &= D_B^* \left[1 - 2KN_1N_2\frac{Z_2}{Z_1}\right] \end{aligned}\right\} \tag{43}$$

The differential interdiffusion coefficient, D_{AB}, is then obtained by substituting equations (43) in equation (16). In those crystalline exchangers which, like chabazite(13) or basic sodalite,(12) do not show limited mutual solid solubility of the end members of the exchange, K is negative in sign with values often in the range $0 > K > -1$, for uni-univalent exchanges.(14) For such values of K, $D_1 > D_A^*$ and $D_2 > D_B^*$ except as N_1 or N_2 approach zero, and D_{AB} exceeds D_{AB} as given by Helfferich and Plesset's equation (1).

Acknowledgement—One of us (R.F.B.) wishes to acknowledge the award of a D.S.I.R. maintenance grant, which allowed him to take part in this work.

REFERENCES

1. HELFFERICH F. and PLESSET M. S., *J. chem. Phys.* **28**, 418 (1958); PLESSET M. S., HELFFERICH F. and FRANKLIN J. N., *ibid.* **29**, 1064 (1958).
2. BEATTIE I. R. and DAVIES D. R., *Phil. Mag.* **8**, **2**, 599 (1957).
3. BARRER R. M., BARTHOLOMEW R. F. and REES L. V. C., *J. Phys. Chem. Solids* **24**, 51 (1963).
4. HELFFERICH F., *J. phys. Chem.* **66**, 39 (1962).
5. FUJITA H., *Text. Res. J.* **22**, 757 (1952); **22**, 823 (1952).
6. CRANK J., *The Mathematics of Diffusion* p. 87. University Press, Oxford (1957).
7. CRANK J., *The Mathematics of Diffusion* p. 246. University Press, Oxford (1957).
8. KIELLAND J., *J. Soc. Chem. Ind.* **54**, 232 (1935).
9. GLUECKAUF E., *Nature, Lond.* **163**, 414 (1949).
10. EKEDAHL E., HOGFELDT E. and SILLEN L. G., *Acta Chem. Scand.* **4**, 556 (1950); **4**, 828 (1950).
11. ARGERSINGER W. J., DAVIDSON A. W. and BONNER O. D., *Trans. Kansas Acad. Sci.* **53**, 404 (1950).
12. BARRER R. M. and FALCONER J. D., *Proc. Roy. Soc.* **A236**, 227 (1956).
13. BARRER R. M. and SAMMON D., *J. chem. Soc.* 2838 (1955).
14. BARRER R. M., *Proc. chem. Soc.* 99 (1958).

J. Phys. Chem. Solids Pergamon Press 1963. Vol. 24 pp. 319–327. Printed in Great Britain.

THE CONDUCTION BAND OF CERIUM SULFIDE $Ce_{3-x}S_4$

M. CUTLER, R. L. FITZPATRICK and J. F. LEAVY

John Jay Hopkins Laboratory for Pure and Applied Science,
General Atomic Division of General Dynamics Corporation, San Diego, California

(*Received* 4 *September* 1962)

Abstract—A study of cerium sulfide, $Ce_{3-x}S_4$, over most of the range of composition, $0 < x < \frac{1}{3}$, has led to information about the conduction band. The compositions, determined by accurate density measurements, permitted evaluation of the electron concentration, n. The room temperature values of the electrical conductivity σ, the thermoelectric power α, and the Hall coefficient R_H, were determined as a function of n over the range from 6×10^{20} cm^{-3} to 6×10^{21} cm^{-3}. The mobility is relatively low (2–3 cm^2/V-sec), but the thermoelectric power varies as $n^{-2/3}$, as required by conventional theory for degenerate systems, and this permitted estimates of the effective mass and width of the conduction band. On the other hand, the Hall coefficient decreases below the value $1/ne$ as n is increased, indicating warping of the Fermi surface as the conduction band is filled. These results, and the analogy to transition metal oxides, suggest the possibility that the conduction band arises primarily from overlapping $5d$ orbitals of the cerium ions.

INTRODUCTION

CERIUM sulfide occurs in several phases with different compositions or ranges of composition as measured by the ratio of sulfur to cerium. The chemical and crystallographic aspects of these compounds and similar sulfides of other rare-earth elements have been the subject of study by a number of investigators;(1,2,3) the most recent and comprehensive discussion is given in a paper by PICON *et al.*(4) The γ-phase of cerium sulfide is metastable at lower temperatures, but it is readily prepared in the high temperature form. It has interesting electronic properties both with regard to thermoelectric applications and also from a fundamental viewpoint; this paper is intended as a contribution to the latter aspect of the subject.

The compound exists in a range of composition between Ce_2S_3 and Ce_3S_4. The crystal structure of Ce_3S_4 is the cubic Th_3P_4 type lattice. The compositions richer in sulfur than Ce_3S_4 have the same crystal structure but with vacancies occurring in the cerium sublattice.(2) Therefore it is helpful to write the formula $Ce_{3-x}S_4$, where x can vary between 0 and $\frac{1}{3}$, the latter extreme corresponding to the composition Ce_2S_3. Crystallographic studies show that the unit cell contains sixteen sulfur atoms and a number of cerium atoms ranging between $10\frac{2}{3}$ and 12.(2) The vacancies are believed to occur in random positions. The lattice constant is 8·6250 Å for $x = 0$, and 8·6347 Å for $x = \frac{1}{3}$.

A significant aspect of the data in the literature consists of magnetic susceptibility measurements which show that the cerium is in a 3+ ionic state with an electronic structure $(4f)^1$.(4) This is true over the whole range of composition. Therefore Ce^{2+} ions do not exist in this compound at room temperature since an additional localized electron would certainly change the magnetic moment.

The interatomic distances in the crystal and the coordination numbers correspond to a largely ionic structure. Since a sulfur ion cannot have more than two electrons, there are extra electrons for compositions with $x < \frac{1}{3}$, and these electrons must be in non-localized states, that is, in a conduction band. As a result, one can characterize the structure in more detail by the formula:

$$(Ce^{+3})_{3-x}V_x(S^{2-})_4(e^{1-})_{1-3x}, \qquad (1)$$

where V indicates vacancies in the cerium ion positions.

The presence of x vacancies requires $(1-3x)$ electrons in a conduction band. This state of affairs is unusual in that the perfect crystal (with no vacancies) has extra electrons, while the compound with the usual chemical stoichiometry (Ce_2S_3) has a high concentration of vacancies.

Since the lattice constant hardly changes with x, the density must vary quite appreciably. Using Vegard's law for the very small change in lattice constant to relate a and x, one can deduce that the density d and vacancy concentration x obey the relation

$$x = (5{\cdot}678 - d)/1{\cdot}51, \tag{2}$$

so that d varies between 5·68 and 5·18 as x goes from 0 to $\frac{1}{3}$. There are $(1-3x)$ electrons for x vacancies in the equation (1), and the lattice constant gives the volume of four $Ce_{3-x}S_4$ units, so that one can then deduce the electron concentration from x by the equation

$$n = 6{\cdot}25 \times 10^{21} \cdot (1-3x)\ \mathrm{cm}^{-3} \tag{3}$$

The conclusion relating composition, for $x < \frac{1}{3}$, with the presence of conduction electrons is borne out in a general way by electrical measurements. Ce_3S_4 is a very good n-type conductor, and compositions approaching Ce_2S_3 have decreasing electrical conductivities. The electronic properties of cerium sulfide were first investigated experimentally by KURNICK, followed by experimental and theoretical studies by a number of other investigators.(5,6,7) They include studies of the *thermoelectric transport coefficients* (electrical conductivity, Seebeck coefficient, and thermal conductivity) over wide ranges of temperature, as well as the effect of doping constituents, and some Hall measurements at room temperature.

The present work is based on a study of the transport coefficients as a function of concentration, the latter being determined from accurate density measurements. We report the results of such measurements at room temperature only; this is sufficient to permit deduction of interesting conclusions about the conduction band. A detailed study of the additional effect of temperature on the transport coefficients is left for a future report, since this would tend to shed light more on transport than on the electronic structure, although the two are closely related. The dependence of transport coefficients on temperature for our samples is generally the same as that reported by previous workers except that our samples have higher electrical conductivities at a given composition; the reasons for this are discussed later in the paper.

PREPARATION AND CHARACTERIZATION OF $Ce_{3-x}S_4$

The samples were prepared by techniques reported previously.(5,6) These techniques involve synthesis of Ce_2S_3 by sulfurization of CeO_2 and then fusion in molybdenum crucibles. The latter process, carried out in an inert atmosphere at 1900–2100°C, leads to an appreciable loss of sulfur from Ce_2S_3. The final material is polycrystalline, and the ultimate sulfur content was affected by the loss of sulfur and by the addition of previously prepared Ce_3S_4 or CeS to the Ce_2S_3. Special care was taken to obtain uniform composition in the frozen melt and conductivity measurements usually showed variations of less than 25 per cent in a given batch.

Our measurements of density aimed at an absolute accuracy of $\pm$ 0·01 g/cm^3, which corresponds to an accuracy in the electron concentration of $\pm 1 \times 10^{20}$/cm^3. We used Archimedes' method, with dried benzene as the fluid. Since the samples usually contained voids and cracks, they were powdered and a platinum bucket was used to hold the powder, Small bubbles clinging to the powder were boiled out by reduction of pressure in a bell jar while the sample in the bucket was immersed in benzene. Errors due to loss of some of the powder on immersion in benzene were made negligible by making weighings in the following sequence: (1) sample plus bucket in benzene, (2) dried sample plus bucket in air, (3) bucket with sample removed, in air, (4) bucket without sample in benzene. The small amount of the powdered sample which tends to stick to the bucket after step (3) causes no appreciable error in the calculated result.

The electrical conductivity provides a simple means for characterizing a sample of $Ce_{3-x}S_4$. One would expect it to be a smooth monotonic function of composition, and therefore of density. Conductivity measurements were made by probing on bars cut from the same chunk of cerium sulfide used to provide the powdered sample. The minimum size of the density sample was 500 mg so that one could obtain the required sensitivity with an analytical balance.

The results of the measurements of density and electrical conductivity for a series of samples are shown in Fig. 1. The relatively small scatter of the points from a smooth curve supports the belief that they represent the properties of homogeneous cerium sulfide. The top abscissa represents the vacancy concentration x corresponding to the density on the bottom scale. The experimental points correspond to a range of electron concentrations between 6×10^{20} and $6 \times 10^{21}/cm^3$, and vacancy concentrations between 0 and 2×10^{21} cm^3. (It should be noted that our densest samples probably still have a high concentration of vacancies on an absolute scale ($\sim 10^{20}/cm^3$), which is the limit of sensitivity of our density measurements.) This curve was used as a master curve to determine the compositions of other samples from their measured electrical conductivities.

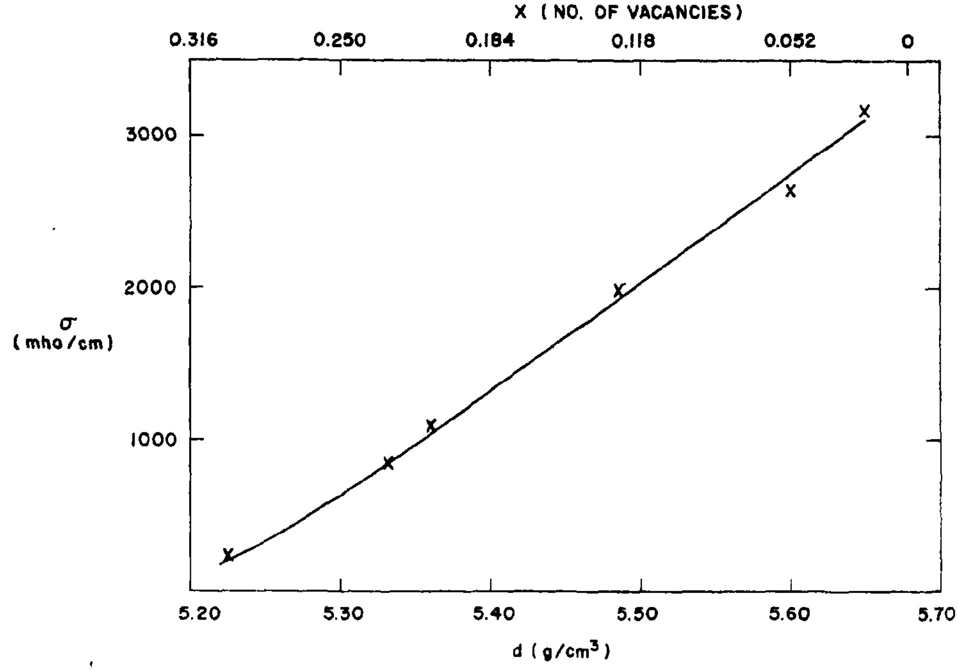

FIG. 1. Electrical conductivity of $Ce_{3-x}S_4$ as a function of density and composition.

In comparison with our results, RYAN *et al.*, who studied mostly sintered samples, found much lower electrical conductivities at compositions near Ce_3S_4.(7) This may have been caused by grain boundary resistance. Their composition determinations were not claimed to be very accurate, but we believe they were largely correct because their values of the thermoelectric power are approximately consistent with the reported composition as judged by our measurements. (Refer to the next Section.) One would expect measurements of the thermoelectric power and Hall coefficient to be affected much less by grain boundary layer resistance; however, this resistance may cause a lower electrical conductivity. Similar erroneous conductivities have been reported in the past from our laboratory, where fused samples were used. Only with considerable care in avoiding contamination by oxygen has it been possible to obtain a consistent relation between the electrical conductivity, σ, and the density, d. Samples contaminated with oxygen were eliminated beforehand by a chemical test.

DEPENDENCE OF ELECTRICAL PROPERTIES ON COMPOSITION AT ROOM TEMPERATURE

Equation (3) allows one to convert the composition parameter x into the electron concentration n, so that one can compute the mobility $\mu = \sigma/ne$

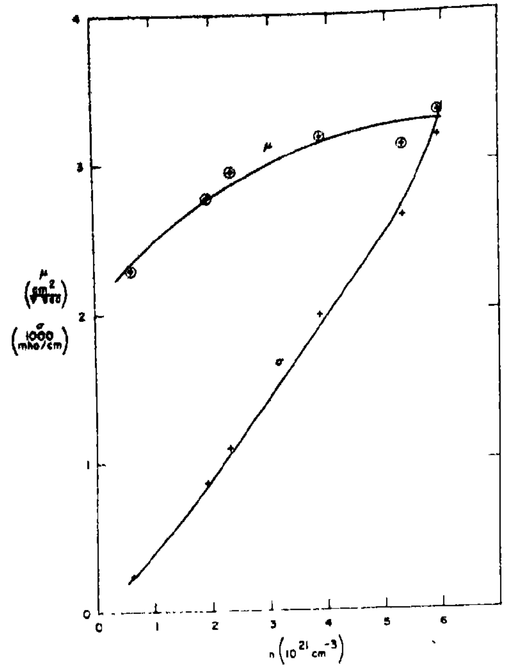

FIG. 2. Electrical conductivity and electron mobility as a function of electron concentration in cerium sulfide.

from $\sigma(n)$. Figure 2 shows the behavior of μ and σ as a function of n. The large electron concentrations and the values of the Seebeck coefficient, discussed below, indicate that degenerate statistics apply. As n decreases from 6×10^{21} to 6×10^{20}, the de Broglie wavelength (the reciprocal of the k vector) increases from 1·8 Å to 3·8 Å, while the scattering distance decreases from 12 to 4·0 Å. Therefore, the experimental range is one in which the scattering distance is larger than the de Broglie wavelength, but approaches it at lower electron concentrations.

Measurements of the Seebeck coefficient were made and the value converted to the absolute thermoelectric power S. The results are shown in Fig. 3. Conventional theory for electron transport in metals based on the free electron model gives rise to the equations:

$$S = \frac{\pi^2}{3}\frac{k^2 T}{\zeta e}\left(1 + \frac{\mathrm{d}\ln\lambda_s}{\mathrm{d}\ln E}\right)_{E=\zeta} \tag{4}$$

and

$$\zeta = \frac{h^2}{8m^*}\left(\frac{3n}{\pi}\right)^{2/3} \tag{5}$$

where ζ is the Fermi energy and λ_s is the scattering distance. Therefore, $S \propto n^{-2/3}$. The data points in Fig. 3 lie fairly well along a line with the required slope for the log–log plot.

Assuming that the fit to conventional theory permits attachment of at least approximate significance to the values of the numerical parameters in the fitted curve, we have plotted $\zeta(n)$ in

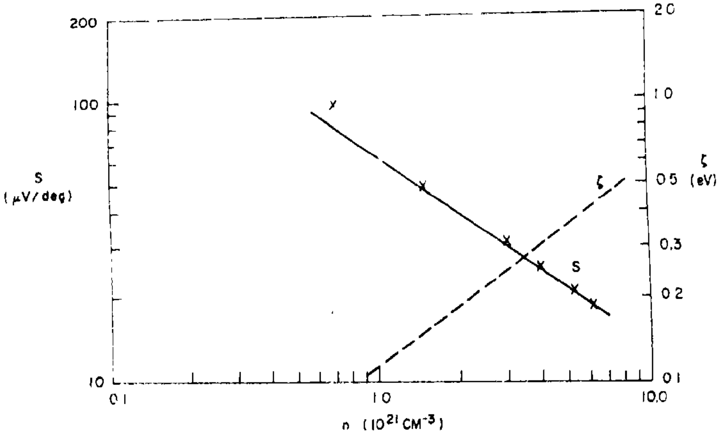

FIG. 3. The absolute thermoelectric power as a function of electron concentration. The dashed curve is the Fermi energy calculated on the basis of $m^*/m_e = 3 \cdot 12$.

Fig. 3, assuming also that $(\mathrm{d}\ln\lambda_s/\mathrm{d}\ln E)_{E=\zeta} = 0$.(4) Corresponding to this also, one obtains $m^* = 3{\cdot}12m_e$. These values for m^* and $\zeta(n)$ are arbitrary, and are subject to revision in the light of further information. There are also reasons, discussed in the next Section, to regard as an approximation the interpretation of m^* as a scalar.

Measurements of the Hall coefficient R_H were carried out with these samples, using essentially the a.c. technique described by KURNICK and FITZPATRICK.(8) Our method included, in addition, means for balancing out the out-of-phase component of the signal across the probes. This permitted a much larger signal-to-noise ratio and a precision of about 5 per cent.

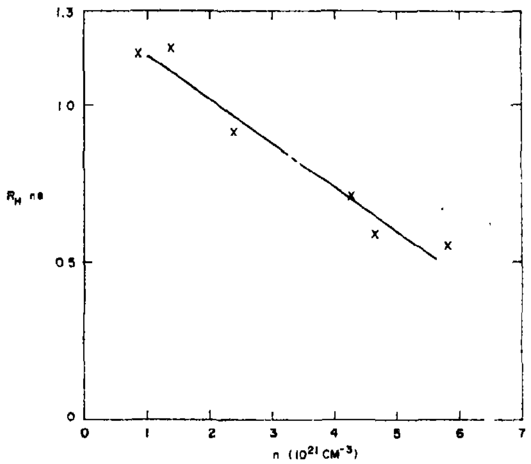

FIG. 4. Plot of R_Hne as a function of electron concentration n.

The experimental values of R_H obtained at large n were considerably smaller than those predicted by the conventional formula, $R_H = 1/ne$. Indeed, the largest value of $(R_He)^{-1}$ exceeded $10^{22}/\mathrm{cm}^3$. This is an impossibly large value for n as can be seen from the considerations involved in deriving equation (3). That particular result was also obtained by a d.c. measurement which was in good agreement with the a.c. value.

Our conclusion is that the observed values of R_H do not obey the usual $(ne)^{-1}$ relation. Therefore, R_Hne was plotted vs. n in Fig. 4. As n decreases, R_Hne increases toward the conventional value of unity. We believe that this behavior is to be explained in terms of distortions of the constant energy surfaces from a spherical shape, reflecting a deviation from the free electron model. This will be discussed further in the next Section.

IMPLICATIONS FOR THE BAND STRUCTURE

The free electron model assumes that the crystal potential provides only a small perturbation to the "particle in a box" picture for electrons. This leads to a constant effective mass and spherical constant energy surfaces over most of the Brillouin zone. Only surfaces near the zone edges are distorted.

For a number of metals, the Fermi surface is close to or intersects the boundaries of the Jones zone,† with consequent deviations from simple transport equations based on a constant effective mass. If the Fermi surface is not spherical, the effective mass is a tensor, and the expressions for the transport coefficients become more complicated. For cubic crystals, they can be found in several sources,(9,10,11) and we present them below in a convenient form. The electrical conductivity, σ, is given by

$$\sigma = \sigma(\zeta) \tag{6}$$

where

$$\sigma(E) = \frac{e^2}{\hbar^2}\left\langle \tau\left(\frac{\partial E}{\partial k_z}\right)^2 \right\rangle_E, \tag{7}$$

and

$$\langle f \rangle_E = 2\int_E f\frac{\mathrm{d}S}{|\nabla_k E|} \tag{8}$$

indicates an integration over a constant energy surface. The scattering time, τ, may be a function of the wave vector $\boldsymbol{k}$.

The thermoelectric power is given by

$$S = \frac{\pi^2k^2T}{3e}\left(\frac{1}{\sigma}\frac{\mathrm{d}\sigma}{\mathrm{d}E}\right)_\zeta \tag{9}$$

---

† We use the expression "Jones" zone or "extended" Brillouin zone to refer to the smallest group of Brillouin zones, containing the Fermi surface, made up by planes which have strong scattering for nearly free electrons, as discussed in Ref. 9, p. 155 *et seq.*

and the Hall coefficient is

$$R_H = \frac{\dfrac{2}{e}\left\langle\left(\dfrac{\partial E}{\partial k_y}\right)^2\dfrac{\partial^2 E}{\partial k_x^2}-\dfrac{\partial E}{\partial k_x}\dfrac{\partial E}{\partial k_y}\dfrac{\partial^2 E}{\partial k_x \partial k_y}\right\rangle_\zeta}{\left\langle\left(\dfrac{\partial E}{\partial k_x}\right)^2\right\rangle_\zeta\left\langle\left(\dfrac{\partial E}{\partial k_y}\right)^2\right\rangle_\zeta} \tag{10}$$

This formula for R_H assumes that τ is isotropic; otherwise a more complicated formula is appropriate.(12)

One may conceivably express $E(\boldsymbol{k})$ in terms of cubic harmonics (as well as $\tau(\boldsymbol{k})$ as was done by COOPER and RAIMES(12)), and attempt to relate measured values of the transport coefficients to the coefficients of this expansion. This kind of analysis is not justified by our present data. However, some pertinent remarks can be made which relate equations (6) through (10) to the shape of the Fermi surface and which provide a qualitative interpretation of our data.

The Hall coefficient is closely related to the curvature of the Fermi surface. In particular, the curvature K of the intersection between the Fermi surface and the $k_x k_y$ plane is given by

$$K = \frac{(\partial E/\partial k_x)(\partial E/\partial k_y)(\partial^2 E/\partial k_x \partial k_y)-(\partial E/\partial k_y)^2(\partial^2 E/\partial k_x^2)}{(\frac{1}{2})\cdot|\nabla_k E|^3} \tag{11}$$

Therefore the Hall coefficient is proportional to this curvature, weighted by $|\nabla_k E|^{-2}$, integrated over the Fermi surface. For many situations, such as a spherical or ellipsoidal Fermi surface, equation (10) reduces to the conventional expression for the Hall coefficient. If the Fermi surface is not entirely convex, the Hall coefficient is decreased below that value; this seems to be the meaning of the experimental results. Models involving two bands do not work, since a second conduction band would not give $R_H ne < 1$, and there is no reasonable theoretical or experimental basis for an overlapping hole band.

Most metals have a large fraction of the Jones zone* filled. The distortions in the Fermi surface arise from proximity to zone boundaries which cause reflection of electron waves even though the interaction of the electrons with the ion cores is weak. For cerium sulfide, there is reason to believe that the Fermi surface is not near zone boundaries which will cause strong reflection of weakly interacting electrons.

There are four $Ce_{3-x}S_4$ units in the cubic unit cell which has a body-centred cubic Bravais lattice. At the highest electron concentration ($x = 0$), there are four conduction electrons per cubic unit cell. For a simple b.c.c. lattice, phase cancellation suppresses reflections at wave vectors for which $k_x + k_y + k_z$ are odd numbers, so that the first extended Brillouin zone with reflecting boundaries is formed by planes of the type (110). In cerium sulfide, however, there is further phase cancellation associated with other symmetries, so that the nearest reflection planes are at (112); this is indicated by the smallest angle for diffraction of X-rays.(13) The volume enclosed by these planes is 4½ times as large as that of a simple b.c.c. lattice, so that it would accommodate 18 electrons. This region of k-space is the Jones zone for the conduction electrons; therefore, strong distortions of the Fermi surface from a spherical shape occur at a large distance from planes of strong reflections as indicated by the behavior of the Hall coefficient. This implies a strong interaction between the electrons and the core potentials of the cerium ions. One likely cause of this (to be discussed further in the next Section) is that the wave functions of the conduction band electrons are derived largely from strongly overlapping 5*d* atomic orbitals of the cerium ions. This could give rise to a relatively narrow conduction band with a width comparable to that found in transition metals (~ 1 eV).(14) In such a band the constant energy surfaces would deviate considerably from a spherical shape, except perhaps at energy extrema.

Figure 5 shows a schematic representation (in two dimensions) of what may be the behavior of the constant energy surfaces as the energy is increased for a narrow band. The lowest energies correspond to spherical surfaces centered on $\boldsymbol{k} = 0$, while the highest energies correspond to spheres with opposite curvature centered on some other point in the Jones zone. Intermediate energies have surfaces which change gradually from positive spheres through convoluted surfaces containing increasing areas of negative curvature, to the final spheres of negative curvature. Corresponding to this, the Hall coefficient would decrease in magnitude from $(ne)^{-1}$ through zero, changing sign, to a positive value approaching $(ne)^{-1}$ as the band is nearly filled and the constant energy surface becomes fully concave. This was shown to be the case for a Bloch tight-binding model in calculations carried out by ROSTOCKER, assuming isotropic scattering.(15) Over the experimental range of electron concentration, the situation for $Ce_{3-x}S_4$ would correspond to surfaces which increase in volume to include at most a small fraction (2/9) of the volume of the Jones zone. Therefore the growth of concave regions will not have completely dominated the primarily convex shape of the low energy surfaces.

---

* See note, p. 323.

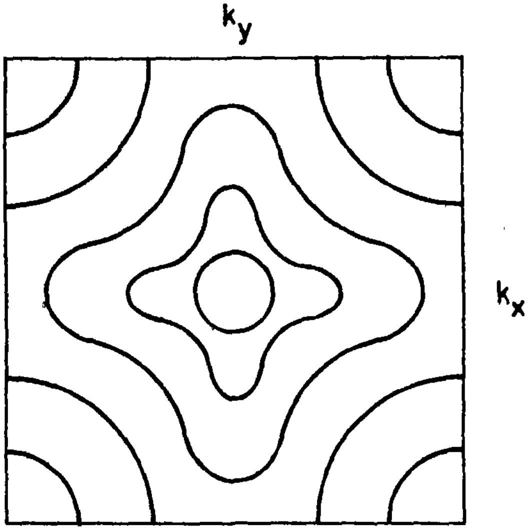

FIG. 5. A schematic diagram for the constant energy surfaces in a conduction band with tightly bound electrons.

It should be noted that anisotropy in the scattering time τ as a function of k can also give rise to smaller values of $R_H ne$. This does not seem likely to occur very strongly except as an indirect result of the anisotropy of $E(k)$, so that we do not offer this in itself as an explanation for our results.

If the observed dependence of R_H on n is to be explained in terms of strong deviations from the free electron model, the question arises as to why the thermoelectric power seems to obey fairly well the theory based on the free electron model. Studies of such deviations for metals have suggested a strong connection between the two. On looking into the problem it would seem that this is not necessarily inconsistent for narrow band systems. Equations (7) and (9) can be interpreted in a very rough way to mean that the electrical conductivity is proportional to the derivative of this area with respect to energy. This would cause the thermoelectric power to go through zero and change sign at an energy for which the area of the Fermi surface goes through its maximum value.

If we put equation (9) in another form:

$$S = \frac{\pi^2 k^2 T}{3e}(E^{-1}\,\mathrm{d}\ln\sigma/\mathrm{d}\ln E)_{E=\zeta} \tag{12}$$

it is clear that if $k(E)$ is to be approximated by any kind of power relation (as is expected), S will depend on n mainly through $E^{-1}(n)$ for $E = \zeta$.(16) Thus, as long as $\mathrm{d}\sigma(E)/\mathrm{d}E$ is not near an extreme value (i.e. zero), $S \propto n^{-2/3}$ implies simply that $E \propto n^{2/3}$. This is exactly true in the free electron approximation, since $E \propto k^2$ and $n \propto k^3$. If the electrons are not free and the constant energy surfaces have distortions from a spherical shape, one might still find, in a first approximation, that the volume of the Fermi surface will be proportional to the cube of some average wave vector (i.e. $n \propto k^{+3}$) and the energy will be proportional to its square. Therefore, the correct interpretation of the results in Fig. 3 is that the Fermi energy apparently varies approximately as $n^{2/3}$, and the calculated value of m^* reflects some average value of $(\mathrm{d}^2E/\mathrm{d}k^2)^{-1}$ over the Fermi surface.

Another approximation in interpretation should be noted with regard to the calculation of the mobility (plotted in Fig. 2), from $\mu = \sigma/ne$. If the constant energy surfaces are distorted from a spherical shape, the effective concentration of electrons is not the same as the true concentration.(27) In such a case, factoring the electrical conductivity, given by equations (6) and (7), into the product of mobility and electron concentration (in addition to the electronic charge) is arbitrary. The mobility given in Fig. 2 then has only an approximate meaning.

NATURE OF THE CONDUCTION BAND

The considerations in the last Section suggest that cerium sulfide has a conduction band whose structure deviates considerably from that expected for the free electron model. The relatively small value for the approximate effective mass ($m^* \cong 3m_e$), on the other hand, indicates that the band is not extremely narrow. Using $m^*/m_e = 3$, and 1·5 electrons per cerium atom in the conduction band, one obtains a band width of 1 eV for a free electron band, and 0·4 eV for a Bloch tight-binding band.

These conclusions seem to be consistent with the suggestion that the conduction band arises from overlapping 5*d* orbitals of the cerium ions. The main support for this hypothesis is derived by analogy to transition metal oxides of the first series; they are believed to have conduction in *d* bands which are fairly wide for the earlier elements. The nature of electronic conduction in transition metal oxides has been reviewed in papers by Morin,(18) and Jonker and van Houten.(19) Morin points out that there is considerable overlap in the 3*d* orbitsls of the type which might be described by the Bloch tight-binding approximation. He presents evidence that *d* band conduction occurs in oxides of titanium and vanadium.(20)

For neutral cerium atoms, the occupied electronic states beyond the xenon shell are $(6s)^2 (5d)^1 (4f)^1$, and their energies are approximately equal. The effect of the neighbouring negative charge of the sulfur ions can be expected to cause relative increases in energy of the (5*d*) state with respect to the (4*f*) state, and the (6*s*) states with respect to the (5*d*), as a result of the decreased shielding of the potential as one goes from 4*f* to 5*d* to 6*s* orbitals. As a result, one has the observed filled $(4f)^1$ levels in the Ce^{3+} ions, and can expect the (5*d*) levels to represent the next highest state. (The possibility that $(4f)^2$ states are lower is excluded by the fact that the corresponding Ce^{2+} ions with the appropriate magnetic moment have never been observed in solids.) In addition to this, one may also expect the interaction to destroy the Russell-Saunders coupling of the atomic $(5d)^1$ states if a conduction band is formed. One would expect the lowest energy states which form the 5*d* band to arise from atomic states whose spacial distribution have the least overlap with the neighboring S^{2-} ions, along the lines of the concepts of crystal field theory.(20) However, these considerations do not provide evidence that the 5*d* band is not overlapped by the 6*s* band in the experimental range of electron concentrations, as is found in transition metals. It may be that the sulfide ions in cerium sulfide will push this band higher in comparison to metals. At any rate, there seems to be no experimental reason to invoke a 6*s* band.

The conclusions arrived at for the 3*d* bands in oxides of the first transition metal series support these ideas. The overlap of the 3*d* orbitals of the transition metal ions increases as one decreases the atomic number. The later members (such as nickel oxide) have small overlap, and the 3*d* levels are believed to form very narrow bands. Electrons in these bands are believed to be localized spacially with strong polarization of the surrounding ions. Their transport involves low mobilities ($\ll 10^{-2}$ cm^2/V-sec—we quote room temperature values) and has been described by a "hopping" model.(21) The earlier members of the series have greater overlap in the 3*d* atomic orbitals, giving rise to wider conduction bands. Titanium oxides have higher electron mobilities (0·1 to 1·0 cm^2/V-sec), corresponding to smaller values for their rigid lattice effective mass.(22)

Scandium oxide, whose conductivity has not been carefully studied, is the first member of the series, and would be expected to have the widest *d* band. Lanthanum is in the same column of the periodic table as scandium, and is immediately followed by cerium. Therefore, cerium sulfide may be regarded as quite analogous to the early transition metal oxides. The greater polarizability of the heavier cerium and sulfur ions can be expected to enhance the width of the *d* band, and, therefore to give rise to larger electron mobilities.

This crude discussion of the character of the electronic levels is in terms of simple atomic orbitals appropriate for purely ionic bonding. Polarization undoubtedly occurs, which would give rise to "mixing" with a fraction of other types of atomic orbitals in the viewpoint used for covalent bonding.

CONCLUSION

The transport coefficients of cerium sulfide have been studied as a function of electron concentration, and they have been found to be consistent, on the whole, with the predictions of conventional theory for degenerate electronic systems. The main exception is the behavior of the Hall coefficient, which seems best explained in terms of increasing distortion of the Fermi surface from a convex shape as the electron concentration is increased.

The proposed behavior of the Fermi surface does not seem to be necessarily inconsistent with the more conventional behavior of the Seebeck coefficient and electrical conductivity. Measurements of the Seebeck coefficient have provided rough estimates of the width of the conduction band and the effective mass. These results are consistent with the suggestion that the conduction band arises largely from the 5*d* states of the cerium ions. This hypothesis is supported largely by analogy with compounds of the transition elements of the first series, such as titanium oxide.

The range of electron concentrations is unusually large compared to other single phase metallic systems that have been investigated. In this regard, comparison should be made with the cubic phase sodium tungsten bronzes, in which the electron concentration varies over a factor of two.(23) The electron concentration varies over a factor of ten in the present study and approaches non-degenerate concentrations at the lower end of the range. As a result, cerium sulfide provides unique opportunity to observe effects on the transport parameters as one fills the conduction band over a wide range with only minor changes in the lattice.

Acknowledgements—We would like to acknowledge, with thanks, the fact that this work has benefitted from discussions with Joachim Appel, Walter Kohn and Brian Coles. Much of the experimental technique and apparatus used in this work was developed by S. W. Kurnick. This work was supported by the Advanced Research Projects Agency (ARPA), under Bureau of Ships Contract NObs-77144.

REFERENCES

1. Eastman E. D., Brewer L., Bromley L. A., Giles P. W. and Longren N. F., *J. Amer. chem. Soc.* **72**, 2250 (1950).
2. Zachariasen W. H., *Acta Cryst.* **2**, 57 (1949).
3. Banks E., Stripps K. F., Newkirk H. W. and Ward R., *J. Amer. chem. Soc.* **74**, 2450 (1952).
4. Picon M., Domango L., Flahaut J., Guittard M. and Patrie M., *Soc. chim. France Bull.* **2**, 221 (1960).
5. Kurnick S. W., Cutler M., Fitzpatrick R. L. and Leavy J. F., *Rare Earth Research* (Edited by Kleber E. V.) p. 241. Macmillan, New York (1961).
6. Appel J. and Kurnick S. W., *J. appl. Phys.* **32**, 2206 (1961).
7. Ryan F. M., Greenberg I. N., Carter F. L. and Miller R. C., *J. appl. Phys.* **33**, 864 (1962); Carter F. L., Miller R. C. and Ryan F. M., *Advanc. Energy Conv.* **1**, 165 (1961).
8. Kurnick S. W. and Fitzpatrick R. L., *Rev. sci. Instrum.* **32**, 452 (1961).
9. Mott N. F. and Jones H., *The Theory of Metals and Alloys* pp. 282, 310. Dover reprint (1958).
10. Jones H. and Zener C., *Proc. Roy. Soc.* **A145**, 269 (1934).
11. Wilson A. H., *The Theory of Metals*, 2nd Edition p. 226. University Press, Cambridge (1954).
12. Cooper J. R. A. and Raimes S., *Phil. Mag.* **4**, 145 (1959).
13. Mott N. F. and Jones H., *The Theory of Metals and Alloys* p. 155. Dover reprint (1958).
14. An extensive discussion of the considerations involved in such a band formation is given in a paper by Goodenough J. R., *Phys. Rev.* **120**, 67 (1960).
15. Rostocker N., private communication.
16. Mott N. F. and Jones H., *The Theory of Metals and Alloys* p. 311. Dover reprint (1958).
17. Mott N. F. and Jones H., *The Theory of Metals and Alloys* p. 97. Dover reprint (1958).
18. Morin F., *Bell Syst. Tech. J.* **37**, 1047 (1958).
19. Jonker G. H. and van Houten S., *Halbleiterprobleme*, **6**, 118 Wieweg, Branschweig (1961).
20. More recent work relating to this question is to be found in (a) Morin F. J., **32**, 2195 (1961) and (b) Frederikse H. P. R., *J. Appl. Phys.* **32**, 2211 (1961).
21. Heikes R. R. and Johnston W. D., *J. chem. Phys.* **26**, 582 (1957).
22. Appel J. and Kurnick S. W., *J. appl. Phys.* **32**, 2206 (1961). This Ref. has an extensive discussion of the implications of polarons in affecting the mobility of electrons in polar crystals such as cerium sulfide and titanium oxide.
23. Ellerbeck L. D., Shanks H. R., Sidles P. H. and Denielson G. C., *J. chem. Phys.* **35**, 298 (1961).

LETTERS TO THE EDITOR

The formation and discharge of Carnauba Wax Electrets in Nuclear Radiation Fields*

(*Received* 29 *June* 1962)

THE PERSISTENT electric polarization of certain photoconducting materials recently has been interpreted on the basis of space charge formation resulting from the localization of electrons and holes in deep traps.(1, 2) The volume polarization of the thermoelectret has been attributed to either hindered dipole orientation(3) or space charge formation resulting from ionic migration at elevated temperature.(4) The discovery of the thermoelectret state in non-polar materials, as well as photo-depolarization of naphthalene thermoelectrets,(5) have raised serious objections to the dipole theory, while the recent finding of uniform volume polarization in Carnauba electrets(6) is difficult to reconcile with the ionic theory.

We have partially depolarized Carnauba wax electrets by gamma-ray bombardment, and have measured the change in the density of unpaired electrons by electron paramagnetic resonance. A 4 Mrad dose of Co^{60} gamma-rays reduced the heterocharge of a Carnauba thermoelectret by a factor of eight, and reduced the density of unpaired electrons by a factor of eighteen. This pairing of spins by radiation could result from neutralization of free radical ions, of trapped electronic charges, or possibly of paramagnetic impurities.

Carnauba wax electrets subsequently were formed by simultaneous action of penetrating radiation and electric field. The term "radioelectret" will be applied to dielectrics polarized by such treatment. Wax disks, 60 mm diameter by 2 mm thickness, were painted on opposite faces with aquadag electrodes and connected to a 1 kV power supply. Beta-rays from a 6 curie Sr^{90} source were allowed to shine alternatively on each face, producing symmetrical irradiation. The average beta dose rate, as determined by ferrous sulfate dosimetry, was 0·38 Mrad-hr^{-1}.

The isothermal decay current of a Carnauba radioelectret is shown in Fig. 1 along with comparative curves for samples electrified in the absence of radiation at 70°C and at room temperature. The small oscillations in the curves are caused by diurnal temperature fluctuations of approximately 1°C. The current, i, from each sample is related to time, t, after the first few hours of decay, by the relation, $i = kt^{-n}$, where k and n are constants. This power law relationship is characteristic of both dipole relaxation and release of electrons from traps characteristically distributed in energy. Decay curves of this type have been useful for determining trap distributions in certain phosphorescent and photo-conducting materials(7) and in irradiated dielectrics.(8)

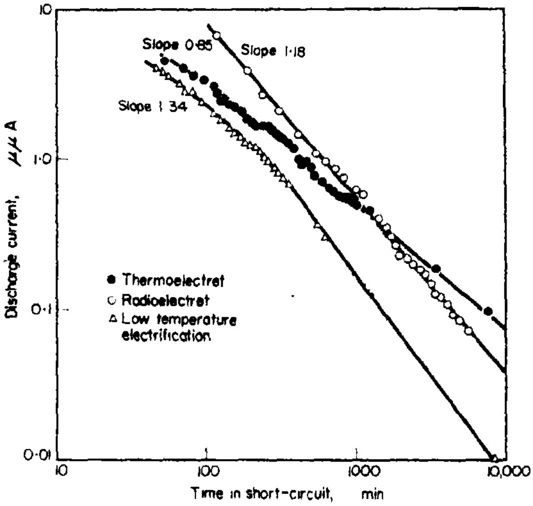

FIG. 1. Decay of electrets at 22 ± 1°C. Identical Carnauba wax disks were electrified at a field strength of 5 kV per cm then measured in short-circuit. The conditions of electrification were as follows: thermoelectret, 4 hr at 70°C, and 18 additional hr after cooling; radioelectret, 37 hr irradiation at 22°C for a total dose of 14 Mrad; low temperature electrification, 48 hr at 22°C.

The residual volume polarization of an electret is determined by reheating the electret in short circuit and integrating the discharge current. This procedure yields the true, volume heterocharge; the contribution of surface homocharge is very

---

* This research was supported by the United States Air Force under Grant No. AF-AFOSR-61-140 monitored by the Air Force Office of Scientific Research, Office of Aerospace Research.

small when electrification is carried out at fields of 5 kV-cm^{-1} or less. Currents were measured by a Cary model 31 electrometer, and the heating system has been described previously.(9) Typical discharge curves for a standard heating rate are shown in Fig. 2. Average values of residual polarization, after two days storage in short circuit, are as follows: 10^{-7} C-cm^{-2} for 4 hr electrifications at 70°C; 7×10^{-10} C-cm^{-2} for 48 hr electrifications at 22°C; and $2{\cdot}5\times10^{-8}$ C-cm^{-2} for 35 hr electrifications at 22°C, in a 0·38 Mrad-hr^{-1} beta irradiation field. The radioelectret polarization was proportional to radiation dose, up to the maximum exposure of 14 Mrad.

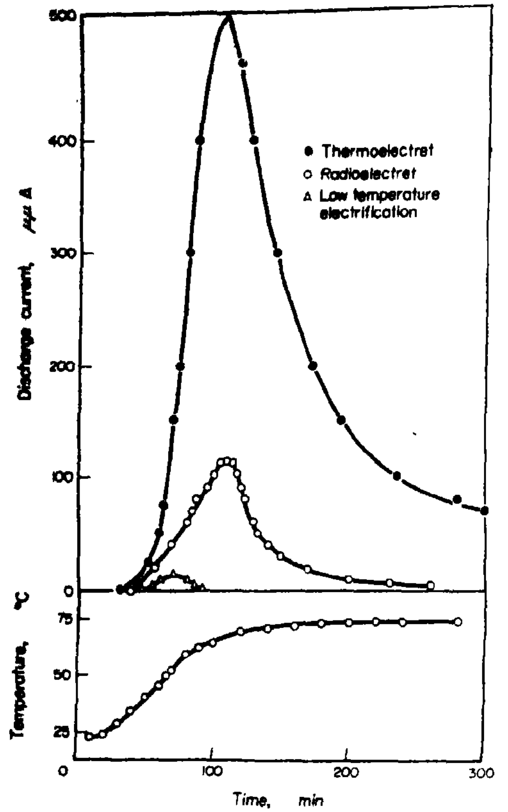

FIG. 2. Thermo-depolarization of electrets. Identical Carnauba wax disks were electrified as in Fig. 1. The samples formed without irradiation were held in short-circuit for two days and the radioelectret for six days before depolarization.

The similarities between Carnauba radioelectrets and thermoelectrets point to common mechanisms. Undoubtedly, the first step in polarization is molecular ionization. This may be followed by electronic charge migration over a microscopic distance in the field direction, with eventual charge capture. The type of charge trapping, such as radical-ion formation, molecular disproportionation, etc., will depend on the nature of the capture site. This model is compatible with the bulk of experimental evidence, including the coexistence of an ionic homocharge, and findings on charge distribution. Measurements of radioelectret charge distribution and electron paramagnetic resonance spectra are needed to verify the existence of a common electret mechanism. A more detailed account of this work, including measurements on other electret forming materials, is in preparation.

Acknowledgements—The author is indebted to S. C. RIBEIRO, F. MILANEZ, and R. J. DE MORAES for their assistance in the experimental work, and to Southwest Research Institute for electron paramagnetic resonance measurements.

Institute of Physics,
Catholic University,
Rio de Janeiro, Brazil

P. V. MURPHY

References

1. FREEMAN J. R., KALLMANN H. P. and SILVER M., *Rev. mod. Phys.* **33**, 553 (1961).
2. FRIDKIN V. M. and ZHELUDEV I. S., *Photoelectrets and Electrophotographic Processes*", p. 56. Academy of Sciences of the USSR, Moscow (1960).
3. GROSS B., *Phys. Rev.* **66**, 26 (1944).
4. GEMANT A., *Phil. Mag.* **20**, 929 (1935).
5. BELYAEV L. M., BELIKOVA G. S., FRIDKIN V. M. and ZHELUDEV I. S., *Kristallografiya* **3**, No. 6 (1958).
6. GROSS B. and DE MORAES R. J., *J. chem. Phys.* **37**, 710 (1962).
7. RANDALL J. and WILKINS M., *Proc. Roy. Soc.* **A184**, 379 (1945).
8. FOWLER J. F., *Proc. Roy. Soc.* **A236**, 464 (1956).
9. GROSS B., *J. chem. Phys.* **17**, 866 (1949).

Availability of high-resolution n-m-r method for the study of molecular motion in the crystalline state

(*Received* 3 *October* 1962)

HIGH-RESOLUTION *n-m-r* technique has been hitherto applied mainly to the study of chemical shift in liquid or solution states. On the other hand, broad line *n-m-r* one has showed its usefulness in the study of molecular motion in the crystalline state. Evidence of the violent thermal motion and the possibility of self-diffusion process found in the so-called plastic crystal(1) by the broad line *n-m-r* and other methods suggested the availability of high-resolution *n-m-r* technique to the study of these problems.

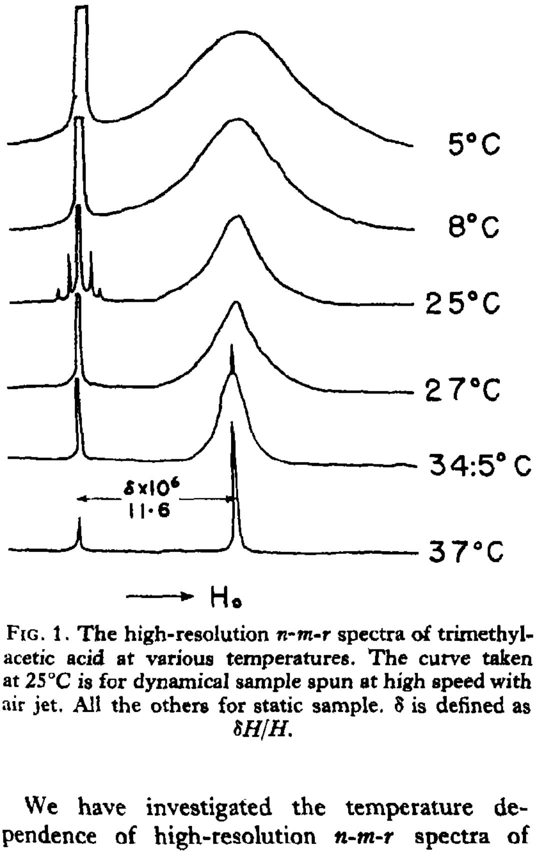

FIG. 1. The high-resolution *n-m-r* spectra of trimethylacetic acid at various temperatures. The curve taken at 25°C is for dynamical sample spun at high speed with air jet. All the others for static sample. δ is defined as $\delta H/H$.

We have investigated the temperature dependence of high-resolution *n-m-r* spectra of trimethylacetic acid crystal which is known to be a kind of plastic crystal by previous thermal,(2) X-ray and other studies.(3) Measurements were performed by use of Varian Associates Model V-4311 High-resolution NMR Spectrometer, covering the temperature region between the transition point (6·9°C) and the melting point (36·4°C). The results are given in Fig. 1.

As is shown, two peaks can be assigned to carboxyl proton and nine methyl protons resonance, respectively, as is evident from the approximate intensity ratio 1:9. When the specimen is spun at high speed with the aid of an air turbine, a set of side spectra was observed around the central OH line at constant separations (see the curve measured at 25°C). This observation consists with the theoretical consideration by ANDREW *et al.*(4) The separation of the two peaks is not so sensitive to the change of state of aggregation, i.e. solid and liquid states, and it is in comparable magnitude with those of other carboxylic acids involving methyl protons.

A gradual reduction in the line width of each peak is observed as the temperature is raised. From the temperature dependence of the line width of the resonance line due to methyl protons we have analysed the kinetic properties associated with the plausible self-diffusion process. The activation energy estimated by use of KUBO–TOMITA theory(5) is found to be about 7·9 kcal/mole. Since this crystal belongs to the face centred cubic lattice, we applied the empirical relationship by NACHTRIEB *et al.*,(6) which holds experimentally in the body and the face centred systems, to calculate the enthalpy of activation for the self-diffusion. By taking our data for the enthalpy of fusion $\Delta H_f = 480$ cal/mole it comes out to be 7·92 kcal/mole, which is fortuitously in good agreement with that given above.

In conclusion, it was revealed that the high-resolution *n-m-r* techniques were also useful for investigating the molecular motions and also for detecting the chemical shifts in the plastic crystals. The above results seem to be significant if we consider the fact that molecules in liquid crystals give the broad line *n-m-r* spectra.(7) A full discussion will be published elsewhere in near future.

Acknowledgements—The authors wish to express their sincere thanks to Dr. E. NAGAI and Mr. S. SATŌ of Kureha Bōseki Co. for their kindness of using the Varian Associates Spectrometer for our purposes and also for their collaboration in the measurements.

Dept. of Chemistry,
Faculty of Science,
Osaka University,
Nakanoshima, Osaka, Japan

HIROSHI SUGA
SYÛZÔ SEKI

References

1. Andrew E. R., *J. Phys. Chem. Solids* **18**, 9 (1961).
2. Suga H., Koide T. and Seki S., Reported at *9th Annual Meeting of chem. Soc. Japan* (1956). To be published.
3. Namba H. and Oda T., *Bull. chem. Soc. Japan* **25**, 225 (1952); Kondo S. and Oda T., *ibid.* **27**, 567 (1954).
4. Andrew E. R. and Newing R. A., *Proc. phys. Soc., Lond.* **72**, 959 (1958).
5. Kubo R. and Tomita K., *J. phys. Soc. Japan* **9**, 888 (1954).
6. Nachtrieb N. H. and Hamdler G. S., *Acta Met.* **2**, 797 (1954).
7. Jain P. L., Lee J. C. and Spence R. D., *J. chem. Phys.* **23**, 878 (1955).

Optical and ESR spectra of irradiated CaO crystals*

(*Received* 5 *November* 1962)

Possible models of various color centers in the alkaline earth oxides have been discussed by Wertz,(1) from spin resonance studies. Clarke(2) presented a tentative energy level scheme for the principal lattice defects in MgO, based largely on optical data. Due to problems in obtaining single crystals, less is known about lattice defects in CaO, SrO, and BaO. (Other information such as the band gaps is also meager.(3)) Certain narrow ESR lines produced in powders of these three oxides have been claimed consistent with an *F*-center model involving oxygen vacancies, based on *g*-shift arguments.(1)

We present here (Fig. 1) the visible and near u.v. absorption spectrum at 300°K of single CaO crystals, obtained from Semi-Elements, Inc., Saxonburg, Penn., and irradiated with 10^{19} nVt fast neutrons in the Oak Ridge ORR reactor. Spectra of non-irradiated CaO, and of an MgO crystal simultaneously irradiated with the CaO samples, are also shown. Broadly speaking, principal absorption lines in the irradiated CaO appear displaced toward the red from the prominent MgO lines. Though we cannot at present establish a correspondence between the CaO and MgO lines, in terms of centers involved, the general trend seems compatible with a more compressed energy level scheme (smaller band gap) in CaO than in MgO. U.V. absorption in non-irradiated CaO sets in around 2700 Å. Our irradiated CaO was too opaque for transmission work beyond 3·7 eV, using 0·1 mm thick samples; further studies in this range are in progress.

The ESR spectrum of neutron irradiated CaO crystals showed a single isotropic line 1 G wide at $g = (2{\cdot}0001 \pm 0{\cdot}0004)$, precisely as reported in irradiated or ground powder.(1) Other lines such as that ascribed to "F_2-centers" in powder(1) were very weak or not noticeable. The spectrum seemed the same at 300, 77 and 4·2°K, except for a T_1 increase to perhaps seconds at 4·2°K. Spin density of samples that received 10^{19} neutrons was $3 \times 10^{18}/\text{cm}^3$ in CaO, $1 \times 10^{18}/\text{cm}^3$ in MgO.

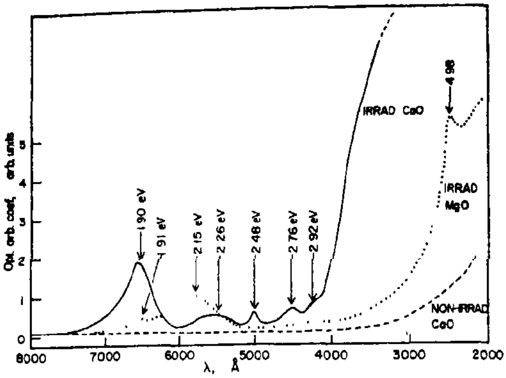

Fig. 1. Optical spectrum of neutron-irradiated CaO single crystals, and spectra of non-irradiated CaO and of irradiated MgO for comparison. Fast neutron dose for both CaO and MgO was 1×10^{19} nVt. Spectra taken on Carey Model 11 spectrograph, using samples 0·1–1·0 mm thick. An "arbitrary unit" on vertical scale corresponds approximately to $k \approx 15\ \text{cm}^{-1}$, though absorption intensities in the u.v. are deemed not reliable.

One or more of the optical bands in irradiated CaO ought to be associated with the paramagnetic center producing the ESR line. Assuming, as seems likely,(1) this center to be an *F*-center, we estimated from the spin density the absorption coefficient expected for a single *F*-like band, assuming unity oscillator strength. The strongest visible peak (1·90 eV) we observed appears 30 times weaker than this estimate; most of the *F*-center absorption presumably then lies beyond the

---

* Supported by the U.S. Air Force and by a Tektronix Foundation grant.

4000 Å absorption edge (Fig. 1). Bleaching experiments in progress have indicated, too, a lack of correlation between the ESR and 1·90 eV absorptions (though not conclusively between the ESR line and the four weaker visible peaks in Fig. 1). After heat treatment at 350°C, the 1·90 eV line was down 65 per cent, the ESR signal only 8 per cent. Heating is expected to anneal positive ion vacancies before oxygen vacancies. So far our observations are consistent with the 1·90 eV band being due to positive ion vacancies, as is assertedly the case with the 2·15 eV MgO line.(2) Such vacancies imply holes trapped on oxygens in both cases, and should give similar optical lines except for probably lower energy in CaO.

Department of Physics,
University of Oregon,
Eugene, Oregon

JAMES C. KEMP
VICTOR I. NEELEY

References

1. WERTZ J. E., ORTON J. W. and AUZINS P. *Disc. Faraday Soc.* **31**, 140 (1961).
2. CLARKE F. P., *Phil. Mag.* **2**, 607 (1957).
3. HANNAY N. B., *Semiconductors* pp. 569–576. Reinhold, New York (1959).

Two crystal forms of ZnP$_2$, their preparation, structure, and optoelectronic properties

(*Received* 14 *September* 1962; *revised* 13 *November* 1962)

WHILE investigating the quaternary system Ga–Si–Zn–P(1) we have synthesized a new crystal form of ZnP$_2$. The new crystal form, monoclinic and black in color, was compared with the tetragonal red crystal form first reported by STACKELBERG and PAULUS.(2)

We have used a sealed quartz system for the synthesis of the ZnP$_2$, rather than the open system used by Stackelberg and Paulus. The open system, in which phosphorus vapor is passed over the heated metallic zinc, yields only the red tetragonal ZnP$_2$ and the well-known black Zn$_3$P$_2$. The sealed system gives only the two forms of ZnP$_2$, their ratios being controlled by the phosphorus pressure. For this procedure zinc and enough excess phosphorus for control of pressure were sealed into an evacuated quartz ampoule. Three distinct temperature regions were maintained on the ampoule. At one extreme of the tube a temperature between 1000 and 1050°C was maintained on the zinc, at the other extreme phosphorus was heated in the region of 460–510°C so that controlled pressures in the range of 3–10 atm could be maintained throughout the system. The intermediate region of the ampoule was kept between 700–850°C. It is here that the single crystals of both forms of ZnP$_2$ grew. The yield of red tetragonal crystals was not easily controlled. For phosphorus pressures of about 3 atm, approximately 50 per cent of the crystal mass was red, while the remainder was black. Phosphorus pressures of about 10 atm gave practically a 100 per cent yield of black crystals. X-ray examination indicated that none of these black crystals were Zn$_3$P$_2$.

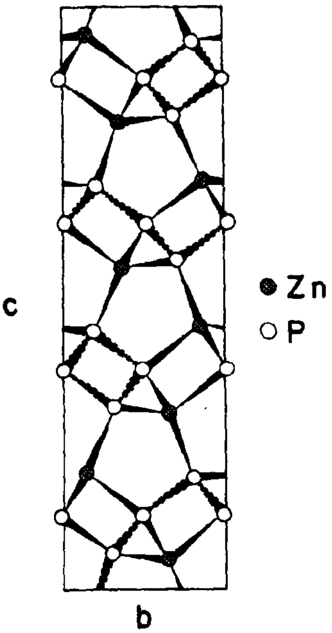

FIG. 1. The crystal structure of the tetragonal modification of ZnP$_2$ projected down the crystal *a* axis. The dotted lines indicate infinite chains of nearest-neighbor phosphorus atoms.

X-ray Weissenberg photographs (Ni filtered CuKα radiation) showed the red crystals to be tetragonal, with unit cell dimensions of $a = 5{\cdot}08 \pm 0{\cdot}01$ Å, and $c = 18{\cdot}59 \pm 0{\cdot}05$ Å. The $00l$ reflections with $l \neq 4n$, and the $h00$ reflections with h odd are extinguished, hence the space group is one of the two enantiomorphs $P4_12_12$ or $P4_32_12$. These data are almost identical with those reported by STACKELBERG and PAULUS.(2) All the atoms are in the 8-fold (*b*) Positions:

xyz; $\bar{x}, \bar{y}, \frac{1}{2}+z$; $\frac{1}{2}-y, \frac{1}{2}+x, \frac{1}{4}+z$; $\frac{1}{2}+y, \frac{1}{2}-x, \frac{3}{4}+z$;

$yx\bar{z}$; $\bar{y}, \bar{x}, \frac{1}{2}-z$; $\frac{1}{2}-x, \frac{1}{2}+y, \frac{1}{4}-z$; $\frac{1}{2}+x, \frac{1}{2}-y, \frac{3}{4}-z$.

The structure was determined from three-dimensional Patterson sections and refined by difference Fourier methods. The refined atomic coordinates are listed in Table I, and a projection of the structure is shown in Fig. 1.

Table 1. *Atomic coordinates in the tetragonal* ZnP_2 *modification*

Atom	*x*	*y*	*z*
Zn	0·154	−0·365	0·050
P_1	−0·184	0·299	0·060
P_2	−0·010	−0·019	0·126

All the atoms are tetrahedrally coordinated. Each Zn atom is bonded to 4 P atoms, while each P atom is bonded to 2 Zn and 2 P atoms. The four independent Zn–P bonds have an average length of 2·40 Å, and the two independent P–P bonds of 2·19 Å. The average values correspond very closely to those calculated from normal covalent radii, 2·41 Å for Zn–P and 2·20 Å for P–P bonds.(3)

The black monoclinic crystals were of two distinct crystal habits. They appeared black when thick with polyhedric shape elongated along the *c* axis. The second form were thin black-greenish platelets of about one micron thin with their length along the *b* direction. The black-green color of these thin platelets can be explained by the presence of a strong absorption band at 1·8 eV which attenuates the red–orange region of the spectrum. The violet part of the spectrum is also attenuated by the generally increasing absorption at higher energies. The remaining blue and yellow portions of the spectrum give rise to the greenish appearance of the platelets. It was often possible to observe epitaxial growth of the monoclinic form on the tetragonal (red) crystals. Sometimes several twins of the monoclinic form rotated within the *bc* plane could be observed. The monoclinic crystals had unit cell dimensions of $a = 8·85 \pm 0·02$ Å, $b = 7·29 \pm 0·02$ Å, $c = 7·56 \pm 0·02$ Å, and $\beta = 102·3° \pm 0·2°$. The systematic extinction of the *h*0*l* reflections with *l* odd and the 0*k*0 reflections with *k* odd determine the space group as $P2_1/c$. The density was measured by water displacement as 3·47 gm cm^{-3} in reasonable agreement with the calculated value of 3·55 gm cm^{-3} for eight molecules per unit cell. In the thin plate crystals *b* and *c* axes lie within the plane of the plate and the normal to the plate is a pseudo orthorhombic axis 34·6 Å in length. The reflection intensities, however, show the true symmetry is monoclinic. All the atoms lie within the 4-fold positions, so that there are two zinc atoms and four phosphorus atoms which are crystallographically independent. The unit cell is closely analogous to the recently-corrected unit cell of $ZnAs_2$,(4) which is monoclinic with $a = 9·28$ Å, $b = 7·68$ Å, $c = 8·03$Å, and $\beta = 102° 19'$, with 8 $ZnAs_2$ units per cell, in space group $P2_1/c$. The crystal structure of the ZnP_2 (monoclinic) was determined by Patterson projections down the three crystallographic axes followed by refinement of the corresponding electron density maps. The refined

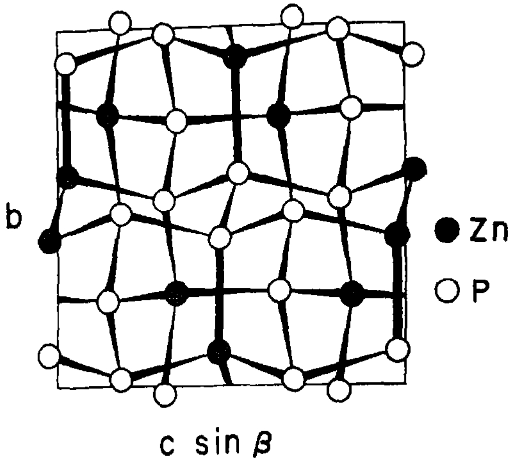

FIG. 2. The crystal structure of the monoclinic form of ZnP_2 projected down the crystal *a* axis.

Table 2. Atomic coordinates in the ZnP_2 *monoclinic modification*

Atom	*x*	*y*	*z*
Zn_1	−0·081	0·244	0·357
Zn_2	0·381	0·089	0·471
P_1	0·394	0·410	0·477
P_2	0·234	0·485	0·190
P_3	0·241	0·017	0·183
P_4	0·078	0·243	0·147

atomic coordinates are given in Table 2, and a projection diagram of the structure is shown in Fig. 2.

Our analysis has shown that in the monoclinic ZnP_2 also, all the atoms are tetrahedrally coordinated. Z_1 is bonded to 4 P atoms and P_2, P_3, and P_4 are each bonded to 2 Zn and 2 P atoms as in the red tetragonal modification. However, Zn_2 and P_1 are each bonded to 1 Zn and 3 P atoms. Because of a very close overlapping of several pairs of atoms in two of the three projections of the structure which have been investigated, the atomic coordinates and bond distances are probably less accurate than those in the tetragonal modification. The coordinates listed above give an average P–P bond distance of 2·27 Å and an average Zn–P distance of 2· 35Å. The Zn–Zn bond has a measured distance of 2·44 Å. This value is very short compared to twice the accepted covalent zinc radius (1·31 Å), but Zn–Zn bonds as short as 2·45 Å have recently been found in $NbZn_2$.(5) The Zn–Zn bonds are in a plane perpendicular to *c* and ± 57° from the *b* axis. Thus, within the *bc* plane there are components of these bonds parallel to *b* but none parallel to *c*.

Optical absorption data provided the basis of energy band gap determination in ZnP_2. For the red tetragonal crystal, Fig. 3 shows the absorption coefficient, α, plotted on a logarithmic scale as ordinate and photon energy $h\nu$, as abscissa. A visual matching of Fig. 3 with the MACFARLANE–ROBERTS(6) expression gives a best-fit value of $E_g = 2{\cdot}05 \pm 0{\cdot}01$ eV. The Macfarlane–Roberts expression for α vs. $h\nu$, for a semiconductor having indirect transitions was plotted separately to the same scale for $T = 300°K$ and assuming $k\theta = 0{\cdot}050$ eV. The value assumed for $k\theta = (0{\cdot}050$ eV) cannot readily be confirmed from the existing

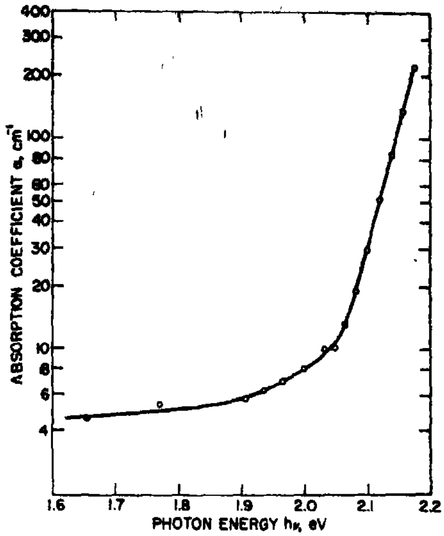

FIG. 3. Optical spectral absorption of red ZnP_2 (tetragonal).

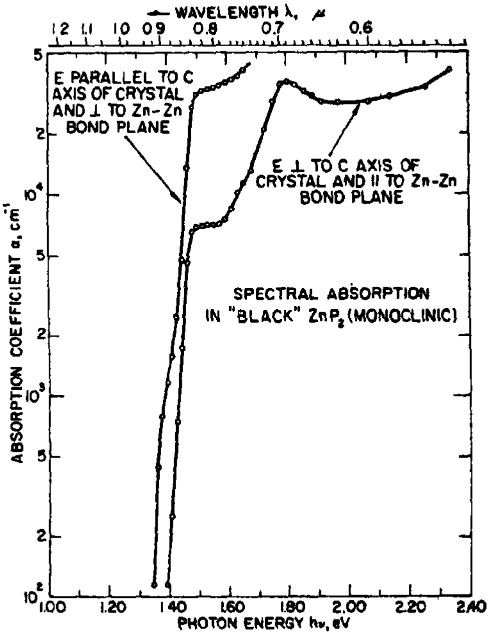

FIG. 4. Optical spectral absorption of black ZnP_2 (monoclinic) with polarized light parallel and perpendicular to long axis of crystal.

optical data and represents an estimate of the energy of the phonon involved in the postulated indirect transition.

In comparison, the optical data for the black form were obtained on very thin crystals and provided absorption coefficient values up to almost 100 times higher than the red form. The very steep slope of α vs. hν probably indicates direct (not phonon-assisted) transitions. A pronounced dichroism has been discovered for α's above 5000 cm^{-1}. The energy band gap is about 1·33 eV for the electric vector of plane polarized light parallel to the *c*-axis and 1·37 eV for the light polarized perpendicular to *c*. (See Fig. 4.) For higher α's this dichroism becomes seven times as large, reaching 0·28 eV at $\alpha = 30{,}000$ cm^{-1}.

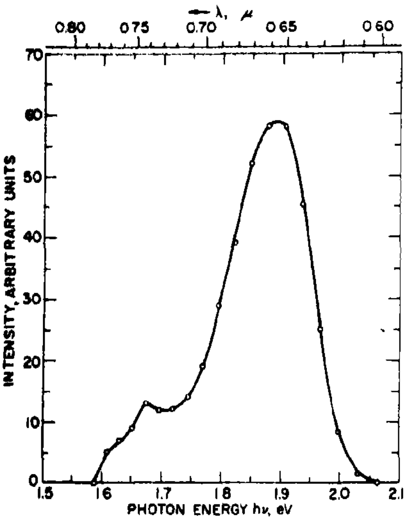

FIG. 5. Photoluminescence of red ZnP$_2$ (tetragonal) with u.v. excitation at liquid nitrogen temperature.

The red ZnP$_2$ (tetragonal) crystals had resistivities in the range of 10^8 Ω-cm while the black (monoclinic) was 10 Ω-cm with an anisotropy of a factor of 2 along the flat and perpendicular direction of the crystal.

Examination of photoluminescence of the tetragonal ZnP$_2$ crystal with u.v. 3650 Å excitation at liquid nitrogen temperature showed a red luminescence with a major peak at 6560 Å (1·89 eV) and a minor peak at 7420 Å (1·67 eV). (See Fig. 5.) Using point contact probes only a very faint electroluminescence at 10^4 V/cm could be observed. Doping with Cu or Mn did not improve the luminous efficiency.

Some photoconductivity data were obtained on the black ZnP$_2$ (monoclinic, see Fig. 6). The photoresponse to unpolarized light (dashed line) has one broad smooth peak covering the region of energy 1·35–1·7 eV. Upon polarization of the incident light, the broad peak was resolved. In the curve "*E* parallel to *c*" the greatest photoconduction peak occurs at about 1·45 eV probably corresponding to the first absorption edge (1·33 eV) obtained in the optical absorption. In the curve "*E* perpendicular to *c*" the maximum peak occurs between 1·65 and 1·85 eV which probably corresponds to the 1·37 eV absorption edge. The minor presence of the characteristic peaks of each polarization on the curves of the other is accounted for by the imperfect polarization in this region of the polaroids used. The energy separation of about 0·3 eV between the two different polarization

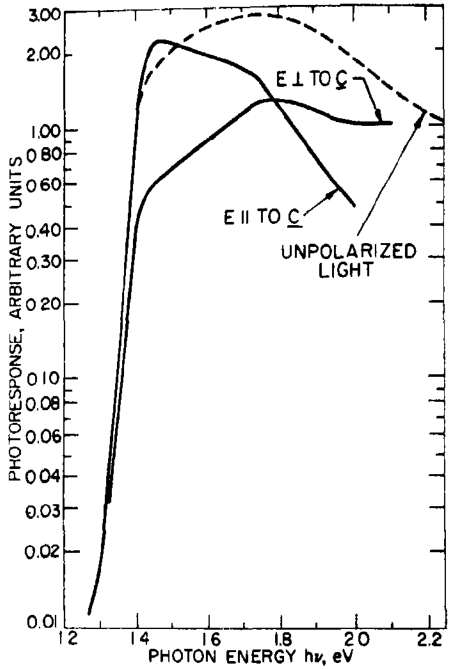

FIG. 6. Photoresponse of black ZnP$_2$ (monoclinic) with unpolarized and polarized light parallel and perpendicular to long axis of crystal.

directions is greater than anything that could be found in the literature. For CdS and CdSe a difference of 0·018 eV has been reported(7) and 0·05 eV for single crystal Te.(8) The related compound $CdAs_2$ reaches a comparable value of 0·2 eV at an absorption coefficient equal to 300 cm^{-1}.(9)

RCA Laboratories,
Princeton, N.J.

I. J. HEGYI
E. E. LOEBNER*
E. W. POOR, Jr.
J. G. WHITE

References

1. LOEBNER E. E., HEGYI I. J. and POOR Jr., E. W., *Metallurgical Society Conferences*, Vol. **12**, pp. 341–369. Interscience, New York–London (1961).
2. STACKELBERG M. and PAULUS R., *Z. phys. Chem.* **B28**, 427–460 (1935).
3. *International Tables for the Determination of Crystal Structures*, Vol. **II**, p. 615, Gebruder Brontraeger–Berlin (1944).
4. SENKO M., DUNN H. M., WEIDENBRONER J. and COLE H., *Acta Cryst.* **12**, 76 (1959).
5. VOLD C. L., *Acta Cryst.* **14**, 1289 (1961).
6. MACFARLANE G. G. and ROBERTS V., *Phys. Rev.* **97**, 1714 (1955); **98**, 1865 (1955).
7. BUBE R. H., *Photoconductivity of Solids*, John Wiley, New York (1960).
8. LOFERSKI J. J., *Phys. Rev.* **93**, 707 (1954).
9. TURNER W. J., FISCHLER A. S. and REESE W. E., *J. appl. Phys.* **32**, 2241 (1961).

---

* Present address: *hp Associates, Palo Alto, California*

BOOK REVIEWS

R. GAY, **Cours de Cristallographie,** Livre III, Gauthier-Villars, Paris (1961). 278 pp. 38 N.F.

THIS is the third book of a series. Book I is entitled *Cristallographie Géométrique*, while Book II is *Cristallographie Physico-Chimique*. The books of the series are individually bound in coarse-textured cloth, and are printed on unsized paper from typescript with both margins justified. Neither the series nor the individual books contain a preface, so that their purpose is not explicitly stated, but they range over a large part of the field of crystallography, including some of what is ordinarily called solid state.

Book III, specifically reviewed here, is subdivided into three parts entitled as follows: First part: Theoretical X-ray crystallography; Second part: Applications of X-ray diffraction—rotating-crystal methods, determination of crystal structures; Third part: applications of X-ray diffraction—powder methods. The subdivisions within the parts do not always appear related to the main title.

"Theoretical X-ray crystallography" (the first part of the book) starts with a short chapter on X-ray tubes, monochromators, filters and collimators. Chapter II continues with some simple physical properties of X-rays. Chapters III, IV, and V are grouped together under the sub-title "The mathematical study of Frauenhoffer diffraction". These are chiefly concerned with various aspects of the Fourier transform. The next group of five chapters (VI through X) conclude the first part of the book. They continue with Fourier transforms and end with three chapters on convolutions. The final chapter is limited to Patterson functions and contains a short section on finding the distribution of atoms by "the method of superpositions".

The second part of the book, "Applications—rotating crystal methods, determination of crystal structures", begins by introducing various diffraction methods based upon a rotating crystal. The rotating-crystal camera is called a "Bragg camera" and the rotating-crystal photograph is called a "Bragg diagram". This is confusing, since the method was invented by Schiebold, developed independently by Polanyi, and later popularized by Bernal. The chapter goes on to describe the Weissenberg and de Jong-Bouman methods briefly. The same chapter continues with a short discussion of the polarization factor, Lorentz factor, absorption, and primary and secondary extinction. Chapter II of this section is entitled "Calculation of the Patterson function" and features only the von Eller analogue computer for two-dimensional Fourier functions. Chapter III discusses absent spectra. Chapter IV is relatively long (30 pages, but including five full pages of illustrations, mainly von Eller photographs) and is devoted to crystal-structure analysis. In it are discussed the method of trial and error, heavy-atom and substituted-atom methods, direct methods in reciprocal space, Patterson methods, and finally refinement.

The third part of the book deals with powder methods. Chapter I treats cameras and indexing. Chapter II discusses some uses of the powder method.

There are several appendices on miscellaneous topics, including the reciprocal lattice, thermal agitation, diffraction spots from small crystals, structures of liquids, Wilson's method of determining F_{000}, small-angle scattering, and Laue photographs.

It is not clear for whom the author intended the book. There is a kind of highlight coverage of topics, but the treatment is neither extensive nor intensive enough to be of much use to those wishing to learn crystal-structure analysis. One is left with the impression that the book is probably a record of a series of lectures given by the author.

Massachusetts Institute of Technology
Cambridge 39, *Mass.*

M. J. Buerger

W. A. Wooster: **Diffuse X-ray reflections from crystals.** University Press, Oxford (1962) 200 pp. 35*s*.

This book is concerned with some of the physical phenomena which can be studied by means of diffuse X-ray scattering. The sections on thermal diffuse scattering are of special interest. There is a good description of the propagation of elastic waves through a crystal and the scattering of X-rays by these waves. Experimental determinations of elastic constants from the absolute magnitude of the thermal diffuse scattering are worked out in sufficient detail to provide some understanding of the technique. The determination of elastic spectra and the dispersion of the velocity of elastic waves are also illustrated. However, the extension of these data to the force constants in the crystal is not undertaken, but this involvement in lattice dynamics is probably beyond the scope of *this book*. The author is well known for his work in the measurement of elastic constants from thermal diffuse scattering, and this section of the book is well written.

The chapter on structural imperfections includes some work on faulting, clustering, short range order and atomic size effects. There is a great deal of ground to be covered, and the author has given a rather brief description of a few investigations in each area. The net result is not very cohesive and lacks the thoroughness of the thermal section. There is also a brief treatment of diffuse scattering from molecular crystals. This chapter is necessarily short, because of the lack of work in this area, but nevertheless welcome.

The introductory portion of the book reviews the theoretical basis of diffuse reflection studies. There is a section on experimental methods, and this leans heavily on the photographic techniques which the author favors. These methods are not as popular here, but the description may still be useful in some cases. There is no mention of recent work on multiple scattering, but perhaps we should not expect to find everything in one book.

The author is misleading in the section on absolute intensity measurements when he indicates that diffuse scattering may be standardized by comparison with the Compton scattering from a material of low atomic number. The total diffuse intensity scattered by the intermediate standard is the quantity which is observed, and although the Compton modified scattering may represent a large portion of the intensity, the remainder should not be ignored.

On the whole, however, the book will be useful for those undertaking experimental work in this area.

B. L. Averbach

NOTICE

Conference on

Sorption Properties of Vacuum Deposited Metal Films

The Institute of Physics and the Physical Society in collaboration with the Joint British Committee for Vacuum Science and Technology announces that it is arranging a conference under the chairmanship of Mr L. HOLLAND, Edwards High Vaccum Ltd., on "Sorption properties of vacuum deposited metal films" at the University of Liverpool from 17 to 19 of April, 1963. It is intended to stress the scientific aspects of the subject rather than detailed techniques. Suggested main topics are as follows:

Structure and properties of metal films.
Sorption and chemical reactivity properties of metal films.
Reaction between ionized gases and metal surfaces.
Application of scientific principles to pumping by metal surfaces.

There will be a number of invited papers covering recent work in the field.

Residential accommodation in a University Hall of Residence will be available. Advance registration for attendance at the conference is necessary. Further details and application forms are available from The Administration Assistant, The Institute of Physics and The Physical Society, 47 Belgrave Square, London, S.W.1.

ERRATUM

H. Schlosser: Symmetrized combinations of plane waves and matrix elements of the Hamiltonian for cubic lattices, *J. Phys. Chem. Solids* 23, 963 (1962).

1. p. 964 *Definition of symbols and notation*

Replace: $\mathscr{A} = \sum_n (I+R_{23})P_{ln}$ by: $\mathscr{A} = \sum_n (I+R_{23})P_{1n}$

$\mathscr{B} = \sum_n (I-R_{23})P_{ln}$ $\mathscr{B} = \sum_n (I-R_{23})P_{1n}$

2. p. 967, line 9 after (15).

Replace: or to different columns of, by: or to different rows of

3. p. 968, *Simple cubic generators* (1,0,0) *axis*

Replace:

Δ_1 $(I+R_{23})[(\pm)i \pm j \pm k]$
Δ_2 $(I-R_{23})[(\pm)i \pm j \pm k]$
Δ_1' $(I-R_{23}-J+JR_{23})[i \pm j \pm k]$
Δ_2' $(I+R_{23}-J-JR_{23})[i \pm j \pm k]$

by:

Δ_1 $(I+R_{23})[i(\pm)j(\pm)k]$
Δ_2 $(I-R_{23})[i(\pm)j(\pm)k]$
Δ_1' $(I-R_{23})\{[i \pm j \pm k]-[i \pm j \mp k]\}$
Δ_2' $(I+R_{23})\{[i \pm j \pm k]-[i \pm j \mp k]\}$

4. p. 969, *Face centered cubic* $(\frac{3}{4}, \frac{3}{4}, 0)$ *point*

Replace: K point has same SCPW as Δ line.

by: K point has same SCPW as Σ line.

ADDENDUM

Add to *Face-centered cubic:*

$(\frac{1}{2}, \frac{1}{2}-m, \frac{1}{2}+m)$ line $m < \frac{1}{2}$

Q_1 $[i\,j\,k]+[-i-k-j]$
Q_2 $[i\,j\,k]-[-i-k-j]$

$(1, \frac{1}{4}, \frac{1}{4})$ *point*

U point has same generators as S axis in s.c.

$(1, m, m)$ line $m < \frac{1}{4}$

S line has same generators as S axis in s.c.

$(m, 1, 0)$ line $m < \frac{1}{2}$

Z line has same generators as Z axis in s.c.

J. Phys. Chem. Solids Pergamon Press 1963. Vol. 24, pp. 341–346. Printed in Great Britain.

WEAK-FIELD MAGNETORESISTANCE OF HOPPING CONDUCTION IN SIMPLE SEMICONDUCTORS*

NOBUO MIKOSHIBA†

Institute for the Study of Metals, University of Chicago, Chicago, Illinois

(*Received* 1 *October* 1962)

Abstract—The weak-field magnetoresistance of phonon-induced hopping conduction is calculated for simple semiconductors, in which the impurity state is represented by the hydrogenic wave function. Emphasis is placed upon the angular dependence of the magnetic perturbation on the wave function, of the elementary transition probability from one to the other impurity sites and of the magnetoresistance coefficients. The quadratic Zeeman perturbation gives rise to an increase of the wave function near the impurity site and a decrease at large distances from the site. Critical distances at which the wave function remains unchanged are given by $\Upsilon_c = 3{\cdot}32a$ (a: Bohr radius) in the direction parallel to the field and $\Upsilon_c = 1{\cdot}63a$ in the perpendicular direction. It is shown that the ratio of the contribution to the magnetoresistance from the shrinkage of each impurity-wave function to the contribution from the phase difference between two neighboring impurity sites is 1·22 at a sufficiently low concentration of impurities. The two magnetoresistance coefficients B and C have the interrelation $C = -B/2$.

1. INTRODUCTION

In two previous papers$^{(1, 2)}$ we have shown that the magnetoresistance of impurity conduction in the phonon-induced hopping region of n-type germanium can be qualitatively explained by a combination of two effects: the shrinkage of each impurity-wave function by the magnetic field and the phase difference produced by the field between two neighboring impurity-wave functions. Since the donor wave function of n-type germanium is fairly complicated, we could not develop a quantitative theory of the relative contributions from the two effects and the anisotropic nature of the magnetic perturbations. In this paper we shall give a quantitative discussion of the impurity-wave function and the hopping process in a weak magnetic field in simple semiconductors, in which the conduction (or valence) band has a spherical energy surface so that the ground state of impurities is represented by a hydrogenic $1s$ function.

For the sake of definiteness, we consider an n-type sample with N_D donors and N_A acceptors ($N_D > N_A$). At low temperatures the acceptors and an equal number of donors are ionized negatively and positively, respectively. The potential energy difference due to the nearby ionized impurities between two donor sites is larger than the resonance energy (or transfer energy). Each of $(N_D - N_A)$ electrons is then localized on one donor site and can hop into the nearby vacant site only by the emission or absorption of a phonon or many phonons. The transition probability of the electron from a neutral donor (i) to the ionized donor site (j) is proportional to the square of the resonance energy W :$^{(3-5)}$

$$W = L + (e^2/\kappa R)S,$$
$$L \equiv (\Psi_i, [-e^2/\kappa \Upsilon_j]\Psi_j), \qquad (1.1)$$
$$S \equiv (\Psi_i, \Psi_j),$$

where κ is the dielectric constant, ν_j is the distance from the site (j) to the position of the electron, R is the distance between the sites (i) and (j).

In the absence of the magnetic field, the basic local function Ψ can be expressed as the product of the envelope function by the Bloch function at the minimum of the conduction band.$^{(6)}$ We can ignore the Bloch function in the calculation of the resonance energy.(4) When we consider the situation at very low temperatures, we can also neglect the excited impurity levels and take the hydrogenic 1*s* function as the basic local function:

---

* Supported in part by the Office of Naval Research.

† On leave of absence from the Electrotechnical Laboratory, Nagatacho, Tokyo, Japan.

1

$$\Psi = (\pi a^3)^{-1/2} \exp(-r/a) \tag{1.2}$$

with

$$a = \kappa\hbar^2/m^* e^2, \tag{1.3}$$

m^* being the effective mass of the conduction band.

In the presence of the magnetic field, we use the symmetric gauge of the vector potential and choose its origin at the donor site (i). When we express $\Psi(r)$ in the coordinate system with the origin on each donor site, we obtain(1, 2, 7)

$$\Psi_i(r) = \Phi_i(H, r), \tag{1.4a}$$

$$\Psi_j(r) = \Phi_j(H, r) \exp\left\{-\frac{ie}{2\hbar c}(H \times R)r\right\}, \tag{1.4b}$$

where $\Phi(H, r)$ is determined by the Schrödinger equation

$$\left\{\frac{1}{2m^*}\left(p+\frac{e}{2c}H\times r\right)^2 - \frac{e^2}{\kappa r}\right\}\Phi(H, r) = E\Phi(H, r) \tag{1.5}$$

One can see the two different effects of the magnetic field on the basic local functions. The exponential factor in (1.4b) represents the phase difference produced by the field between two donor sites and corresponds to the Lorentz force in band conduction. The magnetic-field dependence of $\Phi(H, r)$, as will be shown in what follows, represents the shrinkage of the function at large distances from the impurity nucleus and corresponds to the magnetic-field-induced change in the Bloch function in band conduction. In other words it corresponds to the quantization of the electron orbits, which is negligibly small compared with the effect of the Lorentz force in sufficiently weak fields.

2. HYDROGENIC WAVE FUNCTION IN WEAK MAGNETIC FIELDS

The Schrödinger equation (1.5) or

$$(\mathscr{H}_0+\mathscr{H}')\Phi = E\Phi \tag{2.1}$$

in the abbreviated form, can be solved by the perturbation expansions of the energy and the wave function:

$$\begin{aligned} E &= E^{(0)}+E^{(1)}+ \dots, \\ \Phi &= \Phi^{(0)}+\Phi^{(1)}+ \dots. \end{aligned} \tag{2.2}$$

In order to get information about the wave function at large distances from the donor nucleus, it is convenient to use the method developed by Dargarno and Lewis,(8) and Schwartz.(9) According to their method the first-order changes of the energy and the wave function are given by the expressions.

$$E^{(1)} = (\Phi^{(0)}, \mathscr{H}'\Phi^{(0)}), \tag{2.3a}$$

$$\Phi^{(1)} = F\Phi^{(0)}-(\Phi^{(0)}, F\Phi^{(0)})\,\Phi^{(0)}, \tag{2.3b}$$

where F is the solution of an inhomogeneous differential equation,

$$\Phi^{(0)}\nabla^2 F+2(\nabla F)(\nabla\Phi^{(0)}) = \frac{2m^*}{\hbar^2}(\mathscr{H}'-E^{(1)})\Phi^{(0)}. \tag{2.4}$$

In the problem of the magnetic perturbation on the hydrogenic 1s function, the linear Zeeman term disappears from (1.5) and hence

$$\mathscr{H}' = \frac{e^2H^2}{8m^*c^2} r^2 \sin^2\theta \tag{2.5}$$

in spherical coordinates (r, θ, ζ) with the polar axis in the field direction. Substituting the hydrogenic 1*s* function and

$$E^{(1)} = e^2H^2a^2/4m^*c^2 \tag{2.6}$$

into (2.4), we have

$$\nabla^2 F-\frac{2}{a}\cdot\frac{\partial}{\partial r}F = 6\lambda a\left\{\left(\frac{r}{a}\right)^2 \sin^2\theta-2\right\}, \tag{2.7}$$

where

$$\lambda \equiv \kappa H^2/24m^*c^2. \tag{2.8}$$

Inspection of (2.7) shows that the solution has a form

$$F = \sum_{n=1}^{3}(a_n+b_n \cos^2\theta+c_n \cos^4\theta)r^n. \tag{2.9}$$

Inserting (2.9) into (2.7) we obtain

$$F = -\lambda r^3 \sin^2\theta-\tfrac{5}{2}\lambda r^2 a(1-\tfrac{3}{5}\cos^2\theta). \tag{2.10}$$

The solution of the Schrödinger equation (1.5) is then given by

$$\Phi = \Phi^{(0)}\{1+11\lambda a^3-\lambda r^3 \sin^2\theta - \tfrac{5}{2}\lambda r^2 a \times (1-\tfrac{3}{5}\cos^2\theta)\}. \qquad (2.11)$$

One can see the increase of the wave function at the donor nucleus and the decrease at large distances from the nucleus. To see this quantitatively, the fractional change in the wave function is plotted against (r/a) in Fig. 1, where we define the quantity f:

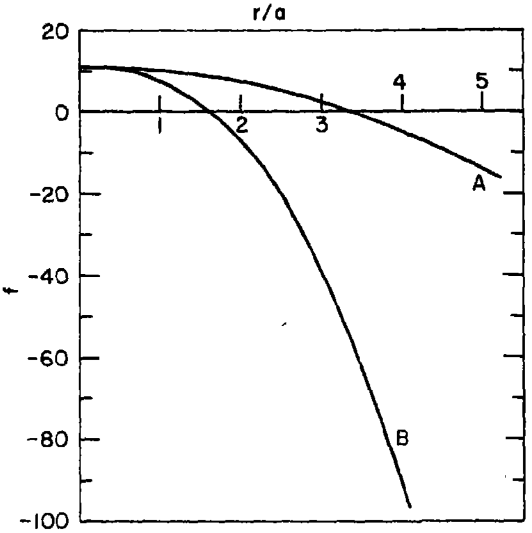

FIG. 1. Fractional change in the hydrogenic wave function in a magnetic field.

$$f \equiv (\Phi-\Phi^{(0)})/\Phi^{(0)}\lambda a^3, \quad \lambda \equiv \kappa H^2/24m^* c^2.$$

r/a is the distance from the impurity nucleus in units of the Bohr radius a. Curves A and B show f's in the direction parallel and perpendicular to H, respectively.

$$f \equiv \frac{\Phi-\Phi^{(0)}}{\lambda a^3\Phi^{(0)}} = 11-\left(\frac{r}{a}\right)^3 \sin^2\theta - \frac{5}{2}\left(\frac{r}{a}\right)^2 \times (1-\tfrac{3}{5}\cos^2\theta). \qquad (2.12)$$

Curve A shows the change in f in the direction parallel to the magnetic field ($\theta = 0°$), Curve B shows the change in the perpendicular direction ($\theta = 90°$). The critical distances at which f vanishes are given by

$$r_c = \begin{cases} 3{\cdot}32\, a & (\theta = 0°), \\ 1{\cdot}63\, a & (\theta = 90°). \end{cases} \qquad (2.13)$$

At large distances from the donor site, there is a strong anisotropic change of the wave function as will be seen in Fig. 2, where we plot f in polar coordinates. Curves A and B show the angular dependence of $(-f)$ at $r/a = 3$ and 4, respectively.

3. MAGNETIC-FIELD-INDUCED CHANGE OF TRANSITION PROBABILITY

In order to calculate the resonance energy for a pair of donors in arbitrary directions, it is necessary to express the basic local function (2.11) in the coordinate system with the z axis inclined from the field direction by ω. It is convenient to use Eulerian angles[10] (ψ, ϕ, ω).

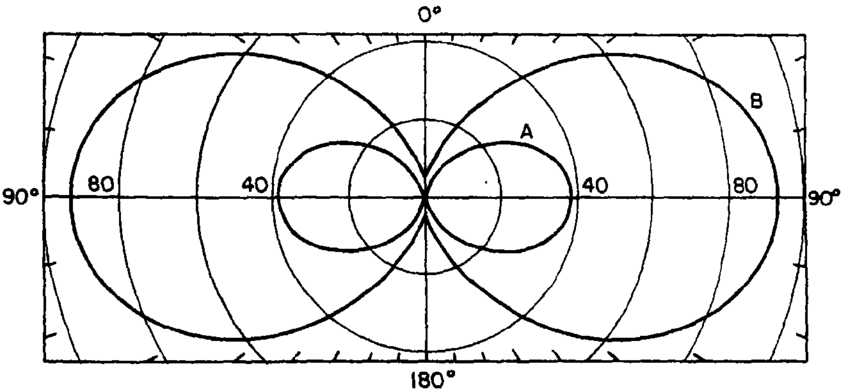

FIG. 2. Anisotropic fractional change in the hydrogenic wave function. Curves A and B show the angular dependences of $(-f)$ at $r/a = 3$ and 4, respectively. The polar angle is measured from the field direction.

Since the wave function (2.11) is symmetric around the field direction, we can choose an arbitrary value of ϕ, for simplicity $\phi = 0$. We therefore have the local function in new coordinates.

$$\Phi = \Phi^{(0)}\{1+11\lambda a^3-\lambda r\,[x^2+(y\cos\omega+z\sin\omega)^2] -\lambda a r^2-\tfrac{3}{2}\lambda a[x^2+(y\cos\omega+z\sin\omega)^2]\}. \quad (3.1)$$

When a pair of donors is in the z direction, the phase factor in (1.4b) can be expressed as

$$\exp\left\{\frac{ieH}{2\hbar c}Rx\sin\omega\right\} = 1+\frac{ieH}{2\hbar c}Rx\sin\omega-\frac{1}{2}\left(\frac{eH}{2\hbar c}\right)^2R^2x^2\sin^2\omega+\ldots, \quad (3.2)$$

where the second term vanishes in the calculation of the resonance energy.

We further perform the transformation of coordinates such that the donor sites (i) and (j) are in the positions $(0, 0, -R/2)$ and $(0, 0, R/2)$, respectively, in new coordinates. Using confocal elliptic coordinates[11] (μ, ν, ζ), the couple of wave functions $\Psi_i\Psi_j$ in the integrands of L and S, (1.1), are now written in the form

$$\begin{aligned}\Psi_i\Psi_j = (\pi a^3)^{-1}\exp(-R\mu/a)\{&1+22\lambda a^3\\ &-(\lambda R^3/4)\mu(\mu^2-1)(1-\nu^2)(\cos^2\zeta+\sin^2\zeta\cos^2\omega)\\ &-(\lambda R^3/4)(\mu^3\nu^2+\mu+2\mu\nu^2)\sin^2\omega\\ &-(\lambda R^2a/2)(\mu^2+\nu^2)\\ &-(3\lambda R^2a/4)[(\mu^2-1)(1-\nu^2)(\cos^2\zeta\\ &\quad+\sin^2\zeta\cos^2\omega)+(\mu^2\nu^2+1)\sin^2\omega]\\ &-(3\lambda R^4/4a)(\mu^2-1)(1-\nu^2)\cos^2\zeta\sin^2\omega\}, \quad (3.3)\end{aligned}$$

where we neglect the term proportional to $y\cdot z$ in (3.1) since it vanishes by integration. The effect of the phase difference is represented by the last term in (3.3). The problem involved in the calculation of the resonance energy is now completely specified. By inserting (3.3) into (1.1) and integrating over μ, ν, ζ we may obtain the resonance energy, and hence the magnetic-field-induced change of the elementary transition probability ($\propto W^2$). The square of the resonance energy is then written in the form

$$W^2 = W_0^2(1-g_s-g_p) \quad (3.4)$$

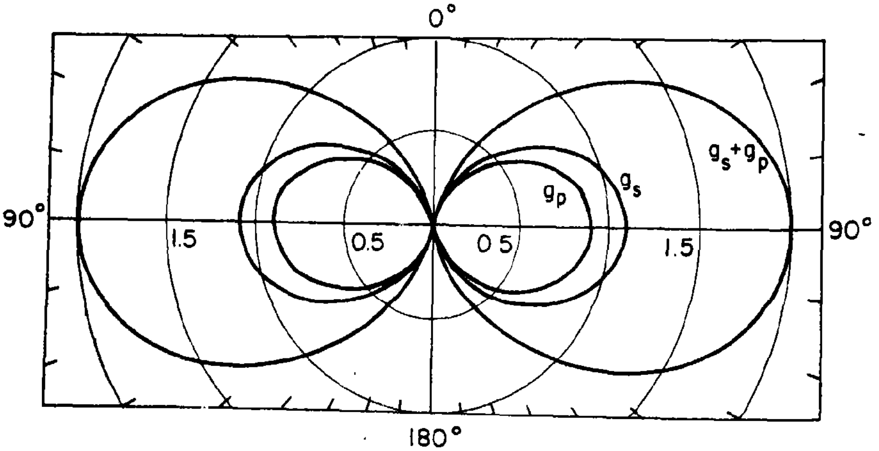

FIG. 3. Contributions to the fractional change in two-center transition probability from the shrinkage effect g_s and the phase-factor effect g_p in units of $\lambda a^3 t^3$.

$$g_s+g_p \equiv (W_0^2-W^2)/W_0^2.$$

The polar angle shows the pair direction relative to H.

with

$$W_0^2 \cong \left(\frac{2e^2R}{3\kappa a^2}\right)^2 \exp(-2R/a), \tag{3.5}$$

$$g_s/\lambda a^3 \cong (1{\cdot}1\, t^3+3{\cdot}6\, t^2)\sin^2\omega$$
$$+0{\cdot}3\, t^2\cos^2\omega+1{\cdot}7\, t^2\,, \tag{3.6}$$

$$g_p/\lambda a^3 \cong (0{\cdot}9\, t^3+0{\cdot}9\, t^2)\sin^2\omega\,, \tag{3.7}$$

$$t \equiv R/a. \tag{3.8}$$

Here, g_s and g_p show the effect of the shrinkage of each donor wave function and the effect of the phase difference between two donor sites, respectively. As long as we are concerned with the case of weak magnetic fields, interference terms between both effects appear only in higher order ($\propto H^4, \ldots$). In deriving (3.4)–(3.7) we use the approximation that $t \gg 1$ and neglect the power of t lower than t^2. At sufficiently large separation of donors we have the ratio of the two effects,

$$g_s/g_p = 1{\cdot}22 \tag{3.9}$$

from (3.6) and (3.7). When the distance R is only several times the Bohr radius, the ratio is somewhat larger than the limiting value of (3.9).

To see the angular dependence of the field-induced change of the elementary transition probability, we plot g_s, g_p and g_s+g_p in the limit of large separation in Fig. 3.

4. MAGNETORESISTANCE COEFFICIENTS

As in the previous papers[1, 2] we assume a simple model, in which the conductivity of the hopping process is proportional to the weighted angular average of W^2, and the average over the radial distribution of impurities is replaced by taking the suitable average distance between donors. If we write $R = sN_D^{-1/3}$, the coefficient s would be somewhat smaller than unity.[2, 5] The weighted angular average of W^2 may be performed using three assumptions: (1) the vacant sites (j) are distributed with equal probability around the occupied site (i), on a sphere with the radius R, (2) the weight of the pair is taken into account by multiplying by the square of the direction cosine of the angle between the pair and the current direction, (3) the average is taken over the hemisphere in the current direction.

The magnetoresistance coefficients[12] B and C in a weak field are defined by the longitudinal and transverse magnetoresistances,

$$\left(\frac{\Delta\rho}{\rho}\right)_{\text{long}} = (B+C)H^2,\quad \left(\frac{\Delta\rho}{\rho}\right)_{\text{trans}} = BH^2 \tag{4.1}$$

in the isotropic medium. The anisotropy term D in cubic crystals such as InSb vanishes in our model. Using the assumptions mentioned above we obtain the weighted angular average of W^2 for the longitudinal and transverse cases:

$$\langle W^2\rangle_{\text{long}} = \langle W_0^2\rangle\{1-\lambda a^3(0{\cdot}8t^3+3{\cdot}68t^2)\}, \tag{4.2}$$

$$\langle W^2\rangle_{\text{trans}} = \langle W_0^2\rangle\{1-\lambda a^3(1{\cdot}6t^3+5{\cdot}36t^2)\}, \tag{4.3}$$

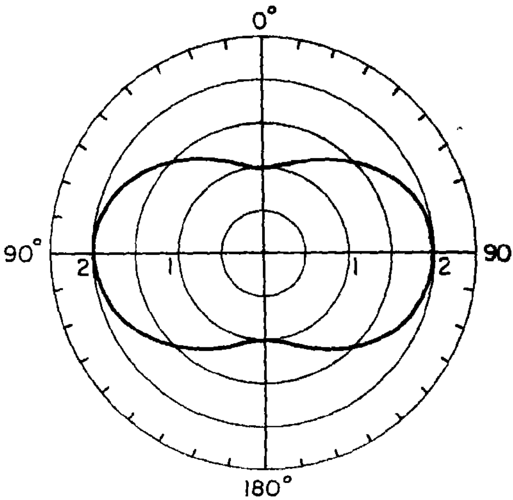

FIG. 4. Angular dependence of the magnetoresistance. The unit is taken to be $\kappa R^3H^2/30m^*c^2$. The polar angle shows the current direction relative to H.

where

$$\langle W_0^2\rangle = W_0^2/3. \tag{4.4}$$

Making use of (4.1)–(4.4) and the relation

$$(\Delta\rho/\rho) = \langle W_0^2\rangle/\langle W^2\rangle-1,$$

we have

$$B = \frac{1}{15}\frac{\kappa R^3}{m^*c^2},\quad C = -\frac{B}{2} \tag{4.5}$$

at a sufficiently low concentration of impurities.

It is interesting to remark that the relation $C = -B/2$ in (4.5) corresponds to the relation

$$C = -B \tag{4.6}$$

in the case of isotropic scattering of conduction electrons in simple semiconductors.(12) In other words, the longitudinal magnetoresistance appears even in the isotropic medium of hopping conduction contrary to the zero magnetoresistance in band conduction.

From the phenomenological relation(12) between the electric field $\boldsymbol{E}$ and the current $\boldsymbol{J}$,

$$\boldsymbol{E} = \rho_0[\boldsymbol{J} + BH^2\boldsymbol{J} + C\boldsymbol{H}(\boldsymbol{J}\boldsymbol{H})], \tag{4.7}$$

we have the magnetoresistance in the case that the current flows in the direction inclined from the magnetic field by θ:

$$\frac{\Delta\rho}{\rho_0} = (2-\cos^2\theta)\frac{\kappa R^3 H^2}{30m^* c^2}. \tag{4.8}$$

Equation (4.8) is plotted in polar coordinates in Fig. 4.

Acknowledgements—I am much indebted to Professor T. Holstein for pointing out the perturbation method used in this paper. I am also indebted to Professors Morrel H. Cohen and J. C. Phillips for helpful comments.

REFERENCES

1. Mikoshiba N. and Gonda S., *Phys. Rev.* **127,** 1954 (1962).
2. Mikoshiba N., *Phys. Rev.* **127,** 1962 (1962).
3. Kasuya T. and Koide S., *J. phys. Soc. Japan* **13,** 1287 (1958).
4. Miller A. and Abrahams E., *Phys. Rev.* **120,** 745 (1960).
5. Mott N. F. and Twose W. D., *Advanc. Phys.* **10,** 107 (1961).
6. Kohn W., *Solid State Physics* (edited by Seitz F. and Turnbull D.), Vol. **5,** p. 257. Academic Press, New York (1957).
7. Holstein T., *Phys. Rev.* **124,** 1329 (1961).
8. Dargarno A. and Lewis J. T., *Proc. Roy. Soc.* **A233,** 70 (1956).
9. Schwartz C., *Ann. Phys., New York* **6,** 156 (1959).
10. Goldstein H., *Classical Mechanics,* p. 107. Addison-Wesley, Cambridge, Massachusetts (1953).
11. Eyring H., Walter J. and Kimball G. E., *Quantum Chemistry,* p. 367. Wiley, New York (1944).
12. Seitz F., *Phys. Rev.* **79,** 372 (1950).

J. Phys. Chem. Solids Pergamon Press 1963. Vol. 24 pp. 347–360. Printed in Great Britain.

THE PREPARATION AND PROPERTIES OF SOME VANADIUM SPINELS

D. B. ROGERS, R. J. ARNOTT, A. WOLD and J. B. GOODENOUGH

Lincoln Laboratory*, Massachusetts Institute of Technology, Lexington 73, Massachusetts

(*Received* 6 *August* 1962; *revised* 26 *October* 1962)

Abstract—In order to study experimentally the properties of outer electrons as a function of interatomic separation through the transition region from narrow-band to localized properties, the spinels MV_2O_4 and M'_2VO_4, where M = Mn, Fe, Mg, Zn and Co and M′ = Fe and Co, were prepared and characterized by X-ray diffraction and chemical analysis. Conductivity measurements could all be represented by the localized-electron relationship $\rho = \rho_0 \exp(q/kT)$, but the measured q was sensitive to room-temperature cation–cation separation R, decreasing in the stoichiometric MV_2O_4 spinels from 0·37 ± 0·01 eV for $R = 3{\cdot}013$ Å in MnV_2O_4 to 0·07 ± 0·005 eV for $R = 2{\cdot}972$ Å in CoV_2O_4. Attempts to prepare NiV_2O_4, which might have had a sufficiently small R for a collective-electron relationship, were unsuccessful. Reduction of R by substitution of Al for V in $CoAl_xV_{2-x}O_4$ introduced a "foreign" ion into the vanadium sublattice, and q increased. Similarly Co_2VO_4, with $R = 2{\cdot}965$ Å and a $Co^{2+}+V^{4+}$ B-site sublattice, has a $q = 0{\cdot}37 \pm 0{\cdot}01$ eV. Further evidence that a small energy is required to create a separated hole-electron pair within the vanadium sublattice comes from maxima at $x \approx 0{\cdot}11$ in the q vs. x and θ vs. x curves for the system $Fe_{1+x}V_{2-x}O_4$, where $0 < x < 1$ and θ is the Seebeck voltage. Magnetization measurements indicate noncollinear spin configurations, which indicates strong antiferromagnetic B–B interactions between vanadium cations. The data are compatible with a predicted V^{3+}–V^{3+} separation in oxides of $R_c \approx 2{\cdot}97$ Å for the transition from collective-electron to localized-electron behavior.

I. INTRODUCTION

Direct cation–cation interactions have been suggested to account for the magnitude and sign of certain magnetic-exchange couplings between localized electrons on neighboring cations, provided overlap of partially filled orbitals is permitted by the crystal geometry.(1) Such interactions have been independently proposed(2) to account for metallic conductivity in several vanadium and titanium oxides. In this latter case, the interacting d electrons presumably form a band of collective-electron states. These observations suggest that there is a critical cation–cation spacing R_c such that for $R < R_c$ the cation-sublattice d electrons are collective, and for $R > R_c$ they are localized. In an earlier paper,(3) these two situations were distinguished as strong and weak interactions, respectively. The concept of a critical separation R_c was also employed in the construction of semi-empirical density-of-states curves for the transition metals and their alloys.(4) This paper represents initial experimental investigations concerning the properties of narrow-band electrons in the range

$$R_c - \delta R < R < R_c + \delta R.$$

II. THEORETICAL BACKGROUND

It is known empirically that for $R \approx R_{eq}$, where R_{eq} is the equilibrium separation for bonding via the electrons under investigation, the collective-electron, band model is adequate and that for $R \gg R_{eq}$, the localized-electron, crystal-field theory is useful. Since the two limiting theories are based on quite different assumptions,(5, 6) it is important to know how sharply defined is R_c, the critical separation at which the collective-electron theory changes to a localized-electron theory.

In order to measure a critical separation R_c, it is necessary to have an operational definition for

---

* Operated with support from the U.S. Army, Navy and Air Force.

collective vs. localized electrons. Of the several physical parameters available, the sharpest criterion is given by the electrical conductivity.(6) However, it must be noted that this criterion cannot be obtained by a simple extrapolation of the conventional conductivity expression for broad-band conductors to the narrow-band limit. As R increases towards R_c, the band of collective-electron states becomes so narrow that it is no longer possible to treat the electron-lattice interaction as a small perturbation. Several workers(7–10) have investigated theoretically the effect of introducing electron-lattice interactions into the zero-order Hamiltonian as a term linear in the atomic displacements. It is found that the charge carrier is no longer a "bare" electron or hole, but consists of an electron or hole trapped in the potential well created by the atomic displacements it introduces. Such an entity is called a "polaron". The size of the polaron, that is the volume of the crystal that it occupies, is inversely proportional to the sixth power of the strength of the electron-lattice interaction.(7) If this interaction is negligible, as in broad-band theory, each charge carrier belongs to the entire crystal; and if it is strong, the charge carrier is localized at a single atomic site. (A localized electron plus near-neighbor atomic displacements is called a "small polaron".) For intermediate interaction strengths, a charge carrier, plus its associated lattice displacements, extends over many atomic sites and is therefore called a "large polaron". Large polarons occupy a band of collective one-particle states, but the bandwidth is strongly temperature dependent:(7)

$$\Delta\epsilon = \Delta\epsilon_0 \exp(-S_T) \qquad (1)$$

where $\Delta\epsilon_0$ is the electronic bandwidth, in tight-binding approximation, for a rigid, periodic array of atoms, and S_T is proportional to the square of the electron-lattice interaction strength and roughly proportional to the temperature. The criterion for band rather than localized states is

$$\Delta\epsilon \geqslant \hbar/\tau \qquad (2)$$

where τ is the mean life time of a large-polaron state. HOLSTEIN(7) has further shown that τ_l can be substituted for τ in equation (2), where τ_l is the mean life time of a small-polaron state. Since τ_l is proportional to the charge-carrier mobility

$$\mu = \mu_0 T^{-3/2} \exp(-E_a/kT) \qquad (3)$$

where E_a is the activation enthalpy for an electron hop,(11) it follows from equations (1–3) that polaron theory calls for a sharply defined transition temperature T_t: The charge carriers are collective, large polarons if $T < T_t$ and localized, small polarons if $T > T_t$. This means that for a given temperature T, there should be a sharply defined critical separation $R_c(T)$, and that for a given material there is a critical range of atomic separations $R_c(T_m) < R < R_c(T_0)$, where $T_0 = 0°\text{K}$ and T_m is the melting point. It was predicted(7) that the collective-electron ($T < T_t$) conductivity, which varies as the bandwidth $\Delta\epsilon$, would decrease more rapidly than exponentially with T and that the localized-electron ($T > T_t$) conductivity $\sigma = ne\mu$ would increase exponentially with T. Such a transition in σ vs. T has never been reported. However, T_t may vary rapidly with the interatomic separation R, so that the transition range $R_c(T_0)$–$R_c(T_m)$ may be quite narrow. The presence of impurities or chemical inhomogeneities will tend to reduce $R_c(T_0)$ more than $R_c(T_m)$, thus further shrinking the experimental range $R_c(T_0)$–$R_c(T_m)$. Only those materials having R within this narrow transition range would exhibit a collective-electron $\rightleftharpoons$ localized-electron transition as a function of temperature. Therefore in order to investigate whether polaron theory provides an adequate description of the collective-electron $\rightleftharpoons$ localized-electron transition, it is necessary to examine a chemical system in which the intercation separation R can be varied more or less continuously through the critical distance R_c. Although we had hoped to accomplish this, and therefore to observe a large-polaron $\rightleftharpoons$ small-polaron transition at a T_t, in the present experimental study, we failed to obtain materials with $R < R_c$. However, several properties, including the sensitivity of the activation energy to interatomic distance R, indicate that the materials studied were in the range $R_c + \delta R$, where δR approaches zero.

In the small-polaron limit ($R > R_c$ or $T > T_t$), it is necessary to distinguish two conditions: extrinsic conditions, where the number of charge carriers n is independent of temperature, and intrinsic conditions, where the number of holes approximately equals the number of electrons and the total number increases exponentially with T. In a stoichiometric (integral number of outer electrons per atom) crystal having $R > R_c$, there are no lattice displacements associated with the localized electrons and therefore no polarons at $T = 0°\text{K}$. However, at a finite temperature, separated hole-electron pairs are created, and each carrier is a small polaron. Such a crystal is intrinsic, whereas a nonstoichiometric crystal may be extrinsic. The conductivity is described by

$$\sigma = ne\mu = A_0 T^{-3/2} \exp(-q/kT) \tag{4}$$

where for extrinsic conditions (n = const) equation (3) gives

$$q = E_a \tag{5a}$$

and for intrinsic conditions ($n = n_0 \exp(-\epsilon_g/2kT)$),

$$q = E_a + \epsilon_g/2 \tag{5b}$$

The energy ϵ_g, which is required to create a separated hole-electron pair, is zero for $R < R_c$ and increases exponentially with $(R-R_c)$ for $R > R_c$. The activation enthalpy should also be sensitive to R. Therefore it is anticipated that as $R > R_c$ decreases towards R_c, the energy q obtained from σ vs. T curves should decrease sensitively with R, especially in stoichiometric crystals.

In the application of this electrical definition for T_t, or R_c, it is necessary to distinguish between the type of transition described above and the type of transition observed in VO_2 or V_2O_3.⁽²⁾ In polar crystals containing transition-element cations, the d electrons may have $R \approx R_c$. In VO_2 and V_2O_3, $R < R_c$ and at low temperatures the d electrons are trapped in homopolar cation–cation bonds.⁽³⁾ Trapped electrons cannot contribute to electrical conductivity, so that cooperative homopolar-bond formation, as in VO_2 and V_2O_3, is manifest by a sharp semiconductor $\rightleftharpoons$ metallic transition at the electron-ordering temperature. On the other hand, the collective-electron $\rightleftharpoons$ localized-electron transition at T_t, given

$$R_c(T_m) < R < R_c(T_0),$$

should be manifest by a metallic $\rightleftharpoons$ semiconductor transition. It should also be noted that homopolar-bond stabilization contains a term linear in the cation displacements that is proportional to the curvature of the cation–cation potential-energy curve. Since the elastic restoring forces are quadratic in the atomic displacements, homopolar-bond stabilization can be anticipated if $R < R_c$ and the curvature of the cation–cation potential vs. distance curve is negative at the undistorted (not bonded) cation–cation separation. This implies that maximum stabilization due to homopolar cation–cation bonding occurs at $R < R_c$, but close to R_c. This fact is mentioned because the possibility of homopolar-bond formation at $R \approx R_c$ can complicate any experimental study of electronic properties as a function of R about $R \approx R_c$.

Since the near-neighbor equilibrium separation in a crystal is primarily determined by outer s and p electrons, it follows that $R < R_c$ for outer $s-p$ electrons. (Molecular crystals may have $R \approx R_c$ for $s-p$ states directed across Van der Waals bonds). For outer $4f$ or $5f$ electrons, $R > R_c$ always occurs. Therefore in order to investigate the properties of electrons in the interatomic range $R_c - \delta R < R < R_c + \delta R$, it is necessary to study the d electrons in a primarily ionic material containing transition-metal or rare-earth cations. In such a material, the outer $s-p$ electrons fill a bonding band, which is primarily associated with the anion sublattice and separated from the $s-p$ conduction (antibonding) band by a large energy gap E_g, so that electron transport is overwhelmingly due to outer d electrons, whose energies fall within E_g. (If outer f electrons are present, they contribute to the magnetic properties, but not significantly to the transport properties because $R \gg R_c^{ff}$.)

In such an ionic material, it is important to distinguish two possible cases: that where electron transport is via an intermediary anion and that where it is direct from cation to cation. This distinction has not always been appreciated in the literature on narrow-band conductivity. For octahedral-site cations, transport of e_g electrons, whose orbitals are directed toward the neighboring anions, can only take place via an anion intermediary. Transport of t_{2g} electrons, whose orbitals are directed in between the anions, may be direct if neighboring cations share either a common octahedral face or edge. It is only direct electron transport for which the estimate of a critical cation–cation separation is meaningful. [In $Li_xNi_{1-x}O$, Ni^{3+} is in a low-spin state so that its t_{2g} levels are filled and only cation–anion–cation interactions via e_g can occur. Cation–anion–cation interactions occur because of cation–anion covalent effects. Admixing of nonbonding e_g states with bonding $e-p$ states gives the nonbonding states with e_g symmetry sufficient radial extension to overlap the nucleus of the anion and hence for cations on opposite sides of the anion to have overlapping orbitals. However, the amount of overlap is always sufficiently small that cation–anion–cation interactions correspond to $R > R_c$. (Indeed the ratio of cation–cation to cation–anion–cation d-electron mobilities appears to be $\sim 10^4$.)].

Finally, in order to select a series of compounds for which $R \approx R_c$, it is necessary to have an estimate of the critical separation. From a consideration of the electric and magnetic properties of Ti_2O_3, V_2O_3, Cr_2O_3, and α-Fe_2O_3, it has been possible to estimate a room-temperature critical separation for $3d$ electrons in oxides:(5)

$$R_c \approx [3{\cdot}05 - 0{\cdot}03\,(Z - Z_{\mathrm{Ti}}) - 0{\cdot}04J(J+1)]\,\text{Å} \qquad (6)$$

where Z_{Ti} and Z are the atomic numbers of titanium and the transition-metal cation in question with total quantum number J.

The vanadium spinels were chosen for study for five reasons:

(1) Chemical preparation is feasible.

(2) The oxygen spinels have lattice parameters compatible with $R_c - \delta R < R < R_c + \delta R$ for V^{3+} or V^{4+}, according to equation (6).

(3) It is possible to vary the B-sublattice V^{3+}–V^{3+} distance, or the concentration of V^{4+}, by varying only the A-sublattice chemistry. (It is assumed that the vanadium spinels are primarily normal.)

(4) It is not possible to propagate near-neighbor antiferromagnetic order over the B-sublattice, so that the possibility of cooperative, homopolar-bond formation in the region $R \lesssim R_c$ is reduced.

(5) V^{3+} has two outer d electrons and V^{4+} only one outer d electron, so that the t_{2g} states are only partially filled and there are no localized e_g electrons present to introduce intra-atomic exchange interactions that would complicate the analysis.

It will be seen in the following discussion that although spinels with $R \gtrsim R_c$ were successfully prepared, attempts to prepare a V^{3+} spinel with $R < R_c$ were unsuccessful. Therefore it was only possible to examine the changes in physical properties as a function of R on one side of R_c.

III. EXPERIMENTAL

Method of synthesis

The compounds studied in the present investigation were the following: MgV_2O_4, ZnV_2O_4, CoV_2O_4, FeV_2O_4, MnV_2O_4, Co_2VO_4, Fe_2VO_4 and the mixed systems $CoV_{2-x}Al_xO_4$ $(0 \leqslant x \leqslant 2)$, $Fe_{1+x}V_{2-x}O_4$ $(0 \leqslant x \leqslant 1)$. Attempts to prepare NiV_2O_4, Zn_2VO_4, CdV_2O_4, and to substitute small amounts of nickel for cobalt in the spinel CoV_2O_4 were unsuccessful. The starting materials used to prepare these compounds were either spectroscopic grade or carefully purified reagent grade.

The preparative technique usually employed in the synthesis of pure mixed oxides involves the careful grinding of equivalent quantities of the component oxides and firing pressed pellets of the mixture to a high temperature under suitable atmospheric conditions. The sequence of grinding, pressing and firing is repeated until a homogeneous, single phase is obtained. The synthesis of pure vanadium spinels is especially difficult because of the necessity of working with starting oxides that are both refractory and relatively unstable with respect to oxidation by air.

The materials reported in this investigation required prolonged grinding using agate mortars and pestles under a nitrogen atmosphere in order to prevent oxidation (exceptions will be noted below). Most of the end-member spinels required two successive grindings and firings before homogeneity was achieved. Lightly pressed pellets of the samples were fired initially at 900°C for 36 hr. The sintered product of this firing was then reground, pressed into bars, and fired at 1100–1200°C for 24 hr.

Atmospheric conditions used in firing were dictated by the material's reactivity toward oxygen. Most of the preparations were made by placing the mixture to be fired in platinum containers, which were in turn sealed in evacuated silica tubes.

General chemical equations for the solid-state reactions can be written as follows:

$$\mathrm{MeO+V_2O_3 \xrightarrow[\text{in vacuo}]{900\text{–}1200^\circ C} MeV_2O_4}$$

$$\mathrm{8MeO+V_2O_3+V_2O_5 \xrightarrow[\text{in vacuo}]{900\text{–}1200^\circ C} 4Me_2VO_4}$$

where Me is Mn, Co, Zn, and Mg. The corresponding equation for the preparation of intermediates in the system $CoV_{2-x}Al_xO_4$ is

$$\mathrm{CoO}+\left(1-\frac{x}{2}\right)\mathrm{V_2O_3}+\frac{x}{2}\,\mathrm{Al_2O_3} \xrightarrow[\text{in vacuo}]{900\text{–}1200^\circ C} \mathrm{CoV_{2-x}Al_xO_4}$$

Manganese vanadite was prepared by reduction of the metavanadate under a stream of hydrogen with slowly increasing temperature up to a final ignition period of 24 hr at 1000°C.

$$\mathrm{Mn(VO_3)_2\cdot 6H_2O+2H_2 \xrightarrow{1000^\circ C} MnV_2O_4+8H_2O}$$

Magnesium vanadite was prepared by grinding together in air equivalent quantities of the component oxides and firing at 1000°C under an atmosphere of flowing hydrogen.

$$\mathrm{MgO+V_2O_3 \xrightarrow[1000^\circ C]{H_2} MgV_2O_4}$$

The preparation of Fe_2VO_4 and FeV_2O_4 has been reported previously by WOLD, ROGERS, ARNOTT and MENYUK.(12) These compounds as well as the intermediate members of the mixed systems FeV_2O_4–Fe_2VO_4 were prepared by grinding together Fe_2O_3 and V_2O_3 in varying mole ratios and firing under various CO–CO_2 atmospheres at 1100°C. Table 1 summarizes those atmospheric conditions imposed which gave best results for the intermediate members studied. A general chemical equation for the preparation of the Fe–V spinels can be written as

$$(1+x)\mathrm{Fe_2O_3}+(2-x)\mathrm{V_2O_3}+\mathrm{CO} \xrightarrow{1100^\circ C} 2\mathrm{Fe}_{1+x}\mathrm{V}_{2-x}\mathrm{O_4}+\mathrm{CO_2}$$

Chemical analysis

Total vanadium content was determined by a method similar to that reported by REUTER and SIEWERT;(13) reducing power was found by the method of WICKHAM and WHIPPLE.(14)

Table 1. Atmospheric conditions used in the synthesis of the system $Fe_{1+x}V_{2-x}O_4$

Compound	CO:CO$_2$
FeV_2O_4	4·5:1·0
$Fe_{1·05}V_{1·95}O_4$	4·3:1·0
$Fe_{1·075}V_{1·925}O_4$	3·9:1·0
$Fe_{1·1}V_{1·9}O_4$	3·8:1·0
$Fe_{1·125}V_{1·875}O_4$	3·6:1·0
$Fe_{1·15}V_{1·85}O_4$	3·3:1·0
$Fe_{1·3}V_{1·7}O_4$	2·8:1·0
$Fe_{1·5}V_{1·5}O_4$	2·0:1·0
$Fe_{1·625}V_{1·375}O_4$	1·3:1·0
$Fe_{1·75}V_{1·25}O_4$	1·0:1·0
$Fe_{1·9}V_{1·1}O_4$	0·6:1·0
Fe_2VO_4	0·33:1·0

Physical measurements

Electrical resistivity as a function of temperature was determined on ceramic bars, approximately 2·5×0·5×0·4 cm, over a temperature range from −160° to +200°C at 10° to 20° intervals. For resistance measurements a Keithley Model 610 A electrometer was used at high resistances (> 500 Ω) and a Keithley Model 502 milliohmeter at low resistances (< 500 Ω). At resistances greater than 3 Ω, the two-probe technique was used, while at lower resistances four probes were employed to eliminate contact resistance. These measurements were correlated by means of the equation $\rho = \rho_0 \exp(q/kT)$, where ρ is resistivity, ρ_0 is essentially a constant for a given conductivity mechanism, q is the activation energy involved, and k is Boltzmann's constant. (In the temperature range investigated, any temperature dependence of ρ_0 would fall within experimental error.) In certain cases, breaks occurred in plots of $\ln \rho$ vs. $1/T$ at low temperatures. For consistency, all q values reported are those determined at temperatures above such breaks.

Seebeck measurements were taken at temperature-difference intervals from $\Delta T \approx 20°C$ to $\Delta T \approx 100°C$, using 0°C as the constant temperature of the cold junction. Reproducibility of the Seebeck coefficient was always within 5μV/°K. Crystallographic parameters for the vanadium spinels were obtained using a Norelco

Diffractometer and vanadium-filtered chromium $K\alpha$ radiation. Low-temperature observations were made using the apparatus described by SCHWARTZ *et al.*(15) Curie points, magnetization curves, and the saturation magnetic moments at 4·2°K and 11,000 G were determined by means of a vibrating-coil magnetometer.

IV. RESULTS AND DISCUSSION

End-member spinels

Successful synthesis of end-member spinels are reported in Table 2, together with the results of chemical analyses for their stoichiometry and oxidation state. The physical properties of these compounds are summarized in Table 3. Cell edges are in excellent agreement with those reported previously in the literature.(16–20)

The vanadium spinels are all semiconductors, possessing a positive temperature coefficient for conductivity. From equation (1), this indicates that $R > R_c$. However, their activation energies are anomalously low for stoichiometric oxides having no mixed valencies and are seen to be strongly dependent on the V–V distance in the MV_2O_4 compounds, decreasing regularly from 0·37 ± 0·01 eV for MnV_2O_4 to 0·07 ± 0·005 eV for CoV_2O_4. The sensitivity of this dependence increases rapidly with decreasing separation at

Table 2. Results of chemical analysis for end member vanadium spinels

Formula	V/M^{2+}*	Reducing power theory	eq/gm Found	Th (%)
MnV_2O_4	2·015 ± 0·005	0·018113	0·01810 ±0·00001	99·90 ± 0·05
FeV_2O_4	1·990 ± 0·006	0·02255	0·02254 ±0·00003	99·95 ± 0·15
MgV_2O_4	1·986 ± 0·004	0·02103	0·02101 ±0·00001	99·90 ± 0·05
ZnV_2O_4	2·003 ± 0·006	0·01730	0·01742 ±0·00002	100·07 ± 0·09
CoV_2O_4	2·009 ± 0·004	0·017790	0·01779 ±0·00001	99·97 ± 0·03
Fe_2VO_4	0·4971 ± 0·0008	0·013236	0·01321 ±0·00001	99·8 ± 0·10
Co_2VO_4	0·5004 ± 0·0005	0·004295	0·004296 ±0·000005	100·0 ± 0·10

* The metal–metal ratio is, with the exception of MnV_2O_4 (where both Mn and V were analyzed), arrived at on the basis of total vanadium content, the other metal being taken by differences.

Table 3. Physical properties of some end-member vanadium spinels

Formula	a_0(Å)	V–V(Å)	T_π(°K)	q(eV)	$\theta\left(\frac{\mu V}{°K}\right)$	$n_B\left(\frac{\text{Bohr mag}}{\text{mol}}\right)$	T_c(°K)
MnV_2O_4	8·522 ± 0·002	3·013	—	0·37 ± 0·01	—	2·10	56
FeV_2O_4	8·454 ± 0·002	2·990	127	0·25 ± 0·01	+400	1·95	109
MgV_2O_4	8·418 ± 0·002	2·976	—	0·18 ± 0·01	−304	—	—
ZnV_2O_4	8·410 ± 0·002	2·973	—	0·16 ± 0·01	−277	—	—
CoV_2O_4	8·407 ± 0·002	2·972	—	0·07 ± 0·005	+ 86	1·33	145
Fe_2VO_4	8·421 ± 0·002	2·975	—	0·27 ± 0·01	− 50	0·72	440
Co_2VO_4	8·379 ± 0·002	2·965	—	0·37 ± 0·01	−167	0·21	158

Definition of symbols: T_π = temperature of observed crystallographic transition; q = activation energy for semiconduction; θ = Seebeck coefficient; n_B = saturation magnetic moments; T_c = Curie temperature.

least down to 2·972 Å. Although these findings are qualitatively in agreement with equation (5b), the data is sensitive to changes in the degree of spinel inversion and total oxidation. Therefore it does not appear meaningful to obtain numbers from this data for the phenomenological parameters in the exponential R dependence of q. However, an important qualitative statement can be made: As the V^{3+}–V^{3+} separation R is reduced toward 2·97 Å, the energy $q = E_a + \epsilon_g/2$ is an extremely sensitive function of R. Since collective-electron properties should occur as $\epsilon_g/2$ vanishes, it would seem from the data that a relatively small further decrease in R, below that in CoV_2O_4, would be sufficient to induce large-polaron behavior below a T_t. This is in excellent agreement with the prediction of equation (6), which calls for $R_c(V^{3+}) \approx$ 2·97 Å given $J \approx 1{\cdot}3$. (The orbital angular momentum of V^{3+} is not completely quenched by the crystalline fields at the B sites.) Unfortunately, it was not possible to reduce R further by preparing NiV_2O_4, nor even to substitute small amounts of Ni^{2+} for Co^{2+} in CoV_2O_4. [The preparation of CdV_2O_4 was also attempted in order to increase R beyond that in MnV_2O_4. Although all syntheses attempted appeared to result in single-phase spinels, chemical analysis of the products indicated that the vanadium content was always high by several per cent.]

The experimentally observed values for saturation magnetic moments deviate considerably from those predicted by a Néel collinear-spin model. Since $R > R_c$, this indicates a complex-spin configuration, which in turn implies strong antiferromagnetic magnetic-exchange interactions between the B-site cations.(21) Magnetization curves were obtained for FeV_2O_4, Fe_2VO_4, MnV_2O_4, and CoV_2O_4. Each of these indicated anomalous changes in slope between their Curie point and 4·2°K. Since these samples were characterized as pure, single-phase materials, the transitions probably correspond to a change from a Néel to a complex spin configuration.(22) If R is close to R_c, antiferromagnetic cation–cation interactions must be strong. Therefore the magnetic data supports the contention that cation–cation magnetic interactions may be important and that in the vanadium spinels R is close to R_c.

Low-temperature crystallography did not reveal any anomalous behavior as a result of cation–cation interactions. The transition observed at 127°K for FeV_2O_4 is tetragonal ($c/a \approx 1{\cdot}014$) to cubic. Tetrahedral Fe^{2+} has the outer-electron configuration $e_g^3\,t_{2g}^3$, so that Jahn–Teller distortions remove the degeneracy of a doubly degenerate state. This means that from first-order theory, equal stabilization is obtained with $c/a > 1$ or $c/a < 1$. However, where the octahedral ion is V^{3+} with electron configuration t_{2g}^2 and the V^{3+} spins are not collinear, optimum additional first-order stabilization is obtained if the sign of the distortion is $c/a > 1$.(23) Thus although $Fe[Cr_2O_4]$ is tetragonal ($c/a < 1$), the second-order term plus anharmonic elastic terms stabilizing $c/a < 1$ at tetrahedral-site Fe^{2+}, a tetragonal ($c/a > 1$) Jahn–Teller distortion is anticipated for cooperative tetrahedral Fe^{2+} and octahedral V^{3+} stabilization. Therefore it appears that the observed transition in FeV_2O_4 may be explained by the Jahn–Teller effect, which is independent of any cation–cation interactions.

The system $CoV_{2-x}Al_xO_4$ $(0 < x < 2)$

An alternate method for reducing the V^{3+}–V^{3+} separation in the MV_2O_4 spinels below $R = 2{\cdot}972$ Å involves partial substitution of Al^{3+} into the B-sites of CoV_2O_4. Table 4 summarizes the results of our studies on the system $CoV_{2-x}Al_xO_4$.

Physical measurements were made on these materials immediately after preparation, but chemical analyses were delayed several months. This was unfortunate since of all the vanadites prepared, these were the only compounds which were highly susceptible to oxidation in the sintered state. The analyses should be considered as a limiting minimum of oxidation purity. Samples that were oxidized were characterized by cell edges deviating considerably from those predicted by Végard's Law. The effect of even small amounts of oxidation on the measured cell edges is large. Only those samples that gave cell edges in agreement with those predicted by Végard's Law were measured electrically. The electrical properties reported in Table 4 are therefore believed to be characteristic of the nominal compositions given.

The energy q as a function of the composition x is shown in Fig. 1. It is apparent that q *increases* initially quite slowly, then more rapidly, with

Table 4. Properties of the system $CoV_{2-x}Al_xO_4$ ($0 \leqslant x \leqslant 2$)

Nominal Composition	Reducing power (Per cent Theor)	Cell edges Measured	Cell edges Vegard	Activation Energy for Semiconduction (eV)
CoV_2O_4	99·95 ± 0·05	8·401 ± 0·002	—	0·070 ± 0·005
$CoV_{1·5}Al_{0·5}O_4$	> 98·0	8·332 ± 0·002	8·332	0·120 ± 0·005
$CoV_{1·2}Al_{0·8}O_4$	> 99·4	8·286 ± 0·002	8·286	0·182 ± 0·010
$CoV_{0·8}Al_{1·2}O_4$	> 98·3	8·233 ± 0·002	8·228	0·339 ± 0·010
$CoV_{0·4}Al_{1·6}O_4$	> 99·6	8·170 ± 0·002	8·165	0·594 ± 0·015
$CoAl_2O_4$	—	8·103 ± 0·002	—	—

increasing aluminum content, and simultaneously with *decreasing* V^{3+}–V^{3+} separation. This would appear to contradict equation (5b) and the findings from the pure, primarily normal, end-member spinels MV_2O_4. However, it must be appreciated that the energy required to create a separated hole–electron pair is decreased by polarization effects that occur via overlap of *d* orbitals on neighbouring atoms. If foreign ions like Al^{3+}, which have no outer *d* electrons to participate in a narrow t_{2g} band, are substituted for V^{3+}, $\epsilon_g/2$ is increased. Also τ of equation (2) is reduced, so that there is an increase in the $\Delta\epsilon$ required for collective-electron behavior, which implies an increase of q_{ex}. Thus both the R_c for $\epsilon_g/2$ and the $R_c(T)$ for q_{ex} are decreased. If the introduction of Al^{3+} decreases R_c more rapidly than it decreases R, q of equation (5b) will *increase* with decreasing R, as observed in $CoV_{2-x}Al_xO_4$. Initial substitutions of Al^{3+} ($x < 0·1$) should have little influence on R_c, but will have an increasing influence for larger x where every V^{3+} ion has at least one near-neighbor Al^{3+} ion.

These results are consistent with the observation from Table 3 that Co_2VO_4, with a *B*-site separation of only 2·965 Å, has a higher activation energy than that of CoV_2O_4. In this case *B*-site Co^{2+} functions as a "foreign" ion.

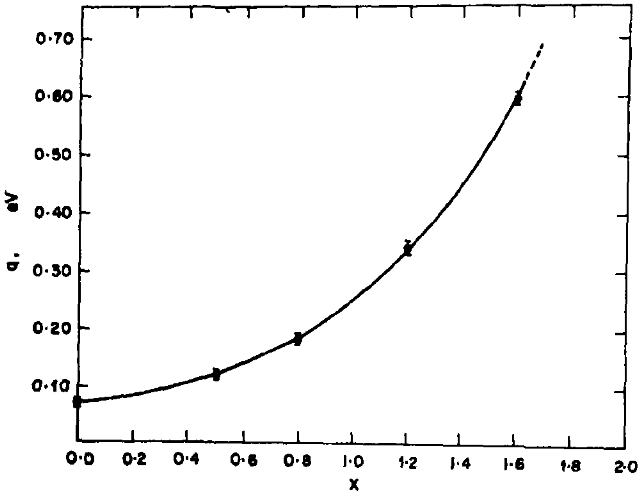

FIG. 1. Compositional dependence of the energy q for the system $CoV_{2-x}Al_xO_4$ ($0 \leqslant x \leqslant 2$).

The system $Fe_{1+x}V_{2-x}O_4$

REUTER *et al.*(24) have reported that the energy q for the mixed system $Co_{1+x}V_{2-x}O_4$ is a minimum at the end member CoV_2O_4 and increases in a uniform manner with the addition of Co_2VO_4. This behavior is inconsistent with a conventional mixed-valency "hopping" model, in which it is assumed that $\epsilon_g = \infty$ so that q (intrinsic) $\gg q$ (extrinsic), as given by equation (5). With this conventional assumption, q decreases rapidly with x initially, reaching a nearly constant value in the extrinsic region, where x equals the number of charge carriers. However, it has been demonstrated that R is close to R_c in CoV_2O_4, so that probably $\epsilon_g < 2E_a$ in this end member. Therefore $Co_{1+x}V_{2-x}O_4$ contains many negative as well as positive charge carriers in the temperature range of measurement for considerable values of x. Where this is so, the energy q is sensitive to $(R-R_c)$ through equation (5b). Therefore it *increases* with x, the number of "foreign" cations on the B-site sublattice. It was decided to study the system $Fe_{1+x}V_{2-x}O_4$ in order to have a similar mixed-valency system for comparison.

Chemical analyses of the intermediates in the $Fe_{1+x}V_{2-x}O_4$ system for total vanadium content and per cent theoretical reducing power indicated that all samples were within one-half per cent of their nominal values of x. Deviations were most apparent in the composition region $0{\cdot}5 \lesssim x \lesssim 0{\cdot}9$. All compositions were carefully examined by x-ray diffraction and appeared to be single-phase spinels.

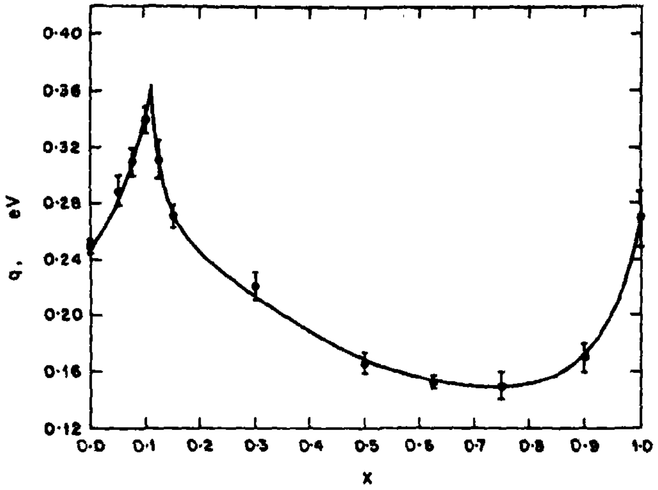

FIG. 2. Compositional dependence of the energy q for the system $Fe_{1+x}V_{2-x}O_4$ $(0 \leqslant x \leqslant 1)$.

Results of physical measurements on the FeV_2O_4–Fe_2VO_4 system were unusual. A plot of q vs. x is given in Fig. 2. This curve is seen to peak sharply at $x \approx 0{\cdot}11$, *increasing* from $0{\cdot}25 \pm 0{\cdot}01$ eV for pure FeV_2O_4 to $0{\cdot}34 \pm 0{\cdot}01$ eV for $Fe_{1{\cdot}1}V_{1{\cdot}9}O_4$, before decreasing to a rather flat minimum at compositions between $x = 0{\cdot}5$ and $x = 0{\cdot}9$. Thus for $x > 0{\cdot}11$, the shape of the q vs. x curve resembles that predicted from a conventional (extrinsic) hopping model. However, the initial increase in q with addition of a different valency of the same ion is, from the conventional viewpoint, a striking property. In this respect the iron system is similar to the $Co_{1+x}V_{2-x}O_4$ system reported by REUTER *et al.*[24] However, the marked maximum in q vs. x is in sharp contrast with the results reported for the cobalt system. It is important, therefore, to inquire into possible mechanisms responsible for this maximum.

From a conventional viewpoint, it is tempting to postulate that for $x < 0{\cdot}11$, the initial iron substitutes for V^{3+} as Fe^{3+}, giving the formula $Fe^{2+}_{1-x}Fe^{3+}_{x}[Fe^{2+}_{x}V^{3+}_{2-x}]O_4$, and that there is ordering of the iron ions on the A-sites. The plausibility of this valence assignment comes from the observation of Fe^{3+}, V^{3+} in the corundum $FeVO_3$.[12] With $x > 0{\cdot}125$, additional A-site Fe^{3+} are randomly distributed, and mixed-valency hopping occurs on the A-sites. Aside from the fact that A-site hopping has never been observed (or looked for) and that ordering on the A-sites is not easily demonstrated, such a model fails to recognize the essential significance of the anomalously low q in FeV_2O_4.

A low q in FeV_2O_4 implies that R is close to R_c and that consequently $\epsilon_g < 2E_a$. This means that in the temperature interval of measurement, the samples remain essentially intrinsic for considerable values of x even though the chemical formula may be $Fe^{2+}[Fe_x^{2+}V_x^{4+}V_{2-2x}^{3+}]O_4$. Since the addition of "foreign" ions into the B-site sublattice decreases R_c, or increases $(R-R_c)$, ϵ_g increases with x relative to E_a. In addition, the Fermi energy decreases with increasing x. These two effects reduce the number of negative charge carriers, thus favoring extrinsic conductivity, as x increases. Therefore at larger x, the material is essentially extrinsic, and $q = E_a$ is given by equation (5a). The effective q that is measured must go through a maximum in the compositional region where the extrinsic and intrinsic contributions to the conductivity are comparable. Although a maximum in q vs. x is anticipated because of the low values of q for the end member FeV_2O_4, the sharpness of the maximum is not obvious from this reasoning, and some additional mechanism probably plays a role.

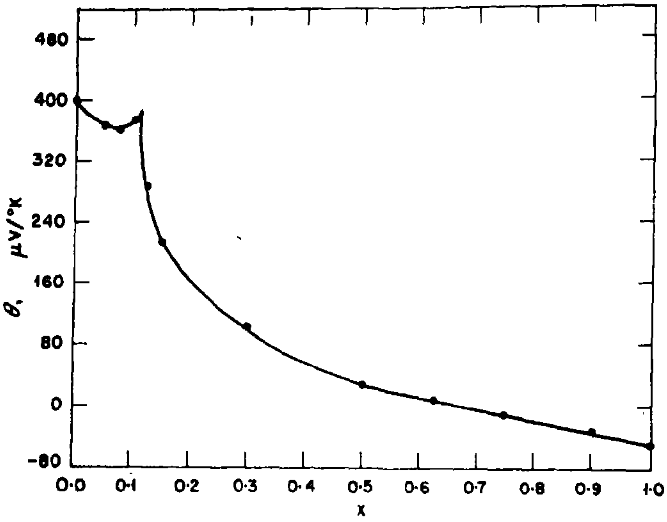

FIG. 3. Compositional dependence of Seebeck coefficient θ for the system $Fe_{1+x}V_{2-x}O_4$ $(0 \leq x \leq 1)$.

This reasoning suggests that there should be a similar maximum in the q vs. x curve of the system $Co_{1+x}V_{2-x}O_4$, but that it occurs at a somewhat larger x. There are two features of the published (23) q vs. x curve for $Co_{1+x}V_{2-x}O_4$ that are inconsistent with this reasoning and with our results for $Fe_{1+x}V_{2-x}O_4$: There is no maximum and the initial rise in q with x is concave to the x-axis. Because of this discrepancy and because the original investigations gave no data for compositions between $x = 0{\cdot}67$ and $x = 1{\cdot}0$, so that any inflection within this region would not have been noted, we have begun a restudy of the electrical transport properties of this system. Preliminary results indicate that q vs. x is initially convex to the x-axis and that a region of lower activation energy does occur where $0{\cdot}67 < x < 1{\cdot}0$ These results are consistent with the model proposed above.

If this model is correct, then the transition from primarily intrinsic to primarily extrinsic character should also be manifest as a maximum in the Seebeck coefficient.(6) Thermoelectric behavior of the system is shown in Fig. 3, and again there is a peak at $x \approx 0{\cdot}11$. However, the high value of θ for very small x is not consistent with primarily intrinsic conduction for $x < 0{\cdot}1$, and the peak at $x \approx 0{\cdot}11$ could be due to other effects.

In the compositional range $0{\cdot}11 < x \lesssim 0{\cdot}8$, the Seebeck coefficients are consistent with those expected for extrinsic conduction. However, in the compositional range $0{\cdot}80 \lesssim x < 1{\cdot}0$, the thermoelectric behavior is only consistent with this mechanism if it is assumed that the end member Fe_2VO_4 is able to provide its own mixed valencies. Although it might be argued that this end member is also intrinsic, the presence of many foreign ions presumably makes ϵ_g relatively high. Nevertheless mixed-valencies are reasonable because the existence of Fe^{3+} and V^{3+} in $FeVO_3$(12) indicates that the energy difference between $Fe^{3+}[Fe^{2+}V^{3+}]O_4$ and $Fe^{2+}[Fe^{2+}V^{4+}]O_4$ is quite small. (It appears necessary to assume that the latter formula is the more stable in order to account for the change in sign of the Seebeck voltage at $x \approx 0{\cdot}67$.)

In summary, the data presented in Figs. 2 and 3 suggest three mechanisms of charge transport within three different compositional regions. In the region $0 \leqslant x \lesssim 0{\cdot}11$, conductivity is due simultaneously to holes and electrons, the energy ϵ_g required to separate a hole-electron pair within the vanadium sublattice being of the order of kT. For $x > 0{\cdot}11$, ϵ_g is large because the effective R_c of equation (5b) has been reduced by the introduction of "foreign" cations. In the region $0{\cdot}11 < x \lesssim 0{\cdot}8$, conductivity is due to the transport of a single type of charge carrier (mixed valency hops). For $x > 0{\cdot}8$, the Fermi level remains nearly constant because the energy required for A-site Fe^{2+}+B-site $V^{4+} \rightarrow A$-site Fe^{3+}+B-site V^{3+} is small (probably less than 0·05 eV). This suggestion is qualitatively supported by the data of Fig. 4. Although measurements on ceramic specimens of "infinite-temperature resistivity" ρ_0 have no quantitative meaning, they are internally consistent, and results were reproducible within a factor of two. Even with the large scatter characteristic of these measurements, the existence of three regions of differing ρ_0 is apparent.

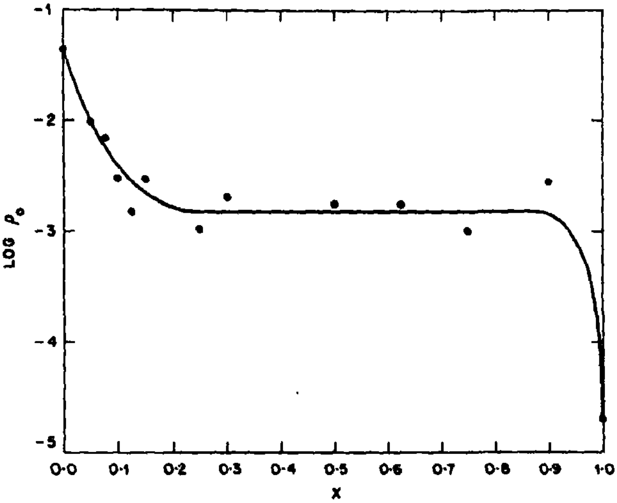

FIG. 4. Compositional dependence of infinite temperature resistivity ρ_0 for the system $Fe_{1+x}V_{2-x}O_4$ $(0 \leqslant x \leqslant 1)$.

Unit cell edges for the FeV_2O_4–Fe_2VO_4 system are plotted in Fig. 5. They are seen to deviate considerably from Végard's Law, being essentially constant where $0{\cdot}0 \leqslant x \lesssim 0{\cdot}20$.

When the intermediate members of the system were studied by x-ray diffraction between room temperature and liquid-nitrogen temperature, three types of crystallographic distortion were observed. The distortion which was found in the end-member FeV_2O_4 with $c/a > 1$ is not present at $x = 0{\cdot}05$, but appears again in $Fe_{1{\cdot}3}V_{1{\cdot}7}O_4$, persisting at least to $x = 0{\cdot}50$. No transitions were observed above 77°K for $x = 0{\cdot}625$, nor for any higher value of x. In the compositional range of

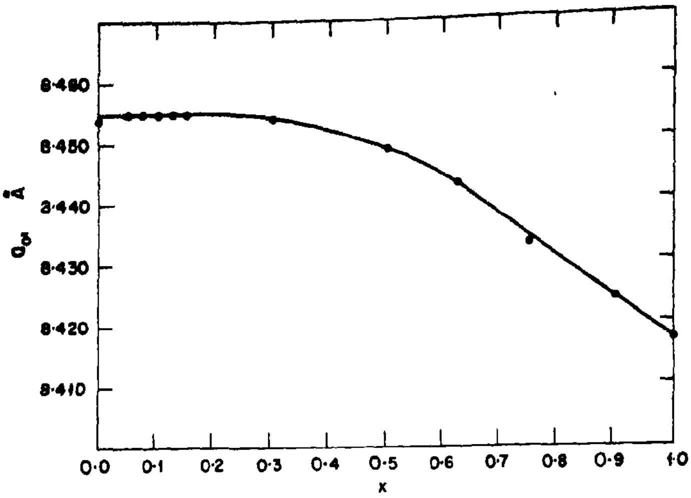

FIG. 5. Compositional dependence of unit cell edge a_0 for the system $Fe_{1+x}V_{2-x}O_4$ ($0 \leq x \leq 1$)

$0{\cdot}05 \lesssim x \lesssim 0{\cdot}15$, two phase changes occur: At intermediate temperatures the structure is tetragonal with $c/a < 1$ (approximately 0·98 to 1·0), and at lower temperatures it appears to be orthorhombic.

For all of the cubic-tetragonal distortions, regardless of the c/a ratio, an exact value of the transition temperature was unobtainable. The experimental method entailed scanning back and forth over the cubic (311) diffraction peak as the temperature was lowered. For these transitions the initial effect was a drastic reduction of the peak height, by at least fifty per cent, before any splitting was observed. This loss of intensity, which takes place over a temperature drop of 30 to 40°C, is probably caused by the tetragonal distortion, but the exact point at which it begins is difficult to determine. In order to obtain a reproducible value, the height of the (311) peak was plotted against temperature for each sample. The steepest portion of the intensity decrease is fairly linear, and the temperature at which fifty per cent of the decrease occurred was taken. These values were found to be reproducible and are internally consistent. These estimates, though probably lower than the true transition temperature, are believed to be qualitatively correct relative to each other.

The second transition, which was observed in samples for which $0{\cdot}05 \lesssim x \lesssim 0{\cdot}15$, is less gradual and can be determined within 3 or 4°C. Since the decrease in intensity, which was observable for the (311) peak, is common to all the diffraction maxima, only the cubic (311) and (220) peaks were sufficiently intense to be studied with any degree of reliability. This second transition results in a splitting of each of these lines into three with considerable overlap. Reasonable agreement of the observed d spacings is obtained with d values calculated on the basis of an orthorhombic cell.

In Fig. 6 an attempt is made to illustrate qualitatively the features of the phase diagram for this system. This diagram should be taken only as an approximation; all of the boundary regions are questionable. The fact that the tetragonal distortion observed for FeV_2O_4 does not occur for values of x greater than 0·50 appears to provide evidence for 3–2–3 valencies in Fe_2VO_4. It has been pointed out that the original distortion is probably due to Jahn–Teller effects. If this is true, then a tetragonal ($c/a < 1$) distortion would be expected for Fe_2VO_4 were the valencies 2–2–4, but no distortions need occur if the valencies are 3–2–3. (However, negative Seebeck voltages indicate a mixture of 2–2–4 and 3–2–3.)

No saturation magnetic moments were determined for the intermediate members of this system; however, several Curie temperatures were measured in the compositional region where unusual electrical and crystallographic properties

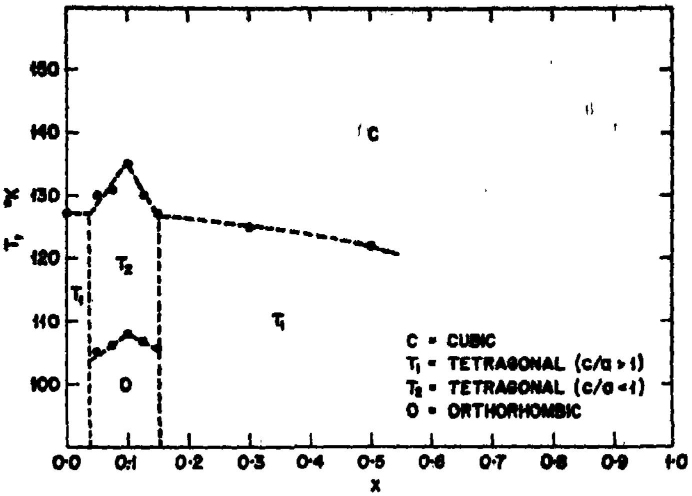

FIG. 6. Qualitative features of low temperature phase diagram for the system $Fe_{1+x}V_{2-x}$ ($0 \leqslant x \leqslant 1$).

were encountered. These were found to go through a minimum in the same region.

To our knowledge, there is no simple explanation for the many unusual properties that occur in the narrow compositional region $0{\cdot}05 \lesssim x \lesssim 0{\cdot}15$. All of these anomalies seem to have their maximum effect at a composition between $x = 0{\cdot}10$ and $x = 0{\cdot}125$, and would appear to indicate a characteristic which is unique to this composition.

V. CONCLUSIONS

The concept of direct cation–cation interactions appears to have been supported by the experimental evidence reported. The critical distances for these interactions should occur for vanadium at slightly less than 2·972 Å. However, these interactions are seen to have an effect on electrical conductivity at separations up to 3·014 Å.

For the MV_2O_4 spinels, several features have been observed that seem to be characteristic of direct interactions between cations whose separations are $R \gtrsim R_c$: The magnetic properties cannot be interpreted on the basis of a Néel configuration between cationic magnetic moments. The electrical transport parameters are not consistent with conventional theories based on $\epsilon_g \gg kT$. There appears to be a strong sensitivity of the physical properties to small changes in cation separation and to the purity of the V^{3+} sublattice.

In a qualitative manner it has been possible to account for the electrical transport properties of the mixed system $Fe_{1+x}V_{2-x}O_4$. Although certain features of the system $Co_{1+x}V_{2-x}O_4$ as reported by Ref. 24, appear to be consistent with these ideas, further clarification of this system is required. Preliminary results indicate that q vs. x is initially convex to the x-axis and that a region of lower q occurs in the interval $0{\cdot}67 < x < 1{\cdot}0$, which would make the system similar to $Fe_{1+x}V_{2-x}O_4$. Certain difficulties of interpretation remain, and electrical properties associated with $Fe^{2+}_{1_{2-x}}Fe^{3+}_x$ on spinel A-sites should be investigated experimentally before a more conventional interpretation for the system $Fe_{1+x}V_{2-x}O_4$ is abandoned.

Inability to obtain samples with $R < R_c$ prohibited a check of the metallic ⇌ semiconducting transition predicted by polaron theory and of the width of the transition region $R_c(T_m) < R < R_c(T_0)$. Several systems with $R \lesssim R_c$ are presently being investigated.

Acknowledgements—The authors would like to acknowledge the help of N. MENYUK and E. J. DELANEY who, respectively, performed the magnetic measurements and many chemical analyses.

REFERENCES

1. WICKHAM D. G. and GOODENOUGH J. B., *Phys. Rev.* **115**, 1156 (1959).
2. MORIN F. J., *Phys. Rev. Letters* **3**, 34 (1959).

3. Goodenough J. B., *Phys. Rev.* **117**, 1442 (1960).
4. Goodenough J. B., *Phys. Rev.* **120**, 67 (1960).
5. Goodenough J. B., *Magnetism and the Chemical Bond*, Suppl. Vol. III of *Progress in Inorganic Chemistry*. Edited by Cotton F. A. Interscience, New York (in press).
6. Goodenough J. B., unpublished research.
7. Holstein T., *Ann. Phys. New York* **8**, 325, 343 (1959).
8. Yamashita J. and Kurosawa T., *J. Phys. Chem. Solids* **5**, 34 (1958); *J. phys. Soc. Japan* **15**, 802 (1960).
9. Tjablikov S. V., *Zh. eksp. teor. fiz. S.S.S.R.* **23**, 381 (1952).
10. Fröhlich J., Pelzer H. and Ziman S., *Phil. Mag.* **41**, 221 (1950).
11. Heikes R. R. and Johnston W. D., *J. chem. Phys.* **26**, 582 (1957).
12. Wold A., Rogers D., Arnott R. J. and Menyuk N. *J. appl. Phys. Supp.* **33**, 1208S (1962).
13. Reuter B. and Siewert J., *Z. anal. Chem.* **162**, 175 (1958).
14. Wickham D. G. and Whipple E., *Talanta* **10** (1963).
15. Schwartz R., Post B. and Fankuchen I., *Rev. sci. Instrum.* **22**, 281 (1951).
16. Rüdorff W. and Reuter B., *Z. anorg. Chem.* **253**, 177 (1947).
17. Lovell G. B. H., *Trans. Brit. ceram. Soc.* **50**, 315 (1951).
18. Richardson H. M., Ball F. and Rigby G. R., *Trans. Brit. ceram. Soc.* **53**, 376 (1954).
19. Reuter B. and Siewert J., *Naturwissenschaften* **44**, 440 (1957).
20. Lensen M., *Ann. Chim. Paris* [13] **4**, 891 (1959).
21. Kaplan T. A., Dwight K., Lyons D. and Menyuk N., *J. appl. Phys. Suppl.* **32**, 13S (1961).
22. Menyuk N., Wold A., Rogers D. and Dwight K. *J. appl. Phys. Suppl.* **33**, 1144S (1962).
23. Goodenough J. B., *J. phys. Soc. Japan* **17**, Suppl. 3-I, 185 (1962).
24. Reuter B., Jaskowsky J. and Riedel E., *Z. Elektrochem.* **63**, 937 (1959).

J. Phys. Chem. Solids Pergamon Press 1963. Vol. 24, pp. 361–370. Printed in Great Britain.

ELECTRICAL RESISTIVITY OF RARE-EARTH ALLOYS*

F. A. SMIDT, Jr.† and A. H. DAANE

Institute for Atomic Research and Department of Chemistry,
Iowa State University, Ames, Iowa

(*Received* 16 *July* 1962)

Abstract—Resistivities of solid solution alloys in the systems Gd–Lu, Tb–Lu, Gd–Er, and Y–Lu were measured from 4·2 to 320°K to determine the behavior of the resistivity in alloy systems with magnetic phenomena arising from localized magnetic moments. A large contribution to the residual resistivity is caused by the random distribution of these localized moments through the lattice. An analysis of the lattice resistivity of the metals shows large variations across the heavy rare-earth series which are possibly correlated with the change of c/a ratio of the metals and the attendant in the Fermi surface geometry.

INTRODUCTION

ONE of the most sensitive and yet one of the most complex physical properties of metals and alloys is their electrical resistivity. It is known to be dependent upon the electronic structure, elastic constants and magnetic interactions but the nature of this dependence is not completely understood, particularly in the case of the transition metals. Scandium, yttrium, and the rare-earth metals, which might be considered as the first members of the transition series by virtue of their incomplete *d* shells, have the same number of conduction electrons, similar elastic constants, atomic sizes, and crystal structures and thus provide excellent subjects for a study of the resistivity behavior in transition metals.

Magnetic phenomena in the rare-earth metals probably arise from an exchange interaction between the unpaired 4*f* electrons localized on the ion core and the conduction electrons, hence the magnetic ordering has a profound effect on the resistivity.(1, 2) This study was undertaken to investigate the dependence of the resistivity on magnetic interactions in rare-earth solid solution alloys. Studies of the alloy systems Gd–Lu and Tb–Lu, where magnetic rare-earth metals were diluted by the weakly paramagnetic metal lutetium, demonstrated the differences between magnetism arising from localized electrons and the collective electron type found in Ni–Pd alloys.(3)

To provide a more meaningful comparison among members of the rare-earth group, the magnetic contribution to the resistivity was subtracted from the total and the variations thus revealed were interpreted as differences in the Fermi surface configuration.

EXPERIMENTAL

The rare-earth metals used in the alloys were prepared by the method described by SPEDDING and DAANE.(4) The alloys were prepared by arc melting the constituents together under an argon atmosphere a sufficient number of times to insure homogeneity. The alloys were obtained as rods by a "manometric" casting method in which the alloys were melted in vacuum and forced up into an inverted tantalum crucible by bleeding a small quantity of argon into the system. A radiographic method of inspection was used to detect the few castings with shrinkage cavities which were rejected. The castings were then machined into rods $\frac{3}{8}$ in. in diameter and 2 in. in length and the rods were stress relief annealed for 3 hr at 350°C.

The resistivity was measured by the standard four probe method with current reversal. A cryostat and temperature controller described by COLVIN, LEGVOLD and SPEDDING(5) were used to attain the desired temperatures over the range 4·2–320°K.

Powder methods were used to obtain the X-ray diffraction data and the lattice constants were

---

* Contribution No. 1169. Work was performed in the Ames Laboratory of the U.S. Atomic Energy Commission.

† Present address: General Electric Co., Hanford Laboratories, Richland, Washington.

Table 1. *X-ray diffraction data*

Sample	a(Å)	c(Å)	c/a	Vol. (Å^3)
Gd	3·639	5·789	1·5907	66·41
Tb	3·606	5·698	1·5804	64·15
Er	3·561	5·594	1·5707	61·44
Lu	3·506	5·555	1·5845	59·14
80·2 Gd-Lu	3·614	5·729	1·5851	64·82
57·3 Gd-Lu	3·589	5·681	1·5829	63·38
40·2 Gd-Lu	3·565	5·644	1·5832	62·11
20·0 Gd-Lu	3·539	5·604	1·5835	60·77
93·4 Tb-Lu	3·601	5·687	1·5793	63·85
66·7 Tb-Lu	3·583	5·655	1·5781	62·87
46·7 Tb-Lu	3·563	5·618	1·5771	61·75
23·3 Tb-Lu	3·537	5·587	1·5798	60·51
81·8 Gd-Er	3·626	5·753	1·5867	65·50
63·7 Gd-Er	3·615	5·719	1·5819	64·73
45·0 Gd-Er	3·601	5·686	1·5791	63·86
25·7 Gd-Er	3·587	5·650	1·5751	62·94

determined by Cohen's method programmed for an I.B.M. 650 computer.

RESULTS

The existence of complete solid solubility in the systems Gd–Lu, Tb–Lu, and Gd–Er was confined by X-ray diffraction and resistivity methods.

Plots of the cell volumes vs. composition indicated that these solid solutions were very nearly ideal as would be expected from their similar

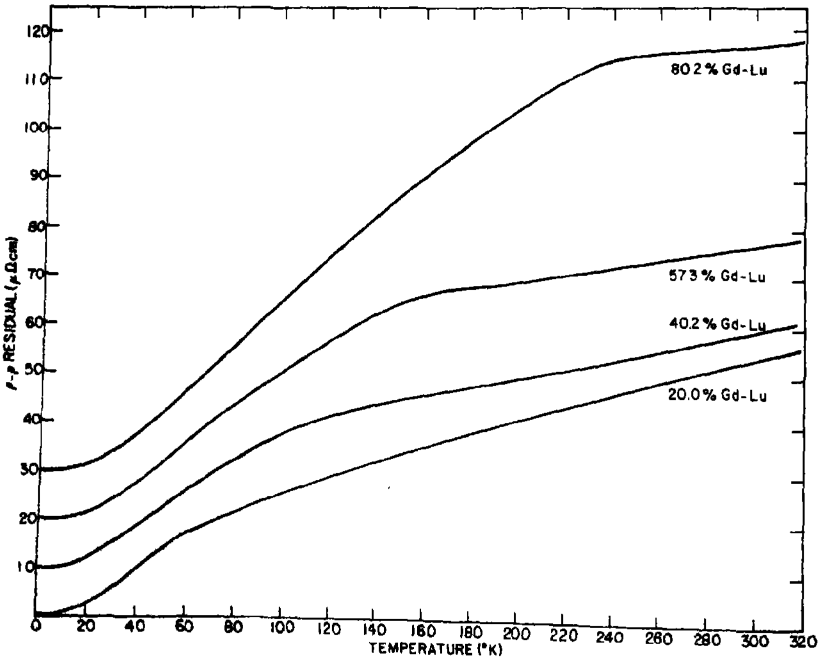

FIG. 1. Resistivity vs. temperature data for Gd–Lu alloys.

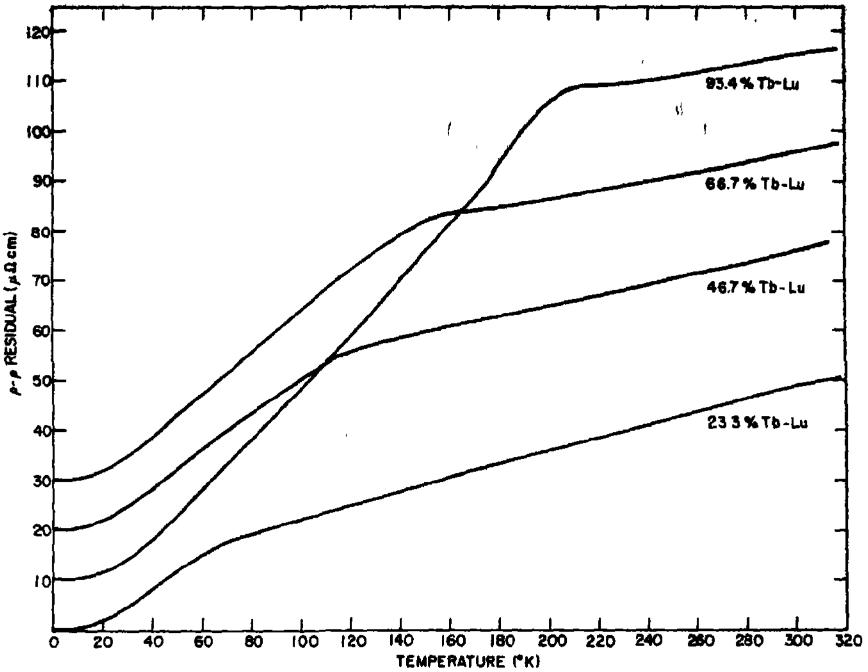

Fig. 2. Resistivity vs. temperature data for Tb–Lu alloys.

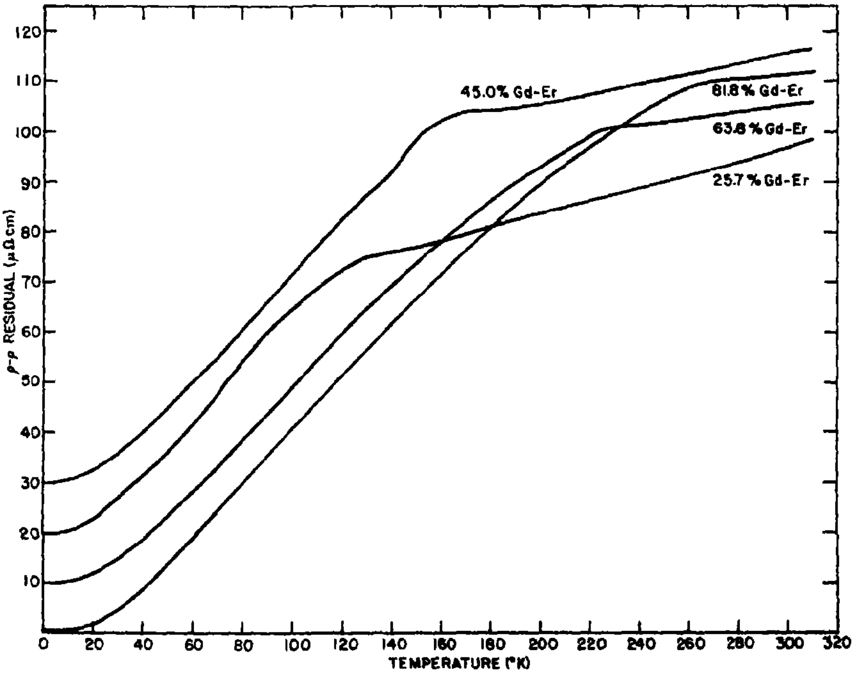

Fig. 3. Resistivity vs. temperature data for Gd–Er alloys.

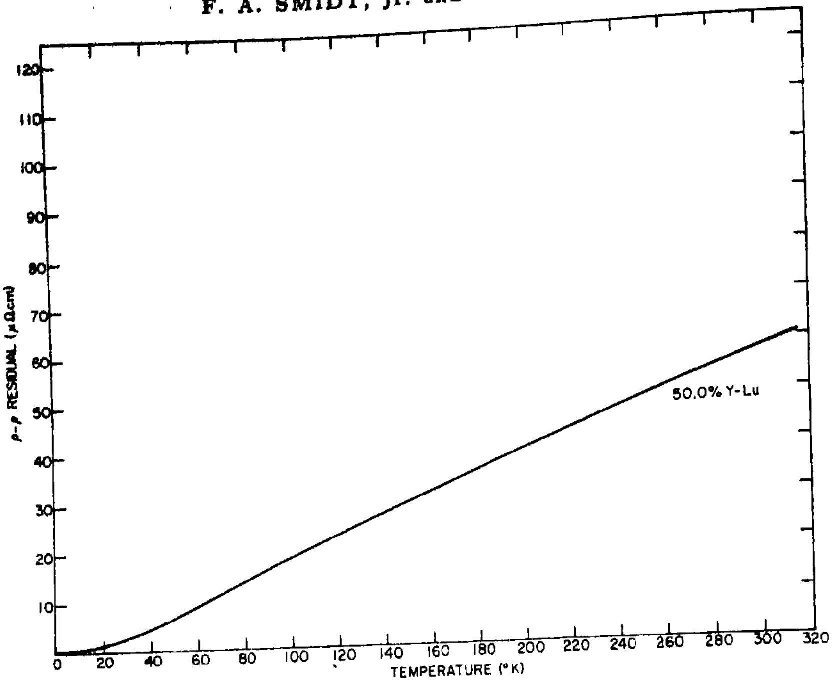

FIG. 4. Resistivity vs. temperature data for 50·0 per cent Y-Lu alloy.

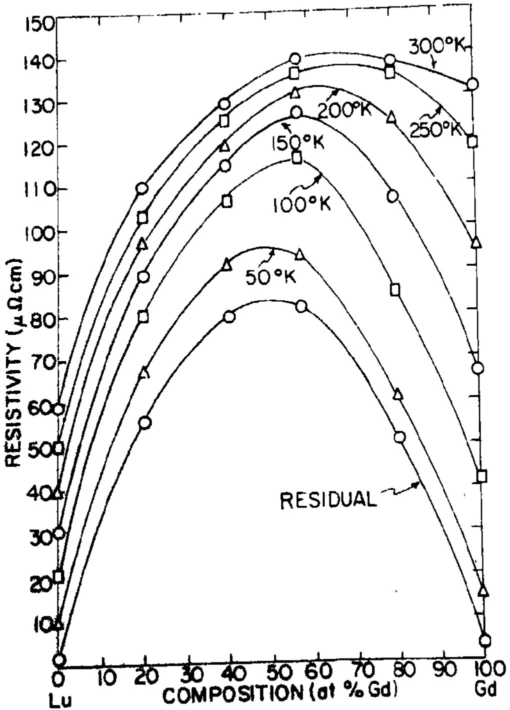

FIG. 5. Resistivity vs. composition isotherms for Gd–Lu alloys.

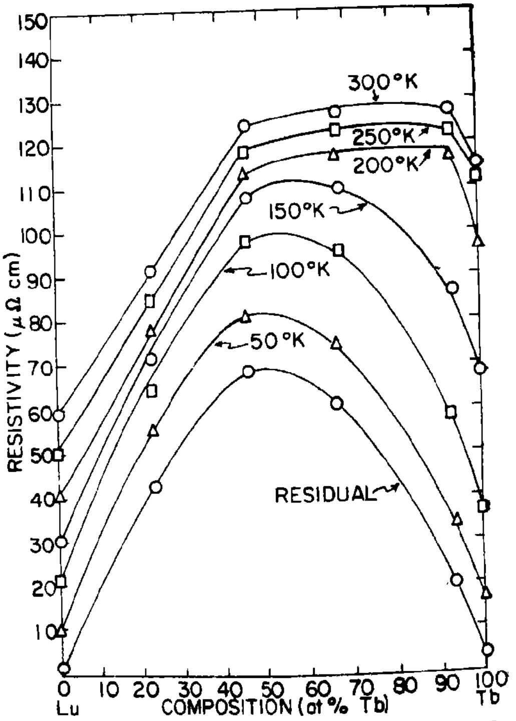

FIG. 6. Resistivity vs. composition isotherms for Tb–Lu alloys.

properties. Plots of the c/a ratio vs. composition for these alloy systems did not follow a linear relation but showed a minimum as shown in Table 1. This behavior is very similar to that observed across the heavy rare-earth series where the c/a ratio decreases from Gd to Er and then rises to Lu.

The temperature dependent portion of the resistivity vs. temperature curves for the alloys is shown in Figs. 1–4. The sharp change in slope in the curves was interpreted as being due to the onset of magnetic ordering. The ordering temperatures given in Table 2 were determined from the discontinuity in plots of $\Delta\rho/\Delta T$ vs. T for each of the alloys. These temperatures varied approximately linearly with composition.

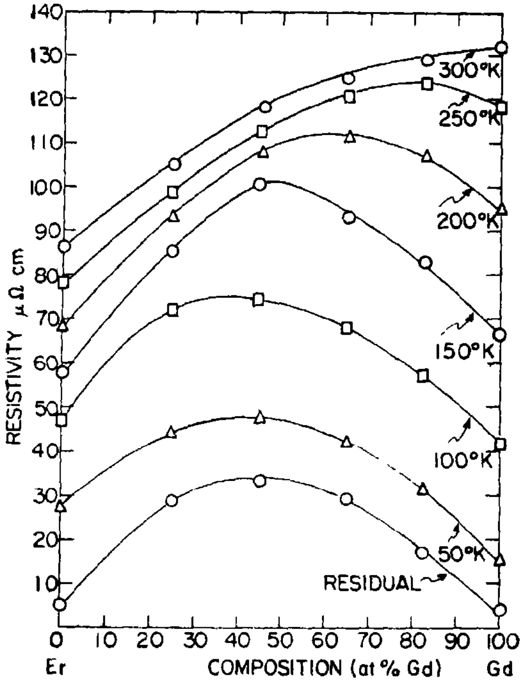

Fig. 7. Resistivity vs. composition isotherms for Gd–Er alloys.

The ρ vs. composition curves are shown in Figs. 5–7 at 50° intervals. The isotherms for the residual resistivities evaluated at 4·2°K conform approximately to the parabolic behavior predicted by Nordheim's rule for solid solution alloys, although the maximum is displaced slightly due to the effects discussed in the succeeding Section on electronic structure. The unsymmetrical shape of the curves at higher temperatures illustrates the necessity for measurements at low temperatures if one wishes to make a meaningful comparison of resistivity data with Nordheim's rule. The unsymmetrical shape of the curves for these alloy systems is due to the presence of magnetic scattering and the large difference between the temperature coefficient of the resistivity above and below the magnetic ordering temperature. This behavior is in direct contrast to that found in Ni–Pd alloys[3] where such curves were unsymmetrical at low temperatures and symmetrical at temperatures above the ordering temperatures of all the alloys.

Table 2. Magnetic ordering temperatures observed in resistivity-temperature curves

Alloy	θ	θ'*
80·2 Gd–Lu	240	
57·3 Gd–Lu	167	
40·2 Gd–Lu	121	
20·0 Gd–Lu	61	
93·4 Tb–Lu	211	181
66·7 Tb–Lu	157·5	
46·7 Tb–Lu	120	
23·3 Tb–Lu	63·5	
81·8 Gd–Er	261·5	
63·7 Gd–Er	255·5	
45·0 Gd–Er	170·5	138
25·7 Gd–Er	128·5	70
Gd†	291·5	
Tb†	229	219
Er†	80	200

* Possible antiferromagnetic–ferromagnetic transition.
† Data from Ref. 5.

The spin-disorder resistivities give a measure of the magnetic interaction in the metal. They were evaluated by extrapolating from linear portions of the ρ–T curves in Figs. 1–3 to $T = 0$°K. Fig. 8 shows that these values for the alloys follow the $(g-1)^2 J(J+1)$ relation (or $S^2(J+1)/J$ for the heavy rare earths) about as well as do the metals themselves. The values of S and J for the alloys were determined from the S and J of the metals by multiplying by the mole fraction of each component in the alloy as done by Weiss and Marotta.[6] The fact that all the points do not

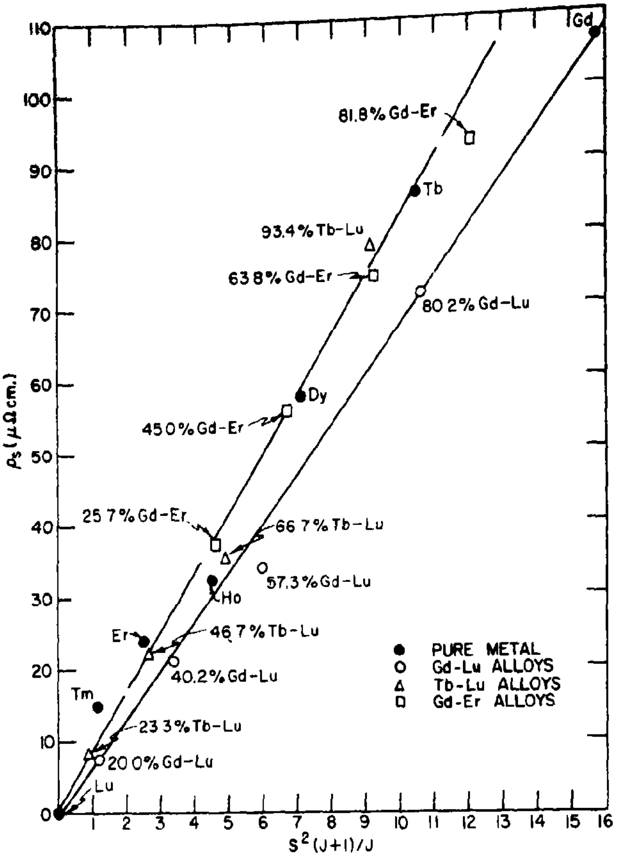

FIG. 8. Spin-disorder resistivities for the alloys and pure metals as a function of average values of $S^2(J+1)/J$.

fall on a straight line is believed to be a function of the variations in electronic structure of the metals rather than a weakness in the assumption that the spin-disorder resistivities should follow a $(g-1)^2 J(J+1)$ dependence.(7) Experiments on dilute alloys have shown that this relation is obeyed quite well where the electronic structure remains essentially constant.(8)

ALLOY STUDIES

The residual resistivity of a solid solution alloy at absolute zero is usually caused by scattering of conduction electrons by two mechanisms; imperfections in the lattice and the difference in electrostatic potential of the two types of atoms in the alloy. The first type is the same as that found in pure metals and includes scattering by dislocations, grain boundaries, impurity atoms, etc. The second type could actually be treated as a very large concentration of impurity atoms but in alloys it is usually treated separately and described by Nordheim's rule, $\rho = Cx(1-x)$, where x is the mole fraction of one component and C is a constant dependent on the difference in the electrostatic potential of A atoms and B atoms.

The alloys examined in this study had much larger residual resistivities than one would expect for alloys with similar electronic structures, crystal structures and atomic sizes (c.f. Ag–Au and Pt–Pd,(9)) and the magnitude of the residual resistivity at a given composition depended upon the difference in angular momentum quantum number of the alloy components. The additional contribution to the resistivity is due to a type of spin-disorder scattering of the conduction electrons found only in alloys where one or more of the components has a localized magnetic moment. The effect is similar to that giving rise to the magnetic anomaly in the pure metals, where no scattering occurs at 0°K, but disorder of the spins with increasing temperature causes a disruption of the perfect periodicity of the lattice and hence scattering and an increase in resistivity. The effect in alloys, however, is present even at 0°K where the spins are completely aligned, for the disorder of the atoms with magnetic moments in the lattice is still a disruption of the periodicity of the lattice. Thus the residual resistivity in these alloys is composed of three parts, $\rho_{\text{residual}} = \rho_{\text{imp}}+\rho_{\text{AE}}+\rho_{\text{AS}}$, the imperfection resistivity, the electrostatic effects of alloying, and the spin-disorder effects of alloying, respectively. The temperature dependent part of the resistivity in the alloys, as in a magnetic rare-earth metal, consists of a thermal vibration or phonon contribution and a spin disorder contribution below the magnetic ordering temperature, and only the phonon term above the ordering temperature.

A qualitative idea of the magnitudes of the various terms in the residual resistivity is provided by a comparison of the results from a 50 per cent Y–Lu alloy (with no magnetic term) with the results for Gd–Lu and Tb–Lu at the same composition. A more quantitative evaluation is possible with dilute alloys as described elsewhere by MACKINTOSH and SMIDT.(8) That work showed the electrostatic term for elements in the sixth period is less than the term for an alloy between a fifth period and sixth period element (Y–Lu). This difference is simply the "a" term in Linde's rule for dilute alloys, $\Delta\rho = a+bz^2$. The rare-earth alloys studied had no bz^2 term because the valences were the same, but would require an additional term $c(g-1)^2\, J(J+1)$ to describe the properties of dilute rare-earth alloys in lutetium; g is the Landé factor, J is the total angular momentum quantum number, and c is a constant.

ELECTRONIC STRUCTURE OF THE RARE-EARTH METALS

Although the rare-earth metals are generally considered to be identical in possessing three conduction electrons (with the exception of Eu, Yb, and α-Ce), a closer scrutiny of the resistivity data on the metals(5, 10) shows rather sizeable differences in the ρ–T curves in the paramagnetic region. This would indicate rather large variations in some of the parameters in the electrical transport equations and suggested a further analysis of the data on the pure metals as well as those obtained from the alloys.

The Bloch–Gruneisen relation predicts a T^5 temperature dependence for metals at low temperatures and a linear dependence for $T > \theta$. WHITE and WOODS(11) have found that the transition metals more generally follow a T^3 dependence in the low temperature region and a similar analysis of the data on rare-earth metals showed the same trend. Table 3 shows the coefficient of T in the expression $\rho = cT^n$ as determined by plotting log ρ vs. log T. The T^2 dependence of ytterbium and europium is perhaps notable but no low temperature data on other cubic divalent metals could be found so it is not known if this effect is typical of divalent metals.

A possible explanation of the T^3 behavior in the magnetic metals has been given by KASUYA(12) as well as others, who have derived a T^2 term for a ferromagnetic and a T^4 term for an antiferromagnetic metal using a spin wave model. Magnetic anisotropy effects(13) and electron–electron(14) interactions probably modify this dependence, however. In addition it is difficult to accept this interpretation when Sc,(15) Y, Lu, and La, which are all weakly paramagnetic, also have a T^3 dependence, while in contrast to the behavior of these metals an alloy, 50 per cent Y–Lu, followed a T^5 dependence very well.

One other feature of the temperature dependence of the resistivity of the rare-earth metals was noted in a qualitative comparison of the curves. The light rare earths, La, Ce, Pr, and Nd, do not follow a linear relation very well above θ, while the heavy rare earths, Gd to Lu and also Y and Sc, follow such a relation quite well. The essential differences between these two groups are the amount of shielding by the $4f$ shell and the more complex crystal structure of the light rare earths.

ZIMAN(14) has shown that the Fermi surface area can be estimated from the resistivity in the linear region ($T > \theta$) (or the temperature coefficient of the resistivity in this region), using a

Table 3. Summary of temperature dependence of the resistivity in the low temperature region

Material	*n*	Material	*n*	*n′*
Gd	3·0 (10–40°)*	80·2 Gd–Lu	3·5 (6–16)	2·8 (17–35)*
Tb	3·2 (14–35)	57·3 Gd–Lu	4·1 (7–15)	2·6 (21–41)
Dy	3·3 (10–32)	40·2 Gd–Lu	6·3 (11–14)	2·4 (14–37)
Ho	2·3 (13–19)	20·0 Gd–Lu	6·0 (6–10)	2·2 (15–40)
Er	3·5 (6–18)	93·4 Tb–Lu	4·3 (11–18)	2·9 (18–34)
Tm	4·5 (6–21)	66·7 Tb–Lu	6·1 (11–17)	2·9 (17–35)
Yb	2·0 (14–40)	46·7 Tb–Lu	4·6 (8–17)	2·5 (17–37)
Lu	2·6 (18–40)	23·3 Tb–Lu	6·6 (7–10)	2·8 (12–29)
Sc†	3·7 (15–28)	81·8 Gd–Er	4·2 (6–13)	2·5 (13–37)
Y	3·1 (11–40)	63·7 Gd–Er	4·2 (8–19)	2·3 (19–40)
La	2·6 (9–26)	45·0 Gd–Er	3·4 (9–15)	2·2 (17–35)
Sm	3·6 (3–14)	25·7 Gd–Er	4·4 (6–13)	2·2 (20–35)
Eu	1·8 (14–32)	50·0 Y–Lu	5·0 (11–22)	2·2 (22–56)

* Temperature range in which *n* is observed.

† Data from Ref. 15.

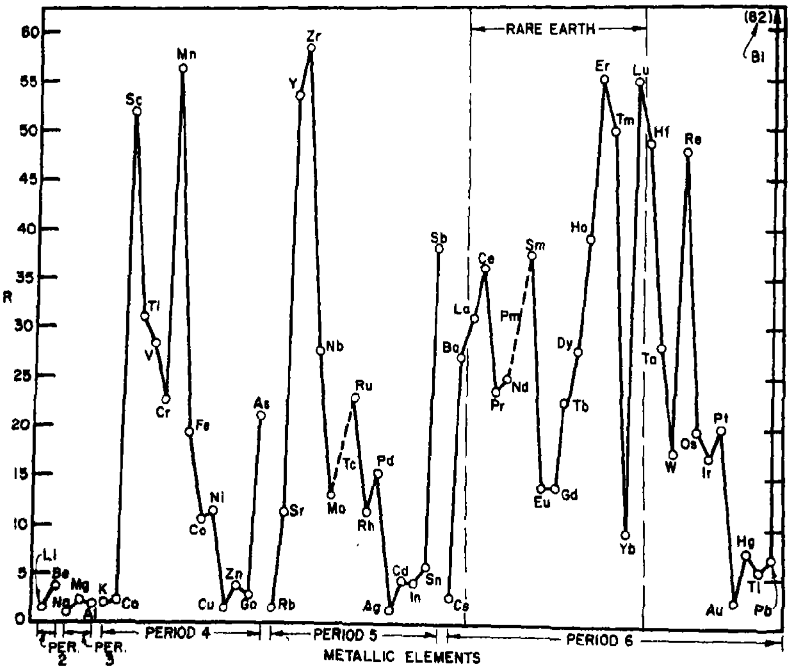

FIG. 9. Ziman *R* parameter for metallic elements. Values taken from Ref. 15 except for Mn, V, Re, and Hf which were calculated from data given in Ref. 12 and the rare earths.

Table 4. *Electronic structure parameters derived from Ziman's equations*

Metals	R	S/S_{free}	N_{eff}
La	30·9	0·259	0·40
Ce	36·2	0·239	0·35
Pr	23·6	0·297	0·49
Nd	24·8	0·289	0·47
Sm	37·4	0·235	0·34
Eu*	14·0	0·34	0·4
Gd	13·6	0·375	0·69
Tb	23·0	0·301	0·50
Dy	27·7	0·274	0·43
Ho	39·2	0·230	0·33
Er	55·1	0·194	0·26
Tm	49·8	0·204	0·28
Yb	9·6	0·407	0·52
Lu	54·8	0·195	0·26
Sc*	52·0	0·20	0·3
Y	53·6	0·197	0·26

* R values calculated with values of θ estimated from Lindeman melting point formula (Eu—94°K, Sc—308°K). Ref. 16 calculated an R value for Sc of 69·0 using a different value of θ.

parameter R, where

$$R = 8{\cdot}125\times 10^{9}\left[\frac{M\theta^{2}\rho}{DT}\right];$$

M being the atomic weight, θ the Debye temperature, ρ the resistivity due to lattice vibrations, D the Debye radius, and T the temperature at which ρ is measured. R is proportional to $n^{2/3}(S_{\text{free}}/S)$ where n is the number of conduction electrons and S and S_{free} are the areas of the actual and free electron Fermi surfaces respectively. A comparison of the calculations with anomalous skin effect

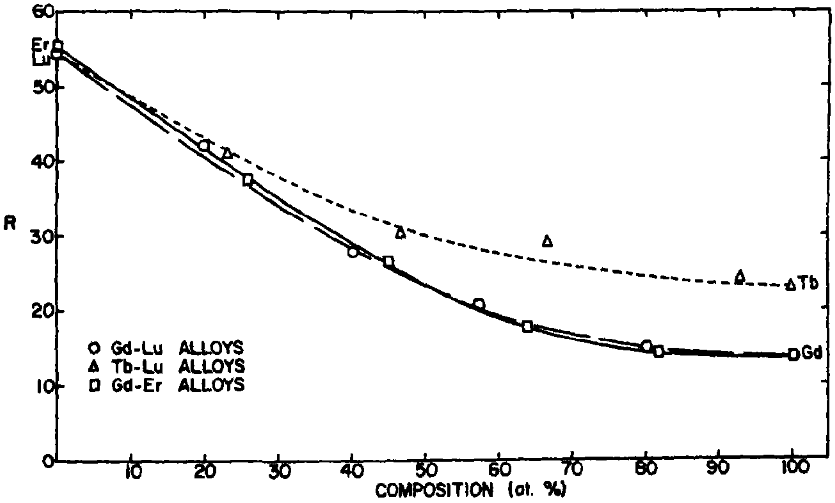

FIG. 10. Variation of Ziman R parameter in alloy system Gd–Lu, Tb–Lu, and Gd–Er.

measurements on metals where the Fermi surface geometries have been determined, shows that the constant of proportionality is 1 for the third period elements but appears to be smaller for other periods.(16)

The values of this parameter for the rare-earth metals were estimated after correcting for the spin-disorder contribution as previously described. These values are shown in Table 4 as well as the ratio S/S_{free}, while a comparison with other metallic elements is shown in Fig. 9. A value for the number of effective electrons, which gives an indication of the fit to the transport equations, has also been calculated from Ziman's equations and is tabulated in Table 4. The absolute values of these parameters may of course be in error because of the uncertainty in the proportionality constant, but the relative values within the rare-earth series are significant and represent facts which remain to be explained. Estimates of R were also made for the alloys assuming a linear change of M, θ, and D across the alloy system and are shown in Fig. 10.

The most striking feature of these calculations of R is the wide variation across the heavy rare-earth series. MACKINTOSH(17) has suggested that the Fermi surface for these metals might be roughly approximated by the free electron Fermi surface. If the transport properties of these metals are dominated by the large piece of Fermi surface in the third Brillouin zone a correlation with the change of c/a ratios for these metals is possible. As the c/a ratio decreases from Gd to Er this surface would shrink and the conductivity would decrease while the increase in c/a ratio for Tm and Lu would produce an increase in the area of this surface and hence in the conductivity.

CONCLUSIONS

Studies of alloy systems among the heavy rare-earth metals have shown that there is a sizeable contribution to the residual resistivity when one or more of the components is magnetic. This contribution results from the random distribution of atoms with localized moments through the lattice.

At temperatures above the ordering temperature of a rare-earth metal or alloy the spin-disorder resistivity can be separated from the total to obtain the lattice resistivity. Sizeable variations in the magnitude of the lattice resistivity were shown to be qualitatively correlated with the change in c/a ratio across the heavy rare-earth series, and the attendant modification thus produced in the Fermi surface.

Acknowledgements—We would like to thank Dr. SAM LEGVOLD for the equipment used in making these measurements and Dr. A. R. MACKINTOSH for many stimulating and enlightening discussions.

REFERENCES

1. KASUYA T., *Progr. theor. Phys. Kyoto* **16,** 45 (1956); *ibid.* **16,** 58 (1956).
2. COLES B. R., *Advanc. Phys.* **7,** 40 (1958).
3. SCHINDLER A. I., SMITH R. J. and SALKOVITZ E. I., *J. Phys. Chem. Solids* **1,** 39 (1956); *Phys. Rev.* **108,** 921 (1957).
4. SPEDDING F. H. and DAANE A. H., *J. Metals* **6,** 504 (1954).
5. COLVIN R. V., LEGVOLD S. and SPEDDING F. H., *Phys. Rev.* **120,** 741 (1960).
6. WEISS R. J. and MAROTTA A. S., *J. Phys. Chem. Solids* **9,** 302 (1959).
7. BROUT R. and SUHL H., *Phys. Rev. Letters* **2,** 387 (1959).
8. MACKINTOSH A. R. and SMIDT F. A. Jr., *Phys. Letters* **2,** 107 (1962).
9. MOTT N. F. and JONES H., *The Theory of the Properties of Metals and Alloys*, Dover, New York (1936).
10. ALSTAD J. K., COLVIN R. V., LEGVOLD S. and SPEDDING F. H., *Phys. Rev.* **121,** 1637 (1961), *ibid.* 123, 418 (1961).
11. WHITE G. K. and WOODS S. B., *Phil. Trans. Roy. Soc.* **251A,** 35 (1959).
12. KASUYA T., *Progr. theor. Phys. Kyoto* **22,** 227 (1959).
13. NIIRA K., *Phys. Rev.* **117,** 129 (1960).
14. ZIMAN J. M., *Electrons and Phonons* University Press, Oxford (1960).
15. COLVIN R. V. and ARAJS S., *Electrical Resistivity of Scandium* U.S. Steel Corporation, Monroeville, Pennsylvania (1962).
16. ZIMAN J. M., *Advanc. Phys.* **10,** 1 (1961).
17. MACKINTOSH A. R., *Rare Earth Research: Proceedings of the Second Conference* (edited by LUNDIN C. E. and NACHMAN J. F.), p. 272 Gordon and Breach, New York (1962).

J. Phys. Chem. Solids Pergamon Press 1963. Vol. 24, pp. 371–378. Printed in Great Britain.

RELATION BETWEEN STRUCTURE ANISOTROPY AND SUPERCONDUCTING ANISOTROPY

J. J. HAUSER and R. G. TREUTING
Bell Telephone Laboratories, Incorporated, Murray Hill, New Jersey

(*Received* 4 *September* 1962)

Abstract—The following four alloys were investigated in this study: 3Mo:2Re, 1Mo:1Re, 3Nb:1Zr, 1Nb:1Zr. Samples of these alloys were cold-rolled by amounts varying from 83·5 to 99 per cent and the variation of the critical current as a function of applied magnetic field was measured. The anomalous current behavior previously described by LEBLANC and LITTLE(1) on Nb and BERLINCOURT *et al.*(2) on Nb–Zr alloys was noted. Besides the known anisotropy with respect to the rolling plane, a strong anisotropy with respect to the rolling direction was observed. Whenever a peak in critical current density was obtained, it was always possible to obtain a curve with a plateau in current density lying above it, thereby showing that the peak is not the anomaly but that the decrease or "valley" in current density preceding the peak is the principal anomaly. The current carrying capacity when measured along the rolling direction was higher with the field perpendicular rather than parallel to the current direction. This effect disappeared upon annealing the sample at high temperature, indicating that the structural effects of deformation were dominating demagnetization effects in these hard superconductors. The ratio of peak to valley was found to increase with increasing degree of cold rolling. This ratio varied in the different materials studied and seemed to be related to the degree of "fiber" structure as revealed by optical microscopy. A tentative explanation in terms of the structural anisotropy present in these cold-rolled materials is proposed.

1. INTRODUCTION

THE general critical current vs. magnetic field curve for a hard superconductor is a monotonically decreasing curve with a plateau region and, in general the transition field is a single valued function of the current. The three different portions of the curve can be interpreted in terms of the "filamentary" model of hard superconductivity.(3) In contrast with this general behavior anomalous current dependence on the magnetic field has been reported first by LEBLANC and LITTLE(1) as well as BERLINCOURT *et al.*(2) on rolled Nb and rolled Nb–Zr alloys respectively. This effect which has now been observed on a variety of alloys was referred to as the "peak effect" by BERLINCOURT and co-workers.(2) The ratio of peak current to minimum current (valley) varied from about 1·2 to 1·5 for the various Nb–Zr alloys investigated. Although some explanations have been offered(4) in terms of trapped flux or interacting filaments, no attempt has been made to correlate the anomalous superconducting behavior with the structure of the material. Furthermore, the proposed explanations, do not explain why this peak effect is more predominant in rolled materials than in materials deformed by other means. It is indeed true, that such an effect has also been observed in drawn Nb–25 per cent Zr wire(4) and in Nb–Hf castings.(5) This last point shows that rolling is by no means necessary to produce the anomalous effect, but on the other hand rolling seems to be the most reproducible deformation process to yield the structural conditions required for such an effect. Thus, cold rolling was employed to discover a correlation between texture and superconducting properties.

2. EXPERIMENTAL PROCEDURE

The various alloys used in this investigation were prepared by arc melting in a water cooled, copper hearth, argon arc furnace the proper stoichiometric mixtures of the metals. The arc melted buttons were then annealed for long times at temperatures ranging from 1250 to 1650°C in a vacuum of 10^{-5} mm in order to homogenize them. The alloys were then cold rolled but annealed several times during the deformation process in order to permit further reduction. The 3Mo:2Re and 1Mo:1Re alloys were last annealed at 15 mils at 1650°C and then cold rolled to two different thicknesses, 2·5 mils and 1 mil corresponding respectively to 83·5 and 93·5 per cent deformation. One of the 3Nb:1Zr samples was last annealed at 95 mils and rolled down to 1 mil (99 per cent), while the other sample tested was subjected to an intermediate anneal at 20 mils at 1250°C and cold-rolled to 2·3 mils (88·5 per cent). The 1Nb:1Zr alloy was last annealed at 31·5 mils at 1250°C and cold-rolled to 1 mil corresponding to 97 per cent reduction. The homogeneity of the alloys was checked microscopically and by X-ray fluorescence analysis. The X-ray fluorescence analysis did not reveal any wide fluctuation in composition and this was taken as evidence for the absence of a second phase. Picklesimer(6) pointed out that some microsegregation on a very fine scale can be revealed by an anodizing process in the Nb–Zr alloys, but this technique was not used in this investigation.

Samples 20 mils wide and usually approximately 1 cm long were sheared out of the rolled sheet. Nickel current leads and potential leads were spot welded on the sample. A copper wire was soldered across the current leads so as to shunt the current when the sample was no longer superconducting. The samples were mounted flat on a phenyl fiber holder and were rigidly cemented with G.E. Adhesive No. 7031. The transition from superconducting to normal was determined by observing the appearance of a voltage across the potential leads using a voltmeter with a sensitivity of about 10^{-9} V.

The critical current versus applied magnetic field curves were measured at 4·2°K. As first suggested by Berlincourt *et al.*(2) some of the curves were established in two manners. (1) the current was increased smoothly and slowly up to the critical current at constant magnetic field and (2) the magnetic field was increased up to the transition field at constant current.

The structure of the various cold-rolled alloys was established by three different means: (1) Optical microscopy to reveal the gross features of the deformed alloy (2) X-ray pole figures to study the crystallographic preferred orientation of the material and (3) electron microscopy to appraise the dislocation distribution in the material.

Figure 1 displays the two different positions in which the samples were measured. When the magnetic field is parallel to the rolling plane in the first position it is also parallel to the rolling direction and in the second position it is perpendicular to the rolling direction. When the magnetic field is perpendicular to the rolling plane, positions 1 and 2 are equivalent. Therefore, any difference between the curves obtained in these two equivalent positions does not reflect any significant physical difference and should disappear under ideal experimental conditions.

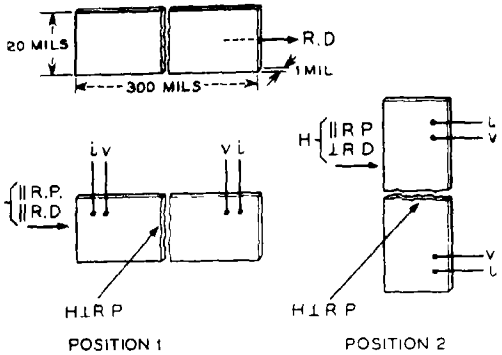

Fig 1. Lead configuration and positions of sample in the magnetic field.

3. EXPERIMENTAL RESULTS

The various experimental results are listed in Table 1 and will be discussed in greater details in the following Section. The two positions used to measure the samples are shown in Fig. 1 and will thereafter be referred to as position 1 or position 2. The critical current versus magnetic field curve for the 3Mo:2Re alloy deformed 93·5 per cent is shown in Fig. 2. The two curves taken with the magnetic field perpendicular to the rolling plane are nearly identical for position 1 and position 2. This provides a good check on the reproducibility in positioning the sample and in obtaining the data. The curve obtained with the magnetic field parallel to the rolling direction in position 1 exhibits a pronounced valley when the magnetic field is 2 kG. This valley disappears

Table 1. Relation between deformation and superconducting properties

	3Mo:1Re				1Mo:1Re		3Nb:1Zr		1Nb:Zr
Cold rolling (per cent)	93·5	83·5	93·5 and annealed ½ hr at 1650°C.	93·5 and etched from 1 mil to 0·7 mil	93·5	83·5	99	88·5	97
Peak to valley ratio	6	3	1	4	4	2	1·5	1	1

when the sample is measured in position 2, i.e. with the magnetic field perpendicular to the rolling direction. When the magnetic field exceeds the value at which the peak occurs, the current versus magnetic field curve is the same for positions 1 and 2. The same gross behavior is exhibited by the 1Mo:1Re alloy deformed 93·5 per cent as shown in Fig. 3. The only difference between 1Mo:1Re and 3Mo:2Re alloys is that in positions 1, the 1Mo:1Re alloys display a plateau after the peak current has been obtained. The ratio of the peak critical current to the minimum critical current in the valley for the 3Mo: 2Re alloy is 6 for the data shown in Fig. 2, but it was found to vary from 5 to 10 in the various samples. The peak to valley ratio for a 1Mo:1Re alloy deformed as severely as a 3Mo:2Re alloy was always found to be smaller; 4 for the sample described in Fig. 3. A 3Mo:2Re alloy and a 1Mo:1Re alloy both deformed 83·5 per cent, had peak to valley ratios

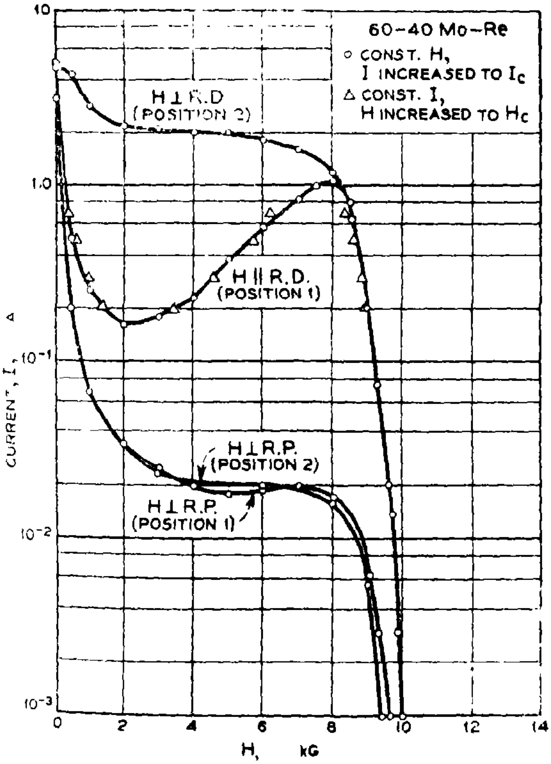

FIG. 2. Critical current vs. magnetic field curves for a 3Mo·2Re alloy cold-rolled 93·5 per cent.

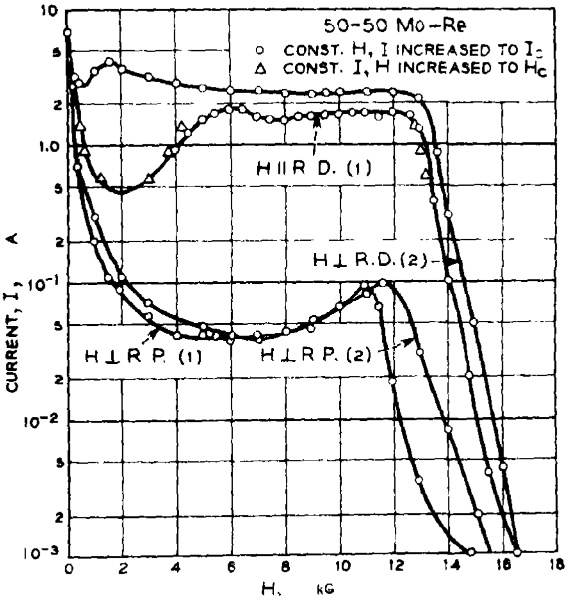

FIG. 3. Critical current vs. magnetic field curves for a 1Mo:1Re alloy cold-rolled 93·5 per cent.

of respectively 3 and 2. A 3Mo:2Re sample deformed 93·5 per cent, 1 mil thick was etched down to 0·7 mil and no appreciable difference was found in its properties except for a reduction of the peak to valley ratio from 7 to 4.

In order to establish the state of the sample in the valley region of the curve the following resistivity measurements were made. The normal resistivity at 4·2°K of a 1 mil thick sample of 3Mo:2Re was obtained by applying a magnetic field of 18 kG and was found to be $2{\cdot}6\times10^{-2}\,\Omega$. In the valley region, at constant current, once the first transition field has been exceeded, the resistance increases with increasing field, passes through a maximum at a field of 3 kG and then decreases to zero at the second transition field. The maximum value of this resistance for the above-mentioned sample was $1{\cdot}63\times10^{-3}\,\Omega$ at a current of 1 A.

A 1 mil thick 3Mo:2Re sample deformed 93·5 per cent was measured in position 1 at the start, i.e. with the magnetic field parallel to the rolling direction. The magnetic field was then rotated from this position in a plane normal to the rolling plane up to an angle of 17° to study how the I_c vs. H curve is affected by an intermediate state. The resulting data is shown in Fig. 4. The same sample was then mounted in position 2 and the magnetic field was rotated in a plane normal to the rolling plane up to an angle of 15°; the results of this experiment are shown in Fig. 5.

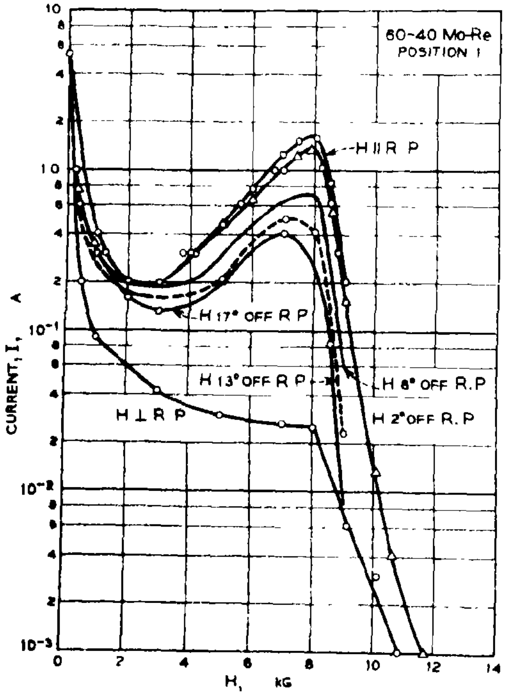

FIG. 4. Critical current vs. magnetic field curves for a 3Mo:2Re alloy cold-rolled 93·5 per cent. (Magnetic field rotated up to 17° from position 1.)

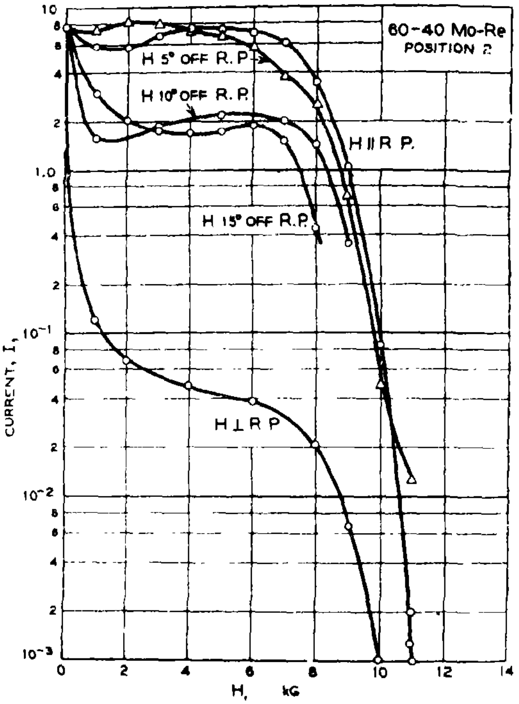

FIG. 5. Critical current vs. magnetic field curves for a 3Mo:2Re alloy cold-rolled 93·5 per cent. (Magnetic field rotated up to 15° from position 2.)

The 1 mil 3Mo:2Re sample of which the superconducting characteristics were described in Fig. 2 was examined by optical microscopy. The microstructure is shown in Fig. 6(a). This microstructure reveals a fiber structure composed of wedge shaped stringers with well defined boundaries approximately 5–10μ in diameter, 30–40μ long. Electron microscopy revealed that most of the dislocations were concentrated in the boundaries of these stringers, and consequently these boundaries are in a state of high strain and disorder. The above mentioned sample was then

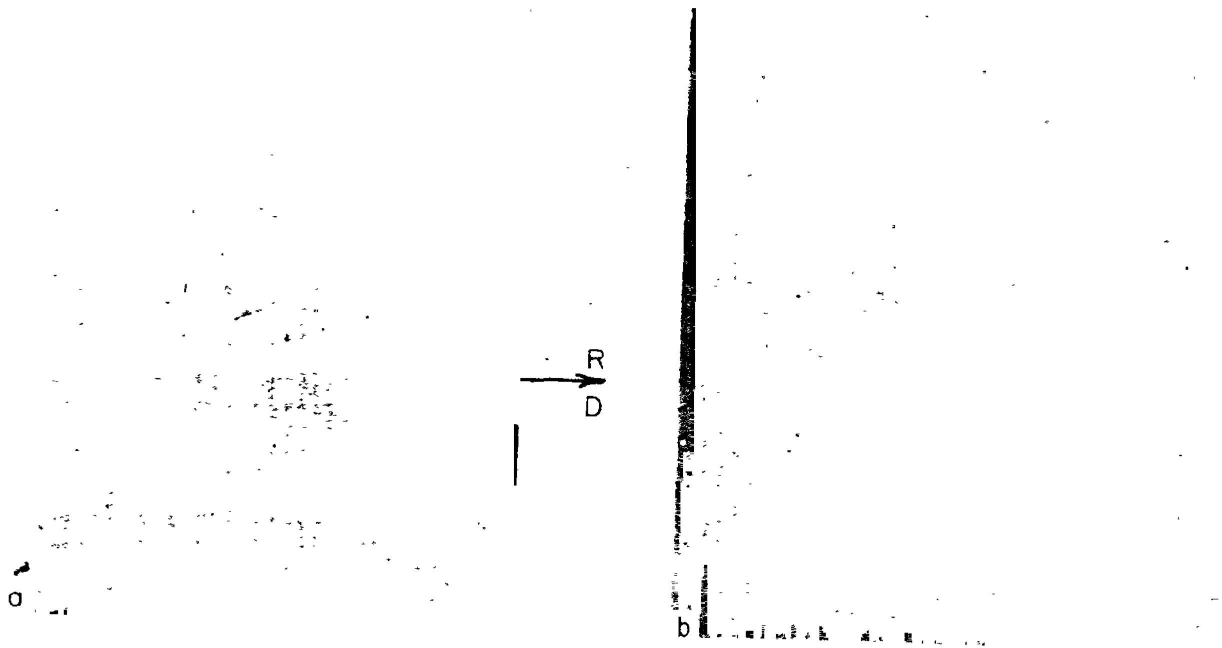

FIG. 6. 60 per cent Mo–40 per cent Re cold-rolled 93·5 per cent to 0·001 in. Electropolished and etched.
(a) Photomicrograph as rolled Magnification 60×. (b) Photomicrograph annealed ½ hr. at 1650°C. Magnification 160×.

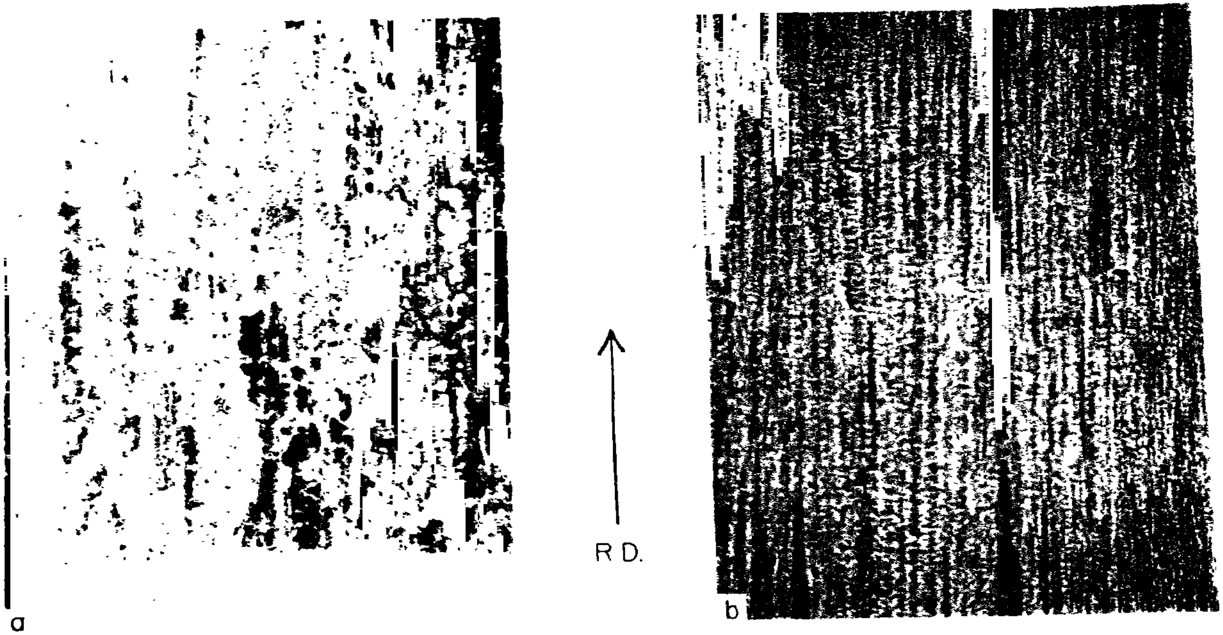

FIG. 8. (a) Photomicrograph of 3Nb:1Zr cold-rolled 99 per cent to 0·001 in. Electropolished and etched. Magnification 60×. (b) Photomicrograph of 1Nb:1Zr cold-rolled 97 per cent to 0·001 in. Electropolished and etched. Magnification 160×.

annealed for $\frac{1}{2}$ hr at 1650°C. The result of this heat treatment was to produce a recrystallized structure shown in Fig. 6(b), composed of equiaxed grains of which the diameter is approximately the thickness of the foil, i.e. one mil. The superconducting characteristics of this annealed sample are shown in Fig. 7. It is obvious from Fig. 7 that the valley effect has disappeared and that the curves obtained in positions 1 and 2 are approximately the same.

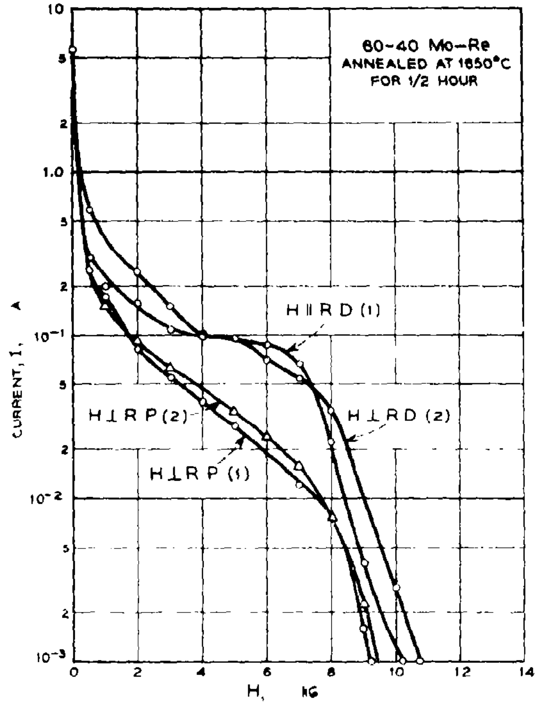

FIG. 7. Critical current vs. magnetic field curves for a 3Mo:2Re alloy cold-rolled 93·5 per cent and then annealed $\frac{1}{2}$ hr. at 1650°C.

The X-ray pole figure study on the Mo–Re alloys revealed a certain degree of crystalline anisotropy. The predominant crystallographic plane parallel to the rolling plane is the {211} but there exists also some {200} preferred orientation. The crystallographic direction parallel to the rolling direction is the ⟨110⟩ direction.

A 3Nb:1Zr alloy similar to that previously studied by BERLINCOURT *et al.*(2) in the cold-rolled form and by ARON and HITCHCOCK(4) in the wire form was cold-rolled 99 per cent down to 1 mil. The resulting microstructure is shown in Fig. 8(a). As compared to Fig. 6(a) the stringers have now very irregular boundaries and their directions are not as well defined as in the Mo–Re alloys. Furthermore, electron microscopy revealed that in this alloy the deformation was of much more homogeneous nature, i.e. the dislocations were not predominantly concentrated in the boundaries of the stringers. The critical current dependence on magnetic field for this alloy is shown in Fig. 9. Again, one can observe that the valley occurs in position 1 and disappears when the sample is measured in position 2. On the other hand the peak to valley ratio for such an alloy is very low, namely 1·5. The 3Nb:1Zr alloy which was cold-rolled 88·5 per cent did not show any valley effect at all.

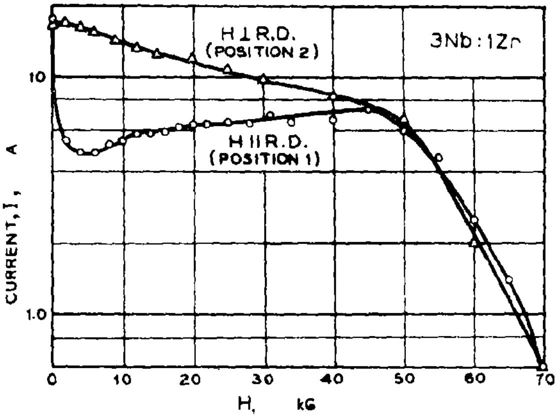

FIG. 9. Critical current vs. magnetic field curves for a 3Nb:1Zr alloy cold-rolled 99 per cent.

A 1Nb:1Zr alloy was cold rolled 97 per cent and the microstructure is shown in Fig. 8(b). The stringer boundaries are ill defined. The superconducting behavior of the alloy is described in Fig. 10 where it is evident that no valley effect is present and that there is no appreciable difference between the current carrying capacity in position 1 or 2.

Finally, a 3Mo:2Re alloy was compression rolled 94·5 per cent i.e. the sample was rotated between successive rolling passes. The microstructure was again characterized by a fiber structure. However, the stringers were not as sharply defined as in the rolled alloy, and the orientation of the stringers varied from region to region in the material. Nevertheless, a predominant fiber texture orientation could be established and measurements taken along this direction yielded the maximum peak to valley ratio. Measurements taken along a direction normal to the predominant fiber structure resulted again in a normal curve with a plateau located above the peak of the curve which exhibited the valley effect.

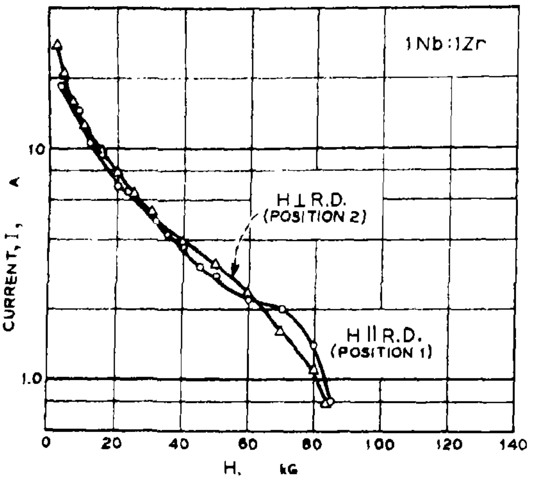

FIG. 10. Critical current vs. magnetic field curves for a 1Nb:1Zr alloy cold-rolled 97 per cent.

4. DISCUSSION

Although the complexity of the metallurgical variables, and the present rather limited understanding of hard superconductors make a complete explanation of the phenomena impossible, certain important conclusions can be drawn from these experiments.

The anomaly in the critical current versus magnetic field curve has been labeled by **BERLINCOURT** *et al.*(2) an anomalous "peak effect". From the data presented here on a variety of alloys in Figs. 2, 3 and 9, it is clear that the peak in current which occurs when the magnetic field is parallel to the rolling direction is invariably below the plateau which is obtained when the sample is measured with the magnetic field normal to the rolling direction. Therefore, the anomaly is not the peak but the valley and the effect should properly be referred to as the valley effect.

As emphasized by previous investigators,(1, 2) these rolled materials display a very strong anisotropy in superconducting properties with respect to the rolling plane. Indeed, as shown in Figs. 2, 3 and 5 there is a difference as large as two orders of magnitude between the current carrying capacities with the magnetic field parallel and normal to the rolling plane. This effect is certainly related to the anisotropic filamentary structure produced by rolling and not to demagnetization effects caused by the ribbon shape of the sample. Indeed, as shown in Fig. 7 where the same ribbon shape is measured in the annealed state, the difference between the current carrying capacities with the field parallel and normal to the rolling plane is at most a factor of 4. Furthermore, this study reveals a very strong anisotropy with respect to the rolling direction. As shown in Figs. 2, 3, 4 and 9, the valley in the critical current vs. magnetic field curve occurs where the magnetic field lies parallel to the rolling direction. Figures 2, 3, 5 and 9 show that the valley is not present when the magnetic field is normal to the rolling direction. The difference could not possibly be caused by the relative orientation of the current and the magnetic field, as shown by Fig. 7. Although in Fig. 7 the same sample geometry and lead arrangement are used as in Fig. 2, the valley has been removed and there is no longer a difference between position 1 and 2. This can only be explained by the fact that the annealing has removed the anisotropy with respect to the rolling direction as shown in the micrograph of Fig. 6(b). The annealing treatment has also reduced the current carrying capacity by a factor of 10 without, however, changing the filamentary critical field. This is consistent with the fact that annealing changes the number of filaments but not their character.(3) As a matter of fact, it can be seen from Figs. 2, 3 and 9 that although the high current density portions of the curves are different in position 1 and 2 because of the different relative orientation of the magnetic field with respect to the fibre structure of the sample, the zero current filamentary critical field is the same for both positions. Consequently, whatever cause is responsible for the valley effect, it does not alter the nature of the filaments.

As mentioned previously, if the magnetic field is increased at a constant current selected in the valley region, the resistance increases up to a maximum which is equal to approximately 1/20 of the normal resistance. Therefore, in the valley region, although a zero resistance current cannot flow any longer, superconductivity has not been destroyed completely and the sample must be in a mixed state. (Mixed state refers to a mixture of normal and superconducting phases produced by chemical or structural inhomogeneities as opposed to the intermediate state where the mixture arises because of geometrical considerations.) Actually, the valley effect can persist in the presence of an intermediate state produced by applying the magnetic field at an angle with respect to the rolling plane. The results of such an experiment are shown in Figs. 4 and 5. It can be seen from Fig. 4 that although the peak to valley ratio decreases as the degree of intermediate state is increased by increasing the angle of the field with the rolling plane, the valley effect still remains. On the other hand, if an intermediate state is produced starting from position 2 where no valley effect exists, as shown in Fig. 5, the general characteristics of the curve (i.e. no valley) are preserved.

The greatest peak to dip ratio was obtained for the 3Mo:2Re alloy and as shown in Fig. 6(a), this alloy shows very pronounced stringers with sharp boundaries. The 3Nb:1Zr alloy which displays stringers with very irregular boundaries and very low directional anisotropy as shown in Fig. 8(a) displays also a very shallow valley in its critical current versus magnetic field curve. The 1Nb:1Zr alloy which does not display any well defined stringer structure (Fig. 8(b)) does not reveal any valley effect at all. The 3Mo:2Re and 1Mo:1Re alloys which were deformed to a lesser extent (83·5 per cent) had a peak to valley ratio reduced by approximately a factor of 2. The 3Nb:1Zr alloy which was deformed only 88·5 per cent did not reveal any valley effect. Consequently, the magnitude of the valley effect can be taken as a measure of the fiber anisotropy present in the material. Up to this point the structure of the material has been used to interpret the superconducting properties. In this particular case it may be possible to use the superconducting properties to deduce the mechanical state of the material. One aspect of this idea can be shown in the case of the compression rolled 3Mo:2Re alloy. As shown in Fig. 7 the valley effect has been removed by destroying the fiber structure by a high temperature anneal. As the valley effect was correlated to the rolling direction, it should be possible to remove the valley effect by compression rolling. This should produce a rolling texture but without an anisotropy with respect to the rolling direction. The experiment was, however, unsuccessful because the first rolling passes produce a directional fiber structure which is not eliminated by the successive passes. Although the direction of the stringers varies from place to place in the material, there is a net direction in which most of the stringers lie and this was also the direction in which the greatest peak to valley ratio was measured.

The explanation for the anomally will have to be, at this stage, of a speculative nature. This explanation must, however, take into account the following factors: (1) the anomaly is a valley effect and not a peak effect (2) the valley effect is related to the direction and presence of a fiber structure (3) the sample is in a mixed state in the valley region (4) the valley effect can be observed upon increasing or decreasing magnetic field. Abrikosov(7) and Goodman(8) have proposed a theory for hard superconductors based on the fact that when the mean free path is short enough, the interfacial energy between the normal and superconducting phases becomes negative and this in turn leads to a reversible breaking up of the material into alternate superconducting and normal lamina parallel to the applied field. On the other hand, hard superconductivity has also been interpreted in terms of a filamentary model(9, 10, 11) in which the filaments are related to real defects of the material such as dislocations.(3, 10) Actually, it is very likely that both theories are correct, but that the critical field of the former one is lower in most cases than that of the latter. As the boundaries of the stringers represent a region of very concentrated dislocation arrays it is very probable that they would pin the normal regions if a mixed state were to develop. Consequently, if one applies a magnetic field parallel to the stringer direction, once the bulk critical field has been exceeded the material will enter a mixed state in which the boundaries of the stringers are normal and the inside of each stringer is superconducting as a whole. Even in such a mixed state, there will always exist some filaments going all the way across the sample which will carry superconducting currents up to the filamentary critical field if the current density is low enough. If the current density is higher than these continuous filaments can carry, as soon as the mixed state extends across the entire cross section of the sample, some normal voltage will develop. This normal voltage increases more and more as the mixed state progresses with increasing field. Finally, the critical field for such a structure will be exceeded and some of the stringers will turn normal as a whole except for the filaments which they contain. This will increase the current carrying capacity, thereby, decreasing the amount of current that must flow in the continuous filaments previously mentioned, until finally the normal resistance will fully disappear. If the magnetic field is increased past this point one will eventually reach the filamentary critical field, where superconductivity will be totally quenched. Such a model applies as well if the magnetic field is decreased instead of increased. If the magnetic field is now applied normal to the rolling direction, the splitting into laminae will again occur according to the ABRIKOSOV–GOODMAN(7, 8) theory but this time without any relationship to the structure of the sample. As a normal lamina will be traversed by superconducting filaments, the valley will not develop and one will observe the normal behavior.

5. CONCLUSIONS

The anomaly in the critical current vs. magnetic field curve which occurs in cold-rolled alloys should be described as a valley effect. This valley effect occurs when the magnetic field is parallel to the rolling direction. Actually, rolling is not necessary for this effect, and any condition which will develop a directional fiber structure with the proper boundaries should yield the same results. The current and magnetic field combination which yields a point in the valley region of the curve, produces a mixed state in the sample. Such a valley effect occurs upon increasing or decreasing magnetic field. The magnitude of the peak to valley ratio is a measure of the degree of fiber structure of the material and can therefore be used to study the properties of such materials. Finally, a speculative explanation of this effect can be given in terms of the ABRIKOSOV–GOODMAN(7, 8) theory and of the filamentary theory.(9, 3, 10)

Acknowledgements—We would like to thank at this time C. V. WAHL who handled most of the rolling operations, H. SCHREIBER who checked by X-ray fluorescence analysis the composition of the alloys and W. H. HAEMMERLE who helped in obtaining the data. It is a great pleasure to acknowledge the help of R. D. HEIDENREICH who examined the samples with light and electron microscopy and without whom no interpretation could have been possible.

REFERENCES

1. LEBLANC M. A. R. and LITTLE W. A., *Proceedings of the 7th International Conference on Low Temperature Physics, Toronto* 1960. Edited by GRAHAM G. M and HOLLIS–HALLETT A. C p. 362 University Press, Toronto (1961).
2. BERLINCOURT T G., HAKE R. R. and LESLIE D. H. *Phys. Rev. Letters* **6,** 671 (1961).
3. HAUSER J. J. and BUEHLER E., *Phys. Rev* **125,** 142 (1962).
4. ARON P. R. and HITCHCOCK H. C , *J. Metals*, **14,** 74 (1962).
5. WERNICK J H., private communication.
6. PICKLESIMER M. L., *O.R.N.L.* Rep. 2296, TID-4500, 13th ed. (1962).
7. ABRIKOSOV A A , *Zh. eksp. teor. fiz. S.S.S.R* **3,** 1442 (1957); *Sov. Phys. J. exptl. theor. Phys* , 1174 (1957)
8. GOODMAN B. B , *Phys. Rev. Letters* **6,** 597 (1961).
9. MENDELSSOHN K , *Proc. Roy. Soc.* **A152,** 34 (1935).
10. HAUSER J. J. and HELFAND E., *Phys. Rev.* **127,** 386 (1962).
11. BEAN C. P., *Phys. Rev. Letters* **8,** 250 (1962)

J. Phys. Chem. Solids Pergamon Press 1963. Vol. 24. pp. 379–382. Printed in Great Britain.

NUCLEAR MAGNETIC RESONANCE IN PLATINUM

L. E. DRAIN
Solid State Physics Division, A.E.R.E. Harwell

(*Received* 31 *October* 1962)

Abstract—Measurements of the nuclear magnetic resonance of Pt^{195} in platinum metal have been made from 24 to 299°K in fields of 1·75 and 9·50 kilogauss. The dependence of line width on field is attributed to line broadening by field inhomogeneities in the powdered sample due to paramagnetism. After allowance for this, a value of the spin–spin relaxation time of 1·1 ± 0·2 msec is deduced. The product of the spin–lattice relaxation time and the absolute temperature is substantially constant and equal to 35 ± 1 msec-deg. These results are in agreement with those obtained by pulse methods. The Knight shift is independent of field but varies from −4·006 ± 0·005 per cent at 24°K to −3·525 ± 0·003 per cent at 299°K relative to chloroplatinic acid. Shifts in some other platinum compounds are given.

RECENTLY measurements have been made of the nuclear spin–spin and spin–lattice relaxation times in platinum metal by pulse techniques.(1, 2) From these measurements it may be deduced that the natural line width of the Pt^{195} resonance due to spin–spin interaction is only about 0·2 G. This is so small that in nuclear magnetic resonance experiments with powdered samples, the line broadening due to field inhomogeneities produced by the paramagnetism of the particles must be considered.(3) The volume susceptibility of platinum is 21×10^{-6} e.m.u. and we may thus estimate the line width from this source to be about 0·6 G at 10 kG applied field.(3) It will thus be important in nuclear magnetic resonance experiments on platinum metal when fields of several kG or more are employed. The presence of this broadening mechanism may explain the apparent discrepancies between values of nuclear magnetic resonance line widths measured directly(4) and those obtained by pulse techniques.(1, 2) Since this broadening mechanism leads to a line width proportional to the field strength, a dependence of line width on field is expected.

Measurements of the Pt^{195} magnetic resonance in platinum metal were therefore made at two frequencies, 1·55 Mc/s and 8·37 Mc/s corresponding to approximately 1·75 and 9·50 kG respectively. The specimen was essentially identical with that used by BUTTERWORTH.(2) It consisted of powdered platinum of Johnson and Matthey superpure grade, particle diameter less than 26μ suspended in vaseline. Line width, defined as the separation of the maximum and minimum of the derivative curve is plotted against temperature in the Fig. 1. There are three contributions to the line width to be considered. They are from spin–spin interaction, spin–lattice relaxation and field inhomogeneity. It is reasonable to assume that the temperature dependence of line width arises from

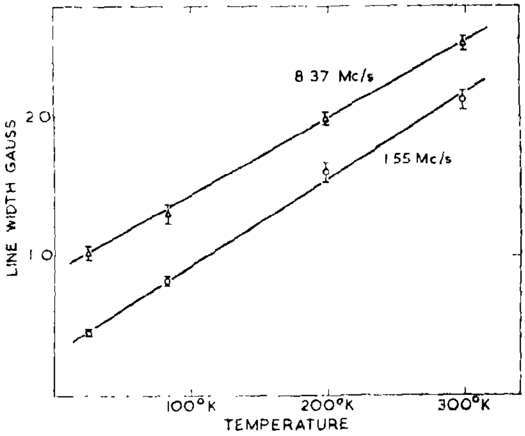

FIG. 1. Temperature dependence of the line width of the Pt^{195} resonance in platinum metal measured at 1·55 and 8·37 Mc/s.

the variation of spin-lattice relaxation time, T_1, and that the field dependence is due to the field inhomogeneity broadening discussed above. Thus extrapolation to 0°K and zero field gives the true line width due to spin–spin interactions. By linear extrapolation a value of 0·18 ± 0·03 G is obtained. This is in substantial agreement with the results of WALSTEDT, DOWLEY, HAHN and FROIDEVAUX(1) and BUTTERWORTH.(2) It is considerably less than the estimated dipolar width of 0·81 G.(4) The explanation is that since platinum contains only one magnetic isotope, indirect coupling of the nuclei via the conduction electrons leads to exchange narrowing of the resonance.(1)

We may also deduce that the field dependent contribution to the line width is 0·8 ± 0·1 G in an external field of 10 kG. This is in fairly good agreement with the estimate for the paramagnetic susceptibility mechanism(3) but of course does not prove conclusively that this mechanism is the only one. It is possible that there is some inhomogeneity of shift for the platinum atoms due to the presence of impurities. This would give a similar field dependent line width but the close agreement of the values of shift obtained from different specimens of platinum suggests that this is a small effect. It will be noted that anisotropy of Knight shift is ruled out by the cubic symmetry of the lattice.

Estimation of the relaxation times

At 1·55 Mc/s, all the Pt^{195} resonance curves measured have Lorentzian shapes within experimental error but at 8·37 Mc/s, deviations occurred at low temperatures where also an appreciable assymetry developed. Where possible, the derivative resonance curves were fitted by an expression of the form $(bh/(a^2+h^2)^2$ where h is the deviation of field from the resonance value and b, an arbitrary constant. The values obtained for the Lorentz line width parameter, a, are given in Table 1. These values will be used to estimate spin–spin and spin-lattice relaxation times.

The fact that at the low field, the line shape is Lorentzian even at 24°K where a large part of the width is due to spin–spin interactions, suggests that the line shape from this cause is at least approximately Lorentzian. This is in agreement with the supposition that the resonance is exchange narrowed and with the observations of WALSTEDT, DOWLEY, HAHN and FROIDEVAUX(1) and BUTTERWORTH.(2) Accordingly we may write the spin–spin contribution to the line width parameter unambiguously as $1/(\gamma T_2')$ where T_2' is the spin–spin relaxation time and γ is the effective magnetogyric ratio (taken as $5{\cdot}51 \times 10^3$ sec^{-1} G^{-1}).

To deduce the spin–lattice contribution to the line width, we note that in a metal, spin–lattice relaxation is the result of the interaction of nuclear moments with magnetic fields produced by conduction electrons. The fluctuation frequency of these fields are very high compared with the nuclear Larmor precession frequency and thus transverse and longitudinal relaxation are effectively the same. Under these circumstances, BLOCH's phenomenological equations are valid(5) with the substitution $T_2 = T_1$ giving a Lorentz

Table 1

Temperature	Knight shift (per cent)	Line width Lorentz parameter (G)	Peak to peak modulation amplitude (G)
Frequency 1·55 *Mc/s*			
24°K	−4·008 ± 0·005	0·37 ± 0·01	0·06
82°K	−3·978 ± 0·010	0·69 ± 0·01	0·14
198°K	−3·792 ± 0·005	1·36 ± 0·06	0·30
299°K	−3·528 ± 0·005	1·76 ± 0·05	0·50
Frequency 8·39 *Mc/s*			
25°K	−4·003 ± 0·004	—	0·17
82°K	−3·977 ± 0·003	—	0·36
198°K	−3·785 ± 0·003	—	0·73
299°K	−3·523 ± 0·003	2·07 ± 0·05	1·10

line of width parameter $1/(\gamma T_1)$. This is therefore the contribution of spin–lattice relaxation to the line width.

The inclusion of the field inhomogeneity term is not straightforward since the line shape from this cause is not Lorentzian and so the line width is not simply additive to the other contributions. However, from the measurements at high field at room temperature, it does seem that when the Lorentzian contribution to the resonance curve exceeds the field inhomogeneity contribution by a factor of three or more, the resulting curve is in fact Lorentzian within experimental error. Any further broadening by a Lorentzian type curve will of course lead to another curve of the same shape, the line width being additive. Thus in the range where the Lorentzian line shape is found to be valid, we may write

$$a = \frac{1}{\gamma T_2}+\frac{1}{\gamma T_1}+\lambda H_0$$

where λ is a constant that depends on the shape of the inhomogeneous field distribution. We have assumed that the width of the distribution is proportional to the applied field H_0. For simplicity the slight dependence of magnetic susceptibility on temperature[(6)] has been neglected. Its inclusion makes no significant difference to the results.

If T_1T is constant as expected for relaxation by conduction electrons in a metal,[(7)] a should vary linearly with the temperature T. From the results at 1·55 Mc/s, it will be seen that this is very nearly true. The best linear representation of the results is as follows:

$$a = 0{\cdot}25+0{\cdot}0052\,T$$

This gives $T_1T = 35 \pm 1$ msec-deg in reasonable agreement with the results of BUTTERWORTH[(2)] and others.[(1)] It must be remarked that the results show a deviation from the linear dependence of a on T that is just outside experimental error suggesting that T_1T increases by about 5–10 per cent over the range of temperature investigated. The best value from the measurements at 24 and 82°K is $T_1T = 33 \pm 2$ msec-deg. A slight increase of T_1T with temperature was also found by BUTTERWORTH.[(2)] The variation is much less than would be expected from the corresponding variation of Knight shift.

Assuming that T_1 and T_2 are independent of field, λ may be deduced from the room temperature results at the two field strengths. $\lambda = 4\times10^{-5}$. Using this and the known value of T_1T, the value of a at 25°K may be used to deduce $T_2 = 1{\cdot}1 \pm 0{\cdot}2$ mseconds, corresponding to a peak to peak line width of 0·19 ± 0·03 G. The good agreement between the values of T_1 and T_2 derived here and those obtained by more direct pulse methods is good evidence for the validity of the assumptions made.

The Knight shift

The results of measurements of the shift of the Pt^{195} resonance defined as $(\nu_m-\nu_r)/\nu_r$ are given in Table 1. ν_m and ν_r are the resonance frequencies in the same field for the metal and reference solution of chloroplatinic acid respectively. It is clear that the shift is independent of field. Where comparable, the results are in agreement with those of ROWLAND.[(4)] The temperatures quoted here are estimated to be correct to better than ± 2°K. They were measured by means of a copper–constantan thermocouple close to the specimen. The thermocouple was calibrated at the boiling points of hydrogen and nitrogen and at the carbon dioxide sublimation point.

The choice of reference compound for measurements of shift is of course arbitrary and it is probable that there is a considerable chemical shift of the Pt^{195} resonance in chloroplatinic acid. To obtain the true value of shift due to conduction electrons it is necessary to correct for this. Some values of chemical shifts in platinum compounds are now available and the results obtained in this laboratory (at 8·71 Mc/s) are given in Table 2. The sample of tetraamine platinous chloride was kindly supplied by the Chemistry Department of Birmingham University. The last three shifts refer to resonances found in a solution of Na_2PtCl_6 which had been reduced by passing SO_2. Although these shifts are by no means negligible, it now seems extremely unlikely that the chemical shift of H_2PtCl_6 is as high as 4 per cent which would be necessary to ensure that the true Knight shift of platinum metal is positive. The lowest chemical shift for platinum so far found is −0·55 per cent in an arsenic complex.[(8)] The highest is that of the reference H_2PtCl_6. It is expected that a systematic study of platinum complexes will enable the position of the unshifted Pt^{195} resonance to be

Table 2

Compound		$\frac{\nu(\mathrm{Pt}^{195})}{\nu(\mathrm{Na}^{23})}$	Shift (per cent)
H_2PtCl_6		0·812667 ± 4	reference
$Pt(NH_3)_4Cl_2$		0·810584 ± 10	−0·256 ± 0·002
Reduction	(i)	0·81135 ± 8	−0·162 ± 0·010
products	(ii)	0·81045 ± 3	−0·273 ± 0·004
(see text)	(iii)	0·80996 ± 3	−0·333 ± 0·004

deduced. A reasonable estimate on the basis of present information would be −0·7 per cent relative to H_2PtCl_6. In this basis, the true Knight shift in platinum metal varies from −3·3 per cent at 20°K to −2·8 per cent at 300°K.

Acknowledgements—The author wishes to thank Mr. J. Butterworth and Dr. T. J. Rowland for valuable comments and Mr. B. Lent for help with the experimental work.

REFERENCES

1. Walstedt R. E., Dowley M. W., Hahn E. L. and Froidevaux C., *Phys. Rev. Letters*, **8**, 406 (1962).
2. Butterworth J., *Phys. Rev. Letters*, **8**, 423 (1962).
3. Drain L. E., *Proc. phys. Soc., Lond.* **80**, 1380 (1962)
4. Rowland T. J., *J Phys. Chem. Solids*, **7**, 95 (1958).
5. Wangsness P. K. and Bloch F., *Phys. Rev.* **89**, 728 (1953).
6. Hoare F. E. and Matthews J. C., *Proc. Roy. Soc.* **A212**, 137 (1952).
7. Korringa J., *Physica*, **16**, 601 (1950).
8. Pidcock A., private communication.

J. Phys. Chem. Solids Pergamon Press 1963. Vol. 24, pp. 383–386. Printed in Great Britain.

PHOTOCONDUCTIVITE EXTRINSÈQUE AVEC EMISSION DE PHONONS DANS LE GERMANIUM

C. BENOIT A LA GUILLAUME et J. CERNOGORA

Laboratoire de Physique de l'Ecole Normale Superieure, Paris

(*Received* 7 *November* 1962)

Résumé—Nous avons étudié la photoconductivité du Germanium dopé avec Zn et Cu. Nous avons observé une série de minima dans la courbe de photoconductivité en fonction de l'énergie des photons incidents. Ces minima sont régulièrement espacés en énergie, la différence entre deux minima successifs est égale à l'énergie d'un phonon optique à $k = 0$. Nous pensons qu'ils sont dûs à la photoionisation des accepteurs avec émission simultanée de 0,1 . . . n phonons-optiques.

Abstract—We have studied the photoconductivity in Ge doped with Zn and Cu. We notice a series of minimum in the photoconductivity response vs. the energy of incident photons. These minima are equally spaced in energy—the difference between the successive minima is just the energy of an optical phonon at $k = 0$. We think they are due to transition of a hole from the acceptor to the valence band with emission of 0,1 . . . n, optical phonons.

1. INTRODUCTION

Nous avons étudié la photoconductivité du Germanium dopé avec Zu et Cu dans le but de construire un détecteur d'infra-rouge jusque vers 40μ.

Nous avons observé une série de minima dans la courbe de photoconductivité en fonction de l'énergie des photons incidents. Ces minima sont régulièrement espacés en énergie, la différence entre deux minima successifs est égale à l'énergie d'un phonon-optique à $k = 0$. Nous pensons qu'ils sont dûs à la photoionisation des accepteurs avec émission simultanée de 0,1 n phonons.

Un tel phénomène a déjà été observé pour des spécimens de Sb In dopés au Cu, Ag, Au, ce qui a permis de retrouver l'énergie de 24 meV du phonon Lo à $K = 0$ (1).

2. TECHNIQUE EXPERIMENTALE

La densité des impuretés dans les échantillons utilisés, (Zn ou Cu) était de l'ordre de 10^{16} par cm^3 (voir tableau ci-dessous). Les échantillons étaient montés dans un cryostat optique et refroidis à 4 K. Leur épaisseur était de l'ordre de 2mm et l'absorption totale—même au voisinage du maximum de l'absorption dûe aux impuretés—était de l'ordre de 0,5. Ceci explique pourquoi la structure de la courbe de réponse dans nos expériences est bien observée.

La lumière incidente était modulée à 13 c/s. La courbe de réponse était obtenue avec un spectromètre à prisme. (Cl Na, KRS5 ou ICs) et comparée à la réponse donnée par un thermocouple.

Tableau des echantillons utilises

	Cristal	Dopage (N/cm^3)
Fig. 1	Ge	Zn = $6{,}7 \times 10^{16}$
Fig. 2		Zn = Sb = 2×10^{16}
Fig. 3		Cu = $2{,}7 \times 10^{16}$

3. RESULTATS EXPERIMENTAUX

Les Figs. 1–4, montrent les courbes de réponse des différents échantillons. On remarque que chaque courbe présente des minima équidistants en énergie mais la position de ces minima dépend de l'impureté. Si on porte (Fig. 5) la position de ces minima en fonction de nombres entiers on obtient des droites de pente 37 meV, qui par extrapolation donnent les énergies d'ionisation des impuretés correspondantes.

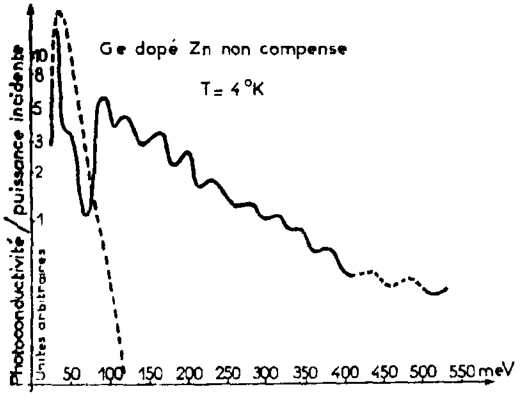

FIG. 1. Spectre de photoconductivité du Ge dopé au Zn.

(a) *Echantillon de* Ge *dopé au* Zn (Fig. 1)

On trouve une énergie d'ionization de 30 meV (Fig. 1) conforme à celle de DUNLAP.(2) FAN et FISHER(3) ont obtenu par absorption optique 32,6 meV. La forme de la courbe entre 30 et 80 meV serait dûe aux raies d'absorption du réseau situé à 43,2 ; 53,2 ; 65,5 ; 69,5 meV ;(4) ce qui expliquerait que l'on ait un minima si prononcé vers 70 meV où l'on a compétition entre l'absorption du réseau et le premier minima de la série.

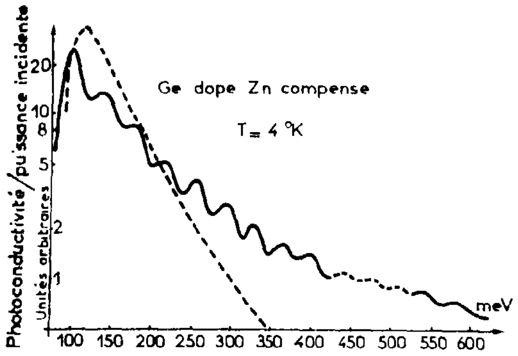

FIG. 2. Spectre de photoconductivité du Ge dopé au Zn et compensé.

On a également observé un minimum secondaire à 147 meV, (non indiqué sur la fig.), que l'on a retrouvé dans les 3 courbes de réponse de Ge et dont on ne connait pas l'origine.

(b) *Echantillon de* Ge *dopé au* Zn *et compensé* (Fig. 2)

On trouve une énergie de 90 meV (Fig. 1) conforme à celle de TYLER.(5) Fan et Fisher avaient trouvé 85,8 meV.

On observe un changement dans la pente générale de la courbe vers 400 meV qui serait dûe au fait, qu'on crée alors des trous libres dans la bande V_3, l'énergie de 400 meV correspondant alors à la distance en énergie V_1–V_3 plus l'énergie d'ionisation de l'impureté.

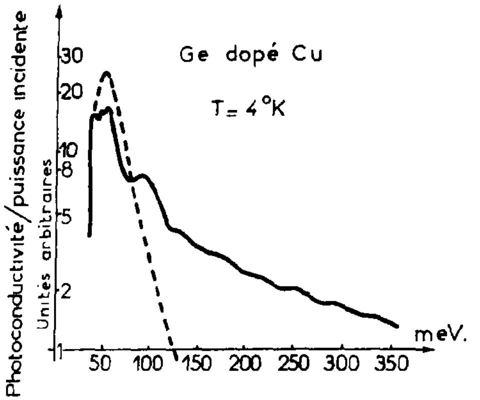

FIG. 3. Spectre de photoconductivité du Ge dopé au Cu.

On a observé d'autre part, dans la partie de la courbe, correspondant à des énergies inférieures à 90 meV (qui serait dûe à une photoconductivité sur des impuretés résiduelles d'énergie d'ionisation inférieure) des minima à 75 meV et 78 meV, qui correspondraient à l'absorption vers les niveaux excités de Zn⁻.(3)

On a observé en outre deux minima à 105,4 et 107 meV dont on ne connait pas l'origine, puis deux autres à 112 et 115 meV qui seraient dûs à l'absorption vers les niveaux excités de Zn avec émission d'un phonon. (On a effectivement 112 = 75+37 et 115 = 78+37.) Ce genre d'absorption a été observé par SMITH(6) dans le diamant.

(c) *Echantillon de* Ge *dopé au* Cu (Fig. 3)

On a trouvé (Fig. 1) une énergie d'ionisation de 43 meV qui est du même ordre que celle trouvée thermiquement par WOODBURY(7) et par ADAMS(8) par des expériences de photoconductivité. On

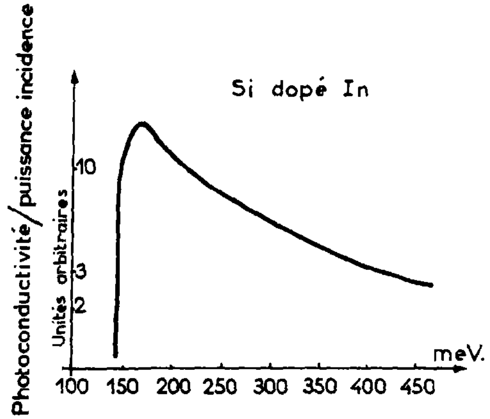

FIG. 4. Spectre de photoconductivité du Si dopé à In.

observe également entre 50 et 100 meV les raies d'absorption du réseau.

(d) *Echantillon de* Si *dopé* à In (Fig. 4)

On observe l'énergie d'ionisation de 150 meV en bon accord avec celle de BURSTEIN(9) mais aucun minima n'a été observé.

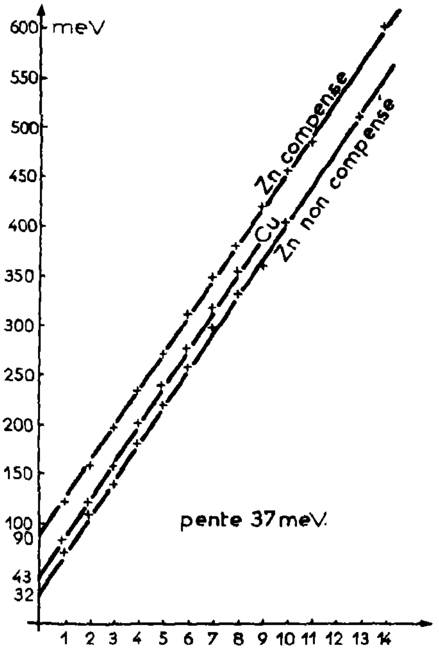

FIG. 5. Position des minima dans les spectres de photoconductivité en fonction de nombres entiérs pour plusieurs niveaux dans le germanium.

4. INTERPRETATION

La pente trouvée de 37 meV est la même quel que soit le niveau de l'impureté, elle correspond donc à une donnée intrinsèque du cristal. Elle est précisément égale à l'énergie des phonons optiques de $k = 0$ du Germanium. BROCKHOUSE et IYENGAR(10) ont d'ailleurs trouvé par des expériences de diffusion de neutrons, la valeur de 37,2 meV, alors que PELAH *et al.*(11) ont trouve 36,9 meV. On est donc amené à penser que le spectre de photoconductivité est dû à la superposition de plusieurs spectres correspondant à l'ionisation de l'impureté avec création de zéro, un, deux ... jusqu'à 17 phonons. Selon le schéma suivant, un trou est ionisé par le photon incident, cette ionisation l'amène vers un état k de la bande de valence, puis le trou est diffusé de l'état k vers l'état k' avec émission de n phonons.

On peut calculer le coefficient d'absorption direct dans le cas d'une impureté hydrogénoïde.

$$\psi_0 = \sum_k A(k) u_k \exp(i\mathbf{kr})$$

est la fonction du trou lié dans son état fondamental

$$\psi_r = u_k \exp(i\mathbf{kr})$$

la fonction d'onde du trou libre (en négligeant l'influence du potentiel coulombien de l'impureté ionisée) on obtient par un calcul analogue à celui de KOHN(12)

$$\alpha = -\frac{n}{cN}\frac{\partial N}{\partial t} = \frac{4\pi^2 Z^2 e^2}{cm^*}\frac{\hbar^2 k^2}{3}|A(k)|^2 \rho(E_f)$$

$$\rho(E_f) = \frac{m^*}{\pi^2 \hbar^3}[2m^*(E_f)]^{1/2}$$

en tenant compte de :

$$h_\omega = E_0 + \frac{\hbar^2 k^2}{2m^*}$$

on obtient

$$\alpha \propto \left(\frac{\hbar_\omega - E_0}{(\hbar_\omega)^6}\right)^{3/2}$$

D'après nos expériences nous avons tracé les courbes représentant le rapport V_{ph}/V_w dont la dépendance en ω est

$$\boxed{f(\omega) = \frac{(\hbar_\omega - E_0)^{3/2}}{(\hbar_\omega)^7}}$$

Si on essaie de superposer la courbe $f(\omega)$ dans les trois cas à la courbe expérimentale (courbe pointillée), on voit que pour le Cu et le Zn (Fig. 2 et 4) la courbe théorique passe effectivement en dessous de la courbe expérimentale, ce qui est compatible avec l'hypothèse d'une superposition de spectre avec émission de un, deux ... plusieurs phonons. Pour le Zn compensé, les deux courbes seraient plutôt superposables, mais on sait que dans ce cas là les hypothèses de Kohn ne sont valables (niveau trop profond).

Des expériences récentes faites par TAYLOR et SMITH(13) ont montré également l'existence de ce phénomène à la température de l'hélium liquide pour des échantillons de Germanium dopés au zinc.

A la température de l'hydrogène le phénomène décroîtrait en intensité. D'autre part le spectre d'absorption, lui, ne présente pas de structure. Les auteurs en concluent que les minima en photoconductivité seraient dûs à la recombinaison vers des états excités—des niveau compensés.

Le fait que le phénomène est moins marqué à l'hydrogène liquide serait dû à l'élargissement des niveaux excités à cette température.

Une telle hypothèse suppose—néanmoins—l'existence de niveaux compensés en quantité suffisante. Elle suppose également que le trou créé soit capturé vers un niveau excité, avant que d'être diffusé vers le haut de la bande de valence.

Remerciement—Nous tenons à remercier Monsieur le Professeur AIGRAIN qui nous a guidés dans ce travail.

BIBLIOGRAPHIE

1. ENGELER W., LEVINSTEIN H. et STANNARD C. S., *J. Phys. Chem. Solids* **22**, 249 (1961).
2. DUNLAP W. C., *Phys. Rev.* **96**, 40 (1954).
3. FISHER P. et FAN H. Y., *Phys. Rev. Letters* **5**, 195 (1960).
4. FAN H. Y. et COLLINS R. J., *Phys. Rev.* **93**, 674 (1954).
5. TYLER W. W. et WOODBURY H. H., *Phys. Rev.* **100**, 1259 (1955).
6. SMITH S. D. et TAYLOR W., *Proc. phys. Soc. Lond.* **79**, 1142 (1962).
7. TYLER W. W. et WOODBURY H. H., *Phys. Rev.* **105**, 84 (1957).
8. ADAMS H. D., BEYEN W. J. et PETRIZ R. L., *J. Phys. Chem. Solids* **22**, 167 (1961).
9. BURSTEIN E., PICUS G., HENVIS B. W. et LAX M. *Bull. Amer. Soc.* 30 n° 2, 13 (1955).
10. BROCKHOUSE B. N. et IYENGAR P. K., *Phys. Rev.* **108**, 894 (1957).
11. PELAH I., EISENHAUER C. M., HUGUES D. J. et PALEWSKY H., *Phys. Rev.* **108**, 1091 (1957).
12. KOHN W., *Solid State Physics* (edited by SEITZ F. and TURNBULL D.) Vol. **5**, Academic Press, New York, p. 258 (1957).
13. TAYLOR W. et SMITH S. D., Communication personnelle.

J. Phys. Chem. Solids Pergamon Press 1963. Vol. 24, pp. 387–403. Printed in Great Britain.

STRUCTURE ELECTRONIQUE DES IMPURETES DANS LE NICKEL.

APPLICATION À LA DIFFUSION MAGNÉTIQUE DES NEUTRONS PAR DES ALLIAGES DÉSORDONNÉS À BASE DE NICKEL

F. GAUTIER

Faculté des Sciences, Groupe II (Service de Physique des Solides).
B.P. No. 11 Orsay (Seine et Oise) France

(*Received* 25 *May* 1962)

Résumé—On calcule la forme asymptotique de la variation de densité électronique $\Delta\rho(r)$ produite dans la bande d du nickel par un atome d'impureté. On adopte un modèle de structure das bandes d du nickel déduit par des calculs de liaisons fortes à l'aide d'un développement pour des vecteurs d'onde proches du haut de la bande. On trouve que $\Delta\rho(r)$ est fortement anisotrope ; elle est localisée dans les plans atomiques (100), (010) et (001) qui contiennent l'atome d'impureté et elle oscille pour les distances r croissantes avec une amplitude décroissante en r^{-2}.

Dans le nickel ferromagnétique, ce changement de densité électronique produit un moment magnétique à grande distance de signe alterné pour les distances r croissantes. Cet effet produit une singularité dans le facteur de forme magnétique pour la diffusion des neutrons par des alliages désordonnés à base de nickel. La singularité observée dans les alliages de Ni–Fe pourrait être due en partie à cet effet. On pourrait observer aussi de telles singularités dans tous les alliages métalliques avec des moments magnétiques désordonnés ; ceci est seulement une conséquence du comportement oscillant à grande distance de ces moments.

Summary—The asymptotic form of the change $\Delta\rho(r)$ in electronic density produced in the d band of nickel by an impurity atom is computed. The structure assumed for the d bands of pure nickel is deduced from tight binding computations by a development in wave vector near to the top of the bands. $\Delta\rho(r)$ is found to be highly *anisotropic*; it is localized on the (100), (010) (001) atomic planes which contain the impurity atom, and oscillates with increasing distance r, with an amplitude decreasing as r^{-2}.

In ferromagnetic nickel, this change in electronic density produces a long range magnetic moment of sign alternating with increasing distance. This effect should produce a singularity in the magnetic form factor for neutron diffusion by disordered nickel base alloys. The singularity actually observed in Ni–Fe alloys might be due in part to this effect. Similar singularities should be observed in all metallic alloys with disordered magnetic moments: they are merely a consequence of the long range oscillating behaviour of these moments.

I. INTRODUCTION

I. 1. Les électrons de conduction d'un métal caractérisé par un potentiel de réseau V_R sont diffusés par une perturbation localisée. La modification de répartition électronique spatiale qui en résulte présente à grande distance de l'impureté des oscillations dont l'amplitude décroît comme r^{-3}.

Dans l'approximation de HARTREE, ROTH(1) et BLANDIN(2, 3) ont lié le comportement asymptotique de ces oscillations à la forme de la surface de Fermi.

On se propose ici de déterminer dans ses grandes lignes la forme des oscillations de densité électronique dans le nickel.

On développe pour cela dans la Section II un modèle approché des bandes d du nickel à partir des calculs de liaisons fortes de FLETCHER.(4)

La théorie générale de Roth–Blandin ne s'applique pas par suite de la forme particulière des surfaces d'énergie constante ; on calcule dans la Section III la forme asymptotique de la variation de densité électronique. On trouve (cf. formule 3.32) qu'elle est localisée au voisinage des plans atomiques (100), (010), (001) passant par l'impureté.

I. 2. La diffusion magnétique des neutrons par un alliage ferromagnétique est sensible aux oscillations de spin introduites par chaque impureté : la courbe donnant l'intensité neutronique diffusée dans une direction déterminée en fonction de la longueur s du vecteur de diffusion présente un point singulier $s = 2k_F$. Dans le cas du nickel, comme dans le cas des électrons libres, $2k_F$ est le nombre d'ondes des oscillations de spin (Section IV).

Les courbes de diffusion obtenues dans le cas d'un alliage Fe–Ni par SHULL(5) et LOWDE(6) présentent un point singulier. On attribue ce phénomène aux oscillations de spin ; si les calculs théoriques ne prédisent pas exactement la forme de la courbe de diffusion, ils donnent cependant une position du point singulier en accord avec les mesures expérimentales.

II. MODELE DE STRUCTURE DE BANDES DES ELECTRONS 3d DU NICKEL

II. 1. *Structure de bande de Fletcher*

Fletcher a développé un calcul de liaisons fortes pour les électrons 3d du nickel. Il a montré que le sommet de la bande est constitué par les diagonales des faces carrées de la zône de Brillouin.

Quand la bande est presque pleine, c'est-à-dire dans la limite où :

$$\delta E = E_F - E_0 \to 0$$

(E_F est l'énergie de Fermi ; E_0 l'énergie du haut de bande),

(a) les surfaces d'énergie constante sont voisines de cylindres ayant pour axes les diagonales des faces carrées de la zône de Brillouin (Fig. 1) ;

(b) la loi de dispersion $E(\mathbf{k}) = E_F$ est donnée sensiblement par une variation parabolique du rayon des cylindres $\mathscr{R}$ en fonction de l'énergie

$$2\delta E = A\mathscr{R}^2. \tag{2.1}$$

A est une constante dépendant des intégrales de

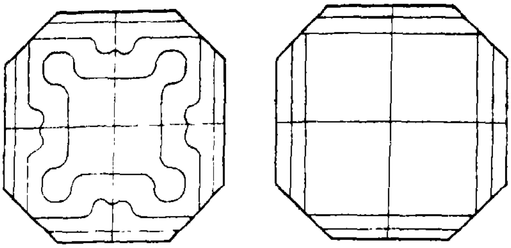

FIG. 1(a). (à gauche) section par le plan $k_z = 0$.

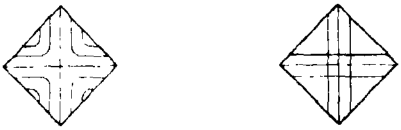

FIG. 1(b). Section par le plan $k_z = 2\pi/a$.

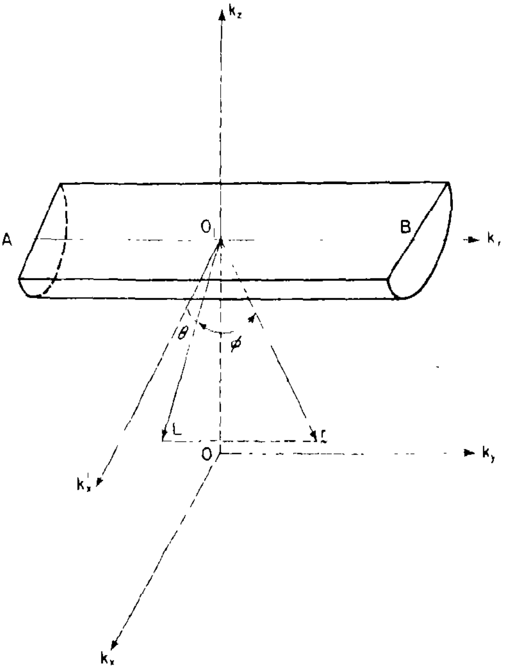

FIG. 1(c)

FIG. 1. On a représenté (à droite) les surfaces d'énergie constante correspondant à notre modèle en comparaison avec les surfaces obtenues par Fletcher.

recouvrement du potentiel :

(c) la fonction d'onde de Bloch $\varphi(\boldsymbol{k},\boldsymbol{r})$ qui, en général, est une combinaison linéaire des cinq orbitales d centrées sur chacun des sites $\boldsymbol{R}_j$ du réseau

$$\varphi(\boldsymbol{k},\boldsymbol{r}) = \frac{1}{\sqrt{N}}\sum_{ij} A_{ji}\phi_i(\boldsymbol{r}-\boldsymbol{R}_j) \tag{2.2}$$

est, pour chaque cylindre, fonction d'une seule orbitale d, les autres coefficients A_{ji} s'annulant.

Ainsi, pour des cylindres ayant leurs axes parallèles à [0,1,0], la seule orbitale

$$\phi_3(\boldsymbol{r}) = \sqrt{\left(\frac{15}{4\pi}\right)}\,\frac{xz}{r^2}\,f(r) \tag{2.3}$$

intervient ; la fonction de Bloch s'écrit :

$$\varphi_3(\boldsymbol{k},\boldsymbol{r}) = \frac{1}{\sqrt{(N)}}\sum_{j} \exp(i\boldsymbol{k}\boldsymbol{R}_j)\phi_3(\boldsymbol{r}-\boldsymbol{R}_j) \quad \text{(Fig. 1c)} \tag{2.4}$$

où N est une constante qui normalise la fonction de Bloch dans l'unité de volume :

$$\frac{1}{\Omega}\int_{\Omega} \varphi(\boldsymbol{k},\boldsymbol{r})\varphi^*(\boldsymbol{k},\boldsymbol{r})\,\mathrm{d}\boldsymbol{r} = 1$$

où Ω est le volume atomique. Dans l'hypothèse du calcul des liaisons fortes

$$N = \Omega^{-1}.$$

II. 2. *Modèle choisi*

On supposera que les résultats précédents (a), (b), (c), trouvés dans la limite où $\delta E \to 0$, sont encore valables pour l'énergie de Fermi.

En fait, le niveau de Fermi du nickel — qu'il soit ferromagnétique ou paramagnétique — est assez loin du haut de bande de sorte que l'approximation est grossière.

La validité de cette approximation est discutée dans l'Appendice A. Remarquons simplement que cette description préserve le caractère dominant de symétrie de la surface de Fermi. La répartition de densité électronique, d'après les résultats de Roth et Blandin, reflète la forme de la surface de Fermi, au moins à grande distance de l'impureté localisée ; on doit s'attendre à avoir une description de la répartition électronique qui dans ses grandes lignes, sinon dans le détail, coïncide avec a densité électronique réelle.

III. OSCILLATIONS DE DENSITE ELECTRONIQUE DANS LE MODELE CHOISI

III

1. La diffusion électronique dans les métaux a été étudiée à partir des équations aux différences de SLATER et KOSTER par KOSTER(11) qui en a déduit la forme asymptotique des fonctions d'onde diffusées. En utilisant directement les fonctions de Bloch, Roth et Blandin ont obtenu les formes asymptotiques de la fonction d'onde et de la variation de densité électronique. C'est ce formalisme que nous utilisons ; on en trouve l'essentiel en référence.(11) Les formules données par Roth et Blandin ne sont d'ailleurs pas applicables ; elles font en effet intervenir le tenseur inverse des masses effectives

$$\boldsymbol{\alpha} = \nabla_{\boldsymbol{k}}\nabla_{\boldsymbol{k}}E$$

qui n'existe pas dans le cas de surfaces cylindriques puisqu'alors le déterminant associé à $\boldsymbol{\alpha}$ est nul. Si on applique brutalement les formules de Roth Blandin, on trouve une densité infinie répartie dans chacun des plans (100), (010) et (001) issus de l'origine.

Il est donc nécessaire de refaire des calculs analogues aux calculs de Roth et Blandin pour trouver dans ce cas particulier la variation de densité. Dans la suite, après avoir établi rapidement les formules générales relatives à la variation de densité électronique (paragraphe III. 2), on examine dans notre modèle la dépendence spatiale de la variation de densité (paragraphe III 3) et on calcule dans l'approximation de Born et dans l'hypothèse d'un potentiel localisé l'amplitude de diffusion (paragraphe III 4) ; dans le paragraphe III. 5, on donne la forme définitive de la variation de densité électronique et on discute rapidement les résultats obtenus (3.32 et 3.33).

III. 2. *Formules générales donnant la variation de densité électronique*

On rappelle rapidement dans ce paragraphe la manière dont on obtient la variation de densité électronique introduite par un potentiel localisé $V_P(\boldsymbol{r})$.

On obtient la forme asymptotique de la fonction d'onde à partir de la forme asymptotique de la distribution de Green $G^+(E)$

$$|\psi^+(\boldsymbol{k})\rangle = |\varphi(\boldsymbol{k})\rangle - \frac{1}{4\pi} G^+(E)V_P|\psi^+(\boldsymbol{k})\rangle. \tag{3.1}$$

Dans cette formule :

$|\psi^+(\boldsymbol{k})\rangle$ est l'onde stationnaire résultant de la diffusion *vers l'avant* de l'onde de Bloch $|\varphi(\boldsymbol{k})\rangle$ par le potentiel localisé V_P.

$G^+(E)$ est l'opérateur de Green dont les éléments de matrice dans une représentation $\{\boldsymbol{r}\}$ satisfont à l'équation

$$\{\Delta + 2(E - V_R)\}\, G^+(\boldsymbol{r},\boldsymbol{r}',E) = -4\pi\delta(\boldsymbol{r}-\boldsymbol{r}') \tag{3.2}$$

où $V_R(\boldsymbol{r})$ est le potentiel du réseau.

Le signe + dans G^+ signifie que $G^+(\boldsymbol{r},\boldsymbol{r}',E)$ a un comportement à l'infini d'onde sortante.

En développant la masse de Dirac $\delta(\boldsymbol{r}-\boldsymbol{r}')$ par rapport au système complet des fonctions de Bloch, on obtient

$$G^+(\boldsymbol{r},\boldsymbol{r}',E) = \frac{1}{2\pi^2}\sum_n \int' \frac{\varphi_n(\boldsymbol{k},\boldsymbol{r})\varphi_n^*(\boldsymbol{k},\boldsymbol{r}')}{E_n(\boldsymbol{k}) - E - i\epsilon}\, \mathrm{d}\boldsymbol{k} \tag{3.3}$$

Dans cette expression $\epsilon > 0$ est un nombre qui tend vers zéro : il fixe le comportement asymptotique de $G^+(\boldsymbol{r},\boldsymbol{r}',E)$; n indice les bandes ; l'intégrale $\int'$ est prise sur la première zone de Brillouin.

A partir du développement de la fonction

$$y(x) = \lim_{\epsilon\to\infty} \frac{1}{x - i\epsilon} = \frac{\mathscr{P}}{x} + \pi i\delta(x) \tag{3.4}$$

$$\left(\frac{\mathscr{P}}{x} \text{ désigne la partie principale de } \frac{1}{x}\right)$$

et en remarquant que les fonctions de Bloch peuvent s'écrire

$$\varphi_n(\boldsymbol{k},\boldsymbol{r}) = u_n(\boldsymbol{r}, -i\boldsymbol{\nabla})\exp(i\boldsymbol{k}\boldsymbol{r}) \tag{3.5}$$

où $u_n(\boldsymbol{r}, -i\boldsymbol{\nabla})$ est l'opérateur obtenu en remplaçant dans la partie périodique de la fonction de Bloch $u_n(\boldsymbol{r},\boldsymbol{k})$, $\boldsymbol{k}$ par l'opérateur $-i\boldsymbol{\nabla}$ qui n'agit que sur la fonction située à droite de u, on trouve :

$$G^+(\boldsymbol{r},\boldsymbol{r}',E) = \frac{1}{2\pi^2}\sum_n u(\boldsymbol{r} - i\boldsymbol{\nabla})u_n^*(\boldsymbol{r}', -i\boldsymbol{\nabla}')$$

$$\times \int' \mathrm{d}E' \left\{\frac{\mathscr{P}}{E'-E} + \pi i\delta(E'-E)\right\}$$

$$\times \int_{S_n(E')}' \frac{\exp[i\boldsymbol{k}(\boldsymbol{r}-\boldsymbol{r}')]}{|\nabla_{\boldsymbol{k}}E|}\, \mathrm{d}S_{\boldsymbol{k}}. \tag{3.6}$$

Dans cette expression on a séparé l'intégration dans l'espace réciproque en intégration sur les surfaces d'énergie constante E',$S_n(E')$ et sur les énergies.

On doit évaluer l'intégrale

$$I_n(E,\boldsymbol{r}) = \int_{S_n(E)} \frac{\exp(i\boldsymbol{k}\boldsymbol{r})}{|\nabla_{\boldsymbol{k}}E|}\, \mathrm{d}S_{\boldsymbol{k}}. \tag{3.7}$$

Si on se limite à la recherche de la forme asymptotique de $\psi^+(\boldsymbol{k},\boldsymbol{r})$, seule une connaissance de la forme asymptotique de $I_n(E,\boldsymbol{r})$ est nécessaire. En effet dans ce cas puisque le potentiel perturbateur est localisé, les seuls points donnant une contribution non nulle dans (3.6) à $I_n(E,\boldsymbol{r}-\boldsymbol{r}')$ sont tels que $|\boldsymbol{r}| \gg |\boldsymbol{r}'|$.

On évalue dans l'Appendice B par la méthode de la phase stationnaire l'intégrale (3.7) dans le cas particulier du modèle choisi au paragraphe II. 2. La Fig. 1(c) précise la géométrie du problème ; deux demi-cylindres i de longueur moyenne $l \simeq \frac{2\pi}{a}$ (a est le côté du cube à faces centrées du nickel), de rayon $\mathscr{R}$ sont symétriques par rapport au centre 0 de la première zone de Brillouin ; leurs axes sont parallèles à $\boldsymbol{k}_i$ (k_x k_y ou k_z) ; π_i est le plan perpendiculaire à $\boldsymbol{k}_i$ passant par 0. Le point d'observation $\boldsymbol{r}$ est repéré par rapport aux deux demi cylindres i par ses projections ρ_i et z_i respectivement sur le plan π_i et l'axe $\boldsymbol{k}_i$.

Les résultats du calcul donnent pour la contribution de la bande d

$$I(E,\boldsymbol{r}) \underset{r\to\infty}{\sim} \frac{4}{A}\sum_i \frac{\sin\frac{l}{2}z_i}{z_i}\, \frac{\cos(\boldsymbol{k}_i(E,\boldsymbol{r})\cdot\boldsymbol{r} - \pi/4)}{\sqrt{\rho_i}} \tag{3.8}$$

Les points de l'espace réciproque $k_i(E,\boldsymbol{r})$ qui interviennent dans (3.8) sont déterminés par la relation :

$$\nabla_{\boldsymbol{k}_i}E = \lambda_i\boldsymbol{\rho}_i \quad \text{avec } \lambda_i < 0 \tag{3.9a}$$

d'après la forme particulière de la surface de Fermi

$$\boldsymbol{k}_i(E,r) = \boldsymbol{k}_{0i} + \mathscr{R}\hat{\rho}_i \tag{3.9b}$$

$\boldsymbol{k}_{0i}$ déterminé par cette dernière relation joint O au centre d'un carré limite de zone de Brillouin ; on a posé en outre $\boldsymbol{p}_i = |\boldsymbol{p}_i|\hat{p}_i$.

On évalue alors séparément partie réelle et partie imaginaire de la fonction de Green ; l'intégration en énergie de la partie imaginaire de (3.6) est immédiate ; pour la partie réelle, on remarque que les contributions importantes proviennent de $E' \simeq E$; on étend alors l'intégration jusqu'à l'infini et en développant la phase au voisinage de l'énergie E, on trouve facilement la valeur de l'intégrale correspondante ; on obtient :

$$G^+(\boldsymbol{r},\boldsymbol{r}',E) \underset{r\to\infty}{\sim} \sum_i u_i(\boldsymbol{r},-i\boldsymbol{\nabla})\left\{\frac{2}{A}\sqrt{\left(\frac{2}{\pi\mathscr{R}\rho_i}\right)}\right.$$

$$\left.\times\frac{\sin\frac{l}{2}z_i}{z_i}\exp\left[i\left(\boldsymbol{k}_i\boldsymbol{r}-\frac{\pi}{4}\right)\right]\varphi^*(\boldsymbol{k}_i,\boldsymbol{r})\right\} \tag{3.10}$$

On a remplacé dans cette formule $\boldsymbol{k}_i(E,\boldsymbol{r})$ par $\boldsymbol{k}_i$. On utilise la forme particulière des fonctions de liaisons fortes (2.4) et grâce à la localisation des fonctions atomiques $\phi_i(\boldsymbol{r})$, on obtient finalement, si $\boldsymbol{r}$ appartient à la cellule C_λ centrée sur le site λ tel que $|R_\lambda| \gg a$:

$$G^+(\boldsymbol{r},\boldsymbol{r}',E) \simeq \frac{2}{A}\sqrt{\left(\frac{2}{\pi\mathscr{R}\rho_{\lambda i}}\right)}\frac{\sin\frac{l}{2}z_{\lambda i}}{z_{\lambda i}}\exp(i\pi/4)$$

$$\times\ \varphi_i(\boldsymbol{k}_i,\boldsymbol{r})\,\varphi_i^*(\boldsymbol{k}_i,\boldsymbol{r}). \tag{3.11}$$

$\rho_{\lambda i}$ et $z_{\lambda i}$ sont respectivement les projections de R_λ sur π_i et $\boldsymbol{k}_i$.

A l'aide des formules (3.1) et (3.11), pour $\boldsymbol{r}$ appartenant à C_λ, l'onde diffusée a la forme asymptotique suivante :

$$\psi^+(\boldsymbol{k},\boldsymbol{r}) \simeq \varphi_i(\boldsymbol{k},\boldsymbol{r}) + \sum_j \frac{a_j(R_\lambda)}{|R_\lambda|^{3/2}} f_{ij}^+(\boldsymbol{k},\boldsymbol{k}_j)\varphi(\boldsymbol{k}_j,\boldsymbol{r}). \tag{3.12}$$

L'amplitude de diffusion vers l'avant est définie de manière habituelle :

$$f_{ij}^+(\boldsymbol{k},\boldsymbol{k}_j) = -\frac{1}{2\pi}\langle\varphi_j(\boldsymbol{k}_j)|V_P|\psi_i^+(\boldsymbol{k})\rangle. \tag{3.13}$$

La grandeur $a_i(\boldsymbol{r})$ est donnée par la formule

$$a_i(\boldsymbol{r}) = r^{3/2}\left\{\frac{l}{A}\sqrt{\left(\frac{1}{2\pi\mathscr{R}}\right)}\frac{\sin\frac{l}{2}z_i}{z_i}\frac{\exp(i\pi/4)}{\sqrt{(\rho_i)}}\right\} \tag{3.14}$$

Elle est liée à $I(E,\boldsymbol{r})$ par la relation

$$I(E,r) = \frac{2\pi}{i}\sum_i\left(\frac{a_i(\boldsymbol{r})}{r^{3/2}}\exp(i\boldsymbol{k}_i\boldsymbol{r}) - CC\right) \tag{3.15}$$

Par un calcul très simple et en tous points analogue à celui de BLANDIN[3] on déduit de (3.12) la variation de densité électronique $\Delta\rho(\boldsymbol{r})$ pour une direction de spin déterminée et intégrée sur toute la bande

$$\Delta\rho(\boldsymbol{r}) = \frac{1}{8\pi^3}\int\Delta\rho_{\boldsymbol{k}}(\boldsymbol{r})\,\mathrm{d}\boldsymbol{k} \text{ avec } \Delta\rho_{\boldsymbol{k}}(\boldsymbol{r})$$

$$= |\psi^+(\boldsymbol{k},\boldsymbol{r})|^2 - |\varphi(\boldsymbol{k},\boldsymbol{r})|^2. \tag{3.16}$$

L'intégration est étendue sur tous les états occupés.

On effectue l'intégration de manière identique à celle de la Réf. 3; rappelons en les étapes. On sépare l'intégration dans le volume en intégration à énergie constante d'abord, puis sur les énergies. L'intégration à énergie constante s'évalue simplement à l'aide de $I(E,\boldsymbol{r})$ en notant que

$$\int\varphi(\boldsymbol{k},\boldsymbol{r})f^+(\boldsymbol{k},\boldsymbol{k}_i)\frac{\mathrm{d}S_{\boldsymbol{k}}}{|\nabla_{\boldsymbol{k}}E|}$$

$$= u(\boldsymbol{r},-i\boldsymbol{\nabla})f^+(-i\boldsymbol{\nabla},\boldsymbol{k}_i)I(E,\boldsymbol{r})$$

et à l'aide de la relation (cf [4] Appendice B)

$$\int f^{+*}(\boldsymbol{k},\boldsymbol{k}_i)f^+(\boldsymbol{k},\boldsymbol{k}_j)\frac{\mathrm{d}S_{\boldsymbol{k}}}{|\nabla_{\boldsymbol{k}}E|}$$

$$= \frac{2\pi}{i}[f^+(\boldsymbol{k},\boldsymbol{k}_j) - f^+(+\boldsymbol{k}_j,\boldsymbol{k}_i)].$$

On obtient

$$\int\Delta\rho_{\boldsymbol{k}}(\boldsymbol{r})\frac{\mathrm{d}S_{\boldsymbol{k}}}{|\nabla_{\boldsymbol{k}}E|} = \frac{1}{4\pi^2 ir^2}$$

$$\times\left\{\sum_{i,j}a_ia_j\varphi(\boldsymbol{k}_j,\boldsymbol{r})\varphi(\boldsymbol{k}_j,\boldsymbol{r})f^+(-\boldsymbol{k}_j,\boldsymbol{k}_i) - CC\right\}$$

Pour évaluer $\Delta\rho(\boldsymbol{r})$, on intègre sur les énergies par parties en ne gardant que le terme prépondérant à grande distance, on obtient alors si $\boldsymbol{r}$ appartient à C_λ telle que $|R_\lambda| \gg a$

$$\Delta\rho(\boldsymbol{r}) \simeq -\frac{1}{4\pi^2 R_\lambda{}^3} \sum_{ij} \frac{a_i(R_\lambda)\, a_j(R_\lambda)}{\dfrac{\rho_{\lambda i}}{|\nabla_{\boldsymbol{k}} E|_i} + \dfrac{\rho_{\lambda i}}{|\nabla_{\boldsymbol{k}} E|_j}}$$

$$\times \varphi_i(\boldsymbol{k}_i,\boldsymbol{r})\varphi_j(\boldsymbol{k}_j,\boldsymbol{r}) f_{ij}^{+}(-\boldsymbol{k}_j,\boldsymbol{k}_i) + CC \qquad (3.17)$$

où CC désigne la partie conjuguée.

$\Delta\rho(\boldsymbol{r})$ dépend de deux facteurs qui traduisent les faits nouveaux introduits par le potentiel de réseau.

(1) *un facteur géométrique* caractérisé par $\boldsymbol{k}_i(E,\boldsymbol{r})$ et par $a_i(\boldsymbol{r})$; il dépend de la forme des familles de surfaces d'énergie constante au voisinage du niveau de Fermi ; il détermine dans une grande partie la dépendance spatiale de $\Delta\rho(\boldsymbol{r})$.

(2) un facteur dépendant de façon complexe des fonctions de Bloch. Comme dans le cas général il y a superposition de différentes ondes électroniques ; notamment il existe des termes d'interférence $\langle ij \rangle$ entre les différentes portions de la surface de Fermi. Mais on verra que la forme particulière des facteurs (1) et (2) fait que ces termes n'existent qu'entre cylindres d'axes parallèles et ne sont pas du tout gênants, cette simplification considérable permet de poursuivre les calculs jusqu'au bout.

III. 3. *Distribution de densité electronique : facteur géométrique*

Chacun des temps $a_i(\boldsymbol{r})$ s'écrit d'après (3.14)

$$\frac{a_i}{r^{3/2}} = \exp(i\pi/4)\,\frac{2}{A}\,\frac{1}{\sqrt{(2\pi\mathscr{R})}}\,\frac{1}{\sqrt{(\rho_i)}}\,\frac{\sin \dfrac{l}{2} z_i}{z_i}$$

Pour une direction $\varphi_i \neq 0$ donnée, la fonction $\dfrac{a_i}{r^{3/2}}$ tend vers zéro comme $\rho_i^{-1/2}$ puisque

$$\lim_{z_i \to \infty} \frac{\sin \dfrac{l}{2} z_i}{z_i} = \frac{2\pi}{l}\,\delta(\rho_i \operatorname{tg} \varphi_i) = \frac{2\pi}{l\rho_i}\,\delta(\operatorname{tg} \varphi_i) \qquad (3.18)$$

Au contraire, pour une direction du plan π_i, $\varphi_i = 0$ et $\dfrac{a_i}{r^{3/2}}$ tend vers zéro comme $\rho_i^{-1/2} = r^{-1/2}$ seulement.

Ceci explique pourquoi, lorsqu'on appliquait brutalement les formules de Roth Blandin, on obtenait une forme asymptotique de la variation de densité strictement localisée dans chacun des plans π_i et de la valeur infinie.

On applique maintenant ces formules pour $\rho_i \gg a$ mais fini.

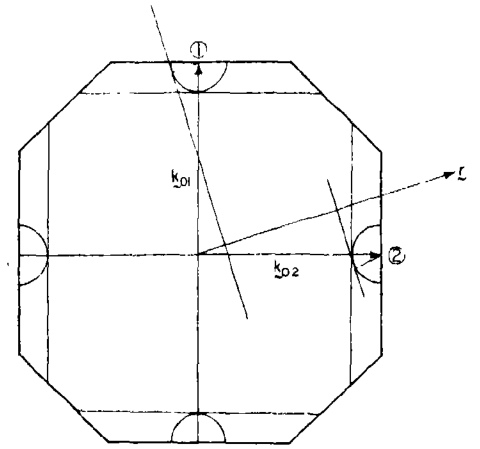

FIG. 2. Interférences entre cylindres d'axes parallèles.

La fonction $\dfrac{a_i(r)}{r^{3/2}}$ est localisée au voisinage du plan π_i ; on a un ordre de grandeur de cette localization en notant que la largeur de la première oscillation de la fonction $\dfrac{\sin l/2\, z_i}{z_i}$ est :

$$2\Delta z_i = \frac{4\pi}{l}. \qquad (3.19)$$

Dans le cas particulier présent

$$l \simeq \frac{2\pi}{a} \text{ et}$$

$$\Delta z_i \simeq a. \qquad (3.20)$$

On distingue deux sortes de termes $\Delta\rho_{ij}(\boldsymbol{r})$

(a) *$\boldsymbol{k}_i$ et $\boldsymbol{k}_j$ correspondent à des cylindres d'axes parallèles.* On a alors $z_i = z_j$, $\rho_i = \rho_j$ et $a_i(\boldsymbol{r})$

$= a_j(\boldsymbol{r})$ (Fig. 1c). Le facteur géométrique qui intervient directement dans $\Delta\rho_{ij}(\boldsymbol{r})$ se réduit à :

$$\frac{a_i a_j}{r^3} = \frac{a_i^2}{r^3} = i\,\frac{l^2}{2\pi A^2 \mathcal{R}}\,\frac{1}{\rho_i}\,\frac{\sin^2 \frac{l}{2} z_i}{z_i^2} \qquad (3.21)$$

Il a une valeur non négligeable seulement au voisinage du plan π_i. Dans la suite *on négligera l'effet des "franges"* de densité électronique correspondant aux oscillations de la fonction $\frac{\sin^2 l/2\, z_i}{z^2}$ et on supposera, d'après (3.21), que seuls les plans réticulaires (100), (010) et (001) sont atteints par une perturbation non nulle à grande distance de l'impureté.*

Le facteur géométrique prend une valeur indépendente du plan π_i quand $\boldsymbol{r}$ appartient à ce plan, comme l'imposent d'ailleurs des raisons de symétrie, il vaut alors :

$$\frac{a^2}{r^3} = \frac{i}{r}\,\frac{l^2}{2\pi A^2 \mathcal{R}}. \qquad (3.22)$$

(b) *k_i et k_j correspondent à des cylindres d'axes non parallèles* ($\pi_i \not\equiv \pi_j$). Le facteur géométrique est nul à grande distance de l'origine ; en effet, φ_i et φ_j ne peuvent être tous deux voisins de zéro que près de la cellule centrale. On verra de plus, dans le paragraphe suivant, que l'amplitude de diffusion $f_{ij}^{+}(\boldsymbol{k}_j,\boldsymbol{k}_i)$, correspondant à deux états $\boldsymbol{k}_i$ et $\boldsymbol{k}_j$ pris sur deux cylindres d'axes non parallèles est nulle pourvu qu'on se limite à l'approximation de Born. *Dans notre modèle, il n'y a donc pas de couplage entre les cylindres d'axes non parallèles.*

III. 4. *Amplitude de diffusion*

III. 4a. Dans le développement (3.18), interviennent les termes $f^+(-\boldsymbol{k}_j,\boldsymbol{k}_i)$. On les évalue dans les approximations suivantes :

— approximation de Born ;

— approximation du potentiel localisé ; le potentiel perturbateur est supposé ne pas déborder de la cellule atomique où se trouve l'impureté.

— On choisit comme fonctions d'onde les fonctions approchées (2.4).

On distingue, comme dans le paragraphe précédent, les cas (a) et (b)

(a) $\boldsymbol{k}_i$ et $\boldsymbol{k}_j$ *correspondent à ces cylindres d'axes parallèles* ($\pi_i \equiv \pi_j$). Les fonctions d'onde (2.4) font intervenir une seule et même orbitale atome $\phi_n(\boldsymbol{r})$ (Fig. 1c).

$$f^+(-\boldsymbol{k}_j,\boldsymbol{k}_i) = -\frac{1}{2\pi N}\sum_{\alpha\beta}\exp(-i\boldsymbol{k}_i\boldsymbol{R}_\alpha) \times \exp(-i\boldsymbol{k}_j\boldsymbol{R}_\beta)\, V_{\alpha\beta}^{(n)} \qquad (3.23)$$

où on a posé :

$$V_{\alpha\beta}^{(n)} = \langle\phi_{n\alpha}|V|\phi_{n\beta}\rangle. \qquad (3.24)$$

On ne conserve de tous ces termes en accord avec l'approximation des liaisons fortes que ceux correspondant à

$$\alpha = \beta = 0 \quad \text{et}\ \alpha = 0 \quad \beta \neq 0$$

$$f^+(-\boldsymbol{k}_j,\boldsymbol{k}_i) = -\frac{1}{2\pi N}\, V_{00}^{(n)} + \alpha(\boldsymbol{k}_i,\boldsymbol{k}_j). \qquad (3.25)$$

Le premier terme est indépendant de $\boldsymbol{k}$; le second n'intervient que pour faire varier sinusoïdalement $f^+(-\boldsymbol{k}_j,\boldsymbol{k}_i)$ autour de la moyenne $V_{00}^{(n)}$.

D'après les approximations précitées, *on négligera $\alpha(\boldsymbol{k}_i,\boldsymbol{k}_j)$ devant $V_{00}^{(n)}$.* Si on suppose, de plus, que le potentiel V a une symétrie sphérique, tous les termes d'amplitude de diffusion sont égaux :

$$V_{00}^{(3)} = V_{00}^{(2)} = V_{00}^{(1)} = V_0$$

et

$$f^+(-\boldsymbol{k}_j,\boldsymbol{k}_i) = -\frac{1}{2\pi N}\, V_0. \qquad (3.26)$$

(b) $\boldsymbol{k}_i$ et $\boldsymbol{k}_j$ *correspondent à des cylindres d'axes non parallèles* ($\pi_i \not\equiv \pi_j$). On peut refaire les mêmes calculs ; on obtient des expressions analogues à (3.24) mais où interviennent des éléments de matrice du potentiel perturbateur.

$$V_{\alpha\beta}^{(mn)} = \langle\phi_{m\alpha}|V|\phi_{n\beta}\rangle \quad m \neq n \qquad (3.27)$$

Dans les approximations faites précédemment *les termes correspondant á $\pi_i \neq \pi_j$ sont négligeables par rapport aux termes $\pi_i \equiv \pi_j$.*

---

* Notons que la valeur de $a_i(\boldsymbol{r})$ n'est pas encore négligeable sur les sites plus proches voisins du plan π_i ; néanmoins on verra que dans ce cas la contribution à la densité électronique est nulle par suite de la forme particulière des fonctions $\varphi(\boldsymbol{k}_i,\boldsymbol{r})$ (cf. Appendice D).

III. 4b. **On peut déterminer la profondeur moyenne du potentiel diffuseur à l'aide de la règle de somme de Friedel.** Puisque nous avons calculé l'amplitude de diffusion dans l'approximation de Born, il suffit d'écrire cette relation au premier ordre en perturbation (approximation des bandes rigides).

Elle s'écrit :

$$Z = n(E_F)f \quad \text{où} \tag{3.28}$$

$$f = \int \varphi^*(\boldsymbol{k},\boldsymbol{r})V_P(\boldsymbol{r})\varphi(\boldsymbol{k},\boldsymbol{r})\,\mathrm{d}\boldsymbol{r} \tag{3.29}$$

et où $n(E_F)$ est la densité d'états au niveau de Fermi par unité d'énergie et de volume et Z la charge déplacée. La densité d'états est donnée par le modèle choisi.

En assimilant le puits de potentiel à un puits carré, on obtient une valeur de l'amplitude de diffusion en fonction de la charge déplacée qu'on utilisera dans le paragraphe III. 4.

III. 5. *Forme définitive de la variation de densité électronique introduite par une impureté dans le nickel*

La forme asymptotique de la variation de densité électronique est donc, si on néglige les "franges", nulle en dehors des cellules de Wigner centrées sur les plans π_n.

Dans une cellule centrée sur le site λ du plan π_n la seule contribution des cylindres d'axes parallèles à k_n n'est pas nulle. D'après (3.17), (3.22) et (3.26) on a alors :

$$\Delta\rho(\boldsymbol{r}) = \frac{i}{32\pi^4}\frac{l^2}{A}\;V_0\Omega\,\frac{A_n(R_\lambda)}{R_\lambda{}^2} \tag{3.30}$$

$A_n(\boldsymbol{r})$ est dans cette formule somme de fonctions oscillantes de (3.17) correspondant aux cylindres d'axes parallèles à $\boldsymbol{k}_n$.

$$A_n(\boldsymbol{r}) = \sum_{ij}{}' \{\varphi_n(\boldsymbol{k}_i,\boldsymbol{r})\varphi_n(\boldsymbol{k}_j,\boldsymbol{r}) - CC\}. \tag{3.31}$$

Rappelons que dans cette formule $k_i(E,\boldsymbol{r})$ sont définis par (3.9).

Un calcul très simple reproduit dans l'Appendice D.1 montre que

$$\text{(D.4)}\quad A_n(\boldsymbol{r}) = 8i\Omega\phi^2_{n\lambda}(\boldsymbol{r})\sin 2\mathscr{R}\hat{\rho}_n\cdot\boldsymbol{R}_\lambda$$

où $\hat{\rho}_n$ est le vecteur unitaire de $\boldsymbol{\rho}_n$.

On obtient pour la valeur de la densité électronique l'expression très simple :

$$\Delta\rho(\boldsymbol{r}) = \mu\,\frac{\sin 2\mathscr{R}R_\lambda}{R^2_\lambda}\,\phi^2_{n\lambda}(\boldsymbol{r}). \tag{3.32}$$

μ est un coefficient entièrement calculable :

$$\mu = -\frac{1}{4\pi^4}\frac{l^2\Omega^2}{A}\,V_0 \tag{3.33}$$

Rappelons que l est la longueur moyenne des cylindres, A la constante de dispersion (2–1), Ω le volume atomique et V_0 l'élément de matrice du potentiel entre les fonctions atomiques (3.26).

Les oscillations de densité dans le nickel sont fortement *anisotropes* ; elles sont localisées dans certains des plans réticulaires (100) (010) et (001) passant par l'impureté. L'amplitude des oscillations de densité dans ces plans décroît avec la distance r comme r^{-2}. Le nombre d'ondes des oscillations est $2\mathscr{R}$ où $\mathscr{R}$ est le rayon des cylindres décrivant la surface de Fermi.

Les résultats obtenus ne sont étonnants ; puisque nous avons fait un développement jusqu'au 2e ordre de la loi de dispersion à partir du haut de la bande nous sommes dans l'approximation des masses effectives ; semi-classiquement, on a donc un gaz de trous dont une des masses effectives est infinie, avec un nombre d'ondes de Fermi $\mathscr{R}$. La perturbation ne s'étend donc qu'au voisinage des plans π_i sur une distance égale à la portée du potentiel ; puisqu'on a supposé que le potentiel localisé ne débordait pas la cellule atomique de l'impureté, il est naturel que les seules cellules atteintes par la perturbation soient les cellules centrées sur π_n.

L'effet du caractère ondulatoire se traduit seulement par :

(a) les "franges" de densité électronique du paragraphe III. 3 que l'on a ici négligées.

(b) les termes d'interférence entre cylindres d'axes parallèles.

Ce calcul ne donne un résultat aussi simple que parce que l'on peut traiter à grande distance de manière *indépendante* les cylindres dont les axes ne sont pas parallèles.

IV. DIFFUSION MAGNETIQUE DES NEUTRONS PAR UN ALLIAGE A BASE DE NICKEL ; INFLUENCE DES OSCILLATIONS A GRANDE DISTANCE D'UNE IMPURETE SUR LA DIFFUSION DES NEUTRONS

IV. 1. *Introduction*

La diffusion des neutrons par un alliage ferromagnétique résulte du couplage des neutrons, d'une part avec les noyaux (diffusion nucléaire), d'autre part avec les électrons (diffusion magnétique). On considère habituellement les électrons de l'alliage comme *localisés* sur les orbitales atomiques des constituants (modèle de Heisenberg). Dans ce cas, la dépendance par rapport au vecteur de diffusion $\boldsymbol{s}$ de l'intensité de désordre magnétique est identique à celle del'intensité de désordre nucléaire ; la section efficace de diffusion s'écrit dans le cas d'un alliage complètement désordonné :

$$\frac{\mathrm{d}\sigma}{\mathrm{d}\Omega}(s) = \alpha C_A C_B (f_A(s) - f_B(s))^2 \qquad (4.1)$$

(formule de Von Laüe (7))

où C_A, C_B, f_A, f_B sont respectivement les concentrations et facteurs de forme du métal de base A et de l'impureté dissoute B ; α est une constante.

Dans le cas présent d'un alliage à base de nickel, les électrons d sont à la base de la diffusion magnétique ; ils ne sont plus localisés sur chaque atome mais répartis sur chacune des orbitales (2.4). Chaque impureté introduit des oscillations de charge à grande distance, donc de spin, puisque dans le nickel ferromagnétique une bande est pleine ; les neutrons sont sensibles à ces oscillations de spin.

Le caractère délocalisé des électrons d (métal) entraîne ainsi qu'on le montre dans le paragraphe IV. 2 l'existence d'une singularité dans la section efficace de diffusion magnétique ; ainsi aux effets éventuels de l'ordre sur le facteur de structure se superpose une singularité purement électronique ; la dépendance de $\mathrm{d}\sigma/\mathrm{d}\Omega(\boldsymbol{s})$ par rapport à $\boldsymbol{s}$ n'est pas la même selon que l'on considère la diffusion magnétique et la diffusion nucléaire. Dans le paragraphe IV. 3 un calcul grossier permet de prévoir le type de singularité obtenu et dans le paragraphe IV. 4 on discute rapidement les résultats expérimentaux de Shull et Lowde.

IV. 2. *Singularité de la section de diffusion d'origine électronique*

La diffusion magnétique de désordre prend son origine dans la répartition électronique, autour de chaque impureté B située au site $\boldsymbol{R}_\lambda$, $\Delta\rho(\boldsymbol{r}-\boldsymbol{R}_\lambda)$. Dans un alliage *dilué* chaque impureté diffuse indépendamment et si le désordre est parfait une formule analogue à la formule de Laüe (4.1) est valable

$$\frac{\mathrm{d}\sigma}{\mathrm{d}\Omega}(s) = \alpha C_A C_B |\widetilde{\Delta\rho}(s)|^2. \qquad (4.2)$$

Dans cette formule et dans la suite le signe ~ signifie la transformée de Fourier définie comme étant:

$$\tilde{f}(s) = \int f(s) \exp(-i\boldsymbol{s}\boldsymbol{r})\, \mathrm{d}\boldsymbol{r}; \qquad (4.3)$$

l'intégrale est étendue sur tout le cristal.

Dans le cas de la diffusion de neutrons incidents non polarisés par un échantillon d'alliage ferromagnétique sans aimantation macroscopique, on peut calculer le coefficient α [8]

$$\alpha = \tfrac{2}{3}(\gamma r_0)^2 S^2$$

γ est le moment magnétique du neutron ($\gamma = 1{,}91$), r_0 est le rayon électronique classique et S le spin électronique.

Les oscillations à grande distance de la variation de densité électronique introduite par une impureté, conséquence du caractère métallique de la matrice, ont un nombre d'ondes voisin de $2k_F$, où $2k_F$ est une dimension caractéristique de la surface de Fermi; on s'attend donc à ce que sa transformée de Fourier présente un point singulier plus ou moins marqué pour $|\boldsymbol{s}| \simeq 2k_F$. Cette remarque est générale et entraîne d'apres (4.2) une singularité dans la section de diffusion magnétique. Dans l'appendice C, on donne les résultats obtenus dans le cas des électrons libres ; on pourrait déceler un tel effet dans les alliages du type Cu–Mn.

Cet effet n'est d'ailleurs qu'un des multiples aspects découlant d'une densité d'états non nulle au niveau de Fermi (effet Kohn ; singularité dans le spectre des ondes de spin. . .).

Dans le cas où les électrons ne sont pas libres, le calcul de $\widetilde{\Delta\rho}(s)$ est difficile parce qu'en général on ne connaît que la forme asymptotique de $\Delta\rho(\boldsymbol{r})$, on la notera dans la suite $\Delta\rho^\infty(\boldsymbol{r})$.

Pour le nickel, la formule (3.32) laisse prévoir une singularité pour $|s| \simeq 2\mathscr{R}$. Le rayon $\mathscr{R}$ pour le nickel ferromagnétique est calculé dans notre modèle de sorte qu'il y ait 0,5 magnéton de Bohr par atome. On trouve $\mathscr{R} = 0{,}7\,\pi/a$; l'angle de diffusion auquel il y aurait une singularité est donc $2\,\theta \simeq 13^\circ$ pour une longueur d'onde neutronique $\lambda = 1{,}1$ Å. On essaye dans la suite de calculer le type de singularité obtenu.

IV. 3. *Allure de la singularité obtenue dans des alliages à base de nickel*

On sépare $\Delta\rho(\boldsymbol{r}$ en deux parties .

$$\Delta\rho(\boldsymbol{r}) = \Delta\rho^{\infty}(\boldsymbol{r}) + \Delta\rho^{0}(\boldsymbol{r}) \qquad (4.4)$$

$\Delta\rho^{0}(\boldsymbol{r})$ décrit l'écart de $\Delta\rho(\boldsymbol{r})$ par rapport à sa forme asymptotique ; la fonction $\Delta\rho^{0}(\boldsymbol{r})$ est essentiellement localisée dans la cellule atomique de l'impureté ; son allure spatiale est donnée par la répartition électronique atomique correspondante.

La transformée de Fourier de $\Delta\rho^{0}(\boldsymbol{r})$ sera une fonction monotone décroissante du type généralement obtenu;(4, 5) elle aura des valeurs non négligeables pour :

$$|s| \lesssim \frac{2\pi}{r_s}$$

où r_s est le rayon de la sphère atomique.

$\widetilde{\Delta\rho}(\boldsymbol{s})$ est alors somme de termes de comportements différents :

(1) $\widetilde{\Delta\rho^{0}}(\boldsymbol{s})$ fonction monotone décroissante,

(2) $\widetilde{\Delta\rho^{\infty}}(\boldsymbol{s})$ fonction présentant une singularité pour $|s| = 2\mathscr{R}$.

$\Delta\rho^{\infty}(\boldsymbol{r})$ ne prenant des valeurs appréciables que dans les cellules centrées sur les plans π_n et en utilisant la formule (3.32), on trouve facilement $\Delta\rho^{\infty}(\boldsymbol{s})$ comme somme de trois termes correspondant aux contributions des trois plans π_n.

$$\Delta\rho^{\infty}(\boldsymbol{s}) = \sum_{n} f_n(\boldsymbol{s}) g_n(\boldsymbol{s}). \qquad (4.5)$$

Dans cette formule, on définit

$$f_n(\boldsymbol{s}) = \int \phi_n^2(\boldsymbol{r}) \exp -(i\boldsymbol{s}\boldsymbol{r})\, \mathrm{d}\boldsymbol{r} \qquad (4.6)$$

$$g_n(\boldsymbol{s}) = \mu \sum_{\lambda}^{n} \frac{\sin 2\mathscr{R} R_\lambda}{R_\lambda^2} \cos \boldsymbol{s}\boldsymbol{R}_\lambda. \qquad (4.7)$$

La somme $\sum\limits_{\lambda}^{n}$ est la somme sur tous les sites $\boldsymbol{R}_\lambda$ du plan π_n hormis le site central. $f_n(\boldsymbol{s})$ est le facteur de structure de l'orbitale n ; dans $g_n(\boldsymbol{s})$ est contenue toute l'information relative aux oscillations de densité électronique ; ce sont ces fonctions $g_n(s)$ ($n = 1,2,3$) qui ont une singularité au voisinage de $|s| = 2\mathscr{R}$. On détermine la contribution de la cellule centrale de la manière suivante :

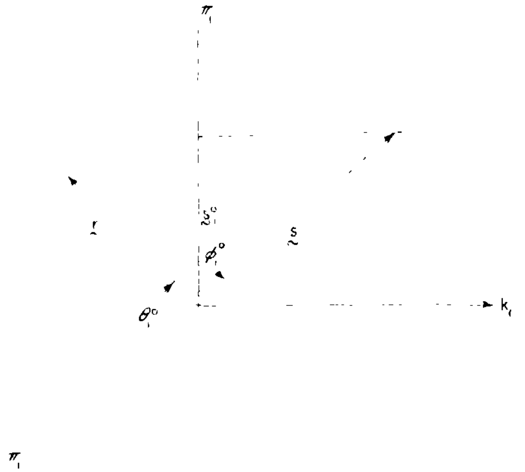

FIG. 3.

(a) On suppose que les électrons dans la cellule centrale sont répartis sur des orbitales atomiques. $\phi_n(\boldsymbol{r})$; on suppose de plus que les trois orbitales d sont également occupées, ce qui, dans l'hypothèse d'un potentiel perturbateur $V_P(\boldsymbol{r})$ à symétrie sphérique est évident par raison de symétrie.

(b) On détermine la densité dans la première cellule par la condition que la charge totale déplacée dans la bande *d* soit égale au supplément de charge nucléaire Z introduit par l'impureté

$$Z = \int \Delta\rho(\boldsymbol{r})\, \mathrm{d}\boldsymbol{r} = \widetilde{\Delta\rho}(0) = \widetilde{\Delta\rho^{\infty}}(0) + \widetilde{\Delta\rho^{0}}(0). \quad (4.8)$$

On peut déterminer entièrement le coefficient μ dans l'hypothèse où le potentiel diffuseur est une perturbation d'après la remarque du paragraphe III. 4b.

Pour que le problème soit entièrement résolu, il suffit donc de calculer $\widetilde{\Delta\rho}^{\infty}(s)$; on alors :

$$\Delta\rho(s) = \sum_{n} f_n(s)\left[\frac{\widetilde{\Delta\rho}^0(0)}{3}+g_n(s)\right] \qquad (4.9)$$

Dans cet article, nous donnons seulement une approximation *très grossière* de $\Delta\rho^{\infty}(s)$; on ne cherche pas à donner de manière précise la forme de la courbe de diffusion mais seulement à *prévoir le type de discontinuité* que peut engendrer la considération d'orbitales moléculaires.

On trouvera dans l'Appendice D.2 les calculs et les approximations faites ; on repère le vecteur s par rapport aux plans π_n par les angles φ_n et θ_n^0(Fig. 3)

$$sr = s_n^0 r \sin\theta_n^0 \quad s_n^0 = |s|\cos\phi_n^0. \qquad (4.10)$$

On trouve alors :

$$f_n(s)g_n(s) \simeq \frac{4\pi\mu}{a^2}\times \begin{matrix} \dfrac{\pi}{2}\ \text{si}\ s_n^0 < 2\mathscr{R} \\ \text{Arc}\sin\dfrac{2\mathscr{R}}{s_n^0}\ \text{si}\ s_n^0 \geqslant 2\mathscr{R} \end{matrix} \qquad (4.11)$$

La courbe représentant cette fonction a une singularité pour $s_n^0 \simeq 2\mathscr{R}$ (Fig. 4a).

En calculant la densité d'états au niveau de Fermi grace â la formule (3.29) on trouve

$$\mu = Z\frac{\Omega}{3\pi a} \qquad (4.12)$$

et

$$\widetilde{\Delta\rho}^{\infty}(0) = \frac{\pi}{2}Z \qquad \widetilde{\Delta\rho}^{0}(0) = \left(1-\frac{\pi}{2}\right)Z$$

On représente sur la Fig. 4(b) la courbe représentant $\widetilde{\Delta\rho}(s)$ dans ces approximations. Elle part de la valeur Z, croît jusqu'à la valeur de $|s| = 2\mathscr{R}$ pour laquelle elle a une *discontinuité de la tangente* $\widetilde{\Delta\rho}(s)$ est assez fortement anisotrope ; notons qu'en vertu des approximations grossières qui ont été faites l'anisotropie provient seulement de $g_n(s)$. Il faudrait ajouter une anisotropie due au facteur de structure qui est assez grande. De plus, le maximum obtenu pour $|s| = 2\mathscr{R}$ sera moins marqué si on tient compte de la décroissance de $f_n(s)$; on pourrait même avoir une coube de la forme donnée par la Fig. 4(c).

Les mêmes remarques sont valables pour $|\Delta\rho(s)|^2$; dans le cas de polycristaux pour lesquels on a fait des mesures, c'est la moyenne de $|\Delta\rho(s)|^2$ calculée pour toutes les orientations du vecteur de diffusion par rapport aux axes cristallographiques ; l'intensité ne dépend alors que du module $|s|$; la singularité est moins marquée par suite des opérations de moyenne. La Fig. 4(d) montre l'intensité diffusée due à la seule variation de densité $\Delta\rho^{\infty}(r)$:

$$\left(\frac{d\sigma^{\infty}}{d\Omega}\right)(s) = 3[|g_1(s)|^2+2\,\overline{g_1(s)g_2(s)}]$$

IV. 4. *Alliages nickel–fer ; discussion des résultats obtenus*

On applique la théorie précédente aux alliages Ni–Fe pour lesquels on a quelques résultats expérimentaux.

La diffusion magnétique des neutrons donne des courbes qui présentent des anomalies par rapport à la diffusion calculée à partir d'alliages désordonnées et dans l'hypothèse de moments localisés ; le type de courbes obtenues est donné par la Fig. 5.(5, 6, 10)

Ces écarts ont été interprétés par ces auteurs comme dû à un ordre local; et en effet l'anomalie est au voisinage des raies de surstructures pour Ni_3Fe (18°15′ et 25°55′). Cependant on obtient ce type de diagrammes non seulement pour des valeurs des concentrations voisines de Ni_3Fe mais dans tout le domaine de concentrations. De plus la région de singularité reste *indépendante de la concentration* et *indépendante du traitement thermique.* Ces faits sont difficiles à interpréter par un ordre chimique local. Récemment, Collins, Jones et Lowde(10) ont mesuré en même temps que la diffusion magnétique d'origine électronique, la diffusion nucléaire. Ils ont montré que les courbes de diffusion montraient l'existence d'un ordre local pour la composition de 30 Fe 70 ^{60}Ni et aussi, mais à un moindre degré, pour 60 Fe 40 ^{60}Ni. Dans ce dernier cas, les courbes experimentales obtenues pour la diffusion magnétique et la diffusion nucléaire montrent cependant des comportements distincts.

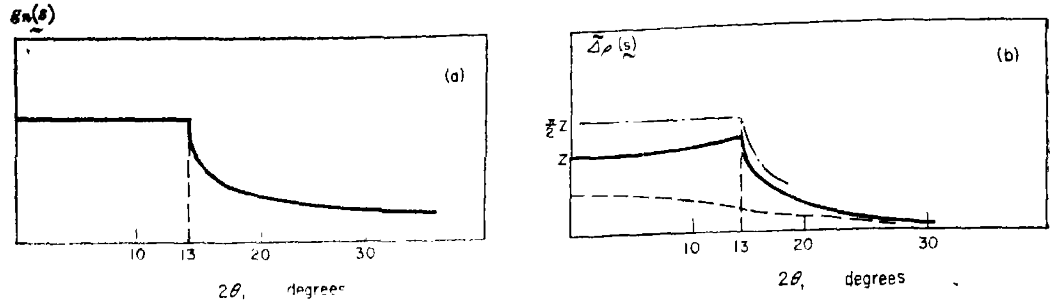

4(a). La courbe $g_n(s)$ a une singularité pour $s_n^0 = 2\mathscr{K}(2\theta = 13°)$.

4(b). Amplitude de diffusion totale dans une direction déterminée,

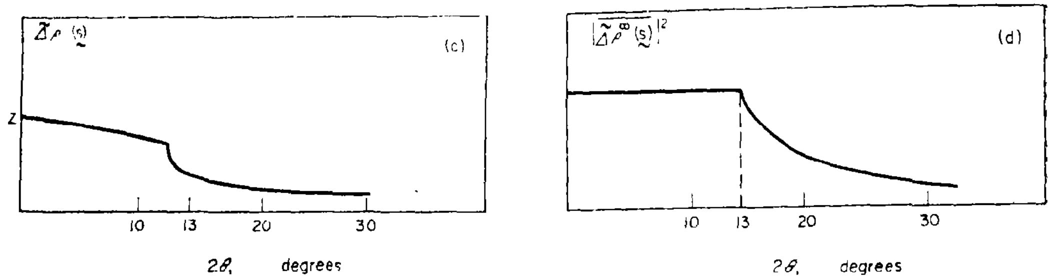

4(c). Amplitude de diffusion totale dans une direction déterminée.

4(d). Section efficace pour une poudre due à $\Delta\rho^{\infty}(r)$, La singularité est moins marquée dans une poudre.

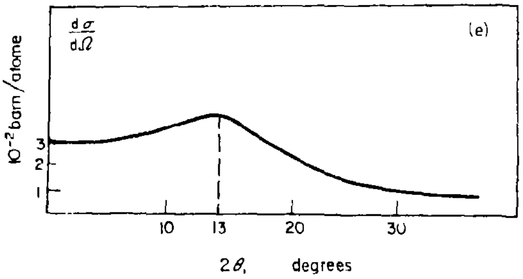

4(e). Section efficace totale prévue pour une poudre.

FIG. 4. Sections efficaces de diffusions.
———— Contribution de la variation de densité à courte distance.
—·—·— Contribution de la variation de densité à grande distance.

Un ordre local ne saurait expliquer tout le phénomène.

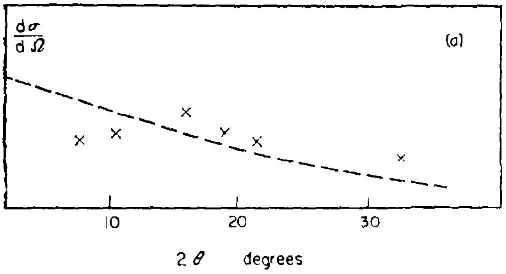

5(a). Mesures de Shull.

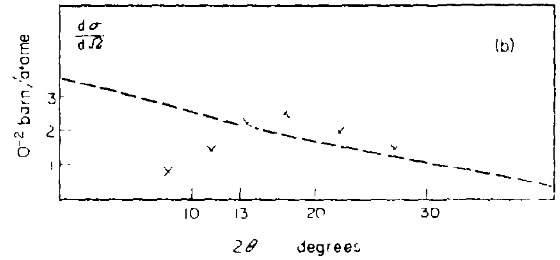

5(b). Mesures de Lowde.

FIG. 5. Mesures expérimentales de la section efficace.

Or, d'après le paragraphe précédent les oscillations de densité de spin à grande distance sont à l'origine d'une singularité dans la courbe de diffusion pour $2\theta \simeq 13°$; les mesures de Shull et Lowde situent en gros cette singularité entre 10 et 20°. Cet effet serait indépendant du traitement thermique et de la concentration pour autant qu'on néglige les interactions entre impuretés. On prévoit ainsi une courbe de diffusion qui a l'allure donnée par la Fig. 4(e). Elle diffère de la courbe expérimentale en ce qu'elle est décalée dans la région des petits angles. Ceci n'a rien d'étonnant par suite des calculs rudimentaires que l'on a faits.

Pour opter de manière indubitable en faveur de l'une ou l'autre interprétation, il est nécessaire, du point de vue expérimental, d'avoir d'autres informations sur la diffusion des neutrons aux petits angles et surtout par un *monocristal.* On aura ainsi une information sur l'anisotropie du facteur de structure.

Du point de vue théorique, il est sans doute nécessaire de connaître de façon plus exacte la charge déplacée $\Delta\rho(\boldsymbol{r})$ dans tout l'espace, mais surtout on doit d'abord calculer de manière plus précise $g_n(\boldsymbol{s})$ et sa dépendance par rapport à $|\boldsymbol{s}|$ dans certaines directions. On pourra alors comparer directement avec des résultats expérimentaux sur les monocristaux ; la comparaison avec des expériences sur des polycristallins est beaucoup plus difficile parce qu'elle nécessite la connaissance de la variation du facteur de structure par rapport à toutes les directions de $\boldsymbol{s}$.

Remerciement—Je suis heureux de remercier ici Monsieur le Professeur J. FRIEDEL qui m'a proposé ce problème et m'a constamment guidé au cours de ce travail.

APPENDICE A

Validité du Modèle

(1) On utilise dans toute la suite les notations de (4). Rappelons qu'à partir d'une fonction d'onde du type (2.2)

$$\Psi(\boldsymbol{k},\boldsymbol{r}) = \sum_{m,j} a_m(\boldsymbol{k}) \exp(i\boldsymbol{k}\boldsymbol{R}_j)\phi_m(\boldsymbol{r}-\boldsymbol{R}_j).$$

On obtient facilement à l'aide des équations de Schrödinger des électrons d dans le potentiel atomique U et dans le potentiel de réseau V_R, la série d'équations linéaires

$$\sum_n a_n(H_{mn}-E\delta_{mn}) = 0 \quad (m,n = 1,2, \dots 5).$$

Dans ces équations H_{mn} sont des quantités dépendant du vecteur d'onde $\boldsymbol{k}$ et des éléments de matrice A_i du potentiel V_R-U pris entre les fonctions d'onde atomiques d centrées sur des sites voisins (équation (7) Ref. (4)) Les relations de dispersion $E = E(\boldsymbol{k})$ sont donc données par l'équation séculaire.

$$\text{(A)} \qquad \det|H_{mn}-E\delta_{mn}| = 0$$

et les coefficients a_n s'en déduisent immédiatement.

Dans la suite on pose2 $(\xi,\ \eta,\ \zeta) = \boldsymbol{a}(k'_x,k'_y,k'_z)$; k'_x, k'_y sont les axes menés du milieu O de AB parallèlement à $\boldsymbol{k}_x$ et $\boldsymbol{k}_y$.

Nous cherchons la relation de dispersion et la fonction d'onde pour des vecteurs d'onde proches de la diagonale AB qui constitue pour une part le sommet de bande. Plus précisément au voisinage du point $\boldsymbol{k}_0$ de AB on écrit

$$E(\boldsymbol{k}_0+\delta k) = E'_0+\delta E.$$

E'_0 étant l'énergie de haut de bande ; on développe alors dans (A) les quantités H_{mn} en fonction de ξ et ζ et on se limite au 2° ordre par rapport *v* ces variables ;

un calcul sans difficulté qui sera reproduit ailleurs donne

(i) les surfaces d'énergie constante sont données par (A.1)

$$2\delta E = A(\eta)\xi^2+B(\eta)\zeta^2 \qquad \text{(A.1)}$$

les quantités $A\,(\eta)$ et $B\,(\eta)$ sont liées aux paramètres A_i et $E_0 = 4\,(A_1+A_2)$ de Fletcher par les relations

$$A(\eta) = b'-a'\cos^2\eta/2 \quad b' = 4(A_1-A_2) = 0{\cdot}524\,E_0$$

$$B(\eta) = b'-a'\sin^2\eta/2 \quad a' = 4\left(A_2-\frac{8\,A_3^2}{A_1+A_2}\right)$$

$$= 0{\cdot}012\,E_0$$

(ii) les fonctions d'onde données par (2 4) ne dépendent que de la seule orbitale d qui pointe dans les directions $\boldsymbol{k}_x$ et $\boldsymbol{k}_z$ perpendiculaires à AB.

(2) *Discussion des hypothèses du paragraphe* II.2 *dans la limite* $\delta E \to 0$ Ces hypothèses sont valables au deuxième ordre si on néglige a′ devant b'. On a d'ailleurs calculé dans les hypothèses des formules (2.4) (A.1) la variation de densité électronique ; on trouve :

(a) une densité électronique localisée dans des régions angulaires très étroites au voisinage des plans (010) (001) (100).

(b) une assez forte anisotropie selon la direction d'observation dans chacun de ces plans. Celle-ci est conséquence de la topologie particulière des surfaces (A.1) (Elles représentent une ligne de singularité).

La répartition électronique présente la même allure générale que celle prévue par le modèle dans le paragraphe III. Ceci justifie entièrement le modèle dans la limite $\delta E \to 0$.

(3) *Validité du modèle jusqu'au niveau de Fermi*

L'extension du modèle jusqu'au niveau de Fermi est justifiée essentiellement par le fait que, même loin du haut de bande, les surfaces présentent une symétrie "cylindrique".

Au-delà du 2e ordre, les calculs deviennent très compliqués. Cependant la signification de l'approximation est assez claire.

Dans notre modèle, les diverses portions cylindriques de la surface de Fermi s'intersectent, ce qui ne saurait avoir lieu que pour un potentiel très particulier. En particulier, quand on fait un développement au 4e ordre, les surfaces s'évitent selon un résultat général de la théorie des bandes. Les déviations importantes par rapport à la symétrie cylindrique sont la conséquence de ce fait.

Ainsi par l'application d'une perturbation du potentiel de réseau $\delta V_R(\boldsymbol{r})$ on passe du modèle "cylindrique" caractéristique du potentiel de réseau $V'_R(\boldsymbol{r})$ au modèle de Fletcher caractéristique du potentiel de réseau du nickel (cf. Figs. 1a et 1b).

$$V_R(\boldsymbol{r}) = V'_R(\boldsymbol{r})+\delta V_R(\boldsymbol{r}) \qquad \frac{\delta V_R}{V_R} \ll 1.$$

En particulier, les surfaces cylindriques délimitent un volume commun dès le haut de la bande ($R > 0$) puis deux volumes dès que $R \geqslant (\pi/2a)$. A chacune de ces parties communes, il correspond une bande distincte dans le modèle de Fletcher. On doit considérer chaque surface limitant une partie commune, comme surface limitant deux bandes. On doit en tenir compte notamment dans l'évaluation de la densité d'états et de l'intégrale $I(E,r)$ (Appendice B).

Le niveau de Fermi ferromagnétique correspond à $\mathscr{R} \simeq 0{,}7\,\pi/a$. Au niveau de Fermi, comme dans le modèle de Fletcher interviennent trois bandes.$^{(4)}$

APPENDICE B

(1) *Surface de Fermi*

Dans le modèle choisi, la surface de Fermi se compose de douze ½ cylindres ; on groupe ces cylindres en trois classes de 4 cylindres, suivant que leurs axes sont parallèles à $\boldsymbol{k}_x$, $\boldsymbol{k}_y$ ou $\boldsymbol{k}_z$.

On traite simultanément deux demi-cylindres symétriques par rapport au centre de la zône de Brillouin.

On veut calculer la fonction $I(E,\boldsymbol{r})$

$$I(E,\boldsymbol{r}) = \sum_i I_i(E,\boldsymbol{r}) \quad 1 \leqslant i \leqslant 6,$$

somme des intégrales de surface.

$$I_i(E,\boldsymbol{r}) = \int_{S_i(E)} \exp(i\boldsymbol{kr})\frac{\mathrm{d}S_{\boldsymbol{k}}}{|\nabla_{\boldsymbol{k}}E|}$$

On évalue dans le paragraphe suivant l'une des intégrales $I_i(E,\boldsymbol{r})$.

(2) Calcul de l'intégrale $I'(E,\boldsymbol{r})$

$$I'(E,\boldsymbol{r}) = \int_{S(E)} \exp(i\boldsymbol{kr})\frac{\mathrm{d}S_{\boldsymbol{k}}}{|\nabla_{\boldsymbol{k}}E|} \qquad \text{(B.1)}$$

L'intégrale est étendue sur les deux cylindres ayant deux axes parallèles à la même diagonale AB de la zône de Brillouin (Fig. 1c).

$$2E = A\mathscr{R}^2.$$

D'après les notations de la Fig. 1(c)

$$\begin{aligned} \boldsymbol{r} &= \boldsymbol{\rho}+\rho\ \mathrm{tg}\ \varphi\boldsymbol{k}_z \\ \boldsymbol{k} &= \mathscr{R}+\eta\boldsymbol{k}_z \end{aligned}$$

$\mathscr{R}$ et $\boldsymbol{\rho}$ sont respectivement les projections de $\boldsymbol{k}$ et de $\boldsymbol{r}$ sur le plan $\boldsymbol{k}'_x\,\boldsymbol{k}_z$

$\hat{\boldsymbol{k}}_z$ est le vecteur unitaire dirigé parallèlement à l'axe $\boldsymbol{k}_z$

$$\boldsymbol{k},\boldsymbol{r} = \mathscr{R}\boldsymbol{\rho}+\eta\rho\ \mathrm{tg}\ \varphi$$

en posant

$$\theta = (\boldsymbol{k}_x,\mathscr{R}) \qquad \theta_0 = (\boldsymbol{k}_x,\boldsymbol{\rho}).$$

L'intégrale devient :

$$AI'(E,\boldsymbol{r}) = \exp(i\boldsymbol{k}_0\boldsymbol{r}) \int_0^{\pi} \exp[i\mathscr{R}\rho\cos(\theta-\theta_0)]_{d\theta} \int_{-l/2}^{+l/2} \times \exp(i\eta\rho\operatorname{tg}\varphi)\,\mathrm{d}\eta + CC \qquad \text{(B.2)}$$

$$= \frac{2}{\rho\operatorname{tg}\varphi}\sin l/2\,\rho\operatorname{tg}\rho\,\{\exp(i\boldsymbol{k}_0\boldsymbol{r}) \times I''(\boldsymbol{r}) + CC\}$$

avec

$$I''(\boldsymbol{r}) = \int_0^{\pi} \exp[i\mathscr{R}\rho\cos(\theta-\theta_0)]_{d\theta}.$$

On peut développer cette intégrale en série de fonctions de Bessel, mais dans la limite des grandes valeurs de $|\boldsymbol{r}|$ elle s'évalue simplement par la méthode de la phase stationnaire.

Les seules contributions proviennent de $\theta \simeq \theta_0$.

On développe $\cos(\theta-\theta_0) = \cos\theta$ au voisinage $\theta' = 0$ et

$$I''(\boldsymbol{r}) \simeq \int_{-\epsilon}^{+\epsilon} \exp(i\mathscr{R}\rho\cos\theta')\,\mathrm{d}\theta'$$

$$= \sqrt{\left(\frac{2}{\mathscr{R}\rho}\right)}\exp(i\mathscr{R}\rho) \int_{-\sqrt{(\mathscr{R}\rho\epsilon/2)}}^{+\sqrt{\mathscr{R}\rho\epsilon/2}} \exp(-iu^2)\,\mathrm{d}u$$

avec la notation

$$u = \sqrt{\left(\frac{\mathscr{R}\rho}{2}\right)}\,\theta'$$

Quand $\rho \to \infty$ l intégrale du deuxième membre tend vers une intégrale numérique classique.

$$\int_{-\infty}^{+\infty} \exp(-iu^2)\,\mathrm{d}u = (1-i)\sqrt{\left(\frac{\pi}{2}\right)} = \sqrt{\pi}\exp\left(-i\frac{\pi}{4}\right)$$

$$\cdot \exp(i\boldsymbol{k}_0\boldsymbol{r})\,I''(\boldsymbol{r}) + CC = 2\sqrt{\left(\frac{2\pi}{\mathscr{R}\rho}\right)}\left\{\exp\left[i\left((\boldsymbol{k}_0\boldsymbol{r} + \mathscr{R}\rho - \frac{\pi}{4}\right)\right] + CC\right\} \qquad \text{(B.3)}$$

D'où en posant :

$$\boldsymbol{k}(E,\boldsymbol{r}) = \boldsymbol{k}_o + \widehat{\mathscr{R}\rho} \qquad \boldsymbol{k}_0 = 0\,0'$$

et en regroupant les résultats de (B.2) et (B.3)

$$I'(E,\boldsymbol{r}) = \frac{4}{A}\sqrt{\left(\frac{2\pi}{\overset{\perp}{\mathscr{R}}}\right)}\,\frac{\sin\frac{l}{2}\rho\operatorname{tg}\varphi}{\rho\operatorname{tg}\varphi} \times \frac{\cos(\boldsymbol{k}(E,\boldsymbol{r})\,\boldsymbol{r} - \frac{\pi}{4})}{\sqrt{\rho}} \qquad \text{(B.4)}$$

ou encore, puisque $r\cos\varphi = \rho$

$$I'(E,\boldsymbol{r}) = \frac{4}{A}\sqrt{\left(\frac{2\pi}{\mathscr{R}}\right)}\frac{\sin\left(\frac{l}{2}\rho\operatorname{tg}\varphi\right)}{\sin\varphi\sqrt{\cos\varphi)}} \times \frac{\sin(\boldsymbol{k}(E,\boldsymbol{r})\cdot\boldsymbol{r} + \frac{\pi}{4})}{r^{3/2}} \qquad \text{(B.5)}$$

Le développement précédent n'est plus valable pour $\theta_0 = 0$, puisqu'alors on a deux extrêma de phase et $I''(\boldsymbol{r}) = \pi J_0(\mathscr{R}\rho)$, où J_0 est la fonction de Bessel d'ordre 0. Cependant puisqu'ici on est dans l'approximation des liaisons fortes, on n'aure pas à calculer cette grandeur $I'(E,\boldsymbol{r})$ que sur un site du réseau $\boldsymbol{R}_\lambda$ de sorte que $\exp i\,\boldsymbol{k}_0\,\boldsymbol{R}_\lambda = \pm 1$; dans ces conditions, on voit aisément que la formule (B.5) est encore valable même pour $\theta_0 = 0$.

Les intégrales $I_i(E,\boldsymbol{r})$, d'après la formule (B.5) ne dépendent que de l'angle $\bar{\varphi}_i$ de $\boldsymbol{r}$ avec π_i. $I(E,\boldsymbol{r})$ est somme de contributions correspondant aux trois groupes de cylindres parallèles à k_x k_y et k_z.

APPENDICE C

Diffusion magnétique des neutrons par un ailliage désordonné dans l'approximation des électrons libres

L'existence d'oscillations à grande distance autour d'une impureté dissoute se traduit nécessairement dans la transformée de Fourier $\widetilde{\Delta\rho}(\boldsymbol{s})$ par une singularité, sinon de la fonction, au moins des dérivées.

Ce fait apparaît dans l'approximation des électrons libres où l'on peut calculer $\widetilde{\Delta\rho}(\boldsymbol{s})$ aisément.

L'introduction d'une charge ponctuelle $Z\delta(\boldsymbol{r})$ dans un gaz d'électrons libres conduit une variation de densité électronique qui a l'une des valeurs suivantes selon le type d'approximation que l'on fait :

(1) Dans le modèle de Thomas Fermi,(2)

$$\widetilde{\Delta\rho}^{TF}(\boldsymbol{r}) = \frac{\lambda^2 Z}{4\pi r}\exp(-\lambda_r) \; ; \; \lambda^2 = \frac{4k_F}{\pi} \qquad \text{(C.1)}$$

$$\widetilde{\Delta\rho}^{TF}(s) = +\frac{4k_F Z}{\pi(s^2+\lambda^2)} \tag{C.2}$$

(2) Dans le modèle de Hartree self consistent et dans l'approximation de Born,$^{(2)}$

$$\widetilde{\Delta\rho}^{HF}(s) = Z\frac{g(s)}{\dfrac{\pi s^2}{2k_F}+g(s)} \tag{C.3}$$

Dans cette formule $g(s)$ est donnée par :

$$g(s) = 1+\frac{k_F}{s}\left(1-\frac{s^2}{4k_F^2}\,\mathrm{Log}\left|\frac{s+2k_F}{2-k_F}\right|\right) \tag{C.4}$$

Dans le modèle de Thomas Fermi $\widetilde{\Delta\rho}^{TF}(s)$ décroît régulièrement avec s sans aucune singularité (Fig. 6a).

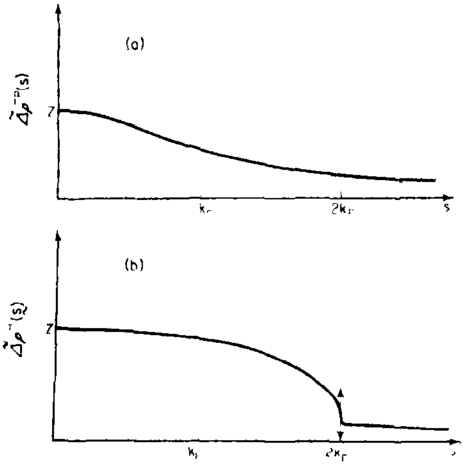

Fig. 6.

Dans le modèle de Hartree self-consistent, l'existence des oscillations à grande distance se traduit sur $\widetilde{\Delta\rho}^{HF}(s)$ par un point singulier (dérivée infinie) pour $s = 2k_F$ (Fig. 6b). La décroissance en $1/r^3$ se traduit d'autre part par une concentration vers $s \simeq 0$ par rapport au modèle de Thomas Fermi.

$$\widetilde{\Delta\rho}^{TF}(s) \underset{r\to\infty}{\sim} 1/s^2 \quad \widetilde{\Delta\rho}^{H}(s) \underset{r\to\infty}{\sim} 1/s^4$$

Pour des neutrons qui ont une longueur d'onde voisine de, 1 Å et pour $k_F \simeq 1\ UA = 0{,}5$ Å, l'angle de diffusion correspondant est $2\theta \simeq (\lambda k_F/\pi) \simeq 10°$.

En dehors des pures difficultés expérimentales, les neutrons n'étant sensibles qu'aux moments magnétiques, la plupart des alliages où l'approximation des électrons libres n'est pas mauvaise ne donnent rien (**Cu**, Zn ...).

Par contre, peut-être peut-on mettre en évidence un tel phénomène dans un alliage **CuMn**.

APPENDICE D

Evaluation de l'amplitude de diffusion

La contribution de la variation de densité au voisinage du plan (010) à la diffusion est donnée par $f_3(s)\, g_3(s)$ que l'on évalue ici ; les autres termes s'obtiennent de manière identique.

(1) Calcul de la fonction $A_n(\boldsymbol{r})$ (définition 3.33).

La fonction $A_n(\boldsymbol{r})$ a une forme très simple par suite de la valeur particulière des fonctions d'onde (liaisons fortes).

Ainsi, si $\boldsymbol{r}$ appartient à la cellule C_λ centrée sur le site du réseau $\boldsymbol{R}_\lambda$

$$A_3(\boldsymbol{r}) = A_{11}(\boldsymbol{r})+2A_{12}(\boldsymbol{r})+A_{22}(\boldsymbol{r}) \tag{D.1}$$

où l'on définit

$$A_{11}(\boldsymbol{r}) = \frac{1}{N}\exp(2i\boldsymbol{k}_{01}\boldsymbol{R}_\lambda)\exp(2i\mathscr{R}\hat{\rho}_3\cdot\boldsymbol{R}_\lambda)$$
$$\times\ \phi_3^2(\boldsymbol{r})-CC \tag{D.2a}$$

$$A_{12}(\boldsymbol{r}) = \frac{1}{N}\exp[i(\boldsymbol{k}_{01}+\boldsymbol{k}_{02})\boldsymbol{R}_\lambda]\exp(2i\mathscr{R}\hat{\rho}_3\cdot\boldsymbol{R}_\lambda)$$
$$\times\ \phi_{3\lambda}^2(\boldsymbol{r})-CC \tag{D.2b}$$

$$A_{22}(\boldsymbol{r}) = \frac{1}{N}\exp[2i(\boldsymbol{k}_{02}\boldsymbol{R}_\lambda)]\exp(2i\mathscr{R}\hat{\rho}_3\cdot\boldsymbol{R}_\lambda)$$
$$\times\ \phi_3^2(\boldsymbol{r})-CC \tag{D.2c}$$

On a posé

$$\boldsymbol{\rho}_3 = \hat{\rho}_3|\rho_3|.$$

D'une manière générale $\exp 2i\boldsymbol{k}_{01}\ R_\lambda = \exp 2i\boldsymbol{k}_{02}\ R_\lambda = 1$ puisque 2 $\boldsymbol{k}_{01}$ et 2 $\boldsymbol{k}_{02}$ sont des vecteurs du réseau réciproque

De plus, dans le cas particulier où R_λ est centré sur le plan π_s et pour le système cubique à faces centrées

$$\exp[i(\boldsymbol{k}_{01}+\boldsymbol{k}_{02})\boldsymbol{R}_\lambda] = 1 \tag{D.3}$$

ainsi qu'on s'en assure très simplement.

Les contributions des termes d'interférence sont égales aux contributions des termes directs

$$A_3(\boldsymbol{r}) = \frac{4}{N}\exp\mathscr{R}\hat{\rho}_3\boldsymbol{R}_\lambda\phi_{3\lambda}^2(\boldsymbol{r})-CC$$
$$= \frac{8i}{N}\phi_{3\lambda}^2(\boldsymbol{r})\sin 2\mathscr{R}\hat{\rho}_3\boldsymbol{R}_\lambda \tag{D.4}$$

[pour $\boldsymbol{r}$ appartenant à C_λ]

Cette expression n'est pas toujours vraie quand $\boldsymbol{R}_\lambda$ est un site quelconque du réseau, car alors

$$\exp[i(\boldsymbol{k}_{01}+\boldsymbol{k}_{02})\boldsymbol{R}_\lambda] = \pm 1$$

et pour la moitié des sites du réseau cristallin les contributions des termes d'interférence détruisent alors simplement les contributions des termes directs (la variation de densité dans la cellule correspondante sera alors nulle).

Dans le cadre de l'hypothèse du paragraphe III. 3a, on néglige les franges de densité électronique alors seules les cellules situées sur les plans π, pour lesquelles la formule (D.4) est valable, sont atteintes par la perturbation. Cette hypothèse est complètement justifiée par le fait, facilement vérifiable, que pour les premiers voisins du plan π_3 $\Delta\rho^\infty(\boldsymbol{r}) = 0$

(2) Evaluation de $f_n(s)\, g_n(s)$.

$g_n(s)$ est une somme sur les différents sites du plan π_n par suite des hypothèses du calcul des liaisons fortes. En vue d'avoir le type de discontinuité pour $|s| \simeq 2\mathscr{R}$, on remplace la somme par une intégrale sur tout le plan π_n. Cette approximation n'est pas justifiée dans la mesure où la longueur d'onde des oscillations $2\mathscr{R}$ est sensiblement de l'ordre de grandeur de l'inverse de la distance interatomique. D'autre part, étendre l'intégrale jusqu'à l'origine surestime certainement la contribution de la partie asymptotique, $\Delta\rho^\infty(\boldsymbol{r})$. Le type de discontinuité obtenu sera cependant probablement le même quelque la valeur calculée pour $\Delta\rho^\infty(s)$ ne soit pas bonne. On a alors :

$$g_n(s) \simeq \frac{2\mu}{a^2}\int_0^\infty \frac{\sin 2\mathscr{R}r}{r}\exp(-isr)\,\mathrm{d}r \quad \text{(D.5)}$$

On évalue facilement $g_n(s)$ à l'aide de la représentation intégrale de la fonction de Bessel d'ordre O, $J_0(u)$

$$g_n(s) \simeq \frac{4\pi\mu}{a^2}\int_0^\infty J_0(s_n^0 r)\frac{\sin 2\mathscr{R}r}{r}\,\mathrm{d}r \quad \text{(D.6)}$$

On obtient d'après la formule de Callop,(9) le résultat de (4.11) à condition de négliger la variation de $f_n(s)$ avec s.

BIBLIOGRAPHIE

1. Roth L., Thèse, Harvard University (1957).
2. Blandin A., Thèse, Université de Paris (1961).
3. Blandin A., *J. Phys. Radium* **22,** 507 (1961).
4. Fletcher, *Proc. phys. Soc. Lond.* **65,** 192 (1952).
5. Shull C. G. et Wilkinson M. K., *Phys. Rev.* **97,** 304 (1955).
6. Lowde R. D., *A.E.R.E. Rep.* **3758** (Harwell, 1961).
7. Guinier A., *Théorie et Technique de la Radiocristallographie*, p. 574. Dunod, Paris (1956).
8. Halperin et Johnson, *Phys. Rev.* **55,** 898 (1939).
9. Magnus et Oberhettinger, *Functions of Mathematical Physics*, Chelsea, London (1954).
10. Collins M. F., Jones R. V. et Lowde R. D., *J phys. Soc. Japan* (sous presse).
11. Koster C. F., *Phys. Rev.* **95,** 1436 (1959).

J. Phys. Chem. Solids Pergamon Press 1963. Vol. 24 pp. 405–423. Printed in Great Britain.

A MAGNETIC AND NEUTRON DIFFRACTION STUDY OF THE Cr_2O_3–Fe_2O_3 SYSTEM

D. E. COX, W. J. TAKEI and G. SHIRANE

Westinghouse Research Laboratories, Beulah Road, Churchill Borough, Pittsburgh 35, Pennsylvania

(*Received* 11 *September* 1962)

Abstract—The magnetic structures of solid solutions $(1-x)Cr_2O_3$-xFe_2O_3 have been determined by neutron diffraction and magnetic measurements. The different antiferromagnetic structures of Cr_2O_3 and Fe_2O_3 are revealed to be connected through cone spiral structures in such a way that continuity is preserved. For the purpose of describing the latter, the fundamental Cr_2O_3 type of magnetic structure is divided into two sublattices, within each of which the spins are coupled ferromagnetically, with antiferromagnetic coupling between the sublattices. The addition of Fe_2O_3 creates a cone spiral within each sublattice, both the cone axis and the spiral wave vector lying along the hexagonal *c*-axis. The cone angle increases with increasing Fe_2O_3 content up to $x = 0{\cdot}15$.

In the region $0{\cdot}2 \leqslant x \leqslant 0{\cdot}35$, the cone axis lies perpendicular to the *c*-axis, although the spiral wave vector remains parallel to the latter, resulting in a cycloidal arrangement. The spin components along the cone axis now have the fundamental Fe_2O_3 type of magnetic structure. As the Fe_2O_3 content increases, the cone angle decreases, until finally when this becomes zero, the Fe_2O_3 type of magnetic structure is attained.

1. INTRODUCTION

BOTH α-Fe_2O_3 and Cr_2O_3 possess the rhombohedral corundum type of crystal lattice,(1) in common with several other sesquioxides, including Ti_2O_3 and V_2O_3. These four compounds in particular have quite complex and differing magnetic properties and have consequently been the subject of numerous investigations. Neutron diffraction studies of Fe_2O_3(2) and Cr_2O_3(3) have revealed the existence of definite magnetic structures, but in spite of the presence of anomalies in the curves of magnetic susceptibility against temperature for Ti_2O_3 and V_2O_3,(4–7) no long range magnetic structure has yet been reported for either of the latter compounds.(8,9)

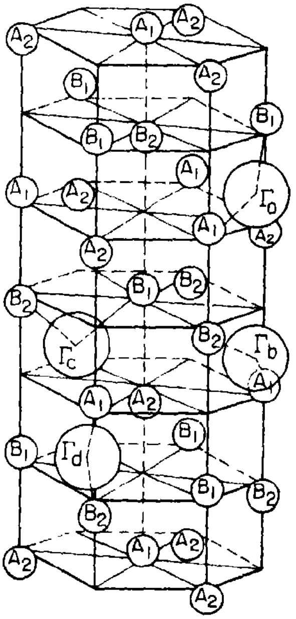

FIG. 1. The crystal structure of α-Fe_2O_3 and Cr_2O_3. Oxygen ions are omitted, except for those used to describe four possible exchange interactions.

Although Fe_2O_3 and Cr_2O_3 are crystallographically isomorphous, their magnetic structures differ. Their crystal structure is illustrated in Fig. 1 and may be considered ideally to consist of layers of cations in the rhombohedral (111) planes, separated by layers of oxygen ions. In actual fact, an individual cation is situated either slightly above or below the plane. The magnetic structure of Fe_2O_3 was established by SHULL, STRAUSER and WOLLAN.(2) At 25°C, the spins within any (111) plane are parallel, and adjacent planes are coupled antiferromagnetically, i.e. $A_1(+)$, $A_2(+)$, $B_1(-)$, $B_2(-)$. As the temperature is lowered, there is a change in the spin direction from within the (111) plane to along the [111] axis in the region of −15°C. Cr_2O_3, on the other hand, has a structure in which the spins are aligned antiparallel within the (111) planes, i.e. $A_1(+)$, $A_2(-)$, $B_1(+)$, $B_2(-)$,(3) and from magnetic measurements the spin direction was found to lie along the [111] axis.(10)

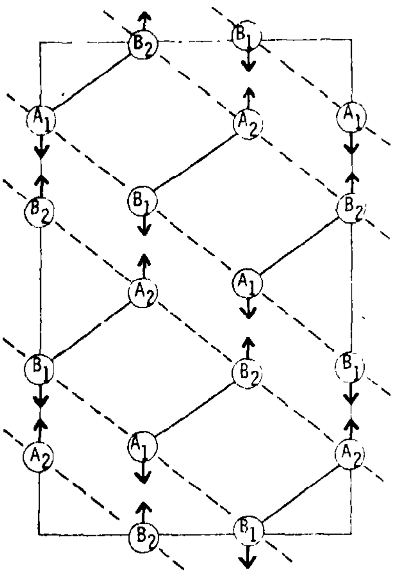

FIG. 2. Hexagonal unit cell of corundum type projected on (110) and showing the Cr_2O_3 spin arrangement. The heavier solid lines indicate the interaction Γ_b and the broken lines Γ_a. It should be noted that the origin differs by (0, 0, $\frac{1}{4}$) from that used in many other publications.

Both types of spin configuration may be derived quite simply by consideration of two exchange interactions.(11,12) Following the notation of ISHIKAWA and AKIMOTO,(13) these may be written as Γ_a and Γ_b (Fig. 1). In the case of Fe_2O_3, both are negative, but in Cr_2O_3, Γ_a is positive and Γ_b negative. A possible reason for this difference has only recently been advanced,(14) from consideration of the overlap of the various cation *d* orbitals with the anion *p* orbitals.

The magnetic structure of Cr_2O_3 may be divided into four sublattices containing the cations A_1, A_2, B_1 and B_2 respectively. It is convenient to combine these into two ferromagnetic sublattices (or more correctly, networks), the one containing cations A_1 and B_1 and the other containing cations A_2 and B_2 as indicated by the broken lines in Fig. 2, the two sublattices being coupled antiparallel by interactions A_1–B_2 and A_2–B_1 of the type Γ_b, shown by the thicker solid lines. In Fe_2O_3, of course, the cations within these particular sublattices are coupled antiferromagnetically, i.e. $A_1(+)$, $B_1(-)$, $A_1(+)$, $B_1(-)$. However, the interactions Γ_b coupling the sublattices are still negative, just as in Cr_2O_3.

In addition to Γ_a and Γ_b there are two other feasible interactions, Γ_c and Γ_d, between adjacent cations within the (111) planes and cation pairs along the [111] axis respectively (Fig. 1). It is not clear which combination of interactions is of predominant importance, but as the latter two have cation–anion–cation angles of about 90°, they might be considered least significant. Details of all four interactions are summarized in Table 1.

Table 1. *Exchange interactions and cation–anion–cation angles in* Fe_2O_3 *and* Cr_2O_3 *for configurations having short cation–anion distances. The number of equivalent neighboring cations is denoted by n*

Interaction	*n*	Fe_2O_3 Sign	Fe_2O_3 Angle	Cr_2O_3 Sign	Cr_2O_3 Angle
Γ_a	6	−	132°	+	133°
Γ_b	3	−	118°	−	121°
Γ_c	3	+	94°	−	93°
Γ_d	1	−	87°	−	82°

As Fe_2O_3 and Cr_2O_3 form solid solutions over the entire composition range(15,16) the influence of competing interactions should lead to anomalous behavior in part of the composition range. In the related Fe_2O_3-$FeTiO_3$ system(17) for example, an interesting feature is the development of an inhomogeneous magnetic structure as the $FeTiO_3$ concentration increases, a structure in which superparamagnetic regions and regions with long range order of Fe_2O_3 type can coexist. In the Fe_2O_3-V_2O_3 system,(18) a gradual breakdown of the Fe_2O_3 type of order occurs, but no other long range magnetic order is observed.

LI(11) has predicted a number of possible situations which might arise in the Cr_2O_3–Fe_2O_3 system when the competitive effect of the different interactions becomes important. One such possibility is the formation of a magnetic structure differing from both those of Fe_2O_3 and Cr_2O_3, and KASPER and DECKER(19) did in fact observe neutron diffraction peaks of magnetic origin in certain solid solutions which did not arise from simple magnetic ordering of Fe_2O_3 and Cr_2O_3 type. However, the magnetic structure remained unsolved.

The present paper describes a detailed magnetic and neutron diffraction study of the Cr_2O_3–Fe_2O_3 system. A very striking feature is the occurrence of a cone spiral arrangement in part of the system. A number of publications have recently appeared in the literature dealing with spiral or helical magnetic structures in various substances, such as Cr,(20–22) a number of rare earth metals,(23–24) $MnAu_2$,(25) MnO_2(26) and $MnCr_2O_4$(27) The latter compound in particular shows many features similar to those displayed by the Cr_2O_3–Fe_2O_3 system, and its spin arrangement is also interpreted on the basis of a cone spiral model. It has been shown by a number of authors(28–32) that a spiral scheme may represent the lowest energy state when the nature of the structure is such that a simple ferromagnetic or antiferromagnetic scheme is not entirely compatible with the various exchange integrals.

2. SAMPLE PREPARATION AND MAGNETIC MEASUREMENTS

The starting materials were "Fisher Certified" reagent grade Fe_2O_3 and Cr_2O_3, the latter being prepared by decomposition and subsequent ignition of "Baker Analyzed" grade ammonium dichromate. A number of mixtures of the two oxides in the desired proportions were prefired at 1000°C in air for 20 hr. The resulting products were finely ground, compacted into discs and fired at 1300°C in air for 20 hr. X-ray powder patterns of the products were obtained on a Norelco diffraction unit with chromium K_α radiation. All the patterns showed extremely sharp lines with very well resolved doublets and only a single rhombohedral phase could be detected in each case. The lattice constants of the solid solutions agreed very closely with the published data of DICERBO and SEYBOLT.(16) Chemical analysis of a few of the materials for iron gave values for x in $(1-x)$ Cr_2O_3–xFe_2O_3 differing by less than 0·01 from the nominal values.

The magnetization of samples was determined by means of the Faraday method over fairly wide temperature ranges. The force acting on the sample was measured with the electromechanical balance described previously.(18) With this apparatus, a maximum field of about 10 kOe can be attained.

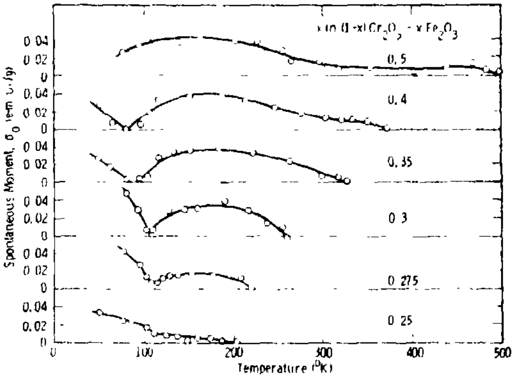

FIG. 3. Variation of parasitic spontaneous moment with temperature for the system $(1-x)$ Cr_2O_3–xFe_2O_3.

On the basis of the magnetic measurements, two regions in the system $(1-x)$ Cr_2O_3–xFe_2O_3 may be defined. The first, extending from approximately $0{\cdot}25 \leqslant x \leqslant 1{\cdot}0$, is characterized by the appearance of a small spontaneous moment below some temperature which is dependent upon the composition (Fig. 3). In the case of Fe_2O_3, this temperature is known to roughly correspond with the Néel temperature as shown by neutron diffraction experiments.(2) DZYALOSHINSKY(33) has proposed that the weak ferromagnetism results from a slightly canted arrangement of moments, a mechanism for which was advanced by MORIYA,(34) as arising from spin-orbit coupling.

The actual measured magnetization σ, is given at sufficiently high fields by the expression

$$\sigma = \sigma_0 + XH$$

where σ_0 is the saturation value of the spontaneous moment, X the susceptibility and H the applied field. Thus by extrapolation to zero field of the linear portion of the magnetization-field curve at a given temperature, σ_0 may be determined. The slope of this line gives χ, of course. In practice, a saturation value for σ_0 appeared to be reached at fields less than 4 kOe, and σ_0 and χ could thus be determined with reasonable accuracy. The estimated possible error in each quantity arising from extrapolation is ± 0·004 e.m.u./g.

A detailed examination of the data in Fig. 3 reveals some interesting features. The region $0{\cdot}5 < x \leqslant 1{\cdot}0$ is not of any special interest, as the behavior merely resembles that of Fe_2O_3, apart from a decrease in the Néel temperature roughly proportional to the decrease in Fe_2O_3 concentration. When $x = 0{\cdot}5$, the variation of σ_0 with temperature is somewhat more complex. Initially, a very small amount appears, barely greater than the estimated possible error. Slightly below room temperature the amount increases fairly rapidly, only to fall again as the temperature approaches 80°K.

This trend is duplicated for $x = 0{\cdot}4$, with the additional feature that σ_0 actually drops to zero at about 80°K, and increases again at still lower temperatures. For $0{\cdot}275 \leqslant x \leqslant 0{\cdot}35$ this latter phenomenon is also clearly shown, but for $x = 0{\cdot}25$, is somewhat less evident owing to the exceedingly small moment initially observed. This type of behavior could arise from a reversal in the direction of the spontaneous moment at some temperature below the Néel point, corresponding superficially at least to the properties of those garnets(35) and spinel systems(36) which show so-called "compensation" temperatures.(37) However, in view of the many orders difference in magnitude of the moments observed, such an analogy is probably misleading.

The second region, with $0 \leqslant x \leqslant 0{\cdot}2$ exhibits fairly straightforward antiferromagnetic characteristics, similar to those of Cr_2O_3. No spontaneous moment is observed, and the Néel temperature can be seen to decrease as the Fe_2O_3 content increases (Fig. 4). At the same time, the antiferromagnetic peak becomes less sharply defined.

On another salient point that may be observed in Fig. 4 is that there is no apparent discontinuity in the susceptibilities of the samples $x = 0{\cdot}3$ and $0{\cdot}4$ at their respective Néel temperatures, although in the former case, at least, there is a small peak at the point where σ_0 falls to zero. The question thus arises whether the assumption that the first appearance of a spontaneous moment indicates the Néel point is necessarily correct. This can be resolved only by the neutron diffraction data to be described in a subsequent Section, and, in fact, the correspondence does exist although the agreement is not exact. Thus, at least in the sample $x = 0{\cdot}3$ there are grounds for believing that a second low temperature magnetic transition may occur through which the susceptibility behaves in a fairly orthodox way. It will be seen later that the continuous increase in susceptibility below the first transition is probably a consequence of the unusually large amount of spin disorder in this region. Moreover, it should be recalled that even in Fe_2O_3 itself, the susceptibility does not decrease between the Néel point and room temperature, but remains roughly constant. As pointed out by LIN,(38) this arises because the applied field aligns the spontaneous moment so as to give the maximum component in the field

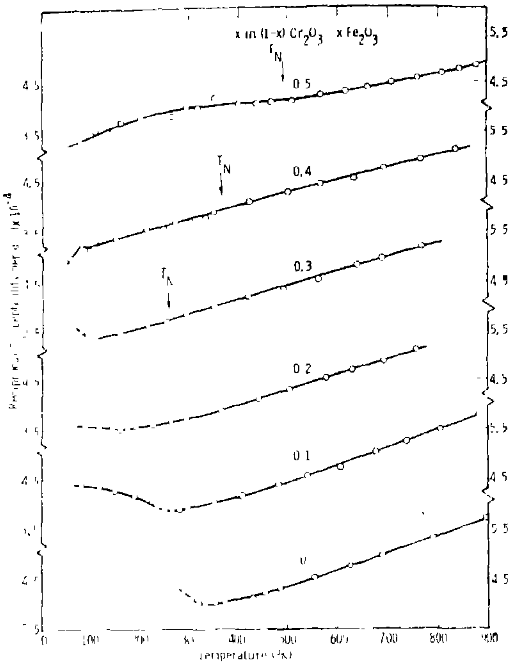

FIG. 4. Variation of reciprocal susceptibility with temperature for the system $(1-x)\ Cr_2O_3$–xFe_2O_3

direction by means of rotation within the (111) planes. As a result, the antiferromagnetic axis lies in the plane perpendicular to the field direction and the susceptibility thus remains constant.

Table 2. Paramagnetic data for the system $(1-x)Cr_2O_3$–xFe_2O_3. θ_a is the asymptotic Néel temperature, μ_{obs} the observed moment per cation and S the corresponding spin quantum number

x	θ_a(°K)	$\mu_{obs}(\mu_B)$	2S
0	−715	4·17	3·29
0·1	−725	4·14	3·26
0·2	−895	4·50	3·61
0·3	−1050	4·68	3·79
0·4	−1170	4·96	4·06
0·5	−1150	5·13	4·23
0·6	−1360	5·29	4·38
0·8	−1640	5·75	4·84
1·0	−1935	6·15	5·23

From the high temperature linear portions of the susceptibility curves, the paramagnetic moments were obtained in the usual way. Values of the observed moment and the asymptotic Néel temperatures are listed in Table 2 for a number of compositions. On account of the rather small slopes involved, particularly for high Fe_2O_3 concentrations, the estimated error in the moment is somewhat high, around $\pm 0{\cdot}2\mu_B$. There is a fairly systematic variation of both quantities, and the values of the moment are consistent with those normally found for Cr^{3+} and Fe^{3+}, with three and five unpaired 3*d* electrons respectively.

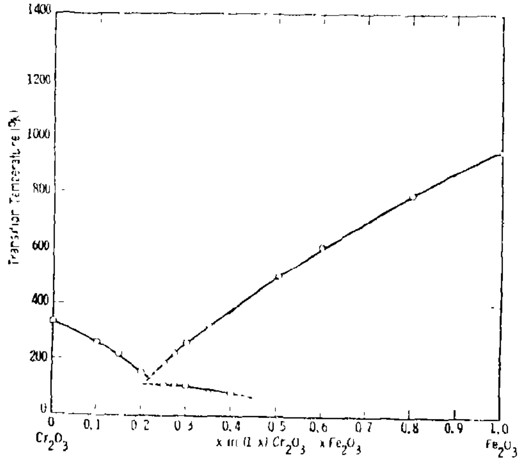

FIG. 5. Variation of magnetic transition temperatures with composition for the system $(1-x)$ Cr_2O_3–xFe_2O_3. The lowest line corresponds to the low temperature discontinuity in the spontaneous moment.

The temperature dependence of the magnetic transitions upon composition is shown in Fig. 5. There is a smooth decrease in the Néel temperature on either side which reflects the effect of competing interactions. There is some disagreement at lower Fe_2O_3 concentrations with the data obtained by POUILLARD,[39] whose measurements were confined to determining the temperature at which the weak spontaneous moment initially appeared. A third line has been inserted to indicate the discontinuities in the spontaneous moments shown in Fig. 3. The neutron diffraction data to be described shortly indicate that this line does in fact correspond to a magnetic phase boundary in this region.

3. CRYSTAL STRUCTURE

The crystal structures of Fe_2O_3 and Cr_2O_3 are described by the rhombohedral space group $R\bar{3}c(D_{3d}^6)$. In the course of the study, it was found more convenient to employ the hexagonal rather than the smaller rhombohedral unit cell, and consequently all subsequent indexing is based upon the former unit cell. In particular, of course, the rhombohedral (111) planes are equivalent to the hexagonal (003) planes.

The ions occupy the following special positions defined in the International Tables.[40]

Fe (or Cr) in 12*c*
O in 18*e*

Thus, in addition to the usual reflection condition arising from trigonal symmetry, that $-h+k+l$ should equal $3n$, there is the condition that reflections of the type $h0l$ or $0kl$ should have l equal to $2n'$.

One factor that should not be overlooked in solid solutions is the possibility of cation order. It has always been assumed that this particular system is completely disordered, which is somewhat presumptious as it is well established that in at least one related rhombohedral system,

Fe_2O_3–$FeTiO_3$, cation ordering of ilmenite ($FeTiO_3$) type occurs, in which the Ti ions are situated on alternate (003) layers with Fe ions on the layers in between.(41) Such an arrangement reduces the symmetry to that of $R\bar{3}$, and leads in particular to the appearance of diffraction peaks $h0l$ for odd values of l, the strongest being (003) and (101). Owing to the small differences in the X-ray scattering factors of Fe and Ti, and Fe and Cr, any such ordering is virtually impossible to detect on X-ray powder patterns. However, the neutron scattering amplitudes are much more favorable in this respect, especially so for the former pair, and ordering has been clearly revealed in this way.(42)

No cation order could be detected from the neutron diffraction patterns, but as the calculated intensities for $(1-x)\,Cr_2O_3$–xFe_2O_3 in the region of interest are barely greater than the observable limit, considerable order could nevertheless exist. A better estimate would be obtained from a neutron diffraction pattern of $x = 0{\cdot}5$ above its Néel point. However, Mössbauer experiments have clearly established the ionic state of Fe in $FeTiO_3$ as Fe^{2+},(43) which suggests a possible reason on energetic grounds for cation ordering, whereas Fe in Fe_2O_3–Cr_2O_3(44) and Fe_2O_3–V_2O_3(45) exists mainly as Fe^{3+}, and in the latter system, no order could be detected by neutron diffraction techniques. Because of this fact, coupled with the close similarity in cation radii, the possibility of cation order in the Fe_2O_3–Cr_2O_3 system is neglected in the subsequent interpretation and discussion of the neutron data.

For the determination of the crystal parameters, the neutron scattering amplitudes tabulated by SHULL and WOLLAN(46) were used, namely, 0·96, 0·35 and 0·58 for iron, chromium and oxygen respectively. Agreement of calculated and observed intensities was generally very satisfactory with the parameters listed in Table 3. These are considered reliable within the limits ± 0·002 for u and ± 0·003 for x. For Cr_2O_3, NEWNHAM and DE HAAN(47) obtained the values 0·3475 and 0·556 for u and x respectively from a single crystal study. In the final column of Table 3 are presented values of the interatomic distance between cations on adjacent layers comprising the c axis pairs A_1 and B_2 or A_2 and B_1 (see Fig. 1). There is a relatively large decrease as the Fe_2O_3 content decreases, which may have some significance as described later.

Table 3. Crystallographic data for the system $(1-x)Cr_2O_3$–xFe_2O_3. The structure parameters u and x refer to cation and anion respectively in the rhombohedral cell. The distance between "cation pairs" A_1B_2 or A_2B_1 situated on the c axis is denoted by d. It should be noted that the origin differs by $(\frac{1}{4}, \frac{1}{4}, \frac{1}{4})$ from that used in many other publications

x	Hexagonal lattice constants (Å) a	c	Structure parameters u	x	d (Å)
0·0	4·958	13 594	0·347	0·554	2·64
0·1	4·969	13·600	0·348	0·556	2·67
0·15	4·974	13·602	0·350	0·556	2·72
0·2	4·981	13·607	0·351	0·554	2·75
0·25	4·985	13·609	0·352	0·554	2·78
0·3	4·991	13·613	0·352	0·553	2·78
0·35	4·995	13·614	0·353	0·554	2·80
0·5	5·015	13·639	0·354	0·554	2·84
1·0	5·034	13·745	0·355	0·552	2·89

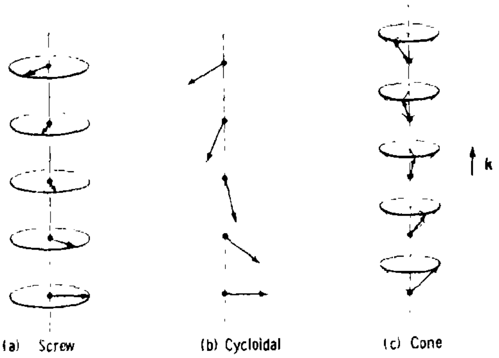

(a) Screw (b) Cycloidal (c) Cone

FIG. 6. Types of simple spiral (a) Screw, (b) Cycloidal, (c) Cone. k is the wave vector.

4. SPIRAL CONFIGURATIONS

In order to discuss the experimental data more clearly, it is worthwhile at this stage to summarize some of the properties of spiral configurations with particular emphasis on the corundum type of structure. A more detailed treatment appears in the Appendix to this paper.

The term "spiral" is somewhat misleading and is used mainly in the sense that the spin vectors lie within a plane such that the components of the spin along two axes at right angles in the plane have a periodic variation along some arbitrary direction in the crystal. If this spin plane is perpendicular to the wave vector $\boldsymbol{k}$, and the variation is sinusoidal, the resulting arrangement gives a "screw" type of structure (Fig. 6a). If the wave vector lies in the spin plane, the arrangement may be termed "cycloidal" (Fig. 6b). A rather more complicated system is the "cone" spiral (Fig. 6c), in which there is also a fundamental (single spin axis) spin component perpendicular to the spiral spin plane.

The neutron diffraction patterns arising from spirals of this kind are characterized by the appearance of pairs of "satellite" magnetic reflections having the reciprocal lattice vectors $(\boldsymbol{R}^* \mp \boldsymbol{k})$, where $\boldsymbol{R}^*$ is the vector $2\pi(h\boldsymbol{a}^*+k\boldsymbol{b}^*+l\boldsymbol{c}^*)$ associated with a conventional Bragg peak of magnetic origin. Thus the positions of the satellites are related to the periodicity $(=2\pi/k)$ of the spiral and in general will not correspond to any small integral multiple of the unit cell dimensions.

As illustrated in Fig. 2, the Cr_2O_3 magnetic structure may be divided into two antiparallel sublattices A_1B_1 and A_2B_2 within each of which the spins are parallel. If now the spins within each sublattice are assumed to spiral such that $\boldsymbol{k}$ is parallel to the c axis, as in Fig. 7(a), it is necessary to assign a phase factor to relate the two sinusoidal functions for the purpose of intensity calculations. A convenient way to express this phase factor is by $k\Delta r_z$, where Δr_z is the difference between the components along the c axis of the position vectors of cations which are coupled antiparallel. Thus, when $k\Delta r_z$ is zero, corresponding to antiferromagnetic coupling within the basal planes of the two sublattices, the two spirals are exactly out of phase. A simple and reasonable assumption is that the spirals are coupled antiferromagnetically by one of the three interactions Γ_b, Γ_c, or Γ_d, each of which is negative in Cr_2O_3 itself (Table 1). The situation for Γ_b negative is depicted in Fig. 7(b) for the spin component perpendicular to the c axis.

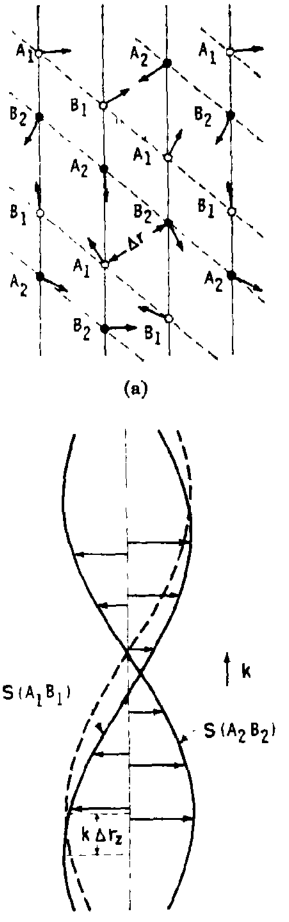

(a)

(b)

FIG. 7. Cycloidal spiral in the Cr_2O_3 type of magnetic structure with Γ_b negative. (a) shows the projection on the (110) plane and (b) shows the phase relationship between the sinusoidal functions for the two sublattices along an axis in the spin plane and perpendicular to c. The spirals are out of phase apart from a small phase factor $\boldsymbol{k}\cdot\Delta\boldsymbol{r}_z$.

For the cycloidal spiral described above, the powder intensities of the satellite reflections are given via equation 14 (see Appendix) by

$$I_{(hkl^-)} = Kp^2\left(\frac{1}{4}+\frac{\sin^2\alpha}{8}\right)\sin^2\left(2\pi lu-\frac{k\Delta r_z}{2}\right) \quad \text{at } \boldsymbol{R}=\boldsymbol{R}^*-\boldsymbol{k}$$

and

$$I_{(hkl^+)} = Kp^2\left(\frac{1}{4}+\frac{\sin^2\alpha}{8}\right)\sin^2\left(2\pi lu+\frac{k\Delta r_z}{2}\right) \quad \text{at } \boldsymbol{R}=\boldsymbol{R}^*+\boldsymbol{k}$$

where K includes proportionality, absorption, temperature, geometrical and multiplicity factors, α is the angle between the scattering vector $\boldsymbol{e}$ and the c axis and the other terms have their usual significance. The reciprocal lattice vector $\boldsymbol{R}^*$ is subject to the conditions $-h+k+l = 3n$ and $l = 2n'$. For the equally possible screw spiral case, the term $(\frac{1}{4}+\sin^2\alpha/8)$ must be replaced by $(\frac{1}{4}+\cos^2\alpha/4)$, both of these representing average q^2 values for equivalent reflections.

The corresponding expression for the Cr_2O_3 structure itself is

$$I_{(hkl)} = Kp^2 \sin^2\alpha \sin^2(2\pi lu) \text{ at } \boldsymbol{R} = \boldsymbol{R}^*$$

The same conditions as before apply to $\boldsymbol{R}^*$.

Intensity calculations were confined to the six cases corresponding to the spiral spin plane parallel or perpendicular to the c axis, combined with the three different phase factors associated with antiferromagnetic coupling of the two spirals through interactions of the type Γ_b, Γ_c and Γ_d.

In the case of a cone spiral, both fundamental and satellite peaks will appear on the diffraction pattern and their relative intensities will clearly depend upon the geometry of the cone. In the subsequent description, the magnitude of the spin is denoted by S, that of its fundamental component by S_0 and that of its spiral or rotating component by S_s. The fundamental component may have either the Cr_2O_3 or Fe_2O_3 type of magnetic order. In the latter case, it should be noted that antiferromagnetic coupling of the spiral components through Γ_c (within the basal plane) does not result in the *spins* being antiparallel, i.e. $\boldsymbol{S}(A_1) = \boldsymbol{S}_0+\boldsymbol{S}_s$ and $\boldsymbol{S}(A_2) = \boldsymbol{S}_0-\boldsymbol{S}_s$. In the former case, however, or when antiferromagnetic coupling of the spiral components is through Γ_b or Γ_d, the spins involved in these interactions are antiparallel, i.e.

$$\boldsymbol{S}(A_1) = \boldsymbol{S}_0+\boldsymbol{S}_s \text{ and } \boldsymbol{S}(A_2) = -\boldsymbol{S}_0-\boldsymbol{S}_s, \text{ etc.}$$

One final point that should be emphasized is that as the periodicity, λ, of the spiral decreases the satellite reflections move away from the positions associated with the reciprocal lattice vectors $\boldsymbol{R}^*$ of Cr_2O_3 type. Finally, when λ has the value of $c/3$, and given Γ_b negative, each of the satellites in a pair coalesces with one from an adjacent pair to give the pattern characteristic of Fe_2O_3, for which the condition necessary for magnetic reflections to appear is $l = 2n+1$. The intensities, of course, will depend upon the orientation of the spiral spin plane, a screw spiral leading to the room temperature magnetic structure of Fe_2O_3. Thus, in this rather artificial sense can be seen a relation between the lattices of Cr_2O_3 and Fe_2O_3 which is of some assistance in the interpretation of the neutron data about to be described.

5. NEUTRON DIFFRACTION DATA

Neutron diffraction data were obtained at the Westinghouse Testing Reactor. Samples were in the form of powders contained in tubes approximately $\frac{3}{8}$ in. dia. and 2 in. long. Initially, aluminum tubes were used, but in the later stages, vanadium tubes were found to be more suitable owing to the coincidence of an aluminum diffraction peak with an important magnetic reflection. The neutron wavelength was 1·14 Å.

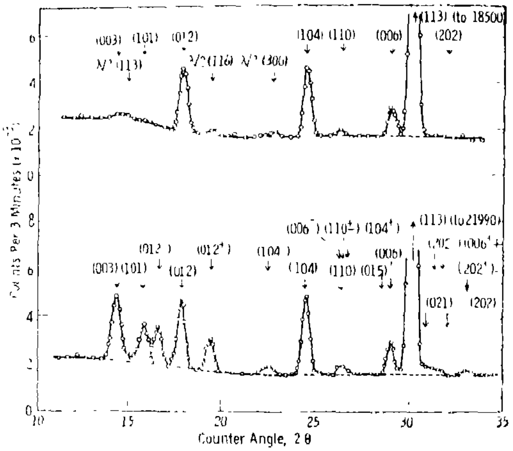

FIG. 8. Neutron diffraction patterns for 0·7 Cr_2O_3-0·3Fe_2O_3. The room temperature pattern is at the top and the pattern at 4°K at the bottom.

Neutron diffraction patterns of a number of solid solutions show many of the general features of the end members. However, for $0{\cdot}1 \leqslant x \leqslant 0{\cdot}35$, the patterns obtained at liquid nitrogen temperature reveal peaks of magnetic origin which cannot be indexed on the basis of the Fe_2O_3 or Cr_2O_3 magnetic structures. The data for $x = 0{\cdot}3$ illustrated in Fig. 8 show these peaks quite clearly. At 4°K (bottom pattern), in addition to reflections of Fe_2O_3 type such as (003) and (101), there are

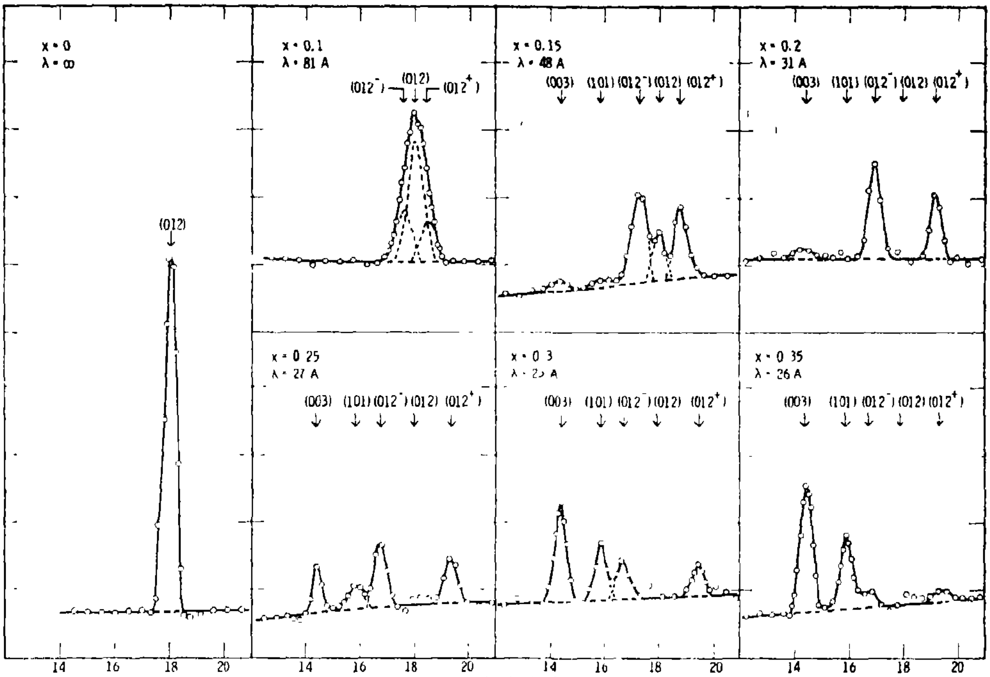

FIG. 9. Neutron diffraction data in the (012) region at 77°K for the system $(1-x)$ Cr_2O_3–xFe_2O_3. The room temperature data have been subtracted so that the nuclear component of (012) is eliminated.

six other observable peaks, distributed in pairs. Four of these namely, (012⁻), (012+), (104⁻) and (202+) are resolved, but the other two cannot be unambiguously indexed. Attempts to index these peaks conventionally were unsatisfactory, although some degree of correspondence could be obtained by doubling the *c* axis. By tripling one or other of the axes, such large unit cells are obtained that any indexing is of little value.

That this approach is inapplicable is clearly demonstrated in Fig. 9, which shows the patterns at 77°K in the (012) region for a number of compositions. In order to resolve the pattern more satisfactorily, the room temperature data have been subtracted so as to eliminate the nuclear component of the (012) peak. Such differences in the general background that exist are believed to arise mainly from slight changes in experimental conditions which proved to be necessary.

It is clear that the patterns in Figs. 8 and 9 show all the general features to be expected from a spiral arrangement with a periodicity which is dependent upon composition. In addition, the presence of fundamental peaks of Fe_2O_3 or Cr_2O_3

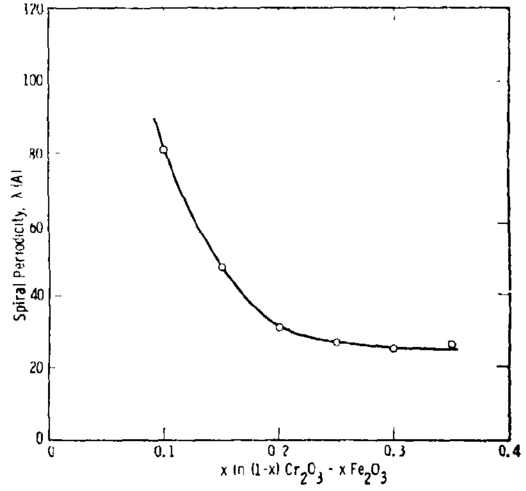

FIG. 10. Variation of the spiral periodicity at 77°K with composition for the system $(1-x)$ Cr_2O_3–xFe_2O_3.

type immediately suggests that some kind of cone spiral exists. A more detailed examination of the data reveals that in all cases the spiral peaks are situated about positions corresponding to the strongest magnetic reflections observed for Cr_2O_3. Calculations show that the wave vector of the spiral must lie along or close to the hexagonal c axis, and the periodicity as a function of composition at 77°K is illustrated in Fig. 10. There is a rapid increase as the composition approaches Cr_2O_3, which may be considered the special case for which the periodicity is infinite. Little, if any, broadening of the spiral peaks occurs and values of λ must be confined within fairly narrow limits throughout the specimens in spite of their being solid solutions. At $x = 0{\cdot}3$ the interplanar turn angle of the spiral component is about 33° and at $x = 0{\cdot}1$, about 10°.

(i) 0·7 Cr_2O_3–0·3 Fe_2O_3

Intensity calculations for the sample $x = 0{\cdot}3$ at 298°K and 4°K are summarized in Table 4. In these and subsequent calculations the form factor for Fe^{3+} quoted by NATHANS, PICKART and ALPERIN[48] has been combined with a form factor for Cr^{3+} determined in the present study from Cr_2O_3 on the assumption that the Cr^{3+} ion carries a moment of $3\mu_B$ at 0°K. Details of the latter will be given in another publication.[49] The neutron half-wavelength contribution has been subtracted from the observed intensities where appropriate, and by consideration of statistical counting errors, the choice of background intensity and errors caused by partial overlap of adjacent peaks, an estimated error in the observed intensities from these sources amounts on the average to around 1000 counts at low angles and 700 counts at high angles. Good agreement is obtained for a cone model in which the two spiral components are coupled antiparallel through Γ_c and the cone axis is perpendicular to c.

Because of the unorthodox magnetic behavior

Table 4. Comparison of observed intensities at 4°K *for* 0·7 Cr_2O_3–0·3 Fe_2O_3 *with those calculated for various models as described in the text*

hkl	I_{nucl} (calc.) $u = 0{\cdot}352$ $x = 0{\cdot}553$	I_{mag} (calc.) Fe_2O_3 component	I_{mag} (calc.) Spiral component Spin plane $\parallel c$ Γ_b	Γ_c	Γ_d	I_{obs} (counts $\times 10^{-2}$) 4°K	298°K
003	—	180	—	—	—	175	—
101	—	93	—	—	—	98	—
012^-	—	—	108	96	90	94	—
012	155	—	—	—	—	161	158
012^+	—	—	47	59	65	61	—
104^-	—	—	5	15	28	18	—
104	159	—	—	—		161	157
006^-	—	—	4	2	1	28	—
110	15	—	—	—	—		11
$110^{\mp}$	—	—	3	0	7		—
104^+	—	—	10	5	1		—
015	—	0	—	—	—	74	—
006	70	—	—	—	—		77
113	961	64	—	—	—	1032	982
021	—	10	—	—	—	16	—
202^-	—	—	13	12	11	16	—
006^+	—	—	1	1	2	<5	—
202	0	—	—	—	—	<5	<5
202^+	—	—	8	10	11	12	—
024^-	—	—	1	3	5	<5	—
024	239	—	—	—	—	221	230
107	—	20	—	—	—	29	
116^-	—	—	6	4	1		—
024^+	—	—	3	1	0	<5	—

of this sample, several scans over the (012) region were performed at various temperatures. Some of the patterns are shown in Fig. 11. Values of the Fe_2O_3 component S_0 and the spiral component S_s, together with the resultant S calculated on the basis of the above cone model are plotted as a function of temperature in Fig. 12. There are several points of interest. The temperature at which the spontaneous moment is first observed is about 30°K lower than that at which coherent magnetic diffraction peaks appear. As the temperature falls, reflections of Fe_2O_3 type increase in intensity, but no satellite peaks are present down to 112°K. At 96°K there is a fairly strong spiral contribution. Thus the point at which the spontaneous moment falls to zero (Fig. 3) is obviously closely connected with a second magnetic ordering transition involving the superposition of a spiral arrangement on the existing Fe_2O_3 type of order. As the temperature is decreased to 4°K, S_s increases much more rapidly than S_0, corresponding to an increase in the cone half angle. At the same time, the periodicity of the spiral retains a constant value of about 25 Å. Comparison of the temperature dependence of the resultant average spin moment S per cation with that expected from an appropriate Brillouin function using the theoretical mean moment at 0°K of $3{\cdot}6\mu_B$ per cation reveals quite a large deficit, this fact implying that the long range ordering scheme is far from perfect.

Thus, as a good approximation the low temperature phase line drawn in Fig. 5 may be taken to indicate the extent of the region in which there is a spiral modulation of the Fe_2O_3 type of spin lattice. It now remains to examine whether any similar low temperature transition, undetectable by magnetic measurements and involving modulation of the Cr_2O_3 type of spin structure, occurs at lower Fe_2O_3 concentrations.

(ii) $0{\cdot}85\ Cr_2O_3$–$0{\cdot}15\ Fe_2O_3$

Figure 13 illustrates the patterns obtained in the (012) region at various temperatures for $x = 0{\cdot}15$. The room temperature data have been subtracted to eliminate the nuclear contribution to (012) and it can be seen that in this case there is a fundamental component of Cr_2O_3 type. A cursory glance leads to the conclusion that there is indeed a second transition between 185 and 163°K. However, a

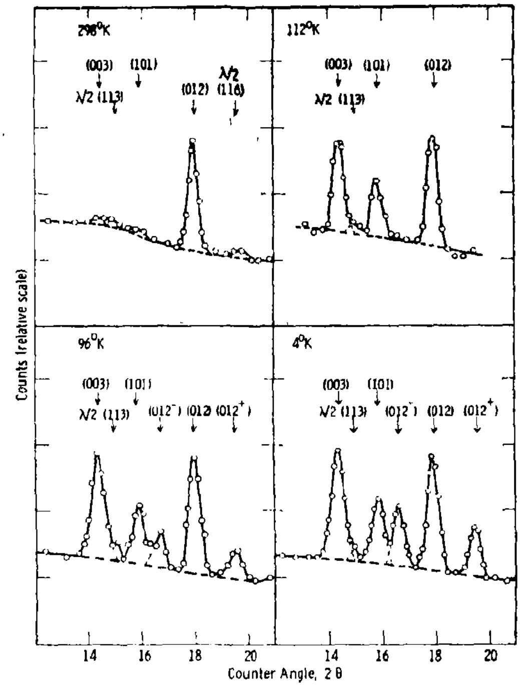

FIG. 11 Neutron diffraction patterns in the (012) region at various temperatures for $0{\cdot}7\ Cr_2O_3$–$0{\cdot}3\ Fe_2O_3$.

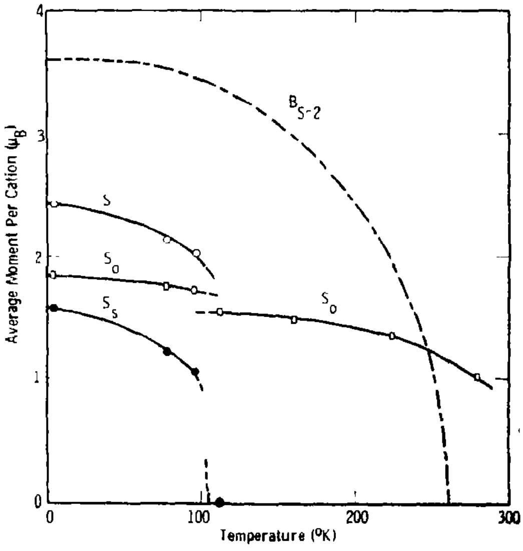

FIG. 12. Variation of neutron diffraction moments with temperature for $0{\cdot}7\ Cr_2O_3$–$0{\cdot}3\ Fe_2O_3$. The broken line represents the Brillouin function for $S = 2$ and $\mu_0 = 3{\cdot}6$ μ_B per cation.

careful assessment of the data shows that there is a fairly rapid increase in the spiral periodicity between 77 and 148°K and an alternative speculation is that at 185°K, the periodicity is large enough for the satellites to be virtually superimposed. Although this may seem to be a rather technical difference, it does carry the implication that there is only one magnetic ordering transition between 298 and 77°K, in agreement with the susceptibility measurements.

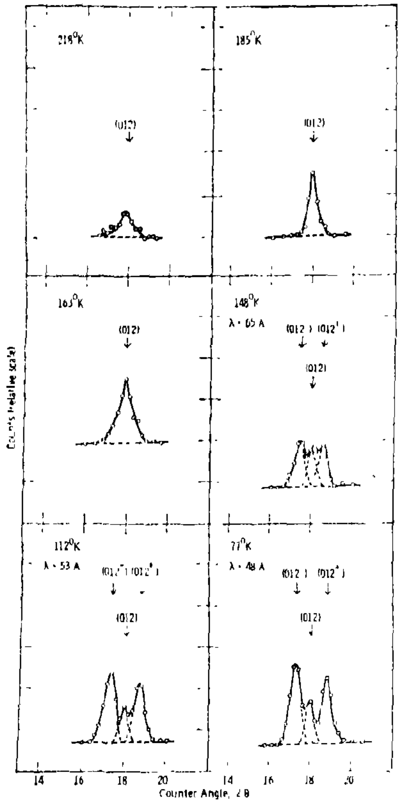

FIG. 13. Neutron diffraction patterns in the (012) region at various temperatures for 0·85 Cr_2O_3–0·15 Fe_2O_3. The room temperature data have been subtracted so that the nuclear component of (012) is eliminated.

Owing to the superposition of the nuclear and fundamental magnetic reflections and the overlap of the $(012\mp)$ satellite peaks with the (012) reflection, neither the orientation of the cone nor the type of spiral coupling can be determined with any certainty by intensity calculations, even though good counting statistics were obtained. Acceptable agreement is given by all four of the combinations obtained with the cone axis parallel or perpendicular to the *c* axis and spiral coupling through Γ_b or Γ_c. However, the choice of model has but little effect on the numerical values of the spin moments obtained and the temperature dependence of these is shown in Fig. 14, for the case in which S_0 is parallel to the *c* axis with spiral coupling through Γ_b. The variation corresponds roughly to a gradual increase in the cone angle as the temperature is lowered. Once again comparison with a suitable Brillouin function having the theoretical spin moment per cation at 0°K of $3{\cdot}3\mu_B$ reveals a considerable deficit in the observed moments.

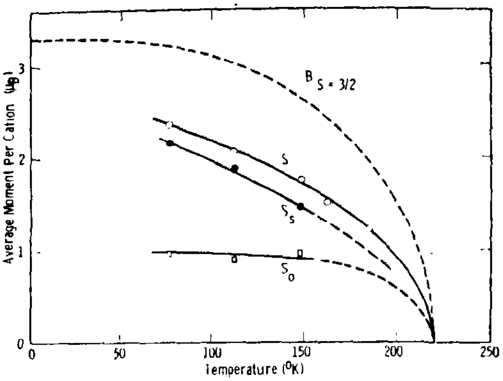

FIG. 14. Variation of neutron diffraction moments with temperature for 0·85 Cr_2O_3–0·15 Fe_2O_3. The broken line represents the Brillouin function for $S = 3/2$ and $\mu_0 = 3{\cdot}3\ \mu_B$ per cation.

It can be seen from Fig. 9 that there is a small but significant contribution to the (003) and (101) reflections amounting to about $0{\cdot}5\mu_B$ which complicates this simple interpretation. It is possible that two magnetic phases exist in this composition range, an Fe_2O_3 type cone spiral perhaps being propagated in regions having a slight local excess of Fe cations.

(iii) 0·9 Cr_2O_3–0·1 Fe_2O_3

Accurate intensity data were also obtained for the sample with $x = 0{\cdot}1$ at 298 and 77°K. In spite of the lack of resolution in the (012) region, intensity calculations definitely favor a model in which the cone axis is directed along the *c* axis. The analysis was performed in the following fashion. The $(104^{\mp})$ peaks are sufficiently resolved for the periodicity to be determined. The relative intensities of the $(012^{\mp})$ and $(202^{\mp})$ peaks can then be calculated for the various models. The total magnetic contributions at 77°K in the unresolved (012) and (202) region are found by subtraction of the nuclear intensities at 298°K. It is fortunate that the nuclear intensity of (202) is negligible, while that of (012) amounts only to about 25 per cent of the total intensity. Scale factors appropriate to S_0 and S_s may then be assessed for the various models, and the calculated intensities for the most satisfactory of these are listed in Table 5. Excellent agreement is given by the arrangement in which S_0 is parallel to *c* and the spirals are coupled antiparallel through Γ_b, although coupling through Γ_c gives almost as satisfactory results. Somewhat poorer, but nevertheless acceptable, numerical agreement is obtained with the model having S_0 perpendicular to *c* and coupling through Γ_b, but a synthesis of the (202) peak from the calculated figures gives a much broader and flatter peak than is actually observed. The first model is therefore preferred.

Table 5. Comparison of observed intensities at 77°K *for* 0·9 Cr_2O_3–0·1 Fe_2O_3 *with those calculated for various models as described in the text*

hkl	I_{nucl} (calc.) $u = 0{\cdot}348$ $x = 0{\cdot}556$	I_{mag} (calc.) Cone axis $\parallel c$			I_{mag} (calc.) Cone axis $\perp c$	I_{obs} (counts $\times 10^{-2}$)
		Γ_b	Γ_c	Γ_d	Γ_b	
012^-	—	72	71	65	147	456
012	111	215	211	213	89	
012^+	—	59	65	68	112	
104^-	—	12	16	19	17	13
104	61	19	19	19	18	83
104^+	—	15	13	10	20	14
110	0	0	0	0	0	<3
$110^{\mp}$	—	0	0	0	0	
006^-	—	3	2	2	3	5
006	76	0	0	0	1	78
006^+	—	1	2	3	1	833
113	839	—	—	—	—	
202^-	—	8	8	7	20	52
202	0	37	36	37	10	
202^+	—	7	8	8	17	

Calculated moments at various temperatures for a number of compositions are summarized in Table 6, together with the cone model found to give the best intensity agreement. The type of spiral coupling should be accepted with some reservation, as in general it is not possible to discriminate between Γ_b and Γ_c coupling with confidence. However, it is probably no accident that Γ_c coupling seems to predominate, as the spiral components are then almost exactly out of phase.

One final observation concerns the effect of a magnetic field of about 12 kOe applied parallel to the scattering vector. No change in the intensities of the magnetic peaks could be detected when an Fe_2O_3 type of spin component was small or absent. However, in the sample $x = 0{\cdot}3$, the intensity of the (101) reflection increased by about 50 per cent, while the intensities of the $(012^{\mp})$ peaks were diminished by about 10 per cent. Qualitatively, this is the expected behavior if it is assumed that the small parasitic ferromagnetic moment associated with the Fe_2O_3 type of structure rotates within the basal planes to give the maximum component in the field direction, thereby aligning the antiferromagnetic axis perpendicular to the field. Effectively this amounts to an increase in

q^2 for (101) and a decrease in q^2 for $(012\mp)$ of roughly the right magnitude. There is no evidence that the periodicity of the spiral or the interaction scheme is disturbed by a field of this strength.

Table 6. Calculated neutron diffraction moments in μ_B per cation at various temperatures for the system $(1-x)\ Cr_2O_3$–$x\ Fe_2O_3$, together with type of spiral coupling and cone half-angles and orientation

x	S_0(Fe_2O_3 type)			S_0(Cr_2O_3 type)			S_s			S			Theoretical S at 0°K	Spiral coupling	S_0	β (77°K)
	4°K	77°K	298°K	4°K	77°K	298°K	4°K	77°K	298°K	4°K	77°K	298°K				
0·1		—	—		2·03	—		1·69	—		2·64	—	3·2	Γ_b	$\parallel_c$	40°
0·15		~0·5	—		0·97	—		2·15	—		2·36	—	3·3	Γ_b(?)	$\parallel_c$(?)	66°
0·2	0·80	0·67	—	—	—	—	2·11	1·92	—	2·26	2·03	—	3·4	Γ_c	$\perp_c$	71°
0·25		1·28	—		—	—		1·56	—		2·02	—	3·5	Γ_c	$\perp_c$	51°
0·3	1·84	1·76	—	—	—	—	1·58	1·22	—	2·43	2·14	—	3·6	Γ_c	$\perp_c$	35°
0·35		2·26	1·36		—	—		0·80			2·40	1·36	3·7	Γ_c	$\perp_c$	19°
0·5			2·66			—			—			2·66	4·0	—	$\perp_c$	—

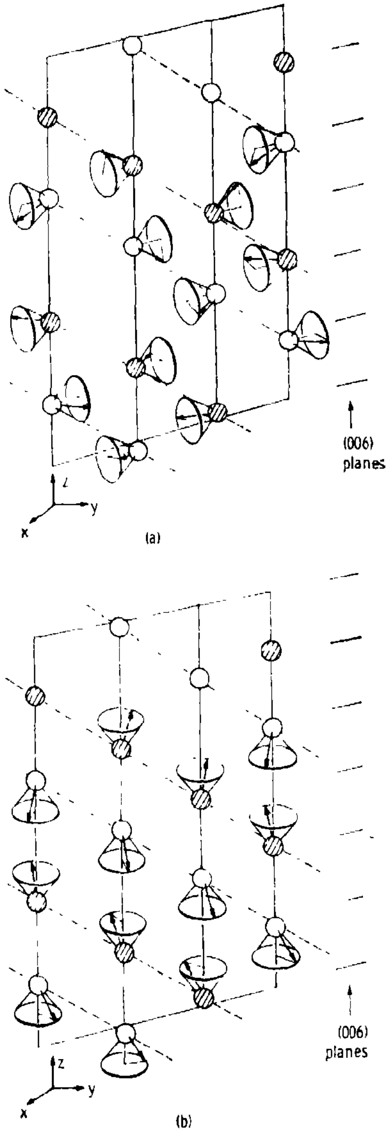

FIG. 15. A (110) section of the corundum lattice showing cone spirals based upon the (a) Fe_2O_3, (b) Cr_2O_3 magnetic structures. The heavy arrows indicate the spin directions. The A_1B_1 sublattice is represented by the shaded circles, and the A_2B_2 sublattice by the open circles.

6. DISCUSSION

An attempt has been made in Fig. 15 to provide a three-dimensional impression of the overall spin structures arising in the two cases in which the fundamental components are of Fe_2O_3 and Cr_2O_3 type respectively. As described earlier in the text, the spiral component is represented by a rotating radius in the cone base, the fundamental component lies along the cone axis and the resultant, indicated by a heavy arrow, lies along a slant edge of the cone. Although the cone axes are shown lying along the $[1\bar{1}0]$ axis in Fig. 15(a), they could, of course, lie in any other direction in the basal plane without causing any change in the powder intensities.

Table 7. Angles between the spins involved in the interactions Γ_a, Γ_b, Γ_c *and* Γ_d *at* 77°K *as a function of composition in the system* $(1-x)Cr_2O_3$–xFe_2O_3

x	Interaction Γ_a	Γ_b	Γ_c	Γ_d	Spiral coupling	S_0
0	0°	180°	180°	180°	—	$\parallel c$
0·1	6°	180°	174°	167°	Γ_b	$\parallel c$
0·15	←	Two phase region?		→	?	?
0·2	46°	155°	142°	155°	Γ_c	$\perp c$
0·25	84°	156°	101°	156°	Γ_c	$\perp c$
0·3	114°	162°	70°	162°	Γ_c	$\perp c$
0·35	143°	170°	39°	170°	Γ_c	$\perp c$
0·5	180°	180°	0°	180°	—	$\perp c$
1·0	180°	180°	0°	180°	—	$\perp c$*

* 298°K.

One very important feature of this model is that it provides a simple mechanism by which continuity is preserved as the Cr_2O_3 magnetic structure passes to the Fe_2O_3 structure, except for a "flip" of the cone axis at some stage. The sample $x = 0{\cdot}15$ probably lies in this range, and as has been briefly mentioned, a narrow essentially two-phase region may exist in the magnetic phase diagram around this composition.

The dependence of the cone half-angle β upon the composition (Table 6) illustrates the continuity of the structures. Initially 0° in Cr_2O_3, β then rises as Fe_2O_3 is substituted to a maximum of about 66°. Around this point, there is a flip of the cone axis and further substitution of Fe_2O_3 leads to a decrease in β. The variation of β, the fact that a pure spiral ($\beta = 90°$) is not observed and the existence of a two-phase region probably reflect the anisotropy requirements of the system.

One of the characteristics of the above cone model is that the interaction scheme may still be considered on the basis of only four interactions involving reasonably close cation–anion–cation contacts, exactly as in Fe_2O_3 and Cr_2O_3. The same notation as before, namely, Γ_a, Γ_b, Γ_c and Γ_d may be used to describe these interactions which, however, are in general no longer parallel or antiparallel. The respective angles which the resultant spin directions make with each other vary according to the composition, and to a lesser extent the temperature. In Table 7 are listed the angles between pairs of spins described by Γ_a, etc. for the various compositions at 77°K. It can be seen that on the whole both Γ_b and Γ_d deviate slightly from 180°.

If one were of overriding importance, the respective spin moments should align antiparallel, thus imposing an angle of considerably less than 180° upon the other interaction. There is thus the implication that Γ_b and Γ_d are of comparable importance, particularly so when it is recalled that the numbers of each interaction are in the ratio 3:1. This fact perhaps arises from the effect of appreciable direct cation–cation interactions of the type proposed by GOODENOUGH.(50) Because of the relatively small separation of cation pairs A_1B_2 and A_2B_1 along the c axis and the favorable configuration of the oxygen octahedra, Goodenough suggests that in Cr_2O_3 at least, there may be sufficient overlap of the 3*d* orbitals to produce direct interactions comparable in strength with the indirect Cr–O–Cr interactions. The cation separation as a function of composition (Table 3) may therefore have some significance.

The model so far adopted is perhaps open to criticism on the grounds that it is difficult to understand why long range order of this sort is propagated in a lattice which on an atomic level is inhomogeneous. A possibly more feasible scheme would involve the coexistence of regions having long range order of either Fe_2O_3 or Cr_2O_3 type and regions having short range order as found in the Fe_2O_3–$FeTiO_3$(42,43) and Fe_2O_3–V_2O_3(18) systems.

However, there is one important difference. There is no evidence that the Ti or V ions in these systems play any role in the long range magnetic order, but it is clear that the Cr ions do. This, together with the fact that a given ion in one of the sublattices A_1B_1 or A_2B_2 can couple with six equivalent neighbors in the same sublattice by means of the interaction Γ_a, provides a means by which the exchange integrals J_A for solid solutions can average out to values intermediate between those for Cr_2O_3 and Fe_2O_3 respectively. Thus at some critical stage, the values of J_A, J_B, J_C and J_D (and perhaps others associated with cations separated by more than one anion which have not been considered) are no longer consistent with a simple antiferromagnetic structure, and in this region a spiral structure has the lowest energy. If Γ_a were strong and negative in Fe_2O_3 and fairly strong and positive in Cr_2O_3 in accordance with their respective Néel temperatures, it would be expected to be rather weak in the region around $x = 0{\cdot}3$.

Simple considerations show that the spin orientations in Table 7 can equally well be achieved by a "canted" structure, which involves two spin axes. In this the interplanar turn angle between spins on A_1B_1, etc. would alternate between positive and negative, in contrast to the spiral structure, in which the spins always rotate in a positive sense. This canted structure corresponds to the special case of the cone spiral with periodicity *c*/3. The fact that a much longer periodicity is actually observed may depend upon the existence of interactions through two layers of oxygen ions. Such interactions are required for the propagation of magnetic order in $FeTiO_3$, for example.(42)

It is nevertheless quite clear that a statistical cation distribution will create fluctuations in the long range magnetic order, which may take the form of regions with short range order or of modulation of the long range sinusoidal function. The fact that the calculated moments fall considerably short of the theoretical ones is believed to result from this. By examination of the background intensity in the (012) region of the diffraction patterns, a considerable amount of short range order is seen to exist. It is hoped that a Mössbauer study which is under way will reveal more exactly the nature of the "missing" moment.

A second criticism is that in the region characterized by a fundamental component of Fe_2O_3 type (cone axis perpendicular to *c*), anisotropy considerations make it very unlikely that the spins will rotate away from the basal plane in the direction of *c* to the same extent as they will rotate within the plane. An elliptic function would probably be more suitable. However, as a change in the orientation of the cone axis is believed to occur around $x = 0{\cdot}15$, the anisotropy may be relatively small in this region and a sinusoidal function may approximate fairly closely to the true state of affairs.

In addition to the proposed model, there is another which deserves some mention. For example, it is possible that the spins rotate away from a single spin axis to some extent such that the component along this axis may be described by the sum of a constant term and a sinusoidal term, while the spin component perpendicular to this axis is disordered. On the Fe_2O_3 side, rotation within the basal plane could occur so that the anisotropy requirements are satisfied. The intensity data do not favor this model on the whole, but are not sufficiently accurate to entirely discriminate against it. Calculations show that the moments thus obtained are very much closer to the theoretical moments, but the simple interaction scheme which is one of the features of the cone model and which correlates so well with the crystal structure no longer exists.

One final point concerns the behavior of the small spontaneous moment through the low temperature transition when $0{\cdot}25 \leqslant x \leqslant 0{\cdot}4$ (Fig. 3). In agreement with DZYALOSHINSKY's theory,(33) this appears only when there is a fundamental component of Fe_2O_3 type present. The decrease in the moment to zero with the onset of the spiral structure could perhaps be attributed to the fact that the MORIYA interaction(34) no longer results in the canted structure being the ground state as in the simple case of Fe_2O_3. However, the origin of the subsequent increase in moment (or possibly reversal in its direction) is not understood.

In conclusion then, as a good approximation the magnetic structures of the Cr_2O_3–Fe_2O_3 system can be described by a cone spiral, and the simple antiferromagnetic structures of the end members merely represent special cases of this spiral. Any change in composition can be accommodated by a change in the geometry of the cone and the periodicity of the spiral in such a way that complete continuity is achieved, apart from a narrow region where the orientation of the cone axis changes. Long, rather than short, range magnetic order is believed to arise because the nature of the crystal structure allows one of the principal exchange integrals, which is negative in Fe_2O_3 and positive in Cr_2O_3, to assume a wide range of intermediate values in solid solutions.

Acknowledgements—We are grateful to Dr. R. NATHANS for helpful discussions, and should like to acknowledge the valuable assistance of Mr. M. JANOCKO and Mr. J. RIEGER in various phases of the experimental study.

REFERENCES

1. PAULING L. and HENDRICKS S. B., *J. Amer. chem. Soc.* **47**, 781 (1925).
2. SHULL C. G., STRAUSER W. A. and WOLLAN E. O., *Phys. Rev.* **83**, 333 (1951).
3. BROCKHOUSE B. N., *J. chem. Phys.* **21**, 961 (1953).
4. FÖEX M. and WUCHER J., *C.R. Acad. Sci., Paris* **241**, 184 (1955).
5. PEARSON A. D., *J. Phys. Chem. Solids* **5**, 316 (1958).
6. CARR P. H. and FONER S., *J. appl. Phys.* **31**, 344S (1960).
7. FÖEX M., GOLDSZTAUB S., WEY R., JAFFRAY J., LYAND R. and WUCHER J., *J. Rech.* **4**, 237 (1952).
8. SHIRANE G., PICKART S. J. and NEWNHAM R., *J. Phys. Chem. Solids* **13**, 166 (1960).
9. PAOLETTI A. and PICKART S. J., *J. chem. Phys.* **32**, 308 (1960).
10. MCGUIRE T. R., SCOTT E. J. and GRANNIS F. H., *Phys. Rev.* **102**, 1000 (1956).
11. LI Y. Y., *Phys. Rev.* **102**, 1015 (1956).
12. IIDA S., *J. phys. Soc. Japan* **11**, 1300 (1956).
13. ISHIKAWA Y. and AKIMOTO S., *J. phys. Soc. Japan* **12**, 1083 (1957).
14. OSMOND W. P., *Proc. phys. Soc., Lond.* **79**, 394 (1962).
15. WRETBLAD P. E., *Z. anorg. Chem.* **189**, 329 (1930).
16. DICERBO R. K. and SEYBOLT A. U., *J. Amer. ceram. Soc* **42**, 430 (1959).
17. SHIRANE G., COX D. E., TAKEI W. J. and RUBY S. L. *J. phys. Soc. Japan* **17**, 1598 (1962).
18. COX D. E., TAKEI W. J., MILLER R. C. and SHIRANE G., *J. Phys. Chem. Solids* **23**, 863 (1962).
19. KASPER J. S. and DECKER B. F., *American Crystallographic Association, Annual Meeting* (1956).
20. CORLISS L. M., HASTINGS J. M. and WEISS R. J., *Phys. Rev. Letters* **3**, 211 (1959).
21. BYKOV V. N., GOLOVKIN V. S., AGEEF N. V., LEVDIK V. A. and VINOGRADOV S. I., *Dokl. akad. nauk. S.S.S.R.* **128**, 1153 (1959).
22. SHIRANE G. and TAKEI W. J., *J. Phys. Soc. Japan* **17**, *Suppl.* **B-III**, 35 (1962).
23. WILKINSON M. K., CHILD H. R., KOEHLER W. C., CABLE J. W. and WOLLAN E. O., *J. phys. Soc. Japan* **17**, *Suppl.* **B-III**, 27 (1962).
24. KOEHLER W. C., CABLE J. W., WOLLAN E. O. and WILKINSON M. K., *J. phys. Soc. Japan* **17**, *Suppl.* **B-III**, 32 (1962).
25. HERPIN A., MÉRIEL P. and VILLAIN J., *C.R. Acad. Sci., Paris* **249**, 1334 (1959).
26. YOSHIMORI A., *J. phys. Soc. Japan* **14**, 807 (1959).
27. HASTINGS J. M. and CORLISS L. M., *Phys. Rev.* **126**, 556 (1962).
28. VILLAIN J., *J. Phys. Chem. Solids* **11**, 303 (1959).
29. KAPLAN T. A., *Phys. Rev.* **116**, 888 (1959).
30. COOPER B. R., *Phys. Rev.* **118**, 135 (1960).
31. OVERHAUSER A. W. and ARROTT A., *Phys. Rev. Letters* **4**, 226 (1960).
32. LYONS D. H., KAPLAN T. A., DWIGHT K. and MENYUK N., *Phys. Rev.* **126**, 540 (1962).
33. DZYALOSHINSKY I., *J. Phys. Chem. Solids* **4**, 241 (1958).
34. MORIYA T., *Phys. Rev.* **120**, 91 (1960).
35. PAUTHENET R., *C.R. Acad. Sci., Paris* **243**, 1499 (1956).
36. GORTER E. W., *Philips Res. Rep.* **9**, 403 (1954).
37. NÉEL L., *Ann. Phys., Paris* **3**, 137 (1948).
38. LIN S. T., *Phys. Rev.* **116**, 1447 (1959).
39. POUILLARD E., *Ann. Chim.* **5**, 164 (1950).
40. *International Tables for X-ray Crystallography*, Vol. **1**, Kynoch Press, England (1952).
41. BARTH T. F. W. and POSNJAK E., *Z. Kristallogr.* **88**, 265 (1934).
42. SHIRANE G., PICKART S. J., NATHANS R. and ISHIKAWA Y., *J. Phys. Chem. Solids* **10**, 35 (1959).
43. RUBY S. L. and SHIRANE G., *Phys. Rev.* **123**, 1239 (1961).
44. KURIYAMA M., SHIRANE G., COX D. E. and FLINN P. (to be published).

45. Shirane G., Cox D. E. and Ruby S. L., *Phys. Rev.* **125**, 1158 (1962).
46. Shull C. G. and Wollan E. O., *Solid State Physics*, Vol. 2 (Edited by Seitz F. and Turnbull D.), Academic Press, New York (1956).
47. Newnham R. E. and de Haan Y. M., *Z. Krystallogr.* **117**, 235 (1962).
48. Nathans R., Pickart S. J. and Alperin H. A., *J. phys. Soc. Japan* **17**, *Suppl.* **B-III**, 7 (1962).
49. Takei W. J., Cox D. E. and Shirane G., *Phys. Rev.* (in press).
50. Goodenough J. B., *Phys. Rev.* **117**, 1142 (1960).
51. Koehler W. C., *Acta Cryst.* **14**, 535 (1961).

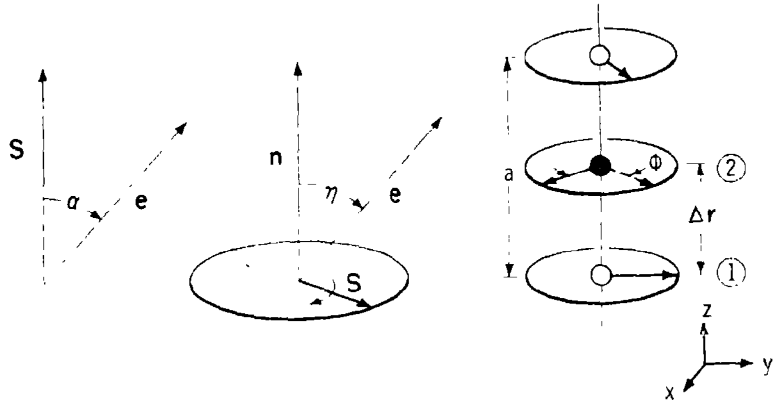

(a) Single spin axis (b) Spiral (c) Two spirals with phase difference Φ

Fig. 16. Types of spin arrangement illustrating the various symbols used in the text.

APPENDIX

DERIVATION OF INTENSITY FORMULAE

Intensity expressions for spiral structures have been described in a number of recent publications; for example, Yoshimori,(26) Koehler(51) and Hastings and Corliss.(27) However, the following simple formulae may prove to be convenient in many cases, in particular where the structure may be represented as two spirals which are not exactly in or out of phase. The latter situation is more likely to arise when the crystal structure is of such a nature that several possible non-equivalent interactions exist, as in the corundum type oxides

The spin vector of a cation in a cone spiral type of magnetic structure is given by

$$\boldsymbol{S} = \mu \sin\beta(\boldsymbol{x} \sin \boldsymbol{k} \cdot \boldsymbol{r}_n + \boldsymbol{y} \cos \boldsymbol{k} \cdot \boldsymbol{r}_n) + \boldsymbol{z}\mu \cos\beta \tag{1}$$

in which μ is the magnitude of the moment, β is the cone half-angle, $\boldsymbol{x}$, $\boldsymbol{y}$ and $\boldsymbol{z}$ are unit vectors along orthogonal axes, $\boldsymbol{r}_n$ is the position vector of the cation and $\boldsymbol{k}(= 2\pi/\lambda)$ is the wave vector of the spins. When $\beta = 0$, the structure reduces to one of single spin axis type, and when $\beta = \pi/2$, a simple spiral is obtained. In the latter event, there are two cases of special interest. If $\boldsymbol{k}$ is parallel to $\boldsymbol{z}$, the arrangement is a screw spiral (Fig. 6a), and if $\boldsymbol{k}$ is perpendicular to $\boldsymbol{z}$, a cycloidal spiral is obtained (Fig. 6b).

Closely related to the spiral is the sinusoidal type of arrangement in which

$$\boldsymbol{S} = \boldsymbol{z}\mu \sin \boldsymbol{k} \cdot \boldsymbol{r}_n \tag{2}$$

By analogy to the former, if $\boldsymbol{k}$ is parallel to $\boldsymbol{z}$ the arrangement may be termed "longitudinal" and if $\boldsymbol{k}$ is perpendicular to $\boldsymbol{z}$, "transverse".

The intensity of the diffracted neutron beam is given by

$$I = Kq^2F^2_{\text{mag}} \tag{3}$$

where K contains a proportionality constant and temperature and geometrical factors, and F_{mag} is the magnetic structure factor. The value of q^2 depends upon the direction of the scattering vector $\boldsymbol{e}$ (normal to the scattering plane) and the spin configuration. For a single spin axis (ferromagnetic or antiferromagnetic) or sinusoidal structure

$$q^2 = \sin^2\alpha \tag{4}$$

where α is the angle between $\boldsymbol{e}$ and $\boldsymbol{S}$ (Fig. 16a). For a spiral structure, a convenient expression is

$$q^2 = \tfrac{1}{2}(1 + \cos^2\eta) \tag{5}$$

where η is the angle between $\boldsymbol{e}$ and $\boldsymbol{n}$, the normal to the spin plane (Fig. 16b). Expressed in this way, q^2 contains an additional factor of $\frac{1}{2}$ which results from splitting of the fundamental peaks.

When the structure is essentially a spiral derived from an antiferromagnetic arrangement, as in chromium, it may be rather more convenient to consider it as the superposition of two ferromagnetic spirals coupled exactly out of phase. The present Cr_2O_3–Fe_2O_3 system provides an example of two cone spirals coupled with a phase difference determined by the various exchange interactions. First a simplified model is considered which is believed to give a clear idea of the physical picture involved.

Two sublattices are depicted in Fig. 16(c) in which it is assumed that $\lambda \geqslant 2a$. The spin vector of an ion in one sublattice (open circles) whose position vector is $\boldsymbol{r}_n$ is given by

$$\boldsymbol{S}_1 = \boldsymbol{x}\sin\boldsymbol{k}\cdot\boldsymbol{r}_n+\boldsymbol{y}\cos\boldsymbol{k}\cdot\boldsymbol{r}_n \qquad (6)$$

In the other sublattice (closed circles)

$$\boldsymbol{S}_2 = \boldsymbol{x}\sin(\boldsymbol{k}\cdot\boldsymbol{r}_m+\Phi)+\boldsymbol{y}\cos(\boldsymbol{k}\cdot\boldsymbol{r}_m+\Phi) \qquad (7)$$

where Φ represents the phase difference between the two spirals. One sublattice is related to the other by the translation vector $\boldsymbol{\Delta r}(\leqslant a/2$ in magnitude) such that

$$\boldsymbol{r}_m = \boldsymbol{r}_n+\boldsymbol{\Delta r} \qquad (8)$$

If the points $\boldsymbol{r}_n$ are taken as origins of the chemical unit cell, the magnetic structure factor is given by the standard summation process as

$$F^-_{\text{mag}} = p(1+\exp[i\Phi]\exp[i\boldsymbol{R}^*\cdot\boldsymbol{\Delta r}]) \quad \text{at } \boldsymbol{R} = \boldsymbol{R}^*-\boldsymbol{k} \qquad (9)$$

$$F^+_{\text{mag}} = p(1+\exp[-i\Phi]\exp[i\boldsymbol{R}^*\cdot\boldsymbol{\Delta r}]) \quad \text{at } \boldsymbol{R} = \boldsymbol{R}^*+\boldsymbol{k} \qquad (10)$$

where $\boldsymbol{R}^* = 2\pi(h\boldsymbol{a}^*+k\boldsymbol{b}^*+l\boldsymbol{c}^*)$ and $p = 0{\cdot}269\times f\times\mu_B$ and is assumed the same for each ion.

A number of special cases will now be considered.

(1) $\Phi = 0$. This is a trivial solution, corresponding to a single spiral.

(2) $\Phi = \pi$. The two spirals are exactly out of phase. If $\boldsymbol{\Delta r} = \boldsymbol{a}/2$, this corresponds to the chromium case, and

$$F^{\mp}_{\text{mag}} = p(1-\exp[i\boldsymbol{R}^*\cdot\boldsymbol{\Delta r}]) \text{ at } \boldsymbol{R} = \boldsymbol{R}^*\mp\boldsymbol{k} \qquad (11)$$

(3) $\boldsymbol{S}_1$ parallel to $\boldsymbol{S}_2$. Then

$$\boldsymbol{k}\cdot\boldsymbol{\Delta r}+\Phi = 0, \text{ or } \Phi = -\boldsymbol{k}\cdot\boldsymbol{\Delta r}$$

$$F^{\pm}_{\text{mag}} = p(1+\exp[i\boldsymbol{R}^*\mp\boldsymbol{k})\cdot\boldsymbol{\Delta r}]) \quad \text{at } \boldsymbol{R} = \boldsymbol{R}^*\mp\boldsymbol{k} \qquad (12)$$

(4) $\boldsymbol{S}_1$ antiparallel to $\boldsymbol{S}_2$. Then

$$\boldsymbol{k}\cdot\boldsymbol{\Delta r}+\Phi = \pi \text{ or } \Phi = \pi-\boldsymbol{k}\cdot\boldsymbol{\Delta r}$$

$$F^{\mp}_{\text{mag}} = p(1-\exp[i(\boldsymbol{R}^*\mp\boldsymbol{k})\cdot\boldsymbol{\Delta r}]) \text{ at } \boldsymbol{R} = \boldsymbol{R}^*\mp\boldsymbol{k} \qquad (13)$$

The Cr_2O_3–Fe_2O_3 system may be considered to fall into category (4) above. $\boldsymbol{S}_1$ and $\boldsymbol{S}_2$ now correspond to the spins involved in one of the three interactions Γ_b, Γ_c or Γ_d, and $\boldsymbol{\Delta r}$ is the appropriate translation vector, originating at A_2, say. As $\boldsymbol{k}$ is parallel to the c axis, $\boldsymbol{k}\cdot\boldsymbol{\Delta r}$ may be replaced by $k\Delta r_z$ where Δr_z is the magnitude of the component of $\boldsymbol{\Delta r}$ along this axis. Summation over the hexagonal unit cell yields through equations (5) and (13) the intensity expression for the spiral case:

$$I^{\mp}_{\text{mag}} = Kp^2\left(\frac{1+\cos^2\eta}{4}\right)\sin^2\left\{2\pi lu\mp\frac{k\Delta r_z}{2}\right\} \quad \text{at } \boldsymbol{R} = \boldsymbol{R}^*\mp\boldsymbol{k} \qquad (14)$$

The usual reflection conditions $-h+k+l = 3n$ and $l = 2n'$ apply to $\boldsymbol{R}^*$. In order to calculate the powder intensity, the intensities must of course be summed over crystallographically equivalent reflections, using the appropriate value of η for each. The corresponding expression for a single spin axis structure of Cr_2O_3 type is

$$I = Kp^2(\sin^2\alpha)\sin^2\{2\pi lu\} \text{ at } \boldsymbol{R}^* \qquad (15)$$

It now remains to select the proper value for $k\Delta r_z$. The three cases in which Γ_b, Γ_c and Γ_d respectively give antiferromagnetic coupling of the two spirals will now be considered (see Fig. 2).

(1) Γ_b negative. Then $A_2(0, 1, \tfrac{1}{2}-u)$ is antiparallel to $B_1(\tfrac{1}{3}, \tfrac{2}{3}, u-\tfrac{1}{3})$. Hence,

$$\frac{k\Delta r_z}{2} = \frac{\pi c}{\lambda}\left(2u-\frac{5}{6}\right) \qquad (16)$$

The Cr_2O_3 structure corresponds to the special case $\lambda = \infty$, and the Fe_2O_3 structure to $\lambda = c/3$. In the latter case, the observed (009) reflection, for example, can be considered to arise from splitting of the (006) and (00,12) reflections in Cr_2O_3 and coalescing of (006^+) and $(00,12^-)$.

(2) Γ_c negative. Then $A_2(1, 0, \tfrac{1}{2}-u)$ is antiparallel to $A_1(\tfrac{2}{3}, \tfrac{1}{3}, u-\tfrac{1}{6})$. Hence,

$$\frac{k\Delta r_z}{2} = \frac{\pi c}{\lambda}\left(2u-\frac{2}{3}\right) \qquad (17)$$

If u has the ideal value $\tfrac{1}{3}$, the two spirals are exactly out of phase. When $\lambda = c/3$, the structure has the configuration $A_1(-)$, $A_2(+)$, $B_1(+)$, $B_2(-)$. This is the only remaining single spin axis structure which does not involve enlargement of the rhombohedral unit cell, and has yet to be reported in oxides of corundum type.

(3) Γ_d negative. Then $A_2(1, 0, \tfrac{1}{2}-u)$ is antiparallel to $B_1(1, 0, u)$. Hence,

$$\frac{k\Delta r_z}{2} = \frac{\pi c}{\lambda}\left(2u-\frac{1}{2}\right) \qquad (18)$$

When $\lambda = c/3$, the structure once more reduces to that of Fe_2O_3.

J. Phys. Chem. Solids Pergamon Press 1963. Vol. 24 pp. 425–429. Printed in Great Britain.

ELECTRON EFFECTIVE MASS IN GALLIUM ANTIMONIDE DETERMINED BY FARADAY ROTATION MEASUREMENTS

HERBERT PILLER

Infrared Division, Research Department, U.S. Naval Ordnance Laboratory, Corona, California

(*Received* 25 *September* 1962)

Abstract—The two-band model is used to calculate the electron effective mass in the [000] conduction band of n-type GaSb using values of the free carrier Verdet coefficient and Hall coefficient measured at 77°K and 296°K. The effective mass was found to be $m^* = (0{\cdot}049\,^{+0{\cdot}005}_{-0{\cdot}008})\,m_e$ for a sample having a carrier concentration of $3{\cdot}77 \times 10^{17}$ cm^{-3} in the [000] band and a ratio of the electron mobilities in the two bands of $\mu_1/\mu_0 = 1/6$. The separation between the [000] and $\langle 111 \rangle$ minima increases with temperature at a rate of $+1{\cdot}1 \times 10^{-4}$ eV °K^{-1}. The density-of-states mass ratio is found to be $m_{d1}/m_{d0} = 14{\cdot}3$. The interband Faraday rotation at the edge indicates a temperature dependence of the direct optical gap in the degenerate n-type sample: $\Delta E_{\text{opt}}/\Delta T = \Delta E_g/\Delta T - 4k$, where E_g is the direct energy gap and k is the Boltzmann constant.

INTRODUCTION

OSCILLATORY magneto-absorption measurements show that the lowest conduction-band minimum is in the center of the Brillouin zone.(1) The fact that this minimum occurs at $k = 0$ is confirmed by elasto-resistance,(2) magneto-resistance,(3) and interband Faraday rotation(4) measurements. The effective mass at the minimum is $0{\cdot}047\,m_e$.(1, 5) Sagar has suggested that there are subsidiary minima along $\langle 111 \rangle$ directions at the zone boundary. These minima lie about 0·08 eV above the [000] minimum at room temperature. He has deduced from the temperature dependence of the piezoresistance a temperature dependence of the separation between the two conduction-band minima of -3×10^{-4} eV °K^{-1}. CARDONA has given evidence that this separation increases with temperature(5) at a rate of 10^{-4} eV °K^{-1}. The temperature dependence of the interband Faraday rotation in GaSb also indicates that the effective indirect gap increases with temperature.(4) The ratio of the mobilities of the electrons in the two conduction bands is about 1/6.(2, 5)

A considerable difference between the electrical properties of samples of GaSb doped with tellurium and those doped with an equal concentration of selenium has been reported. STRAUSS has suggested that the observed differences arise from impurity conduction.(6) The results obtained for 77°K are consistent with the assumption that a selenium donor level is located about 0·07 eV above the principal conduction-band edge.(7) BECKER, RAMDAS and FAN deduced from absorption, magneto-resistance, and Hall-effect measurements(3) the density-of-states mass ratio 17·3, the mobility ratio 0·06, and the energy separation 0·08 eV between the two sets of valleys at 4·2°K.

Reflectivity experiments in the u.v.(8, 9) show, as do the other experiments, that the band structure of GaSb has a marked similarity to that of germanium. EHRENREICH has synthesized, from existing experimental information, the band structure in the $\langle 100 \rangle$ and the $\langle 111 \rangle$ direction.(10) He calculated the spin-orbit splitting of the valence band at [000] as $\Delta = 0{\cdot}86$ eV and $E_P = 20$ eV; ($E_P = (2m/\hbar)P^2$, where P is the momentum matrix element).

These results show that a large amount of information about the conduction-band structure of GaSb has been obtained. The differences in some parameters, however, show that still more quantitative information is needed.

The Faraday rotation technique has given accurate values of the electron effective mass.(11) This technique is very sensitive in the free carrier region, where the rotation is proportional to the square of the wavelength of the incident radiation and inversely proportional to the square of the effective mass.(12)

EXPERIMENTAL PROCEDURE

The single crystal n-type GaSb was supplied through the courtesy of Battelle Memorial Institute, Columbus, Ohio. The slice was cut approximately perpendicular to a $\langle 211\rangle$ axis. The doping material is tellurium. The samples used for the Faraday rotation and Hall effect measurements were rectangular parallelepipeds 10^{-1} to 1 mm thick, 3 mm wide and 9 mm long. The sample surfaces were mechanically finished with a Buehler No. 3 polish.

The leads were soldered with indium. The Hall effect was measured in a field of 6·7 kG. The Faraday rotation was measured in magnetic fields up to 20 kG using a conventional technique described in an earlier paper.(13) The measurements were made at 77 and 296°K. Transmission measurements made at room temperature have shown that the absorption increases beyond the wavelength of 5μ.

CALCULATION OF THE EFFECTIVE MASS IN THE [000] BAND

The two-band model is used to calculate the carrier concentrations and the effective mass in the [000] band. It is assumed that the donors are completely ionized at both temperatures and therefore that, in the first approximation, the total concentration of the electrons in the conduction bands is independent of temperature. According to the two-band model, considering two conduction bands, the expression for the Hall coefficient is

$$R_H = \frac{1}{n_0 e}\frac{\mu_{0H}}{\mu_0}\frac{1+(n_1\mu_1\mu_{1H})/(n_0\mu_0\mu_{0H})}{[1+(n_1\mu_1)/(n_0\mu_0)]^2} \tag{1}$$

where e is the electronic charge, n is the carrier concentration, μ is the drift mobility, and μ_H is the Hall mobility. The subscripts 0 and 1 refer to the [000] and the $\langle 111\rangle$ conduction band. The ratio between the Hall and drift mobilities is assumed to be 1. This assumption is justified in the [000] band where the degeneracy is high. (For a carrier concentration of $3{\cdot}8\times 10^{17}$ in the [000] band, the degeneracy temperature is more than 400°K.) For the $\langle 111\rangle$ band, this might not be the case. However, no large error is introduced by this assumption.(5) The terms containing $(\mu_1/\mu_0)^2$ in equation (1) are small with respect to 1 in samples with small carrier concentrations; neglecting these terms, the Hall coefficient is

$$R_H = \frac{1}{n_0 e}\left(1+2\frac{n_1}{n_0}\frac{\mu_1}{\mu_0}\right)^{-1} \tag{2}$$

The error which is introduced by that neglection is smaller than the error in the Hall effect measurement itself.

The free carrier rotation in GaSb is the sum of the rotations resulting from the carriers in both conduction bands

$$\theta = \frac{e^3 B l}{\omega^2 2 n c \epsilon_0}\left(\frac{n_0}{m_0^{*2}}+\frac{n_1}{m_1^{*2}}\right) \tag{3}$$

where B is the magnetic induction, l is the thickness of the sample, n is the refractive index, c is the velocity of light, ϵ_0 is the dielectric constant of vacuum, and ω is the angular frequency of the incident radiation.

The effective mass in the $\langle 111\rangle$ band, m_1^*, is much larger than the effective mass in the [000] band. An increase in temperature will result in an increase in n_1 with respect to n_0, because the energy separation between the two conduction-band minima is of the order kT. Equation (3) shows that in this case, the Faraday rotation will decrease. There will be a change in the effective mass with temperature: an increase caused by the spread of the Fermi distribution and a decrease caused by the thermal expansion of the lattice.(14) There will also be a decrease in the effective mass that occurs with decreasing carrier concentration in the [000] band because of the curvature of the conduction band. As a result, the actual change in the effective mass with temperature in the [000] band should be very small and is probably not detectable.

Under the condition of temperature-independent effective masses, the ratio of the Faraday rotations at temperatures T_a and T_b, is

$$\frac{\theta_a}{\theta_b} = \frac{n_{0a}+n_{1a}(m_0^*/m_1^*)^2}{n_{0b}+n_{1b}\,(m_0^*/m_1^*)^2} \tag{4}$$

For a small value of $(m_0^*/m_1^*)^2$ and small carrier concentrations in the $\langle 111 \rangle$ band that ratio is approximately

$$r = \theta_a/\theta_b = K n_{0a}/n_{0b} \qquad (4a)$$

where K is a correction factor depending on the density-of-states mass ratio and the carrier-concentration ratios. The average effective mass m_1^* in the $\langle 111 \rangle$ band is about one-third of the density-of-states mass $m_{d1} = 17{\cdot}3\, m_0^*$ (assuming $m_0^* = m_{d0}$).(3) In this case, taking $K = 1$ introduces a negligible error in equation (4a).

From equations (2) and (4a) the carrier concentration in the [000] band at temperature T_a is

$$n_{0a} = \frac{r(1/R_{Ha} - 1/R_{Hb})}{e(r-1)(1-2\mu_1/\mu_0)} \qquad (5)$$

This equation together with the first term in equation (3) determines the effective mass in the [000] conduction band.

RESULTS AND DISCUSSION

Figure 1 shows the Faraday rotation in n- and p-type GaSb at room temperature. The n-type material shows the expected wavelength-square dependence well below the frequency corresponding to the energy gap. At the absorption edge, the Faraday rotation changes in sign corresponding to direct transitions between the valence band and the conduction band.(4) The small shift of the edge corresponds to the filling of the conduction band. The p-type material shows no free carrier rotation.

Figure 2 shows the Faraday rotation at liquid-nitrogen temperature for the same samples used in the measurements shown in Fig. 1. The free carrier rotation increased by a factor of $r = 2{\cdot}84$. The shift at the edge is much larger than at room temperature. This indicates the following temperature dependence of the direct optical gap in that degenerate sample: $\Delta E_{\text{opt}}/\Delta T = \Delta E_g/\Delta T - 4k$ where E_g is the direct gap and E_{opt} corresponds to an energy about $4kT$ below the Fermi level.(15) Using Burstein's relation, the Fermi level is found to be about 115 meV above the bottom of the conduction band at 77°K, which is too large for the carrier concentration in the [000] band at this temperature by about a factor of 3.

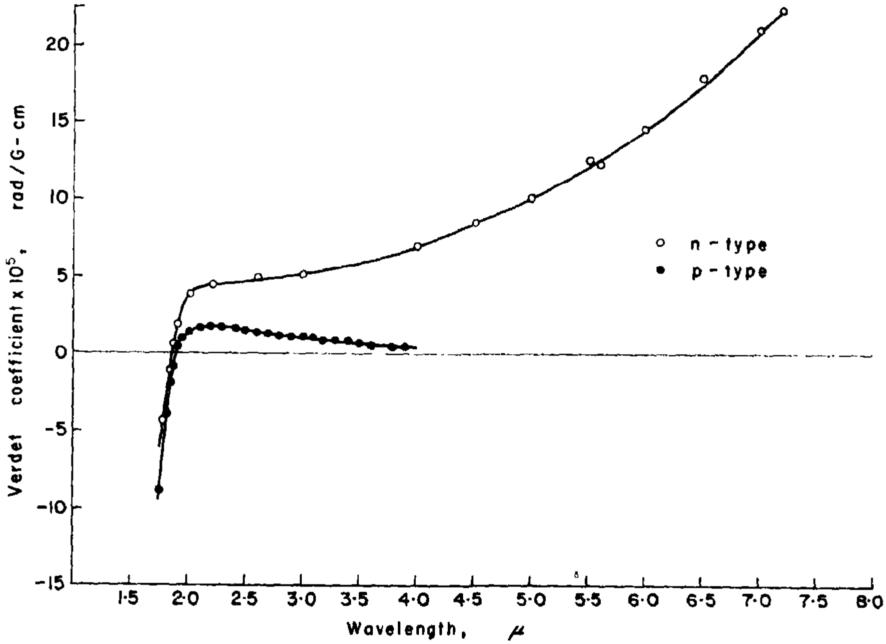

FIG. 1. Faraday rotation in n- and p-type gallium antimonide at room temperature.

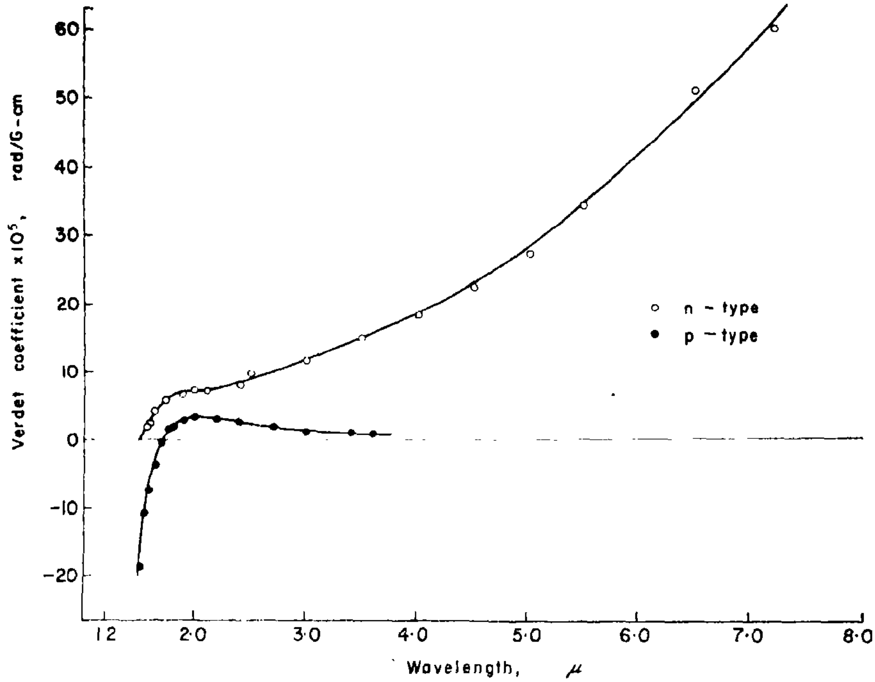

FIG. 2. Faraday rotation in *n*- and *p*-type gallium antimonide at liquid-nitrogen temperature.

Further experiments on samples with different dopings and on compensated samples might explain the observed difference. If this difference is real, it would indicate the presence of two or more surfaces of different curvatures at $k = 0$.

The Hall-effect measurements on the *n*-type sample gave the Hall coefficients, $R_{Ha} = 15$ cm³ C⁻¹ at $T_a = 77$°K, and $R_{Hb} = 24{\cdot}6$ cm³ C⁻¹ at $T_b = 296$°K.

Using the mobility ratio, 1/6, one obtains from equations (2), (4a), and (5) the carrier concentrations in the [000] band

$n_{0a} = 3{\cdot}77 \times 10^{17}$ cm⁻³ at 77°K, $n_{0b} = 1{\cdot}33 \times 10^{17}$ cm⁻³ at 296°K, and in the ⟨111⟩ band $n_{1a} = 1{\cdot}20 \times 10^{17}$ cm⁻³ at 77°K, $n_{1b} = 3{\cdot}65 \times 10^{17}$ cm⁻³ at 296°K.

Using the refractive index $n = 3{\cdot}6$,⁽⁵⁾ and the Faraday rotation and carrier concentration at 77°K, one obtains the effective mass in the [000] band from equation (3)

$$m^* = (0{\cdot}049\,^{+0{\cdot}005}_{-0{\cdot}003})\,m_e$$

The conduction band is not parabolic; the curvature decreases with increasing energy. Under the condition in which the energy $E < E_g + \frac{2}{3}\Delta$, the conduction band around the [000] minimum is given by the following approximation⁽¹⁴, ¹⁶⁾

$$E = -E_g/2 + (E_g^2/4 + k^2\gamma^2)^{1/2} \qquad (6)$$

where

$$\gamma^2 = P^2(E_g + \tfrac{2}{3}\Delta)/(E_g + \Delta)$$

Applying this approach to GaSb with $\hbar^2/m^* = \left(\frac{1}{k}\frac{\mathrm{d}E}{\mathrm{d}k}\right)_F$ for $T = 0$, where the subscript F refers to the Fermi level, the effective mass is given by

$$m^* = (E_g^2/4 + k_F^2\gamma^2)^{1/2}/\gamma^2 \qquad (7)$$

Using the values for Δ and E_P given by EHRENREICH,⁽¹⁰⁾ $\gamma^2 = 0{\cdot}305$ atomic units. For a carrier concentration $n_0 = 3{\cdot}9 \times 10^{17}$ cm⁻³, one obtains $k_F = 1{\cdot}19 \times 10^{-2}$ atomic units. With these values one obtains from equation (7) the effective mass for that carrier concentration $m^* = 0{\cdot}053\, m_e$, which is in agreement with the effective mass determined by Faraday rotation.

The Fermi level with respect to the [000] minimum and the temperature dependence of the separation between the [000] and ⟨111⟩ minima can be obtained by solving the equations

$$n_0 = (4\pi(2kT)^{3/2}/h^3)m_0^{*3/2}F_{1/2}(E_F/kT) \tag{8}$$

$$\frac{n_1}{n_0} = \frac{\nu_1 m_{1l}{}^{1/2} m_{1t}}{m_0^{*3/2}} \frac{F_{1/2}[(E_F-\Delta E)/kT]}{F_{1/2}(E_F/kT)} \tag{9}$$

where $F_{1/2}$ is the Fermi integral,(17) ν_1 is the number of equivalent minima in the first Brillouin zone, E_F is the Fermi level, m_{1l} is the longitudinal effective mass, m_{1t} is the transverse effective mass in the ⟨111⟩ band, and ΔE is the energy separation between the [000] and ⟨111⟩ minima.

Using the effective mass, $m_0^* = 4{\cdot}9\times 10^{-2}\, m_e$, the carrier concentrations given above, and $\Delta E_b = 80$ meV at 296°K, one finds $\Delta E_a = 56$ meV at 77°K. This indicates that the separation between the [000] and ⟨111⟩ minima increases with temperature at a rate of $+1{\cdot}1\times 10^{-4}$ eV °K^{-1}. Equation (9) gives $m_{d1}/m_{d0} = 14{\cdot}3$ for the density-of-states mass ratio. With this large mass ratio the error introduced in the determination of the effective mass in the given sample is negligibly small. The free carrier Faraday rotation, with the Hall effect, and the interband Faraday rotation could be used to determine the Fermi level, the direct optical gap, and the location of the postulated donor level in selenium doped GaSb.(7) As the concentration of the doping material increases the Fermi level reaches the impurity level. At low temperature a part of the impurities will be neutral and at high impurity concentration the Fermi level should be stable at the corresponding impurity level.

Acknowledgements—The author is indebted to H. G. Ford, V. A. Patton, and G. Zaeschmar for their assistance in making measurements and calculations. The samples of GaSb were skillfully prepared by J. C. Jerome.

REFERENCES

1. Zwerdling S., Lax B., Button K. J. and Roth L. M., *J. Phys. Chem. Solids* **9**, 320 (1959).
2. Sagar A., *Phys. Rev.* **117**, 93 (1960).
3. Becker W. M., Ramdas A. K. and Fan H. Y., *J. appl. Phys. Suppl.* **32**, 2094 (1961).
4. Piller H. and Patton V., *Bull. Amer. phys. Soc.* **7**, 184 (1962).
5. Cardona M., *J. Phys. Chem. Solids* **17**, 336 (1961).
6. Strauss A. J., *Phys. Rev.* **121**, 1087 (1961).
7. Bate R. T., *J. appl. Phys.* **33**, 26 (1962).
8. Tauc J. and Abraham A., *Proceedings of the International Conference on Semiconductors*, Prague, (1960).
9. Cardona M., *Z. Phys.* **161**, 99 (1961).
10. Ehrenreich H., *J. appl. Phys. Suppl.* **32**, 2155 (1961).
11. Moss T. S., Smith S. D. and Taylor K. W., *J. Phys. Chem. Solids* **8**, 323 (1959).
12. Moss T. S., *Optical Properties of Semiconductors*, Butterworth, London (1959).
13. Piller H. and Patton V. A., *Foundational Research Projects, Jan.–Mar.* 1962 (NAVWEPS Report 7219) p. 47. Naval Ordnance Laboratory, Corona, California.
14. Cardona M., *Phys. Rev.* **121**, 752 (1961).
15. Burstein E., *Phys. Rev.* **93**, 632 (1954).
16. Kane E. O., *J. Phys. Chem. Solids* **1**, 245 (1957).
17. McDougall J. and Stoner E. C., *Proc. Roy. Soc.* **237A**, 67–104 (1938).

J. Phys. Chem. Solids Pergamon Press 1963. Vol. 24. pp. 431–435. Printed in Great Britain.

CALCULATION OF WORK FUNCTIONS FOR SURFACES COMPOSED OF IONIC CRYSTALS

A. G. BUYERS

Hughes Research Laboratories, Malibu, California

(*Received* 29 *August* 1962; *revised* 16 *October* 1962)

Abstract—Values for the work functions of thermionic emitter surfaces composed of alkaline earth oxides have been approximated by means of a closed energy balance cycle which is a modification of the Born–Haber Method ordinarily used to estimate lattice energies or electron affinities. Comparison of calculated surface potentials with reported work functions for alkaline earth oxides disclosed reasonable agreement. The modified Born–Haber cycle includes, among other terms, the lattice energy, the heat of sublimation, and the molecular electron affinity of the gaseous, neutral, diatomic molecules under consideration. Justification for the incorporation of these quantities into the energy balance, together with the general implications of this method of estimating work functions, is discussed.

1. INTRODUCTION

RICHARDSON work function values for thermionic cathodes coated with inorganic compounds have not been theoretically estimated, but two approaches have yielded procedures for predicting work function values.(1, 2) A compilation of these elemental work function values is found in Ref. (3).

This article presents a new procedure for estimating work functions of electron emission surfaces composed of ionic crystals. This procedure employs the principles used in the BORN–HABER cycle,(4, 5) which is ordinarily utilized for determining lattice energies and nonmetal electron affinities. The significance of this new calculation lies in its use for predicting unknown values of work functions characteristic of ionic crystal surfaces. The energy balance cycle depicted for baria in Fig. 1 represents emitting surface processes that permit work functions for alkaline earth oxide surfaces to be calculated by summation of the energy terms (representing the different chemical and physical phenomena) which follow the cycle in one direction. This sum is then equated to the single quantity evaluating one process selected to originate at the initial point of departure and terminate at the same part of the cycle as the summation. Thus, the work function ϕ is calculated from the equation:

$$\phi = [U_0 - \Delta H^0_{0(s)} - D^0_0 - I + E + X]/F \qquad (1)$$

where

U_0 = the lattice energy of the ionic compound

$\Delta H^0_{0(s)}$ = the heat of sublimation of the solid

D^0_0 = the bond energy of the vaporized molecular species

I = the total ionization potential of the metal atom

E = the nonmetal electron affinity for the anionic component of the molecule comprising the surface and vapor species

X = the electron affinity of the molecule defined as the difference in potential between an electron in the gas existing within a pore in the emission surface and the conduction band of the ionic crystal comprising the surface.

This new calculation incorporated factors which establish the potential barrier an electron must overcome prior to escape into a vacuum from an ionic emitting surface, i.e. the Fermi level of the electrons within the bulk of the material, the temperature, the nature of chemical bonding, the various forces characteristic of the crystal matrix, and the physical nature of the surface.

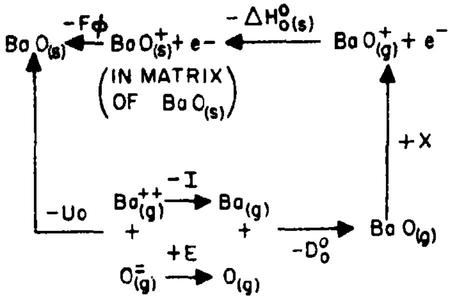

FIG. 1. Modified Born–Haber cycle for the calculation of work functions for alkaline earth oxides.

2. EXPERIMENTAL DATA

Work functions for the alkaline earth oxide series (magnesia, calcia, strontia, and baria) are calculated by employing the best values of lattice energies, heats of sublimation, bond energies, ionization potentials, anionic electron affinities, and molecular electron affinities. Results of these approximations and the data used in calculation are summarized in Table 1.

This tabulation discloses significant uncertainties for the energy terms used to calculate the relatively small work function values. Despite this, agreement between reported and calculated work functions is reasonable for all of the alkaline earth oxides. It is recognized, however, that the magnitude calculated for a given work function by the modified Born–Haber method can be in error by an amount far in excess of those data in Table 1.

3. DISCUSSION

The work function is not a property of the surface alone but is primarily dependent upon the bulk solid properties.(14) The following discussion is offered to substantiate this opinion, further supported by the results of the Born–Haber calculations. The implications of using, in the modified Born–Haber cycle, energy terms such as lattice energy U_0, heat of sublimation $\Delta H^0_{0(s)}$, and molecular electron affinity X are examined below. The use of the bond energy D^0_0, the ionization potential I, and the nonmetal electron affinity E need no further discussion.

Table 1. Thermochemical data and comparison of work function values*

	(Kcal/mole)						(eV)	(eV)
Inorganic surface	Lattice energy(6) U_0 (Error Est. ± 10 per cent)	Heat of sublimation $\Delta H^0_{0(s)}$	Bond energy(8) D^0_0	Ionization potential(7) I (Error Est. ± 10 per cent)	Nonmetal electron affinity(6) E (Error Est. ± 10 per cent)	Molecular electron affinity X (Error Est. ± 30 per cent)(12)	Reported	Work function of surface Estimated
MgO	940 ± 94	149 ± 10(9)	92 ± 16	521 ± 52	−168 ± 17	70 ± 21†	3·1(13)	3·5 ± 0·9
CaO	842 ± 82	150 ± 8(10)	100 ± 15	413 ± 41	−168 ± 17	35 ± 11†	1·7(14)	2·0 ± 0·5
SrO	791 ± 79	155 ± 5(9)	83 ± 5	384 ± 38	−168 ± 17	25 ± 8†	1·4(15)	1·1 ± 1·0
BaO	748 ± 75	104 ± 4(11)	130 ± 5	349 ± 35	−168 ± 17	14 ± 4(12)	1·0(16)	0·5 ± 0·8

* All thermochemical values were rounded off to the nearest whole number.

† Values estimated from that for BaO using the equation $X_i = (I_i - I_r) + X_r$, where X_i is the estimated molecular electron affinity, I_i is the first ionization potential of the cationic component of the molecule, X_r is a reported, experimentally determined molecular electron affinity for the most ionic member of a series with a common anion, and I_r is the cationic component of that molecule.

Lattice energy

The lattice energy of an inorganic crystal can be calculated from the BORN–HABER cycle,(4, 5) or from the equation:

$$U_0 = \frac{e^2z^2NA}{r_0}\left(1-\frac{1}{n'}\right) \tag{2}$$

where

e = the unit of electrical charge
A = the Madelung constant, a correction factor reflecting the type of crystal lattice
z = the highest common factor of the oxidation numbers of the two ions comprising the molecule
N = Avogadro's number
r_0 = the interionic distance
n' = the Born exponent, representing a measure of the repulsive forces which arise from interpenetration of the two ions.

A more precise expression for the lattice energy U_0 was developed by BORN and MAYER.(17) This provided better agreement with quantum mechanical results by the incorporation of two modifications: replacement in (2) of e^2/r_0 with an exponential, and addition of a term for the Van der Waal's interaction, later modified even further by MAYER.(18, 19)

The heat of sublimation

The use of the heat of sublimation in the modified Born–Haber calculation requires discussion on two counts: 1. Should the physical nature of the surface appear mathematically in the equation for this heat? 2. Does the heat of sublimation of a neutral molecule have the same magnitude as that for a singly ionized species? First, the heat of sublimation cannot be expressed mathematically to include a parameter determined by the physical nature of the surface, as it is a basic thermodynamic principle that the energy change representing a shift from one equilibrium state to another is independent of the path. The difference in energy is a function of the initial and final states, and in this instance, the heat of sublimation is dependent only upon the energy content of the initial or solid state and that of the final or gaseous state. Second, the heat of sublimation for a neutral molecule should equal that for a singly ionized species. The following documentation is offered in support of this contention: The heat of sublimation of neutral barium is reported to be equal to 41·1 kcal/mole,(20) and the heat of sublimation for single charged barium ion, determined from a plot of positive ion current vs. reciprocal temperature, is reported to be equal to 39·0 ± 1·0 kcal/mole.(21) Thus, it is postulated that the heats of sublimation of neutral baria and singly ionized baria differ negligibly.

The molecular electron affinity

The molecular electron affinity X of the gaseous diatomic molecule is assumed to be the difference in potential between an electron in the gas existing within the pore in an emission surface and the conduction band of the specific crystal lattice characteristic of the ionic interaction of the atomic components of the crystal.

The magnitude of the molecular electron affinity for the adsorbed gaseous molecule is expressed by the equation:

$$X = \left[kT \ln \frac{el}{v}(2m\pi kT)^{-1/2}\right] \tag{3}$$

where

k = the Boltzmann constant
T = absolute temperature
e = the charge upon the electron
l = the mean dimension of the pores in the solid surface
m = the mass of the electron
v = the mobility of the electrons in the solid

The calculation of the molecular electron affinity, X, locates the bottom of the conduction band for an ionic crystal, namely, the potential existing between an electron at the bottom of the conduction band and the vacuum just outside the crystal surface. Accordingly, it is noted that the temperature dependence of the Richardson Work Function is small. Uncertainties introduced in values of the work function for high temperatures, incorporating X in their calculation by the new Born–Haber method, lie within inaccuracies arising from temperature differences and the surface potential associated with an electron of given energy and origin in the crystal.

The use of the molecular electron affinity permits incorporation of the physical nature of the emission surface into the work function calculation, since the quantity, l, is the mean pore dimension in the surface. This equation is obtained by equating the conductivities of the solid particles and the pores.[12]

The temperature needed to satisfy the equation is determined at the break in slope in an experimental plot of the logarithm of the conductivity of the solid emitter vs. reciprocal temperature. **Hensley** has explained the break in slope by stating that it is this temperature at which solid particle and pore conductivities are equal.[22]

The quantity X is assumed to be a measure of the ionization energy for the gaseous molecule, adsorbed upon the emitting surface. This assumption is based upon the method by which X is determined, i.e. high temperature measurement of electrical conductivity. It is conceivable that an ionized, gaseous, diatomic molecule exists within a pore or on the emission surface at high temperatures. Thus a positive molecular electron affinity represents the ionization potential of the gaseous molecule.

Values of X for strontia, calcia, and magnesia were estimated from the value experimentally determined for baria.[12] The following equation was used:

$$X_t = (I_t - I_r) + X_r. \tag{4}$$

where X_t is the molecular electron affinity estimated from the value X_r reported for baria, I_t is the first ionization potential of the alkaline earth metal whose oxide molecular electron affinity is being estimated, and I_r is the first ionization potential of barium metal.

The development of this equation is deductive. Differences in ionic character for inorganic molecules with a common anion and within the same family in the periodic table can be estimated from the difference between the first ionization potentials of the metals considered, provided parameters are known for the most ionic member of the group.

4. CONCLUSIONS

The described Born–Haber procedure for calculation of work functions for ionic crystal surfaces is a new approach to the problem of estimation of work function values. Although this method is not suitable for thermionic emissions which occur in the presence of an ionized metal plasma, it seems applicable to surfaces emitting electrons into a vacuum or into an inert gas plasma. Accordingly, it is necessary to describe and identify the ionic nature of the inorganic compounds and the molecular and ionic gaseous species for estimation of the work functions representative of a given inorganic emission surface or series of surfaces. It is also necessary to obtain accurate values for (1) the lattice energy, (2) the heat of sublimation of the neutral molecule, (3) the molecular electron affinity for the most covalent or most ionic member of a given series of compounds with a common anion, (4) the bond energy or energies of vapor species as they may exist and are represented in the energy valance cycle, (5) the total ionization potential of the gaseous cationic component of the molecule or molecules, and (6) the electron affinity of the anionic component of the gaseous molecule or molecules.

The proposed procedure is not limited to pore conductors or alkaline earth oxides, but can find wide application in the estimation of work functions for ionic surfaces by using appropriate values for representative chemical and physical processes properly summed throughout a closed energy balance cycle.

REFERENCES

1. Gyftopoulos E. P. and Levine J. D., *J. appl. Phys* **33**, 67–73 (1962).
2. Rasor N. S., Summary of presentation by Atomics International at the Second Round Table Discussion on Thermionic Conversion, Appendix **B**, June 1961.
3. Hodgman C. D. Ed., *Handbook of Chemistry and Physics* pp. 2344–2352. Chemical Rubber Publishing Co., Cleveland Ohio (1955).
4. Born M., *Verh. dtsch. phys. Ges.* **21**, 13 (1919).
5. Haber F., *Verh. dtsch. phys. Ges.* **21**, 750 (1919).
6. Sherman L., *Chem. Rev.* **11**, 93 (1932).
7. Moeller T., *Inorganic Chemistry, An Advanced Textbook* p. 162. John Wiley, New York (1959).
8. Cottrell T. L., *The Strength of Chemical Bonds*, Academic Press, London (1958).
9. Porter R. F., Chupka W. A. and Inghram M. G., *J. chem. Phys.* **23**, 1347–1348 (1955).
10. Brewer L., *Chem. Rev.* **52**, 1–75 (1953).
11. Ingham M. G., Chupka W. A. and Porter R. F., *J. chem. Phys.* **23**, 2159–2165 (1955).

12. HENSLEY E. B., Report on the Fifteenth Annual Conference of Physical Electronics, Cambridge Mass., March 24–26 p. 18–21 (1955).
13. *Thermoelectricity*, (Edited by EGLI P. H.) p. 219. John Wiley, New York (1960).
14. HOPKINS B. J. and VICK F. A., *Brit. J. appl. Phys.* **9**, 257–264 (1958).
15. EISENSTEIN A. S., *Advances in Electronics* pp. 41–42. Academic Press, New York (1948).
16. YOUNG J. R., *J. appl. Phys.* **23**, 1129–1138 (1952).
17. BORN M and MAYER J. E., *Z. Phys.* **75**, No. 1 (1932).
18. MAYER J. E., *J. chem. Phys.* **1**, 270 (1933).
19. MAYER J. E. and MAYER M. G., *Phys. Rev.* **43**, 605 (1933).
20. *Selected Values of Chemical Thermodynamic Properties*, (Edited by ROSSINI F. D.) p. 757. NBS 500, U.S. Govt. Printing Office (1952).
21. WERNING J. R., UCRL–8455, September (1958).
22. HENSLEY E. B., *J. appl. Phys.* **23**, 1122–1129 (1952).

J. Phys. Chem. Solids Pergamon Press 1963. Vol. 24. pp. 437–441. Printed in Great Britain.

BEHAVIOR OF SELENIUM IN GALLIUM ARSENIDE*

L. J. VIELAND† **and I. KUDMAN**‡

Radio Corporation of America, Semiconductor and Materials Division,
Somerville, New Jersey

(*Received* 25 *June* 1962; *revised* 17 *September* 1962)

Abstract—Selenium is not fully active electrically when present in gallium arsenide in concentrations over 4×10^{17} atoms/cm^3. Part of the selenium enters the lattice as an optically active $[V_{Ga}Se_3]$ complex, giving rise to an added absorption starting at approximately 0·9 eV. A model is developed to explain the dependence of the carrier concentration on the total selenium concentration, and it is shown to have general applicability to the doping of $A^{III}B^{V}$ compounds with group VI elements.

INTRODUCTION

THE group VI elements sulfur, selenium, and tellurium have generally been assumed to behave as normal donors in the $A^{III}B^{V}$ compounds when present in low concentrations; that is, to be randomly distributed throughout the crystal on B sites, and to introduce one shallow donor level for each atom incorporated. However, a great deal of experimental evidence has been obtained which suggests that the doping behavior of these elements is not simple. WOOLEY and co-workers have investigated both the phase equilibria(1) and electrical and optical(2–4) properties of many of the pseudo binary $A^{III}B^{V}$, $A_2^{III}B_3^{VI}$ systems over the entire composition range. The systems studied all show a minimum in the Hall coefficient near 100 per cent $A^{III}B^{V}$. Gallium selenide [probably] forms a continuous series of solid solutions with gallium arsenide,(1, 5) with a minimum in the Hall coefficient at five mole per cent‡ gallium selenide.(6) The carrier concentration is about 10^{19}/cm^3, so that only a small fraction of the selenium in the crystal appears to be electrically active at this composition. The object of this investigation is to examine in greater detail the properties of crystals close to 100 per cent GaAs, where the band structure of the system may be reasonably taken to be that of pure GaAs.

EXPERIMENTAL

All crystals studied were grown by the horizontal Bridgman technique at 0·3 in. per hour, and were single over most or all of their length. The doping element was added to the gallium prior to its reaction with arsenic and crystal growth. The crystals were found to be essentially unoriented with respect to the growth interface. Undoped crystal would be expected to be n-type with carrier concentrations below 5×10^{16}/cm^3.

Hall measurements were made at room and liquid nitrogen temperatures. In no case did the Hall coefficients or resistivities differ by more than 20 per cent at the two temperatures, which is within experimental error, and in most samples the differences were less than 10 per cent. Field strengths of about 5 kG were used. In subsequent discussion the carrier concentrations used have been obtained from the relationship $n = 1/R_H e$.

Optical transmission measurements were made on optically polished wafers taken from slices adjacent or close to the Hall sample, using a Perkin–Elmer model 112 spectrometer with a fused quartz prism. The absorption coefficient was calculated taking into account the effect of multiple internal reflection.

Since the selenium is not fully active electrically, several crystals were analyzed chemically for total selenium by the method of CHENG.(7)

---

* The work described was performed under the sponsorship of the United States Air Force.

† Present address: RCA Laboratories, David Sarnoff Research Center, Princeton, New Jersey.

‡ Based on the ratio Ga_3As_3/Ga_2Se_3, or the fraction of Se atoms on arsenic lattice sites.

Table 1. *Hall and chemical data for selenium and silicon doped gallium arsenide*

Crystal	Dope	Conc. in melt atoms/cm^3	n cm^{-3}	μ 300°K cm^2/V-sec	Conc. in solid atoms/cm^3
A	Se	$1{\cdot}6\times10^{18}$	4×10^{17}	3300	$4{\cdot}5\times10^{17}$
B	Se	$4{\cdot}0\times10^{18}$	$1{\cdot}0\times10^{18}$	3130	
C	Se	$9{\cdot}2\times10^{18}$	$2{\cdot}4\times10^{18}$	2320	$5{\cdot}8\times10^{18}$
D	Se	$2{\cdot}9\times10^{19}$	$4{\cdot}2\times10^{18}$	2040	
D_1	Se	$6{\cdot}9\times10^{19}$	$5{\cdot}2\times10^{18}$	1700	
E	Se	$6{\cdot}5\times10^{19}$	$4{\cdot}8\times10^{18}$		$1{\cdot}6\times10^{19}$
F	Se	$1{\cdot}1\times10^{20}$	$5{\cdot}7\times10^{18}$	1610	
F_1	Se	$2{\cdot}5\times10^{20}$	$7{\cdot}5\times10^{18}$	1420	
G	Se	$5{\cdot}0\times10^{20}$	$9{\cdot}3\times10^{18}$	1240	$1{\cdot}8\times10^{20}$
G_1	Se	$1{\cdot}0\times10^{21}$	$1{\cdot}2\times10^{19}$	1430	$2{\cdot}2\times10^{20}$
H	Si	$2{\cdot}3\times10^{19}$	$2{\cdot}6\times10^{18}$	1700	$3{\cdot}2\times10^{18}$
H_1	Si	$7{\cdot}9\times10^{19}$	$4{\cdot}1\times10^{18}$	1280	$1{\cdot}1\times10^{19}$

RESULTS

Results of Hall and chemical measurements are given in Table 1. In crystals D, F, and G, samples were cut from the front and rear of the bar. The concentration of Se in the melt toward the rear of the ingot was calculated using $k_s = 0{\cdot}5$(8) and the curves for normal freezing given by PFANN.(9) Data for two silicon doped crystals are also given. These crystals provide standards for the optical measurements, as explained below. The electrical data for these crystals are in excellent agreement with the results of WHELAN *et al.* for both the segregation coefficient(8) and the degree of self compensation.(10)

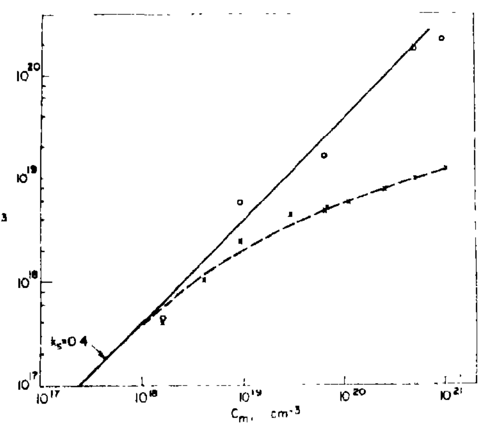

FIG. 1. Concentration in the solid as a function of the selenium concentration in the melt.

× electron concentration
○ selenium atom concentration
- - - - theoretical electron concentration

Figure 1 shows the selenium and carrier concentrations in the solid as a function of the selenium concentration in the melt. It is seen that the total selenium concentration in the solid as measured chemically is proportional to the concentration in the melt, the segregation coefficient being in adequate agreement with the radiotracer value.(8) The selenium is fully active electrically only at low concentrations. For n greater than about 4×10^{18}/cm^3 the carrier concentration rises as the cube root of the total concentration.

In Fig. 2 the absorption coefficient is shown as a function of wavelength for various doping levels. A portion of the fundamental edge is shown for comparison. This was obtained from measurements of 7×10^{15}/cm^3 n-type material. The heavily doped selenium samples show a displacement of the absorption edge to higher energies due to the penetration of the Fermi level into the conduction band. At the lowest energy portion of the curve an added absorption resulting from a combination of free carrier excitation and transitions from the $k = (000)$ conduction band minimum to a higher lying minimum(11) is present. Since the transition probabilities are low for these processes at higher energies, a minimum in the absorption coefficient might be expected to occur close to the fundamental edge, as in silicon(12) and gallium antimonide.(13) The anomalous absorption of the selenium doped samples in this region is made apparent by comparison with the silicon doped samples of the same carrier concentration, which show the expected behavior. In order to compute the excess absorption attributable to selenium, it is necessary to subtract the absorption due to other, known, transitions. This has been done by taking the curves for the silicon doped samples as representing the normal decrease of free carrier and interband transition absorption with increasing energy. In the case of the heavily doped samples, it has been assumed that the curve for the [hypothetical] silicon doped sample of the same carrier concentration would be parallel to that for sample H, and coincide with the silicon doped crystals at energies below about 0·9 eV. Curves for the excess absorption as a function of incident energy are shown in Fig. 3. It is apparent that the excess absorption rises more rapidly than the carrier concentration.

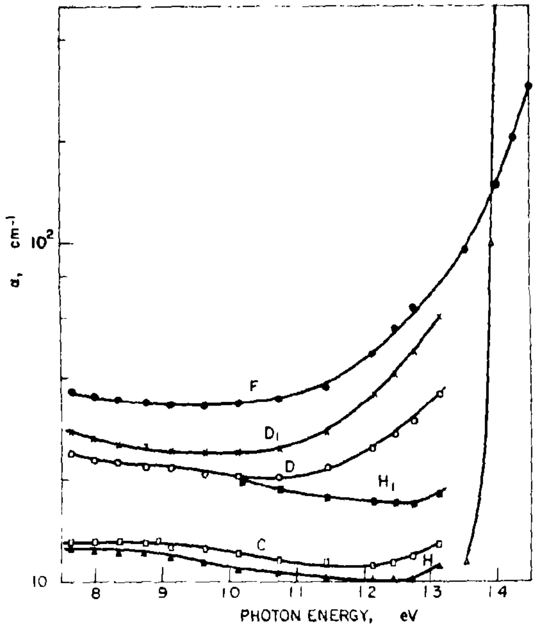

FIG. 2. Absorption coefficient as a function of photon energy.

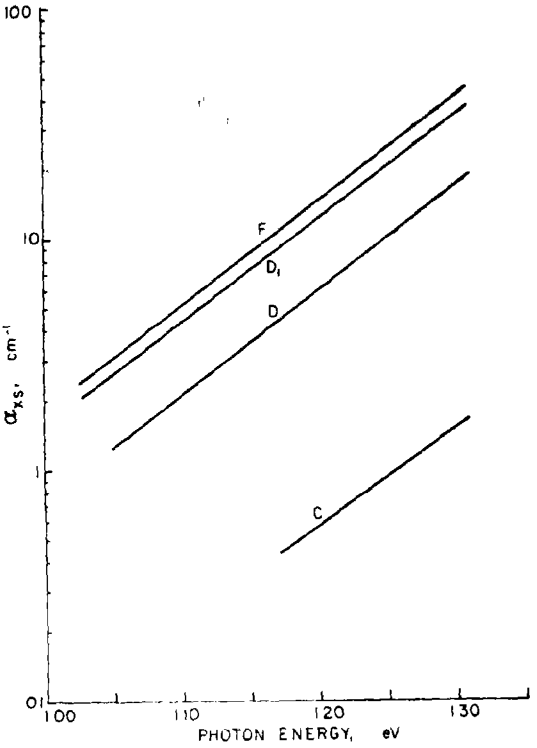

FIG. 3. Excess absorption as a function of photon energy.

DISCUSSION

Gallium selenide crystallizes with a defect zinc-blende structure,(14) the electronic requirements for tetrahedral bonding being fulfilled by the incorporation of a lattice vacancy on one-third of the cation sites. It follows that one might expect its alloys with gallium arsenide to have the composition $[\mathrm{Ga}_{(2+x)}V_{\mathrm{Ga}(1-x)}]\ [\mathrm{As}_{(3x)}\ \mathrm{Se}_{3(1-x)}]$ where x is the mole fraction $\mathrm{Ga_3As_3}$, and to be electrically intrinsic. It is seen that the Hall data is consistent with such a model except in the most dilute solid solutions, since at higher concentrations only a small fraction of the selenium is electrically active. That this fact is not attributable to electrical compensation is apparent from a comparison of the mobilities of the heavily selenium doped crystals with the silicon doped (compensated) crystals of Table 1. To the first approximation the selenium gives rise to no acceptor levels, and the inactive portion makes no contribution to the scattering process even when present in concentrations an order of magnitude higher than the ionized impurity concentration. Consistent with these experimental observations and the above formula, the inactive selenium is taken to be present in the form of a $[V_{Ga}Se_3]$ complex—the three selenium atoms on second nearest neighbor sites tetrahedrally bonded around the gallium vacancy and supplying the three extra electrons required to fill the octet.

The complex gives rise to a deep level, situated roughly 0·9 eV below the conduction band. In Fig. 4 it is seen that the excess absorption at fixed energy can be taken as proportional to the concentration of unionized selenium $(k_s C_m - n)$, as expected.

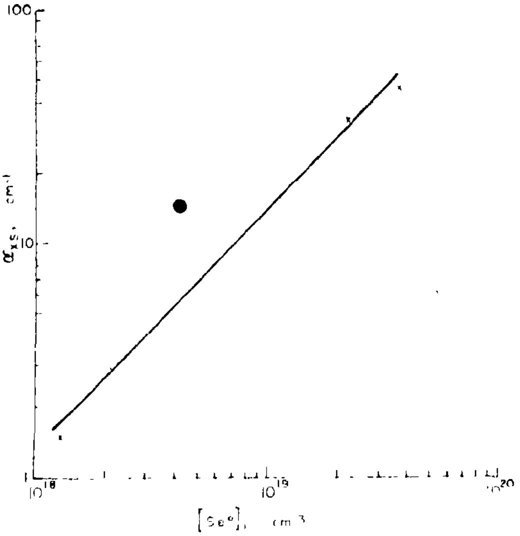

FIG. 4. Excess absorption at 1·3 eV as a function of the unionized selenium concentration.

A simple thermodynamic interpretation can be given to the data. The necessary reactions are written schematically as follows:

$$Ga_2Se_{3(m)} \overset{K}{\leftrightarrows} 2\,Ga_{(m)} + 3\,Se_{(m)} \qquad (1)$$

$$Ga_2Se_{3(m)} \overset{k_3}{\leftrightarrows} 2\,Ga_{(m)} + V_{Ga}Se_{3(s)} \qquad (2)$$

$$Se_{(m)} \overset{k_1}{\leftrightarrows} Se_{(s)}\ (\rightarrow Se^{+} + n) \qquad (3)$$

where (m) designates the melt (or the growth interface) and (s) the solid. The segregation coefficients can be obtained from the data in the regions where essentially all of the selenium is present exclusively in one form or the other. K is then deduced from the relationship

$$K = (Se_{(s)})^3 k_3 / (VSe_{3(s)}) k_1^3 \qquad (4)$$

by substituting experimental concentrations at any point. It can be seen from equation (4) that in the region where the bulk of the selenium is unionized the carrier concentration should vary as the cube root of the total concentration in the solid (or melt). The theoretical curve of Fig. 1 has been calculated on the basis of the above relationships, with $k_1 = k_3 = 0{\cdot}4$. In general, however, these values would not be expected to be equal.

Since there is considerable evidence that these results are perfectly general, it is of interest to examine some of the anomalies reported for InSb and GaSb doped with group VI elements in the light of this discussion. MULLIN and HULME,(15) using both radiotracer and Hall measurements, found the segregation coefficient of Te in InSb to be greater than unity on a [111] facet and less than unity off the facet. ALLRED and WILLARDSON,(16) using electrical measurements obtained similar results with Se doping. Anisotropic segregation was also observed in undoped crystal, leading to the conclusion that the residual impurity was a group VI element. Magnetoresistance measurements(17) also reveal a scattering anisotropy which is a function of the pull rate and seed orientation. As emphasized by Mullin and Hulme, these effects cannot be explained in terms of the diffusion limited variations of k treated by BURTON *et al.*,(18) and in some respects appear to be unique to the group VI elements in the $A^{III}B^{V}$ [InSb] compounds. A clue to the reason for this unusual behavior may be found in the following arguments:

If we assume that the crystal growth takes place by the development of [many] fundamental atomic planes, and that part of the impurity is incorporated into the crystal as the complex, then the [111] (and $[\bar{1}\bar{1}\bar{1}]$) facets are unique in that it is only on these facets that the atoms of the complex can be deposited co-planarly. For example, on the [100] faces two bonds are already directed into the crystal, so that only two second nearest neighbors can be bound to a lattice site in the next layer. On the [110] one bond is directed inward, two are available co-planarly, and one can be satisfied in the next layer. Differences might be expected even on opposite [111] faces. In the cast of an *A* face, three second nearest neighbors are deposited and the vacancy occurs in the next layer, whereas on the *B* face the impurity deposits around a vacant lattice site. For non [111] interfacial regions the segregation coefficient k_3, which is not a true equilibrium constant, will have some average value governed by the fraction of the growth interface exposing [111] planes.

This reasoning accounts for the facet effect only for the electrically inactive species. However, it is reasonable to suppose that the existence of the complex at the interface can have a large effect upon the segregation coefficient even though the bulk of the impurity may be present in the crystal in the atomic form.

In the case of GaSb, STRAUSS(19) found substantial differences in the behavior of selenium and tellurium doped crystal which could not be explained on the basis of the accepted band structure alone. In particular, the mobilities of Se doped crystals show an abnormal decrease with decreasing Hall coefficient. BATE(20) proposed an unusual band model to account for this behavior, the chief feature of which is that it leads to incomplete ionization of the impurities at higher carrier concentrations, thereby predicting the onset of neutral impurity scattering at low Hall coefficients. From this work, and the work of Wooley *et al.*, it is apparent that the mobility can be correlated with the Hall coefficient only in those regions where the scattering is due entirely to the ionized impurities, and that it is possible to have large differences in the total impurity content for the same value of the Hall coefficient, depending on the specific impurity. Indeed, Strauss' data for Se doped GaSb appear to include the region of the minimum of the Hall coefficient, so that the mobility is not a single valued function of the Hall coefficient. In general, the group VI element concentration in the region of the minimum is no longer small, so that appreciable regions of different band gap and/or opposite conductivity type are possible, and the mobilities are best approached in the manner outlined by WEISBERG.(21) In this connection it is of interest to note that the substitution of a group V atom into the $A_2^{III} B_3^{VI}$ lattice should result in *p*-type conductivity, which is observed for As doped Ga_2Se_3.(6)

Acknowledgements—The authors express their appreciation to W. OSHINSKY for preparing some of the crystals used in this study, and to G. HORNBERGER for performing the chemical analysis.

REFERENCES

1. WOOLEY J. C. and SMITH B. A., *Proc. phys. Soc. Lond.* 72, 867 (1958).
2. WOOLEY J. C., GILLETT C. M. and EVANS J. A., *J. Phys. Chem. Solids* **16**, 138 (1960).
3. WOOLEY J. C., PAMPLIN B. R. and EVANS J. A., *J. Phys. Chem. Solids* **19**, 147 (1961).
4. WOOLEY J. C. and KEATING P. N., *Proc. phys. Soc. Lond.* **78**, 1009 (1961).
5. GORYUNOVA N. A. and GRIGOR 'EVA U. S., *J. Tech. Phys. U.S.S.R.* **26**, 10, 2157 (1956).
6. NASLEDOVE D. N. and FELTIN'SH I. A., *Sov. Phys. Solid State* **1**, 510 (1959).
7. CHENG L. K., *Analyt. Chem.* **28**, 1738 (1956).
8. WHELAN J. M., STRUTHERS J. D. and DITZENBERGER J. A., *Properties of Elemental and Compound Semiconductors.* (Edited by GATOS H. C.) p. 141. Interscience, New York (1960).
9. PFANN W. G., *Trans. Amer. Inst. min. (metall.) Engrs.* **194**, 747 (1952).
10. WHELAN J. M., STRUTHERS J. D. and DITZENBERGER J. A., *Proceedings of the* 1960 *International Conference on Semiconductors* (Prague), Publishing House of the Czechoslovak Academy of Sciences, Prague (1961).
11. SPITZER W. and WHELAN J. M., *Phys. Rev.* **114**, 59 (1959).
12. SPITZER W. and FAN H. Y., *Phys. Rev.* **108**, 268 (1957).
13. BECKER W. M., RAMDAS A. K. and FAN H. Y., *J. appl. Phys.* **32**, 2094 (1961).
14. HAHN H. and KLINGER W., *Z. anorg. Chem.* **259**, 135 (1949).
15. MULLIN J. B. and HULME K. F., *J. Phys. Chem. Solids* **17**, 1 (1960).
16. ALLRED W. P. and WILLARDSON R. K., Abstracts of the Chicago Meeting of the Electrochemical Society, p. 178. Spring (1960).
17. RUPPRECHT H., *Acta Cryst.*, **16a**, 395 (1961).
18. BURTON J. A., PRIM R. C. and SLICHTER W. P., *J. chem. Phys.* **21**, 1987 (1953).
19. STRAUSS A. J., *Phys. Rev.* **121**, 1087 (1961).
20. BATE R. T., *J. appl. Phys.* **33**, 26 (1962).
21. WEISBERG L. R., *J. appl. Phys.* **33**, 1817 (1962).

J. Phys. Chem. Solids Pergamon Press 1963. Vol. 24, pp. 443–451. Printed in Great Britain.

ON THE MAGNITUDE OF VACANCY SUPERSATURATIONS IN SILVER DURING DEFORMATION AT ELEVATED TEMPERATURES*

R. B. MINCH and R. W. BALLUFFI

University of Illinois, Urbana, Illinois

(*Received* 3 *October* 1962; *revised* 9 *November* 1962)

Abstract—The electrical resistivity of large silver single crystals was measured during and directly after plastic deformation under essentially isothermal conditions near 700 and 800°C. Strain rates of $11{\cdot}6 \times 10^{-5}$ and $58{\cdot}3 \times 10^{-5}$ sec^{-1}, and total strains between 0·07 and 0·09 were employed. Particular efforts were made to detect transient resistivity decays directly after the cessation of deformation such as would be produced by the possible decay of deformation-induced crystal defects. In two runs no resistivity decay greater than the experimental sensitivity of about $2{\cdot}6 \times 10^{-10}$ Ω cm was found. In three runs extremely small apparent decays of the order of 10^{-9} Ω cm were found. These small effects could conceivably have been due, in whole or in part, to: (1) experimental factors not related to the actual relaxation of defects in the specimens; (2) decay of excess dislocations; and, (3) decay of excess point defects. Possibility (1) could not be confirmed or rejected by any independent means. Possibility (2) was practically eliminated by approximate calculations which indicated that the resistivity due to the excess dislocations was well below the level of detection. Possibility (3) was shown to correspond to vacancy supersaturations in the specimens during deformation no larger than those in the range between 6 and 50 per cent.

The experimental results are therefore completely consistent with the diffusion-deformation measurements of Savitskii and Darby *et al.* which predict vacancy supersaturations less than ≃ 50 per cent during similar deformation in silver but are in marked disagreement with the diffusion-deformation experiments of Forestieri and Girifalco and Lee and Maddin which imply supersaturations at least two orders-of-magnitude larger.

1. INTRODUCTION

THERE is extensive experimental evidence(1–3) that excess point defects are generated during the plastic deformation of face-centered cubic metal crystals. Forced non-conservative dislocation motion evidently occurs during the deformation, leading to the formation of point defects. Extensive investigation of this phenomenon has been carried out at, and below, room temperature using a variety of techniques such as the measurement of changes of electrical resistivity, stored energy, density, X-ray lattice parameter, flow stress, etc., and also direct observation by means of transmission electron microscopy.

No comparable experiments of this type have been carried out during high temperature deformation (i.e. at temperatures greater than half the absolute melting temperature), since the defects anneal out with great rapidity at these temperatures making observation difficult. However, in recent years a number of investigations have been carried out of diffusion rates in metals at elevated temperatures in the presence of simultaneous deformation at a constant strain rate. Under these conditions it might be expected that the steady state vacancy concentration should be increased above the equilibrium value as a result of the generation of excess vacancies, and that

$$C_v - C_v^0 = \Delta\dot{N}_v\tau, \tag{1}$$

where C_v is the steady state vacancy concentration, C_v^0 is the usual equilibrium value, $\Delta\dot{N}_v$ is the rate of generation of excess vacancies due to the

---

* This research was supported by the United States Air Force through the Air Force Office of Scientific Research.

deformation, and τ is the effective lifetime of the excess vacancies. Since the diffusion coefficient is proportional to the vacancy concentration, this situation leads to an enhancement of the diffusivity given by

$$D_s/D_u = 1+\frac{\Delta\dot{N}_v\tau}{C_v^0}, \qquad (2)$$

where D_s is the diffusivity during straining, and D_u is the usual static diffusivity in the unstrained material. The magnitude of the diffusion enhancement therefore depends directly on the rate of excess vacancy production and the length of the vacancy lifetime. At the present time there is considerable disagreement among investigators as to whether or not measurable increases in the vacancy concentration and in the diffusivity arise from deformation-produced vacancies at elevated temperatures. The disagreement is particularly marked in the case of silver, where in one group of experiments no detectable effects have been found,(4, 5) and in another group of experiments large enhancements have been reported(6, 7) under rather similar experimental conditions. An extensive analysis of the entire problem of strain enhanced diffusion has been carried out recently by RUOFF and BALLUFFI(8–10) which leads to the following main conclusions: (1) the rate of excess vacancy production and the vacancy lifetime are sufficiently small during the high temperature deformation of typical metals so that any perturbations of the usual vacancy concentration should be below the limit of detection in standard diffusion experiments; (2) the large apparent enhancement reported in Refs. 6 and 7 were due solely to experimental difficulties with specimen distortion resulting from the deformation; (3) under certain circumstances the bulk diffusivity in metals may be noticeably enhanced by fast diffusion short-circuiting along static or moving dislocations and grain boundaries.

In view of the above situation the present work was carried out in order to measure directly any possible excess vacancy concentration present in deformed silver at elevated temperatures using a different technique, i.e. the well established electrical resistivity technique. This method has a number of advantages over the diffusion method of measuring excess vacancies, since: (1) it is a bulk measurement sensitive mainly to the presence of vacancies (it will be shown later that the resistivity of the associated excess dislocation is most probably negligible); (2) it is highly sensitive to the presence of vacancies. The diffusion measurement on the other hand may be affected by short-circuiting, and by the geometrical distortion of the specimen. Also, when the diffusion rate is measured inward from the free specimen surface (as is commonly the case) the vacancy concentration is only sampled in a narrow region near the specimen surface which may be heavily depleted of vacancies by the sink action of the surface. This phenomenon has been extensively analyzed in Ref. 8.

Silver was an ideal metal for the present work, since: (1) the equilibrium concentrations of vacancies are known;(11) (2) the resistivity per atomic per cent of vacancies(12) is known; and (3) an estimate of the dislocation density and the dislocation resistivity can be made.

The investigation consisted essentially of deforming silver single crystals at a constant strain rate at 700 and 800 C, while making simultaneous resistivity measurements, and then abruptly stopping the deformation and looking for a possible resistance decay due to the annealing of excess vacancies.

2. EXPERIMENTAL PROCEDURE

A. Specimen geometry and preparation

Massive single crystal resistivity specimens were desired in order to minimize the effects of grain boundaries and free surfaces as sources and sinks for vacancies and to ensure that the geometry of the deformation and the dislocation structure were those characteristic of large bulk specimens. The geometry shown in Fig. 1 was, therefore, employed. Each specimen assembly consisted of two legs joined at one end by a large cylinder which acted as a riser during casting and a low resistance connection during the electrical measurements. The free end of each leg was provided with a rectangular block as shown in order to facilitate gripping during deformation. With this arrangement each leg (having a gauge length of 30 cm and a diameter of 5 mm) could be twisted independently of the other. By measuring the resistance change of the two legs in series as one leg was

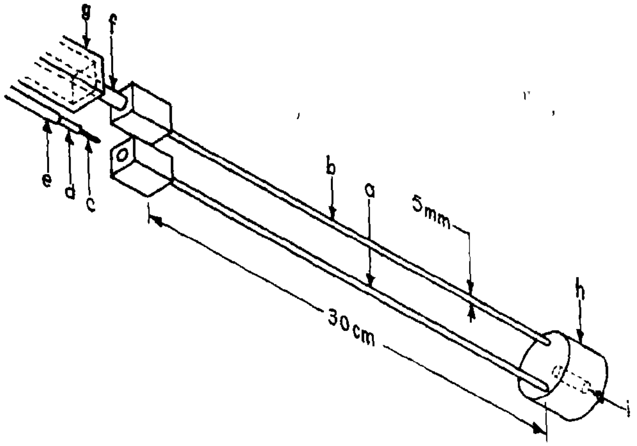

FIG. 1. Resistivity specimen assembly geometry: two silver specimen legs *a* and *b* cast together as single crystal connected by low resistance silver cylinder *h*. Potential lead *c* and current lead *e* are separated by quartz tube *d* and are shown threaded into specimen at *f*. Torsion grip is shown at *g* and the thermocouple well at *i*.

twisted while the other remained static it was possible to determine the resistivity changes in the twisted leg. Each specimen assembly therefore, provided two resistivity specimens. The rectangular end of each leg was drilled and tapped to receive concentric current and potential leads shown as *e* and *c* respectively in Fig. 1.

The specimen assemblies were cast in spectroscopically pure graphite molds under vacua of 10^{-6} mm Hg by the standard Bridgman technique. To study the possible effect of purity, specimens were made from two grades of silver. One group was cast from 99·99 per cent Ag obtained from the Handy and Harmon Company and was from the same lot used by Darby, Tomizuka and Balluffi.(5) The second group was cast from 99·9999 per cent Ag supplied by the Consolidated Mining and Smelting Company of Canada. The main impurities in the initial materials are listed in Table 1.

B. Deformation apparatus

A schematic view of the overall apparatus is shown in Fig. 2. The furnace was heated by six separate windings in order to allow adjustment for minimizing the longitudinal temperature gradient in the region of the specimen. Voltage stabilizers in the power input, and a large thermal inertia kept thermal drift during the experiments to less than 0·005°C per min. The specimen temperature was determined by means of a chromel–alumel thermocouple inserted in the well shown at *h* in Fig. 1.

The specimen was supported on a quartz liner from the cylindrical upper end in order to maintain electrical insulation. Torque was transmitted through insulating ceramic grips to the lower rectangular ends of the specimen as shown in Fig. 1. The ceramic grips were driven by stainless steel tubes through which the current and potential leads ran concentrically, the current leads being

Table 1. *Purity of the two grades of silver used (in parts per million)*

	Al	Ca	Fe	Mg	Si	Cu	Sn	Pb
99·9999 per cent Ag	0·1	0·1	0·2	0·1	0·1	—	0·2	—
99·99 per cent Ag	—	—	< 10	—	—	70	—	< 10

in the form of tubes themselves and insulated with concentrically running quartz tubes. The torsion tubes were driven by a motor and gear reducer subjecting the specimen to a constant torsional strain rate. Vacua of 10^{-6} mm Hg or better were maintained.

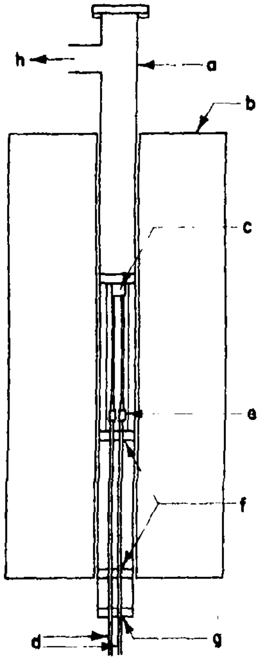

FIG. 2. Furnace and torsion apparatus: furnace tube *a* rests vertically in furnace *b*. Specimen *c* is deformed by torsion rods *d* connected to grips *e*. *f* and *g* are alignment bushings, *h* goes to diffusion pump. Torsion rods enter furnace tube through rotating vacuum seals.

C. Electrical Measurements

Electrical resistivity changes were determined with a Leeds and Northrup Precision Kelvin Double Bridge as shown in Fig. 3. This arrangement employed separate current and potential leads with high resistances in the latter to render lead and contact resistances relatively insignificant.(13) Care was taken in positioning the current and potential leads in the specimens in order to minimize end effects. The bridge current was held constant by measuring the potential drop which it produced across a 0·001 Ω standard resistor with a Leeds and Northrup Type K-3 potentiometer and varying the circuit resistance with a series of oil-cooled rheostats. The bridge was calibrated independently in terms of galvanometer deflection thus avoiding continuous balancing of the circuit.

The parameters of the present bridge circuit differed somewhat from those usually employed, since the current lead resistance α was larger than usual relative to the small resistance of the large specimen used. In this case the standard bridge equation for the absolute specimen resistance contains a non-negligible additive term linear in α.(13) However, this term drops out in difference measurements as long as α remains constant. In the present difference measurements α was maintained constant by always connecting it to the static specimen in order to avoid any deformation by twisting.

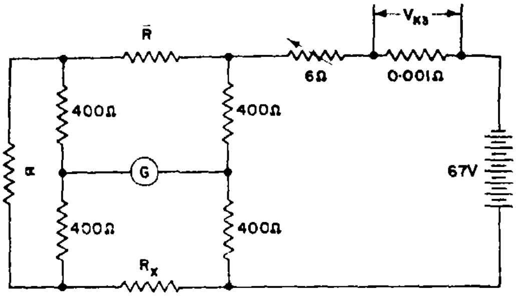

FIG. 3. Resistance measuring circuit: standard Kelvin double bridge. Specimen is $\bar{R}$; low resistance standard is R_x, and V_{K3} is held constant by varying 6Ω variable resistance. α is lead resistance.

In order to check for general consistency in the measurements, the absolute specimen resistance was calculated roughly by neglecting the term in α. The resulting value was observed to agree in every case with published values(14) within about 2 per cent. Of more importance, the temperature dependence of the specimen resistance calculated in this way was found to be in excellent agreement with published data.(14) This result was as expected, since the measurement of the temperature dependence is actually a difference measurement, and is therefore independent of α.

The smallest detectable resistance change in the present work was 4×10^{-8} Ω.

D. Measuring procedure

The bridge current was applied 12 hr before each determination to allow the circuit and the specimen to reach thermal equilibrium. Temperature drift was monitored for 1 hr before deformation and had to be closely linear and of small magnitude before conditions were considered acceptable. The short term thermal drift during all runs was less than could be determined accurately by the standard thermocouple technique used. The specimen was then deformed at a constant strain rate and the resistance changes were measured during deformation as well as for 1 hr afterward. Measurements were taken every minute during deformation and for 10 min afterwards; during the remaining time they were taken every 2 min.

3. RESULTS

A. Specimen structure

Initially all specimens were single crystals of undetermined orientations. Deformation caused recrystallization in only one specimen leg; however, the resulting grain size ($\geqslant 3$ mm) was too large to have caused an appreciable vacancy sink effect.

The strain appeared macroscopically uniform over the specimen lengths as judged by the distribution of surface undulations. In addition to the pronounced surface undulations, there was a marked tendency for each specimen axis to twist into a helix.

B. Resistance measurements

Since resistance changes are a volume effect, the average strain rate, $\bar{\dot{\epsilon}}$, and total average strain, $\bar{\epsilon}_t$, were obtained by integrating the local values over the specimen volume. It is readily shown that these average values in torsional deformation are 2/3 of the respective maximum values at the specimen surface. The experimental values employed are listed in Table 2.

The specimen resistance changes as functions of time are shown in Figs. 4 through 8 for temperatures near 700 and 800°C. Since torsional deformation is inhomogeneous, and since any resistivity changes throughout the specimens must have been non-uniform, we shall designate the specimen resistance as an average value, i.e. by $\bar{R}$. The two runs shown in Figs. 4 and 5 are characterized by an immeasurably small resistance change in the period before deformation, as a

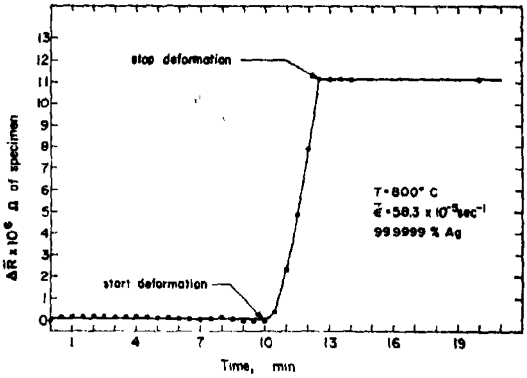

FIG. 4. Resistance changes of specimen as a function of time before, during, and after deformation at 800°C.

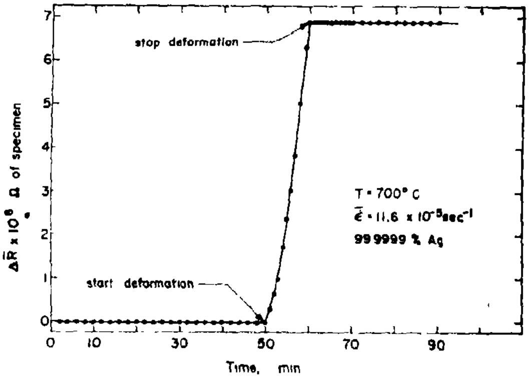

FIG. 5. Resistance changes of specimen as a function of time before, during, and after deformation at 700°C.

Table 2. Deformation data, and values of the maximum apparent resistance decay. $\Delta\bar{R}_{\max}$, and resistivity decay $\Delta\bar{\rho}_{\max}$

Temp. (°C)	$\bar{\dot{\epsilon}}$ ($\sec^{-1} \times 10^5$)	$\bar{\epsilon}_t$	$\Delta\bar{R}_{\max}$ ($\Omega \times 10^7$)	$\Delta\bar{\rho}_{\max}$ (Ω cm $\times 10^{10}$)
		99·9999% Ag		
800*	58·3	0·07	$\leqslant$ 0·4	$\leqslant$2·6
807	11·6	0·07	2·2	14
700	11·6	0·086	$\leqslant$ 0·4	$\leqslant$ 2·6
		99·99% Ag		
800	11·6	0·09	1·2	7·9
700	11·6	0·07	1·0	6·5

* Recrystallized: grain size $\geqslant$ 3 mm.

result of an exceedingly small temperature drift, followed by an abrupt resistance increase beginning and ending with the deformation period. This increase is clearly due to the geometrical shape change of the specimen associated with the deformation. Directly after deformation the resistance again becomes essentially constant with time. No evidence was found for a resistance decay directly after the cessation of deformation which was larger than the sensitivity of the experiment. It should be pointed out that a resistance increase due to the specimen shape change in the present torsional deformation appears quite reasonable. It is readily shown that a single crystal deformed in pure torsion in the absence of other restraints (e.g. gripping effects) will twist into a helix and that the arc length of the helical axis will be the same as the axial length before deformation to at least first order. The projected crystal length will be shorter, however, and the undeformed ends will not remain parallel to the original axial direction. In the present experiment the gripping arrangement maintained the alignment of the ends by bending the crystal and also provided some restraint on the tendency of the projected crystal length to decrease. These effects could easily have caused the ~ 0·1 to ~ 0·5 per cent increase in effective specimen length indicated by the data. As mentioned previously, the crystals actually twisted into rather irregular helices, and therefore, no attempts were made to carry out accurate measurements of the actual arc lengths of the specimens after deformation.

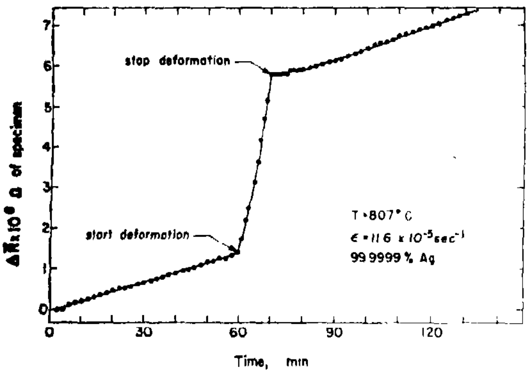

FIG. 6. Resistance changes of specimen as a function of time before, during, and after deformation at 807°C.

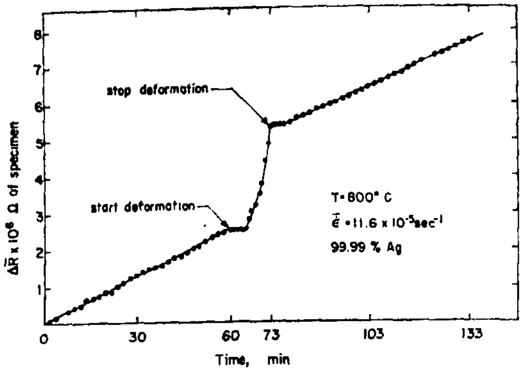

FIG. 7. Resistance changes of specimen as a function of time before, during, and after deformation at 800°C.

The results in Figs. 6, 7 and 8 indicate a higher rate of thermal drift during the runs as shown by the measurable monotonic resistivity changes with time both before and after the deformation. In addition, there are slight perturbations of the resistivity for a short period after deformation. In these three cases the perturbations are negative indicating very small apparent resistance decays. The apparent decay periods vary between about 5–10 min and no increase in decay time with decreasing temperature is apparent. We have no simple explanation (see discussion below) as to why these effects appeared in certain cases (Figs. 6 to 8) and not in others (Figs. 4 and 5). We note

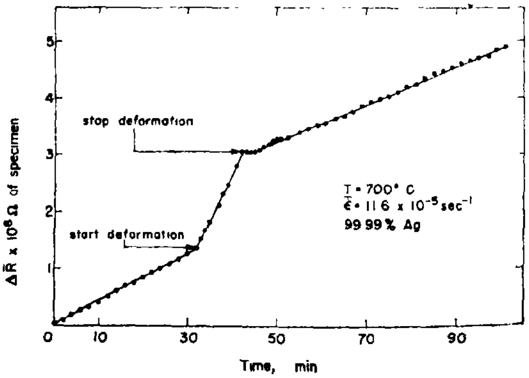

FIG. 8. Resistance changes of specimen as a function of time before, during, and after deformation at 700°C.

that there are no apparent effects of specimen purity within the limited range of the experiments. The maximum apparent resistance decay in each specimen after deformation was taken as the difference between the resistance value at the instant deformation ceased and the resistance value at this same time obtained by a backwards extrapolation of the linear curve which was always accurately obtained after the decay of the perturbation. The small maximum resistance increments. $\Delta\bar{R}_{\max}$, obtained in this way are listed in Table 2. The corresponding increments in Figs. 4 and 5 were taken to be the estimated accuracy in the measurement of $\Delta\bar{R}$. All of these average resistance increments were converted to average resistivity increments, $\Delta\bar{\rho}_{\max}$, which are also given in Table 2.

4. INTERPRETATION AND DISCUSSION

The maximum resistivity decreases directly after the cessation of deformation which are listed in Table 2 could conceivably be due, in whole or in part, to: (1) experimental factors not related to the actual relaxation of crystal defects in the specimens; (2) decay of excess dislocations; and, (3) decay of excess point defects. Let us consider these possibilities in turn.

It is, of course, conceivable that small specimen movements and temperature relaxations may have occurred leading to slight apparent resistance perturbations directly after the deformation. In view of the small resistance increments involved it was not possible to check these possibilities by any independent method. We conclude that possibility(1) can be neither confirmed nor rejected.

Possibility (2) may be investigated by comparing the experimentally observed resistivity increments with estimates of the expected resistance decay due to annealing of the excess dislocations. For this purpose it is necessary to arrive at estimates of both the resistivity per unit dislocation density, ρ_d, and the dislocation density change during the decay. Previous work(15, 16) indicates that $\rho_d = 2\times10^{-19}$ Ω cm per unit dislocation density is a reasonable value for silver.(17) An order-of-magnitude estimate of the total dislocation density, N_d(cm^{-2}) may be made by following an approximate method discussed by BALLUFFI and RUOFF(8) where

$$N_d \simeq 1{\cdot}85\times10^{8}\,[\sigma(20^{\circ}\mathrm{C})\cdot(G_{\mathrm{Cu}}/G)]^2. \quad (3)$$

Here, $\sigma(20^{\circ}\mathrm{C})$ is the flow stress of the dislocated crystal at 20°C in units of kg/mm^2, G_{Cu} is the shear modulus of copper, and G is the shear modulus of the metal in question. LIVINGSTON(18) has found that this relation holds for copper at room temperature.

Since silver should not differ greatly from copper, we shall use equation (3) for silver. (The ratio of shear moduli are inserted in order to take into account differences in elastic properties.) We now require values of $\sigma(20^{\circ}\mathrm{C})$. DARBY *et al.*(5) found that $\sigma(800^{\circ}\mathrm{C}) = 0{\cdot}28$ kg/mm^2 and $\sigma(700^{\circ}\mathrm{C}) = 0{\cdot}42$ kg/mm^2 for silver single crystals strained at the rate $\bar{\dot{\epsilon}} = 14{\cdot}7\times10^{-5}$ sec^{-1}. The corresponding values of σ at the present strain rate of $\bar{\dot{\epsilon}} = 11{\cdot}6\times10^{-5}$ sec^{-1} may be obtained using the relation(17)

$$\sigma \propto \bar{\dot{\epsilon}}^{1/4}.$$

Also, the ratio of the flow stress at the elevated temperature to that at 20°C may be estimated for silver from the measurements of HIRSCH and WARRINGTON(19) on copper by using their flow stress ratio data at temperatures corresponding to the appropriate fraction of the absolute melting temperature. The results are: $\sigma(20^{\circ}\mathrm{C}) = 0{\cdot}43$ kg/mm^2 for silver deformed at 800°C at $\bar{\dot{\epsilon}} = 11{\cdot}6\times10^{-5}$ sec^{-1}; $\sigma(20^{\circ}\mathrm{C}) = 0{\cdot}57$ kg/mm^2 for silver deformed at 700°C at $\bar{\dot{\epsilon}} = 11{\cdot}6\times10^{-5}$ sec^{-1}. This procedure is not completely accurate, of course, since silver and copper are known to possess different stacking fault energies. However, the error introduced should be relatively small, since Hirsch and Warrington found that the flow stress ratio data for the dissimilar metals, copper and aluminum, normalized fairly well on a scale of temperature relative to that of the melting point.

From equation (3), therefore, the total estimated dislocation densities are $N_d\,(800^{\circ}\mathrm{C}) \simeq 9\times10^{7}$ cm^{-2} and $N_d\,(700^{\circ}\mathrm{C}) \simeq 1{\cdot}6\times10^{8}$ cm^{-2} respectively. The resistivities due to the total dislocation contents at the end of the deformation period were then $\simeq 0{\cdot}18\times10^{-10}\,\Omega$ cm at 800°C, and $\simeq 0{\cdot}32\times10^{-10}$ Ω cm at 700°C. Since only a fraction of the total dislocation density would anneal out in the few minutes after deformation, we conclude that the resistivity decays due to dislocation annealing were probably smaller than the increments listed in Table 2 by factors considerably larger than one order-of-magnitude. It is, therefore, unlikely that dislocation annealing effects were of any importance in the present measurements.

It seems unlikely that the resistivity decays were due to the annealing of excess vacancies, because of the erratic appearance of the decays amongst the various runs and the observation that the length of the decay period in the few available measurements does not have the proper temperature dependence. Nevertheless, it is instructive to calculate the maximum possible vacancy concentration decays, $\Delta\bar{C}_{v\max}$, which could have occurred in the present experiments on the assumption that the maximum average resistivity increments listed in Table 2 resulted entirely from this cause. The results are given in Table 3 where the values of $\Delta\bar{C}_{v\max}$ are also directly compared to the vacancy concentration in equilibrium at each temperature. The calculations were made using the following expressions:(11, 12)

$$1{\cdot}3\times 10^{-4}\cdot\Delta\bar{C}_{v\max} = \Delta\bar{\rho}_{\max}(\Omega\,\mathrm{cm});$$

$$C_v^0 = \exp(1{\cdot}5)\cdot\exp(-1{\cdot}09\ \mathrm{eV}/kT).$$

Here, T is the absolute temperature, and k is Boltzmann's constant.

The results in Table 3 indicate that the maximum possible vacancy supersaturations in the present specimens ranged between about 0·06 and 0·50. This finding is completely consistent with the results of the group of self-diffusion experiments on deformed silver(4, 5) which indicated no detectable diffusion enhancements as a result of deformation at these temperatures. The present results, however, are in marked disagreement with the other group of deformation-diffusion experiments reporting large enhancements.(6, 7) For purposes of comparison we have included in Table 3 the approximate vacancy supersaturations predicted for the present conditions by the data reported in these latter experiments.(6, 7) The values were compared on the basis that

$$\Delta\rho(r) \propto \Delta C_v(r) \propto \dot{\epsilon}(r),$$

where the first two quantities are the incremental increases due to the deformation at the radial position r. For a torsional specimen it is readily shown that

$$\begin{aligned}\Delta\bar{\rho} &= 2/3\cdot\Delta\rho(r=a),\\ \Delta\bar{C}_v &= 2/3\cdot\Delta C_v(r=a),\\ \bar{\dot{\epsilon}} &= 2/3\ \dot{\epsilon}(r=a);\end{aligned}$$

where a is the specimen radius.

The supersaturations predicted by LEE and MADDIN(7) and by FORESTIERI and GIRIFALCO(6) are seen to be at least two orders of magnitude larger than the maximum possible values derived from the present direct resistivity experiment. We conclude that these diffusion experiments were

Table 3. Maximum excess vacancy concentrations based on measured resistivity changes, and comparison with some previous diffusion experiments

Temp °C	$\bar{\dot{\epsilon}}$ (sec$^{-1}\times 10^5$)	C_v^0 ($\times 10^5$)	$\Delta\bar{C}_{v\max}$ ($\times 10^6$)	$\left[\dfrac{\Delta\bar{C}_{v\max}}{C_v^0}\right]^*$	$\left[\dfrac{\Delta\bar{C}_{v\max}}{C_v^0}\right]^\dagger$	$\left[\dfrac{\Delta\bar{C}_{v\max}}{C_v^0}\right]^\ddagger$
			99·9999% Ag			
800	58·3	3·4	$\leqslant$ 2·0	$\leqslant$ 0·06	$\simeq$ 176	—
807	11·6	3·7	10·8	0·29	$\simeq$ 35	—
700	11·6	1·0	$\leqslant$ 2·0	$\leqslant$ 0·20	$\simeq$ 55	$\simeq$ 280
			99·99% Ag			
800	11·6	3·4	6·1	0·18	$\simeq$ 35	—
700	11·6	1·0	5·0	0·50	$\simeq$ 55	$\simeq$ 280

* Present results.

† Suggested by diffusion data of LEE and MADDEN.(7)

‡ Suggested by diffusion data of FORESTIERI and GIRIFALCO.(6)

influenced by effects other than those due to excess vacancies. This same conclusion has already been reached independently in the analysis of RUOFF and BALLUFFI,(8–10) where it has been suggested that experimental difficulties with interface roughening were largely responsible for the large apparent diffusion enhancements. We emphasize that these experimental differences cannot be explained by differences in specimen purity or grain size,(7) since the 99·99 per cent pure silver used in the present work was nominally of the same composition as the silver used in Refs. (6) and (7), and, since single crystals were used throughout.

The present results indicate that the vacancy supersaturations present during high temperature deformation must be comparatively small. Evidently, the excess vacancy production rates due to deformation, and the lifetimes of these vacancies, are sufficiently small so that the steady state excess concentrations supported by the deformation are small compared to the concentrations normally present in thermal equilibrium. Numerous independent arguments supporting this conclusion have been given by RUOFF and BALLUFFI(8–10) using detailed models for high temperature deformation and diffusion.

REFERENCES

1. COTTRELL A. H., *Vacancies and other point defects in Metals and Alloys.* p. 1. The Institute of Metals, London (1958).
2. BROOM T. H. and HAM R. K., *Vacancies and Other Point Defects in Metals and Alloys.* p. 41. The Institute of Metals, London (1958).
3. BALLUFFI R. W., KOEHLER J. S. and SIMMONS R. O., Tech. Rep. No. 26 to the A.E.C. under Contract AT(11-1)182, University of Illinois, (1962). To be published in the Proceedings of the Symposium on *Recovery and Recrystallization of Metals, Amer. Inst. min. (metall.) Engrs.* Annual Meeting (1962).
4. SAVITSKII A. V., *Phys. Met. Metall.* **10**, 4, 71 (1960; or *Fiz. metal. metalloved.* **10**, No. 4, 564 (1960).
5. DARBY J. B., Jr., TOMIZUKA C. T. and BALLUFFI R. W., *J. appl. Phys.* **30**, 104 (1959); **32**, 840 (1961).
6. FORESTIERI A. F. and GIRIFALCO L. A., *J. Phys. Chem. Solids* **10**, 99 (1959).
7. LEE C. H. and MADDIN R., *Trans. Amer. Inst. min. (metall.) Engrs.* **215**, 397 (1959); *J. appl. Phys.* **32**, 1846 (1961).
8. BALLUFFI R. W. and RUOFF A. L., *Materials Science Center Report* No. 46, Cornell University (to be published, *J. appl. Phys.*).
9. RUOFF A. L. and BALLUFFI R. W., *Materials Science Center Report* No. 47, Cornell University (to be published, *J. appl. Phys.*).
10. RUOFF A. L. and BALLUFFI R. W., *Materials Science Center Report* No. 48, Cornell University (to be published, *J. appl. Phys.*).
11. SIMMONS R. O. and BALLUFFI R. W., *Phys. Rev.* **119**, 600 (1960).
12. DOYAMA M. and KOEHLER J. S., *Phys. Rev.* **127**, 21 (1962).
13. LAWS F. A., *Electrical Measurements* 2nd Ed. p. 186. McGraw-Hill, New York (1938).
14. See: *American Institute of Physics Handbook* (edited by GRAY D. E.) pp. 4–13. McGraw-Hill, New York (1957).
15. KLEIN M. J. and HUGGINS R. A., *Acta Met.* **10**, 55 (1962).
16. LIVINGSTON J. D., *Acta Met.* **10**, 229 (1962).
17. CALRBROUGH L. M., HARGREAVES M. E. and LORETTO M. H., *Phil. Mag.* **7**, 115 (1962).
18. SCHOECK G., in *Creep and Recovery* p. 199. American Society for Metals, Cleveland (1957).
19. HIRSCH P. B. and WARRINGTON D. H., *Phil. Mag.* **6**, 735 (1961).

J. Phys. Chem. Solids Pergamon Press 1963. Vol. 24, pp. 453–467. Printed in Great Britain.

THE DETERMINATION OF THE VIBRATIONAL ENTROPIES OF SOLUTE ATOMS IN DILUTE COPPER SOLID SOLUTIONS BY THE MEASUREMENT OF VAPOUR PRESSURES

R. B. McLELLAN and R. SHUTTLEWORTH

Metallurgy Department, Leeds University

(*Received* 17 *January* 1962; *revised* 5 *September* 1962)

Abstract—An effusion method has been used to investigate the equilibrium between dilute copper based solid solutions and their vapours over a large range of temperature. Neutron irradiated alloys were used and a gamma-ray spectrometer enabled measurements on very dilute alloys to be carried out. The change of vibrational entropy $S_u^+ - S_v^0$ occurring when a solvent atom is replaced by a solute atom and the corresponding enthalpy change $H_u^+ - H_v^0$ were derived from the experimental data. The results are given in the table together with the values of H_u^+, the energy of a solute atom in the solution with respect to a solute atom at rest in a vacuum.

System	$H_u^+ - H_v^0$ kcal/mole	H_u^+ kcal/mole	$\dfrac{S_u^+ - S_v^0}{k}$
Cu–0·1 At. % Ag	26·6 ± 0·69	−45·9 ± 0·69	4·71 ± 0·29
Cu–0·5 At. % Au	2·01 ± 0·29	−70·5 ± 0·29	7·07 ± 0·12
Cu–2·5 At. % Au	1·84 ± 0·26	−70·7 ± 0·26	6·85 ± 0·11

To explain the very large increases in vibrational entropy two models have been discussed. In the first, atomic force constants were used to estimate the change in vibrational frequency with solute diameter for a cluster of 13 atoms. In the second model elastic theory was used to calculate the change in entropy due to the shear and dilational strains around a solute atom. The experimental values of $S_u^+ - S_v^0$ lie between those derived from the two models.

Experimental values of the vibrational entropies deduced by other workers from solvus curves and e.m.f. measurements are also compared with the calculated values.

INTRODUCTION

MANY theories of metallic solutions such as the Bragg and Williams theory and the quasi-chemical theory are based on the assumption that there are no changes in vibrational entropy when a solution is formed and that only changes in configurational entropy need to be taken into account.

A number of measurements have shown that this approximation is not always valid and the topic has been discussed by ORIANI.[1] Gold-nickel alloys have been investigated by SEIGLE, COHEN and AVERBACH,[2] who found that at all concentrations the partial entropies were greater than for a random solution. In the present work the partial excess entropies, $(S_u^+ - S_u^0)$, of silver and gold atoms in dilute solid copper solutions have been deduced. For the silver solute $\exp\{(S_u^+ - S_u^0)/k\} \approx 30$ and for the gold solute $\exp\{(S_u^+ - S_u^0)/k\} \approx 150$. These large values are to be compared with unity, the value assumed for these exponentials in the quasi-chemical theory.

There are two principal methods available for determining the vibrational entropies of solids. In one method the low temperature specific heat is measured; in the other method the equilibrium between the solid and either a gas or another solid of known thermodynamic properties is determined.

The first method has been employed by DE SORBO,(3) who measured the low temperature specific heat of a quenched 50/50 Au–Ni alloy; the measured excess *integral* entropy is about the same as the configurational entropy of a 50/50 random solution. However this method cannot be used for dilute solutions because the small amount of solute will make no appreciable difference to the specific heat, even when the *partial* excess entropy is large.

The second method utilizing the equilibrium between two solid phases has been employed by SEIGLE, COHEN and AVERBACH(2), who measured the e.m.f. of a cell with Ni–Au alloy and pure nickel electrodes, and by Nowick and Freedman who deduced values of the partial excess entropies from phase diagrams. In a binary system where there are no intermediate phases the solid solubility curve (solvus) is the composition of the alloys containing an atomic fraction c_u of the solute that is in equilibrium with the essentially pure solvent. When c_u is small it varies with temperature according to the equation,

$$c_u = \exp(S_u^+ - S_u^0)/k \cdot \exp(H_u^+ - H_u^0)/kT \qquad (1)$$

where $(S_u^+ - S_u^0)$ and $(H_u^+ - H_u^0)$ are the changes in vibrational entropy and energy which occur on transferring a solute atom from the pure solute to the dilute solution. NOWICK and FREEDMAN(4) deduced values of $\exp\{(S_u^+ - S_u^0)/k\}$ that ranged between 0·33 and 8·2 and Seigle *et al.* found that for a gold–nickel alloy containing 5 At. per cent Au $\exp\{(S_u^+ - S_u^0)/k\}$ was 33.

In the present paper, equilibrium was measured between the solution and the vapour. The use of radioactive isotopes enabled very dilute solutions to be used (copper containing 0·1 At. per cent Ag and 0·5 At. per cent Au) and for these solutions the entropy of mixing can be assumed to be ideal. The quantities directly measured in these experiments were $(S_u^+ - S_v^0)/k$ and $(H_u^+ - H_v^0)/k$, the changes in vibrational entropy and energy on replacing a solvent atom by a solute atom.

HUNTINGTON, SHIRN and WAJDA(5) gave the formal equation relating the change in vibrational entropy on replacing a solvent atom (v) by a solute atom (u):

$$\frac{S_u^+ - S_v^0}{k} = \sum_{i=1}^{i=3N} \ln \nu_i/\nu_i' \qquad (2)$$

where ν_i and ν_i' are the frequencies of the $3N$ normal(6) modes before and after the replacement of a solvent atom by a solute atom. The quantity $(S_u^+ - S_v^0)/k$ thus defined is related to the quantity $(S_u^+ - S_u^0)/k$ estimated by Nowick and Freedman by the equation:

$$(S_u^+ - S_v^0) = (S_u^+ - S_u^0) + (S_u^0 - S_v^0) \qquad (3)$$

where S_u^0 and S_v^0 are the entropies per atom of the pure solute and solvent.

The change of entropy of the electrons on alloy formation must also be considered; however for the alloys formed from monovalent copper, silver, and gold this will be negligible in comparison to the effect measured. Even for nickel–gold alloys DE SORBO(3) has justified the neglect of this term.

ZENER(7) has made a simple estimate of $(S_u^+ - S_v^0)/k$ for solute atoms in solid solutions and detailed calculations of the vibrational entropies of vacancies and interstitial atoms have been made by HUNTINGTON, SHIRN and WAJDA.(5) In this paper an elastic model has been used to estimate $(S_u^+ - S_v^0)/k$.

More qualitatively the increase of entropy can be estimated by considering a diatomic molecule in which one of the atoms is replaced by a larger atom. If the potential between the two atoms can be written in the form

$$V(r) = \lambda r^{-s} - \mu r^{-t} \qquad (4)$$

where λr^{-s} and μr^{-t} are the repulsive and the attractive potentials, the equilibrium separation r_0 is given by

$$s\lambda r_0^{-(s+1)} = t\mu r_0^{-(t+1)}. \qquad (5)$$

The curvature of the potential field in which the atoms vibrate can be written in terms of r_0

$$\mathrm{d}^2V/\mathrm{d}r^2 = (s-t)t\mu r_0^{-(t+2)}. \qquad (6)$$

When one of the atoms is replaced by a larger atom it will be supposed that the increase in r_0 is due to the increase in the repulsive coefficient λ whilst s, t, and μ remain constant. Then the vibrational frequency changes from ν to ν' where

$$\nu'/\nu = (1+\delta)^{-(t+2)/2} \tag{7}$$

and $\delta = (r_0' - r_0)/r_0$ is the fractional increase in the separation of the atoms. The vibrational entropy of a 1-dimensional harmonic oscillator is given by(6)

$$S/k = \ln kT/h\nu + 1 \tag{8}$$

so that the increase of entropy when one of the atoms of the molecule is replaced by a larger atom is simply

$$\begin{aligned} \Delta S/k &= \tfrac{1}{2}(t+2)\ln(1+\delta) \\ &= 4\delta \text{ for } t = 6 \end{aligned} \tag{9}$$

A model for a solid solution would be a central atom surrounded by 12 neighbouring atoms. When the diameter of the central atom is increased the vibrational entropy of each of the neighbouring atoms would increase by an amount similar to that given by equation (9). Furthermore the stiffness of the field in which the neighbouring atoms vibrate towards each other would decrease on increasing the size of the central atom. Thus the total increase of entropy would be about 15x that given by equation (9), so that,

$$(S_u^+ - S_v^0)/k \simeq 60\delta \tag{10}$$

For silver and gold dissolved in copper $\delta = 13 \times 10^{-2}$ and this simple calculation predicts a value of $7{\cdot}8/k$ compared to the experimentally determined values of $3{\cdot}92/k$ and $4{\cdot}30/k$; in this comparison the entropy change due to the different masses of the solute and solvent atoms have been subtracted from the experimental values.

EQUILIBRIUM BETWEEN THE VAPOUR AND A DILUTE SOLID SOLUTION

In the present measurements the composition of the vapour is compared with the composition of the dilute solid solution with which it is in equilibrium.

In equilibrium the chemical potentials of both components in the solid and vapour are equal. The chemical potentials of the solute and solvent in the dilute solid substitutional solutions are(8)

$$\left.\begin{aligned} \mu_u^s &= \mu_u^+ + kT\ln c_u \\ \mu_v^s &= \mu_v^0 + kT\ln c_v \end{aligned}\right\} \tag{11}$$

The term $k\ln c_u$ accounts for the configurational entropy since in a dilute solid solution ordering is negligible. The term μ_u^+ can be written

$$\mu_u^+ = H_u^+ - TS_u^+ \tag{12}$$

where H_u^+ is the increase in enthalpy and S_u^+ the increase in entropy due to the addition of a solute atom to the pure solvent, i.e.

$$\left.\begin{aligned} H_u^+ &= \operatorname*{Lt}_{c_u\to 0}\left(\frac{\partial H}{\partial n_u}\right), \\ \text{and}\quad S_u^+ &= \operatorname*{Lt}_{c_u\to 0}\left(\frac{\partial S}{\partial n_u}\right) + k\ln c_u \end{aligned}\right\} \tag{13}$$

where H and S are the enthalpy and entropy of the alloy.

The chemical potential of the solute atoms in the perfect monatomic vapour is given by(9)

$$\mu_u^g = kT\ln\left(\frac{h^2}{2\pi m_u kT}\right)^{3/2}\frac{1}{\omega_u} + kT\ln C_u \tag{14}$$

where C_u is the number of solute atoms per unit volume and ω_u is the statistical weight of the solute atom in the vapour. The energy zero is that of atoms at rest in the gas.

In equilibrium $\mu_u^g = \mu_u^s$ so that

$$\frac{C_u}{c_u} = \left(\frac{2\pi m_u kT}{h^2}\right)^{3/2}\omega_u \exp\left(-\frac{S_u^+}{k}\right)\exp\left(\frac{H_u^+}{kT}\right). \tag{15}$$

A similar equation holds for the solvent so that

$$\frac{C_u/c_u}{C_v/c_v} = \left(\frac{\omega_u}{\omega_v}\right)\left(\frac{m_u}{m_v}\right)^{3/2}\exp\left(-\frac{S_u^+ - S_v^0}{k}\right) \times \exp\left(\frac{H_u^+ - H_v^0}{kT}\right). \tag{16}$$

and $(S_u^+ - S_v^0)$ and $(H_u^+ - H_v^0)$ are the increase of vibrational entropy and enthalpy when a solute atom is substituted for a solvent atom.

This thermodynamic treatment of the equilibrium is similar to that used by Johnson and

SHUTTLEWORTH(10) for the solubility of krypton in metals.

In these experiments the composition of the vapour was determined by allowing it to effuse through a small orifice in a Knudsen cell and condense on a target. The number of solute or solvent atoms passing through the aperture is proportional to the number of atoms per unit volume in the vapour and to the mean velocity with which they move. The mean velocity of an atom is inversely proportional to its mass so that the quantity determined by experiment

$$\frac{N_u/N_v}{n_u/n_v} = \frac{C_u/C_v}{c_u/c_v}\left(\frac{m_v}{m_u}\right)^{1/2} \qquad (17)$$

where N_u, N_v, n_u and n_v are the numbers of atoms of solute and solvent condensed on the target and in a sample of the solid. Hence

$$\sigma = \exp\left(-\frac{S_u^+ - S_v^0}{k}\right)\exp\left(\frac{H_u^+ - H_v^0}{kT}\right)$$

where

$$\sigma = \frac{N_u/N_v}{n_u/n_v}\cdot\frac{\omega_v M_v}{\omega_u M_u} \qquad (18)$$

where M_u and M_v are the atomic weights of the solute and solvent. The statistical weights ω for copper, silver and gold atoms are all two.

A plot of $\ln \sigma$ against $1/T$ gives a line of slope $(H_u^+ - H_v^0)/k$ and an intercept of $-(S_u^+ - S_v^0)/k$; this is valid even when H and S are temperature dependant because of the thermodynamic relations(11) $G = H - TS$ and $H = \partial(G/T)/\partial(1/T)$.

EXPERIMENTAL METHOD

A Knudsen effusion method has been used to investigate the equilibrium between solid dilute alloys and the vapour phase. The composition of the vapour in equilibrium with the solid was determined by condensing the vapour effusing from a Knudsen orifice. Prior to effusion the alloys were made radioactive by irradiation in a neutron flux of 12×10^{11} n/cm^2 per sec. for one week; the composition of the condensate and a sample of the alloy were determined from the γ-ray activity. The use of a γ-ray spectrometer enabled quantities of gold as small as 10^{-10} g to be estimated.

(a) *Preparation of the alloys*

When σ is either greater or less than unity the vapour that effuses from the cell will contain a greater proportion of either solute or solvent than does the alloy; the composition at the surface will remain constant only if the rate of evaporation is small compared to the rate of diffusion. To make the surface changes negligible the rate of evaporation per unit area was reduced by rolling the specimens into foils of large area.

In non-steady state diffusion problems, the characteristic distance is $\sqrt{(Dt)}$ where D is the diffusion coefficient and t is the time. Thus concentration gradients will be small, provided that the amount of the more volatile component that effuses is small compared with the amount within a distance $\sqrt{(Dt)}$ of the surface. For effusions with silver alloys ($\sigma \sim 10^3$) the ratio of the amount of silver effused to the amount in the thickness $\sqrt{(Dt)}$ was 10^{-4} at the highest temperature, and 4×10^{-2} at the lowest temperature. For effusions with gold alloys ($\sigma \sim 10^{-2}$) the ratio of the amount of copper that effused to the amount in thickness $\sqrt{(Dt)}$ ranged from 10^{-5} at the highest temperature, to 10^{-6} at the lowest temperatures.

In order to produce the foils 2 cm lengths were cut off the cast cylinders and after removal of the outer layers these were rolled into $1 \times 30 \times 0{\cdot}001$ cm foils. Copper-beryllium was used since experience had shown that the use of steel rolls leads to pick-up of iron. Before rolling the rolls were cleaned with metal polish and then washed in alcohol and the foil and rolls were again washed in alcohol after each 10 passes. The foils were then coiled, sealed up in silica ampoules, and dispatched to Harwell for irradiation.

(b) *The effusions*

The effusion apparatus used, shown in Figs. (1) and (2) is that used by PYLE and SHUTTLEWORTH(12) to investigate liquid–vapour equilibrium in dilute copper alloys. The apparatus has been used by McLELLAN and SHUTTLEWORTH(13) to determine the vapour pressure of solid copper absolutely down to 714°C.

Before the effusions were carried out the alloy specimens were annealed in the apparatus for 1½ hr at a temperature of 10–15°C below the melting point. Experience had shown that it was necessary to follow this procedure in order to obtain reproducible results.

The furnace was supplied with current from a constant voltage transformer and the temperature of the furnace and specimen was determined by a Pt–Pt/Rh thermo-couple spot welded to the base of the crucible. Manual adjustments were made to the mains input to the furnace transformer with a "Variac" to maintain a constant temperature. Even at temperature about 1000°C the temperature control was within ± 2°C. The temperature measurement was checked by measuring the melting points of copper, silver and antimony in the furnace and agreement to within ± 2°C was found.

The effusions were carried out down to a temperature at which the minimum measurable amount of radio-activity was obtained on the target when using a large Knudsen orifice and long effusion times (8 hr). Several effusions were carried out on the same alloy specimen after it had been annealed and small samples of the alloy were taken before and after the effusions.

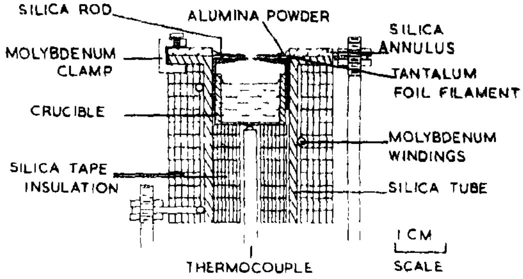

FIG. 2. Furnace.

The Knudsen condition, that the ratio of the orifice diameter to the mean free path of the copper atoms should be much less than unity was always satisfied. Even at the highest vapour pressures this ratio was less than 0·1.

In these experiments the quantity measured is the ratio of the numbers of solute and solvent atoms effusing and this ratio should not be sensitive to the geometry of the apparatus since geometrical factors would be expected to affect the effusion of both types of atom equally.

After each effusion the targets were removed and the radio-active material adhering was dissolved in a standard volume (2 cm^3) of a suitable acid; (10 per cent nitric acid in the case of the Cu-Ag alloys and aqua-regia in the case of the Cu-Au alloys.)

(c) *Radio-active assaying*

From equation (18) it is seen that the essential measurement is the ratio $(N_u/n_u)/(N_v/n_v)$. This can be derived by measuring the activities of the solute and solvent on the target and in a sample of the alloy from the crucible. It is not necessary to know the specific activity of the solute and solvent; however, for the Cu–Au system small pieces of copper and gold were irradiated along with the alloy and this enabled the actual masses of gold and copper on the target and the composition of the alloy in the crucible to be estimated. Because the solutes Ag and Au gave very different

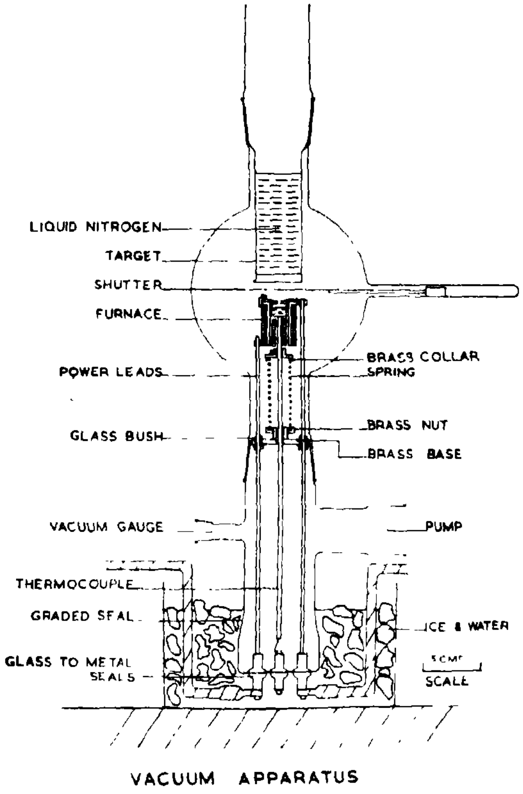

FIG. 1. The vacuum apparatus.

Table 1. Cu – 0·1 *per cent* Ag *effusions; Target radius* = 2·0 *cm*

Effusion temperature (°C)	Effusion time (min)	Orifice area (10^{-3}cm^2)	$\frac{N_u/n_u}{N_v/n_v}$ (10^2)
1065	20	1·96	1·96
1040	20	1·96	2·20
1029	20	1·96	2·63
1014	20	1·96	2·84
999	25	1·96	3·50
977	30	1·96	4·03
954	35	1·96	4·98
931	40	1·96	5·60
915	40	1·96	6·87
899	50	1·96	9·25
860	60	1·96	12·8
844	45	7·85	14·1
828	50	7·85	14·4
812	65	7·85	17·8
796	90	7·85	30·6

Table 2. Cu – 0·5 *per cent* Au *effusions; Target radius* = 2·0 *cm*

Effusion temperature (°C)	Effusion time (min)	Orifice area (10^{-2} cm^2)	Target to orifice distance (cm)	$\frac{\text{Mass Au}}{\text{Mass Cu}}$ in crucible (10^{-2})	At. % Au in crucible	Mass Cu on target (10^{-6} g)	Mass Au on target (10^{-10} g)	$\frac{N_u/n_u}{N_v/n_v}$ (10^{-8})
1029	40	7·85	0·75	1·79	0·58	13·8	14·3	5·79
1029	40					13·9	14·8	5·95
1029	40					13·0	13·4	5·76
1054	30	12·7	0·75	1·67	0·54	43·2	42·1	5·84
1014	35					15·2	12·9	5·06
999	40					13·1	12·9	5·90
984	50					11·5	11·5	5·96
964	75					12·1	11·7	5·77
949	90					9·44	11·0	6·98
931	120					6·18	6·08	5·89
951	35	70·7	1·76	1·67	0·54	3·38	3·51	6·22
899	45					3·20	3·51	6·56
844	70					3·06	3·17	6·21
868	135					4·01	4·18	6·24
852	240					4·17	4·51	6·47
836	180	83·0	1·76	1·59	0·52	2·08	2·21	6·69
820	300					2·36	2·46	6·56
804	480					1·70	1·72	6·35

Table 3. Cu – 2·5 *per cent* Au *effusions; Target radius* = 2·0 *cm*

Effusion temperature (°C)	Effusion time (min)	Orifice area (10^{-2} cm^2)	Target to orifice distance (cm)	$\frac{\text{Mass Au}}{\text{Mass Cu}}$ in crucible (10^{-2})	Atomic %Au in crucible	Mass Cu on target (10^{-6} g)	Mass Au on target (10^{-10} g)	$\frac{N_u/n_u}{N_v/n_v}$ (10^{-3})
1040	25	1·77	2·29	9·56	3·3	9·04	58·8	6·80
1022	50					13·9	92·7	6·96
1007	60					11·0	71·2	6·79
984	75					9·21	59·5	6·76
961	90					6·74	43·3	6·73
946	100					6·97	44·1	6·61
931	120					4·04	25·9	6·71
915	40	4·94	3·81	7·90	2·7	1·22	6·99	7·25
891	50					0·661	4·19	8·02
876	60					0·536	3·15	7·41
852	75					0·407	2·45	7·63
828	100	8·30	2·29	6·35	2·1	1·07	4·88	7·18
812	180					1·23	5·82	7·48
796	340					1·48	7·13	7·62
780	420					3·17	15·4	7·65
780	420					3·17	15·8	7·83
780	420					3·14	15·8	7·92

values of $(N_u/n_u)/(N_v/n_v)$ and have very different half-lives and specific activities, somewhat different methods of assaying had to be used for the two systems. The most difficult measurement was that of the material on the target because of the small mass.

The Cu–Ag *system.* The value of σ was large and ranged, from $3{\cdot}7\times10^2$ at high temperatures to $6{\cdot}7\times10^3$ at low temperatures. Thus although the specific activity of silver is 200 times less than that of gold, the ^{110}Ag-activity on the target was considerable due to the high value of σ. At high temperatures the activity on the target was predominantly due to ^{64}Cu and at low temperatures to ^{110}Ag. The activities due to ^{64}Cu and ^{110}Ag could be estimated separately by counting immediately after effusion and then about a week later since the half-lives of ^{64}Cu and ^{110}Ag are very different (12·8 hr for ^{64}Cu and 270 days for ^{110}Ag). The samples of crucible alloy obtained before and after the effusions were analysed in a similar fashion and no change in n_u/n_v was detected.

The samples were counted in a Dynatron scintillation counter using a 3 in. diameter Th-activated NaI well-shaped crystal surrounded by a 4 in. thick iron castle to reduce the background activity.

The Cu-Au *system.* For this system the value of σ was small, about 10^{-2}, and did not vary much with temperature. Due to the small value of σ there was only a small amount of ^{198}Au-activity on the target even though the specific activity of ^{198}Au is about 10^3 times that of ^{64}Cu. It was not possible simply to use the different half-lives of ^{64}Cu and ^{198}Au to separate the copper and gold because there is not a large difference in the half-lives (2·7 days for ^{198}Au) and by the time the ^{64}Cu-activity had decayed away the low ^{198}Au-activity would have decayed to less than the background level. Therefore a γ-ray spectrometer$^{(14)}$ was used to separate the ^{64}Cu and ^{198}Au.

The copper was estimated immediately after effusion by focussing the spectrometer on the ^{64}Cu-peak (0·51 MeV). This reduces the ^{198}Au-activity by a factor 0·01. This correction factor was determined by counting a sample of pure gold both on the ^{64}Cu-peak and the ^{198}Au-peak.

The gold was estimated by focussing the instrument on the ^{198}Au-peak (0·41 MeV). This count was taken later than the copper count, at such a time when the proportion of ^{64}Cu-activity had been reduced by decay but the ^{198}Au-activity was still much above the natural background. Focusing on the ^{198}Au-peak reduces the ^{64}Cu-activity counted by a factor of about 0·2. This correction factor was determined by measurements on a pure copper sample.

Because of the low ^{198}Au-activities on the target it was essential, despite the use of the spectrometer, to increase the signal-to-background ratio as much as possible. To this end the natural background was reduced by enclosing the crystal and photomultiplier in a 4 in. thick iron castle. Using the iron castle the background activity counted on the ^{198}Au-peak corresponded to 3×10^{-11} g of gold.

The single-channel Philips γ-ray spectrometer incorporated a Th-activated NaI flat crystal 2 in. in diameter and 2¼ in. high in contact with a 13 stage photomultiplier. The resolution achieved, measured on a ^{137}Cs-peak from a standard source, was 9 per cent. The gate-width, i.e. the width of the energy band in the spectrum in which the pulses were counted was chosen so that the ratio of the number of pulses counted of the isotope to be estimated to the number of pulses from the interfering isotope, was a maximum.

Despite the use of the iron castle the ^{198}Au activity was only about 3 times the background activity for the low temperature effusions, and this necessitated counting for several hours in order to obtain an accurate estimate of the activity. Hence it was essential to ensure that the spectrometer remained stable during the counting periods. Before and after each session of counting the activity of the ^{137}Cs-standard was estimated at the position of the ^{198}Au-peak since this count will be very sensitive to peak-drift. In no case was any appreciable peak-drift observed.

(d) *Experimental results*

A summary of the experimental details of the effusions and the measured values of $(N_u/n_u)/N_v/n_v)$ are given in Tables 2 and 3 for the gold solute and in Table 1 for the silver solute. In Fig. (3) values of ln σ are plotted against $1/T$ where σ has been defined in equation (18).

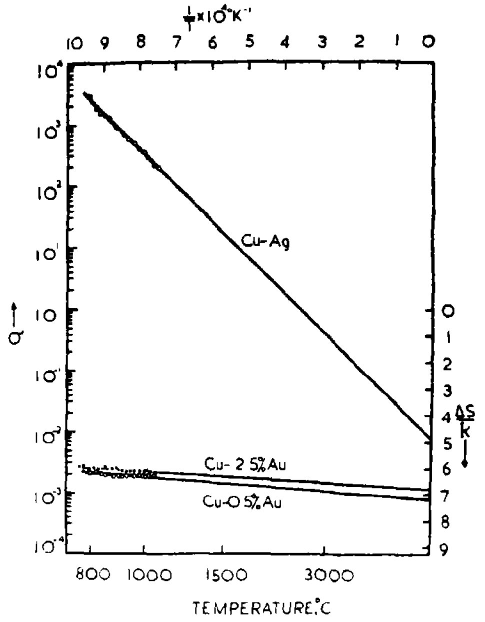

FIG. 3. The variation of lnσ with $1/T$.

Samples of gold and copper were irradiated along with the gold–copper alloys and measurements of the specific activities enabled the masses of copper and gold on the target to be estimated and the vapour pressures to be calculated from the equation(15)

$$p = \frac{w}{a^2}\left(\frac{r^2+l^2}{r^2}\right)\left(\frac{2\pi RT}{M}\right)^{1/2} \tag{19}$$

where w is the mass of copper condensing on the target per sec. from an orifice of area a^2 distant l from a target of radius r.* The vapour pressure of copper thus estimated is given in Fig. (4) together with values determined by McLELLAN and SHUTTLEWORTH for pure copper.(13)

Values of the partial enthalpies $H_u^+ - H_u^\circ$ were calculated from the values of $H_u^+ - H_v^\circ$ and previously determined values of the sublimation energies by the equation,

$$H_u^+ - H_u^0 = (H_u^+ - H_v^0) - (H_u^0 - H_v^0) \tag{20}$$

---

* In the article by McLELLAN and SHUTTLEWORTH(13) this equation was misprinted; however, the correct equation was used to calculate the vapour pressure.

Table 4. Experimental results

System	Temperature range (°C)	$H_u^+ - H_v^\circ$ (kcal/mole)	$\dfrac{S_u^+ - S_v^\circ}{k}$
Cu-0·1 % Ag	253	26·6 ± 0·69	4·71 ± 0·29
Cu-0·5 % Au	242	2·01 ± 0·29	7·67 ± 0·12
Cu-2·5 % Au	260	1·84 ± 0·26	6·85 ± 0·11

and these values are given in Table 5 together with values of H_u^+. The heats of sublimation, $-H_u^\circ + 5/2 \cdot RT$, were taken as 79·2, 64·1, and 83·6 kcal/mole for copper,(13) silver,(16) and gold.(17) (The last quantity has been corrected to 1200°K from the value given at 0°K.). The partial enthalpies are probably much less accurate than $H_u^+ - H_v^\circ$ since they involve the combination of the results of different experimenters.

Similarly the partial entropies were calculated from the standard entropies of the pure metals by equation (3) and these are also given in Table 5. The standard entropies of 1200°C were calculated from the entropies at 298°K and the specific heat data;(18) the values of S_v° are given in Table 6.

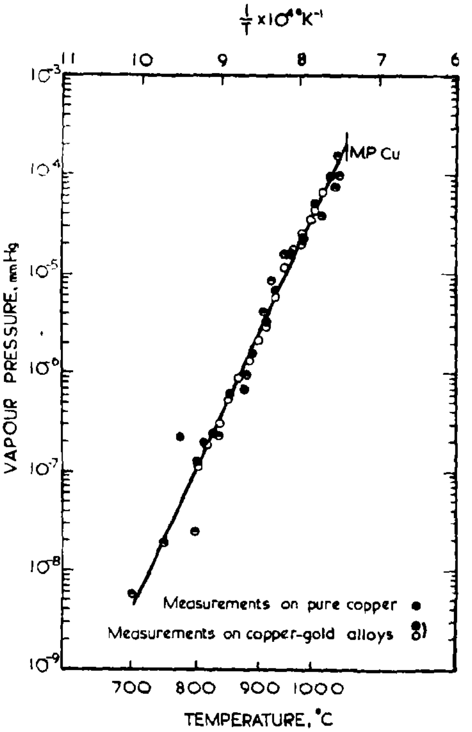

FIG. 4. The variation of the vapour pressure of copper with temperature.

Values of $(H_u^+ - H_v^\circ)$ and $S_u^+ - S_v^\circ)/k$ and their standard deviations were determined by the method of least squares and the results are given in Table 4, together with the temperature range over which they were measured. Values of H_u^+ are given in Table (5); this is the increase in enthalpy occurring when a solute atom at rest in the vapour is dissolved in the pure solvent.

(e) *Results of other workers*

Values of $(S_u^+ - S_u^\circ)$ deduced by Nowick and Freedman(4) from equilibrium diagrams, and by Seigle, Cohen and Averbach(2) from e.m.f. measurements on Au–Ni alloys are given in Table 6 together with the values of the standard entropies used to reduce them to the form $(S_u^+ - S_v^\circ)/k$. The values for Au–Ni alloys have been extrapolated to zero concentration from 5 At. per cent Au.

It is possible that the values deduced by Nowick and Freedman may not be very accurate since the solvus measurements on which they are based were made for alloys of different compositions, although they did attempt to correct for this. In particular they obtained a value for $S_u^+ - S_v^\circ$ of 2·7 k for the Cu–Ag system as compared with the value of 4·71 k found in this work.

By an e.m.f. method Weibke and von Quadt measured the partial enthalpies of copper in Cu–Au alloys.(19) From these results Oriani(20) determined the partial enthalpies of gold using the Gibbs–Duhem relation. At the lowest concentration of 15 At. per cent Au he gives a value of the partial enthalpy for gold of −4 kcal/mole; this is to be compared with the value of +6 kcal/mole given in Table 5 at 0·5 and 2·5 At. per cent Au.

Table 5. Partial enthalpies and entropies

System	$H_u^+ - H_u^0$ kcal/mole	H_u^+ kcal/mole	$\frac{S_u^+ - S_u^0}{k}$
Cu–0·1 At. % Ag	11·5 ± 0·69	−45·9 ± 0·69	3·40 ± 0·29
Cu–0·5 At. % Au	6·4 ± 0·29	−70·5 ± 0·29	5·25 ± 0·12
Cu–2·5 At. % Au	6·2 ± 0·26	−70·7 ± 0·26	5·03 ± 0·11

Table 6. Reduction of $(S_u^+ - S_u^0)/k$ values to values of $(S_u^+ - S_v^0)/k$

Solvent	Solute	$\frac{S_u^+ - S_u^0}{k}$	$\frac{S_v^0}{k}$	$\frac{S_u^0}{k}$	$\frac{S_u^+ - S_v^0}{k}$
Cu	Ag	(1·4)	8·400	9·718	(2·72)
	Fe	(3·0)		6·677	(1·28)
	Co	(0·64)		8·590	(0·83)
Ag	Pb	(2·5)	9·718	12·81	(5·59)
	Cu	(1·4)		8·400	(0·09)
	Ni	(−1·1)		8·655	(−2·16)
Pb	Sb	(0·77)	12·81	10·15	(−1·89)
	Cd	(0·81)		11·24	(−0·76)
	Ni	(1·8)		8·655	(−2·35)
Au	Co	(2·5)	10·23	8·590	(0·87)
	Ni	3·0		8·655	1·44
Ni	Au	3·5	8·655	10·23	5·07

HALL(17) measured the vapour pressures of gold over a series of gold–copper alloys and the equal slopes of his curves suggest that at gold concentrations of between 5 and 100 per cent the partial heat is zero.

Thus the suggestion is that the partial heat is positive at low gold concentrations and becomes negative about 10 per cent Au, but of course goes to zero at 100 per cent Au. However, this conclusion is tentative since it depends on the combination of a number of experimental determinations.

DISCUSSION

As indicated by equation (2) a theoretical estimate of the change in vibrational entropy due to the introduction of a solute atom into a crystal of pure solvent, could be made by evaluating the change in the frequency spectrum of the crystal. Such an approach has been made by MONTROLL and POTTS(21) who have used an approximate method to calculate the change in the frequency spectrum of a crystal due to the introduction of (a) an isotope of slightly different mass but not involving a change in interatomic coupling coefficient, and (b) an atom having the same mass but a slightly different coupling coefficient. However a detailed calculation of the change in frequency spectrum due to the substitutional replacement of a lattice atom by a solute atom of very different mass and coupling coefficient has not yet been undertaken, nor have the corresponding changes in the thermodynamic functions been calculated. HUNTINGTON, SHIRN and WAJDA(5) have calculated the vibrational entropies of vacancies and interstitial atoms in copper by considering separately vibrations localized around the defect and the elastic vibrations at appreciable distances. The local entropy contribution is calculated by assuming an Einstein model in which each atom is considered to move in a potential minimum established by its interaction with each of its neighbours presumed to be held fixed. The entropy contributions from the elastic vibrations were calculated from the temperature coefficient of the shear modulus, and the pressure coefficients of c_{11} and c_{44}.

As pointed out in the introduction the experimental values are consistent with those values calculated by considering the vibrations of a cluster of 13 atoms. In the following Sections the opposite approximation is made of treating the solid solvent as an elastic continuum which contains a spherical cavity into which a solute atom of different radius is inserted. It is supposed that the solvent expands so that the potential field in which the solute atom vibrates is unchanged so that apart from changes of entropy due to the different masses of the solute and solvent atoms, the changes in entropy are due to the elastic strain of the matrix.

In the same three-dimensional potential field a heavy atom will vibrate more slowly than a light atom and the entropy will be greater by an amount

$$\Delta S_M/k = 3/2 \ln M_u/M_v \qquad (21)$$

Owing to the insertion of a solute atom of different size into the cavity the continuum will be both sheared and dilated. In the next Sub-Section the entropy changes due to the dilational and shear strains are calculated and in the following Sub-Section the magnitudes of the dilational and shear strains due to placing a sphere of radius $r(1+\delta)$ into a cavity of radius r are estimated. In the final Sub-Section the magnitudes of the entropy changes are calculated.

Thermodynamics of strained solids

(1) *Dilational entropy*. The variation of entropy of a solid with hydrostatic pressure is related to the temperature coefficient of its volume by the Maxwell relation,

$$(\partial S/\partial P)_T = -(\partial V/\partial T)_P \qquad (22)$$

The equation of state of a solid is given to a first approximation by the equation,

$$V = V_0(1+b-P/K) \qquad (23)$$

Where V_0 is its volume at 0°K and zero pressure, K is the bulk modulus, and b a function of temperature related to the linear thermal expansion coefficient β by the relation $db/dT = 3\beta$.
Thus

$$(\partial V/\partial T)_P = V_0\left\{3\beta+\frac{P}{K^2}\left(\frac{dK}{dT}\right)\right\} \qquad (24)$$

Integrating,

$$\Delta S_D = -3V_0\beta P-\frac{V_0}{2}\frac{P^2}{K^2}\frac{dK}{dT} \qquad (25)$$

since

$$\beta \sim \frac{1}{K}\left(\frac{dK}{dT}\right) \text{ and } P/K \ll 1$$

the last term is negligible compared to the first and the dilational entropy becomes,

$$\Delta S_D = -3V_0P\beta \qquad (26)$$

(2) *Shear entropy*. The work done on a cube of volume V on increasing the shear strain from ϕ to $\phi+d\phi$ is

$$dw = \tau V d\phi \qquad (27)$$

where τ is the shear stress. The corresponding change in the Helmholtz free energy dF is

$$dF = -SdT+\tau V d\phi \qquad (28)$$

Hence

$$(\partial S/\partial\phi)_\tau = -(\partial(\tau V)/\partial T)_\phi \qquad (29)$$

The shear modulus μ is related to τ and ϕ by the equation

$$\phi = \tau/\mu \qquad (30)$$

Hence

$$(\partial(\tau V)/\partial T)_\phi = \phi(\partial(\mu V)/\partial T)_\phi \qquad (31)$$

and

$$\Delta S_s = -\tfrac{1}{2}\phi^2(\partial(\mu V)/\partial T)_\phi \qquad (32)$$

Equation (32) must result in a positive value for ΔS_s since experiment shows that $d(\mu V)/dT$ is negative. There is no term in equation (32) corresponding to the first term in equation (25). This is because a change of temperature at zero shear stress does not produce a shear strain and hence there is no term in (30) corresponding to b in (23).

From equations (27) and (30) $\frac{1}{2}\phi^2\mu V$ is the work needed to shear the cube through an angle ϕ. Thus equation (32) can be generalized: The change in entropy on shearing a body is simply minus the temperature coefficient of the shear strain energy.

Entropy change on elastically straining a spherical shell

The change of entropy on replacing a sphere of radius $a+u_0$ into a spherical shell of internal and external radii a and b can be calculated from elastic theory and the equations (26) and (32). When a pressure p is applied to the interior of the shell the circumferential and radial stresses Q and R in the shell at a distance r from the centre of the hole are,(22)

$$\left.\begin{aligned} R &= a^3p(-1/r^3+1/b^3) \\ Q &= a^3p(-\tfrac{1}{2}r^3+1/b^3) \end{aligned}\right\} \text{for } a \ll b \tag{33}$$

By symmetry Q, Q and R are the principal stresses.

The hydrostatic pressure in the shell is given by

$$\begin{aligned} P &= -\tfrac{1}{3}(R+2Q) \\ &= -a^3p/b^3 \\ &= -4\pi a^3p/3V_0 \end{aligned} \tag{34}$$

where V_0 is the volume of the shell.

The pressure p can be expressed in terms of u_0 the radial displacement of the inner surface,(22)

$$p = 4\mu u_0/a \quad \text{for } a \ll b \tag{35}$$

so that the hydrostatic pressure is

$$P = -16\mu a^2\pi u_0/3V_0 \tag{36}$$

The pressure is larger the smaller the volume but the total dilation and thus the dilational entropy is independent of the volume. By equation (26) the dilational entropy is:

$$\Delta S_D = 16\pi\mu\beta a^2u_0 \tag{37}$$

The shear entropy is calculated from the shear energy. The shear energy density is given by(23)

$$\{(\sigma_x-\sigma_y)^2+(\sigma_y-\sigma_z)^2+(\sigma_z-\sigma_x)^2\}/12\mu$$

where σ_x, σ_y, σ_z are the principal stresses. For the shell $\sigma_x = \sigma_y = Q$ and $\sigma_z = R$ and the energy density is

$$v = 6\mu a^4u_0/r^4 \tag{38}$$

The total shear energy, found by integrating, is

$$24\pi u_0^2\mu a^4 \int_a^\infty \mathrm{d}r/r^4 = 8\pi\mu a u_0^2 \tag{39}$$

and the corresponding entropy change due to shear in the elastic continuum is,

$$\Delta S_s = -8\pi a u_0^2(\partial\mu/\partial T) \tag{40}$$

Thus when an internal pressure is used to increase the radius of a hole in a thick elastic shell from a to $(a+u_0)$ the corresponding increase of entropy is:

$$\Delta S = 6\cdot\tfrac{4}{3}\,\pi a^3\left\{2\mu\beta\frac{u_0}{a}-\frac{\mathrm{d}\mu}{\mathrm{d}T}\left(\frac{u_0}{a}\right)^2\right\} \tag{41}$$

Vibrational entropy and size factor

The change of entropy on replacing a solvent atom by a solute atom can be estimated from equation (41) together with the term $\frac{3}{2}k \ln M_u/M_v$ due to the different masses. The atomic volume of the face-centred solvent $4\sqrt{(2)}r_v^3$ is put equal to the volume of the hole $4\pi a^3/3$, where $2r_v$ is the nearest-neighbour distance. Somewhat arbitrarily u_0/a is replaced by $(r_u-r_v)/r_v = \delta$ where $2r_u$ is the atomic diameter of the solute and δ is the size factor of the solution. Thus the calculated change of entropy is,

$$\begin{aligned} \frac{S_u^+-S_v^0}{k} &= \frac{24\sqrt{(2)}r_v^3}{k}\left\{2\mu\beta\delta-\frac{\mathrm{d}\mu}{\mathrm{d}T}\,\delta^2\right\} \\ &\quad + \frac{3}{2}\ln\frac{M_u}{M_v} \end{aligned} \tag{42}$$

In Fig. 5, for a copper solvent, the first two terms of equation (42) and their sum are shown separately. Up to about 12 per cent size difference the linear dilation term is larger than the quadratic shear term.

It is to be noted that in equation (42) only the parameters M_u and δ depend on the solute, the other parameters are properties of the solvent. In Table 7 values of M_v, μ, $\mathrm{d}\mu/\mathrm{d}T$ and β are given for various solvents to enable a comparison of the

Table 7. Properties of the solvents

Solvent	r_v (10^{-8} cm)	μ (10^{11} dyne/cm^2)	β (10^{-5} °C^{-1})	$24\sqrt{(2)}r_v^3/k$ (10^{-7} °C cm^2/dyne)	$2\mu\beta$ (10^7 dyne/cm^2 per °C)	$-\mathrm{d}\mu/\mathrm{d}T$ (10^7 dyne/cm^2 per °C)	M_v
Cu	1·275	4·62	1·70	5·10	1·57	14·2	63·5
Ag	1·442	2·76	1·91	6·07	1·05	12·5	108
Au	1·439	2·76	1·41	7·33	0·778	6·98	179
Ni	1·245	7·93	1·33	4·75	2·11	26·8	58·7
Pb	1·745	0·552	2·90	13·07	0·320	6·62	207

relative magnitudes of the first two terms in equation (42) to be made. The values of $\mathrm{d}\mu/\mathrm{d}T$ were estimated from KÖSTER's(24) measurements of the temperature coefficient of the Young's Modulus and the approximation $\mathrm{d}\mu/\mathrm{d}T = \frac{3}{8}\,\mathrm{d}E/\mathrm{d}T$.

To test equation (42) the calculated quantities $(\Delta S_D + \Delta S_S)/k$ and the experimentally determined quantities $(S_u^+ - S_v^0)/k - \frac{3}{2}\ln M_u/M_v$ are compared in the last two columns of Table 8. The values in curved brackets are due to Nowick and Freedman and those in square brackets are due to Seigle, Cohen and Averbach. These two quantities are also compared in Fig. 5 by plotting each as a function of δ.

CONCLUSIONS

From Fig. 5 it is seen that the experimentally determined values of the vibrational entropy for silver and gold dissolved in copper lie between the values calculated for the cluster of 13 atoms and the values calculated by the elastic theory. Generally values calculated by the elastic theory are within $2k$ of those determined by experiment. The greatest discrepancy is for Ni dissolved in Pb where the calculated value is $5{\cdot}9k$ and the value determined from the solvus is $-0{\cdot}43k$. However, the solvus curve determined by TAMMANN and OELSEN(25) is in some doubt.

It is thought that the experimental values are

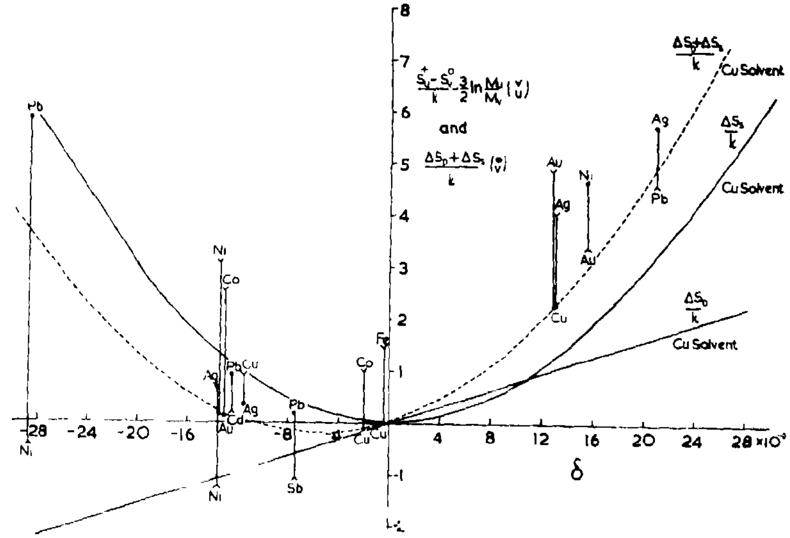

FIG. 5. Dependence of the measured and calculated vibrational entropies on the size factor δ. The theoretical values are indicated by full circles and the solvent is adjacent to them. The experimental values are marked with arrow heads and the solutes are adjacent to them.

Table 8. Comparison of results calculated from elastic model and experimental results

Solvent	Solute	δ (10^2)	M_u	ΔS_M/k	ΔS_D/k	ΔS_S/k	$\Delta S_D + \Delta S_S$/k	$(S_u^+ - S^0) - \Delta S_M$/$k$
Cu	Ag	13·1	108·0	0·79	1·05	1·20	2·25	3·92
	Au	12·86	197·0	1·70	1·03	1·24	2·27	5·30
	Fe	−0·392	55·85	−0·19	−0·031	0·028	−0·003	(1·48)
	Co	−1·961	58·94	−0·11	−0·16	0·001	−0·156	(0·94)
Ag	Pb	21·01	207·0	0·98	1·62	4·07	5·69	(4·59)
	Cu	−11·58	63·54	−0·79	−0·89	1·24	0·342	(0·88)
	Ni	−13·66	58·70	−0·91	−1·05	1·71	0·655	(−1·24)
Au	Co	−13·13	58·94	−1·67	−0·75	0·882	0·133	(2·54)
	Ni	−13·48	58·70	−1·67	−0·76	0·930	0·166	[3·10]
Ni	Au	15·58	197·0	1·67	1·56	3·09	4·65	[3·38]
Pb	Sb	− 7·507	122·0	−0·80	−0·31	0·49	0·173	(−1·07)
	Cd	−12·48	112·0	−0·92	−0·54	1·43	0·890	0·19
	Ni	−28·65	57·80	−1·89	−1·20	7·10	5·90	(−0·43)

reliable for the systems Au dissolved in Ni and for Ag and Au dissolved in copper. For the other systems the discrepancy may be due to an error in the determination of the solvus.

The vibrational entropies of solute atoms presented in this paper may be compared with vibrational entropies found by SIMMONS and BALLUFFI[26] for monovacancies in solid aluminium. The variation of monovacancy concentration with temperature for a crystal in thermal equilibrium is given by,

$$c = \exp(S/k)\exp(-H/kT), \qquad (43)$$

where S/k is the vibrational entropy and H the enthalpy of formation of a monovacancy. The $/Sk$ is comparable to the quantity $(S_u^+ - S_v^0)/k$ for a solute atom since the number of atoms remains unchanged (c.f. equation 2). By measuring simultaneously the change in length and lattice parameter of an aluminium specimen Simmons and Balluffi measured the monovacancy concentration absolutely and thus estimated S/k from equation (43). The best straight line between the high temperature measurements of Simmons and Balluffi and the best low temperature values of vacancy concentration found by measuring the electrical resistivity of quenched aluminium[27] gives a vibrational entropy of 3·6 k.

Acknowledgement—The authors are indebted to the A.E.R.E., Harwell for providing a grant which enabled this work to be carried out.

REFERENCES

1. ORIANI R. A., *N.P.L. Symposium No.* 9 Vol. **1**, (1959).
2. SEIGLE L. L., COHEN M. and AVERBACH B. L., *Trans. Amer. Inst. min. (metall.) Engrs.* **196,** 1320 (1952).
3. DE SORBO W., *Acta Met.* **3**, 227 (1955).
4. NOWICK A. S. and FREEDMAN J. F., *Acta Met.* **6,** 176 (1958).
5. HUNTINGTON H. B., SHIRN G. A. and WADJA E. S., *Phys. Rev.* **99,** 1085 (1955).
6. MAYER J. and MAYER M., *Statistical Mechanics,* Wiley, New York (1940).
7. ZENER C., *Acta Cryst* **2,** 1963 (1949).
8. GUGGENHEIM E. A., *Thermodynamics,* equation (5.19.3) p. 226. North Holland, Amsterdam (1959).
9. FOWLER R. and GUGGENHEIM E. A., *Statistical Thermodynamics,* equation (3.10.6) p. 81. University Press, Cambridge (1949).
10. JOHNSON G. and SHUTTLEWORTH R., *Phil. Mag.* **4,** 957 (1959).
11. GUGGENHEIM E. A., *Thermodynamics,* equations 5 and 9, p. 24. North Holland, Amsterdam (1950).
12. PYLE T. and SHUTTLEWORTH R., *Radioisotopes in Scientific Research, UNESCO Conference, Paris* (1957) Vol. **1**, U.N. Publication.
13. McLELLAN R. B. and SHUTTLEWORTH R., *Z. Metallk* **51,** 143 (1960).

14. CROUTHAMEL C. E., *Applied Gamma-Ray Spectrometry*, Pergamon Press, London (1960).
15. SPEISER R. and SPRETNAK J. W., *Vacuum Metallurgy, Symposium of the Electrochemical Society*, Boston, Mass. (1954).
16. SCHADEL E. and BIRCHENALL C. E., *I. Metals, New York* **2**, 1134 (1950).
17. HALL L. D., *J. Amer. chem. Soc.* **757** (1951).
18. KUBASCHEWSKI O. and EVANS E. LL., *Metallurgical Thermochemistry*, 2nd revised ed., Pergamon Press, London (1958).
19. WEIBKE F. and VON QUADT U., *Z. Elektrochem* **45,** 715 (1939).
20. ORIANI R. A., *Acta Met.*, **1,** 144 (1953).
21. MONTROLL E. W. and POTTS R. B., *Phys. Rev.* **102,** 72 (1956).
22. PRESCOTT J., *Applied Elasticity*, equations 25 and 26, p. 329, and equation 7, p. 327. Longmans, Green, London (1924).
23. TIMOSHENKO S. and GOODIER J. N., *Theory of Elasticity*, equation 149, p. 88. McGraw-Hill, New York (1951).
24. KÖSTER W., *Z. Metallk* **39,** 1 (1948).
25. TAMMANN G. and OELSEN W., *Z. anorg. chem.* **186,** 266 (1933).
26. SIMMONS R. O. and BALLUFFI R. W., *Phys. Rev.* **117,** 52 (1960).
27. DE SORBO W. and TURNBULL D., *Acta Met.* **7,** 83 (1959).

J. Phys. Chem. Solids Pergamon Press 1963. Vol. 24. pp. 469–473. Printed in Great Britain.

THERMAL DECOMPOSITION OF SODIUM AZIDE CRYSTALS*

E. A. SECCO†

Physics and Chemistry of Solids, Cavendish Laboratory, Cambridge, England

(*Received* 18 *October* 1962)

Abstract—A study of the kinetics of thermal decomposition of sodium azide crystals, in the form of platelets, obtained by crystallization from aqueous solution is reported. The experimental results for the rate of decomposition fall approximately into three temperature regions: (a) below 300°C; (b) 300–345°C; and (c) above 350°C.

Below 300°C the rate follows, after a rapid initial stage (c.a. 5 per cent), a linear relation leaving a white residue in the shape of the original crystal. The reaction begins on preferred crystallographic faces and moves along a two-dimensional path towards the center of the crystal. During the progress of decomposition a sharp line of demarcation is observed at the undecomposed azide and white residue interface. Between 300–345°C the rate is of the sigmoid type leaving white residue enclosing a central cavity. Above 350°C two different linear rates are observed, the latter being 100 times faster than the first with no detectable residue. The enhanced rate is attributed to adsorbed sodium which catalyses the reaction.

These results are discussed in the light of the early data on NaN_3 thermal decomposition and the parallel case of ammonium perchlorate.

VERY little work has been done on the thermal decomposition of sodium azide since the early study by GARNER and MARKE(1) some twenty-five years ago. Much of the recent work on azide decomposition has been concentrated on potassium, silver and thallous azides and the alkaline earth azides.(2) The usual experimental approach is to follow the rate of nitrogen evolution in a closed system and observe the general characteristics of the overall process assuming the decomposition to be of the general type

$$MN_{3(s)} \rightarrow M_{(s)} + 3/2N_{2(g)}$$

During the decomposition of the heavier azides such as calcium azide, some nitride is also formed(3) but it was pointed out(4) that the nitride is not an intermediate in the decomposition but results from the secondary reaction of metallic calcium with gaseous nitrogen formed during the decomposition. Garner and Marke reported a white amorphous residue in the decomposition of sodium azide which "possessed the properties of an azide".

The accepted mechanism of decomposition of an ionic azide is assumed to develop by an electron transfer mechanism

$$N_3^- \rightarrow N_3 + e^-$$

followed by,

$$2N_3 \rightarrow 3N_2$$

and

$$M^+ + e^- \rightarrow M$$

where metallic nuclei have been observed on the surface of a crystal. This mechanism postulated for the heavier ionic azides in the broad sense was believed to be generally applicable to sodium azide.

The sodium azide used by Garner and Marke was not as single crystals but as star-shaped aggregates. They state that the decomposition reaction occurs partly on the external surface of the crystal and partly in the interior. It was desirable therefore to study the thermal decomposition of sodium azide single crystals to compare with the results of Garner and Marke and the mechanism postulated for the ionic azide decomposition.

---

* This work was carried out during the tenure of a NATO Overseas Science Fellowship at the University of Cambridge.

† Present address: Chemistry Department, St. Francis Xavier University, Antigonish, Nova Scotia, Canada.

EXPERIMENTAL

Single crystals, transparent and colorless, of sodium azide in the form of platelets were obtained by crystallization from aqueous solution.

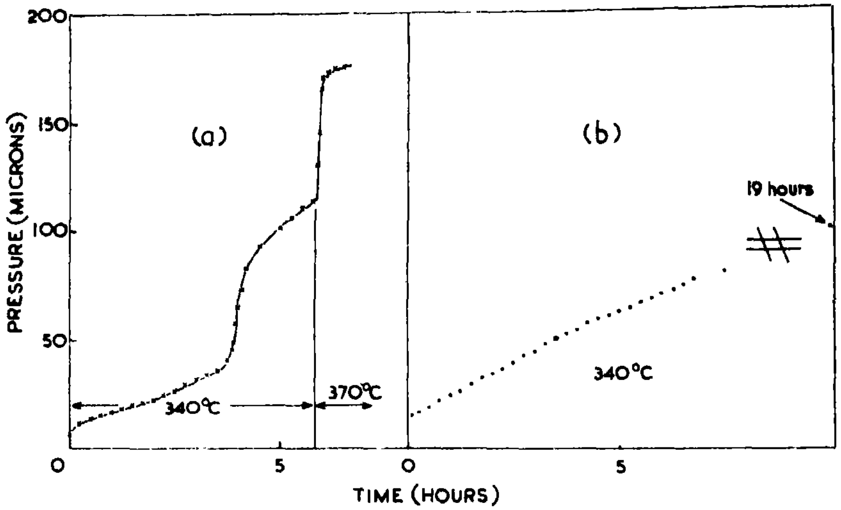

FIG. 4 (a) Pressure versus time plot at 340 and 370°C for azide platelet. (b) Pressure vs. time plot at 340°C for small crystal (0·35 mg).

Technical grade sodium azide was dissolved in distilled water and filtered. The solution was saturated by slow evaporation at 45–50°C and allowed to cool slowly (3–4 hr) to room temperature. The crystals were recovered by filtration, dried and stored in a dessicator with P_2O_5. These crystals had the *c*-axis parallel to the plane of the plate.

A single crystal of sodium azide was selected from the batch of crystals, weighed (0·3–1·5 mg) and placed in a quartz bucket. The bucket with crystal was suspended in a conventional vacuum system and degassed at room temperature. Under a final holding vacuum of 2×10^{-6} mm Hg, the bucket was lowered into the furnace maintained at the required temperature. The temperature of the furnace was maintained constant to ± 2°C by use of an electronic controller.

The progress of the reaction was followed with a Pirani gauge connected to Fielden Servograph (5 sec full scale deflection) previously calibrated with a McLeod gauge.

After a fraction of the crystal had decomposed, the crystal was withdrawn and examined with a microscope (Carl Zeiss, Germany) and photographed on Kodachrome 135 A.

RESULTS

Figure 1(a) is a photograph by reflected light of a crystal decomposed at 275°C in a closed system. The print shows that the decomposition begins on preferred crystallographic faces and moves towards the center of the crystal. The relative rates of reaction on the various edges can be judged by the amount of white residue. The other significant features are the sharp purple line of demarcation at the undecomposed azide and residue interface and the absence of reaction on the surface. Figure 1(b) is a photograph of the same crystal in transmitted light showing a number of microscopic defects and imperfections which appear to have no observable effect on the path of the decomposition. Macroscopic fissures or imperfect surface growths, are, however, favorable regions for decomposition to occur.

a

FIG. 1 (a) Photograph of azide platelet by reflected light partially decomposed at 275°C in a closed system under vacuum. Magnified ×8; exposure time 8–10 sec.

b

(b) Photograph of azide platelet in transmitted light treated as in (a)

FIG. 2 (a) Photograph of azide platelet by reflected light partially decomposed at 315°C in an open system under vacuum. Magnified ×8; exposure time 8–10 sec.

(b) Photograph in (a) magnified × 25.

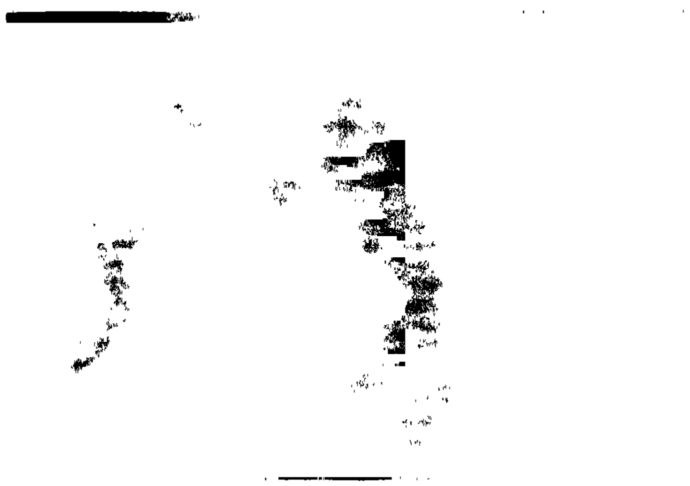

Fig. 3. Photograph of residue by reflected light after complete decomposition of azide platelet at 320°C in an open system under vacuum.

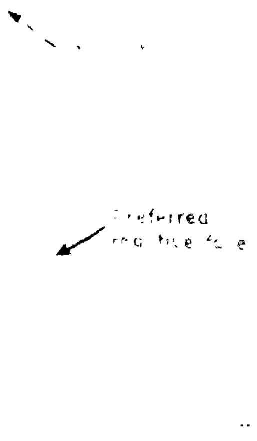

Fig. 7. Photograph of an azide platelet by reflected light showing preferred reactive face.

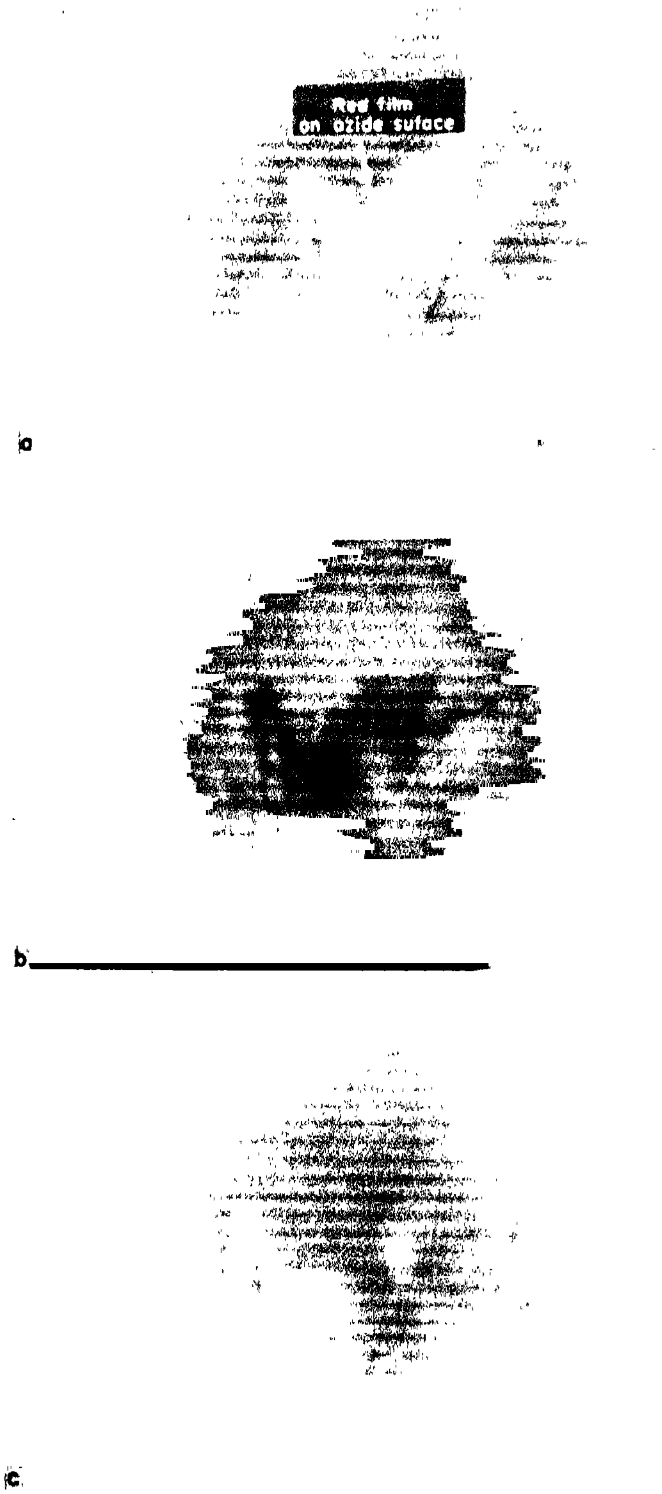

FIG. 8 (a), (b), (c) Sequence of photographs at 15 sec intervals showing the disappearance of red color on azide surface.

Figure 2(a) is a photograph of a crystal decomposed at 315°C in an open system under vacuum, that is, the products were continuously pumped out and the pressure of N_2 did not exceed 5×10^{-6} mm Hg. This crystal shows similar characteristics to those in Fig. 1(a) along with the additional feature of black surface ripples on the edge of the residue, a magnified print of the black surface is given in Fig. 2(b). The black deposit was later shown to be carbon resulting from the decomposition of grease which adhered to the bucket when lowered into the furnace. The reaction when complete gave a white residue, porous in structure, which was c.a. 50 per cent of the original weight.

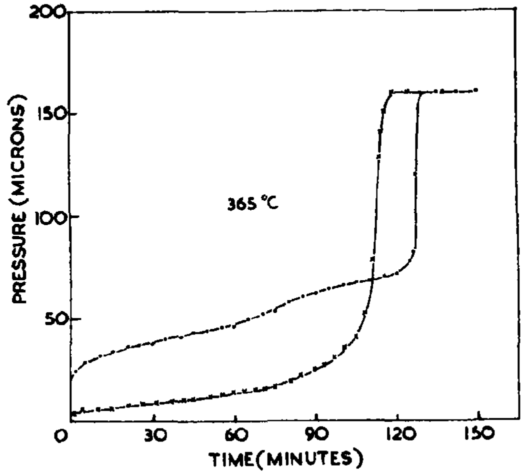

FIG. 5. Pressure vs. time plots at 365°C for decomposition of azide platelets.

In the decomposition of an azide crystal below 300°C in a closed system under vacuum or between 300–345°C in an open system under vacuum the white residue always retained the shape of the original crystal. On the other hand, decomposition of the azide between 300–345° in a closed system yields a residue as shown in Fig. 3, that is, the usual white material enclosing a central cavity.

Pressure vs. time plots for single crystals at different temperatures are given in Figs. 4 and 5. Figure 4(a) represents decomposition at a temperature of 340°C with the commonly observed sigmoid character up to 6 hr. The residue had the features shown in Fig. 3. Raising the temperature to 370°C after outgassing brought about complete decomposition of the white material. Figure 4(b) shows a predominantly linear rate up to 8 hr at the same temperature but with a smaller crystal. The linear behaviour as typified by Fig. 4(b) is observed below 300°C with a large crystal (0·7 mg) and between 300–345°C with a small crystal (0·35 mg). Figure 5 with two experiments carried out at the same temperature (365°C) shows the different extent of the initial reaction, the different rate of the second stage and the accelerated linear third stage. It was observed that the onset of the accelerated rate usually occurred when the crystal had decomposed to the extent of 35–45 per cent.

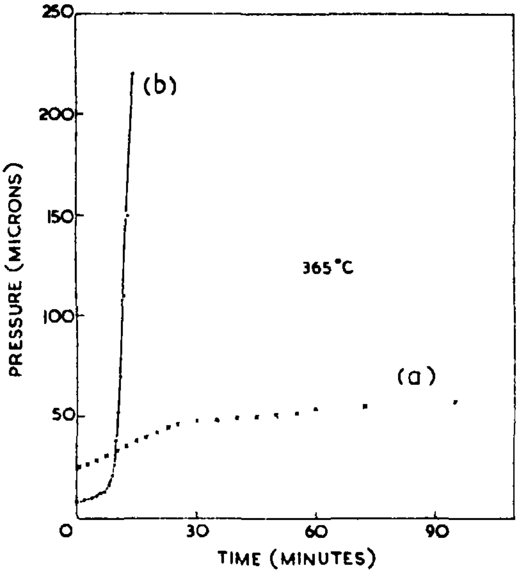

FIG. 6. Pressure vs. time plots for sodium azide powder, untreated BDH laboratory reagent.

For comparison purposes a few experiments were done with azide powder, untreated BDH laboratory reagent, and pressure versus time plots are given in Fig. 6. The outgassing treatment prior to decomposition was identical since the initial reaction was speculated to be desorption. Neither desorption nor surface area can account for the observations on the initial reaction. The initial reactivity can be associated with preferred faces or imperfect active sites as demonstrated in Figs. 1 and 2. A preferred reactive face is brought out very clearly in Fig. 7.

The linear rate constant was 2–4 times greater in the case of the powder at the same temperature.

The linear rate constant for the initial reaction is equal to the rate constant for the accelerated third stage. The activation energy for the intermediate stage was found to be 50 ± 5 kcal/mole from a plot of the logarithm of the linear rate constant versus the reciprocal of the absolute temperature in the region 345–365°C. It must be pointed out that there was great difficulty in obtaining reproducible results since each crystal, not being crystallographically identical, presented different faces and hence the rates varied. This value, however, is in good agreement with the value of 49 kcal/mole found by JACOBS and TOMPKINS(5) with potassium azide but higher than the value of 35 kcal/mole for sodium azide reported by GARNER and MARKE.(1) Because of the lack of reproducibility no activation energy could be determined for the initial reaction while the accelerated third process appears to be temperature independent.

The infra-red spectra of both undecomposed sodium azide and the residue from a decomposition at low temperatures were determined in Nujol mull using standard technique.* No difference between the two spectra was evident. This observation is consistent with the residue being chemically identical with the original salt in agreement with the observation of GARNER and MARKE.(1)

The crystal shown in Fig. 1 was scanned† in an electron spin resonance spectrometer with particular emphasis on detection of a signal associated with the purple line at the interface since it was previously observed(6) that a purple color in irradiated NaN_3 crystal gave a strong ESR signal attributed to unpaired electrons from colloidally dispersed sodium in the azide lattice. No ESR signal was discernible in this scan but the negative result does not preclude the presence of colloidal sodium in the interface, because of the very limited volume of the purple color and the concentration of sodium might be below the detection limits of the spectrometer.

With the object of obtaining a sufficient quantity of white residue for purposes of analysis, about five single crystals of NaN_3 were decomposed overnight at 310°C. The crystals were withdrawn and examined with the microscope. In addition to the usual features exhibited in Fig. 1 each crystal surface was covered with islands of deep red color. These colored islands reacted quite rapidly in the atmosphere accompanied by bubbling (*i.e.* gas evolution) leaving behind a colorless liquid-like product. The reaction was complete in less than three minutes. Figure 8 shows a sequence of magnified photographs (×16) of the crystal shortly after exposure to the atmosphere. This same crystal was examined the following day and the liquid-like product was replaced by islands of white powder. The red color was reproducible but the color intensity is a function of decomposition time, temperature, pressure, and crystal size.

The original islands of red color observed were beyond doubt adsorbed sodium on the azide surface. The subsequent observations are the usual reactions(7) of sodium with water vapor to yield NaOH with H_2 evolved and finally, in the presence of CO_2, the white carbonate Na_2CO_3 is formed.

The white residue from the decomposition at low temperature was found to decompose at 315°C with a rate nearly equal to the rate of the accelerated third stage at 365°C. On the other hand, white residue maintained under vacuum decomposes at 365°C at a rate slower than the third stage by a factor of 10. Exactly similar observations of rejuvenation on exposure to the atmosphere have been made on the residue from ammonium perchlorate decomposition.(8) The rejuvenation in the case of NH_4ClO_4 residue was thought to be due to some type of interface recrystallization.

DISCUSSION

It is not possible on the evidence available to elucidate completely the mechanism of decomposition of sodium azide. The decomposition of the azide crystals will be discussed in the light of the major points of our results.

The first important point to consider is the white residue obtained at low temperatures. This residue, which was confirmed to be chemically identical to the original salt, can arise from decomposition of strained material in the intermosaic grain boundaries. The intermosaic boundary reaction hypothesis(9) has been advanced to account for the residue in the case of ammonium perchlorate decomposition. An alternative explanation may be found in two types of azide molecules in the azide lattice possessing different stabilities. The structure of sodium azide is usually given as rhombohedral with Na atoms at each of the corners of the unit cell and the N atoms linearly arranged along the longest diagonals of the cell. There may be some dispute as to whether or not the three N atoms are centrosymmetric(10, 11, 12) but it is generally accepted that the N_3^- is a linear symmetric(2) triatomic group. Alternatively, a hexagonal cell(13) may be chosen with the *c*-axis parallel to the azide ion. No X-ray examination of the white residue nor of the azide lattice as a function of temperature have yet been reported but this is planned to be the subject of a future study. There exists one other possibility and that is, decomposition of the sodium azide by $NaN—N_2$ bond fission, with the subsequent reaction of the intermediate NaN to sodium and the azide. The fission of the $N—N_2$ bond is a typical mode of azide decomposition where the N—N bond lengths differ but is considered rather remote on the basis of the available thermochemical data(14) in the ionic azides. The azide residue does not however result from a back reaction of the products as the experiment with continuous pumping demonstrated.

---

* Spectra done by Dr. Dennis Chapman of the University Chemical Laboratory, Lensfield Road, Cambridge.

† ESR scan done by Dr. A. CARRINGTON of the University Chemical Laboratory, Lensfield Road, Cambridge.

The accelerated linear rate of the third stage in the pressure vs. time plot above 350°C is novel and most interesting. This rapid rate is believed to be due to adsorbed sodium on the undecomposed surface. Two dimensional decomposition of the azide occurs during the extended second stage with no perceptible reaction on the surface. As the reaction proceeds adsorbed sodium exerts a catalytic effect, as previously observed,(1) by disrupting the stable surface layer with the subsequent bulk decomposition. There appears to be two requisite conditions for the accelerated third stage, temperature above 350°C and critical concentration of adsorbed sodium. This latter condition is supported by the observations that the accelerated rate occurs at 35–45 per cent decomposition and the absence of an accelerated rate with small crystals, i.e. linear rate to completion with small crystals.

Acknowledgements—The author is indebted to the National Research Council of Canada for the award of a NATO Overseas Science Fellowship, to Dr. F. P. Bowden for providing laboratory facilities, and to Dr. A. D. Yoffe for many helpful discussions. The author is grateful to Dr. A. Carrington and Dr. Dennis Chapman for the ESR and Infra-red analyses, respectively.

REFERENCES

1. Garner W. E. and Marke D. J. B., *J. chem. Soc.* 657 (1936).
2. Evans B. L., Yoffe A. D. and Gray P., *Chem. Rev.* **59**, 515 (1959).
3. Andreev K. K., *Phys. Z. Sowjet* **6**, 121 (1934).
4. Tompkins F. C. and Young D. A., *Disc. Faraday Soc.* **23**, 202 (1957).
5. Jacobs P. W. M. and Tompkins F. C., *Proc. Roy. Soc.* **215A**, 265 (1952).
6. Miller B. S., *J. chem. Phys.* **33**, 889 (1960).
7. Partington J. R., *Textbook of Inorganic Chemistry*, 6th Edition pp. 685, 689. McMillan, London (1953).
8. Bircumshaw L. L. and Newman B. H., *Proc. Roy. Soc.* **A227**, 115 (1954); **A227**, 228 (1955).
9. Galwey A. K. and Jacobs P. W. M., *Proc. Roy. Soc.* **254A**, 455 (1960).
10. Hendricks S. B. and Pauling L., *J. Amer. chem. Soc.* **47**, 2904 (1925).
11. Frevel L. K., *J. Amer. chem. Soc.* **58**, 779 (1936).
12. Bassiere M., *J. chim. phys.* **36**, 71 (1939); *C.R. Acad. Sci. Paris* **208**, 659 (1939).
13. Wyckoff R. W. G., *Crystal Structures* Vol. **II**, chap. 6, table, p. 7 Interscience, New York (1957).
14. Franklin J. L., Dibeler V. H., Reese R. M. and Krauss M., *J. Amer. chem. Soc.* **80**, 298 (1958).

J. Phys. Chem. Solids Pergamon Press 1963. Vol. 24, pp. 475–477. Printed in Great Britain.

SPIN ORDERING IN THE SUPERCONDUCTING STATE

S. H. LIU

International Business Machines Corporation,
Thomas J. Watson Research Center,
Yorktown Heights, New York

(*Received* 17 *August* 1962)

Abstract—It is argued that the spin ordering in the so-called ferromagnetic superconductors is essentially the same as that in normal dilute magnetic alloys such as manganese in copper. The range of ordering of the localized spins is much smaller than the coherence length.

IN DILUTE magnetic alloys such as manganese in copper the spins of the manganese ions are believed to be coupled by the RUDERMAN–KITTEL interaction.(1, 2) MARSHALL(3) showed that the peculiar specific heat curves(4) of these alloys can be explained on this basis. He observed that (1) the Ruderman–Kittel interaction can have either sign depending on the distance between the participating spins and (2) in a random alloy system, the neighbors of a given spin can be at various distances from it, he concluded that the effective field acting on a spin may be of either sign or zero. In fact, the low temperature specific heat comes mainly from the motion of those spins which are at the low effective field points. From this argument, one can readily see that the spins are very unlikely to have long range order. The recent calculation of BROUT and KLEIN(5) seems to indicate that the range of correlation of the spins is of the order of the average nearest neighbor distance. Experimentally, the specific heat curves of these alloys have no sharp peak or discontinuity that is characteristic of long range order–disorder transition. Therefore, the spin ordering in these alloys is almost certainly of short range.

It will be shown that this kind of magnetic ordering is also to be expected in the so-called ferromagnetic superconductors discovered by MATTHIAS(6) and his co-workers. One first shows that in the superconducting state the Ruderman–Kittel interaction is practically identical in strength and space dependence as in the normal state. Following YOSIDA(2) one writes the interaction between the conduction electrons and the magnetic ions in the following form

$$H = N^{-1}\sum_{\mathbf{k},\mathbf{k}'}\sum_{i} I(\mathbf{k}-\mathbf{k}')[(a^*_{\mathbf{k}'\uparrow}a_{\mathbf{k}\uparrow}-a^*_{\mathbf{k}'\downarrow}a_{\mathbf{k}\downarrow})S_i^z + a^*_{\mathbf{k}'\uparrow}a_{\mathbf{k}\downarrow}S_i^- + a^*_{\mathbf{k}'\downarrow}a_{\mathbf{k}\uparrow}S_i^+]\exp[i(\mathbf{k}-\mathbf{k}')\cdot\mathbf{R}_i], \tag{1}$$

where $I(\mathbf{k}-\mathbf{k}')$ is the exchange interaction matrix element, N the total number of atoms in the sample, $\mathbf{R}_i$ the position of the i-th spin $a^*_{\mathbf{k}s}$ and $a_{\mathbf{k}s}$ are the creation and annihilation operators of a conduction electron in the state with momentum $\mathbf{k}$ and spin s. In the second order perturbation calculation the energy of the system is(1, 2)

$$E = E_0 - \sum_{ij} J(R_{ij})\mathbf{S}_i\cdot\mathbf{S}_j \tag{2}$$

where E_0 is the energy of the unperturbed electron system and

$$J(R_{ij}) = N^{-2}\sum_{\mathbf{k}\,\mathbf{k}'}\frac{|I(\mathbf{k}-\mathbf{k}')|^2[f(\mathbf{k})-f(\mathbf{k}')]}{\epsilon_{k'}-\epsilon_k} \times \exp[i(\mathbf{k}-\mathbf{k}')\cdot\mathbf{R}_{ij}] \tag{3}$$

ϵ_k is the energy of the state $\mathbf{k}$, $f(\mathbf{k})$ is the Fermi distribution function. Assuming $|I(\mathbf{k}-\mathbf{k}')|^2 = I^2$ for $k, k' \simeq k_F$ one finds for free electrons at 0°K that

$$J(R) = -\frac{9\pi I^2Z^2}{8\epsilon_F}F(2k_FR), \tag{4}$$

where k_F is the Fermi wave vector, Z is the valence of the ion, and

$$F(x) = (x \cos x - \sin x)/x^4. \tag{5}$$

Equations (4) and (5) define the Ruderman–Kittel interaction in a normal metal. In a superconductor the B.C.S.[(7)] theory shows that the elementary excitations are the quasi-particle states which are related to the free electron states by the Bogoliubov transformation[(8)]

$$\begin{aligned} \alpha_{\boldsymbol{k}} &= (1-h_k)^{1/2}a_{\boldsymbol{k}\uparrow}+h_k^{1/2}a^*_{-\boldsymbol{k}\downarrow} \\ \beta_{\boldsymbol{k}} &= (1-h_k)^{1/2}a_{-\boldsymbol{k}\downarrow}-h_k^{1/2}a^*_{\boldsymbol{k}\uparrow}. \end{aligned} \tag{6}$$

The energy of the quasi-particles is

$$E_k = [(\epsilon_k-\epsilon_F)^2+\Delta_0^2]^{1/2}, \tag{7}$$

where Δ_0 is the energy gap. The coefficient h_k is related to ϵ_k by

$$h_k = \frac{1}{2}\left[1-\frac{\epsilon_k-\epsilon_F}{E_k}\right]. \tag{8}$$

If one works out the second order perturbation calculation in the quasi-particle representàtion, one obtains

$$J'(R) = N^{-2}\sum_{\boldsymbol{k}\boldsymbol{k}'} |I(\boldsymbol{k}-\boldsymbol{k}')|^2 L(\epsilon_k,\epsilon_{k'}) \times \exp[i(\boldsymbol{k}-\boldsymbol{k}')\cdot\boldsymbol{R}]$$

where $L(\epsilon_k,\epsilon_{k'})$ is defined by equation (4.22) of Ref. 7. Taking

$$|I(\boldsymbol{k}-\boldsymbol{k}')|^2 \cong I^2,$$

one can evaluate

$$J(R)-J'(R) = \frac{I^2}{N^2}\sum_{\boldsymbol{k}\boldsymbol{k}'}\left[\frac{f(k')-f(k)}{\epsilon_k-\epsilon_{k'}}-L(\epsilon_k,\epsilon_{k'})\right] \times \exp[i(\boldsymbol{k}-\boldsymbol{k}')\cdot\boldsymbol{R}]$$

in a way very similar to the calculation of the B.C.S. non-local kernel function. The result is

$$J(R)-J'(R) = \frac{9\pi I^2Z^2\Delta_0}{16\epsilon_F^2}\frac{1}{(2k_FR)^2}\int_{2R/\pi\xi_0}^{\infty} K_0(y)\,\mathrm{d}y, \tag{10}$$

where $K_0(y)$ is the modified Bessel function. Since the function on the right-hand side of equation (10) is a monotonic function, the new coupling energy $J'(R)$ has the same oscillatory property of $J(R)$. This is to be expected because the period of oscillation depends on k_F which is not affected by the onset of superconductivity. In a 1 per cent alloy, which is the typical concentration of these alloys, the average nearest neighbor distance is approximately $5c$ where c is the lattice constant. Since for ordinary superconductors $\Delta_0 \cong 10^{-4}\epsilon_F$ and $k_F \cong 2\pi/c$, one finds

$$[J(R)-J'(R)]/J(R) \cong 10^{-2}$$

for nearest neighbors. At larger distances the right-hand side of equation (10) drops off exponentially. Hence, the effect of superconductivity on the spin coupling is entirely negligible. Thus, the same spin alignment described by Marshall and Brout and Klein must also apply to these materials.

To make the above argument self-consistent, one must also show that the spin alignment has a negligible effect on the superconductivity so that the latter can still be described by the B.C.S. theory. There is so far no conclusive theory on the range of ordering of the spins. If one uses the Brout and Klein theory as a guide, one measures the range of ordering by the average nearest neighbor distance, i.e. about 10 Å in a 1 per cent alloy. This is two or three orders of magnitude smaller than the coherence length of most superconductors. Hence, it seems safe to conclude that, as far as the superconducting electrons can tell, the spins are essentially randomly oriented. Therefore, there is no long range polarization of the conduction band[(9)] and the material behaves essentially like a dirty superconductor.[(10)] Although there are conflicting ideas about the theory of dirty superconductors,[(11)] it seems all right in the present problem to use the simple theory for making a crude estimation of the important effect. The final result that the superconductivity has negligible effect on the spin coupling should be insensitive to the detail of the theory of superconductivity.

The specific heat measurements of Phillips and Matthias[(12)] on ferromagnetic superconductors also lend support to the conclusion that the spin correlation in the superconducting state is the same in nature as that in the normal state. There are striking similarities between the specific heat curves of Ref. 12 and those of Ref. 4

for CuMn alloys; e.g. the linear dependence on temperature in the low temperature region and the broad peak in the higher temperature region. Using the theory of Marshall, one may estimate from the data that the electron-ion coupling constant in these alloys is of the order of 0·1 eV, which is the correct order of magnitude for Gd ions. Since the measurements of Ref. 12 were not carried out over a wide enough concentration range, it is not possible to compare the concentration dependence of the specific heat for these two groups of alloys.

One can readily see the similarity between the "cryptoferromagnetic" structure suggested by ANDERSON and SUHL(13) for ferromagnetic superconductors and the magnetic structure proposed here. However, in contrast to Anderson and Suhl, it is argued that the short range correlation is due to the nature of the Ruderman-Kittel interaction and the random space distribution of the magnetic spins. Furthermore, no distinction can be made between the magnetic structure of ferromagnetic superconductors and that of normal dilute magnetic alloys.

In the sum of equation (2) the terms with $i = j$ are also included. These are the self-energy terms of the spins and have no effect on the spin ordering. It was shown by HERRING,(14) SUHL and MATTHIAS(15) and BALTENSPERGER(16) that these terms are mainly responsible for the suppression of the superconducting critical temperature. The calculation of Herring assumes that the transition from the superconducting state to the normal state for an impure superconductor remains of the second order whereas the calculations of Suhl and Matthias and Baltensperger assume a first order transition. Recent experimental evidence seems to be in favor of the first point of view.(17) The linear dependence of the critical temperature on the concentration as obtained by Herring is also in better agreement with the experiment.

It was found that normal dilute magnetic alloys(18) as well as ferromagnetic superconductors(19) show hysteresis and coercive properties when magnetized. In the latter case there is definite evidence of remnant magnetization in addition to the trapped flux by the superconductivity. This phenomenon is often regarded as the experimental evidence of the existence of long range ferromagnetism. However, as pointed out by Marshall, there are loosely coupled spins in the Ruderman-Kittel model even at low temperatures. These spins can be lined up by an external field and be locked in approximately aligned positions by local anisotropy after the field is removed. This simple mechanism may explain the observed magnetization in both normal and superconducting magnetic alloys. The smallness of the remnant magnetization seems to be consistent with this model.

Of course, most of the above ideas are highly speculative in nature. However, it is hoped that some of them can be checked theoretically or experimentally, and in the course of doing so we may add new knowledge or new understanding to the general problem of magnetism in metals.

Acknowledgement—The author wishes to thank Dr. D. C. MATTIS for suggesting the investigation.

REFERENCES

1. RUDERMAN M. A. and KITTEL C., *Phys. Rev.* **96**, 99 (1954).
2. YOSIDA K., *Phys. Rev.* **106**, 893 (1957).
3. MARSHALL W., *Phys. Rev.* **118**, 1519 (1960).
4. ZIMMERMAN J. E. and HOARE F. E., *J. Phys. Chem. Solids* **17**, 52 (1960).
5. KLEIN M. W., *Unpublished Thesis*, Cornell University (1962); KLEIN M. W. and BROUT R. *Bull. Amer. phys. Soc.* **7**, 263 (1962).
6. MATTHIAS B. T., SUHL H. and CORENZWIT E., *Phys. Rev. Letters* **1**, 449 (1958).
7. BARDEEN J., COOPER L. N. and SCHRIEFFER J. R., *Phys. Rev.* **108**, 1175 (1957).
8. BOGOLIUBOV N. N., *Zh. eksp. teor. fiz. S.S.S.R.* **34**, 58 (1958). Translation: *Sov. Phys. -JETP* **7**, 41 (1958).
9. VONSOVSKII S. V. and SVIRSKII M. S., *Zh. eksp. teor. fiz. S.S.S.R.* **39**, 384–392 (1960), [Translation: *Sov. Phys. -JETP* **12**, 272 (1961)].
10. ANDERSON P. W., *J. Phys. Chem. Solids* **11**, 26 (1959).
11. BLATT J. M., *Progr. theor. Phys.* **24**, 851 (1960).
12. PHILLIPS N. E. and MATTHIAS B. T., *Phys. Rev.* **121**, 105 (1961).
13. ANDERSON P. W. and SUHL H., *Phys. Rev.* **116** 898 (1959).
14. HERRING C., Kamerlingh Onnes Memorial Conference on Low-Temperature Physics, Leiden, Holland, 1958; *Suppl. Physica* **24**, S184 (1958).
15. SUHL H. and MATTHIAS B. T., *Phys. Rev.* **114**, 977 (1959).
16. BALTENSPERGER W., *Helv. Phys. Acta.* **32**, 197 (1959)
17. PARKS R. D., *Bull. Amer. phys. Soc.* **7**, 322 (1962).
18. OWEN J., BROWNE M. E., ARP V. and KIP A. F., *J. Phys. Chem. Solids* **2**, 85 (1957).
19. BOZORTH R. M., DAVIS D. D. and WILLIAMS A. J., *Phys. Rev.* **119**, 1570 (1960).

J. Phys. Chem. Solids Pergamon Press 1963. Vol. 24, pp. 479–485. Printed in Great Britain.

THE CRYSTAL STRUCTURE OF $Bi_2Te_{3-x}Se_x$

SEIZO NAKAJIMA

Research Laboratory, Matsushita Electronics Corporation,
Takatsuki, Osaka, Japan

(*Received* 9 *July* 1962; *revised* 14 *November* 1962)

Abstract—It has been confirmed that Bi_2Te_3 and Bi_2Se_3 form complete solid solutions, their space group being D_{3d}^5-$R\bar{3}m$. The unit cell dimensions for the specimens having various compositions are given. The atomic parameters are found to be $u = 0{\cdot}4000$ and $v = 0{\cdot}2097$ for Bi_2Te_3, $u = 0{\cdot}3958$ and $v = 0{\cdot}2118$ for Bi_2Te_2Se, $u = 0{\cdot}3985$ and $v = 0{\cdot}2115$ for Bi_2TeSe_2, and $u = 0{\cdot}4008$ and $v = 0{\cdot}2117$ for Bi_2Se_3. Two kinds of bond length for Bi–Te (Se) are found. They lie in a range between covalent and ionic extremes. The temperature factors of each atom are also estimated. Relations between the crystallographic data and physical properties are discussed.

1. INTRODUCTION

In recent years extensive studies of V–VI compounds including Bi_2Te_3 have been made[(1–6)] in order to develop efficient materials for thermoelectric elements.

The crystal structure of Bi_2Te_3 has been first reported by Lange.[(7)] The crystal has a rhombohedral unit cell with one chemical formula and the space group is D_{3d}^5-$R\bar{3}m$. By transformation of axes, the unit cell can also be given as a hexagonal unit with three chemical formulae. The crystal has a layer structure stacked in the following order along the c_H axis of the hexagonal lattice,

$$Te^{[1]}—Bi—Te^{[2]}—Bi—Te^{[1]}.$$

The $Te^{[1]}$ atom has as the nearest neighbours three Bi atoms on one side and three Te atoms on the other side, whereas the $Te^{[2]}$ atom is surrounded by six Bi atoms; i.e. there exist two essentially different sites for the Te atoms. It has, moreover, been found by thermal and X-ray powder analysis that Bi_2Te_3 and Bi_2Se_3 form a complete solid solution in any proportion,[(8)] the solid solution ($Bi_2Te_{3-x}Se_x$) having the same crystal structure as Bi_2Te_3.[(4, 9)]

Besides the above cited work on the lattice parameters of the $Bi_2Te_{3-x}Se_x$ system atomic parameters have been determined for the compositions $x = 0$,[(7, 9, 10, 11)] $x = 1$[(12)] and $x = 3$.[(10)]

It is the purpose of this paper to present new crystallographic data (lattice parameters, atomic parameters and temperature factors) on the composition $x = 2$, which seem to correlate in an interesting way with some of the known physical properties of this system. A further object is to present briefly our own results on the compositions which were already investigated, as they may be slightly more accurate and as they provide an independent check on the data published already.*

In Section 2 the experimental procedure is described. Then our data are presented and compared with those of other authors. Finally, in Section 4 some conclusions are drawn about the possible correlation of our results with some of the physical properties.

2. EXPERIMENTAL PROCEDURES

A. Preparation of specimens

Chemical analyses by means of a square-wave polarograph showed that the component elements have purities higher than 99·999 per cent.† They were mixed in a given composition, placed in a quartz tube, sealed after evacuation and heated at 800°C for 6 hr. After quenching in water, the specimens were annealed for 6 hr at temperature slightly below their melting points, followed by slow cooling to room temperature at a rate of

---

* In fact the above mentioned work on the compositions $x = 1$ and $x = 3$ were brought to the author's attention only after the present work was finished.[(13)]

† Chemical analyses were carried out by Mr. Kakumoto of our Laboratory.

50°C per hr. Four specimens (Bi_2Te_3, Bi_2Te_2Se, Bi_2TeSe_2 and Bi_2Se_3), synthesized in this way, were used for the analysis.

B. Determination of lattice parameters

Lattice parameters along the a_H and c_H axis of the hexagonal unit cell were determined by the least-squares method and the extrapolation method, respectively. The measurements were carried out by a diffractometer, using powder specimens for the determination of a_H and single crystals for that of c_H. Diffraction angles were calibrated with quartz powder of Brazilian origin.

C. Measurements of diffraction intensities

Small pieces of specimens, which were cleaved off from grown crystals and proved to be single crystals by the Laue method, were placed on a glass plate and the diffraction profiles were recorded by an X-ray diffractometer with Ni filtered $CuK\alpha$ radiation. The receiving slit of the equipment was opened wide enough to catch K_{α_1} and K_{α_2} at the same time and the dispersion slit was made as narrow as possible, limited however by the condition that the X-ray beam should cover the whole area of the specimens. Additional conditions of the recording were 10 sec for the time constant and 1/10° per min for the scanning speed. Corrections on coincidence loss of the Geiger–Müller counter of the diffractometer were made for all diffraction profiles. The area surrounded by the corrected profile was taken to be proportional to the diffraction intensity. To carry out the correction, the dead time of the counter was determined by the multiple-foil method (14) The measurements were repeated five times and the standard deviations of structure factors were 3 ~ 6 per cent. Since the space group of this system is $D_{3d}^5-R\bar{3}m$, $(00l)$ reflections occur only when $l = 3n$ according to the extinction law. Twelve reflections were measured in each case.

3. RESULTS

3.1 *Structure analysis*

Lattice parameters of the hexagonal unit cell are shown in Table 1. The atomic positions in the rhombohedral unit cell are as follows;

2Bi	$\pm\ (u\ u\ u)$
$2X^{[1]}$ (site 1)	$\pm\ (v\ v\ v)$
$1X^{[2]}$ (site 2)	$(0\ 0\ 0)$

where $X^{[1]}$ and $X^{[2]}$ show the Te or Se atoms.

Approximate values of the atomic parameters are obtained by comparisons between relative values of observed intensity and those of calculated intensity. Overall values of the temperature factor are obtained from usual plots of $\ln|Fo|/|Fo|$ vs. $(\sin\theta/\lambda)^2$.

As a function of atomic parameters values of reliability factor R for Bi_2Te_3, Bi_2Te_2Se and

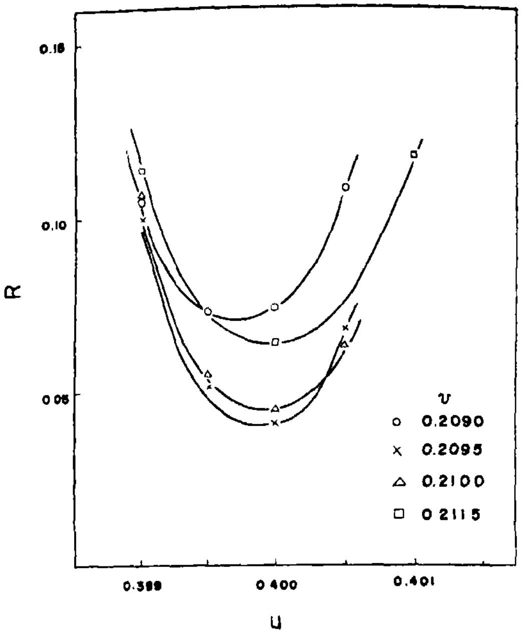

FIG. 1. Reliability factor R of Bi_2Te_3 vs. atomic parameters u and v.

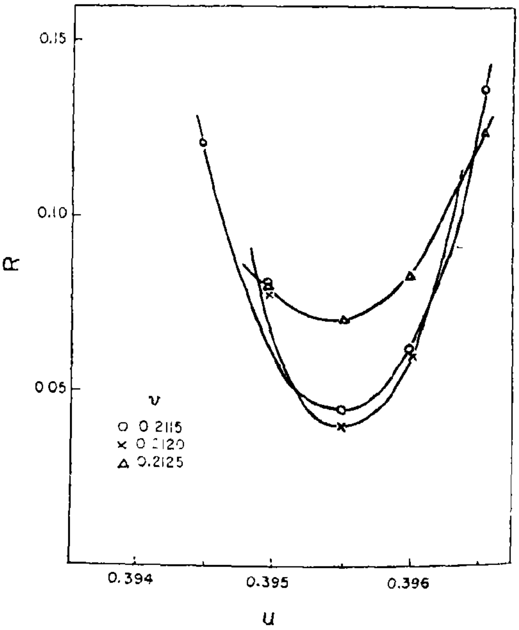

FIG. 2. Reliability factor R of Bi_2Te_2Se vs. atomic parameters u and v.

Bi_2Se_3 are shown in Figs. 1, 2 and 3, respectively.

In the case of Bi_2TeSe_2, values of R are obtained as a function of atomic parameters and a distribution parameter α, which is given by the quantity of Se at site (2). Then the distribution of atoms are expressed by the following formula.

$$Bi_2Te_{\alpha}^{[1]}\ Se_{2-\alpha}^{[1]}\ Te_{1-x}^{[2]}\ Se_{\alpha}^{[2]}.$$

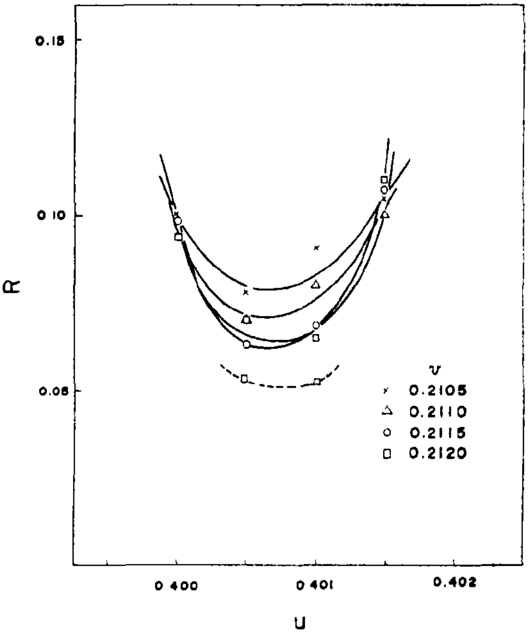

FIG. 3. Reliability factor R of Bi_2Se_3 vs. atomic parameters u and v.

Table 1. Lattice parameters

Specimen	Hexagonal lattice	
	a_H(Å)	c_H(Å)
Bi_2Te_3	4·386 ± 0·005	30·497 ± 0·020
$Bi_2Te_2Se_1$	4·298	29·774
$Bi_2Te_1Se_2$	4·218	29·240
Bi_2Se_3	4·143	28·636

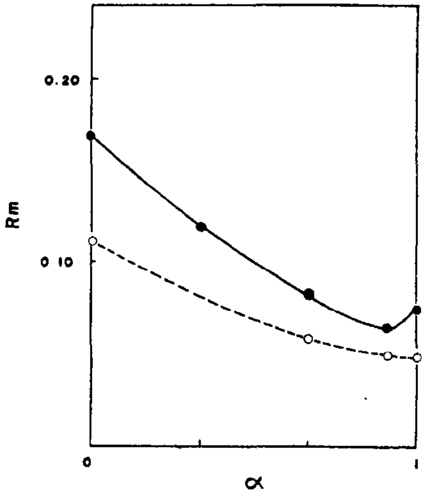

FIG. 4. Minimum reliability factor Rm of Bi_2TeSe_2 vs. distribution parameter α. Distribution of atoms is shown as $Bi_2Te_{\alpha}^{[1]}\ Se_{(2-\alpha)}^{[1]}\ Te_{(1-\alpha)}^{[2]}\ Se_{\alpha}^{[2]}$ by the parameter α. Solid line indicates Rm obtained from overall temperature factor. Broken line indicates Rm obtained from temperature factors of each atom.

Table 2. Atomic parameters

Specimen	u	v	B	Reference
				(u, v)
Bi_2Te_3	0·4000 ± 0·0007	0·2097 ± 0·0009	1·45	(0·399, 0·208)(7) (0·4001, 0·2095)(9)
	0·4000*	0·2095*	1·50*	(0·400, 0·212)(10) (0·399, 0·211)(11)
Bi_2Te_2Se	0·3958 ± 0·0007	0·2118 ± 0·0010	1·85	($0·396_1$, $0·211_7$)(12)
Bi_2TeSe_2	0·3985 ± 0·0008	0·2115 ± 0·0018	2·00	
Bi_2Se_3	0·4008 ± 0·0008	0·2117 ± 0·0015	1·50	(0·399, 0·206)(10)

* atomic parameters corrected with anomalous dispersion
u atomic parameter for Bi
v atomic parameter for atom at site (1)
B overall temperature factor

The solid line in Fig. 4 indicates the minimum value of $R(R_m)$ for given α.

In the above mentioned approximation, overall temperature factors are used. In order to arrive at a more detailed structure, temperature factors of each atom, as estimated by the least-squares method, are introduced into the calculation. The atomic parameters u and v were again refined by the least-squares method. Final values obtained in this way are summarized in Table 2. Temperature factors of each atom are plotted in Fig. 5 as a function of composition.

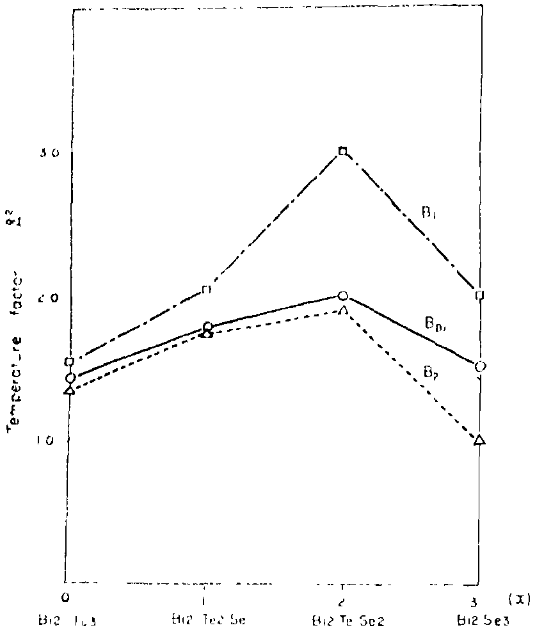

FIG. 5. Temperature factors of each atom

B_{Bi} : temperature factor of Bi
B_1 : temperature factor of atom at site (1)
B_2 : temperature factor of atom at site (2)

The minimum values of R for Bi_2TeSe_2 and Bi_2Se_3 are higher than those for Bi_2Te_3 and Bi_2Te_2Se. The former, however, decrease to the same level as the latter by further calculations as shown in Figs. 2 and 4 when the temperature factors of each atom are taken into account. Throughout all the specimens, the finally obtained values of R range between 4 and 5 per cent, which are almost of the same order as the range of the standard deviations of *Fo*, (3 ~ 6 per cent).

In the case of Bi_2TeSe_2, the difference in R values between the models corresponding to $\alpha = \frac{2}{3}$ and $\alpha = 1$ is so small that it is difficult to determine the most likely model merely by comparing the values of R. However it does not seem reasonable to take the model with $\alpha = \frac{2}{3}$, because in that case *Fo* and *Fc* for (0012) do not agree satisfactorily and B takes an unreasonable value as shown in Table 3. Finally, the results obtained in Refs. 12 and 13, which show that for $x = 1$ all Se are on site (2), make it very plausible that only those Se atoms which cannot be placed on site (2) occupy the site (1).

Table 3. Comparison of Fc with Fo for Bi_2TeSe_2

		Fc	
l	*Fo*	$\alpha = \frac{2}{3}$ $B_{Bi} = 2\cdot0$ $B_1 = 2\cdot8$ $B_2 = 2\cdot8$	$\alpha = 1$ $B_{Bi} = 2\cdot0$ $B_1 = 3\cdot0$ $B_2 = 1\cdot9$
3	32·9	41·4	31·7
6	$\overline{89\cdot0}$	$\overline{89\cdot7}$	$\overline{95\cdot9}$
9	$\overline{38\cdot2}$	$\overline{35\cdot8}$	$\overline{36\cdot2}$
12	$\overline{9\cdot6}$	0·4	$\overline{8\cdot7}$
15	147·2	156·6	155·6
18	77·7	80·7	79·8
21	$\overline{72\cdot2}$	$\overline{72\cdot6}$	$\overline{77\cdot1}$
24	$\overline{26\cdot5}$	$\overline{28\cdot0}$	$\overline{27\cdot6}$
27	11·4	10·2	9·4
30	51·7	51·3	50·5
33	50·7	48·9	50·6
36	$\overline{25\cdot8}$	$\overline{24\cdot4}$	$\overline{24\cdot7}$

Extinction effects were examined by plotting *Ic*/*Io* as a function of *Ic*. The ratio *Ic*/*Io* is constant and apparently this effect can be disregarded for further refinement. Anomalous dispersion of

X-ray scattering(15) gives trivial effects on the atomic parameters. For Bi_2Te_3 the corrected parameters are shown in Table 2. Different electronic states of atoms give no appreciable effect on the scattering factors(16) for all reflections observed in the experiment.

3.2 *Bond length*

Bond lengths are calculated from lattice and atomic parameters. Three kinds of bonds in the crystal are denoted by d_1, d_2 and d_3 as shown in Fig. 6. The length d_1 is shorter than d_2. Both values are always found in the range between the two extremes of purely ionic and purely covalent length, as calculated from published data.(17)

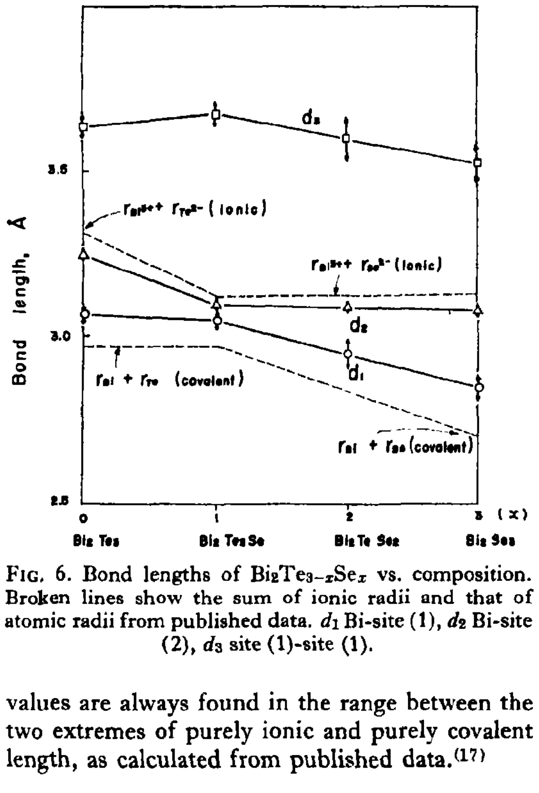

FIG. 6. Bond lengths of $Bi_2Te_{3-x}Se_x$ vs. composition. Broken lines show the sum of ionic radii and that of atomic radii from published data. d_1 Bi-site (1), d_2 Bi-site (2), d_3 site (1)-site (1).

3.3 *Comparison with previous work*

The comparison of our results with those obtained by other investigators is summarized in Table 2. As can be seen from this table our data on Bi_2Te_2Se are in excellent agreement with those obtained by BLAND and BASINSKI.(12) However, our data are believed to be slightly more reliable because in the present investigation the standard deviation of *Fo*'s are satisfactorily small as mentioned above, because the temperature factors of each type of atom are taken into account separately in calculating *Fc* and because the finally obtained reliability factor *R* is less than that of Bland and Basinksi by a factor of about 4.

The previously published data on Bi_2Se_3(10) have been obtained by means of electron diffraction study. These data are probably slightly less satisfactory, because the bond lengths calculated from these data take unreasonable values if they are compared with those obtained for other compositions of our system. It is quite generally not justified to expect very accurate results from the study of electron diffraction.

4. DISCUSSION

4.1 *Bond length and conductivity character*

Although it is impossible to make unique quantitative statements about the degree of ionicity of a mixed chemical bond,(18, 19) qualitative statements may still make sense. Our results on the bond length (Fig. 6) might indicate that the bond d_2 is more ionic than d_1. This conclusion is drawn from the fact that the bond length d_2 is closer to the purely ionic value. It is interesting to observe that this conclusion ties up in a satisfactory way with the conductivity character (*n*-type or *p*-type) in the undoped $Bi_2Te_{3-x}Se_x$ system.

As was shown by OFFERGELD and VAN CAKENBERGHE(20) Bi_2Te_3 and Bi_2Se_3 are nonstoichiometric with an excess of Bi. Therefore we may apply KRÖGER's suggestion(21) about the nature of lattice defects in nonstoichiometric crystals. If this is done for our system, we come to the conclusion that an antistructure type of disorder leads to *p*-type conductivity whereas an interstitial or vacancy mechanism would lead to *n*-type conductivity.

It can be considered as a general rule that the antistructure mechanism predominates at not too high temperature when Bi and X (where X shows Te or Se) differ only slightly in atomic radius and electronegativity, whereas the interstitial or vacancy mechanism predominates at higher temperatures. The observation of *p*-type conductivity in Bi_2Te_3 must therefore be attributed to the predominance of the antistructure mechanism.(20)

With an increase of the quantity of Se the interstitial or vacancy mechanism becomes dominant owing to an increasing difference in atomic radius and electronegativity and *n*-type properties are observed at x = ca.1. We believe that the alternation in the dominant disorder mechanism causes this inversion from *p*-type to *n*-type in the $Bi_2Te_{3-x}Se_x$ system. It goes without saying that site (1) is more favorable for antistructure, because according to our results the bond d_2 is of a more ionic nature.

Additional support for the connection between bond length and conductivity mechanism suggested here may be obtained from observations on the $Bi_{2-w}Sb_wTe_{3-x}Se_x$ system.(22) In fact the inversion point from *p*-type to *n*-type conductivity is shifted to higher values of x if the Sb content becomes larger. As the bond between Sb and X is doubtlessly more covalent than that between Bi and X, the change in dominant disorder mechanism must occur at higher values of x.

4.2 *Temperature factor, bond strength and thermal conductivity*

As can be seen from Fig. 5, B_1 becomes extraordinarily large at $x = 2$. This can be taken as an indication for an appreciable weakening of the bond d_2 and especially d_3. As also the other individual temperature factors are larger for this composition than for others, it may be concluded that all the bonds in Bi_2TeSe_2 are weakened to some extent.

We believe that this weakening of the bonds at $x = 2$ can explain some of the characteristic results found in the behavior of the thermal conductivity.

Thermal conductivity of this system has been measured by several investigators.(4, 6, 23) Although perfect agreement has not been obtained, an interesting common tendency can be observed. Rosi *et al.*(23) have found two minima in the lattice component (κ_L) of the conductivity at $x = 0{\cdot}7$ and $1{\cdot}9$. Fuschillo *et al.*(6) have also found two minima at $x = 1{\cdot}0$ and $2{\cdot}2$; however, they did not separate the lattice component from the total thermal conductivity. The minimum around $x = 2$ is most probably connected with the maximum in the temperature factor we found for this composition. The variation in temperature factors between $x = 0$ and $x = 1$ are relatively small. The other minimum which lies somewhere between $x = 0$ and $x = 1$ must therefore be mainly attributed to a relative maximum in alloy scattering of phonons which could be expected in this region.

5. SUMMARY AND CONCLUSION

1. The crystal structure of Bi_2Te_3, Bi_2Te_2Se and Bi_2Se_3 are refined.
2. The distribution of the atoms in Bi_2TeSe_2 are determined. From the results obtained on the distribution and the change in bond length, it can be concluded that all Se atoms preferentially occupy site (2) when $x \leqslant 1$, whereas one Se atom occupies site (2) and the others $(x-1)$ are distributed at random in site (1) when $3 > x > 1$.
3. The bond lengths are calculated from the lattice and atomic parameters. Two kinds of bonds between Bi and Te or Se are found. The length d_1 (Bi-site (1)) has a close correspondence to the sum of covalent radii, whereas the length d_2 (Bi-site (2)) corresponds to that of ionic radii.
4. The temperature factors of atoms are estimated by the least-squares method. The magnitude of the factors changes with the specimens and the atoms. A possible interpretation is proposed on the basis of the bond strength.
5. Physical properties of this system are discussed from a standpoint of the structure.

Acknowledgements—The author wishes to express his sincere thanks to Prof. T. Watanabe and Dr K. Ōsaki of Osaka University, Prof. A. Shimada of Osaka City University, and Dr. H. J. G. Meyer of Philips Research Laboratories for their helpful discussions. Thanks are also due to Dr. M. Ozasa for his support and to Mr. H. Okazaki for his assistance throughout the course of this work. Last but not least, thanks are due to Mr. I. Teramoto, who prepared specimens and, moreover, whose interesting investigations on the electrical properties of the Bi–Sb–Te–Se system has stimulated the author to closer analysis of structure.

REFERENCES

1. Black J., Conwell E. M., Seigle L. and Spencer C. W., *J. Phys. Chem. Solids* **2**, 240 (1957).
2. Satterthwaite C. B. and Ure R. W., *Phys. Rev.* **108**, 1164 (1957).
3. Goldsmidt H. J., Sheard A. R. and Wright D. A., *Brit. J. appl. Phys.* **9**, 365 (1958).
4. Birkholz U., *Z. Naturf.* **13a**, 780 (1958).
5. Aoki M. and Chang Z. P., *Oyo Buturi* **28**, 82 (1959). (In Japanese).

6. FUSCHILLO N., BIERLY J. N. and DONAHOE F. J., *J. Phys. Chem. Solids* **8**, 430 (1959).
7. LANGE P. W., *Naturwissenschaften* **27**, 133 (1939).
8. MCHUGH J. P. and TILLER W. A., *Trans. Amer. Inst. min. (metal.) Engrs.* **215**, 651 (1959).
9. WIESE J. R. and MULDAWER L., *J. Phys. Chem. Solids* **15**, 13 (1960).
10. SEMILETOV S. A., *Trud. inst. krit. akad. nauk S.S.S.R.* **10**, 76 (1954).
11. AIRAPETIANTS S. V. and EVIMOVA B. A., *J. Tech. Phys. Moscow* **8**, 1632 (1958).
12. BLAND J. A. and BASINSKI S. J., *Canad. J. Phys.* **39**, 1040 (1961).
13. OKAZAKI H. and NAKAJIMA S., *Oyo Buturi Gakkai, Tokyo*. The 8th Conference of Applied Physics of Japan, Tokyo (1961) Prelim. Rep. **8**, 284 (1961). (In Japanese).
14. KLUG H. P. and ALEXANDER L. E., *X-ray Diffraction Procedures*, p. 282. John Wiley, New York (1954).
15. DAUBEN C. H. and TEMPLETON D. H., *Acta Cryst.* **8**, 841 (1955).
16. SAGEL K., *Tabellen zur Röntgen Strukturanalyse*, p. 106. Springer, Berlin (1958).
17. KIRIYAMA R., *Structural Inorganic Chemistry* **I**, p. 219. Kyoritu, Tokyo (1952). (In Japanese).
18. DRABBLE J. R. and GOODMAN C. H. L., *J. Phys. Chem. Solids* **5**, 142 (1958).
19. SUCHET J. P., *J. Phys. Chem. Solids* **16**, 265 (1960).
20. OFFERGELD G. and VAN CAKENBERGHE J., *J. Phys. Chem. Solids* **11**, 310 (1959).
21. KRÖGER F. A., *J. Phys. Chem. Solids* **7**, 277 (1958).
22. TERAMOTO I. and TAKAYANAGI S., *J. Phys. Chem. Solids* **19**, 124 (1961).
23. ROSI F. E., ABELES B. and JENSEN R. V., *J. Phys. Chem. Solids* **10**, 191 (1959).

J. Phys. Chem. Solids Pergamon Press 1963. Vol. 24, pp. 487–491. Printed in Great Britain.

STRUCTURE ET PROPRIÉTÉS MAGNÉTIQUES DE L'OXYSULFURE D'URANIUM UOS

R. BALLESTRACCI, E. F. BERTAUT et R. PAUTHENET

Laboratoire d'Electrostatique et de Physique du Métal,
et
Centre d'Etudes Nucléaires, Grenoble, France.

(*Received* 20 *September* 1962)

Resumé—UOS quadratique est antiferromagnétique avec une température de Néel de $T_N = 55$°K et une température paramagnétique $\Theta_p = -51$°K. Dans la région antiferromagnétique, il y a une forte anisotopie uniaxiale. Chaque atome d'uranium est porteur d'un moment de 2 μ_B environ, dirigé selon l'axe *c*. Les interactions U–O–U sont fortement négatives. La succession des moments selon *c* est + + − −. La maille magnétique est deux fois la maille chimique selon *c*.

Dans la région paramagnétique, l'inverse de la susceptibilité magnétique en fonction de la température possède deux régions rectilignes auxquelles correspondent deux constantes de Curie $C_1 = 0,9$ (aux basses températures) et $C_2 = 1,2$ (pour $T > 450$°K).

Abstract—UOS is tetragonal and antiferromagnetic with a Néel temperature $T_N = 55$°K and a paramagnetic Curie temperature $\Theta_p = -51$°K. In the antiferromagnetic region, there is a strong uniaxial anisotropy. Every uranium atom has a moment of about 2 μ_B, directed along the *c*-axis. The interactions U–O–U are strongly negative. The succession of moments along *c* is + + − −. The magnetic unit cell is twice the chemical one along *c*.

In the paramagnetic region, the inverse of the magnetic susceptibility versus temperature shows two linear portions with corresponding Curie constants $C_1 = 0,9$ (at low temperatures) and $C_2 = 1,2$ (at $T > 450$°K).

STRUCTURE CRISTALLOGRAPHIQUE

On a préparé UOS par sulfuration ménagée de UO_2 dans un courant de H_2S à 1000°C. La structure de UOS[(1)] est isotype de celle de PbFCl.[(2)] Le groupe d'espace est $P4/nmm$, centro-symétrique. Les paramètres de la maille sont[(1)] $a = 3,835$ kX et $c = 6,681$ kX. U et S sont dans les positions 2*c*) $00z$; $\frac{1}{2}\,\frac{1}{2}\,\bar{z}$. 0 est en 2*a*) $\frac{1}{2}\,0\,0$; $0\,\frac{1}{2}\,0$. Une représentation équivalente, ayant le centre de symétrie à l'origine, est U et S en 2*c*) $\pm\,(\frac{1}{4}\,\frac{1}{4}\,z)$, 0 en 2*a*) $\pm\,(\frac{3}{4}\,\frac{1}{4}\,0)$. Dans la structure les plans d'atomes se succèdent selon *c* comme O–U–S–S–U–O–U–S–S– . . . La Fig. 1 représente 2 mailles cristallographiques.

DIFFRACTION NEUTRONIQUE

La diffraction neutronique à température ordinaire confirme entièrement la structure déterminée par Zachariaesn aux rayons-X,[(1)] la précision de nos paramètres $z_U = 0,199$; $z_S = 0,643$ étant probablement meilleure. Il en résulte que U a pour voisin 4 atomes 0 à 2,33 kX, 4 atomes S à 2,91 kX et un atome S à 2,97 kX.

A la température de l'hélium liquide (4,2°K), les raies nucléaires ne changent pas tandis que de nouvelles raies apparaissent que l'on parvient à indexer dans une maille doublée selon *c*. (cf. Figs. 2 et 3). Ces raies sont donc caractéristiques d'un vecteur de propagation $\boldsymbol{k} = [0\ 0\ \frac{1}{2}]$. Pour un vecteur de propagation unique donné, le nombre de modèles possibles est égal au nombre de réseaux de Bravais magnétiques dans la maille cristallographique.[(3)] Il n'y a alors que deux modèles possibles correspondant respectivement aux successions + + − − et + − − + des plans de moments magnétiques situés aux cotes $z = 0,2$; 0,8 ; 1,2 ; 1,8*c* de la maille chimique. L'absence de toute réflexion (00*l*) d'origine magnétique conduit à identifier la direction des spins avec l'axe 0_z.

Un examen même qualitatif des intensités des raies magnétiques d'indices $(101)_M$ $(111)_M$ et $(113)_M$ élimine le modèle + − − +. La Fig. 1 représente la structure magnétique de UOS.

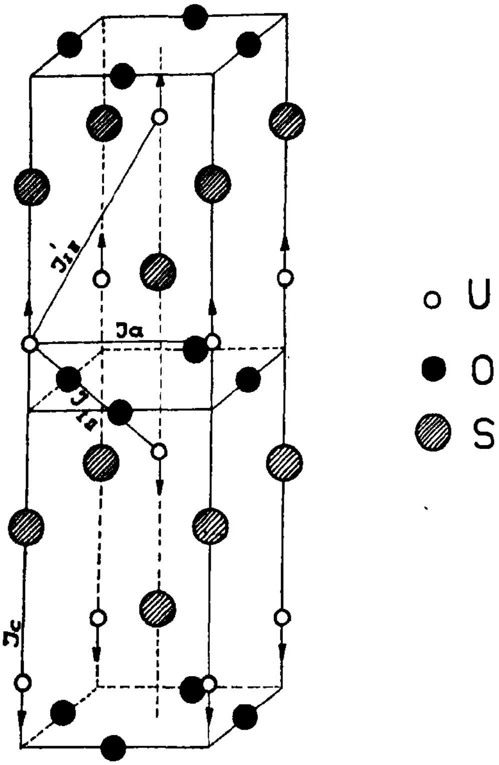

FIG. 1. Structure cristallographique et magnétique de UOS.

En l'absence de facteurs de forme magnétiques f publiés pour l'uranium, nous nous sommes basés sur une courbe moyenne de f que nous devons à l'obligeance de BROCKHOUSE et HENSHAW.(4) Elle est relative à UO_2, les spins étant supposés dirigés selon [100]. De la comparaison de la réflexion magnétique $(101)_M$ avec l'ensemble des réflexions nucléaires $(101)_N$ et $(002)_N$, non séparées, on déduit $\langle S^2 \rangle = 0{,}91$, soit une valeur apparente de spin égale à 0,954. La précision sur $\langle S^2 \rangle$ est estimée à ± 6 pour cent. Les valeurs déduites des raies magnétiques $(111)_M$ et $(113)_M$ dont les intensités sont déterminées par la différence des diagrammes des Figs 2 et 3 sont moins certaines, la valeur moyenne de S^2 étant $0{,}99 \pm 0{,}25$. (Les intensités observées ayant servi à établir ces résultats sont, après correction de Lorentz et en unités arbitraires $I(101)_M = 3434 \pm 150$; $I(111)_M = 1114 \pm 300$; $I(113)_M = 849 \pm 300$. Les carrés des facteurs de forme magnétiques respectifs sont selon(4) 0,805 ; 0,655 et 0,57. L'intensité nucléaire de l'ensemble $I[(101)_N+(002)_N]$ est 445,4).

En résumé, la diffraction neutronique indique un moment magnétique de $1{,}9 \pm 0{,}11\ \mu_B$, voisin de la valeur de "spin seul".

PROPRIÉTÉS MAGNÉTIQUES DE UOS

Entre 2,5°K et l'ambiante on a mesuré la variation de l'aimantation spécifique en fonction du champ magnétique interne H_i. Au-dessus de la température ambiante jusqu'à environ 1100°K on a déterminé directement la susceptibilité χ_m, relative à la molécule gramme au moyen d'une balance de translation. Au-dessus de 50°K, les isothermes (σ, H_i) sont des droites dont les pentes représentent χ_m ; au-dessous de 50°K s'ajoute un très faible ferromagnétisme dont l'aimantation spécifique est de l'ordre de 0,03 u.é.m./g. L'allure de $1/\chi_m$ en fonction de la température T (Fig. 4) est caractéristique d'un comportement antiferromagnétique avec une température de Néel T_N = 55°K.

Dans la région paramagnétique, $(1/\chi_m, T)$ n'est pas une droite, mais présente une légère courbure avec une inflexion vers 450°K. Des mesures à basses températures, on peut déduire un point de Curie paramagnétique $\Theta_{p1} = -51$°K et une constante de Curie $C_1 = 0{,}96$; par contre des mesures à haute température (au-dessus de 450°K) on déduit des valeurs légèrement différentes, soit $\Theta_{p2} = -108$°K et $C_2 = 1{,}2$. Si le moment magnétique était dû au spin seul, on déduirait des valeurs de C_1 et de C_2 que U^{4+} est porteur de 1,94 et 2,24 μ_B respectivement.

Des relations*

$$\Theta_p = \tfrac{1}{2}C(n+n'); \quad T_N = -\tfrac{1}{2}C(n-n')$$

où n et n' sont les coefficients du champ

---

* On convient ici de représenter les coefficients de champ moléculaire et les intégrales d'échange par des quantités positives pour des interactions ferromagnétiques et par des quantités négatives pour des interactions antiferromagnétiques.

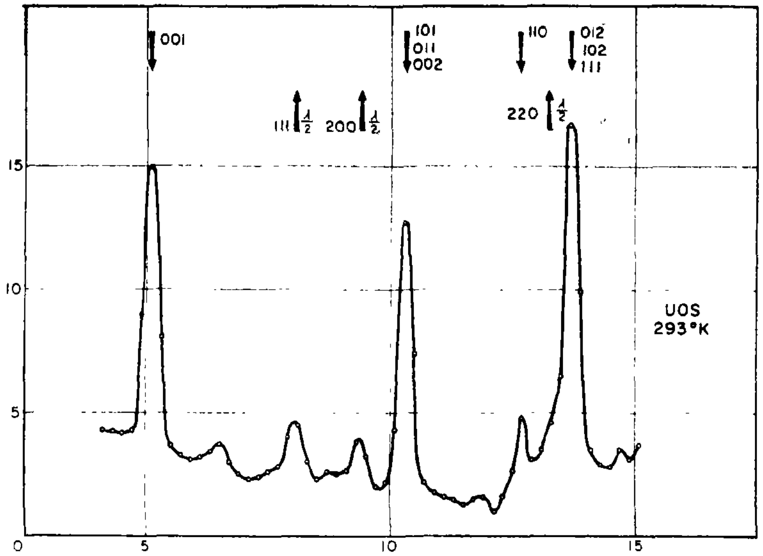

FIG. 2. Diagramme neutronique de UOS. Température ordinaire = 1,198 Å.

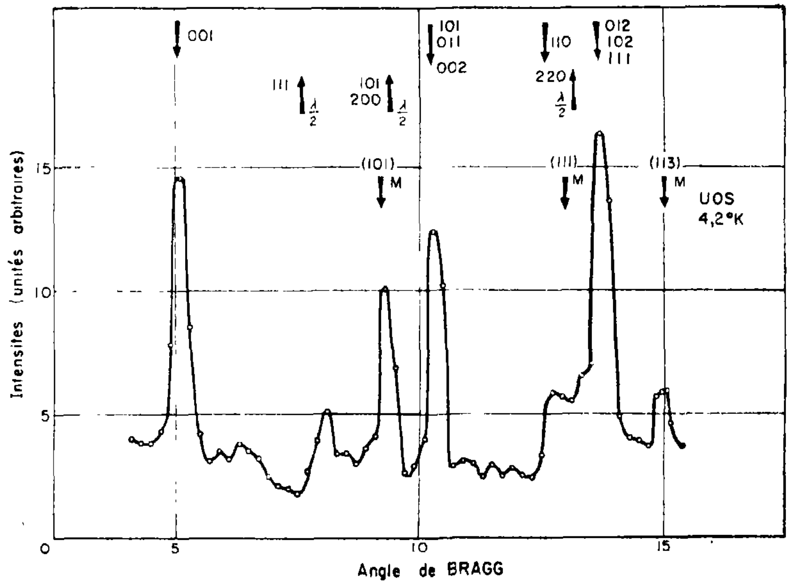

FIG. 3. Diagramme neutronique de UOS à 4,2°K.

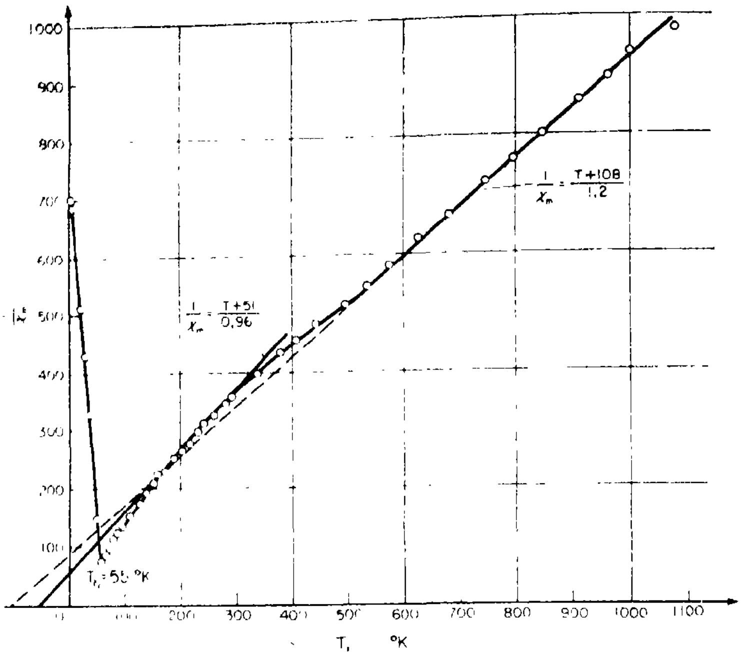

FIG. 4. Susceptibilité magnétique de UOS.

moléculaire représentant respectivement les interactions entre deux sous-réseaux* de Néel différents et celles entre ions sur un même sous-réseau, on déduit aux basses températures

$$n_1 = -111; \; n_1' = +4,2$$

et aux températures élevées (au-dessus de 450°K)

$$n_2 = -136; \; n_2' = -42$$

Pour $T = T_N$, la valeur expérimentale de $1/\chi_m$ est 80 alors que les valeurs calculées peuvent être égales à 111 ou 136. Au zéro absolu la valeur extrapolée de $1/\chi_m$ est environ quatre fois plus grande (cf. Fig. 4) que la valeur calculée $\frac{3}{8}$ $|n|$.

Nous admettrons que l'écart est dû à l'anisotropie magnéto-cristalline. En représentant cette dernière par le terme $K_1 \sin^2 \theta$ où θ est l'angle entre l'aimantation spontanée J_s avec l'axe de facile aimantation, l'expression théorique de $1/\chi_m$ est au zéro absolu

$$(1/\chi_m)_{T=0} = \frac{3}{2}\left(n + \frac{2K_1}{J_s^2}\right)$$

On en déduit que K_1 est de $7{,}5 \cdot 10^7$ erg/g ; valeur élevée, mais compatible avec l'ordre de grandeur des constantes d'anisotropie des substances uniaxes.

INTERACTIONS MAGNÉTIQUES

Les atomes d'uranium occupent dans la structure cristallographique deux réseaux de Bravais d'origines $00z$ (réseau I) et $\frac{1}{2}\,\frac{1}{2}\,\bar{z}$ (réseau II). Les intégrales d'échange significatives sont (cf. Fig. 1) $J_{\mathrm{I,II}}$ de l'espèce U–O–U à la distance $d_{\mathrm{I,II}} = 3{,}81$ kX, J_a à la distance $a = 3{,}835$ kX, $J'_{\mathrm{I,II}}$ à la distance 4,84 kX. L'intégrale d'échange J_c est probablement négligeable, la distance correspondante étant de 6,681 kX. Nous avons montré ailleurs[3] que l'étude d'une certaine matrice $\zeta(\boldsymbol{k})$ fournit directement les valeurs de l'énergie d'échange, les configurations de spin possibles et les critères de stabilité locale lorsque le vecteur de propagation $\boldsymbol{k}$ est unique. La matrice $\zeta(\boldsymbol{k})$ a ici la forme

---

* Un sous-réseau de Néel est l'ensemble des réseaux de Bravais d'atomes magnétiques de même espèce et de même direction de spin.

$$\zeta(\boldsymbol{k}) = \begin{bmatrix} A & B \\ B^* & A \end{bmatrix}$$

où $A = 2(J_a(\cos X + \cos Y) + J_c \cos Z$

$$B = 4 \exp \tfrac{1}{2}i(X+Y) \cos \tfrac{1}{2}X \cos \tfrac{1}{2} Y J_{\mathrm{I,II}} + J'_{\mathrm{I,II}} \exp{-iZ})$$

$$X = 2\pi h \; ; \; Y = 2\pi k \; ; \; Z = 2\pi l$$

La valeur propre λ de la matrice $\zeta(\boldsymbol{k})$ se réduit pour $\boldsymbol{k} = [0\ 0\ \tfrac{1}{2}]$ à

$$\lambda = 4(J_a + J'_{\mathrm{I,II}} - J_{\mathrm{I,II}}) - 2J_c$$

L'énergie d'échange par unité cristallographique est $H = -2\lambda$. L'examen de la stabilité locale (maximum de λ) conduit alors aux conditions suivantes (en négligeant J_c)

$$J_{\mathrm{I,II}} < 0 \; ; \quad J'_{\mathrm{I,II}} > 0$$

$$2J_a - J_{\mathrm{I,II}} + J'_{\mathrm{I,II}} > 0$$

Dans la théorie du champ moléculaire on a

$$4J_a - 2J_c + 4(J'_{\mathrm{I,II}} - J_{\mathrm{I,II}}) = \rho T_N$$

$$4J_a + 2J_c + 4(J'_{\mathrm{I,II}} + J_{\mathrm{I,II}}) = \rho \Theta_p$$

où ρ est une constante (qui, dans le cas de spin seul, prend la valeur $\rho_s = 3/\,2S(S+1)$).
On en déduit (en négligeant J_c)

$$J_a + J'_{\mathrm{I,II}} = \tfrac{1}{8}\, \rho(T_N + \Theta_p)$$

$$J_{\mathrm{I,II}} = \tfrac{1}{8}\, \rho(-T_N + \Theta_p)$$

de sorte que la 3e condition de stabilité devient

$$J_a + \tfrac{1}{4}\, \rho T_N > 0$$

J_a peut donc être négatif dans les limites permises par l'inégalité précédente.

Retenons encore que $J_{\mathrm{I,II}}$ est proportionnel à n tandis que $J_a + J'_{\mathrm{I,II}}$ est proportionnel à n'.

DISCUSSION

Il y a au moins deux faits remarquables, d'abord le changement de signe de n', ensuite le fait que la constante de Curie, voisine de 1, et le moment trouvé par diffraction neutronique semblent indiquer un état de spin *seul* $S = 1$.

Comme n' est proportionnel à $J'_{\mathrm{I,II}} + J_a$, il se peut qu'aux basses températures $J'_{\mathrm{I,II}}$ (positif) prédomine tandis qu'aux températures élevées où uniquement les voisins proches contribuent à n', J_a seul entre en ligne de compte. Or, J_a peut être négatif.

Le fait que la constante de Curie est voisine de l'unité peut être une pure coincidence numérique. En effet C a la forme

$$C = \frac{1}{3} \frac{N\mu_B^2}{k}\, g^2 \sum_i | \; \langle i|J_z|i \rangle|^2$$

avec

$$\tfrac{1}{3}\, N\mu_B^2/k = 0{,}125$$

Si U^{4+} est dans l'état ${}^3H_4$ ($S = 1$, $L = 5$, $J = 4$), alors $g = 4/5$. Dans un site *cubique* (par exemple dans UO_2) la matrice U affecte la forme suivante(5, 6)

$$J = \frac{5}{2} \begin{bmatrix} 1 & \cdot & \cdot \\ \cdot & 0 & \cdot \\ \cdot & \cdot & -1 \end{bmatrix}$$

de sorte que C se réduit à $0{,}125 \times 16/25 \times 25/2 = 1$. Or c'est exactement la valeur que l'on trouverait dans l'hypothèse d'un "spin seul" ($C = 0{,}125\, g^2S(S+1)$ avec $g = 2$ et $S = 1$).

AYANT et BELORIZKY ont entrepris des calculs quantiques pour expliquer la grandeur de l'anisotropie cristalline due au champ cristallin, la valeur du moment magnétique dans un site de symétrie *quadratique* (aussi bien dans la région antiferro- que para-magnétique) et enfin la variation de la constante de Curie de $C_1 = 0{,}96$ aux basses températures à $C_2 = 1{,}2$ aux températures élevées.

BIBLIOGRAPHIE

1. ZACHARIASEN W. H., *Acta Cryst.* **2,** 291 (1949).
2. *Strukturberichte*, 1928–1932, **II,** p. 45. *Akad. Verlagsges. Leipzig* (1937).
3. BERTAUT E. F., *C.R. Acad. Sci., Paris* **252,** 76 2078 (1961); *J. Phys. Chem. Solids.* **21,** 256 (1961); *J. appl. Phys.* **33,** 1138 (1962).
4. BROCKHOUSE B. N. et HENSHAW D. G., *Amer. phys. Soc.* meeting, New York, (1957) (unpublished); see also *Bull Amer. phys. Soc.* **2. 9** (1957).
5. HUTCHISON C. A. et CANDELA G. A., *J. Chem. Phys.* **27,** 707 (1957).
6. AYANT Y. et BELORIZKY E., *J. Phys. Radium,* **22,** 461 (1961).

LETTERS TO THE EDITOR

Spectral photoresponse of Si, GaAs and Ge shallow junction in the region 1–5 eV

(*Received* 24 *September* 1962)

THE reflectance measurement on a number of semiconducting crystals in the intrinsic region has recently been the active interest of several laboratories.(1) The fine structure in the reflectance spectral reveals direct interband transitions and hence provides important information on the band structure of the semiconductor. The spectral photoresponse measured on a semiconductor in the intrinsic region may yield similar data. Furthermore, it may provide the information on the behavior of excited carriers in different parts of the *k*-space.

This Letter reports the spectral photoresponse measured on shallow *p–n* junctions of silicon, germanium, and gallium arsenide crystals in the intrinsic region up to 5 eV at room temperature. The measurement shows that the spectral photoresponse of each crystal has fine structure, which can be related to the photoconduction of carriers excited by major interband transitions. (See the following letter.)

Shallow *p–n* junctions of Si, GaAs, and Ge crystals with junction depth from a fraction of a micron to a few microns were reversely biased at room temperature during spectral photoresponse measurements.

The Perkin–Elmer spectrometer, Model 112, equipped with a fused quartz prism and operated with a single beam pass was used. Emission lines from the G.E. mercury lamp, AH4, with glass envelope removed were used as the light source. A power stabilizer of the conventional hydrogen lamp source was used as the power input of the mercury lamp transformer. The relative intensity of mercury emission lines in the measured range was essentially constant as checked by either the Reeder's thermocouple with CsI window, or the photomultiplier 1P28 on different days. The reflectance spectrum from the surface of the *p–n* junction was measured by the Reeder's thermocouple at the place of the photodiode for direct beam and nearby for the reflected beam.

The photoresponse spectra of shallow *p–n* junctions of GaAs, Si, and Ge crystals are shown in the upper part of Fig. 1 by curves joining the solid circles. These solid circles have photon energies corresponding to the mercury lamp emission lines. The spectral photoresponse, which is computed by dividing the measured photoconductive signal by the product of measured direct beam intensity, calibrated wavelength, and the known value of (1 – reflectivity), is proportional to the product of quantum yield and carrier collection efficiency. Because of the size limitation of the thermocouple and the diffused portion of the reflection from the surface of the photodiode, it is not accurate to obtain the reflectivity of the photodiode by simply using a thermocouple to measure the direct beam intensity shining on the diode and the reflected beam from the diode. Therefore the published value of reflectivity(1) of

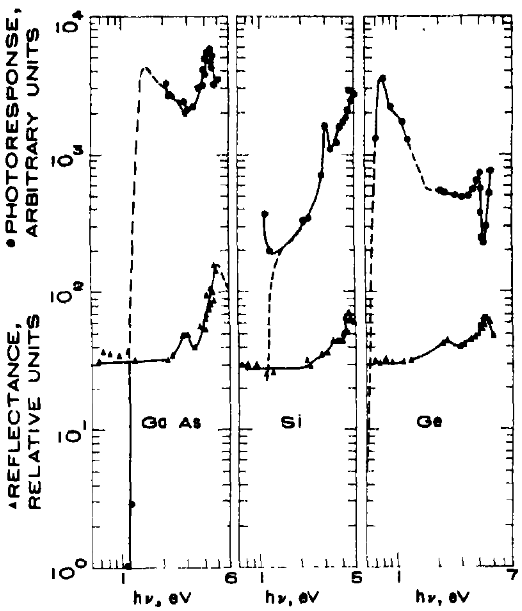

FIG. 1. Spectral photoresponse and reflectance spectra of GaAs, Si and Ge shallow junctions at room temperature. The solid points were taken using mercury emission lines and the dashed curve using a tungsten lamp.

these crystals was used in the computation of photoresponse. However, the general feature of the measured reflection spectrum, as shown in the lower part of Fig. 1 in arbitrary units, resembles the published spectra.(1)

It is known that the general trend of the spectral photoresponse of a semiconductor in the intrinsic region can rise, such as the Si junction on one hand, or fall, like the Ge and GaAs photodiode on the other hand, depending on the factors such as surface recombination velocity,(2) junction depth, etc. The fine structure* which is superimposing on the general background of photoresponse in Fig. 1, can be interpreted as due to the photoconduction of excited carriers in different parts of the k-space. (See the following Letter). Because of the intense light source used in the experiment, the np product of excited carriers is large and the recombination is fast. They may lead to the incomplete thermalization of the carriers before recombination which can explain the shape of the observed structure. (See the following Letter.)

Similar photoconductive measurement has also been made on a highly resistive Ge bar, n-type and 45 Ω-cm in room temperature resistivity, with the cleaved surface facing the incident beam and biased at a current density about 60 mA per cm^2. The photoresponse rises slightly in the visible region. In the ultraviolet region, a similar structure as that of the Ge photodiode in Fig. 1 is also observed. (For GaAs and Si bars the photoconductive signal is too weak in the intrinsic region, probably because of a number of possible reasons such as surface, contacts, etc.). It is therefore suggestive that although the structure shown in Fig. 1 was obtained from the reversely bias photo-diodes (n-type diffused shallow layer on p-type Ge and Si and p-type diffused thin layer on n-type GaAs) the observed structure is intrinsic and it depends essentially on the band structure of the crystal.

The bias current dependence of the spectral photoresponse has also been measured(5) for Si and GaAs junctions, only in the vicinity of the band edge, by varying the reverse bias voltage. By using bias voltage up to about 100 V, the reverse current changes also about two orders of magnitude. The overall photoresponse is raised by the increasing reverse bias voltage, especially in the long wavelength region, and hence the shoulder or peak of the photoresponse near the band edge appears to be shifted toward longer wavelength. However, the amount of the apparent shift, 5×10^{-2} eV for Si under 80 V bias, and 10^{-2} eV for GaAs under 100 V is not too large, and the general spectrum near the band edge has not been significantly altered.

For regions of higher photon energy, it would be expected that the bias voltage effect on the spectral spectrum may be similar or even less effective. In short, the order of magnitude of the bias current density, 5 μA through 1·6 cm^2 Si junction, $10^{-2}\,\mu$A through 15×10^{-2} cm^2 GaAs junction, and 200 μA through $2{\cdot}3 \times 10^{-1}$ cm^2 Ge junction, and the intensity of the excitation light through the monochromator used in the experiment are probably too low to wash out the structure in the photoresponse due to electron–electron scatterings.

Acknowledgements—It is a great pleasure to acknowledge Helen Farran's work in fabricating the Si and Ge detectors, R. H. Harada for providing the cadmium diffused GaAs photodiodes, E. Matovich for supplying the diffused Ge junctions, and G. S. Picus for frequent discussions.

The author is greatly indebted to Professor J. C. Phillips of the University of Chicago for his special interest in the photoresponse data and several stimulating exchanges of correspondence.

Hughes Semiconductor Division,
Newport Beach, California
Eugene Loh†

References

1. Ehrenreich H., Phillip H. R. and Phillips J. C., *Phys. Rev. Letters* **8**, 59 (1962); Phillip H. R., and Taft E. A., *Phys. Rev.* **113**, 1002 (1959); **120**, 37 (1960).
2. Smith R. A., *Semiconductors*, p. 311. University Press, Cambridge (1959).
3. Vavilov V. S., *J. Phys. Chem. Solids* **8**, 223 (1959).
4. Tauc J., *J. Phys. Chem. Solids* **8**, 219 (1959).
5. Loh E., *Bull. Amer. phys. Soc.* **7**, 506 (1962).

---

* Vavilov(3) and Tauc(4) have measured the photoresponse of Ge and Si junctions in the same region of photon energy with no fine structure observed. The difference between the results of these authors and the present one, is probably due to the sensitivity in the detection.

† Present Address: Hughes Research Laboratories
Malibu, Calif., U.S.A.

Band structure effects in photoconductivity of semiconductors

(*Received* 24 *September* 1962)

SEVERAL empirical theories have been advanced(1,2) to describe the conductivity of semiconductors in the presence of electric fields strong enough to produce carriers with kinetic energies several eV above the band edge. These models treat the carriers as free and make the simplifying assumption that mean free paths for phonon emission and pair production are energy-independent. On the other hand, the previous Letter reports marked structure in the spectral photoresponse in the visible and ultraviolet, where the carriers that are produced have kinetic energies of order several eV. Here we show that this structure can be interpreted as a non-equilibrium effect by using the same band structure used to explain reflectance data.(3, 4)

We assume that after the photon has produced the initial electron-hole pair, the hole diffuses to the top of the valence band $\Gamma_{25'}$. Because of the low mobilities at the top of the valence band, the holes contribute a small current independent of the initial photon. The high-mobility carriers are all assumed to be electrons which have diffused to the L_1 and Δ_1 (near X_1) band edges. Broadly speaking, whenever $h\nu$ may take an electron from the valence band to near one of these high mobility edges, a peak in the photoresponse results. (When the carrier is produced near the band edge, it emits optical phonons ($\sim 0{\cdot}05$ eV) every 50 Å until it diffuses to the band edge, where it has high mobility. The small momentum losses at the end of the diffusion path will be produced partly by impurity scattering.) Large peaks can be obtained if the lifetime for recombination in the junction layer is sufficiently short that not all carriers thermalize to the lowest band edge before recombining. The amplitude of the variations in the photoresponse is governed by the degree of incomplete thermalization. With complete thermalization, little variation in the photoresponse should be observed when the absorption length ($\sim 10^{-6}$ cm in this spectral region) is much smaller than the junction depth ($\sim 10^{-4}$ cm). From the data of the preceding Letter, it appears that thermalization to L_1, Δ_1, and $\Gamma_{2'}$ band edges is rapid, but that complete thermalization before recombination from the higher band edges to the lowest band edges is not achieved. The higher band edges up to 1 eV above the lowest band edge appear to be thermally metastable.

These assumptions are sufficient to explain most of the structure reported in the preceding Letter. They do not explain the most striking feature of the data, however, which is the great difference in photoresponse of Ge, Si, and GaAs near the largest reflectance peak (about 4·5 eV). To understand this one must analyze recombination processes in more detail.

Indirect recombination is in general about 100 times slower than direct recombination, which takes place from $\Gamma_{2'}$ to $\Gamma_{25'}$. When intervalley scattering from some other edge in the conduction band to $\Gamma_{2'}$ is strong, the mobility of that edge will be greatly reduced. For this reason we sketch in Fig. 1 the band structures of Ge and Si(3, 4, 5) and GaAs.(3, 6, 7) Using these we may explain the structure in the photoresponse data as follows.

(1) In GaAs, there is a peak at 2·7 eV corresponding to the production of L_1 carriers from the transition $L_{3'} \rightarrow L_1$. This is followed by a dip at 3.0 eV because the Λ_1 carriers tend to diffuse to $\Gamma_{2'}$ where they recombine directly. The increasing yield up to the peak at 4·3 eV is due to the production of electrons near X_1. These decay slowly to the $\Gamma_{2'}$ edge, which is 0·35 eV ($\approx 13T$ at room temperature) lower in energy. Beyond 4·3 eV, absorption takes place for k nearer the (110) direction.(4) Carriers near (110) may scatter into $\Gamma_{2'}$ as well as X_1, which reduces the current.

(2) In Si only the L_1 and X_1 band edges are important. The X_1 carriers give a high current because only indirect recombination to the $\Gamma_{25'}$ holes is feasible. The narrow, high peak in the current at 3·2 eV corresponds to the $L_{3'} \rightarrow L_1$ threshold in the reflectance.(4) The sharp dip at 3·4 eV corresponds to the $\Gamma_{25'} \rightarrow \Gamma_{15}$ peak in the reflectance.(4) Because of direct recombination Γ_{15} carriers contribute little current. Note that just as for L_1 and X_1 in GaAs, the L_1 carriers are metastable against decay. The current rises again as we approach the $X_4 \rightarrow X_1$ edge in the reflectance. In this case, however, the (110) carriers which are produced beyond the X_1 reflectance edge cannot decay to $\Gamma_{2'}$, but only to X_1. Therefore, the photocurrent continues to rise up to 5 eV.

(3) Ge is the most interesting case because of the near degeneracy of the three band edges: $\Gamma_{2'}$ and X_1 are about 0·15 eV higher than L_1. The L_1 carriers should have a long lifetime because they recombine only indirectly. We see a small hump in the current beginning about 1·9 eV, in agreement with the $L_{3'} \rightarrow L_1$ threshold.(4) On the other hand, X_1 carriers may have a very short lifetime because they can scatter with just one phonon to $\Gamma_{2'}$ and thence recombine directly. Thus as we approach the X_1 reflectance edge there is a striking drop in photoresponse, with minimum at 4·3 eV. This drop can be explained only by intervalley resonance scattering from X_1 to $\Gamma_{2'}$. Beyond 4·3 eV carriers are produced near (110) and near X_3, and these may diffuse to the (111) edge, so that the current rises to its previous level. It is interesting that the intervalley resonance gives a much stronger effect than the $L_{3'} \rightarrow L_1$ threshold at 1·9 eV.

In the vacuum u.v., above 5 eV, there is another peak in the reflectance associated with $L_{3'} \rightarrow L_3$ transitions.(3, 4, 5) This should give a peak in the photoresponse because L_3 carriers decay directly to the high-mobility L_1 band edges.

To give a complete quantitative analysis, a detailed knowledge of the rates of long- and short-wave length phonon emission during the thermalization process is required. Such knowledge could be obtained in principle from the results of Ref. 4. With this knowledge the thermalization process could be studied by the Monte Carlo method.

The salient feature of the thermalization process is the metastable higher band edges (e.g. in Si, L_1 is 0·75 eV above Δ_1). This may be due to the small volume of phase space near X_1. If we make the effective mass approximation with a density-of-states mass $m^+ = 0{\cdot}3\ m$, the isoenergetic surface near X_1 that the L_1 carriers may be scattered to, will be smaller than that at higher energies, where the free electron approximation is valid, by about 0·75 eV/20 eV $\simeq$ 0·04.

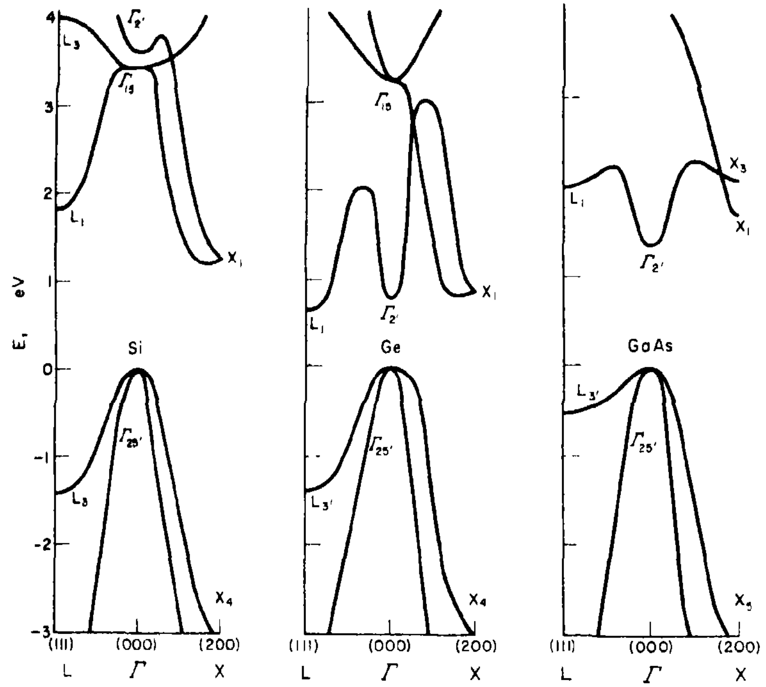

FIG. 1. A sketch of the energy bands of Si, Ge, and GaAs near the energy gap, according to experiments described in Refs. 3–7.

Because the structure in the preceding Letter is insensitive to junction depth, it appears that surface recombination may not play a decisive role. Depending on the surface preparation and geometry, it appears that qualitatively:

(1) The details of recombination (surface or volume) may not wash out band-structure effects.

(2) For current densities from 1 μA/cm^2 to 1 mA/cm^2 electron–electron scattering can be neglected.

Near the largest reflectance peak the absorption coefficient is as high as $2 \cdot 10^6$ cm^{-1}. Variations in photoresponse near this peak may provide a valuable *microscopic* probe of the effects of junction geometry and external fields on carrier distribution near the surfaces of *p–n* junctions.

Ordinarily one expects to measure intrinsic properties of a system by effects first-order in applied fields. If, as we have assumed, high photon flux can produce non-linear structure in the photoresponse associated with higher band edges, then the opposite situation obtains here. It would be desirable to have these effects studied independently to make certain that they are indeed intrinsic and not structure-sensitive.

Acknowledgements—One of us (J.C.P.) wishes to thank C. Herring, E. O. Kane, D. G. Thomas, and P. A. Wolff for critical discussions.

Hughes Semiconductor Division, EUGENE LOH*
Newport Beach, California

Department of Physics and J. C. PHILLIPS
Institute for the Study of Metals
University of Chicago
Illinois

References

1. WOLFF P. A., *Phys. Rev.* **95**, 1415 (1954).
2. SHOCKLEY W., *Suppl. Czech. J. Phys.* (Prague Conference), **11**, 81–121 (1961). Shockley emphasizes that his model is phenomenological and that a correct theory would include the band structure effects we discuss.
3. EHRENREICH H., PHILIPP H. and PHILLIPS J. C., *Phys. Rev. Letters* **8**, 59 (1962).
4. BRUST D., PHILLIPS J. C. and BASSANI F., *Phys. Rev. Letters* **9**, 94 (1962).
5. PHILLIPS J. C., *Phys. Rev.* **125**, 1931 (1962).
6. EHRENREICH H., *Phys. Rev.* **120**, 1951 (1960).
7. GREENAWAY D., *Phys. Rev. Letters* **9**, 97 (1962).

---

* Present Address: Hughes Research Laboratories
Malibu, Calif., U.S.A.

BOOK REVIEWS

Magnetostatic Principles in Ferromagnetism of Selected Topics in Solid State Physics. Vol. I. Series edited by E. P. Wohlfarth. William Fuller Brown Jr., North Holland, Amsterdam (1962). 202 pp.

Prospective readers should not be deterred by the title; the subject of magnetostatics is usually dealt with in such a dull fashion that it may come as a surprise to learn that it can be treated in a logical yet stimulating way. Using as his starting point dipole moments, rather than free-poles, the author develops the theory of domains, single domain particles, resonance and spin waves.

Throughout the book Professor Brown takes every opportunity to comment unfavourably upon much of the domain theory developed over the last thirty years, and which must be considered as "old fashioned" in the view of "modern" authors. He uses a method of criticism which is dearly loved by the great debaters; he ascribes to his opponents opinion which they do not hold, then attacks them for being so misguided as to hold them. The great heresy is the "childish faith in free poles" which he asserts is held by other authors. In fact the introduction of fictitious free poles to magnetostatic problems is a perfectly legitimate device, which Professor Brown himself uses "without shame", and there is no more reason to suggest a belief in free magnetic poles in the mind of the user than to suggest that Hans Andersen believed in fairies.

Again in a discussion of hysteresis curves the author writes, "The conventional *B-H* curve is, in any strict sense, a myth. However, for structurally homogeneous material in bulk it seems to be a sufficient empirical approximation under ordinary conditions, provided we measure *H* and *B* on a large scale and ignore the microscopic magnetization distribution". Except for the myth, this is a conventional old fashioned statement of the conventional old fashioned position.

It is rather difficult to know from this book what exactly Professor Brown wants in the way of a well developed domain theory. He considers, as many do, that Néel's treatment of domains is too sophisticated for the simple model to which it was applied; yet he looks with scepticism upon the use of a one dimensional calculation of the energy of the three dimensional domain wall. Professor Brown is hard to please; this is one reason why this book should be read by all who have an interest in ferromagnetism.

R. S. Tebble

Studies in Optics. A. A. Michelson, University of Chicago Press, 1927, republished in 1962 as Phoenix Science Series No. 514 paperback, 176 pp. Illustrated, $1.75.

How can one judge a "republishing" of a book originally issued in 1927—if the content and language are now partly obsolete? Had the book been of vast breadth and depth, many parts might yet be of value; but this book is narrow and shallow, having been written to interest young students. Had it dealt with Michelson's career systematically, it would be of permanent value as a biography; but it has little resemblance to a biography, despite the retrospective foreword by H. B. Lemon. Had it contained first class illustrations, the reader would feel some warmth for it even today: but the illustrations are mediocre and the captions non-existent.

The *coup de grâce* is the publisher's failure to issue adequate warning as to the book's age and partial obsolescence. The glossy, glamorous cover gives no hint that the book is anything other than brand new (it is 35 years old). Nor does the back cover, nor the title page. Michelson's preface bears no date. Even Lemon's foreword bears no date, though I deduce that it is about 27 years old at least.

The glossed-over obsolescence is certainly harmful. The obsolete language is likely to frustrate the student and the obsolete concepts are likely to lead him into dead-end paths. Had the publisher annotated the book, putting each chapter in proper perspective, the harm would be less. But there are no notes to the individual chapters, and the reader is exposed to the full force of several authoritative statements that, today, are grossly misleading. On the very first page, for example, he finds the statement that, as regards "... the phenomena of light ... the undulatory theory satisfies all requirements without the necessity of accessory hypothesis ..." Does this mean that MICHELSON—and LEMON—are convinced that the photon theory of light is superfluous?

MICHELSON's contributions were enormous. The present book—when new in 1927—was undoubtedly a valuable one. But to whom is it valuable now? An old book in new covers can be as dangerous as an old egg in a new omelet.

Cambridge Electron Accelerator,
Harvard University,
Cambridge, Mass.

WILLIAM SHURCLIFF

Superconductivity, Methuen's Monographs on Physical Subjects. ERNEST A. LYNTON. Methuen, London (1962). pp. 174. 21*s*.

DURING the past fifteen years liquid helium has become widely available. This technology, coupled with a growing commercial interest in solid state physics, has led to a tremendous upsurge in studies of the superconducting state, but the results are scattered widely through the periodical literature. This little book by E. A. LYNTON can be of major assistance in getting a view of the field as it currently stands. It can be of great help to one undertaking to make a first acquaintance with the subject, as well as to one whose efforts to keep up with new developments have been handicapped by the rate at which such studies have been appearing.

It consists of a brief outline of superconductivity in all its aspects and an extensive list of references to the original papers. The outline itself is rarely sufficient to enable the reader to form his own judgment as to the validity of the conclusions presented, but the references to the original work provide an outline for as thorough a study as may be desired.

The book opens with an outline of the basic facts about ideal superconductors. This is followed by chapters on the phenomenological thermodynamic treatment of Gorter and Casimir and on the electrodynamic equations of the London brothers. The succeeding chapters deal with Pippard's concept of a coherence range and the Ginzberg–Landau description of the boundary between a superconducting and a normal phase in a single substance.

The analysis of thermal conductivity in the superconducting state is presented as leading to the idea of an energy gap, and the experimental studies of the energy gap and its effect on electrical properties are clearly indicated. The Bardeen–Cooper–Schrieffer microscopic theory of superconductivity is succinctly described, and the very recent work on quantized flux is cited as giving particular support to the idea of electron pairing as a major feature of the superconducting state. In this connection, however, the author gives less attention to the various papers of Blatt and of Schafroth than might have been expected.

After discussing the theory the book closes with a chapter on superconducting alloys and compounds and one on superconducting devices. This last chapter gives a brief account of the development of superconducting magnets and of the use of superconducting elements in high speed computers.

W. V. HOUSTON

NOTICES

Publication of Proceedings of Conference

THE Proceedings of the International Conference on the Physics of Semiconductors held at Exeter from 16 to 20 July, 1962 are to be published shortly by the Institute of Physics and The Physical Society. It is hoped that the book will be available by the end of the year.

The volume contains over 130 papers classified under the headings of: Transport (experimental and theoretical), Disordered semiconductors, Effective mass determination, Optical properties, Lattice vibrations, Band theory, Magnetic properties, Materials, Surface effects and Recombination. The main points which arose during discussion are also included.

The price of the book is 10 guineas, and the distributors are Chapman and Hall Ltd., 37 Essex Street, London, W.C.2. The book may be ordered through any bookseller.

International Conference on Lattice Dynamics

AN INTERNATIONAL CONFERENCE on Lattice Dynamics will be held at the Technical University in Copenhagen, Denmark on August 5–9, 1963.

The Conference is sponsored by the International Union of Pure and Applied Physics, NORDITA, the Danish Physical Society, the U.S. National Science Foundation and the U.S. Office of Naval Research. It will be concerned with the following major topics: dispersion (frequency vs. wavelength) curves; anharmonicity; elastic properties; dielectric properties; vibrations in lattices with impurities and imperfections and in disordered lattices; surface vibrations and dynamical models and their limitations. Emphasis will be placed on those experimental and theoretical contributions which lead to a better understanding of the interactions between atoms in solids and their role in lattice dynamics.

The program is expected to consist of approximately 8 invited papers and 24 contributed papers. They will be divided among five morning and four afternoon sessions. In order to achieve a program of maximum interest and value, the Program Committee consisting of Dr. W. Cochran, England, Chairman; Professor E. Burstein, U.S.A.; Professor G. Leibfried, Germany; Dr. S. Lundquist, Sweden; Professor J. P. Mathieu, France and Professor K. B. Tolpygo, U.S.S.R., will make a careful selection among contributed papers.

The deadline for submission of abstracts of contributed papers is March 31, 1963. Six copies of the abstract, limited to no more than 200 words, should be sent to the Conference Secretary, Dr. Stig Lundquist, Department of Mathematical Physics, Chalmers University of Technology, Göteborg, Sweden. Requests for further information concerning the meeting should be addressed to the Secretary of the Conference.

The Conference Proceedings will be published approximately five months after the Conference as a special issue of *The Journal of The Physics and Chemistry of Solids* (Pergamon Press, Ltd.).

ERRATUM

Rotational properties of paramagnetic resonance spectra of non-cubic crystals, by M. SACHS: *J. Phys. Chem. Solids* **15**, 291–305 (1960).

1. In the entries under the column in Table 1 that is headed $U_2(n)$,* the factor $\lambda+2\mu/n$ should be replaced by $\lambda+(2\mu/n)+\mu$.
2. In equations (49) and (50) replace $\mu = 12m$ with $\mu = 6m$.

J. Phys. Chem. Solids Pergamon Press 1963. Vol. 24, pp. 501–506. Printed in Great Britain.

THE THERMOELECTRIC POWER IN CHROMIUM AND VANADIUM*

A. R. MACKINTOSH and L. SILL

Institute for Atomic Research and Department of Physics,
Iowa State University, Ames, Iowa

(*Received* 18 *December* 1962)

Abstract—The thermoelectric power in pure chromium and vanadium has been measured between 4·2 and 340°K and found to be positive in both metals over the whole temperature range. Maxima in the curves of thermopower against temperature at low temperatures are interpreted in terms of a phonon drag component. An anomaly in the results for both monocrystalline and polycrystalline chromium at the Néel temperature is interpreted in terms of the LIDIARD–OVERHAUSER model of conduction electron antiferromagnetism. Hysteresis in the measurements on chromium over the whole temperature range is attributed to the effect of antiferromagnetic domains. An anomaly in the thermopower of vanadium at approximately 217°K is attributed either to a transition to an antiferromagnetic state or to a structural phase transition, possibly involving ordering of impurities. Experiments for distinguishing between these possibilities are suggested.

INTRODUCTION

CONSIDERABLE interest has been evinced recently in the exact nature of the antiferromagnetic phase of chromium and in the possibility of the existence of such a phase in vanadium. The transition to the ordered state in chromium manifests itself through a variety of physical properties,(1–5) and the nature of the magnetic ordering has been explored using neutron diffraction techniques.(6–10) OVERHAUSER(11) has proposed that the antiferromagnetic phase is characterized by the existence of a static spin density wave in which the conduction electron spin density varies sinusoidally through the metal. He has shown that the experimental data can be understood on the basis of three spin density waves, with their wave vectors in the [100] directions. The observation by various workers of small anomalies in various properties of vanadium(12–15) has raised the possibility that a phase with a small amplitude spin density wave might exist in it, and possibly also in other metals.

The thermoelectric power in a metal is determined by the equation

$$S = \frac{\pi^2}{3}\frac{k^2T}{e}\left[\frac{\partial \log \bar{l}}{\partial \epsilon}+\frac{\partial \log \Sigma}{\partial \epsilon}\right]_{\epsilon_F} \tag{1}$$

where $\bar{l}$ is the mean free path of electrons on a Fermi surface of area Σ, and the derivatives are evaluated at the Fermi surface. It thus provides an excellent tool for the study of small changes in the state of metals, since it is extremely sensitive both to changes in the electronic structure and to the mechanisms which scatter the electrons. The experiments described in this paper were undertaken primarily in order to elucidate further the nature of the magnetic transition in chromium and to gather more evidence about the possibility of a phase transformation in vanadium.

THE EXPERIMENTAL PROCEDURE

The experimental procedure used was basically the same as that described by BORN *et al.*(16) A temperature difference of about 2°K was maintaind across the specimens by means of a heater soldered to one end, and the mean sample temperature varied by using a heat-leak chamber. The temperature at each end of the sample and its mean

---

* Contribution No. 1249. Work was performed in the Ames Laboratory of the U.S. Atomic Energy Commission.

temperature were measured with copper–constantan thermocouples. The thermoelectric voltage between the specimen and copper leads was measured with a thermofree Rubicon microvolt potentiometer and the absolute thermoelectric power of the specimen determined by standardizing with a piece of pure lead, whose absolute thermopower is known.(17)

The relative accuracy of the measurement is estimated to be within ± 0·05 μV/°K for the thermoelectric power and within ± 0·05°K for the temperature. The systematic errors are more difficult to evaluate, but above 20°K the absolute accuracy of the thermoelectric power measurements is estimated to be within ± 0·1 μV/°K, and that of the temperature to be within ± 0·5°K. Below 20°K the results are somewhat less precise because of the difficulty of establishing equilibrium and the lack of reproducibility of the thermocouples. In addition, non-reproducible results were initially obtained for vanadium above 20°K on account of adsorption of helium exchange gas. In order to overcome this difficulty the temperature range was covered in three stages; in order, 70 to 340°K using liquid nitrogen in the bath, 20 to 90°K using liquid hydrogen and finally 4·2 to 30°K using liquid helium.

Measurements were made on a single crystal and a polycrystal of chromium and a polycrystalline vanadium sample. In each case the specimen was in the form of a rod, approximately 15 mm by 2 mm. The ratio of the resistivity at 300°K to that at 4·2°K was about 150 for the chromium samples and the orientation of the axis of the single crystal was at 10° from the [111] direction in a (110) plane. The resistivity ratio of the vanadium was considerably lower, about 30, probably due to the presence of a considerable quantity of adsorbed gases.

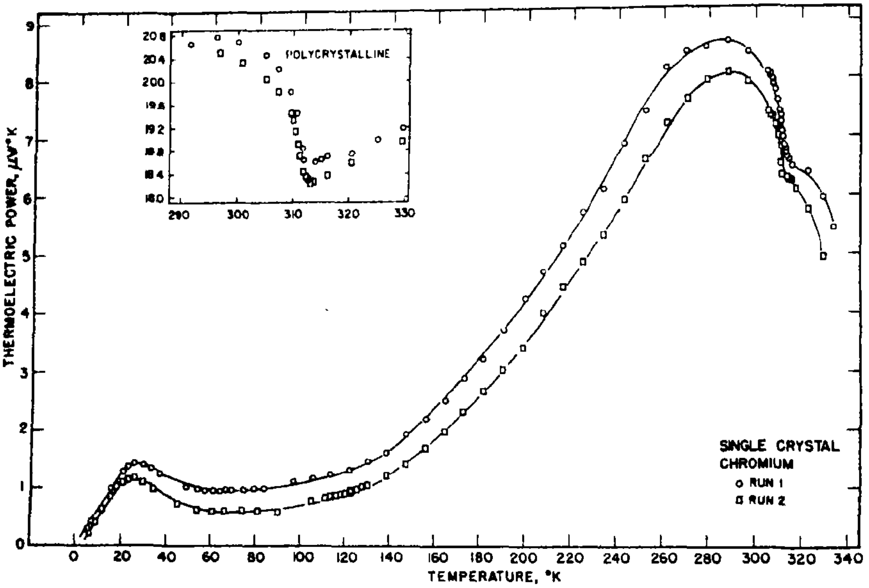

FIG. 1 The thermoelectric power of chromium as a function of temperature.

THE RESULTS

The observed temperature variation of the thermoelectric powers of chromium and vanadium are shown in Figs. 1 and 2. The thermopower of both metals was positive over the whole temperature range.

The measurements on both the single crystal and the polycrystal of chromium revealed an abrupt change in the slope of the curve of thermopower against temperature at about 311°K, the antiferromagnetic Néel temperature. Immediately below this temperature there is a large hump in the curve, and the single crystal results show another, smaller one, with a maximum at about 25°K. No clear evidence for any anomaly was observed in the temperature range near 120°K, where a further magnetic transition is known to take place,(7) even though a careful search was made in this region in run 2.

Considerable hysteresis was observed between runs over the whole range from 4·2°K to 340°K, both below and immediately above the Néel temperature. In addition, the thermoelectric power was observed to decrease with temperature immediately above the Néel temperature in the single crystal while in the polycrystal it increases with temperature. These effects are thought to be genuine, and not due to the experimental technique since measurements on non-magnetic metals, both before and after these experiments using essentially the same technique, yielded completely reproducible results. Similar hysteresis near the Néel temperature in measurements of the electrical resistivity has been reported by ARAJS *et al.*(18)

A small but reproducible anomaly, consisting of an abrupt change in slope of the thermopower curve, was observed in vanadium at about 217°K when the temperature was increased, but not when the temperature was decreased through this value. In addition, a reproducible hysteresis was observed in this region. At low temperature, a rather distinct hump was observed, with a maximum at about 75°K, and the thermoelectric power went abruptly to zero at about 5°K, the superconducting transition temperature.

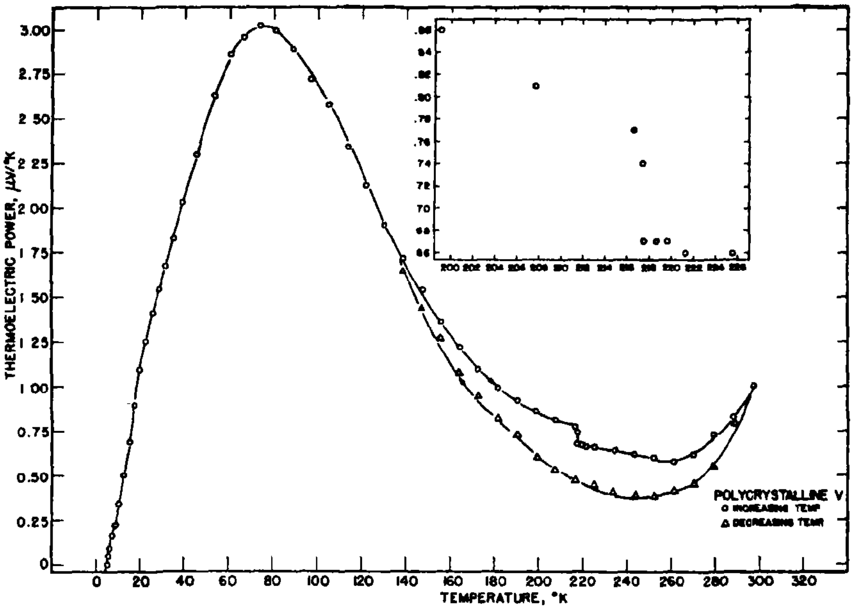

FIG. 2. The thermoelectric power of vanadium as a function of temperature.

DISCUSSION

The thermoelectric powers of both chromium and vanadium are positive over the whole temperature range studied and this can be interpreted, according to equation (1), as indicating that the energy surfaces just above the Fermi level have a smaller area than the Fermi surface itself, since $\partial \bar{l}/\partial \epsilon$ is usually positive. This implies that the Fermi surfaces in these metals are predominantly hole-like. In view of the well known difficulty of interpreting the sign of the thermoelectric power,(19) however, this conclusion should be treated with caution.

The low temperature humps in the thermoelectric powers of both chromium and vanadium can probably be ascribed to phonon-drag. In chromium the humps are not sufficiently distinct to allow a detailed analysis, but the low temperature data for vanadium, excluding the first two points, which, as determined separately by resistivity measurements, are affected by the superconducting transition, give a good fit to the formula

$$S = aT+bT^3 \qquad (2)$$

where the two terms represent, respectively, the diffusion and phonon-drag contributions. The values of the coefficients are

$$a = 6{\cdot}5\times 10^{-3}\,\mu\text{V deg}^{-2}$$

$$b = 2{\cdot}4\times 10^{-4}\,\mu\text{V deg}^{-4}$$

These can be compared with the values of $-9{\cdot}8\times 10^{-3}\,\mu$V deg^{-2} and $-3{\cdot}5\times 10^{-4}\,\mu$V deg^{-4}, respectively, deduced by GOLD and PEARSON(20) for pure lead from the results of CHRISTIAN *et al.*(21)

LIDIARD(22) first suggested that the antiferromagnetism of chromium is associated with the conduction electrons and showed that the small anomalies in the specific heat and magnetic susceptibility can be understood in this way. OVERHAUSER(11) developed this idea and proposed that the antiferromagnetic phase in chromium is described by three static spin density waves which have wave vectors along the [100] directions and are transversely polarized between the Néel temperature and about 120°K and longitudinally polarized below 120°K. He has shown that this model can account satisfactorily for the change in the physical properties associated with the magnetic transition. The onset of a spin density wave state can also explain the behavior of the thermoelectric power near the magnetic transition. The change in slope of the curve and the rapid increase in magnitude just below the transition is probably caused by the appearance of extra planes of energy discontinuity in the Brillouin zone structure due to the magnetic ordering, together with a rapid variation of magnetic disorder scattering. This is analogous to the behavior of the transport properties of the rare-earth metals near magnetic ordering transitions, which has been discussed by one of us.(23) In the case of the rare earths, however, a localized moment is present on the ions above the Néel temperature, whereas the neutron diffraction results of WILKINSON *et al.*(24) and the observation of a nuclear magnetic resonance by BARNES and GRAHAM(25) strongly indicate that no localized moment is present on the chromium ions above the Néel temperature. It is conceivable that the transition is one in which the metal goes from a state with no localized moment to one in which localized moments are present and are ordered. This would happen, for instance, if the free energy curve for the non-localized state cut that for the state with localized moments below the hypothetical ordering temperature of the latter. In this case, however, a sudden change in the electronic structure would be expected and consequently a discontinuity in the thermoelectric power, which is not observed. The amplitude of the nuclear magnetic resonance, which goes continuously to zero at the transition,(25) and the small specific heat anomaly(4) also provide evidence against this possibility. It seems, therefore, that the antiferromagnetism of chromium must be associated with the conduction electrons and that it is adequately represented by a spin density wave model.

No evidence for the spin-flip transition at lower temperatures was detected in this work, but this transition does not lead to any new periodicities in the lattice, so the changes in electronic structure and scattering which it causes are probably relatively minor. The large amount of magnetic hysteresis observed both below and above the Néel temperature might tentatively be attributed to antiferromagnetic domain structure. A domain wall in a single crystal is presumably a region over which the phase of the spin density wave varies abruptly. Similar effects in the resistivity of pure chromium have been observed by ARAJS *et al.*(18) near the Néel point and magnetomechanical damping experiments have been interpreted on the same basis by DE MORTON.(26) The fact that the hysteresis persists above the transition shows that there is a considerable amount of residual short range ordering in the paramagnetic phase. The persistence of order above the Néel temperature was also observed in the neutron diffraction experiments of BACON,(9) although the effect was much greater in a polycrystalline sample than in a single crystal.

The small but distinct and reproducible anomaly in the thermoelectric power of vanadium at about 217°K is also suggestive of some kind of phase change. Small anomalies in the electrical resistivity in this region have been observed by LOOMIS and CARLSON(12) and by others. BURGER and TAYLOR(13) have observed a very small change in the magnetic susceptibility. LOOMIS and CARLSON(12) and BOLEF, DE KLERK and BRANDT(15) have reported anomalies in the elastic constants and thermal expansion coefficients at temperatures which are extremely sensitive to the impurity content of the vanadium. The two most likely explanations for these phenomena appear to be either that there is a transition to a very weakly antiferromagnetic phase or that there is a structural phase change, possibly involving ordering of impurities. In either case the non-appearance of the anomaly when the sample is cooled through the transition is probably due to local supercooling in the polycrystalline sample. A similar effect has been observed at the ferroelectric transition of $SrTiO_3$ by KROGSTAD and MOSS.(27)

LOOMIS and CARLSON(12) have shown that a brittle-ductile transition occurs in vanadium at about 200°K. They conclude that this transition is due to the interaction of dislocations with minute amounts of impurity and suggest that it may be accentuated by the ordering of impurities. They cite as evidence for this conclusion the internal friction peak at around 200°K and the change in the slope of the lattice parameter vs. temperature curve in crystal bar vanadium at about the same temperature.(12) One would expect that such a transformation would have a considerable effect on the elastic moduli, but it is not so clear that it should affect the transport properties. If, as is likely, however, it alters the lattice vibration spectrum, it will affect the electron-lattice scattering probability and hence the transport properties, in addition to any possible effect on the electronic structure. In particular the thermoelectric power, which is very sensitive to the electronic relaxation time, might be appreciably affected.

If, alternatively, there is a small amplitude spin density wave in vanadium at low temperatures, all of the anomalies can readily be explained in terms of the modification of the electronic structure which this entails. This mechanism would also account for the small anomaly in the magnetic susceptibility.(13) On the other hand, BARNES and GRAHAM(25) observed only a very small change in the KNIGHT shift of the V^{51} resonance in pure vanadium on cooling to liquid nitrogen temperature through the region of the anomalies, and this contrasts strongly with the abrupt vanishing of the Cr^{53} resonance at the Néel point in pure chromium. To make this result compatible with the occurrence of a magnetic transition in vanadium, it appears necessary to assume that the electrons participating in the antiferromagnetic ordering have no S-character so that they do not penetrate the nucleus, and this seems rather unlikely. If vanadium is antiferromagnetic then there is particular interest in the fact that it is superconducting also. Because of the small number of electrons participating in the magnetic ordering it is in principle energetically possible for a metal to undergo successively transitions to an antiferromagnetic state and, at some lower temperature, to a superconducting state.

There does not yet appear to be sufficient evidence to distinguish definitely between the hypotheses of a structural or a magnetic transition, although the experiments of Barnes and Graham appear to favor the former. It is, of course, possible that both occur and that they are related. Further experimental data therefore seem to be required to settle this point. A careful neutron diffraction study at low temperatures might reveal the presence of magnetic ordering, although failure to discover magnetic reflections need not imply its absence.(11) It would be interesting to determine whether there is any magnetic field dependence of the transport properties near the anomaly, as would be expected if it were magnetic in origin. Perhaps the most valuable effort, however, would be directed towards the preparation of purer vanadium crystals. Many workers have observed that the temperature of the anomalies is very dependent on impurity concentration. In particular LOOMIS and CARLSON(12) have shown that removing gaseous impurities lowers the transition temperature. It would be of great interest to determine whether this process can be continued indefinitely.

Acknowledgements—We are very grateful to Professor O. N. CARLSON for supplying the chromium and vanadium samples used in these experiments. Valuable discussions with R. G. BARNES, S. LEGVOLD, J. F. SMITH, A. V. GOLD and D. I. BOLEF are gratefully acknowledged.

REFERENCES

1. Pursey H., *J. Inst. Metals* **86,** 362 (1958).
2. de Vries G. and Rathenau G. W., *J. Phys. Chem. Solids* **2,** 339 (1957).
3. Collings E. W., Hedgcock F. T. and Siddiqui A., *Phil. Mag.* **6,** 155 (1961).
4. Beaumont R. H., Chihora H. and Morrison J. A., *Phil. Mag.* **5,** 188 (1960).
5. White G. K., *Austral. J. Phys.* **14,** 359 (1961).
6. Corliss L., Hastings J. and Weiss R., *Phys. Rev. Letters* **3,** 211 (1959).
7. Bykov V. N., Golovkin V. S., Ageev N. V., Levdik V. A. and Vinogradov S. J., *Dokl. akad. nauk. S.S.S.R.* **128,** 1153 (1959).
8. Wilkinson M. K., Wollan E. O. and Koehler W. C., *Bull. Amer. phys. Soc.* **5,** 456 (1960).
9. Bacon G. E., *Acta Cryst.* **14,** 823 (1961).
10. Shirane G. and Takei W. J., *J. phys. Soc. Japan* (to be published).
11. Overhauser A. W., *Phys. Rev.* **128,** 1437 (1962).
12. Loomis B. A. and Carlson O. N., *Reactive Metals* (Edited by Claugh W. R.) Vol. **2,** p. 227. Interscience, New York (1959).
13. Burger J. P. and Taylor M. A., *Phys. Rev. Letters* **6,** 185 (1961).
14. White G. K. and Woods S. B., *Phil. Trans. Roy. Soc.* **251,** 273 (1959).
15. Bolef D. I., de Klerk J. and Brandt G. B., *Bull. Amer. phys. Soc.* **7,** 236 (1962).
16. Born H. J., Legvold S. and Spedding F. H., *J. appl. Phys.* **32,** 2543 (1961).
17. Christian J. W., Jan J. P., Pearson W. B. and Templeton I. B., *Proc. Roy. Soc.* **A245,** 213 (1958).
18. Arajs S., Colvin R. V. and Marcinkowski M. J, *J. Less-Common Metals* **4,** 46 (1962).
19. MacDonald D. K. C., *Thermoelectricity*, p. 103. John Wiley, New York (1962).
20. Gold A. V. and Pearson W. B., *Canad. J. Phys.* **39,** 445 (1961).
21. Christian J. W., Jan J. P., Pearson W. B. an Templeton I. M., *Phil. Mag.* **5,** 765 (1960).
22. Lidiard A. B., *Proc. phys. Soc. Lond.* **A66,** 1188 (1953).
23. Mackintosh A. R., *Phys. Rev. Letters* **9,** 90 (1962).
24. Wilkinson M. K., Wollan E. O., Koehler W. C. and Cable J. W., *Phys. Rev.* **127,** 2080 (1962).
25. Barnes R. G. and Graham T. P., *Phys. Rev. Letters* **8,** 248 (1962).
26. de Morton M. E., *Phil. Mag.* **6,** 825 (1961).
27. Krogstad R. S. and Moss R. W., *Bull. Amer. phys. Soc.* **7,** 192 (1962).

J. Phys. Chem. Solids Pergamon Press 1963. Vol. 24, pp. 507–516. Printed in Great Britain.

THE UNIAXIAL MAGNETIC ANISOTROPY OF THE F.C.C. COBALT PRECIPITATE IN COPPER

C. W. BERGHOUT

Philips Research Laboratories, N.V. Philips' Gloeilampenfabrieken,
Eindhoven, Netherlands

(*Received* 17 *September* 1962)

Abstract—An experimental investigation of magnetic annealing in single crystals of a copper 2·6 wt per cent cobalt alloy yielded the following results.

(a) During magnetic annealing the crystals acquire in addition to the cubic crystal anisotropy of the cobalt precipitate a uniaxial anisotropy in that cube direction which makes the smallest angle with the field.
(b) As a function of particle size the uniaxial anisotropy exhibits a sharp maximum.
(c) The experimental value of the anisotropy constant is a factor of ten higher than the value calculated on the basis of existing hypotheses.

The existing hypotheses which assume an ellipsoidal change of shape by the spherical particles of cobalt precipitate under the influence of the magnetostatic energy, are also in conflict with points (a) and (b). Moreover, since the maximum occurs in a stage where the particles undergo a transition from a coherent to a non-coherent state an explanation based on the elastic strains present in the precipitate particles appears to be more plausible.

INTRODUCTION

As has been shown by several authors,(1, 2) copper alloys containing a few per cent of cobalt exhibit uniaxial anisotropy after magnetic annealing in the two-phase region. It was found that this anisotropy occurs in a stage where all cobalt has already precipitated in the form of very small spheres (10^{-18}–10^{-16} cm^3). It is commonly assumed that the anisotropy is due to a shape anisotropy of the precipitated cobalt particles. This shape anisotropy is due to the magnetostatic energy, which tries to make the particles as elongated as possible. This tendency is opposed by the surface free energy. Because the rate of growth of the particles is small compared to the rate of attaining equilibrium of shape an expression due to Néel(3) may be used for the anisotropy constant

$$K_N = \frac{\pi^2 M_a^2 M^2 d}{5\gamma} \qquad (1)$$

In this expression M_a and M are the saturation magnetizations at the temperatures at which magnetic annealing takes place and at which the measurement is made: γ is the surface free energy and $d = \sqrt[3]{(6V/\pi)}$ is a kind of mean diameter.

Our original object was to measure, with the aid of (1), the surface free energy of a coherent phase boundary. Hillert(4) has recently published calculations on the development of modulated structures in precipitation systems. His method can also be used for the calculation of the surface free energy of coherent phase boundaries. An experimental verification of such calculations can be of interest in connection, for example, with the assumption made in the calculations that only the interaction between nearest neighbours is important. Another reason for subjecting copper–cobalt alloys to further investigation was that Mitui(1) some years ago showed that the anisotropy passes through a maximum during the growth of the extremely fine cobalt precipitate.

We believed that this might suggest a transition from a state of low to a state of high surface free energy.* In such a case one might think, for example, of the transition from the coherent to the non-coherent state.

Our experiments have shown, however, that the view on which equation (1) is based cannot be applied to magnetic annealing in copper–cobalt alloys. In this article we shall substantiate this statement, after which we shall consider what can be the real cause of uniaxial anisotropy in magnetically annealed copper–cobalt alloys.

PREPARATION OF THE SPECIMENS

As we did not wish to assume beforehand that the anisotropy produced by magnetic annealing is independent in magnitude and direction on the crystallographic orientation, we performed our measurements on single crystals. This has a further advantage, for, by also measuring the magnetic crystal anisotropy, one can see whether the crystallographic orientation of the cobalt in relation to the matrix has changed during the growth of the precipitate.

We had available for our experiments a rod-shaped single crystal measuring 5 mm in diameter and 60 mm in length. This crystal had been pulled by the well-known Czochralski method from a melt containing 2·5 wt. per cent Co. The cobalt content of the crystal was 2·65 wt per cent; the rod axis coincided to within a few degrees with a cube direction. The crystal was divided with a fine saw into a number of short cylindrical sections roughly 5 mm high. After a layer of a thickness of about 0·3 mm had been removed by etching, the sections were homogenized for 100 hr at 1050°C. This removed the segregations, formed during solidification, which could clearly be demonstrated before this treatment.

The relatively high stability of the single crystals proved to be a fortunate circumstance. After any given heat treatment, the crystals could again be homogenized without risk of recrystallization, and this made it possible to use the same crystals for different experiments. It was necessary, however, to exercise caution when quenching the crystals in the course of a heat treatment. This can considerably alter the orientation of the precipitate in relation to the matrix. Since this is no doubt due to the quenching strains, we observed the following three precautions during the heat treatments: (a) No specimen was cooled at a rate exceeding 10°C sec^{-1}; (b) the specimens were brought directly, without intermediate quenching, from the homogenizing temperature (T_h) to the required precipitation temperature (T_a); (c) the precipitation annealing of a specimen was always preceded by a homogenizing treatment (Fig. 1). A drawback of the relatively low cooling rate is the fact that appreciable quantities of cobalt may precipitate during the cooling process.

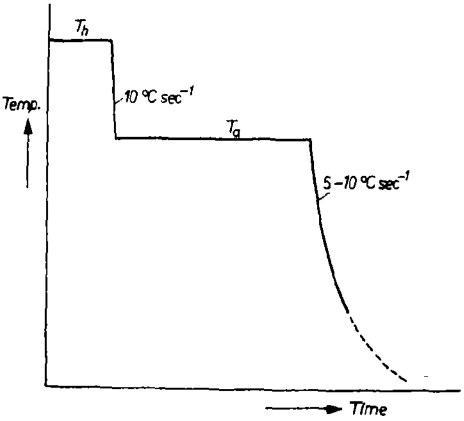

FIG. 1. Heat-treatment of the crystals.

Most anneals were carried out with the field parallel to the axis of the specimen because the specimen then could easily be oriented with respect to the field. The cube direction parallel to the axis of the specimen will henceforth be denoted by [001]. For anneals with a field in the [100] or the [111] directions, the precise orientation of the specimens was determined from the directions of preferred magnetization (⟨111⟩) which can be found when the specimen can rotate freely in a magnetic field. These orientations were determined with an accuracy of ± 5°.

---

* This view differs from that held by BECKER(2) and MITUI.(1) They believe that this maximum is related to the transition from magnetic single domain to multi-domain. Since Mitui himself, however, has shown that the maximum also occurs with annealing fields of 8000 Oe, where the cobalt particles are certainly saturated, this view does not seem to be tenable.

During the precipitation anneals the magnetic field (H_a) must be strong enough to saturate the spherical precipitate particles. Since the saturation magnetization can at the most be that of pure cobalt at the relevant temperature ($M_a \sim 1100$) a field strength of $(4\pi/3)\times 1100 = 4600$ Oe is always sufficient. The field strength (H_a) used in the experiments was 6500 Oe. All heat treatments were performed in an atmosphere of purified hydrogen.

MEASUREMENT OF THE MAGNETIC ANISOTROPY

We investigated the magnetic anisotropy of the crystals after a heat treatment by measuring, on a registrating torque balance,$^{(5)}$ the torque (T)

Table 1

No. of experiment†	Magnetic annealing		Plane of measurement	θ*	$2K_c/M$	$2K_a/M$
	T_a (hr at °C)	H_a (Oe)				
11	1 815	110	$(1\bar{1}0)$	58·9°	1255	206
21	1 740	110	$(1\bar{1}0)$	65·8	1650	740
31	1 780	001	$(1\bar{1}0)$	32·0	1520	1070
32	1 700	001	$(1\bar{1}0)$	43·7	1460	442
33	1 660	001	$(1\bar{1}0)$	48·1	1390	217
34	From 1000°C cooled with 100°C sec^{-1}	no field	$(1\bar{1}0$	54·6	1365	6
35	1 760	001	$(1\bar{1}0)$	25·7	1805	1450
36	1 800	001	$(1\bar{1}0)$	48·6	1170	196
37	From 1000°C cooled with 10°C sec^{-1}	110	$(1\bar{1}0)$	56·2	1330	112
38	8 820°C	001	$(1\bar{1}0)$	—	1500	161
41	15′ 740	001	—	44·2	—	(367)
42	30′ 740	001	—	41·0	—	(482)
43	1 740	001	—	34·0	—	(723)
44	2 740	001	—	27·0	—	(943)
45	4 740	001	—	32·1	—	(789)
46	8 740	001	$(1\bar{1}0)$	47·1	1390	228
47	15′ 740	001	$(1\bar{1}0)$	45·2	1300	331
48	1 740	001	$(1\bar{1}0)$	35·0	1375	714
49	8 740	001	$(1\bar{1}0)$	—	1360	308
51	1 780	110	$(1\bar{1}0)$	83	1810	1890
61	1 700	110	$(1\bar{1}0)$	61	1730	404
71	From 1000°C quenched in brine	no field	—	—	Non-magnetic	
81	From 1000°C cooled with 10° sec^{-1}	001	$(1\bar{1}0)$	51·6	1450	130
82	1 660	001	$(1\bar{1}0)$	47·7	1290	216
83	1 700	001	—	—	—	—
84a	1 740	111	$(1\bar{1}0)$	—	1565	160
84b			(001)	—	1370	138
85	1 700	110	(001)	—	1370	159
86	1 820	110	(001)	—	1330	40
87	1 760	010	(001)	—	1540	1230
88a	1 760	110	(001)	—	1485	360
88b			$(1\bar{1}0)$	—	1540	1192

* θ is the angle between the [001] direction and the nearest preferred direction of magnetization.

† The first figure in this column refers to the crystal, the second to the heat treatment.

exerted by the crystal as a function of angle during rotation of the magnetization in a particular plane. The latter will be found in Table 1 in the column headed "Plane of measurement". The magnetization is rotated with the aid of a magnetic field of at least 25,000 Oe.

When no magnetic field was applied during annealing only a cubic anisotropy is found. Magnetic annealing alters the orientation-dependence. It is found that the extra anisotropy is uniaxial with the preferred direction along that cube direction which makes the smallest angle with H_a (Fig. 2). Our results are described with sufficient accuracy by the sum of two energies namely the (cubic) magnetic crystal anisotropy energy

$$E_c = -K_c(\alpha_1^2\alpha_2^2 + \alpha_2^2\alpha_3^2 + \alpha_3^2\alpha_1^2) \tag{2}$$

and a uniaxial term,

$$E_a = -K_a\,\alpha_{1,2,3}^2 \tag{3}$$

$\alpha_{1,2,3}$ is the cosine of the angle between magnetization and that cube direction which, during magnetic annealing, makes the smallest angle with H_a. If H_a makes equal angles with two or three cube directions, the preferred directions of the cobalt particles are distributed randomly over these cube directions. We have for example with H_a in [110],

$$E_a = -\frac{K_a}{2}\alpha_1^2 - \frac{K_a}{2}\alpha_2^2 \tag{3a}$$

In Table 2 $E_c + E_a$ is presented for the cases given in Fig. 2 as a function of the most suitable variable. Note that no extra anisotropy is induced in experiment No. 84 (H_a in [111]).

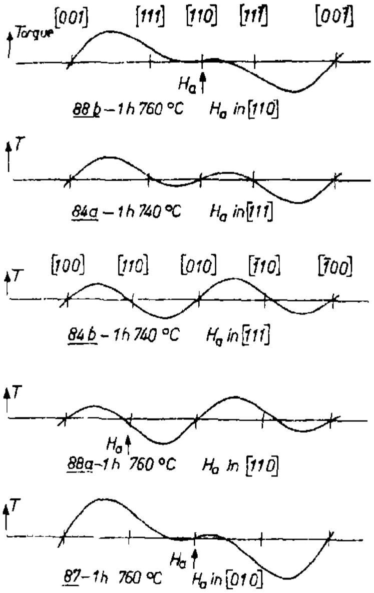

FIG. 2. Torque measurements after some characteristic magnetic anneals.

The constants $2K_c/M$ and $2K_a/M$, derived from our measurements, are given in Table 1. From the fairly constant value of K_c we conclude

Table 2

Annealing Field	Plane of measurement	Energy		Specimen
001	(1$\bar{1}$0)	$-K_c\,(\frac{1}{2}\alpha_3^2-\frac{3}{4}\alpha_3^4)-K_a\alpha_3^2$	(4)	
110	(1$\bar{1}$0)	$-K_c\,(\frac{1}{2}\alpha_3^2-\frac{3}{4}\alpha_3^4)+K_a/2\alpha_3^2$	(5)	88(b)
111	(1$\bar{1}$0)	$-K_c\,(\frac{1}{2}\alpha_3^2-\frac{3}{4}\alpha_3^4)$	(6)	84(a)
111	(001)	$-K_c\,(\alpha_1^2-\alpha_1^4)$	(7)	84(b)
110	(001)	$-K_c\,(\alpha_1^2-\alpha_1^4)$	(8)	88(a)
100	(001)	$-K_c\,(\alpha_1^2-\alpha_1^4)-K_a\alpha_1^2$	(9)	87

FIG. 6. Electron micrograph of specimen No. 51 (1 hr 780°C) after 10 sec etching in ferric chloride. The magnetic field during magnetic annealing was in the plane of the photograph.

FIG. 7. Electron micrograph of specimen No. 61 (1 hr 700 C) after 10 sec etching in ferric chloride. The magnetic field during magnetic annealing was in the plane of the photograph. The small-angle boundaries are only faintly visible.

that always in our experiments the cobalt precipitate had the f.c.c. structure with the same orientation as the matrix. This too is a justification for the use of formula (2). The average value of K_c ($1{\cdot}0\times10^6$ erg/cm^3) is somewhat higher than the value found by Anderson(6) (0·4–0·6 erg/cm^3) but agrees with the values found by Bean(7) $1{\cdot}17\times10^6$ erg/cm^3 and Rodbell(8) ($0{\cdot}9\times10^6$).

The values of K_c and K_a in Table 1 were calculated from the energy values obtained from the torque curves, after integration and adaptation to the formulae in Table 2. Since the specific moment M of the copper-saturated cobalt is not exactly known, we give the values of $2K/M$. These values are obtained from those of the anisotropy (h) and of the saturation moment (m_s) of the specimens, using the expression $2K/M = 2\,h/m_s$ (10). The torque measurements pertaining to experiments 84(a) and (b), 85, 86 and 88(a) do not, owing to small errors in the orientation of H_a, fulfil exactly the equations (6), (7) and (8) in Table 2. These measurements were therefore analyzed with the aid of equations (4), (5) and (9). It is then clear that the value found for K_a is small compared with that found for measurements where H_a is situated in one of the cube directions.

No torque curve was measured after the heat treatments 42 to 45. Assuming $2K_c/M = 1370$ Oe for these experiments, we calculated $2K_a/M$ from θ using the expression:

$$2K_a/M = (3\cos^2\theta - 1)\,K_c/M \qquad (11)$$

In experiments 42 and 44 to 48 we also measured the (002) reflection of the copper crystal using Co$K\alpha$ radiation. Fig. 3 shows the change in resolution of the $K\alpha$ doublet. When after 2 hr at 740°C K_a has a maximum (Fig. 3a) the resolution is at its worst. The (002) reflex of the cobalt precipitate is not visible until after 8 hr at 740°C.

MEASUREMENT OF PARTICLE DIAMETER

To determine the particle diameter in a given experiment, we used two calibration curves. In Fig. 4 the particle dia. is represented as a function of annealing temperature for an annealing time of 1 hr, and Fig. 5 gives the dia. as a function of annealing time at 740°C. The particle dia. could not be found from the calibration curve in experiments 37, 38 and 81. In those cases, therefore, separate measurements were necessary. As calibration points for the curves in Figs. 4 and 5 we used the specimens 11, 21, 47, 49, 51, 61, 82 and 83. For Nos. 11, 21, 49, 51 and 61, and also for the separate measurements of 38 ($d = 1030$ Å) use was made of electron micrographs of direct carbon replicas shadowed with platinum. Magnetic methods were used for determining the diameters in experiments 47, 81 ($d = 150$ Å), 82 and 83.

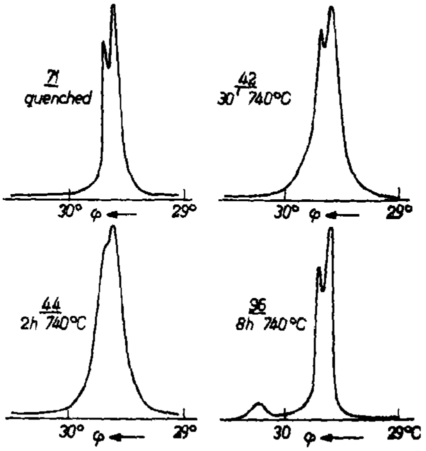

Fig. 3. Change of line-profile of the (002) reflection of CoK radiation during magnetic annealing at 740°C.

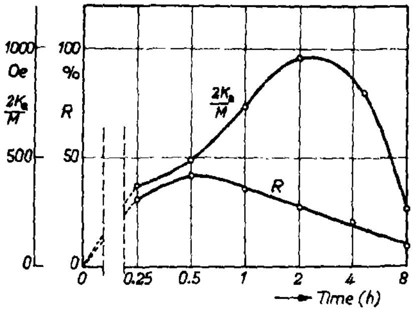

Fig. 3(a). Induced anisotropy and remanence ($R = m_R/m_s$) as a function of annealing time at 740°C.

Figures 6 and 7 show the surfaces of specimens 51 and 61 after etching for 10 sec in ferric chloride. These electron micrographs were not used for determining particle diameters because, owing to the etching, the cobalt particles appear to be larger than they are in reality. The diameters were determined using replicas taken directly after electrolytic polishing of the surface. The electron micrographs reproduced, however, are meant to show that the growth of the precipitate is influenced by the presence of small-angle grain boundaries only when the particles are relatively large. In the case of specimens 11 and 51 the small-angle grain boundaries are clearly visible, but not in specimens 21 and 61.

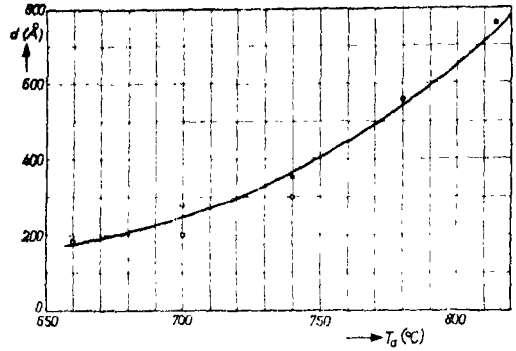

FIG. 4. Particle diameter of the cobalt-precipitate for a 1 hr anneal at the given temperature. Full circles from electron micrographs. Open circles from magnetic remanence.

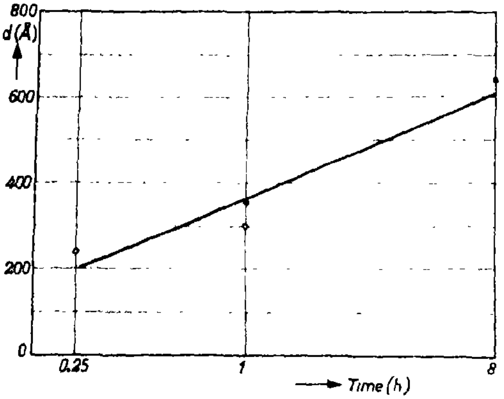

FIG. 5. Particle diameter as a function of time at 740 °C.

The magnetic method employed to determine the smallest particle-diameters consisted of measuring the remanence as a function of temperature.$^{(9)}$ The magnetizing field was oriented in the [001] direction. The curves given in Fig. 8 relate to a time of 10 sec between switching off the field and measuring the remanence. The remanence is given as a percentage of the maximum possible remanence ($m_s \cos\theta$). As appears from the relatively slight decrease of $m_R/(m_s \cos\theta)$ with temperature in Fig. 8, *there is a distribution of* particle sizes. However, since we are constantly concerned with average quantities in our calculations, we shall directly compute here too the average particle diameter. We assume for the purpose that the particles with average diameter have a relaxation time (τ) of 10 sec at the temperature where the remanence has dropped to half its original value.* The particle size then follows from the following formula:

$$\tau = \tau_0 \exp(W_j/kT) \tag{12}$$

where

$$W_j = V(K_c/12 + K_a/3 + K_a^2/3K_c) \tag{13}$$

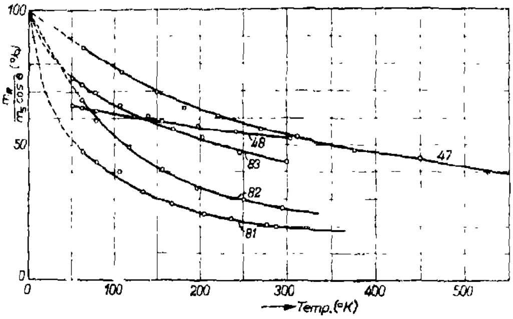

FIG. 8. Temperature dependence of the remanence.

Here τ is the relaxation time of a particle and V is the volume. The constant τ_0 was separately determined in an experiment in which, with the same specimen, the remanence was measured as a function of time at various temperatures. It was found that $\tau_0 = 1{\cdot}7 \times 10^{-10}$ sec.

Figure 8 also shows the temperature-dependence of the remanence for experiment 48. This curve cannot be treated in the manner described, since a certain percentage of the particles is too large to show magnetic single-domain behaviour and therefore no longer contributes to the remanence. From the extrapolation shown by the dotted curve in Fig. 8, it appears that this percentage is roughly 30 per cent. We can use this information for estimating the average particle size for experiment 48, as the diameter at which f.c.c. cobalt particles lose their single-domain properties can be computed from the saturation magnetization and the energy of a Bloch wall (σ_w)

---

* If $\cos\theta$ were identical for all cobalt particles, this assumption would imply averaging over the *volume*. However, since $\cos\theta$ in fact depends on the magnitude of the particles, this introduces an error. As a result, the diameter determination by this magnetic method is not more accurate than ± 30 per cent. The error in the measurement using electron micrographs is estimated, however, to be of the same order of magnitude.

$$d_{\text{crit}} = 1{\cdot}4\frac{\sigma_w}{M^2} = \frac{1{\cdot}4}{M^2}\sqrt{\left(\frac{2kT_cK_c}{a}\right)} \tag{14}$$

Assuming $M = 1300$ erg G^{-1}, $T_c = 1400$°K, $K_c = 10^6$ erg/cm^3 and $a = 2{\cdot}5\times10^{-8}$ cm, it then follows that 30 per cent of the particles have a volume greater than 19×10^{-18} cm^3. On the other hand, using (12) and (13), we can derive from Fig. 8 that 20 per cent of the particles in experiment 48 must be smaller than $7{\cdot}3\times10^{-18}$ cm^3. A reasonable estimate of the average volume in experiment 48 therefore seems to be 14×10^{-18} cm^3 ($d = 300$ Å).

DISCUSSION

In Fig. 9 K_a/K_c is plotted vs. diameter as read from Figs. 4 and 5. The values of K_a shown in Table 1 for experiments 84a and b, 85, 86 and 88a are not of course included in Fig. 9. For comparison, we have indicated in the same figure what the relation between K_a/K_c and d would be if the hypothesis underlying (1) were correct. For this purpose we have kept to the value of 1500 Oe for $2K_c/M$. It is evident from the figure that the experimental and theoretical results differ by a factor of 10. A second discrepancy is the absence of any linear relation between the experimental values of K_a and d predicted by (1). The third and most important difference between theory and experiment is the presence of a very pronounced dependence upon direction. This latter point in particular suggests that the anisotropy of the precipitate does not have a magnetic but an elastic cause. We can best illustrate this with the calculation underlying the theoretical curve in Fig. 9.

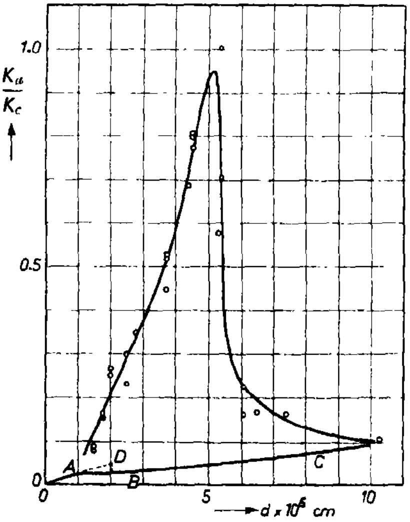

FIG. 9. The anisotropy induced by magnetic annealing as a function of the diameter of the cobalt particles. The values of K_a and K_c are taken directly from Table 1 but the values of the diameter are taken from the interpolated curves in Figs. 5 and 6.

The theoretical curve consists of three parts: O–A, A–B and B–C. In the part O–A a particle having a coherent boundary represents the most stable state. The free energy in this case consists of three terms, viz: the surface-free energy, the energy of the magnetic field, and an elastic term

$$F = \gamma_1 S + 2\mu V\delta^2\frac{1+\sigma}{1-\sigma} + 2\pi M_a^2 V N \tag{15}$$

Here γ_1 is the surface free energy, μ the torsion modulus, $\delta = (a_{\text{Cu}} - a_{\text{Co}})/a_{\text{Cu}}$ the misfit between the copper and cobalt lattices, σ is Poisson's ratio, $4\pi N$ is the demagnetizing factor and S the surface of the nearly spherical particles.

For coherent particles the elastic term is independent of shape.(10, 11) Since S and N, however, are both shape-dependent, slight ellipsoidal deformation occurs. Assuming that the relative difference ϵ between the long and short axes of the ellipsoid is small, we can approximate S and N with:

$$S = \pi d^2(1 + \tfrac{8}{45}\epsilon^2) \tag{16}$$

$$N = \tfrac{1}{3}(1 - \tfrac{4}{5}\epsilon) \tag{17}$$

At constant volume, equilibrium is reached where $\epsilon = \pi M_a^2 d/4\gamma_1$, which gives rise to the magnetic anisotropy given by (1).

If we wish to know the free energy as a function of particle size, we can disregard the magnetic term. The free energy then follows directly from (15):

$$F_1/V = 6\gamma_1/d + 2\mu\delta^2(1+\sigma)/(1-\sigma) \tag{18}$$

In the part *B–C*, ($d > d_D$) particles with an incoherent boundary represent the most stable situation. The elastic energy then ceases to be a volume energy because the stresses now become concentrated at the surface. The free energy of a fully non-coherent particle can therefore be calculated with a surface free energy $\gamma_2(>\gamma_1)$ and the elastic energy term equal to zero.

$$F = \gamma_2 S + 2\pi M_a^2 V N \tag{19}$$

From the equilibrium condition at constant volume we again calculate the anisotropy with $\gamma = \gamma_2$ as given by (1). Here too the magnetic term is small, and therefore the free energy as a function of d is given by

$$F_2/V = 6\gamma_2/d \tag{20}$$

The particle size above which the incoherent particles are stable is found from $F_1 = F_2$. We then find:

$$d_D = \frac{3(\gamma_2-\gamma_1)(1-\sigma)}{\mu\delta^2(1+\sigma)} \tag{21}$$

Figure 10 shows how F_1 and F_2 vary as a function of d. The transition from coherent to incoherent can, however, also take place more gradually than via *D*. As an example we assume that the surface of a particle can be partly incoherent and that the elastic energy is then equal to

$$E_{el} = 2\mu V\delta^2 \frac{1+\sigma}{1-\sigma}\left(\frac{S_c}{S}\right)^2 \tag{22}$$

(S_c is the coherent part of the surface). The free energy now becomes

$$F = \gamma_1 S_c + \gamma_2(S-S_c) + 2\mu V\delta^2 \frac{1+\sigma}{1-\sigma}\left(\frac{S_c}{S}\right)^2 + 2\pi M_a^2 V N \tag{23}$$

Apart from ϵ we now have S_c/S as an independent variable. In the same way as from (15) and (19), it then follows from (23) for $d \geqslant d_A$ that

$$K_a = \frac{\pi^2 M_a^2 M^2 d}{5\gamma_2\left(1-\dfrac{d_A}{d}\dfrac{(\gamma_2-\gamma_1)}{\gamma_2}\right)} \tag{24}$$

the particle diameter in *A* being given by

$$d_A = \frac{3(\gamma_2-\gamma_1)(1-\sigma)}{2\mu\delta^2(1+\sigma)} = \frac{d_D}{2} \tag{25}$$

Neglecting again the magnetic term the free energy is given by

$$\frac{F_3}{V} = \frac{6\gamma_2}{d} - \frac{9(\gamma_2-\gamma_1)^2(1-\sigma)}{2\mu\delta^2 d^2(1+\sigma)} \tag{26}$$

In Fig. 10 the curve of F_3 as a function of d is also represented. The following numerical values were adopted in the calculations:

μ = $0{\cdot}5 \times 10^{12}$ dyne/cm^2
σ = 1/3
M_a = 1100 erg G^{-1}
γ_2 = 520 erg/cm^2
γ_1 = 240 erg/cm^2
δ = 2·15 per cent

The value of δ is found by correcting the difference in lattice constants at room temperature (1·73 per cent) for the difference in the thermal expansion of copper and cobalt between 20 and 800°C. No value is known for γ_2. Since this surface free energy will not, however, differ much from that of the phase boundary f.c.c. Fe against Cu, the value of γ_2 has been taken from the latter.(12) We calculated the value of γ_1 by a method indicated by HILLERT(4) for computing the free energy

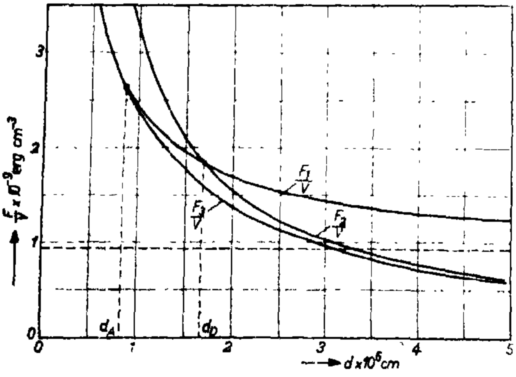

FIG. 10. Free energy of cobalt particles in copper as a function of the particle diameter. F_1—coherent particles; F_2—non-coherent particles; F_3—partly coherent particles.

of coherent phase boundaries. Our calculation is based on a boundary parallel to $\langle 100 \rangle$ planes. This is of little significance since the energy of a coherent phase boundary depends only very slightly,(13) if at all, on the orientation.(14) In calculating γ_1 we assume that, at the magnetic annealing temperatures, copper and cobalt have a mutual solubility of 1·22 at. per cent.

With the assumptions used no agreement between experiment and calculations can be reached. (Fig. 9). We neglected, however, one factor. It was shown by NABARRO(10) that the elastic energy of particles with a non-coherent boundary is no longer shape-independent. Therefore formula (22) has to include a function of ϵ. Because this function depends on ϵ in such a way that E_{el} decreases as the particles become more and more non-spherical, a strong shape anisotropy must develop from the moment the particles enter the transition stage ($d > d_A$). Owing to the anisotropy of the elastic constants, this shape anisotropy will exhibit a marked preference for certain crystallographic orientations.(15, 10) This view is in excellent agreement with our observations. One can also understand the absence of strong anisotropy at large particle sizes. In these large particles the misfit between the copper and cobalt lattices is eliminated by diffusion of extra vacancies and/or slip. Because of the absence of elastic strains these particles again acquire the spherical shape, apart from a small anisotropy in accordance with (1). In this way the maximum in K_a as a function of particle size can be understood qualitatively. A quantitative explanation will not be given. We can only predict the value of d where shape-anisotropy begins to develop (~ 001 Å). For a calculation of the dependence of K_a on d much extra information is needed since the elimination of the misfit between the cobalt and copper lattices will at first proceed at a rate comparable to or less than the growth rate of the particles.

It is perhaps necessary to give two refinements on this schematized view. In the first place the absence of an influence of the shape of the particles on the elastic energy of a coherent precipitate has only been proven for isotropic and identical elastic constants of precipitate and matrix. Therefore shape anisotropy can also be present in the coherent state. But as NABARRO(16) has shown the effect will certainly be smaller than in the non-coherent state. Secondly we want to stress that it is not necessary to rely on the occurrence of a transition state with a partly coherent boundary. Also, when the particles enter directly the non-coherent state (via D) strains will be present since the rate of elimination of the misfit is at first small compared with the growth rate of the particles. Recently PHILLIPS and LIVINGSTON(17) published a work on direct electron microscopy of copper cobalt alloys which indicated that particles of 350 Å diameter were still surrounded by coherency strains.

It is interesting that our experimental results are satisfactorily described only with particles having a rod-like anisotropy in one of the cube directions. When we calculate K_a from our experiments on the assumption that the particles have a preferential plane, we do not obtain the fairly smooth curve given in Fig. 9. The experiments with H_a along [110] then give K_a values four times lower than the values calculated from experiments with H_a along [100]. Therefore results of RODBELL(8, 18) obtained with ferromagnetic resonance do not agree with the experiments given in this paper. He found the particles to be plate-like on $\langle 100 \rangle$ planes. However, his conclusion is reached using second order effects, because no magnetic annealing was employed in his experiments.

A factor that should not be overlooked in these considerations is the magnetic anisotropy that may arise due to internal strains in the cobalt. In the coherent state this factor can never give rise to uniaxial anisotropy, since the strain field does not possess the necessary symmetry. Nor can this factor have any importance in the non-coherent state, for the internal strains have already become too small. But in the transitional state this magnetic anisotropy may well be significant. When the surface is partly coherent, strain fields are possible which no longer possess cubic symmetry. This can give rise to an anisotropy equal at maximum to

$$K_E = \tfrac{3}{2}\, E\lambda\delta_r$$

(E = Young's modulus, λ = magnetostriction.)

Assigning the values 2×10^{12} dyne/cm² to E and -10×10^{-6} to λ*) we obtain disregarding the sign

---

* From measurements of the magnetostriction of a copper 2·65 wt per cent cobalt alloy heated for 10 min at 740°C.

($\delta_r = 0{\cdot}017$): $2K_E/M = 730$ Oe. This in itself is not sufficient to explain the value found for K_a. Moreover strains will in general be smaller than $E\delta_r$. Only in the beginning of the transition stage A–B this effect may be of some importance.

In connection with the foregoing, some remarks should finally be made about Figs. 6 and 7. In the first place, it does not appear from these photographs that the precipitate particles possess uniaxial shape anisotropy. If shape anisotropy were present, however, the axial ratio of 1·27, which we calculated for Fig. 6 from the magnetic measurements, differs too little from unity to be made visible with the aid of replicas.

Another aspect of Figs. 6 and 7 that should be considered is the presence of depleted zones at the low-angle crystal boundaries in the specimens having particle sizes greater than 500 Å. This phenomenon too can be regarded as an indication that particles enter the fully incoherent stage at about 500 Å. The slip and the diffusion of extra vacancies, which are necessary in this stage, occur easily at a small-angle crystal boundary. As a result, particles on the boundary reach equilibrium sooner and are thus in the better position for further growth. Their faster growth takes place, however, at the expense of particles in their immediate vicinity.

Acknowledgements—The author would like to thank Mr. H. J. Feil for preparing the electron micrographs and Mr. Th. Thijssens for performing the torque measurements.

REFERENCES

1. Mitui T., *J. phys. Soc. Japan* **13**, 549 (1958).
2. Becker J. J., *Trans. Amer. Inst. min. (metall.) Engrs.* **212**, 130 (1958).
3. Néel L., *C.R. Acad. Sci., Paris* **225**, 109 (1947).
4. Hillert M., *Acta Met.* **9**, 525 (1961).
5. Enz U., to be published in *Philips Tech. Rev.*
6. Anderson J. C., *Proc. phys. Soc. Lond.* **75**, 33 (1960).
7. Bean C. P., Livingston J. D. and Rodbell D. S., *J. Phys. Radium* **20**, 298 (1959).
8. Rodbell D. S., *J. appl. Phys.* **29**, 311 (1958).
9. Weil L. and Gruner L., *C.R. Acad. Sci., Paris* **243**, 1629 (1956).
10. Nabarro F. R. N., *Proc. Roy. Soc.* **A175**, 519 (1940).
11. Eshelby J. D., *Proc. Roy. Soc.* **A241**, 376 (1957).
12. Van Vlack L. H., *Trans. Amer. Inst. min. (metall.) Engrs.* **191**, 251 (1951).
13. Meijering J. L., private communication.
14. Cahn J. W. and Hilliard J. E., *J. chem. Phys.* **31**, 688 (1958).
15. Bragg W. L., *Proc. phys. Soc. Lond.* **52**, 105 (1940).
16. Nabarro F. R. N., *Proc. phys. Soc. Lond.* **52**, 90 (1940).
17. Phillips V. A. and Livingston J. D., *Phil. Mag.* **7**, 969 (1962).
18. Bean C. P., Livingston J. D. and Rodbell D. S. *Acta Met.* **5**, 682 (1957).

J. Phys. Chem. Solids Pergamon Press 1963. Vol. 24, pp. 517–528. Printed in Great Britain.

ORDER–DISORDER TRANSFORMATION AND REVERSE THERMO-REMANENT MAGNETISM IN THE $FeTiO_3$–Fe_2O_3 SYSTEM

YOSHIKAZU ISHIKAWA*
The Institute for Solid State Physics, University of Tokyo
and
YASUHIKO SYONO
Geophysical Institute, University of Tokyo, Japan

(*Received* 19 *July* 1962; *revised* 23 *November* 1962)

Abstract—The order–disorder transformation and the reverse thermo-remanent magnetization (reverse T.R.M.) have been investigated in detail in synthesized solid solutions of xFeTiO$_3$–(1 $-x$) Fe$_2$O$_3$ with x around 0·5. It has been confirmed that the reverse T.R.M. is closely related to the order–disorder transformation which exists in this system; the reverse T.R.M. is observed only in a state of metastable equilibrium, and not in specimens either completely ordered or completely disordered. The reverse T.R.M. is found to be the result of antiparallel superexchange interaction between the magnetic moments of the ordered phase and the moments of an Fe-rich metastable phase which is created around the ordered structure in the process of the development of order. The detailed kinetic process of the development of order in this system has also been elucidated. The origin of the metastable phase has been investigated in detail and a model which can consistently explain the experimental results on the reverse T.R.M. is presented.

1. INTRODUCTION

REVERSE thermo-remanent magnetism (reverse T.R.M.) is the phenomenon whereby a specimen is cooled through the Curie point in a magnetic field and the remanent magnetization is in a direction opposite to that of the field originally applied. This self-reversal phenomenon of remanent magnetization was first discovered by the NAGATA group(1) in certain minerals extracted from Haruna rocks and it attracted great attention throughout the world in the fields of rock magnetism and paleomagnetism. Until this time, the existence of rocks which have the natural remanent magnetization direction nearly in the opposite direction to the earth's present magnetic field had been believed uniquely to be due to the reversal of the geomagnetic field in the past.

The most extensive investigation of this phenomenon has been carried out by UYEDA.(2) It has been found that the reverse T.R.M. is an intrinsic property of the solid solution of FeTiO$_3$ and Fe$_2$O$_3$ (xFeTiO$_3$–(1 $-x$)Fe$_2$O$_3$), which constitute the ferromagnetic minerals of the rock. Furthermore, he has found that the reverse T.R.M. is observed only in the specimen with x around 0·5, whose magnetic properties are sensitive to heat treatment.(2) The effect of heat treatment was examined in detail by one of the authors and specimens in this range of composition have been found to show the order–disorder transformation of the atomic arrangement of titanium and iron ions.(3) The disordered specimen is parasitic ferromagnetic with the crystal symmetry $R\bar{3}C$, while the ordered one is ferrimagnetic with the crystal symmetry $R\bar{3}$. The reverse T.R.M. is, therefore, expected to be closely related to the order–disorder transformation of this system.

On the basis of his experimental results, UYEDA proposed a tentative explanation that the reverse

---

* Present address: Laboratoire d'Électrostatique et de Physique du Métal, Institut Fourier, B.P. 319, Grenoble, France.

T.R.M. is the result of antiparallel coupling between the magnetic moments of ordered and disordered phases coexisting in a specimen.(2) Magnetic interaction was expected to be the superexchange interaction. Uyeda's model of the exchange coupling of two phases was supported by MEIKLEJOHN and CARTER(4) who observed a slight shift of the hysteresis loop of 0·6 $FeTiO_3$–0·4 Fe_2O_3 at 300°K after cooling in a magnetic field through the Curie point.(4)

Uyeda's model is, however, too simple to explain the complex features of the reverse T.R.M. of this system. He had to assume in his model that the disordered region has a Curie point higher than that of the ordered region, in order to produce the reverse T.R.M. This assumption contradicts the experimental results that the disordered phase has a Curie point 20–30°K lower than that of the ordered phase, if the compositions are the same. Furthermore, both Uyeda and Meiklejohn noticed in their experiments that the characteristics of the reverse T.R.M. were different sample by sample, even if the composition of the samples were the same. This made their results very complicated, and the detailed mechanism of this phenomenon has remained uncertain.

We have suggested in the previous paper(3) that this phenomenon may be closely related to a metastable phase which is created on the boundary of the ordered phase, so that a careful study of this phenomenon might make clear not only the mechanism of the reverse T.R.M., but also the kinetic process of the order-disorder transformation of this system.

In this paper, we describe the results of our experiments carried out to find the relation between order-disorder transformation process and the reverse T.R.M. A model is proposed which explains consistently the various features of the reverse T.R.M. of this system. Some information about the kinetic process of the order–disorder transformation in this oxide system which has been elucidated by this investigation is also presented. The results on the reverse T.R.M. have already been reported briefly.(5)

2. EXPERIMENTAL RESULTS

1. *Kinetic process of order–disorder transformation*

Specimen with x around 0·5, which show the most prominent order–disorder transformation, were used in our experiments. They were prepared by the same method as previous reported(6) and were shown by X-ray analysis to be single phase. The compositions were determined by an X-ray method which give results in good agreement with chemical analysis.(6) Each specimen was sealed carefully into an evacuated silica tube in order to avoid oxidation or reduction during heat treatment at high temperature, and all measurements were carried out with the specimen still sealed. The long range order parameter $S(T)$ of the specimen at a temperature T was determined by quenching the specimen from this temperature and measuring the magnetization in a magnetic field of 8500 Oe at room temperature, which has been shown to be approximately proportional to the long range order parameter S.(3) The temperature dependence of the equilibrium value of $S(T)$, obtained by keeping the specimens for a long time at the temperature T, is shown in Fig. 1. The number of each curve in the figure indicates mole percentage of ilmenite in the specimen. It should be noted that the maximum values of magnetization at room temperature of the specimen with x = 0·48 and 0·465, which were annealed for more than 3 days at low temperatures

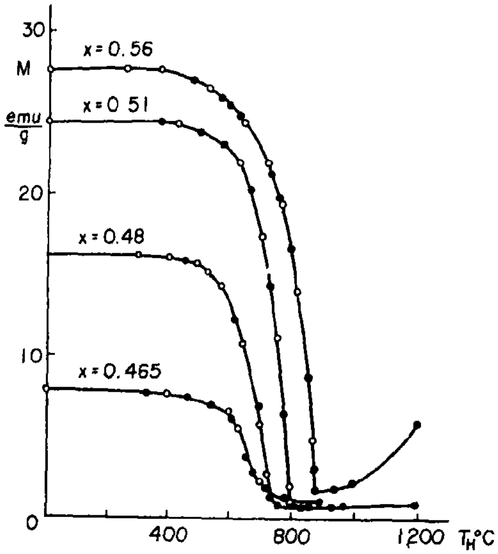

FIG. 1. Magnetization at room temperature vs. quenching temperature.

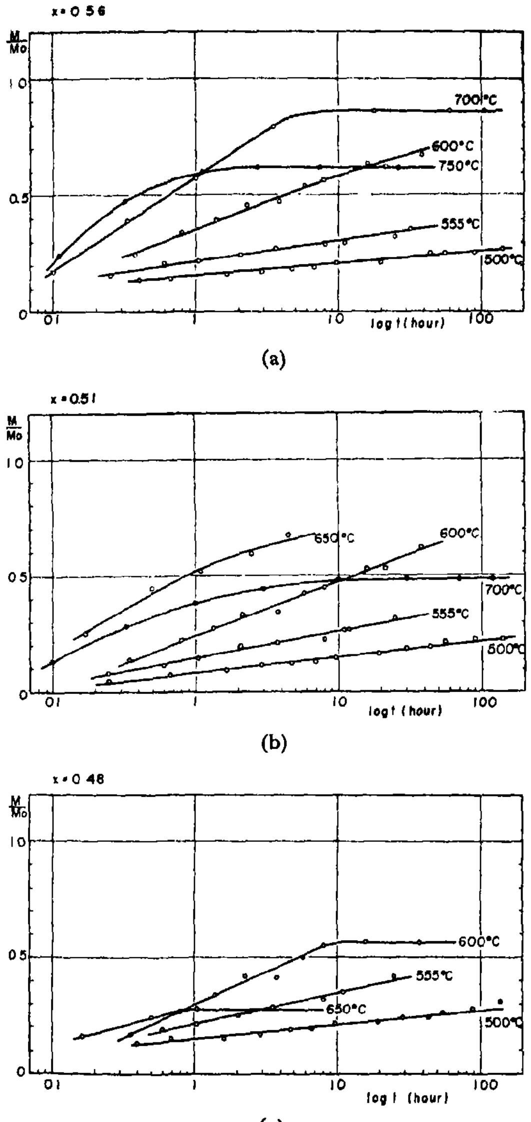

(a)

(b)

(c)

FIG. 2. Isothermal time variations of long-range order (magnetization at room temperature) for various temperatures

(a) 56 mole per cent $FeTiO_3$
(b) 51 mole per cent $FeTiO_3$.
(c) 48 mole per cent $FeTiO_3$.

are fairly small compared with those of $x = 0{\cdot}51$ and $0{\cdot}56$. This suggests that the perfect order cannot be established in the former specimens.

In Fig. 2(a) (b) and (c), the isothermal variations of the long range order parameter (magnetization at room temperature) measured at various temperatures are presented for three different compositions. These results were obtained by annealing the disordered specimen at a temperature T_H for a certain time interval t, and quenching it to room temperature. The ordinate of these figures are normalized to M_0, the magnetization at room temperature of complete ordered 56 mole per cent $FeTiO_3$. This approximate normalization may be permitted, because a decrease of the concentration of ilmenite in the specimen reduces the magnetic moment at 0°K while it raises the Curie point, so that the room temperature magnetizations of these three specimens are expected to remain nearly constant in the completely ordered state.

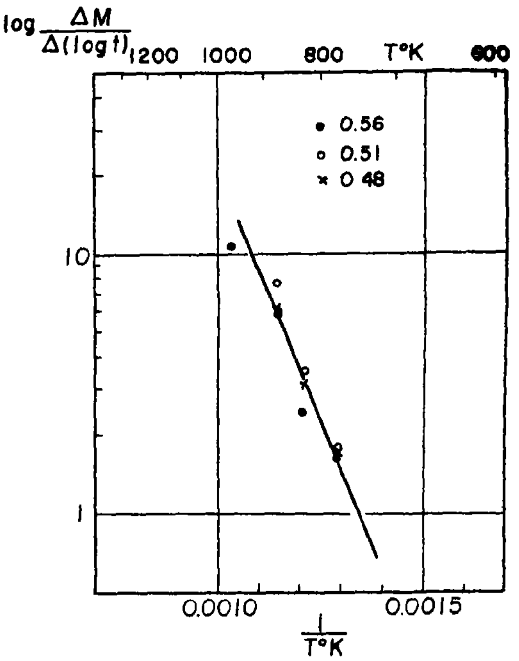

FIG. 3. Temperature dependence of slopes of logarithmic increase of long-range order, obtained from Fig. 2 for three compositions.

These figures show that the isothermal variation of the long range order parameter, $S(T)$ is proportional to the logarithm of the annealing time over a wide time range. The initial stage of the ordering process ($t \leq 5$ min) cannot be detected by our method. The slopes A of the time variation curves obtained from Fig. 2(a), (b) and (c) are plotted in Fig. 3 as a function of temperature. From this figure, we find that A is approximately proportional to $\exp(-E/kT)$ and is almost independent of the composition. The isothermal change of long range order S in this system is, *therefore, expressed by the following relation,* as long as the specimen is in a state far from equilibrium.

$$S(T) = A_0 \exp(-E/kT) \log t,$$

where E, obtained from Fig. 3 is 0·33 eV.

This relation indicates that the velocity of development of order is strongly temperature dependent and an appreciable increase of order can hardly be expected at temperatures below 500°C. Accordingly the ordered structure can never be developed in a specimen with x less than 0·40, because they have the order–disorder transformation temperature less than 500°C.

2. *The reverse T.R.M. of the specimen in the course of development of order*

The thermo-remanent magnetization of the specimen in various stages of order was produced by the following procedure. A specimen was annealed at a temperature T_H ($\geqslant$ 500°C) for a certain time t, quenched to room temperature to detect the state of order, reheated to 450°C, and finally cooled to room temperature with a magnetic field of 100 Oe applied only from 450°C down to some temperature T_a. The thermo-remanent magnetization at room temperature thus produced was measured by an ordinary ballistic method. The Curie point of the ferrimagnetic phase responsible for T.R.M. in the specimen was determined by measuring the temperature at which the thermo-remanent magnetization disappeared. After a series of magnetic annealing from 450°C to various temperatures T_a, the specimen was reheated to T_H and annealed at this temperature for a further long time. One of the advantages of this system is such that a repetition of the magnetic annealing between 450°C and room temperature does not disturb the arrangements of ions as was discussed in the previous section. In Fig. 4(a), the thermo-remanent magnetization measured at room temperature for the 56 mole per cent FeTiO$_3$ is plotted against T_a. Each

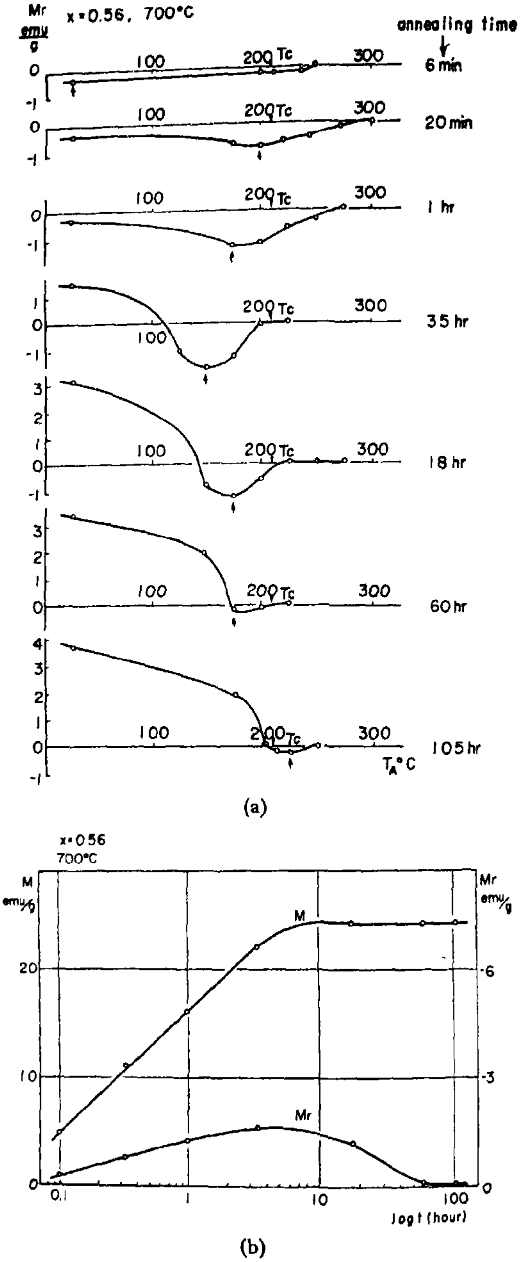

(a)

(b)

FIG. 4. (a) Thermo-remanent magnetizations of 56 mole per cent FeTiO$_3$ annealed at 700°C for various times. Abscissa is the temperature down to which a magnetic field was applied during cooling. (b) Isothermal changes of long-range order (upper curve) and maximum reverse T.R.M. at 700°C in 56 mole per cent FeTiO$_3$.

curve corresponds to the results obtained for a different annealing time at $T_H = 700°C$. The Curie point of the thermo-remanent magnetization T_c, determined by the method described above, is also indicated in the figure. No appreciable change of the Curie point was observed in the process of development of order at 700°C. From these figures we find that, for a specimen in the early stages of development of order, the reverse T.R.M. was found to be produced even if the magnetic field was applied only down to a temperature appreciably above the Curie point of the induced thermo-remanent magnetization. Since the T.R.M. is known to be produced if the magnetic field is applied down to below the Curie point of the phase,(7) this fact suggests that another phase (or phases) exist with a range of Curie temperature higher than that of the thermo-remanent magnetization, which is presumably that of the ordered phase. This unknown phase is designated hereafter as the x-phase. As the Curie point of the disordered phase is lower than that of the ordered phase of the same composition, the x-phase must be an Fe-rich region as compared with both the ordered and disordered phases. If the magnetic moment of the x-phase is fairly small compared with that of the ordered phase, the anti-parallel coupling between the magnetic moment of the ordered phase and that of the x-phase, which was locked in the direction of the field applied during the magnetic annealing process, results in the self reversal of the remanent magnetization. Fig. 4(a) also shows that the Curie points of the x-phase, which are distributed over a range of temperature, change with the development of order.

When the specimen was cooled to a temperature far below the Curie point of the ordered phase, a normal T.R.M. was superimposed on the reverse T.R.M. This effect was more pronounced if the specimen is annealed for a long time. The maximum values of the reverse T.R.M. obtained from Fig. 4(a) are plotted in Fig. 4(b) as a function of the annealing time at 700°C. The upper curve in the figure indicates the long range order parameter developed by the annealing process, while the lower curve is the maximum reverse T.R.M. of the specimen. The striking result is that the reverse T.R.M. exists only in the intermediate state, and is not found in either the fully ordered state or in the disordered state. These facts indicate clearly that the x-phase which is responsible for the reverse T.R.M. is only a metastable phase: that is, it is created in the process of the formation of order and tends to disappear if the crystal reaches equilibrium.

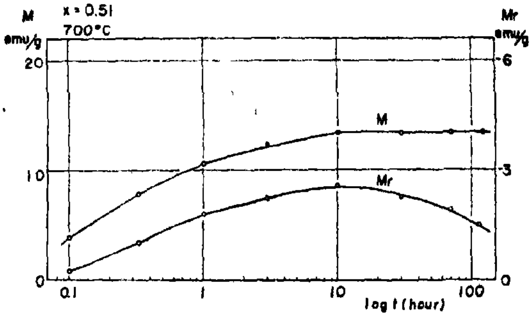

FIG. 5. Isothermal changes of long-range order (upper curve) and maximum reverse T.R.M. at 700°C in 51 mole per cent $FeTiO_3$. (Cf. Fig. 4b).

Similar experiments were carried out for specimens with $x = 0{\cdot}51$ and the results are presented in Figs. 5 and 6. The result obtained by annealing the specimens at 700°C is almost the same as that

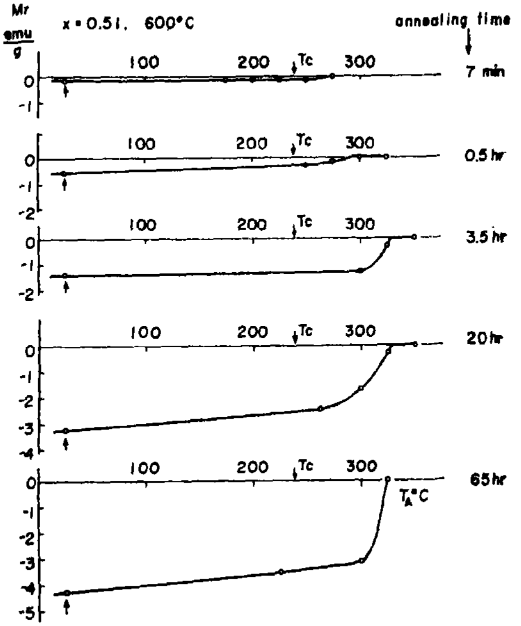

FIG. 6. Thermo-remanent magnetization of 51 mole per cent $FeTiO_3$ annealed at 600°C for various times (Cf. Fig. 4a).

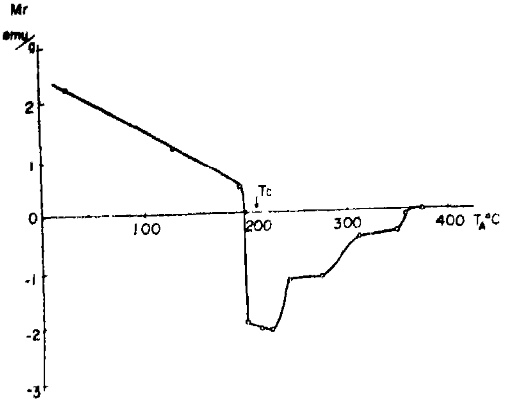

FIG. 7. Thermo-remanent magnetization of 51 mole per cent $FeTiO_3$ furnace-cooled from 1000°C. Abscissa is the temperature down to which a magnetic field was applied during cooling.

of $x = 0{\cdot}56$, but in this case, the reverse T.R.M. (the metastable phase) does not disappear completely, even after annealing for more than 100 hr at 700°C, as shown in Fig. 5. When the specimen was annealed at 600°C, however, the characteristics of magnetic annealing were found to be fairly different from those at 700°C. As shown in Fig. 6, the Curie points of metastable phase still increase after annealing for more than 65 hr, indicating that the difference in composition between the metastable phase and matrix increases with prolonged annealing. Furthermore, in this case, the maximum reverse T.R.M. is always produced when the magnetic field is applied down to room temperature during cooling from 450°C. These figures indicate that the metastable phase created in the annealing process at 600°C has the same characteristics as that created only in the early stage of annealing at 700°C ($t \simeq 6$ min). In a later Section we shall discuss in more detail such a difference in the kinetic process with temperature and composition.

We have thus found that the characteristics of the reverse T.R.M. were quite different, even if the long range order is the same. The most prominent case was found for the specimen with $x = 0{\cdot}56$ which was cooled with the furnace from 1000°C. After this heat treatment, the magnetization at room temperature is about 85 per cent of that of the perfectly ordered specimen, indicating that the long range order is fairly well developed in the specimen. The characteristics of the magnetic annealing of this specimen, however, are quite different from the previous cases, as shown in Fig. 7, which was obtained by the same method as described previously. The Curie points of the

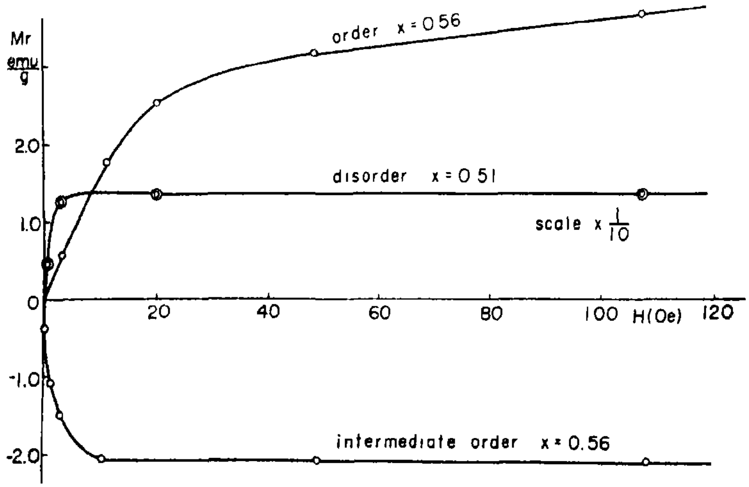

FIG. 8. Field dependence of the thermo-remanent magnetization. Magnetic field was applied only down to a temperature above the Curie point for the reverse T.R.M.

metastable phase are distributed over a range of 200°C above the Curie points of the ordered phase. This is an indication that a considerable amount of metastable phase with compositions quite different from the matrix still exists in combination with the ordered phase as a result of such furnace-cooling.

3. *Magnetic properties of* x-*phase*

It is difficult to measure the magnetic properties of the metastable x-phase by any direct means, because the x-phase always exists in combination with the strong ferrimagnetic ordered phase. Therefore the magnetic properties of the x-phase were estimated from the reverse T.R.M., which indicates indirectly their magnetic properties. In Fig. 8 the field dependence of the reverse T.R.M. is shown, together with the field dependence of the normal T.R.M. for both the ordered phase ($x = 0{\cdot}56$) and the disordered phase ($x = 0{\cdot}51$). The reverse T.R.M. was produced in the specimen with $x = 0{\cdot}56$, which was previously furnace-cooled from 1000°C, by applying a magnetic field H from 450°C down to a temperature just above the Curie point of the ordered phase, so as not to produce the normal T.R.M. The field dependence of the reverse T.R.M. obtained by this procedure is presumably that of the pure x-phase. This figure shows that the characteristics of the x-phase are quite similar to those of the disordered phase, that is, in the case of both the disordered phase and the x-phase, a magnetic field of 10 Oe is sufficient to produce the saturated thermo-remanent magnetization, while for the ferrimagnetic ordered phase, more than 100 Oe is necessary to saturate the T.R.M. The field dependence of the disordered state is a characteristic of the parasitic ferromagnet;$^{(8)}$ that is, in this case, the demagnetizing field, which prevents the saturation of the remanent magnetization, is very small. The x-phase has, therefore, the very weak magnetic moment and is presumably in the disordered state.

In Fig. 9, the field dependence of the reverse T.R.M. for a specimen with $x = 0{\cdot}56$, annealed at 700°C, is shown for various annealing times. The reverse T.R.M. was produced by the same method as described above for each annealing time. The field dependence of the reverse T.R.M. thus obtained is found to be almost the same throughout the ordering process; that is, even for the specimen annealed for only 10 min at 700°C, the reverse T.R.M. was saturated by a weak field. This fact indicates that the x-phase is not present in regions as small as one or two atomic layers thick on the boundary of the ordered phase even in the early stage of ordering. If the x-phase region were fairly small, it would behave as superparamagnetic particles at high temperature and it should become very difficult to saturate the magnetic moment of the x-phase, which, in turn, should result in hard saturation of the reverse T.R.M.

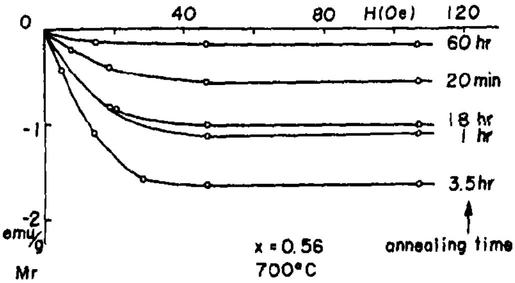

FIG. 9. Field dependence of the reverse T.R.M. of 56 mole per cent $FeTiO_3$ annealed for different times at 700°C. Magnetic field was applied only down to a temperature above the Curie point.

4. *Magnetic interaction between the ordered phase and the* x-*phase*

In order to estimate the order of magnitude of magnetic coupling between the magnetic moments of the order phase and the x-phase, we have measured the hysteresis of the remanent magnetization produced at room temperature. In Figs. 10 and 11, the results obtained for specimens with $x = 0{\cdot}465$ and $x = 0{\cdot}51$ are shown. They are annealed at 600°C for 2 hr and 20 min respectively beforehand, and the reverse T.R.M. was produced by applying a magnetic field of 100 Oe from 450°C down to room temperature. A magnetic field was then applied at room temperature in the direction opposite to the reverse T.R.M., and the remanent magnetization was measured by the ballistic method. Each point in the figure corresponds to the remanent magnetization obtained after applying the magnetic field indicated on the abscissa. As Fig. 10 shows, more than 14,000 Oe is

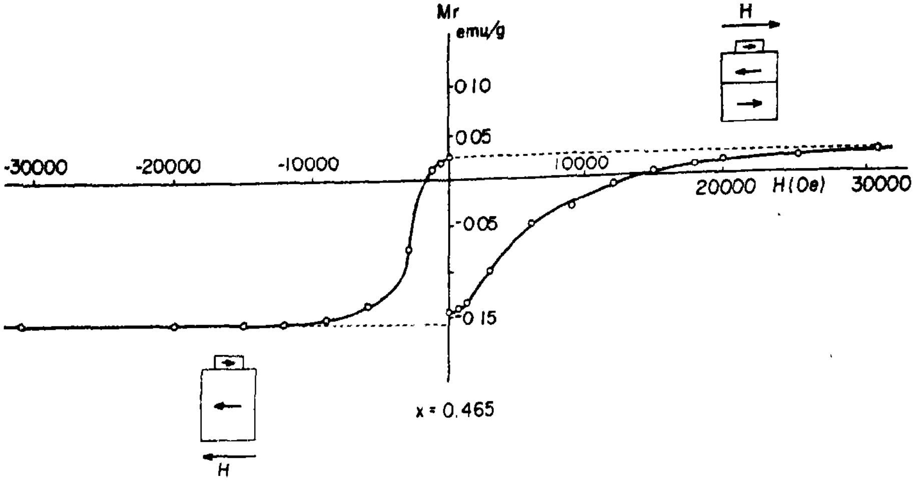

FIG. 10. Remanence hysteresis of 46·5 mole per cent FeTiO3 with reverse T.R.M.

necessary to destroy the reverse T.R.M. of the specimen in which $x = 0{\cdot}465$. On the other hand, the remanent magnetization produced in the opposite direction to the reverse T.R.M. at room temperature by a field strength of 30,000 Oe can be easily destroyed by a field of 1000 Oe applied in the direction of the reverse T.R.M. Such an asymmetric hysteresis suggests that the magnetic moments of the x-phase, which were fixed in the direction of the applied field during magnetic annealing, do not change their directions even if an external field as strong as 30,000 Oe is applied in the opposite direction. This situation is schematically illustrated in the figure. In the case of $x = 0{\cdot}51$, we have also an asymmetric hysteresis as shown in Fig. 11, although the remanence coercivity is reduced to 3400 Oe. In the case of $x = 0{\cdot}56$, a remanence coercivity of 760 Oe was obtained for the specimen annealing 600°C for 20 min. Such a decrease in remanence coercivity is not due to decrease in the strength of magnetic coupling but due to increase in the normal remanence magnetization produced from the part which does not couple with the metastable x-phase. The remanent hysteresis was also measured for both a completely ordered specimen ($x = 0{\cdot}56$) and a disordered specimen ($x = 0{\cdot}51$). The remanent coercivities are found to be 200 Oe and 3000 Oe respectively, indicating that the coercive force is fairly small even for the disordered specimen. Accordingly the asymmetry hysteresis observed in a magnetic field of 30,000 Oe is the most clear evidence that the magnetic moments of the ordered phase and x-phase are coupled through a superexchange interaction.

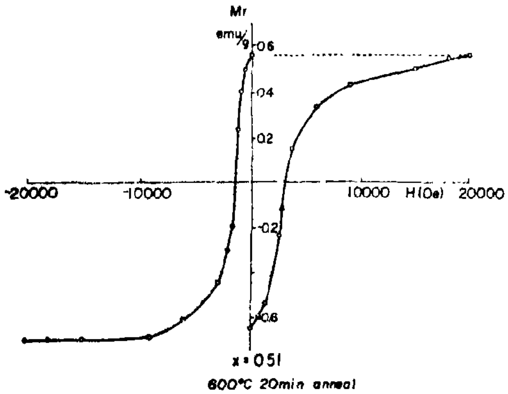

FIG. 11. Remanence hysteresis of 51 mole per cent FeTiO3 with reverse T.R.M.

DISCUSSION

1. *Discussion of reverse T.R.M.*

We have suggested that the reverse T.R.M. is the result of anti-parallel coupling between the magnetic moments of the ordered phase and an

Fe-rich metastable phase. Moreover the x-phase must be atomically in antiphase with respect to the ordered phase in order that the resultant magnetic moments of the two phases can be aligned antiparallel through a superexchange interaction. The possibility of the existence of such a metastable phase was examined by following graphically the development of the ordered phase in the disordered matrix. Fig. 12(a) is a two dimensional representation of disordered 0·5 $FeTiO_3$–0·5 Fe_2O_3. The positions of Ti ions, indicated by black circles in the figure, were chosen by means of a table of random digits. An ordered phase was developed in the disordered matrix by rearranging the metal ions as shown by the arrows in the figure. Here we assume that diffusion of ions takes place more easily within the same layer than between the layers. Figure 12(b) indicates schematically the ordered phase thus produced, on the boundary of which we find the Fe-rich metastable regions. These regions may correspond to the "x-phase" although their boundaries cannot be clearly determined. As the Ti ions rejected from the Fe layers in the ordered phase are displaced to the same layers in the metastable phase, the x-phase is always in antiphase to the ordered phase. Therefore a superexchange interaction acting between the neighbouring layers can align the resultant magnetic moments of the two phases antiparallel. Of course, Ti-rich metastable regions are also created on the boundary. However, they do not affect the reverse T.R.M., because the Curie point of this phase is lower than that of the ordered phase. Thus, the graphical study shows that our antiphase-contact two-phase model is fairly promising, and we believe that the phenomenon of the reverse T.R.M. of the Haruna type is satisfactory explained by our model. The assumption of the preferential diffusion of Ti ions within the C-plane, which is essential for our model, is hoped to be examined experimentally in near future.

2. *Discussion of the kinetic process of ordering*

In this Section we summarize the results concerning with the kinetic process of order–disorder transformation in the ilmenite–hematite system, which was elucidated by the investigation of the reverse T.R.M. The various features of the reverse T.R.M. observed in the ordering process, which were presented in Figs. 4, 5 and 6, are also explained on the basis of the kinetic process.

(1) When a disordered specimen is annealed at a temperature T below the order–disorder transformation temperature, long range order is developed in the disordered matrix. The isothermal change of the long range order parameter $S(T)$ is approximately expressed by the following relation, so long as the specimen is in a state far from equilibrium,

$$S(T,t) = A_0 \exp(-E/kT) \log t$$

where E is found to be about 0·3 eV and is independent of the concentration of Ti ions in the crystal.

Similar logarithmic time dependence has been observed in the case of the magnetic after effect in Alnico V(9) and other materials(10) and has been interpreted by NÉEL(12) and by STREET and WOOLEY(9) as a relaxation phenomenon where the relaxation times are distributed over a wide range of time. It is possible that the relaxation times or the activation energies of diffusion of Ti ions by which the ordered structure is developed in the ilmenite–hematite system are distributed over a wide range, because they may depend on various configurations of surrounding ions and vacancies.(13) According to a simple calculation based on the assumption of a square-type distribution function of the relaxation times, the slope A of the logarithmic curve is proportional to the absolute temperature T. This relation is actually observed for Alnico V(9) and Fe_3O_4.(11) The kinetic process of ordering in this system is, however, apparently quite different from such a simple case.

(2) In the early stage of the ordering process, a metastable phase with a concentration of Ti ions different from both the ordered and disordered phase is created on the boundary. The difference in concentration between the metastable phase and the ordered phase first increases and then decreases again with further annealing. The composition of the ordered phase remains almost unaltered throughout the whole process of the development of order. The metastable phase does not disappear even after the long-range order attains its equilibrium value, and further annealing is necessary in order to remove the metastable phase.

(3) The ordered phase is developed by diffusion

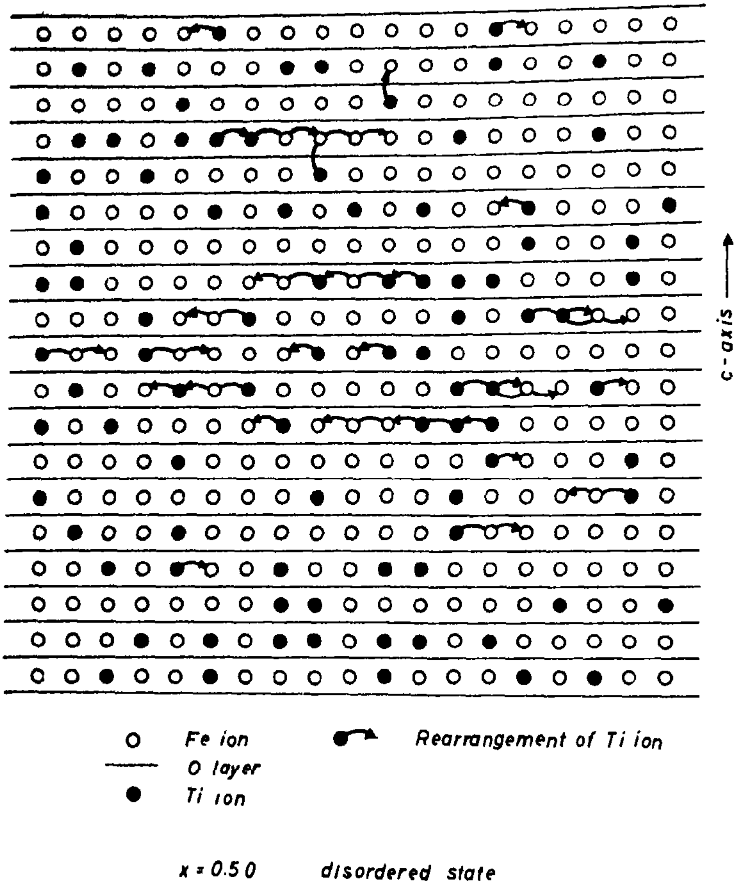

(a)

FIG. 12. (a) Two dimensional representation of disordered 50 mole per cent FeTiO$_3$.

of Ti ions, which is expected to take place preferentially within the C-plane. The metastable phase created on the boundary by this diffusion process is always atomically antiphase to the ordered phase. The reverse T.R.M. of this system is the result of antiparallel coupling of the spins of the ordered phase and of the metastable phase, through a superexchange interaction.

(4) If the annealing temperature is fairly low ($T \leqslant 600°C$), only small size ordered regions are developed, always in contact with metastable regions. The ordered region is presumably magnetically single domain, so that the reverse T.R.M. is produced even if the magnetic field is applied down to room temperature as really observed in Fig. 8(a).

On the other hand, if the specimen is annealed at a high temperature ($T \geqslant 700°C$), the ordered regions grow in size rather than number. Therefore, if the specimen is annealed at 700°C for a long time, most of the ordered regions are too large in size to be affected by the metastable phase on the boundary and the normal T.R.M. is produced if the magnetic field is applied down to below the Curie point of the ordered phase which was shown in the last two figures of Fig. 4(a).

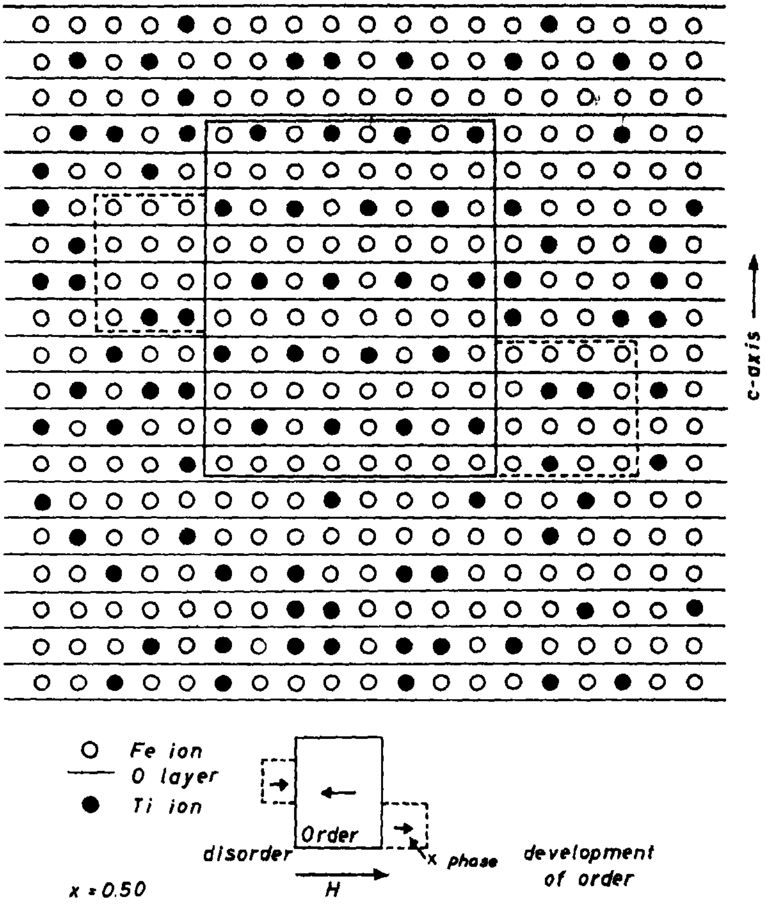

(b)

FIG. 12. (b) Ordered phase and x-phase developed in the disordered matrix. The boundary of x-phase, which is presumably not definite in the actual crystal, is shown schematically in the figure.

In the intermediate stage of ordering, however, we found that the normal T.R.M. was produced if the magnetic field was applied down to almost 100°C below T_c (cf. the third and the fourth curve of Fig. 4a). We may expect that, in this stage of ordering, the ordered phase has reached a size such that it remains magnetically single domain (or almost single domain) near the Curie point, but becomes multidomain at low temperatures. A similar situation was first suggested by RATHENAU(14) in order to explain the fact that the coercive force of barium-ferrite has a maximum at a temperature below the Curie point. When the multidomain structure becomes stable at low temperature and the coercive force becomes less than the applied field, some of magnetic moments, which were directed in the direction opposite to the applied field by the negative coupling field just below the Curie point of the ordered phase may change their direction to that of the applied field by domain wall motion and a normal T.R.M. is produced.

(5) If the concentration of Ti ions in the specimen is decreased, the tendency that the ordered phase grown in size is decreased. It becomes, therefore, difficult to remove the metastable phase for the specimen with low concentration of Ti ions, as is indicated in Fig. 5.

Acknowledgements—The authors wish to express their thanks to Professors S. Chikazumi, T. Nagata and S. Akimoto for valuable discussion and advice. Their thanks are also due to Dr. C. D. Graham, Jr. for reading and criticizing the manuscript, and to Mr. H. Hashiura for his preparation of specimens. This research was partly supported by a research grant of the Ministry of Education.

REFERENCES

1. Nagata T., Uyeda S. and Akimoto S., *J. Geomagn. Geoelect., Kyoto* **4**, 22 (1952).
2. Uyeda S., *Japanese J. Geophys.* **2**, 1 (1958).
3. Ishikawa Y., *J. phys. Soc. Japan* **13**, 828 (1958).
4. Meiklejohn W. H. and Carter R. E., *J. appl. Phys.* **30**, 2020 (1959).
5. Ishikawa Y. and Syono Y., *J. phys. Soc. Japan* **17S, BI**, 714 (1962).
6. Ishikawa Y. and Akimoto S., *J. phys. Soc. Japan* **12**, 1083 (1957).
7. Nagata T., *Rock magnetism.* Revised edition by Maruzen p. 147 (1961).
8. Syono Y. and Nagata T., *J. Geomagn. Geoelect. Kyoto* (in press).
9. Street R. and Wooley J. C., *Proc. phys. Soc. Lond.* **A62**, 562 (1949).
10. Barbier J. C., *Ann. Phys. Paris* **9**, 84 (1954).
11. Shimizu Y., *J. Geomagn. Geoelect. Kyoto* **11**, 125 (1960).
12. Néel L., *J. Phys. Radium* **11**, 49 1950); **12**, 339 (51).
13. Ida S. and Inoue T., *J. phys. Soc. Japan.* **17S**, BI 281 (1962).
14. Rathenau G. W., *Rev. mod. Phys.* **25**, 297 (1953).

J. Phys. Chem. Solids Pergamon Press 1963. Vol. 24, pp. 529–536. Printed in Great Britain.

LONG-RANGE ANTIFERROMAGNETISM IN DISORDERED Fe–Ni–Mn ALLOYS

J. S. KOUVEL and J. S. KASPER
General Electric Research Laboratory, Schenectady, New York

(*Received* 23 *October* 1962)

Abstract—Neutron diffraction measurements at 77 and 298°K reveal long-range antiferromagnetic ordering in the atomically-disordered face-centered cubic alloys with more than about 50 at. per cent Fe in the ternary series $(Ni,Fe)_3Mn$. Consistent with these results, the Néel temperatures of these alloys, deduced from the temperature dependence of their electrical resistivities, rise from 210 to 425°K as the iron concentration increases from 50 to 75 at. per cent. An antiferromagnetic structure that conforms to the neutron diffraction polycrystal data is the collinear, tetragonal configuration previously reported for the Mn-rich Mn–Cu alloys. However, quite unlike Mn–Cu, the Fe–Ni–Mn alloys give no detectable X-ray diffraction evidence for a tetragonal (or any other) distortion of their cubic atomic arrangement. Hence, an alternative structure proposed for these alloys is one that is cubic though not collinear, the moments on four equivalent sublattices being oriented along different $\langle 111 \rangle$ directions such that their vector sum is zero. Both these magnetic structures are then shown to be special cases of a general set of non-collinear, tetragonal configurations which produce the same neutron diffraction pattern for a given magnitude of the average atomic moment $\bar{\mu}$. For the $(Ni,Fe)_3Mn$ series it is found that $\bar{\mu}$ increases from 1·1 to 1·7 μ_B with increasing iron concentration from 50 to 75 at. per cent, which is shown to be at least in part due to an improved degree of long-range magnetic order. The results of the present work are compared and related to the unusual ferromagnetic–antiferromagnetic behavior of the more Ni-rich alloys in this ternary series and to the low-temperature antiferromagnetic structure recently reported for γ-iron.

INTRODUCTION

UNUSUAL magnetic properties were recently observed[1] in disordered face-centered cubic alloys of composition $(Ni,Fe)_3Mn$. When cooled to very low temperatures in a magnetic field, the alloys with up to approximately 35 at. per cent iron exhibit hysteresis loops that are displaced from their symmetrical positions about the origin. In this respect and in the anomalous temperature and field dependencies of their magnetizations, these Ni-rich alloys are all qualitatively similar to disordered Ni_3Mn in which these properties had been previously discovered and attributed to an inhomogeneous ferromagnetic–antiferromagnetic state.[2] The justification for such a state in Ni_3Mn had been based on the combined effects of statistical composition fluctuations (inherent to an atomically disordered system) and the existence of both positive and negative exchange interactions between different nearest-neighbor atom pairs. It was therefore concluded that a complex magnetic state of this type also obtained in the alloys in which as much as 35 at. per cent nickel in Ni_3Mn has been replaced by iron.

The alloys in this $(Ni,Fe)_3Mn$ series with about 50 and 56 at. per cent iron, however, were found to have a much simpler magnetic behavior, with no measurable effects due to cooling in a field.[1] The magnetization of each of these iron-rich alloys is at all temperatures essentially proportional to the applied field and is characterized by a susceptibility having a maximum value somewhat below room temperature. At higher temperatures, the susceptibility follows a Curie–Weiss relation, $\chi = C/(T-\theta)$, with a large negative θ. This behavior is so strongly suggestive of a long-range antiferromagnetic spin alignment that we decided to explore this possibility with neutron diffraction measurements. We were previously[3] unable to detect any neutron diffraction evidence for long-range magnetic order in atomically disordered Ni_3Mn, which is consistent with the microscopically inhomogeneous magnetic state visualized for this alloy.[2] Hence, any long-range antiferromagnetism in the iron-rich $(Ni,Fe)_3Mn$ alloys revealed by neutron diffraction would be definitive support of the susceptibility results in indicating that the iron and nickel atoms of these face-centered cubic alloys are significantly different in their magnetic interactions with neighboring atoms.

We chose for the present study a series of $(Ni,Fe)_3Mn$ compositions which extended from the 50 and 56 at. per cent Fe alloys mentioned above all the way to Fe_3Mn. Even though a partial intrusion of a hexagonal ϵ-phase could be anticipated in Fe_3Mn,[4] it was hoped that most of this alloy would be retained in f.c.c. form and that any ambiguities in its neutron diffraction pattern caused by the presence of the ϵ-phase would be resolved by extrapolation of the data on the f.c.c. alloys containing some nickel. This procedure was considered preferable to suppressing the ϵ-phase by doping the material heavily with carbon, as was done in a recent magnetic study of Fe–Mn(–C) alloys.[5]

Since the magnetic susceptibility of the iron-rich $(Ni,Fe)_3Mn$ alloys decreases rapidly with increasing iron concentration[1] and eventually becomes too small for convenient measurement in our apparatus, we decided on electrical resistivity measurements as an alternative means of determining the temperatures of any magnetic transitions in our alloys. This information was then used as a guide in our neutron diffraction experiments.

A preliminary oral report[6] was recently given on some of the results presented in this paper.

Table 1. *Compositions in atomic per cent for nominal* $(Ni,Fe)_3Mn$ *alloys*

Fe	Ni	Mn
49·6	25·1	25·3
56·5	18·2	25·3
65·5	9·7	24·8
69·5	5·0	25·5
74·7	0·0	25·3

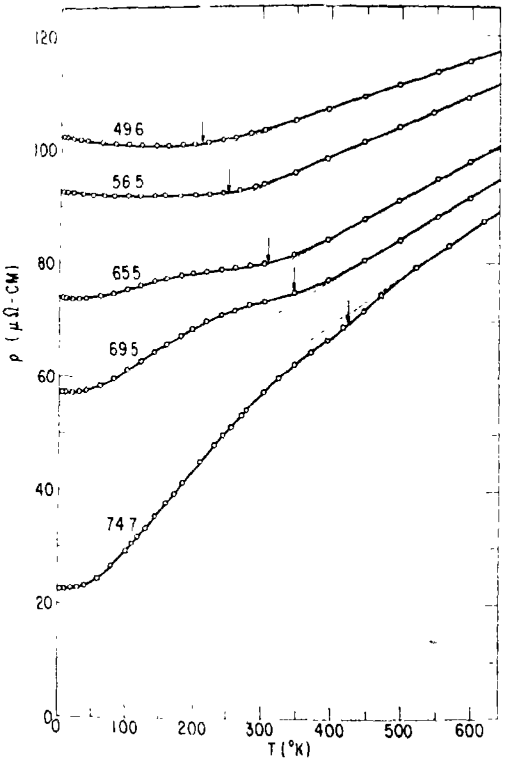

Fig. 1. Electrical resistivity vs. temperature for $(Ni,Fe)_3Mn$ alloys, designated by at. per cent Fe. Arrows indicate temperatures at which resistivities deviate by 3μΩ-cm from extrapolated high-temperature curves.

EXPERIMENTAL RESULTS AND DISCUSSION

The alloys of this investigation were prepared by induction-melting under argon. The compositions of the ingots obtained by chemical analysis are listed in Table 1. A 0·02 in. diam. wire was cold-drawn from each ingot for electrical resistivity measurements, and the remainder of each ingot was divided into small chips for neutron diffraction. The wires and chips (as well as some fine filings made for X-ray diffraction work) of all these materials were sealed in quartz under a partial pressure of helium, annealed 15 hr at 900°C and then water-quenched. X-ray diffraction study indicated that all the alloys containing nickel were entirely face-centered cubic, with lattice parameters (a_0) lying within the range 3·603 ± 0·003 Å. The nominal Fe_3Mn alloy, however, although retained predominantly in f.c.c.

form (a_0 within the above range), contained some (volume fraction approximately ¼) of the hexagonal close-packed phase ($a_0 = 2{\cdot}546 \pm 0{\cdot}002$ Å, $c_0 = 4{\cdot}114 \pm 0{\cdot}002$ Å, $c_0/a_0 = 1{\cdot}616$).

Conventional potentiometric techniques were used in measuring the electrical resistivities of these alloys from 4.2 up to about 600°K. The data are presented in Fig. 1, and it is evident that below some temperature (marked approximately by an arrow) the resistivity of each material begins to deviate significantly from its linear variation at higher temperatures. For the 49·6 and 56·5 at. per cent Fe alloys, this temperature agrees closely with that of the maximum susceptibility;(1) there is also agreement with the susceptibility-temperature anomaly recently observed at about 400°K in a f.c.c. Fe_3Mn alloy containing about 2 at. per cent carbon.(5) It therefore seems reasonable to assume that for each alloy this temperature is the antiferromagnetic Néel point. However, under this assumption, Fig. 1 would indicate that the resistivities of all but the 74·7 at. per cent Fe alloy are increased by the magnetic ordering, which is an unusual situation attributable perhaps to the random (or near-random) arrangement of different moment-bearing atoms in these materials. The Néel temperatures (T_N) determined from the resistivity–temperature anomalies are plotted vs. iron concentration in Fig. 2. In this figure we have also plotted the paramagnetic Curie temperatures (θ) and the temperatures of maximum magnetic hysteresis losses (T_l) obtained recently for this $(Ni,Fe)_3Mn$ alloy series.(1) Since T_l also signifies the temperature at which the displaced hysteresis loop effect (mentioned earlier) disappears, the decrease of T_l to zero is consistent with the values of T_N and θ in suggesting that the iron-rich $(Ni,Fe)_3Mn$ alloys, in contrast to those rich in nickel, have some type of long-range antiferromagnetic order below T_N.

The neutron diffraction data were obtained at 77 and 298°K for the polycrystalline chips of each alloy packed into a cylindrical aluminum container. The patterns for the 56·5 at. per cent Fe alloy are shown in Fig. 3, where the angular positions of possible Bragg reflections for a cubic system with $a_0 \simeq 3{\cdot}60$ Å are labelled with the appropriate indices and the Bragg peaks from the aluminum container are marked accordingly. It is evident that at 298°K the alloy specimen gives rise only to those reflections corresponding to a face-centered cubic structure; moreover, the relative intensities of these reflections are consistent with a random distribution of the different atoms among the various lattice sites. However, in addition to the reflections characteristic of a disordered f.c.c. structure, the pattern for this alloy at 77°K contains a fairly conspicuous peak which can be readily indexed as (110) and a peak that is just barely detectable at the (210) position. The same two extra reflections were also observed only at 77°K for the 49·6 at. per cent Fe alloy, whereas for the 65·5, 69·5 and 74·7 at. per cent Fe compositions they were also found to be present at 298°K, though somewhat diminished in relative intensity from those at 77°K. In all these cases, as in that of the 56·5 at. per cent Fe alloy, the rest of the reflections were those appropriate for a disordered f.c.c. system, except for the nominal Fe_3Mn alloy whose patterns also showed reflections that were identifiable with the h.c.p. ε-phase.

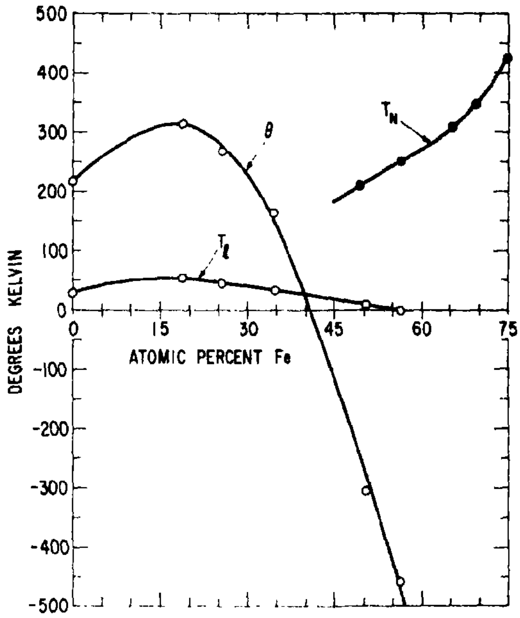

FIG. 2. Néel temperature (T_N) obtained from Fig. 1, paramagnetic Curie temperature (θ) and temperature of maximum magnetic hysteresis losses (T_l) obtained from Ref. 1, as functions of iron concentration in $(Ni,Fe)_3Mn$ alloy series.

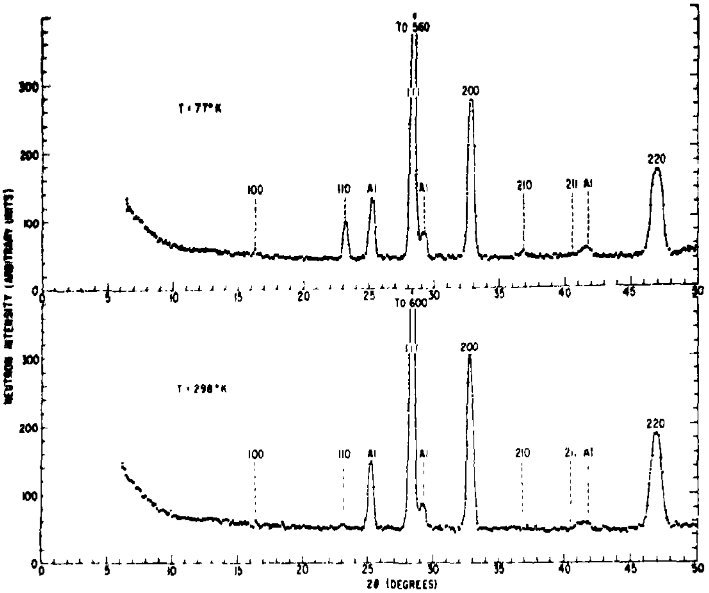

FIG. 3. Neutron diffraction data obtained at 77 and 298°K for $(Ni,Fe)_3Mn$ alloy of 56·5 at. per cent Fe.

The change in the intensities of the (110) and (210) peaks with temperature, as described for each of these alloys, is definite evidence that these extra peaks arise entirely from the existence of long-range antiferromagnetic order below the temperature T_N determined from the resistivity-temperature anomaly. The fact that in all cases the (210) peak is much weaker than the (110) peak is consistent with the rapid decrease of the magnetic form factor with increasing Bragg angle. The occurrence of (110) and (210) peaks and the absence of certain other reflections, notably the (100), suggest that a possible antiferromagnetic structure for these $(Ni,Fe)_3Mn$ alloys is essentially that deduced by BACON *et al.*(7) from their neutron diffraction data on Mn-rich Mn–Cu alloys. Below the Néel temperature, the f.c.c. atomic structure of the Mn–Cu alloys becomes tetragonally distorted, and with reference to the tetragonal atomic cell the magnetic structure consists of ferromagnetic (001) sheets with their moments antiparallel to those in nearest-neighbor sheets and directed along the *c*-axis. This tetragonal antiferromagnetic structure (henceforth referred to as the γ-Mn structure) is in the space group *P4/mnc* and is shown in Fig. 4(a) in terms of a *C*-centered cell with the origin shifted by $\frac{1}{4}\,\frac{1}{4}\,\frac{1}{4}$ from its conventional position in this type of cell. The low-index magnetic reflections allowed by this structure are (110), (201) and (112).

An alternative to the γ-Mn magnetic structure, also based on a face-centered atomic arrangement and giving the same magnetic reflections with even the same relative intensities, is shown in Fig. 4(b) designated by the space group *Pn*3. Unlike the γ-Mn structure, it is not a collinear magnetic structure; as indicated in the figure, the moments on four equivalent sublattices are oriented along different ⟨111⟩ directions such that their vector sum is zero. Furthermore, this structure is cubic and may therefore be particularly relevant to the $(Ni,Fe)_3Mn$ alloys whose atomic structures below their Néel temperatures show no departure from cubicity, according to X-ray and neutron diffraction measurements described thus far.

In order to learn if indeed there is some very small distortion of the f.c.c. atomic arrangement in these alloys suggestive of a non-cubic magnetic structure, we investigated the back-reflection region of an X-ray diffractometer pattern for a

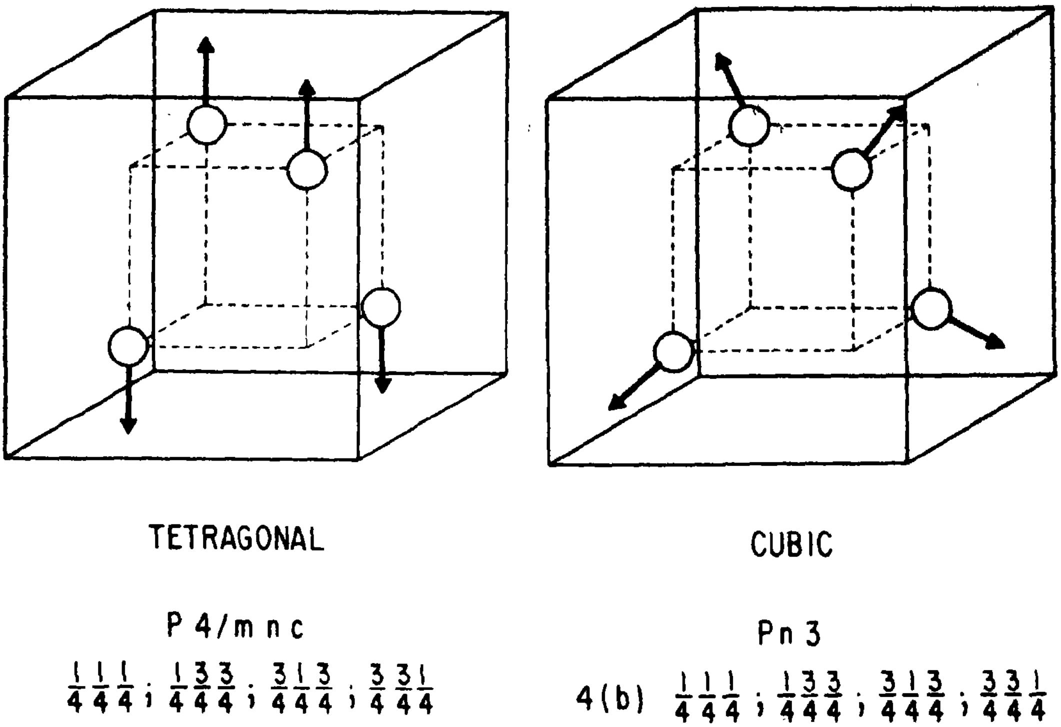
TETRAGONAL
P 4/m n c
$\frac{1}{4}\frac{1}{4}\frac{1}{4}$; $\frac{1}{4}\frac{3}{4}\frac{3}{4}$; $\frac{3}{4}\frac{1}{4}\frac{3}{4}$; $\frac{3}{4}\frac{3}{4}\frac{1}{4}$
CUBIC
Pn 3
4(b) $\frac{1}{4}\frac{1}{4}\frac{1}{4}$; $\frac{1}{4}\frac{3}{4}\frac{3}{4}$; $\frac{3}{4}\frac{1}{4}\frac{3}{4}$; $\frac{3}{4}\frac{3}{4}\frac{1}{4}$

(a) (b)

FIG. 4. Alternative antiferromagnetic structures for $(Ni,Fe)_3Mn$ alloys.

polycrystalline specimen of the 69·5 at. per cent Fe alloy. This was done at room temperature which is below the estimated Néel temperature of this material. For CuK_α radiation, the (420) reflection proved the most suitable for detailed study. K_{α_1}, K_{α_2} were clearly resolved with the appropriate intensity ratio, but no additional splitting caused by a lowering of the atomic symmetry could be detected. Assuming a tetragonal distortion such that the separation between (420) and (204) reflections is at most about half the K_{α_1}, K_{α_2} splitting, we estimate that the c_0/a_0 ratio does not deviate from unity by more than 10^{-3}. Although this upper limit is much less than the 3 to 4 per cent by which the c_0/a_0 ratios of the Mn–Cu alloys depart from unity, it does not eliminate the possibility that the γ-Mn antiferromagnetic structure also obtains in the $(Ni,Fe)_3Mn$ alloys but gives rise to a much smaller tetragonal distortion. Hence, until this distortion (or lack of it) is established more definitely, symmetry arguments cannot be used to discriminate between the tetragonal and cubic structures depicted in Fig. 4, both of which are consistent with our neutron diffraction data.

The antiferromagnetic structure of the $(Ni,Fe)_3Mn$ alloys becomes even more ambiguous when it is realized that the two configurations in Fig. 4 are special cases of a set of magnetic structures all of which produce the identical neutron diffraction pattern. As shown in Fig. 5 all these structures are based on a f.c.c. atomic arrangement and share the additional feature of four magnetic sublattices, each having a different moment direction at an angle ϕ with respect to the same cube-edge axis (the z-axis in the figure). Two of the sublattice moments lie in each of the two face-diagonal planes that include this axis, such that the vector sum of all four sublattice moments is zero. Although the magnetic unit cell has the

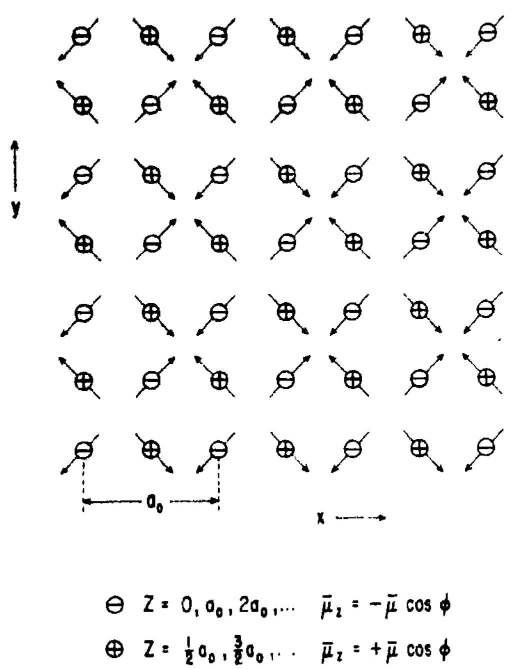
y
x
a_0
⊖ $Z = 0, a_0, 2a_0, \ldots$ $\bar{\mu}_z = -\bar{\mu} \cos\phi$
⊕ $Z = \frac{1}{2}a_0, \frac{3}{2}a_0, \ldots$ $\bar{\mu}_z = +\bar{\mu} \cos\phi$

FIG. 5. General set of tetragonal antiferromagnetic structures based on f.c.c. atomic cell of disordered $(Ni,Fe)_3Mn$ alloys. Moment vectors (of magnitude $\bar{\mu}$) shown in projection on basal (xy) plane.

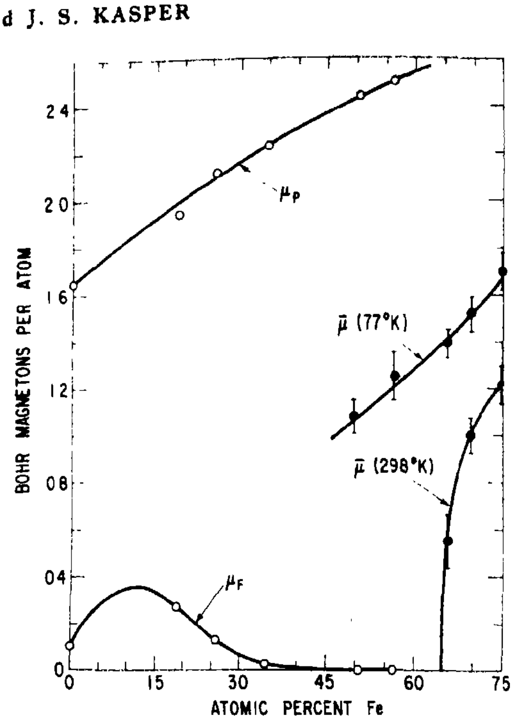

FIG. 6. Average atomic moment ($\bar{\mu}$) obtained from neutron diffraction data at 77 and 298°K, ferromagnetic and paramagnetic moments (μ_F and μ_P, respectively) obtained from Ref. 1, as functions of iron concentration in $(Ni,Fe)_3Mn$ alloy series.

dimensions of the cubic atomic cell, the magnetic symmetry for arbitrary ϕ is tetragonal (the z-axis in Fig. 5 being the unique axis). It is obvious that for $\phi = 0$ and $\phi = \cos^{-1}(1/\sqrt{3})$ the magnetic configuration reduces to those shown in Figs. 4(a) and 4(b), respectively. In general, the neutron diffraction intensities for each of the following groups of reflections: (110) (101) (011), (201) (210) (102) and (112) (211) (121), are predicted to be in the ratio of $\cos^2\phi : \frac{1}{2}\sin^2\phi : \frac{1}{2}\sin^2\phi$. Hence, if there is no detectable tetragonal distortion of the atomic structure, as in the $(Ni,Fe)_3Mn$ alloys, the reflections within each of these groups will merge and their total intensity will be invariant with ϕ.

It should also be noted that the total exchange energy for the antiferromagnetic configuration in Fig. 5 is independent of the angle ϕ if this energy is taken to be the sum of isotropic interactions of the form $J_{ij}\mathbf{S}_i \cdot \mathbf{S}_j$ where the exchange coefficient J_{ij} depends only on the distance between the ith and jth atoms. Since this statement is particularly valid when the atomic structure is cubic, which appears to be the case for the $(Ni,Fe)_3Mn$ alloys, it follows that this simple exchange energy consideration does not favor any particular value of ϕ for the magnetic structures of these alloys.

Fortunately, the determination of the average atomic moments of our $(Ni,Fe)_3Mn$ alloy specimens does not depend on the choice of ϕ. For any value of this angle and for a given magnetic moment, the antiferromagnetic structure shown in Fig. 5 gives rise to the same magnetic reflection intensities in the neutron diffraction pattern. In our data for each of these alloys, the (110) reflection was the only magnetic reflection ever strong enough to be measured with reasonable accuracy. Normalizing its intensity to those of the nuclear reflections associated with the disordered f.c.c. lattice (for Fe_3Mn, using only reflections not overlapped by those of the ϵ-phase), we evaluated the average magnetic moment $\bar{\mu}$ at both 77 and 298°K.

The $\bar{\mu}$ values thus obtained are plotted vs. alloy composition in Fig. 6; the estimated uncertainty in each $\bar{\mu}$ value is indicated. The disappearance of the average moment evaluated at 298°K for (Ni,Fe)$_3$Mn compositions having less than about 65 at. per cent Fe simply reflects the fact that their Néel temperatures fall below 298°K, consistent with the T_N values shown in Fig. 2. However, since the Néel temperatures of all our alloy specimens are much higher than 77°K, the values of $\bar{\mu}$ obtained at this lower temperature are almost certain to be very nearly equal to the moment values at 0°K.

It is clear from Fig. 6 that $\bar{\mu}$ (77°K) decreases almost linearly from about 1·7 to 1·1μ_B as the composition of this (Ni,Fe)$_3$Mn alloy series is changed from 75 to 50 at. per cent Fe. If it is assumed that the atomic moments of Fe, Ni and Mn in all these alloys are fixed in magnitude and that they contribute additively to $\bar{\mu}$, the observed change of $\bar{\mu}$ with composition would require that the atomic moment of Fe exceed that of Ni by about 2·5μ_B. This difference in moment seems quite excessive especially since it is even larger than the average moment of the Fe$_3$Mn alloy, in which the moment of Fe is probably smaller than that of Mn. Moreover, since unreasonably large changes in the atomic moments of Fe, Ni and Mn would have to be evoked in order to justify this abnormally large composition dependence of $\bar{\mu}$, we believe that it must be attributed at least in part to a gradual disordering of the antiferromagnetic structure with decreasing iron concentration.

In Fig. 6 we have also plotted the values for the low-temperature ferromagnetic moment (μ_F) and for the paramagnetic moment (μ_P) recently reported for these (Ni,Fe)$_3$Mn alloys.(1) Although the smallness of μ_F compared to μ_P was only a minor part of the evidence offered for a mixed ferromagnetic–antiferromagnetic state in the alloys of low Fe concentration, the contrasting variations of μ_F and μ_P with composition (together with the composition dependence of θ shown in Fig. 2) were very important in defining the different couplings responsible for this state. Specifically, it was concluded that the nearest-neighbor interactions between Mn–Mn and Fe–Mn atom pairs are antiferromagnetic and that those between Ni–Ni, Ni–Mn and Ni–Fe pairs are ferromagnetic; the only decision reached on the Fe–Fe interactions was they cannot be strongly ferromagnetic. On this basis, it is reasonable to expect that in the alloys of sufficiently high iron content the antiferromagnetic interactions are so predominant in concentration that they extend into all parts of the material, thereby preventing the ferromagnetic–antiferromagnetic inhomogeneity that exists in the more Ni-rich alloys and generating instead a long-range antiferromagnetic structure of the type indicated by our neutron diffraction data. It also follows, however, that this long-range antiferromagnetic order would not be perfect but would gradually improve as the nickel content of the alloys is reduced to zero, which we also concluded from the composition dependence of $\bar{\mu}$ (77°K) shown in Fig. 6.

Furthermore, in the Fe$_3$Mn composition the antiferromagnetic ordering can be expected to be essentially perfect as long as the short-range Fe–Fe interactions in this alloy are antiferromagnetic, even though they may be only weakly so. The average moment of about 1·7μ_B obtained from our neutron diffraction data on this alloy would then represent a simple weighted sum of the atomic moments of iron and manganese (μ_{Fe}, μ_{Mn}). Setting μ_{Mn} equal to 3 or 4μ_B, which are approximately the μ_{Mn} values in the ordered alloys Ni$_3$Mn(8) and NiMn,(3) we find that μ_{Fe} is about 1·3 or 0·9μ_B, respectively. Although these μ_{Fe} values are considerably less than the 2·2μ_B of ferromagnetic b.c.c. iron, it is more pertinent that they are fairly close to the atomic moment of 0·7μ_B recently determined for the low-temperature antiferromagnetic structure of iron retained in f.c.c. form as a fine-particle precipitate in copper.(9) The collinear magnetic configuration deduced from this neutron diffraction work on γ-Fe is a simple variant of the γ-Mn configuration shown in Fig. 4(a), in which the moments are inclined at about 19° from the (001) axis; its Néel temperature was estimated to be about 8°K. The fact that the Néel temperature of disordered Fe$_3$Mn is so much higher is probably to a large extent the result of very strong antiferromagnetic interactions between manganese and its neighboring atoms. However, as indicated by recent pressure experiments on Fe–Ni alloys,(10) the possibility that antiferromagnetic interactions between iron atoms may be stronger in some f.c.c. alloys than in the pure f.c.c. element cannot be discounted.

Acknowledgements—We are very grateful to A. ABRAHAMSEN and H. N. TREAFTIS for their assistance in the neutron diffraction experiments and electrical resistivity measurements, respectively.

REFERENCES

1. KOUVEL J. S., *J. Phys. Chem. Solids* **16**, 152 (1960).
2. KOUVEL J. S. and GRAHAM C. D., Jr., *J. Phys. Chem. Solids* **11**, 220 (1959).
3. KASPER J. S. and KOUVEL J. S., *J. Phys. Chem. Solids* **11**, 231 (1959).
4. HANSEN M., *Constitution of Binary Alloys*. 2nd ed. pp. 664–667. McGraw-Hill, New York (1958).
5. SEDOV V. L., *Sov. Phys. JETP* **15**, 88 (1962).
6. KOUVEL J. S. and KASPER J. S., *Bull. Amer. phys. Soc.* **5**, 456 (1960).
7. BACON G. E., DUNMUR I. W., SMITH J. H. and STREET R., *Proc. Roy. Soc.* **A241**, 223 (1957).
8. SHULL C. G. and WILKINSON M. K., *Phys. Rev.* **97**, 304 (1955).
9. ABRAHAMS S. C., GUTTMAN L. and KASPER J. S., *Phys. Rev.* **127**, 2052 (1962).
10. KONDORSKY E. I. and SEDOV V. L., *J. appl. Phys. Suppl.* **31**, 331 (1960); KOUVEL J. S. and WILSON R. H., *J. appl. Phys.* **32**, 435 (1961).

J. Phys. Chem. Solids Pergamon Press 1963. Vol. 24, pp. 537–548. Printed in Great Britain.

EFFECTS OF REACTOR RADIATIONS ON THE CHEMISORPTION EQUILIBRIUM OF OXYGEN ON NICKEL OXIDE

I. MAXIM and T. BRAUN

Institute of Atomic Physics, Bucharest, Rumania

(*Received* 7 *September* 1962)

Abstract—On irradiating non-stoichiometric nickel oxide—in vacuum—in a nuclear reactor, it was found that the amount of surface oxygen (determined by iodometric titration) increases. The greater the initial non-stoichiometry of the irradiated oxide, the greater this increase. The catalytic activity of the nickel oxide in the decomposition of hydrogen peroxide also increases as a consequence of the irradiation. The radio-induced effect is annealed after a thermal treatment. The activation energy of this annealing process is 0·8 eV. Both the appearance and annealing of the effect observed are explained on basis of the presence, on the nickel oxide surface, of some weakly bound forms of oxygen, in keeping with Wolkenstein's theory.

1. INTRODUCTION

1.1. THE effect of ionizing radiations on the adsorption process of oxygen on oxidic semiconductors has been investigated in both experimental(1, 2, 3) and theoretical(5, 4) studies. The possibility of modifying the kinetics and the adsorption equilibrium has been proved in these works.

Thus, by irradiating Cr_2O_3, pure or supported on Al_2O_3 or SnO_2, in the nuclear reactor in an oxygen atmosphere it was found that(1) the amount of chemisorbed oxygen increases while in the case of irradiation in vacuum a small desorption could be observed. Other authors(2, 3, 4) have been able to make evident the change in the kinetics of hydrogen and iso-butylene adsorption and oxygen desorption on ZnO during gamma irradiation from a ^{60}Co source.

1.2. WOLKENSTEIN(5) demonstrated in a recent theoretical work that irradiation with ionizing radiations may modify both the kinetics and the adsorption equilibrium of gases on semiconductors. The absolute magnitude and sense of displacement of the equilibrium will depend on the electronic affinity of the gas and on the initial position of the Fermi level for the semiconductor subjected to irradiation. The Fermi level is determined, in its turn, by the sample history, by the gas pressure and the temperature. The effect of irradiation for the same system can be, as a function of the above conditions, either an adsorption or a desorption of the gas.

1.3. It is the object of this work to report on the detailed study of some of the above-mentioned problems, in the case of the oxygen–nickel oxide system. This model system was chosen on account of the possibility of preparing nickel oxide samples with various concentrations of oxygen initially adsorbed on the surface, and also because of the possibility of determining this concentration relatively simply.

These investigations may also contribute to a better understanding of the mechanism of nuclear radiation effects on the catalytic properties of oxidic semiconductors.

2. EXPERIMENTAL

2.1. *Preparation of samples*

Nickel oxide samples of various stoichiometries were obtained by 5 hr pyrolysis of Riedel de Haen A.R. grade $NiCO_3$. The pyrolysis temperatures were 300, 400, 500, 600, 700 and 1000°C. The decomposition process of the initial $NiCO_3$ was followed by means of differential thermal analysis

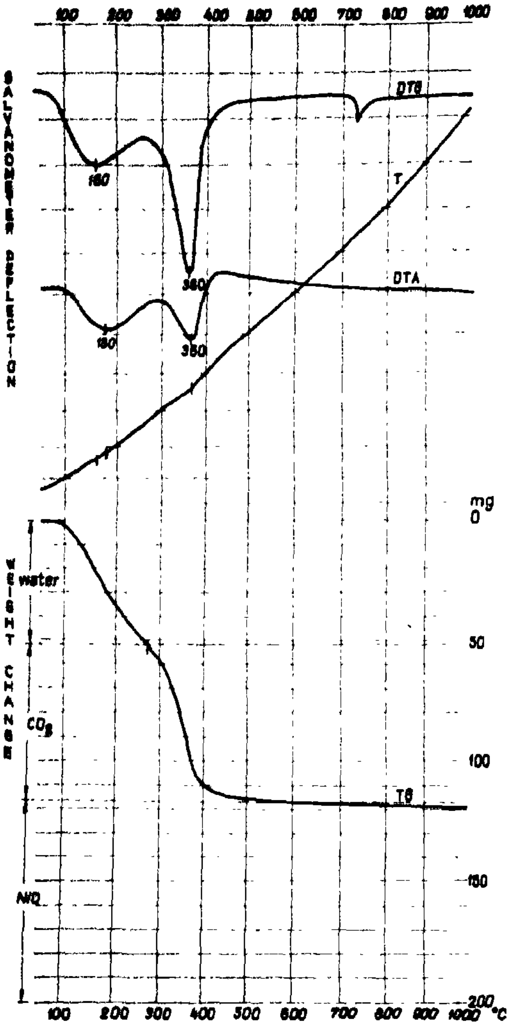

Fig. 1. Derivatogram of NiCO$_3$ decomposition: DTG = Derivated thermogravimetric curve; TG = Thermogravimetric curve; DTA = DTA curve; T = Temperature curve.

and thermogravimetry, using a Paulik–Paulik–Erdey (Orion–Gyem, Hungary) type "Derivatograph". The derivatogram of the NiCO$_3$ decomposition recorded in the 20–1000°C temperature range is shown in Fig. 1.

2.2. *Determination of the non-stoichiometry*

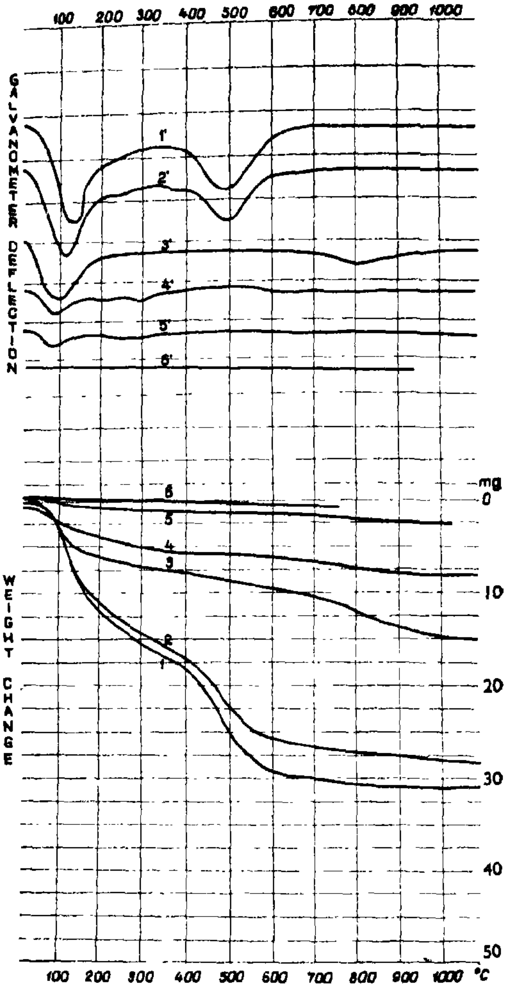

Fig. 2. Derivatograms of the NiO samples of various non-stoichiometries.

1:1', Thermogravimetric and derivative thermogravimetric curves for NiO obtained by pyrolysis of NiCO$_3$ at 300°C.

2:2', *Idem* for 400°C.
3:3', *Idem* for 500°C.
4:4', *Idem* for 600°C.
5:5', *Idem* for 700°C.
6:6', *Idem* for 1000°C.

The non-stoichiometry of the various NiO samples was determined in two ways:

(a) By the iodo-amperometric method described in the previous paper.(1)

(b) By thermo-gravimetry

By iodometric titration, in fact, the amount of Ni^{3+} is determined. The result is nevertheless expressed in per cent atoms of oxygen in excess, considering that two Ni^{3+} ions correspond to one ion of O^{2-}. By thermogravimetry, the weight of the non-stoichiometric oxygen is obtained directly.

It was found that by recording the derivatograms of the NiO samples of various stoichiometries in the 20–1000°C range, the curves have the aspect shown in Fig. 2.

It can be seen in the figure that most of the thermogravimetric curves have two plateaus reflecting the presence of two processes: the one at low temperatures (about 100°C) is due to the evaporation of the physically bound water, the other occuring at increasingly higher temperatures as a function of the sample preparation temperature, reflects the desorption of the non-stoichiometric oxygen. It was possible to calculate the amount of excess oxygen from the thermogravimetric curve.

Table 1

Preparation temperature of NiO (°C)	300	400	500	600	700
Excess oxygen at. per cent iodometric	1·2	0·9	0·5	0·3	0·07
Excess oxygen at. per cent thermogravimetric	13·6	9·5	5·7	1·9	0·5
$\frac{\text{Excess oxygen at. per cent iodometric}}{\text{Excess oxygen at. per cent thermogravimetric}}$	11·3	10·5	11	6	7

The results of the determination of non-stoichiometry by the two procedures for the case of our series of samples are shown in Table 1.

As it can be seen from Table 1 there are noticeable differences between the results obtained by the two procedures. More will be said hereafter about these differences.

2.3. *Catalytic activity determination in the* H_2O_2 *decomposition*

The catalytic activity of the samples was determined by using the decomposition of H_2O_2 as a model reaction. The apparatus used was identical to the one described in Ref. 1. The working temperature was 40°C and the H_2O_2 concentration 3 per cent.

2.4. *Irradiation of samples*

The irradiation was performed both in the humid and in the dry channels of the VVR-S 2 MW reactor of the Institute for Atomic Physics, Bucharest. In the case of irradiation in oxygen atmosphere or in vacuum, quartz ampoules were used, the technique of ampoule filling being identical to the one described in Ref. 1. The temperature during irradiation did not exceed 60°C. In order to follow the influence of temperature on the radio-induced effect, irradiations were also made at the temperature of 100°C, a small electric oven being used to heat the sample during irradiation.

2.5. *Thermal treatment*

In view of determining the stability of the effect, the samples were submitted to an isothermal treatment, with the aim of following the annealing of the radio-induced effect. The treatment was repeated at various temperatures in the 60–90°C range. This treatment was performed in a thermostat accurate within ± 0·1°C.

3. RESULTS

3.1. *Irradiation of* NiO *of various non-stoichiometries in oxygen atmosphere*

The samples were irradiated in quartz ampoules filled with oxygen at atmospheric pressure. The flux of fast neutrons was 7×10^{12}n cm^{-2} sec^{-1} that of thermal neutrons $1{\cdot}5 \times 10^{13}$n cm^{-2} sec^{-1}.

Table 2

Preparation temperature of NiO (°C)	300	400	500	600	700
Excess oxygen at. per cent iodometric					
Before irradiation	1·2	0·9	0·5	0·3	0·07
After irradiation	2.2	1·7	0·8	0·4	0·07
$\mu = \dfrac{\text{After irradiation}}{\text{Before irradiation}}$	1·8	1·6	1·6	1·3	1

The results obtained in the case of samples of various non-stoichiometries are tabulated in Table 2.

3.2. *Irradiation of* NiO *of various non-stoichiometries in vacuum*

The samples were irradiated in quartz ampoules evacuated at room temperature down to 10^{-3} mm Hg. The fluxes were the same as in 3.1.

A previous checking was made, to ensure that the non-irradiated evacuated samples had not modified their non-stoichiometry.

The results obtained after irradiation are tabulated in Table 3.

3.3. *Variation of radio-induced non-stoichiometry with radiation flux*

In order to determine the extent to which the radio-induced non-stoichiometry varies as a function of the radiation flux, three samples were irradiated in three different positions with respect to the active zone of the reactor.

The time of irradiation was the same in the case of the three samples, only the flux of neutrons was different and, obviously also the integral fluxes.

The results are shown in Table 4.

3.4. *Kinetics of the annealing process*

The curves showing the kinetics of the annealing process at temperatures ranging between 65 and 87·5°C are presented in Fig. 3.

The quantity $Y = x_t - x_0/x_t - x_0$, which represents the relative value of the radiation effect left over after a time t of thermal treatment is given in the ordinate.

Table 3

Preparation temperature of NiO (°C)	300	400	500	600	700
Excess oxygen at. per cent iodometric					
Before irradiation	1·2	0·9	0·5	0·30	0·07
After irradiation	2·1	1·7	0·8	0·36	0·07
μ as in Table 2	1·7	1·7	1·6	1·2	0·9

Table 4

Flux ncm^{-2} sec^{-1}		Excess oxygen at. after irradiation	μ as in Table 2
Fast neutrons	Thermal neutrons		
7×10^{17}	$1·5\times10^{18}$	2·2	1·8
$9·3\times10^{16}$	2×10^{17}	1·7	1·4
$3·8\times10^{16}$	$8·2\times10^{16}$	1·3	1·08

The excess oxygen (determined iodometrically) before irradiation, after irradiation and, respectively, after a time t (min) of thermal treatment is represented by x_0, x_i and x_t. It is clearly seen from the figure that the effect of irradiation is quite unstable. It is totally annealed at the temperature of about 90°C after approximately 180 min.

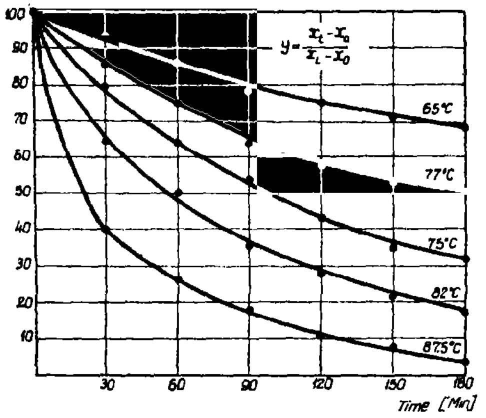

FIG. 3. Variation of the value $Y = (x_t - x_0)/(x_i - x_0)$ with the time of the isothermal treatment.

x_0 = Amount of non-stoichiometric oxygen before irradiation. x_i = Amount of non-stoichiometric oxygen after irradiation. x_t = Amount of non-stoichiometric oxygen after the time t of thermal treatment.

3.5. *Influence of the irradiation of non-stoichiometric* NiO *on its catalytic activity in the* H_2O_2 *decomposition*

The kinetic curves of the H_2O_2 decomposition on an unirradiated (curve B), respectively irradiated (curve A), NiO catalyst are plotted in Fig. 4.

The influence of the thermal treatment of the irradiated catalyst on its catalytic activity was investigated in a series of experiments.

The curves representing the change of radio-induced non-stoichiometry (curve A) and of catalytic activity (curve B) as a function of time in the case of an isothermal treatment at the temperature of 82°C are plotted in Fig. 5.

4. DISCUSSION OF RESULTS

4.1. It can be seen from the analysis of the experimental results reported, that the irradiation of the NiO in the reactor has as a consequence the increase of the amount of oxygen (determined iodometrically) chemisorbed on the surface.

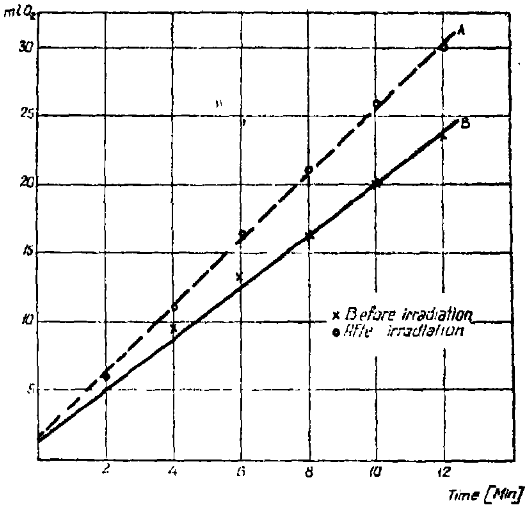

FIG. 4. Amount of oxygen liberated vs. time in H_2O_2 decomposition. A, Decomposition by unirradiated NiO catalyst; B, Decomposition by irradiated NiO catalyst.

Several hypotheses can be suggested in view of explaining this phenomenon:

(a) The radiochemisorption of gaseous oxygen on the surface of NiO, similar to the case of Cr_2O_3,(1) can explain the appearance of the

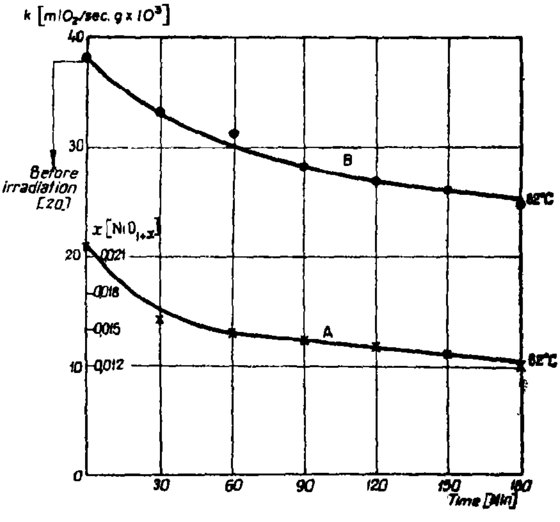

FIG. 5. Reaction rate, k, of H_2O_2 decomposition and non-stoichiometry, x, of NiO_{1+x} vs. time of isothermal treatment at 82°C.

phenomenon in the case of irradiation in oxygen atmosphere. This hypothesis cannot, however, explain why the phenomenon appears in the case of irradiations in vacuum.

As can be seen in Table 3, the amount of chemisorbed oxygen following the irradiation in vacuum is approximately equal to the one chemisorbed on irradiation in an oxygen atmosphere. A simple calculation shows that even if one admitted that the oxygen still present in the ampoules after evacuation at 10^{-2} mm Hg has been integrally radiochemisorbed on the sample surface, its amount is much smaller than the one determined experimentally.

Hence, although the radiochemisorption of the gaseous oxygen is not excluded it nevertheless cannot, in the present case, explain the phenomenon observed.

(b) *The existence of a "post-effect" might* explain the appearance of the phenomenon in the case of irradiation in vacuum. It is well known that irradiation produces transformations in the structure of solids and it might be possible that these transformations, in our case, could generate a potentially metastable state favourable to the oxygen adsorption. Owing to this fact, after irradiation, when the oxide comes in contact with atmospheric oxygen a marked adsorption could occur. In order to verify this hypothesis, samples containing accurately weighed amounts of NiO were irradiated in vacuum. After irradiation the ampoules were opened under water (in the solution of potassium iodide in which non-stoichiometry was determined iodometrically).

Thus, after irradiation, the surface of the sample no longer comes in contact with the air and hence, in this case, the post-effect could no longer appear. The results showed, however, that under these conditions the effect of irradiation appeared with the same intensity.

(c) It is shown by the analysis of the derivatograms shown in Fig. 2, that the irradiated NiO samples contain at their surface a certain quantity of water (adsorbed physically), this quantity being larger the lower the preparation temperature of the sample. It is, on the other hand, well known[6] that the radiolysis of the liquids adsorbed on the surface of solids is much greater than that of the respective liquids in a non-adsorbed state. Since from the radiolysis of water there also results atomic oxygen, it could be possible for the chemisorbed oxygen to originate from this source. In order to verify this hypothesis the water at the surface of the samples was removed by evacuation and heating at 300°C for 1 hr. Then, the quartz ampoules in which the treatment was performed were sealed under vacuum and then irradiated. The increase in the quantity of oxygen chemisorbed consequently to irradiation was approximately the same as for untreated samples. Therefore the radiolysis of water does not constitute the main source of oxygen.

(d) Under the action of nuclear radiations, atom displacements occur in the crystalline lattice of semiconductors. If an oxygen atom is displaced, owing to its large volume it cannot be accommodated in the interstice but falls into a vacancy, it accumulates in pouches, or leaves the solid, passing into the gaseous phase. Since, in this paper, a desorption of oxygen as a consequence of irradiation was not recorded, this process cannot have made a very large contribution. When, however, a nickel atom is displaced, it can remain in the interstice, as Ni^0, leaving a vacancy in the lattice. To restore the local electrical equilibrium after such a process, two ions of Ni^{2+} from the lattice will have to pass into the Ni^{3+} form. This state will be metastable, hence when the lattice receives energy (thermal treatment) the recombination of the interstitial with the vacancy will occur, a fact which will also lead to the disappearance of the Ni^{3+} ions. As can be seen, this mechanism could explain both the appearance of the phenomenon and the process of thermal annealing. We should, however, notice that if this mechanism is correct, the phenomenon should not be dependent on the sample preparation temperature. As it can, however, be seen from Table 2, the magnitude μ which characterizes the effect of irradiation is dependent on this temperature. It could, however, happen that this dependence is only caused by the different specific surface of the samples, the more so since by the iodometric procedure used in this work only the surface non-stoichiometry is determined (see Refs. 7 and 8 for details).

The following experiment was performed in order to eliminate the influence of the sample surface size: the $NiCO_3$ was decomposed in ampoules evacuated at 300 and 400°C ($p = 10^{-2}$ mm Hg), samples of NiO without chemisorbed oxygen on their surface being thus obtained, the samples having, however, a large specific surface. These samples sealed under vacuum into ampoules were irradiated in the same conditions as those of NiO obtained by the CO_3Ni pyrolysis in air.

In the case of these samples the phenomenon no longer appeared, hence the hypothesis of the displacement of atoms cannot explain the appearance of the radio-induced phenomena.

(e) The existence of several forms of oxygen chemisorbed on the surface, among which only some are detectable by iodometric titration, could explain the appearance of radio-chemisorption, by displacement of the equilibrium in favour of the form iodometrically detectable.

We believe that the forms physically adsorbed should not be taken into consideration when discussing the mechanism since the phenomenon of radiochemisorption observed also appears in the case of the samples evacuated at 300°C, a treatment which practically removes the whole amount of physically adsorbed oxygen. Consequently, we shall hereafter only consider the chemisorbed forms of oxygen. At present, there are two theories which endeavour to explain the phenomenon of chemisorption on semiconductors starting from the relationship between their electronic and adsorptive properties.

The electronic theory of adsorption, elaborated and developed by WOLKENSTEIN(9) asserts that the particles chemisorbed on the surface of a semiconductor may be found in three forms: neutral N^0 (weakly bound), in the form of electropositive N^+ ions and in the form of electronegative N^- ions (both forms being strongly bound). The weak form of the bond is achieved without the participation of the free carriers of the adsorbant lattice, while its strong form, with their participation.

The theory promoted by a series of other authors,(10) known under the name of "Randschichttheorie der Chemisorption", ignore the existence of the weak form, only taking into consideration the strong forms, i.e. the ionic forms. In other words these authors understand by chemisorption, exclusively "ionosorption".

Experimental facts seem, however, also to point to the existence of the weak form. It appears that the phenomena made evident in this paper, in the case of NiO irradiation, can be explained in the most satisfactory manner on the basis of the existence of this form and of its passage to the strong form under the action of the radiations.

The analysis of the data in the literature, about the non-stoichiometry of nickel oxide, indicated a disagreement between the results obtained by different methods. Thus, in YIDA's paper(11) a disagreement stands out between the amounts of excess oxygen determined by the reduction of NiO with hydrogen at 700°C (gravimetric method) and the one determined by iodometric titration as shown in Table 5.

The calculation of the amount of excess oxygen starting from the value of Ni^{3+} was performed on basis of the formula $Ni^{2+}_{1-2\delta}\,Ni^{3+}_{2\delta}\,O_{1+\delta}$.

It can be seen from Table 5 that the excess oxygen determined by the reduction with hydrogen is 6–20 times larger than the one determined iodometrically. Generally, all the authors who

Table 5

Preparation temperature of NiO (°C)	400	500	600	700	800
Excess oxygen at. per cent By hydrogen reduction	10·0	4·0	1·0	—	—
Ni^{3+} at. per cent By iodometry	1·07	0·41	0·31	0·27	0·11
Excess oxygen at. per cent calculated from iodometric Ni^{3+}	0·5	0·205	0·155	0·135	0·055
Excess oxygen at. per cent By reduction ——— Excess oxygen at. per cent By iodometry	20·0	19·0	6·4	—	—

determine the non-stoichiometry by the method of reduction with hydrogen(11, 12) or electrogravimetrically,(8) hence by a gravimetric method, find for the NiO obtained through the pyrolysis of its salts in the 300–600°C temperature range, a value of the non-stoichiometry 5–20 times larger than the one determined by the iodometric method.(8, 11) In this work the determination of the surface non-stoichiometry (oxygen chemisorbed on the surface) was performed both iodometrically and thermogravimetrically. The thermogravimetric curves of Fig. 2 show that one of the processes occurs in the case of all the samples, whatever be their preparation temperature, in the same temperature range, and consists in the elimination of the water physically adsorbed on the surface. In the case of the second process, it can be seen on the curve that it begins at a temperature somewhat higher than the preparation temperature of the sample and consists in the desorption of the oxygen adsorbed on the surface. Having in view the high temperature at which the second process occurs, the contribution of the oxygen physically adsorbed is negligible.

By comparing the results obtained for the non-stoichiometric oxygen, by thermogravimetry on the one hand, by iodometry on the other hand, it can be seen that the gravimetric procedure yields results approximately ten times larger than the procedure by titration. This great difference cannot be due to experimental errors but only to the fact that there are, on the surface, several forms of chemisorbed oxygen, of which only part are revealed by titration. Owing to the strong electronegativity of oxygen, out of the three possible forms of chemisorption, only the weakly adsorbed form N^0 and the strongly negative form N^- appear. By iodometric titration the ion I^- is oxidized to I^0 by the ion Ni^{3+} which passes to Ni^{2+}. But Ni^{3+} only appears in the lattice if Ni^{2+} loses another electron, which is trapped by the chemisorbed oxygen. The appearance of Ni^{3+} means the modification of the number of free carriers in the lattice, hence the form of adsorption which could lead to this modification can only be the strong negative adsorption.

The weak adsorption does not cause the appearance of Ni^{3+}, hence it is not observed by iodometric titration. Hence, by the iodometric method, only the strongly negative adsorption form is determined, while by the gravimetric procedures (reduction with hydrogen, electrogravimetry, thermogravimetry) both the strong and the weak form are determined. This seems to be the cause leading to such different results through the two methods.

In his considerations regarding the influence of external factors on the adsorption equilibrium, WOLKENSTEIN(9) assumes the case of a non-degenerate semiconductor with a small degree of surface covering. Under these conditions and for a constant pressure, the number of weakly adsorbed particles is not influenced by the external agent (e.g. irradiation), i.e. $N_0^0 = N^0$ (N_0^0 = number of weakly adsorbed particles, before irradiation; N^0 = number of weakly adsorbed particles, after irradiation). In the case where, in this work also, we find ourselves in similar conditions (it should be mentioned that even if this were not the case, the error is not large, particularly for a qualitative analysis of the phenomenon), then, by irradiation of the NiO only, the number of particles strongly adsorbed from N_0^- (before irradiation) to N^- (after irradiation) is modified. The ratio $\mu = N^-/N_0^-$ will characterize the effect of the radiations. The sign and the absolute magnitude of μ will be determined by the position of the Fermi level in the initial sample.(5) It can be seen from Table 2 that, for all the samples we have used, μ is greater than unity (the equilibrium moves towards the strongly negative form).

The increase in the amount of chemisorbed oxygen experimentally observed, is the result of the radiative displacement of the adsorption equilibrium, i.e. of the passing of the weak form into the strong form.

4.2. The particle weakly chemisorbed on the semiconductor surface creates a full donor level and an empty acceptor level.

The electrons from the conduction or from the valence bands can reach the acceptor level. In this case the acceptor level is partially filled and the particle passes from the weak to the strong acceptor form. The electrons from the donor level can reach the conduction or the valence bands, the level becoming partially empty, the particle passing from the weak to the strong donor form. After the adsorption equilibrium is established the donor and the acceptor levels are filled to a certain degree which is dependent on the characteristics of the gas, on the nature of the semiconductor, and on the temperature.

If the concentration of the free carriers is changed by any means whatever (irradiation, injection of carriers, etc.), the surface levels generated by the adsorbed particles will then become centres of recombination in the case when the incoming rate of electrons is equal to the incoming rate of holes.(13) In this case the degree of filling of the level remains unchanged and consequently no change in the adsorption equilibrium will take place. If, however, the incoming rate of electrons to the level is much greater than those of holes, then the level will become trapping centre for electrons and consequently its degree of filling will also change and the adsorption equilibrium will be displaced in favour of the strong acceptor form.

In the case of irradiation of the NiO in the reactor field the NiO is strongly ionized, while electrons and holes are formed. These are consumed by direct or indirect recombination, in addition electrons are also consumed by the trapping process on the surface acceptor levels of the weakly chemisorbed oxygen, an equivalent number of holes appearing in the valence band. Through the trapping of the electrons the degree of filling of the acceptor level is increased and the weak form passes into the negative strong form. The radiochemisorption of hydrogen and of isobutylene on ZnO(3) is likewise explained by a mechanism of trapping. In this case, trapping of the holes occurs on the hydrogen and isobutylene molecules adsorbed on the surface. Here, too, it is a question of passing from the weak to the strong form of chemisorption, though the authors do not explain this phenomenon by using the adsorption theory suggested by Wolkenstein. The same authors also describe the desorption of oxygen in the case of the irradiation of ZnO with chemisorbed oxygen on its surface.(2) In this case the partially full acceptor level of the oxygen constitutes traps for holes, the degree of filling decreases, and the strong form passes into the weak one and then, probably, the bond is completely broken with the oxygen passing into the gaseous phase (which causes an increase of the ZnO conductivity).

In conclusion, the displacement of the adsorption equilibrium, due to irradiation, depends on the part played by the surface levels associated with the chemisorbed particles. If these levels are recombination centres the equilibrium remains unchanged, while if they are trapping centres of the minority carriers the equilibrium is modified either in the direction of the strong forms (adsorption), or towards the weak forms (desorption).

4.3. The magnitude and sense of the radio-induced effect depends on the initial state of the sample, on the gas pressure, on the temperature of the system during irradiation and, obviously, on the type of radiations.

a. Initial state of sample. As described in the experimental part the NiO samples used, were obtained by pyrolysis of the CO_3Ni at temperatures ranging between 300 and 1000°C. These samples differed from one another through the quantity of oxygen adsorbed and through the specific area.

It can be seen from Table 2 that the sign of the effect remains unchanged but its size varies as a function of the preparation temperature of the samples, i.e. as a function of the initial amount of oxygen chemisorbed, the effect being a maximum in the case of the maximum quantity of oxygen present on the surface.

b. Gas pressure. The pressure of the oxygen in the interval 10^{-2}–760 mm Hg has no influence that can be recorded by the measuring procedures used in this work. The irradiations in oxygen, respectively in vacuum (10^{-2} mm Hg) yield the same results.

This fact is probably due to the large initial concentration of oxygen weakly bound on the surface and to its independence on pressure at low temperatures. Actually, DEREN *et al.*(8) show that the oxygen present on the surface of the NiO (whatever the form of binding) is not desorbed by evacuation at temperatures below 300–400°C.

Therefore, in the case of NiO, the concentration of the weak form N^0 is not dependent on the pressure and hence, the relation $N_0^0 = N^0$ suggested by WOLKENSTEIN(9) does not hold. But the variation of N^0 through irradiation is one order of magnitude smaller than N_0^0, so that one may consider $N_0^0 \simeq N^0$ and hence maintain the relations resulting therefrom.

c. Temperature. The temperature of the system during irradiation has a strong influence on the effect observed. This influence is due to the fact that a great part of the effects achieved by irradiation are unstable or metastable. If the radiation tends to displace the equilibrium in the direction of these states, the temperature will tend to bring the system back to its initial state of equilibrium. The result of irradiation will, in fact represent the result of the competition between the two processes. The higher the temperature, the smaller the effect of irradiation. This effect is also made clear in BARRY's work,(2) where he establishes that the desorption of the oxygen on the ZnO during irradiation with γ-radiations, only occurs at temperatures below room temperature. Irradiation above 50°C no longer produces any noticeable effect.

In this work the irradiations were performed in the 40–50°C range. An irradiation performed at 100°C showed that the effect noticed at lower temperatures ceases to appear at this temperature.

4.4. After interrupting irradiation, the process of thermal annealing continues at a rate which is dependent on the temperature at which the sample is stored.

In the case of a sample stored for several months at the temperature of 28–30°C, an annealing in the ratio of $\sim$ 40 per cent was observed. Since a study of the annealing process can give indications of the size of the radio-induced effect, the irradiated samples were subjected to an isothermal annealing treatment, the curves in Fig. 3 being obtained. The plotting of these data in the system of coordinates $\log Y = f(t)$ in Fig. 6 points to a process of the first order. The activation energy of the annealing, calculated according to these curves on basis of the Arrhenius equation, yielded the value of 0·9 eV (Fig. 7). A VAND–PRIMAK treatment(14) was also applied to the annealing process. A spectrum of activation energies distributed in a 0·07 eV wide range was found, having a single maximum at 0·71 eV. A rather close value, 0·79 eV, was also obtained by applying the formula:

$$E_{\text{act.}} = 25\, kT_{\text{max}}.$$

suggested for the phenomena of luminescence(15) and used by GIBSON(16) to estimate the emission of exo-electrons from iron oxide catalysts irradiated with γ-rays.

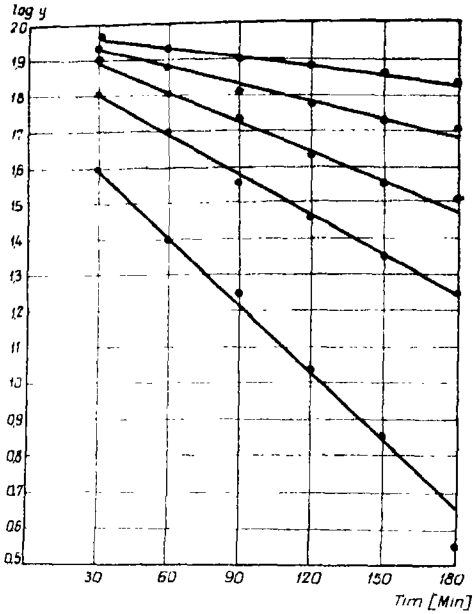

FIG. 6. Variation with time of the logarithm of the fraction $Y = (x_t - x_0)/(x_t - x_0)$.

By comparing these three values, one obtains for the activation energy of the annealing process a value of approximately 0·8 eV. In accordance with the mechanism of the radio-chemisorption process, assumed by us in (4.1) the annealing process would consist of the passing of the electron

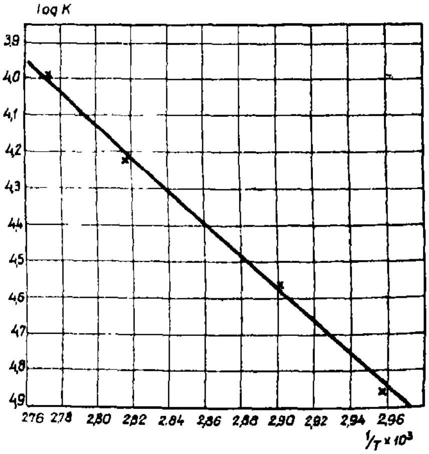

FIG. 7. Logarithm of the apparent rate constant as a function of the absolute temperature.

from the acceptor level of the oxygen in the valence band, respectively the trapping on this level of the hole from the valence band, and its recombination with the electron. Consequently, the degree of filling of the level decreases, the oxygen passing from the strong to the weak form. As a result, the electrical conductivity of the sample should decrease. The electrical phenomena which might accompany the effects studied above will be investigated in a subsequent paper.

It was assumed in the above description that the oxygen is radio-chemisorbed on the NiO, increasing the relative quantity of the strong form existing before irradiation at a greater value than the the one corresponding to equilibrium. However, the possibility is not excluded either, for other forms of strongly chemisorbed oxygen of lower stability—which did not exist on the non-irradiated sample—to appear also, this lower stability causing their disappearance when the temperature increases. The existence of several forms of negative oxygen ions adsorbed on the surface is discussed in the literature.(17, 18) In fact the existence of several types of negative oxygen ions chemisorbed on the surface, O_2^-, O^-, O^{2-}, means that the weak adsorption produces not one, but several acceptor levels in the forbidden band.

4.5. From Fig. 4 it can be seen that the catalytic activity of the irradiated sample (curve A) is greater than that of the unirradiated sample (curve B). As it was shown above, by the trapping of the electrons and the passing of the oxygen in the strongly chemisorbed form the number of holes in the NiO increases. The conclusion may be drawn that there is a symbatic relation between the catalytic activity and the number of holes. In view of obtaining more conclusive data on the relation between the number of holes and the catalytic activity, the variation of these two quantities was studied after the annealing process. Curve A in Fig. 5 represents the variation of the amount of strongly chemisorbed oxygen and Curve B the variation of the catalytic activity as a function of the annealing time at the temperature of 82°C. It can be seen that the two magnitudes vary in the same sense. This fact shows that in the process of decomposition of H_2O_2 on NiO the phase determining the rate is that in which the free holes participate.

5. CONCLUSIONS

5.1. The oxygen chemisorbed on the surface of nickel oxide is found in two forms: the neutral form (form of weak chemisorption) and in the form of negative ions (form of strong chemisorption). The total amount of chemisorbed oxygen is large for the NiO samples obtained by pyrolysis of $NiCO_3$ at low temperatures (300–400°C) and it decreases down to 0 for those obtained at 1000°C. Most of the oxygen is chemisorbed in the weak form.

5.2. The oxygen chemisorbed in the weak form creates one or more empty acceptor surface levels.

5.3. The acceptor surface levels, owing to their position in the forbidden band constitute trapping centres for electrons which, in the case of NiO, are minority carriers. The trapping of electrons on these levels cause the passing of the weak form of chemisorbed oxygen into the strong form.

5.4. The NiO is strongly ionized in the field of radiations of the reactor. Owing to the large initial concentration of holes, particularly in the NiO samples obtained by pyrolysis at low temperatures, the increase in the number of holes through ionization is insignificant. In exchange, the concentration of the electrons increases to a great extent, thus modifying the electrical equilibrium.

The consumption of the electrons is realized mostly through a trapping process on the acceptor surface levels of the weakly chemisorbed oxygen.

5.5. The consequence of the trapping of electrons on the acceptor surface levels is the displacement of the chemisorption equilibrium towards the strong form (i.e. passing of the weak form into the strong form).

5.6. The value of this displacement, in the case of NiO, is independent of the pressure of oxygen and of the temperature during the irradiation. In the range studied the effect increases with the increase of the time of exposure.

5.7. The radiochemisorption of oxygen increases the catalytic activity of NiO in the decomposition reaction of H_2O_2.

5.8. The adsorption equilibrium obtained after irradiation is metastable and tends to anneal. The activation energy of the annealing process is 0·8 eV.

REFERENCES

1. NACHMAN M., MAXIM I. and BRAUN T., *J. Phys. Chem. Solids* **20**, 307 (1961).
2. BARRY T. I., *Proceedings of the International Conference on Catalysis, Paris* 1960. Paper 70.
3. BARRY T. I. and KLIER K., *Disc. Faraday Soc.* **31**, 219 (1961).
4. KLIER K. and BARRY T. I., *Coll. Trav. Chim. Tchécosl.* **27**, 1320 (1962).
5. WOLKENSTEIN Th., *Disc. Faraday Soc.* **31**, 209 (1961).
6. CAFFREY J. M. and ALLEN A. O., *J. phys. Chem.* **62**, 33 (1958).
7. GOSSEL H., *Z. Elektrochem.* **65**, 98 (1961).
8. DEREN J., HABER J. and SLOCZYNSCHI J., *Bull. Acad. Sci. Polsk. Ser. Sci. Chim.* **IX**, 245 (1961).
9. WOLKENSTEIN Th., *Elektronnaia teoria cataliza na poluprodnicah*, Fizmatghiz, Moscow (1960).
10. HAUFFE K., *Advanc. Catalys* **9**, 187 (1957); Academic Press, New York (1960).
11. YIDA I., *Bull. chem. Soc. Japan* **33**, 10 (1960).
12. KUTZEVA L. N., *Dokl. akad. nauk.* **198**, 409 (1961).
13. LAW J. T., *Semiconductors*, edited by HANNAY N. D.
14. PRIMAK W., *Phys. Rev.* **100**, 1677 (1955).
15. RANDALL J. T. and WILKINS M. H. F., *Proc. Roy. Soc.* **A184**, 366 (1945).
16. GIBSON E. J., *J. Phys. Chem. Solids* **17**, 220 (1960).
17. BARRY T. I. and STONE F. S., *Proc. Roy. Soc.* **255**, 124 (1960).
18. MARGOLIS L. YA., *Usp khim* **28**, 615 (1959).

J. Phys. Chem. Solids Pergamon Press 1963. Vol. 24, pp. 549–556. Printed in Great Britain.

ZINC BLENDE TYPE HgTe–MnTe SOLID SOLUTIONS—I

R. T. DELVES* and **B. LEWIS**

The General Electric Company Limited, Central Research Laboratories,
Hirst Research Centre, Wembley, England

(*Received* 5 *November* 1962)

Abstract—The ternary phase diagram Hg–Mn–Te is discussed with special emphasis on the stability and phase limits of the solid solution range which has the zinc blende type structure. Up to about 80 per cent of the mercury atoms in HgTe can be replaced by manganese atoms with the retention of the zinc blende type structure. The possible concentration of tellurium vacancies in the lattice increases to approximately 13 per cent as the manganese content increases.

1. INTRODUCTION

WE HAVE found that HgTe–MnTe solid solutions of the zinc blende structure-type, designated the α-phase, can be prepared in the range 0 to about 80 molar per cent MnTe. This paper discusses the physical chemistry and phase diagram of these alloys. The results of electrical measurements will be reported in a second paper.

The interest in this system, compared with the HgTe–ZnTe system for example, is the possible influence of the half-filled "*d*" shell of the Mn^{2+} ions on the electrical transport properties. These alloys, HgTe–MnTe, belong to one of the few systems which contain appreciable quantities of paramagnetic ions, and in which high mobilities are observed for either electrons or holes.

The electrical properties of HgTe were first described by NIKOL'SKAYA and REGEL,(1) and later by other authors.(2–6)

HgTe–CdTe alloys have been investigated by LAWSON, NIELSON, PUTLEY and YOUNG,(3) HARMAN *et al.*,(7) and SCHNEIDER and GAVRISHCHAK.(8)

2. PREPARATIVE TECHNIQUE

2.1. *Purity of starting materials*

Manganese was obtained as electrolytic flake of a stated purity of 99·9 per cent, and was melted under hydrogen to remove sulphur. The tellurium was melted in an atmosphere of hydrogen, and zone-refined with ten passes, which gives a purity of at least 99·99 per cent. The major impurities detected spectrographically after the zone-refining process were bismuth, antimony and selenium. The mercury used had been purified by the triple distillation method, which according to LAWSON *et al.*(3) gives a purity of 99·999 per cent.

2.2. *Preparation of Alloys*

Alloys were prepared by sintering powders of HgTe and MnTe together. HgTe was prepared as a cast ingot by melting mercury and tellurium together in an evacuated silica tube. The silica tube was initially heated to 450°C, at which temperature mercury and tellurium react rapidly, and the mass of HgTe which forms can block off unreacted mercury from the remaining tellurium. The tube was therefore slowly heated to 700°C, and continuously rocked to ensure complete mixing of the elements. In this way we avoided the formation of pockets of free mercury which might have caused explosions at the temperatures of the melting points of the alloys. The tube was quenched to 550°C and then slowly cooled to room temperature overnight. The tube was inspected for traces of free mercury before it was opened.

Alternatively, mercury and tellurium powder of less than 250μ size were heated together for one day at 550°C in a hard glass tube. The HgTe which formed was porous, but suitable for milling to a powder.

Manganese and tellurium were separately milled to a particle size of 75μ, and appropriate weights of the mixed powders were placed in silica tubes. The total weight of material used was about 40g. These operations were carried out in an atmosphere of argon. The silica tubes were then evacuated and sealed. The reaction between the elements was initiated by warming one end of the silica tube; the reaction was violent and the heat generated was sufficient to melt the MnTe momentarily. However, the tubes quickly cooled to room temperature. No attack on the silica occurred during the few seconds that the MnTe was molten, and no tube ever cracked or exploded.

---

* Now at Ministry of Aviation R.R.E., Great Malvern.

The cast ingots of HgTe and MnTe were separately milled to a particle size of less than 75μ and appropriate quantities weighed out, thoroughly mixed, and pressed into cylinders at a pressure of 5×10^3 kg/cm². These operations were also carried out in an atmosphere of argon. The pressed cylinders were sintered in sealed, evacuated hard glass tubes at various temperatures—treatment for three days at 450°C was found to be suitable for most alloy composition. The free space in the tubes was filled by glass discs to minimize the loss of volatile constituents. When an excess or deficiency of tellurium was required, the necessary compositional adjustment was made to the HgTe component of the alloy. The result of the single sintering treatment was in all cases a homogeneous alloy, provided that the alloy was a stable phase. No resintering was necessary, and the sintered cylinders were used for various experiments including preliminary electrical measurements.

3. EXAMINATION OF ALLOYS

3.1. *X-ray examination*

The sintered cylinders were crushed in air to a particle size of 75μ and the powders were annealed at various temperatures for one day in evacuated, sealed tubes in which the free space was kept to a minimum. Hard glass tubes were used up to 550°C, and silica tubes from 550 to 700°C. Since manganese rapidly attacks silica above 700°C, the powders to be annealed above this temperature were placed in small alumina tubes which were sealed inside silica tubes. Samples annealed above 550°C were quenched in water, and those annealed below 550°C were allowed to cool in air after removal from the furnace.

The powders were examined by conventional X-ray powder diffraction techniques, using an 11·46 cm diameter camera and CuKα radiation. The values of $1{\cdot}5405_0$ and $1{\cdot}5443_4$ Å were assumed for the wavelengths of the α_1 and α_2 radiations respectively in calculating the structure-cell dimensions from X-ray patterns of the alloy specimens.

3.2. *Differential thermal analysis (DTA)*

The sintered cylinders were crushed to 250μ size and about 12g of powder were packed into a silica tube provided with the usual re-entrant thermocouple well. Temperature differences between the sample and dummy were measured to ½°C, and the absolute temperature was known to 2°C. Heating and cooling rates were 1 to 2°C/min, and little attack took place on the silica during the short time that the samples were molten. The results are summarized in Table 1.

The volume of the sample was only about one half of the volume of the tube after the sample had melted. Therefore some evaporation of mercury from the sample must have taken place to maintain the necessary vapour pressure of mercury. If we assume that the latter is 30 atm over HgTe at the melting point, the loss of mercury is about 2 at. per cent. This is probably an over-estimate for most of our samples, but the point must be considered in discussing the results.

3.3 *Vapour phase equilibration*

The following method was used to explore the tellurium-deficient phase boundary of the α-phase solid solution range.

Samples of $Hg_xMn_{1-x}Te_{1\cdot0}$ were treated at 550°C in a controlled pressure of mercury vapour from a reservoir at 500 or 520°C. The increase in weight of the sample was recorded, and the phases present analyzed by X-ray powder diffraction.

Approximately 2g of sample were used, either as a sintered cylinder or as a powder, and the increase in weight of the sample after treatment was measured to 0·2 mg. The decrease in weight of the mercury in the reservoir was also checked. We believe that the major source of error in experiments such as these is the loss of tellurium from the sample; this tellurium is normally observed as HgTe condensed on the walls of the containing tube. Thus, to minimize the loss of tellurium, heat treatments were carried out for one day only. This treatment was considered to be adequate, since diffusion

Table 1. *Results of DTA runs on* HgTe/MnTe *preparations*

Molar per cent MnTe	Arrest on heating run (°C)	Identification	Arrest on cooling run (°C)	Identification
0	665	m.p.	669	f.p.
5	670	m.p.	680	f.p.
10	677	m.p.	698	f.p.
15	671	m.p.	709	f.p.
17·5	675	m.p.	729	f.p.
20	669	m.p.	775?	f.p.
20	—	—	720	$MnTe_2$ forms
25	650	m.p.	—	No f.p. found
25	—	—	720	$MnTe_2$ forms
35	c.600°C	—	—	No f.p. found*
35	—	—	720	$MnTe_2$ forms

* F.P. is between 850 and 800°C judged by the appearance of the sample after heating runs.

of mercury through the sample is rapid. We assumed that the mercury vapour pressure was high enough to produce a composition in the sample corresponding with that of an α-phase close to the tellurium-deficient phase boundary. The results of our experiments are summarized in Table 2.

Table 2. Results of Mercury vapour equilibration of HgTe/MnTe *preparations, samples at* 550°C

Molar % MnTe	Temperature of reservoir of Hg (°C)	At. % Additional Hg in sample	Phases observed	Lattice parameter of α-phase (Å)	Nominal Composition after Treatment
10	500	3	α (zinc blende type)	—	
25	525	4	α	6·431	$Hg_{0\cdot75}Mn_{0\cdot25}Te_{0\cdot978}$
50	520	10	α	6·406	$Hg_{0\cdot545}Mn_{0\cdot455}Te_{0\cdot91}$
75	520	14	α, $MnTe_2$*	6·373	$Hg_{0\cdot35}Mn_{0\cdot65}Te_{0\cdot87}$
85	500	16	α, $MnTe_2$*, MnTe*	6·367	$Hg_{0\cdot27}Mn_{0\cdot73}Te_{0\cdot86}$
90	500	16	α, $MnTe_2$*, MnTe*	6·362	$Hg_{0\cdot21}Mn_{0\cdot79}Te_{0\cdot88}$

* Traces of these phases were found.

4. DISCUSSION OF RESULTS

4.1. *Binary phase system* Mn–Te

There is little published information on any of the three binary systems involved. The Hg–Mn system does not concern us.

In the Mn–Te system, it is known that only two intermediate phases exist; MnTe with a nickel arsenide type structure, and $MnTe_2$ with a pyrites type structure.

According to FURBERG(9) the phase limits of $MnTe_2$ lie between $MnTe_{1\cdot7}$ and $MnTe_{1\cdot8}$ on the manganese-rich side, and between $MnTe_{1\cdot8}$ and $MnTe_{2\cdot0}$ on the high tellurium side of the phase range. Furberg also reports that the limits of the MnTe phase at 500°C are between $MnTe_{0\cdot8}$ and $MnTe_{0\cdot9}$ on the manganese-rich side, and between $MnTe_{1\cdot0}$ and $MnTe_{1\cdot1}$ on the tellurium-rich side. This agrees with our findings, except that we observe that all our preparations of $MnTe_{1\cdot0}$ at 500°C contain a trace of $MnTe_2$.

The melting point of MnTe is 1167°C(10) and DUDKIN(11) states that $MnTe_2$ decomposes peritectically at 735°C [See Section 4.3].

4.2. *Binary phase system* Hg–Te

Though it is known that HgTe is the only intermediate phase, only a few liquidus points for tellurium-rich compositions have been given.(12) The melting point of HgTe is variously given as 600°C(3) and 675 ± 5°C.(5)

We have determined the main features of the phase diagram near the composition HgTe by DTA and vapour phase equilibration. As was explained in Section 3.2, the actual compositions of the alloys could have been 2 at. per cent deficient in mercury near the melting point compared to the nominal composition, due to the loss of mercury vapour. The temperatures of the arrests were measured to ± 1°C, so that our results are qualitative only, and are shown in the schematic phase diagram (Fig. 1).

The maximum in the liquidus lies on the tellurium-rich side, between 2·5 and 4 at. per cent. The melting point of HgTe is 670 ± 1°C. The solid solubility of mercury in HgTe at 450°C is substantially less than 2 at. per cent and probably approaches 0 per cent; the solid solubility of tellurium in HgTe is appreciable, perhaps 2·5 at. per cent. In agreement with the value quoted by HANSEN,(12) we observed the tellurium–HgTe eutectic at 409 ± 2°C. The lattice parameter of HgTe does not appear to alter appreciably as tellurium is added.

4.3. *The* HgTe–MnTe *section of the ternary phase diagram*

Our results are summarized in Fig. 2. There is no difficulty in preparing single phase alloys containing up to 35 molar per cent MnTe by sintering the components at 450°C, but beyond this composition the α-phase appears to be metastable. All our alloy preparations with more than 35 molar

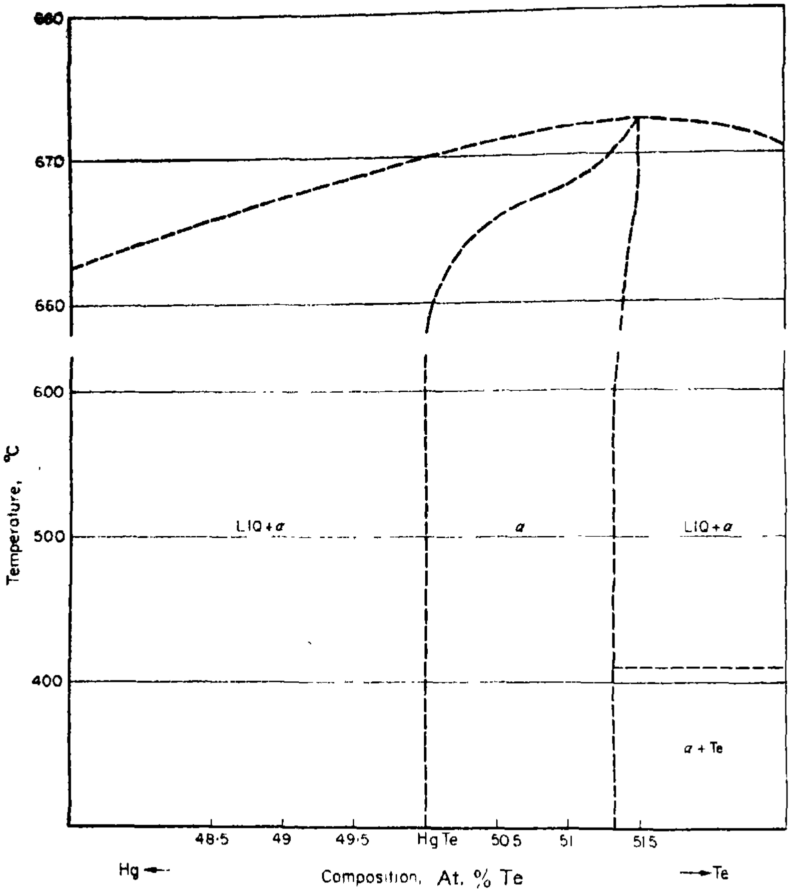

FIG. 1. Schematic phase diagram for the system Hg–Te, at the composition HgTe. *N.B.* Expanded scale used in temperature range 660–670°C.

per cent MnTe contained a trace of $MnTe_2$ after sintering at 450°C for 3 days, the amount observed increasing as the period of heat treatment was extended. It appears that the first product of reaction in this composition range is an α-phase which decomposes slowly into $MnTe_2$ and a mercury-rich α-phase. If free mercury had been present in these alloys, we would have expected to observe traces condensed on the walls of the heat-treatment tube after cooling to room temperature, and we obtained no evidence of this nature for any of our alloy preparations.

We attempted to prepare single phase material of the composition 50 molar per cent MnTe by sintering the components at 250°C, but even after 20 days at this temperature the reaction was not complete. No improvement was observed when a sample sintered at 450°C for 3 days was annealed at 250°C.

The presence of $MnTe_2$ in alloy preparations containing more than 35 molar per cent MnTe accounts for the scatter that we observe in the lattice parameters of the α-phases which are plotted in Fig. 3. Nevertheless, Vegard's Law which is closely obeyed in the composition range 0–35 molar per cent MnTe, still appears to be followed well towards the limiting composition of the α-phase.

During DTA runs we observed only a diffuse arrest for the liquidus when the sample contained

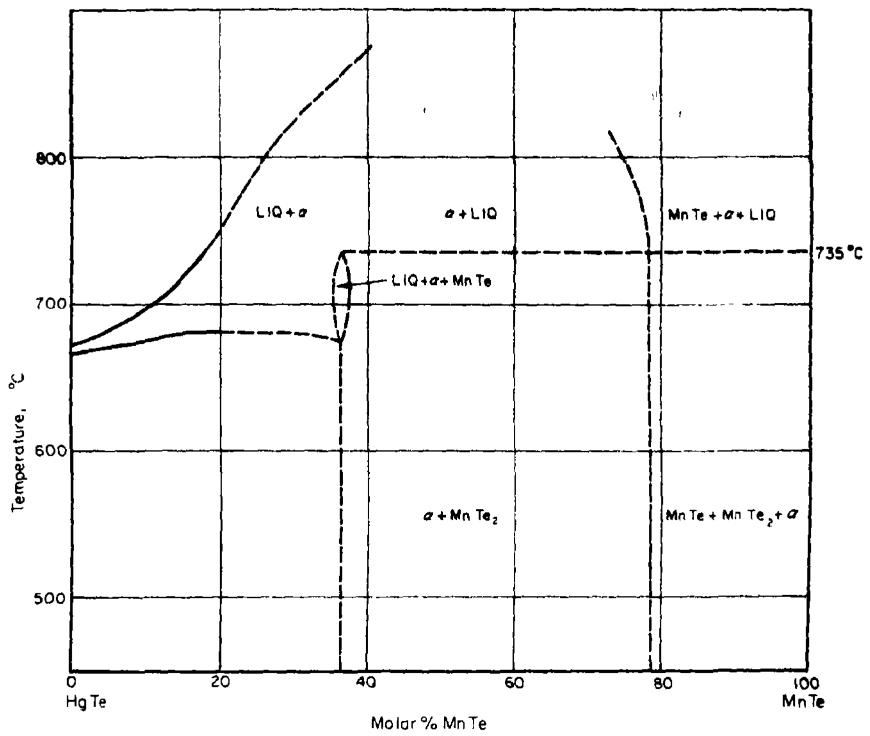

FIG. 2. HgTe–MnTe section of the ternary phase diagram.

10–20 molar per cent MnTe, and failed to observe any arrest for alloys containing more than 20 molar per cent MnTe. Presumably, during the cooling runs the α-phase that first freezes out is appreciably deficient in tellurium compared with the liquid composition, and this accounts for the diffuseness of the arrest. The excess tellurium can then accumulate in the liquid phase, and at 720°C we observe a sharp arrest which we attribute to the formation of $MnTe_2$. DUDKIN(11) states that $MnTe_2$ decomposes peritectically at 735°C.

The materials from the DTA runs were examined by X-ray powder diffraction without further annealing. An inhomogeneous α-phase was observed in each case, the measured range of lattice parameter increasing with increasing manganese content. No trace of $MnTe_2$ was found in any sample. Moreover, during the heating runs on these alloys, no arrest at 720°C could be detected. We conclude, therefore that in our experiments, $MnTe_2$ is not in equilibrium with the α-phase at room temperature, when the concentration of MnTe in the alloys is less than 35 molar per cent. During the cooling runs, mercury from the mercury-rich α-phase which originally solidifies out can diffuse into any $MnTe_2$ formed, to give an α-phase of another composition.

We attempted to determine the phase constitution of alloys in the range 35–70 molar per cent MnTe at temperatures above 720°C. Powders were annealed at 770°C for 1 day and then quenched into water. $MnTe_2$ was observed in some samples, but in randomly varying concentrations, indicating that the high temperature phases were not always retained. A 35 molar per cent MnTe sample contained some free tellurium and an inhomogeneous α-phase. A 50 molar per cent MnTe sample contained MnTe, possibly some free tellurium and an α-phase with a limited range of composition. A sample with 75 molar per

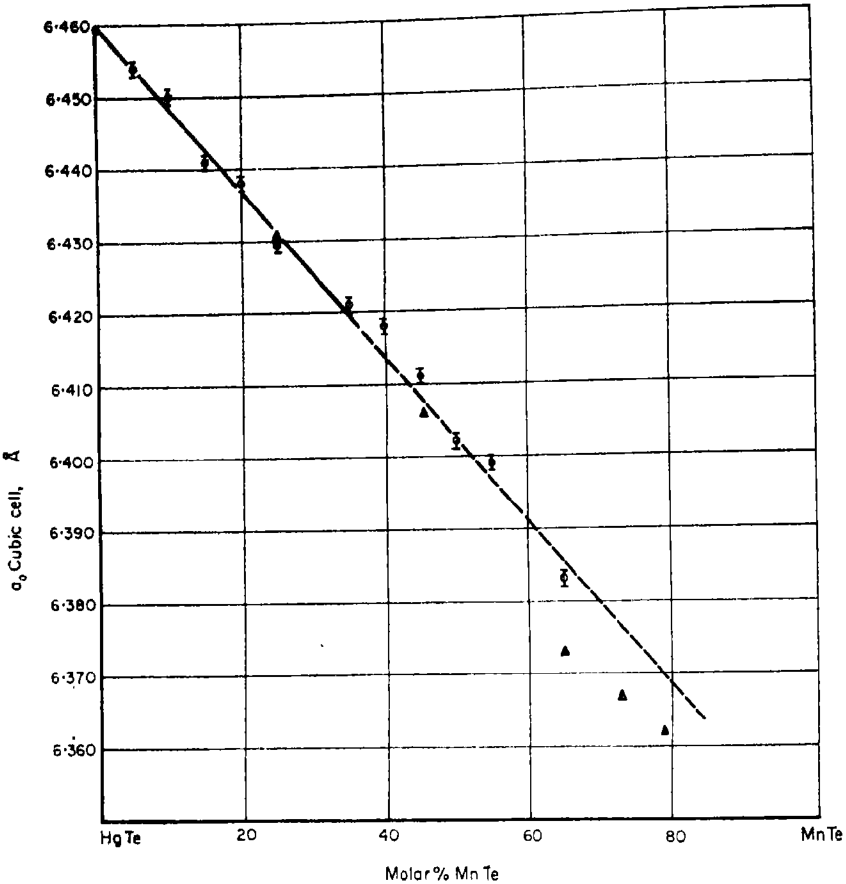

FIG. 3. Variation in structure cell dimensions of α-phases with change in composition.

○ As prepared

△ Heat-treated in Hg vapour

Values of a_0 obtained from the measurement of one sample only for each alloy composition.

cent MnTe contained MnTe as the major phase, and the percentage of MnTe observed was substantially greater than that in a similar sample annealed at 550°C. It would appear, therefore, that the amount of manganese that the zinc blende type lattice can accommodate decreases with increasing temperature.

4.4 *Tellurium-deficient α-phases* (550°C *isotherm*)

We explored the tellurium-deficient boundary of the α-phase solid solution range at 550°C, by diffusing mercury into $Hg_xMn_{1-x}Te_{1.0}$ alloy samples as described in Section 3.3. Our results are summarized in Table 2 and Fig. 4 which represents the isotherm at 550°C. It can be seen that as the manganese content increases substantial deficiencies of tellurium are observed in the zinc blende type α-phase, reaching a maximum of about 13 per cent.

We have noted that the compound $Hg_{0.5}Mn_{0.5}Te_{0.9}$ is stable up to 770°C, but we have not studied it at higher temperatures.

4.5. *Non-stoichiometric* $Hg_{0\cdot9}Mn_{0\cdot1}Te$ *alloys*

As the mercury-rich end of the α-phase range has the most interesting electrical properties, the alloy $Hg_{0\cdot9}Mn_{0\cdot1}Te$ was studied in further detail. The solubility of excess tellurium in this alloy at 450°C is more than 2·5 at. per cent, and of excess mercury 3 at. per cent. The lattice parameters for alloys containing 2·3 at. per cent excess tellurium and 1·8 at. per cent excess mercury are $6{\cdot}452_5$ and 6·443 Å respectively. The liquidus of this section of the system has a flat maximum at 700°C, occurring at a composition of 1·8 at. per cent excess mercury.

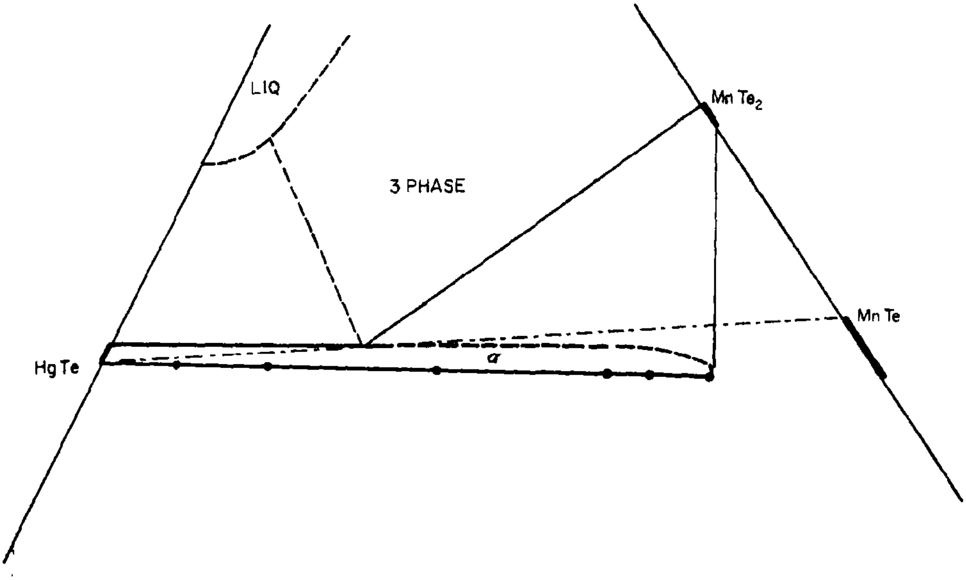

FIG. 4. Ternary isotherm at 550°C showing the α-phase region. —·—·—·— Construction line joining stoichiometric compositions HgTe and MnTe.

4.6. *Other transition metal alloy systems*

In this Section we consider that other alloys might exist which are semiconducting, have a reasonably high mobility, and contain a transition metal with an incompletely filled "*d*" shell.

The close similarity in properties between HgTe and HgSe leads us to predict that HgSe–MnSe alloys will exist, and that their properties will be similar to the HgTe–MnTe alloys described in this present work. It would be interesting to attempt to dissolve transition metals other than manganese in either HgTe or HgSe. We have tried, without success, to dissolve nickel and chromium in HgTe. It is worth noting that MnTe is the only first row transition metal telluride that is semiconducting, all the others being metallic.(13) We suggest, therefore, that only transition metal chalcogenides which are semiconducting will form solid solution alloys with HgS, HgSe and HgTe. In the selenide systems, it is known that MnSe, CrSe and perhaps FeSe are semiconducting, so that these compounds may form zinc blende type solid solutions with HgSe.

Although HgS itself has the cinnabar structure, REGEL(1) reports that solid solutions of HgS with less than 1 per cent HgTe have the zinc blende type structure. CrS, FeS, MnS and possibly NiS and CoS are semiconducting, and these compounds also are likely to form appreciable ranges of zinc blende type solid solutions with HgS containing a little Te. These alloys are being investigated.

We now consider other Group II metal tellurides. JUZA *et al.*(14) report ZnTe–MnTe alloys with the zinc blende type structure and we have prepared CdTe–MnTe alloys containing at least 75 molar per cent MnTe. These alloys are semiconductors with high energy gaps and probably have low mobilities. HARMAN(7) and PUTLEY(8) have shown that $Hg_{0.9}Cd_{0.1}Te$ has a mobility of 100,000 cm^2/V sec at 80°K. Alloys of this compound with MnTe should be of interest.

JOHNSTON(10) reports that above 900°C MnTe has the rock salt type structure, and that GeTe–MnTe alloys exist which have this structure at room temperature, and show a wide range of composition. These alloys are of interest as thermoelectric generating materials, but they are unlikely to have high mobilities. We have tried, unsucessfully, to dissolve manganese in PbTe. The large size difference of the Pb^{2+} and Mn^{2+} ions may well account for our failure.

REFERENCES

1. NIKOL'SKAYA E. I. and REGEL A. R., *Zh. tekh. fiz.* **25,** 1352 (1956).
2. BRACH B. Ya, ZHDANOVA V. V. and LEV E. Ya, *Sov. Phys. Solid State* **3,** 571 (1961).
3. LAWSON W. D., NIELSON S., PUTLEY E. H. and YOUNG A. S., *J. Phys. Chem. Solids* **9,** 325 (1959).
4. HARMAN T. C., LOGAN M. J. and GOERING H. L., *J. Phys. Chem. Solids* **7,** 228 (1958).
5. HARMAN T. C. and STRAUSS A. J., *J. appl. Phys.* **32,** 2265 (1961).
6. CARLSON R. O., *Phys. Rev.* **111,** 476 (1958).
7. HARMAN T. C., STRAUSS A. J., DICKEY D. H., DRESSELHAUS M. S., WRIGHT G. B. and MAVROIDES J. G., *Phys. Rev. Letters* **7,** 403 (1961).
8. SCHNEIDER A. D. and GAVRISHCHAK I. V., *Sov. Phys. Solid State* **2,** 1865 (1961).
9. FURBERG S., *Acta Chem. Scand.* **7,** 693 (1953).
10. JOHNSTON W. D. and SETRICH D. E., *J. inorg. nucl. Chem.* **19,** 229 (1961).
11. DUDKIN L. D. and VAIDANICH V. I., *Sov. Phys. Solid State* **2,** 1384 (1961).
12. HANSEN M. and ANDERKO K., *Constitution of Binary Alloys*, p. 840. McGraw-Hill, New York (1958).
13. DUDKIN L. D., *Sov. Phys. Solid State* **2,** 371 (1960).
14. JUZA R., RABENAU A. and PASCHER G., *Z. anorg. Chem.* **285,** 61 (1956).

J. Phys. Chem. Solids Pergamon Press 1963. Vol. 24, pp. 557–558. Printed in Great Britain.

ON THE TRANSITION FROM WHITE TIN (β-Sn) TO THE BODY-CENTRED CUBIC FORM UNDER PRESSURE

M. J. P. MUSGRAVE

Basic Physics Division, National Physical Laboratory, Teddington, Middlesex

(*Received* 21 *November* 1962)

Abstract—The recently reported transition from white tin to a body-centred cubic structure, which occurs under a pressure of 110–115 kbars at room temperature, is given a lattice dynamical interpretation. The necessary atomic displacements to effect the phase change may be specified in terms of optical lattice modes in white tin which have been shown to have low stiffness. Since pressure tends to destabilize these modes still further, it is suggested that the transition may occur as a result of their instability.

It has recently been found (Jamieson(1)) that, under a pressure of 110 kbars at room temperature, white tin undergoes a change of phase to a body-centred cubic structure. Stager *et al.*(2) have also reported a transition from white tin at a pressure of 113–115 kilobars but have not specified the subsequent structure. This note offers an interpretation of the transition in terms of a lattice dynamical model whose analysis is being fully reported elsewhere (Musgrave(3)).

In the course of that analysis, it was found that the lattice modes of least stiffness in the model of white tin are the transverse optical and acoustic modes of wave vector $q = 2\pi/a'$ [1,0,0] or $2\pi/a'$ [0,1,0] having displacement vectors $(0,0,\pm 1)$ in the constituent Bravais lattices (b.c. tetragonal) of the structure; the unit vectors of the tetragonal lattices are $(a',0,0)$, $(0,a',0)$ and $(0,0,c)$ and $c/a' = 0{\cdot}54$. The angular frequency of the *TO* and *TA* modes with $q = 2\pi/a'$ [1,0,0] (*A*) is $0{\cdot}39\times 10^{13}$ c/s and for the zero wave vector mode with (0,0,1) displacement (*B*) it is $0{\cdot}67\times 10^{13}$ c/s; the maximum frequency for the model is $3{\cdot}22\times 10^{13}$ c/s.

Table 1 indicates how a superposition of the modes of low stiffness can yield a simple b.c. tetragonal structure with axial ratio 0·83, whose *x*, *y* crystal axes are rotated 45° about the *z*-axis from those of white tin. Column 1 contains the co-ordinates of 8 atoms of the white tin structure in their equilibrium positions; column 2 lists their positions when at maximum displacement by mode *A*, while column 3 gives the positions after superposition of mode *B* and a shift of origin; column 4 refers the co-ordinates of column 3 to axes rotated 45° about the tetragonal axis. The configuration represented in column 4 has a body-centred atom with 8 equivalent neighbours, the former first and third neighbours in white tin. Minimum energy is commonly attained when the angles between "bonds" are equal and, if such a principle is applicable in this case, the configuration having co-ordination number 8 will pass to b.c.c. Figure 1 illustrates the initial and final configurations.

That a critical pressure should be necessary to cause the instability is reasonable in the light of other findings. In the course of computations on the model mentioned above, it was found that the stability of the relevant lattice modes was most sensitive to the value of the elastic constant c_{13}. For values of this constant above a critical maximum, the mode proved unstable. The effect of pressure on elastic constants of the type c_{ij} $(i,j = 1,2,3;\ i \neq j)$ is to raise their value, viz. $c_{ij}(P) = c^{*}_{ij}+P$, where c^{*}_{ij} is the elastic constant of the structure having the reduced dimensions caused by the pressure (Musgrave and Pople;(4) Musgrave(5).) In the absence of information about the variation of elastic constants when atomic

Table 1. Superposition of lattice modes yielding a simple body-centred tetragonal structure

Co-ordinates of atom in white tin structure			Effect of mode *A* amplitude *c*/4			Effect of mode *B* amplitude *c*/8 and shift of origin by (0, 0, *c*/8)			Axes rotated by 45° about *z*-axis*		
a'	*a'*	*c*	*a'*	*a'*	*c*	*a'*	*a'*	*c*	$a'/\sqrt{2}$	$a'/\sqrt{2}$	*c*
0	0	0	0	0	$-\frac{1}{4}$	0	0	0	0	0	0
0	0	1	0	0	$\frac{3}{4}$	0	0	1	0	0	1
$\frac{1}{2}$	0	$\frac{3}{4}$	$\frac{1}{2}$	0	$\frac{1}{2}$	$\frac{1}{2}$	0	$\frac{1}{2}$	$\frac{1}{2}$	$\frac{1}{2}$	$\frac{1}{2}$
$\frac{1}{2}$	0	$-\frac{1}{4}$	$\frac{1}{2}$	0	$-\frac{1}{2}$	$\frac{1}{2}$	0	$-\frac{1}{2}$	$\frac{1}{2}$	$\frac{1}{2}$	$-\frac{1}{2}$
0	$\frac{1}{2}$	$\frac{1}{4}$	0	$\frac{1}{2}$	$\frac{1}{2}$	0	$\frac{1}{2}$	$\frac{1}{2}$	$-\frac{1}{2}$	$\frac{1}{2}$	$\frac{1}{2}$
0	$\frac{1}{2}$	$-\frac{3}{4}$	0	$\frac{1}{2}$	$-\frac{1}{2}$	0	$\frac{1}{2}$	$-\frac{1}{2}$	$-\frac{1}{2}$	$\frac{1}{2}$	$-\frac{1}{2}$
$\frac{1}{2}$	$\frac{1}{2}$	$\frac{1}{2}$	$\frac{1}{2}$	$\frac{1}{2}$	$\frac{3}{4}$	$\frac{1}{2}$	$\frac{1}{2}$	1	0	1	1
$\frac{1}{2}$	$\frac{1}{2}$	$-\frac{1}{2}$	$\frac{1}{2}$	$\frac{1}{2}$	$-\frac{1}{4}$	$\frac{1}{2}$	$\frac{1}{2}$	0	0	1	0

* The axial ratio of the structure represented in column 4 is $c\sqrt{2}/a' = 0{\cdot}83$.

dimensions are altered, no better value can be assigned to c^*_{ij} than that for zero pressure $c_{ij}(0)$; the implications of the effects of pressure are then in satisfactory accord with the results obtained from the model.

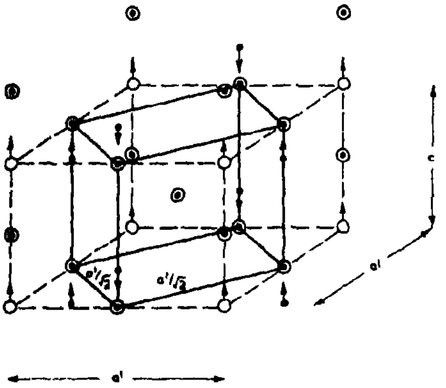

○ ● Atoms of the constituent body-centred tetragonal lattices of white tin; axial ratio 0·54

● Atoms of the simple body-centred structure; axial ratio 0·83

FIG. 1. The initial (Col. 1) and final (Cols. 3 and 4) configurations of the atoms.

A decrease in volume is to be expected with the transition but it is not easy to offer an estimate of its magnitude since it is sensitive to the axial ratio of the tetragonal form under applied pressure. From the elastic constants of white tin, it is possible to discover the initial trend of the variation since the axial ratio will increase or decrease as the ratio of strains

$\epsilon_{zz}/\epsilon_{xx} = [c_{11}+c_{12}-2c_{13}]/[c_{33}-c_{13}] < \text{or} > 1$. In this respect it is worth remarking that the observed constants of MASON and BÖMMEL(6) yield the former result while those of RAYNE and CHANDRASEKHAR(7) yield the latter. BRIDGMAN(8) has listed coefficients for the expression of these longitudinal strains to quadratic approximation in *P*; from this data also, the value of the above ratio proves greater than unity.

Acknowledgement—The work described above has been carried out as part of the research programme of the National Physical Laboratory and this paper is published by permission of the Director of the Laboratory.

REFERENCES

1. JAMIESON J. C., *Houston Meeting of Geological Society of America* (1962).
2. STAGER R. A., BALCHAN A. S. and DRICKAMER H. G., *J. chem. Phys.* **37**, 1154 (1962).
3. MUSGRAVE M. J. P., *Proc. Roy. Soc.* **A** (1963). In press.
4. MUSGRAVE M. J. P. and POPLE J. A., *J. Phys. Chem. Solids* **23**, 321 (1962).
5. MUSGRAVE M. J. P., *Academic Session, Diamond in Industry Symposium, Paris* (1962).
6. MASON W. P. and BÖMMEL H. E., *J. acoust. Soc. Amer.* **28**, 930 (1956).
7. RAYNE J. A. and CHANDRASEKHAR B. S., *Phys. Rev.* **120**, 1658 (1960).
8. BRIDGMAN P. W., *The Physics of High Pressure* Table V. Bell, London (1958).

J. Phys. Chem. Solids Pergamon Press 1963. Vol. 24, pp. 559–562. Printed in Great Britain.

PARAMAGNETIC RESONANCE OF IRRADIATED FERROELECTRIC $LiN_2H_5SO_4$

R. BLINC, M. SCHARA and S. POBERAJ
Nuclear Institute J. Stefan, Ljubljana, Yugoslavia

(*Received* 2 *July* 1962; *revised* 16 *November* 1962)

Abstract—The electron spin resonance spectra of γ-ray damaged ferroelectric lithium hydrazinium sulphate (LiHzS) and deuterated LiHzS have been studied. A comparison of experimental and theoretical resonance patterns indicated that: (a) the principal impurity centers produced by γ-rays in LiHzS and deuterated LiHzS are $\dot{N}_2H_4^+$ and $\dot{N}_2D_4^+$, respectively; (b) the unpaired electron spin densities on both nitrogens are nearly equal to each other, and the charge distribution has local cylindrical symmetry about both nitrogen nuclei; (c) the approximate values of the isotropic and anisotropic nitrogen hyperfine coupling constants are $A_1 = 14$, $A_2 = 12$ and $B_1 = 8$, $B_2 = 7$ G, respectively.

INTRODUCTION

It has been found by Chynoweth⁽¹⁾ that the dielectric properties of ferroelectric crystals are modified when the crystals are subjected to γ-ray damage. The mechanism of these effects is not yet fully understood. The purpose of the present paper was to study by electron spin resonance the impurity centers produced by γ-rays in lithium hydrazine sulphate (LiHzS), one of the few crystals exhibiting ferroelectricity at room temperature.

It was hoped that a knowledge of the nature of the impurity centers would eventually lead to an understanding of the mechanism producing the changes in the ferroelectric properties.

EXPERIMENTAL

The LiHzS crystals were grown by evaporation from an aqueous solution of $N_2H_6SO_4$ and Li_2CO_3, and their crystal symmetry was checked by taking Debye–Scherrer photographs. The unit cell dimensions agreed with the ones given by Pepinsky *et al.*⁽²⁾ within the limits of experimental error. The deuterated samples were prepared by exchange with D_2O and the amount of deuteration checked by measuring the i.r. spectra. The irradiations of the LiHzS crystals and powder samples were carried out at room temperature with a Co^{60} γ-ray source. The dose rate at the sample was about $0\cdot1\ 10^6$ r/hr and the irradiation time varied between ten and sixty hours. Unirradiated samples did not show any paramagnetic absorption. The electron spin resonance spectra were measured with a home built spectrometer working at 9375 Mc/s with recorder presentation of the derivative of the absorption curve.

Spectroscopic splitting factors were measured by comparing the position of the centre of the spectrum with that of DPPH. Mn^{2+} doped ZnS was used as a scale marker.

RESULTS AND DISCUSSION

The results obtained demonstrate that stable impurity centers are formed in irradiated LiHzS. Figures 1(a) and 1(b) show the spectra of irradiated polycrystalline LiHzS and LiHzS single crystals, respectively. The spectra taken 1 hr after irradiation and the spectra of a crystal, aged for 1 month at room temperature, were exactly the same. The spectroscopic splitting factors are very close to the free spin value. The symmetry of the powder spectra as well as the angular dependence of the single crystal spectra, indicate that the anisotropy in the g tensor can be neglected. The powder as well as the single crystal spectra exhibit hyperfine structure. In the former, eleven strong components with an average spacing of 13 G could be detected. The number of the components in the single crystal spectra, on the other hand is strongly orientation dependent and varies between seven and nineteen. The anisotropy of the single crystal spectra shows that the centers are fixed in the crystal lattice.

In order to simplify the analysis and interpretation of the spectra, deuterated polycrystalline LiHzS was prepared and the paramagnetic spectra measured after irradiation with γ-rays. As it can be seen from Fig. 2, the spectrum of the deuterated samples is considerably simpler than that of the hydrogen analogue. It consists of five broad, widely spaced components. The spacing between the central absorption maximum and the first outer maximum amounts to 21 G, whereas the spacing between the first and second outer maximum equals 28 G.

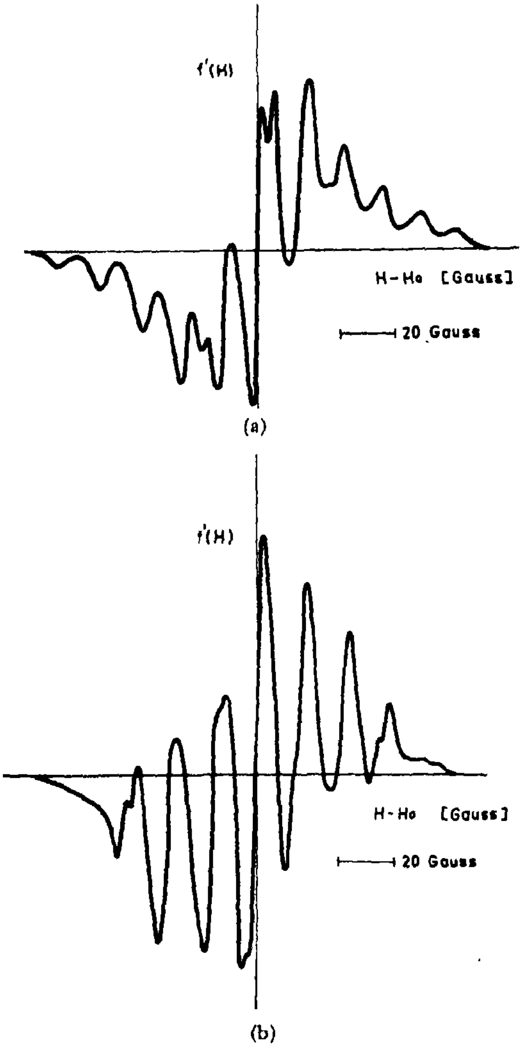

Fig. 1. ESR derivative spectrum of irradiated LiHzS: (a) powdered sample; (b) single crystal. $c \perp H_0$, $\phi = 45^\circ = \sphericalangle (H_0, b)$.

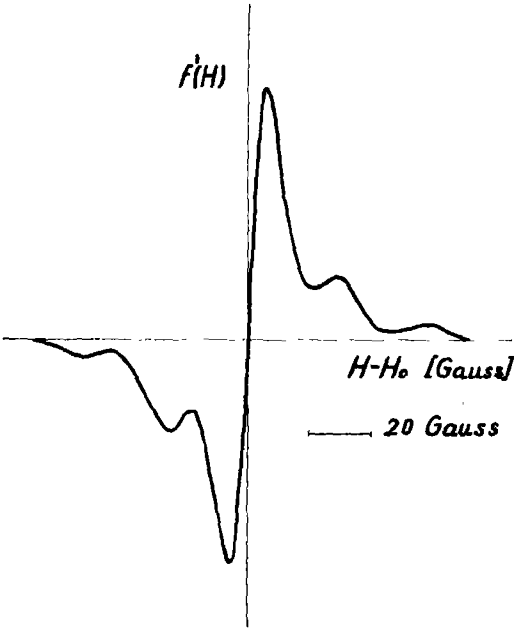

Fig. 2. ESR derivative spectrum of irradiated deuterated LiHzS polycrystaline sample.

The appearance of a five peak hyperfine structure in the spectrum of deuterated polycrystalline LiHzS strongly suggests that the hyperfine structure is due to interactions of the unpaired electron spin density with the two central nitrogen nuclei and that the deuteron hyperfine structure, in contrast to the proton hyperfine structure in "normal" LiHzS, is not fully resolved. The line shapes in deuterated LiHzS accordingly represent envelopes of the fully resolved deuteron hyperfine structures. The impurity center in both "normal" and deuterated LiHzS would thus be produced from the parent molecule by the destruction of one of the NH or ND bonds, respectively.

In order to verify the above hypothesis and to throw further light on the nature of the impurity center, the line shape has to be evaluated. The spin Hamiltonian for Zeeman and magnetic hyperfine interactions, involving one unpaired electron and two magnetic nuclei(8) is

$$\mathscr{H} = -g\mu_0 HS + A_1 SI_1 + A_2 SI_2 + SB_1 I_1 + SB_2 I_2 \tag{1}$$

with

$$AS = -gg_I\mu_0\mu_N(8\pi/3)\left\langle \sum_k \delta(r_k)S_k \right\rangle \tag{2}$$

and

$$B = -gg_I\mu_0\mu_N \left\langle 3rrr^{-5} - \mathscr{T}r^{-3} \right\rangle \tag{3}$$

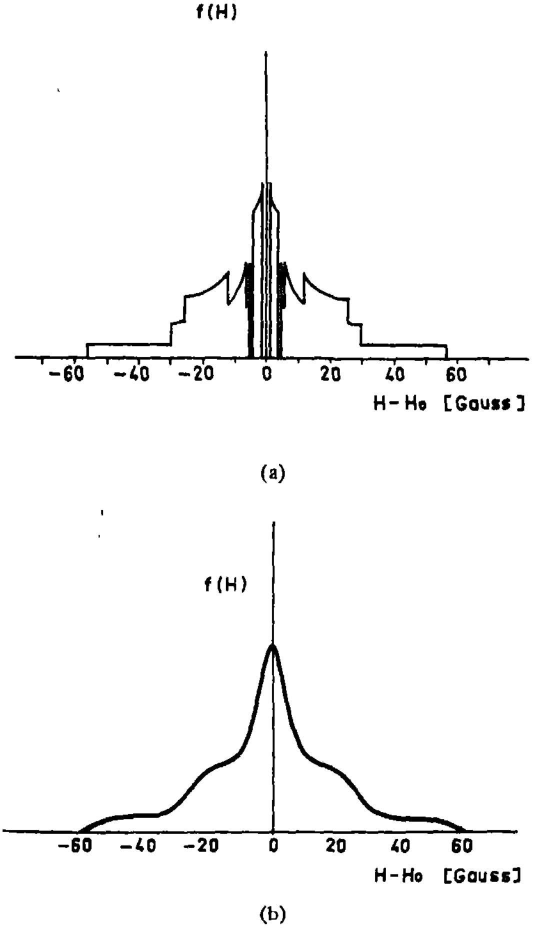

FIG. 3. Deuterated LiHzS: (a) theoretical line shape; (b) theoretical line shape after broadening.

Here the notation of BLINDER(8) is used. The five parts of (1) represent, respectively, the electron Zeeman energy and the isotropic and tensor hyperfine couplings to the two magnetic nuclei. The hyperfine coupling of a nucleus is thus characterized by three parameters: the isotropic Fermi coupling constant A and two of the principal values of the traceless tensor B which become degenerate in case of cylindrical symmetry.

Following the method of LORD and BLINDER,(4) it was possible to fit the spectrum of deuterated polycrystalline LiHzS to the above spin Hamiltonian with the following assumptions:

(a) $I_1 = I_2 = 1$, i.e. the unpaired electron interacts with the two nitrogen nuclei:

(b) $C_1 = C_2 = \frac{1}{2}\,(B_{xx}-B_{yy}) = 0$, the unpaired electron charge distribution has local cylindrical symmetry about both nitrogen nuclei with the two z-axis parallel;

(c) the tensor coupling constants are $B_1 = \frac{1}{2}$ $B_{1,zz} = 8$, G $B_2 = \frac{1}{2}\,B_{2,zz} = 7$ G, indicating that the spin densities on both nitrogen nuclei are approximately the same.

(d) the Fermi coupling constants are $A_1 = 14$, $A_2 = 12$ G. Each isotropic parameter has the same sign as the corresponding anisotropic coupling constant. Since the assumption of cylindrical symmetry implies that the unpaired electron's orbital contains principally s and p character, $B > 0$ for the nitrogen coupling, and all hyperfine coupling constants are almost certainly positive.

The theoretical powder line shape is reproduced on Fig. 4. Following (4),* we took

$$\frac{1}{gM_1M_2(\nu)} = \frac{1}{gM_1(\nu)} + \frac{1}{g_0M_2(\nu)}$$

with

$$gM(\nu) = \frac{\nu(\theta)}{(6AB+3B^2)M^2\cos\theta} \tag{4}$$

and

$$\nu(\theta) = [A^2+2AB(3\cos^2\theta-1) + B^2(3\cos^2\theta+1)]^{1/2}\,M_I.$$

The derivative of the theoretical line shape with the inclusion of Gaussian broadening ($\sigma = 4$ G) is compared with the experimental spectrum in Fig. 4.

---

* The symbols used are the same as in Ref. (4).

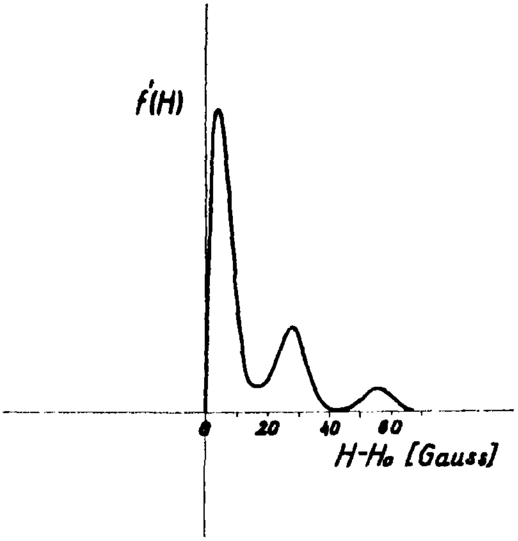

FIG. 4. Theoretically computed derivative spectrum of $\dot{N}_2D_4^+$.

The quantitative agreement between theory and experiment in deuterated LiHzS constitutes strong evidence that the above hypothesis on the nature of the impurity centers in LiHzS is correct. This conclusion is further supported by the fact that it seems to be possible to obtain the spectrum of "normal" polycrystalline LiHzS from the above theoretical spectrum just by accounting for the resolved proton hyperfine structure. The small changes in the spectrum of normal LiHzS observed on cooling to liquid N_2 temperature can be as well explained by the above model as a consequence of the freezing in of the protonic motion in the $\dot{N}_2H_4^+$ radical. This is also consistent with the results of an earlier proton magnetic resonance study,[(5)] where a line width transition was observed below −100°C.

The isotropic and anisotropic hyperfine coupling constants contain certain informations about the nature of the wave function of the unpaired electron. As already stated above, the assumption of cylindrical symmetry implies that the singly occupied orbital in the impurity centrum contains principally *s* and *p* admixtures. From the magnitude of the anisotropic coupling constants we can further deduce that this orbital has principally *p* character. The sum $B_1+B_2 = 15$ G, namely, is comparable to the coupling constant B_n, evaluated for an atomic nitrogen 2*p* orbital.[(4)] This is also consistent with the magnitude of the isotropic hyperfine coupling constants $A_1 = 14$, $A_2 = 12$ G which puts an upper limit of 1–2 per cent *S* admixture into the unpaired electron's orbital.

REFERENCES

1. CHYNOWETH A. G., *Phys. Rev.* **113**, 159 (1959).
2. PEPINSKY R., VEDAM K., OKAYA Y. and HOSHINO S., *Phys. Rev.* **111**, 1467 (1958).
3. BLINDER S. M., *J. chem. Phys.* **33**, 748 (1960).
4. LORD N. W. and BLINDER S. M., *J. chem. Phys.* **34** 1693 (1961).
5. BLINC R. and PIRKMAJER E., to be published.

J. Phys. Chem. Solids Pergamon Press 1963. Vol. 24, pp. 563–571. Printed in Great Britain.

DIFFUSION AND SOLID SOLUBILITY OF SILVER IN SINGLE-CRYSTAL BISMUTH TELLURIDE*

J. D. KEYS and H. M. DUTTON†

Mines Branch, Department of Mines and Technical Surveys, Ottawa, Canada

(*Received* 24 *October* 1962)

Abstract—The anisotropic diffusion and the solid solubility of silver in single-crystal bismuth telluride have been measured by radioactive tracer techniques employing silver-110 and silver-111. The diffusion coefficient perpendicular to the cleavage planes is given by

$$D_{\perp} = 5{\cdot}1^{+2\cdot1}_{-1\cdot6}\times10^{-3}\exp\left(\frac{-0{\cdot}92\text{ eV}}{kT}\right)$$

and that parallel to the cleavage planes by

$$D_{\parallel} = 5{\cdot}4^{+2\cdot6}_{-1\cdot7}\times10^{-3}\exp\left(\frac{-0{\cdot}45\text{ eV}}{kT}\right)$$

The solid solubility has a maximum of $1{\cdot}5\times10^{20}$ atoms/cm^3 (2·5 atom per cent) and the variation of solid solubility with temperature is shown to be consistent with the existing knowledge of the silver–bismuth–tellurium system.

INTRODUCTION

THE widespread use of bismuth telluride as the basis for alloys in the thermoelectric industry has resulted in several investigations of diffusion in this compound. The first investigators(1) used polycrystalline material, but the more recent results(2, 3, 4, 5) have been obtained with single-crystal specimens. The deleterious effects of certain doping materials, in particular copper, have received the attention of several workers and, in view of their results, it appeared worthwhile to extend the diffusion investigations to include the remaining Group IB metals, silver and gold. In a previous communication(6) preliminary measurements of the diffusion of silver into bismuth telluride were reported. It is the object of this paper to present results for the anisotropic diffusion and solubility of silver in this compound, and to discuss in detail the experimental techniques employed.

The structure of bismuth telluride has been well established as belonging to the rhombohedral class $R\bar{3}m$.(7) For the purposes of this work it is more convenient to refer to the equivalent hexagonal cell with "c" axis of 30·487 Å and an "a" value of 4·384 Å. When viewed in this manner, a layered structure is readily apparent with the atoms lying in planes perpendicular to the [0001] direction as follows:

$$\ldots\,\mathrm{Te_1}][\mathrm{Te_1}\text{—}\mathrm{Bi}\text{—}\mathrm{Te_2}\text{—}\mathrm{Bi}\text{—}\mathrm{Te_1}][\mathrm{Te_1}\,\ldots$$

This structure, together with the relatively weak bonding between the adjacent Te$_1$ layers, is responsible for the ease with which the material may be cleaved and has led to the adoption of a modified form of cleaving in carrying out the present investigation.

Because of this highly anisotropic nature the diffusion coefficients perpendicular and parallel to the cleavage planes have been measured separately. In the following discussion the terms "perpendicular" and "parallel" will be used to refer

---

* Published by permission of the Director, Mines Branch, Department of Mines and Technical Surveys, Ottawa, Canada. Crown Copyright Reserved.

† Permanent address, Bishop's University, Lennoxville, P.Q.

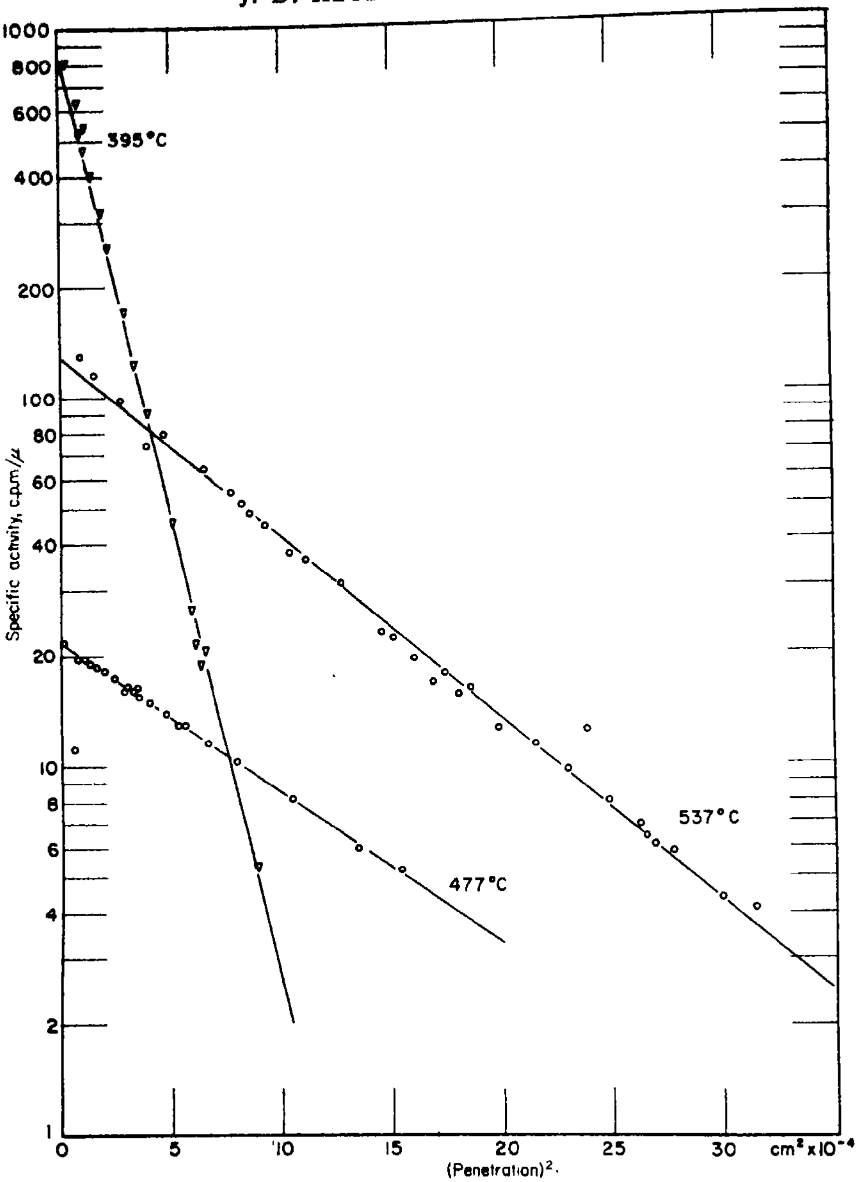

FIG. 1. Typical penetration profiles of the diffusion of Ag into Bi_2Te_3 perpendicular to the cleavage plane.

to diffusion in these directions with respect to the cleavage planes.

EXPERIMENTAL METHODS

Samples employed in this work were cleaved from zone-refined ingots of stoichiometric Bi_2Te_3 obtained by reacting bismuth (99·999 per cent pure)* and tellurium (99·999 per cent pure).†

---

* Consolidated Mining and Smelting Company of Canada, Ltd., Montreal, P.Q.

† A. D. Mackay Inc., New York, N.Y. American Smelting and Refining Company, New York, N.Y.

Single crystals obtained in this manner ranged in size from 5 × 2 × 20 to 10 × 8 × 100 mm. The usual methods of cutting were found to be useless for this material because of the ease with which it cleaved and it was necessary to employ an Airbrasive Unit.* With this unit sample-size crystals (approximately 8 × 8 × 2 mm) were cut from the larger pieces. For the solubility determinations the thickness was reduced by cleaving to 150–400 μ.

In the perpendicular diffusion and solubility experiments radioactive silver-110 was deposited electrolytically on the diffusing surfaces from a cyanide solution, the edges being suitably masked to prevent end effects. The samples were then sealed in Pyrex ampoules under a pressure of 10^{-2} torr and annealed at temperatures ranging from 270 to 540°C. The temperature control during annealing was ± 2°C.

Attempts to grind the specimens in order to obtain penetration profiles proved unsatisfactory due to chipping, tearing and smearing. However, this manner of preparation was unavoidable for samples used in parallel diffusion experiments. For the perpendicular diffusion and solubility measurements it was found that uniform layers could be peeled from a sample (by means of "Scotch" tape) sufficiently thin to permit an accurate determination of the penetration profile. Knowing the sample area and density, the thickness peeled off was readily calculated from the weight of the removed slice. The activities of the slices thus obtained were counted in a standard scintillation counting apparatus using a 2 in. NaI(Tl) crystal. In order to obtain the solubilities the system was calibrated with a standard silver-110 source.

In the parallel direction the penetration profiles were obtained by autoradiography using Kodak SA 1 spectrographic plates and silver-111 as the tracer. This isotope was preferred for autoradiography as 91 per cent of the disintegrations are by beta emission only. The emulsion was calibrated for its response to silver-111 over a range of transmissions from 1–90 per cent. Radioactive silver was deposited on the end of the sample by evaporating a drop of a dilute silver nitrate solution. Diffusion anneals were carried out in the same manner as in the perpendicular experiments. Annealed specimens were cleaved and samples of different thicknesses were exposed simultaneously in order to determine whether sample thickness influenced the diffusion profile. The resulting profiles were examined with a Leeds and Northrup recording densitometer and it was concluded that the measured diffusion coefficient was independent of sample thickness to within 10 per cent.

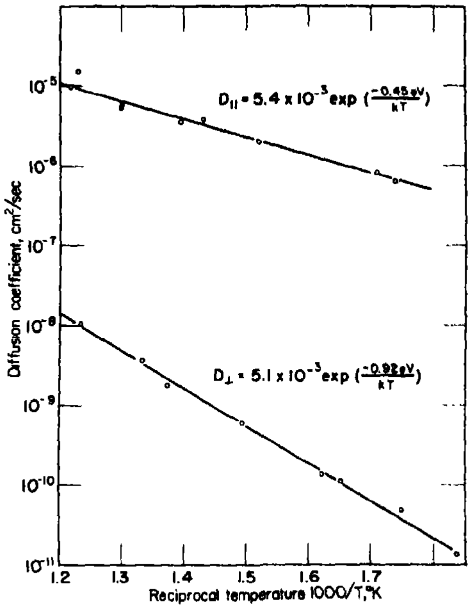

FIG. 2. Temperature dependence of the diffusion coefficient for both perpendicular and parallel diffusion.

RESULTS

1. *Perpendicular diffusion*

Specific activity was plotted against the square of the penetration and the diffusion coefficient calculated from the slope of the resulting straight line. Typical penetration profiles are shown in Fig. 1. This was done for each sample over the range of temperatures from 270 to 540°C and the logarithm of the diffusion coefficient was plotted against reciprocal temperature. The result, shown in Fig. 2, is a straight line and a least squares fit

---

* Industrial Airbrasive Unit, Model C, made by S. S White Dental Mfg. Co., New York 16, N.Y.

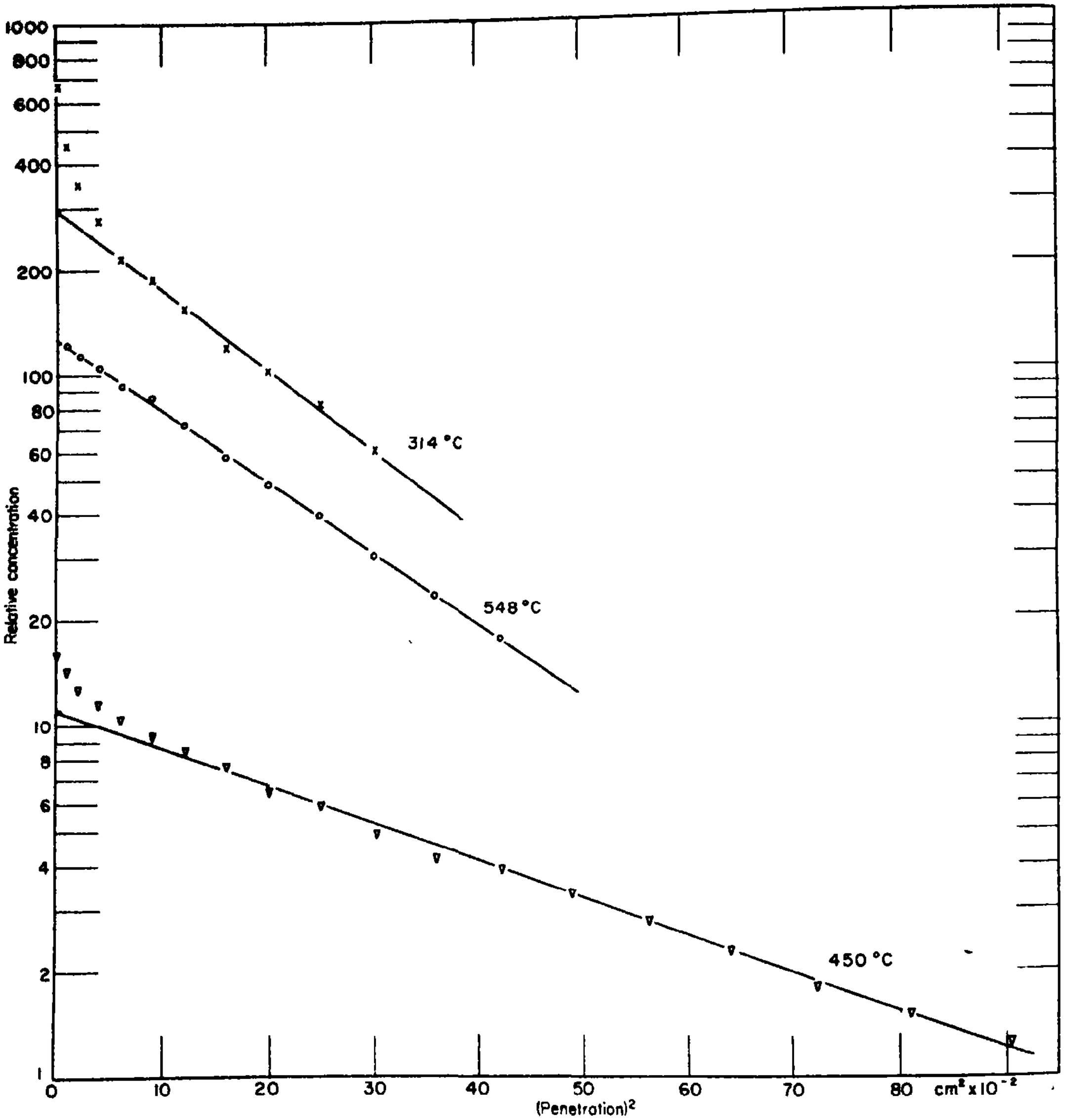

FIG. 4. Typical penetration profiles of the diffusion of Ag into Bi_2Te_3 parallel to the cleavage plane obtained from densitometer measurements of autoradiographs.

gives

$$D_{\perp} = 5{\cdot}1^{+2\cdot1}_{-1\cdot6}\times 10^{-3}\exp\left(\frac{-0{\cdot}92\text{ eV}}{kT}\right)$$

The estimated uncertainty in the activation energy is 0·01 eV.

2. *Parallel diffusion*

A typical autoradiograph is shown in Fig. 3. Densitometer readings were analysed to give a plot of specific activity against square of penetration. Results were obtained over the temperature range from 300 to 550°C and typical

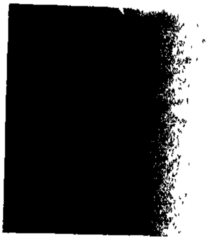

FIG. 3. Autoradiograph showing penetration of silver parallel to the cleavage plane.

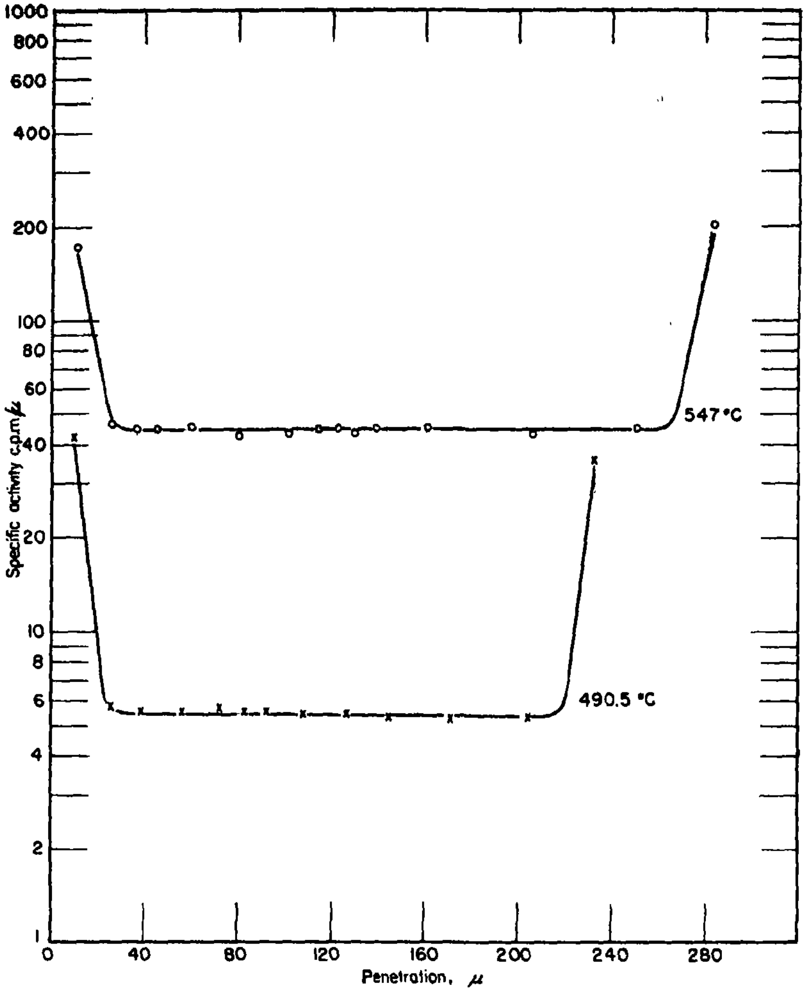

FIG. 5. Penetration profiles showing saturation conditions of Ag in Bi_2Te_3.

penetration profiles are shown in Fig. 4. The temperature dependence of the diffusion coefficient is also shown in Fig. 2, and can be expressed by the equation

$$D_{\parallel} = 5{\cdot}4^{+2{\cdot}6}_{-1{\cdot}7}\times 10^{-3}\exp\left(\frac{-0{\cdot}45\text{ eV}}{kT}\right)$$

Estimated uncertainty in activation energy is 0·01 eV.

In this direction the penetration profiles were straight lines, except that in some cases increased concentrations were found at small penetrations (up to 2–3 mm). These deviations were not present at high temperatures.

3. *Solubility*

For these measurements both faces of a fairly thin sample were plated with silver-110 and the sample was then annealed. It proved relatively easy to saturate the sample if the anneal time and the amount of silver deposited were carefully controlled. Penetration profiles (Fig. 5) across the sample were obtained using the peeling technique and from the constant value of the concentration the solubility was calculated. Figure 6 shows the relation between solubility and temperature.

DISCUSSION

Attempts to formulate diffusion theories compatible with experimental results have been made by many authors.(8, 9, 10) The majority of the proposed theories and their modifications have dealt with self-diffusion in cubic structures, impurity diffusion in cubic structures and diffusion in binary alloys. Although theoretical calculations have been made of the enthalpies and entropies of diffusion and vacancy formation in semiconductors with the diamond lattice, the structure of bismuth telluride is considerably more complicated than the ones referred to above and no attempts have been made to modify existing theories to fit this case.

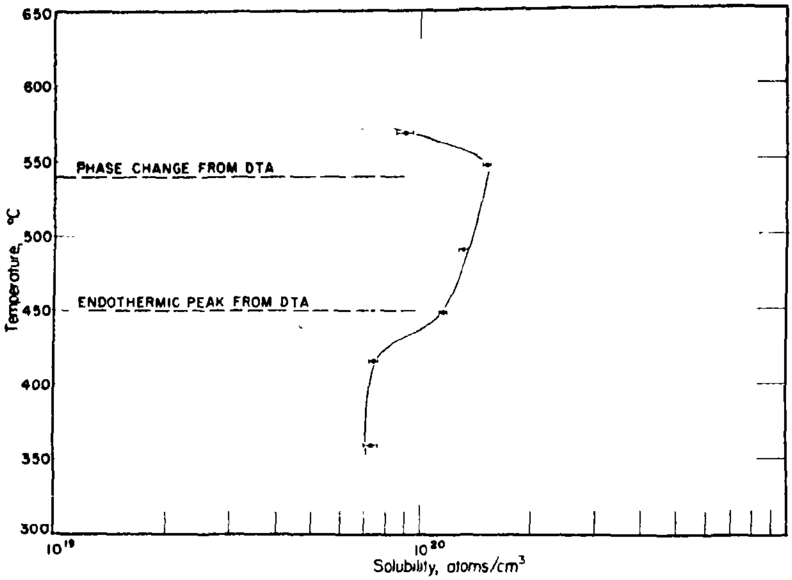

FIG. 6. Temperature dependence of Ag solubility in Bi_2Te_3.

Zener's theory of metallic diffusion has been applied to the diffusion of copper in bismuth telluride(2) and, with some approximations, has been shown to give a reasonable interpretation of the experimental results. Following similar arguments, our results obtained for the diffusion of silver parallel to the cleavage planes agree well with a model based on interstitial diffusion between the weakly bound Te_I layers, but the value of D_0 obtained in the perpendicular case leads to the assumption of a negative entropy of activation. Although the quantitative details of the interactions that might give rise to this situation are not known, a qualitative explanation may be arrived at from a consideration of the special properties associated with semiconducting materials.

Zone-refined bismuth telluride is *p*-type with a carrier concentration of the order of 10^{18}/cm^3, which, it is assumed, arises from the occupation of tellurium sites by bismuth. It becomes intrinsic at about 200°C and it is to be expected that diffusion of silver above this temperature will be influenced by electron–hole interactions and/or ion pairing.

Electron–hole equilibria and ion pairing have been investigated in the case of silicon, germanium, and gallium arsenide, and proposed theories have been shown to be closely followed.(11, 12) For either type of interaction, the effect on the diffusion coefficient and solid solubility has been found to be pronounced. In the present case all diffusion anneals were performed at temperatures above that at which bismuth telluride becomes intrinsic and, therefore, it may be expected that ion pairing interactions will be relatively unimportant.

Electron–hole interactions, on the other hand, could influence the migration of silver through the lattice to a considerable extent. The presence of free electrons will cause an equilibrium to be established between silver as an atom and silver as a positive ion. The equilibrium value of silver as an atom will be governed by the relationship

$$\begin{array}{rcccc} \mathrm{Ag} & \rightleftharpoons & \mathrm{Ag}^{+} & + & e^{-} \\ & & + & & + \\ \mathrm{Lattice} & \rightleftharpoons & e^{-} & + & e^{+} \\ & & \upharpoonleft\downharpoonright & & \upharpoonleft\downharpoonright \\ & & \mathrm{Ag} & & \mathrm{Lattice} \end{array}$$

The number of electrons available increases with temperature and, therefore, the equilibrium amount of atomic silver should increase with temperature. Assuming that the silver diffuses mainly as an ion, the effect of electron–hole interaction will be more pronounced at the higher temperatures. This interaction will reduce the diffusion coefficient at all temperatures. The result of this is to give a lower apparent activation energy than in the absence of this interaction and hence a low value of D_0. Although no estimate of the magnitude of the effect can be made at this time, a relatively small shift would be sufficient to account for the observed deviations from values obtained in metals.

A similar argument may be advanced in the case of diffusion parallel to the cleavage planes. In this case, however, since the diffusion is more rapid by at least one order of magnitude, the concentration of silver ions is smaller than in the perpendicular case and, therefore, the interaction will be less, reducing the effect on the diffusion coefficient.

One feature of the penetration profiles obtained in the parallel case that was not present in the perpendicular diffusion was the appearance of a pronounced upward "hook" at small penetrations. This "hook" was present in only a few samples and appeared in a random manner over the experimental temperature range. The effect is attributed to deformation of the surface layer due to grinding prior to the deposition of the silver. In the worst case, this "hook" extended to a depth of 3 mm, and in the others it was somewhat less. Although this depth may be considered large, it represents less than 30 per cent of the total penetration profile analysed and its presence has been ignored in the calculation of the diffusion coefficients.

The solubility results showed some unexpected features and it was considered advisable to perform a differential thermal analysis (DTA) on stoichiometrically prepared $AgBiTe_2$. This compound is known to be stable above 428°C, dissociating below this temperature to Bi_2Te_3 and Ag_2Te.[13] Under the thermal treatment used in DTA, these two compounds may undergo transitions before combining at 428°C. The results are shown in Fig. 7. Endothermic reactions were observed at 325, 450 and 540°C. The 325°C peak has no obvious correlation with a known phase change in the system; the 450°C peak cannot be precisely related to changes unless the formation of $AgBiTe_2$ (428°C) is responsible. The 540°C peak corresponds to the m.p. of $AgBiTe_2$ (542°C).

Breaks in the solubility curve, Fig. 6, are reasonably compatible with the above DTA data.

CONCLUSIONS

The results of this investigation agree partially with the recently published results of an independent similar investigation by BOLTAKS and FEDOROVICH.[5] The frequency factor and activation energy for diffusion parallel to the cleavage planes agree to within experimental error, but there exist considerable discrepancies between values for the same quantities measured perpendicular to the cleavage planes. Our solubility temperature curve shows features that are absent in theirs and indicates a maximum for the solubility that is one order of magnitude greater than that obtained by the above authors. The reasons for the wide divergence of results are not clear at this time, since the discrepancies are greatest for the measurements in which we have the greatest confidence.

The results reported here are in qualitative agreement with the previously published data on copper diffusion in bismuth telluride,[2] and indicate considerable anisotropy in the diffusion of silver in the directions perpendicular and parallel to the cleavage planes. The values obtained for the activation energies in each case suggest an interstitial mechanism of diffusion, and although the small values for the frequency factors give rise

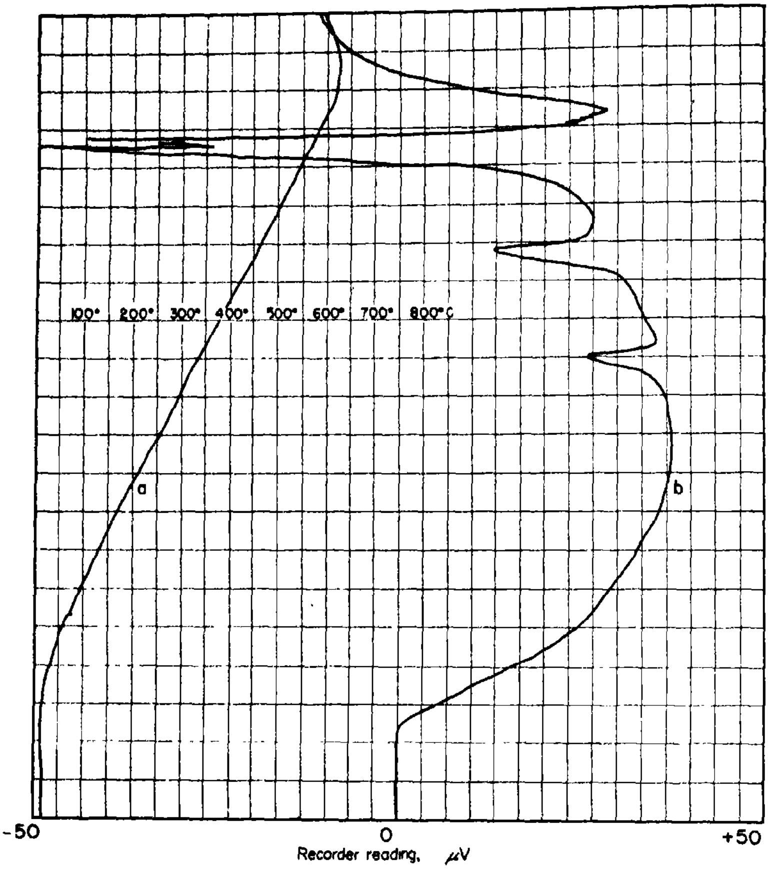

FIG. 7. Differential thermal analysis curves for $AgBiTe_2$.
Curve (a): temperature calibration.
Curve (b): differential temperature of the sample.

to a negative entropy term in the perpendicular case, they are not sufficiently small to be accounted for by large interconnecting dislocations in the crystals. Some modification of the existing diffusion theory for metals, incorporating the special properties of semiconductors as outlined above, could bring the results of this experiment into at least qualitative agreement with the theory of diffusion in metals as currently understood.

The solubility-temperature curve shows a discontinuity in the range 420–450°C, corresponding to the combination of the phases Ag_2Te and Bi_2Te_3, or to a re-arrangement of the silver-containing Bi_2Te_3 structure, to form the disordered NaCl-type structure of $AgBiTe_2$. This change is considered responsible for the abrupt increase by a factor of two in the silver solubility at the temperature at which this phase is reported to form.

Acknowledgements—The authors are indebted to Mr. R. H. LAKE for performing the differential thermal analyses, to Mr. A. F. SEELEY and Mr. H. INHABER for technical assistance and to Dr. G. G. EICHHOLZ and Dr. A. T. PRINCE for useful discussions and encouragement during the course of the investigation.

REFERENCES

1. BOLTAKS B. I., *Zh. tekh. fiz. S.S.S.R.* **25,** 767 (1955).
2. CARLSON R. O., *J. Phys. Chem. Solids* **13,** 65 (1960).
3. MANLEY O. P. M.I.T. *Res. Lab. of Electron. Tech. Rep.* 376 (1960).
4. WEISS K., FIELDING P. and KRÖGER F. A., *Z. phys. Chem.* **26,** 145 (1960).
5. BOLTAKS B. I. and FEDOROVICH N. A., *Fiz. tver. tela* **4,** 550 (1962); translation *Sov. Phys. Solid State* **4,** 400 (1962).
6. KEYS J. D., *J. Phys. Chem. Solids* **23,** 820 (1962).
7. LANGE P. W., *Naturwissenschaften* **27,** 133 (1939).
8. ZENER C., *Imperfections in Nearly Perfect Crystals,* pp. 289–314. John Wiley, New York (1952); FRANCOMBE M. H., *Brit. J. appl. Phys.* **9,** 415 (1958).
9. LAZARUS D., Solid State Physics (edited by SEITZ F. and TURNBULL D.) Vol. **10,** pp. 71–126, Academic Press, New York (1960).
10. LE CLAIRE A. D., *Phil. Mag.* **7,** 141 (1962).
11. REISS H., FULLER C. S. and MORIN F. J., *Bell Syst. tech. J.* **35,** 535 (1956).
12. WHELAN J. M., *Proceedings of the International Conference on Semiconductor Physics, Prague.* Czechoslovak Academy of Sciences (1960).
13. WERNICK J. H., GELLER S. and BENSON K. E., *J. Phys. Chem. Solids* **7,** 240 (1958).

J. Phys. Chem. Solids Pergamon Press 1963. Vol. 24, pp. 573–577. Printed in Great Britain.

CHANGE OF SODIUM CHLORIDE SURFACES IN ELECTRIC DISCHARGES

GIANNA L. PETRICONI, T. W. ZAWIDZKI, ALBERTO C. MONTEFINALE
and HENRY M. PAPÉE

Centre for Aerosol Nucleation, National Research Council of Italy
Via Vettore 4 (Monte Sacro), Rome

(*Received* 25 *July* 1962; *revised* 2 *October* 1962)

Abstract—A convenient and simple laboratory method for introducing surface defects into some powdered solids is described. The method is applied to monodisperse sodium chloride particles, and the extent of the chemical change associated with the defects is found to depend linearly on the specific surface of the halide.

1. INTRODUCTION

DURING the recent years extensive investigations have been carried out by many workers on the physical and optical properties of colour centres and colloidal metal dispersions in alkali halide crystals. It appears, however, that the approach to the problem of introducing colour centres into the lattice of the substance studied, has so far been limited to the use of X- or gamma-ray irradiation of *monocrystals* suitably prepared, or to the heating of salts in metal vapours. It was recently noticed(1) that sodium chloride *microcrystals*, in which large amounts of surface defects had been induced, exhibited under some circumstances an electrical charge, and it was suggested(2) that this may be partly due to photoelectron emission from colloidal sodium incorporated in the lattice of the product. This hypothesis recently appeared to be confirmed in this laboratory,(3) since it was observed that substantial positive charges (of the order of an e.s.u. per sec/cm^2 of surface) may arise on sodium chloride particles which have previously been activated in electric discharges, whenever such particles are illuminated with a strong source of visible light, of a wavelength shorter than that corresponding to the work function of sodium.

Exoelectron emission due to lattice defects in crystals has been observed recently by other workers(4, 5, 6) and it is possible that the phenomenon may partly be due to shallow electron traps associated with dislocations(7) and which seem to be generated when the crystals are irradiated with X-rays.(8)

It has recently been suggested(9) that the ability to cause nucleation of water in the atmosphere, which some substances seem to possess, may be largely due to the electrical effects, e.g. the high local field, which such particles may be capable of producing. Hence it was desirable to find a simple laboratory method for obtaining monodisperse particles into which lattice defects could be introduced. Furthermore, since such particles, after compression under vacuum, could easily be used for photometric research on colour centres, it was considered that the results obtained and presented in the present contribution might also be of interest to workers in the above related field.

2. EXPERIMENTAL

Reagent grade sodium chloride was desiccated at 160°C, ground mechanically under nitrogen in a heated agate mortar, and sieved through an A.S.T.M., standard screen of 270 Mesh × in.$^{-1}$ The fine powder fraction was separated into monodisperse batches using a "Bahco" centrifuge, manufactured by the Etablissements Neu, Lille, France. An electrical heating tape was wound around the shield of the rotor, in the upper part of which the fractionation took place, and which was protected from the atmosphere by a suitably fitted cover. The rotor was thus kept heated to about 100°C and hot air was blown over the inlet of the centrifuge during the fractionation. These precautions prevented caking, sticking and agglomeration of particles by the effects of atmospheric humidity. After fractionation, and until use, the particles were stored in a desiccator which was pumped down to a vacuum of 10^{-5} mm Hg by means of a diffusion pump; when the samples were required for study pure, dry nitrogen was bled into the desiccator.

The size of the particles obtained was measured microscopically using an ocular-micrometer attachment. Photomicrographs of samples of particles fractionated are shown in Fig. 1, while Table 1 gives their dimensions and the specific surfaces computed.

Table 1. *Dimensions* (*obtained on the basis of* 50 *microscopic readings per particle fraction*) *and corresponding specific surfaces of the monodisperse samples of sodium chloride*

Diameter ($cm \times 10^4$)	Specific surface ($cm^2 \times 10^{-3}$)
5·3 ± 0·4	5·23 ± 0·4
12·2 ± 1·0	2·28 ± 0·2
18·6 ± 3·0	1·49 ± 0·1
27·8 ± 3·0	1·0 ± 0·1
42·2 ± 4·0	0·66 ± 0·06
49·0 ± 5·0	0·57 ± 0·06

Quantities of about 100 g of the monodisperse, dry solid were introduced into the discharge tube shown in Fig. 2. The tube was connected to the vacuum assembly by a suitable rubber line, and to a radiofrequency oscillator by an electrodeless, capacitative coupling. In contrast with previous work, where defect sodium chloride was prepared for purposes of microcalorimetric studies of adsorption of water vapour,[(10)] and where agitation of the solid particles was carried out by rotating the container; in the present work, mixing of the salt was achieved by vibrating the discharge reactor electromagnetically. This improvement enabled the evolved chlorine to be pumped off continuously (with consequent continuous operation of the discharge assembly) and better control of the defect introduction process could hence be achieved by preventing agglomeration.

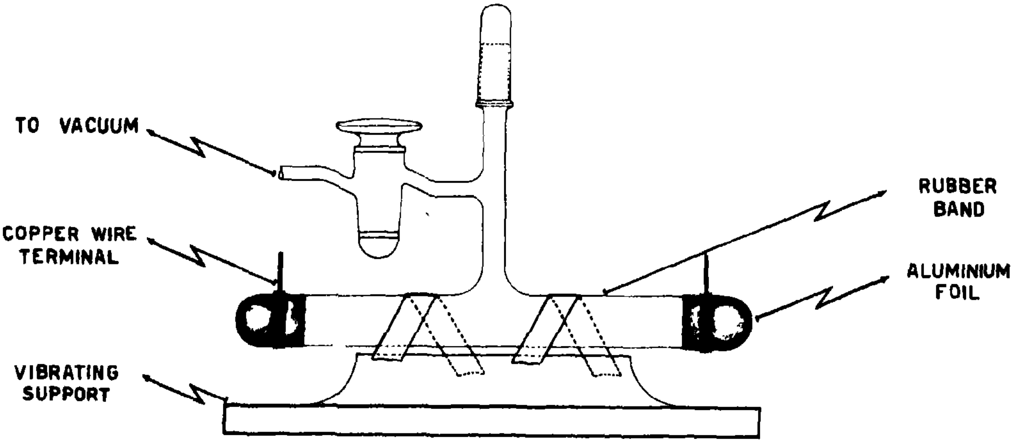

FIG. 2. Discharge tube assembly. × ¼ (schematic).

After filling the tube, the samples were outgassed by evacuating the vibrating container for several hours by means of the diffusion pump. A discharge was then passed in the tube using a stabilized 25 Mc radiofrequency oscillator operating at about 2 kV peak to peak potential at a controlled output of 200 W. Timing was initiated at the commencement of the discharge. After suitable

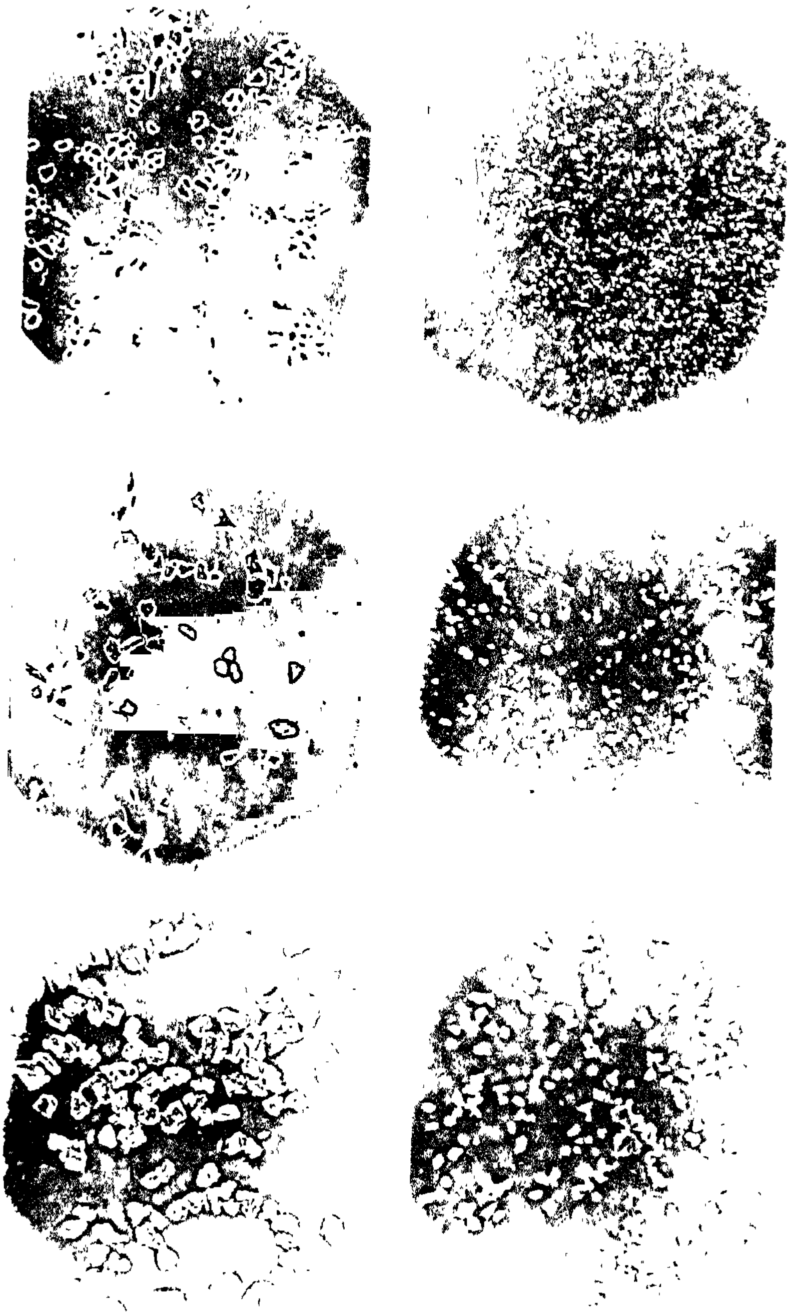

FIG. 1. Photomicrographs of monodisperse particles used. Visual field is $0{\cdot}78_0$ mm in diameter.

periods of time during the runs, the discharge was interrupted, the tube filled with pure, dry nitrogen, and a sample of the salt taken; the procedure of evacuation and discharge treatment was then repeated. The increase of alkalinity of the product was monitored by *pH* determination on samples of 300·0 mg. of substance brought to the volume *of* 100 *cm*^{3} *with distilled water. A sensitive* pH-meter (Beckman 9600) was used for the above measurements. An average of fifteen readings was taken for the determination of pH of pure, monodisperse NaCl fractions, while averages of six readings were used to obtain the values presented in this paper. The results are given in Table 2.

Table 2. *Experimental values of* pH *increments obtained upon dissolving* 300·0 mg. *of monodisperse* NaCl *salt previously treated for* t *seconds in a discharge tube, with respect to control values for untreated salt. Standard deviation of* ΔpH *values is* 0·015 pH *units*

Specific surface (cm^2 × 10^{-3})	5·23		2·28		1·49		1·00		0·66		0·57	
	t × 10^{-3}	ΔpH	t × 10^{-3}	ΔpH	t × 10^{-3}	ΔpH	t × 10^{-3}	ΔpH	t × 10^{-3}	ΔpH	t × 10^{-3}	ΔpH
	1·2	0·25	1·2	0·16	1·2	0·21	1·2	0·09	1·2	0·03	1·2	0·06
	2·4	0·65	2·4	0·24	2·4	0·24	2·4	0·15	2·4	0·10	2·4	0·08
	3·6	0·76	4·2	0·51$_5$	4·2	0·43	4·2	0·22	4·2	0·14	4·2	0·11
	5·0	0·80	7·3	0·65	7·2	0·48	7·2	0·36	7·2	0·18$_5$	7·2	0·19$_5$
					10·8	0·60	10·8	0·45	10·8	0·23	10·3	0·25
					15·0	0·83			15·0	0·28	15·0	0·34
					17·5	0·85			17·5	0·36	17·5	0·37
					20·0	0·94			20·0	0·42	20·0	0·42

3. RESULTS AND DISCUSSION

It can be assumed that the rate of escape of chlorine from the surface of the crystals will be approximately proportional to the surface exposed to ions and electrons. Since the amount of chlorine evolved from the surface of the salt will be equal to the stoichiometric excess of sodium, and therefore to OH$^-$ (the hydroxyl ions generated by dissolving the defect salt in water) it follows that:

$$\frac{\mathrm{d}[\mathrm{OH}^-]}{\mathrm{d}t} = KS \qquad (1)$$

where S represents the area of surface bombarded. Since the product is constantly mixed and the intervals between sampling are large, and since the specific surface of the sodium chloride does not change appreciably during the treatment,$^{(10)}$ equation (1) can obviously be integrated for a particular sample treated, to give $\Delta[\mathrm{OH}^-]$, the quantity of OH$^-$ ions (in gramme equivalents per unit surface of salt) generated indirectly by the loss of Cl$^-$ ions up to time t and resulting from dissolution of 1 g of salt treated in the discharge, *compared with the control amount of* OH$^-$ *ions* present in a solution prepared with the same salt at t_0 irradiation time. This increase is equal to the corresponding quantity of chlorine which has "escaped".

The results obtained are shown in Fig. 3, the plots indicate that during the time of discharge, depletion of the surface in Cl$^-$ was sufficiently small not to affect the linear behaviour shown. It is furthermore apparent that the continuous pumping maintained the concentration of species bombarding the surface at a fairly constant level, which is reflected in the small dispersion of the experimental values about the mean lines in Fig. 3. We expect (equation 1) that the rate of evolution of chlorine will be linear with respect to time when the specific surface of the salt under discharge changes; this is substantiated by Fig. 4. In this case, the constant K is found to be

$$K = (7{\cdot}8 \pm 0{\cdot}2)\ 10^{-16}\ \mathrm{g\ eq\ sec^{-1}\ cm^{-2}}.$$

4. CONCLUDING REMARKS

Under appropriate conditions, the *flux* of

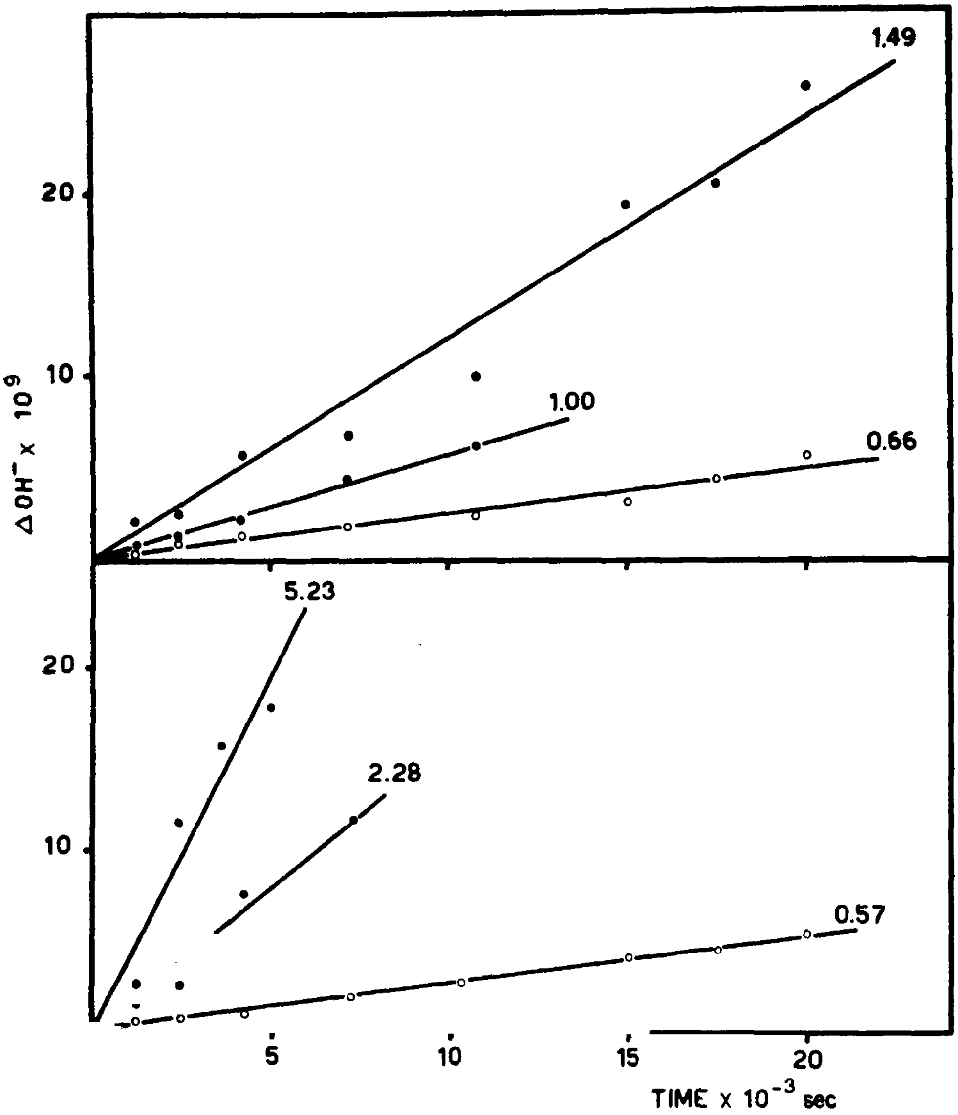

FIG. 3. Plot of the increment of hydroxyl ions in gram-equivalents per unit weight of salt and due to dissolving irradiated NaCl, with respect to the content of OH^- in a solution prepared with sample prior to discharge treatment, against time of treatment (in sec.), ΔOH^- is taken to equal the excess of sodium and thus the escaped chlorine. Specific surfaces (in $cm^2 \times 10^{-3}$) are indicated near least square lines.

electron emission from solids largely depends on the surface available. The method outlined enables the introduction of surface defects and surface non-stoichiometry into solid particles of large specific surface areas to be carried out simply, and on a relatively large scale, without the use of X-ray equipment. Furthermore it permits a variety of surface reactions between a *substrate* and gases

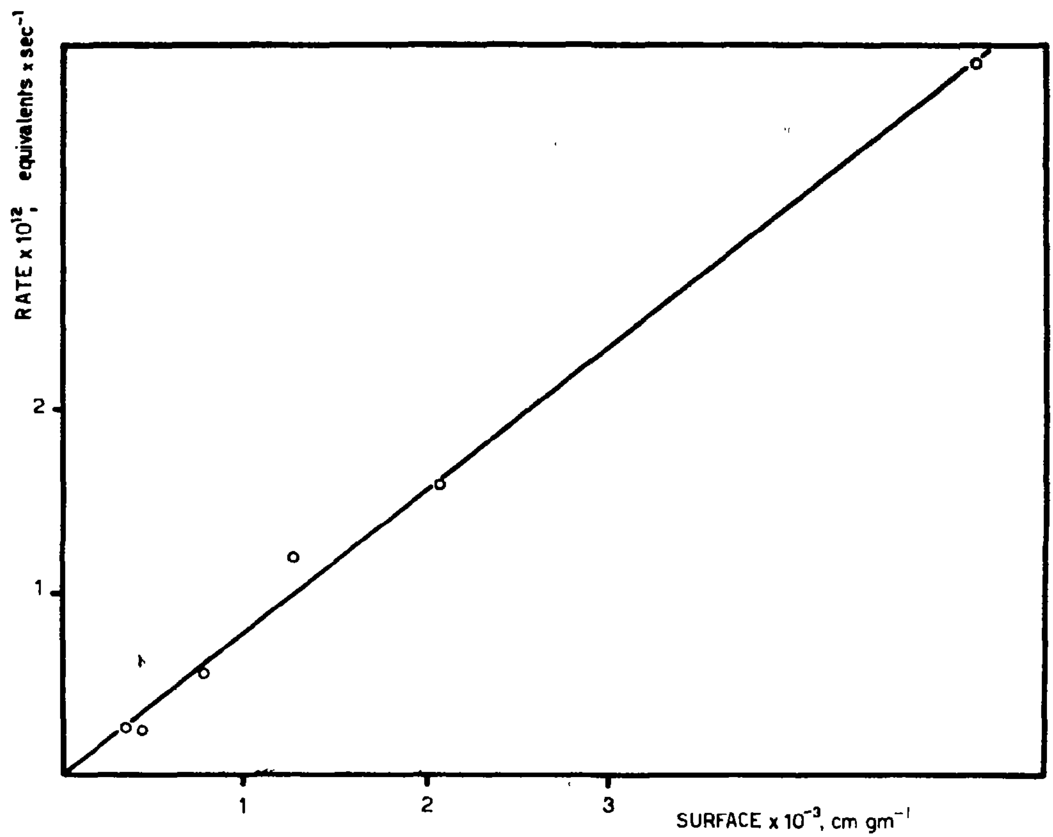

FIG. 4. Plot of the rates of escape of chorine from sodium chloride under conditions discussed, against specific surface of salt.

(for example, the reduction of some metallic salts by hydrogen). Finally, since it is known[(11)] that catalytic activities of some substances may be enhanced by ionic bombardment, it is thought that the use of the technique outlined could, with some modification, be profitably applied to problems of catalyst activation or re-activation, as well as to deposition of finely dispersed metals on inert surfaces, e.g. by radiation-induced decomposition of absorbed salts.

Acknowledgements—We are indebted to Prof. V. CAGLIOTI for his interest and encouragement, and to Mr. M. ARMENI for technical assistance.

The work described in this contribution was carried out with partial financial support from the Società Generale Elettrica della Sicilia and the Cassa per il Mezzogiorno.

REFERENCES

1. PAPÉE H. M., *J. Meteorol.* **16**, 295 (1959).
2. PAPÉE H. M. and SMITH A. C., *Geofis. pura. appl.* **44**, 216 (1959).
3. PAPÉE H. M., ZAWIDZKI T. W., MONTEFINALE A. C. and PETRICONI G. L., to be published.
4. KRAMER J., *Z. phys. chem. N.F.* **25**, 19 (1960).
5. SEIDL R., *Czech. J. Phys.* **B10**, 931 (1960).
6. SZAYNOK A., *J. appl. Phys.* **31**, 211 (1960).
7. OHKURA H., *J. phys. Soc. Japan* **16**, 881 (1961).
8. HIBI T. and ISHIKAWA K., *J. phys. Soc. Japan* **13**, 709 (1958).
9. PAPÉE H. M., *Z. angew. Math. Phys.* **13**, 186 (1962).
10. PAPÉE H. M., *J. Meteorol.* **16**, 244 (1959).
11. SOSNOVSKY H. M. C., *J. Phys. Chem. Solids* **10**, 304 (1959).

J. Phys. Chem. Solids Pergamon Press 1963. Vol. 24, pp. 579–581. Printed in Great Britain.

TEMPERATURE–PRESSURE PROJECTION OF LEAD TELLURIDE PHASE DIAGRAM

RICHARD F. BIS*

U.S. Naval Ordnance Laboratory, White Oak, Silver Spring, Maryland

(*Received* 14 *September* 1962; *revised* 8 *November* 1962)

Abstract—We have determined the partial pressure of diatomic tellurium in equilibrium with Te-saturated PbTe between 567°C and 910°C. The partial pressure was $1\cdot4\times10^{-2}$ atm. from 910°C to 730°C and then dropped linearly on a log vs. $1/T$ plot to $1\cdot6\times10^{-3}$ atm. at 567°C. A double furnace was employed which allowed the partial pressure of Te over the PbTe crystal at a fixed temperature to be varied until the crystal melted, which gave one point on the three-phase line. The partial pressures of Te corresponding to pure Pb and the $P_{\min}$ line were calculated thermodynamically.

1. INTRODUCTION

PREVIOUS work which has been reviewed by KRÖGER and VINK[1] indicates that crystals of controlled stoichiometry can be prepared by annealing crystals in a controlled atmosphere. Work on the Te vapor in equilibrium with solid PbTe has not been reported thus far, and since research and practical applications require the preparation of samples with controlled stoichiometry, the study of the Te vapor in equilibrium with solid PbTe was undertaken. Also the correct model for the disorder in PbTe must account for the thermodynamic properties of the vapor in equilibrium with solid PbTe.

For an ideal gas the chemical potential of $Te_2(\mu_{Te_2})$ is related to the partial pressure of $Te_2(P_{Te_2})$ by the relation

$$\mu_{Te_2} = 1/2[RT \ln P_{Te_2}]+\mu_0, \qquad (1)$$

where R is the gas constant, T the absolute temperature, and μ_0 is the reference state chemical potential. The determination of the temperature–pressure projection of the PbTe phase diagram, (hereafter referred to as the the T–P projection) gives μ_{Te_2} in PbTe at the Te-rich limit of stability as a function of temperature. A double furnace[1, 2, 3] (see Fig. 1) was employed so that the P_{Te_2}[4] over the crystal at a fixed temperature could be varied until solid, liquid, and vapor coexisted. According to the data of MAXWELL and MOSLEY,[5] diatomic tellurium is the only species present in saturated Te vapor over the temperature and pressures encountered in this experiment.

2. EXPERIMENTAL

The PbTe was prepared from A. D. McKay 99·999 per cent pure lead and tellurium. About 3 g of stoichiometric PbTe and 5 g of pure tellurium were placed in a silica tube and sealed off under a vacuum of about 10^{-5} mm of Hg. The tube was then placed in the furnaces as shown in Fig. 1. Both the crystal and tellurium temperatures were controlled to better than ± 1°C. The temperature distributions were such that the temperature was flat to better than 1°C over 4 in. in the tellurium furnace and 5 in. in the crystal furnace. The temperature distributions were determined by probing with a thermocouple both with and without a tube in the furnace.

Since the temperature in the Te furnace is the lowest in the system, it determines the partial pressure of Te_2 in the system. The temperature of the crystal was then fixed and the partial pressure of diatomic tellurium was raised until

---

* Based on a thesis submitted to the Graduate School of the University of Maryland in partial fulfilment of the requirements for the degree of Master of Science.

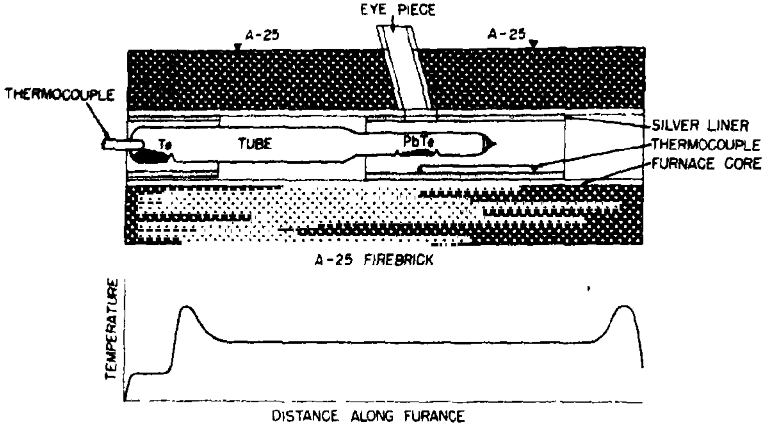

FIG. 1. Furnace arrangement and temperature distribution along furnace.

melting was observed, then lowered until freezing was observed. Both the melting and freezing were observed visually. The range between melting and freezing was narrowed until they were within 10^{-4} atmospheres of each other giving one point on the *T–P* projection.

Each tube was run until the crystal had sublimed away and then a fresh tube was placed into the furnace and the last point taken was repeated to check for contamination of the tellurium reservoir. If the reservoir were contaminated, then the P_{Te_2} determined with the old tube would appear to be higher than the P_{Te_2} determined with the fresh tube. The points determined with fresh tubes were within ½ per cent of those determined with old tubes indicating that contamination was not a problem. Examination of the old tubes revealed that most of the PbTe condensed on the walls of the tube about 4 in. from the Te reservoir.

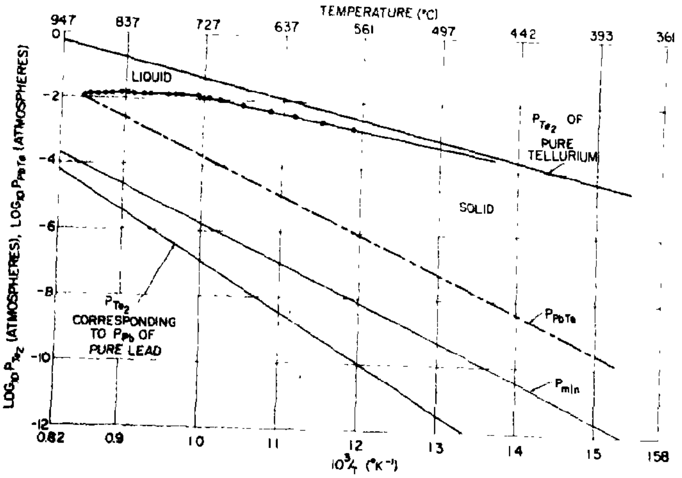

FIG. 2. Three-phase line of PbTe.

3. RESULTS

The T–P projection was measured between 567°C and 910°C as shown in Fig. 2. Below 567°C the time for the crystal to come into equilibrium with the vapor was too long (of the order of 3 hr), while above 910°C the crystal sublimed away. This sublimation near 910°C is consistent with PbTe vapor pressure measurements. These measurements have been made between 511 and 679°C by condensing the effusion products of a calibrated Knudsen cell containing solid PbTe and weighing the condensate.(6) The results are interpreted here as the partial pressure of gaseous PbTe over solid PbTe and are shown as the P_{PbTe} line in Fig. 2. An alternative explanation of this rapid sublimation would be that the $P_{\min}$ line* intersects the three-phase line in the same region. However, a calculation places the $P_{\min}$ line well below P_{PbTe} as shown in Fig. 2. This high vapor pressure of PbTe also causes difficulty when one wishes to pull crystals of PbTe in that the PbTe vapor condenses on the pulled crystal.(7)

The partial pressure of Te_2 corresponding to pure Pb has been calculated and is plotted in Fig. 2. In order to make the calculation one needs a relationship between the partial pressure of lead and the partial pressure of diatomic tellurium in equilibrium with the crystal. Such a relationship may be arrived at in the following manner:

The lead and diatomic tellurium partial pressures are not independent but are coupled by the equilibrium constant of the reaction

$$\mathrm{PbTe}(s) = \mathrm{Pb}(g) + 1/2\mathrm{Te}_2(g), \tag{2}$$

where s and g stand for solid and gas respectively.

The calculation of the equilibrium constant follows that of DE NOBEL(2) for CdTe and assumes the vapor is ideal and the molar Gibb's free energy of formation of solid PbTe is not significantly dependent upon composition over the narrow range of stability of PbTe. The free energy values of MCATEER and SELTZ(8) were extrapolated linearly on a G vs. T plot from the 623 to 683°K range of experimental determination to 723°K, the melting point of Te where the slope was changed by the entropy of melting of Te.(9) The values of G thus obtained were adjusted to a standard state of ideal monoatomic Pb gas and diatomic Te gas.

Since P_{PbTe} is always higher than the vapor pressure of pure Pb and therefore always higher than the partial pressure of Pb in equilibrium with crystalline PbTe, it is not possible to determine the Pb-rich limit of stability by the method used here. However, a limit can be established in that the Pb-rich limit lies inside P_{Te_2} corresponding to pure Pb.

4. SUMMARY

We have measured the partial pressure of Te_2 in equilibrium with Te-saturated PbTe as a function of temperature. The Pb-rich limit of stability could not be studied with either a Pb or Te reservoir as the partial pressure of PbTe is always higher than the partial pressure of Pb and Te in equilibrium with Pb-saturated PbTe.

Acknowledgements—The author wishes to express his gratitude to Drs. BLAND B. HOUSTON, Jr. and ROBERT F. BREBRICK for their many helpful suggestions during the course of the experimental work, and during the preparation of the manuscript.

REFERENCES

1. KRÖGER F. A. and VINK H. J., *Solid State Physics* Vol. 3 (Edited by SEITZ F. and TURNBULL D.), p. 307. Academic Press, New York (1956).
2. DE NOBEL D., Thesis, University of Leiden (1958).
3. BREBRICK R. F. and SCANLON W. W., *Phys. Rev.* **96,** 598 (1954).
4. BROOKS L. S., *J. Amer. Chem. Soc.* **74,** 227 (1952).
5. MAXWELL L. R. and MOSLEY V. M., *Phys. Rev.* **57,** 21 (1940).
6. PASHINKIN A. S. and NOVOSELOVA A. V., *Russ. J. inorg. Chem.*, English translation, *Chem. Soc. London* 1229 (1959).
7. HOUSTON B. B., *Bull. Amer. phys. Soc.* **5,** 166 (1960).
8. MCATEER J. H. and SELTZ H., *J. Amer. chem. Soc,* **58,** 2081 (1936).
9. STULL D. R. and SINKE G. C., *Thermodynamic Properties of the Elements*, Advances in Chemistry Series, *Amer. chem. Soc.*, Washington, D.C. (1956).

---

* For a discussion of the $P_{\min}$ line, see Ref. 2.

LETTERS TO THE EDITOR

Comments on "A study of neodymium substituted yttrium iron garnet" by T. H. Ramsey Jr., H. S. Steinfink and E. J. Weiss

(*Received* 15 *October* 1962)

IN CONNECTION with the above paper,[1] we wish to call attention to a rather detailed study[2] of neodymium substituted yttrium iron garnet as well as neodymium substituted gadolinium iron garnet published over a year ago but not included in its list of references. We wish especially, however, to discuss a conclusion of this paper with which we disagree.

The Nd substituted YIG's are not similar to the perovskite-like Mn^{3+}–Mn^{4+} ion containing compounds[3] as implied by RAMSEY *et al.*[1] In the latter compounds the moments of *all* magnetic ions are presumably in parallel alignment and the net moment appears to arise only from spin.[3] In the Nd substituted YIG's the Fe^{3+} ion moments in the two different magnetic sublattices are aligned antiparallel; it is these antiferromagnetic interactions which establish the ferrimagnetism of the crystals. As in the case of rare earth ions with configuration $4f^7$ to $4f^{13}$, the main magnetic interaction between the Nd^{3+} and tetrahedral Fe^{3+} ions is antiferromagnetic in spin moment. It is only because $\boldsymbol{J}$ is oppositely directed to $\boldsymbol{S}$ that the Nd^{3+} ion net moment is aligned parallel to the resultant moment of the Fe^{3+} ion sublattices.[1, 4, 5]

There are in fact other ways[6] of obtaining garnets in which the moment of the *c* sublattice is parallel to the resultant iron sublattice moment. An example is $\{Gd_{1\cdot 5}Ca_{1\cdot 5}\}[Fe_2](Fe_{1\cdot 5}Si_{1\cdot 5})O_{12}$[6]. In this case the octahedral sublattice moment is greater than the tetrahedral one and the effective Gd^{3+} ion sublattice moment therefore parallel to the resultant iron sublattice moment. Here again the spin moments of the Gd^{3+} and tetrahedral Fe^{3+} ions are antiparallel—*not* different from the Nd substitutions discussed above or from GdIG itself. We would hardly refer to the substituted GdIG example above as ferromagnetic as opposed to ferrimagnetic. The strong interactions in this garnet are all antiferromagnetic.

We can carry the illustrations a step further. It is probable, though we have not tried it yet, that the analogous $\{Nd_{1\cdot 5}Ca_{1\cdot 5}\}[Fe_2](Fe_{1\cdot 5}Si_{1\cdot 5})O_{12}$ garnet could be made. In this case, the net moment of the Nd^{3+} ion sublattice would be *anti*parallel to the net moment of the iron sublattices although still parallel, of course, to the tetrahedral sublattice moment.

There is perhaps some question as to what name should be given to the magnetic behavior of an *intermetallic* compound such as $NdCo_5$.[7] The compound $GdCo_5$[8] is experimentally ferrimagnetic, the net moment of the Co sublattices being antiparallel to that of the Gd sublattice. In $NdCo_5$, the net moment of the cobalt sublattices is parallel to that of the Nd sublattice. This case, however, also is not one which is analogous, for example, to the ferromagnetism in iron, but again probably occurs through antiferromagnetic interaction of the spins of the two different kinds of atoms. It is therefore reasonable to consider $NdCo_5$ to be ferrimagnetic also.

In any case, it seems hardly proper to refer to the Nd substituted YIG's as ferromagnetic.

Bell Telephone Laboratories,
Inc.,
Murray Hill, New Jersey

S. GELLER
H. J. WILLIAMS
R. C. SHERWOOD

References

1. RAMSEY T. H. Jr., STEINFINK H. and WEISS H. J., *J. Phys. Chem. Solids* **23**, 1105 (1962).
2. GELLER S., WILLIAMS H. J. and SHERWOOD R. C., *Phys. Rev.* **123**, 1692 (1961). *See also* GELLER S., WILLIAMS H. J. and SHERWOOD R. C., *Bull. Amer. phys. Soc.* **6**, 230 (1961).
3. JONKER G. H. and VAN SANTEN J. H., *Physica* **16**, 337 (1950).
4. WOLF W. P., *J. appl. Phys.* **32**, 742 (1961).
5. WHITE R. L., *J. appl. Phys.* **32**, 1178 (1961).
6. GELLER S., WILLIAMS H. J., ESPINOSA G. P. and SHERWOOD R. C., *Bull. Amer. phys. Soc.* **7**, 279 (1962).
7. NESBITT E. A., WILLIAMS H. J., WERNICK J. H. and SHERWOOD R. C., *J. appl. Phys.* **33**, 1674 (1962).
8. NESBITT E. A., WERNICK J. H. and CORENZWIT E., *J. appl. Phys.* **30**, 365 (1959).

High voltage photovoltaic effect at low temperatures

(*Received* 19 *December* 1962)

ANODIZED zirconium electrodes that have been coated with a thin evaporated layer of copper or gold develop photopotentials of the order of 1–2 V at room temperature when irradiated with u.v. light.(1) It has been found that at temperatures in the vicinity of $-175°C$ photopotentials as large as 35 V are produced with both copper and gold coated electrodes. Electrodes coated with tin develop potentials as large as 90 V under similar conditions.

The zirconium bars, supplied by the Wah Chang Corporation, are polished on an emery wheel and etched in a $HF–HNO_3$ solution. This is followed by anodization of the etched face in a borate–boric acid solution of pH 8. The anodization is carried out for 12 or more hr at a temperature of 30°C. The polarization voltages are 75 or 100 V. The electrode is then placed in a Bendix Vacuum Evaporator with a specially designed brass cover. A thin, semi-transparent layer of copper, gold or tin is evaporated on to the anodized face. Care is taken to eliminate edge effects by suitable masking. Electrical contact to the evaporated metal is made by means of a previously mounted platinum wire. The electrode is cooled to low temperatures by a conduction method. A copper–constantan thermocouple connected to the electrode is used to measure the temperature.

Light from a G. E. UA-2 Uviarc mercury lamp is passed through a quartz window on to the electrode face. The photopotential is measured with a high impedance electrometer. An auxilliary bucking circuit is provided for high voltage measurements. Upon irradiation the zirconium becomes negative with respect to the evaporated metal. The photopotential rises slowly and reaches a steady value in about 30 sec.

PENSAK(2) observed an anomously large photovoltage across an evaporated layer of Cd–Te on a glass substrate. The photovoltage increased as the temperature was lowered and was of the order of 100 V at $-169°C$. In the case of the anodized zirconium electrode the potential is developed across an oxide whose thickness is about 2000 Å. The origin of this large photovoltage is unknown at present. VAN GEEL *et al.*(3) proposed a theory to explain the behavior of similarly prepared aluminium and tantalum photovoltaic cells. In this theory the maximum photovoltage attainable is equal to the difference between the work functions of the two metals. These large photopotentials are probably due to several effective photovoltaic cells arranged in series. Further work aimed at determining the cause of this effect is in progress.

Chemistry Department,
Temple University,
Philadelphia 22,
Pennsylvania

P. N. RAMACHANDRAN
R. E. SALOMON

References

1. SALOMON R. E., thesis, Univ. of Oregon (1960).
2. PENSAK L. *Phys. Rev.* **109**, 601 (1958).
3. VAN GEEL W. C., PISTORIUS C. A. and WINKEL P. *Philips res. Rep.* **13**, 265 (1958).

Magnetostriction of yttrium iron garnet

(*Received* 15 *October* 1962)

WE HAVE measured the magnetostriction of yttrium iron garnet single crystals(1) as a function of temperature. The measurements were performed with an apparatus previously used for measuring thermal expansion at low temperatures.(2) No strain gauges are used in this type of experiment, the change in length being directly measured with a mechanical–optical device. Measurements were made at room temperature, at liquid air temperature and at 1·5°K. The field was always applied in the direction of the long axis of the specimen. Two single crystals approximately 2 cm long and 3 mm thick with their long axis oriented in the (100) and (111) directions were investigated.

The results are shown in Figs. 1 and 2, where $\Delta L/L$ is the relative change of length as a function of the applied magnetic field. In all cases, $\Delta L/L$ tends to a saturation value. No hysteresis effects were observed.

In the theory of magnetoelasticity,(3) the magnetostriction for cubic materials is given by the formula

$$\frac{\Delta L}{L} = \frac{3}{2}\lambda_{100}\left(\alpha_1^2\beta_1^2+\alpha_2^2\beta_2^2+\alpha_3^2\beta_3^2-\tfrac{1}{3}\right)$$
$$+3\lambda_{111}(\alpha_1\alpha_2\beta_1\beta_2+\alpha_1\alpha_3\beta_1\beta_3+\alpha_2\alpha_3\beta_2\beta_3) \qquad (1)$$

where $(\alpha_1, \alpha_2, \alpha_3)$ are the direction cosines of the magnetization relative to the principal axis of the crystal and $(\beta_1, \beta_2, \beta_3)$ the direction cosines of the direction in which $\Delta L/L$ is measured. The magnetostriction constants λ_{100} and λ_{111} are related to the magnetoelastic coupling constants B_1 and B_2 as follows:

$$\lambda_{100} = -\tfrac{2}{3}\,B_1/(c_{11}-c_{12}) \quad \lambda_{111} = -\tfrac{1}{3}\,B_2/c_{44} \quad (2)$$

(c_{ik} = elastic constants)

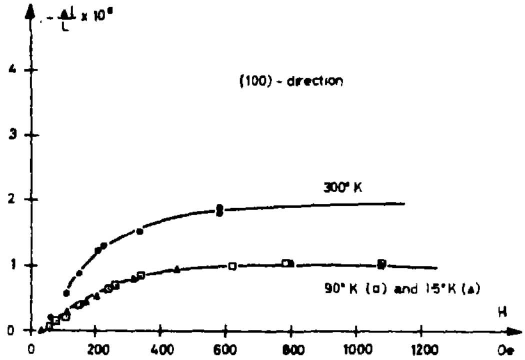

FIG. 1. Magnetostriction of a YIG crystal oriented in (100)-direction as a function of magnetic field and temperature.

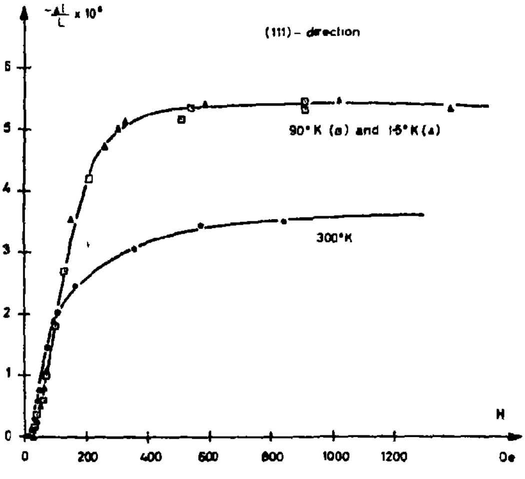

FIG. 2. Magnetostriction of a YIG crystal oriented in (111)-direction as a function of magnetic field and temperature.

According to equation (1), our measured saturation values in the (100) and (111) directions are identical with the constants λ_{100} and λ_{111}, respectively. At 300°K, we obtain for the magnetoelastic constants (using known experimental values for the elastic constants[4]) $B_1 = 4{\cdot}8 \times 10^6$ erg/cm^3 and $B_2 = 8{\cdot}3 \times 10^6$ erg/cm.^{3}

In the literature, only magnetostriction values for polycrystalline yttrium iron garnet at 300°K are reported[5] giving $\lambda_s = -3{\cdot}7 \times 10^{-7}$. From our values, using the customary formula for the average[6] $\lambda_s = 1/5(2\lambda_{100}+3\lambda_{111})$, we find $\lambda_s = -3 \times 10^{-6}$ in very bad agreement with the measured polycrystalline value. It should be noted that we could not test equation (1) with our apparatus since we could only apply longitudinal fields. Therefore we cannot be certain that the relation (1) applies because of possible disturbing domain effects in zero magnetic field.

To search for the physical mechanism which accounts for our observed value of the magnetostriction, one can calculate the contribution due to dipole–dipole interaction.[5] The values thus obtained are $\lambda_{100} = 5{\cdot}8 \times 10^{-7}$ and $\lambda_{111} = -4 \times 10^{-7}$. The dipole contribution is, therefore, small and of the wrong sign for λ_{100}.

Since the Fe^{3+}-ion is in an S-state, all usual processes which involve the orbital momentum state fail for the explanation of the magnetostriction. However, GESCHWIND[7] has shown that the magnetic anisotropy of yttrium iron garnet can be explained to a large extent by the single ion crystal field anisotropy. In close analogy one can calculate the anisotropy energy for a deformed lattice, which gives the magnetoelastic energy. If we take as an example the process which combines the $3d^5$ configuration with the $3d^4\,4s$ by a combined action of the intra spin–spin interaction and the deformed crystal field potential,[8] we find the measured order of magnitude for the magnetoelastic energy.

The results in Table 1 show that the temperature dependence of λ_{100} and λ_{111} and, therefore, also of the magnetoelastic coupling constants B_1 and B_2 (the elastic constants should not vary considerably with temperature) does not follow an

Table 1

	λ_{100} ($\times 10^6$)	λ_{111} ($\times 10^6$)	*M* (G)
300°K	−2·0	−3·6	138
77°K	−1·1	−5·4	195
1·5°K	−1·1	−5·4	—

M^3-law as it should in the one ion model,(9) (M is the saturation magnetization). The anomalous temperature dependence especially of λ_{100} has probably to be attributed to a domain effect as mentioned above. A similar magnetostriction experiment, using a strain gauge method, is being carried out by Crapo.(10)

Acknowledgements—We are grateful to Prof. P. Grassmann and Prof. J. L. Olsen for their support. This work was supported partly by the Schweizerischer Nationalfonds.

Institut für kalorische Apparate und Kältetechnik der Eidgenössischen Technischen Hochschule,
Zurich, Switzerland
K. Andres

International Business Machines CorporationResearch Laboratory,
Rüschlikon-Zurich,
Switzerland
B. Lüthi

References

1. The YIG crystals were kindly supplied by Dr. P. E. Seiden from the IBM Research Center, Yorktown Heights.
2. Andres K., *Cryogenics*, **2**, 93 (1961).
3. Kittel C. and Galt K., *Solid State Physics* Vol. **3** (Edited by Seitz F. and Turnbull D.) p. 470. Academic Press, New York (1955).
4. Clark A. E. and Strakna R. E., *J. appl. Phys.* **32**, 1172 (1961).
5. Nakamura A. and Sugiura Y., *J. phys. Soc. Japan* **15**, 1704 (1960).
6. Becker R. and Döring W., *Ferromagnetismus*, p. 166. Springer, Berlin (1939).
7. Geschwind S., *Phys. Rev.* **121**, 363 (1961).
8. Tsuya N., *Sci. Rep. Tôhoku Univ.* **B8**, 161 (1958).
9. Kittel C. and Van Vleck J. H., *Phys. Rev.* **118**, 1231 (1960).
10. Crapo W. A. (private communication).

Investigation of optical absorption in irradiated CsF

(*Received* 17 *December* 1962)

In recent studies of alkali halides with the CsCl-type lattice it has been found that the principal optical absorption band displays fine structure. The components of this structure are partially resolved in the vicinity of liquid helium temperature,(1) while at temperatures of liquid nitrogen and above only a general distortion in the band shape is observed.(1–3) Since this absorption exhibits typical properties normally expected of the F-band, the question arises as to the origin of the structure.

At present one may speculate that the structure is the result of splitting in either the excited state of the F-center or the ground state. The latter possibility is unlikely in that e.p.r. observation of the F-center in CsCl shows no characteristics which may be due to a split ground state.(4) If the splitting occurs in the excited state, it might be related to either (a) the CsCl-type lattice, or (b) the cesium ion, both of which are common to the cesium halides studied to date (CsCl, CsBr, and CsI). The strongest evidence against postulate (a) comes from the observation of the F-band in the CsCl-phase of RbCl induced by the application of high pressure.(5) This F-band is not complex but retains its simple shape characteristic of that observed in the NaCl-phase at normal pressure.

The present work deals with CsF. This crystal is unique in that it is the only cesium halide with the NaCl-type lattice under standard temperature and pressure, and thus offers the further possibility of reflecting on postulate (a) as well as (b).

Single CsF crystals obtained from the Harshaw Chemical Co, and Semi-Elements Inc. were employed in these measurements. The spectrographic analysis shown in Table 1 indicates that the Semi-Elements crystal had the smaller metallic impurity content. Since CsF is particularly deliquescent, all operations that required atmospheric exposure of the crystals were carried out in a dry box containing dried nitrogen gas.

Table 1. *Spectroscopic analysis in p.p.m.*

Element	Harshaw CsF	Semi-Elements CsF
Fe	1000	< 1
Al	5	5
Ca	50	< 1
Cu	1	< 1
Ag	< 1	< 1
Si	50	< 1
Mg	5	1
Mn	1	< 1
Na	< 1	< 1
K	< 1	< 1

The solid curves of Fig. 1 show the principal absorption structure in Harshaw CsF at 295, 80 and 18°K after X-ray irradiation at 295°K. No absorption structure was observed to longer wavelengths (in the range to 1700 mμ), and to shorter wavelengths weak and poorly defined absorption was observed at about 300 mμ extending to what appears to be the tail of the fundamental absorption near 210 mμ. The absorption structure at room temperature consists of a principal triplet (636, 667, and 707 mμ) with a weak component to shorter wavelength at approximately 570 mμ. Additional resolution at 18°K, Fig. 1, indicates that the short wavelength component of the triplet consists of at least two overlapping absorption bands; for purposes of convenience this structure will continue to be referred to as the "triplet", even though it consists of at least four bands. In order to verify that the X-ray induced structure was the result of a trapped electron center, a Harshaw CsF crystal was additively colored with cesium. These data are shown at 80°K in Fig. 1, and the principal triplet is again in evidence. The fact that the short wavelength component appearing near 570 mμ is enhanced relative to the triplet absorption tends to indicate that this band is unrelated to the triplet. Unfortunately, it could not be established with certainty that the absorptions near 570 mμ in the X-rayed and additively colored crystals were identical. The weakness of the 570 mμ band in the X-rayed crystal in the presence of overlapping absorption to longer wavelength, coupled with limitations in the additive coloring process of an extremely deliquescent crystal prevented such a determination. It was clear, however, that the components of the triplet itself maintained a fixed relative ratio, as confirmed by the following observations.

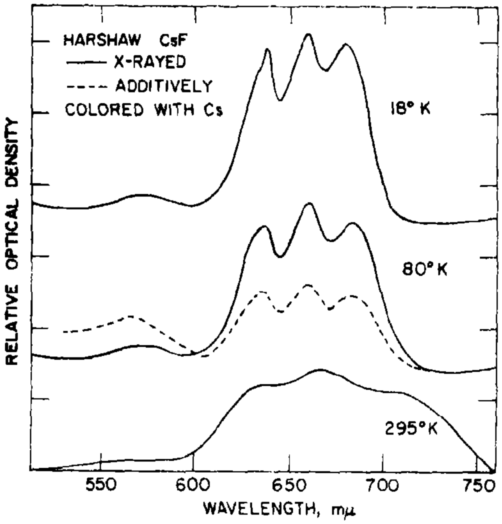

FIG. 1. Solid curves, Harshaw CsF X-ray irradiated at 295°K and thereafter measured successively at 295, 80 and 18°K. X-irradiation was performed with a Machlett OEG-60 tungsten-target tube operated at 50 kV and 40 mA. Dashed curve, Harshaw CsF additively colored with cesium (625°C for 12 hr) and measured at liquid nitrogen temperature. All optical data were obtained with a Cary, Model 14 MR, spectrophotometer.

(1) Attempts to selectively bleach the three components of the room temperature triplet proved unsuccessful. The relative proportion of the triplet structure was maintained during optical bleaching independent of the bleaching wavelength.

(2) Crystals were irradiated at low temperature as well as room temperature to show that the same structure was produced. Irradiations at 80°K resulted in absorption spectra that are essentially identical to that shown at 80°K in Fig. 1. X-raying at 18°K resulted in the production of additional absorption bands which overlapped and distorted the data of Fig. 1, but fortunately this additional structure could be selectively bleached and the essential character of the data of Fig. 1 at 18°K could be reproduced. It was furthermore confirmed that the room-temperature triplet of Fig. 1 could be produced by first X-raying at low temperature, and subsequently observing the crystal at room temperature.

(3) The behavior of the triplet in a wide variety of X-ray exposures did not show any significant variation in the Harshaw and Semi-Element-specimens which differed considerably in impurity content.

Attempts were also made to induce dichroism in the triplet absorption by bleaching with linearly polarized white light. These measurements were carried out on X-irradiated crystals at 18°K to minimize possible reorientation that might take place at higher temperature. If one defines a dichroism factor as $\eta = \dfrac{(\text{O.D.})_{\parallel} - (\text{O.D.})_{\perp}}{(\text{O.D.})_{\parallel} + (\text{O.D.})_{\perp}}$ then a change $\Delta\eta$ induced by bleaching with light polarized in the perpendicular direction would indicate that the triplet center was anisotropic and thus not the *F*-center. Within the limits of experimental error ($\Delta\eta \leqslant 0{\cdot}05$ for [100] dichroism, and $\Delta\eta \leqslant 0{\cdot}1$ for [110] dichroism) no dichroism was observed.

Although it is clear that both the 570 mμ band and the triplet absorption are candidates for the *F*-band, unfortunately no *F*-electron paramagnetic resonance was observed. The only observed e.p.r. absorption in irradiated CsF was a seven-line pattern about 50 Oe wide. This could be due to an electron interacting with two or more sets of equivalent nuclei. Since an identical absorption has been observed in irradiated CsCl and CsBr[6] there seems to be no basis for associating it with the optical bands in CsF. Due to e.p.r. spectrometer sensitivity considerations, measurement of the *F*-center e.p.r. absorption in CsF is expected to be marginal; thus, the absence of the resonance at present may not be construed as either positive or negative evidence that the optical bands are due to the *F*-center.

The anticipated position of the *F*-band in CsF on the basis of the Ivey relation does not seem to add any further clarification. Both the 570 mμ band and the triplet structure lying to longer wavelengths are considerably displaced from the 531 mμ *F*-band position predicted by Ivey.[7] Since the peak position of the *F*-band in at least two other alkali fluorides, namely NaF and KF, also fall to the long wavelength side of the Ivey curve, it seemed desirable to determine the *F*-band peak position in RbF which does not appear to have been previously reported. Examination of the optical absorption spectrum of X-ray irradiated RbF shows an *F*-like band at 525 mμ at room temperature which shifts to 511 mμ at 80°K. The room temperature peak position for RbF is plotted together with the data for other alkali fluorides in Fig. 2. The CsF data includes the 570 mμ band (uppermost point) and the positions of the components of the triplet (three lower points). The solid curve gives the Ivey equation for NaCl-type alkali halides at room temperature which appears to show wide deviation from the plotted points. In a search for a simple common denominator to explain this deviation the empirical observation was made that the ratio of the positive-ion radius to the negative-ion radius appeared to be critical. At least in all cases in which this ratio is large, *F*-band positions fall to the long wavelength side of the predicted Ivey position as shown in Fig. 2. In the instance of a low radius ratio for LiF the experimental *F*-band peak falls to shorter wavelength. At present no theoretical basis for this observation is known. Since it appears that *F*-bands in most of the fluorides fall to the long wavelength side of the Ivey curve, a deviation of some 140 mμ for the CsF triplet may not necessarily rule out its assignment as the *F*-band in view of its unusually large positive-ion to negative-ion radius ratio.

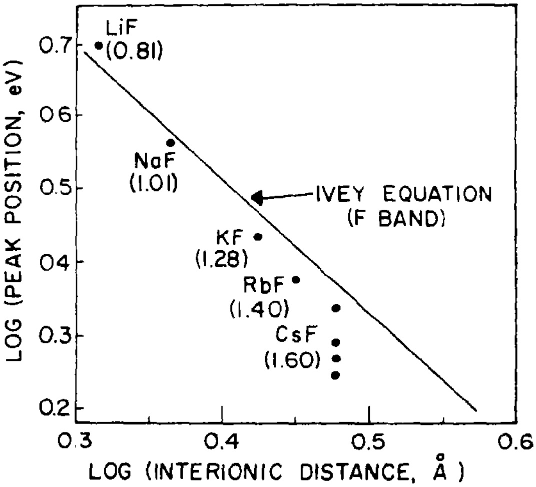

FIG. 2. The solid line gives the Ivey equation for the *F*-band in NaCl-type alkali halides at room temperature, and the plotted points are experimentally determined *F*-band positions for various alkali fluorides. The four CsF points are for the 570 mμ absorption band and the three components of the triplet absorption to longer wavelength, shown in the 295°K curve of Fig. 1. The data given in parentheses for each salt are the ratios of the positive-ion radius to the negative-ion radius computed from the data of GOURARY and ADRIAN.[8]

At present the possibility exists that a complex *F*-band in CsF, similar to those observed in other cesium halides, is in some way related to the cesium ion and not the type of lattice involved, i.e. postulate (b) is valid rather than postulate (a).

Acknowledgements.—The authors are indebted to F. G. ADRIAN, C. C. KLICK, and J. H. SCHULMAN for a number of interesting discussions and to M. HASS for providing

CsF and RbF crystals used in this work. The authors are also appreciative for receipt of an early copy of Dr. FITCHEN's thesis from Professor DAVID LAZARUS. S. CRESS very kindly performed the CsF spectrographic analysis.

U.S. Naval Research Laboratory, FLOYD HUGHES
Washington, D.C. HERBERT RABIN

References

1. RABIN H. and SCHULMAN J. H., *Phys. Rev. Letters* **4**, 280 (1960); *Phys. Rev.* **125**, 1584 (1962).
2. AVAKIAN P. and SMAKULA A., *Phys. Rev.* **120**, 2007 (1960).
3. LYNCH D. W., *Phys. Rev.* **127**, 1537 (1962).
4. HUGHES F. and ALLARD J. G., *Phys. Rev.* **125**, 173 (1961).
5. FITCHEN D. B., Thesis, University of Illinois, 1962.
6. HUGHES, F. (unpublished).
7. IVEY H. F., *Phys. Rev.* **72**, 341 (1947).
8. GOURARY B. S. and ADRIAN F. J., *Solid State Physics* (edited by SEITZ F. and TURNBULL D., Vol. **10**, p. 144. Academic Press, New York (1960).

Absence of antiferromagnetism in palladium

(*Received* 17 *December* 1962)

THE magnetic susceptibility of palladium has been reported to exhibit a maximum at about 80°K.(1) The recent work of BOZORTH *et al.*(2) indicates the maximum in the susceptibility occurs at 90°K. LIDIARD(3) considered the earlier susceptibility data to be indicative of antiferromagnetism in palladium. Further interest has been raised in this possibility by the large moment found associated with cobalt when in a solution as dilute as 0·1 at. per cent in palladium:(2) at this dilution, a moment of 9–10 Bohr magnetons per cobalt atom is obtained. A mechanism accounting for this result postulates(2) a moment of 0·6 Bohr magnetons on each of the twelve nearest-neighbor Pd atoms. An alternative explanation of the maximum in the palladium susceptibility has been given by ELCOCK *et al.*(4) in terms of the density-of-states curve. They showed that a maximum in the susceptibility–temperature relation is to be expected for certain simple band shapes.

A distinction between the antiferromagnetic and the density-of-states theories for palladium could be made by neutron diffraction. The interaction of an antiferromagnetic lattice with a neutron beam would allow observation of reciprocal lattice points forbidden by the nuclear lattice. An attempt to observe such magnetic neutron scattering was made in three separate experiments. In the first, a polycrystalline sample of 99·99 per cent pure palladium was used to obtain a neutron diffraction pattern at room temperature and at liquid helium temperature. The "powder" cryostat and diffractometer used(5) were kindly made available by Dr. S. PICKART. The nuclear peaks corresponding to the f.c.c. unit cell were observed, but no additional coherent scattering was detected at 4·2°K corresponding to the forbidden lines of a possible antiferromagnetic P_I lattice at (100) or (110). The maximum but unobserved structure factors for these reflections and the corresponding upper limit for the atomic moments of an antiferromagnetic array are given in columns 2 and 3 of Table 1. The nuclear structure factors were used to establish the absolute scale.

The sensitivity of the neutron diffraction experiment was then increased by use of the single crystal technique. The first of two single crystals was grown from 99·8 per cent pure palladium and ground into a cylinder, with [110] along the cylinder-axis.(6) The cryostat(7) and the Single Crystal Automatic Neutron Diffractometer(8) have been described previously. A careful search of the *hhl* zone at 4·2°K indicated no fractional order reflections to be present. There is also no evidence for any large change in lattice constant.

Table 1. Structure factors and upper limits of antiferromagnetic moments on palladium atoms

hkl	*F*(powder) 10^{-12} cm/cell	μ Bohr mag.	*F*(cryst. No. 1) 10^{-12} cm/cell	μ Bohr mag.	*F*(cryst. No. 2) 10^{-12} cm/cell	μ Bohr mag.
100	< 0·222	< 0·37	< 0·017	< 0·028	< 0·016	< 0·027
110	< 0·220	< 0·44	< 0·026	< 0·054	< 0·018	< 0·037

The observed value of a at 4·2°K is 3·884 Å, as compared with 3·890 Å at 298°K. The *hhl* reflections were filtered through plutonium foil, to remove the $\lambda/2$ component. The corresponding upper limits on $F(100)$ and $F(110)$, together with the limits on the largest moments that could be associated with the palladium atoms and still not be observed, are given in columns 4 and 5 of Table 1. In these calculations, the nuclear scattering length of Pd was taken(9) as $0{\cdot}585 \times 10^{-12}$ cm, the magnetic form factor of Ni was used,(10) and a single spin-axis model was assumed.

After completion of these measurements it was found, by spectrochemical and by X-ray fluorescent analyses, that this crystal (No. 1) contained the ferromagnetic impurities Fe, Mn and Ni in the concentration range 0·01–0·1 per cent. In order to be sure that the limits on the maximum possible antiferromagnetic moment given in Table 1 apply to *pure* palladium, a second single crystal was grown by E. Buehler. Johnson Matthey Company 99·999 per cent-pure palladium wire was floating-zone refined in an argon atmosphere. A single pass more than doubled the residual resistance ratio,(11) as compared with the unannealed cold-worked original wire sample. This pass produced a sufficiently large single crystal of palladium for a sample to be cut out for the neutron diffraction measurement, in which the crystal was oriented about [110] as rotation axis.

A study of the *hhl* zone with this second crystal at 4·2°K, confirmed the absence both of fractional order reflections as well as those allowed by a P_I chromatic lattice. The upper limits of the absolute magnitudes of F(100) and F(110) for crystal No. 2, scaled by comparison with the nuclear structure factors, are given in column 6 of Table 1. The corresponding limits on the moments are in column 7.

The absence of magnetic scattering both in pure palladium and in low concentration—ferromagnetically contaminated palladium at 4·2°K thus indicates that the largest single spin-axis moment per palladium atom that could be present in these two single crystal samples is less than 0·03 Bohr magnetons. The absence of antiferromagnetism in palladium is also indicated by the observation(12) of Pd^{105} n.m.r. at temperatures between 1·4 and 20·2°K. A similar absence of antiferromagnetism in the 4*d* transition element molybdenum has recently been reported.(13) The only 3*d* transition elements in which antiferromagnetism has been unambiguously demonstrated, at present, are chromium,(14) α-manganese(15, 16) and γ-iron.(17)

Acknowledgements—It is a pleasure to thank E. J. Loeser for operating S.C.A.N.D., D. L. Nash for the spectrochemical analysis and H. Schreiber for the X-ray fluorescent analysis of crystal No. 1, E. Buehler for zone refining and growing crystal No. 2 and J. L. Bernstein for grinding and orienting crystal No. 2.

Bell Telephone Laboratories, S. C. Abrahams*
Murray Hill, N.J.

---

* Guest Scientist: Brookhaven National Laboratory.

References

1. Hoare R. E., Matthews J. C., *Proc. Roy. Soc.* **A212**, 137 (1952).
2. Bozorth R. M., Wolff P. A., Davis D. D., Compton V. B. and Wernick J. H., *Phys. Rev.* **122**, 1157 (1961).
3. Lidiard A. B., *Proc. Roy. Soc.*, **A224**, 161 (1954).
4. Elcock E. W., Rhodes P. and Teviotdale A., *Proc. Roy. Soc.* **A221**, 53 (1953).
5. Pickart S., Ph.D. Thesis, University of Maryland (1958).
6. I am indebted to R. M. Bozorth and A. J. Williams for this.
7. Abrahams S. C., *Rev. sci. Instrum.* **31**, 174 (1960).
8. Prince E. and Abrahams S. C., *Rev. sci. Instrum.* **30**, 581 (1959).
9. Bergsma J. and Goedkoop J. A., *Physica*, **26**, 744 (1960).
10. Watson R. E. and Freeman A. J., *Acta Cryst.* **14**, 27 (1961).
11. Buehler E. and Berry E., *Trans. Amer. Inst. min. (Metalls.) Engrs.* **224**, 874 (1962).
12. Gossard A. C. and Jaccarino V., *Bull. Amer. phys. Soc.* Ser. II, **7**, 556 (1962).
13. Abrahams S. C., *J. Phys. Chem. Solids* **23**, 1348 (1962).
14. Corliss L. M., Hastings J. M. and Weiss R. J., *Phys. Rev. Letters* **3**, 211 (1959).
15. Shull C. G. and Wilkinson M. K., *Rev. Mod. Phys.* **25**, 100 (1953).
16. Kasper J. S. and Roberts B. W., *Phys. Rev.* **101**, 537 (1956).
17. Abrahams S. C., Guttman L. and Kasper J. S., *Phys. Rev.* **127**, 2052 (1962).

Detection of oxygen-17 n.m.r. in solid MgO*

(*Received* 4 *December* 1962)

THIS note is to report what is believed to be the first observation of oxygen-17 nuclear magnetic resonance (n.m.r.) in a solid. While several studies have been reported on the O^{17} n.m.r. signal from various liquid samples, repeated attempts to observe the O^{17} signal from solids have been unsuccessful. This failure has been attributed to the broadening of the resonance due to the interaction of the electric quadrupole moment of the O^{17} nucleus with the electric field gradient at the oxygen site in the crystal lattice. Difficulty is also sometimes experienced in studying O^{17} n.m.r. in highly viscous aqueous solutions. As the solute concentration exceeds about 8 molar (depending on solute), the H_2O^{17} signal becomes broadened and very difficult to detect. This is presumably due to the fact that the quadrupolar interactions which are reduced by the random motions in less viscous samples are no longer averaged sufficiently to prevent broadening of the resonance.

An O^{17} n.m.r. signal was detected several years ago in this laboratory in a sample of ice produced by freezing 1 ml. of water enriched to 1·3 per cent O^{17}. The signal from this sample, however, was extremely weak and barely detectable. If the broadening effects of quadrupolar intreactions are responsible for the difficulty in observing O^{17} n.m.r. in solids, then choice of a crystal lattice in which the oxygen is located at a site with cubic symmetry should reduce the quadrupole interaction.

Extensive searches were made in an attempt to detect the O^{17} signal from several oxides with cubic structure such as MgO, with O^{17} in natural abundance (0·04 per cent.). These were all unsuccessful. A sample of MgO powder enriched to 0·7 per cent O^{17} was then prepared. A search for the dispersion signal from this sample was successful. Several runs were made at different values of r.f. power, modulation width, etc. Fig. 1 shows the best trace obtained (derivative of dispersion curve). Experimental techniques were similar to those reported previously.(1) H_1 was measured directly by a 1-turn search coil inserted into the probe of the spectrometer.

This trace was obtained under the following conditions: $f = 8$ Mc/s, $H_0 = 13860$ G, $H_1 = \sim\frac{1}{2}$ G, $\omega_m = 40$ c/s, modulation amplitude = 0·5 G, spectrometer response time = 80 sec, scan rate = 0·1 part/10^4 per min, temperature = 20°C. The

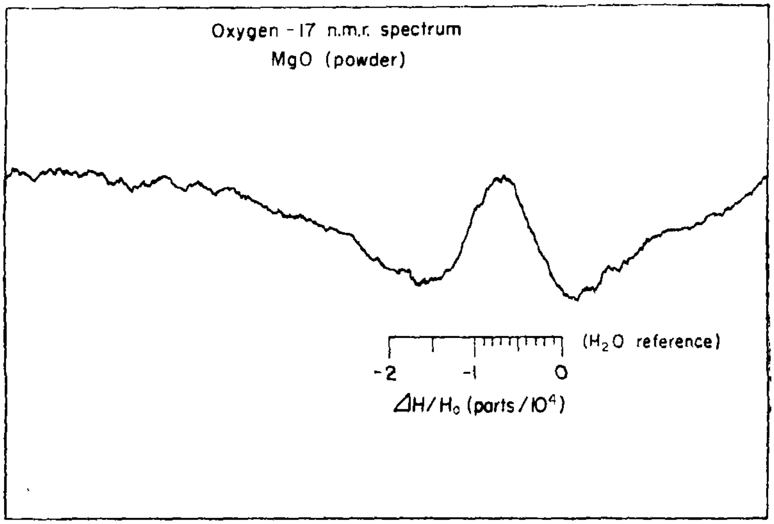

FIG. 1. Oxygen-17 n.m.r. in MgO powder. O^{17} enriched to 0·7 per cent. Derivative of dispersion curve.

---

* Work performed under the auspices of U.S. Atomic Energy Commission.

peak is shifted $-0{\cdot}7$ part/10^4 with respect to the O^{17} position in H_2O.

It is apparent from the shape of the trace in Fig. 1 that the r.f. power level of $\frac{1}{4}$ G is saturating the resonance. This is confirmed by the fact that in the present studies the absorption signal was found to saturate at very low power levels, and at the power level used in Fig. 1 is completely undetectable.

Since the O^{17} relaxation time in a site of pure cubic symmetry is evidently too long for optimum detectability, a search was made for the O^{17} resonance in samples of MgO which had been doped with a paramagnetic ion. The first attempt was with a sample of five single crystal chips aggregate volume = ~ 1 cm^3) of MgO (O^{17} in natural abundance) which had been doped with 0·05 per cent Cr_2O_3.(2) This search was unsuccessful. An attempt was then made to detect the O^{17} signal from 28 single crystal chips (aggregate volume = ~ 3 cm^3) of MgO (O^{17} in natural abundance) doped with 1 per cent MnO_2.(2) This search was successful and the best trace is shown in Fig. 2. It can be seen that the resonance shows much less saturation than the undoped sample of Fig. 1, thus permitting detection of the signal in natural abundance O^{17}.

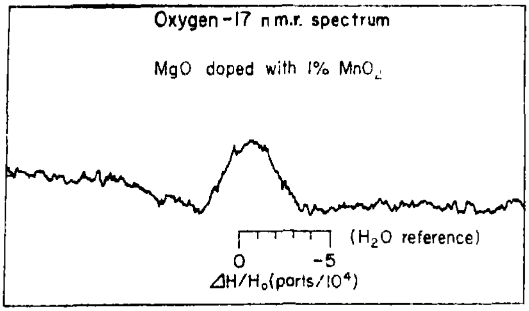

FIG. 2. Oxygen-17 n.m.r. in MgO single crystal chips doped with 1 per cent MnO_2. O^{17} in natural abundance (0·04 per cent). Derivative of dispersion curve.

The signal to noise ratio in these experiments is too small to make reliable estimates of relaxation times. However, they confirm that the principal difficulty in observation of the O^{17} n.m.r. resonance in many solids is the broadening due to electric quadrupole interactions of the oxygen nucleus. Further experiments are continuing in an effort to detect the resonance in other crystals.

Acknowledgements—The author wishes to thank Dr. S. W. RABIDEAU for preparing the O^{17} enriched MgO powder sample, and Dr. W. B. LEWIS for suggesting the source of doped MgO crystals, and for valuable discussions. The author is also indebted to Dr. B. B. MCINTEER and Mr. R. M. POTTER of this laboratory for supplying the oxygen-17 essential to this investigation.

University of California,
Los Alamos Scientific
Laboratory,
New Mexico

JASPER A. JACKSON

References

1. JACKSON J. A., LEMONS J. F. and TAUBE H., *J. chem. Phys.* **32,** 553 (1960); LEWIS W. B., JACKSON J. A., LEMONS J. F., and TAUBE H., *Ibid.*, **36,** 694 (1962).
2. Obtained from Semi-Elements, Inc., Saxonburg, Pennsylvania.

Pressure induced stacking faults in zinc sulphide crystals

(*Received* 5 *December* 1962)

IN A recent study of thin zinc sulphide single crystal plates (wurtzite) in the Siemens Elmiskop I electron microscope, unusual stacking faults have been observed (CHADDERTON *et al.*(1)) by the transmission technique. These stacking faults can be divided into two categories, those on planes perpendicular to the *c*-axis, ((00·1) planes), and those on planes containing the *c*-axis which are thought to lie at 60° to the crystal growth surface ((11·0) and ($1\bar{2}{\cdot}0$)) The crystals usually contain regions which have only (00·1) stacking faults, but close to these regions there are often other areas containing all the stacking faults discussed above. A typical area containing both (00·1) stacking faults and stacking faults on (11.0) and ($1\bar{2}{\cdot}0$) planes is shown in Fig. 1. The stacking fault fringes from the faults on planes either parallel or perpendicular to the *c*-axis are seen to intersect orthogonally. The system of fringes either runs throughout the crystal ending on an edge or else forms closed fault surfaces.

A new technique has been developed in this laboratory whereby crystals thin enough for examination in the electron microscope can be subjected to approximately hydrostatic pressures

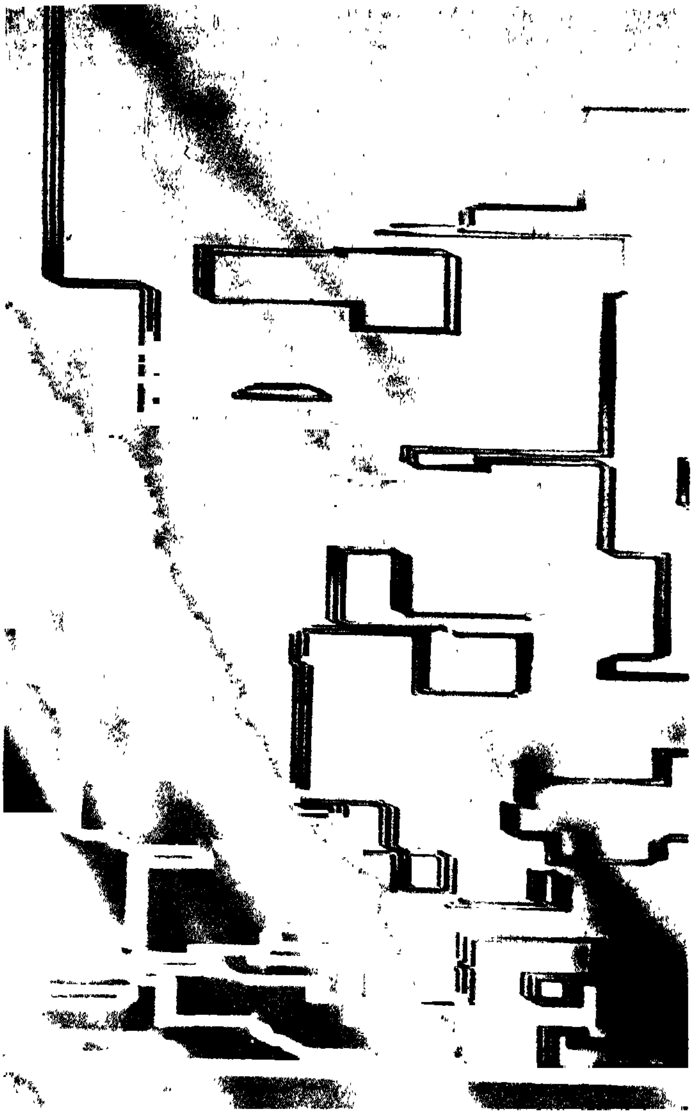

FIG. 1. Electron micrograph showing orthogonally intersecting fringes from stacking faults in zinc sulphide crystals. × 60,000.

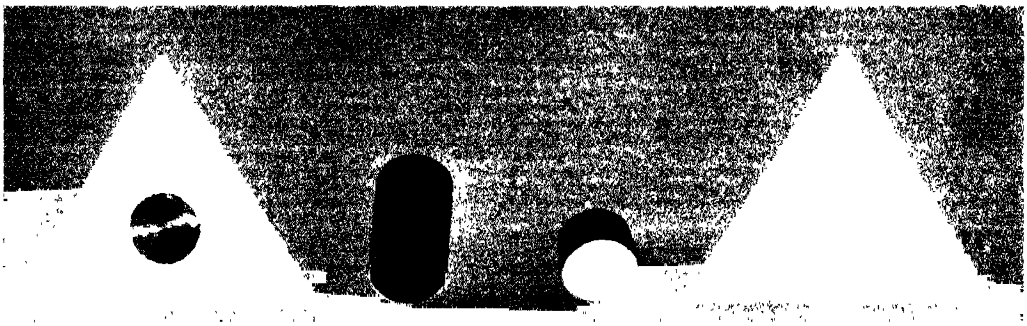

FIG. 2. High pressure cell for subjecting thin crystals to pressures of 60 kbars. This figure shows the various parts and assembled tetrahedron.

[*facing page* 592

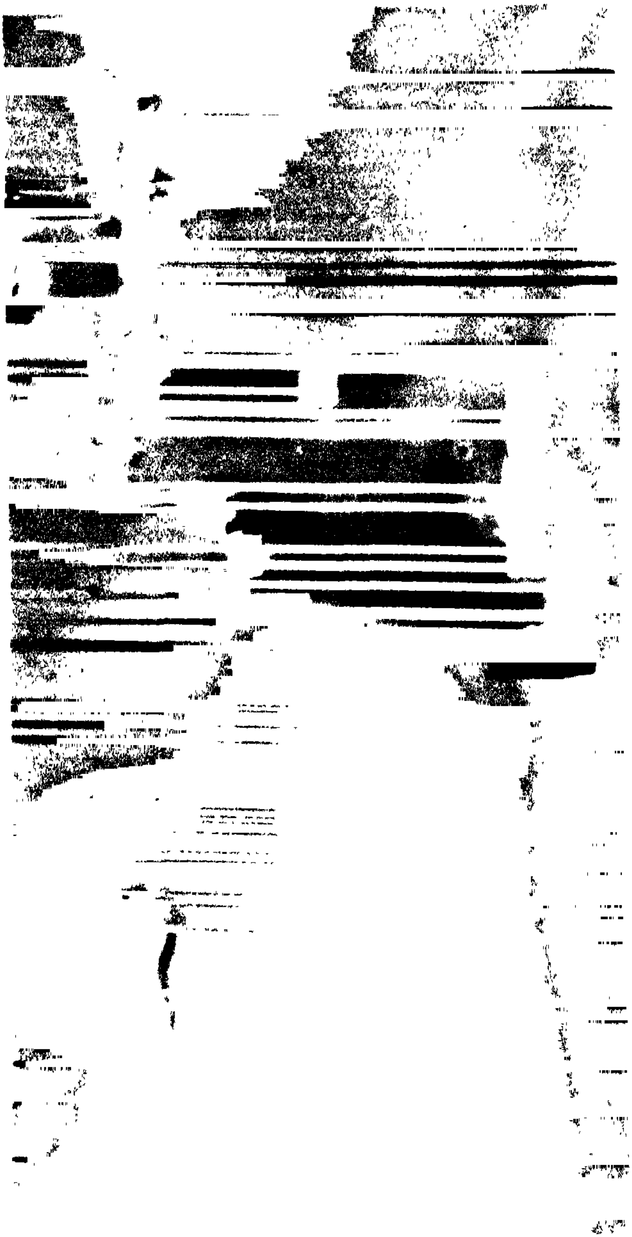

FIG. 3. Electron micrograph showing the effects of pressure on stacking faults in zinc sulphide. ×80,000.

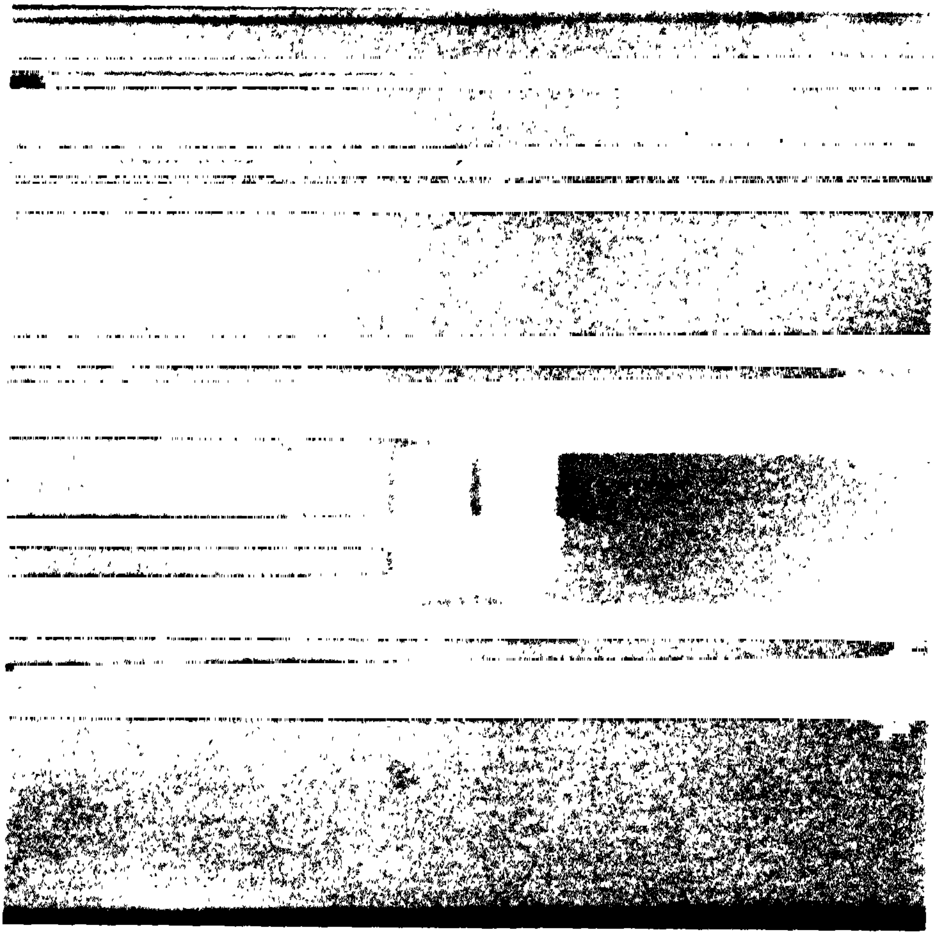

FIG. 4. Delineated area of Fig. 3. × c.320,000.

of up to 70 kbars and to temperatures of the order of a thousand degrees centigrade. In the work described in this note the crystals were subjected to a pressure of 60 kbars at room temperature. The apparatus used was the "Tetrahedral Anvil Arrangement" (HALL⁽²⁾). Details of the high pressure cell for subjecting crystals to pressure are shown in Fig. 2. The zinc sulphide crystals were deposited on the copper electron microscope grids before the experiment. A stainless steel capsule (Fig. 2) containing the grids was filled with the high pressure oil, sealed with an aluminium stopper, and placed in the pyrophyllite tetrahedron. The pressure calibration was made in the normal way by measuring the resistance of Bi, Tl, and Ba in AgCl. Several checks were also made by D. R. NORRIS using Tl wire inside the oil filled capsules, and the agreement was reasonably good.

It is possible that the oil solidifies above about 30 kbars, though when the copper electron microscope grids are examined after a pressure run they are never found to be distorted, nor are the crystals deformed in any way except for the pressure induced defects which are reported in this paper.

Fig. 3 shows the effect of pressure on an area of the crystal similar to that in Fig. 1. The fringes due to diffraction contrast at stacking faults on prismatic planes can be seen to be distorted, and new stacking faults are introduced. It would appear that partial dislocations derive from the prismatic fault planes, move across the crystal in the basal plane, and leave (00·1) stacking faults behind. A particular example of this phenomenon is given in Fig. 4, the inset to Fig. 3. There is further evidence for this conclusion. When pressure treated crystals are examined with a high intensity electron beam, Shockley partials are observed to move at high speed across the crystal, and the introduction of further stacking faults can be followed in the electron microscope.

It may be concluded that the effect of high compressive stress on the wurtzite modification of zinc sulphide is to introduce an extensive array of stacking faults in the basal plane.

Acknowledgements—The authors are grateful to I. DEV for kindly supplying the zinc sulphide crystals and to F. P. BOWDEN for constant encouragement.

Physics and Chemistry of Solids,
Cavendish Laboratory,
Cambridge

L. T. CHADDERTON
A. G. FITZGERALD
A. D. YOFFE

References

1. CHADDERTON L. T., FITZGERALD A. G. and YOFFE A. D., *Phil. Mag.* (in press).
2. HALL H. T., *Rev. sci. Instrum.* **29**, 267 (1958).

Sub-eutectic solubilities of impurities in germanium and silicon

(*Received* 26 *July* 1962; *revised* 10 *December* 1962)

IN A recent paper⁽¹⁾ solidus curves for binary systems involving germanium and silicon and several three- and five-valent impurities were calculated in reasonable agreement with experimental data. In view of the technological importance of such systems an extension of these calculations to temperatures below a eutectic point may be warranted, although there are no experimental data yet available to check these calculations.

In the referred paper⁽¹⁾ equation (44) provides the concentration of neutral impurities in the semiconductor, which is in equilibrium with a partial vapor pressure of the monoatomic impurity gas. This equation remains valid below the eutectic temperature and can be used to obtain the sub-eutectic solidus concentration by inserting the vapor pressure of the impurity coexisting with the impurity-rich solidus. Since the solid solubility of the semiconductor in the impurity element is quite small for the systems considered here, the vapor pressure of the pure solid "impurity"-element can be used. The factor $P^I/P^{0,I}$ of equation (44) thus becomes $\exp(-\Delta H_F^I/RT)$, where ΔH_F^I is the heat of fusion of the impurity element (neglecting differences in the specific heats of solid and liquid impurity elements). The expression (20) of Ref. (1) has been used for the factor Γ in equation (44). Equation (44) was derived by assuming that the change of heat content when inserting a mole of impurities into the semiconductor is independent of temperature, and this change in heat content was expressed in terms of the distribution coefficient of impurities at the melting point of the semiconductor. The ionization equilibrium in the semiconductor is then taken into account in order to proceed from the concentration of neutral impurities to the total impurity concentration. Dividing the total concentrations of impurities by that of atoms in the pure solid impurity element, the distribution coefficients k plotted in Fig. 1 were obtained for the systems Ge–Sb, Ge–Al and Si–Al, using eutectic temperatures from Hansen(2) and other numerical data (activity coefficients and distribution coefficients at the melting point of the semiconductor; intrinsic carrier concentration and partition sums for electrons and holes) as in Ref. (1).

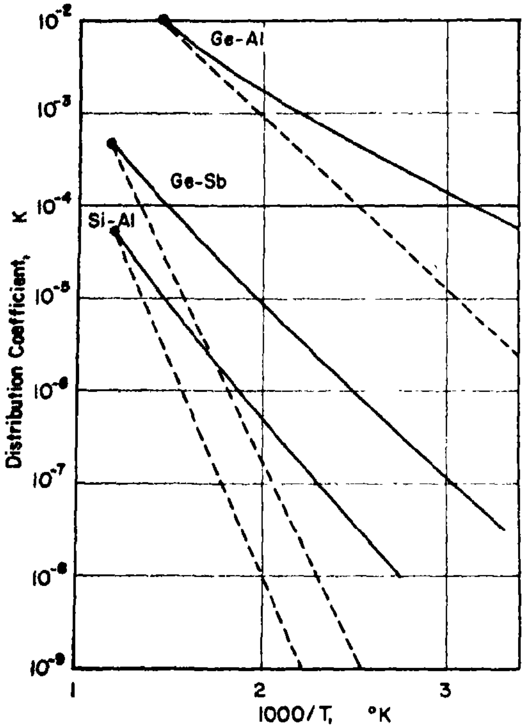

Fig. 1. Theoretical distribution coefficients for Al and Sb in Ge and for Al in Si at sub-eutectic temperatures. The dotted lines are the values suggested by Hall.(4)

The accuracy of such calculations might be indicated by comparison of the theoretical solid solubilities of the impurities at the eutectic temperature with experimental values(3)* listed in parentheses in what follows (units are atoms/cm^3): Ge–Sb: $1{\cdot}6\times10^{19}$ ($5{\cdot}6\times10^{18}$); Ge–Al: $6{\cdot}0\times10^{20}$ ($3{\cdot}7\times10^{20}$); and Si–Al: $3{\cdot}4\times10^{18}$ ($6{\cdot}0\times10^{18}$).

The only other estimate of sub-eutectic solidus curves of such systems is that by Hall,(4) who proposed a linear relationship of $\ln k$ vs. $1/T$, which is defined by $k = 1$ at $T = 2{\cdot}3\ T^S_M$ (where T^S_M is the melting point of the pure semiconductor) and by the value of k at the eutectic temperature. Using our theoretical value at the eutectic temperature, Hall's proposed k-values are indicated as dotted lines in Fig. 1. Hall's estimate is based on an empirical value for an apparently strong temperature dependence of the heat content change when incorporating impurities in the solid, which arises if one neglects to take into account the ionization equilibrium of impurities. It should be pointed out that Hall and we obtain the same change of $\partial \ln k/\partial T$ at the eutectic temperature, but that his $\partial \ln k/\partial T$ above the eutectic temperature differs considerably from ours. This reflects in the discrepancy of the slopes below the eutectic temperature shown in the figure.

Sprague Electric Company, Kurt Lehovec
North Adams, Mass. Alexis Slobodskoy

References

1. Lehovec K., *J. Phys. Chem. Solids*, **23**, 695 (1962).
2. Hansen M., *Constitution of Binary Alloys*, 2nd edition, McGraw-Hill, New York (1958).
3. Trumbore F. A., *Bell Syst. tech. Journal* **39**, 205 (1960).
4. Hall R. N., *J. Phys. Chem. Solids* **3**, 63 (1957).

---

* The impurity concentration at the eutectic temperature for the Si–Al system is extrapolated from experimental solid solubilities at more elevated temperatures.

BOOK REVIEWS

Creep in Structures. (Edited by Nicholas J. Hoff), Springer Verlag, Berlin, 1962. 375 pp., $13.50.

This book constitutes the proceedings of a colloquium on the creep of structures held under the auspices of the International Union of Theoretical and Applied Mechanics at Stanford University in July, 1960. The twenty papers in the volume were written upon special invitation of a scientific committee. The range of topics covers just about every phase of the subject and the book serves as a very good summary of the state-of-the-art. There are more papers (eight) on stress distribution in plates and shells (including thin-walled beams) than any other one topic. Five papers were devoted to buckling problems of columns, plates, and shells. Another six are primarily concerned with mathematical methods of analysis of creep problems (elastic analogs, variational principles, integral transforms, etc.) but include examples of application to various problems. Four papers deal with constitutive relations. All four of these papers are at least partially devoted to new experimental results of the authors. Two of them shed some light on the effects of changing stress level during creep, a problem which badly needs attention. There is one paper on linear viscoelasticity and one paper on damping due to creep. Some papers belong in more than one of the categories mentioned.

Almost any problem of structural analysis previously solved in the elastic domain can be made into a problem involving creep. Because of this the new element in many of the papers is not the problem but the method used to solve the horribly nonlinear equations. Judging from the success of the authors on a variety of problems it would seem that, thanks to computing machines, most, if not all, of the creep counterparts of the classical problems can indeed be solved. There would be enough material here to fill the journals for years if it were not for the fact that many such problems are not of practical importance where creep is concerned and fewer still are worth the effort.

The appearance of the book is proof that the subject of creep analysis of structures has come very far in the last ten years or so (almost all the references date since 1950). The editor of the collection has himself been responsible for more than his share of the progress.

J. Lyell Sanders, Jr.

Luther E. Preuss (Editor): **1961 Transactions of the Eighth National Vacuum Symposium and the Second International Congress.** Pergamon Press, Oxford (1962). Two Volumes £15 per Set.

The Eighth National Vacuum Symposium of the American Vacuum Society was held jointly with the Second International Vacuum Congress of the International Organization for Vacuum Science and Technology in Washington, D.C. in October, 1961. The proceedings of this large conference are now available in these two weighty but beautifully edited and published volumes.

These volumes perform the invaluable service to all workers using high vacuum techniques of bringing together nearly all significant references in the field to date and summarizing the present state of the art. This is particularly important since the development of this field has undoubtedly been retarded by lack of good intercommunication in the past. The quality of the 200 papers is generally high. It is apparent that in only a few years much of the vacuum industry has caught up with the techniques of ultrahigh vacuum (i.e. 10^{-10} Torr) that were formerly practised in only a few laboratories. Some of the work reported, however, still attests to the lack of communication mentioned.

The subject matter covers from both a practical and theoretical viewpoint all the current technical problems encountered in producing and measuring ultrahigh vacua, and the application of vacuum techniques to the technologies of sputtering, thin film production and vacuum metallurgy.

The two volumes are separated in content to the extent that the sections on sputtering, adsorption and mass spectrometry are all in Volume I, while those on Vacuum Metallurgy, the use of high energy electron beams for fusing and welding, and the production, measurement and properties of thin films are in Volume II. Both volumes, however, contain many papers on general and ultrahigh vacuum problems and techniques.

There is heavy emphasis on getter and ion pumping, cryo-pumping and use of high speed diffusion pumps, and the application of all these to large chambers such as space simulators and particle accelerators.

Useful summaries are given on the latest data on degassing behavior of many materials, on the sorption properties of gettering surfaces, and on residual gas analysis under many operating conditions. There is extensive data on behavior of materials exposed to the conditions of high vacuum, temperature fluctuation and u.v. intensity encountered in space.

Recent developments of interest in the vacuum field include new low vapor pressure pump oils that permit attainment of 10^{-9} Torr without trapping; four different types of ion gauges that will extend by up to three orders of magnitude the present limit of $\sim 10^{-11}$ Torr of the conventional Bayard–Alpert gauge; and a mechanical (molecular) pump magnetically suspended that can produce vacua of 4×10^{-10} Torr.

It is clear that vacuum technology is rapidly coming of age. LUTHER PREUSS and the Pergamon Press are to be congratulated for this contribution.

F. G. ALLEN

J. Phys. Chem. Solids Pergamon Press 1963. Vol. 24, pp. 597–606. Printed in Great Britain.

RESONANCE AND HIGH FREQUENCY SUSCEPTIBILITY IN CANTED ANTIFERROMAGNETIC SUBSTANCES

G. F. HERRMANN*

General Telephone and Electronics Laboratories Inc., Palo Alto, California

(*Received* 15 *November* 1962)

Abstract—Canting in essentially antiferromagnetic substances can be caused by two distinct interactions, i.e. single ion anisotropy and antisymmetric exchange. Starting from a general expression for the free energy which includes contributions from both types of interactions, expressions are derived for antiferromagnetic resonances, and for r.f. and d.c. susceptibilities. The dependence of the dynamic behavior on the particular mechanism responsible for canting enters into the expressions for the resonances as a linear term in the canting parameters, whereas in the case of the susceptibilities it appears only in terms of higher order. The measurement of resonance frequencies as functions of an applied magnetic field appears to offer the most effective method for assessing the separate contributions of the canting mechanisms. The role of anisotropic exchange is briefly discussed.

INTRODUCTION

THE canting effect responsible for weak ferromagnetism in essentially antiferromagnetic materials is attributed primarily to two types of mechanisms, i.e. single ion anisotropy and antisymmetric exchange. The first arises from a magnetocrystalline anisotropy for which the easy direction of magnetization is tilted relative to the crystalline axes in a manner depending on the ion site. The second is due to an exchange interaction of the form $\boldsymbol{D}_{ij} \cdot \boldsymbol{S}_i \times \boldsymbol{S}_j$ introduced by MORIYA.(1) In elementary treatments the effect of canting on antiferromagnetic resonance is usually described in terms of an artificial "canting field." This greatly simplifies the calculation, but the results can throw no light on the origin of canting, and at times may be quite misleading.

Whether single ion anisotropy or antisymmetric exchange does in fact predominate depends, of course, on the substance in question. In a recent study of orthoferrites, TREVES(2) pointed out that the susceptibility depended strongly on the type of mechanism responsible for canting. On the basis of his experimental data Treves concluded that in orthoferrites the antisymmetric exchange effect predominated. From theoretical considerations MORIYA(1) predicts that antisymmetric exchange predominates in the case of αFe_2O_3, whereas single ion anisotropy predominates in NiF_2. The latter probably holds also in the case of $KMnF_3$(3) and related crystals. There may be other substances where both interactions are significant. The study of such substances requires a procedure which is capable not only of deciding which is the principal mechanism but of establishing the exact magnitude of each interaction. Unfortunately, susceptibility measurements are extremely difficult to perform and their accuracy is poor. The following calculation indicates that a more accurate and more clear-cut method is available in the study of antiferromagnetic resonance. The calculation is based on a fairly general form of the free energy which includes both types of interactions. This formulation, while rather elaborate, brings out clearly the separate dependence of the resonance on the two canting mechanisms. The expressions for resonance contain, as a special case, those obtained for αFe_2O_3 by PINCUS,(4) who considered only antisymmetric exchange. Expressions obtained by ORBACH(5) are in partial disagreement with our own, owing to his use of the simplifying "canting field" concept. Expressions are also given for the r.f. susceptibility,

---

[*] Now at Lockheed Missiles and Space Company, Palo Alto, California.

and the resonance modes are briefly discussed. For the sake of completeness we present, also, expressions for d.c. susceptibility which are more general than those of TREVES[(2)] in that they include simultaneously the coefficients associated with both interactions.

FREE ENERGY AND THE DYNAMIC EQUATIONS

The symmetry properties of canted antiferromagnetic solids are discussed in detail by several authors.[(2,3)] In most cases the configuration is almost antiferromagnetic and there are four inequivalent ion sites. The dynamical behavior is excellently approximated by a two sublattice model, which is obtained by combining the magnetization vectors corresponding to the four sublattices in pairs so as to yield two magnetization vectors, $\boldsymbol{M}_1$ and $\boldsymbol{M}_2$, of constant magnitude M which lie in almost opposite directions. This simplification results in the loss of two resonance modes. These, however, are optically almost inactive, and their interaction with active modes is negligible.

The free energy, F, is composed of a part caused by exchange interactions and a part caused by the anisotropy at the (composite) sites associated with $\boldsymbol{M}_1$ and $\boldsymbol{M}_2$. The free energy is expanded as a power series in the magnetization components and only quadratic terms are retained. In substances with orthorhombic symmetry this approximation probably holds well for arbitrary orientations of $\boldsymbol{M}_1$ and $\boldsymbol{M}_2$. In substances with higher than two-fold symmetry axes, e.g. αFe_2O_3, the expressions should be considered as valid only in the neighborhood of the equilibrium position. It is convenient to describe the free energy and the parameters appearing in it in units of magnetic field. To this end we define a normalized free energy, V, given by

$$V = F/M, \tag{1}$$

and unit directional vectors

$$\begin{aligned} \boldsymbol{R}_1 &\equiv (X_1Y_1Z_1) = \boldsymbol{M}_1/M; \\ \boldsymbol{R}_2 &\equiv (X_2Y_2Z_2) = \boldsymbol{M}_2/M. \end{aligned} \tag{2}$$

At this point we introduce a convention in the choice of coordinates and in the labeling of $\boldsymbol{M}_1$ and $\boldsymbol{M}_2$ which is consistently adhered to in the following. We choose the Y-axis to be normal to $\boldsymbol{M}_1$ and $\boldsymbol{M}_2$ at equilibrium, with the Z-axis bisecting the angle between the vectors, and $\boldsymbol{M}_1$ and $\boldsymbol{M}_2$ lying, respectively, in the first and the fourth quadrant of the (Z,X)-plane (Fig. 1). This convention agrees with the standard crystallographic convention for orthoferrites, but not necessarily for other substances. From symmetry considerations it follows that V is invariant to a reversal in the sign of Y_1 and Y_2 and may therefore include only even terms in these variables.

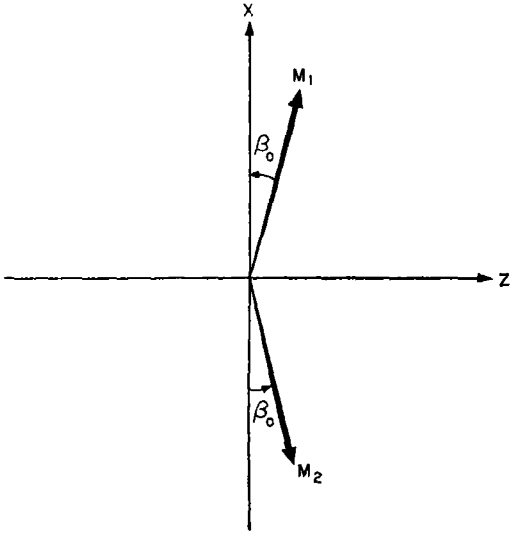

FIG. 1. Normal equilibrium position for canted two sublattice model.

The anisotropy energy associated with the site corresponding to $\boldsymbol{M}_1$ assumes the form

$$-(A_{xx}X_1^2 + A_{zz}Z_1^2 + A_{xz}X_1Z_1).$$

There is no need to include a term with Y_1^2 since a scalar of the form $X_1^2 + Y_1^2 + Z_1^2$ can always be added to the free energy as an arbitrary constant.

In orthorhombic substances the anisotropy tensor can be represented by an ellipsoid (TREVES[(2)]), one of whose axes coincides with the Y-axis and whose other axes make an angle of θ with the X, Y axes (Fig. 2), where

$$\tan 2\theta = A_{xz}/(A_{xx} - A_{zz}).$$

From symmetry, one obtains the anisotropy energy for $\boldsymbol{M}_2$ as

$$-(A_{xx}X_2^2 + A_{zz}Z_2^2 - A_{xz}X_2Z_2).$$

Here the ellipsoid axes make an angle of $(-\theta)$

with the X, Y-axes. The exchange energy can be written as the sum of a scalar, pseudovector, and tensor part given, respectively, by

$$E\boldsymbol{R}_1\cdot\boldsymbol{R}_2, \quad -D(X_1Z_2-X_2Z_1),$$
$$\text{and } E_xX_1X_2+E_zZ_1Z_2,$$

where E is referred to as symmetric, D as antisymmetric, and (E_x, E_z) as anisotropic exchange fields. The anisotropic exchange term is much smaller than the others⁽¹⁾ and is left out of the detailed calculation. Its role is discussed briefly in the concluding paragraph of this paper.

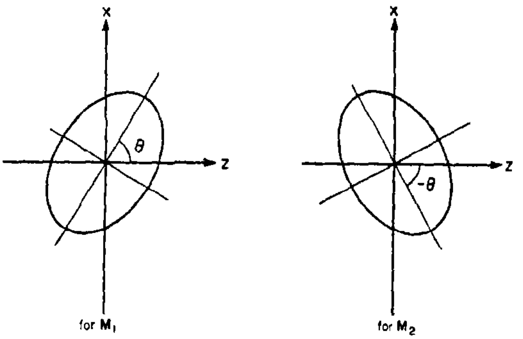

FIG. 2. Anisotropy ellipsoids for M_1 and M_2.

The complete expression for the normalized free energy is

$$V = E\boldsymbol{R}_1\cdot\boldsymbol{R}_2-D(X_1Z_2-X_2Z_1)-A_{xx}(X_1^2+X_2^2)$$
$$-A_{zz}(Z_1^2+Z_2^2)-A_{xz}(X_1Z_1-X_2Z_2). \qquad (3)$$

A short discussion of the magnitudes of the coefficients will be useful in order to clarify the approximation procedures used below. The exchange energy, E, is quite large compared to the other coefficients, and this forms the basis for all approximations. The calculation is, however, complicated by the fact that the canting energy in some substances is quite large compared to the anisotropy energy. In order not to commit oneself in advance one must use an approximation procedure valid for both large and small values of the canting parameters D and A_{xz}, and retain terms of the form D^2/EA_{xx}, $A^2{}_{xz}/EA_{xx}$, etc., which in some substances may be of the order of unity.⁽²⁾ We neglect higher than quadratic terms in the applied magnetic field.

The dynamic equations for M_1 and M_2 in an applied magnetic field $\boldsymbol{H}$, neglecting dissipation terms, can be given in the form

$$(1/\gamma)\dot{\boldsymbol{R}}_1 = -\boldsymbol{R}_1\times(\boldsymbol{H}-\nabla_1V),$$
$$(1/\gamma)\dot{\boldsymbol{R}}_2 = -\boldsymbol{R}_2\times(\boldsymbol{H}-\nabla_2V), \qquad (4)$$

where γ is the gyromagnetic ratio and where ∇_1 and ∇_2 are gradients with respect to $X_1Y_1Z_1$ and $X_2Y_2Z_2$, respectively, the coordinates being treated as independent variables. The auxiliary conditions $X_1^2+Y_1^2+Z_1^2 = 1$ and $X_2^2+Y_2^2+Z_2^2 = 1$ are imposed upon completion of the operation.

Since ∇_1V and ∇_2V appear formally in the role of a magnetic field they have been frequently replaced in the above equations by effective "anisotropy fields" and "canting fields." This procedure can be grossly misleading since in actuality these "fields" must themselves depend on the orientation of both M_1 and M_2. In fact, as TREVES⁽²⁾ has shown with respect to the susceptibility and as we shall show below, the dynamic behavior depends strongly on whether the so-called "canting fields" are associated with the coefficient D or with A_{xz} in equation (3).

THE EQUILIBRIUM POSITIONS

According to the convention described above, the equilibrium position of lowest energy is given by Fig. 1. It can be shown that V is, in fact, minimized for such a configuration provided the coordinate axes and the labels 1 and 2 are chosen so as to make $A_{xx} > A_{zz}$ and $D+A_{xz} > 0$. The equilibrium position is obtained by applying equations (4) to the specific form of V given by equation (3) and setting $\dot{R}_1 = \dot{R}_2 = 0$ and $\boldsymbol{H} = 0$. Let β_1 denote the angle measured from M_1 to the positive X-axis and β_2 the angle measured from the negative X-axis to M_2. Then at equilibrium one has

$$\beta_1 = \beta_2 = \beta_0$$

where

$$\tan 2\beta_0 = \frac{A_{xz}+D}{E+A_{xx}-A_{zz}} \sim \frac{A_{xz}+D}{E}. \qquad (5)$$

This relation is only slightly modified by the application of a magnetic field H_0 along the Z-axis. To a very good approximation

$$\tan 2\beta_0 = \frac{A_{xz}+D+H_0}{E+A_{xx}-A_{zz}}. \tag{6}$$

A sufficiently strong field along the X-axis may cause the resultant magnetization to "flip" into the X-direction. In an orthorhombic configuration one may assume that equation (3) is reasonably valid for all orientations. In that case, the stability condition for the flipped configuration is given by

$$\begin{aligned}-4E(A_{xx}-A_{zz})+4A_{xz}(A_{xz}-D)\\ +(5A_{xz}-D)H_x+H_x^2 > 0.\end{aligned} \tag{7}$$

For $D = 0$ a stable equilibrium along the X-direction can exist even in the absence of a magnetic field provided $A_{xz}^2 > E(A_{xx}-A_{zz})$. A comparison of the case $A_{xz} = 0$ and $D = 0$ will show that in the former M_1 remains to the left of M_2, whereas in the latter it is found to the right of M_1 (Fig. 3). The results obtained below for the case where H_0 is along the Z-direction can be applied directly to the flipped configuration, provided that appropriate changes in the sign of A_{xz} or D are made.

RESONANCE FREQUENCIES AND R.F. SUSCEPTIBILITIES

We now present an outline of the calculation of the resonance frequencies and r.f. susceptibilities. In considering the effect of an applied field we may immediately conclude from the symmetry that whereas there may be terms which are linear in H_z, there will be, at most, quadratic terms in H_x and H_y. The case where H_0 lies along the Z-axis provides the most sensitive experimental configuration which, moreover, avoids difficulties connected with the domain structure of the material. We therefore confine the detailed discussion to this configuration. The other configurations are briefly discussed at the end of this Section.

To obtain resonance frequencies and r.f. susceptibilities one must resort to the usual small signal approximation by expressing the motion in terms of small deviation from equilibrium. We follow the customary procedure of transforming to two separate coordinate systems, $(S_1T_1Y_1)$ and $(S_2T_2Y_2)$, which describe, respectively, the motion of M_1 and M_2, where the S_1 and S_2-axes are chosen so as to coincide, respectively, with the equilibrium positions of M_1 and M_2 (Fig. 4). The transformation equations are given by

$$\begin{aligned}Z_1 &= S_1\sin\beta_0-T_1\cos\beta_0,\\ Z_2 &= S_2\sin\beta_0+T_2\cos\beta_0,\\ X_1 &= S_1\cos\beta_0+T_1\sin\beta_0,\\ X_2 &= -S_2\cos\beta_0+T_2\sin\beta_0,\end{aligned} \tag{8}$$

where β_0 is given by equation (6). Note that both systems remain right-handed in the given order. By applying the transformation, equation (8) to

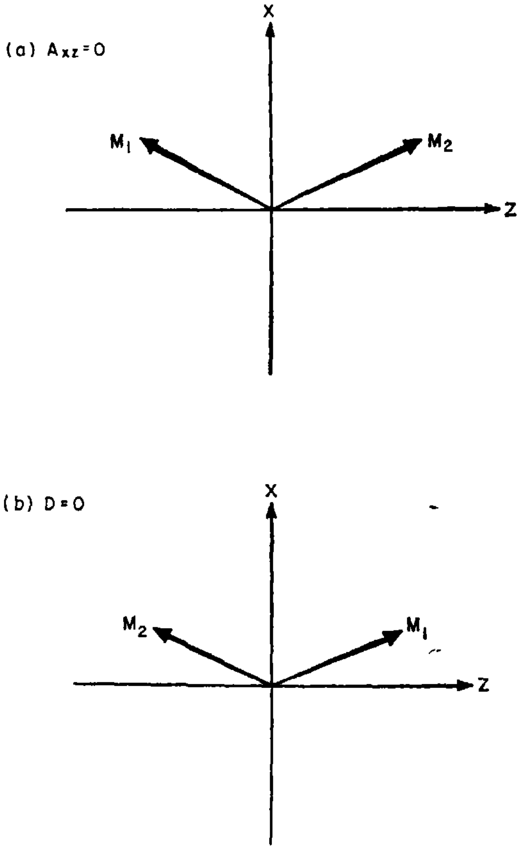

FIG. 3. Flipping of the magnetization caused by high magnetic field in X-direction. (a) Anti-symmetric exchange predominant. (b) Single ion anisotropy predominant.

equation (3) one obtains

$$\begin{aligned} V = {} & EY_1Y_2-(E\cos 2\beta_0+D\sin 2\beta_0)(S_1S_2+T_1T_2) \\ & +(E\sin 2\beta_0-D\cos 2\beta_0)(S_1T_2-S_2T_1) \\ & -(A_{xx}\cos^2\beta_0+(\tfrac{1}{2})A_{xz}\sin 2\beta_0+A_{zz}\sin^2\beta_0)(S_1^2+S_2^2) \\ & -[(A_{xx}-A_{zz})\sin 2\beta_0-A_{xz}\cos 2\beta_0][(S_1T_1-S_2T_2)] \\ & -(A_{xx}\sin^2\beta_0-(\tfrac{1}{2})A_{xz}\sin 2\beta_0+A_{zz}\cos^2\beta_0)(T_1^2+T_2^2) \end{aligned} \tag{9}$$

The dynamic equations can be written as

$$\begin{aligned} 1/\gamma\, \dot{T}_1 &= -Y_1(H_{s1}-\partial V/\partial S_1)+S_1(H_{y1}-\partial V/\partial Y_1), \\ 1/\gamma\, \dot{Y}_1 &= -S_1(H_{t1}-\partial V/\partial T_1)+T_1(H_{s1}-\partial V/\partial S_1) \end{aligned} \tag{10}$$

where H_{s1}, H_{t1} and H_{y1} are components of the *total* magnetic field along the S_1, T_1, and Y_1-axes, with a similar pair of equations for $\dot{T}_2$ and $\dot{Y}_2$. The equations for $\dot{S}_1$ and $\dot{S}_2$ are omitted since they play no role in the following approximation.

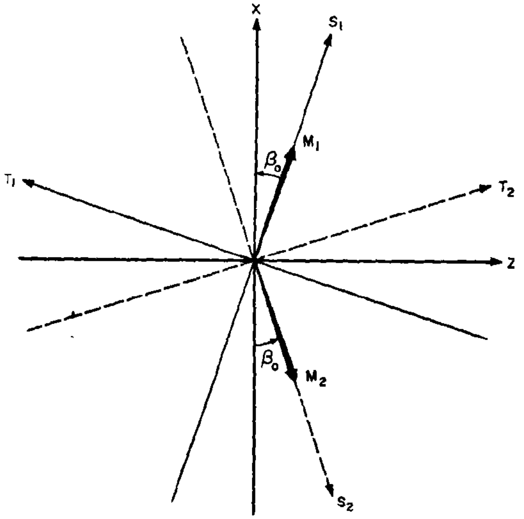

FIG. 4. Special coordinate systems for describing small precessions.

The small signal approximation is now applied as follows. We put $\boldsymbol{H} = \boldsymbol{H}_0+\boldsymbol{h}$ where $\boldsymbol{H}_0$ is a constant field along the Z-direction and $\boldsymbol{h}$ is a small r.f. field with arbitrary components and a time variation of the form $e_{i\omega t}$. We next expand equation (10) about the equilibrium position $S_1 = S_2 = 1$, $Y_1 = Y_2 = T_1 = T_2 = 0$ and retain only linear terms in $\mathrm{d}T_1 = T_1$, $\mathrm{d}T_2 = T_2$, $\mathrm{d}Y_1 = Y_1$, $\mathrm{d}Y_2 = Y_2$.

By making use of the symmetry properties of V and of the fact that the only non-vanishing derivative of V with respect to either Y_1 or Y_2 is $\partial^2V/\partial Y_1\partial Y_2$, one obtains after suitable rearrangement:

$$i(\omega/\gamma)T_1-aY_1+bY_2 = h_y, \tag{11a}$$

$$i(\omega/\gamma)Y_1-cT_1-dT_2 = -h_{t1}, \tag{11b}$$

$$i(\omega/\gamma)T_2-aY_2+bY_1 = h_y, \tag{11c}$$

$$i(\omega/\gamma)Y_2-cT_2-dT_1 = -h_{t2}, \tag{11d}$$

where

$$\begin{aligned} a &= \frac{\partial V}{\partial S_1}-H_0\sin\beta_0, \\ b &= \frac{\partial^2 V}{\partial Y_1\partial Y_2}, \\ c &= \frac{\partial^2 V}{\partial T_1^2}-\frac{\partial V}{\partial S_1}+H_0\sin\beta_0, \\ d &= \frac{\partial^2 V}{\partial T_1\partial T_2}, \end{aligned} \tag{12}$$

where β_0 is given by equation (6).

From equation (11) one can obtain two uncoupled systems of equations—the first, by adding (c) to (a) and (d) to (b); the second, by subtracting (c) from (a) and (d) from (b). Thus,

$$\begin{aligned} & i(\omega/\gamma)(T_1+T_2)+(b-a)(Y_1+Y_2) = 2h_y \\ & -(d+c)(T_1+T_2)+i(\omega/\gamma)(Y_1+Y_2) \\ & \qquad = -(h_{t1}+h_{t2}) = -2h_x\sin\beta_0 \end{aligned} \tag{13}$$

and

$$\begin{aligned} & i(\omega/\gamma)(T_1-T_2)-(b+a)(Y_1-Y_2) = 0 \\ & -(d-c)(T_1-T_2)+i(\omega/\gamma)(Y_1-Y_2) \\ & \qquad = h_{t2}-h_{t1} = 2h_z\cos\beta_0. \end{aligned} \tag{14}$$

Consider first the resonance frequencies. These are obtained by setting $\boldsymbol{h} = 0$ and searching for non-vanishing solutions. The condition for this is that the determinants of either equation (13) or equation (14) vanish.

One thus obtains two resonance frequencies:

$$\omega_{xy}^2/\gamma^2 = (b-a)(d+c) \tag{15}$$

and

$$\omega_z^2/\gamma^2 = (b+a)(d-c). \tag{16}$$

If $\omega = \omega_{xy}$, then $T_1 = T_2$ and $Y_1 = Y_2$; and, hence,

$$\bar{X}_1 = \bar{X}_2,\ \bar{Y}_1 = \bar{Y}_2,\ \text{and}\ \bar{Z}_1 = -\bar{Z}_2,$$

where the barred symbols represent r.f. amplitudes in the original coordinate system. Since $\bar{Z}_1 + \bar{Z}_2 = 0$, there is no resultant r.f. magnetization in the Z-direction for the ω_{xy} mode.

If $\omega = \omega_z$, then $T_1 + T_2 = 0$ and $Y_1 + Y_2 = 0$ and $\bar{X}_1 + \bar{X}_2 = 0$, $\bar{Y}_1 + \bar{Y}_2 = 0$, and $\bar{Z}_1 = \bar{Z}_2$.

The resultant r.f. magnetization is now polarized entirely in the Z-direction.

To obtain r.f. susceptibilities, one solves equations (13) and (14) to obtain

$$T_1 + T_2 = \frac{2i\gamma^2}{\omega_{xy}^2 - \omega^2}\,[i(\omega/\gamma)h_y + (b-a)h_x \sin\beta_0],$$

$$Y_1 + Y_2 = \frac{2\gamma^2}{\omega_{xy}^2 - \omega^2}\,[-i(\omega/\gamma)h_x \sin\beta_0 + (d+c)h_y], \tag{17}$$

$$T_1 - T_2 = \frac{2\gamma^2}{\omega_z^2 - \omega^2}\,(b+a)h_z \cos\beta_0,$$

$$Y_1 - Y_2 = \frac{2\gamma^2}{\omega_z^2 - \omega^2}\,i(\omega/\gamma)h_z \cos\beta_0.$$

For small displacements from equilibrium one can put

$$\bar{X}_1 + \bar{X}_2 = (T_1 + T_2)\sin\beta_0;$$

$$\bar{Z}_1 + \bar{Z}_2 = -(T_1 - T_2)\cos\beta_0.$$

Hence,

$$\bar{X}_1 + \bar{X}_2 = \frac{2\gamma^2}{\omega_{xy}^2 - \omega^2}\,[(b-a)h_x \sin^2\beta_0 + i(\omega/\gamma)h_y \sin\beta_0];$$

$$\bar{Y}_1 + \bar{Y}_2 = \frac{2\gamma^2}{\omega_{xy}^2 - \omega^2}\,[-i(\omega/\gamma)h_x \sin\beta_0 + (d+c)h_y];$$

$$\bar{Z}_1 + \bar{Z}_2 = -\frac{2\gamma^2}{\omega\ \ - \omega^2}\,(b+a)h_z \cos^2\beta_0.$$

In terms of the r.f. magnetization vector $\boldsymbol{m} = M(\mathbf{R}_1 + \mathbf{R}_2)$, one can write these relations in the form

$$\boldsymbol{m}_x = [2\gamma^2 M/(\omega_{xy}^2 - \omega^2)][(b-a)h_x \sin^2\beta_0 + i(\omega/\gamma)h_y \sin\beta],$$

$$\boldsymbol{m}_y = [2\gamma^2 M/(\omega_{xy}^2 - \omega^2)]\,[-i(\omega/\gamma)h_x \sin\beta_0 + (d+c)h_y], \tag{18}$$

$$\boldsymbol{m}_z = -[2\gamma^2 M/(\omega_z^2 - \omega^2)]\,(b+a)h_z \cos^2\beta_0.$$

A detailed calculation gives

$$b+a = E - A_{xx} - A_{zz} - (E + A_{xx} - A_{zz}) \times \cos 2\beta_0 - (A_{xz} + D)\sin 2\beta_0 - H_0 \sin\beta_0,$$

$$b-a = E + A_{xx} + A_{zz} + (E + A_{xx} - A_{zz}) \times \cos 2\beta_0 + (A_{xz} + D)\sin 2\beta_0 + H_0 \sin\beta_0,$$

$$d+c = 2(A_{xx} - A_{zz})\cos 2\beta_0 + 2A_{xz}\sin 2\beta_0 + H_0 \sin\beta_0, \tag{19}$$

$$d-c = -2(E + A_{xx} - A_{zz})\cos 2\beta_0 + 2(A_{xz} + D) \times \sin 2\beta_0 - H_0 \sin\beta_0.$$

Into these equations one can substitute β_0 from equation (6) and obtain accurate expressions for the resonance frequencies and the susceptibility tensor. For most purposes, expressions based on the approximation discussed above suffice. These are given by

$$b+a \sim -2A_{xx} - \frac{(A_{xz}+D)^2}{2E} - \frac{(A_{xz}+D)H_0}{2E},$$

$$b-a \sim 2E + 2A_{xx},$$

$$d+c \sim 2(A_{xx} - A_{zz}) + \frac{2A_{xz}(A_{xz}+D)}{E} + \frac{5A_{xz}+D}{2E}H_0 + \frac{1}{2E}H_0^2, \tag{20}$$

$$d-c \sim -2E - 2(A_{xx} - A_{zz}).$$

With this approximation one obtains the following resonances

$$
\begin{aligned}
\omega_{xy}^2/\gamma^2 &= 4E(A_{xx}-A_{zz})+4A_{xx}(A_{xx}-A_{zz})\\
&\quad +4A_{xz}(A_{xz}+D)+(5A_{xz}+D)H_0+H_0^2,\\
\omega_z^2/\gamma^2 &= 4EA_{xx}+4A_{xx}(A_{xx}-A_{zz})\\
&\quad +(A_{xz}+D)^2+(A_{xz}+D)H_0,
\end{aligned}
\qquad (21)
$$

for the resonance frequencies. This result includes as a special case the equations obtained by PINCUS(4) for αFe_2O_3, leaving out the anisotropy canting effect.

The components of the r.f. magnetization (see equation (18)) are given by

$$
\begin{aligned}
m_x &= \frac{M}{(\omega_{xy}^2-\omega^2)E}\,[\gamma^2(A_{xz}+D+H_0)^2h_x\\
&\qquad +i\gamma M(A_{xz}+D+H_0)h_y],\\
m_y &= \frac{M}{(\omega_{xy}^2-\omega^2)E}\,[-i\gamma M(A_{xz}+D+H_0) \qquad (22)\\
&\qquad \times\ h_x+\omega_{xy}^2h_y],\\
m_z &= \frac{M\omega_z^2}{(\omega_z^2-\omega^2)E}\,h_z.
\end{aligned}
$$

These results can be expressed in terms of an r.f. susceptibility tensor whose components are given in the Summary Section.

The geometrical aspects of the two precession modes are displayed in Fig. 5. In either mode, the quasi-elliptic trajectories traversed by the end points of M_1 and M_2 are extremely narrow, the large axis lying along an optically inactive direction—i.e. predominantly along the Z-direction for the ω_{xy} mode and along the Y-direction for the ω_z mode. The ratio of the minor to the major axis at resonance is best given in terms of the amplitudes T and Y. For the ω_{xy} mode one has

$$\frac{|Y|}{|T|} = (1/E)\,[E(A_{xx}-A_{zz})+A_{xz}(A_{xz}+D)]^{1/2} \qquad (23)$$

and for the ω_z mode

$$\frac{|T|}{|Y|} = (1/4E)\,[8EA_{xx}+2(A_{xz}+D)^2]^{1/2}. \qquad (24)$$

These ratios represent small numbers. Most of the precessional motion is therefore optically inactive. This may result in a disadvantageous ratio between radiation losses and losses associated with the internal motion.

When H_0 is along the X or Y-direction, the symmetry of the equilibrium configuration is reduced. As a result, the four dimensional secular

ω_{xy} MODE

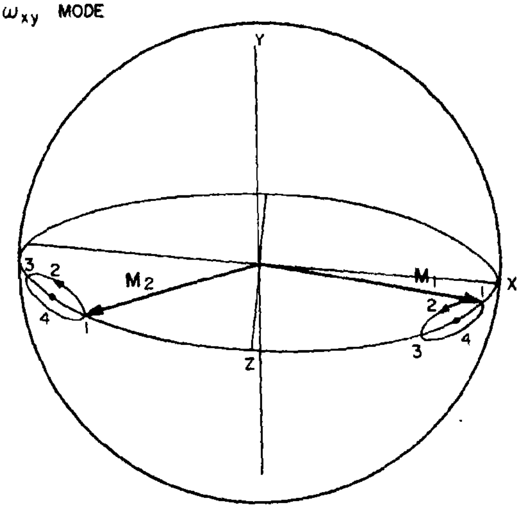

ω_z MODE

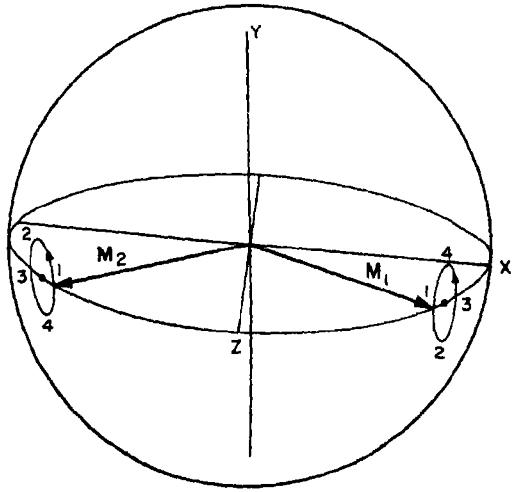

FIG. 5. Resonant precession modes. The numbers 1, 2, 3, 4 indicate successive orientations of the precessing magnetization vectors.

equation is not separable. The general procedure in calculating the resonance frequency is analogous to but considerably more complicated than the one followed above. The values of ω_{xy} and ω_z for H_0 along the Y-direction are given in the Summary. For H_0 along the X-direction the expressions become too cumbersome to be of much use. As mentioned before, the lowest term is quadratic in H_0. The coefficient of H_0^2 varies roughly from zero to the order of unity, depending on the basic parameters.

THE D.C. SUSCEPTIBILITY

From symmetry consideration one can show (see, e.g. TREVES[(2)]) that the magnetization σ is given, up to quadratic terms in the constant field H, by expressions of the form

$$\sigma_x = \chi_{xx}H_x + 2C_{xxz}H_xH_z,$$

$$\sigma_y = \chi_{yy}H_y + 2C_{yyz}H_yH_z,$$

$$\sigma_z = \sigma_{z0} + \chi_{zz}H_z + C_{xxz}H_x^2 + C_{yyz}H_y^2 + C_{zzz}H_z^2.$$

To obtain the coefficients, one makes a number of substitutions in equation (22) after setting $\omega = 0$. One replaces m_x by σ_x, m_y by σ_y, m_z by $(\sigma_z - \sigma_{z0})$; H_0 by H_z, h_x by H_x, and h_y by H_y. σ_{0z} is obtained directly from the canting angle given by equation (5). The results are listed in the Summary. The coefficients C_{yyz} and C_{zzz} are negligible in this approximation.*

SUMMARY OF RESULTS

D.C. susceptibilities

The magnetization σ is given by the expressions

$$\sigma_x \simeq \chi_{xx}H_x + 2C_{xxz}H_xH_z,$$

$$\sigma_y \simeq \chi_{yy}H_y,$$

$$\sigma_z \simeq \sigma_{z0} + \chi_{zz}H_z + C_{xxz}H_x^2,$$

where

$$\sigma_{z0} \simeq \frac{M(A_{xz}+D)}{E},$$

$$\chi_{xx} \simeq \frac{(A_{xz}+D)^2M}{4E[E(A_{xx}-A_{zz})+A_{xz}(A_{xz}+D]},$$

$$\chi_{yy} = \chi_{zz} \simeq M/E,$$

$$C_{xxz} \simeq \frac{(A_{xz}+D)[8E(A_{xx}-A_{zz})+(A_{xz}+D)(3A_{xz}-D)]}{32E[E(A_{xx}-A_{zz})+A_{xz}(A_{xz}+D)]}.$$

*R.F. susceptibilities (**H_0** in Z-direction)*

$$\bar{\chi}_{xx} \simeq \frac{\gamma^2M(A_{xz}+D+H_0)^2}{(\omega_{xy}^2-\omega^2)E},$$

$$\bar{\chi}_{yy} \simeq \frac{M\omega_{xy}^2}{(\omega_{xy}^2-\omega^2)E}$$

$$\bar{\chi}_{xy} = -\bar{\chi}_{yx} \simeq \frac{i\gamma\omega M(A_{xz}+D+H_0)}{E}$$

$$\bar{\chi}_{zz} \simeq \frac{M\omega_z^2}{(\omega_z^2-\omega^2)E}.$$

For $H_0 = 0$,

$$\bar{\chi}_{xx} \simeq \chi_{xx}\frac{\omega_{xy}^2}{\omega_{xy}^2-\omega^2},$$

$$\bar{\chi}_{yy} \simeq \chi_{yy}\frac{\omega_{xy}^2}{\omega_{xy}^2-\omega^2},$$

$$\bar{\chi}_{zz} \simeq \chi_{zz}\frac{\omega_z^2}{\omega_z^2-\omega^2}.$$

where bars denote r.f. magnitudes.

Resonance Frequencies

With $H_0 = 0$,

$$\omega_{xy}^2(0)/\gamma^2 = 4E(A_{xx}-A_{zz})+4A_{xx}(A_{xx}-A_{zz}) + 4A_{xz}(A_{xz}+D),$$

$$\omega_z^2(0)/\gamma^2 = 4EA_{xx}+4A_{xx}(A_{xx}-A_{zz})+(A_{xz}+D)^2$$

With H_0 in Z-direction

$$\omega_{xy}^2/\gamma^2 = \omega_{xy}^2(0)/\gamma^2+(5A_{xz}+D)H_0+H_0^2,$$

$$\omega_z^2/\gamma^2 = \omega_z^2(0)/\gamma^2+(A_{xz}+D)H_0.$$

---

* The result obtained by Treves according to which C_{zzz} may vary as $1/E^2$ rather than $1/E^3$ is based on an error in the calculation.

With H_0 in Y-direction,

$$\omega_{xy}^2/\gamma^2 = \omega_{xy}^2 0)/\gamma^2 - \frac{4A_{xz}^2}{4A_{zz}E+(D+A_{xz})(D-3A_{xz})} H_0^2,$$

$$\omega_z^2/\gamma^2 = \omega_z^2(0)/\gamma^2 + \frac{4A_{zz}E+(D-A_{xz})^2}{4A_{zz}E+(D+A_{xz})(D-3A_{xz})} H_0^2.$$

RELATION TO "EFFECTIVE FIELD" APPROACH

The canting angle at equilibrium depends, according to equation (6), directly on $A_{xz}+D+H_0$, where H_0 is along Z. It is tempting to regard $A_{xz}+D$ as representing an effective field, denoted $H_\perp$, also along Z, and consider the precession of the sublattice magnetization vectors as determined by a total perpendicular field $H_0+H_\perp$. The inadequacy of this approach can be made apparent from purely physical considerations. Consider, for example, the ω_{xy} mode for $H_0 = 0$, $A_{xz} = 0$. The canting energy in this case depends exclusively on the angle between M_1 and M_2, but this angle remains virtually constant during the precession, leading to the conclusion that $H_\perp$ is not operative with respect to this mode. Other difficulties arise when a field H_0 is introduced, which not only adds to the torques, but also changes the equilibrium positions. It is therefore not surprising that our results show no simple dependence on $A_{xz}+D+H_0$, but depend in an intricate manner on each of the separate parameters. They are thus in disagreement with, for example, the results of ORBACH[5] who describes the effect of canting and of an external perpendicular field by means of the single parameter $|H_\perp+H_0|$. Where coupling between several sublattices is involved, it is evidently advisable to avoid the introduction of effective fields.

CONCLUSION

The relations listed in the summary indicate that the anisotropy-canting energy, A_{xz}, and the antisymmetric exchange energy, D, play distinct roles and should not, in general, be combined as a single canting field. This is most clearly displayed in the expressions for the resonance frequencies. It will be noted that the linear coefficient of H_0 (H_0 along Z-direction) is given by $(5A_{xz}+D)$ and $(A_{xz}+D)$, respectively, for the two modes. A measurement of resonance as a function of H_0 can therefore yield accurate values of A_{xz} and D without previous knowledge of other constants.

The expressions for susceptibility are not as clear cut. The first order dependence of σ_{z0}, χ_{xx}, and C_{xxz} on the canting coefficient is given in terms of the parameter $A_{xz}+D$, which does not bring out the distinct roles of A_{xz} and D. Only when A_{xz} or D is comparable in magnitude to $[E(A_{xx}-A_{zz})]^{1/2}$ is there a hope of extracting A_{xz} and D separately from the susceptibility data by simultaneous solution of the equations for σ_{z0}, χ_{xx}, and C_{xxz}. Thus, TREVES[2] was able to show that in orthoferrites the susceptibility data are, on the whole, consistent with the assumption that $D \gg A_{xz}$.

His results, however, rely heavily on the value of the second order coefficient C_{xxz}, which is extremely difficult to determine accurately. Because of this inaccuracy there remain severe discrepancies between the values of C_{xxz} and χ_{xx} as calculated and measured by Treves. The reliance on high order coefficients also seems rather questionable when one considers that the expression for the free energy from which these are derived is itself given in a somewhat over-simplified form.

A word might be added concerning the inclusion in the free energy of an anisotropic exchange term of the form $E_xX_1X_2+E_zZ_1Z_2$. According to MORIYA,[1] E_x and E_z would be roughly of the order of D^2/E. According to TREVES,[2] the anisotropy energy in several orthoferrites is actually of this order. It is therefore conceivable that in these orthoferrites the anisotropy is caused entirely by exchange effects. The results of the above calculation can be easily modified to include the anisotropic exchange effect by introducing additional terms in equation (20). One adds $(-E_x)$ to the expression for $(b+a)$, E_x to the expression for $(b-a)$, (E_x-E_z) to the expression for $(d+c)$, and $(-E_x-E_z)$ to the expression for $(d-c)$. One then finds that E_x and E_z become submerged in other constants. Thus, at present, there appears to be no procedure by which a separate measurement of anisotropic exchange could be made.

Acknowledgements—The author would like to express his total indebtedness to the stimulation, advice, and interest of R. L. White. This work was sponsored in part by the Air Force Cambridge Research Laboratories, Office of Aerospace Research, under Contract AF 19(628)–387.

REFERENCES

1. Moriya T., *Phys. Rev.* **120**, 91 (1960).
2. Treves D., *Phys. Rev.* **125**, 1843 (1962).
3. Heeger A. J., Beckman O. and Portis A. M., *Phys. Rev.* **123**, 1652 (1961).
4. Pincus P., *Phys. Rev. Letters* **5**, 13 (1960).
5. Orbach R., *Phys. Rev.* **115**, 1189 (1959).

J. Phys. Chem. Solids Pergamon Press 1963. Vol. 24. pp. 607–616. Printed in Great Britain.

NONLINEAR EFFECTS IN SOLIDS

P. L. KELLEY

Lincoln Laboratory,* Massachusetts Institute of Technology, Lexington 73, Massachusetts

(*Received* 1 *October* 1962; *revised* 23 *November* 1962)

Abstract—The current response of Bloch electrons is calculated to second order in the external electromagnetic field by operator perturbation theory. Using a simple energy band transition scheme, the results are applied to the production of second harmonic radiation. The dependence of the intensity of the second harmonic light on energy band parameters is found and an estimate of the second harmonic power is made.

INTRODUCTION

A NUMBER of experiments[1–5] have been performed recently in which the harmonic generation of light has been observed. Two theoretical explanations of the results have been given: the first, by LAX *et al.*[5] using a classical nonlinear harmonic oscillator model of electronic motion and the second, by ARMSTRONG *et al.*[6] using time dependent perturbation theory to evaluate the second order polarization of localized electrons. Armstrong and co-workers have also considered, in some detail, the macroscopic electromagnetic effects of the nonlinear polarization.

It is the purpose of this paper to present a theory of second harmonic generation in solids with the assumption that the electromagnetic wave interacts with Bloch electrons. The induced electronic current is calculated to second order in the electromagnetic field in a manner analogous to the first order calculation of KUBO[7,8] and the higher order calculations of BERNARD and CALLEN[9] for the problem of noise in driven systems. A third order nonlinear response tensor connecting the induced current with the applied electromagnetic field to second order is obtained. The nonlocal character of the Bloch electrons is taken into account. The nonlinear current response is used as a source term to obtain a second harmonic electromagnetic wave. Two second harmonic waves are found, one propagating parallel and the other antiparallel to the direction of propagation of the fundamental. The amplitudes of these second harmonic waves are found, in the crystal, to be oscillatory functions of position. Finally, the frequency dependent part of the nonlinear response is evaluated in the dipole approximation for a three band transition scheme in a solid with filled valence and empty conduction bands.

OPERATOR PERTURBATION THEORY

In the one-electron picture, the expectation value of the electronic current density after an external field has been applied can be written as:

$$\langle J^{\mu}(rt) \rangle = Tr J^{\mu}(r)\rho^{s}(t), \tag{1}$$

where $J^{\mu}(r)$ is the μth component electron current density operator, and s denotes the Schrödinger representation. $\rho^{s}(t)$, the density operator for an electron, obeys the Liouville equation ($\hbar = 1$)

$$\frac{\partial \rho^{s}}{\partial t}(t) = -i[\mathscr{H}^{s}(t), \rho^{s}(t)], \tag{2}$$

where $\mathscr{H}^{s}(t)$ is the electronic Hamiltonian including the effect of the external field. $\mathscr{H}^{s}(t)$ is separated as follows:

$$\mathscr{H}^{s}(t) = \mathscr{H}_0 + \mathscr{H}^{s}_{A}(t), \tag{3}$$

where $\mathscr{H}_0$ is the electronic Hamiltonian in the absence of the electromagnetic field and $\mathscr{H}^{s}_{A}(t)$ represents the interaction with the Maxwell field.

---

* Operated with support from the U.S. Army, Navy, and Air Force.

The initial condition on the density operator is taken to be that of thermal equilibrium, i.e.

$$\rho^s(t = t_0) = f(\mathscr{H}_0), \tag{4}$$

where $f(\mathscr{H}_0)$ is the Fermi distribution operator. In order to obtain the response to second order in the external field, the density operator is calculated to second order in $\mathscr{H}_A(t)$. To facilitate this calculation, the operators are transformed to the interaction representation. The Liouville equation in the interaction representation is given by:

$$\frac{\partial\rho(t)}{\partial t} = -i[\mathscr{H}_A(t), \rho(t)], \tag{5}$$

where an operator in the interaction representation is related to one in the Schrödinger representation by

$$A(t) = \exp(i\mathscr{H}_0 t)A^s(t)\exp(-i\mathscr{H}_0 t). \tag{6}$$

By forward integration, we obtain to second order in the interaction Hamiltonian

$$\rho(t) = \rho(t_0) - i\int_{t_0}^{t}[\mathscr{H}_A(t'), \rho(t_0)]\,\mathrm{d}t' - \int_{t_0}^{t}\mathrm{d}t'\int_{t_0}^{t'}\mathrm{d}t''\Big[\mathscr{H}_A(t'), [\mathscr{H}_A(t''), \rho(t_0)]\Big]. \tag{7}$$

Substituting this result into (1), the current to second order in $\mathscr{H}_A$ is given by

$$\langle J^\mu(rt)\rangle = -i\int_{t_0}^{t} Tr\rho(t_0)[J^\mu(rt), \mathscr{H}_A(t')]\,\mathrm{d}t' - \int_{t_0}^{t}\mathrm{d}t'\int_{t_0}^{t'}\mathrm{d}t''\,Tr\rho(t_0)\Big[[J^\mu(rt), \times\mathscr{H}_A(t')], \mathscr{H}_A(t'')\Big]. \tag{8}$$

Thus, the current response to second order in the interaction Hamiltonian has been obtained.

SECOND ORDER RESPONSE

The response to second order in the external field can now be obtained from (8). In order to accomplish this, the Hamiltonian and the current density operators are written explicitly in terms of the Maxwell field. In this treatment electron spin will be neglected. The total Hamiltonian operator is given by

$$\mathscr{H}^s = \frac{1}{2m}\left(\boldsymbol{p} - \frac{e}{c}A\right)^2 + V. \tag{9}$$

The interaction Hamiltonian is, therefore, given in the interaction representation by

$$\mathscr{H}_A(t) = -\frac{e}{2mc}\{A(t)\cdot\boldsymbol{p}(t) + \boldsymbol{p}(t)\cdot A(t)\} + \frac{e^2}{2mc^2}A^2(t). \tag{10}$$

The interaction Hamiltonian may be rewritten in terms of momentum space integrals as follows:

$$\mathscr{H}_A(t) = -\frac{e}{mc}\sum_{\mu}\iint \mathrm{d}\boldsymbol{q}'\mathrm{d}\boldsymbol{q}''\{p^\mu(\boldsymbol{q}', t)A^\mu(\boldsymbol{q}', t) \times\delta(\boldsymbol{q}''-\boldsymbol{q}') - \frac{e}{2mc}P(\boldsymbol{q}'+\boldsymbol{q}'', t) \times A^\mu(\boldsymbol{q}', t)A^\mu(\boldsymbol{q}'', t)\}. \tag{11}$$

Here, $p^\mu(q)$ is the momentum space transform of the momentum density operator $p^\mu(\boldsymbol{r})$. In other words,

$$p^\mu(\boldsymbol{q}) = \int \mathrm{d}\boldsymbol{r}\exp(i\boldsymbol{q}\cdot\boldsymbol{r})p^\mu(\boldsymbol{r}) \tag{12}$$

where

$$p^\mu(\boldsymbol{r}) = \tfrac{1}{2}\{|\boldsymbol{r}\rangle\langle\boldsymbol{r}|p^\mu + p^\mu|\boldsymbol{r}\rangle\langle\boldsymbol{r}|\}. \tag{13}$$

Similarly, $P(\boldsymbol{q})$ is the momentum space transform of the mass density operator $P(\boldsymbol{r})$. $A^\mu(\boldsymbol{q}t)$ is related to the configuration space vector potential in the following manner:

$$A^\mu(\boldsymbol{r}, t) = \int \mathrm{d}\boldsymbol{q}\exp(i\boldsymbol{q}\cdot\boldsymbol{r})A^\mu(\boldsymbol{q}, t). \tag{14}$$

Note that the A's are no longer operators.

The current density operator is given by

$$J_\mu(rt) = \frac{e}{m}\left(p^\mu(rt) - \frac{e}{mc}P(rt)A^\mu(rt)\right). \tag{15}$$

Using (12), (14) and (15), the momentum space transform of that part of (8) which is second order in the vector potential is given as follows:

$$
\begin{aligned}
\langle J^{\epsilon}(qt)\rangle^{\text{N.L.}} &= \int \mathrm{d}\boldsymbol{r} \exp(i\boldsymbol{q}\cdot\boldsymbol{r})\langle J^{\epsilon}(\boldsymbol{r}t)\rangle^{\text{N.L.}} \\
&= \frac{-e^3}{2m^3c^2}\int\int \mathrm{d}\boldsymbol{q}'\mathrm{d}\boldsymbol{q}'' \sum_{\mu\nu}[i\int_{t_0}^{t} \mathrm{d}t'\{Tr\rho(t_0) \\
&\quad \times [p^{\epsilon}(\boldsymbol{q}, t), P(\boldsymbol{q}'+\boldsymbol{q}'', t')]\delta_{\mu\nu}A^{\mu}(\boldsymbol{q}'t')A^{\mu}(\boldsymbol{q}''t'') \\
&\quad + 2Tr\rho(t_0)[P(\boldsymbol{q}''+\boldsymbol{q}, t), p^{\mu}(\boldsymbol{q}', t')]\delta_{\epsilon\nu}A^{\mu}(\boldsymbol{q}'t')A^{\nu}(\boldsymbol{q}''t)\} \\
&\quad + 2\int_{t_0}^{t} \mathrm{d}t' \int_{t_0}^{t'} \mathrm{d}t'' Tr\rho(t_0)[[p^{\epsilon}(\boldsymbol{q}, t), p^{\mu}(\boldsymbol{q}', t')], p^{\nu}(\boldsymbol{q}'', t'')] \\
&\quad \times A^{\mu}(\boldsymbol{q}'t')A^{\nu}(\boldsymbol{q}''t'')]. \qquad (16)
\end{aligned}
$$

Here N.L. indicates the second order response. It will be convenient to use this momentum space transform of the nonlinear current in obtaining the electromagnetic response to the nonlinear current. Since the vector potential is zero when $t < t_0$, the lower limit on the integrals can be extended to minus infinity; the upper limits are extended to infinity by introducing step functions into the integrands. Further, the invariance of the trace under time translations is used to rewrite the time arguments of the operators. The second order current becomes

$$
\begin{aligned}
\langle J^{\epsilon}(\boldsymbol{q}, t)\rangle^{\text{N.L.}} &= \frac{-e^3}{2m^3c^2}\int\int \mathrm{d}\boldsymbol{q}'\mathrm{d}\boldsymbol{q}'' \sum_{\mu\nu}\int_{-\infty}^{\infty}\mathrm{d}t'\int_{-\infty}^{\infty}\mathrm{d}t'' \\
&\quad \times \{iTr\rho(t_0)[\exp\{i\mathscr{L}_0(t-t')\}p^{\epsilon}(\boldsymbol{q}), P(\boldsymbol{q}'+\boldsymbol{q}'')]\delta_{\mu\nu}\eta(t-t')\delta(t'-t'') \\
&\quad + 2iTr\rho(t_0)[\exp\{i\mathscr{L}_0(t-t')\}P(\boldsymbol{q}''+\boldsymbol{q}), p^{\mu}(\boldsymbol{q}')]\delta_{\epsilon\nu}\eta(t-t')\delta(t-t'') \\
&\quad + 2Tr\rho(t_0)[\exp\{i\mathscr{L}_0(t'-t'')\}[\exp\{i\mathscr{L}_0(t-t')\}p^{\epsilon}(\boldsymbol{q}), p^{\mu}(\boldsymbol{q}')], p^{\nu}(\boldsymbol{q}'')] \\
&\quad \times \eta(t-t')\eta(t'-t'')\}A^{\mu}(\boldsymbol{q}'t')A^{\nu}(\boldsymbol{q}'', t''), \qquad (17)
\end{aligned}
$$

where $\eta(t)$ is given by

$$\eta(t) = \begin{cases} 1 & t > 0 \\ 0 & t < 0. \end{cases} \qquad (18)$$

The Liouville operator $\mathscr{L}_0$ is defined in terms of the matrix elements in the energy representation of the product of a function of $\mathscr{L}_0$, namely $F(\mathscr{L}_0)$, and an operator, B,

$$\langle\alpha|F(\mathscr{L}_0)B|\beta\rangle = F(\mathscr{H}_{0\alpha\alpha} - \mathscr{H}_{0\beta\beta})B_{\alpha\beta}. \qquad (19)$$

The expectation value of the nonlinear current is now transformed into frequency space, introducing the transformation

$$\langle J^{\epsilon}(\boldsymbol{q}, t)\rangle^{\text{N.L.}} = \frac{1}{2\pi}\int_{-\infty}^{\infty}\mathrm{d}\omega \exp(-i\omega t)\langle J^{\epsilon}(\boldsymbol{q}\omega)\rangle^{\text{N.L.}}, \qquad (20)$$

Using the convolution theorem, we readily obtain, from (17),

$$\langle J^{\epsilon}(\boldsymbol{q}, \omega)\rangle^{\text{N.L.}} = \int\int \mathrm{d}\boldsymbol{q}'\mathrm{d}\boldsymbol{q}'' \sum_{\mu\nu} \int_{-\infty}^{\infty}\mathrm{d}\omega_1 \int_{-\infty}^{\infty}\mathrm{d}\omega_2 \alpha^{\epsilon\mu\nu}(\boldsymbol{q}, \boldsymbol{q}', \boldsymbol{q}'', \omega_2+\omega_1, \omega_1)$$

$$\times A^{\mu}(\boldsymbol{q}', \omega_2)A^{\nu}(\boldsymbol{q}'', \omega_1)\delta(\omega-\omega_1-\omega_2); \tag{21}$$

here the response function $\alpha^{\epsilon\mu\nu}$ is given by

$$\alpha^{\epsilon\mu\nu}(\boldsymbol{q}, \boldsymbol{q}', \boldsymbol{q}'', \omega_2+\omega_1, \omega_1)$$

$$= \frac{-e^3}{(2\pi)2m^3c^2}\{iTr\rho(t_0)[\eta(\mathscr{L}_0+\omega_2+\omega_1)p^{\epsilon}(\boldsymbol{q}), P(\boldsymbol{q}'+\boldsymbol{q}'')]\delta_{\mu\nu}$$

$$+2iTr\rho(t_0)[\eta(\mathscr{L}_0+\omega_2)P(\boldsymbol{q}+\boldsymbol{q}''), p^{\mu}(\boldsymbol{q}')]\delta_{\epsilon\nu}$$

$$+\frac{1}{\pi}Tr\rho(t_0)[\eta(\mathscr{L}_0+\omega_1)[\eta(\mathscr{L}_0+\omega_1+\omega_2)p^{\epsilon}(\boldsymbol{q}), p^{\mu}(\boldsymbol{q}')], p^{\nu}(\boldsymbol{q}'')]\}. \tag{22}$$

Here $\eta(\omega)$ is given by $1/(\omega+i\epsilon)$, where $\epsilon \to 0^+$. Note that $A(\boldsymbol{q}, \omega)$ is the frequency transform of $A(\boldsymbol{q}, t)$. The resulting expression may now be evaluated by explicitly calculating the trace. Since $J(\boldsymbol{r}t)$ and $A(\boldsymbol{r}t)$ are real, the following condition on α is obtained:

$$\alpha^{*\epsilon\mu\nu}(\boldsymbol{q}, \boldsymbol{q}', \boldsymbol{q}'', \omega_2+\omega_1, \omega_1)$$

$$= \alpha^{\epsilon\mu\nu}(-\boldsymbol{q}, -\boldsymbol{q}', -\boldsymbol{q}'', -(\omega_2+\omega_1), -\omega_1). \tag{23}$$

If the states are of Bloch character, the momentum space transform of an operator, such as the probability density operator or the momentum density operator, may be written in the following manner:

$$B(\boldsymbol{q}) = \int \mathrm{d}\boldsymbol{r}\exp(i\boldsymbol{q}\cdot\boldsymbol{r})B(\boldsymbol{r}) = \Delta(\boldsymbol{q}+\boldsymbol{\kappa})\bar{B}(\boldsymbol{q}), \tag{24}$$

where $$\Delta(\boldsymbol{q}) = \frac{1}{N}\sum_{n}\exp(i\boldsymbol{q}\cdot\boldsymbol{R}_n)$$

and $$\bar{B}(\boldsymbol{q}) = N\int_{\text{cell}}\mathrm{d}\boldsymbol{r}\exp(i\boldsymbol{q}\cdot\boldsymbol{r})B(\boldsymbol{r}). \tag{25}$$

$\boldsymbol{R}_n$ is the position vector of the nth unit cell; κ is the analogue of the Liouville operator for the crystal momentum. This operator is defined as follows: a matrix element of the product of a function $F(\kappa)$ and an operator B between Bloch states is given by

$$\langle nk|F(\kappa)B|n'k'\rangle = F(\boldsymbol{k}-\boldsymbol{k}')B_{nk,n'k'} \tag{26}$$

It is worthwhile noting that for Bloch electrons, κ and $\mathscr{L}_0$ commute. $\Delta(\boldsymbol{q})$ has the following property

$$\Delta(\boldsymbol{q}-\boldsymbol{q}')\Delta(\boldsymbol{q}-\boldsymbol{q}'') = \Delta(\boldsymbol{q}-\boldsymbol{q}')\Delta(\boldsymbol{q}'-\boldsymbol{q}'') \tag{27}$$

Note that $\rho(t_0)$ is a diagonal operator in the Bloch representation and thus, only the diagonal part of the commutators in (22) contribute to the trace. With the above results in mind, the response function can be rewritten:

$$\alpha^{\epsilon\mu\nu}(\boldsymbol{q}, \boldsymbol{q}', \boldsymbol{q}'', \omega_1+\omega_2, \omega_1) = \frac{V}{(2\pi)^3}\Delta(\boldsymbol{q}+\boldsymbol{q}'+\boldsymbol{q}'')$$

$$\times \Gamma^{\epsilon\mu\nu}(\boldsymbol{q}, \boldsymbol{q}', \boldsymbol{q}'', \omega_1+\omega_2, \omega_1) \tag{28}$$

where V is the volume of the crystal. The function $\Gamma^{\epsilon\mu\nu}$ is given by

$$
\begin{aligned}
&\Gamma^{\epsilon\mu\nu}(q, q', q'', \omega_2+\omega_1, \omega_1) \\
&= \frac{-e^3(2\pi)^3}{2m^3c^2V} Tr\rho(t_0)\{[\eta(\mathscr{L}_0+\omega_1+\omega_2)\bar{p}^{\epsilon}(q), \Delta(\kappa+q'+q'')\bar{P}(q'+q'')]\delta_{\mu\nu} \\
&\quad +2[\eta(\mathscr{L}_0+\omega_2)\bar{P}(q+q''), \Delta(\kappa+q')\bar{p}^{\mu}(q'')]\delta_{\epsilon\nu} \\
&\quad + \frac{1}{\pi}[\eta(\mathscr{L}_0+\omega_1)[\eta(\mathscr{L}_0+\omega_1+\omega_2)\bar{p}^{\epsilon}(q), \Delta(\kappa+q')\bar{p}^{\mu}(q')], \Delta(\kappa+q'')\bar{p}^{\nu}(q'')]\} \qquad (29)
\end{aligned}
$$

The above separation of α into a sum of exponential terms and Γ will be useful for the evaluation of the spatial dependence of the electromagnetic wave produced by this nonlinear polarization. As shall be shown presently, the sum of exponential terms will determine the spatial dependence of the wave at frequency $\omega_1+\omega_2$, while the Γ part, which is a slowly varying function of the q's, will not affect the spatial dependence.

It should be noted that it is extremely difficult to evaluate the expression Γ as it now stands; however, since the operators have been expressed as integrals over a unit cell, the exponential in the spatial integral may be expanded as a power series in $(q \cdot r)$, using the condition $|q|a \ll 1$ (for q's in the optical region) to truncate the series. For systems without inversion symmetry, it is sufficient to keep only the lowest order term in the series, i.e. $\exp(iq \cdot r)$ may be replaced by 1, this being the dipole approximation. In the case of systems with inversion symmetry, the lowest order term vanishes and it is necessary to keep at least the next higher order term in the series. For the dipole approximation, the single commutator terms vanish and Γ becomes

$$
\begin{aligned}
\Gamma^{\epsilon\mu\nu}_{\text{dipole}}(\omega_2+\omega_1, \omega_1) &= \frac{-e^3(2\pi)^2}{m^3c^2V} \\
&\times Tr\rho(t_0)[\eta(\mathscr{L}_0+\omega_1)[\eta(\mathscr{L}_0+\omega_1+\omega_2)\bar{p}^{\epsilon}(0), \\
&\times \delta_{\kappa,0}\bar{p}^{\mu}(0)], \delta_{\kappa,0}\bar{p}^{\nu}(0)]. \qquad (30)
\end{aligned}
$$

Here, the Δ-functions have been replaced by Kronecker deltas (or by Dirac delta functions in the continuous limit) and q has been set equal to zero, since in most cases, $q \ll k$. Thus, the contributions to Γ will be nonvanishing for vertical transitions only. Use is made here of the property that in the summations over wave vectors indicated by the trace operation $\Delta(\kappa)$ is a sharply peaked function about $\kappa = 0$ (in the reduced zone scheme). However, the replacement of $\Delta(q+q'+q'')$ in (28) by $\delta(q+q'+q'')$ is not correct. One would obtain from this replacement a polarization wave spread through all space, and which would not take into account the finite nature of the crystal. In the next Section, the finite array of lattice points involved in the Δ-function in (28) will be used together with the condition that the second harmonic wave from each unit cell be outgoing to find the spatial dependence of the second harmonic wave.

Writing the trace in terms of matrix elements between Bloch states α, β, γ, the nonlinear response Γ becomes

$$
\begin{aligned}
\Gamma^{\epsilon\mu\nu}(\omega_1+\omega_2, \omega_1) &= \frac{-(2\pi)^2 e^3}{m^3c^2V} \sum_{\substack{\alpha\beta\gamma \\ k=k_\alpha=k_\beta=k_\gamma}} f(\omega_\alpha) \\
&\times \left\{ \frac{1}{\omega_{\alpha\beta}(k)+\omega_1+\omega_2+i\epsilon} \frac{1}{\omega_{\alpha\gamma}(k)+\omega_1+i\epsilon} p^{\epsilon}_{\alpha\beta} p^{\mu}_{\beta\gamma} p^{\nu}_{\gamma\alpha} \right. \\
&- \frac{1}{\omega_{\alpha\gamma}(k)+\omega_1+i\epsilon} \frac{1}{\omega_{\beta\gamma}(k)+\omega_1+\omega_2+i\epsilon} p^{\mu}_{\alpha\beta} p^{\epsilon}_{\beta\gamma} p^{\nu}_{\gamma\alpha} \\
&- \frac{1}{\omega_{\beta\gamma}(k)+\omega_1+\omega_2+i\epsilon} \frac{1}{\omega_{\beta\alpha}(k)+\omega_1+i\epsilon} p^{\nu}_{\alpha\beta} p^{\epsilon}_{\beta\gamma} p^{\mu}_{\gamma\alpha} \\
&\left. + \frac{1}{\omega_{\beta\alpha}(k)+\omega_1+i\epsilon} \frac{1}{\omega_{\gamma\alpha}(k)+\omega_1+\omega_2+i\epsilon} p^{\nu}_{\alpha\beta} p^{\mu}_{\beta\gamma} p^{\epsilon}_{\gamma\alpha} \right\} \qquad (31)
\end{aligned}
$$

where

$$\omega_{\alpha\beta}(k) = \langle\alpha|\mathscr{H}|\alpha\rangle - \langle\beta|\mathscr{H}|\beta\rangle.$$

MAXWELL'S EQUATION WITH A NONLINEAR SOURCE

In this Section, the spatial dependence of an electromagnetic wave with a nonlinear source will be calculated. The equation for the vector potential is taken to be

$$\left(\nabla^2 - \frac{\mu_0\epsilon}{c^2}\partial_t^2\right)A^\epsilon(rt) = -\frac{4\pi}{c}\langle J^\epsilon(rt)\rangle^{NLS}. \quad (32)$$

Here the constitutive equations have been used to obtain the dielectric constant from the linear response. It will be assumed that ϵ is real: in other words, the linear effects are assumed purely dispersive, i.e. nonabsorptive. The NLS superscript indicates the nonlinear source current; this differs from the nonlinear current calculated previously due to the inclusion of local field corrections. The Fourier transform of (32) is now introduced, where

$$A^\mu(\boldsymbol{r}t) = \frac{1}{(2\pi)^4}\int \mathrm{d}\omega \mathrm{d}\boldsymbol{q} \exp[-i(\omega t + \boldsymbol{q}\cdot\boldsymbol{r})]A(\boldsymbol{q}\omega). \quad (33)$$

The equation for the Fourier transformed $A^\mu(\boldsymbol{k}\omega)$ is

$$(\boldsymbol{q}^2 - \mu_0\epsilon\omega^2)A^\mu(\boldsymbol{q}\omega) = \frac{4\pi}{c}\langle J^\epsilon(\boldsymbol{q}\omega)\rangle^{NLS}. \quad (34)$$

The vector potential then becomes

$$A^\epsilon(\boldsymbol{r}t) = \frac{2}{(2\pi)^3 c}\int_\gamma \mathrm{d}\boldsymbol{q}\int_{-\infty}^{\infty}\mathrm{d}\omega\frac{\langle J^\epsilon(\boldsymbol{q}\omega)\rangle^{NLS}}{q^2 - \mu_0\epsilon\omega^2}$$
$$\times \exp[-i(\omega t + \boldsymbol{q}\cdot\boldsymbol{r})]. \quad (35)$$

The contours γ in the q planes are defined so that the wave will be outgoing. Equation (21) is used to obtain

$$A^\epsilon(\boldsymbol{r}t) = \frac{2}{(2\pi)^3 c}\int_\gamma \mathrm{d}\boldsymbol{q}\frac{\exp[-i\{(\omega_1+\omega_2)t + \boldsymbol{q}\cdot\boldsymbol{r}\}]}{q^2 - \mu_0\epsilon\omega^2}$$
$$\times \int\int \mathrm{d}\boldsymbol{q}'\mathrm{d}\boldsymbol{q}'' \sum_{\mu\nu}\int \mathrm{d}\omega_1\int \mathrm{d}\omega_2$$
$$\times \alpha'^{\epsilon\mu\nu}(\boldsymbol{q}, \boldsymbol{q}', \boldsymbol{q}'', \omega_2+\omega_1, \omega_1)$$
$$\times A^\mu(\boldsymbol{q}', \omega_1)A^\nu(\boldsymbol{q}'', \omega_2). \quad (36)$$

Here, the prime indicates that local field effects have been taken into account. The connection between α and α' has been shown by ARMSTRONG *et al.*⁽⁶⁾ to be

$$\alpha'^{\epsilon\mu\nu} = \sum_{\epsilon'\nu'\mu'} R_{\epsilon'}^{\epsilon}R_{\mu'}^{\mu}R_{\nu'}^{\nu}\alpha^{\epsilon'\mu'\nu'}, \quad (37)$$

where the R's are related to the dielectric tensor of the medium. The self-polarization corrections for Bloch electrons have been omitted; these are discussed in some detail by ADLER⁽¹⁰⁾ and are assumed small. At this point, attention will be confined to the frequency doubling case. A^μ and A^ν are assumed to have only one frequency component, i.e. ω_1, and to have the same spatial dependence: in other words, $\boldsymbol{q}' = \boldsymbol{q}'' = \boldsymbol{q}_1$. The frequency doubled vector potential for times $t > t_0$ is given by

$$A^\epsilon(\boldsymbol{r}t) = \frac{2}{(2\pi)c}\sum_{\mu\nu}\exp(+i\omega_2 t)A_1^\mu A_1^\nu$$
$$\times \int_\gamma \frac{\mathrm{d}\boldsymbol{q}}{(2\pi)^3}\frac{\exp(-i\boldsymbol{q}\cdot\boldsymbol{r})}{q^2 - q_2^2}v_c\sum_n \exp[i(\boldsymbol{q}+2\boldsymbol{q}_1)\cdot\boldsymbol{R}_n]$$
$$\times \Gamma^{\epsilon\mu\nu}(\boldsymbol{q}, \boldsymbol{q}_1, \boldsymbol{q}_1, \omega_2, \omega_1), \quad (38)$$

where $q_2^2 \equiv \mu_0\epsilon\omega_2^2$ and $\omega_2 = 2\omega_1$. Equation (28) has been used to eliminate α. In obtaining the above result, only those contributions to the frequency integration due to poles in the frequency transform of the vector potentials A^μ and A^ν have been taken into account. There will, of course, be contributions from the singularities in the response function, but these are in the nature of branch line integrals which damp out in time.

Assuming Γ is a slowly varying function of q, and converting the summation over cells into an integration and integrating over q and the cells, the following result is obtained:

$$A^{\epsilon}(rt) = \frac{1}{(2\pi)^2 c}\frac{1}{q_2}\exp(i\omega_2 t)A_1^{\mu}A_1^{\nu}$$
$$\times\sum_{\mu\nu}\left\{\exp(-iq_2 x)\exp[-i(q_1-q_2/2)x]\frac{\sin\{(2q_1-q_2/2)x\}}{(2q_1-q_2)/2}\Gamma'^{\epsilon\mu\nu}(q_2, q_1, q_1, \omega_2, \omega_1)\right.$$
$$-\exp[iq_2(x-L)]\exp[i(q_1+q_2/2)(x-L)]\exp(-i2q_1L)\frac{\sin\{(q_1+q_2/2)(x-L)\}}{((2q_1+q_2)/2)}$$
$$\left.\times\Gamma'^{\epsilon\mu\nu}(q_2, q_1, q_1, \omega_2, \omega_1)\right\}. \tag{39}$$

The wave q_1 is travelling through the crystal in the x direction from $x = 0$ to $x = L$. The solutions outside the solid may be found from the above by using the appropriate solutions at the boundary of the nonlinear dielectric.

In this treatment, we have neglected reflection and refraction at the boundaries. The first harmonic will be reflected at $x = L$; thus, there will be more than one Fourier component in the source term. In addition, the internal reflection of the second harmonic will give rise to additional second harmonic components neglected in (39). To obtain the correct result, (39) must be modified to include the additional Fourier components in the source term and homogeneous terms must be added to satisfy the second harmonic boundary conditions. It should be pointed out that BLOEMBERGEN and PERSHAN(11) have treated the effects of the boundaries in great detail. Because of the finite distribution in space of the source terms and the neglect of reflection, the first term in (39) is zero at $x = 0$ and the second, zero at $x = L$.

The first term in (39) is a wave of frequency $\omega_2 = 2\omega_1$ propagating in the direction of the wave of frequency ω_1; the second term is a wave propagating in a direction 180° from the wave of frequency ω_1. The first ω_2 wave builds up initially as x increases from zero, then oscillates; the second builds up as x decreases from L and then oscillates. It should be noted that there exists the possibility of phase matching for the first term in (39), since the argument of the sine function $(q_2-2q_1)x/2$ might be made to go to zero. However, the second term can never be phase matched. In materials where phase matching is difficult, the second term in (39) might be of the same order of magnitude as the first.

Confining attention to the first term in (39), it is seen that, in the dipole approximation, this becomes

$$A^{\epsilon}(xt) = \frac{1}{(2\pi)^2 cq_2}\exp(i\omega_2 t)$$
$$\times\sum_{\mu\nu}\exp(-iq_2x)\exp[i(q_2/2-q_1)x]$$
$$\times\frac{\sin((2q_1-q_2)/2)x}{(2q_1-q_2)/2}\Gamma'^{\epsilon\mu\nu}(2\omega_1, \omega_1)A_1^{\mu}A_1^{\nu}, \tag{40}$$

where Γ′ is related to Γ in the same way that α' is to α. In order to study the frequency dependence, (31) will be used to evaluate Γ for simple band structure.

THE EVALUATION OF THE RESPONSE FUNCTION FOR VIRTUAL INTERBAND TRANSITIONS

In this Section, the response function will be calculated for a simple energy band model. First, it should be noted that the states of a system which has inversion symmetry can be chosen to have a definite parity and that the momentum operator only connects states of opposite parity. The product $p_{\alpha\beta}p_{\beta\gamma}p_{\gamma\alpha}$ (where α, β, and γ are states of definite parity) must vanish. This follows, since α must have opposite parity from β for $p_{\alpha\beta}$ not to vanish, and β from γ for $p_{\beta\gamma}$ not to vanish;

therefore, γ must have the same parity as α and $p_{\gamma\alpha}$ must vanish. Thus, crystals which do not have inversion symmetry must be chosen for the pure dipolar process. It should be noted that the interaction of electrons with phonons should allow the dipolar process to occur even in systems with inversion symmetry.

We will consider a solid with a completely filled valence band and empty conduction bands with band maxima or minima at $k = 0$. It is assumed that a perturbation calculation for the p matrix elements about the band edge can be performed. For the sake of simplicity, only the zeroth order terms in k will be kept, i.e. just the band edge matrix element.

If the process were to involve only two bands, then one of the matrix elements of p in (31) would have to involve an intraband transition. However, an intraband matrix element of p vanishes at the band edge and thus the nonlinear response has no contribution from the band edge matrix elements. It may be noted that if higher order terms in k were to be included in the intraband matrix element, then higher order terms in k would also have to be included in the interband p's in order to obtain a product which is even in k and does not vanish on summation over k. The fact that intraband matrix elements can contribute at all is in contrast to the linear case where intraband matrix elements do not contribute to the polarization or absorption.

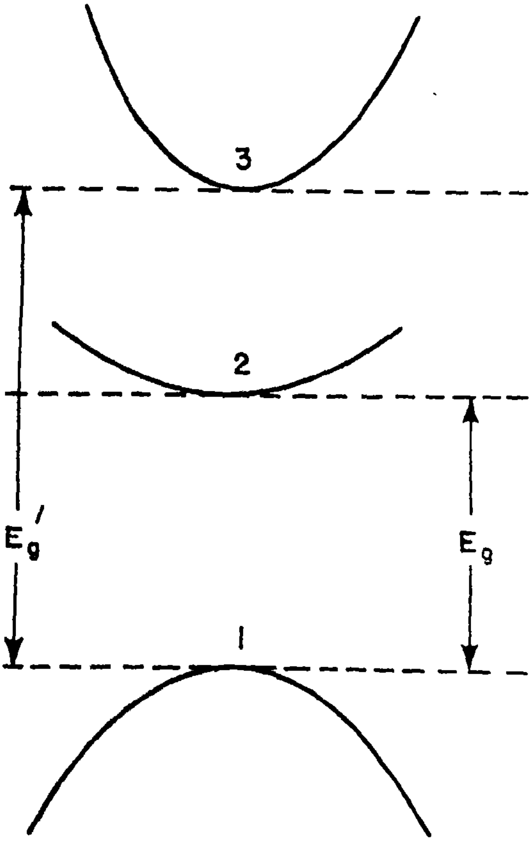

FIG. 1. Three-band model.

In order that the band edge matrix elements be nonvanishing, a three-band process, where dipole transitions between the three bands are allowed, must be considered. The symmetry of the crystal restricts the various components of the momentum matrix elements which are nonvanishing between the bands, but this will be neglected at present. The band structure is indicated in Fig. 1.

The valence band has the following energy vs. wave vector dependence:

$$E_1(k) = -\frac{k^2}{2m_1}; \tag{41}$$

while the conduction bands have the E vs. k dependence

$$E_2(k) = E_g + \frac{k^2}{2m_2}, \tag{42}$$

$$E_3(k) = E_g' + \frac{k^2}{2m_3}. \tag{43}$$

Parabolic bands have been chosen for simplicity in calculation. The transitions are assumed to be virtual, in other words, $\omega_1 < E_g$, $2\omega_1 < E_g'$. In the situation where $2\omega_1 > E_g$, the second harmonic light would be reabsorbed. However, if $\omega_1 \sim E_g$ and $2\omega_1 \sim E_g'$, the energy denominators may be small enough so that the layer within an absorption length of the surface may act as a second harmonic source. The leading term in (31) for the frequency doubling case gives

$$\Gamma^{\epsilon\mu\nu}(2\omega_1, \omega_1) \approx \left(\frac{-e^3(2\pi)}{m^3c^2V}\right) p_{13}^{\epsilon} p_{32}^{\mu} p_{21}^{\nu} \times \sum_k \frac{1}{\omega_{31}(k) - 2\omega_1} \frac{1}{\omega_{21}(k) - \omega_1}, \tag{44}$$

where $\omega_{31}(k) = E'_g + k^2/2\mu_{31}$, and $\omega_{21}(k) = E_g + k^2/2\mu_{21}$. The reduced effective mass μ has been introduced and is given by

$$\mu_{ij} = \frac{m_i m_j}{m_i + m_j}. \tag{45}$$

Converting the sum over k into an integral in the case $k^2_{\text{max}} > 2\mu_{21}(E_g - \omega_1)$, $2\mu_{31}(E_g - 2\omega_1)$, the following is obtained:

$$\Gamma^{\epsilon\mu\nu}(2\omega_1, \omega_1) \simeq \frac{1}{4}\left(\frac{-e^3}{\hbar^3 m^3 c^2}\right) \times \sqrt{[\mu^2_{31}\mu_{21}]} f(\omega_1) p^{\epsilon}_{13} p^{\mu}_{32} p^{\nu}_{21}, \tag{46}$$

where $f(\omega_1)$ is given by

$$f(\omega_1) = \frac{\sqrt{[(\mu_{31}/\mu_{21})(E'_g - 2\hbar\omega_1)]} - \sqrt{[E_g - \hbar\omega_1]}}{(\mu_{31}/\mu_{21})(E'_g - 2\hbar\omega_1) - E_g - \hbar\omega_1}. \tag{47}$$

$\hbar$'s have been reintroduced into (46) and (47). Figure 2 is a graph of $f(\omega_1)$ when $\mu_{31}/\mu_{21} = 1$ for two cases: (1) $E_g/E' = 0{\cdot}64$ (the dashed line) and (2) $E_g/E'_g = 0{\cdot}505$ (the solid line). $f(\omega_1)$ is finite except for the very special situation where $E_g/E'_g = 0{\cdot}5$. In this case, $f(\omega_1)$ has a square root infinity when $2\hbar\omega_1 = E'_g$.

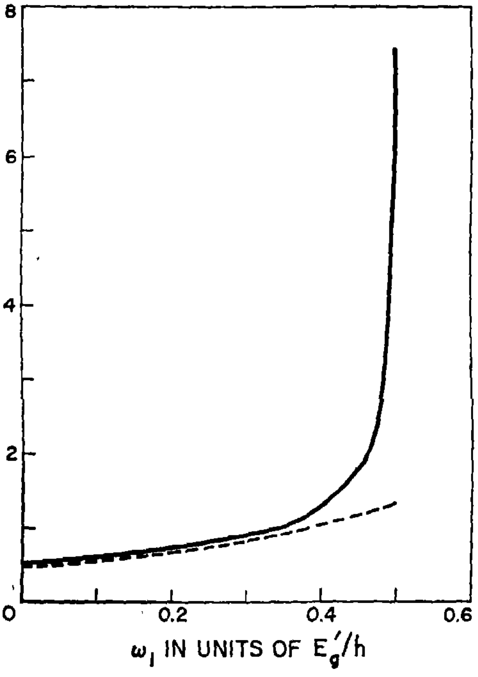

FIG. 2. Plot of $f(\omega_1)$.

The above results may be used to estimate the intensity of the doubled beam due to ruby laser light ($\lambda = 0{\cdot}69\,\mu$). Equations (40), (46) and (47) are used to find the second harmonic amplitude as a function of $f(\omega_1)$, the momentum matrix elements, and the masses. The relation between the vector potential A and the power per unit area S is then used to obtain the following result:

$$S_2 = (10^{-16}\, m^2/W) S_1^2 \tag{48}$$

Here S_2 and S_1 are the power per unit area of the doubled and incident beams respectively. The following values are taken for the parameters: $f(\omega_1) = (E'_g)^{-1/2}$, $E_g = \frac{1}{2}E'_g = \frac{5}{4}\hbar\omega_1 = 2{\cdot}2$ eV and $\sqrt{(\mu^2_{13}\mu_{12})} p^{\epsilon}_{13} p^{\mu}_{32} p^{\nu}_{21} = \frac{1}{2}(m_0^2 E_g)^{3/2}$. The last relation is obtained by approximating the relation between effective masses and momentum matrix elements. The sine function in (40) is taken to be 1 and the phase mismatch is assumed to be given by $|q_2 - 2q_1| = q_1/4$.

CONCLUSIONS

The foregoing derivation has given the nonlinear response function for Bloch electrons to second order in the external fields. The shape of the second order response as a function of frequency has been given for a three-band transition scheme in the dipole approximation. The intensity of the second harmonic increases as the second harmonic frequency approaches one absorption edge and the first harmonic another edge. There are other interband processes which should be considered such as a two-band transition scheme where, although the contribution at the absorption edge may vanish, terms away from the edge may give a contribution. In solids with inversion symmetry where dipole effects vanish, the above results may be used to extend the analysis to higher order multipole processes.

Acknowledgements—The author would like to thank Dr. J. G. MAVROIDES and Dr. A. L. MCWHORTER for many useful discussions. He would also like to thank Dr. LAURA M. ROTH and Dr. G. DRESSELHAUS for reviewing the manuscript.

REFERENCES

1. Franken P. A., Hill A. E., Peters C. W. and Weinreich G., *Phys. Rev. Letters* **7**, 118 (1961).
2. Bass M., Franken P. A., Hill A. E., Peters C. W. and Weinreich G., *Phys. Rev. Letters* **8**, 18 (1962).
3. Giordmaine J. A., *Phys. Rev. Letters* **8**, 19 (1962).
4. Maker P. D., Terhune R. W., Nisenoff M. and Savage C. M., *Phys. Rev. Letters* **8**, 21 (1962).
5. Lax B., Mavroides J. G. and Edwards D. F., *Phys. Rev. Letters* **8**, 166 (1962).
6. Armstrong J. A., Bloembergen N., Ducuing J. and Pershan P. S., *Tech. Rep. No.* 358, *Cruft Laboratory, Harvard University* (1962).
7. Kubo R. and Tomita K., *J. phys. Soc. Japan* **9**, 888 (1954).
8. Kubo R., *J. phys. Soc. Japan* **12**, 570 (1957).
9. Bernard W. and Callen H. B., *Rev. mod. Phys.* **4** 1017 (1959).
10. Adler S. L., *Phys. Rev.* **126**, 413 (1962).
11. Bloembergen N. and Pershan P. S., *Tech. Rep. No.* 367, *Cruft Laboratory, Harvard University* (1962).

J. Phys. Chem. Solids Pergamon Press 1963. Vol. 24, pp. 617–624. Printed in Great Britain.

A STUDY OF ROTATIONAL FREEDOM IN SEVERAL AMMONIUM SALTS BY SLOW NEUTRON INELASTIC SCATTERING*

V. BRAJOVIC,† **H. BOUTIN**, **G. J. SAFFORD**‡ and **H. PALEVSKY**
Brookhaven National Laboratories, Upton, New York

(*Received* 15 *November*, 1962)

Abstract—Differential inelastic cross sections for 0·005 eV incident neutrons scattered at 90° from polycrystalline samples of NH_4PF_6, $NH_4K_xI_{1+x}$, $(NH_4)_2S_2O_8$, and NH_4SO_3F have been studied. Measurements were made at $T = 294°K$ for all four samples, at $T = 103°K$ for NH_4PF_6 and at $T = 348°K$ for $(NH_4)_2S_2O_8$. The observed shapes of the energy spectra for neutrons gaining energy are compared at each temperature with shapes calculated on the basis of a Kreiger–Nelkin approximation, assuming free three-dimensional rotation of the NH_4^+ ions. The results show that the energy spectra of neutrons scattered from NH_4PF_6 and $NH_4K_xI_{1+x}$ at $T = 294°K$ ($kT \sim 0{\cdot}6$ kcal/mole) approach the expected shape for free rotations of the ammonium ion with effective masses of 2·8 and 2·0, respectively. The neutron spectra from NH_4SO_3F and $(NH_4)_2S_2O_8$ at $T = 294°K$ ($kT \sim 0{\cdot}6$ kcal/mole) have nearly the same shape and show a considerable departure from the shape expected for free rotation, but at $T = 348°K$ ($kT \sim 0{\cdot}7$ kcal/mole) the neutron-energy-gain spectrum from $(NH_4)_2S_2O_8$ closely approaches the shape expected for free rotation with an effective mass of 2·0 mass units. At $T = 103°K$ ($kT \sim 0{\cdot}2$ kcal/mole) the neutron spectrum from NH_4PF_6 departs in shape significantly from the shape expected for free rotation. These results are consistent with previous rough estimates of rotational barriers of 0·2 kcal/mole for NH_4PF_6 and 0·7 kcal/mole for $(NH_4)_2S_2O_8$ and NH_4SO_3F.

INTRODUCTION

THERE has been much interest in both theoretical and experimental studies of rotational motions of ions of molecules in gases and liquids. Recent measurements have shown that in certain polycrystalline ammonium salts there exists a high density of low energy levels which are available to inelastically scattered neutrons and that these levels may be associated with a nearly unhindered rotational motion of the ammonium ions.(1) Study of the structure of NH_4PF_6 shows that the 6 fluorine ions are arranged in a very symmetrical way around the ammonium ions so that resulting forces, which hinder any rotational motions of this ion, are expected to be weak. A mixed salt $NH_4K_xI_{1+x}$ was studied to determine if the 2–5 per cent replacement NH_4^+ ions in KI could rotate freely. Nuclear magnetic resonance measurements as a function of temperature for $(NH_4)_2S_2O_8$ predict a low barrier to rotation for the ammonium ions in this molecule.(2) This barrier to rotation appears to have a similar magnitude in NH_4SO_3F as in $(NH_4)_2S_2O_8$.(1) In cases where there are no phase transitions that would affect the rotational freedom and where the rotational barrier does not change much with temperature, the ammonium ion is expected to act more like a molecule trapped in an almost spherical cell (clathrate)(3) where it rotates almost freely, than like a molecule in a one-component solid state where the rotation of the molecule affects and is affected by its neighbors. However, the number of solids where it has been established that molecules can rotate with nearly the same freedom as in the gaseous phase is indeed small.

---

* Work performed under the auspices of the U.S. Atomic Energy Commission.

† Present address: Institute B. Kidric, Beograd, Yugoslavia.

‡ Also at Columbia University, Physics Department.

In the present experiment the differential inelastic cross sections for incident neutrons scattered at 90° from polycrystalline samples of NH_4PF_6, $NH_4K_xI_{1+x}$, $(NH_4)_2S_2O_8$, and NH_4SO_3F have been studied. Measurements were made at $T = 294°K$ for all four samples, at $T = 343°K$ for $(NH_4)_2S_2O_8$ and at $T = 103°K$ for NH_4PF_6. The incident neutrons had an energy of 5×10^{-3} eV which was in all cases small compared to the thermal excitation energy kT. In addition, only those neutrons which had gained energy in a single scattering event in the thin target sample are observed. Thus, the energy gains observed represent transitions from thermally populated levels of the scattering system. Due to the small coherent scattering cross section for hydrogen, and the large total scattering cross section of hydrogen compared to those of the other elements in these compounds, the observed neutron spectra represent almost entirely the independent motions of the scattering units (NH_4^+ ions) in which the hydrogen is bound. Previous total cross section measurements(1) had yielded rough estimates of the rotational barriers of $\sim 0{\cdot}2$ kcal/mole for NH_4PF_6 and $\sim 0{\cdot}7$ kcal/mole for $(NH_4)_2S_2O_8$ and NH_4SO_3F. In addition, measurements of the total cross section as a function of temperature for 8 Å incident neutrons has shown that for NH_4PF_6 and $(NH_4)_2S_2O_8$ there are no phase changes that would modify the hindering potential in the temperature range of 294–90°K.

The shapes of the observed inelastic spectra at each temperature for each compound were compared with the shapes computed on the basis of the KRIEGER–NELKIN approximation of the scattering cross section assuming free rotation of the ammonium ions.(4) The ammonium ion has been assumed to be in the ground state with regard to internal vibrations, and known frequencies for the ammonium ion have been used in the calculations of the vibrational term in the expression for the cross section. At each temperature the observed shapes of the spectra were compared with the computed shapes for a range of effective masses between 1 and 6 proton mass in steps of 0·1 mass units. A comparison was first made to see if the observed shape could be accounted for by any of the calculated shapes with effective masses within this range and then to determine that value of the effective mass which gave the best over-all agreement in shape. The velocity spectrum of neutrons scattered in the Krieger–Nelkin free gas approximation is expected to peak at an energy $E = kT$ corresponding to the most probable velocity: $V_P = \sqrt{(2kT/m)}$. The value of the effective masses obtained by this shape fitting procedure were then compared with those computed on the basis of the BROWN–ST. JOHN type calculation.(5)

THEORY

The quantum mechanical treatment of the energy levels of a molecule with hindered rotational motion has been investigated by PAULING, STERN and others.(6, 7) In general, such motion is described in terms of a potential of the type $V_0 (1-\cos n\Phi)$ where n is an integer and depends upon the rotational symmetry of the rotor. In addition, it is necessary to introduce the moments of inertia of the rotating molecule through its rotational constant $B = \hbar^2/2I$ to completely specify the energy levels of the system. It can then be shown that for such a system excited by the thermal energy kT, when $kT \ll V_0$ the levels approach those of a harmonic oscillator with a level separation $\sqrt{(2V_0B)}$, while for $kT > 2V_0$ the levels approach those of a freely rotating molecule with the rotational constant B. In order to specify the differential cross section for the inelastic scattering of neutrons from such a system in the most general form that could be compared with inelastic neutron scattering data, a calculation of $d^2\sigma/d\Omega dE$ as a function of V_0, B, kT, the effective translational mass, the incident and final neutron energies, and the scattering angle would be needed.

While, at present, no such general formulation is available, Krieger and Nelkin have derived an expression for the differential cross section for neutrons scattered by a gas of non-rigid molecules with rotational freedom. This expression is valid in the limit where $K^2/2M$ is large compared with the rotational level spacing and the energy transfer is not too different from $K^2/2M$. This model includes a Doppler correction to the cross section, and it is assumed that the internal vibrations are in the ground state level. An effective mass M_e is obtained for the "scattering units" by incorporating the SACHS–TELLER mass tensor(8, 9) into the problem using the simplifying approximation of Brown and St. John that $1/M_e$ is the average of the principal values of the reciprocal mass tensor. In addition, there has been derived an improved expression for the Brown–St. John effective mass, which gives better agreement between scattering from a free molecule and scattering from a classical rotor, as obtained by the high energy limit of the quantum mechanical formulation of ZEMACH and GLAUBER.(10) The expression for the differential scattering cross section is:

$$\sigma_T(\theta,\epsilon) = \exp[-\gamma\kappa^2]\sigma_0(\theta,\epsilon)$$

where

$$\sigma_0(\theta,\epsilon) = a^2\left(\frac{k}{k_0}\right)\left(\frac{M}{2\pi T\kappa^2}\right)^{1/2} \times\exp\left[-\frac{M}{2T\kappa^2}\left(\epsilon+\frac{\kappa^2}{2M}\right)^2\right]$$

is the cross section for a monoatomic gas of mass M and temperature T.

k_0 = initial momentum of neutron, $E_0 = \dfrac{k_0^2}{2m}$

k = final momentum of neutrons

$\kappa = (k-k_0)$ = momentum transfer

$\epsilon = (2m)^{-1}(k^2-k_0^2)$ = energy transfer

θ = scattering angle in laboratory system

$$\gamma = \frac{1}{6}\sum_{\lambda}\frac{(c^{(\lambda)^2})}{\omega^{(\lambda)}}$$

where

$c^{(\lambda)}$ is amplitude vector corresponding to the νth nucleus and λth mode

$\omega^{(\lambda)}$ is the angular frequency of the λth mode

EXPERIMENTAL APPARATUS

The present experiment utilized the cold neutron facility at the Brookhaven National Laboratory research reactor, which has been described in the literature.(11) The neutron beam incident on the scatterer is produced by filtration through 8 in. of refrigerated beryllium. No Bragg (elastic) scattering can occur for the low energy ($\simeq 0{\cdot}005$) incident neutrons, and the neutrons which are scattered at 90° by the sample are those which have gained energy or have been elastically scattered by the sample. The energy spectrum of the scattered neutrons was determined by chopper time-of-flight technique.

The polycrystalline samples were contained in an aluminum sample holder which was shielded by cadmium so that neutrons could only be scattered off the samples. The effective thickness of the polycrystalline material was approximately (1–2 mm) so that the probability of multiple scattering was negligible.

RESULTS AND DISCUSSION

The observed spectra are shown in Figs. 1–6 together with the computed shapes for values of the ratio M_e/m_{proton} defined as R, which lie close to the value giving the best fit. The ordinates of these curves are the scattered neutron intensity in arbitrary units. The abscissa is proportional to the neutron times of flight and the corresponding energies are given at the top of each graph. The elastic peak which corresponds to the energy of the incident neutrons appears at 5×10^{-3} eV. The energy gained by a neutron is the energy shown by up-scale minus 5×10^{-3} eV.

Figures 1–6 show that the best over-all agreement with a free rotational spectrum shape is obtained for NH_4PF_6 at $T = 294$°K, $(NH_4)_2S_2O_8$ at $T = 343$°K, and for $NH_4K_xI_{1+x}$ at $T = 294$°K, with values of $R = 2{\cdot}8$, $R = 2{\cdot}0$, proton masses, respectively. In the case of $(NH_4)_2S_2O_8$ as the temperature is lowered from $T = 343$°K ($kT \sim 0{\cdot}7$ kcal/mole) to $T = 294$°K ($kT = 0{\cdot}6$ kcal/mole) a definite departure from a free rotational shape is observed. For NH_4PF_6 a large departure from a rotational shape is also observed as the temperature is lowered to $T = 103$°K ($kT \sim 0{\cdot}2$ kcal/mole). It is important to realize that in no case has perfect agreement, with regard to shape, been obtained between theory and experiment within the over-all statistical accuracy of the data. A departure from the free rotational limit which would be expected when kT is not very large compared to $2V_0$ reflects qualitatively an increase of the types of molecular motions associated with hindered rotations or torsional oscillations. The onset of hindered rotations would be associated with an increase in the effective rotational mass, while the onset of torsional oscillations, which, in general, are associated with lower frequencies than molecular vibrations, would increase the vibrational constant γ. Indeed, if many torsional

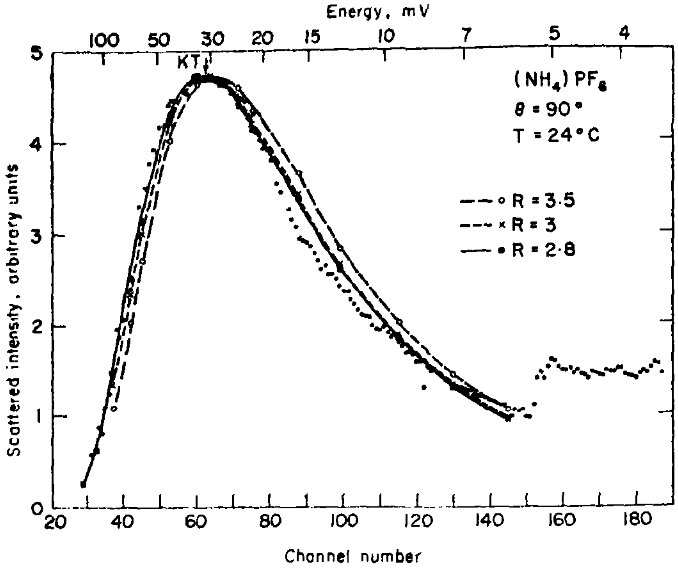

FIG. 1. The time-of-flight spectrum of neutrons scattered at 90° by a 2 mm polycrystalline sample of NH_4PF_6 at room temperature. The edge of the elastic peak occurs approximately at channel 153. The black dots represent the experimental points. The dashed and solid lines represent theoretical curves computed on the basis of the expression for the differential cross section as given by Krieger and Nelkin, with different values of R, ratio of the effective mass to the mass of the proton.

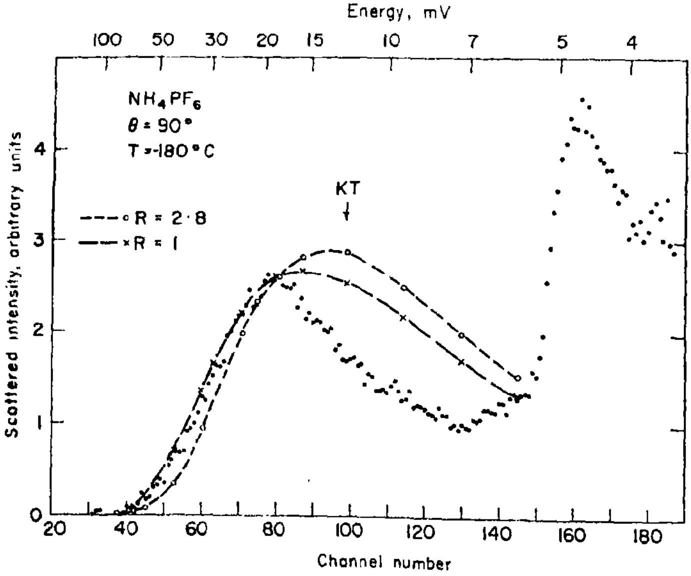

FIG. 2. The polycrystalline sample of NH_4PF_6 is cooled down to −180°C. Theoretical curves are also represented.

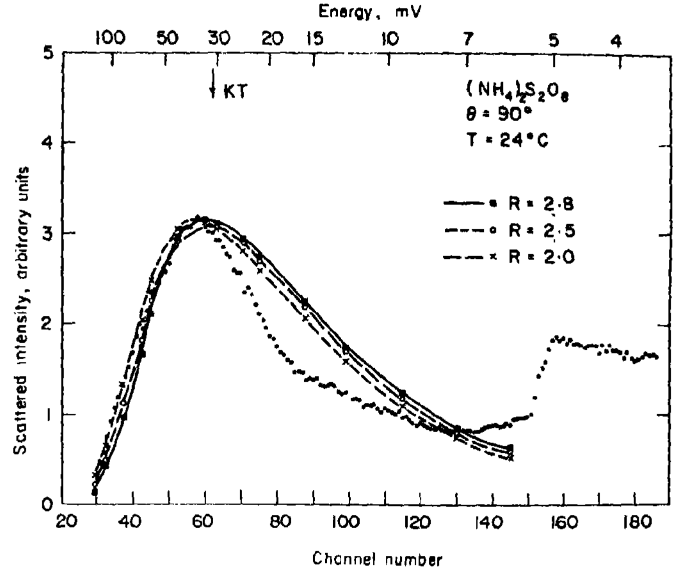

FIG. 3. The time-of-flight spectrum of neutrons scattered at 90° by a 2 mm polycrystalline sample of $(NH_4)_2S_2O_8$ at room temperature. Experimental points (black dots) are compared with calculated curves. There is now a rather large discrepancy in the low energy region of the inelastic peak.

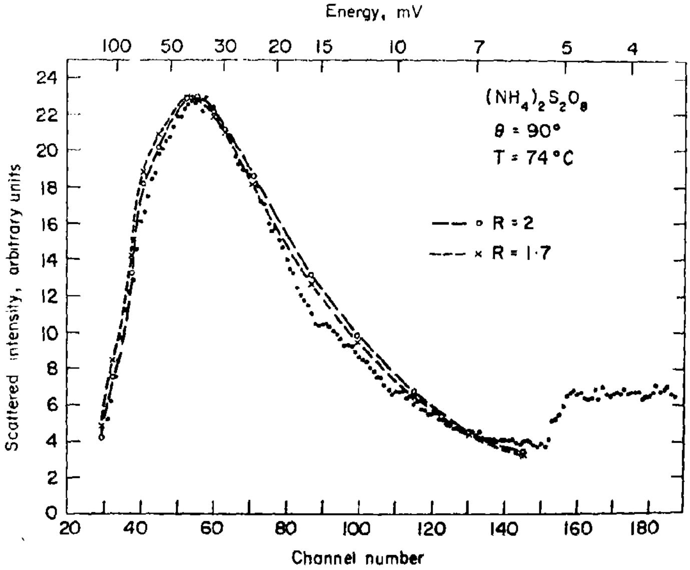

FIG. 4. The same sample of $(NH_4)_2S_2O_8$ is now heated to +74°C. There is a much better agreement between observed and calculated spectra.

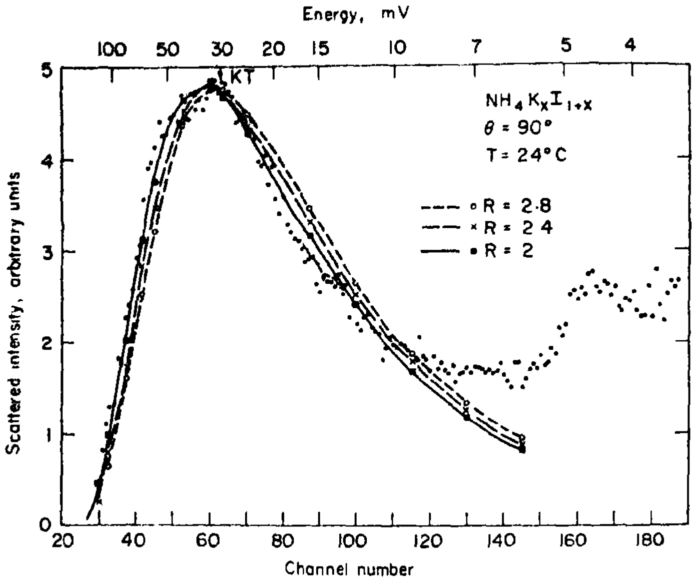

FIG. 5. The time of flight spectrum of neutrons scattered at 90° by a 2 mm polycrystalline sample of NH$_4$K$_x$I$_{1+x}$ containing 2 to 5 per cent ammonium ions. Three theoretical curves have been computed for different values of *R* and compared to the experimental curve (black dots).

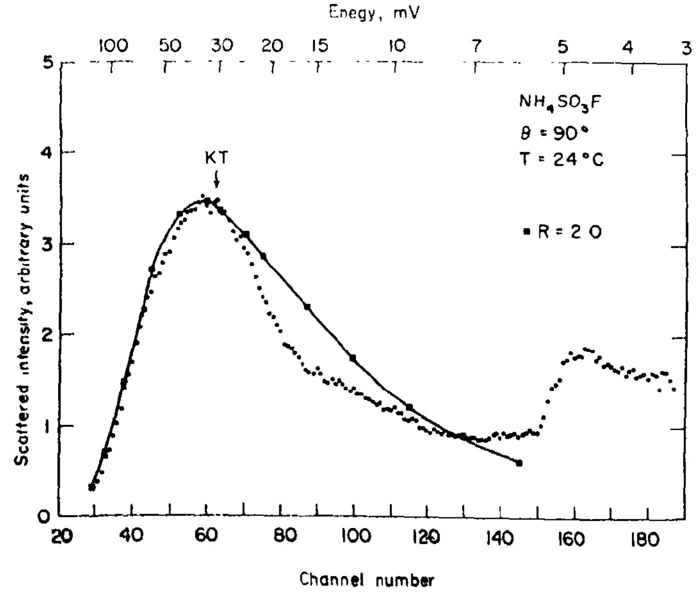

FIG. 6. The time-of-flight spectrum of neutrons scattered at 90° by a 2 mm polycrystalline sample of NH$_4$SO$_3$F at room temperature. There is no agreement between the observed and calculated spectra.

levels are excited (i.e. the torsional oscillator is not in its ground state) or the initial neutron energy is not large compared to the level spacing, the above model is not valid. In the cases where the data most closely approach free rotational curves, it was found that the fitted shape was sensitive to within a few tenths of a proton mass for R. Too large a value of R would make the theoretical curve drop too rapidly above kT and too slowly below kT. The reverse behavior is obtained for a value of R that is too small. In addition, at low temperature where the condition $kT \gg 2V_0$ is certainly no longer satisfied and where the level density for torsional oscillation becomes important, the experimental curve peaks above kT and the low energy side below kT drops rapidly. In view of this behavior, even where reasonable agreement between the Krieger–Nelkin theory and the observed shapes has been obtained, it would be expected that any small residual hindrance would have the effect of yielding a value of R (from a shape comparison as described above) that would be too small. Indeed, it is observed that the three values of R obtained for NH_4PF_6, $(NH_4)_2S_2O_8$ and $NH_4K_xI_{1+x}$ range between 2·0 and 2·8 proton mass units.

In order to compare the values of the effective masses obtained by the above procedure with the effective rotational masses expected for the NH_4^+ ion, values of the effective rotational masses were calculated according to the BROWN–ST. JOHN approximation[5] and the "improved Brown–St. John" approximation. These calculations yield values of $M_{rot} = 4{\cdot}00$ and $4{\cdot}50$ proton masses, respectively. If a total effective mass M_e is calculated by including a translational mass $M_t = 18$ for the ammonium ion, then $1/M_e = 1/M_{rot} + 1/M_t$ and the two resulting values of M_e of 3·27 and 3·48 proton masses are obtained. These values for a total effective mass do appear to be in better agreement with the experimental values of R with range between 2 and 2·8 than do the pure rotational effective mass values of 4·00 and 4·50. However, with incident neutrons of 0·005 eV it is difficult to justify that the ammonium ion is sufficiently weakly bound to have an effective translational mass of 18. This casts doubts in the validity of computed effective masses of 3·27 and 3·48. Two features of this expression should be noted with regard to comparing it with experimental data:

(a) If $E_0 \gg kT$ the cross section will be peaked at the recoil energy $kT^2/2M$ while if $kT \gg E_0$ the cross section will be peaked at $E \sim kT$.

(b) In the case of a molecule or ion in a crystal, it would not be expected that completely free translation could occur as in the case of a gas. However, even though the NH_4^+ ions may not be completely free, it is possible to treat their translational motions under certain conditions as those of a perfect gas of mass 18. If for example, the motion of the molecule or ion as a whole may be described by a shallow potential such that the level spacing was small compared to both E_0 and kT, then a product term is introduced into intermediate scattering function of the type $\langle \chi \rangle = \exp[-K^2/2M(it + Tt^2)]$ with M equal to the mass of the molecule or ion. However, this expression for χ is identical to that expected for neutrons scattered by a perfect gas of molecules which are free to translate. This approximation should only be good for higher energy incident neutrons or for molecules moving in a very shallow potential (harmonic oscillator). In such cases the level separation could be small compared to kT and E_0.

CONCLUSION

The experimental neutron data are very sensitive to the details of the rotational motions of the NH_4^+ ion as is seen from the temperature variations in the scattered spectrum. While the observed peaks for these three salts approach free rotational shapes as kT is increased and peak at kT, in no case has a perfect shape agreement been obtained. In addition, the values of the effective mass obtained by the shape-fitting procedure are not in agreement with the values computed from a Brown–St. John approximation. Indeed, as $\hbar^2/2I = 0{\cdot}0006$ eV for the NH_4^+ ion, the condition that $K^2/2M$ be larger than the level spacing may not be fulfilled and the applicability of the Krieger–Nelkin approximation is in doubt. What is needed, at present, in order to get a better understanding of these spectra is the framework of a theory that would allow one to calculate the neutron kinematics for a system as a function of the degree of rotational freedom. Such a theory would start with a torsional harmonic oscillator, then proceed to the transition region where the ammonium ion oscillates and eventually makes a rotational jump and finally would consider the freely rotating system. Whereas the two limiting cases are now understood under certain conditions, no theory* exists for the transitional region.

---

* NELKIN has pointed out (private communication) that in the spirit of the short collision time approximation some effects from the hindrance of the molecular rotations can be included in a generalized form of the Krieger–Nelkin model. Then the appropriate adjustable parameter is not the effective mass but an effective rotational temperature T' which represents the increased rotational kinetic energy in the presence of a hindering potential. Then the simple formula

$$\sigma_0(\Theta,\epsilon) = a^2 \left(\frac{k}{k_0}\right) \left(\frac{M}{2T'K^2}\right)^{1/2} \times \exp\left[\frac{\epsilon}{T} - \frac{M}{2T'K^2}\left(\epsilon - \frac{K^2}{2M}\right)^2\right]$$

where $\epsilon = (2M)^{-1}(k^2 - k_0^2)$ is assumed positive, T is the actual temperature, and T' is an adjustable effective temperature.

However, this procedure is not expected to give as good a fit as obtained in the present cases above with a reasonable T'. In addition, it is difficult to predict the value of T' expected for these compounds. Therefore, an extensive fit to the present data using this model has not been carried out.

REFERENCES

1. RUSH J. J., SAFFORD G. J., TAYLOR T. I. and HAVENS W. W. Jr., to be published in *J. Nucl. Sci. Eng.*
2. RICHARDS R. E. and SCHABFER T., *Trans. Faraday Soc.* **57**, 210 (1961).
3. STAVELEY L. A., *J. Phys. Chem. Solids* **18**, 46 (1961).
4. KRIEGER T. J. and NELKIN M. S., *The Scattering of Slow Neutrons by Hydrogeneous Moderation.* G. E. C. Rep., August 1 (1955).
5. BROWN H. D. and ST. JOHN A. S. (a) D. P. 33. *Neutron Energy Spectrum in D_2O.* February (1954). (b) BROWN H. D., D. P. 64. *Neutron Energy Spectra in Water.* February (1955).
6. PAULING L., *Phys. Rev.* **36**, 430 (1930).
7. STERN T. E., *Proc. Roy. Soc.* **A130**, 551 (1930).
8. SACHS R. G. anv TELLER E., *Phys. Rev.* **60**, 18 (1941).
9. MESSIAH A. M. L., *Phys. Rev.* **84**, 204 (1951).
10. ZEMACH A. C. and GLAUBER R. J., *Phys. Rev.* **101**, 118, 129 (1956).
11. HUGHES D. J., PALEVSKY H., KLEY W. and TUNKELO E., *Phys. Rev.* **119**, 872 (1960).

J. Phys. Chem. Solids. Pergamon Press 1963. Vol. 24. pp. 625–630. Printed in Great Britain.

THE DIFFERENCE BETWEEN GILBERT'S AND LANDAU-LIFSHITZ'S EQUATIONS

S. IIDA*

Department of Physics, University of Tokyo, Tokyo, Japan

(*Received* 21 *November* 1962)

Abstract—The difference between the Gilbert equation and the Landau–Lifshitz equation is discussed. An interpretation is presented that both equations assume viscous type damping, and the damping action is isotropic in the Gilbert equation, but is strongly anisotropic in the Landau–Lifshitz equation. It seems more reasonable to assume the Gilbert equation physically, if we do not know anything about the detailed mechanism of the damping of a problem.

1. INTRODUCTION

It is well known that there are two basic kinetic equations for the movement of the magnetization of a ferromagnet. These are the Landau–Lifshitz equation,(1) and the Gilbert equation,(2) as shown below.

$$\frac{\mathrm{d}\boldsymbol{M}}{\mathrm{d}t} = -\gamma'(\boldsymbol{M}\times\boldsymbol{H})-\gamma\frac{\boldsymbol{M}}{M}\times\left(\frac{\boldsymbol{M}}{M}\times\boldsymbol{H}\right) \quad (1)$$

$$\frac{\mathrm{d}\boldsymbol{M}}{\mathrm{d}t} = -\gamma(\boldsymbol{M}\times\boldsymbol{H})+\alpha\frac{\boldsymbol{M}}{M}\times\frac{\mathrm{d}\boldsymbol{M}}{\mathrm{d}t} \quad (2)$$

Here, the second term represents the damping of the motion. Although the first term can be derived quantum mechanically, there is no intrinsic general derivation for the second term.

Equation (1) was presented by Landau–Lifshitz(1) and equation (2) was presented by Gilbert.(2,3)† Gilbert thought that equation (2) should be considered a more fundamental equation than equation (1). He emphasized that in a case of eddy-current damping equation (2) is a direct result of Lagrangian analysis. His paper, however, is not well explained and the physical meaning of the two equations was not made clear. Kittel has employed the form of equation (1) in his analysis of the heavy damping phenomena of rare earth iron garnets in ferromagnetic resonance experiments.(4) He mentions the Gilbert form of damping in that paper and concludes that equation (2) cannot describe the heavy damping phenomena intrinsically. His paper, however, does not clearly explain the reason for the intrinsic inadequateness of the Gilbert equation. One of the reasons mentioned is the lack of success of the equation for the description of the experimental results on rare earth iron garnets. This evidence, however, is not conclusive since there are alternative explanations(5) for this experimental result.

Kikuchi(6) has pointed out mathematically that, in the rotational switching phenomena of spherical single domain ferromagnets, the Gilbert equation gives the highest switching speed when α is equal to one, but there is no limit for the speed as a function of γ in Landau–Lifshitz equation. Gyorgy found experimentally(7) that in the range‡ of the switching which follows after the wall displacement range as a function of applied field, the switching coefficient

$$S_\omega = \frac{\mathrm{d}\tau_s}{\mathrm{d}(1/H)} \quad (3)$$

---

* Temporary address, Bell Telephone Laboratories, Murray Hill, New Jersey.

† Suhl and Walker have suggested this equation in *Bell Syst. tech. J.* **33**, 568 (1954).

‡ This region is described by him as a nonuniform rotational range.

of rectangular hysteresis loop ferromagnets, both for thin films and ferrites, is in good agreement with the minimum switching coefficient that can be expected from the Gilbert equation, i.e. with that which is obtained by putting α equal to one. Although, since we have deduced another form of description of this phenomenon,(8) the experimental results of the rotational switching phenomena do not necessarily indicate the intrinsic adequateness of the Gilbert equation, this is another field of interest in which the difference between the two equations may possibly become quite important.

In these connections, we feel that the past interpretations of the two equations are quite uncertain. Here we hope to present our own interpretation.

2. MATHEMATICAL EQUIVALENCE

It is already well known that the two equations are mathematically equivalent when we use the following transfer relations.

$$\gamma' = \frac{\gamma}{1+\alpha^2} \tag{4}$$

$$\lambda = \gamma M \frac{\alpha}{1+\alpha^2} \tag{5}$$

or

$$\gamma = \gamma'\left(1+\frac{\lambda^2}{M^2\gamma'^2}\right) \tag{6}$$

$$\alpha = \frac{\lambda}{M\gamma'}. \tag{7}$$

It is noticed that these are all one-to-one relations. The relation of equations (4) and (5) are shown in Fig. 1. It may be noted that λ has the same value for two different values of α, but γ' does not have this character.

Mathematically, the Landau–Lifshitz equation is more convenient because it has no time derivative on the right-hand side and when we define θ and ϕ as is shown in Fig. 2, it is easily deduced that

$$\frac{d\phi}{dt} = \gamma' H \tag{8}$$

$$\frac{d\theta}{dt} = -\lambda\frac{H}{M}\sin\theta \tag{9}$$

Thus, mathematically, the two principal components of the movement are separately represented by the two constants of the Landau–Lifshitz equation. Therefore this equation seems more convenient as a phenomenological equation of the problem.

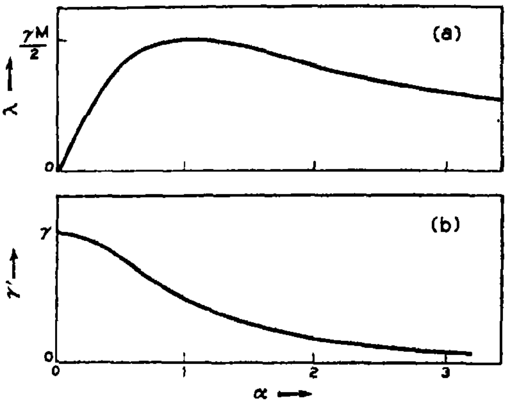

FIG. 1. Constant λ or γ' in the Landau–Lifshitz equation as a function of α of the Gilbert equation.

The corresponding expressions of the Gilbert equation are obtained by transforming γ' and λ in equations (8) and (9) into expressions in terms of γ and α with the aid of equations (4) and (5). The relation between γ' and λ and γ, α is already illustrated in Fig. 1.

Now, the two equations are quite different physically when γ' or γ is regarded as a true gyromagnetic constant

$$\frac{e}{2mc}\cdot g' \tag{10}$$

and the second term is assumed to represent the energy dissipation of the magnetic system to other systems which are discarded in the equation. This is the main subject of the following discussion.

It is, however, also well known that, even in this case, the two equations are practically equivalent when the dissipation of the energy is very small. Mathematically, when

$$\alpha = \frac{\lambda}{M\gamma'} \ll 1 \tag{11}$$

and α^2 can be neglected, equations (4), (5), (6), and (7), become

$$\gamma' = \gamma \tag{12}$$

$$\lambda = \gamma M\alpha \tag{13}$$

so that the two equations become equivalent physically as well. Since, in most cases, equation (11) can be assumed, the difference between the two equations is usually not significant.

of ferromagnets where the magnetic field applied is much smaller than the exchange field. Of course it is possible to have long wavelength spin waves which destroy the constancy of $|M|$ without consuming much exchange energy. In this case, however, only a limitation is required for the size of the region where the equations can be applied to a certain small unit where M can be assumed uniform.

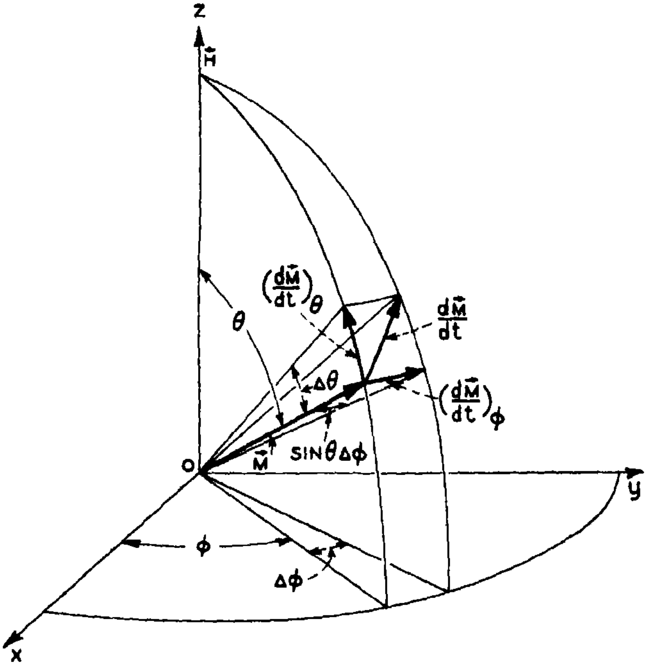

FIG. 2. Definitions of θ, ϕ, $(dM/dt)_\theta$ and $(dM/dt)_\phi$.

3. BASIC ASSUMPTIONS OF THE TWO EQUATIONS

There are several assumptions present as a basis of the two equations.

The first is the constancy of the absolute magnitude of the magnetization, $|M|$. The basis of this assumption is the presence of a strong exchange field between every neighboring unit component of M. Since we know that even if a considerable amount of spin waves is excited, still $|M|$ can be assumed unchanged up to a first order of the amplitudes of spin waves; this assumption is quite reasonable in the usual phenomena

The second assumption is the isotropic nature of the ferromagnet. If an anisotropic nature of the crystal is to be taken into account then γ or γ' and damping constant α or γ must be a function of the direction of M referred to the crystal axes. It is noticed, however, that even under this assumption, the crystal can still be anisotropic because of the presence of the applied field H. This is the case for the Landau-Lifshitz equation as is shown next.

The third and most important assumption that we have concluded is the assumption of the presence of viscous type damping. By viscous damping we mean that the damping force at each instant is only a function of the location and the rate of movement of M at that instant and is a negative linear function of the rate of the movement. In a magnetic system, the magnitude of the direct force operating is implicit in general and this is represented by an equivalent magnetic field. In the GILBERT equation,(2) it is obvious that this damping field is

$$-\frac{\alpha}{\gamma}\frac{1}{M}\frac{\mathrm{d}\boldsymbol{M}}{\mathrm{d}t} \tag{14}$$

and obviously is proportional to and opposes the velocity of the motion, $\mathrm{d}\boldsymbol{M}/\mathrm{d}t$. In the Landau–Lifshitz equation, equation (1) can be transformed into

$$\frac{\mathrm{d}\boldsymbol{M}}{\mathrm{d}t} = -\gamma'(\boldsymbol{M}\times\boldsymbol{H})+\frac{\lambda}{\gamma' M}\frac{\boldsymbol{M}}{M}\times\left(\frac{\mathrm{d}\boldsymbol{M}}{\mathrm{d}t}\right)_{\phi} \tag{15}$$

where $(\mathrm{d}\boldsymbol{M}/\mathrm{d}t)_{\phi}$ is the ϕ component of $\mathrm{d}\boldsymbol{M}/\mathrm{d}t$, as has been shown in Fig. 2. Therefore in this case the damping field is

$$-\frac{\lambda}{\gamma'^2 M^2}\left(\frac{\mathrm{d}\boldsymbol{M}}{\mathrm{d}t}\right)_{\phi} \tag{16}$$

and is always proportional to ϕ, i.e. the precessional component of $\mathrm{d}\boldsymbol{M}/\mathrm{d}t$. This means that a viscous type damping is operating for the movement along ϕ direction but is not operating for the movement along θ direction. Therefore, the Landau–Lifshitz equation represents a motion of the magnetization in an extremely highly anisotropic medium for damping. According to the second assumption, this highly anisotropic damping must be introduced merely from the presence of magnetic field H, since the material itself is assumed to be isotropic.

4. GENERAL EXPRESSION FOR THE TWO EQUATIONS

Based on the discussion of the previous Section, the following general expression is obtained for the dynamical equation of the magnetic system. It is

$$\frac{\mathrm{d}\boldsymbol{M}}{\mathrm{d}t} = -\gamma^{+}(\boldsymbol{M}\times\boldsymbol{H})+\alpha_{\phi}\frac{\boldsymbol{M}}{M}\times\left(\frac{\mathrm{d}\boldsymbol{M}}{\mathrm{d}t}\right)_{\phi} +\alpha_{\theta}\frac{\boldsymbol{M}}{M}\times\left(\frac{\mathrm{d}\boldsymbol{M}}{\mathrm{d}t}\right)_{\theta} \tag*{(17)*}$$

Here the second term represents the viscous type damping for the ϕ component and the third term that for the θ component. If we put

$$\alpha_{\phi} = \alpha_{\theta} = \alpha. \tag{18}$$

Equation (17) coincides with the Gilbert equation and if we put

$$\alpha_{\theta} = 0$$
$$\alpha_{\phi} = \frac{\lambda}{\gamma^{+}M}. \tag{19}$$

Equation (17) coincides with the Landau–Lifshitz equation. As is the case of the Gilbert equation, equation (17) again can be reduced to a Landau–Lifshitz form mathematically as

$$\frac{\mathrm{d}\boldsymbol{M}}{\mathrm{d}t} = -\frac{\gamma^{+}}{1+\alpha_{\theta}\alpha_{\phi}}(\boldsymbol{M}\times\boldsymbol{H}) -\frac{M\alpha_{\phi}\gamma^{+}}{1+\alpha_{\theta}\alpha_{\phi}}\left[\frac{\boldsymbol{M}}{M}\times\left(\frac{\boldsymbol{M}}{M}\times\boldsymbol{H}\right)\right] \tag{20}$$

Therefore

$$\gamma' = \frac{\gamma^{+}}{1+\alpha_{\theta}\alpha_{\phi}} \tag{21}$$

$$\lambda = \frac{\gamma^{+}M\alpha_{\phi}}{1+\alpha_{\theta}\alpha_{\phi}}. \tag{22}$$

It is noticed that in the other extreme case where

$$\alpha_{\phi} = 0 \tag{23}$$

Equation (20) reduces to the original Zeeman term only. The damping is inactive in this case.

---

[*] An equation with combined damping terms:

$$\frac{\mathrm{d}\boldsymbol{M}}{\mathrm{d}t} = -\gamma(\boldsymbol{M}\times\boldsymbol{H})+\frac{\boldsymbol{M}}{M}\times\left(\frac{\mathrm{d}\boldsymbol{M}}{\mathrm{d}t}\right)-\lambda\frac{\boldsymbol{M}}{M}\times\left(\frac{\boldsymbol{M}}{M}\times\boldsymbol{H}\right)$$

was suggested by L. R. WALKER in private discussion.

5. DISCUSSION

As is shown, the Landau–Lifshitz equation describes one of the extreme cases in which no resistance is present for the movement of magnetization along θ direction. This is so unusual that we feel that the Gilbert equation that assumes isotropic damping is the more normal expression which should be taken as a zero order approximation, so far as we know nothing about the detailed mechanism of the damping. The Landau–Lifshitz equation can then regarded as a simplified form of the Gilbert equation which is derived mathematically by eliminating the time derivative term in the right-hand side of the Gilbert equation, and employing the meaning of the constants γ' and λ as given in equations (4) and (5). In this connection it is interesting to illustrate the vector relations of the two equations on a plane which is normal to M. They are shown in Figs. 3(a) and (b). In the Landau–Lifshitz equation, the damping torque

$$-\lambda\frac{M}{M}\times\left(\frac{M}{M}\times H\right) \tag{24}$$

always operates at a right angle to the driving torque

$$-\gamma'(M\times H) \tag{25}$$

The actual movement, therefore, of the magnetization dM/dt is always larger than the driving and damping torques. Further, this equation allows the possibility that the damping torque can become even larger than the driving torque when

$$\lambda > \gamma' M \sim 10^{10}\,\mathrm{sec}^{-1} \tag{26}$$

Since, in this magnetic system, movement is always a result of the presence of a certain torque and the presence of a damping torque is a result of the presence of a driving torque, the fact mentioned seems quite unusual. It is noticed, however, that this is not illogical since this torque does not do any more work than that which is allowed by the energy conservation law. Obviously this unusual situation is a result of the mentioned extreme condition implied for damping.

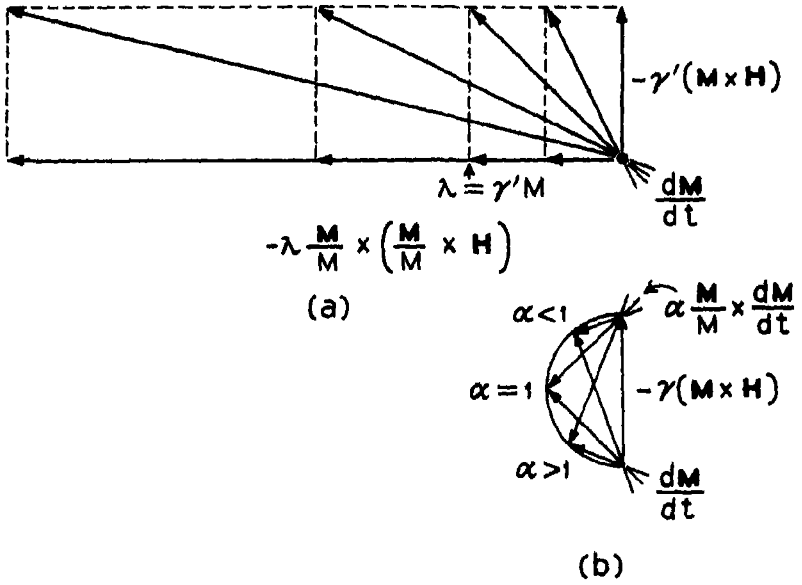

FIG. 3. Vector relations in the Landau–Lifshitz and the Gilbert equations, illustrated on the normal plane to the magnetization M.

In Fig.2(b), it is shown that the damping torque

$$\alpha\frac{M}{M}\times\frac{dM}{dt} \tag{27}$$

of the Gilbert equation is always at right angles to the movement of magnetization $\mathrm{d}\boldsymbol{M}/\mathrm{d}t$ and less than the driving torque

$$-\gamma(\boldsymbol{M}\times\boldsymbol{H}) \tag{28}$$

As a result, the movement of magnetization $\mathrm{d}\boldsymbol{M}/\mathrm{d}t$ is always less than the driving torque $-\gamma(\boldsymbol{M}\times\boldsymbol{H})$. This is quite normal.

In the case of rotational switching of a spherical single domain ferromagnet, the employment of the Gilbert equation gives an essential limitation for the speed as a function of damping constant α, as is discussed by Kikuchi, Gyorgy *et al.* and is shown here in equations (9) and (5). We feel this is a correct conclusion for normal ferromagnets. It is emphasized, however, that if we could find a material which has a quite anisotropic damping mechanism in which α_θ is quite small and α_ϕ is quite large, then equations (9) and (22) say that this material can exhibit a very high speed switching without limitation. This theoretical standpoint seems somewhat analogous to the case of the ferroxplana problem. It is, however, noticed again that this theory can be applicable only in the case of ideal spherical single domain ferromagnets and not the cases of the switching of polycrystalline ferrites or thin films.[8]

The assumption of viscous type damping is not a unique mechanism of damping. We are familiar with frictional type damping in classical dynamics, and also nonlinear damping effects in fluid dynamics. In the case of damping by spin-wave generation, we know also that many nonlinear effects are introduced by the mutual interactions of spin waves and the uniform mode. Therefore, the applicability of equation (17) depends always on whether in the physical situation of the problem viscous type damping can be assumed or not. It is noted that so far as a linear relation can be assumed between the damping field and the velocity of the movement of the magnetization, the equation can be reduced always to a Landau–Lifshitz form. (This is equivalent to regarding α_ϕ and α_θ in equation (17) as tensors which operate on $(\mathrm{d}\boldsymbol{M}/\mathrm{d}t)_\phi$ or $(\mathrm{d}\boldsymbol{M}/\mathrm{d}t)_\theta$.)

As mentioned in Section 2, the difference of the two equations can be appreciable only in the case where the damping term is quite larg We feel so far that there is no experimental evidence that can differentiate between the two equations clearly, except the case of eddy-current damping of Gilbert. In this connection the experiment of magnetic damping of rare earth garnets seems quite interesting. But in this case again, if we made the experiment on single crystals, the anisotropies of γ, α_θ and α_ϕ referred to the crystal axes and to the direction of the applied field, may be found to be significant. We feel, therefore, that the main purpose of this paper is to make clear the physical situation of the two equations. Practical application of this paper should be made carefully, taking into account many additional factors.

Acknowledgement—The author expresses his sincere appreciation to Dr. L. R. Walker for his valuable discussion of the problem.

REFERENCES

1. Landau L. and Lifshitz E., *Phys. Z. Sowjetunion* **8**, 153 (1935).
2. Gilbert T. L., *Phys. Rev.* **100**, 1243 (1955).
3. Gilbert T. L. and Kelly J. M., *Proceedings of the Pittsburgh Conference on Magnetism and Magnetic Materials*, 1955. AIEE Special Publication T-78, p. 253.
4. Kittel C., *Phys. Rev.* **115**, 1587 (1959).
5. Smit J. and Kasuya T., private communications.
6. Kikuchi R. *J. appl. Phys.* **27**, 1345 (1956).
7. Gyorgy E. M., *J. appl. Phys.* **31**, 110 S (1960).
8. Iida S., to be reported shortly.

J. Phys. Chem. Solids Pergamon Press 1963. Vol. 24, pp. 631–640. Printed in Great Britain.

LAWS OF PHASE TRANSFORMATION IN A SERIES OF NORMAL PARAFFINS

YU. V. MNYUKH
Institute of Organo-Element Compounds, Academy of Sciences, Moscow, U.S.S.R.

(*Received* 16 *October* 1962)

Abstract—The crystal lattice energy of n-paraffins (n-C_nH_{2n+2}) is represented as

$$U = \epsilon \cdot n + \Delta$$

where $\epsilon \cdot n$ is the energy of molecular side-packing and Δ is the end-group packing energy independent of n. By analyzing molecular packing of n-paraffin crystalline modifications R, T and M_R it was found that $\Delta_T < \Delta_{M_R} < \Delta_R$ but $\epsilon_T > \epsilon_R$. A qualitative interpretation of polymorphism and melting laws in the n-paraffin series is based on these relations. The calculations of the crystal lattice energy at 0°K and free enthalpy at 200°K given for the C_9 to C_{18} n-paraffins are in full accord with the previous conclusions and, as a matter of fact, substantiate thermodynamically, by way of n-paraffins, the molecular close packing principle in organic crystals.

1. INTRODUCTION

CRYSTAL structure studies on n-paraffins started in the twenties of this century with the excellent works by Müller. Many studies on n-paraffins that followed were stimulated by the desire to investigate the cause of polymorphism evinced by this significant class of substances. At that time, however, the basic principles of molecular crystal packing were still not duly recognized and, in addition, the information available on n-paraffins structure was not adequate.

The homologous series of n-paraffins

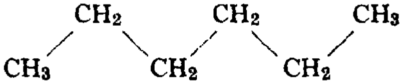

represents interesting material for phase-transition law analysis. The n-paraffins permit consideration of polymorphism as a function of both temperature and the n number of C atoms in a molecular chain. This approach applies equally to melting points because they are related logically to the solid-phase structure.

The phase transition pattern for the n-C_8 to n-C_{36} paraffins (dealt with here) is shown by plots in Fig. 1(a).* Some of its features are demonstrated by the diagram (Fig. 1b) which specifies crystalline modifications for each individual n-paraffin. A detailed examination of the n-paraffin structure based on the theory of chain molecule close-packing developed by KITAIGORODSKII is given in Refs 2 and 3. The literature on the topic mentioned is listed in Ref. 3.

Although some features of the transition pattern of n-paraffins have been discussed previously(2, 3) they will be repeated here for completeness.

2. CRYSTAL STRUCTURE

The shape of n-paraffin molecules in any crystals is similar. The C-atoms of the CH_2 groups lie in one plane to form a zigzag about the axis that passes along the molecule. The C–C bond is 1·54 Å long and the C–C–C angles are 112°. Thus, the length of a chain molecule depends on n, the distance between the centres of CH_3 end-groups being $(n-1) \cdot 1{\cdot}27$ Å). However, the molecules with n_{even} differ from those with n_{odd}, a difference which is conditioned by their symmetry; the topic will be discussed below.

Packing of long-chain molecules in crystals is in complete accord with the general rules of organic chemical crystallography(2) but has a specific character of its own. Since this topic has been examined in detail in Refs. 2 and 3, here we shall only briefly mention its characteristic features.

---

* The graph was compiled by SCHAERER *et al.*(1) on the basis of literature data and their own refinements.

The crystal lattice formed by individual n-paraffins consists of layers stacked on one another. All molecules in the crystal have their long axes parallel and directed along the normal to the layer plane (rectangular layer) or at a small angle with the normal (oblique layer). Thus, the thickness of a molecular layer, limited by two planes drawn mentally through CH_3 end-groups, depends on the molecular chain length of a particular n-paraffin, that is on n.

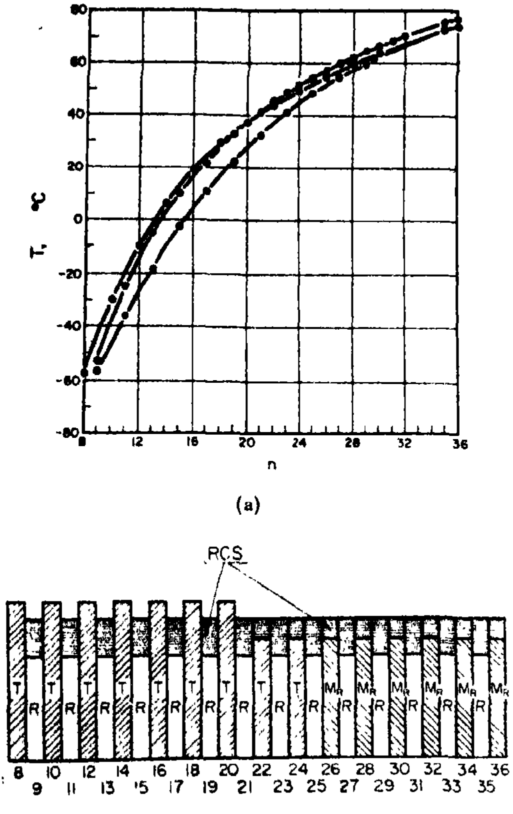

(a)

(b)

FIG. 1. (a) Melting points and phase transition from crystalline state to RCS vs. n number of C atoms in n-paraffin molecule. (The graph was compiled by SCHAERER *et al.*[1] and summarizes all reliable informations on n-paraffins.) (b) Diagram illustrating crystalline modifications of n-paraffins and the main features of (a). Diagram reflects the even–odd alternations of structural forms and phase transition temperatures.

Accordingly, the molecular side-packing (packing in a layer) and the end-group packing (layer stacking) should be distinguished. The mode of side-packing in a layer is specified by a sub-cell (Fig. 2). Sub-cell and layer stacking mode knowledge represents the entire information on crystal structure.

The n-paraffins can form four crystalline modifications (Fig. 2): triclinic T (T-subcell, oblique layers), orthorhombic R (R-subcell, rectangular layers) monoclinic M_R (R-subcell, oblique layers) and hexagonal (rotational-crystalline state,[*] rectangular layers).

3. MOLECULAR PACKING DENSITY

Let us compare molecular packing density in the case of the low-temperature crystalline modifications T, R, M_R. The density of layer stacking and that of molecular packing in a layer will be considered separately.

From the point of view of molecular close-packing theory (see Ref. 2); arbitrary displacement of layers when stacked on one another is always more advantageous (i.e. denser) than the displacement which maintains monoclinic and, all the more, orthorhombic symmetry. This is caused by the restrictions which crystal symmetry imposes on the displacement of layers relative to each other. That is why the layer stacking in triclinic (T) structure of n-paraffins, where layer mutual displacement is set only by their maximum stacking-density condition,[†] is closer than M_R. In turn, the molecular layer stacking in monoclinic (M_R) structure is denser as compared with R.

Molecular packing density in a sub-cell is determined by S, the cross section area per molecule perpendicular to the chain. It was found (Ref. 3) that for the R-sub-cell (based on n-C_{30}) and the T-sub-cell (based on n-C_{18}) this area is equal to $S_R = 18{\cdot}5_6$ Å^2 and $S_T = 18{\cdot}7_3$ Å^2, respectively. Thus, in this case $S_T > S_R$, but not more than about 1 per cent. This inequality is supposed to be common for all n-paraffins. For example, it is known that polyethylene exists both in R and T modifications (Refs. 4 and 5) but the latter is unstable. It may be supposed that this is caused by the lower density

---

[*] See below.

[†] Thermal vibration factor is discussed in Section 7, where its role is shown to be negligible.

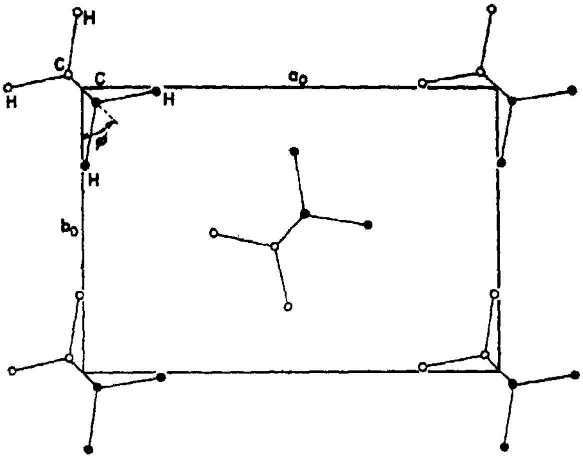

(a)

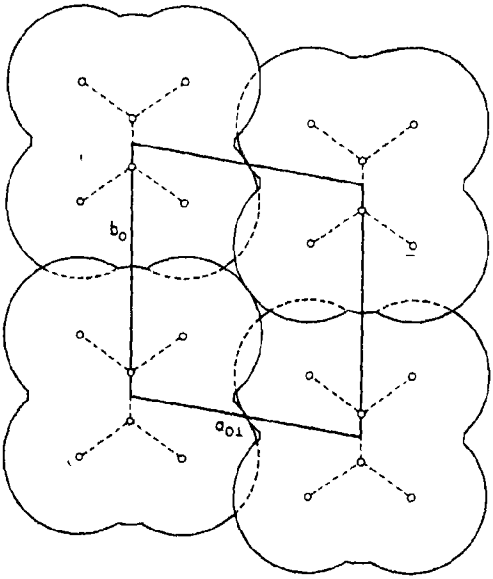

(b)

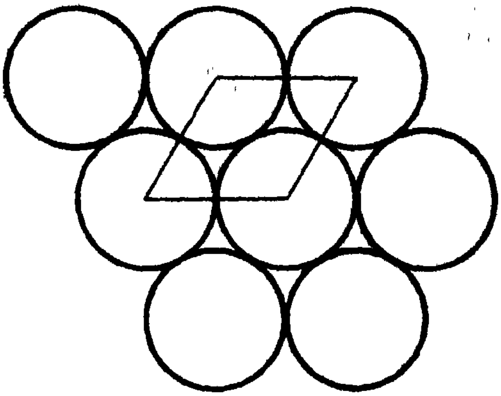

(c)

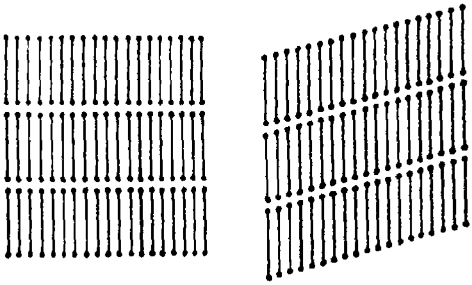

(d) (e)

FIG. 2. Structures of different modifications of *n*-paraffins.

1. Molecular packing inside the layer (cross-section being perpendicular to chains).

(a) Subcell in *R* and M_R structures.

Parameters: $a_0 = 7{\cdot}45$ Å
$b_0 = 4{\cdot}95$ Å
$c_0 = 2{\cdot}54$ Å
$\phi = 41°$

(b) Subcell in *T* structure. Contains two CH_2 groups.

Parameters: $a_0 = 4{\cdot}3$ Å $\alpha_0 = 90°$
$b_0 = 4{\cdot}8$ Å $\beta_0 = 107{\cdot}5°$
$c_0 = 2{\cdot}54$ Å $\gamma_0 = 107°$

$a_{0\perp}$ is projection of a_0 on plane.

(c) Subcell in rotational-crystalline state (RCS).

2. Layer stacking scheme.

(d) rectangular layers (*R*, RCS)

(e) oblique layers (*T*, M_R).

of triclinic side-packing of the molecular chains. It was also established that when adding some impurities, such as adjacent series members, to the individual *n*-paraffins having a *T* structure, the latter transforms to an *R* one. We shall see below, that at $S_T > S_R$, this fact can be easily explained (see footnote, page 637).

The rotational-crystalline structure of *n*-paraffins is a hexagonal packing of cylinders with rectangular layers. RCS* is a special mesomorphic state of a substance. The chainlike molecules in such a state rotate about their longitudinal axes. The packing density in this structure is lower than in those considered above, due to the fact that additional space is needed for the thermal molecular rotation ($S_{RCS} = 19{\cdot}7$ Å^2, compared with S_T and S_R; layer stacking in RCS is also less close). This density loss is associated with substantial increase in the internal energy. However, entropy advantage caused by rotational freedom appears to be sufficient to ensure RCS stability within some temperature range, limited from above by the melting point.

The crystal lattice energy of *n*-paraffins is the sum of the CH_2 group side-packing energy in a layer and the CH_3 end-group packing energy of layer stacking. It is very fruitful for our consideration to represent it as $U = \epsilon \cdot n + \Delta$, where U is energy per molecule, ϵ is side-packing energy related to one C-atom and Δ is interlayer packing energy of molecular end-groups:

$$\begin{aligned} U_T &= \epsilon_T \cdot n + \Delta_T \\ U_R &= \epsilon_R \cdot n + \Delta_R \qquad (1) \\ U_{M_R} &= \epsilon_R \cdot n + \Delta_{M_R} \end{aligned}$$

In accordance with the basic concept of organic chemical crystallography (Ref. 2) that high molecular packing density ensures lower lattice energy, and, taking into account the above information concerning packing density of different crystalline modifications of *n*-paraffins we can write:

$$\Delta_T < \Delta_{M_R} < \Delta_R \qquad (2)$$

and

$$\epsilon_T > \epsilon_R \qquad (3)$$

Equations (1) and inequalities (2) and (3) contain everything required for the qualitative explanation of reasons for, and peculiarities of, the phase behaviour of *n*-paraffins. That these relations are correct will be confirmed below by their full agreement with all reliable experimental data available.

4. EVEN-ODD ALTERNATION OF STRUCTURAL MODIFICATIONS

Figure 1(b) expresses the factual alternation as a function of *n*-even or odd of the T and R (for n = 8–25) and M_R and R (for n = 25–36) structural modifications. In this Section we shall try to answer the following questions: (1) What are the reasons for the phenomenon mentioned? (2) Why do all *n*-paraffins with n_{odd} crystallize in the R form but those with n_{even} in T and M_R forms? (3) What is the reason for T to M_R transition when the *n*-paraffin molecular chain with $n = n_{even}$ becomes longer? (4) Why do *n*-paraffins with n = 21–36 have no RCS alternation?

Despite the crystal structures of all *n*-paraffins being analogous, the series members with n_e and n_0 have a difference, which results in an alternation of some properties. It has already been noted, that the difference lies in the dissimilarity of the molecular symmetry: even molecules have $2/m$-symmetry while odd ones have $m \cdot m$ (Fig. 3a, b). Organic chemical crystallography states (see Ref. 2, pp. 89 and 191), that the former retain their inversion centre in the crystal while the latter retain one reflection plane, namely the plane which coincides with the layer plane ($m_{\parallel}$ in Fig. 3b). This means that the layers of odd *n*-paraffins can only be rectangular. The retention of the inversion centre in the crystal of even *n*-paraffin molecules is compatible with producing both rectangular

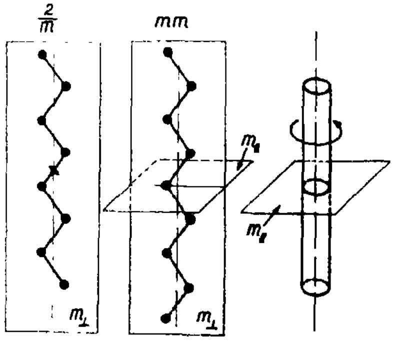

a. $n = n_e$ b $n = n_0$ c. RCS

Fig. 3. Symmetry of *n*-paraffin molecules.

---

* Abbreviation for rotational-crystalline structure or state of substance.

and oblique layers. The experimental data are in perfect agreement with these conclusions, namely, all odd members of the homologous series, without exception, have the rectangular layer structure (R), while even ones have the oblique layer structure (T and M_R).

With regard to the high-temperature RCS, the case is somewhat different. Everything mentioned about molecular symmetry dependence on n odd or even has nothing to do with the RCS, since axial rotation of the molecules in this state provides for them, independently of n, statistical mean cylindrical symmetry. The formation of rectangular layers is caused by the mirror symmetry $m_\parallel$ (Fig. 3c) of these molecules. Hence, it is not difficult to understand why RCS is formed both by odd and even n-paraffins. In particular, this symmetry is inherent in all members of the series beginning from n-C_{21}.

It is thus clear why odd members of the n-paraffin series have the R-type structure: it is the only one of the three (R, T and M_R) that has the $m_\parallel$ mirror symmetry of the molecular layer. It is also clear why there may be no even–odd alternation in relation to RCS. But the following problem still remains: why do even n-paraffins with shorter chains crystallize in the T-form and with longer chains-in the M_R form. The relations (1), (2) and (3) answer this question.

First of all, as follows directly from these relations, $U_{M_R} < U_R$. Alternatively, the fact that even n-paraffins with shorter chain crystallize in the T-form enables one to conclude that $U_T < U_{M_R}$ and, therefore, $U_T < U_{M_R} < U_R$. The relation $U_T < U_R$ will be proved in Section 7 independently.

Comparison between energies such as U_T with U_{M_R} and U_T with U_R based on one carbon atom

$$\frac{U_{M_R}-U_T}{n_e} = \underbrace{\frac{\Delta_{M_R}-\Delta_T}{n_e}}_{\substack{\vee\\0}} - \underbrace{(\epsilon_T-\epsilon_R)}_{\substack{\vee\\0}}$$

$$\frac{U_R-U_T}{n_e} = \underbrace{\frac{\Delta_R-\Delta_T}{n_e}}_{\substack{\vee\\0}} - \underbrace{(\epsilon_T-\epsilon_R)}_{\substack{\vee\\0}} \tag{4}$$

shows that the advantage of the molecular T-packing is explained by energy gain specific for the triclinic mode of molecular layer packing. These advantages gradually diminish as n_e increases, and by

$$n_e = \frac{\Delta_{M_R}-\Delta_T}{\epsilon_T-\epsilon_R}$$

a situation when $U_T = U_{M_R}$ arises. The experimental data (Fig. 1) show that this value is $24 < n < 26$. The reason for the T to M_R but-not-to-R transition is quite obvious. It should be noted, that as $\Delta_R > \Delta_{M_R}$, the $T \to R$ transition would have occurred by

$$n_e = \frac{\Delta_R-\Delta_T}{\epsilon_T-\epsilon_R} > 26 \tag{5}$$

Summing up all mentioned above concerning alternation of structure modifications one may say that it is caused by closer molecular packing (which ensures lower lattice energy) specific for even members of the series, whilst in the case of odd members this packing is prohibited by the rules of symmetry.

5. MELTING POINT AS A FUNCTION OF n

In this Section we shall consider the common features of the $T_{\text{melt}}(n)$ curve, and in the following Section we shall investigate the causes for the presence or absence of the even–odd alternation effects of melting points near the general curve $T_{\text{melt}}(n)$.

TIMMERMANS(6) was the first who stated that the m.p. curve of n-paraffins gradually approaches the polyethylene melting point as n increases. It should be noted, that the law of n-paraffin melting point dependence on n is in approximate accord with crystallographic density change. As shown above, all n-paraffin crystal structures are, in general outline, of one type, namely, they consist of layers whose thickness depends on n. As n increases the structure density increases too because of the decrease in the number of interlayer distances.

The volume per molecule may be represented as $V_{\text{mol}} = A \cdot n + B$, where A is the volume per C atom of the molecular side-packing and B is the interlayer volume per molecule. Therefore, the density is approximately proportional to $n/(An+B)$.

In general, $T_{melt}(n)$ changes follow about the same law. Such correlation between melting point and crystallographic density inside one series of the same type structures seems to be natural. According to LINDEMANN,(7) the melting point can be represented as bond breaking as a result of increasing the amplitude of particle fluctuations. As the density increases (which might be envisaged as the result of successive replacement of weak van der Waals' bonds by strong chemical ones (see Fig. 4), atomic vibrations become more difficult as they require more "cooperativeness".

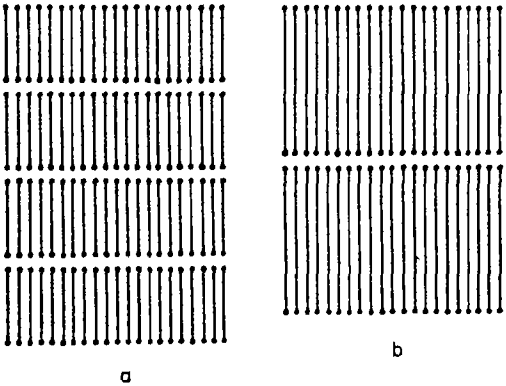

FIG. 4. Increase in molecular layer thickness (in this case from (a) to (b) two times) may be represented as replacement of a part of weak van der Waals' bonds by strong chemical ones. Structure density and "stiffness" increase. Atomic and molecular oscillations become more difficult because of their being more "cooperative". This results in melting point increase. Upper limit is the case of displacement of all intermolecular contacts by chemical bonds—that is, polyethylene case.

Our discussion is, undoubtedly, over-simplified but it helps us to understand, at least to a first approximation, the T_m dependence on n and the tendency of this melting point to the fixed limit, namely the polyethylene m.p., as molecular packing tends to its fixed limit, namely polyethylene packing.

6. EVEN-ODD ALTERNATION OF PHASE TRANSITION TEMPERATURES

The data given in Fig. 1 for the analysis of n-paraffin phase transitions has yet to be exploited to the full. A variety of data so far remained outside the scope of our examination, such as:

(1) Substances with n_{even} from 8 to 20 do not form a rotational-crystalline phase whilst all the other series members do.

(2) Substances with n = 8–20 show melting point alternation, the m.p. of even homologues being higher.

(3) There is no such alternation for n = 20–36 but, instead, here we see transition point alternation from solid state to RCS; the M_R–RCS transition points being higher than R–RCS ones.

To predict the melting point of the crystal, it is necessary to know the free energy of both crystalline and liquid phases. Such calculations are practically impossible. However, it will be possible to give a qualitative explanation of the m.p. alternation (as a function of n being even or odd) about the average curve $T_{melt}(n)$, discussed in the previous Section, when if we turn our attention to the following two facts:

(a) crystals with lower lattice energy melt at higher temperatures and

(b) isomorphic structures have their melting points (as well as lattice energies) falling on a smooth curve. (By the way, this allows a conclusion to be drawn that the free energy of the liquid phase in the n-paraffin series is a monotonic and, apparently, weak function of n.)

Alternation effects are absent not only in the liquid phase but already in RCS. As noted above, all structures in RCS, independently of n being even or odd, may be considered isomorphic; and this permits even, as well as odd molecules to form a rotational-crystalline phase. For the same reason, n-paraffins with n = 20–36 have no even–odd alternations of melting points (See Fig. 1). Now it is not difficult to understand why n-paraffins with n = 8–20 have even–odd alternation of melting points whilst members of the series with n_{even} = 8–20 have no rotational-crystalline phase. Indeed, the RCS melting curve is a lower melting limit for any n-paraffins. It is quite evident, that if the crystal lattice of any n-paraffin appears to be stable up to a higher temperature than that determined by the RCS melting curve, such an n-paraffin is incapable of forming RCS. The latter concerns triclinic crystals, such as n-C_8, n-C_{10}, n-C_{12}, n-C_{14}, n-C_{16} and n-C_{18} whose melting points (due to the low value of the crystal lattice energy, see Sections 4 and 7) fall above the RCS melting curve.

The equations (4) show that the T-lattice energy advantage must gradually disappear with n increasing. Experimentally this is revealed by their melting points as the melting curves of even and odd n-paraffins become closer to each other. To the right of their crossing point, two T-paraffins (n-C_{22} and n-C_{24}) are already found to give polymorphic transition to RCS and their m.p.s are on the RCS melting curve. In this connection, it is of interest to draw attention to the problem of previous discussions related to presence or absence of polymorphism of n-C_{16}, n-C_{18} and n-C_{20}. The fact is that the melting points of these substances, thoroughly purified from adjacent homologue impurities, fall near to the RCS melting curve but somewhat above it. Hence, they give no transition to RCS. But even small quantities of the impurities present decrease the melting point of these substances.* Therefore they show a small range of rotational-crystalline phase, and their melting points fall on the over-all RCS melting curve. The mistake of those authors who found n-C_{16}, n-C_{18}, and n-C_{20} to have polymorphism arose from experimental difficulties of separation of individual n-paraffins.

In conclusion we shall briefly consider the even–odd alternation of transition temperatures to RCS for n-paraffins with $n = 20$–36. It is caused by alternation of the low-temperature forms: odd series members have R structure while even ones have $T(n = 22$ and $24)$ or $M_R \times (n_e = 26$–$36)$ structure. Comparison of the lattice energy

$$U_R - U_{M_R} = (\epsilon_R \cdot n + \Delta_R) - (\epsilon_R \cdot n + \Delta_{M_R})$$
$$= \Delta_R - \Delta_{M_R} > 0$$

shows that $U_{M_R} < U_R$, therefore, the $M_R \rightarrow$ RCS transition temperatures exceed that of $R \rightarrow$ RCS. As n increases, the relative contribution of Δ_R and Δ_{M_R} to the lattice energy decreases. Therefore, we find in Fig. 1(a) gradual attenuation of the transition point alternation.

7. THERMODYNAMIC CALCULATIONS OF CRYSTAL LATTICE ENERGY OF C_9–C_{16} n-PARAFFINS

The crystal lattice energy of n-paraffins was calculated as the heat of its sublimation at 0°K. This energy characterizes van der Waals' (intermolecular) molecular interaction in the lattice (at 0°K) and it is obviously closely related to the mode and density of their packing.

The scheme of thermodynamic cycle (See Table 1) is that used by Billmeyer[(8)] in calculating the lattice energy of polyethylene. But unlike that author, who averaged all available reliable data for n-paraffin heats to find the corresponding increments in heat content per CH_2 group, we made calculations for each n-paraffin separately and were interested in the differences between their lattice energies.

To elucidate the effect of thermal vibrations on phase behaviour of n-paraffins, free enthalpy was also calculated as

$$\phi(T) = \int_0^T C_p \, dT - T \int_0^T \frac{C_p \, dT}{T} \tag{6}$$

up to two limits—that is 150 and 200°K. The initial experimental data for our calculations we took from Refs. 8 and 9. All the results are summarized in Table 2 and also given in Fig. 5. The analysis of these results allows us to draw the following conclusions:

1. Linear dependence of the lattice energy on n, assumed in the expressions (1), is fulfilled very well:

$$\begin{aligned} U_T &= \epsilon_T \cdot n + \Delta_T \\ U_R &= \epsilon_R \cdot n + \Delta_R \end{aligned} \tag{7}$$

The energy increments ϵ and Δ evince in Fig. 5 the following geometrical meaning: ϵ ($= \operatorname{tg} \alpha$) is a slope of corresponding straight line and Δ is a segment on the U-axis when extrapolating to $n = 0$.

---

* This is a general rule. As to n-paraffins, the entrance into their lattice of molecules with other chain lengths first of all resulted in a decrease of the layer stacking density. As regards to the T-lattice, this influence is particularly strong, since its low energy depends on high density of molecular layer stacking. If the quantity of impurities exceeds a certain percentage, T-packing does not occur at all, and R-structure is formed below the temperature range of RCS existence. The R-structure offers the advantage of somewhat higher density of molecular packing inside a layer.

Table 1. *Thermodynamic cycle for calculations of the sublimation energy of n-paraffins at* 0°K

No.	Thermodynamic process	Thermal effect kcal/mole	Notes
1	2	3	4
1	Crystal (0°K) → crystal (T_m°K) + liquid (T_m °K → liquid (298°K)	$-\left\{\int_0^{T_m} C_p\,dT + \int_{T_m}^{298} C_p\,dT\right\}$	a
2	Crystal (T_m°K) → liquid (T_m°K) + Crystal (T_m °K) → RCS (T_{tr} °K)	$-\{Q_m + Q_{tr}\}$	b
3	Liquid (298°K) → gas (298°K)	$-\{1.17\,(n-2)+2.88\}$	c
4	Gas (298°K) → gas (0°K)	$+\ 1.023n$	d
5	Crystal (0°K) → gas (0°K)	$\Sigma = -U_{\text{lattice}}$ (0°K)	

Notes: (a) The values were calculated in (8) from (9) data.

(b) For the *n*-paraffins which have no transition, Q_m alone is taken into account.

(c) Supposed to have a uniform dependence on *n*; 1·17 is the increment in heat content per CH_2 group; 2.88 is the increment in heat content per two CH_3 groups.

(d) Supposed to be uniform dependence on *n*.

The value 1.023 is given in (8).

Table 2. *Data for the lattice energy calculations of n-paraffins at* 0°K (*by Table* 1 *scheme*) *and free enthalpy* (*by expression* 6)

n	Thermal effect (kcal/mole) (See line No. in Table 1)				U(0°K) (kcal/mole)	$-\phi_T{}^0$ (cal/mole)	
						T° = 150°K	T° = 200°K
	1	2	3	4	5		
9	10.81	5.24	11.07	9.21	17.91	2336	4348
10	11.32	6.87	12.24	10.23	20.20	2473	4621
11	12.32	6.89	13.41	11.25	21.37	2665	4981
12	12.87	8.77	14.58	12.28	23.94	2824	5280
13	13.85	8.64	15.75	13.30	24.94	3011	5641
14	14.39	10.77	16.92	14.32	27.76	3174	5945
15	15.42	10.46	18.09	15.35	28.62	3354	6301
16	15.87	12.53	19.26	16.37	31.29	3524	6606

From the calculated values of the lattice energy for n-C$_{13}$ to n-C$_{16}$, we find the following ϵ and Δ values (kcal/mole):

$$\epsilon_T = -1{\cdot}77, \quad \epsilon_R = -1{\cdot}84,$$
$$\Delta_T = -2{\cdot}98 \quad \text{and} \quad \Delta_R = -1{\cdot}03$$

2. Comparison between the $U(n)$ graph at 0°K and the $\phi(n)$ graph at 150 and 200°K indicates that thermal vibrations has no appreciable effect on even–odd alternation of structural forms (this alternation is expressed by $U_T(n)$ and $U_R(n)$ at 0°K being separate lines spaced about 1 kcal/mole apart, whilst the difference between $\phi_T(n)$ and $\phi_R(n)$ at 200°K is as small as about 0·02 kcal/mole).

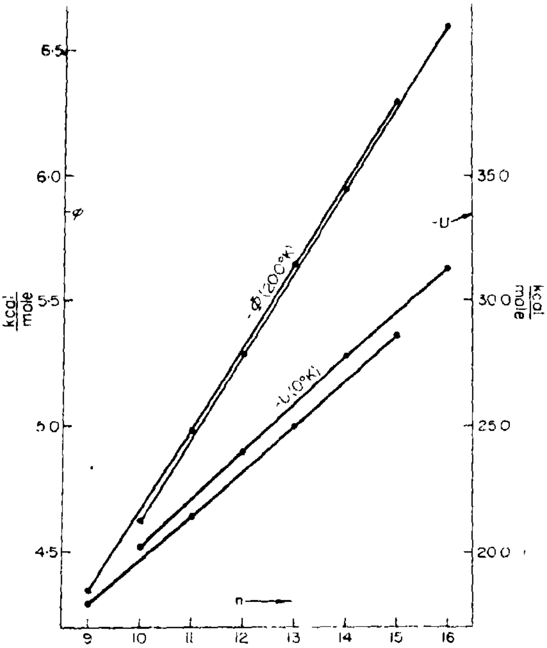

FIG. 5. Lattice energy U at 0°K and free enthalpy ϕ at 200°K vs. n.

This conclusion about the predominance of the molecular packing energy in a crystal over thermal vibrational energy may be considered as experimental thermodynamic substantiation (by way of n-paraffins) of the principle of molecular close-packing in the molecular crystal, the fundamental idea of organic chemical crystallography (See Ref. 2). The correctness of the above-mentioned analysis of the laws of phase transition of n-paraffins, in which thermal vibrational energy was not taken into account, is confirmed.

3. The lattice energy of even n-paraffins with n = 9–16 is substantially (by approx. 1 kcal/mole) lower than that of odd ones:

$$U_T < U_R,$$

which proves one of the fundamental propositions set forward when interpreting the above-considered phenomena.

The following fact is also worthy of notice: while the line $U(n)$ for odd n-paraffins lies above the corresponding one for even n-paraffins, the situation in the case of $\phi(n)$ is the reverse.

4. The accuracy of the experimental data, on which $U(n)$ calculations are based, does not appear to be good enough to confirm directly the relations:

$$\epsilon_T > \epsilon_R \quad \text{and} \quad \Delta_T < \Delta_R \tag{8}$$

The error is mainly caused by inaccuracy of measurements of melting heats and transition heats to RCS; this is expressed by disagreement between data given by different authors. Figure 5 still shows, that the ϵ_T and ϵ_R slopes of the lines (7) differ but slightly, as was to be expected. Graphically, the inequalities (8) imply that the lines (7) should cross when extrapolating to the right. To describe requirements for the accuracy needed to prove the inequalities (8), we suppose that this crossing occurs at n = 30 (it was shown above (5)), that n should be > 26). This gives $\epsilon_T - \epsilon_R \simeq 0{\cdot}1$ kcal/mole. This value shows that the experimental data must be very precise in this field.

Alternatively, the inequalities (8) would have been proved, if such an n_θ (> 26) could be demonstrated at which the lines (7) are crossed—that is, the T structure is replaced by R. From a practical point of view, for the reasons considered above, one can observe the $T \rightarrow M_R$ transition rather than the $T \rightarrow R$. Unfortunately, this complication obscures the possibility of proving the inequalities in that way. However, it should be noted that the $T \rightarrow M_R$ transition still favours the inequalities (8).

Thus, thermodynamic data are only indirectly in support of the inequalities, but one may console oneself with the fact that the latter naturally result from the geometric analysis of molecular packing and completely conform to the n-paraffin phase behaviour pattern.

Acknowledgement—The author wishes to thank Professor A. I. Kitaigorodskii for detailed discussions of this work and valuable suggestions.

REFERENCES

1. Schaerer A. A., Bayle G. G. and Mazee W. H., *Rec. Trav. chim. Pays—Bas.* **75**, 513 (1956).
2. Kitaigorodskii A. I., *Organic Chemical Crystallography*, Consultants Bureau, New York (1961).
3. Mnyukh Yu. V., *Zh. strukt. khim.* **1**, 370 (1960).
4. Kitaigorodskii A. I. and Mnyukh Yu. V., *Dokl. akad. nauk. S.S.S.R.* **121**, 115 (1958).
5. Tear, P. W. and Holmes D. R., *J. Polym. Sci.* **24**, 496 (1957).
6. Timmermans J., *Les constantes physiques des composés organiques cristallises*, p. 258. Paris (1953).
7. Lindemann F. A., *Phys. Z.* **11**, 609 (1910).
8. Billmeyer F. W., *J. appl. Phys.* **28**, 1114 (1957).
9. Finke H. L., Gross M. E., Waddington G. and Huffman, H. M., *J. Amer. chem. Soc.* **76**, 333 (1954).

J. Phys. Chem. Solids Pergamon Press 1963. Vol. 24, pp. 641–648. Printed in Great Britain.

CALCULATED SPECIFIC HEAT CONTRIBUTION OF F_2^- CENTERS IN LiF

W. C. OBERMOELLER* and W. A. BARKER

Physics Department, Saint Louis University, St. Louis, Missouri

(*Received* 1 *November* 1962)

Abstract—The Schottky heat capacity of F_2^- centers in LiF has been computed using the molecular ion model, the spin Hamiltonian, and the associated eigenvalue equation in terms of which spin resonance and optical absorption data have been so adquately interpreted. An anisotropic hyperfine peak occurs at $T_{p_1} \approx \dfrac{g_0\beta_0 b \cos\theta}{3{\cdot}72k} \approx 10^{-2}$ °K where b is a hyperfine constant and θ is the angle between the molecular bond axis and the magnetic field. An isotropic "hole" spin Zeeman peak occurs at $T_{p_2} \approx \dfrac{g_0\beta_0 H}{2{\cdot}4k} \approx 10^{-1}$ °K for H between 1 and 10 kg. For $10^{18}/\text{cm}^3$ centers, the hyperfine heat capacity maximum is ~ 100 erg/°K cm^3 and the "hole" heat capacity maximum is ~ 65 erg/°K cm^3. If the related experiment were performed, these contributions would greatly exceed the lattice heat capacity for $T < 1$°K, but would probably be partially disguised by other paramagnetic contributions.

1. INTRODUCTION

THE PROPERTIES of X_2^- centers, produced by the X-irradiation of alkali halides at liquid N_2 temperatures, have been investigated both by electron spin resonance$^{(1)}$ and by optical techniques.$^{(2)}$ The resonance data can be understood by postulating a halogen $_2^-$ molecular ion model described in terms of an effective spin Hamiltonian,$^{(3)}$

$\mathcal{H}$:

$$\frac{\mathcal{H}}{g_0\beta_0} = \frac{g}{g_0} HS_z + a\boldsymbol{I}\cdot\boldsymbol{S} + bI_{z'}S_{z'} \qquad (1)$$

where g_0 is the free electron spin Landé splitting factor, β_0 is the Bohr magneton, g is the observed electron splitting factor, H is the static magnetic field, $\boldsymbol{S}$ is the electron spin angular momentum operator, $\boldsymbol{I}$ is the superposition of the nuclear spin angular momentum operators of the two halide nuclei, a and b are empirical hyperfine constants, Z and Z' are the magnetic field and molecular bond axes respectively. The significance of these centers has been stressed by SLICHTER$^{(4)}$ who considers them to bear the same relation to solid state physics as the fundamental particles do to nuclear physics.

The energy levels of any of the X_2^- centers may be computed from the eigenvalue equation

$$E(m_I, m_s) = [g\beta_0 H + g_0\beta_0(p^2+q^2)^{1/2} m_I]m_s + \frac{g_0^2\beta_0(2a+b)^2 q^2 m_I^2 m_s}{2g(p^2+q^2)[H+(p^2+q^2)^{1/2}m_I]} \qquad (2)$$

where $m_s = \pm 1/2$ is the projection of the electron spin operator, $\boldsymbol{S}$ on the Z axis, $m_I = m_{I_1} + m_{I_2}$ is the projection of the hyper-nuclear spin operator $\boldsymbol{I}$ along Z and p and q are abbreviations:

$$p \equiv a + b\cos^2\theta$$
$$q \equiv b\sin\theta\cos\theta \qquad (3)$$

Equation (2) is obtained by second order perturbation theory$^{(3)}$ from equation (1).

It is the purpose of this paper to use equation

---

* This represents research done in partial fulfilment of the requirements for an M.S. (R) at Saint Louis University. Present address: Research Division, McDonnell Aircraft Co., St. Louis, Missouri.

(2) and conventional statistical mechanics to obtain theoretical expressions and numerical values for the heat capacity contribution of F_2^- centers in LiF.

2. ENERGY LEVELS, INTERNAL ENERGY AND HEAT CAPACITY

A. *Energy levels*

The F^{19} nucleus has a spin of 1/2 and a natural abundance $\sim$ 100 per cent. Hence the F_2^- centers are simpler to analyze than the other X_2^- centers which have higher spin value and/or several abundant isotopes.

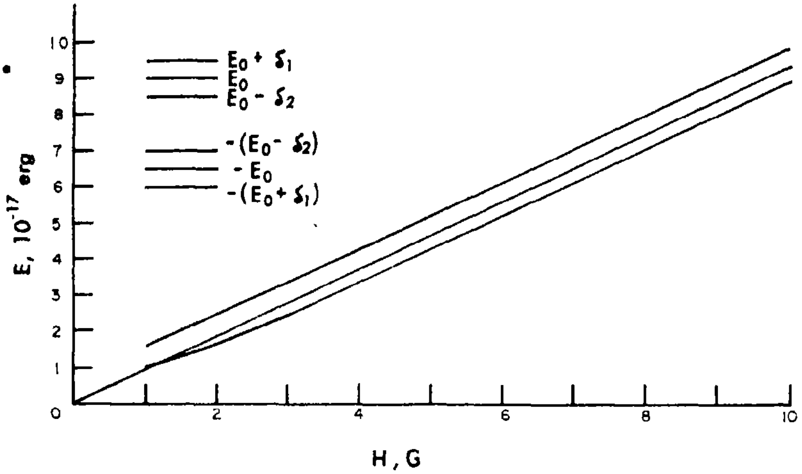

FIG. 1. Energy of levels 4, 5, 6 vs. magnetic field strength and schematic of energy levels.

The energy level splitting and the corresponding internal energy and heat capacity are anisotropic, depending on the orientation of the F_2^- centers with respect to H_0. Let us choose H_0 parallel to the (110) plane of the LiF crystal. Unless optically reoriented by polarized light,(5) the F_2^- molecular axes lie with equal probability parallel to the six equivalent $\langle 110 \rangle$ crystal directions. Our choice of field direction means that 2/3 of the centers make an angle $\theta = 60°$ with H. The other 1/3 make angles of $\theta = 0°$ and $\theta = 90°$ in equal proportions. We calculate the contribution of the centers whose angle $\theta = 60°$.

Numerical values for the parameters in equation (2) appropriate to the F_2^- centers are:(1, 2)

$$g \simeq g_0 = 2{\cdot}0023;\ \beta_0 = 9{\cdot}273\times 10^{-21}\,\text{erg G}^{-1};$$

$$|a| = 59\text{ G};\ (a+b) = 887\text{ G};\ m_s = \pm\tfrac{1}{2}, m_I = 1, 0, -1.$$

There are six energy levels symmetrically arranged about $E = 0$ as depicted in Fig. 1: $\delta_1 \equiv (E_2-E_1) = (E_6-E_5)$; $\delta_2 \equiv (E_3-E_2) = (E_5-E_4)$. Numerical values for the E_i ($i = 1,2,\ldots,6$) were calculated with the aid of an IBM 610 computer. E_4, E_5, and E_6 are plotted in Fig. 1. vs. the magnetic field strength for $0 \leqslant H \leqslant 10$ kG.

B. *Internal energy and heat capacity*

The F_2^- center concentration, N, depends on the type, duration, and intensity of the irradiation and also on the type and concentration of electron traps which inhibit recombination. N may range from 10^{17} to $10^{19}/\text{cm}^3$. In any case we are safe in assuming (with Kastner and Kanzig) that the average distance between centers is sufficiently large so that the mutual interaction between centers is negligible. The molecular ions are assumed to be in thermal equilibrium at temperature T with the LiF host. We treat the system as a canonical ensemble with an individual F_2^- centre as a subsystem.

The internal energy U and heat capacity $C_{H,\theta}$

may be calculated in the customary manner from the partition function: Z:

$$Z = \sum_{i=1}^{n} \exp(-E_i/\tau) \quad \text{where } \tau = kT \text{ and } n = 6 \text{ for the } F_2^- \text{ case,} \tag{4}$$

$$\bar{\epsilon} = \tau^2 \frac{\partial}{\partial\tau} \ln Z \tag{5}$$

$$U = N\bar{\epsilon} \tag{6}$$

and

$$C_{H,\theta} = \left(\frac{\partial U}{\partial T}\right)_{H,\theta} = Nk\left(\frac{\partial\bar{\epsilon}}{\partial\tau}\right)_{H,\theta} \tag{7}$$

Carrying out the steps indicated, we may write the following prescriptions suitable for numerical calculation of the internal energy and heat capacity.

$$\frac{U}{N} = \bar{\epsilon} = \frac{\sum\limits_{i=1}^{n} E_i \exp(-E_i/\tau)}{\sum \exp(-E_i/\tau)} \tag{8}$$

$$\frac{C_{H,\theta}}{Nk} = \left(\frac{\partial\bar{\epsilon}}{\partial\tau}\right)_{H,\theta} = \frac{1}{\tau^2}\left\{\frac{\sum\limits_{i=1}^{n} E_i^2 \exp(-E_i/\tau)}{\sum\limits_{i=1}^{n} \exp(-E_i/\tau)} - \left[\frac{\sum\limits_{i=1}^{n} E_i \exp(-E_i/\tau)}{\sum\limits_{i=1}^{n} \exp(-E_i/\tau)}\right]^2\right\} \tag{9}$$

These equations apply for a set of non-degenerate levels which are arbitrarily spaced.

Suppose we had $n = 2J+1$ equally spaced levels of separation ΔE. From equations (8) and (9), after some manipulation, we find that

$$\bar{\epsilon} = -J\Delta E\left[\frac{2J+1}{2J} \operatorname{ctnh} \frac{2J+1}{2J} x - \frac{1}{2J} \operatorname{ctnh} \frac{x}{2J}\right] = -J\Delta E B_J(x) \tag{10}$$

and

$$\frac{\partial\bar{\epsilon}}{\partial\tau} = \left(\frac{\Delta E}{\tau}\right)^2 \left[\tfrac{1}{4} \operatorname{csch}^2 \frac{x}{2} - (J+\tfrac{1}{2})^2 \operatorname{csch}^2 (J+\tfrac{1}{2})x\right] = -\left(\frac{\Delta E}{\tau}\right)^2 \frac{\partial B_J(x)}{\partial\tau} \tag{11}$$

where

$$x = \frac{J\Delta E}{\tau}$$

These are well known results expressed in terms of the Brillouin function $B_J(x)$.

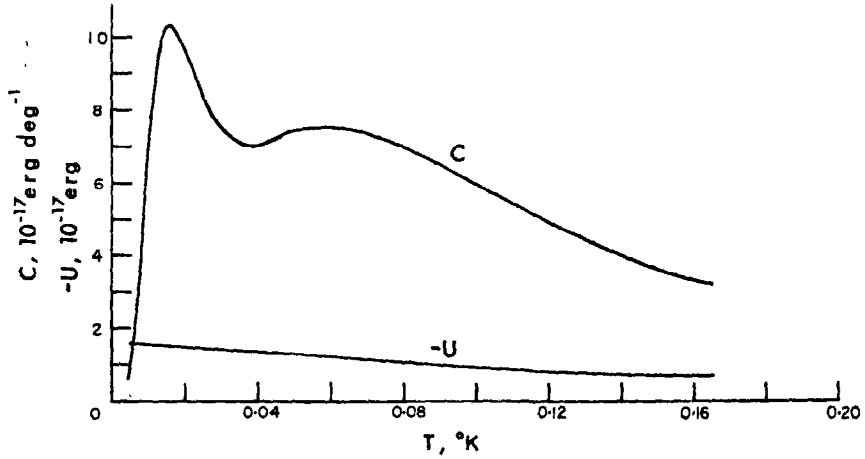

FIG. 2. Specific heat C, and internal energy U, vs. temperature for magnetic field strength of 1000 G.

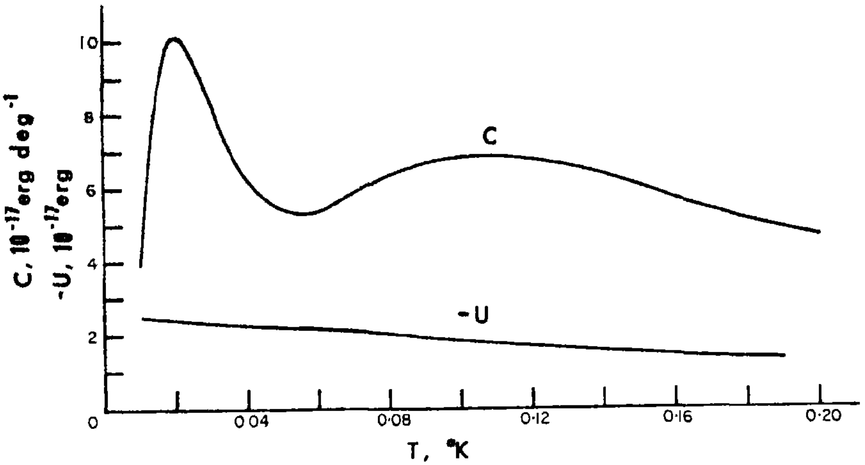

Fig. 3. Specific heat C, and internal energy U, vs. temperature for magnetic field strength of 2000 G.

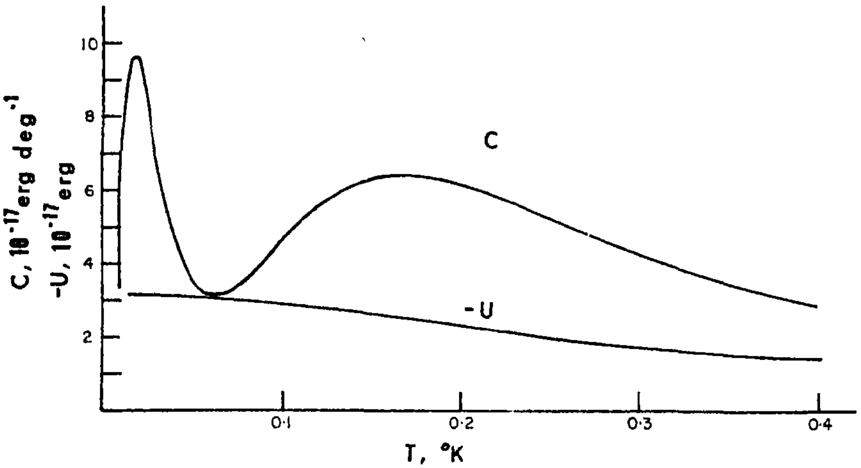

Fig. 4. Specific heat C, and internal energy U, vs. temperature for magnetic field strength of 3000 G.

Values for the E_i obtained from equation (2) Fig. 1 may now be inserted into equations (8) and (9) to obtain numerical values for the internal energy and heat capacity. This was done, with the aid of the IBM 610 computer, for an assumed magnetic field of 1, 2, 3, 4, 5 and 10 kG over a wide enough low temperature range to adequately describe the T dependence for each selected value of H. The results for $\bar{\epsilon}$ and $\left(\frac{\partial \bar{\epsilon}}{\partial T}\right)_{H,\theta}$, the internal energy and heat capacity per F_2^- center respectively, are plotted vs. T in Figs. 2–7 inclusive.

3. APPROXIMATE ANALYSIS

A striking feature of the theoretical specific heat vs. temperature curves is the appearance of

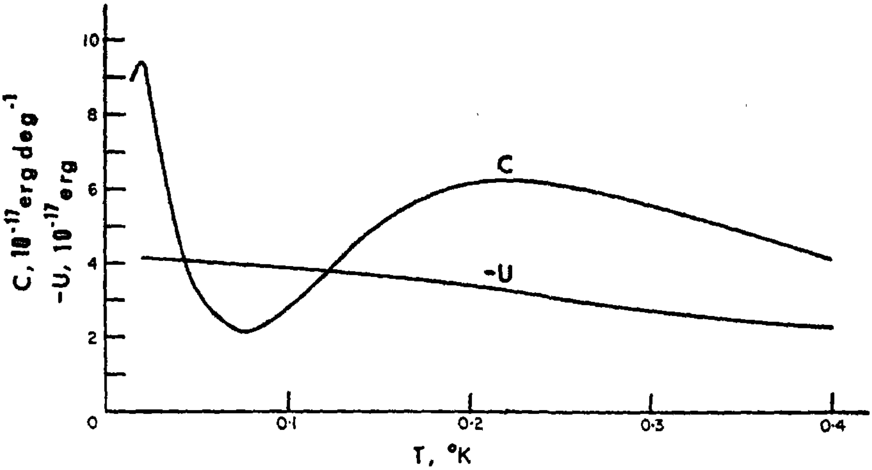

FIG. 5. Specific heat C, and internal energy U, vs. temperature for magnetic field strength of 4000 G.

two peaks. It is well known that for a system of equally spaced levels one SCHOTTKY(6) peak occurs. It is the unequal spacing which accounts for the appearance of more than one peak.

We can understand the appearance of the two peaks by making an approximate analysis suggested by a study of the energy level separations depicted in Fig. 1.

A. *Three level model*

For values of $T \ll 2E_0/k$, the occupation of the three upper energy levels may be neglected. In fact for $T = T_c = \dfrac{2(\delta_1+\delta_2)}{k}$ and $H = 5{,}000$ G the three lower energy states are occupied by ~ 500 times as many ions as the upper energy levels. Hence, for values of $0 \leqslant T \ll T_c$, we may,

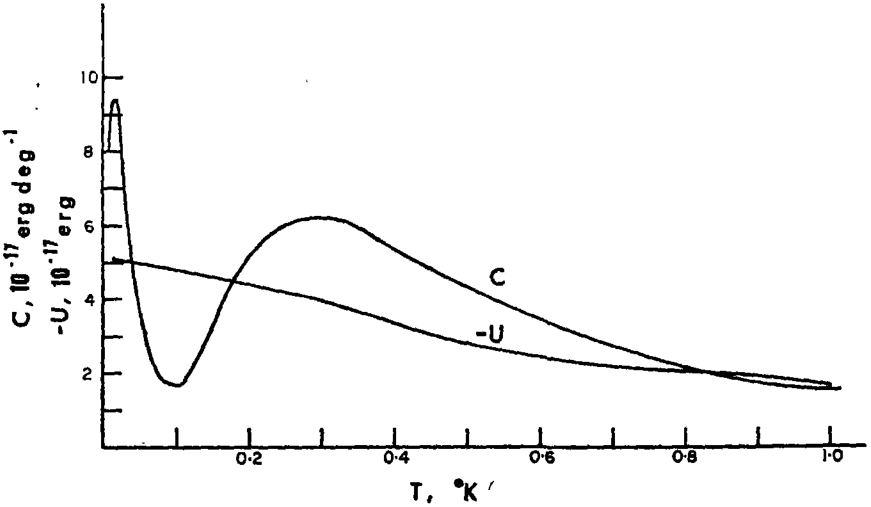

FIG. 6. Specific heat C, and internal energy U, vs. temperature for magnetic field strength of 5000 G.

to a first approximation, consider an equally spaced three level system. We neglect the contribution of the relatively unoccupied higher energy states and take the spacing $\Delta E = \frac{\delta_1+\delta_2}{2}$. Equation (11) may now be used with $J = 1$. A single peak occurs at $\frac{\Delta E}{2kT} = 0{\cdot}93$. The temperature at which this maximum occurs is predicted on this simple model to be

$$T_{p1} \approx \frac{(\delta_1+\delta_2)}{3{\cdot}72k}, \quad T \ll T_c \qquad (12)$$

For $H = 5$ kg, $\delta_1 = 0{\cdot}497\times10^{-17}$ ergs, $\delta_2 = 0{\cdot}375 \times 10^{-17}$ ergs, equation (12) gives $T_{p1} \approx 0{\cdot}0166$°K. This approximate value is to be compared with $T_{p1} = 0{\cdot}0175$°K obtained from the exact equation (11). For values of $H > 5$ kg, the approximation given by equation (12) is better because $(\delta_1-\delta_2) \to 0$ with increasing H. The approximation is not as good for $H < 5$ kg.

B. 2 *Level system*

Now when T is comparable to $\frac{2E_0}{k}$ we can expect all six levels to play a role. In this range let us construct another simple model. Consider a two level system in which the energy separation $\Delta E = E_5 - E_2 = 2E_0 = g\beta_0 H$. Equation (11) is again applicable with $J = \frac{1}{2}$. The specific heat maximum occurs for $\frac{\Delta E}{2kT} = 1{\cdot}20$. The temperature for which this peak occurs is

$$T_{p2} = \frac{g_0\beta_0 H}{2{\cdot}4k}, \quad T > T_c \qquad (13)$$

For $H = 5$ kg, $g_0 H = 0{\cdot}927\times10^{-16}$ ergs, and equation (13) gives $T_{p2} \approx 0{\cdot}28$°K in comparison with $T_{p2} = 0{\cdot}28$°K obtained from equation (11). For other values of $H_0 > 1$ kg, T_{p2} values from equation (13) agree within 1 per cent of values from equation (11). This close agreement is not fortuitous but rather depends on the fact that $E_0 \ll \delta_{1,2}$ for $H > 1$ kg.

In Fig. 7, for $H = 10$ kg, only the second peak is shown. The first peak should occur at about $T_{p1} \approx 0{\cdot}018$°K.

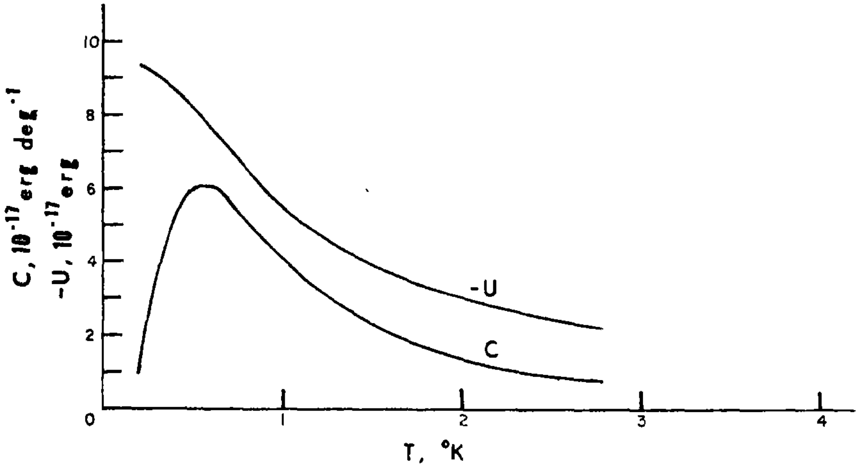

FIG. 7. Specific heat C, and internal energy U, vs. temperature for magnetic field strength of 10,000 G.

4. COMPARISON WITH OTHER CONTRIBUTIONS TO THE HEAT CAPACITY

In Table 1, numerical values for T_{p1}, T_{p2} and the corresponding Schottky heat capacity maxima are compiled for a number of magnetic field values ranging between 1 and 25 kg. The number of F

centers is taken as $N = 10^{18}/\text{cm}^3$. For comparison the lattice contribution to the heat capacity, C_L, is tabulated for T_{p1} and T_{p2}. Numerical values for C_L were obtained from the low temperature Debye formula

$$C_L = 234\,N'k\left(\frac{T}{\Theta}\right)^3 \tag{14}$$

with the Debye temperature, Θ, taken as 736°K for LiF.(7) Note that although N', the number of LiF molecules/cm³, exceeds N by a factor of $\sim 10^4$, nevertheless $C_{H,\theta} \gg C_L$ for all $T \leqslant 1$°K.

Table 1. Heat capacity maxima and the corresponding temperatures for 10^{18} F_2^- centers cm^{-3} in various magnetic fields. The lattice heat capacity contribution is given at T_{p1} and T_{p2}

H (kg)	T_{p1} (°K)	$C_{H,\theta}(1)$ (erg/°K cm³)	$C_L(1)$ (erg/°K cm³)	T_{p2} (°K)	$C_{H,\theta}(2)$ (erg/°K cm³)	$C_L(2)$ (erg/°K cm³)
1	0·015	102·75	$1{\cdot}68\times10^{-5}$	0·060	74·88	0·0018
2	0·020	101·03	$3{\cdot}97\times10^{-5}$	0·110	68·70	0·0066
3	0·0175	96·33	$2{\cdot}66\times10^{-5}$	0·170	63·79	0·0244
4	0·020	93·42	$3{\cdot}97\times10^{-5}$	0·225	62·45	0·056
5	0·0175	93·43	$2{\cdot}66\times10^{-5}$	0·280	61·81	0·109
10				0·56	60·93	0·873
25				1·40	60·90	13·60

Clearly F centers and possibly other paramagnetic centers would be present along with F_2^- centers in an irradiated LiF crystal and these would make contributions to the heat capacity of comparable order of magnitude, particularly at T_{p2}. It should be possible to unscramble the various contributions by a suitable combination of experimental and analytical techniques. F center production during irradiation can be inhibited in favor of X_2^- center production by adding suitable dopants (Pb^{2+} in KCl works quite well). X_2^- centers can be annealed out of the host after production by heating to temperatures above 120°K.

5. DISCUSSION OF RESULTS

F_2^- centers in LiF are known from a more exact analysis given by WOODRUFF and KANZIG(8) to have eight rather than six energy levels. The two additional levels lie quite close to levels 5 and 2 of Fig. 3. We do not believe that any of the numerical results reported will be altered by more than a few per cent by the inclusion of these additional levels.

The six levels treated have an unequal spacing. The separations δ_1, δ_2, E_0 should in principle lead to three rather than two peaks in the heat capacity curves. However, δ_1 and δ_2 are sufficiently close so that our machine calculation did not resolve the two lower peaks. A related experiment conducted at $T \sim 10^{-2}$ °K would also probably not resolve these two peaks.

The approximate analysis of Section III illuminates the physics of the problem. The first heat capacity peak occurs at a temperature given to a good approximation by equation (12). With the aid of equation (2) this may be written as follows:

$$T_{p1} \approx \frac{g_0\beta_0 b\cos\theta}{3{\cdot}72k} \tag{15}$$

Where use has been made of the fact that $b \gg |a|$ and H is considered sufficiently large so that the second term of equation (2) may be dropped. Equation (15) clearly demonstrates that the first peak is associated primarily with the hyperfine interaction. It is field independent but angle dependent. At the outset we chose a field H parallel to the 110 plane for which 2/3 of the centers make an angle $\theta = 60°$ with H, 1/6 make an angle $\theta = 0°$ and 1/6 make an angle $\theta = 90°$. Equation (15) predicts, therefore, two low temperature peaks one at 0·015°K and a second at 0·030°K. Detailed calculations in Section II were made only for the more abundant centers.

The second heat capacity peak occurs for $T > T_c$ where

$$T_c \simeq \frac{2g_0\beta_0 b\cos\theta}{k} \approx 1{\cdot}86\, T_{p1} \qquad (16)$$

Equation (13) for T_{p2} clearly shows that the second peak is associated primarily with the "hole" Zeeman splitting. It is field dependent and angle independent.

At 10 kg it would be possible to detect the "hole" spin Zeeman peak by pumping on liquid He.[8] However, the more interesting anisotropic hyperfine peak occurs at a temperature which at best is 0·03°K, and hence would only be observable by going to temperatures attainable by adiabatic demagnetization.

REFERENCES

1. Delbecq C. J., Smaller B. and Yuster P. H., *Color Center Symposium at Argonne National Laboratory* (1956) unpublished; Yuster P. H., Delbecq C. J. and Smaller B., *Bull. Amer. phys. Soc.* Ser. II, **2**, 302 (1957); Kastner T. G. and Kanzig W., *J. Phys. Chem. Solids* **3**, 178 (1957); Woodruff T. O. and Kanzig W., *J. Phys. Chem. Solids* **5**, 268 (1958).
2. Delbecq C. J., Smaller B. and Yuster P. H., *Phys. Rev.* **111**, 1235 (1958); Hayes W. and Nichols G. M., *Phys. Rev.* **117**, 993 (1960); Delbecq C. J., Hayes W. and Yuster P. H., *Phys. Rev.* **121**, 1043 (1961).
3. See the papers by Kastner T. G. and Kanzig W. and by Woodruff T. O. and Kanzig W., listed in Ref. 1.
4. Slichter C. P., Invited paper on Electron Spin Resonance, *Midwest Conference on Solid State Physics, Argonne National Laboratory* (1961) unpublished.
5. Delbecq C. J., Hayes W. and Yuster P. H., *Phys. Rev.* **121**, 1043 (1961).
6. Schottky W., *Phys. Z.* **22**, 1 (1921); *ibid.* **23**, 9, 448 (1922).
7. Jones G. O. and Martin D. L., *Phil. Mag.* **45**, 649 (1954).
8. Last paper listed in reference 1. Woodruff T. O. and Kanzig W., *J. Phys. Chem. Solids* **5**, 268 (1958).

J. Phys. Chem. Solids. Pergamon Press 1963. Vol. 24. pp. 649–666. Printed in Great Britain.

FERMI SURFACE OF WHITE TIN FROM MAGNETOACOUSTIC MEASUREMENTS

TORE OLSEN

Department of Physics, Brown University, Providence, Rhode Island
and Fysisk Institutt, Universitetet i Oslo, Blindern, Norway.*

(*Received* 5 *October*, 1962; *revised* 17 *November* 1962)

Abstract—Magnetoacoustic measurements have been made on single crystals of white tin at several frequencies in the range 10–100 Mc/s. From the magnetoacoustic oscillations some dimensions of the Fermi surfaces of tin have been deduced. The results are in agreement with experimental data obtained by other investigators, and they agree to some extent with the surface suggested by the free electron approximation. It is suggested that the hole surface in zone 4 has a main open direction along [110] and a secondary one along [100]. The high field attenuation was also studied, and the results are consistent with the topology of the surface indicated by the magnetoacoustic oscillations.

1. INTRODUCTION

FOLLOWING the pioneer work by BÖMMEL,(1) the magnetoacoustic effect was first studied in any detail by MORSE and coworkers.(2) The magnetoacoustic method has since been employed to furnish data relating to the structure of the Fermi surface in a number of metals.(3–13) A main advantage of the method is that results can be interpreted in terms of a few basic properties.

This paper describes a magnetoacoustic investigation of white tin, and also a few acoustic measurements in the absence of a magnetic field. Parts of these data have been published previously(6,9,14) as preliminary reports. In Section II we shall review very briefly the important features of existing theories. Magnetoacoustic measurements contain more information than presently can be interpreted usefully, and this is especially true in a complicated metal like tin. Therefore, in Section III we give the experimental data as completely as space permits us. Finally, in Section IV we interpret the data in light of the existing theories and other experimental investigations regarding the Fermi surface of white tin.

2. THEORY

PIPPARD(15) has calculated the attenuation α in the absence of a magnetic field. He found that

$$\alpha/\alpha' = \frac{6}{\pi}\left(\frac{ql_e}{3}\frac{a}{1-a} - \frac{1}{ql_e}\right) \tag{1}$$

where q is the wave-vector of the soundwave, l_e the electron mean free path, $a = \operatorname{arctg} ql_e/ql_e$, and α' is the limiting value of the attenuation when $ql_e \rightarrow \infty$.

The theory of magnetoacoustic effects has been treated by a great number of authors. A complete semi-classical theory for the free electron case has been given by KJELDAAS and HOLSTEIN(16) and by COHEN *et al.*(17) Quantum theoretical treatments have been attempted by SKOBOV,(18) ZYRYANOV(19) and STOLZ.(20)

Magnetoacoustic effects in real metals have been studied semiclassically by GURVEITCH,(21) KANER(22) and PIPPARD.(23) It has been shown that when $ql_e > 1$ the attenuation changes periodically with H^{-1}. According to GUERVITCH(21) the oscillations depend in a fundamental way on the topology of the Fermi surface. He found that for closed surfaces and $q \perp H$ the oscillations are harmonic and associated with electron orbits having an extremum in the direction of sound propagation. The attenuation is given as

---

* Present address.

$$\alpha(H) \sim \alpha' \frac{l_e}{r}\{1 + A(k_{\text{ext}} \cdot \beta)^{-1/2} \sin(k_{\text{ext}} \cdot \beta \pm \pi/4)\} \tag{2}$$

where α' is the zero field attenuation, $A \sim 1$, r the orbit radius, $\beta = 2\pi\hbar c/\lambda eH$, λ the sound wave length, and k_{ext} the extremal diameter of the Fermi surface along $[q \times H]$ in k-space. Oscillations can also be found with open surfaces(10) if the wavevector q is parallel the average direction of the open orbits. Then k_{ext} will be the difference $(k_{\text{max}} - k_{\text{min}})$ perpendicular H.

PIPPARD(28) found that the observed attenuation will be a sum of contributions from all orbits depending on integrals like

$$I_n \approx A_n(\beta k^*)\eta_n^{(\text{ext})} \sin(\beta k^* + \delta) \tag{3}$$

Here k^* is the total extension of the orbit in the $[q \times H]$ direction, and the detailed shape of the orbit will determine the phase factor and the amplitude factor.

In principle it should be possible to map the entire Fermi surface on the basis of measurements of the oscillations in α for all directions of q and a perpendicular field.

3. EXPERIMENTS

The samples

As a Bravais lattice for white tin one can choose a body-centred tetragonal lattice as shown in Fig. 1. At liquid helium temperatures the lattice constants in the [100]- and [001]-directions are 5·81 Å and 3·16 Å respectively.(24)

Two single crystal samples were used in the experiments, and both were grown from 99·9999 per cent pure tin by the Virginia Institute for Scientific Research, Richmond, Virginia. Two sets of parallel faces were cut on one of the samples, the faces being perpendicular the [001]- and the [110]-axes respectively. The same sample was later reshaped to permit a sound transmission along the [100]-axis as well. On the second sample two parallel faces were cut perpendicular a direction 18° off the [100]-axis in the (001) plane.

Ordinary machine tools were used in the cutting of the sample, but care was taken to make the cuts as fine as possible. The faces were later lapped by hand until they were flat and parallel within 0·0003 cm across the faces (1–2 cm in diameter). Finally the damaged surface layers were removed by etching, and the faces checked to be within one degree perpendicular to the crystalline axis.

Experimental method

The ultrasonic attenuation was measured by a pulse method using pulses of one microsecond duration in the frequency range 5–100 Mc/s. A schematic diagram of the experimental apparatus is shown in Fig. 2. A quartz transducer was attached to the sample, and the center frequency of the electronic pulse was tuned to one of the resonant frequencies of the transducer. The

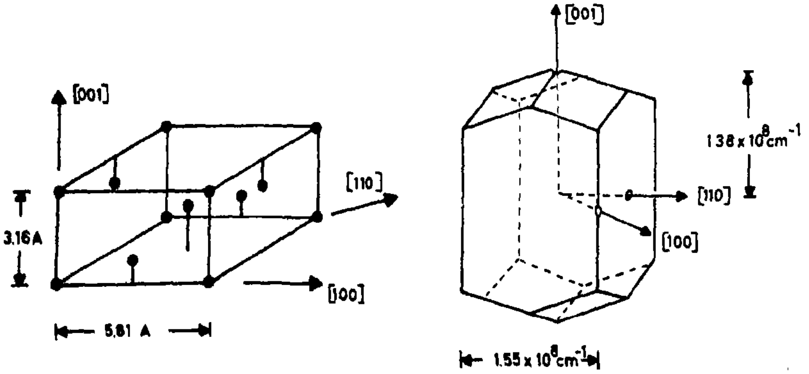

FIG. 1. Crystal structure and zone structure of white tin. The lattice constants a and c are equal to 5·81 and 3·16 Å respectively. The zone contains one electron per atom.

ultrasonic pulse thus generated was reflected back and forth between the parallel faces of the sample, and the transducer, which also served as a receiver, picked up a train of pulses (echoes). The received signals were amplified, rectified, and displayed on an oscilloscope where the attenuation of the sound could be measured. A detailed account of this method in the low temperature region has been given by MORSE,(25) and CHICK *et al.*(26) have described the electronic part of the apparatus.

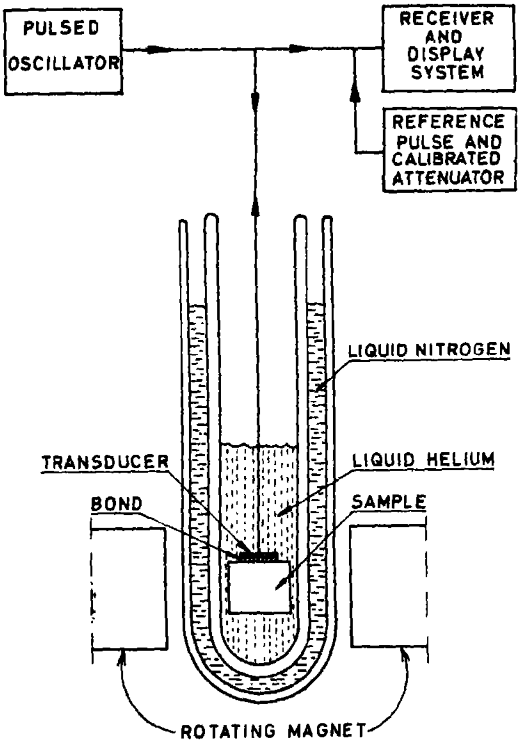

FIG. 2. Experimental method (schematic).

The bond between the transducer and the sample was made of a very thin layer of "Nonaq"-stopcock grease, but considerable difficulty was experienced in making this bond. It tended to crack when cooled down, and especially so on surfaces perpendicular to axes of low symmetry, and here again more often with shear wave transducers than with longitudinal ones. This was probably due to the anisotropic thermal stresses. The best results were obtained by cooling the sample rapidly by plunging it into liquid air. This procedure presumably allowed the tin samples to undergo most of the thermal contraction before the bond became solid.

The main part of the present experiments were done with the direction of propagation along [100], [110] and [001]. WATERMAN(27) found that pure longitudinal as well as pure shear waves can be propagated along these three directions. However, some of the experiments were performed with the direction of propagation in the (001) plane, 18° off the [100]-axis. In the Appendix it is shown that the quasilongitudinal mode generated by a longitudinal transducer along this direction is nearly a pure longitudinal mode.

In the shear wave experiments the direction of particle motion was always kept parallel to a principal axis. But it was found difficult to align this plane of polarization to the crystalline axis better than within ± 2°. However, the shear wave observations were reproducible from one run to another, proving that this alignment was not critical.

The sample was suspended directly in the liquid helium bath. The magnet was a Varian 4 in.-laboratory model, and the dewars allowed a pole gap of 6 cm, limiting the maximum field to 6500 Oe. The field was found to be homogeneous within 1 per cent in the central region where the sample was located. The temperature of the sample could be reduced from 4·2 to 1·05°K by pumping directly on the helium bath. The temperature was measured by a 130-Ω Speer carbon resistor calibrated against the vapor pressure of the liquid helium, giving an accuracy better than 0·01°K.

Because of reflection and diffraction effects, the total attenuation cannot be accurately determined. However, the variation of the electronic part as function of the external parameters T and H can be accurately studied from the relative attenuation of one of the echoes. Furthermore, this method is the only one possible when the electronic attenuation becomes so large that only the first echo is observable. The validity of the relative method rests upon the fact that none of the other effects contributing to the attenuation will change with H or with T in the liquid helium temperature range as shown by MORSE and BOHM.(25)

Experimental results

The attenuation of longitudinal waves was measured as a function of the following parameters: the sound frequency, the strength of the magnetic field, and the direction of this field. However, all measurements were restricted to those cases where the field was perpendicular to the direction of sound propagation. The temperature dependence of the attenuation in high fields was also measured but this is treated in more detail in a separate paper.(28)

The attenuation of shear waves was measured as a function of the same parameters. However, the direction of the magnetic field was kept either along the direction of polarization or perpendicular to it only. In the compressional case the magnetic field and the sound wave always have the same relationship to each other, and consequently any anisotropic effect must be attributed to the anisotropy of the Fermi surface. With shear waves, however, the anisotropy will be masked by the geometric anisotropy introduced by the changing angle between the plane of polarization and H when the latter is rotated.

The sound frequency was measured by a calibrated grid dip meter, and the sound velocity was calculated from the time between the echoes on the oscilloscope. From the knowledge of the pathlength the velocity was then calculated within 2 per cent, and it is estimated that the total error in the wavelength determinations is 3 per cent.

The different velocities found at 4·2°K are listed in Table 1. The velocities agree within the experimental error with those measured by other investigators.(24,29) One exception is for the longitudinal wave along [100] where we found a somewhat lower value.

Table 1. *Measured sound velocities in white tin at* 4·2°K

Direction of propagation q	Direction of particle motion ϵ	Velocity ($T = 4{\cdot}2$ °K) (cm/sec)
[100]	[100]	$3{\cdot}19 \cdot 10^5$
	[001]	$1{\cdot}91 \cdot 10^5$
	[010]	$1{\cdot}92 \cdot 10^5$
[001]	[001]	$3{\cdot}78 \cdot 10^5$
	[100]	$1{\cdot}88 \cdot 10^5$
	[110]	$1{\cdot}92 \cdot 10^5$
[110]	[110]	$3{\cdot}61 \cdot 10^5$
	[001]	$1{\cdot}88 \cdot 10^5$
[$\phi = 18°, \psi = 90°$]	long.	$3{\cdot}40 \cdot 10^5$

Absence of a magnetic field

The electronic contribution to α will decrease towards zero below the transition temperature (T_c). In tin the decrease will be exponential around 1°K, and the electronic part of the attenuation can be found within 1 per cent by extrapolation to $T = 0$°K.(30) We have done this for longitudinal waves with q along the three principal crystalline directions and in each case for several frequencies between 10 and 100 Mc/s. The data have been compared with equation (1) by the following procedure: Normalize the frequencies, i.e. the ql_e-values, divide the measured attenuation by the frequency and fit the outcoming set of data to the α/α'-curve. In this way α' and l_e can be determined from the experiments. The validity of this comparison rests on the assumption that an expression similar to (1) can be found in real metals as well, and that the real metal effects are taken care of by the parameter α'. According to Olsen(28) this can be done, and the attenuation when $ql_e \gg 1$ can be written as

$$\alpha' = \frac{[n/N(E_F)]^2 q}{4\pi\rho_0 u_q} \oint \frac{1}{\partial^2 E/\partial k_x^2} \frac{dk_\eta}{v_k} \qquad (4)$$

for a general Fermi surface. Here $n/N(E_F)$ is the ratio of the total number of electrons to the density of electrons at the Fermi surface. u_q and ρ_0 are the velocity of the wave and the mass density respectively, and v_k is the group velocity. Here we have supposed q to be along the x-axis and the integral is to be taken along the curves where $(\partial E/\partial k_x)q - \hbar\omega_q = 0$.

Writing (4) as $\alpha' = A_q \cdot q$ we can calculate A_q for the different direction of propagation. This quantity contains information about the Fermi surface, and is listed in Table 2.

Magnetoacoustic oscillations with q along [100]

Figure 3 shows the attenuation of a longitudinal wave propagating along [100] as a function of field strength and field directions in the (100)-plane.

The attenuation is given in dB/cm and the abscissa is the parameter $1/H\lambda$. Smooth curves have been drawn through the observed points. Since we are mainly interested in the oscillatory effects and not the absolute magnitude of the electronic attenuation, the attenuation in the absence of a magnetic field is set equal to zero. Unless anything else is said this will be the case for all of the following curves showing the magnetoacoustic oscillations. From Table 2 we see that the zero field electronic attenuation is large for this direction of q, and 45·5 Mc/s was the maximum frequency at which the oscillations could be studied conveniently. The oscillations are of the geometric resonance type as is illustrated in Fig. 4. We see that the location of the oscillations scales in the parameter $1/H\lambda$ as to be expected of a geometric resonance. Furthermore, the low frequency curve in Fig. 4 reveals another oscillation in the high field region. This illustrates that in spite of the fact that measurements taken at lower frequencies yield fewer oscillations, they offer a valuable supplement to the observations taken at higher frequencies because in the latter case the high field attenuation is often too large to be measureable.

Table 2. The magnitude of the attenuation in the absence of a magnetic field when $ql_e \gg 1$

Direction of q	$\alpha' = A_q \cdot q$ A_q
[100]	$2{\cdot}58 \cdot 10^{-3}$
[001]	$2{\cdot}10 \cdot 10^{-3}$
[110]	$1{\cdot}02 \cdot 10^{-3}$

In some cases the oscillations show up more clearly for shear waves, and the reason for this is probably the low shear wave velocity giving larger ql_e-values. Figure 5 shows the attenuation of a shear wave with the plane of polarization along [010] and the magnetic field along [010] and [001]

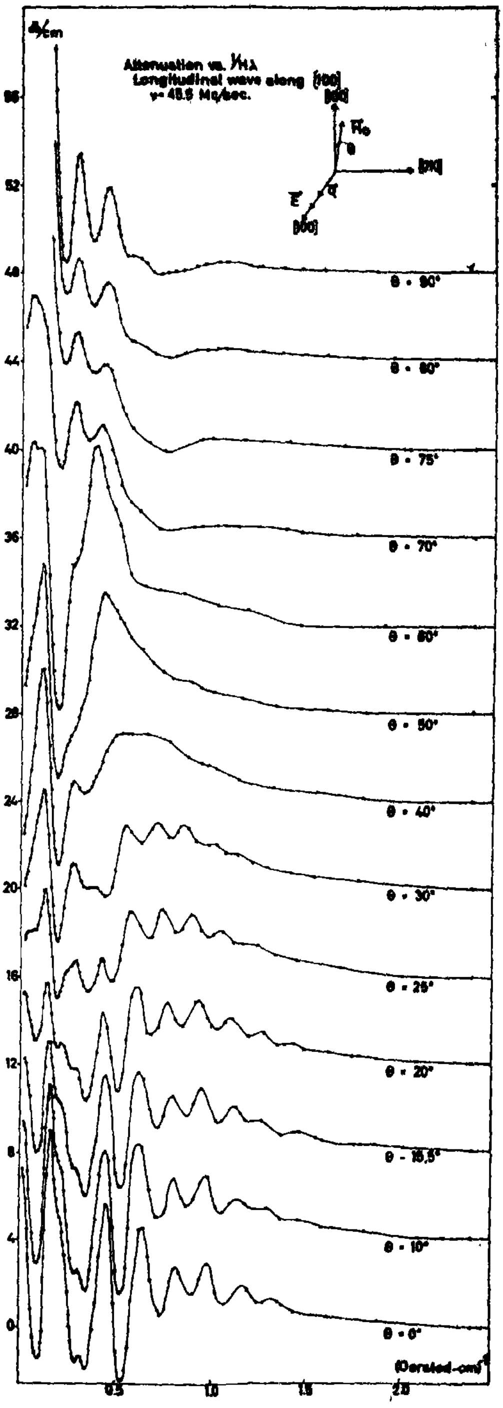

FIG. 3. Attenuation of a longitudinal wave propagating along [100] as a function of $1/H\lambda$ and field direction in the (100) plane. All curves have been displaced 4 dB/cm in the interest of clarity. The zero field attenuation is set equal to zero.

respectively. Contrary to the transverse case ($H \perp \epsilon$) no oscillations could be detected when $H \parallel \epsilon$. The results obtained with the plane of polarization along [001] are given in Fig. 6. It should be noted that, with respect to the electron orbits, the $H \perp \epsilon$ case in Fig. 5 is identical to the $H \parallel \epsilon$ case in Fig. 6. However, the interaction with the two different sound waves yield different sets of periods.

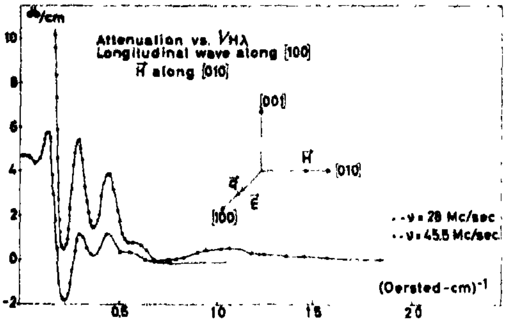

FIG. 4. Attenuation of a longitudinal wave propagating along [100] and with the field along [010] as a function of $1/H\lambda$. The two curves are taken at different frequencies and show that the oscillations are of the geometric resonance type.

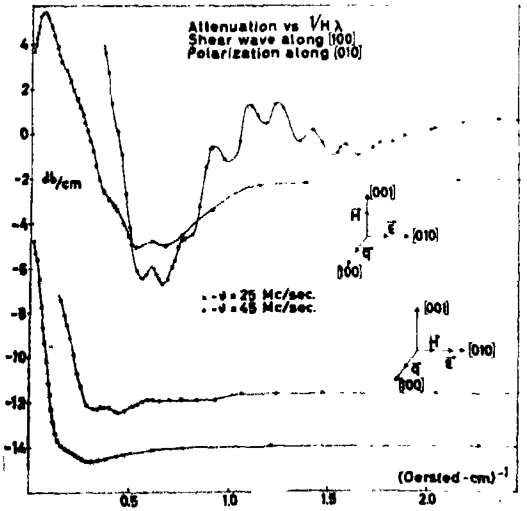

FIG. 5. Attenuation of shear waves propagating along [100] as a function of $1/H\lambda$. Plane of polarization along [010] and H along [010] and [001]. The curves have been displaced by (from top to bottom) -2, -12, and -14 dB/cm.

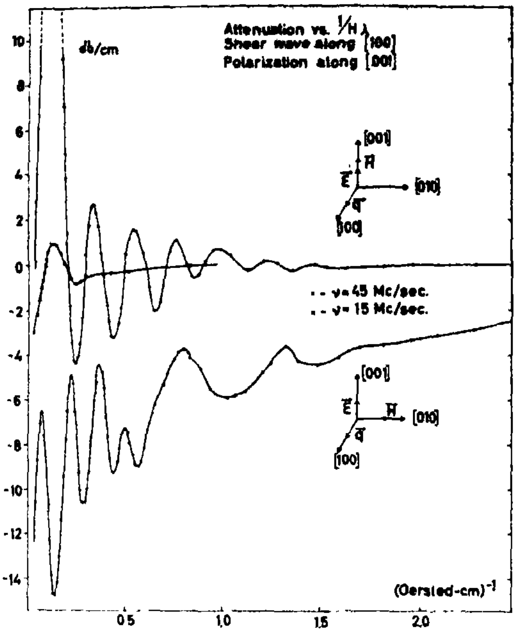

FIG. 6. Attenuation of shear waves propagating along [100] as a function of $1/H\lambda$. Plane of polarization along [001], and H along [010] and [001]. The lower curve has been displaced -2 dB/cm.

Magnetoacoustic oscillations with q along [001]

Figure 7 shows the attenuation of a longitudinal wave propagating along the [001] axis as function of field strength and of field directions between [100] and [110]. The oscillatory behavior of the attenuation was best measured at 76·5 Mc/s but for the purpose of studying the oscillations in the region of small $1/H\lambda$ similar measurements were also made at lower frequencies. This is illustrated in Fig. 8 for the cases $H \parallel [100]$ and $H \parallel [110]$.

Two sets of measurements were done with shear waves, one with the plane of polarization along [110] and one with the same plane parallel [100]. In either case the attenuation was measured for $H \parallel \epsilon$ and $H \perp \epsilon$. Figure 9 shows the attenuation when the plane of polarization was along [110]. Two features about the $H \perp \epsilon$ curve should be noticed. Firstly, the double-maximum and secondly the tremendous range over which the attenuation varies. This range is greater than 28 dB/cm for a modest change in H. Because the [001] axis is one of fourfold symmetry the $H \perp \epsilon$ and $H \parallel \epsilon$ cases represent the same electron orbits but these orbits lead to very different interactions with the two sound waves.

Figure 10 shows the attenuation vs. $1/H\lambda$ when the plane of polarization is kept parallel [100].

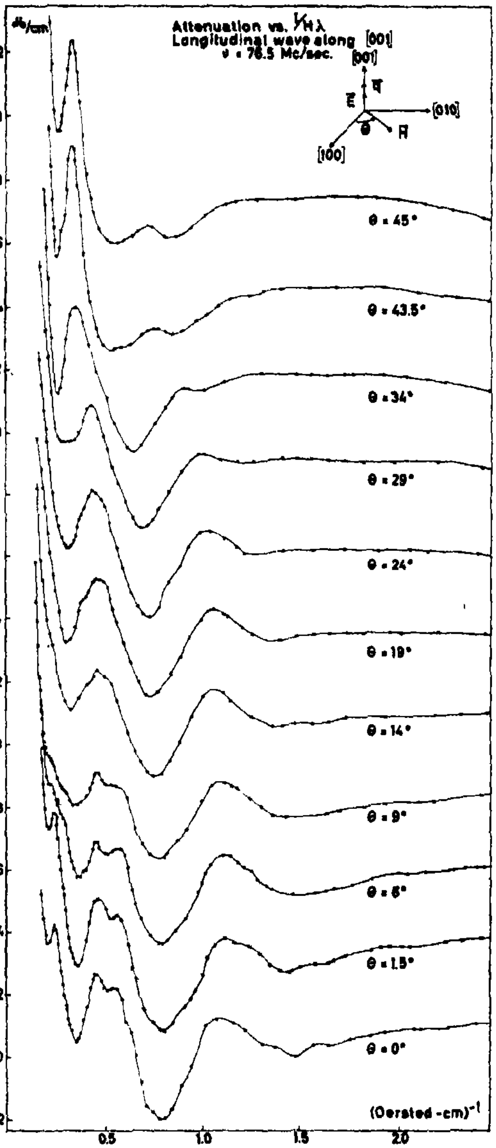

FIG. 7. Attenuation of a longitudinal wave propagating along [001] as a function of $1/H\lambda$ and field directions between [100] and [110]. All curves have been displaced by 2·5 dB/cm.

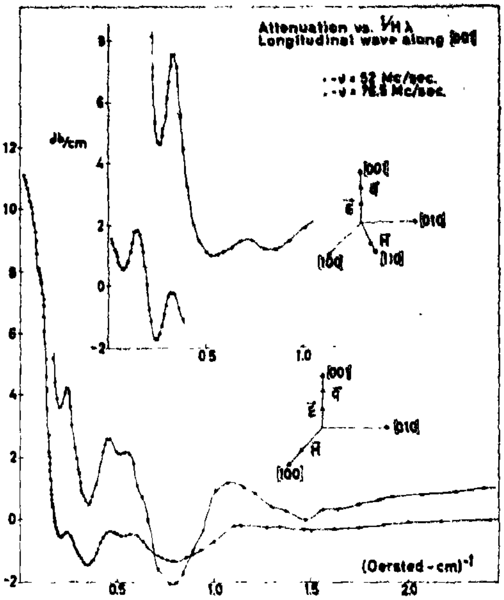

FIG. 8. Attenuation of a longitudinal wave propagating along [001] as a function of $1/H\lambda$ and with the field along [100] and [110]. The observations taken at $\nu = 52$ Mc/s reveal oscillations in the region of small $1/H\lambda$.

For free electrons the shear wave attenuation finally decreases to zero for increasing field intensity. However, this was not always so in tin, and the upper curve in Fig. 10 shows the opposite case. The increase continued down to the smallest, observable values of the parameter $1/H\lambda$.

Magnetoacoustic oscillations with **q** *along* [110]

Figure 11 shows the attenuation of a longitudinal wave propagating along [110], as a function of the field strength and of the field direction in the (110)-plane. For small values of $1/H\lambda$ at the higher frequencies the attenuation increased out of the measureable range and made this set of data less informative than desirable. An improvement could have been obtained by the use of a smaller pathlength. However, this meant impairing other faces on the sample, and therefore, it was necessary to run a similar set of measurements at lower frequencies to locate possible maxima for small values of $1/H\lambda$. This is illustrated in Fig. 12 for $H \| [001]$ and $H \| [\bar{1}10]$.

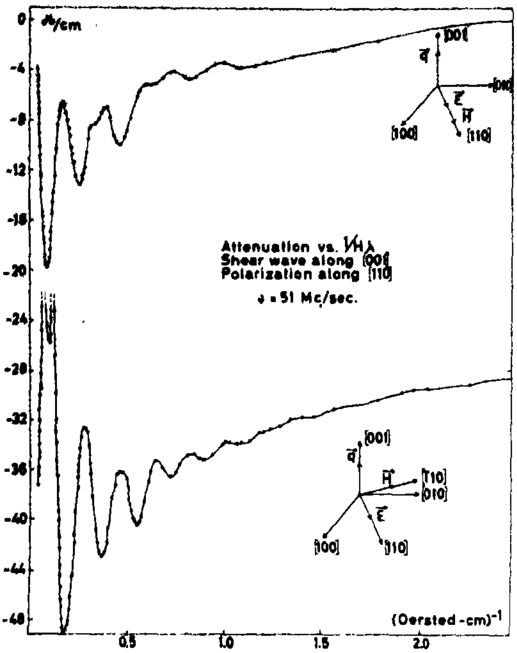

FIG. 9. Attenuation of shear waves propagating along [001] as a function of $1/H\lambda$. Plane of polarization along [110] and H along [110] and $[\bar{1}10]$. The lower curve has been displaced by -28 dB/cm.

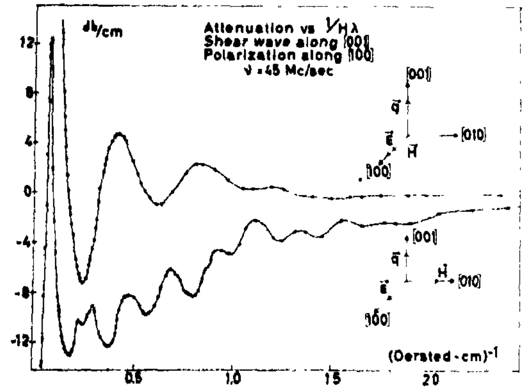

FIG. 10. Attenuation of shear waves propagating along [001] as a function of $1/H\lambda$. Plane of polarization along [100] and H along [100] and [010].

Shear waves were propagated along [110] with the plane of polarization along both [001] and $[\bar{1}10]$. In the latter case the attenuation at liquid helium temperatures for $H = 0$ was so large, that no trace of even the first echo could be detected at any frequency down to 10 Mc/s. Under the influence of a magnetic field the echoes appeared for the smallest values of $1/H\lambda$ that could be obtained, i.e. frequencies around 10 Mc/s and fields larger than 1000 Oe. However, no oscillations were found in the measurable range, but a decreasing attenuation with decreasing $1/H\lambda$ was observed both with $H \parallel \epsilon$ and $H \perp \epsilon$. A somewhat smaller zero field attenuation was encountered when the plane of polarization was along [001]. But only for the lowest obtainable frequencies could the attenuation be measured in the whole range from zero field to $H = 6500$ Oe.

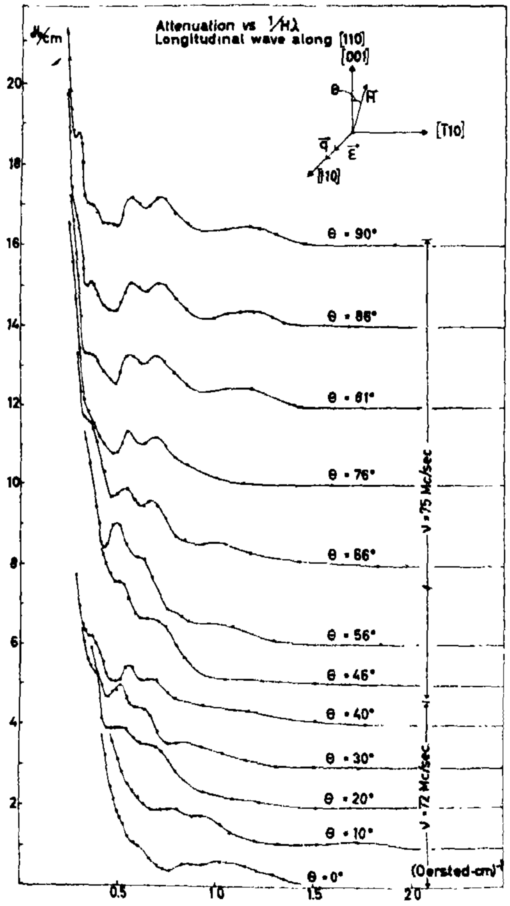

FIG. 11. Attenuation of longitudinal waves propagating along [110] as a function of $1/H\lambda$ and field direction in the (110) plane. The curves for $\theta = 0°$, 10°, 20°, 30°, 40°, 46°, and 56° are separated by 1 dB/cm and the remaining by 2 dB/cm.

No oscillations could be observed in this experiment either. However, as observed for $\epsilon \| [\bar{1}10]$ the attenuation for $\epsilon \| [001]$ also showed a tendency for decrease when $1/H\lambda$ decreased, both when $H \| \epsilon$ and when $H \perp \epsilon$.

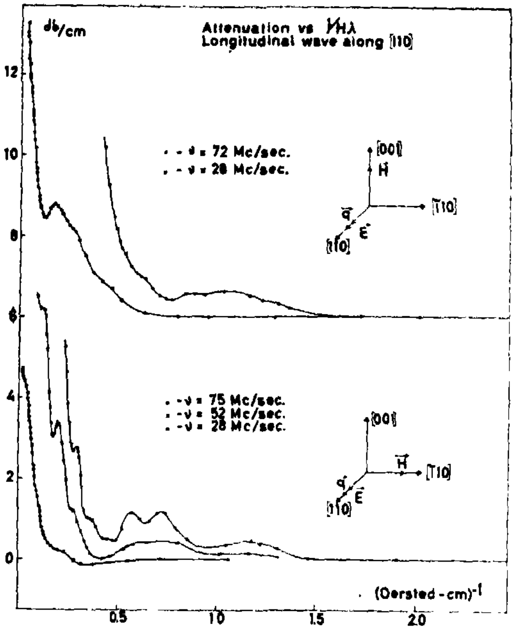

FIG. 12. Attenuation of longitudinal waves propagating along [110] as a function of $1/H\lambda$ and with the field along [001] and $[\bar{1}10]$. The observations taken at lower frequencies reveal oscillations in the region of small $1/H\lambda$.

Magnetoacoustic oscillations with q *along* $[\phi = 18°, \psi = 90°]$

Figure 13 shows the attenuation of a longitudinal wave propagated in the (001) plane 18° off the [100]-axis as function of the strength and the direction of a perpendicular field. No shear wave measurements were done along this direction.

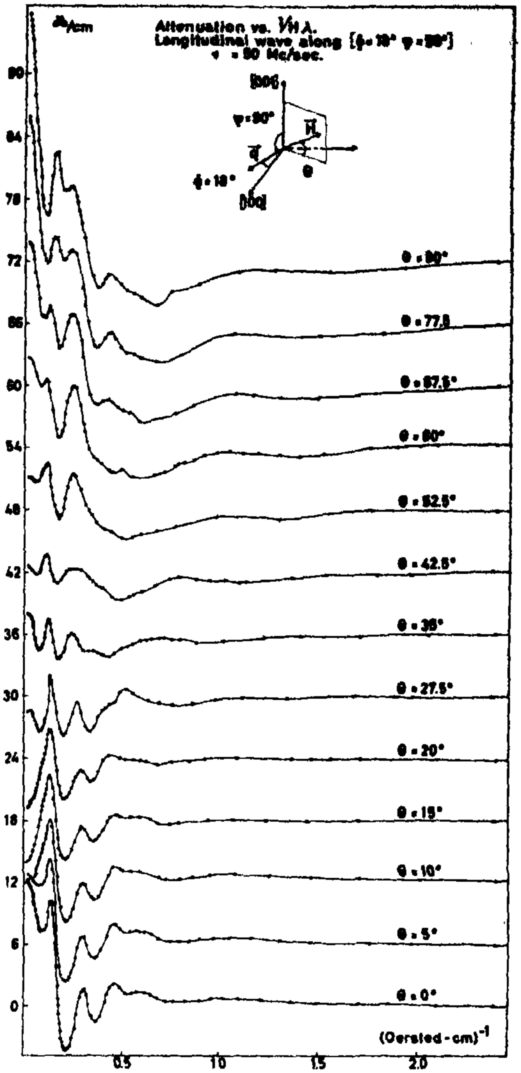

FIG. 13. Attenuation of longitudinal waves propagating in the (001)-plane 18° off the [100]-axis as a function of $1/H\lambda$ and the direction of a perpendicular field. All curves have been displaced by 4 dB/cm.

High field attenuation

From Figs 3, 4, 7, 8, 11, 12, and 13, all showing the attenuation of longitudinal soundwaves in a perpendicular field, it is clear that superimposed on the oscillatory behavior is an increase in the attenuation with increasing magnetic field. This high field attenuation reached a saturation value that usually was larger than the attenuation in the absence of a magnetic field. However, for the smallest values of ql_e the attenuation when $H \to \infty$ could be lower than in zero field. This has also been observed by GALKIN *et al.*,(10) and is easily understood if one plots $\alpha(H)/\alpha'$ vs. ql_e, where $\alpha(H)$ is the total electronic attenuation in a high field. We have done this in a separate paper,(28) and we found that all investigated directions of sound propagation and field directions gave straight lines on such plots. This proves that $\alpha(H)$ is proportional to $q^2 l_e$. However, the magnitude of the saturation values, and hence the slopes of the $\alpha(H)/\alpha'$-lines, vary drastically with direction of the field. Since this must be due to the anisotropy of the electronic distribution, the high field attenuation represents another possible way to study the Fermi surface.

In Figs. 14, 15, 16 and 17 we have shown the saturation value of the attenuation for the four different directions of q vs. the direction of a perpendicular field of 6500 Oe. The attenuation in the absence of a field is set equal to zero in the Figs.

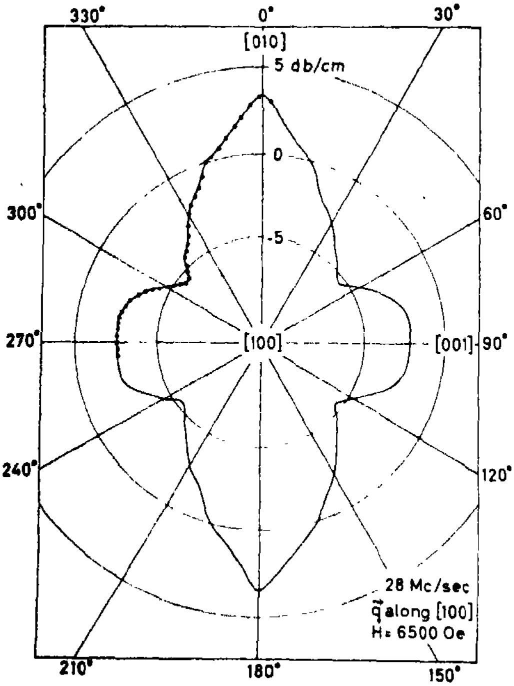

FIG. 14. The saturation value of the attenuation for q along [100] vs. the direction of the perpendicular field. The attenuation in the absence of a field is set equal to zero.

IV. INTERPRETATION OF THE EXPERIMENTAL RESULTS

The extremal momenta appearing in (2) can be calculated from the relation

$$k = e/2c\hbar P \tag{5}$$

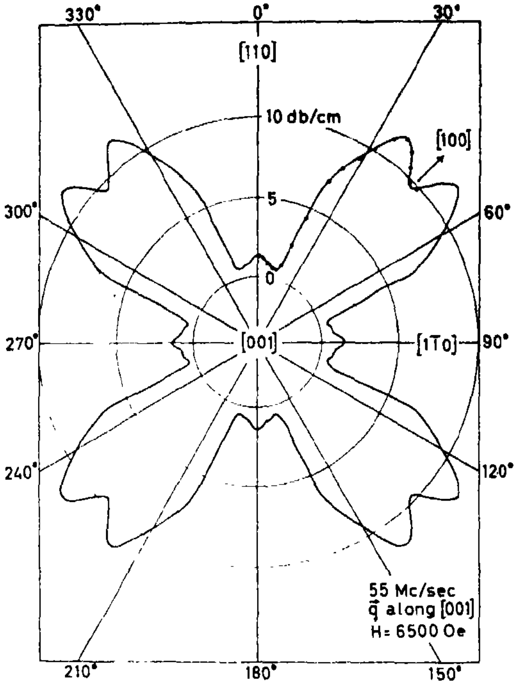

FIG. 15. The saturation value of the attenuation for q along [001] vs. the direction of the perpendicular field.

where P is the period in $1/H\lambda$. On the other hand PIPPARD(23) found that all orbits contribute to the oscillations, and consequently it is difficult to find the dominating momentum. However, GUREVITCH'(21) very simple result seems to be supported by magnetoacoustic work in metals where the Fermi surface also can be determined by other experimental methods.(9) We will, therefore, tentatively use (5) to calculate the momenta and consider it safe to assume the outcoming values to be reasonable first approximations of the actual Fermi momenta.

It is evident from Figs. 3–13 that the electronic distribution in tin is very anisotropic. Maxima from several different periods interfere with each other, so that the grouping of some of the maxima becomes ambiguous. However, up to seven or eight maxima of some periods have been observed. In this case the magnitude of the corresponding momentum can most accurately be calculated by plotting the $1/H\lambda$-values of the maxima vs. their number. The slope of the outcoming straight line gives the momentum. Some such plots have been shown in Fig. 18. From such plots it should also be possible to find the phasefactor in (2) and (3).

The most interesting oscillatory behavior was found when $q \| [100]$, and longitudinal waves yielded a particularly strong oscillation when the field was along or ± within 30° off the [001]-axis (Fig. 3). The maxima number vs. $1/H\lambda$ for this period is shown in Fig. 18, and the plot gives $k = 0{\cdot}45 \cdot 10^{8}$ cm^{-1} when $H \| [001]$. Another strong oscillation appeared when the field approached [010] and from Fig. 18 we get $k = 0{\cdot}49 \cdot 10^{8}$ cm^{-1} when $H \| [010]$.

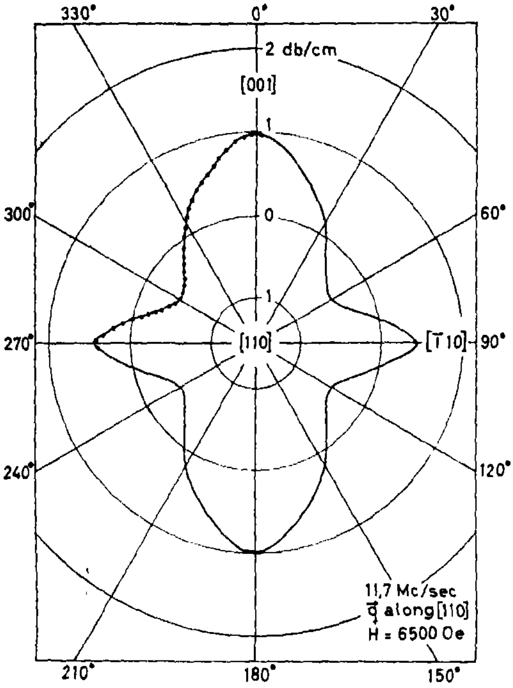

FIG. 16. The saturation value of the attenuation for q along [110] vs. the direction of the perpendicular field.

But it is clear from Fig. 3 that other than the two above mentioned periods are present. These are: one with a very low period and one interfering with the two first maxima of the main period when $H \| [001]$, and finally one with a very low period when $H \| [010]$. It is not possible to make plots like Fig. 18 from these periods, and the momenta had to be calculated from the location of one or two maxima alone. Therefore, large

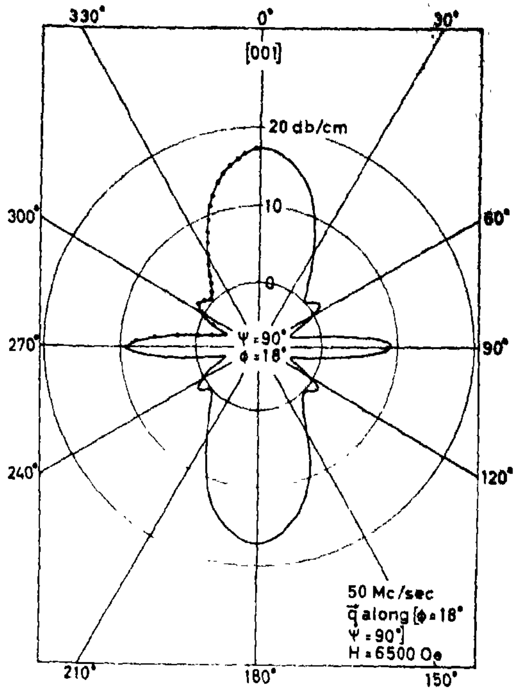

FIG. 17. The saturation value of the attenuation for q in the (001)-plane 18° off the [100]-direction vs. the direction of the perpendicular field.

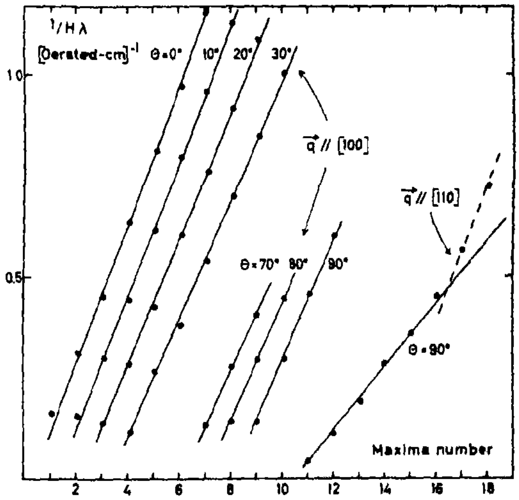

FIG. 18. Values of $1/H\lambda$ for successive maxima. The lines have been displaced in the interest of clarity.

uncertainties are attached to the k-values. Another source for errors exists when only one maximum is observable. Namely, the possibility of attaching the wrong number to the observed maximum.

In Section I of Fig. 19 we have plotted the momenta found with $q \| [100]$ i.e. momenta in the (100)-plane of the reciprocal space. In order to distinguish between those momenta that can be calculated from plots like Fig. 18 and the more uncertain ones, we have drawn smooth curves through the former. As can be seen from Figs. 5 and 6, shear waves yield the same periods, although with slightly different values of the momenta. We have plotted these momenta in Fig. 19. It should be noted that the magnitude of the low periods are uncertain.

We have marked the different branches of the momenta in Section I of Fig. 19 with letters from a to e, and it is interesting to note that the observations taken when q was 18° off the [100]-axis in the (001) plane (Fig. 13), give a similar system of branches. These are plotted in Section IV of Fig. 19 and marked correspondingly a' to e'.

As can be seen from Figs. 7 and 8, longitudinal waves propagating along [001] yield a considerably more complex oscillatory behavior and the interpretation is difficult. However, when $H \| [100]$ two maxima of a low period ($k = 0{\cdot}14 \cdot 10^8\ \mathrm{cm}^{-1}$) can be detected and superimposed on this is a relatively rapid period giving $k = 0{\cdot}71 \cdot 10^8\ \mathrm{cm}^{-1}$. This latter period (branch g in Section II of Fig. 19) disappears when H is turned more than

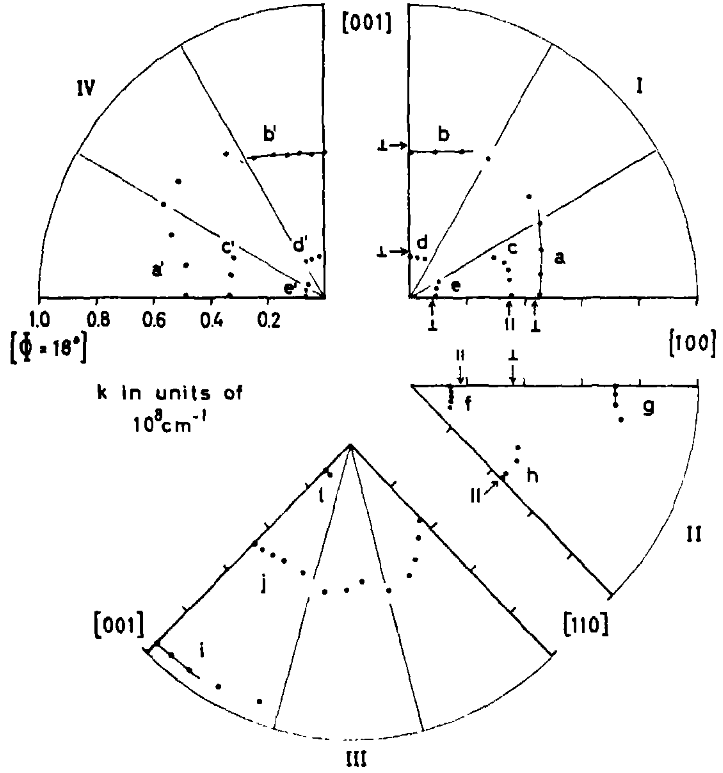

FIG. 19. Momenta calculated from the oscillations. In Sections I, II, and III the direction of sound propagation was along [100], [001], and [110], respectively and in Section IV along a direction in the (001)-plane 18° off the [100]-direction. Smooth curves have been drawn through the momenta that can be determined from plots like Fig. 18. Momenta found with shear waves are marked ∥ and ⊥ for H parallel and perpendicular ϵ respectively.

10° away from [100]. The low period (*f* in Section II of Fig. 19) might possibly exist for all directions of H, but it cannot be separated from the other oscillations. When $H \| [110]$ or within 15° off this direction, two maxima from another period can be observed. The corresponding momentum has been marked h in Fig. 19.*

The case $\epsilon \| [100]$ in Fig. 10 gives $k = 0{\cdot}18 \cdot 10^8$ cm^{-1} and $k = 0{\cdot}36 \cdot 10^8$ cm^{-1} with $H \| \epsilon$ and $H \perp \epsilon$ respectively. Furthermore, some very feeble oscillations belonging to a large momentum can be seen. It is estimated that this momentum is close to $1{\cdot}1 \cdot 10^8$ cm^{-1}. The case $\epsilon \| [110]$ yields $k = 0{\cdot}42 \cdot 10^8$ cm^{-1} both when $H \perp \epsilon$ and $H \| \epsilon$. However, in the first case with the phase factor $\frac{1}{2}$ and in the latter case approximately zero. A very feeble period appears when $H \| \epsilon$ in Fig. 9 but no momentum can be deduced. The sharp second maximum on the lower curve in Fig. 9 might be an open orbit resonance of the type reported by Gavenda and Deaton,$^{(11)}$ but the $1/H\lambda$ value of the maximum is somewhat higher than expected.

As can be seen from Figs. 11 and 12 a particularly complicated oscillatory behavior appeared when $q \| [110]$. When $H \| [1\bar{1}0]$ a high period giving a momentum $k = 0{\cdot}95 \cdot 10^8$ cm^{-1}, can easily be observed, as illustrated in Fig. 18. This period can be traced as long as H is less than 10° off $[1\bar{1}0]$ but disappears rapidly for larger angles. We have called this branch of the momentum i in Section III of Fig. 19. Figure 18 also shows the two maxima previously$^{(9)}$ interpreted as a "double"-maximum, i.e. the first maxima of two closely spaced momenta. However, a more careful study of the data seems to favour a different interpretation as indicated in Fig. 18. Here we have considered the two maxima as belonging to the same period, and this gives a momentum of approximately $0{\cdot}47 \cdot 10^8$ cm^{-1}. Furthermore, the shapes of the $\theta = 90°$ curves in Figs. 11 and 12 indicate that these two maxima are superimposed on the first maximum of a very low period ($k = 0{\cdot}12 \cdot 10^8$ cm^{-1}). The latter period (branch e in Fig. 19) disappears when H is turned away from $[1\bar{1}0]$, but the "double" maximum can be followed for all directions of the field. A very anisotropic branch in the momentum plot results (branch j in Fig. 19). However, the interpretation is rather ambiguous.

The different theoretical treatments of the high field attenuation of longitudinal waves differ essentially on some points. According to Pippard$^{(23)}$ open orbits, contrary to closed ones, could cause the attenuation to increase with H^2 at high fields. On the other hand, Kaner$^{(22)}$ found that open and closed orbits lead to the same kind of attenuation dependence in high fields, i.e. a saturation proportional to $q^2 l_e$. This work gave the result that the high field attenuation reached a saturation value for all the investigated directions of the field. According to other measurements of the Fermi surface in tin$^{(10)}$ some of the field directions we have used should cause open orbits, and we therefore take Kaner's approach to be a better description of the high field phenomena. However, all theoretical approaches give extremely cumbersome expressions for $\alpha(H)$, and the amount of information that can be drawn from the Figs. 14, 15, 16, and 17 is limited. But following Kaner,$^{(22)}$ some qualitative statements can be made from these plots. Whenever the angle between q and a direction of open orbits is of the order $1/ql_e$ one should expect large changes in $\alpha(H)$ with a small change in the angle. As can be seen from Figs. 14–17 several regions with rapidly changing $\alpha(H)$ were observed, the most spectacular case being the one with $q \| [001]$ (Fig. 15) and H approximately 20° off [110]. These regions can then be interpreted as directions where the types of orbit change drastically and this should be helpful in a topological study of the Fermi surface. In agreement with such a viewpoint one finds that the oscillatory effect is particularly complex for the same directions of the field.

Using the obtained values of A_q listed in Table 2 together with (4) we can make a few general statements about the Fermi surface. The large value of A_q found when $q \| [100]$ indicate that the extremal areas of the surface with respect to this direction should have a relatively high density of states. The opposite can be said about the extremal sections with respect to the [110]-axis.

It is obvious that the magnetoacoustic effect represents a powerful tool in the study of Fermi surfaces, but it is not possible to deduce unambiguously a model of the surface from such measurements, and especially not in a complicated metal like tin. However, Sections I and IV of Fig. 19 show that important features of the Fermi surface can be deduced from this type of experiments if one propagates the sound along directions not too widely spaced. We see that turning the field 18° off [100] in the (001) plane does not create principally new electron orbits, and this fact throws light on the topology of the Fermi surface.

---

* It should be noted that the axes [100] and [110] have erroneously been interchanged in Section II of Fig. 5 p. 242 in Ref. (9).

The Fermi surface of tin

On the basis of our measurements, supplemented by other published data and available theories, we shall suggest a shape of the Fermi surface in tin.

The primitive Brillouin zone (Fig. 1), contains one electron per atom. The surface of a sphere accommodating the four electrons of tin will have a radius of $1{\cdot}64 \cdot 10^8$ cm^{-1} and hence enclose completely the first zone. Therefore, the Fermi surface must lie entirely in higher zones in the extended zone scheme. The simplest way to construct the Fermi surface in the reduced zone scheme is the method given by HARRISON.(31) GOLD and PRIESTLEY(32) have done this and Fig. 20 shows the result when all sharp corners have been rounded off. Taking the X-ray structure factor into consideration they suggest that the second zone is full, that the sixth is empty, and that the "intersecting pancake" surface in the fifth zone might be absent. The extremal portions of the resulting modified free electron surface, on which it should be possible to shed light by ultrasonic observations, are $4(a)\eta$, 3γ, $4(b)\xi$, and $5\xi'$ with the field along [100], and when $H \| [110]$ the orbits 3ϵ and $4(a)\epsilon'$. The electron orbits 3δ, $4(a)\zeta$, 5σ, and 5μ should appear when the field is along the tetragonal axis.

Some points of agreement can be found when the momenta in Fig. 19 are compared with the above orbits. The strong oscillation found when $q \| [100]$ and $H \| [001]$, is most likely, caused by the orbit $4(a)\zeta$ and hence the calculated momentum of $k = 0{\cdot}45 \cdot 10^8$ cm^{-1} is the distance from the point L toward the center of the zone, i.e. to the intersection between $4(a)\zeta$ and η. By the same argument branch *a* in Fig. 19 sect. I is part of the extremal section $4(a)\eta$ as measured from L. We interpret branch *b* (Fig. 19 Section I) as caused by electrons orbiting around the extremal section $4(a)\eta$ since it appears when $H \| [010]$ and $q \| [100]$. This means that the orbit $4(a)\eta$ will be given approximately by the free electron model close to ζ, but that it has to be modified close to the [001]-axis where it will pass below W instead of above. In Fig. 21 is drawn a cut through the [001]- and [100]-axes showing the section η

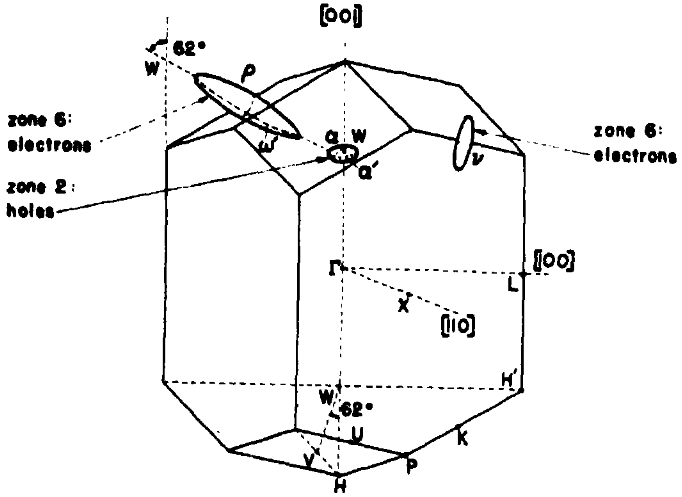

FIG. 20 (a)

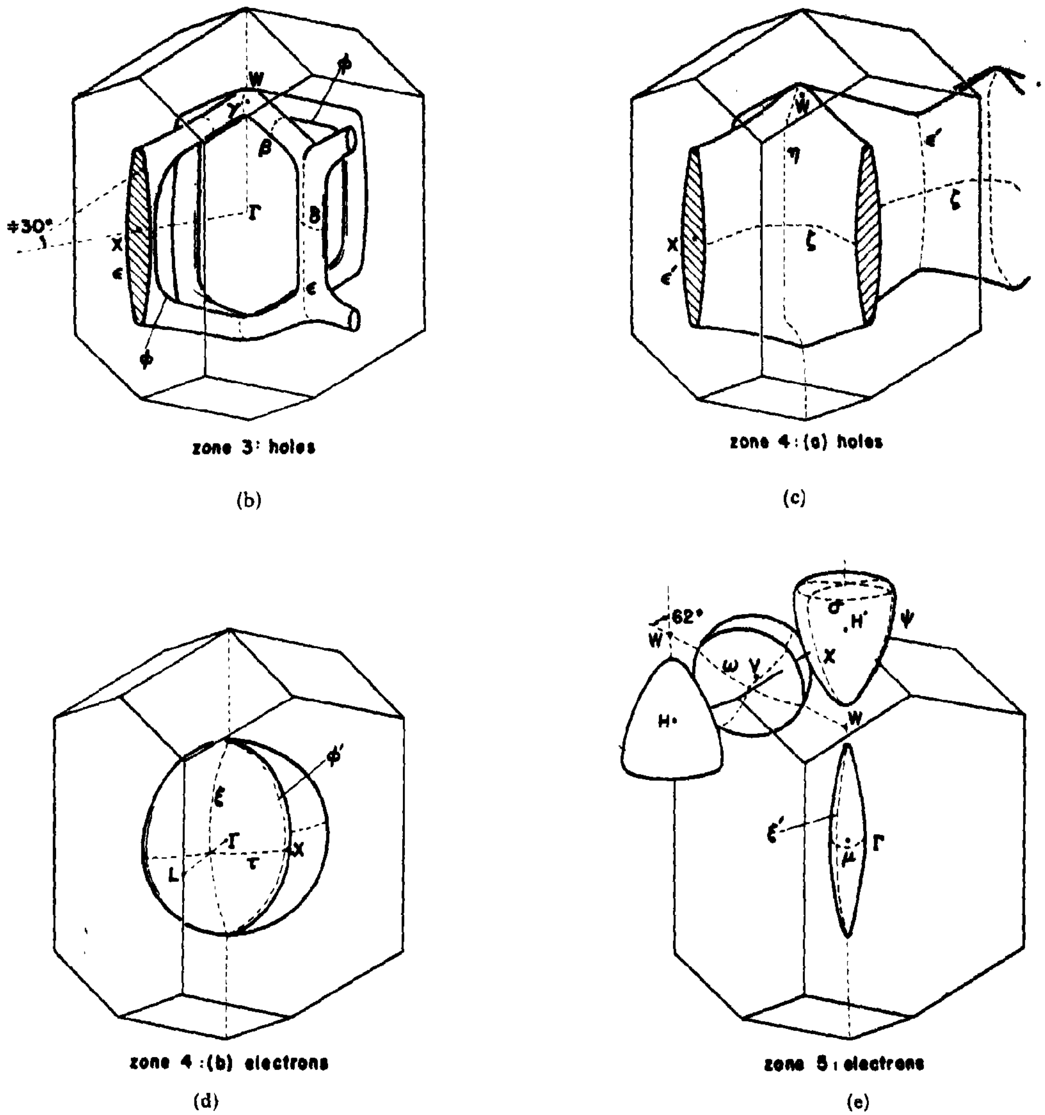

FIG. 20. The free electron Fermi surface in the reduced zone scheme (after Gold and Priestley).

in zone 4. The shaded areas indicate the parts of the zone filled with electrons.

The orbit $4(a)\eta$ should also give oscillations when $H \| [100]$ and $q \| [001]$, but now with a period corresponding to the distance from the center (Γ) of the zone. We interprete branch g as this momentum. This interpretation is supported by the fact that within the experimental error we have

$$k_a + k_g \sim L\Gamma$$

Figure 19 shows that along [110] we have

$$k_f + k_h \sim LX$$

We can now use these two equations to make a plot of the orbit ζ in zone 4(a), and this is shown in Fig. 21. The shaded areas indicate those parts filled with electrons.

An important observation concerning open orbits can be made from Fig. 21. The connectivity and the surface is such that a broad band of open orbits appear when $H \| [110]$ and a narrow band when $H \| [100]$. This is in correspondence with the high field attenuation plot in Fig. 15, and with the possible occurence of an open orbit resonance when $H \| [\bar{1}10]$ and $q \| [001]$ as in Fig. 9.

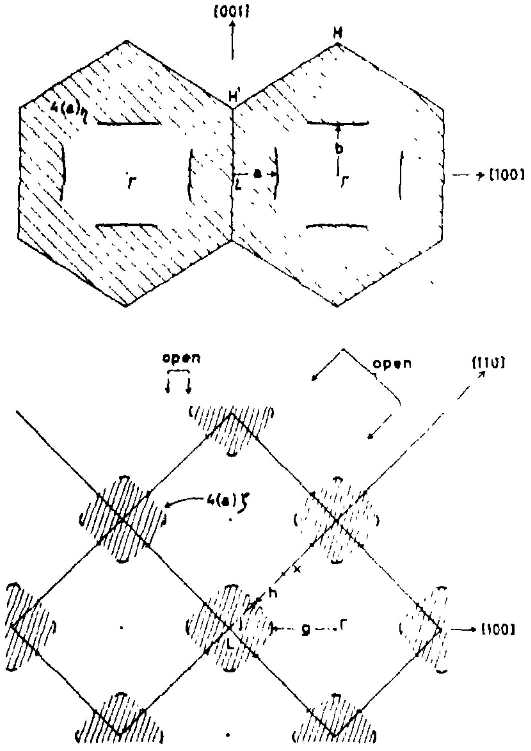

FIG. 21. Cut through the [001] and [100] axes and through the [100] and [110] axes of the hole surface in zone 4. Open directions occur along [110] and along [100]. Shaded areas are filled with electrons.

Furthermore, Fig. 19 Section III strongly suggests that branch j close to [001] gives the dimension of orbit 4 (a) ϵ' in this direction. But out of the remaining branches in Fig. 19 none can be unambiguously interpreted through the free electron model. Tentatively we may attribute the branches c and d to the surface in zone 4 (b). However, several interpretations exist for the branches e, f, and l. They can be extremal sections on some of the many pockets suggested by the free electron model. But branch l and possibly also branch d, can be attributed to the open orbits for $H \| [100]$ and $H \| [110]$, i.e. they represent $(k_{\max} - k_{\min})$ on such orbits. Finally, we suggest that branch i could be due to the hole surface in zone 3, but nothing definite can be said.

GALKIN *et al.*(10) have also studied magnetoacoustic effects in tin and two of the four directions of propagation, that they have used coincide with this investigation i.e. $q \| [001]$ and $q \| [110]$. In the former case they find only one period yielding the momenta $0 \cdot 1 \cdot 10^8\ \text{cm}^{-1}$ and $0 \cdot 15 \cdot 10^8\ \text{cm}^{-1}$ along [100] and [110] respectively. We identify this period as our branch f in Fig. 19. With $q \| [110]$ GALKIN *et al.* found two periods, one with a momentum of $0 \cdot 5 \cdot 10^8\ \text{cm}^{-1}$ along [001] and one considerably smaller. We suggest that these two momenta are identical with our branches j and l. The fact that they observe fewer and smaller momenta can be explained by the higher frequency they used. This could cause the higher momenta to be hidden by the high field attenuation. The authors report a new type of oscillatory behavior when the sound was propagated along two directions of low symmetry. They attribute these oscillations to the open orbits and conclude that tin has open orbits along [110] and that the dimensions of the open surface are given by the momenta mentioned above. The work of GALKIN *et al.*(10) is, therefore, in agreement with this investigation. However, we feel that their conclusion about the dimensions of the open surface in the (001)-plane might be based on a wrong set of periods. The magnetoacoustic work of MACKINTOSH(33) suggests open orbits along [100] and [110], but no details are given.

ALEKSEEVSKII *et al.*(34,35) have studied the Fermi surface of tin from galvanomagnetic properties. They propose an open surface consisting of a plane net of corrugated cylinders with axes parallel [110] and [100]. The surface can also be looked upon as two corrugated planes jointed with tubular bridges. In their first paper, ALEKSEEVSKII *et al.*(34) suggested that the [100]-direction was the main direction of open orbits and that the [110]-direction was an additional one. However, in their last note(35) they corrected this and brought the proposed surface in correspondence with zone 4 (*a*) of the free electron model, i.e. they suggest the [110]-direction to be the principal direction of open orbits. Furthermore, they give the diameter of the bridges as approximately $1{\cdot}2 \cdot 10^{8}\ \mathrm{cm}^{-1}$ and the distance between the planes as $1{\cdot}1 \cdot 10^{8}\ \mathrm{cm}^{-1}$. We find this to be in good agreement with this investigation.

Gold and Priestley(32) have given a detailed study of the Fermi surface of tin through measurements of the de Haas–van Alphen effect. They found that the electronic distribution in tin has much the same complexity as that predicted by the free electron model. But they also found serious discrepancies in a detailed comparison. We can only make a quantitative comparison for the surface proposed in Fig. 21. From these plots the areas of the extremal orbits 4 (*a*) η and ζ can be evaluated approximately and hence compared with the de Haas–van Alphen periods. Good agreement is found between the area of the 4 (*a*) η orbit and the similar area given by Gold and Priestley. However, the orbit 4 (*a*) ζ in Fig. 21, having an area of approximately $4{\cdot}9 \cdot 10^{15}\ \mathrm{cm}^{-2}$, should correspond to a de Haas–van Alphen period of $1{\cdot}9 \cdot 10^{8}\ \mathrm{G}^{-1}$. Gold and Priestley found a period close to this value ($1{\cdot}8 \cdot 10^{8}\ \mathrm{G}^{-1}$), but they have suggested this to be orbit 5 σ. For orbit 4 (*a*) ζ they list $0{\cdot}88 \cdot 10^{-8}\ \mathrm{G}^{-1}$, but the topology of the surface in zone 4 (*a*) seems to favour our interpretation.

Khaikin(36) has recently investigated the Fermi surface of tin by a modified cyclotron resonance method. He points out that the momentum he deduces agrees with our branch *a* in Fig. 28 I, although he finds a somewhat larger numerical value. His interpretation of this momentum agrees with this investigation.

We conclude that tin has a full first Brillouin zone and that probably also the second zone is full. The higher zones all up to the sixth can contain parts of the total Fermi surface area. The hole surface in zone 4 can be described as two corrugated planes connected with tubular bridges as illustrated in Figs. 20 and 21. The main direction of open orbits is along [110], but the dimensions of the bridges are such that also the [100]-direction becomes open.

Furthermore, the free electron model seems to give a good idea of the complexity of the Fermi surface, but rather large deviations are to be expected. However, to speculate about the shape of the other parts of the surface, which quite obviously is complex, seems fruitless without more detailed experimental data and a better theoretical model.

Acknowledgements—The author is indebted to members of the low-temperature group at Brown University, and especially Professor R. W. Morse and Dr. J. D. Gavenda.

REFERENCES

1. Bömmel H. E., *Phys. Rev.* **100**, 758 (1955).
2. Morse R. W., Bohm H. V. and Gavenda J. D., *Phys. Rev.* **109**, 1394 (1958).
3. Reneker D. H., *Phys. Rev.* **115**, 303 (1959).
4. Morse R. W. and Gavenda J. D., *Phys. Rev. Letters* **2**, 250 (1959).
5. Galkin A. A. and Korolyuk A. P., *Zh. eksp. teor. fiz. S.S.S.R.* **36**, 1307 (1959); English translation. *Sov. Phys. JETP.* **9**, 925 (1959); *Zh. eksp. teor. fiz. S.S.S.R.*, **37**, 310 (1959); English translation. *Sov. Phys. JETP.* **10**, 219 (1960); *Zh. eksp. teor. fiz. S.S.S.R.* **33**, 1688 (1960); English translation. *Sov. Phys. JETP.* **11**, 1218 (1960).
6. Olsen T., *Phys. Rev.* **118**, 1007 (1960).
7. Roberts B. W., *Phys. Rev.* **119**, 1889 (1960).
8. Morse R. W., Myers A. and Walker C. T., *Phys. Rev. Letters* **4**, 605 (1960).
9. *The Fermi Surface* (edited by Harrison W. A. and Webb M. B.), Wiley, New York (1960).
10. Galkin A. A., Kaner E. A. and Korolyuk A. P., *Zh. eksp. teor. fiz. S.S.S.R.* **39**, 1517 (1960), English translation. *Sov. Phys. JETP.* **12**, 1055 (1961).
11. Gavenda J. D. and Deaton B. C., *Phys. Rev. Letters* **8**, 208 (1962).
12. Rayne J. A. and Chandrasekhar B. S., *Phys. Rev.* **125**, 1952 (1962).
13. Rayne J. A. and Sell H., *Phys. Rev. Letters* **8**, 199 (1962).
14. Olsen T., *Proceedings of the Third International Congress on Acoustics* (edited by Cremer L.) p. 578. Elsevier, Amsterdam (1961).
15. Pippard A. B., *Phil. Mag.* **46**, 1104 (1955).
16. Kjeldaas T. and Holstein T., *Phys. Rev. Letters* **2**, 340 (1959).
17. Cohen M. H., Harrison M. J. and Harrison W. A., *Phys. Rev.* **117**, 937 (1960).
18. Skobov V. G., *Zh. eksp. teor. fiz. S.S.S.R.* **40**, 1446 (1961); English translation. *Sov. Phys. JETP.* **13**, 1014 (1961).
19. Zyryanov P. S., *Zh. eksp. teor. fiz. S.S.S.R.* **40**, 1353 (1961); English translation. *Sov. Phys. JETP.* **13**, 953 (1961).
20. Stolz H., *Phys. stat. sol.* **1**, 328 (1961).

21. Gurevich V. L., *Zh. eksp. teor. fiz. S.S.S.R.* **37,** 71 (1959); English translation. *Sov. Phys. JETP.* **10,** 51 (1960). *Zh. eksp. teor. fiz. S.S.S.R.* **37,** 1680 (1959); English translation. *Sov. Phys. JETP.* **10,** 1190 (1960).
22. Kaner E. A., *Zh. eksp. teor. fiz. S.S.S.R.* **33,** 212 (1960); English translation. *Sov. Phys. JETP* **11,** 154 (1960). *Zh. eksp. teor. fiz. S.S.S.R.* **39,** 1071 (1960); English translation. *Sov. Phys. JETP.* **12,** 747 (1961).
23. Pippard A. B., *Proc. Roy. Soc.* **A 257,** 165 (1960).
24. Rayne J. A. and Chandrasekhar B. S., *Phys. Rev.* **120,** 1658, (1960).
25. Morse R. W., *Progress in Cryogenics* **I,** Heywood, London (1959).
26. Chick B., Anderson G. and Truell R., *J. acoust. Soc. Amer.* **32,** 186 (1960).
27. Waterman P. C., *Phys. Rev.* **113,** 1240 (1959).
28. Olsen T., *J. Phys. Chem. Solids* **24,** 187 (1963).
29. Mason W. P. and Bömmel H. E., *J. acoust. Soc. Amer.* **28,** 930 (1956).
30. Morse R. W., Olsen T. and Gavenda J. D., *Phys. Rev. Letters* **3,** 15 (1959); *Erratum, ibid.* **3,** 193 (1959).
31. Harrison W. A., *Phys. Rev.* **118,** 1190 (1960).
32. Gold A. V. and Priestley M. G., *Phil. Mag.* **5,** 1089 (1960).
33. See Refs. 9 and 32.
34. Alekseevskii N. E., Gaidukov Yu. P., Lifshitz I. M. and Peschanskii V. G., *Zh. eksp. teor. fiz. S.S.S.R.* **39,** 1201 (1960); English translation. *Sov. Phys. JETP.* **12,** 837 (1961).
35. Alekseevskii N. E. and Gaidukov Yu. P., *Zh. eksp. teor. fiz. S.S.S.R.* **41,** 1079 (1961); English translation. *Sov. Phys. JETP.* **14,** 770 (1962).
36. Khaikin M. S., *Zh. eksp. teor. fiz. S.S.S.R.* **41,** 1772 (1961); English translation. *Sov. Phys. JETP.* **14,** 1260 (1962).
37. Love A. E. H., *A treatise on the Mathematical Theory of Elasticity,* Dover, New York (1944).

APPENDIX

Following Love(37) we can write the equation giving the velocity of a plane wave in an aeolotropic solid as

$$|\lambda_{ij} - \rho u^2 \delta_{ij}| = 0$$

where

$$\lambda_{ij} = c_{ik,jl} \cdot \alpha_k \alpha_l$$

Here $c_{ik,jl}$ is the elasticity tensor, and the direction cosines of the propagation vector are denoted by α_i. For a tetragonal crystal the nonzero λ_{ij} are:

$$\begin{aligned}
\lambda_{11} &= c_{11}\alpha_1^2 + c_{66}\alpha_2^2 + c_{44}\alpha_3^2 \\
\lambda_{22} &= c_{66}\alpha_1^2 + c_{11}\alpha_2^2 + c_{44}\alpha_3^2 \\
\lambda_{33} &= c_{44}(\alpha_1^2 + \alpha_2^2) + c_{33}\alpha_3^2 \\
\lambda_{12} &= (c_{12} + c_{66})\alpha_1\alpha_2 \\
\lambda_{23} &= (c_{13} + c_{44})\alpha_2\alpha_3 \\
\lambda_{31} &= (c_{13} + c_{44})\alpha_3\alpha_1
\end{aligned}$$

Here the 3-axis is along the *c*-axis and the 1- and 2-axes along the *a*-axes.

For a propagation direction 18° off the [100]-axis in the (001)-plane, we get the determinantal equation ($\alpha_3 = 0$, and $\alpha_1^2 + \alpha_2^2 = 1$).

$$\begin{vmatrix}
c_{11}\alpha_1^2 + c_{66}\alpha_2^2 - \rho u^2 & (c_{12} + c_{66})\alpha_1\alpha_2 & 0 \\
(c_{12} + c_{66})\alpha_1\alpha_2 & c_{66}\alpha_1^2 + c_{11}\alpha_2^2 - \rho u^2 & 0 \\
0 & 0 & c_{44} - \rho u^2
\end{vmatrix} = 0$$

This equation yields that a pure shear mode can be generated with $\boldsymbol{\epsilon} \| [001]$, corresponding to $\rho u^2 = c_{44}$. But the remaining two modes are quasi-shear and quasi-longitudinal with velocities given as

$$\begin{aligned}
\rho u^2 = \tfrac{1}{2}(c_{11} + c_{66}) \pm [\tfrac{1}{4}(c_{11} - c_{66})^2 \\
+ (c_{12}^2 + c_{66}c_{12} + 2c_{11}c_{66} - c_{11}^2)\alpha_1^2\alpha_2^2]^{1/2}
\end{aligned}$$

Using the elastic constants given by Rayne and Chandrasekhar(24) this equation gives a longitudinal velocity

$$u_L = 3 \cdot 48 \cdot 10^5 \text{ cm/sec}$$

This compares favourably with the observed value of $3 \cdot 40 \cdot 10^5$ cm/sec.

The particle motion for the quasi-longitudinal mode makes an angle β with the direction of propagation. This angle will be given by the equation

$$\operatorname{tg}[2(18° + \beta)] = \frac{2\lambda_{12}}{\lambda_{11} - \lambda_{22}} = \frac{2(c_{12} + c_{66})\alpha_1\alpha_2}{(c_{11} - c_{66})(\alpha_1^2 - \alpha_2^2)}$$

or $\beta \sim 6°$, and hence our mode is close to a pure longitudinal one.

J. Phys. Chem. Solids. Pergamon Press 1963. Vol. 24. pp. 667–669. Printed in Great Britain.

ORIGIN OF *F*-CENTERS IN X-RAY IRRADIATED NaCl CRYSTALS

M. GEUDEKE and W. G. BURGERS

Technological University, Laboratory for Physical Chemistry of the Solid State, Delft

(*Received* 14 *September* 1962; *revised* 23 *November* 1962)

Abstract—Etching of NaCl crystals X-ray irradiated at room temperature does not reveal a displacement of dislocation lines such as might be expected according to various mechanisms suggested in the literature for the generation of *F*-centers at dislocations.

RECENT experiments by CRAWFORD and YOUNG(1) do not support a theoretical suggestion by SEITZ,(2) according to which *F*-centers in alkalihalide crystals X-ray irradiated at low temperatures might be formed by "evaporation" (and subsequent ionization) of vacancies from dislocations. Crawford and Young showed for NaCl crystals irradiated with γ-rays that no displacement of the dislocation lines due to climb was observed. If present, it was in any case much less than what might be expected on the basis of Seitz' theory for the concentration of *F*-centers formed during the given exposure.

The position of the dislocation lines in these experiments was located by applying a "double etching" technique, in which a cleaved (100)-face was etched before and after irradiation. The NaCl crystal had been exposed to a flux of 10^6 r/hr from a Co^{60}-source at 40°C up to a maximum absorption detectable optically.

BAUER and GORDON(3) suggest that the negative result of Crawford and Young's experiment with the double etching technique might be caused by a pinning of the ends of the dislocations at the free surface by the first etching used. However, a result similar to that obtained by Crawford and Young was reached in the following experiments with crystals exposed to a strong flux of X-rays. In this case for the detection of a possible displacement use was made of the experimental fact that two matched cleavage faces show identical etch patterns, as first shown by GILMAN and JOHNSTON(4) for LiF crystals. One cleavage plane was etched whereas its "opposite" was exposed to X-rays from a Wo-tube (50 kV; 20 mA; $3 \cdot 10^4$ r/sec) for several hours and thereafter etched (reactive: 400 mg $HgCl_2$ and 200 mg $BaBr_2$ in a mixture of 100 cm^3 C_2H_5OH and 50 cm^3 CH_3OH: cf. MORAN(5)).

After such exposure the crystals were deepblue and completely opaque over a depth of several mm. Comparing the dislocation density in our crystals as shown by etching with that present in the crystals used by Crawford and Young, a displacement of the etch pits over at least 1–3 dia. might be expected on the basis of Seitz' mechanism. Figures 1 and 2 give examples of such pairs of corresponding etched cleavage faces. A comparison of two corresponding photographs does not give any indication of a displacement of the anticipated magnitude although in this case no double etching was applied. The only observable change concerns the size of the etch pits which is slightly reduced for the irradiated crystal, whereas its surface obtains a grainy appearance.

The question thus remains whether one must conclude from these results that dislocations do not play a major part in the production of *F*-centers on irradiation at room temperature. In the conception of *F*-center formation at room temperature given by VARLEY,(6) interstitially formed chlorine atoms may be trapped at dislocation jogs and so cause climb. Varley suggests that the negative evidence obtained in Crawford and Young's experiments, and now obtained again in the present investigation, may be due to a migration of interstitial atoms along the dislocation to the surface of the crystals, forming fresh layers as observed by HIBI and ISHIKAWA.(7) By such a process dislocation climb would not be observed at the surface, but might still take place inside the crystal.

If this were the cause of the non-displacement of the dislocations, it would mean that the migration extends deeper than the depth of an etch pit. We have at present no experimental evidence whether a still deeper etching would reveal a displacement. However, in Crawford and Young's experiments, the double etching technique used does not show such an effect. On the other hand the fact that the intensive coloration of the crystals goes hand in hand with a general roughening of the surface shows that structural changes have taken place in the surface region.

We wish to raise one other possibility in this connection. One might ask whether the visible etch pits reveal the complete dislocation pattern of the crystals.* Naturally, if only part of the dislocations were revealed by etching, the actual number would be larger and the mean displacement to be expected after formation of a definite number of F-centers correspondingly smaller.

The question of a one-to-one correspondence between etch pits and dislocations was raised in the researches of GILMAN and JOHNSTON(4) in lithium fluoride crystals and, on the basis of their experimental evidence, answered in the affirmative. It was found, however (GILMAN and JOHNSTON(8)), that different reagents could distinguish between dislocations present in the crystals as grown and dislocations introduced by plastic deformation. Also MENDELSON,(9) in experiments with rocksalt, affirmed the one-to-one correspondence. On the other hand etching experiments by BRIGHT and RIDGE(10) with gypsum give evidence that etch pits may reveal only a fraction of the dislocations cut by the surface.† However, it must be kept in mind that these observations refer to a structure very different from rocksalt. A deciding answer must be left open at the present.

Acknowledgement—One of the authors (M.G.) is indebted to the Delfts Hogeschoolfonds for the grant of a *stipendium*.

REFERENCES

1. SEITZ F., *Proceedings of the International Conference on Theoretical Physics, Kyoto-Tokyo* (1953), p. 839; *Rev. mod. Phys.* **26**, 7 (1954).
2. CRAWFORD Jr., J. H. and YOUNG Jr., F. W., *J. appl. Phys.* **31**, 1688 (1960).
3. BAUER CH. L. and GORDON R. B., *Phys. Rev.* **126**, 73 (1962).
4. GILMAN J. J. and JOHNSTON W. G., *J. appl. Phys.* **27**, 1018 (1956).
5. MORAN P.R., *J. appl. Phys.* **29**, 1768 (1958).
6. VARLEY J. H. O., *J. Phys. Chem. Solids* **23**, 985 (1962).
7. HIBI T. and ISHIKAWA K., *J. phys. Soc. Japan* **13**, 709 (1958).
8. GILMAN J. J. and JOHNSTON W. G., *Dislocations and Mechanical Properties of Metals*, p. **116**. Wiley, New York (1957).
9. MENDELSON S., *J. appl. Phys.* **32**, 1579 (1961).
10. BRIGHT J. E. and RIDGE M. J., *Phil. Mag.* **6**, 441 (1961).

---

* We are indebted to F. W. SCHAPINK from the Koninklijke/Shell Laboratory at Amsterdam for bringing this possibility to our attention.

† Note added in proof: A similar conclusion can be drawn from a recent paper by A. W. RUFF JR. (*J. appl. Phys.* **33**, 3392 (1962)) for thin copper crystals.

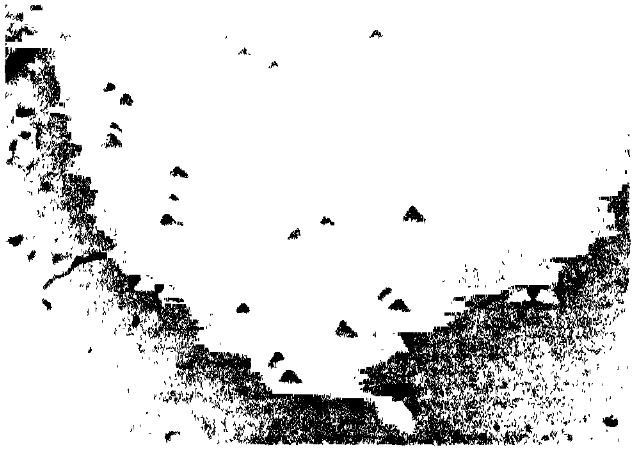

(a)

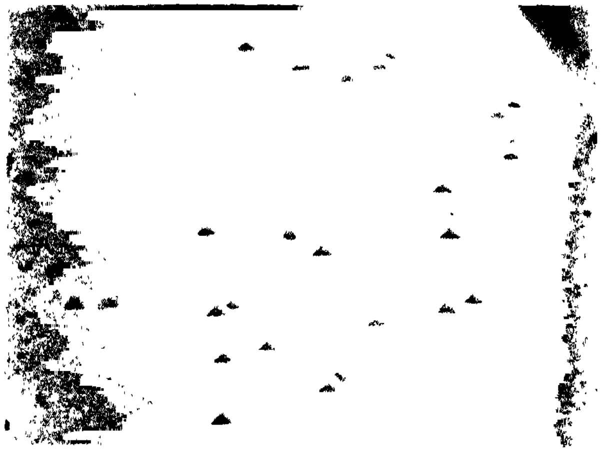

(b)

FIG. 1. NaCl crystal. Opposite (100) cleavage planes. ×360. (a) etched, not exposed to X-rays. (b) etched after intensive X-ray irradiation.

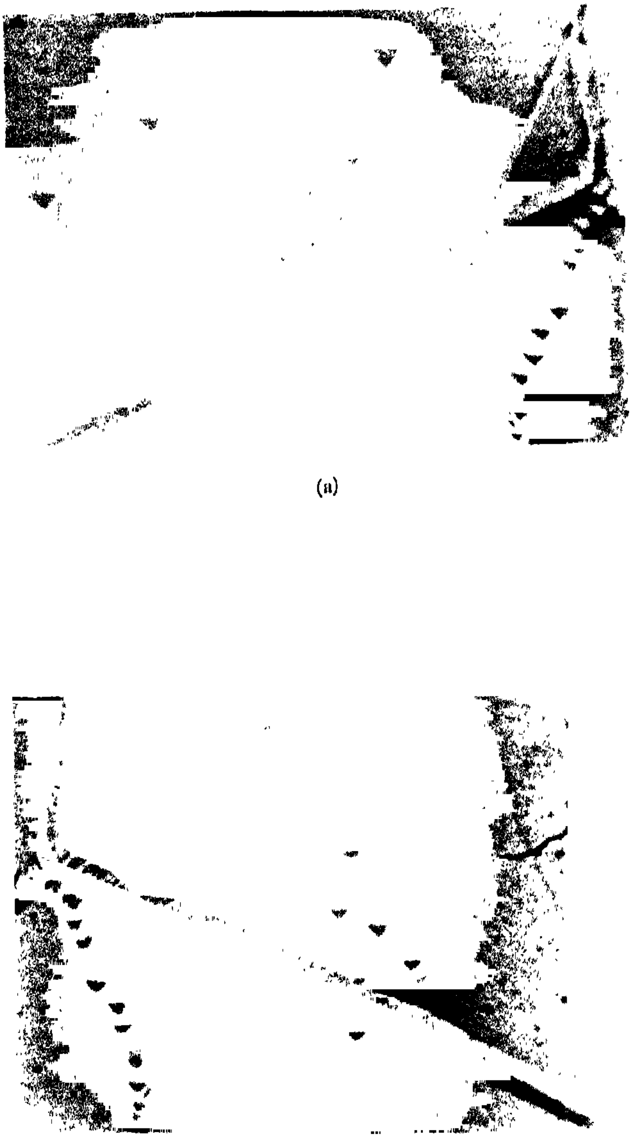

(a)

(b)

Fig. 2. NaCl crystal. Opposite (100) cleavage planes. ×360. (a) etched, not exposed to X-rays. (b) etched after intensive X-ray irradiation.

J. Phys. Chem. Solids Pergamon Press 1963. Vol. 24, pp. 669–679. Printed in Great Britain.

SOME EFFECTS OF A PERTURBATION IN A LATTICE ON THE NORMAL MODES*

T. N. CASSELMAN and JORDAN J. MARKHAM

Physics Division, Armour Research Foundation, Chicago, Illinois

(*Received* 2 *March* 1962; *revised* 17 *September* 1962)

Abstract—A one-dimensional, monatomic chain with an isotopic defect at the center has been considered. The effect of the defect on the crystalline modes has been calculated. It is shown that small changes in the frequencies of the crystalline modes make the most important contributions to the ion displacements near the defect. It is shown that the broadening of the absorption line can be calculated independently of the knowledge of the normal modes as long as an effective frequency approximation can be made. As an illustration of the effect of the defect on the crystalline modes, the broadening for several isotopic defects has been calculated. The several bands of modes which contribute to the broadening are shown and it is pointed out how the position of these bands on the spectrum is strongly dependent on the mass of the defect.

1. INTRODUCTION

POINT imperfections in a lattice cause perturbations to the modes of vibration. The most dramatic effect is the appearance of local modes whose frequencies lie in the forbidden bands. These modes undergo a complete change in character, becoming damped and non-propagating.(1) In addition, the frequencies of the crystal modes are shifted an infinitesimal amount.(2) Finally, the effect of the crystal modes on the displacement of a given atom (or ion) is perturbed. If the atom is some distance from the imperfection, the change is very small, and of no importance; however, near the imperfection, the change can be large and of major importance. This last effect is not the same as the first since it occurs even when no local modes are produced. For reasons to appear later, we shall refer to this as the "eigenvector" effect.(3)

For long-range effects, all three items are of little importance. Thus, for an electron in the conduction band, if self-trapping is ignored, the elementary treatment of the normal modes is meaningful. Measurements of the mobility of long wavelength electrons in the conduction band give an excellent agreement with the elementary treatment of this problem.(4) For short-range effects, the perturbation of crystal mode frequencies is of little importance, but the local modes and the eigenvector effect must be taken into account.

Traditionally, one has divided the modes in a crystal into two groups—"local" and "crystal". For problems which involve short-range forces, one must include the eigenvector effect. This is true for the broadening associated with the *F*-center, for calculations of the interaction of the exciton with the lattice, and certainly for a tightly bound polaron. This means that one has to make a much more refined calculation than has been made so far in many problems. We shall indicate that some of our ideas regarding normal modes apply only to a limited class of problems and not to every case of interest. One of these is the boundary condition on the chain.

Unfortunately complete calculations on realistic models of a lattice with an imperfection are extremely involved and so far have not been done, except in a formalistic manner. During the last 50 years, physicists have carried through calculations on unrealistic models hoping to gain some insight into the physical properties of phonons and

---

* Research supported by the Atomic Energy Commission.

phonon–electron interactions. Calculations on phonons associated with a linear chain in general do not apply to a solid, unless modified. Consider for a moment a Debye solid and the distribution function $d(\nu)\Delta\nu$, i.e. the number of modes between ν and $\nu+\Delta\nu$. For a solid, it is proportional to ν^2; for a vibrating square membrane it is proportional to ν, while for a string it is a constant. Since the physical properties many times involve a function of ν, to obtain a realistic calculation, one must modify the results on simple models. This paper is no exception to this rule, and this explains why some modifications have been made which at first sight seem unrealistic. We believe, however, that these calculations give a basic insight into some phonon problems of major importance which at present are not understood.

An example of a model which lacks realism is found in the recent paper of ROSENSTOCK and KLICK[5] who calculated the relative displacement of the next-nearest ion in a linear chain. To handle the problem, these authors had to assume an extremely simple geometry which in reality can only apply to a "forbidden" transition. This permitted them to ignore completely the eigenvector effect, the major topic of this paper. The eigenvector problem would be of major import if these authors varied the spring constant (our α, see Part II). In any realistic case we know that the spring constant near the defect varies and that the F-band is due to an allowed transition. They also did not consider the fact that the high frequency modes have to be weighted more heavily than the low frequency modes if one is to obtain a "realistic picture" which applies to a three dimensional solid. The authors of this paper do not mean this as a criticism of the work of Rosenstock and Klick, rather as a statement of the difficulties in making progress in this field and as an "explanation" of the assumptions we have made to gain an insight into the eigenvector problem.

BJORK and KRUMHANSL[6] have developed a theorem regarding the relative magnitude of the eigenvectors associated with the local and crystal modes. Their arguments were very general and apply to actual solids. They do not, however, apply to the actual displacement as we shall show and can not be related simply to the concept of a configurational coordinate.

In this paper, we shall study the eigenvector effect by making detailed calculations on a one-dimensional linear chain in which there is an isotopic mass defect at the center. As an illustration, we shall calculate the broadening of the optical absorption associated with a "one dimensional F-center". This is a completely fictitious problem and is employed simply as an example. In this calculation, we shall be forced to modify some of the equations relating to the broadening of optical absorption lines. In this regard, it is an extension of the treatment which has recently been published[7] (referred to as M). It is useful to formulate this problem in its most general form, i.e. in terms of the normal modes. Actual calculations require that one considers the true displacement of the atoms. We shall also indicate why the configurational coordinate model works in practice, although it does not seem to have a good theoretical foundation.

2. THE DYNAMICAL PROBLEM

Consider a one-dimensional chain of $2N+1$ particles fixed at both ends, i.e. only $2N-1$ degrees of freedom. We place an isotopic impurity at the center, see Fig. 1. The appropriate equations of motion are:

$$m\frac{d^2}{dt^2}u_l = \alpha[u_{l+1}-2u_l+u_{l-1}] \tag{1a}$$

$$M\frac{d^2}{dt^2}u_0 = \alpha[u_1-2u_0+u_{-1}] \tag{1b}$$

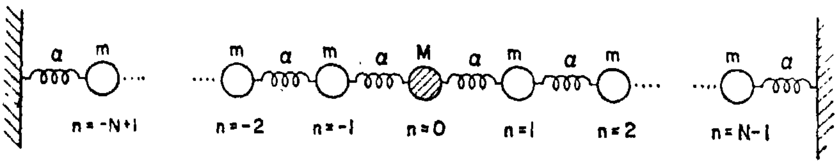

FIG. 1. A schematic diagram of the finite, linear monatomic chain with an isotopic impurity. Particles N and $-N$ are fixed and are represented by the walls.

Following MAZUR, MONTROLL, and POTTS,(1) a time-dependent solution of these equations which satisfies the boundary condition is:

$$\begin{aligned} u_l &= \sum_j A(j)\sin(N-l)\theta_j \exp(i\omega_j t) \qquad \text{if } l \geqslant 0 \\ &= \sum_j B(j)\sin(N+l)\theta_j \exp(i\omega_j t) \qquad \text{if } l < 0 \end{aligned} \tag{2}$$

where $A(j)\ \sin(N-l)\ \theta_j$ is an eigenvector of a dynamical equation which determines ω_j. Substituting (2) into (1a), it follows that:

$$\omega_j^2 = [2\alpha/m]\,(1-\cos\theta_j). \tag{3a}$$

One may classify the modes into symmetric ($u_l = u_{-l}$) and antisymmetric ($u_l = -u_{-l}$). For an antisymmetric mode with any value of $M/m = P$, $u_0 = 0$, θ_j has the values:

$$\theta_j = j\pi/2N, \quad j = 2, 4, \ldots, 2N-2. \tag{4a}$$

Further, $A(j) = -B(j)$.

To obtain the symmetric modes, we must solve the following equation obtained from (1b):

$$\cot N\theta_j = (P-1)\tan(\tfrac{1}{2})\theta_j. \tag{3b}$$

For $P = 1$ it gives

$$\theta_j = j\pi/2N, \quad j = 1, 3, 5, \ldots, 2N-1 \tag{4b}$$

and $A(j) = B(j)$.

If $P > 1$, there are N independent solutions of (3b) and we may express the motion of the lth particle in terms of (2). If $P < 1$, there are only $N-1$ independent solutions and one additional mode must be introduced. This is done by allowing θ in (3b) to be complex ($\pi+i\phi$) and solving for θ_{local} by means of (3b). An analytic solution can be found in the limit $N \to \infty$.

The substitution changes the nature of equation (2), introducing complex numbers for A and B. It also causes neighboring particles to vibrate out of phase. Another simple way to obtain a solution is to assume that the local mode is of the form

$$u_l(\text{local}) \to [f(P)]^{|l|}$$

The above is a solution to our problem only when $N \to \infty$; otherwise, the boundary conditions are not obeyed. Since we have considered a finite chain with fixed boundary conditions, there does not seem to be a simple way to describe the actual local mode. One could, of course, return to equation (2) and substitute sinh for sin. This would lead to more complex equations for the frequency of the local mode. For this reason, we shall assume that u_l(local) and θ_{local} for the infinite chain are valid for the finite chain.

We digress to comment upon the boundary conditions. For finite boundary conditions, the position of the defect with respect to the boundaries will affect the symmetry of the normal modes. Only if the defect is in the center, or for more than one defect, if they are placed symmetrically about the center, can one classify the modes as symmetric or antisymmetric with respect to the center. The length of the crystal has no effect on this conclusion. If one uses periodic boundary conditions, the implication is that since the number of particles is very large, the defect is at the "center", no matter what its position is, and therefore the modes can always be classified as symmetric or antisymmetric. This can best be seen by considering the periodic boundary condition from the viewpoint of a ring. The same situation applies for an infinite chain with one defect. In an actual crystal, however, it is incorrect to attach any physical meaning to the concept of even or odd modes, as has been done in relation to the odd "breathing" modes. The importance of the odd modes has arisen from the very special geometry assumed, which is not typical. We also have placed our impurity at the center to simplify the problem. In a more realistic case the impurity should be placed at a random point.

In an actual problem, one has to find the Hamiltonian corresponding to (1a) and (1b) so as to introduce canonical conjugate variables.(8) Equations (2) and (3) are used only to simplify this problem. The Hamiltonian for the chain is:

$$\mathscr{H} = \frac{1}{2}\sum_{-(N-1)}^{N-1} m_l\left[\frac{\mathrm{d}u_l}{\mathrm{d}t}\right]^2 + \tfrac{1}{2}\sum_{-(N-1)}^{N-1}\alpha(u_{l+1}-u_l)^2 \tag{5}$$

where $m_l = M$ for $l = 0$

$= m$ for $l \neq 0$.

One may reduce (5) to the desired form:

$$\mathscr{H} = \frac{1}{2}\sum_j\left(\frac{\mathrm{d}q_j}{\mathrm{d}t}\right)^2 + \tfrac{1}{2}\sum_j \omega_j^2 q_j^2 \tag{6}$$

by the substitution:

$$u_l = (m_l)^{-1/2} \sum_j e(l|j) q_j. \tag{7}$$

The reduction is an eigenvector problem where $e(l|j)$ is the lth component of the jth eigenvector and ω_j is the eigenvalue; hence the name. The transformation (7) must be unitary, and the e's have the properties;[9]

$$\sum_l \sum_\alpha e_\alpha(l|j) e_\alpha(l|j') = \delta_{jj'} \tag{8a}$$

$$\sum_j e_\alpha(l|j) e_\beta(l'|j) = \delta_{ll'}\delta_{\alpha\beta} \tag{8b}$$

The subscripts α and β refer to the three dimensional case, see Ref. 9, p. 173. The q's of (7) are determined from a canonical ensemble and hence are a definite function of the temperature θ. The mean displacement of the lth particle of the chain due to the jth symmetric mode is:

$$\begin{aligned}\overline{u_l(j)} &= (m_l)^{-1/2}\{[N - \tfrac{1}{2}\sin 2N\theta_j \cot\theta_j]^{-1/2} \\ &\quad \times \bar{q}_j \sin(N-l)\theta_j\} \\ &= \frac{1}{(m_l)^{1/2}} e(l|j)\bar{q}_j \end{aligned} \tag{9}$$

where $(\bar{q})^2$ is the canonical average of the quantum mechanical expectation value of q^2. It is given by

$$\bar{q}_j = \left[\frac{\hbar}{2\omega_j}\coth\frac{\hbar\omega_j}{2k\theta}\right]^{1/2} \tag{10}$$

The correction in the second term of the denominator of (9) is very small except when $\theta_j = 0$ or π, which never occurs; hence it will be omitted.

If $P = 1$, $e(l|j)$ oscillates, but there is no damping in the net amplitude of the displacement. When $P < 1$, the local mode causes a decrease in the amplitude of the eigenvectors of the crystal modes about the imperfection. To see why this occurs, we return to (8b) and write:

$$\sum_j^{\text{local}} e_\alpha^2(l|j') + \sum_j^{\text{crystal}} e_\alpha^2(l|j'') = 1 \tag{11}$$

Equation (11) is written in a general form. For our model, the first sum consists of only one term. Since all the terms are positive in (11), it means that the second sum decreases as the first sum increases. The dominance of the eigenvector for the local mode over any one eigenvector for the crystal modes, first pointed out by BJORK and KRUMHANSL,[6] led them to a possible explanation of the success of WILLIAMS's[10,11] configurational-coordinate model for the optical absorption spectrum of Tl-doped KCl. This model correctly describes the temperature dependence of the broadening, assuming a single effective normal coordinate to describe the latice.

Bjork and Krumhansl argued that since the local eigenvector dominates, the assumption of a single normal coordinate is reasonable. This is not correct, as the important factor is not the eigenvector, but the actual displacement which, from (9) and (10), contains $\bar{q}_j$. It depends on j in a complex fashion and one may not conclude from (11) alone that the displacement is due primarily to the local modes. At high temperatures, the following approximation applies:

$$\bar{q} = \frac{1}{\omega}(k\theta)^{1/2}.$$

Since the local modes have higher frequencies, one cannot tell which of the two effects—the decrease in $\bar{q}$ of the local mode or the increase in the e's—is more important. Only detailed calculations can answer this question; hence, one must include the effect of $\bar{q}$.

Even if the displacement due to the local mode is large compared to that from any one crystalline mode, it is not correct to assume that the local mode dominates in the electron–lattice interaction. In considering the contribution of the crystal modes to the interaction, one must compare the sum of the displacements due to the crystal modes with the contribution from the local modes.[7] This has been done by ROSENSTOCK and KLICK[5] for a particular model. In their case, the contribution from both types of modes was of the same order of magnitude.

When $P > 1$, there are no local modes; however, the e's change for small values of l. This is significant if P is large, as we shall show. For large values of l this does not occur. In view of the complexity of equation (9) (we are dealing with small changes in θ_j due to variations in P), the only way to illustrate what happens, so far as the authors know, is to carry through detailed calculations.

With the use of a digital computer, we calculated the θ_j and the e's for the symmetric modes for a chain of 101 particles ($N = 50$). In Fig. 2, we have plotted the positive e's for the symmetric modes against θ_j. P was set equal to $\frac{1}{2}$, 1, and 2, while $l = 1$. The Bjork–Krumhansl effect, the redistribution of the e's, is illustrated in the case when $P = \frac{1}{2}$. Most of the displacement of the high frequency modes vanishes, but an e for the local mode appears. When $P = 2$, there has again been a redistribution; the high frequency modes seem to be of greater importance, although no local mode appears.

In a very crude fashion, one may say that the motion of the first particle is made of two frequencies, one associated with the lower values of j and the other associated with the higher.(12) When $P = 1$, the displacement of both types is approximately equal. $P = \frac{1}{2}$ shifts both frequencies to higher values. One of these resides in the local mode. $P = 2$ also decreases the effect of the lower frequency and increases the importance of the higher lattice modes. The band of crystal modes that makes the major contribution to the eigenvectors will shift to a lower frequency as P decreases. This has been verified by a calculation of $e(l|j)$ for $P = \frac{1}{4}$.

One cannot attach any physical significance to the direction of the shift as a function of P. This is because the model assumes only an isotopic defect and hence, as P decreases, the local mode eigenvector approaches zero.

In Fig. 3 we have made similar calculations for $l = 5$. This figure indicates the redistribution is less important as one gets further away from the defect. The dependence of the eigenvectors on l is noticeable even when $P = 1$ (the perfect chain) and arises from using finite boundary conditions; with periodic boundary conditions it would disappear. BORN and HUANG(13) have shown that for a perfect lattice, the frequency distribution is independent of the boundary conditions. Our calculation indicates that this is not the case for the eigenvectors.

In Figs. 4 and 5 we have plotted the actual displacement of the $l = 1$ particle at low $[\bar{q}\,(1/\omega^{1/2})]$

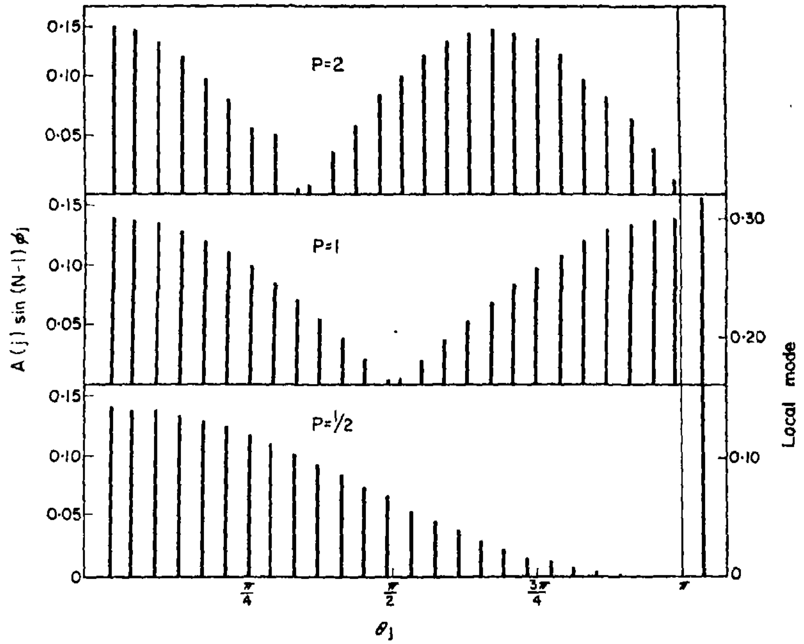

FIG. 2. The positive eigenvectors of the symmetric crystal modes as a function of θ_j for $l = 1$. Three isotopic defects are considered, $P = 2$, 1, $\frac{1}{2}$. The eigenvector of the local for $P = \frac{1}{2}$ is also shown. The y-axis is really $e(l|j)$.

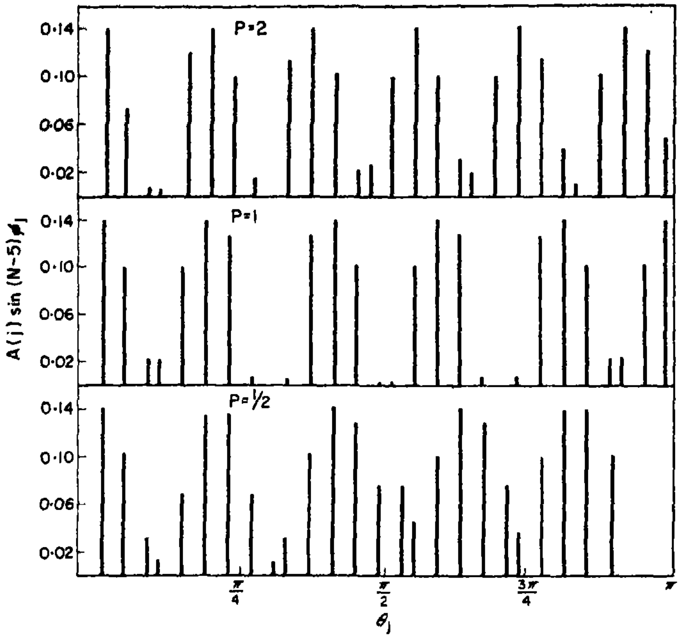

FIG. 3. The positive eigenvectors of the symmetric crystal modes as a function of θ_j for $l = 5$. The same defects considered in Fig. 2 are shown but the local mode for $P = \frac{1}{2}$ is negligible. The y-axis is really $e(s|j)$.

and at high $\bar{q}\,[(1/\omega)]$ temperatures. The reader is reminded that the mode distribution in an actual solid is roughly proportional to ω^2, so that it might be more appropriate to multiply the eigenvectors by $\omega^{3/2}$ and ω.

Since the u's, not the q's, determine the actual physical behavior of an imperfection, these redistributions can be of major importance. As an illustration, we now consider the contribution each mode makes to the broadening of an optical absorption band.

3. THE BROADENING OF AN ABSORPTION LINE

Using the formalism reviewed previously, (M), we relate the eigenvector shift discussed in Section 2 to the breadth of the optical absorption band associated with an imperfection. This is an extension of the recent review.

Relatively little is known regarding the modes which broaden absorption lines in solids, either experimentally or theoretically. In only one case has it been established that the broadening is due to modes of a single effective frequency. This is the case of the F-center in KCl.(14) In the case of the F-center in NaCl the situation is not clear. The calculation made by WILLIAMS and co-worker(10, 11) is extremely important, but far too crude to answer this question. The actual measurements by PATTERSON(15) do not suggest that a single effective frequency exists, but that the absorption in the 5 eV region is more complex. It may be due to several overlapping bands. The measurement of Russell and Klick does not establish a single effective frequency for various F-centers. The assumption of a single effective frequency will be made later in this Section, however, so that we may examine the consequences of this hypothesis. This is based on *experimental*, not theoretical arguments.

Consider an electron at a point defect and assume a deep trap with two bound electron levels. Several quantities can be used to characterize the absorption, $\alpha(\epsilon)$. (ϵ is the absorbed photon energy.) One of these is:

$$m^2 = \frac{M_2}{M_0} - \bar{\epsilon}^2 \tag{12}$$

where M_n is the nth moment and $\bar{\epsilon}$ is the average, M_1/M_0. The half-width of the line H is defined as $H = \epsilon_V - \epsilon_r$ where ϵ_V and ϵ_r are the half-width energies to the violet and red, respectively, of the peak absorption. To first order (see *M*, Sections 7 and 10:)

$$H^2 = cm^2 = c \sum_j \epsilon_j^2 \frac{\hbar}{2\omega_j} \coth\left[\frac{\hbar\omega_j}{2k\theta}\right], \qquad (13)$$

$$H^2(0) = c \sum_j \epsilon_j^2 \frac{\hbar}{2\omega_j} = \sum_j \epsilon_j^2(0), \qquad (13a)$$

where c is a function of the shape (*M*, Section 7) and we have neglected higher order terms. ϵ_j is

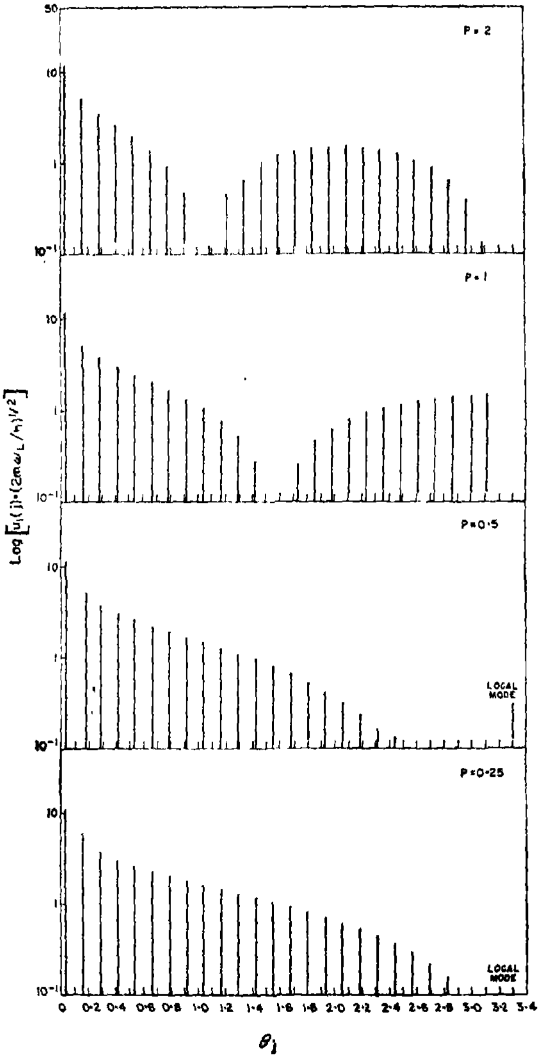

FIG. 4. The low temperature contributions to the positive displacement of the $l = 1$ particle, due to the symmetric crystalline modes. The local modes for $P = \frac{1}{2}, \frac{1}{4}$ are also shown.

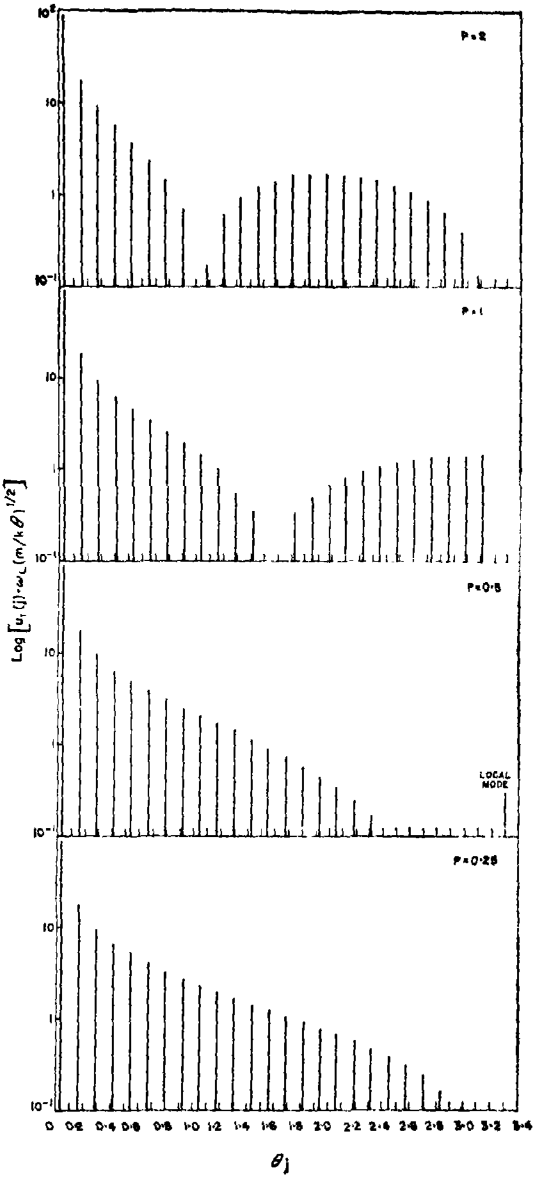

FIG. 5. The high temperature contributions to the positive displacement of the $l = 1$ particle due to the symmetric crystalline modes. The local mode for $P = \frac{1}{2}$ is shown; that for $P = \frac{1}{4}$ is negligible.

given by the relation (M, 3.18a)

$$\epsilon_j = \frac{\partial}{\partial q_j}\{\epsilon_u(q_j)-\epsilon_g(q_j)\} = \frac{\partial \Delta\epsilon}{\partial q_j} \tag{14}$$

ϵ_u and ϵ_g are the eigenvalues associated with the electronic part of the wavefunction (see M, Section 3). The derivation of (13) makes use of only two assumptions—the Condon principle (see M) and that terms such as $\partial^2\Delta\epsilon/\partial q_j\partial q_{j'}$ can be neglected. Equation (14) is evaluated for the equilibrium position of the ions associated with the ground state.

We shall now connect the eigenvectors to the broadening by considering a three-dimensional lattice. Later, the results will be reduced to a linear chain. Defining u^α_l as the displacement from equilibrium of the lth ion in the αth direction, we have:

$$u^\alpha_l = X^\alpha_l - (X^\alpha_l)g, \tag{15}$$

where the equilibrium value of X depends on the electronic eigenvalue. The eigenvalues enter into H_j, since

$$\epsilon_j = \sum_l \sum_\alpha \left(\frac{1}{m_l}\right)^{1/2} \left(\frac{\partial\Delta\epsilon}{\partial X^\alpha_l}\right)_{R_g} e_\alpha(l|j) \tag{16}$$

where equation (7) has been employed. Substituting into (13), results in:

$$H^2(0) = c\sum_j \frac{\hbar}{2\omega_j} \times \left[\sum_l \sum_\alpha \left(\frac{1}{m}\right)^{1/2} \left(\frac{\partial\Delta\epsilon}{\partial X^\alpha_l}\right)_{R_g} e_\alpha(l|j)\right]^2 \tag{17}$$

The meaning of $\dfrac{\partial\Delta\epsilon}{\partial X^\alpha}$ can be understood by Feynman's theorem (M, 3.1). The total potential relative to the equilibrium positions of the ions, when the electron is in the ground state must have the form:

$$V = \sum_l V_1(\mathbf{r},u_l) + \sum_{l'l''} V(u_{l''},u_{l'}). \tag{18}$$

where $\mathbf{r}$ is the position of the "extra" electron. The actual potential is more complex, since the terms involving the interaction between the bound electrons and the "extra" electron exist. This could be written in terms of the polarization of the ions. This complexity though physically necessary, adds little to the problem at hand and will be neglected.

Using (M, 3.16),

$$\frac{\partial\Delta\epsilon}{\partial u^\alpha_l} = \left\langle \phi_n \left| \frac{\partial V_1}{\partial u^\alpha_l} \right| \phi_u \right\rangle - \left\langle \phi_g \left| \frac{\partial V_1}{\partial u^\alpha_l} \right| \phi_g \right\rangle, \tag{19}$$

where ϕ is the adiabatic eigenfunction, i.e. it depends on the u's. Equation (19) then represents the change in force on the ions due to the electron when it is excited into a higher state.

Assuming the wavefunctions of the electron are known, the force on the ions due to the electron can be evaluated from electrostatics as follows. If the amount of charge enclosed in a volume of radius r due to an electron in the nth state is:

$$-e\rho_n(r) = -\int_0^r e|\phi_n(r)|^2\, 4\pi r^2\, dr, \tag{20}$$

then the force on an ion of charge Ze, located at a distance a_l, from the imperfection is:

$$-\frac{Ze^2}{(a_l)^2}\rho_n(a_l). \tag{21}$$

Hence,

$$\frac{\partial\Delta E}{\partial X^\alpha_l} = -\frac{Ze^2}{(a_l)^2}[\rho_u(a_l)-\rho_g(a_l)]. \tag{22}$$

If a single effective frequency (ω_e) exists as shown experimentally by the measurements on the F-center in KCl, equation (17) can be greatly simplified and the eigenvectors can be completely eliminated as follows:

$$\begin{aligned} H^2 &= \frac{c\hbar}{2\omega_e}\coth\frac{\hbar\omega_e}{k\theta}\sum_{\substack{j,l,\alpha\\ l',\beta}} \frac{1}{(m_l m_{l'})^{1/2}}\frac{\partial\Delta\epsilon}{\partial u^\alpha_l}\frac{\partial\Delta\epsilon}{\partial u^\beta_{l'}} \\ &\qquad \times e_\alpha(l|j)e_\beta(l'|j) \\ &= \frac{c\hbar}{2\omega_e}\coth\frac{\hbar\omega_e}{k\theta}\sum_{l,\alpha}\frac{1}{m_l}\left[\frac{\partial\Delta\epsilon}{\partial u^\alpha_l}\right]^2 \end{aligned} \tag{23}$$

where use has been made of (8b). In the case where $\theta = 0$,

$$H^2(0) = \frac{c\hbar}{2}\frac{1}{\omega_e}\sum_{l,\alpha}\frac{1}{m_l}\left[\frac{\partial\epsilon}{\partial u_l^\alpha}\right]^2 \tag{24}$$

Equation (23) shows that assuming $1/\omega_e$ exists, one can calculate H^2 without any knowledge of the normal modes. Since $1/\omega_e$ can be determined approximately from experimental measurements (see M), one can readily evaluate H^2 if the wavefunctions are known approximately.

Examination of (23) gives some insight into the configurational coordinate model described by Williams. It shows that the predicted shape and temperature dependence of H^2 is based on the assumption of a single effective frequency, and not of a single normal mode. The sum in (23) represents the difference in the force exerted on the ions by the defect when it undergoes a transition to an excited state. If we assume that the electronic wavefunctions are spherically symmetric, then the forces will be radial, as will the displacements. Williams made this assumption in the case of Tl-doped KCl where it seems quite reasonable. His assumed normal coordinate was calculated from the largest value of $\left(\frac{\partial\Delta\epsilon}{\partial u}\right)^2$ and hence the sum in equation (24). Thus, the assumption made (Refs. 10 and 11) of a single coordinate is immaterial to their correct prediction of the absorption.

For the case of the linear chain, we may omit the superscript α and write:

$$H^2(0) = c\sum_j\frac{\hbar}{2\omega_j}\left[\sum_j\left(\frac{1}{m_l}\right)^{1/2}\frac{\partial\Delta\epsilon}{\partial u_l}e(l|j)\right]^2 \tag{25}$$

4. A SIMPLE CALCULATION TO SHOW THE EIGENVECTOR EFFECT

We should like to apply our knowledge of the eigenvectors of the linear chain to a problem with an element of reality. This should answer the question: Are the eigenvector shifts present in Figs. 2 and 3 of physical importance? One may combine Parts II and III provided one assumes wavefunctions for the ground and excited states, replaces $e(l|j)$ by its absolute value, and introduces a density distribution appropriate for a solid. In addition, the change in equilibrium positions of the ions due to the presence of the trapped electron, is ignored. One cannot justify these assumptions; but unless they are made it is impossible to tell if the eigenvector effect is of any physical importance.

It might be argued that the antisymmetric modes, which for our model are not perturbed by the defect, make the major contribution to the electron–lattice interaction and hence to the broadening. This will be true in an actual solid only if the defect makes a transition between two spherically symmetric states. In the case where one electron state is non-spherically symmetric, the symmetric modes must also make a large contribution to the broadening.

For the wavefunctions we use the angular independent wave-functions calculated for the F-center by SIMPSON.(16) His wavefunctions have the simple form:

$\phi_1 = A_1e^{-\lambda r}$, ground state ($\lambda = 0{\cdot}52$ atomic unit for NaCl). (26a)

$\phi_2 = A_2re^{-\mu r}\cos\theta$, excited state ($\mu = 0{\cdot}36$ atomic unit for NaCl). (26b)

If we neglect the angular dependence of ϕ_2, $\frac{\partial\Delta\epsilon}{\partial X_l}$ may be evaluated as a function of λ, μ, and l. After some lengthy but straight-forward calculations, one obtains the result:

$$\frac{\partial\Delta\epsilon}{\partial X_l} = Ze^2\Big\{e^{-2\lambda x}\left[\frac{2}{3}\lambda^4x^2+\lambda^3x+4\lambda^2+\frac{2\lambda}{x}+\frac{1}{x^2}\right] - e^{2\mu x}\Big[2\mu^2+\frac{2\mu}{x}+\frac{1}{x^2}\Big\}\Big], \tag{27}$$

where $x = la$ and a is the distance between neighbouring ions, assumed in this case to be $2a{\cdot}u$. $\frac{\partial\Delta\epsilon}{\partial X}$ was evaluated for $l = 1$, 2, and 3. Beyond this value, ρ_g was set equal to ρ_u and $\frac{\partial\Delta\epsilon}{\partial X}$ equals zero for $l > 3$. It is not correct, of course, to neglect the angular part of ϕ_2. First, the electronic transition must be an allowed one; hence the symmetry of the two states cannot be the same.

Secondly, we will be considering only the symmetric modes' contribution to the broadening as they are the only modes affected by the defect.

If we should simply combine (27) and (25) using the ϵ's from equation (9a), we would obtain a misleading result, since, in an actual crystal, there are many more high frequency modes than low. As stated before, the simplest way out is to assume a Debye frequency distribution, i.e. proportional to ω^2 and cut it off at the highest frequency. In view of the crudeness of the model, no refinement in the distribution could possibly be justified. The one-dimensional frequency distribution arising from a solution of the equations in Section 2 would be completely misleading, since our interest is in a three-dimensional lattice. Hence, the quantity:

$$\mathscr{H}_j^2(0) \approx \omega_j^2 H_j^2(0) \tag{28}$$

instead of $H^2(0)$ has been plotted in Fig. 6 where a chain of alternating positive and negative ions has been considered.

The reader should note that for every P certain spectra regions are important. Thus when $P = 1$ the important region is about $\omega = \omega_L$, when $P = 2$, $\omega = 0{\cdot}92\ \omega_L$. The y-axis is a logarithmic scale and we assume a density of crystal modes and only a single local mode when it exists. This is a crude theoretical justification for assuming that a "single effective" frequency exists as was done in Section 3. The reader will further note that the important regions for $H_j^2(0)$ cannot be obtained in any simple manner from the eigenvectors or the displacements in Figs. 2 through 4.

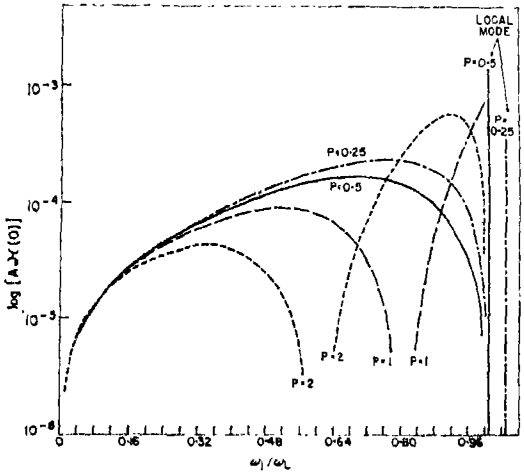

FIG. 6. The contribution to the optical broadening as a function of the frequencies of the crystal and local modes. The electron is in a deep two-level trap in a system defined by the linear chain described in the text. The frequency distribution function is that associated with a Debye solid. ω_L is the maximum crystal mode frequency and A is given by $m/\hbar Ze^2$.

5. CONCLUSIONS

The calculations show that the vibrations around an imperfection are strongly influenced by it. Certain bands of modes will make the major contribution to the displacement of any given ion. The position of these bands in the crystalline mode spectrum will be strongly dependent upon such parameters as the mass and the force constant of the defect. This is true whether or not there are local modes. For any short-range effect which involves the displacement of the atoms (or ions), one must by all means carry through calculations in full detail. Little reliance can be placed on the calculation of $H(0)$ factor carried through by Pekar and by Huang and others, since they did not include the eigenvector problem. We hesitate to draw general conclusions from these calculations. These do, however, stress that $H(0)$ cannot be obtained realistically without taking into consideration the above problem.

If we have a free electron in a solid, we may employ the unmodified normal mode approach as long as the interaction is extremely weak. As the interaction increases, the wavelength decreases and a localized imperfection occurs. At this point, the electron starts to distort the crystal modes and if the interaction is strong enough, the lattice modes are completely distorted about the electron. Here the eigenvector effect becomes of primary importance. To calculate the electron–lattice interaction in this case, one must first calculate the changes in the lattice modes.

Acknowledgement—We thank Dr. McCombie for several helpful discussions of these problems.

REFERENCES

1. At this time, the authors want to be extremely unsophisticated in their analysis; hence, the reader is referred to an elementary development of this problem by MAZUR P., MONTROLL W. and

Potts R. B., *J. Wash. Acad. Sci.* **46**, 1 (1956). See also Appendix E, Montroll W. and Potts R. B., *Phys. Rev.* **100**, 525 (1953).

2. These small shifts are related to the effect of changes of the boundary conditions. This problem has been discussed in some detail by Born M., *Proc. phys. Soc. Lond.* **54**, 362 (1942).
3. The eigenvector effect was "discovered" independently by the group working with Dr. C. W. McCombie, University of Aberdeen, Scotland. Their work preceded ours by several months and they kept us informed of their progress. Actually, their models as far as this effect (perturbation of lattice modes) were limited to a linear chain where the force constant was changed about the central imperfection. However, our realization and understanding of the effect were actually made independently. We have published this paper since we are using a radically different model from that employed by McCombie and coworkers. We believe it brings out certain effects of extreme importance in a simple manner and thus complements the work of the Aberdeen group. See McCombie C. W., Matthew J. A. and Murray A. M., *J. appl. Phys. Suppl.* **33**, 359 (1962).
4. Brown F. C. and Inchauspe N., *Phys. Rev.* **121**, 1303 (1961).
5. Rosenstock H. N. and Klick C. C., *Phys. Rev.* **119**, 1198 (1960).
6. Krumhansl J. A., oral presentation at the *Argonne National Laboratory Color Center Conference* (1956) and subsequently Bjork R. J., *Phys. Rev.* **105**, 456 (1957).
7. Markham J. J., *Rev. mod. Phys.* **31**, 956 (1959).
8. An exception might occur if one were dealing with an actual linear chain but this problem is of little interest today. The "standard" introduction which we have outlined here must have confused more than one scientist who wanted to obtain an understanding of the theory; this includes the authors.
9. Born M. and Huang K., *Dynamical Theory of Crystal Lattices* p. 173. University Press, Oxford (1954). We employ their notation.
10. Williams F. E., *J. chem. Phys.* **19**, 457 (1951).
11. Williams F. E. and Hebb M. H., *Phys. Rev.* **84**, 1181 (1951).
12. These double frequencies remind one of the old specific heat theory of Nernst and Lindermann, although there is no connection. For $l = 2$, there are three groups of importance.
13. Williams F. E., *J. chem. Phys.* **19**, 391 (1951).
14. Konitzer J. D. and Markham J. J., *J. chem. Phys.* **32**, 843 (1960); and Markham J. J. and Konitzer J. D., *J. chem. Phys.* **34**, 1936 (1961).
15. Patterson D. A., *Phys. Rev.* **112**, 296 (1958).
16. Simpson J. H., *Proc. Roy. Soc.* **A197**, 269 (1949).

J. Phys. Chem. Solids Pergamon Press 1963. Vol. 24, pp. 681–685. Printed in Great Britain.

EXCITATION SPECTRA OF ZnS PHOSPHORS
PART 1: THEORETICAL ANALYSIS

GY. GERGELY*

Industrial Research Institute for Telecommunication Techniques, Budapest

(*Received* 7 *September* 1962; *revised* 10 *December* 1962)

Abstract—A theoretical analysis of the excitation spectra of ZnS phosphors is given. The analysis is based on the Schön–Klasens model and assumes a constant quantum efficiency, being independent of the exciting photon energy. The diffusion and surface recombination of carriers generated by photon excitation are considered. The drop of sensitivity on the high energy side of the excitation spectrum is explained by the surface recombination of carriers. The long wave tails of the excitation spectra are associated with center (activator) excitation and they are determined by optical effects. Generalized curves are derived for the evaluation of the experimental excitation spectra.

INTRODUCTION

THE phenomenological study of excitation spectra in ZnS phosphors was undertaken by several authors, but no attempt has been made to give an explanation of the experimental results. In this paper an analysis of excitation spectra will be given, taking into consideration surface recombination and diffusion of carriers. A similar analysis of cathodoluminescence processes was given in a previous paper(1) in this journal. The influence of several factors on excitation spectra will be discussed.

ANALYSIS OF THE EXCITATION SPECTRUM

The analysis is restricted to high quality ZnS and ZnCdS phosphors, containing only two sets of levels in the forbidden band associated with luminescent centers (A) and deep traps (H), respectively.

In the analysis the following simplifying assumptions have been used:

1. The crystal is free from internal imperfections and killer centers.
2. The quantum efficiency is unity, independent of the energy of the exciting photons.
3. Non-radiative recombinations in the bulk (direct or via H traps) are fully neglected. The surface recombination is radiationless.
4. Thermal generation of carriers (thermal release from traps) is negligible. The analysis is not valid above room temperature.
5. The effects of space charge accumulated in traps are neglected.
6. The current density is zero within the crystal.
7. Possible effects due to excitons are neglected.
8. A uniform, parallel beam of photons is normally incident on the front surface of the crystal.
9. The crystal is a thin plane parallel infinite slab. In the analysis a one dimensional plane geometry is adopted.

The plane parallel crystal model can be applied also to microcrystals. This model was successfully adopted by BODÓ(2) and JOHNSON(3) in the optical analysis of absorption on diffuse microcrystalline layers.

In practice assumptions 1–9 may be applied for high quality ZnS–Ag–Cl and e.g. for 50ZnS–50CdS–Ag–Cl phosphors, containing a high density of activator centers [$A = 10^{18}$–$10^{19}/\text{cm}^3$] and a low density of deep traps [$H = 10^{14}$–$10^{15}/\text{cm}^3$].(4) A scheme of electronic transitions in the crystal is represented in Fig. 1.

---

* Present address, Semiconductors Laboratory, Physics Department, University of Buenos Aires, Argentina.

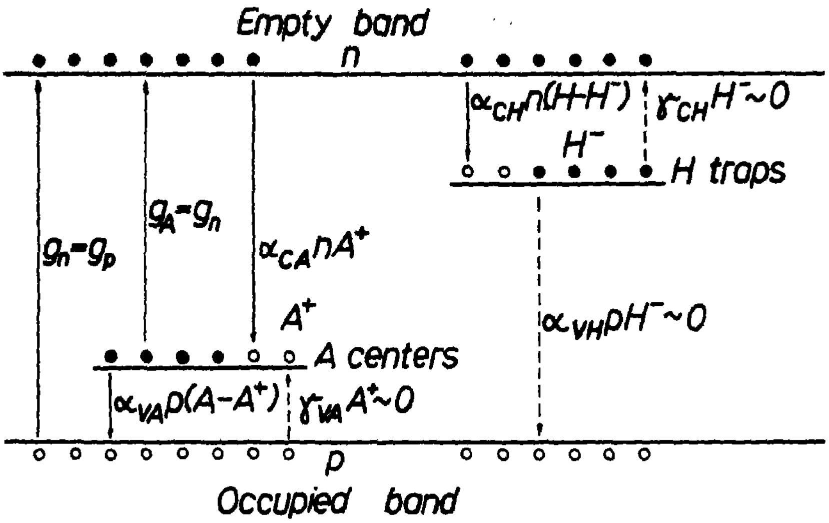

FIG. 1. Schematic drawing representing electronic transitions in the crystal.

The distribution and electronic transitions of carriers can be calculated by solving the fundamental system of kinetic equations of SCHÖN[5] and KLASENS[6] discussed in detail by HOOGENSTRAATEN.[13] In steady state equilibrium, the equations have the following form:

$$0 = g_n(x) - \alpha_{CA} n A^+ - \alpha_{CH} n (H - H^-) + \gamma_{HC} H^- + D_n \frac{d^2 n}{dx^2} + \mu_n \operatorname{div}(En) \quad (1)$$

$$0 = g_A(x) - \alpha_{CA} n A^+ + \alpha_{VA} p (A - A^+) - \gamma_{VA} A^+ \quad (2)$$

$$0 = \alpha_{CH} n (H - H^-) - \alpha_{VH} p H^- - \gamma_{HC} H^- \quad (3)$$

$$0 = g_p(x) + \gamma_{VA} A^+ - \alpha_{VA} p (A - A^+) - \alpha_{VH} p H^- + D_p \frac{d^2 p}{dx^2} - \mu_p \operatorname{div}(Ep) \quad (4)$$

$$\operatorname{div} E = \frac{4\pi}{\epsilon} e (p + A^+ - n - H^-) \quad (5)$$

The following symbols will be used:

n = density of free electrons
p = density of free holes
H = density of electron traps
H^- = density of electrons trapped in H centers
A = density of luminescent centers
A^+ = density of holes captured by A centers
$g_n(x)$ = density of optical excitation for free electrons
$g_p(x)$ = density of optical excitation for free holes
$g_A(x)$ = density of optical excitation for A centers
α_{CH} = capture coefficient of vacant H traps for free electrons. $\alpha_{CH} = 10^{-9}$ cm^{3}sec^{-1}
α_{VH} = recombination coefficient between free holes and trapped electrons. $\alpha_{VH} = 10^{-8}$ cm^{3}sec^{-1}
α_{CA} = capture coefficient of A^+ centers for free electrons. $\alpha_{CA} = 10^{-12}$ cm^{3}sec^{-1}
α_{VA} = capture coefficient of A centers for free holes, $\alpha_{VA} = 10^{-9}$ cm^{3}sec^{-1}
γ_{HC} = probability for thermal release of trapped electrons from H centers
γ_{VA} = probability for thermal generation of a free hole
μ_n = mobility of electrons
μ_p = mobility of holes
D_n = diffusion coefficient of electrons
D_p = diffusion coefficient of holes
τ_p = lifetime of free holes
L_n = diffusion length of electrons
L_p = diffusion length of holes
S = surface recombination velocity of holes
$E(x)$ = electric field

e = electronic charge
ϵ = dielectric constant
N_λ = density/cm²sec of incident photons for wave-length λ
α_λ = absorption coefficient for wave-length λ
R_λ = reflection coefficient for wave-length λ [defined by the Fresnel formula]
l = thickness [dia.] of the crystal
$L(\alpha_\lambda)$ = luminescence brightness for excitation by wave-length λ

The rigorous solution of equations (1–5) is a hopeless task, nevertheless, by making use of assumptions 1–9, a practical approximate solution may be given for the excitation spectrum.

The luminescence processes in high quality ZnS–Ag–Cl and ZnCdS–Ag–Cl phosphors may be characterized by code numbers 122122, 121122 and 121112 of Klasens. The conditions for the processes are determined for host crystal excitation by the inequalities:

$$\begin{array}{cc} 122122 & 121122 \\ g_n > \alpha_{CH}H^2 & \gamma_{VA}H < g_n < \alpha_{CH}H^2 \end{array}$$

and 121112

$$\gamma_{VA}\alpha_{VH}\tau_p H^2 < g_n < \gamma_{VA}H \qquad (6)$$

For the three cases it holds :

$$n \gg p \quad A^+ \ll A \quad \tau_p = \frac{1}{\alpha_{VA}A} = \text{const.} \qquad (7)$$

Case 122122 corresponds to high excitation densities, the recombination of free electrons is bimolecular and the density relationship between free electrons and holes is:

$$n = \text{const.}\ \sqrt{p} \qquad (8)$$

Thermal generation of holes is negligible in comparison to optical excitation.

For lower excitation densities—this is rather the case for excitation spectrum studies—code number 121122 may be used. The recombination of free electrons and holes is monomolecular and their density relationship is:

$$n = \text{const.}\ p$$

Thermal generation of holes [$\gamma_{VA}H$ = const.] may be considerable.

For still lower excitation densities code number 121112 holds, thermal generation of holes is predominant. In both of the latter cases the density of holes is given by the superposition of thermal and optical generation; the diffusion of free carriers, however, is determined mainly by the spatial distribution of optical excitation.

In the following analysis two cases of excitation will be discussed.

A. *Host crystal excitation*

The excitation density is given by:

$$g_n(x) = g_p(x) = N_\lambda(1-R_\lambda)\alpha_\lambda \exp(-\alpha_\lambda x) \qquad (10)$$

$g_A(x) \simeq 0$, in view of the low density of A centers:

In consequence of simplifying assumption 1–9 the terms $\alpha_{VH}\ \gamma_{HC}$ and γ_{VA} in equations (1–4) may be neglected. Using the approximation $E \simeq 0$ for cases 122122 and 121122, from equations (2), (4) and (7) it follows:

$$0 = \frac{p}{\tau_p} - \alpha_{CA}nA^+ \qquad (11)$$

$$0 = g_p(x) - \frac{p}{\tau_p} + D_p \frac{d^2p}{dx^2} \qquad (12)$$

Equation (11) expresses the steady state recombination balance between free electrons and holes via A centers. The number of photons emitted by the crystal per unit time [$L(\alpha_\lambda)$] can be calculated by the recombination of electrons or holes. The solution of equation (12) gives the distribution of holes. This, however, is analogous to the distribution of carriers in an illuminated photoconductor slab, a problem discussed in details by DEVORE(7) and TANG TING-YUAN.(8) Making use of DeVore's results

$$L(\alpha_\lambda) = \int_0^l \frac{p}{\tau_p}\, dx \qquad (13)$$

and

$$L(\alpha_\lambda) = \frac{N_\lambda(1-R_\lambda)}{1-L_p{}^2\alpha_\lambda{}^2}\left\{1-\exp(-\alpha_\lambda l) - \frac{\alpha_\lambda S L_p[1+\exp(-\alpha_\lambda l)] + \alpha_\lambda{}^2 D_p L_p[1-\exp(-\alpha_\lambda l)]}{D_p/L_p + S \operatorname{cth}(l/2L_p)}\right\} \qquad (14)$$

$$L_p = \sqrt{(D_p\tau_p)} \qquad (15)$$

In a more rigorous analysis the neutrality and zero current conditions should be taken into consideration, as this was done in Refs. 9 and 10. The conditions can be fulfilled for monomolecular and bimolecular recombinations by a slight modification of equation (12) taking 3/2 D_p or $2D_p$ instead of D_p for processes 122122 and 121122 respectively. Consequently, in equations (14) and (15) 3/2 D_p and $2D_p$ respectively have to be used.*

For equal number of exciting photons in the total spectrum [N_λ = const.] equation (14) gives the short wave side of the excitation spectrum.

Below certain wave-length (λ_c) the experimental excitation spectra of ZnS Phosphors exhibit a nearly constant short wave tail. In this section $\alpha_\lambda = \alpha_c$ = const., being in accordance with experimental absorption spectra as found by MOLLWO(11) and DUTTON.(12)

B. *Impurity excitation*

The long wave edge of excitation spectrum is associated with the generation of electrons from incorporated impurity [activator] centers. The luminescence processes can be characterized now by code numbers 122112 [$g_n > \alpha c_A H^2$] and 121112 respectively. The absorption coefficient takes moderate values and multiple internal reflections of incident photons have to be considered. The spatial distribution of excitation is given by an expression of TANG TING-YUAN.(8)

$$g_n(x) = g_A(x) = \frac{\alpha_\lambda N_\lambda(1-R_\lambda)}{1-R_\lambda{}^2\exp(-2\alpha_\lambda l)}\{\exp(-\alpha_\lambda x) + R_\lambda \exp(-2\alpha_\lambda l+\alpha_\lambda x)\} \qquad (16)$$

and $g_p(x) = 0$ for photon energies below the band gap.

In this case, holes are generated by thermal excitation. The solution of the fundamental equations (1–5) is very complicated, but a simple approximate solution can be given by assuming that the absorption in the bulk of any incident photon yields luminescence emission and all carriers generated in the surface diffusion layers [$x < L_n$ or $x > l-L_n$] suffer non-radiative surface recombinations. This corresponds to $S = \infty$. The other limiting case, $S = 0$ is equivalent to $L_n = 0$. Thus:

$$L(\alpha_\lambda) = \int_{L_n}^{l-L_n} g_n(x)\,dx \qquad (17)$$

and

$$L(\alpha_\lambda) = \frac{N_\lambda(1-R_\lambda)}{1-R_\lambda{}^2\exp(-2\alpha_\lambda l)} \times \{\exp(-\alpha_\lambda L_n)-\exp[-\alpha_\lambda(l-L_n)] + R_\lambda\exp(-2\alpha_\lambda l)[\exp\alpha_\lambda(l-L_n)-\exp(\alpha_\lambda L_n)]\} \qquad (18)$$

The maximum of excitation spectrum is associated with total absorption of excitation energy without considerable (< 5–6 per cent) surface recombination losses:

$$L(\alpha)_{\max} \simeq 0{\cdot}95(1-R_\lambda)N_{\lambda\max} \qquad (19)$$

In the constant short wave tail $\alpha_c = 10^6$–10^5 cm^{-1} thus equation (14) becomes very simple. Comparing equations (14) and (19), from the ratio $L(\alpha)_{\max}/L(\alpha_c)$ an estimation of S may be made.

THE GENERALIZED EXCITATION SPECTRUM

The shape of the excitation spectrum is determined by L_p, S, R_λ and particularly by α_λ. Omitting the term $(1-R_\lambda)$ in equations (14–18), a set of curves may be derived without knowing the variation of α_λ with the wave-length. [In equation (18) R_λ varies only slightly with λ in the absorption tail].

Figure 2 represents the generalized excitation spectra of a cubic ZnS–Ag–Cl phosphor for $L_p = 0{\cdot}1\mu$, $l = 10\mu$ and varying S.

Comparing these curves with the experimental curves of α_λ and $L(\alpha_\lambda)$, the surface recombination velocity S may be determined. In practice, however, reliable data relating to α_λ are seldom available. In lack of data, the absorption spectra of microcrystalline ZnS and ZnCdS phosphors may be derived by their excitation spectra. This may be of special interest in the domain of strong [lattice] absorption.

The experimental results are described in Part II of this issue.

---

* Some more details on carrier diffusion are given in Ref. 10.

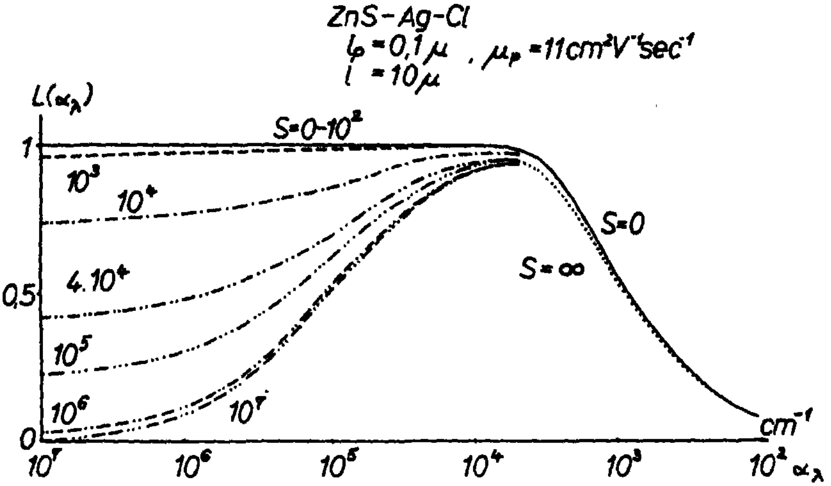

FIG. 2. Generalized excitation spectra of a ZnS phosphor.

REFERENCES

1. GERGELY GY., *J. Phys. Chem. Solids* **17**, 112 (1960).
2. BODÓ Z., *Acta phys. Hung.* **1**, 135 (1951).
3. JOHNSON P. P., *J. opt. Soc. Amer.* **42**, 978 (1952).
4. KALLMANN H. and SUCOV E., *Phys. Rev.* **109**, 1473 (1958).
5. SCHÖN M., *Physica* **20**, 930 (1954).
6. KLASENS H. A., *J. Phys. Chem. Solids* **7**, 175 (1958).
7. DEVORE H. B., *Phys. Rev.* **102**, 86 (1956).
8. TANG TING-YUAN, KAO KOU-YU., *Arbeitstagung Festkörperphysik, Erfurt.* p. 62. Akademie, Berlin (1957).
9. AUTH J., *Ann. Phys. Lpz.* **20**, 210 (1957).
10. GERGELY GY., *J. Phys. Chem. Solids* **21**, 105 (1961).
11. MOLLWO R., *Reichsber. Phys.* **1**, 1 (1944).
12. DUTTON D., *Phys. Rev.* **112**, 788 (1958).
13. HOOGENSTRAATEN W., *Philips res. Rep.* **13**, 515 (1958).

J. Phys. Chem. Solids Pergamon Press 1963. Vol. 24, pp. 687–691. Printed in Great Britain.

EXCITATION SPECTRA OF ZnS PHOSPHORS

PART II: EXPERIMENTAL RESULTS

GY. GERGELY,* J. ADAM, and GY. T. BAUER

Industrial Research Institute for Telecommunication Techniques, Budapest

(*Received* 4 *September* 1962; *revised* 10 *December* 1962)

Abstract—The excitation spectra of several ZnS and ZnCdS phosphors were studied in various gas atmospheres. The high energy tail of the spectrum is strongly reduced by grinding. The shift of the long wave tail with crystal grain size corresponds to the theoretical analysis. No change of excitation spectra was observed applying various gas atmospheres. The surface recombination velocity of ZnS and ZnCdS phosphors varied between $2\cdot10^3$–$1\cdot4\cdot10^5$ and $7\cdot10^5$–$2\cdot10^6$ cm sec^{-1} respectively. The absorption spectrum can be deduced from the excitation spectrum.

INTRODUCTION

IN PART II of this paper experimental studies of excitation spectra on ZnS phosphors are described. The experimental results are evaluated by equations quoted in parentheses and discussed in Part I of the paper.

EXPERIMENTAL TECHNIQUES

A Zeiss quartz prism monochromator and a high pressure xenon arc light source (Tungsram XBO 160) served to determine the excitation spectra of several microcrystalline ZnS and ZnCdS phosphors. The samples were tested in a chamber mounted on the exit slit of the monochromator. The light detector was a 1P21 multiplier phototube, combined with suitable filters. Stray light was carefully eliminated. The spectral slit width was 30–100 Å.

The preparative data of phosphors studied are summarized in Table 1.

Measurements were carried out at room temperature in various gas atmospheres, such as oxygen, ozone, nitrogen, molecular and atomic hydrogen and vacuum. Atomic hydrogen was produced by heating a tungsten coil in hydrogen at 0·5 Torr pressure.

In order to eliminate diffuse optical effects of multiple powder layers, thin elementary layers of microcrystals (settled in pure alcohol) were tested. Up to now, excitation spectra were studied on

Table 1.

Phosphor	Activator (g/g)	Firing Temperature (°C)	Time (hr)	Flux
Hex. ZnS–Ag–Cl	$2\cdot10^{-4}$ Ag	1160	1	4% NaCl
Cub. ZnS–Ag–Cl	10^{-4} Ag	960	1	4% NaCl
Hex. ZnS–Cl	—	1160	1	4% NaCl
Cub. ZnS–Cl	—	960	1	4% NaCl
49 ZnS–51CdS–Ag–Cl	10^{-4} Ag	960	1	4% NaCl

All samples fired in covered quartz crucibles.

---

* Present address, Semiconductors Laboratory, Physics Department, University of Buenos Aires, Argentina.

thick powder layers, thus some important effects had been masked by multiple scattering.

EXPERIMENTAL RESULTS

The experimental results are summarized on Figs. 1–4. Figures 1–2 represent the excitation spectra of several ZnS and ZnCdS phosphors. They are similar to those published in the literature[1-6] and exhibit a nearly constant section in their short wave tail. This constant section begins at ~ 3100 Å for ZnS and at 3600 Å for ZnCdS phosphors.

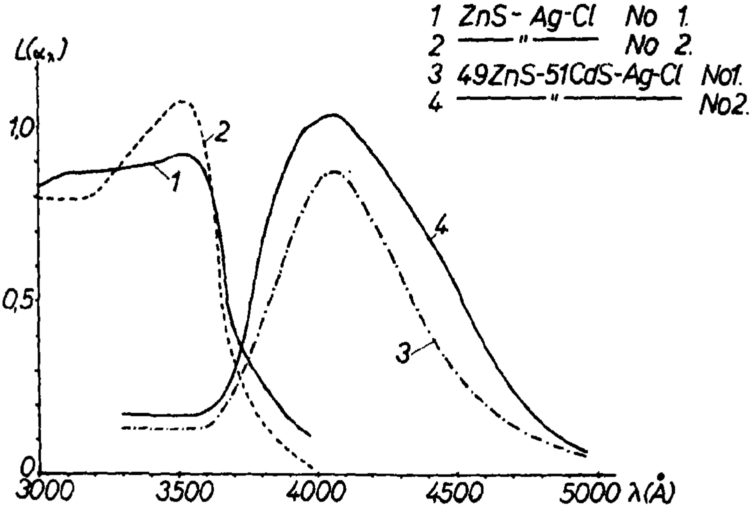

FIG. 1. Excitation spectra of some ZnS and ZnCdS phosphors. $L(\alpha_\lambda)$ plotted in arbitrary units.

Figure 3 represents the variation of excitation spectra with the grain size of crystals, separated by sedimentation from a 49ZnS–51CdS–Ag–Cl sample. The spectra are fitted in their maxima. The congruence of their short wave side and the shift of the long wave tails are remarkable and correspond to Equations (17) and (18).

Figure 4 shows the change of excitation spectra of a 49ZnS–51CdS–Ag–Cl and a cubic ZnS–Ag–Cl phosphor with grinding. The curves are normalized in their maxima. The surface deterioration decreases the short wave sensitivity of the crystals. This is analogous to the case of sandblasted silicon, germanium and CdS crystals.[7]

No change of excitation spectra was observed using various gas atmospheres including atomic hydrogen.[8] In spite of this, Friedrich found a strong (20-fold) enhancement of the blue luminescence on a CdS crystal excited by 3650 Å photons and previously subjected to a glow discharge surface treatment.[9]

Further studies with various surface treatments are being pursued in our laboratory, they will be discussed in a forthcoming paper.

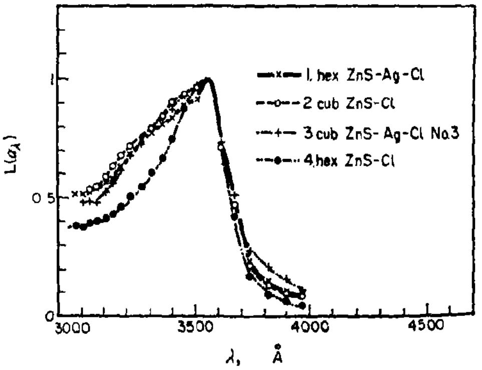

FIG. 2 Excitation spectra of some ZnS phosphors. $L(\alpha_\lambda)$ plotted in arbitrary units.

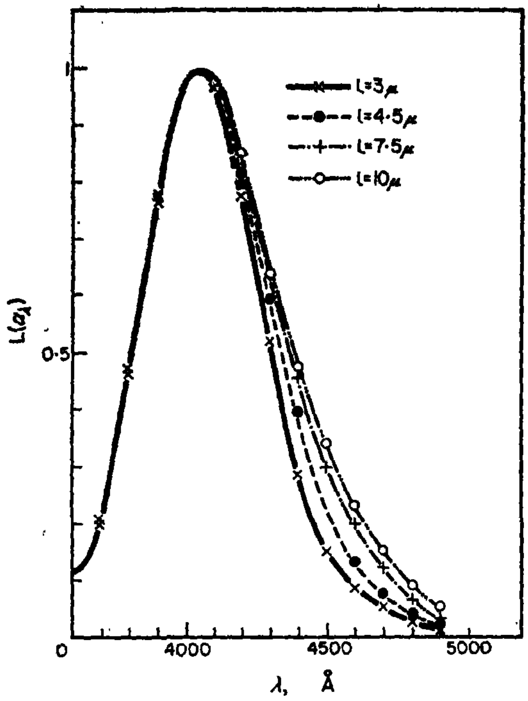

FIG. 3. Variation of excitation spectra with grain size of a 49 ZnS–51CdS–Ag–Cl phosphor. $L(\alpha_\lambda)$ plotted in arbitrary units.

EVALUATION OF EXPERIMENTAL RESULTS AND DISCUSSION

The experimental excitation spectra exhibit a nearly constant short wave tail. As shown in Part I Fig. 2 in the maximum $L(\alpha_\lambda)_{\max}$ surface recombination produces losses attaining less, than 5–6 per cent. The ratio $L(\alpha_0)_{\max}/L(\alpha_\lambda)_{\max}$ is varying for the individual samples of the same type of phosphor. Comparing $L(\alpha_0)$ and $L(\alpha_\lambda)_{\max}$ using Equations (14) and (19) respectively, an estimation for S may be made. For evaluating experimental results in the constant short wave tail $\alpha_0 = 10^6$ cm^{-1} (a limiting value found by MOLLWO(10)) was used. The results are summarized in Table 2 for the phosphor samples represented in Figs. 1–4.

The strong enhancement of S with grinding is remarkable. Grinding produces surface deterioration of crystals creating a high density of recombination centers. It is interesting to note, that S is considerably larger for ZnCdS phosphors than for ZnS ones. All the ZnS samples (cubic, hexagonal, with activator and without), exhibit the same character, they are, however, different in their long wave tail. The effect of silver activator and the shift of long wave edge with cubic crystal structure may be noted in Fig. 2.

Figure 5 represents the theoretical $L(\alpha_\lambda)$ spectra for a cubic ZnS–Ag–Cl phosphor sample with

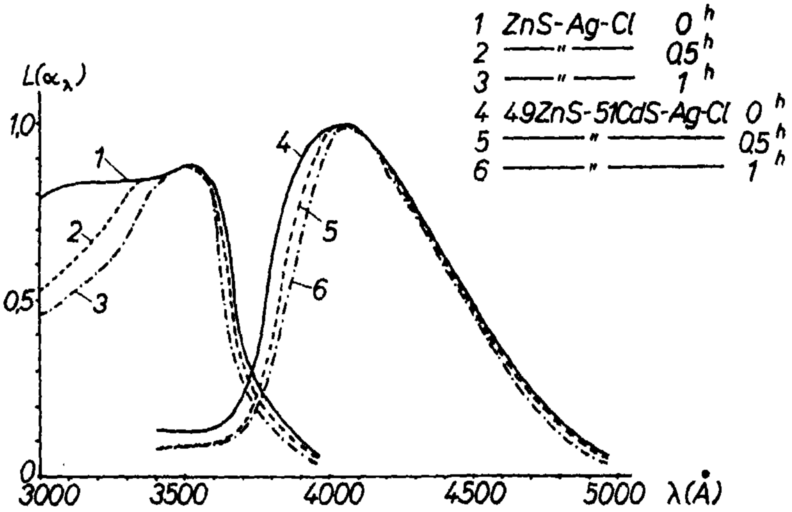

FIG. 4. Effect of grinding on the excitation spectra. $L(\alpha_\lambda)$ plotted in arbitrary units.

Table 2.

Phosphor	Surface recombination velocity (cm sec^{-1})	
cub. ZnS–Ag–Cl No. 1.	$2 \cdot 10^{3}$	
cub. ZnS–Ag–Cl No. 2.	$1 \cdot 3 \cdot 10^{4}$	
cub. ZnS–Cl	$2 \cdot 9 \cdot 10^{4}$	
hex. ZnS–Ag–Cl	$2 \cdot 9 \cdot 10^{4}$	
hex. ZnS–Cl	$1 \cdot 4 \cdot 10^{5}$	
49ZnS–51CdS–Ag–Cl No. 1.	$7 \cdot 10^{5}$	
49ZnS–51CdS–Ag–Cl No. 2.	$2 \cdot 10^{6}$	
Effect of grinding		
cub. ZnS–Ag–Cl No. 1.	$1 \cdot 9 \cdot 10^{4}$	0·5 hr
cub. ZnS–Ag–Cl No. 1.	$2 \cdot 8 \cdot 10^{4}$	1 hr
49ZnS–51CdS–Ag–Cl No. 1.	$5{:}10^{6}$	0·5–1 hr

$l = 10\mu$ grain size. The absorption coefficient α_λ was taken from MOLLWO[10] in the domain of strong absorption. In the long wave tail of absorption edge, our own results [11] were applied. The parameters $L_p = 0 \cdot 1\mu$ and $\mu_p = 11$ cm^2 V^{-1} sec^{-1} were taken from cathodoluminescence measurements.[12] The discrepancies between theoretical and experimental curves might be presumably

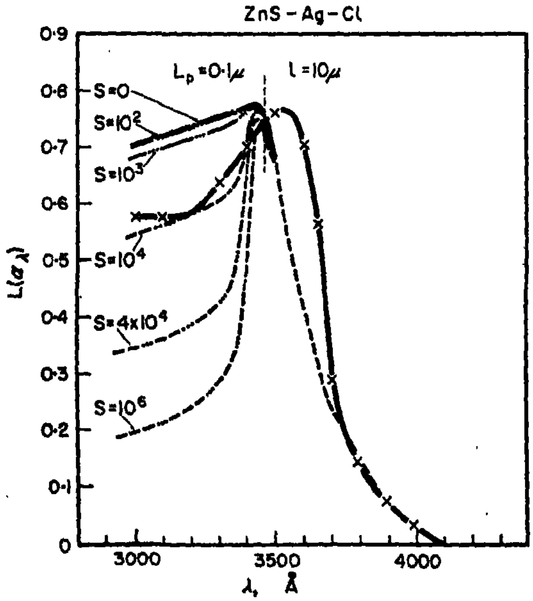

FIG. 5. Theoretical and experimental excitation spectra of a cubic ZnS–Ag–Cl phosphor. Experimental curve denoted by ——x——x——.

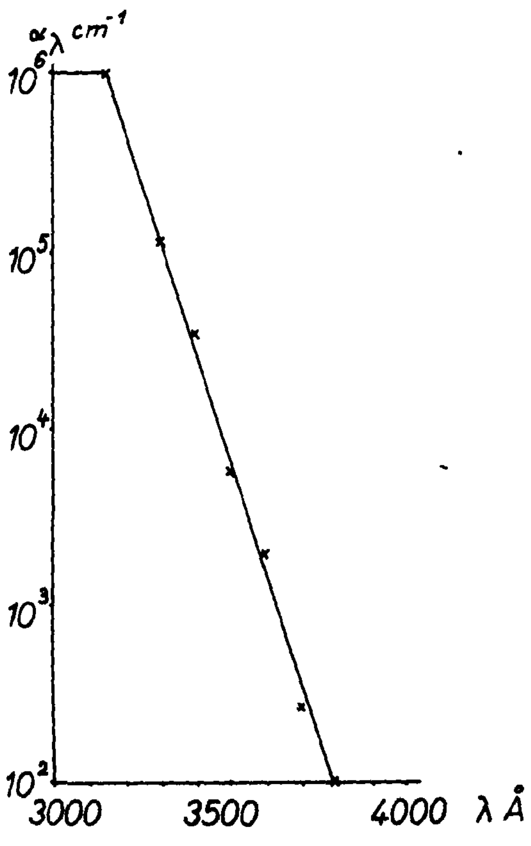

FIG. 6. Absorption spectrum of a cubic ZnS–Ag–Cl phosphor, as deduced from its excitation spectrum.

explained by the uncertainties of α_λ. MOLLWO's data were determined on thin films prepared without added impurities (activator). On the other hand, the comparison of generalized curves with experimental excitation spectra enables the approximate determination of absorption spectra of luminescent microcrystals even in the domain of strong absorption. The diffuse optical methods (reflection and transmission measurements) used up to the present are in practice unadequate for determining values of $\alpha_\lambda > 10^4\,\text{cm}^{-1}$. Figure 6 represents the absorption spectrum of the cubic ZnS–Ag–Cl sample, deduced from its excitation spectrum. It is similar to Mollwo's result.

Unfortunately low temperature measurements were not made, this however, would be of special interest in order to reveal possible exciton lines, as observed by HALPERIN and ARBELL.$^{(13)}$

Summarizing the results and comparing the theoretical analysis with experiments, the following conclusions may be drawn:

The behaviour of various ZnS–Ag–Cl phosphors (cubic, hexagonal, with and without activator), the change of excitation spectra with grinding and their variation with crystal grain size are in full accordance with theory and confirm the adequacy of the model used. Friedrich's experiment is a further strong support of the model. The uneffectiveness of various gas atmospheres may be caused presumably by a passive layer on the surface of microcrystals, having a large specific surface. In Friedrich's experiment, this passive surface layer was successfully removed by a gas discharge.

Acknowledgements—The authors are indebted to Mrs. M. STEINBACH for her help in the calculation.

REFERENCES

1. GARLICK G. F. J. and GIBSON A. F., *Nature, Lond.* **161**, 359 (1948).
2. ANTONOV ROMANOVSKY V. V. and EPSTEIN N. I., *Dokl. Akad. Nauk. S.S.S.R.* **64**, 483 (1949).
3. BUBE R. H., *Phys. Rev.* **90**, 70 (1953).
4. ALENCEV M. N., *Opt. Spectrosc.* **1**, 240 (1956).
5. BROSER I. and BROSER–WARMINSKY R., *Z. Elektrochem.* **61**, 209 (1957).
6. KELLER S. P. and PETTIT G. D., *Phys. Rev.* **115**, 526 (1959).
7. GROSS E. F. and NOVIKOV B. V., *Fiz. tverd. tela. S.S.S.R.* **1**, 1882 (1959).
8. BERGER H., BÖER K. W. and WEBER E. H., *Z. Phys.* **158**, 501 (1960).
9. FRIEDRICH M., *Monatsber. Dtsch. Akad. Wiss*, Berlin **3**, 283 (1961); *Z. Naturf.* **16a**, 1106 (1961).
10. MOLLWO R., *Reichsber. Phys.* **1**, 1 (1944).
11. BAUER GY. T., GERGELY GY. and ÁDÁM J., *Tagung Festkörperphysik, Balatonfüred,* 1959, p. 263. Akademie, Berlin (1961).
12. GERGELY GY, *Acta phys. hung.* **12**, 221 (1960); *J. Phys. Chem. Solids* **21**, 105 (1961).
13. HALPERIN A. and ARBELL H., *Phys. Rev.* **113**, 1216 (1959).

J. Phys. Chem. Solids Pergamon Press 1963. Vol. 24, pp. 693–697. Printed in Great Britain.

MAJORITY-CARRIER MOBILITY ON GERMANIUM SURFACES

N. B. GROVER* and **R. OREN**

Department of Physics, The Hebrew University, Jerusalem, Israel

(*Received* 2 *November* 1962)

Abstract—Measurements are reported of the majority-carrier surface mobility at several temperatures and following various etches in a large number of both *n*- and *p*-type germanium samples and the results are compared with theoretical calculations based on the diffuse scattering model. The pulsed field-effect technique is used, advantage being taken of the relatively slow thermal release of charge from most of the surface states into the majority-carrier band at reduced temperatures.

The results indicate good qualitative agreement with the diffuse scattering model, but some degree of specularity is necessary to account for the data obtained. The less-than-predicted sensitivity to such parameters as impurity concentration and temperature as well as the marked effect of etchants may very well be the results of the overriding influence of surface states and their variation with surface treatment.

INTRODUCTION

In order to be able to determine the barrier height from surface conductivity measurements,(1, 2) a knowledge of the surface mobilities(3) is necessary. Several attempts have been made to calculate these theoretically,(4, 5, 6) but the results of any such attempt must depend on the particular model of surface scattering chosen. It is thus highly desirable to measure experimentally the surface mobility because, first of all, this will permit quantitative interpretation of surface measurements and, secondly because a knowledge of the surface mobility may help elucidate the scattering mechanism prevalent at the semiconductor surface.

Results have been reported before(7) of majority-carrier surface mobility on a few *n*- and *p*-type germanium samples. In the present paper, these measurements are extended to include the investigation of influences due to crystallographic orientation, etchants, and impurity concentration in a large number of samples of both conductivity types. The *p*-type germanium samples were studied for the most part at 185°K while the *n*-type samples were measured at other temperatures as well, particularly at 257 and at 80°K. A special light-tight cryostat was used at the lower temperatures to prevent optical generation of minority carriers which in this range can become significant if no special precautions are taken. Several etchants were tested and systematic studies were carried out on all samples using two of them.

The pulsed field-effect technique was used to measure the majority-carrier surface mobility in accumulation layers. This procedure, which has been described in detail elsewhere,(7) consists essentially in applying a succession of constant-amplitude, square-wave pulses in series with a variable d.c. biasing voltage while measuring the sample conductance in such a way that the bias determines the operating point of the barrier and the pulses repel the majority carriers from the surface. In this way, advantage is taken of the relatively slow thermal release of charge from many of the surface states into the majority-carrier band at reduced temperatures. By the use of the pulsed field-effect technique, a rapid decrease in majority-carrier concentration within the space-charge region is effected. The change in surface conductance, determined at the onset of

---

* Present address: Rockefeller Institute, New York 21, N.Y.

the pulse before the deficit induced can be redistributed between the states and the majority-carrier band, then becomes a direct measure of majority-carrier surface mobility. The latter is obtained as a function of barrier height provided that the d.c. swing is sufficient to enable the barrier to pass through the conductance minimum. Results obtained by this method represent the lowest possible limit to the actual values.

RESULTS

Preliminary measurements of the effect of various etchants on the surface mobility showed that the results obtained on any particular sample are usually reproducible following polishing and re-etching. The investigation reported here was restricted to two etchants after it became clear that a third, warm hydrogen peroxide, resulted in no measurable difference in surface mobility before and after the etch. In general the samples were etched first in one etchant and, following measurements, were again polished and etched in the second etchant. Occasionally this procedure was reversed, and then the results agreed well with those obtained on the same sample using the standard procedure. Etch I consists of HF, CH_3COOH, HNO_3 in the ratio 3:3:5 and the etching was carried out at 35°C for $\frac{1}{2}$ min. Etch II consists of the same acids but in the ratio 1:12:6 and with the addition of 0·25 mg KI for every ml HF. The samples were etched in etch II for 1 min. also at 35°C.

Typical results of the surface mobility for *n*-type samples at 80°K are shown in Fig. 1 as a function of barrier height v_s. (Note that in accumulation layers v_s is always positive for *n*-type and negative for *p*-type samples. At $v_s = 0$ the bands are straight up to the surface; as $|v_s|$ increases, the potential well for the *majority* carriers at the surface becomes deeper and the accumulation layer stronger.) The circles, squares, rings, and triangles refer to different samples having impurity concentrations lying between 10^{13} and 10^{14} cm^{-3}. The filled points are obtained following etch I, the empty ones following etch II. The effect of the etchant is seen to overshadow almost completely any effect due to variations in impurity concentration. The solid line is a typical theoretical curve based on the diffuse scattering model.(8)

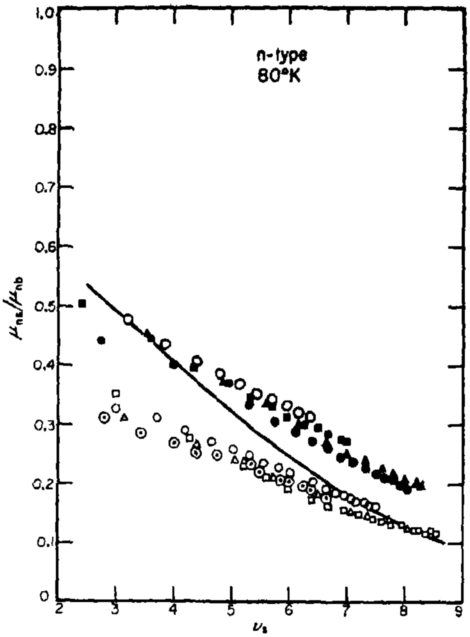

FIG. 1. Typical results of electron surface mobility in accumulation layers of *n*-type germanium samples at 80°K as a function of barrier height. The circles, squares, rings, and triangles refer to different samples having impurity concentrations lying between 10^{13} and 10^{14} cm^{-3}. The solid line is a typical theoretical curve for diffuse scattering. Filled points—etch I; Empty points—etch II.

Figure 2 illustrates results obtained at 185°K on four different *p*-type samples having impurity concentrations lying between 10^{14} and 10^{15} cm^{-3}. Here too, the filled points refer to etch I and the empty points to etch II. The striking result in these data is the opposite effect of these etchants on *n*-and *p*-type samples, caused perhaps by the overriding influence of the surface states and the different way they are affected by surface treatment in the two conductivity types.

The influence of temperature on four different *n*-type samples of comparable impurity concentration is shown in Fig. 3. The upper set of points was obtained with the cryostat immersed in a crushed-ice and salt solution (257°K) while the lower set is from measurements in liquid air (80°K). The temperature of the middle set of points is not as well defined as in the other two cases. Variations about the mean value (185°K), however, were never more than a few degrees.

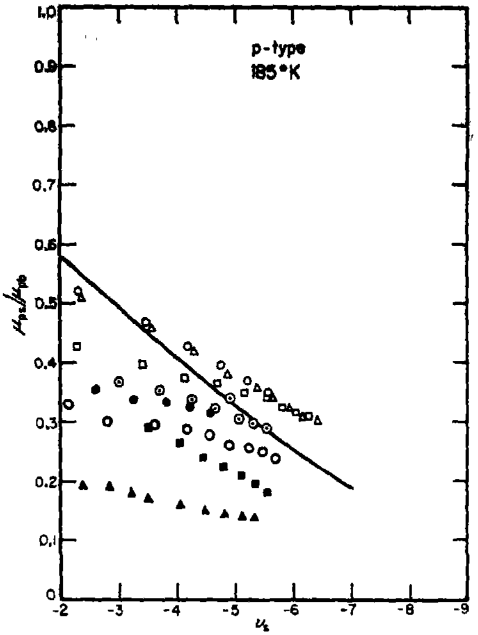

FIG. 2. Typical results of hole surface mobility in accumulation layers of p-type germanium samples at 185°K as a function of barrier height. The circles, squares, rings, and triangles refer to different samples having impurity concentrations lying between 10^{14} and 10^{15} cm^{-3} The solid line is a typical theoretical curve for diffuse scattering. Filled points—etch I; Empty points—etch II.

The results shown here are typical. At the highest temperature the experimental points lie well above the corresponding theoretical curve, while at the lowest temperature some of the points are above and some are below. The surface mobility decreases more slowly than as predicted by the theoretical curve, so that for large values of barrier height (strong accumulation layers) all the points lie above the curve. The situation is somewhat different in the results obtained at the solid CO$_2$ temperature. Here almost all the points lie below the corresponding curve but they give every indication that they will cross it at a value of v_s slightly beyond the range of measurement.

Data accumulated on various n-type samples are shown in Fig. 4 in order to illustrate the influence of impurity concentration at the two lower temperatures. The filled circles, triangles, and squares (185°K) refer to impurity concentrations of 3·2, 6·3, 9·5 × 10^{13} cm^{-3} respectively. The empty points (80°K) refer to 3·2, 8·6, 18 × 10^{13} cm^{-3} respectively. These results indicate the general trend expected for different impurity concentrations, but by their very nature are less reliable than those obtained above—it is nearly impossible to vary the impurity concentration of an individual sample, so that the data must be accumulated on different samples.

These results are to be compared with the data for six p-type samples at 185°K shown in Fig. 5. Despite the spread in impurity concentrations of from 10^{14} to 10^{15} cm^{-3}, no trend is noticeable in the experimental points. Thus another mechanism must be dominant in the case of p-type material.

CONCLUSIONS

All the results presented above have several features in common. In many cases the experimental points lie above the corresponding

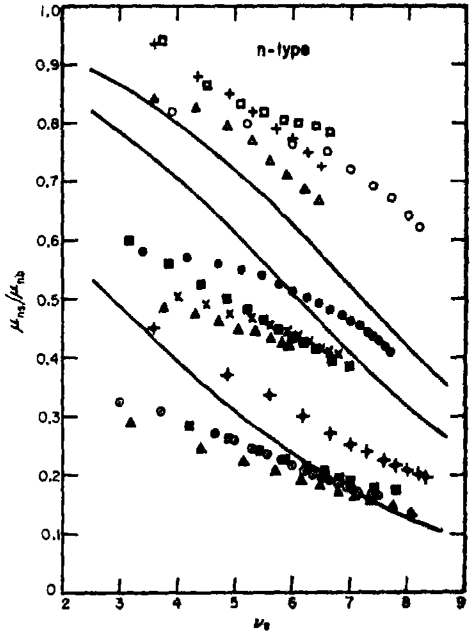

FIG. 3. Typical results of electron surface mobility in accumulation layers of n-type germanium samples at three different temperatures as a function of barrier height. The circles, squares, crosses, and triangles refer to four different samples of comparable impurity concentrations. The upper set of points (empty) was obtained at 257°K, the middle set (filled) at 185°K, and the lower set (dotted) at 80°K. A typical theoretical curve (for diffuse scattering) is shown for each temperature.

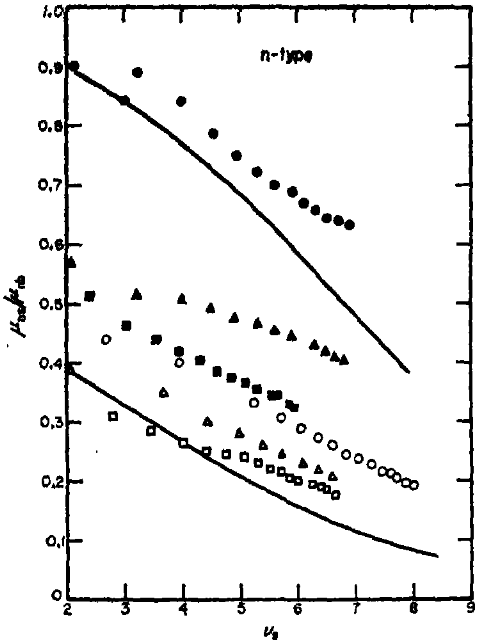

FIG. 4. Typical results of electron surface mobility in accumulation layers of *n*-type germanium samples at 185°K (filled) and 80°K (empty) as a function of potential barrier. A typical theoretical curve (for diffuse scattering) is shown for each temperature.

Symbol	Impurity concentration	Symbol	Impurity concentration
●	$3\cdot 2\times 10^{13}$ cm^{-3}	●	$3\cdot 2\times 10^{13}$ cm^{-3}
▲	$6\cdot 3\times 10^{13}$ cm^{-3}	▲	$8\cdot 6\times 10^{13}$ cm^{-3}
■	$9\cdot 5\times 10^{13}$ cm^{-3}	■	18×10^{13} cm^{-3}

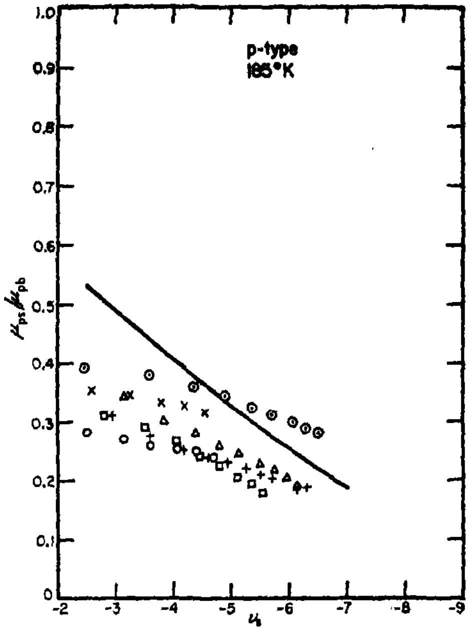

FIG. 5. Typical results of hole surface mobility in accumulation layers of *p*-type germanium samples at 185°K as a function of potential barrier. The various symbols refer to different samples having impurity concentrations lying between 10^{14} and 10^{15} cm^{-3}. A typical theoretical curve (for diffuse scattering) is also shown.

theoretical curves (for diffuse scattering) throughout the entire range of barrier height. In other cases the stronger the accumulation layer the less is the separation between the points and the curve, until either the curve passes under the points or gives every indication that it is about to do so at values of v_s slightly beyond the range of measurement. The effect of etchants is much more marked than that of sample doping (particularly in *p*-type germanium), while the crystallographic orientation of the surface seems to be of secondary importance. The influence of temperature is more or less as predicted by the theory, perhaps somewhat less.

In the processing of the data we have tacitly assumed that the experimental procedure employed eliminated effects arising from all surface states. Actually, the occurrence of any states with release times shorter than the experimental resolution time (for example, states close to the majority-carrier band edge) would result in the mobile charge being less than the total charge induced by the pulse. The effect of such states, if present, would then be to raise the actual surface mobility above its measured value on the one hand and, on the other, to lower the values of v_s below those calculated on the basis of no surface states. As the barrier height for strong accumulation layers depends only logarithmically on the induced mobile charge, however, the deduced values of v_s would not be appreciably affected in this range. The results obtained by the field-effect technique thus represent the lowest possible limit to the actual values.

The general picture which emerges from the results of these measurements indicates good agreement between the experimental data and the theoretical model, but in most cases (particularly in the case of *n*-type samples) the scattering is definitely not completely diffuse, especially when the carriers are confined to deep wells, and some degree of specularity must be involved. Such information, however, is far from being capable of determining the dominant mechanism of surface scattering, and considerable work is still required.

Acknowledgements—The authors wish to thank Prof. A. Many for suggesting this problem and for his help and encouragement. Thanks are also due to Messrs. J. Weisman and S. Bell for their help in carrying out the measurements and to Mr. Y. Aharonow for his technical assistance.

REFERENCES

1. Kingston R. H. and Neustadter S. F., *J. appl. Phys.* **26**, 718 (1955).
2. Garrett C. G. B. and Brattain W. H., *Phys. Rev.* **99**, 376 (1955).
3. Schrieffer J. R., *Phys. Rev.* **97**, 641 (1955).
4. See the review article by Greene R. F., *J. Phys. Chem. Solids* **14**, 291 (1960).
5. Goldstein Y., Grover N. B., Many A. and Greene R. F., *J. appl. Phys.* **32**, 2540 (1961).
6. Grover N. B., Goldstein Y. and Many A., *J. appl. Phys.* **32**, 2538 (1961).
7. Many A., Grover N. B., Goldstein Y. and Harnik E., *J. Phys. Chem. Solids* **14**, 186 (1960).

LETTERS TO THE EDITOR

Maximum solid solubility and distribution coefficient of impurities in germanium and silicon

(*Received* 26 *December* 1962)

FISCHLER(1) has found empirically a relation between the maximum molar solid solubility x_M of impurities in Germanium and Silicon and the distribution coefficient k at the melting point

$$x_M = 0{\cdot}1k. \tag{1}$$

A theoretical explanation for this relation can be given as follows:

LEHOVEC(2) has given an expression for the ratio of the solidus and liquidus concentrations x^0 and x_L^0 of neutral impurities applying the mass action law to the transfer of neutral impurities from the liquid to the solid semiconductor:

$$\frac{x^0}{x_L^0} = \gamma\Gamma\left(\frac{k\delta}{\gamma\Gamma}\right)_\Theta^{\Theta/T} \tag{2}$$

Θ is the melting point of the pure semiconductor. The expressions in the parentheses have to be taken at the melting point as indicated by the subscript Θ. γ means the activity coefficient of the impurities at the liquidus and Γ can be approximated by

$$\Gamma \approx \exp\left\{-\frac{\Delta H_I}{R\Theta_I}\right\}, \tag{3}$$

where ΔH_I and Θ_I are the heat of fusion and the melting temperature of the impurity. R is the gas constant. δ means the fraction of neutral impurities in the solid phase. In equation (2), the neutral impurity concentration x_L^0 at the liquidus can be assumed to be equal to the total impurity concentration x_L as was pointed out by LEHOVEC.(2)

In order to obtain an explanation of equation (1), we now express x_L in equation (2) by the ideal liquidus equation

$$x_L = 1-\exp\left\{-\frac{\Delta H}{R}\left(\frac{1}{T}-\frac{1}{\Theta}\right)\right\}, \tag{4}$$

where we did not allow for an activity coefficient different from unity. This can be done with good approximation as long as the temperatures are near the melting point. Differentiation of equation (2) with respect to T, where we assume $\gamma\Gamma$ to be independent of temperature, gives us the temperature of maximum solid solubility. We insert the expression for this temperature into equation (2) and obtain for the maximum solid solubility of neutral impurities

$$x_M^0 = \frac{B\delta_\Theta}{B-\ln A}\exp\left\{-\frac{1}{B}\ln A\ln\frac{-\ln A}{B-\ln A}\right\}k. \tag{5}$$

A and B stand for $\left(\frac{k\delta}{\gamma\Gamma}\right)_\Theta$ and $\frac{\Delta H}{R\Theta}$, respectively.

B takes the values 3·37 for Ge and 3·62 for Si. In the case of Ge, δ at the melting point is equal to 0·29 and 0·42 for donor and acceptor type impurities, respectively. In the case of Si, the corresponding values are 0·18 and 0·36.(2) In all four cases the ionization energy of the impurities is assumed to be small compared to the thermal energy.

The right hand side of equation (5) shows approximately the same functional dependence on k as in equation (1) because the factor

$$F = \frac{B}{B-\ln A}\exp\left\{-\frac{1}{B}\ln A\ln\frac{-\ln A}{B-\ln A}\right\} \tag{6}$$

turns out to be nearly constant over a wide range of A as can be seen from Fig. 1.

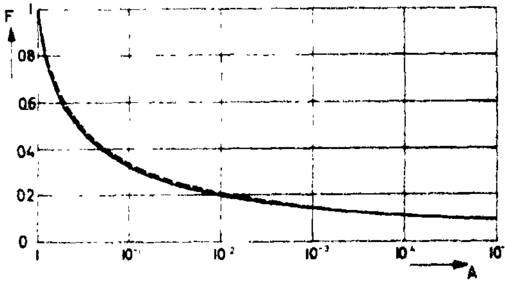

FIG. 1. F as function of A. For the explanation of the abbreviations see text. The solid line corresponds to Ge, and the dotted line to Si.

Table 1. *The neutral and the total maximum molar solid solubility* x_M^0 *and* x_M *divided by the distribution coefficient* k *at the melting point for various impurities in* Ge *and* Si *as calculated from equation* (5) (*columns* 7 *and* 8). x_M^0/x_M *is taken from* LEHOVEC.[2] *Columns* 3 *through* 6 *contain the parameters used in the calculation. The last column gives the experimental values as reported by* FISCHLER.[1]

		k	$\delta\Theta$	$\gamma\Theta$	Γ	x_M^0/k (theor.)	x_M/k (theor.)	x_M/k (exp.)
Ga		0·087	0·42	0·94	0·11	0·20	0·20	0·13
Al		0·073		0·53	0·25	0·18	0·18	0·13
In		0·001		1·46	0·40	0·06	0·14	0·09
Zn		4×10^{-4}		1*	0·31	0·06	0·16	0·15
Cu	in	$1{\cdot}5\times10^{-5}$		2·23	0·32	0·03	0·09	0·05
Pt	Ge	5×10^{-6}		1*	0·28	0·03	0·08	?
Cd		1×10^{-5}		2·30	0·29	0·04	0·10	?
As		0·02	0·29	0·79	0·048	0·11	0·14	0·10
Sb		0·0030		1·46	0·073	0·06	0·14	0·09
Li		0·002		1*	0·29	0.05	0·14	0·08
Ga		0·0080	0·36	1·7	0·11	0·08	0·16	0·10
Al		0·0020		0·54	0·25	0·07	0·21	0·19
In	in	4×10^{-4}		5·61	0·40	0·04	0·14	?
As	Si	0·3	0·18	3·9	0·048	0·09	0·10	0·11
Sb		0·023		6·0	0·073	0·04	0·11	0·06
Li		0·01		1*	0·29	0·04	0·14	0·12

In order to obtain the total maximum solid impurity concentration x_M, we have to divide equation (5) by δ_T, where δ_T means δ at the temperature at which the maximum value of x^0 appears. This holds approximately only, because as a consequence of the dependence of δ on temperature and concentration the maximum values of x^0 and x are not exactly at the same temperature.

Table 1 gives the calculated values of x_M^0/k and x_M/k for some impurities in germanium and silicon. δ_T can be evaluated for small impurity ionization energies from data given by LEHOVEC.[2] The values of k are taken from TRUMBORE.[3] Γ is calculated from equation (3) and γ at the melting point is calculated from

$$\gamma_\Theta = \exp\left\{\frac{a-b\Theta}{R\Theta}\right\} \tag{7}$$

(see LEHOVEC[2]). The values of a and b are given by THURMOND and KOWALCHIK.[4] If a and b are not available γ is approximated by unity. This is marked by an asterisk. It may be emphasized that inaccuracies of the values contained in A have little influence on the resulting x_M/k (see Fig. 1).

The dependence of γ and δ on temperature was not fully considered in our calculation. So we cannot expect overall agreement between theoretical and experimental values. Nevertheless, our calculation gives the proper functional dependence of x_M on k (equation 5) which corresponds satisfactorily with the empirical relation (1). Moreover, the deviations of our calculated values $(x_M/k)_{\text{theor}}$ from equation (1) are at most of the same order of magnitude as the deviations of the experimental values $(x_M/k)_{\text{exp}}$ from equation (1) (columns 8 and 9 of Table 1).

IBM Laboratories,
Boeblingen,
Germany.

HORST STATZ

References

1. FISCHLER S., *J. appl. Phys.* **33**, 1615 (1962).
2. LEHOVEC K., *J. Phys. Chem. Solids* **23**, 695 (1962).
3. TRUMBORE F. A., *Bell Syst. tech. J.* **39**, 205 (1960).
4. THURMOND C. D. and KOWALCHIK M., *Bell Syst. tech. J.* **39**, 169 (1960).

The thermodynamic activity of the semiconductor

(*Received* 2 *January* 1963)

IN EXACT formulations of the intrinsic ionization equilibrium as, for example,(1)

$$kT \ln np = -(\mu_n^0 + \mu_p^0) - kT \ln \gamma_n \gamma_p f_n f_p \quad (1)$$

or its statistical equivalent

$$kT \ln np = kT \ln \mathcal{N}_C \mathcal{N}_V - \Delta\epsilon_G - kT \ln f_n f_p \quad (2)$$

the thermodynamic activity of the semiconductor does not appear explicitly. The reason can be shown to lie in the thermodynamic definition of the hole. Thus, expressing the intrinsic ionization process as an electronic transition

$$e^-(\text{valence band}) = e^-(\text{conduction band}) \quad (3a)$$

or as a self-ionization of the semiconductor (GaAs will be used as an example)

$$\text{GaAs} = \text{GaAs}^+ + e^-(\text{conduction band}) \quad (3b)$$

the hole is alternatively conceived as a missing valence-band electron, whence $\mu_p \equiv -\mu_{e^-}(\text{v.b.})$, or as a constituent of the ionized atom pair, whence $\mu_p \equiv \mu_{\text{GaAs}^+} - \mu_{\text{GaAs}}$. By either route, the intrinsic ionization reaction comes to be reformulated as

$$\text{zero} = e^-(\text{c.b.}) + e^+(\text{v.b.}) \quad (3c)$$

thereby indicating the equivalence of the two definitions of the hole.

The second definition may be expanded to give

$$\mu^0_{\text{GaAs}^+} - \mu^0_{\text{GaAs}} - \mu^0_p = kT \ln \frac{a_p}{a_{\text{GaAs}^+}/a_{\text{GaAs}}} \quad (4)$$

Equation (4) shows that at each temperature the activity of holes a_p is proportional to the ratio $a_{\text{GaAs}^+}/a_{\text{GaAs}}$. In order to preserve the symmetry in properties between holes and electrons, we require that the activity of holes become equal to their concentration as the total concentration of imperfections decreases indefinitely; under the same conditions, the activity of the semiconductor, which is approximated by its mole fraction, will approach unity:

$$\text{as } \sum c_i \to 0,\ a_{\text{GaAs}} \to 1 \text{ and } a_p \to a_{\text{GaAs}^+} \to p \quad (5)$$

Stated in another way, the standard state for holes has, for convenience, been chosen so as to make the left-hand side of equation (4) identically zero.

In terms of thermodynamic properties of actual chemical species,* the activity coefficient $\gamma_p f_p$ for holes is $(\gamma f)_{\text{GaAs}^+}/a_{\text{GaAs}}$, $(\gamma f)_{\text{Si}_2^+}/a^2_{\text{Si}}$, etc. The hole is, therefore, an abstraction of such nature that the thermodynamic activity of holes is an implicit function† of the activity of the semiconductor species.

Lincoln Laboratory,‡ WALTER W. HARVEY
Massachusetts Institute of
Technology,
Lexington 73,
Massachusetts.

References

1. HARVEY W. W., *J. Phys. Chem. Solids* **23**, 1545 (1962).
2. EIGEN M. and DE MAEYER L., *The Structure of Electrolyte Solutions*, (edited by HAMER W. J.). Chap. 5. John Wiley, New York (1959).

Surface states at the germanium–electrolyte cathode

(*Received* 11 *December* 1962)

WHEN germanium, immersed in an electrolyte, is polarized negatively, hydrogen is evolved and the germanium surface is covered by about a monolayer of chemisorbed hydrogen atoms.(1, 2) The surface chemistry of the germanium cathode is fairly well defined, and it is both reasonable and useful to ask what the density and energy of surface states will be at such a surface. A knowledge of the surface state configuration of the germanium

---

[*] The consideration that the ionized atom pairs are, owing to the thermal velocity of the hole, capable of only transitory existence does not disqualify them as chemical entities; the lifetime of an individual H_3O^+ ion, for example, in water or ice is comparably short.(2)

[†] If by analogy to electronic semiconductors, a defect proton π^- is conceived as $\pi^- \equiv OH^- - H_2O$, the chemical equation for the self-ionization of water becomes zero $= H^+ + ^-$, and the activity of water molecules is contained within the activity coefficient of the abstract species π^-.

[‡] Operated with support from the U.S. Army, Navy, and Air Force.

electrode is important in the theory of semiconductor electrochemistry(3, 4) and even more important as part of the experimental basis of a theory of surface states.

A modification of the field-effect experiment has been used to investigate the germanium cathode, Ge|(intrinsic) 2M HCl, H_2 (gas). The physical arrangement of the germanium electrode is shown in Fig. 1. It consists of a uniformly thin Ge disc waxed (paraffin wax, not a serious source of electrode contamination) to the bottom of the cathode compartment. An ohmic contact, in the form of a ring concentric with, and having an inner diameter the same as the inner diameter of the glass tube which makes the bottom of the cathode compartment, is made on the air side of the germanium disc. Provision was made to measure the potential of the ohmic contact with respect to a reference hydrogen electrode; under conditions of electrolysis, this gives the overpotential of the germanium electrode at its periphery. A tungsten needle was used to probe the potential difference between the ohmic contact (periphery) and any known point along a diameter (2 cm) of the disc. The electrolysis current (from a constant current source) was applied at the ohmic contact, whence the current distribution in the Ge disc is axially symmetrical.

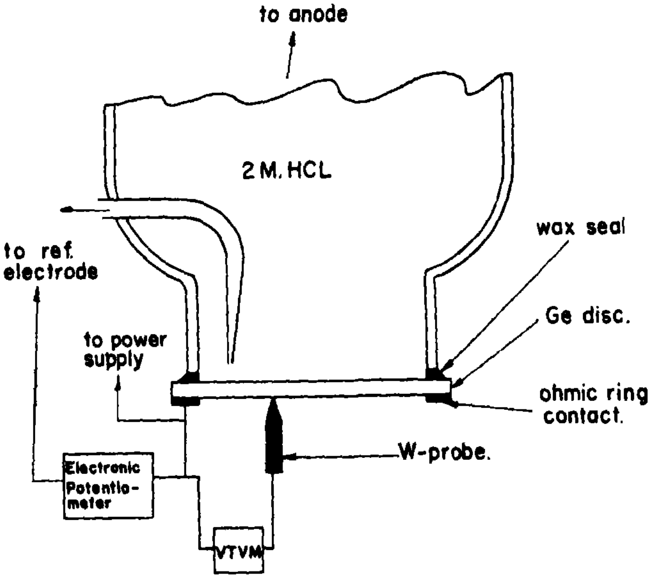

FIG. 1. Arrangement of Ge disc electrode and electrical connections.

The entire apparatus was cooled to 4°C in an air thermostat. The resistivity of the Ge disc (as a function of temperature) had been previously measured, and the material found to be uniform and intrinsic from 28 to 0°C. Furthermore, measurements on very thin discs (10^{-2} cm thick) showed that C.P.4 etch caused essentially no surface space charge, i.e. resistance (per square) vs. reciprocal thickness extrapolated to zero. The disc was cut parallel to the (111) plane and etched in C.P.4 etch which was subsequently flooded out.(5) Electrolysis was carried out under conditions of high purity, and stable hydrogen overpotential curves were obtained.

The immediate object of the experiment is to obtain the experimental relation between the lateral resistance of the Ge and the hydrogen overpotential. First of all we obtain the value of the Tafel slope, b, and the exchange current, i_0, by placing a mercury contact over the back of the Ge disc and running the electrolysis current through the mercury rather than through the ohmic contact. We measure the potential difference between the ohmic contact and the reference electrode.

The results used in this work for a run at 4°C were, $b = 175$ mV and $i_0 = 4{\cdot}4 \times 10^{-10}$ A cm^{-2}. The mercury contact was removed and the arrangement of Fig. 1 resorted to.

Since the hydrochloric acid resistivity was less than 1/100 that of the Ge and the Ge disc was thin (0·32 mm) the equivalent circuit shown in Fig. 2

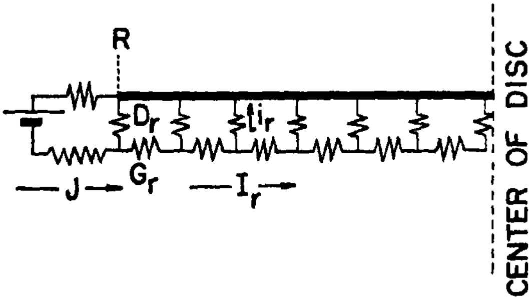

FIG. 2. Equivalent circuit of Ge–electrolyte electrode in connection with the electrolysis cell.

can be used to represent the electrode. The resistance, D_r, is the electrical double layer resistance, which is related to the current i_r passing through the interface at point r (radius measured from the center of the disc) by the relation

$$D_r = (b/i_r) \log_{10} (i_r/i_0), \tag{1}$$

where i_r is the current density at r (A cm^{-2}); i_0 is the exchange current density (A cm^{-2}); and, b is the Tafel slope (volts per decade of current) for the electrochemical reaction. This relation is obeyed for $i \gtrsim 10\, i_0$. G_r is the lateral resistance of the Ge disc at r in ohms per square. J is the total electrolysis current. Finally I_r is the total current passing along the disc at r: $I_r = J$, for $r = R$, at the periphery.

Since we can probe the potential difference ΔV along the disc we know the overpotential (η) as a function of r, i.e.

$$\eta_r = \eta_R - \Delta V_r \tag{2}$$

We also now know the relation between i and η, i.e.

$$\eta_r = b \log_{10} (i_r/i_0) \tag{3}$$

We can therefore obtain I_r, viz.

$$I_r = J - 2\pi \int_r^R i_r\, r\, \mathrm{d}r. \tag{4}$$

The gradient of potential along the Ge disc is given by

$$\left(\frac{\mathrm{d}\Delta V}{\mathrm{d}r}\right)_r = \frac{I_r \rho_r}{2\pi r} \tag{5}$$

where ρ_r is the lateral resistance of the Ge disc at r in ohms per square.

It is now possible to obtain η vs. ρ. A partial check of the method is obtained by plotting $2\pi r i_r$ vs. r and evaluating the integral in equation (4) graphically; it should equal J, and was found to do so. At low current densities, such that ρ_r is essentially invarient with r (i.e. $\Delta V \lesssim 15$ mV), $2\pi r i_r$ vs. r gives a straight line. Under these conditions we can simplify the measuring procedure by just measuring the lateral potential difference between the periphery and the center of the disc, when

$$\Delta V = I\rho/4\pi \tag{6}$$

The results of η vs. ρ measurements for the condition fulfilling equation (6) are shown in Fig. (3). The surface is n-type(6) and the surface conductivity (knowing ρ and the flat band disc conductivity) at two values of η is $2{\cdot}3 \times 10^{-4}$ and $4{\cdot}15 \times 10^{-4}$ mhos per square at $\eta = 470$ and -860 mV respectively. Using a value of electron mobility(7) in the space charge region of 2000 cm^2 V^{-1} sec^{-1}, and the appropriate constant at 4°C for the solution of the static space relations,(8) we obtain $(u_s)_{-470} = 10{\cdot}2$ and $(u_s)_{-860} = 11{\cdot}0$, where u_s is the number of units of kT which separates the center of the energy gap from the Fermi level at the germanium surface.

It can readily be demonstrated that this must be a surface with a high density of surface states. Thus, on going through a $\Delta\eta$ change of 390 mV we have only changed the excess charge in the space charge region of the semiconductor by $5{\cdot}8 \times 10^{11}$ cm^{-2}. Whereas, for no surface states(3) we should have observed a change of $4{\cdot}3 \times 10^{13}$ cm^{-2} for a compact Helmholtz double layer 3 Å thick with a dielectric constant for water of 6.

Knowing the exact shape of the η vs. ρ curve it is possible to calculate the density, N_s, and energy, E_t, of the surface states, for a simple single energy level model. Our experimental uncertainty is somewhat too high for such a calculation, and we have therefore taken $N_s = 5 \times 10^{14}$. We select

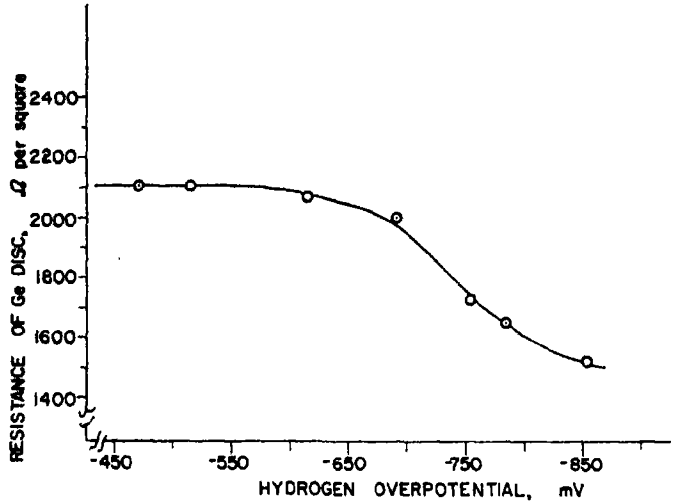

FIG. 3. Resistance of Ge disc as a function of hydrogen overpotential. (Bulk resistivity at 4°C is 131·8 Ω cm.)

N_s as equal to the surface concentration of chemisorbed hydrogen atoms (N_s must be $\gtrsim 10^{14}$, and therefore should have a value which is rational in terms of the chemistry of the surface). In this way we determine that E_s, which can only be donor type states in order to be consistent with the experimental results, is 0·22 eV above the center of the energy gap.

The results of this experiment are entirely consistent with the electrode kinetics(9) and the capacity values(10) found for germanium cathodes. They provide confirmation of the theory of the semiconductor–electrolyte interface(3, 4) and should provide useful data against which to test a theory for impurity surface states.

Acknowledgements—We would like to thank the Philco Corporation for partial support of this research, and one of us (J. McB) would like to thank the A.R.P.A. Agency operating at the University of Pennsylvania for a research grant.

The Electrochemistry Laboratory, MINO GREEN
The University of Pennsylvania, V. JENDRASIC*
Philadelphia 4, J. McBREEN
Pennsylvania.

References

1. BARDELEBEN J., *Z. phys. Chem.* **17,** 39 (1958).
2. HARVEY W. W., SHEFF S. and GATOS H. C., *J. electron. chem. Soc.* **107,** 560 (1960).
3. GREEN M., *Modern Aspects of Electrochemistry,* Vol. 2, Chap. 5, Butterworths, London (1959).
4. GREEN M., *J. chem. Phys.* **31,** 200 (1959).
5. GREEN M. and LIBERMAN A., *J. Phys. Chem. Solids,* **23,** 1407 (1962).
6. BRATTAIN W. H. and GARRETT C. G. B., *Bell Syst. tech. J.* **34,** 129 (1955).
7. GREENE R. F., FRANKL D. R. and ZEMEL J., *Phys. Rev.* **118,** 967 (1960).
8. KINGSTON R. H. and NEUSTADTER S. F., *J. appl. Phys.* **26,** 718 (1955).
9. ERDELYI V. R. and GREEN M., *Nature, Lond.* **182,** 1592 (1958).
10. ENGELL H. J. and BOHNENKAMP K., *Surface Chemistry of Metals and Semiconductors,* p. 232. John Wiley, New York (1960).

Electric properties of gray tin single crystals grown in tin–mercury alloys

(*Received* 31 *October* 1962)

SOME measurements of electric properties of gray tin single crystals have been carried out on samples prepared according to the method described by VAN LENT.(1, 2)

---

* This work was carried out in partial fullfilment of the requirements for the degree of Doctor of Philosophy at The University of Zagreb.

The samples were prepared from six alloys, three (R) of tin purified by zone-melting[1] and 1, 3 and 10 wt. per cent spectroscopic pure mercury, and three alloys (O) of Johnson and Matthey tin (99·999 per cent) and the same amounts of this mercury. Strips of the alloys, with linear dimensions of $0{\cdot}2\times 3\times 20$ mm were placed between glass slides and nucleated at one side with gray tin. The glass slides were put in a refrigerator at a temperature of $-9{\cdot}0 \pm 0{\cdot}2$°C. At this temperature the transformation velocity of the relatively impure alloys is about 0·3 mm/24 hr and of the pure alloys about 0·5 mm/24 hr.

The resulting gray tin is a single crystal, which is perfect and strain-free when grown in alloys with 3 and 10 per cent Hg, and deformed when grown in alloys with 1 per cent Hg, as appeared from Laue X-ray photographs. The mercury content of the perfect crystals is about 0·2 wt. per cent, and of the deformed crystals about 1 per cent. This mercury is present at room temperature for the greater part in the form of inclusions of a metallic tin–mercury alloy ($HgSn_{12}$ van Lent[1, 2, 3]).

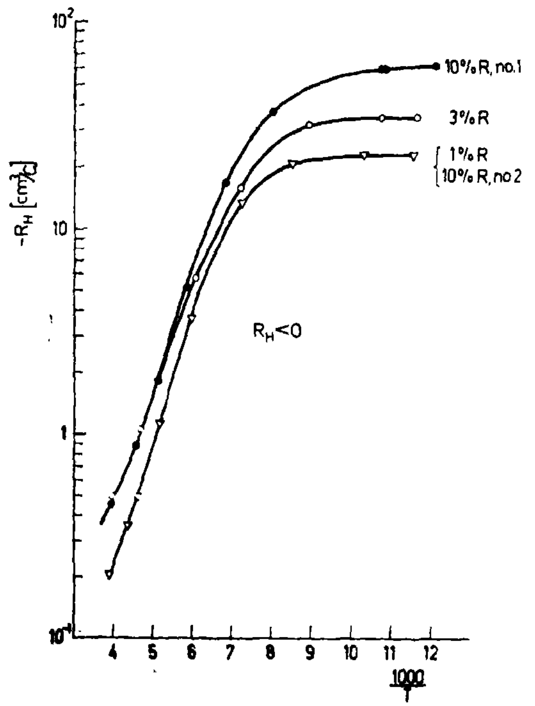

FIG. 1. Hall coefficients of gray tin samples made from alloys (containing 1, 3, 10 wt. per cent mercury) of zone molten tin.

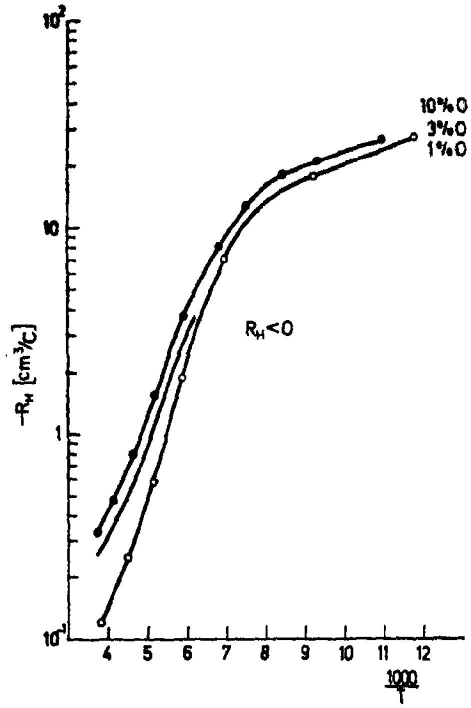

FIG. 2. Hall coefficients of gray tin samples made from alloys containing 1, 3, 10 wt. per cent mercury) of tin (99·999 per cent).

For the measurements samples with a length of 12 mm were cut from the slabs. Electrical contacts were soldered with a low melting point In–Ga solder. The d.c. measured Hall coefficients are given in Figs. 1 and 2, from these measurements it appears that all samples are *n*-type and contain about the same net donor concentration ($N_d - N_a \simeq 10^{17}/\mathrm{cm}^3$), although a deep lying donor impurity has been removed by zone-melting the tin. The specific conductivity σ as a function of the temperature is given in Fig. 3.

The Hall-mobilities $\mu_H = \sigma R_H$ are plotted in Fig. 4. With the exception of the sample 3 per cent (R) the Hall-mobilities between $8 < 1000/T < 9$ obey a $1/T3/2$ law, indicating lattice scattering. At lower temperatures the curves have a tendency to flatten, which is probably due to impurity scattering.

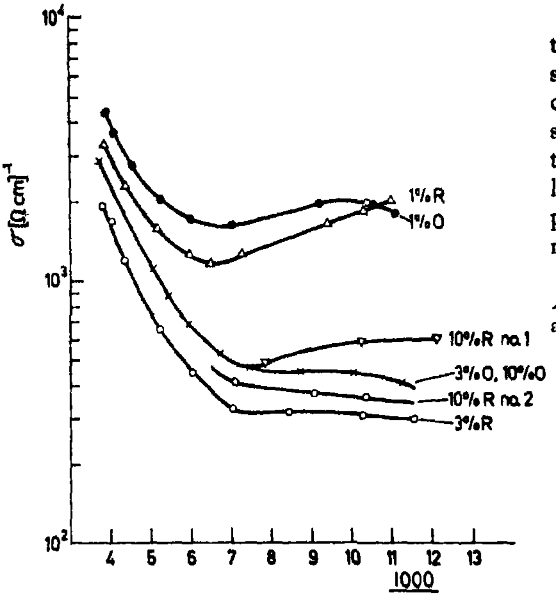

FIG. 3. Conductivity of the gray tin samples.

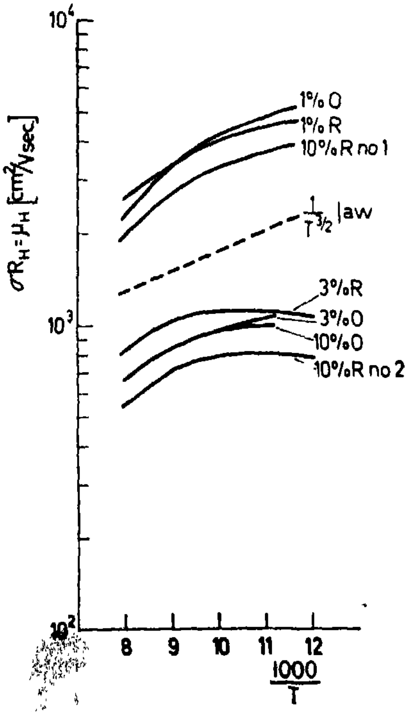

FIG. 4. Hall mobility of the gray tin samples.

The Hall-mobilities at liquid nitrogen temperature are higher than those found in polycristalline samples,[4] although the high mobilities of 10^5 cm^2/Vsec in single crystals grown from a liquid solution[5, 6] are not reached. Thus we conclude that, although this growth method produces larger crystals and is simpler to operate, their purity is inferior to that of crystals grown by the method of Ewald and Tufte.

Acknowledgement—Thanks are due to Mr. VERWEY for assistance with the measurements.

References

1. VAN LENT P. H., *Thesis*, Delft (1962).
2. VAN LENT P. H., *Acta Met.* **10**, 1089 (1962).
3. VAN LENT P. H., *Acta Met.* **9**. 125 (1961).
4. BUSCH G. and KERN A., *Solid State Physics* (edited by SEITZ F. and TURNBULL D.). Vol. **11**, 1 (1960).
5. EWALD A. W. and TUFTE O. N., *J. Phys. Chem. Solids* **8**, 523 (1959).
6. TUFTE O. N. and EWALD A. W., *Phys. Rev.* **122**, 1431 (1961.

Physics Laboratory of the
National Defence Research
Organization, T.N.O.
The Hague,
Netherlands.

H. BOKHOUT
P. H. VAN LENT

Atomic Polarizabilities in III–V Compounds

(*Received* 28 *January* 1963)

RECENTLY, HASS and HENVIS[1] have shown that the effective charges of III–V compounds as defined by Szigeti's formula satisfy a linear dependence on the difference $\alpha_V - \alpha_{III}$ of the atomic polarizabilities. This relation was considered to be unexpected. But it is understandable indeed if a simple classical model of effective charges[2] of homopolar diatomic molecules is adopted as being valid also in the case of the III–V lattices. According to this model, which is based on electrostatic interactions, the effective charge, defined here as the derivative of the dipole moment with respect to interatomic distance, is given as

$$e^* = \frac{\sigma e}{r^2}\left[\frac{d(\alpha_V - \alpha_{III})}{dr} - \frac{2(\alpha_V - \alpha_{III})}{r}\right].$$

Here, α_V and α_{III} are the respective atomic polarizabilities, r is the interatomic distance, and σ is a screening factor taking into account the influence of overlapping of electronic shells on the atomic fields.

If the values of the Szigeti effective charges derived by Hass and Henvis are used instead of the differently defined "dynamic" effective charges meant in the above formula, it is possible to calculate the screening factors and the values of $d(\alpha_V-\alpha_{III})/dr$ from the straight line smoothing out the observations of Hass and Henvis. The results of the calculation are given in Table 1.

Table 1. *Polarizability data for* II–IV *compounds*

Compound	r,	$\alpha_V-\alpha_{III}$	$\frac{d(\alpha_V-\alpha_{III})}{dr}$	σ
GaP	2.36 Å	6·8 Å	14 Å^2	0·40
GaAs	2·44	8·1	13·5	0·44
GaSb	2·64	11·0	12·5	0·56
InP	2·54	4·7	13	0·50
InAs	2·61	5·7	12·65	0·54
InSb	2·81	8·5	11·75	0·68

Data for AlSb are left out; it does not obey the linear relation.

Although the applicability of the molecular model to lattices may be doubtful and although the effective charges used in the model and those derived by Hass and Henvis are not necessarily identical, it is felt that the close structural similarity of the III–V compounds would permit the use of the functional relation, while at most the absolute values of the calculated parameters might be affected by the deviation from the basic assumptions. The observed linear relation implies that σ is proportional to r^3, and this is a strong indication that the present approach is fundamentally adequate. The decrease of $d(\alpha_V-\alpha_{III})dr$ with increasing r is also readily understandable from a model based on interatomic interactions. It is remarkable, furthermore that here as well as in the interpretation of Raman effect data$^{(2)}$ it is necessary to assume $d\alpha/dr$ to be different from zero.

The equation given above is not valid for ionic molecules. Therefore, we do not expect a similar linear relation to hold for effective charges in alkali halides, and actually none is observed.

Universität Freiburg i.Br.
West Germany.

FRANK MATOSSI

References

1. HASS M. and HENVIS B. W., *J. Phys. Chem. Solids* **23**, 1099 (1962).
2. MATOSSI F., *Z. Naturf.* **8a**, 61 (1953); *J. chem. Phys.* **20**, 819 (1952).

BOOKS RECEIVED

JOHN C. SLATER: **Quantum Theory of Molecules and Solids Vol. 1, Electronic Structure of Molecules.** McGraw-Hill, New York and London (1963). xv, 485 pp. $12.50.

ROBERT K. WILLARDSON and HARVEY L. GOERING (Editors): **Compound Semiconductors Vol. 1, Preparation of III–V Compounds.** Reinhold, New York, (Chapman and Hall, London) (1963). xxii, 553 pp., illus., $25.00.

NOTICE

Publishing houses are asked to note that, apart from those outstanding at present, no further book reviews will be published in this Journal.

J. Phys. Chem. Solids Pergamon Press 1963. Vol. 24, pp. 709–714. Printed in Great Britain.

INSTABILITIES OF TRANSVERSE WAVES IN A DRIFTED PLASMA

J. BOK and P. NOZIERES

Laboratoire de Physique, Ecole Normale Supérieure, Paris, France

(*Received* 30 *November* 1962)

Abstract—In this paper we study the propagation of transverse electromagnetic waves in a drifted plasma, in the presence of a longitudinal d.c. magnetic field.

We first derive the complex conductivity of such a plasma containing two kinds of particles of opposite charge (for instance electrons and holes in a semiconductor).

From the dispersion relations, we then deduce the conditions for instability or amplification of the wave.

We derive the threshold drifting electric field E_{D0} as a function of the longitudinal magnetic field B_0 and the frequency of the wave. This formula is applied to a practical case, namely InSb at 77°K and 300°K.

1. INTRODUCTION

IN A DRIFTED plasma with two types of carriers of opposite sign, there may occur a number of instabilities, the so called "two stream" instabilities. The literature is mostly concerned with longitudinal instabilities in a solid state plasma(1,2) and screw instabilities.(3,5)

This paper deals with transverse electromagnetic waves, and we show that instability can occur in certain conditions. We discuss these conditions in the case of semiconductors such as InSb.

2. DERIVATION OF THE TRANSVERSE CONDUCTIVITY OF A DRIFTED PLASMA

We shall use a Boltzmann equation technique. Such an analysis for an electron gas at equilibrium has been done long ago (see e.g. GROSS(6)): we wish to extend these results to the case of a drifted plasma.

For the sake of simplicity, we consider only the simplest geometry:

The d.c. magnetic field B_0 points in the positive z-direction.

The d.c. electric field E_D, which produces the drift velocity of the carriers, is parallel to B_0. The d.c. conditions are thus stable, the drift current undergoing no Hall effect.

On this d.c. structure, we superimpose a small a.c. wave, with a wave vector $\boldsymbol{k}$ parallel to B_0, a frequency ω.

We only consider transverse polarization, the electric field $\boldsymbol{E}$ and magnetic field $\boldsymbol{B}$ of the wave being perpendicular to $\boldsymbol{k}$.

We write the distribution function $f(v)$ as

$$f = f_0 + \bar{g}$$

where f_0 is the static value, $\bar{g}$ the a.c. perturbation induced by the electromagnetic wave. f_0 is roughly maxwellian, such that

$$\begin{aligned} \int f_0 \, \mathrm{d}^3v &= n \\ \int f_0 v_z \, \mathrm{d}^3v &= n v_D \end{aligned} \tag{1}$$

where n is the equilibrium density, v_D the average drift velocity of the carriers. The a.c. perturbation g is of the form $\bar{g} = g \exp i(\omega t - kz)$. As usual, we linearize the Boltzmann equation with respect to the a.c. terms E, B, and $\bar{g}$. We thus get

$$\begin{aligned} i(\omega - kv_z)g + \frac{g}{\tau} + q\frac{\boldsymbol{v}\times\boldsymbol{B}_0}{m^*}\cdot\boldsymbol{\nabla}_v g + q\frac{\boldsymbol{E}_D\cdot\boldsymbol{\nabla}_v g}{m^*} \\ = -\frac{q}{m^*}\boldsymbol{v}\times\boldsymbol{B}\cdot\boldsymbol{\nabla}_v f_0 - \frac{q}{m^*}\boldsymbol{E}\cdot\boldsymbol{\nabla}_v f_0 \end{aligned} \tag{2}$$

m^* and q are the effective mass and charge of the carriers under consideration. τ is a collision time, which may eventually depend on the energy $\epsilon = \frac{1}{2}m^*v^2$ of the carriers.

Let us first consider the usual case of a non-drifted plasma ($E_D = 0$). The equilibrium distribution f_0 depends only on the energy ϵ. The driving term due to the a.c. magnetic field then disappears (since it maintains the carriers on constant energy surfaces). Let us use cylindrical coordinates (v_z, v_t, ϕ). Equation (2) reduces to the well known form

$$i(\omega-kv_z)g+g/\tau-\omega_c\frac{\partial g}{\partial \phi} = -q\boldsymbol{v}\cdot\boldsymbol{E}\cdot\frac{\partial f_0}{\partial \epsilon} \quad (3)$$

where

$$\omega_c = \frac{qB_0}{m^*}$$

In order to solve (3), we consider a circularly polarized wave, such that

$$\left.\begin{aligned} E_z &= 0 \\ E_y &= -i\nu E_x \end{aligned}\right\} \quad \nu = \pm 1 \quad (4)$$

When $\nu\omega > 0$, the electric field E rotates in the same direction as would do negative charges around the magnetic field B_0. The sign $\nu\omega < 0$ corresponds to the rotation of positive charges. With this choice, (3) yields the following result

$$g_\nu = \frac{-iqE_t v_t \exp(i\nu\phi)\partial f_0/\partial\epsilon}{\omega-kv_z+\nu\omega_c-(i/\tau)} \quad (5)$$

From g, we can compute the current density

$$J_\nu = q\int \boldsymbol{v}g\,\mathrm{d}^3v \quad (6)$$

and the conductivity $\sigma = J/E$ (which, in the present case, is scalar):

$$\sigma_\nu = \frac{q^2}{2}\int \frac{v_t^2(\partial f_0/\partial\epsilon)\,\mathrm{d}^3v}{i(\omega-kv_z+\nu\omega_c)+1/\tau} \quad (7)$$

Remark that σ_ν is invariant if we change both the orientation of the wave ($\nu \to -\nu$) and of the cyclotron rotation ($\omega_c \to -\omega_c$).

We shall only be interested in quasistatic conditions, such that

$$\left.\begin{aligned} \omega &\ll \omega_c \\ k\bar{v} &\ll \omega_c \end{aligned}\right\} \quad (8)$$

where $\bar{v}$ is the average thermal velocity. Under these conditions, (7) is equivalent to the usual expression for the mobility and Hall constant. If we replace $\tau(\epsilon)$ by some suitable average τ, the integration of (7) yields the well known result:

$$\sigma_\nu = \frac{nq^2}{m^*}\frac{1}{1/\tau+i\nu\omega_c} \quad (9)$$

The dependence on ν yields the Faraday effect.

From equation (9), we derive the dielectric constant of the medium for the two circularly polarized modes:

$$\epsilon_\nu = \epsilon_l - \frac{i\sigma_\nu}{\epsilon_0\omega}$$

where ϵ_l is the dielectric constant of the lattice and ϵ_0 the electrical permittivity of vacuum. (We use M.K.S.A. units.) We obtain

$$\epsilon_\nu = \epsilon_l - \frac{\omega_p^2}{\omega(\nu\omega_c - i/\tau)} \quad (10)$$

where

$$\omega_p = (nq^2/\epsilon_0 m)^{1/2}$$

is the plasma frequency. Formula (10) is identical to that obtained by AIGRAIN(7) and LIBCHABER and VEILEX(8) for Helicon waves.

Let us proceed to the case of a drifted plasma. We restrict ourselves to the limit $\omega \ll \omega_c$, $k\bar{v} \ll \omega_c$, thus neglecting the first term of equation (2). We must now take into account the driving force due to the a.c. magnetic field; the latter is given by Maxwell's equation:

$$\boldsymbol{B} = \frac{\boldsymbol{k}\times\boldsymbol{E}}{\omega} \quad (11)$$

This causes no difficulty. In addition, we must consider the action of the d.c. electric field E_D on the a.c. distribution: that is more tricky.

In order to simplify the calculation, we shall assume that the collision time is energy independent, equal to some suitable average of the actual τ. Keeping this assumption in mind, we multiply (2) by $q\boldsymbol{v}$, and integrate over the whole velocity space. We thus get:

$$\frac{\boldsymbol{J}}{\tau} - \frac{q}{m^*}\boldsymbol{J}\times\boldsymbol{B}_0 - \frac{q}{m^*}\boldsymbol{E}_0\rho = \frac{Nq^2}{m^*}\boldsymbol{E} + \frac{Nq^2}{m^*}\boldsymbol{v}_D\times\boldsymbol{B} \quad (12)$$

where ρ is the density fluctuation induced by the a.c. field:

$$\rho = q\int g\,\mathrm{d}^3v = \frac{\boldsymbol{k}\cdot\boldsymbol{J}}{\omega} \tag{13}$$

We shall first suppose k real, positive, and look for time instabilities, i.e. for $Im(\omega) < 0$.

From equation (16) it is easy to deduce ω, since this equation is linear in ω. We find

$$\boxed{\omega = \frac{k^2c^2(\omega_{c1}\omega_{c2}-\gamma_1\gamma_2)-\nu k(\omega_{p1}^2v_1\omega_{c2}+\omega_{p2}^2v_2\omega_{c1})+i[-\nu k^2(\omega_{c1}\gamma_2+\omega_{c2}\gamma_1)+k(\omega_{p1}^2v_1\gamma_2+\omega_{p2}^2v_2\gamma_1)]}{-\nu(\omega_{p1}^2\omega_{c2}+\omega_{p2}^2\omega_{c1})+i(\omega_{p1}^2\gamma_2+\omega_{p2}^2\gamma_1)},}$$

In our simple geometry, $\rho = 0$: the d.c. electric field E_D exerts no driving force on the a.c. perturbation. Let us replace B by its expression (11), we finally obtain

$$\frac{J}{\tau}-\frac{q}{m^*}J\times B_0 = \frac{Nq^2}{m^*}E\left(1-\frac{kv_D}{\omega}\right) \tag{14}$$

The only new feature brought in by the drift of the plasma is the factor $(1-kv_D/\omega)$.

3. PLASMA INSTABILITIES

We now deal with a plasma made up of electrons and holes. We suppose that the particles do not interact. The electrical permittivity is then obtained by adding the contributions of the two kinds of particles. We thus have, neglecting ϵ_l:

$$\epsilon_\nu = \frac{-\omega_{p1}^2(1-kv_1/\omega)}{\omega(\nu\omega_{c1}-i/\tau_1)}-\frac{\omega_{p2}^2(1-kv_2/\omega)}{\omega(\nu\omega_{c2}-i/\tau_2)} \tag{15}$$

where the subscripts 1 and 2 denote electrons and holes, respectively. (v_1 and v_2 are abbreviations for v_{D_1} and v_{D_2}.) In equation (15), we have neglected ω as compared to ω_c: we are thus left with a finite contribution. In the special case of a non-drifted, undamped plasma with $n_1 = n_2$, this leading term vanishes; one must keep the term ω in the denominators: instead of helicon waves, one gets the usual "ALFVEN" waves.[9]

From equation (15), we then obtain the dispersion relation:

$$k^2c^2 = \frac{\omega_{p1}^2}{-\nu\omega_{c1}+i/\tau_1}(\omega-kv_1)+\frac{\omega_{p2}^2}{-\nu\omega_{c2}+i/\tau_2}(\omega-kv_2) \tag{16}$$

Since electrons and holes have opposite charges, ω_{c1} and v_1 have a sign opposite to that of ω_{c2} and v_2. (Since v_1 and v_2 are obtained by applying a d.c. electric field to the medium.)

where $\gamma_1 = 1/\tau_1$, and $\gamma_2 = 1/\tau_2$.

After some simple algebra, we deduce from this equation the condition of instability $Im(\omega) < 0$:

$$[\omega_{p1}^2\tau_1(1+\omega_{c2}^2\tau_2^2)+\omega_{p2}^2\tau_2(1+\omega_{c1}^2\tau_1^2)]k^2c^2 + \nu k\omega_{p1}^2\omega_{p2}^2\tau_1\tau_2(\omega_{c2}\tau_2-\omega_{c1}\tau_1)(v_1-v_2) < 0 \tag{17}$$

For electrons, we have $\omega_{c1}\tau_1 < 0$ and for holes $\omega_{c2}\tau_2 > 0$ (this results from our assumption $B_0 > 0$). Therefore, equation (17) can only be satisfied if

$$k\nu(v_1-v_2) < 0 \tag{18}$$

We remark that v_1 and v_2 have opposite signs. Thus (v_1-v_2) has the same sign as v_1; condition (18) may be written as

$$k\nu v_1 < 0$$

If $kv_1\omega > 0$ (electrons going in the direction of the propagation), we must have $v\omega < 0$ (wave rotating in the direction of the holes). Conversely, if $kv_1\omega < 0$, the above condition implies $v\omega > 0$. In short, condition (18) means that those particles which run opposite to the phase velocity must rotate in the same direction as the wave: remark that for a given drifting field, only one polarization of the wave may lead to instabilities.

Let us write:

$$v_1 = -\mu_1E_D, \qquad v_2 = +\mu_2E_D$$

$$\omega_{c1}\tau_1 = -\mu_1B_0, \quad \omega_{c2}\tau_2 = \mu_2B_0$$

where μ_1, μ_2 are the mobilities of the carriers. Let e be the charge of a hole. We have

$$\omega_{p1}^2\tau_1 = \frac{n_1e\mu_1}{\epsilon_0}$$

$$\omega_{p2}^2\tau_2 = \frac{n_2e\mu_2}{\epsilon_0}$$

This supposes that the d.c. relaxation time of the carriers is the same as that for high frequency. We also assume that the drift mobility is the same as the Hall mobility. If this is not true, it is easy to modify adequately equation (19), but this will not lead to any major change in our conclusions.

The threshold electric field E_{D_0} for instability is then derived from equation (17)

$$E_{D_0} = \frac{\epsilon_0 k c^2}{e(\mu_1+\mu_2)^2 B_0}\left[\frac{1+\mu_1^2 B_0^2}{n_1\mu_1}+\frac{1+\mu_2^2 B_0^2}{n_2\mu_2}\right] \quad (19)$$

Usually, the density of holes equals that of electrons. The expressions for E_{D_0} and B_M then take the much simpler form

$$E_{D_0} = \frac{\epsilon_0 c^2 k}{neB_0}\frac{(1+\mu_1\mu_2 B_0^2)}{\mu_1\mu_2(\mu_1+\mu_2)}$$

$$B_M^2 = \frac{1}{\mu_1\mu_2}$$

where we have set $n_1 = n_2 = n$.

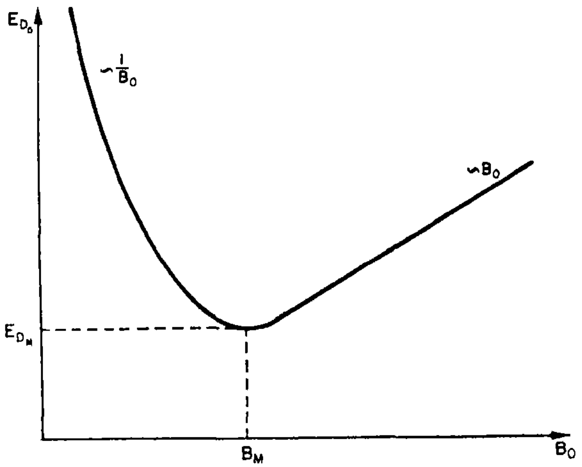

FIG. 1. The threshold d.c. electric field E_{D_0} as a function of the longitudinal d.c. magnetic field B_0.

This general rule calls for the following comments:

(a) We see that there is no instability if the *two* types of carriers are not present. If n_1 or n_2 becomes 0, E_{D_0} becomes infinite.

(b) The threshold electric field decreases with increasing mobility μ_1 and μ_2 of the carriers.

(c) The variation of E_{D_0} with the longitudinal magnetic field B_0 is given by Fig. 1. The minimum critical electric field occurs for a value of the magnetic field B_M given by:

$$B_M^2 = \left[\frac{1}{n_1\mu_1}+\frac{1}{n_2\mu_2}\right]\left[\frac{\mu_1}{n_1}+\frac{\mu_2}{n_2}\right]^{-1}$$

4. AMPLIFICATION

Instead of considering k as real and looking for instabilities, one can consider ω as real and positive, and regard whether there is space amplification (growing waves).

We adopt an energetic point of view. The energy loss from the wave to the medium is $Re(\sigma_\nu)E^2$, where σ_ν is the conductivity defined in Section 1.

In order to have amplification, we need $Re(\sigma_\nu) < 0$, or $Im(\epsilon_\nu) > 0$.

From equation (15) we deduce

$$Im(\epsilon_\nu) = \frac{1}{\omega^2}[-(A_1+A_2)\omega+k(A_1v_1+A_2v_2)]$$

where

$$A_i = \frac{\omega_{pi}^2 \tau_i}{1+\omega_{ci}^2 \tau_i^2} \qquad (i = 1, 2).$$

$A_i \epsilon_0$ is simply the longitudinal conductivity of the i^{th} type of carriers in the presence of the magnetic field B_0.

The condition $Im(\epsilon_\nu) > 0$ implies:

$$k[A_1 v_1 + A_2 v_2] > 0 \tag{20}$$

Under typical conditions, the concentrations of holes and electrons are roughly equal, while the electron mobility is much higher than that of the holes. One then has:

$$A_1 |v_1| \gg A_2 |v_2|$$

Condition (20) then leads to $kv_1 > 0$: the electrons must be drifted in the direction of k. The condition for amplification is:

$$\frac{A_1 v_1 + A_2 v_2}{A_1 + A_2} > \frac{\omega}{k}; \tag{21}$$

ω/k is the phase velocity v_ϕ of the wave. If we assume $A_2 \ll A_1$, (21) becomes:

$$v_1 > v_\phi$$

Therefore, we have amplification when the drift velocity of the more mobile carriers is greater than the phase velocity of the wave. Let us point out the analogy with the travelling wave tubes, where the same condition holds for amplification.

Condition (21) is not sufficient to have an amplification; it ensures a net transfer of energy from the particles to the wave, but that wave can be evanescent (see for instance STURROCK$^{(10)}$). We must also satisfy the condition $Re(\epsilon_\nu) > 0$, which ensures propagation.

From equation (15), we derive $Re(\epsilon_\nu)$

$$\omega^2 Re(\epsilon_\nu) = -\nu[C_1(\omega - kv_1) + C_2(\omega - kv_2)] \tag{22}$$

where

$$C_i = \frac{\omega_{pi}^2 \omega_{ci} \tau_i^2}{\omega_{ci}^2 \tau_i^2 + 1} = A_i \omega_{ci} \tau_i \quad (i = 1, 2)$$

The condition $Re(\epsilon_\nu) > 0$ therefore fixes the sign of ν: again we see that only one circular polarization may be amplified. The general result (22) is difficult to analyze. In the special case where electrons dominate the behaviour of the plasma ($|C_1| > |C_2|$), the condition for amplification becomes

$$\nu C_1(\omega - kv_1) < 0$$

C_1 is always negative; condition (21) implies $(\omega - kv_1) < 0$. Therefore, ν is negative: the wave must rotate in the direction of the holes: as in the preceding Section, the wave must rotate as those particles which run opposite to k.

The mechanism of the amplification can be understood in the following way:

The plasma allows propagation of an Helicon wave with small attenuation. If the density of carriers is large, the dielectric constant becomes very high and the phase velocity of the Helicon wave is very small. In the presence of the drifting field E_D, the electrons run much faster than the holes, since they have a higher mobility. When their velocity reaches v_ϕ, we have amplification as in a travelling wave tube. However, at the onset of the instability ($v_1 = v_\phi$), the electron contribution to the dielectric constant (15) vanishes. The holes are therefore essential to maintain the dielectric constant at a very large value.

The threshold conditions are given by

$$\left.\begin{aligned} &\frac{A_1 v_1 + A_2 v_2}{A_1 + A_2} = \frac{\omega}{k} \\ \text{and} \\ &-\nu k^2 c^2 = C_1(\omega - kv_1) + C_2(\omega - kv_2) \end{aligned}\right\} \tag{23}$$

By eliminating k we find the following condition for the threshold velocities

$$(A_1 v_1 + A_2 v_2)(v_1 - v_2) = \frac{-\nu (A_1 + A_2)^2 c^2 \omega}{A_1 C_2 - A_2 C_1}$$

Let us use the relations

$$v_1 = -\mu_1 E_D \qquad C_1 = -\mu_1 B_0 A_1$$

$$v_2 = +\mu_2 E_D \qquad C_2 = \mu_2 B_0 A_2.$$

The critical electric field is then given by

$$E_{D_0} = \frac{\nu \omega c^2 (A_1 + A_2)^2}{(\mu_1 + \mu_2)^2 (\mu_2 A_2 - \mu_1 A_1) A_1 A_2 B_0} \tag{24}$$

For small values of B_0, E_{D_0} varies as $B_0^{-1/2}$. For large values of B_0, E_{D_0} varies as $B_0^{1/2}$, except when $n_1 = n_2 = n$, in which case E_{D_0} varies as $B_0^{3/2}$.

In the latter case (the most usual in practice), (24) reduces to

$$E_{D_0}^2 = \frac{\epsilon_0 \nu \omega c^2}{n e B_0} \frac{(1+\mu_1\mu_2 B_0)^2}{\mu_1\mu_2(\mu_2^2-\mu_1^2)} \tag{25}$$

As was pointed out earlier, if $\mu_1 > \mu_2$, we must choose $\nu = -1$.

The critical field E_{D_0} is minimum when the magnetic field B_0 takes the value B_M given by

$$B_M = \frac{1}{\mu_1\mu_2}$$

We find the same condition as in the preceding Section. This is hardly surprising. This minimum of B_0, being independent of k and ω, corresponds to the onset of instabilities, which should not depend on the chosen point of view.

We shall illustrate this conclusion by a few numerical applications. Let us consider InSb; at room temperature this material is intrinsic, and we have

$$n_1 = n_2 = n = 1{\cdot}6\ 10^{22}\ \mathrm{m}^{-3}$$

$$\mu_1 = 7\ \mathrm{m}^2/V\mathrm{sec}$$

$$\mu_2 = 0{\cdot}1\ \mathrm{m}^2/V\mathrm{sec}$$

which leads to $B_M = 12{,}000$ G. For a reasonable value of the drift field $E_D = 2 \cdot 10^4$ V/m, one can have amplification up to a frequency $\omega = 2 \cdot 10^6$ c/s. At 77°K, under avalanche conditions, we can obtain

$$\mu_1 = 50\ \mathrm{m}^2/V\mathrm{sec}$$

$$\mu_2 = 1\ \mathrm{m}^2/V\mathrm{sec}$$

$$n_1 = n_2 = n = 10^{22}\ \mathrm{m}^{-3}.$$

We then get $B_M = 1{,}500$ G. With $E_D = 2 \cdot 10^4$ V/m, we can amplify up to $\omega = 6 \cdot 10^8$ c/s.

Acknowledgements—We wish to thank Professor P. Aigrain and Mrs. N. Hulin for many stimulating discussions on the subject of this paper.

REFERENCES

1. Bohm D. and Gross E. P., *Phys. Rev.* **75**, 1865 (1949).
2. Pines D. and Schreffer R., *Phys. Rev.* **124**, 1387 (1961).
3. Kadomtsev B. B. and Nedospasov A. V., *J. Nucl. Energy, Part C. Plasma Phys.* **1**, 230 (1960).
4. Glicksmann M., *Phys. Rev.* **124**, 1655 (1961).
5. Johnson R. R. and Jerde D. A., *Boeing Res. Lab. Rep.* No. D1-82-0127 (1962).
6. Gross E., *Phys. Rev.* **82**, 232 (1951).
7. Aigrain P., *Proceedings of the International Conference on Semiconductor Physics, Prague,* 1960.
8. Libchaber A. and Veilex R., *Phys. Rev.* **127**, 774 (1962).
9. Alfven H., Cosmical Electrodynamics, University Press, Oxford, London (1950).
10. Sturrock P. A., *Phys. Rev.* **112**, 1488 (1958).

J. Phys. Chem. Solids Pergamon Press 1963. Vol. 24, pp. 715–718. Printed in Great Britain.

EPITAXIAL GROWTH OF ICE ON ORGANIC CRYSTALS

N. FUKUTA and B. J. MASON
Imperial College, London

(*Received* 30 *November* 1962)

Abstract—The epitaxial growth of ice crystals on organic crystalline substrates has been studied in some detail and is illustrated by a number of photographs. The highest temperature at which ice crystals appear on a particular substance is very close to the threshold temperature at which an aerosol of the same substance nucleates a supercooled soap film. The most effective substances are the steroids, several of which form ice crystals at temperatures close to −1°C. The ice-nucleating ability of these compounds does not appear to be closely related to their lattice dimensions but the presence and arrangement of hydrogen-bonding groups on their surfaces seems to be an important factor. Ice crystals appear preferentially at steps and cracks on the surface where OH groups are likely to be exposed.

1. INTRODUCTION

IN RECENT years many studies have been made of the ice-nucleating properties of inorganic crystals —see, for example, MASON(1) and FLETCHER.(2) One technique has been to introduce the substance, in finely-divided form, into a cloud of supercooled water droplets and to measure the highest (threshold) temperature at which, say, one particle in about 10^4 produces an ice crystal. A second, and more satisfactory technique, is to observe under the microscope the epitaxial growth of ice crystals on the surfaces of single crystals of the nucleant and to determine critical values for the temperatures and supersaturations at which the ice crystals appear. Such a detailed study of 10 inorganic substances has been described by BRYANT, HALLETT and MASON,(3) the three most effective nucleating substances being AgI (−4°C), PbI_2 (−6°C) and CuS (−6°C) having the threshold temperatures shown in brackets.

Little is known about the ice-nucleating ability of organic crystals. BASHKIROV and KRASIKOV(4) reported that phloroglucinol was active at temperatures as high as −6°C but little interest was aroused until HEAD's(5) discovery that 7 out of 30 steroid compounds, which he tested by observing the formation of ice crystals around particles on a microscope cold stage exposed to moist air, were almost as effective as silver iodide. The activity of the steroid crystals was greatly enhanced when they were melted and recrystallized quickly near the melting point. Particles of $d > 0{\cdot}03$ mm of the following substances: androstenolone, androstan-3,17-dione, pregnenolone, androsterone, testosterone, 3α-methylcholestan-3β-ol, and cholesterol nucleated ice crystals at temperatures as high as −5°C. To this list HEAD(6) has recently added stigmasterol (−3°C), methyl androstan-3,17-diol (−2·5°C), 17α-oestradiol (−4°C) and progesterone (−7°C), and the following substituted fluorenes: 9-hydroxyl methylfluoren-9-ol (−2·5°C), 1,1-diphenylethane-1,2,-diol (−4°C), 9-fluorenone (−4°C) and fluorenol (−6°C).

KOMABAYASI and IKEBE(7) tested a number of aromatic compounds by introducing the finely powdered material into a supercooled cloud, allowing the ice crystals so formed to fall into a tray of supercooled sugar solution, and measuring the highest temperature at which 1 particle in 10^4 produced an ice crystal. They found that the following substances, mostly monoclinic, were effective at the threshold temperatures shown in brackets: terephthalic acid (−10°C), phthalic acid (−10°C), β-naphthoquinone (−10°C), phthalic anhydride (−11°C), salicylic acid (−11·5°C), anthraquinone (−13°C), isophthalic acid, phthalic aldehyde and terephthalic aldehyde (−13·5°C).

Lastly, POWER and POWER(8) have reported the following amino-acids to be active at temperatures above −10°C: l-leucine (−4·5°C), l-tryptophane (−5·5°C), dl-aspartic acid (−6°C) and dl-alanine (−7°C).

In the present investigation the technique employed by BRYANT, HALLETT and MASON(3) for inorganic crystals has been used to study the nucleation and growth of ice crystals on crystals of several organic compounds under accurately controlled conditions of temperature and supersaturation.

2. EXPERIMENTAL

In order to screen a large number of organic compounds for ice-nucleating ability they were tested by the supercooled soap film technique of MASON and MAYBANK.(9) A small quantity of a finely-ground compound was ejected from a polyethylene squeeze bottle into a closed cold chamber, previously flushed with clean, filtered air, and containing a stable soap film supported on a metal ring. Evaporation from the film provided a supply of water vapour for the formation of ice on the organic particles and, if activated particles fell on the soap film, they nucleated the supercooled water in the film and produced large ice crystals which were readily seen and counted. The highest temperature at which 10 crystals appeared on the film for an injection of about 10^4 organic particles was measured with a thermocouple placed close to the soap film. In this way, several highly effective ice nucleants, having threshold temperatures above −5°C, were isolated (see Table 1), many of them having been discovered meanwhile by HEAD.(6)

Large crystals of these substances were then prepared for microscopic study of epitaxial growth. Among the preparation methods tried were crystallization of the compound from an aqueous or alcohol solution followed by cleavage of the larger crystals for test, and evaporation of the compound on to cleaved mica in vacuo. But crystals having the highest density of nucleation sites were prepared by placing a sample between two sheets of cleaved mica and heating the sandwich on a metal plate. After melting, the specimen was slowly cooled, when nucleation began at a few points to produce thin crystals about 1 cm^2 in which numerous shrinkage cracks appeared. The specimen was prepared for use by stripping the top layer of mica and was then placed in the experimental chamber.

Here it was stuck by a thin layer of vacuum grease on to the flat end of a copper rod dipping into a Dewar flask of liquid nitrogen. The temperature T_1 of the copper surface was controlled by an electric heater wound on the copper rod and was measured by a 38 s.w.g. thermocouple soldered immediately below the surface. The temperature and vapour pressure of the air surrounding the specimen crystals were controlled by stirring it and bringing it into equilibrium with the ice-lined walls of a surrounding copper chamber cooled by circulating chilled alcohol. The temperature T_2 of the ice layer was measured with a thermocouple. The supersaturation of the air surrounding the specimen was then given by the ratio of the saturation vapour pressures of ice at temperatures T_2 and T_1. The cold unit was mounted on the travelling stage of a microscope so that the crystal surface could be scanned. With the specimen in position and the chamber temperature T_2 fixed, the copper rod was cooled slowly to the required temperature, which was maintained for 2 min before the microscope was lowered and the illumination switched on. This pause allowed the ice crystals to grow when the substrate was not being heated by radiation from the microscope objective and light source. The specimen was then illuminated by light from a tungsten lamp passing through heat filters and a vertical illuminator, viewed by an 8 mm objective and ×20 eyepiece, and photographed in reflected light. Observations of the onset of evaporation and melting of ice crystals indicated that the temperature of their formation was being determined within an accuracy of ± 0·1°C.

3. OBSERVATIONS OF EPITAXIAL GROWTH

The experimental observations are summarized in Table 1 which shows the threshold temperature at which each substance nucleated the soap film and the highest temperature at which an oriented deposit of ice crystals appeared on the organic crystal substrate. Substances which failed to nucleate the soap film at −15°C were regarded as ineffective and were not examined for epitaxial growth.

Table 1. Properties of active organic ice-forming nuclei

Substance	Formula	Symmetry	*a*	*b*	*c*				Threshold Temp.(°C) on soap film	Threshold Temp.(°C) Epitaxy
Pentaerythritol	$C(CH_2OH)_4$	Tetragonal	6·10	6·10	8·73				−7	> −12
dl-leucine	$CH(CH_3)_2CH_2CH(NH_2)COOH$	Triclinic	5·18	5·39	14·60	96°	103°	111°30′	−5	−5
dl-α-alanine	$CH_3 \cdot CH(NH_2)COOH$	Orthorhombic	12·06	6·05	5·82				−9	
dl-tryptophane	$C_6H_4 \cdot NH \cdot CH : C \cdot CH_2 \cdot CH(NH)COOH$	Triclinic	5·30	8·61	16·20	103°	107°	98°	−8·5	
β-naphthol	$C_{10}H_7OH$	Monoclinic	8·09	5·94	17·80		120°		−8·5	
Fluorenone	$C_{13}H_8O$	Orthorhombic	16·0	12·5	18·63				< −17	−8
Cholesterol	$C_{27}H_{46}O{\cdot}H_2O$	Triclinic	12·3	6·23	42·3	90°	124°	90°	−2	−1
Cholesterol(anhyd)	$C_{27}H_{46}O$	Triclinic	14·0	10·46	37·8	94°	117½°	90°	−2	−1
Testosterone	$C_{13}H_{28}O_2$	Monoclinic	14·73	11·09	11·01		125°		−2	−1
Pregnenolene	$C_{21}H_{32}O_2$								−2	−1
Diosgenin	$C_{27}H_{42}O_3$								−1·5	−1
Stigmasterol	$H_2O \cdot C_{29}H_{48}O$	Monoclinic	9·51	7·59	37·2		100°		−8	−1

(a) *Pentaerythritol*

Of the aliphatic compounds tested only pentaerythritol was found to be effective. It nucleated the soap film at −7°C and oriented deposits of ice crystals were observed at −12°C (which was not the threshold temperature) on cleaved crystals grown from aqueous solution. Figure 1 shows ice crystals growing in two different orientations at −15°C. Substitution of bromine for the OH groups of pentaerythritol produced orange monoclinic crystals of pentaerythritol-tetrabromide that failed to nucleate the soap film at −17°C.

(b) *Amino-acids*

Among the amino-acids, l-leucine nucleated the soap film at −5°C agreeing with Power and Power's result of −4·5°C. Ice crystals were also observed on a cleaved surface at −4·5°C but they were few in number and did not show parallel orientation. However, water drops condensing on the cleaved surface of the crystal at temperatures near −5°C showed hexagonal symmetry with fairly sharp edges that were in parallel orientation—see Fig. 2. Ice crystals appearing on the substrate at lower temperatures were randomly oriented. dl-α-alanine and l-tryptophane nucleated the soap film at −9°C, that is, at rather lower temperatures than reported by Power and Power. We found the simple amino-acid, glycine, to be effective only below −15°C.

(c) *Aromatic compounds*

Of the several aromatic compounds tested, phloroglucinol and p-aminophenol were the most effective, having threshold temperatures of −6°C and −10°C respectively when sprinkled on the soap film. Cleaved crystals of phloroglucinol prepared from aqueous solution had a rather low density of active nucleation sites at −10°C but, when the temperature was lowered to −17°C, ice prisms appeared in three different orientations, mainly on cleavage steps as shown in Fig. 3. Sometimes a few oriented hexagonal ice plates appeared simultaneously with the prisms.

3-phenanthrol and β-naphthol nucleated the soap film at −7°C and −8·5°C respectively. Epitaxial growth of ice was observed on the latter substance, also reported to be an effective ice nucleus by Head. Fluorenone, which Head reported effective at $-4°C$, failed to nucleate the soap film at $-17°C$, but crystals formed from the melt between mica sheets nucleated ice crystals at $-8°C$ on the cold stage; perhaps the latter were of a different polymorphic form.

(d) *Steroids*

Steroid compounds, prepared by the mica sandwich technique were the most effective group of substances tested. Epitaxial deposits of ice crystals were observed at temperatures as high as $-1{\cdot}0°C$ on cholesterol, pregnenolone, diosgenin and stigmasterol, and on testosterone at $-1{\cdot}3°C$. The nucleation of these steroids was also observed on the soap film at about $-1{\cdot}5°C$ except for stigmasterol which was effective only below $-8°C$.

Figure 4 shows oriented hexagonal ice plates growing at $-1{\cdot}5°C$ on cholesterol crystals produced by melting and recrystallization between mica sheets. Figure 5 shows a deposit of oriented ice prisms growing on a similarly produced crystal at $-2{\cdot}3°C$. Nucleation of ice crystals was observed to occur preferentially at shrinkage cracks in the substrate and ice crystals growing at both edges of a crack are shown in Fig. 6. Figure 7 shows carpets of small water droplets condensing preferentially on sites formerly occupied by ice crystals that had disappeared by sublimation.

The epitaxial growth of ice plates at $-1{\cdot}5°C$ and $-2{\cdot}1°C$ on pregnenolone is illustrated in Figs. 8 and 9 in which the crystals show a tendency towards trigonal symmetry. Ice crystals are shown growing in several different orientations at $-1{\cdot}1°C$ on diosgenin in Figs. 10–12. Although the different orientations tend to be grouped in separate domains they are geometrically related, which suggests that this crystal face is nearly equally effective for the nucleation of all three ice crystal forms.

Both oriented ice plates (Fig. 13) and oriented prisms (Fig. 14) have been observed to form on stigmasterol at temperatures as high as $-1{\cdot}3°C$. The strong tendency for ice crystals to form at shrinkage cracks and to align themselves with the local crystal orientation is clearly shown. Finally, Fig. 15 shows ice crystals grown on testosterone at $-5°C$.

Discussion

Any attempt to explain the high ice-nucleating ability of organic compounds is complicated by the existence of polymorphic forms stable at room temperatures, by the fact that, in several cases, the detailed crystalline structures are not known, and that both the predominant crystal form and the density of nucleating sites are strongly dependent on the method of preparation.

It will be seen from Table 1 that steroids of very similar ice-nucleating ability differ considerably in their unit cell dimensions and that there is not, in general, a close correspondence between these dimensions and those of the ice lattice. Probably a more important factor is the presence and arrangement of rather flexible hydrogen-bonding groups on the faces of the organic crystals for, as both HEAD[6] and ourselves find, compounds lacking such groups are inactive as ice nuclei. Taking cholesterol as an example, the OH groups are arranged in a regular pattern 7 Å × 9 Å that matches the prism plane of ice (4·52 Å × 7·37 Å) quite closely. The exposure of OH groups at steps and cracks may explain their being preferred sites for ice nucleation.

Acknowledgement—We wish to thank Professor D. H. R. BARTON, F.R.S. for kindly providing us with samples of several steroid compounds.

REFERENCES

1. MASON B. J., *The Physics of Clouds*, Chap. IV, Clarendon Press, Oxford (1957).
2. FLETCHER N. H., *The Physics of Rainclouds*, University Press, Cambridge (1962).
3. BRYANT G. W., HALLETT J. and MASON B. J., *J. Phys. Chem. Solids* **12,** 189 (1959).
4. BASHKIROV G. M. and KRASIKOV P. N., *Trud. glav. geofiz. obs.* **72,** 118 (1957).
5. HEAD R. B., *Nature, Lond.* **191,** 1058 (1961).
6. HEAD R. B., *J. Phys. Chem. of Solids* **23,** 1371 (1962).
7. KOMBAYASI M. and IKEBE Y., *J. met. Soc. Japan* Ser. II, **39,** 82 (1961).
8. POWER B. A. and POWER R. F., *Nature, Lond.* **194,** 1170 (1962).
9. MASON B. J. and MAYBANK J., *Quart. J. R. met. Soc.* **84,** 235 (1958).

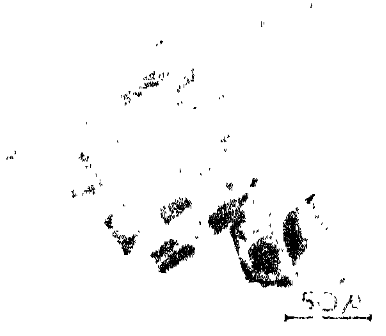

FIG. 1. Epitaxial growth of ice crystals on pentaerythritol at −15°C.

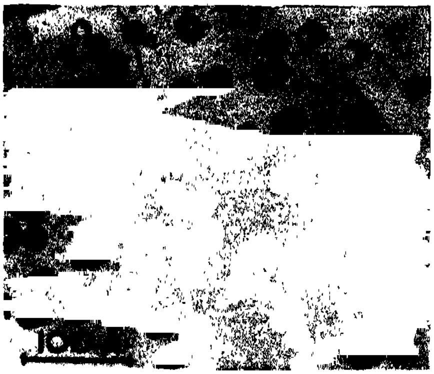

FIG. 2. Water droplets with pseudo-hexagonal outlines condensed on to a leucine crystal at −5·8°C.

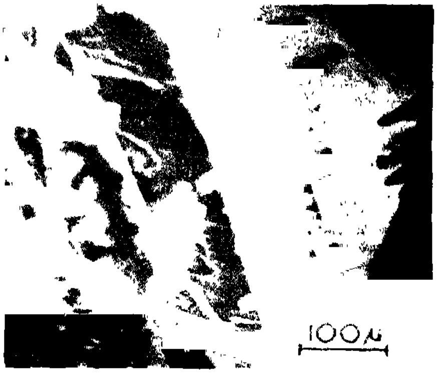

FIG. 3. Prismatic ice crystals formed on cracks in a cleaved crystal of phloroglucinol at −17°C.

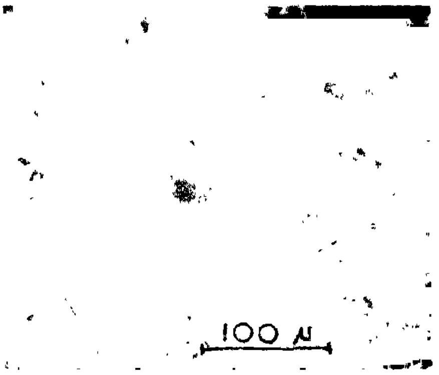

FIG. 4. Epitaxial deposit of ice plates on cholesterol at −1·5°C.

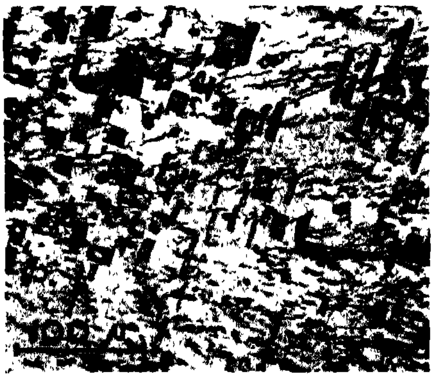

FIG. 5. Epitaxial deposit of ice prisms on cholesterol at −2·3°C.

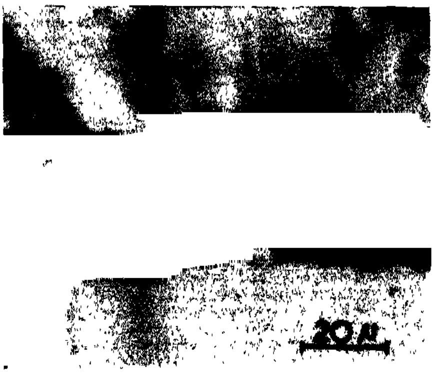

FIG. 6. Ice formation in a crack of a cholesterol crystal at −1·1°C.

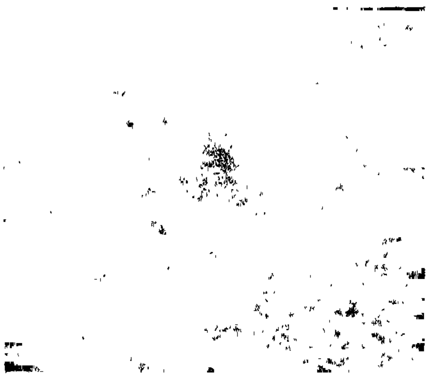

FIG. 7. Condensation of small water droplets at −1·8°C on sites left by evaporated ice crystals.

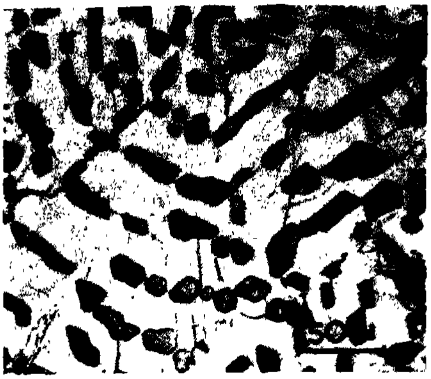

FIG. 8. Preferential growth of ice crystals on cracks in the surface of pregnenolone at −1·5°C.

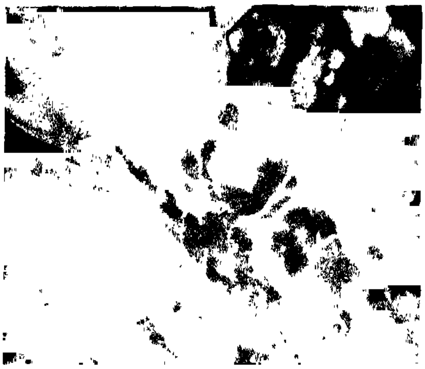

FIG. 9. Ice crystals of trigonal symmetry growing on pregnenolone at −2·1°C.

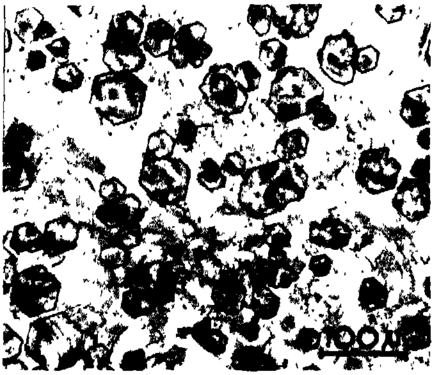

FIG. 10. Ice plates growing on diosgenin at −1·8°C.

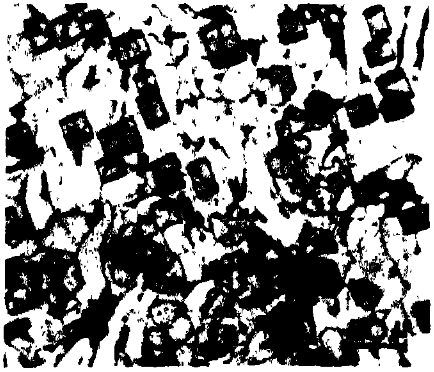

FIG. 11. Oriented prisms and plates on diosgenin at −1·1°C.

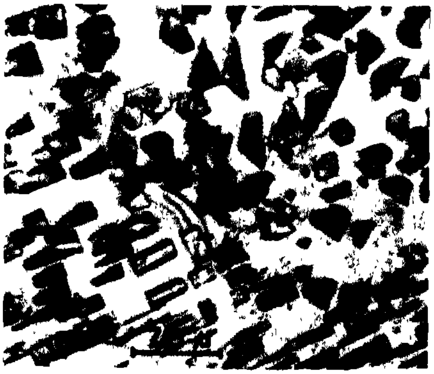

FIG. 12. Prisms, plates and pyramidal ice crystals on diosgenin at −1·1°C.

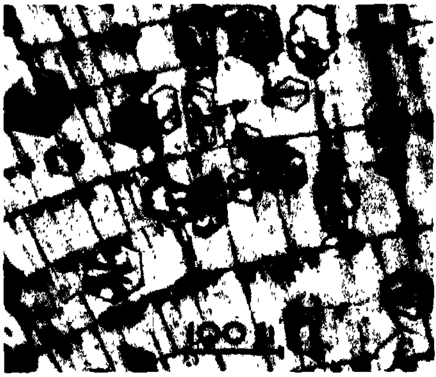

FIG. 13. Oriented ice plates on stigmasterol showing preferential nucleation at shrinkage cracks.

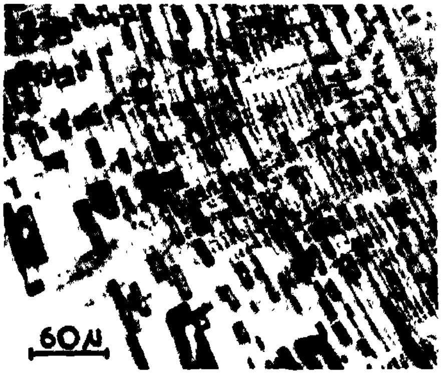

FIG. 14. Nucleation of prisms at cracks on stigmasterol at −2·3°C.

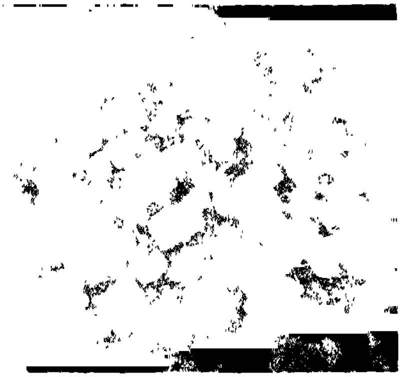

FIG. 15. Epitaxial deposit of ice prisms on testosterone at −5°C.

J. Phys. Chem. Solids Pergamon Press 1963. Vol. 24, pp. 719–728. Printed in Great Britain.

CORRELATION OF EPR AND ELECTRO-OPTICAL MEASUREMENTS IN ZnS

F. F. MOREHEAD and R. S. TITLE

International Business Machines Corporation, Thomas J. Watson Research Center,
Yorktown Heights, New York

(*Received* 15 *August* 1962; *revised* 31 *December* 1962)

Abstract—A recent publication(1) by one of us describes an optically stimulated e.p.r. spectrum in ZnS doped with various amounts of Al. On the basis of the experimentally observed decrease in the optical energy required to excite the e.p.r. spectrum, which was due to Al^{2+}, with increasing aluminum, a model was proposed. The model involved two major assumptions: (1) increasing association of aluminum ions and zinc vacancies with increasing aluminum concentration and (2) a direct, optically induced transfer of charge between these two centers. The present work describes measurements of luminescence and d.c. photoconductivity in these same powder samples which are in disagreement with this model. A second model involving a doubly ionizable center and indirect optical transfer of charge from this center to the Al^{2+} via the conduction band is proposed which is in agreement with all of the available data.

INTRODUCTION

A PREVIOUS report(1) has described the results of e.p.r. measurements on a series of ZnS powder samples to which various amounts of Al had been added. On illumination these samples all showed an e.p.r. spectrum peaking at $g = 2{\cdot}00$. The resolvable structure was attributed to six equally spaced peaks arising from the hyperfine structure of Al^{27}. The dependence of the magnitude of this e.p.r. spectrum on the wavelength of the illumination was a peak which broadened and shifted to longer wavelengths with increasing amounts of added Al. Figure 1 shows this wavelength dependence for an unactivated (no added Al) sample and for samples to which 5 p.p.m. and 15 p.p.m. Al had been added. Figure 2 shows position of the peak of the e.p.r. excitation spectrum as a function of the concentration of the added Al. From this data it was found that the change in the energy of the radiation producing the maximum e.p.r. response increased roughly as the cube root of the concentration of the total Al, up to about 15 p.p.m., beyond which a saturation was observed. From this analysis it was concluded that the optically induced charge transfer responsible for the e.p.r. was directly from a zinc vacancy to a nearby Al^{3+}, without involvement of the conduction band. Increasing the concentration of Al^{3+} should decrease the average separation of the zinc vacancies and the Al^{3+} and hence lower the energy required to make a direct charge transfer, as shown in Figs. 3(a) and 3(b). Since this average separation is expected to decrease as the cube root of the concentration of the Al, the observed dependence of the position of the peak of the e.p.r. excitation spectrum on the concentration of added Al appeared reasonable on the basis of the proposed model. The depth of

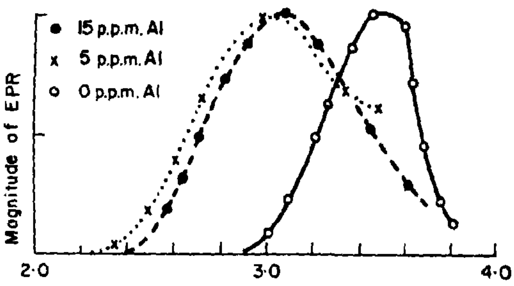

FIG. 1. The wavelength dependence of the e.p.r. response in ZnS:Al at 300°K.

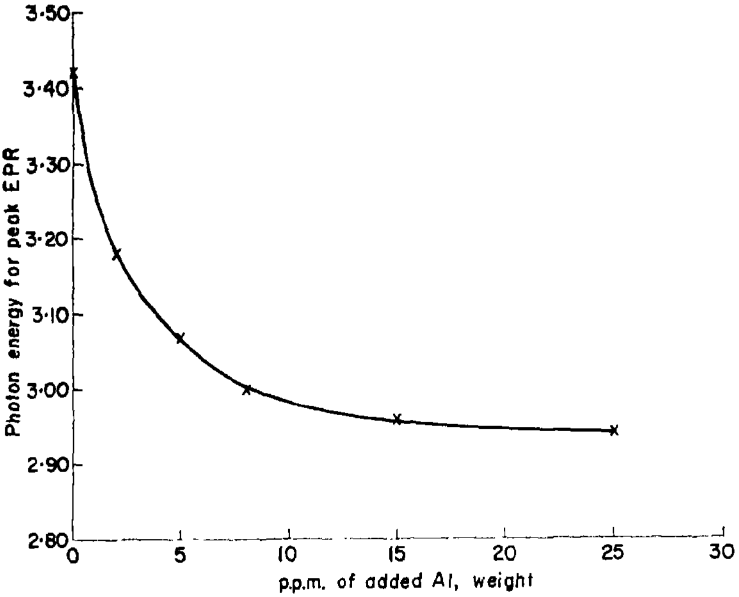

FIG. 2. The photon energy of the radiation producing the maximum e.p.r. response as a function of added Al.

the trap associated with the Al^{3+} should be large compared to the total shift in energy of the peak of the e.p.r. excitation spectrum observed (about 0·5 eV). Further, one might expect the effective thermal depth of the trap to decrease with increasing aluminum. Thermal glow curve and optical stimulation measurements were undertaken to verify these points. Measurements of both direct and alternating photocurrent were also made to indicate whether or not any charge transfer occurred via the conduction band. Measurements of emission, excitation, and quenching spectra as well as thermal quenching data were taken to characterize the samples and to provide data with which to test the model.

These additional measurements showed the model originally proposed to be inadequate. An alternative model consistent with all the measurements is presented.

MATERIALS

As described in the previous publication, R.C.A. luminescent grade ZnS was fired at 1100°C for 2 hr in an H_2S atmosphere and is therefore hexagonal. Spectrochemical analysis showed that the material contained no impurities in greater concentrations than 3 p.p.m. Al was added as $Al_2(SO_4)_3$ under the same conditions of firing.

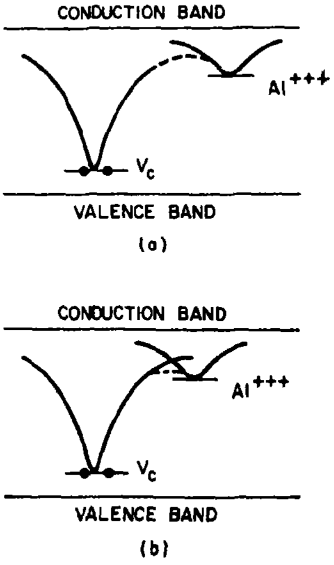

FIG. 3(a). The energy required to transfer charge directly for sites not too close. (b). The lower energy required for direct charge transfer between sites closer than in 3(a).

The samples were cooled in H_2S to room temperature in one-half hour.

APPARATUS

A high-pressure Xe arc lamp with a 250 mm, Bausch and Lomb grating monochromator served as the source of high energy radiation. For the longer wavelengths required for quenching and stimulation measurements, a Sylvania type DXL movie lamp and a Perkin Elmer Model 98 monochromator with a quartz prism were used. The slit widths of both monochromators were adjusted at each wavelength to give a constant photon flux. The visible emission spectra were measured with the Perkin Elmer monochromator and a 1P22 photomultiplier detector. The samples were mounted on a copper block inside a metal Dewar with a quartz window that permitted measurements at 80°K. The insertion of a heater permitted the measurements of the thermal glow and the temperature dependence of the visible luminescence from 80° to 500°K. The thermoluminescence and other optical effects were measured with a 1P21 photomultiplier with the appropriate Corning filters. Electrical contact was made to the powders by means of a silica disc with a conducting coating of tin oxide, which is transparent from 0·3 to 2·5 μ.

MEASUREMENTS

Emission and excitation of luminescence

Figure 4 shows the emission spectra of the three phosphors examined in this work. These spectra were measured at liquid nitrogen temperature and show in each case two bands peaking at 2·4 and 2·75 eV. The relative heights have been normalized and are not meant to be significant. The striking increase in the 2·4 eV band in the samples containing added Al should be noticed here.

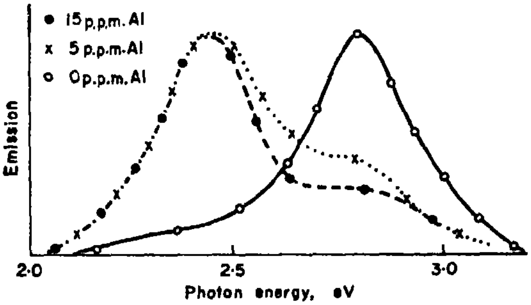

FIG. 4. Emission spectra of ZnS:Al at 80°K.

Figures 5(a) and 5(b) show excitation spectra for the three samples measured at 80° and 300°K. The luminescence excited by each wavelength was measured with a 1P21 photomultiplier with a Corning C.S. 4-64 green filter. Here one need only note that there is substantially stronger relative excitation away from the edge extending to lower energies for the two samples containing added Al.

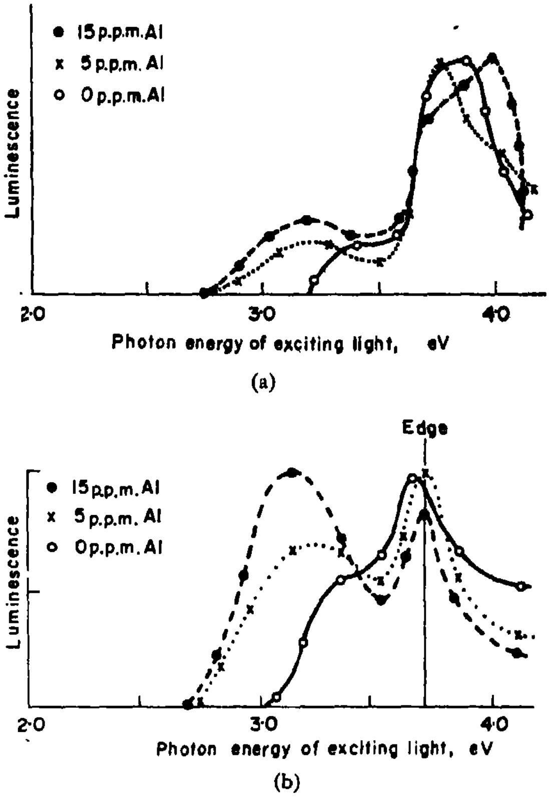

(a)

(b)

FIG. 5. Excitation spectra of ZnS:Al at 80°K (a) and 300°K (b).

Thus, both excitation and emission data indicate with increasing Al either a shift in the Fermi level toward the conduction band, or a lowering of the energy required to excite luminescence within a center. There is no inconsistency with the original model, which would require the latter interpretation.

Quenching and stimulation of luminescence

Figures 6(a) and 6(b) display the quenching (and enhancement) spectra of the ZnS:Al phosphors at 300 and 80°K. At room temperature the 0 p.p.m. sample showed no effects produced by infrared illumination. For the quenching measurements the fluorescence is excited with extrinsic light near the band edge and the long wavelength radiation allowed to fall on the phosphor. At 80°K there is a stimulated burst in the fluorescence followed by a fall to a steady level below the original fluorescence. This latter difference in fluorescence is plotted as quenching in Fig. 6(b). The 0 p.p.m. Al sample showed only enhancement, no quenching of the fluorescence.

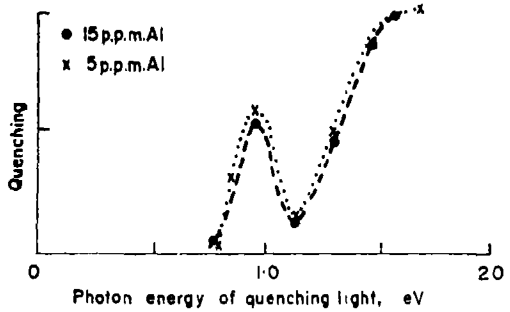

FIG. 6(a). Spectra of the quenching of the luminescence in ZnS:Al at 300°K.

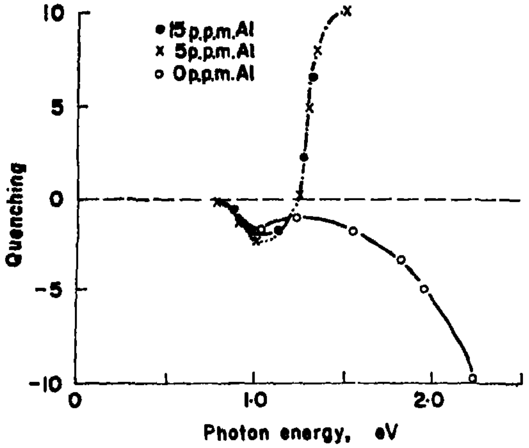

FIG. 6(b). Spectra of the quenching or enhancement of the luminescence in ZnS:Al at 80°K.

To measure the stimulation spectra the short wavelength, exciting light is turned off and the long wavelength radiation turned on; a stimulated burst of phosphorescence is observed, which then decays more or less exponentially. The peak height of this burst is plotted as stimulation against the energy of the long wavelength light in Fig. 7. At room temperature the phosphorescence as well as the fluorescence is quenched by the long wavelength radiation.

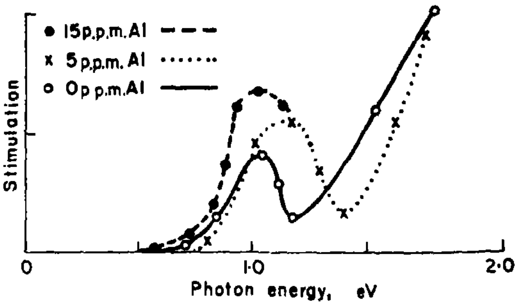

FIG. 7. Spectra of the stimulation of the phosphorescence of ZnS:Al at 80°K.

It should be noted that the 0·95 eV quenching peak which occurs in the quenching spectra at 300°K for the two samples containing added Al (Fig. 6(a)) does not occur at 80°K (Fig. 6(b)). In the latter case one observes quenching only above the 1·3 eV edge and enhancement below that point. The steady state effect of long wavelength radiation on the fluorescence of the 0 p.p.m. Al sample at 80°K (Fig. 6(b)) is essentially the same as its transient effect on the phosphorescence (Fig. 7). This latter effect (stimulation spectrum) is essentially the same for all three samples.

The quenching data indicate that, if optical quenching is due to the removal of holes from recombination centers via the valence band, then an increased occupancy of states lying higher in the forbidden band is favored by increased Al, since quenching effects are observed at room temperature for the Al doped samples and not for the 0 p.p.m. samples. Where the states are close to the valence band, thermal release of the hole into the valence band will dominate at room temperature, and small optical effects will be observed, as in the case of 0 p.p.m. sample. The stimulation data show that the same trapping level is involved in all three samples. The measured optical depth is either to the conduction band or in accordance with the original model, to the top of the energy barriers shown in Fig. 3 as dashed lines.

Thermoluminescence and the temperature dependence of the efficiency of the photoluminescence

Figure 8 shows both the glow curves (TL) and the temperature dependence of the photoluminescence efficiency (TPL). Since measurable glow is obtained beyond the temperature at which the photoluminescence is thermally quenched, the glow curves have been "corrected"; that is, the TL plotted here is the measured thermoluminescence divided by the TPL. The activation energy E_a for the high temperature glow peaks (370–385°K) was found to be about 0·85 eV from analyses of the leading edge of the glow peaks.

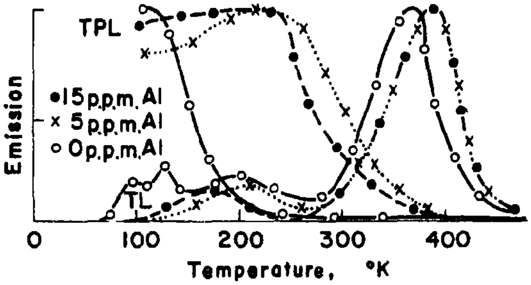

FIG. 8. Glow curves (TL) and the temperature dependence of the photoluminescence efficiency (TPL) of ZnS:Al.

The thermal activation energies corresponding to the low temperature (100–200°K) peaks for the three phosphors fall in the range 0·1–0·35 eV. The activation energies E_a obtained by fitting the TPL data to the usual expression

$$B = B_0/(1+\exp[-E_a/kT])$$

were around 0·5 eV for the two activated phosphors and 0·2 eV for the unactivated ZnS. This thermal activation energy E_a corresponds to the thermal escape into the valence band of holes trapped at radiative recombination centers. The photon energy required for this same transition is seen to be at least 1·3 eV from Fig. 6(b). The photon energy required to empty the traps with thermal activation energy E_a is greater than 0·9 eV, as shown by Fig. 7.

Experiments with 0·95 and 0·6 eV (the optical energy usually associated with the trap responsible for thermal glow)[2] showed that the latter radiation is ineffective in either reducing the amount of thermal glow (even for the low temperature peaks) or in stimulating phosphorescence (negligible in the present case). On the other hand an exact correspondence between the amount of stimulated phosphorescence and the reduction in thermoluminescence was obtained for the 0·95 eV light. Both high and low temperature peaks were reduced proportionally. These experiments, performed on the 5 p.p.m. Al sample, serve to associate all of the thermal glow peaks with activation energies from 0·1 to 0·85 eV with the 0·95 eV optical stimulation edge. Further discussion of this point will be presented later.

These thermal data are energetically reasonably consistent with the optical quenching and stimulation data. In the absence of photoconductivity data they support either the original model, involving transitions within the associated center, or a model invoking transitions which involve the conduction and valence bands of the host lattice.

Optical trap filling experiments

The experiment from which the data in Fig. 9 were taken is the following: A constant number of photons of the energy plotted as the abscissa in Fig. 9 was allowed to fall upon the sample at 80°K.

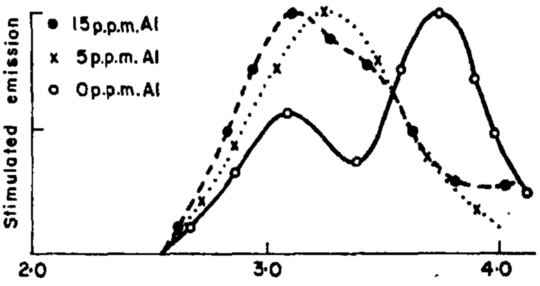

FIG. 9. Stimulated emission (1·05 eV stimulating light) after the traps have been filled by the indicated short wavelength radiation at 80°K.

After the phosphorescence had decayed to a negligible value, 1·05 eV radiation of a high constant intensity was shone upon the phosphor, producing a burst of stimulated visible emission, the peak of which is plotted as the ordinate in Fig. 9. Figure 9, therefore, shows the relative effectiveness of the short wavelength radiation in transferring charge to the traps and is to be compared with the e.p.r. data in Fig. 1. (1·05 eV light was chosen since, as shown in Fig. 6(b), the stimulating effect of this radiation is not diminished by competitive quenching processes.)

The essential difference between Fig. 9 (luminescence) and Fig. 1 (e.p.r.) is that the former suggests that with increasing Al a low energy excitation band becomes dominant over another such band of higher energy. One would not expect this type of change with Al from the original model which suggests a continuous shift in a broad excitation spectra which should not contain definite sub-bands.

Photoconductivity measurements

Figure 10 shows the spectral dependence of the direct photocurrent measured in two of the powder ZnS:Al samples at room temperature. The electric field is applied to the powders by means of a transparent conducting silica disc which serves as one electrode, the copper block as the other electrode. The passage of the direct current, therefore, depends on particles pressed together by means of the two electrodes, the separation of which is about 200 μ. It did not prove feasible to measure photoconductivity at 80°K. It will be noted that photoconductive response extends to as low values as the photon energies in the e.p.r. response plotted in Fig. 1.

Long wavelength radiation enhances the steady state direct photocurrent produced by radiation of photon energy greater than 2·4 eV. The dependence of this enhancement on the energy of the long wavelength radiation is identical with the spectral dependence of the optical quenching of the photoluminescence at room temperature, as shown in Fig. 6(a). The enhancement is apparently a contact effect since with the application of a 1 kc/s alternating field, long wavelength radiation quenches both the dissipative and capacitative contributions to the alternating photocurrent. In the case of the enhancement of the direct photocurrent, holes released by the long wavelength radiation can migrate to the cathode side of a particle, concentrating the field at that point, and possibly increasing the probability of barrier penetration and producing a larger photocurrent. Bulk processes dominate in the case of the alternating photocurrent which is quenched along with the photoluminescence by the transfer of holes from the slow radiative centers to sites where recombination with conduction electrons is faster and non-radiative.

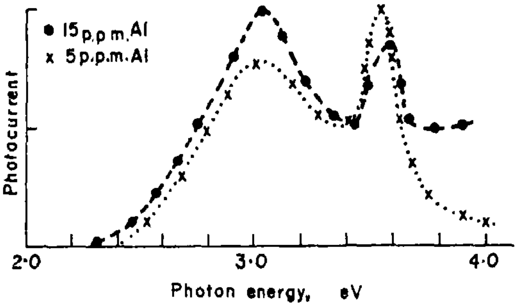

FIG. 10. Direct photocurrent measured at 300°K for powder samples of ZnS:Al.

A stimulated direct photocurrent produced by the long wavelength radiation is also observed, at room temperature. The low energy radiation is applied after the photocurrent exciting wavelength is removed and the current allowed to decay to its dark value. A burst of current followed by an exponential decay is observed when the long wavelength radiation is applied. The dependence of the heights of the burst on the energy of the stimulating radiation is again identical with that of the quenching of the photoluminescence as in Fig. 6 (a). The dependence of the amount of stimulated photocurrent on the energy of the light used to excite the original photocurrent is shown in Fig. 11. This plot, like Fig. 9, represents the relative effectiveness of different wavelengths in causing the charge transfer from the emission centers to the traps. Like Fig. 9, it is also to be compared with the e.p.r. data in Fig. 1. Unfortunately a good measurement of photoconductivity effects in the "unactivated" sample (0 p.p.m. Al) was not obtained. None of the samples showed measurable photoconductive effects at 80°K.

The photoconductivity data offer the most insuperable obstacle to acceptance of the original model, since transfer of change via the conduction band is clearly indicated. An alternative must be considered.

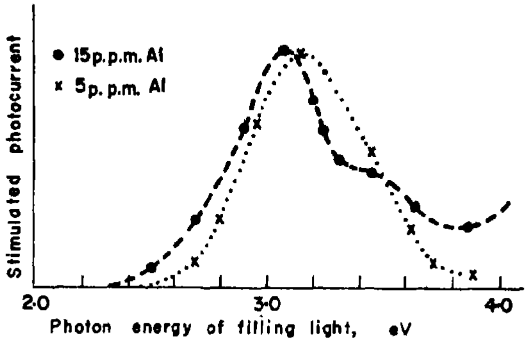

FIG. 11. Direct photocurrent stimulated by long wavelength radiation after exposure to light of the indicated energy at 300°K.

DISCUSSION

The possibility of direct transfer of charge between emission center(1) (indicated as V_c in Fig. 3) and trap (Al^{3+}) must be ruled out since a direct photocurrent can be excited by the same wavelengths that bring about the charge transfer. The dependence of the direct photocurrent on wavelength is shown in Fig. 10. The e.p.r. and stimulability data for photocurrent and photoluminescence (Figs. 1, 9 and 11) are all measures of the effectiveness of different energies of radiation in transferring charge to the traps. The near coincidence of the low energy edge of these latter three spectra and that for photoconductivity shows that the conduction band is involved in the filling of the traps.

The doubly peaked structure of the luminescence stimulability spectrum for the unactivated sample in Fig. 9 suggests an explanation for the shift in the e.p.r. spectra with added Al (Figs. 1 and 2). As Al is added, the number of centers requiring only 2·9 eV to ionize electrons into the conduction band is increased and becomes dominant with respect to those centers requiring nearly the band gap energy. The average energy required shifts to lower energies with increasing Al. The absence of any low energy response in the e.p.r. spectrum for this sample (0 p.p.m. Al) may be due to the difference in temperature. It will be remembered that no stimulation of the phosphorescence was observable at room temperature (where the e.p.r. measurements were made).

A model involving a doubly ionizable center is introduced to explain the results. The origin of this center will be considered after discussion of the model. This model is shown schematically in Fig. 12. The ionization of the first electron from C^{2-} gives C^-, which can recombine with a conduction band electron, producing green emission. Ionization of the electron from C^- gives C, which recombines with a conduction electron with blue emission. Transitions of valence electrons into C^- and C quench the green and blue emission respectively, since the holes left in the valence band can migrate to non-radiative recombination centers (not indicated on the diagram). The transition within C^- can lead to quenching at room temperature since a valence electron can be thermally excited into the vacated lower level. At liquid nitrogen temperature this transition can lead to infra-red emission, but not quenching. The model accounts for the presence of the 0·95 eV quenching peak at room temperature and its absence at 80°K. Optical or thermal emptying of the trapping level T accounts for the stimulated emission and the thermoluminescence. The presence of electrons in T has been detected paramagnetically in the present case. The e.p.r. spectrum is consistent with identifying T with an Al^{2+} ion at a Zn^{2+} site and T^+ as Al^{3+}. At low concentrations of aluminum the C^- centers are

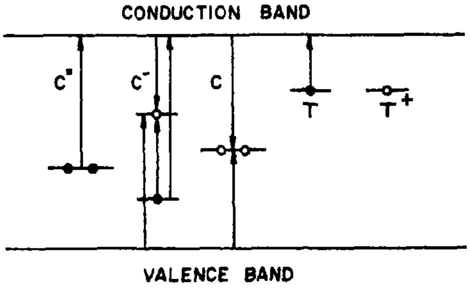

FIG. 12. ZnS model showing the doubly ionizable center, C^{2-}.

dominant and the emission will be blue, as observed. The addition of coactivating Al, in which an additional electron is transferred to the C^- centers, converts them to C^{2-}, leading to the dominance of green emission. The average energy required to ionize an electron from the centers into the conduction band and thence to a T^+ level is reduced by increasing the ratio of C^{2-} to C^- centers, accounting for the observed shift in the e.p.r. excitation spectra (Fig. 1) with added Al. The disturbing absence of any indication of two different levels in any of the e.p.r. excitation spectrum (in contrast to the corresponding luminescence data in Fig. 9) is not explained by the model in any obvious way.

Two possibilities for the origin of the C centers are considered. A zinc vacancy would be a doubly ionizable center. Another possibility is to associate the C center with the presence of copper in the sample. The latter possibility is suggested from the photoluminescence emission spectra for the three samples (Fig. 4), which shift from blue to green with increasing Al. The self activated luminescence in ZnS is invariably blue,(3) while the Cu-activated luminescence is blue for low concentrations of Cu and an excess of Cu over coactivator. With excess of coactivator (Al in this case) over Cu, green emission becomes more prominent.(2, 4)

A comparison of the thermal and optical values for the energies required to ionize holes from C^- or electrons from T with those for Cu doped ZnS is *not* as favorable to the identification of the C center as due to copper. In our samples the optical edge for the ionization of holes from C^- is about 1·3 eV (Fig. 6(b)) while the thermal activation energy for this process is about 0·5 eV, as obtained from the TPL data in Fig. 8. Highly doped ZnS:Cu_2Cl (1000 p.p.m.) phosphors exhibiting an identical quenching spectra to that in Fig. 6(b) have exhibited thermal activation energies over 1·0 eV in the temperature dependence of their luminescence efficiency.(4) The optical edge for emptying the T levels is about 0·9 eV, as shown in Fig. 7. The peak in these spectra at around 1·1 eV is due to the onset of the quenching effect starting at 1·3 eV which produces a decrease in the observed stimulation at that point.(4) The greatest trap depth observed in the glow curves of these materials was 0·85 eV, which is in good agreement with the optical edge. However, for the ZnS:Cu,Cl phosphors mentioned above,(4) the stimulation spectrum is identical with those in Fig. 7, but no trap deeper than 0·4 eV was found in its glow curve. Further, heating the ZnS:Cu,Cl samples to 200°K, the highest temperature below which glow was observed, completely eliminated all optical stimulability at 80°K. One might note that the optical energies involved in the quenching and stimulation processes appear to be much the same for ZnS in general, while the activation energies for the corresponding thermal processes are much more sensitive to the details of preparation. The use of thermal data to assign the position of various levels within the forbidden gap is probably a questionable procedure since in the case of ZnS multistep processes may be involved.

A zinc vacancy is a doubly ionizable acceptor. The identification of the C center with a zinc vacancy would require that C^{2-} correspond to the completely ionized state of the zinc vacancy, C^- to the zinc vacancy with a single hole trapped in it, and C correspond to the zinc vacancy with its full complement of two holes.

Of these only the zinc vacancy with a single trapped hole (C^-) is paramagnetic. This center differs from the A center reported by KASAI and OTOMO(5,6) in that all neighboring ions are sulfur ions. In the A center one sulfur ion is replaced by a halogen. Analysis for this center shows that an isotropic resonance near $g = 2$ would be expected. A large resonance at this position was observed in addition to the aluminum resonance and was in fact attributed to a hole trapped in a zinc vacancy in Ref. 1. The model proposed in this paper (Fig. 12) would require for low concentrations of aluminum the presence of C^- centers even in the absence of ionizing radiation. The resonance was however seen in all samples only in the presence of light. If the proposed model is to be applicable a different origin of this resonance is required or an alternative identification of the C center. The identification of the C center with Cu would require that C^{2-} correspond to Cu^0, C^- to Cu^+, and C to Cu^{2+}. The paramagnetic character of copper will depend not only on the valence state but will also be determined by any rearrangement of the chemical bonding necessary to incorporate that particular valence state. The effect of the bonding will depend on the covalent or ionic character of the bond. ZnS has a mixture of both types of bonding.(7)

The incorporation of neutral copper Cu^0 is rather unlikely. If it were incorporated a resonance due to the 4*s* electron would be observable. No such resonance is detected whereas the model predicts a large concentration of C^{2-} centers as the aluminum concentration is increased.

Incorporation of Cu^+ at a zinc site leaving the bonding orbitals at neighboring sulfur sites intact would lead to a non-paramagnetic center since Cu^+ has a non-magnetic $3d^{10}$ configuration. A missing electron on one of the neighboring sulfur sites would result in a paramagnetic site. The resonance can in this case be regarded as due to a trapped hole centered at the Cu^+ site. An isotropic resonance near $g = 2$ is expected which should show a hyperfine structure interaction with the Cu nuclei. No such resonance was observed.

The Cu^{2+} ion has a $3d^9$ configuration and should therefore show a paramagnetic resonance due to the unpaired spin. It is rather surprising that although Cu^{2+} resonances have been seen in many compounds, their detection in II–VI compounds has been difficult.(8,9) It is only recently that the first report of a Cu^{2+} resonance in a II–VI compound, ZnO, has been made.(10,11) The g values of the resonance(11) $g_{\parallel} = 0{\cdot}6$, $g_{\perp} = 1{\cdot}5$, are very different from the range 2·0–2·5 usually found for Cu^{2+}. There is a significant difference however between ZnO and the other compounds in which Cu^{2+} has been measured. In ZnO Cu^{2+} is tetrahedrally coordinated whereas in the other compounds it is surrounded by an octahedron of negative charges. The effect of the crystalline field of these charges on the ^2D level of the $3d^9$ configuration of Cu^{2+} will be different in both cases as shown in Figs. 13 and 14.

A phenomenological model to predict the total angular momentum J and the orbital degeneracy L' for the various $3d^n$ configurations in tetrahedral symmetry has been given by LUDWIG, WOODBURY and HAM.(12) Applying this model to the $3d^9$ configuration of substitutional copper, one finds $S = 1/2$, $L' = 1$ and $J = 1/2$ or $3/2$. For $J = 1/2$ one would predict $g = 2/3$ which is in the range of the measured g values in ZnO.(11)

Failure so far to detect Cu^{2+} in ZnS may be due simply to the fact that insufficient experiments have been carried out at the high magnetic fields and low temperatures required to find the resonance.

A firm conclusion as to whether the doubly ionizable C center is due to a zinc vacancy or to copper cannot be reached from the available data. That part of the resonance spectrum which was in Ref. 1 ascribed to a hole trapped at a zinc vacancy may in fact be due to a small amount of chromium. Chromium enters substitutionally for zinc as Cr^{2+} and acts as an electron trap to become Cr^+.(13)

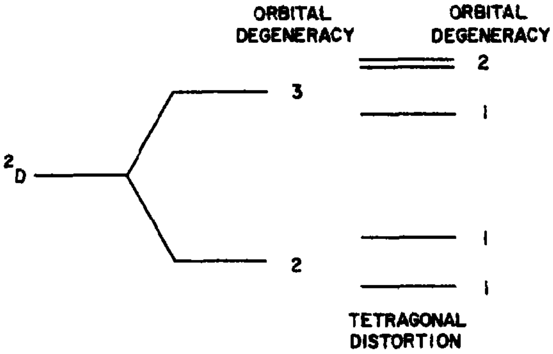

FIG. 13. $Cu^{2+}3d^9$ Octahedral coordination.

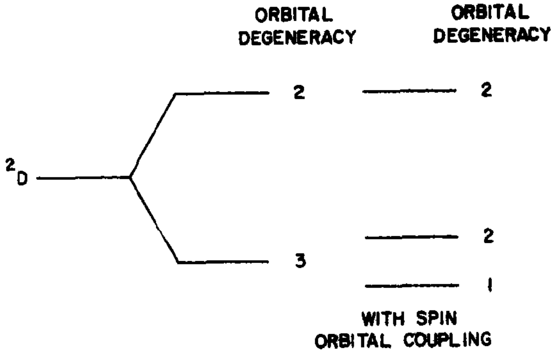

FIG. 14. $Cu^{2+}3d^9$ Tetrahedral coordination.

SUMMARY AND CONCLUSION

The luminescence and photoconductivity data obtained on the ZnS samples have failed to support the original model invoking a direct transfer of charge from the emission center to the trap. The decrease in the average energy required to affect this paramagnetically detected transfer with increased amounts of added Al was originally explained on the basis of a direct transfer and a lowering of the energy barrier as the emission center and trap approached one another (Figs. 3(a) and (b)). A more conventional model has been proposed which involves charge transfer to the Al trapping site via the conduction band. A doubly ionizable center has been proposed; the state of ionization of this center and hence the average energy required to release an electron into the conduction band is decreased with added Al. This model satisfactorily accounts for all of the observed data. The exact nature of the doubly ionizable centre is not known and may be due to either a zinc vacancy or to some unadded Cu.

Acknowledgements—The authors wish gratefully to acknowledge the valuable discussions and encouragement of Drs. S. P. KELLER, W. V. SMITH and R. W. KEYES and to express thanks to Mr. J. A. KUCZA for the preparation of the samples and to Messrs. E. E. TYNAN and W. N. HAMMER for assistance in carrying out the measurements.

REFERENCES

1. TITLE R. S., *J. Phys. Chem. Solids* **22,** 235 (1961); *Advances in Quantum Electronics*, p. 404. Columbia University Press (1961).
2. BROSER I. and SCHULZ H. J., *J. electrochem. Soc.* **108,** 545 (1961).
3. PRENER J. S. and WEIL D. J., *J. electrochem. Soc.* **106,** 409 (1959).
4. MOREHEAD F., *J. Phys. Chem. Solids* **24,** 37 (1963).
5. KASAI P. H. and OTOMO Y., *Phys. Rev. Letters*, **7,** 17 (1961).
6. KASAI P. H. and OTOMO Y., *J. chem. Phys.*, to be published.
7. PAULING L., *The Nature of the Chemical Bond*, 3rd ed. p. 98. Cornell University Press, Ithaca, New York (1960).
8. BOWERS R. and MELAMED N. T., *Phys. Rev.* **99,** 1781 (1955).
9. Unpublished data of various workers.
10. YARIV A., *Comment at First International Conference on Paramagnetic Resonance, Jerusalem, Israel*, July 1962.
11. ESTLE T., to be published.
12. LUDWIG G. W. and WOODBURY H. H., *Solid State Physics*, Vol. 13 (edited by SEITZ F. and TURNBULL D.) p. 266. Academic Press, New York (1962); HAM F. S., to be published.
13. DIELEMAN J., TITLE R. S. and SMITH W. V., *Phys. Letters*, **1,** 334 (1962).

J. Phys. Chem. Solids Pergamon Press 1963. Vol. 24, pp. 729–733. Printed in Great Britain.

THE TEMPERATURE DEPENDENCE OF THE NUCLEAR MAGNETIC RESONANCE OF Co^{59}

RICHARD CONLEY LA FORCE, LOUIS E. TOTH and S. FREDERICK RAVITZ
Department of Mineral Technology, University of California, Berkeley, California

(*Received* 18 *January* 1963)

Abstract—The temperature dependence of the nuclear magnetic resonance spectrum of pure cobalt from 25°C to 600°C has been re-examined with the aid of more sensitive apparatus. The resonances from the hexagonal phase disappear at 490°C on heating and re-appear at 440°C on cooling. The principal resonance lines of the face-centered-cubic and hexagonal phases start to split into two lines each at about 235°C and 260°C, respectively; the fractional splitting increases with temperature, and is approximately the same for the two phases. The absolute intensities of the split resonances decrease in an externally applied magnetic field, but the relative intensities are independent of the external field.

INTRODUCTION

In an earlier study we determined the temperature dependence of the nuclear magnetic resonance absorption in powdered samples of Co^{59} metal.(1) Our results differed somewhat from those of similar studies made by Jaccarino(2) and Koi *et al.*;(3) we observed a splitting of the principal resonance from each phase into two lines as the temperature was increased, whereas they did not. We have since extended our original measurements in order to determine the conditions under which splitting occurs and the degree of splitting as a function of temperature.

EXPERIMENTAL

In our previous study powdered cobalt metal was used as the sample. The metal particles, however, tended to sinter together at higher temperatures and thereby greatly increased the noise level of the spectrometer. To avoid this difficulty we have used a solid cobalt rod as the sample in the present experiments. The rod, made of Johnson–Matthey cobalt nominally 99·999 per cent pure, was 3/16 in. in diameter and 2 in. long, and formed part of the inner conductor of a shorted coaxial line. The shorted coaxial line was then incorporated as the inductive element in the grid circuit of a marginal oscillator (see Fig. 1). A detailed description of the marginal oscillator may be found elsewhere.(4)

The end of the spectrometer containing the sample was completely enclosed in a thin-walled stainless steel tube and surrounded by a furnace. The tube contained the desired atmosphere for the sample. A thermocouple, inserted into the center of the cobalt rod, monitored the temperature which was controlled to 0·5°C.

Before a series of experiments, the cobalt rod was first annealed at 600°C for 1 hr in a hydrogen atmosphere and then electropolished in a solution of 77 per cent glacial acetic acid and 23 per cent perchloric acid. A reducing atmosphere of hydrogen in the spectrometer protected the specimen against oxidation. No change in experimental results could be detected when argon was substituted for hydrogen as the atmosphere.

EXPERIMENTAL RESULTS

The frequencies of the principal resonance absorption for both the hexagonal and cubic phases in the solid cobalt sample are shown in Fig. 2 as a function of temperature between 350° and 885°K. A splitting of the main resonance was first observed at 509°K in the f.c.c. phase and at 533°K in the hexagonal phase. The resonance frequency of the principal absorption from the f.c.c. phase in surface-oxidized cobalt powder is also shown as a function of temperature in Fig. 2; no splitting was observed. We found that if the surface of the solid cobalt sample was allowed to

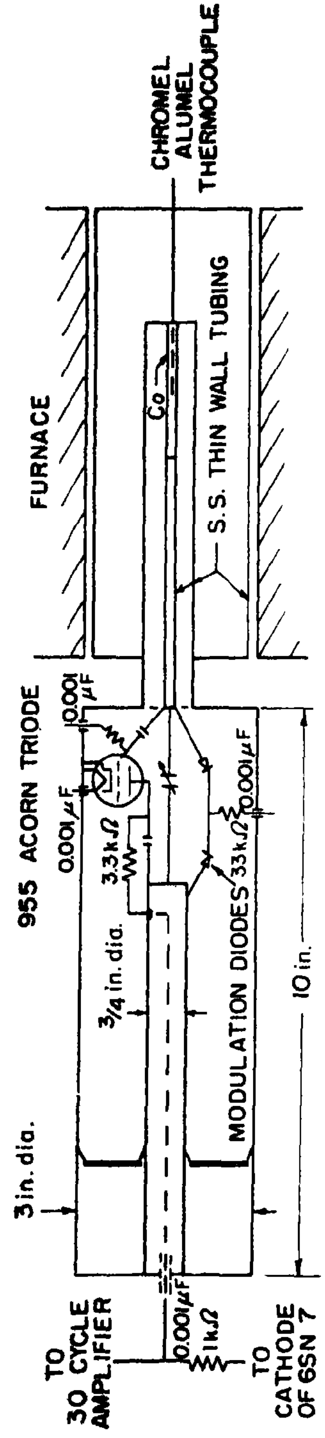

Fig. 1. Schematic diagram of spectrometer with Co^{59} rod used as an inner conductor of the shorted coaxial inductance.

oxidize, the splitting in the resonance line decreased markedly, but if the surface was then reduced at 600°C in hydrogen for one hour the splitting returned to its maximum value.

Spectra taken at room temperature and at an elevated temperature are shown in Figs. 3 and 4 respectively. At the elevated temperature the main resonance for the hexagonal phase and that for the cubic phase are each seen to split into an unsaturated resonance at the higher frequency and a saturated resonance, with its consequent dispersive shape, at the lower frequency. At first, the former was believed to originate from nuclei in the bulk, because there is no r.f. magnetic field enhancement there and consequently it was expected that a signal from these nuclei, if observed, would not be saturated. In order to explore this conjecture more thoroughly, we studied the dependence of the amplitude of the resonance lines on an externally applied magnetic field. The intensity of a resonance signal from a domain wall (Bloch wall) depends on the product of the r.f. field enhancement caused by movement of the wall and the number of nuclei experiencing a given hyperfine field. The application of an external magnetic field reduces the ease with which domain walls move in response to the applied r.f. field and hence decreases the enhancement factor. One expects, therefore, that the intensity of a signal from nuclei in domain walls will decrease more as a function of applied magnetic field than the intensity of a signal from nuclei in the bulk material. With the applied magnetic field perpendicular to the long axis of the rod, we observed no change in the relative intensities of the resonance lines in fields up to 7000 kOe. At fields greater than 7000 kOe the lines could no longer be observed. We conclude, therefore, that the splitting results either from nuclei in different preferred positions within a given type of domain wall or from nuclei in different types of walls where the direction of magnetization passes through nonequivalent crystallographic directions.

The spectra at 743 and 764°K showed an additional splitting in the f.c.c phase which disappeared at higher temperatures. This behavior strongly suggests that there are several preferred orientations in a domain wall where the product of enhancement factor and number of nuclei

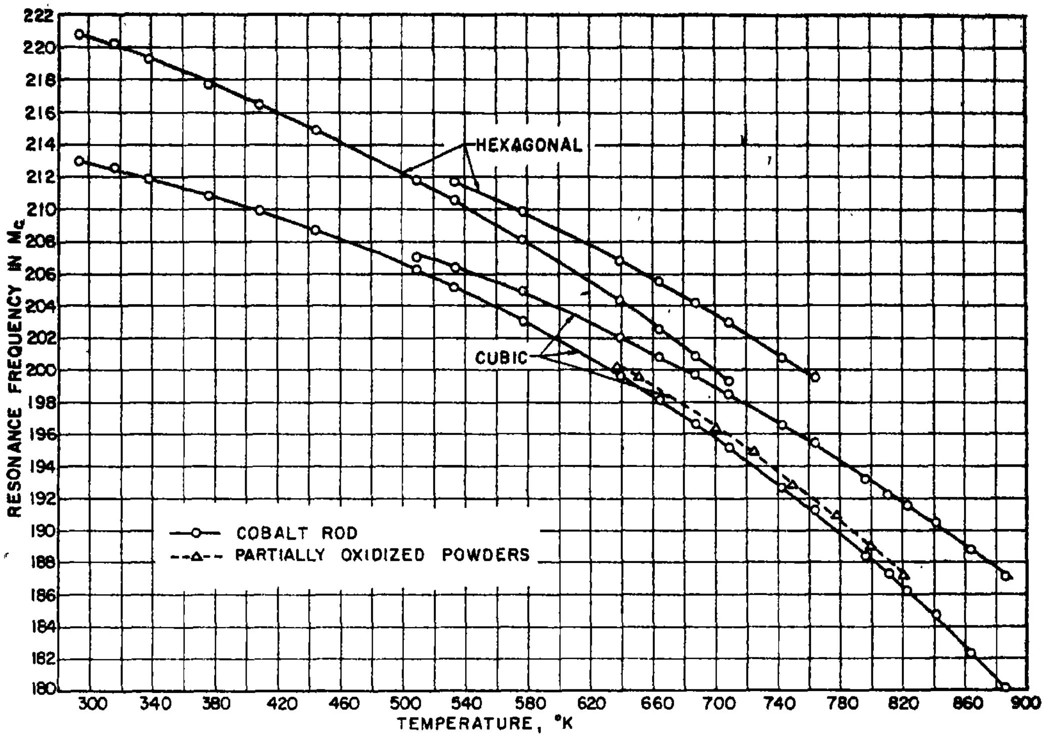

FIG. 2. The resonance frequencies for h.c.p. and f.c.c. Co^{59} are shown as a function of temperature. Splitting occurs in both the f.c.c. and h.c.p. phases but not in the oxidized sample.

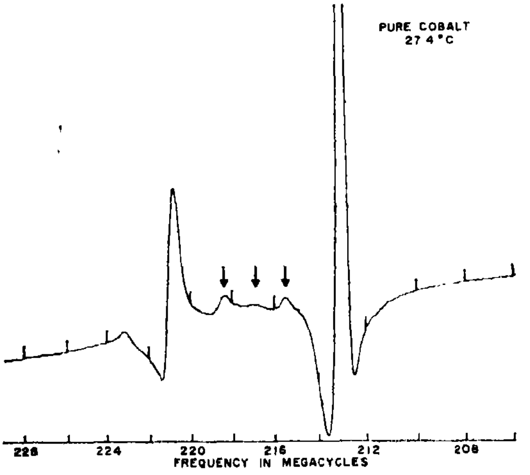

FIG. 3. Spectrum of Co^{59} at room temperature, showing the f.c.c. and h.c.p. main resonances at 213·1 and 221·0 Mc/s respectively. The arrows mark resonances due to stacking faults.

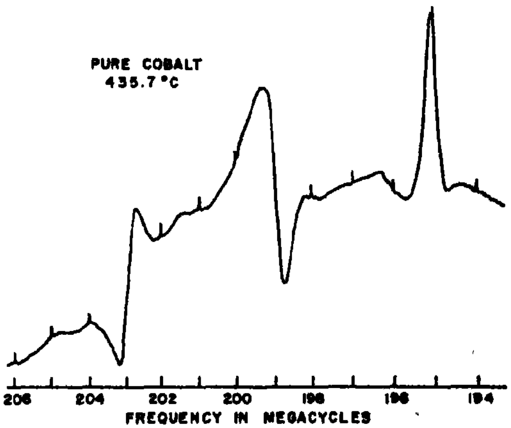

FIG. 4. Typical spectrum of Co^{59} at elevated temperature showing the main resonances for h.c.p. and f.c.c. phases each split into two resonances.

produces relative maxima in the absorption spectrum (see Fig. 5).

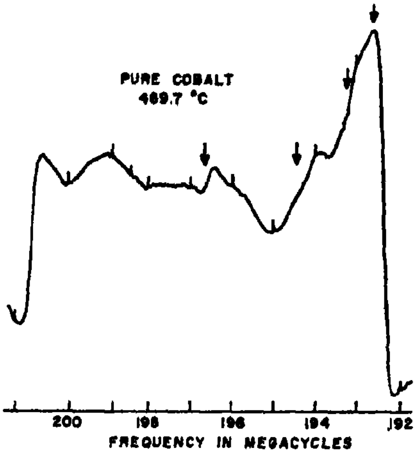

FIG. 5. The cobalt resonance at 469°C showing additional splitting. The four resonances in the f.c.c. phase, three of dispersive shape and one of absorptive shape, are marked by arrows.

The resonance from the hexagonal phase disappeared at 490°C with increasing temperature and reappeared at 440°C with decreasing temperature. These temperatures for the hexagonal-cubic transformation are considerably higher than the equilibrium value of 417°C reported by HOUSKA *et al.*(5)

DISCUSSION

Within the experimental error the fractional splitting as a function of temperature is the same for both the hexagonal and cubic phases. This fact leads us to believe that the major domain wall in both phases is of the same type and that the splitting is due to preferred orientations of spin within the domain wall. We have tried, therefore, to estimate the variation of magnetization with position within the domain wall.

WINTER(6) has estimated the variation with temperature of the magnetization across a 180° domain wall in a simple cubic lattice, assuming a $T^{3/2}$ law for the variation with temperature of magnetization in a uniform ferromagnet. He obtained the following expression for the difference in resonance frequency between the edge of the wall and the center of the wall:

$$\frac{\nu_{\text{edge}}-\nu_{\text{center}}}{\nu_0} = \frac{1}{3}\left(\frac{2KS}{kT}\right)^{1/2}\left(\ln\frac{K}{K^1}\right)\left(\frac{\Delta M}{M_0}\right)_{\text{uniform}} \quad (1)$$

Here K^1 is the apparent wall anisotropy associated with demagnetizing fields, K the bulk anisotropy, and $\Delta M/M_0$ the fractional decrease of magnetization below the value for $T = 0$.

RODBELL(7) has measured the temperature dependence of the bulk anisotropy K between 4 and 850°K and gives the following empirical fit to the data:

$$K(T) = K(0)\left(1+\frac{\Delta M}{M_0}\right)^{8 \cdot 8} \quad (2)$$

where $K(0) = 850$ G. Using Rodbell's results equation (1) becomes:

$$\frac{\nu_{\text{edge}}-\nu_{\text{center}}}{\nu_0} = \frac{1}{3}\left(\frac{2K(0)S}{kT}\right)^{1/2}\left(1+\frac{\Delta M}{M_0}\right)^{4 \cdot 4}\frac{\Delta M}{M_0}\ln\frac{K}{K^1} \quad (3)$$

Using our experimental values for

$$\frac{\nu_{\text{edge}}-\nu_{\text{center}}}{\nu_0} \quad \text{and} \quad \frac{\Delta M}{M_0},$$

together with equation (3), we have evaluated K/K^1 as a function of temperature. We find that

$$\ln(K/K^1) = 0 \cdot 21\ T \quad (4)$$

fits the data from the cubic phase rather well. But the values of K^1 implied by equation (4) are smaller by orders of magnitude than one would expect. For a reasonable value of K^1, perhaps 0·1 G, one would predict a broadening of the resonance rather than the observed splitting. We are forced to conclude that the explanation of the splitting is not yet completely resolved.

Acknowledgements—We would like to express our appreciation for the interest taken in this work by Professor A. PORTIS. This work was supported by the National Science Foundation.

REFERENCES

1. LA FORCE R. C., RAVITZ S. F. and DAY G. F. *J. phys. Soc. Japan*, **17**, 99 (1962).
2. JACCARINO V., *Bull. Amer. phys. Soc.*, Ser. II, **4**, 461 (1959).
3. KOI Y. and TSUJIMURA A., *J. phys. Soc. Japan*. **17**, 96 (1962).
4. LA FORCE R. C., *Rev. sci. Instrum.* **32**, 1387 (1961).
5. HOUSKA C. R., AVERBACH B. L. and COHEN M., *Acta Met.* **8**, 81 (1960).
6. WINTER J. M., *Phys. Rev.* **124**, 452 (1961).
7. RODBELL D. S., *J. phys. Soc. Japan* **17**, 313 (1962).

J. Phys. Chem. Solids Pergamon Press 1963. Vol. 24, pp. 735–739. Printed in Great Britain.

INDUCED CONDUCTIVITY IN CADMIUM SELENIDE BY ELECTRON BOMBARDMENT

H. W. STURNER and C. E. BLEIL

Research Laboratories, General Motors Corporation, Warren, Michigan

(*Received* 8 *January* 1963)

Abstract—The effects of generated X-radiation on induced conductivity in cadmium selenide under electron bombardment shows that cadmium selenide and cadmium sulfide behave in much the same manner. The specific role of certain X-radiations is more evident for cadmium selenide than for cadmium sulfide. On the other hand no measure of the exciton diffusion length was possible for cadmium selenide.

INTRODUCTION

THE interaction of electrons with solids has been a subject of considerable interest for many years. This paper deals only with conductivity changes in cadmium selenide under excitation by electrons of 0 to 50 keV. A review of some of the literature pertinent to this work has recently been given by one of us(1) and will not be repeated here. The earlier work reported on cadmium sulfide showed conclusively that the X-rays generated in the bombarded crystal contributed significantly to the conductivity observed. However, there was some doubt with regard to the X-radiation wavelength ranges responsible. The suggestion was made that perhaps the Cd_K and Cd_L or S_K characteristics played a significant role. For the case of cadmium selenide the K absorption edge of selenium falls between the Cd_K and Cd_L and is well separated from both. This material therefore might permit direct verification of previous suggestions for cadmium sulfide. Also, because of the general similarity between the materials it is expected that many of the results observed should coincide very closely with previous work reported on cadmium sulfide.(1)

EXPERIMENTAL

The crystals used in these experiments were grown by the vapor phase technique reported earlier.(1) Those selected were about 2 mm × 6 mm × 200 μ. The surface bombarded was the $(12\bar{3}0)$ in most cases and the electron beam was always perpendicular to the c-axis. Experimental arrangements used are shown schematically in the first three figures. The aluminum foil and the screen permit the X-ray effects to be studied independently. Detailed techniques and procedures were the same as those reported by BLEIL.(1)

BRIEF DESCRIPTION

The experimental arrangements and the results of induced conductivity vs. distance for the non-bombarded crystal with and without the aluminum foil in place are shown in Figs. 1 and 2 respectively. The case for the bombarded crystal is shown in Fig. 3. In experiments of this type a significant effect was always observed when the aluminum foil was removed or introduced. It was determined that this effect was not due to scattered electrons. There was no visible luminescence and very little radiation could be detected in the wavelength range of the band edge for cadmium selenide. It is apparent that the soft X-ray absorption of the foil must be considered.

Figures 4 and 5 show the induced conductivity per unit power plotted against the DeBroglie wavelength of the bombarding electrons. Shown also on these figures are the curves of the mass absorption coefficient for cadmium selenide as a function of wavelength. In Fig. 4 with the aluminum foil present all of the effect caused by the Se_K is masked whereas in Fig. 5, without the foil, the Se_K absorption is clearly visible. A similar set of curves for cadmium sulfide is shown in Figs. 6 and 7.

Thus the two slopes shown in Figs. 1 and 2 are undoubtedly associated with the two *K* X-ray absorption edges of cadmium and selenium respectively. Where the crystal is bombarded directly (Fig. 3) only two slopes were observed. For the case of cadmium sulfide a third slope was observed which was ascribed to excitons. If one supposes that the first slope in Fig. 3 characterizes the exciton diffusion length for cadmium selenide then a value of about 1·5 mm is obtained. We believe that this value is several times too high and that this slope is not due to excitons.

CONCLUSIONS

The results of this series of experiments on a related compound adds confirmation to the general observations made on cadmium sulfide. In the case of cadmium sulfide no clear cut identification was made of the two ranges of X-rays found to predominate. For cadmium selenide however the effectiveness of the Cd_K and Se_K absorption peaks is clearly demonstrated, and by inference from Figs. 5 and 6, and corresponding assignment to the Cd_K and Cd_L absorption edge should be made for cadmium sulfide.

Finally, no measurement of the exciton diffusion length for cadmium selenide was possible but on the basis of general observations of many crystals, it is believed to be less than that for cadmium sulfide.

REFERENCE

1. Bleil C. E., *J. Phys. Chem. Solids*, **23**, 1729 (1962).

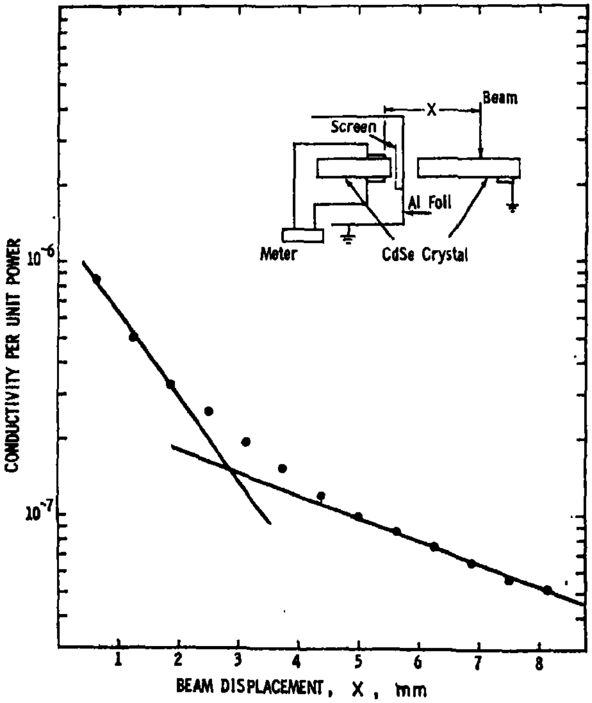

Fig. 1. Induced conductivity in nonbombarded crystal vs. the beam to contact distance *X*. An aluminum foil is in place between the two crystals as shown. The accelerating voltage is 40 kV.

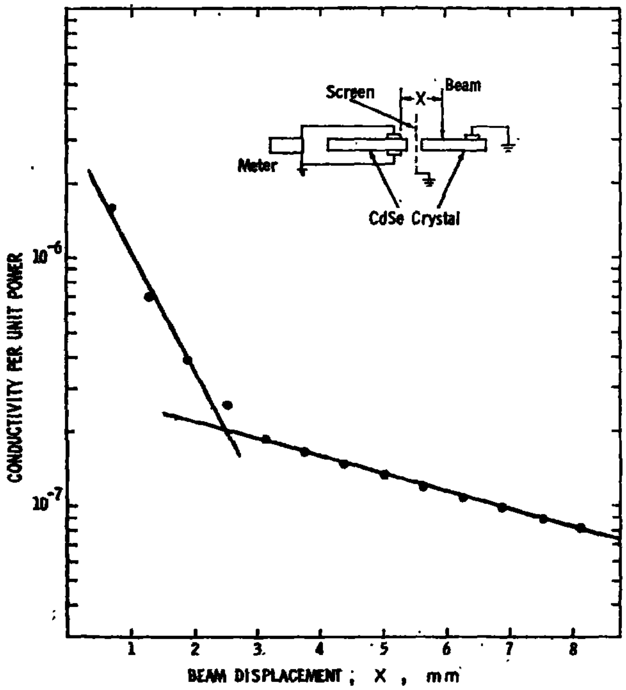

FIG. 2. Induced conductivity in nonbombarded crystal vs. the beam to contact distance X. The aluminum foil has been removed from between the crystal.

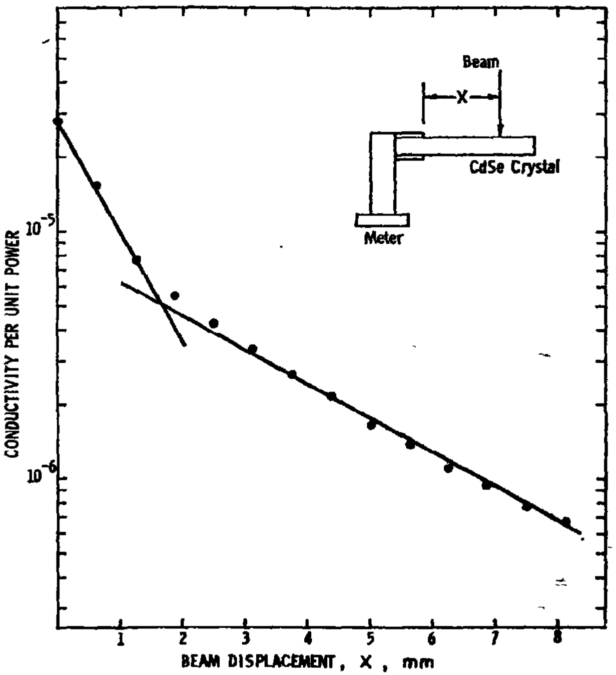

FIG. 3. Induced conductivity in a bombarded crystal vs. the beam to contact distance X.

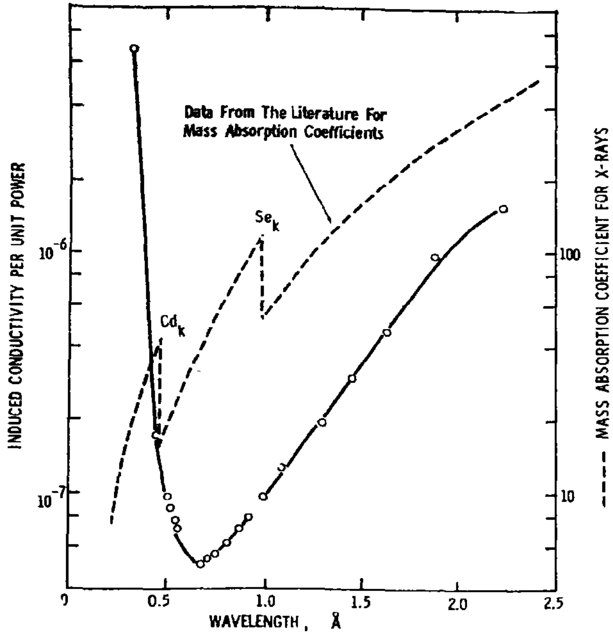

FIG. 4. Induced conductivity in a nonbombarded crystal vs. the DeBroglie wavelength of the bombarding electrons. The mass absorption coefficient for cadmium selenide is also shown. The experimental arrangement is the same as that shown in the schematic of Fig. 1. An aluminum foil is in place between the crystals.

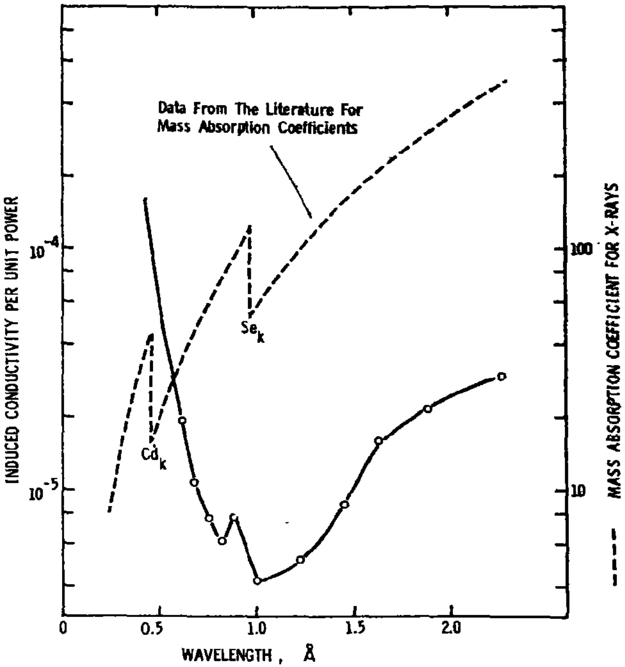

FIG. 5. Induced conductivity in a nonbombarded crystal vs. the DeBroglie wavelength of the bombarding electrons. The mass absorption coefficient for cadmium selenide is also shown. The experimental arrangement is the same as that shown in the schematic of Fig. 2. The aluminum foil has been removed from between the crystals.

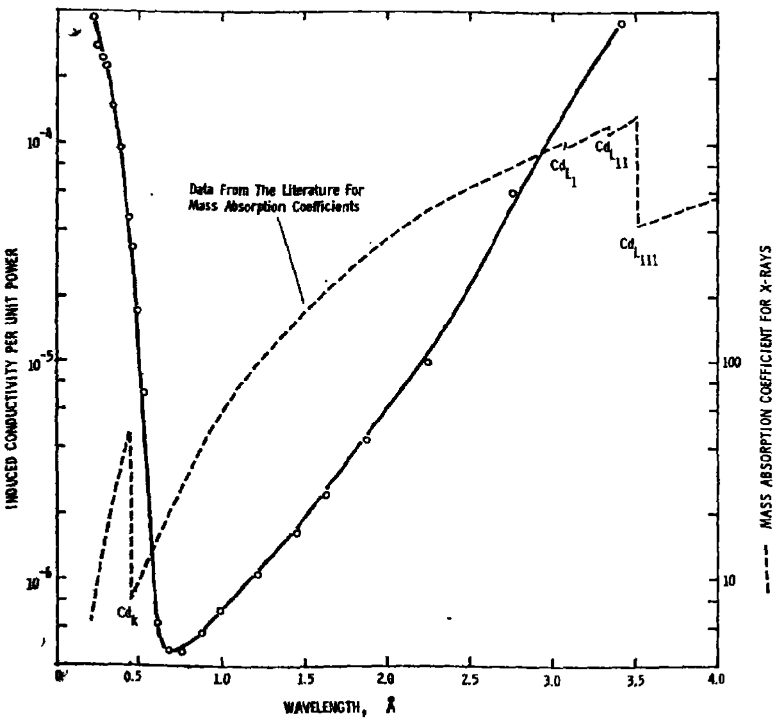

FIG. 6. Induced conductivity in a nonbombarded cadmium sulfide crystal vs. the DeBroglie wavelength of the bombarding electrons. The mass absorption coefficient for cadmium sulfide is also shown. The experimental arrangement is the same as that shown in the schematic of Fig. 1.

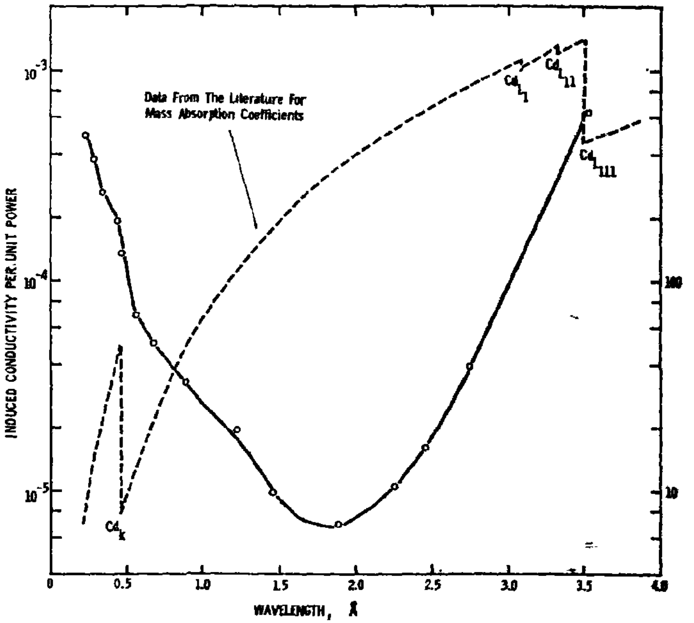

FIG. 7. Induced conductivity in a nonbombarded cadmium sulfide crystal vs. the DeBroglie wavelength of the bombarding electrons. The mass absorption coefficient for cadmium sulfide is also shown. The experimental arrangement is the same as that shown in the schematic of Fig. 2.

J. Phys. Chem. Solids Pergamon Press 1963. Vol. 24, pp. 741–749. Printed in Great Britain.

ETUDE DE LA RESISTIVITE ELECTRIQUE DES ALLIAGES BINAIRES ORDONNES

R. PICK

Centre d'Etudes Nucléaires de Saclay, France

(*Received* 28 *November* 1962)

Résumé—On développe un formalisme liant l'anomalie de résistivité à l'ordre à grande distance qui règne à l'intérieur d'un alliage métallique binaire ordonné. Les formules que l'on obtient sont applicables quels que soient: le type d'ordre envisagé (ordre normal ou antiphasé), la composition de l'alliage, et la portée des interactions. Les corrections apportées par l'ordre à courte distance sont calculées dans l'approximation du champ moléculaire.

Abstract—We establish a relation between long range order existing in a binary alloy and the corresponding anomaly in resistivity. General formulae are obtained under the following assumptions: quasi-free conduction electrons, and order due to binding forces between metallic ions. These formulas are valid whatever the range of the binding forces, the type of order (normal or periodically antiphased) and the relative concentration of the two components. The correction due to short range order is calculated with a molecular field approximation.

INTRODUCTION

Il est bien connu que la résistivité des alliages binaires qui s'ordonnent au-dessous d'une température critique T_c possède une anomalie de résistivité liée à l'ordre qui règne à l'intérieur de ceux-ci. Depuis les premiers travaux de Mott et Jones[1] et de Muto,[2] de nombreux auteurs se sont intéressés à ce problème ; en dehors d'études telles que celle de Krivoglaz[3] qui a étendu au domaine des électrons collectifs les idées de Mott et Jones, ou celle de Gibson[4] qui a cherché si les mesures de résistivité et de corrélation à courte distance déjà faites étaient compatibles, on s'est sourtout intéressé à l'aspect thermodynamique du problème :[5–7] comment la résistivité varie-t-elle en fonction de l'ordre et de la température dont ce dernier dépend ?

Jusqu'ici, on s'est toujours limité aux approximations suivantes : seuls les ions métalliques voisins interagissent entre eux et, en dessous de T_c, il n'existe que deux types de sous-réseaux qui sont occupés préférentiellement par les atomes A, et par les atomes B respectivement. De plus, en dessous de T_c, on s'est surtout intéressé aux alliages stoechiométriques.

Nous nous proposons ici d'établir une relation générale, valable en dessous de T_c, entre l'anomalie de résistivité et la fonction décrivant l'ordre à grande distance d'un tel alliage. Cette relation sera assez générale pour englober aussi bien les alliages ordonnés normaux (laiton β, Au–Cu I, ...) que les antiphases périodiques (Au–Cu II, Au Cu_3 antiphasé ...), quelles que soient les proportions relatives des deux constituants et la portée des interactions entre ceux-ci.

Nous montrerons que cette anomalie contient :

(a) Un terme principal dont l'origine est indépendante de toute approximation statistique. Ce terme, que l'on peut facilement relier à l'intensité des taches de diffraction obtenues par rayons X, est, dans les cas usuels, proportionnel à $1-a^2$ (où a est un paramètre d'ordre à longue distance, qui tend vers l'unité lorsque la température décroît).

(b) Un terme supplémentaire correspondant aux fluctuations par rapport à l'ordre moyen, dues aux corrélations à courte distance entre ions. Nous calculerons cette correction dans l'approximation du champ moléculaire, et montrerons qu'elle est toujours en $1/kT$, et, en général, proportionnelle à $(1-a)^2$.

Nous commencerons par indiquer succinctement comment les antiphases périodiques peuvent être considérées comme des alliages binaires ordonnés particuliers. Cette étude nous permettra d'introduire le formalisme général utile à la deuxième partie.

Après un bref rappel de la manière dont on lie la résistivité anormale aux fonctions de corrélations de l'alliage, nous calculerons celles-ci dans le cas d'alliages ordonnés et en déduirons la relation cherchée entre l'ordre à grande distance et la résistivité.

Nous appliquerons enfin ces résultats à différents types d'alliages. En particulier nous retrouverons et généraliserons, pour les alliages stoechiométriques, les résultats déjà établis⁽⁷⁾ pour les structures du laiton-β et de $AuCu_3$ normal ; nous les étendrons à Au–Cu I. Dans les cas non stoechiométriques, nous retrouverons, comme cas particulier, les formules de KRIVOGLAZ.⁽³⁾

1. ANTIPHASES DANS L'APPROXIMATION DU CHAMP MOLECULAIRE

Nous allons, ici, rappeler comment il est possible de décrire et, dans l'approximation du champ moléculaire, d'expliquer thermodynamiquement l'existence d'antiphases périodiques dans les alliages binaires.*

Soit un alliage A–B avec des concentrations respectives F_A et F_B. Considérons une configuration γ de cet alliage ; soit π_R la fonction de présence d'un atome de type A sur le noeud R, fonction qui vaut 1 ou 0 suivant le noeud et posons :

$$\pi_R = F_A(1+\sigma_R) \qquad (1,1)$$

Nous désignerons par P_R et S_R les moyennes thermiques de π_R et σ_R.

S_R est soumis aux conditions évidentes :

$$-1 \leqslant S_R \leqslant \frac{F_B}{F_A} \qquad (1,2a)$$

$$\sum_R S_R = 0 \qquad (1,2b)$$

Nous allons postuler que les phénomènes d'ordre que nous étudions sont uniquement dus à des interactions entre paires d'ions métalliques, l'intensité des forces dépendant seulement de la nature des ions en présence et de leur distance relative.†

Pour une configuration donnée l'énergie liée à l'ordre sera

$$E_c = \tfrac{1}{2}\sum_{R,R'}\{\pi_R\pi_{R'}\, J_{AA}(\boldsymbol{R}'-\boldsymbol{R}) + [\pi_R(1-\pi_{R'}) + \pi_{R'}(1-\pi_R)]J_{AB}(\boldsymbol{R}'-\boldsymbol{R}) + (1-\pi_R)(1-\pi_{R'}) \times J_{BB}(\boldsymbol{R}'-\boldsymbol{R})\} = NU_0 + \tfrac{1}{2}F_A^2\sum_{R,R'} J(\boldsymbol{R}'-\boldsymbol{R})\sigma_R\sigma_{R'} \qquad (1,3)$$

Avec

$$U_0 = \tfrac{1}{2}\sum_{(\boldsymbol{R}'-\boldsymbol{R}} [F_A^2 J_{AA}(\boldsymbol{R}'-\boldsymbol{R}) + 2F_AF_B \times J_{AB}(\boldsymbol{R}'-\boldsymbol{R}) + F_B^2 J_{BB}(\boldsymbol{R}'-\boldsymbol{R})] \qquad (1,4a)$$

$$J(\boldsymbol{R}'-\boldsymbol{R}) = J_{AA}(\boldsymbol{R}'-\boldsymbol{R}) + J_{BB}(\boldsymbol{R}'-\boldsymbol{R}) - 2J_{AB}(\boldsymbol{R}'-\boldsymbol{R}) \qquad (1,4b)$$

L'énergie d'un ion métallique comprend donc, en sus de son énergie propre U_0, un terme que l'on peut décrire comme l'interaction de σ_R avec un champ $\mathscr{H}_R$

$$\mathscr{H}_R = F_A^2 \sum_{R'} \sigma_{R'} J(\boldsymbol{R}'-\boldsymbol{R}) \qquad (1,5)$$

L'approximation du champ moléculaire consiste à postuler qu'à chaque température, σ_R interagit en fait avec un champ moyen H_R obtenu en remplaçant dans (1,5), les σ_R par leurs valeurs moyennes S_R.

$$H_R = F_A^2 \sum_{R'} S_{R'} J(\boldsymbol{R}'-\boldsymbol{R}) \; ; \qquad (1,5a)$$

---

* Une description plus complète de ces questions pourra être trouvée dans Refs. 8 et 9.

† Ceci exclut apparemment toute explication d'existence des antiphases périodiques par un mécanisme tel que celui proposé par SATO.⁽¹⁰⁾ Mais, même si les raisons qu'il invoque sont déterminantes pour la fixation de la longueur de la période, la valeur de l'ordre à grande distance qui règne dans celles-ci est très certainement liée aux mécanismes que nous invoquons ici. Cet ordre varie d'ailleurs en fonction de la température comme le démontrent des expériences de ANQUETIL⁽¹¹⁾ comparées à (3,3).

on en déduit tout de suite la valeur moyenne thermique S_R de σ_R

$$\boxed{S_R = \frac{(F_B/F_A)\exp[-\beta(F_B/F_A)(H_R+\lambda)]+(-1)\exp[\beta(H_R+\lambda)]}{\exp[-\beta(F_B/F_A)(H_R+\lambda)]+\exp[\beta(H_R+\lambda)]}\,;\ \beta = \frac{1}{kT} \qquad (1,6)}$$

équation dans laquelle on a ajouté au champ H_R agissant sur σ_R un potentiel thermodynamique λ indépendant de R qu'il est nécessaire d'introduire si l'on veut que 1,2b soit satisfait.

D'où :

$$\mathrm{Log}\frac{1+S_R}{1-(F_A/F_B)\,S_R} = -\frac{F_A}{kT}\left[\sum_{R'} J(\bar{R}'-\bar{R})\,S_{R'} + \frac{\lambda}{F_A^2}\right] + \log\frac{F_B}{F_A} \qquad (1,7)$$

On vérifie facilement que les équations (1,7) sont celles que l'on obtient en cherchant le minimum de la fonction à N variables

$$F = \tfrac{1}{2}F_A^2 \sum_{R,R'} J(\boldsymbol{R}'-\boldsymbol{R})S_R S_{R'} - kT\sum_R(-) \times [F_A(1+S_R)\mathrm{Log}(1+S_R)+F_B(1-F_A/F_B\,S_R) \times \mathrm{Log}(1-F_A/F_B)\,S_R)] \qquad (1,8)$$

où les S_R sont en plus soumis à (1,2b).

L'interprétation thermodynamique de (1,8) est aisée : l'énergie libre F du système d'ions métalliques est égale à son énergie moyenne (valeur de (1,3) où les σ_R ont été remplacés par les S_R correspondants), diminuée de kT fois l'entropie liée à l'ordre.

L'équation (1,8) est, en fait, d'un maniement plus aisé que (1,7). Il est en particulier possible de chercher directement si elle peut être minimisée par des fonctions périodiques. Nous avons été capables de montrer[8] que, dans certaines conditions (liées en particulier à l'existence de maximums de J_k (transformée de FOURIER de $J(\boldsymbol{R}'-\boldsymbol{R})$) pour des vecteurs $\boldsymbol{k}$ qui ne sont pas des vecteurs de réflexion de BRAGG), des fonctions périodiques, de période incommensurable avec celle du réseau, pouvaient fournir une énergie libre inférieure à celle que l'on calcule pour un alliage classiquement ordonné. De telles fonctions représentent clairement des antiphases périodiques telles que Au–Cu II par exemple. Ces solutions ont toujours un domaine d'existence limité en température vers le haut par une température critique T_{c_2} au-dessus de laquelle règne le désordre; elles peuvent être aussi limitées vers le bas, à une température T_{c_1} par une transition antiphase–ordre normal.

La transformation qui se produit à T_{c_2} peut être du deuxième ou du premier ordre suivant les cas ; celle qui a lieu à T_{c_1} semble toujours être du premier.

La recherche pratique de ces solutions est difficile et demanderait une connaissance précise des J_k. Nous verrons que l'étude de l'anomalie de résistivité fait aussi intervenir ces mêmes J_k mais n'apporte en fait sur elles aucune information supplémentaire.

2. FORMALISME GENERAL

Nous allons calculer l'expression générale de la résistivité anormale liée à l'ordre dans le cadre suivant :

(1) Les électrons sont diffusés par les ions métalliques, chaque ion créant un potentiel qui est un simple puits carré, et dépend de sa seule nature ;

(2) Les électrons de conduction sont des électrons presque libres ;

(3) Les sections efficaces de diffusion sont calculées dans l'approximation de Born.

MOTT et JONES[1] ont montré que de telles approximations étaient parfaitement justifiées dans l'étude de la résistivité des alliages métalliques non ordonnés, et leurs arguments restent valables dans le cas qui nous intéresse ici.

Nous choisirons l'origine des énergies de telle sorte que la valeur moyenne du potentiel soit nulle. Cette définition est indépendante de la configuration γ de l'alliage puisque

$$\begin{aligned} V(\boldsymbol{r}) &= \sum_R [F_A(1+\sigma_R)V_A(\boldsymbol{R}-\boldsymbol{r})+(F_B-F_A\sigma_R) \times V_B(\boldsymbol{R}-\boldsymbol{r})] \\ &= \sum_R [F_A V_A(\boldsymbol{R}-\boldsymbol{r})+F_B V_B(\boldsymbol{R}-\boldsymbol{r})] + F_A\sum_R \sigma_R(V_A(\boldsymbol{R}-\boldsymbol{r})-V_B(\boldsymbol{R}-\boldsymbol{r})) \qquad (2,1) \end{aligned}$$

Commes les potentiels sont des puits carrés, on en déduit que la valeur moyenne du deuxième membre est nulle d'après (1,2b).

Il suffit donc d'imposer :

$$F_A\langle V_A\rangle + F_B\langle V_B\rangle = 0 \tag{2,2}$$

ce qui rend le premier terme de (2,1) nul quel que soit $\boldsymbol{r}$.

On peut montrer⁽¹⁾ que la résistivité supplémentaire $\Delta\rho$ produite par la présence d'une différence entre les potentiels diffusants des ions A et B est égale à :

$$\sum_{\boldsymbol{k},\boldsymbol{k}'} A(\boldsymbol{k},\boldsymbol{k}',\boldsymbol{x})\,|\langle\boldsymbol{k}|V(\boldsymbol{r})|\boldsymbol{k}'\rangle|_T^2 \tag{2,3}$$

où $\boldsymbol{k}$ et $\boldsymbol{k}'$ sont deux vecteurs de Fermi, $\boldsymbol{x}$ la direction du champ électrique, $A(\boldsymbol{k},\boldsymbol{k}',\boldsymbol{x})$ un coefficient indépendant de la température et,

$$|\langle\boldsymbol{k}|V(\boldsymbol{r})|\boldsymbol{k}'\rangle|_T^2 \equiv |\langle\boldsymbol{k}|(V_A-V_B)|\boldsymbol{k}'\rangle|^2F_A^2 \\ \times \ll |\sum_R \sigma_R \exp[i(\boldsymbol{k}'-\boldsymbol{k})\cdot\boldsymbol{R}]|^2 \gg_T$$

Dans cette dernière expression $\ll\ \gg_T$ signifie que l'on a pris la valeur moyenne thermique du terme entre crochets. Le but de ce travail est de montrer que

$$I_X = F_A^2 \ll \sum_{R,R'} \sigma_R\sigma_{R'} \exp[i(\boldsymbol{k}-\boldsymbol{k}')\cdot(\boldsymbol{R}-\boldsymbol{R}')]\gg_T \tag{2,4}$$

possède, en fonction de l'ordre à grande distance, la dépendance qui a été brièvement décrite dans l'introduction.

Remarque

Nous n'expliciterons guère plus par la suite la forme exacte de $\Delta\rho$ qui ne prend une forme simple que si la surface de Fermi est sphérique.

En particulier, cette surface n'est certainement pas la même à haute température, où le cristal est désordonné, à basse température où la zone de Brillouin est plus petite par suite de l'existence de surstructures, et dans la région intermèdiare où peuvent exister des antiphases; ceci explique en particulier que nous ne serons pas capables de relier entre elles les différentes anomalies correspondant aux différents types d'ordre d'un même alliage. Nous pourrons seulement étudier la variation de l'anomalie à l'intérieur de chaque domaine de température séparément.

Une telle limitation peut avoir une grande importance pratique: dans les alliages pour lesquels le paramètre d'ordre a ne tend pas vers zéro lorsqu'on s'approche de la température critique, on ne possède aucune information expérimentale sur la valeur de la résistivité aux petits a. Une extrapolation de cette dernière à partir des valeurs obtenues dans le domaine désordonné ne peut pas être ici justifiée a priori : dans l'alliage Au_3 Cu, par exemple, la résistivité de l'état ordonné est supérieure à celle de l'état désordonné⁽¹²⁾ ce qui serait incompatible avec les formules que nous allons obtenir, si l'on admettait la possibilité d'une telle extrapolation.

Nous sommes maintenant débarrassés de tout l'aspect "électrique" de notre problème et avons à étudier, en fonction de la température, la variation de :

$$I_X = F_A^2 \sum_{R,R'} \exp[i\boldsymbol{X}\cdot(\boldsymbol{R}-\boldsymbol{R}') \ll \sigma_R\sigma_{R'} \gg_T ;$$

$$\boldsymbol{X} = \boldsymbol{k}-\boldsymbol{k}' \tag{2.5}$$

Nous simplifierons notre problème en introduisant, en sus des probabilités simples, des probabilités conditionnelles qui remplaceront les fonctions de corrélation de (2,5).

Nous poserons par définition que

$$F_A(1+S_R+S^{(\alpha)}_{R\,R'}) \tag{2,6}$$

est la probabilité de trouver un atome A en R' lorsqu'en R (où $\ll\sigma_R\gg_T = S_R$) il y a un atome de type α.

Les $S^{(\alpha)}_{R,R'}$ sont reliés par l'équation suivante, qui exprime la probabilité inconditionnelle d'avoir un atome A en R'

$$S_{R'} = F_A(1+S_R)\,(S_{R'}+S^{(A)}_{R,R'}) \\ +(F_B-F_AS_R)(S_{R'}+S^{(B)}_{R\,R'})$$

Soit

$$F_A(1+S_R)S^{(A)}_{R\,R'}+(F_B-F_AS_R)S^{(B)}_{R\,R'} = 0 \tag{2,7}$$

On peut alors transcrire (2,4) en fonction de nos nouvelles notations en exprimant que chaque noeud est occupé par un atome A ou B avec la probabilité correspondante :

$$I_X = F_A^2 \sum_{R,R'} \exp[i\boldsymbol{X}\cdot(\boldsymbol{R}-\boldsymbol{R}')][F_A(1+S_R) \\ \times (F_B/F_A)(S_{R'}+S^{(A)}_{R,R'})+(F_B-F_AS_R)(-1) \\ \times(S_{R'}+S^{(B)}_{R,R'})] = F_A^2 \sum_{R,R'} \exp[i\boldsymbol{X}\cdot(\boldsymbol{R}-\boldsymbol{R}')] \\ \times [S_RS_{R'}+(1+S_R)S^{(A)}_{R,R'}] \tag{2,8}$$

Cherchons à quelle équation satisfait $S^{(A)}_{R,R'}$. Nous pouvons établir immédiatement une expression de $S^{(\alpha)}_{R,R'}$ en fonction des $S^{(\alpha)}_{R,R'}$ par une méthode analogue à celle qui nous a fourni l'équation (1,6). Si $H_{II\,R'}$ est le champ moléculaire qui s'exerce en R' il vaut :

$$H_{II\,R'} = F_A^2 \sum_{R''} (S_{R''} + S^{(\alpha)}_{R,R''}) J(R'' - R')$$
$$= H_{R'} + H_{I\,R'} \qquad (2,9)$$

Soit en introduisant un potentiel chimique $\mu_{R'}$ destiné à ce que (2,7) soit satisfait

$$S^{(\alpha)}_{R,R'} = \frac{(F_B/F_A - S_{R'}) \exp[-\beta\, F_B/F_A(H_{R'}+\lambda+H_{IR'}+\mu_{R'})] + (-1-S_{R'}) \exp[\beta(H_{R'}+\lambda+H_{IR'}+\mu_{R'})]}{\exp[-\beta\, F_B/F_A\,(H_{R'}+\lambda+H_{IR'}+\mu_{R'})] + \exp[\beta(H_{R'}+\lambda+H_{IR'}+H_{R'})]} \qquad (2,10)$$

En éliminant $H_{R'}+\lambda$ par l'intermédiaire de (1,6) il vient

$$S^{(\alpha)}_{R,R'} = \frac{(F_B - F_A S_{R'})(1+S_{R'})(\exp[-\beta(H_{IR'}+\mu_{R'})/F_A]-1)}{1+F_A(1+S_{R'})(\exp[-\beta(H_{IR'}+\mu_{R'})/F_A]-1)} \qquad (2,11)$$

Ces équations ne sont évidemment valables que pour $R' \neq R$; par définition :

$$S^{(A)}_{R,R} = (F_B/F_A - S_R) \; ; \; S^{(B)}_{R,R} = -(1+S_R)$$

quantités qui satisfont bien (2,7).*

Si l'on limite le développement de l'exponentielle à son terme linéaire en $H_{I\,R}$, (ce que nous justifierons plus loin) on obtient :

$$S^{(\alpha)}_{R,R'} = -(F_B - F_A S_{R'})(1+S_{R'})(F_A/kT)$$
$$\times \left[\sum_{R''} J(R''-R') S^{(\alpha)}_{R,R''} + \frac{\mu_{R'}}{F_A^2}\right] \qquad (2,12)$$

Il est alors aisé de voir que l'on peut faire $\mu_{R'} = 0$ quel que soit R'. En effet (2,12) est identique pour $\alpha = A$ et $\alpha = B$; il s'ensuit que, si tous les $\mu_{R'}$ sont nuls, le rapport $S^{(A)}_{R,R'}/S^{(B)}_{R,R'}$ ne dépendra pas de R' et vaudra $S^{(A)}_{R,R}/S^{(B)}_{R,R}$; (2,7) est alors automatiquement satisfait.

Montrons que le passage de (2,11) à (2,12) est justifié. Outre des valeurs moyennes thermiques $S^{(A)}_{R,R''}$ qui sont certainement petites, $H_{IR'}$ contient $J(R'-R)\; S^{(A)}_{R,R}$ qui en est le terme principal, et n'est pas, a priori, petit devant kT. Mais S_R ne varie beaucoup qu'autour de T_c et tend assez vite vers sa limite lorsque la température décroît. $J(R'-R)S^{(A)}_{R,R}/kT$ sera toujours petit devant l'unité si l'atome A est "à sa place" (c'est-à-dire sur un site où S_R tend vers F_B/F_A) et le développement sera valable. Ce dernier peut paraître plus discutable pour les sites où se placent préférentiellement des atomes B. Mais, en fait, on peut remplacer, dans (2,8), $(1+S_R)S^{(A)}_{R,R'}$ par $-F_B/F_A - S_R)S^{(B)}_{R,R'}$ pour chacun de ces sites, puis linéariser l'exponentielle correspondante dans (2,11). Ceci est parfaitement correct et conduit au même résultat final (2,14), ce qui justifie, à posteriori, notre façon de procéder. Le développement n'est donc discutable que juste en dessous de T_c, domaine de température où $J(R-R')S^{(\alpha)}_{R,R}/kT$ est au plus de l'ordre de l'unité. Nous pourrons donc toujours nous contenter de (2,12).

Si nous négligeons alors tous les $S^{(A)}_{R,R''}$ pour $R'' \neq R$ dans le membre de droite de (2,12) on obtient :

$$S^{(A)}_{R,R'} = -(1/kT)(F_B - F_A S_R)(F_B - F_A S_{R'})$$
$$\times (1+S_{R'}) J(R-R') \qquad (2,13)$$

qui est la solution de (2,11) à

$$\left[\frac{J(R-R')(F_B - F_A S_{R'})(1+S_{R'})}{kT}\right]^2 \text{ près.}$$

---

* Notons qu'avec ces définitions, il a été correctement tenu compte dans (2,9) du rôle particulier joué par l'atome situé en R.

On en déduit alors :

$$I_X = F_A^2 \sum_{R,R'} S_R S_{R'} \exp[iX \cdot (R-R')] + F_A \,[\sum_R (F_B - F_A S_R)(1+S_R) - F_A/kT \times \sum_{R,R'} (F_B - F_A S_R)\,(1+S_R)(F_B - F_A S_{R'})(1+S_{R'}) J(R-R') \exp\{iX \cdot (R-R')\}] \tag{2,14}$$

En introduisant les transformées de Fourier de $J(R'-R)$, S_R et $(F_A - F_B\, S_R)(1+S_R) = F_R$

$$S_k = [1/\sqrt{(N)}] \sum_R S_R \exp(ik \cdot R) \; ; f_k = [1/\sqrt{(N)}] \sum_R (F_B - F_A S_R)(1+S_R) \exp(ik \cdot R) \; ; \quad J_k = [1/\sqrt{(N)}] \sum_{(R-R')} J(R-R') \exp(ik \cdot (R-R')] \tag{2,15}$$

il vient

$$I_X = F_A^2\, N S_X\, S_{-X} + \sqrt{(N)} F_A [f_0 - F_A/kT \sum_q f_{-q} f_q\, J_{X-q}] \tag{2,16}$$

Dans la plupart des cas que nous étudierons, nous considérerons des alliages ordonnés. Pour ceux-ci, S_R est une fonction périodique : seuls quelques S_k et f_k (en particulier f_0) ne sont pas nuls, alors que J_k a un spectre continu. Nous pourrons donc en général négliger le premier terme de (2,16) devant les deux autres.

Nous avons ainsi démontré que I_X et, partant, l'anomalie de résistivité, était proportionnelle au deuxième terme de (2,16). Nous consacrerons la dernière partie de cet article à la discussion de cette formule et à son application à un certain nombre de cas particuliers.

3. DISCUSSION—APPLICATIONS DIVERSES

Discussion générale

(1) Nous allons commencer par discuter la forme de (2,16) et montrer que celle-ci découle directement de (2,5).

$$I_X = F_A^2 \sum_{R,R'} \exp[iX \cdot (R-R')] \ll \sigma_R \sigma_{R'} \gg_T$$

Le premier terme de (2,16) provient de l'approximation :

$$\ll \sigma_R \sigma_{R'} \gg_T \; = \; \ll \sigma_R \gg_T \ll \sigma_{R'} \gg_T \tag{3,1}$$

Cette approximation est évidemment très mauvaise pour tous les termes de la somme pour lesquels $R' = R$. Il faut donc la compenser pour ceux-ci en ajoutant :

$$F_A^2 \sum_R (\ll \sigma_R^2 \gg_T - S_R^2) \tag{3,2}$$

Par définition de S_R ceci est égal à :

$$F_A^2 \sum_R [(F_A(1+S_R)(F_B/F_A)^2 + (F_B - F_A S_R)(-1)^2 - S_R^2]$$

qui est le deuxième terme de (2,16). (3,2) découle donc de la seule notion de fonction d'ordre S_R et, par conséquent, est indépendant de toute approximation statistique.

L'approximation est aussi insuffisante pour des couples R,R' où R et R' sont peu éloignés l'un de l'autre. Mais, expérimentalement, nous savons qu'il s'agit cette fois-ci d'une faible correction aux températures largement supérieures à T_c[13] et d'une plus faible encore en dessous de T_c[14]. Nous nous sommes donc contentés de calculer :

$$\sum_{R,R' \neq R} \exp[iX \cdot (R-R')] \ll \sigma_R \sigma_{R'} \gg_T - \ll \sigma_R \gg_T \times \ll \sigma_{R'} \gg_T)$$

dans l'approximation du champ moléculaire. C'est ce qui nous a fourni le dernier terme de (2,16) qui s'exprime en fonction de S_R et de la température. On peut remarquer qu'il s'agit d'une correction : il est donc loisible de remplacer, dans son expression, les S_R correspondant à l'approximation du champ moléculaire par leurs valeurs expérimentales.

(2) I_X, sous sa forme tronquée, dépend bien de l'ordre à longue distance comme il a été dit. En effet, comme S_R tend vers F_B/F_A ou -1, f_R tend toujours vers 0 lorsque la température décroît. Nous verrons en (C) et (D) que, dans le cas des alliages normaux, chaque f_R, séparément, est proportionnel à $(1-a)$, où a tend vers 1 lorsque la température tend vers zéro. On en déduit donc que le premier terme de I_X est proportionnel à $(1-a)$ et le deuxième à $(1-a)^2$.

(3) Le terme principal peut être interprété commodément même dans le cas des antiphases. $\sqrt{(N)}f_0$ s'écrit en effet :

$$\sqrt{(N)}f_0 = \sum_R (F_B - F_A S_R^2) = N[F_B - (F_A/N) \sum_k |S_k|^2] \qquad (3,3)$$

Or les $|S_k|^2$ sont des quantités qui sont mesurées directement dans les études d'antiphases par rayons X. (3,3) permet donc une comparaison directe entre les deux types d'expériences. Les seuls résultats que l'on possède à l'heure actuelle sont encore trop imprécis pour que l'on spécule davantage sur le terme supplémentaire.

Applications

Nous ne nous occuperons plus maintenant que des alliages ordonnés normaux. Pour exploiter plus aisément la forme de I_X nous allons expliciter J_q. Comme $J(\boldsymbol{R}'-\boldsymbol{R})$ est une fonction paire, on peut écrire :

$$I_X = F_A\sqrt{(N)}\,[f_0 - (F_A/kT)\,(1/\sqrt{(N)}) \sum_q |fq|^2 \times \Big(\sum_{(\boldsymbol{R}'-\boldsymbol{R})} J(\boldsymbol{R}'-\boldsymbol{R}) \cos \boldsymbol{q}_0(\boldsymbol{R}'-\boldsymbol{R}) \cos \boldsymbol{X}(\boldsymbol{R}'-\boldsymbol{R})\Big)] \qquad (3,4)$$

A. *Surface de* FERMI *sphérique*

Une simplification supplémentaire peut être apportée à (3,4) si l'on suppose la surface de FERMI sphérique. $A(\boldsymbol{k},\boldsymbol{k}',\boldsymbol{x})$ et $\langle \boldsymbol{k}|(V_A - V_B)|\boldsymbol{k}'\rangle$ ne dépendent plus que de $|\boldsymbol{k}-\boldsymbol{k}'| = |\boldsymbol{X}|$ et $\boldsymbol{X}$ peut prendre toutes les orientations par rapport au réseau. On peut alors dans (2,3) ne conserver qu'une sommation sur $|\boldsymbol{X}|$ à condition de remplacer (3,4) par sa moyenne sur toutes les orientations relatives de $\boldsymbol{X}$ et $\boldsymbol{R}-\boldsymbol{R}'$:

$$I_X = \sqrt{(N)}F_A \Bigg[f_0 - (F_A/kT)\,(1/\sqrt{(N)}) \sum_q |fq|^2 \Bigg(\sum_{(\boldsymbol{R}'-\boldsymbol{R})} J(\boldsymbol{R}'-\boldsymbol{R}) \cos \boldsymbol{q}\cdot(\boldsymbol{R}'-\boldsymbol{R}) \frac{\sin(|\boldsymbol{X}|\,|\boldsymbol{R}'-\boldsymbol{R}|)}{|\boldsymbol{X}|\,|\boldsymbol{R}'-\boldsymbol{R}|}\Bigg)\Bigg] \qquad (3,5)$$

On voit alors que les interactions éloignées, qui peuvent être importantes dans la formation de l'ordre à longue distance, ont un rôle beaucoup plus faible dans la résistivité.

Remarque. Ceci est aussi vrai à haute température. Le formalisme développé ici est tout aussi valable au-dessus de la température critique, en prenant S_R identiquement nul. Dans ce cas, seul f_0 est différent de zéro et vaut $\sqrt{(N)}F_B$. (3,5) se réduit à :

$$I_X = N\,F_B F_A \Bigg[1 - \frac{F_A F_B}{kT} \sum_{(\boldsymbol{R}'-\boldsymbol{R})} J(\boldsymbol{R}'-\boldsymbol{R}) \times \frac{\sin(|\boldsymbol{X}|\,|\boldsymbol{R}'-\boldsymbol{R}|)}{|\boldsymbol{X}|\,|\boldsymbol{R}'-\boldsymbol{R}|}\Bigg] \qquad (3,6)$$

qui est une généralisation évidente de la formule (20) de Ref. 7a.

On peut d'autre part remarquer que (2,16) non tronqué peut redonner d'une autre façon la valeur de $\Delta\rho$ pour un alliage complètement désordonné, en supposant que S_R vaut -1 ou F_B/F_A de façon parfaitement aléatoire. Dans ce cas f_R est nul quel que soit R et il reste :

$$I_X = N|S_X|^2 F_A^2 \qquad (3,6a)$$

Comme le spectre des S_k est forcément blanc on a

$$|S_X|^2 = F_B/F_A$$

en vertu de l'égalité de Parceval:

$$\sum_k |S_k|^2 = \sum_R S_R^2.$$

(3,6a) est donc le premier terme de (3,6) ce qui est normal puisque nous avons négligé ainsi toute corrélation entre les différentes sites et que ce sont celles-ci qui amènent le terme en $F_A F_B/kT$.

B. *Alliages stoechiométriques du type A-B: (laiton β* (C.C.), AuCu I (C.F.C.)).

On a $F_A = F_B = \frac{1}{2}$; $S_R = \pm\, a$; $f_R = \frac{1}{2}(1-a^2)$

S_R prend deux valeurs opposées suivant les sites mais f_R se réduit à une constante. Donc seul f_0 est différent de zéro.

On a donc :

$$I_X = (N/4)\,(1-a^2)\left(1 - \frac{N(1-a^2)}{4kT} J_X\right) \qquad (3,7)$$

On peut relier J_X à la température critique dans le seul cas où l'on suppose simultanément que (3,5) est valable et qu'il n'y a d'interactions qu'entre premiers voisins :

$$I_X = N\left(\frac{1-a^2}{4}\right)\left[1 - \frac{(1-a^2)}{4kT} zJ \frac{\sin Xc}{Xc}\right] \qquad (3,7a)$$

où z est le nombre de voisins d'un atome donné, c la distance entre voisins et J la valeur de $J(\boldsymbol{R}-\boldsymbol{R}')$ pour $|\boldsymbol{R}-\boldsymbol{R}'| = c$. En tirant la valeur de T_c de l'équation (1,7) (équation dans laquelle il est facile de voir que $F_A = F_B$ entraîne $\lambda = 0$), on obtient :

$$I_X = N\left(\frac{1-a^2}{4}\right)\left(1-(1-a^2)\frac{T_c}{T}\frac{\sin Xc}{Xc}\right) \text{ (C.C.)} \tag{3,8a}$$

$$I_X = N\left(\frac{1-a^2}{4}\right)\left(1-(1-a^2)\frac{3T_c}{T}\frac{\sin Xc}{Xc}\right) \text{(C.F.C).} \tag{3,8b}$$

C. *Alliages stoechiométriques du type* A_3-B (C.F.C.).

$F_A = \frac{3}{4}$; S_R prend les deux valeurs $-a$ et $a/3$ suivant les sites. f_k possède cette fois deux valeurs différentes suivant que $k = 0$ ou qu'il est l'un des trois vecteurs: $0, 0, 2\pi/\boldsymbol{b}$ où $\boldsymbol{b}$ est la longueur de l'arête du cube

$$f_0 = \sqrt{(N)}\left(\frac{1-a^2}{4}\right) ; f_{k\neq 0} = \sqrt{(N)}(1-a)\frac{a}{6}$$

Soit :

$$I_X = \frac{3N}{16}\left[(1-a^2)-\frac{3}{16}\frac{(1-a)^2}{kT}\sum_{(\boldsymbol{R}'-\boldsymbol{R})} J(\boldsymbol{R}'-\boldsymbol{R}) \times \cos \boldsymbol{X}\cdot(\boldsymbol{R}'-\boldsymbol{R})\left((1+a)^2+\sum_{k\neq 0}\cos \boldsymbol{k}\cdot(\boldsymbol{R}'-\boldsymbol{R})\frac{4a^2}{9}\right)\right] \tag{3,9}$$

Il nous faut alors distinguer, dans la somme sur $(\boldsymbol{R}'-\boldsymbol{R})$, entre les noeuds (I) pour lesquels $\boldsymbol{R}'-\boldsymbol{R}$ est de la forme $(p,q,r)\,b$ et ceux (II) pour lesquels il s'écrit $(p, q+\frac{1}{2}, r+\frac{1}{2})b$. Dans le premier cas $\sum_{k\neq 0} \cos \boldsymbol{k}\cdot(\boldsymbol{R}'-\boldsymbol{R}) = 3$; dans le second cette somme vaut -1.

D'où :

$$I_X = \frac{3N}{16}\left[(1-a^2)-\frac{3}{16}\frac{(1-a)^2}{kT}\left(\sum_{(\boldsymbol{R}'-\boldsymbol{R})}^{I} J(\boldsymbol{R}'-\boldsymbol{R}) \times \cos \boldsymbol{X}\cdot(\boldsymbol{R}'-\boldsymbol{R})\frac{3+6a+7a^2}{3} + \sum_{(\boldsymbol{R}'-\boldsymbol{R})}^{II} J(\boldsymbol{R}'-\boldsymbol{R})\cos \boldsymbol{X}\cdot(\boldsymbol{R}'-\boldsymbol{R})\frac{(3+a)(3+5a)}{9}\right)\right] \tag{3,10}$$

Dans le cas particulier d'une surface de Fermi sphérique et d'interactions entre premiers voisins, (3,10) s'écrit* :

$$I_X = \frac{3N}{16}(1-a^2) \times \left[1-\frac{(1-a)(3+a)(3+5a)}{4(1+a)}\frac{J}{kT}\frac{\sin Xc}{Xc}\right] \tag{3,10a}$$

D. *Alliages normaux non stoechiométriques*

D'un point de vue purement mathématique, la forme de la fonction S_R n'est pas connue, car elle ne peut plus, ici, être déterminée par des raisons de symétrie comme dans les alliages stoechiométriques.

Expérimentalement, on constate que ces alliages s'ordonnent comme les stoechiométriques dont ils sont le plus voisins : par exemple dans des alliages AuCu, on obtient la même surstructure pour $0{,}37 < F_A < 0{,}63$. Nous pouvons donc supposer qu'à toute température non nulle (cette restriction étant due au théorème de Nernst, imposant à l'alliage d'être rigoureusement ordonné au zéro absolu) S_R est une fonction qui ne prend de valeurs distinctes que sur des sous-réseaux différents.

Les résultats de (B) et (C) sont alors légèrement modifiés ; pour les alliages de type AB par exemple, seul f_0 est encore non nul, mais ses propriétés sont un peu différentes. Avec les mêmes hypothèses simplificatrices qu'en (3,8), et pour la surface de Fermi, et pour la détermination de T_c, on obtient :

$$I_X = F_A F_B N\left(1-\frac{F_A}{F_B}a^2\right)\left(1-\left(1-\frac{F_A}{F_B}a^2\right) \times\frac{T_c}{T}\frac{\sin Xc}{Xc}\right) \text{ (C.C.)} \tag{3,11a}$$

$$I_X = F_A F_B N\left(1-\frac{F_A}{F_B}a^2\right)\left(1-\left(1-\frac{F_A}{F_B}a^2\right) \times\frac{3T_c}{T}\frac{\sin Xc}{Xc}\right) \text{ (C.F.C.)} \tag{3,11b}$$

---

[*] La formule 12 de Ref. 7b est presque identique mais contient une légère erreur de calcul que (3,10a) corrige.

Pour le C.C., ces résultats sont peu différents de ceux de KRIVOGLAZ(3) (seul cas explicité dans son article) et plus généraux puisqu'ils s'étendent immédiatement à des interactions entre voisins éloignés, et ne sont pas liés à la petitesse de X_C devant l'unité.

Il faut remarquer que :

(a) Le terme provenant de l'ordre à longue distance ne s'annule pas à basse température. En effet, pour $F_B > F_A$ par exemple, la valeur maximum de a^2 est 1. Le terme vaut alors $F_A(F_B - F_A)$. Ceci traduit simplement l'existence d'un désordre résiduel sur un sous-réseau où coexistent, avec des atomes A, les atomes B qui n'ont pu se loger sur l'autre sous-réseau.

(b) Le terme correspondant aux corrélations à courte distance devient maintenant infini à basse température ; ceci est dû à ce que, f_R ne tendant plus vers zéro avec T, la linéarisation (2,16) n'est plus valable à basse température. Physiquement, ceci n'a aucune importance, car aucune transformation n'a lieu à des températures inférieures à 150°C environ, température où l'ordre est déjà presque entièrement réalisé et pour laquelle (3,11) est parfaitement valable.

Remerciements—Je tiens à remercier Messieurs A. HERPIN et J. FRIEDEL pour l'intérêt qu'ils ont constamment porté à ce travail, ainsi que Mlle M. T. BEAL pour ses nombreuses remarques et de fructueuses discussions.

BIBLIOGRAPHIE

1. MOTT N. F. et JONES H., *The Theory of the properties of metals and alloys*, Chap. VII, para. 12, University Press, Oxford (1936).
2. MUTO T., *Sci. Pap. Inst. phys. chem. Res. Tokyo* **30**, 99 (1936).
3. KRIVOGLAZ M. A., et MATSYNA Z. A., *Sov. Phys. JETP*, **1**, 103, (1955).
4. GIBSON J. B., *J. Phys. Chem. Solids*, **4**, 177 (1958).
5. SMIRNOV A. A., *J. exp. theor. Phys.* **17**, 743, (1947).
6. DIENES G. J., *J. appl. Phys.* **22**, 1020 (1951).
7. BEAL M. T., *J. Phys. Chem. Solids* **15**, 72 (1960); **18**, 156 (1961).
8. PICK R., *J. Phys. Radium*, à paraître.
9. VILLAIN J., Communication présentée au *Colloque sur les solutions solides, Orsay juillet* 1962, *J. Phys. Radium* (à paraître).
10. SATO H. et TOTH R. S., *Phys. Rev.*, **124**, 1833 (1961).
11. ANQUETIL M. C., *J. Phys. Radium* **23**, 113 (1962).
12. HIRABAYASCHI M., *J. phys. Soc. Japan* **14**, 262 (1959).
13. COWLEY J. M., *J. appl. Phys.* **21**, 24 (1950).
14. ROBERTS B. W. et VINEYARD G. H., *J. appl. Phys.* **27**, 103 (1956).

J. Phys. Chem. Solids Pergamon Press 1963. Vol. 24, pp. 751–757. Printed in Great Britain.

OPTICAL PROPERTIES OF THE PHTHALOCYANINES

LEWIS T. CHADDERTON

Physics and Chemistry of Solids, Cavendish Laboratory, Cambridge

(*Received* 12 *December* 1962)

Abstract—The optical properties of some of the phthalocyanines have been investigated for molecules in different degrees of association. If the spectral shifts arising from temperature dependence and the broadening due to crystal field effects are accounted for there appears to be a one-to-one correspondence between peaks observed in vapour, sublimed film, and single crystal absorption spectra.

It is proposed that the simple band model offers a reasonably good description of crystalline copper, platinum, and metal-free phthalocyanines. The sharp energy levels of the free molecule transform into broad quasi-continuous bands on crystallization.

THE semiconduction properties of some of the phthalocyanine derivatives have stimulated interest(1–14) in the electrical, photoconductive, and optical properties of the same compounds. FIELDING and GUTMAN(1) have reported on the relation between absorption spectra of thin sublimed films and the temperature dependence of resistivity, while VARTANYAN and KARPOVICH(2–4) have been concerned with the spectral dependence of the photoconductivity and optical activation energy. The Russian authors TERENIN, PUTZEIKO and AKIMOV(5) point out the importance of such studies because of the similarity of the phthalocyanine and chlorophyll molecules, and, more recently, TOLLIN, KEARNS and CALVIN(6,7) have published a detailed treatment of the kinetics of conductivity in metal-free phthalocyanine. These treatments generally deal with sublimed layers of the compound. The only investigation of the optical properties of single crystals is that reported by LYONS, WALSH and WHITE(8) who give the reflection absorption spectra of phthalocyanine.

This communication describes a number of features in the optical properties of the phthalocyanines which have been investigated in the course of a research programme concerned with radiation damage in the solid state.(15,16)

EXPERIMENTAL

Platinum phthalocyanine is difficult to prepare in large quantities and metal-free phthalocyanine(17) itself exists in distinctly separate forms (α, β, and γ) which are stable in different temperature regions. Hence the results which are reported mostly concern copper phthalocyanine, though some values have been obtained for the platinum and metal-free compounds. It will be evident, however, that there are close similarities in spectra obtained for the three compounds, so little is lost in generalizing the results obtained for the copper derivative.

Absorption spectra were obtained for molecules in different degrees of association:

(a) *Vapour*

Crystals of copper phthalocyanine were obtained from the Imperial Chemical Industries Ltd. and these were purified by repeated vacuum sublimaton. A little of the purified material was vacuum-sealed in a 1-ft silica tube with optically flat quartz terminal faces and the latter was placed at the centre of a 3-ft cylindrical furnace. Light from a tungsten strip source was passed through the copper phthalocyanine vapour and focused into the slit of a Hilger D 187 wavelength spectrometer. The absorption spectrum was recorded photographically on Kodak 0·250 rapid ortho metallographic plates, and the procedure was repeated with purified metal-free phthalocyanine.

Vapour absorption spectra for the two compounds are shown in Fig. 1. Densitometer traces are given in Fig. 2.

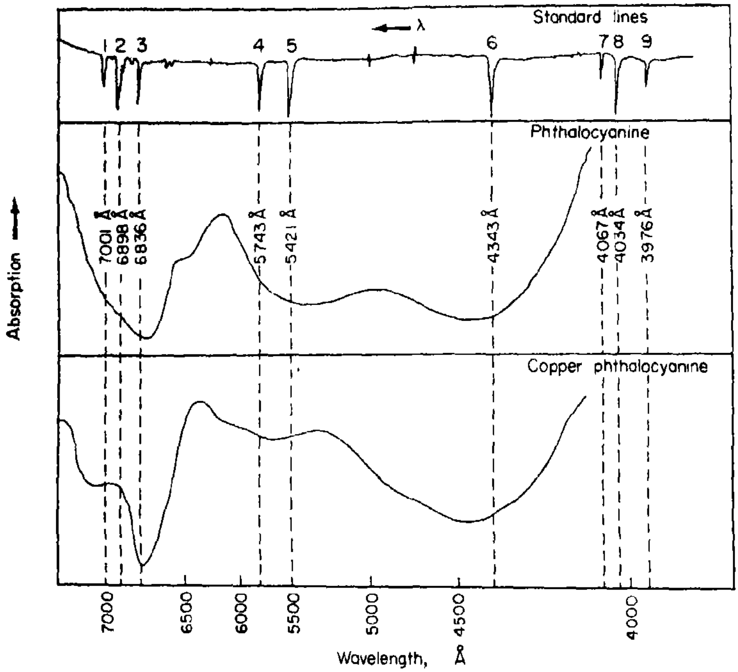

FIG. 2. Densitometer traces of the absorption spectra in Figure 1.

(b) *Evaporated films*

These were prepared by direct sublimation of a very small quantity of the purified material onto quartz discs. A Unicam S.P.500 absorption spectrophotometer was used to determine the absorption spectra at room temperature. The results obtained for metal-free, copper and platinum phthalocyanines are shown in Fig. 3.

(c) *Single crystals*

Thin flat crystalline ribbons of copper phthalocyanine were grown by entrainer-gas vacuum sublimation in a sealed silica tube in a furnace. At temperatures between 600°C and 700°C and pressures of about 10 cm of argon or nitrogen beautiful thin crystals of copper phthalocyanine in the (001) orientation were formed. Thicknesses ranged from about one tenth of a micron up to several microns and the crystals were blue when observed in transmission. Specimens of phthalocyanine were prepared in a similar manner and two good crystals of the platinum derivative were obtained with an apparatus which has been described previously.(16)

Single crystal absorption spectra were obtained with the Unicam S.P. 500 absorption spectrophotometer—the crystal being placed over a small hole in a piece of copper foil. Crystal thicknesses were measured in a high-powered optical projection microscope and the absorption coefficients were corrected for reflection losses. The liquid nitrogen Dewar flask which is shown in Fig. 4(a) was used to obtain the low temperature absorption spectrum of the copper derivative, and this was further investigated at higher resolution in the 4000 Å to 6000 Å range by using a Hilger D 187 wavelength spectrometer in conjunction with a quartz EMI 6255B photomultiplier and a Solartron D.C. AA900 amplifier. The results which have been obtained are illustrated in Figs. 5–8.

In addition to the measurements of absorption reported in (a)–(c) above, the spectral dependence of photoconductivity in the range 4000 Å to 10,000 Å was investigated for single crystals of copper phthalocyanine. Long flat crystalline needles, up to 3 cm in length, were obtained from the vapour phase. The crystal, which was mounted on a quartz disc and secured at each end with

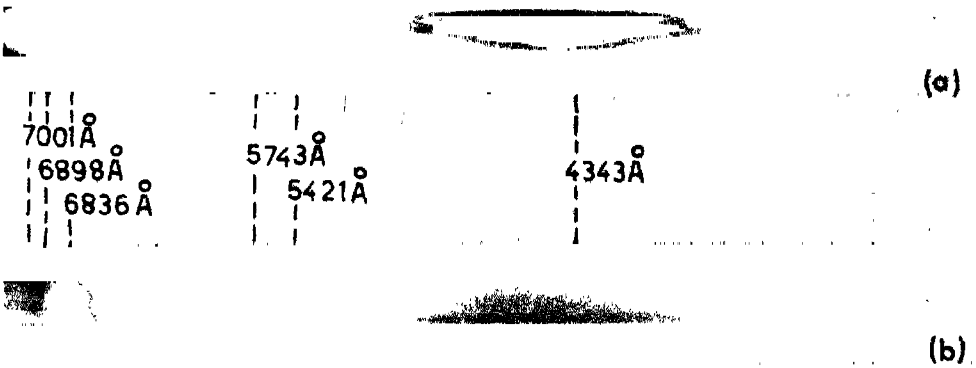

FIG. 1. Vapour absorption spectra of: (a) Metal-free phthalocyanine (at 605°C). (b) Copper phthalocyanine (at 640°C).

platinum terminals, was bathed with radiation from a Hilger D 222 monochromator and chopped light source, and the spectral response was observed with a Vibron 33C electrometer. For experiments at liquid nitrogen temperatures the Dewar flask shown in Fig. 4(b) was assembled.

The spectral response curve for the photocurrent in a single crystal of copper phthalocyanine surrounded by air at room temperature is given in Fig. 9. The curve obtained for a crystal in vacuum was identical but was considerably reduced in intensity, while at liquid nitrogen temperatures the photocurrent was only just detectable.

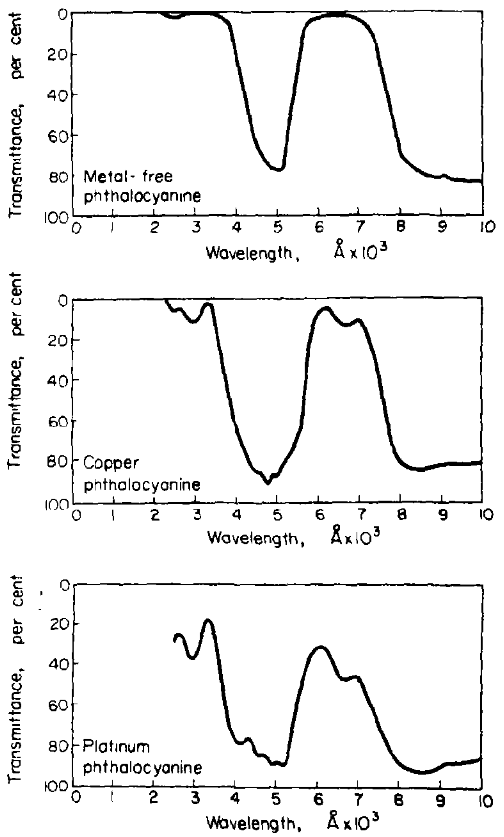

FIG. 3. Absorption spectra in the visible region for thin sublimed films of metal-free, copper, and platinum phthalocyanines.

INTERPRETATION OF THE RESULTS

A most reasonable explanation for the transmission absorption spectra of thin single crystals of phthalocyanine and its derivatives involves a consideration of the π-electrons in the conjugated double bond systems. If a crystal is illuminated, or if energy is supplied in some other manner, electrons are lifted to an excited level in the same molecule and the type of semiconductivity and photoconductivity observed is dependent on the mode of communication of the energy to the surrounding crystal environment. There is evidence that, in crystals composed of small molecules, the electron and resulting hole travel together in the form of an exciton and the theory of molecular crystals presented by Davydov(18) is then involved. For larger molecules the electron and hole which comprise the exciton may diffuse independently through the crystal and the wavelength dependences of the photoconductivity and optical absorption are then closely similar.

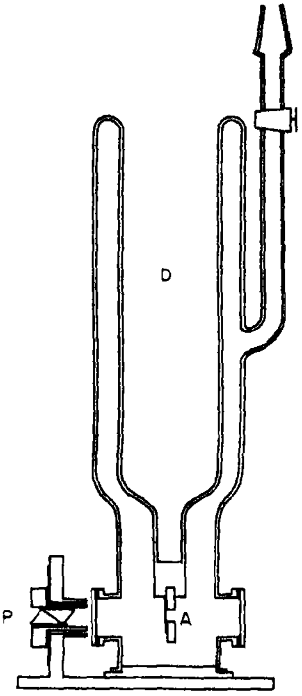

FIG. 4(a). Diagrammatic representation of the holder used for the measurement of the absorption spectra of single crystals of copper, platinum, and metal-free phthalocyanines. The crystal is held over the aperture *A*. *D* is a Dewar flask. The Nicol prism *P* may be used to polarize the light in any required direction.

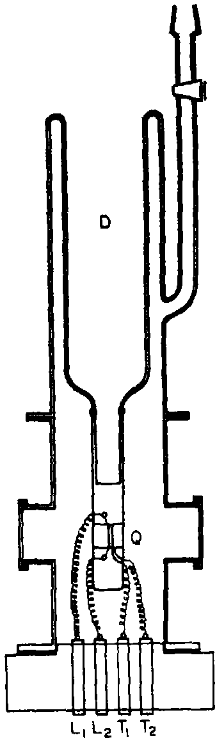

FIG. 4(b). Diagrammatic representation of the holder used for the measurement of the spectral response of photocurrent in single crystals of copper phthalocyanine. The crystal is secured on the quartz disc *Q* by platinum terminals. T_1 and T_2 are thermocouple leads, and L_1 and L_2 are leads to the crystal. *D* is a Dewar flask.

In the case of metal-free phthalocyanine we have a large conjugated molecule containing thirty-eight π-electrons. In the crystalline form the planar molecules lie at an angle of 44° to the *a–c* plane, alternate molecules pointing above and below the plane. Stereochemistry(19) suggests a possible overlap of $\pi(p_2)$ orbitals between one molecule and its neighbour along the *c*-axis, but BASU(20) calculates that the extreme values of the π-electron density occur in the vicinity of the nitrogen atoms, in the central part of the molecule. It is therefore probable that π-electron overlap from molecule to molecule will occur between adjacent stacks, and that energy levels of π-electrons in the molecule will be important in considering interpretations of single crystal absorption spectra.

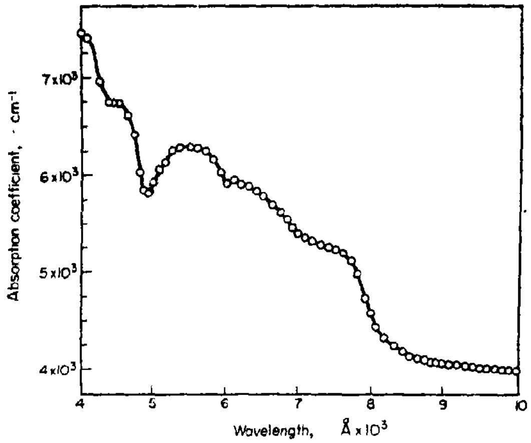

FIG. 5. Absorption spectra for single crystal of metal-free phthalocyanine. Unpolarized light was used.

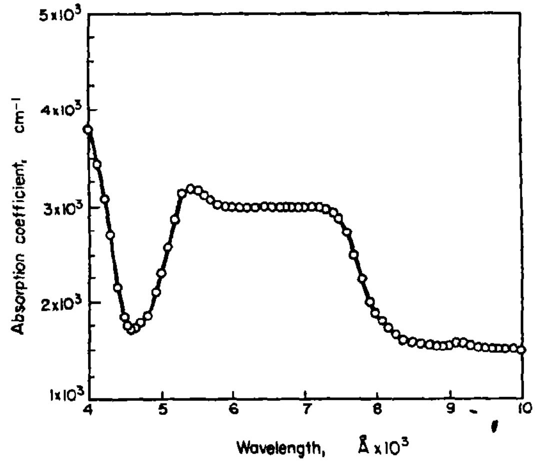

FIG. 6. Absorption spectra for single crystal of platinum phthalocyanine. Unpolarized light was used.

It is evident that, for copper phthalocyanine, the photoconductivity response curve closely follows the optical absorption spectrum for a single crystal. This also suggests that, for molecular crystals like copper phthalocyanine, the energy required to jump the π-electron across an intermolecular barrier is negligible compared with the energy required to lift the electron to the excited state. The quasi-continuous bands shown in the single crystal absorption spectra of metal-free and

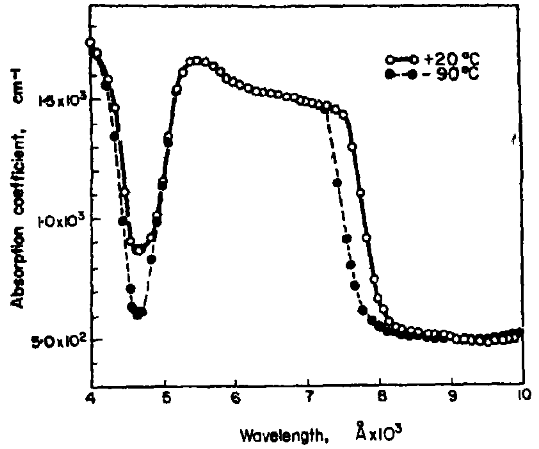

FIG. 7. Absorption spectra for single crystal of copper phthalocyanine. Unpolarized light was used.

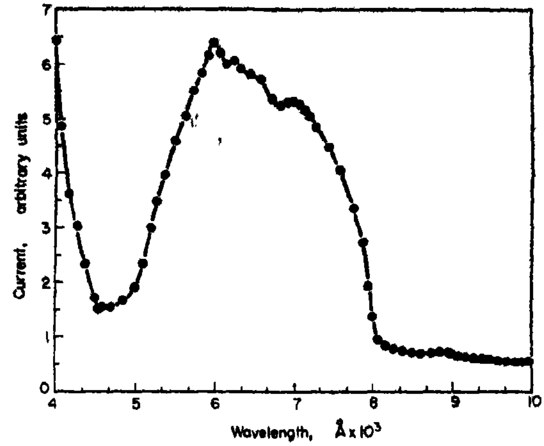

FIG. 9. The spectral dependence of photocurrent in the range 4000 Å to 1,000 Å for a single crystal of copper phthalocyanine at room temperature and in air.

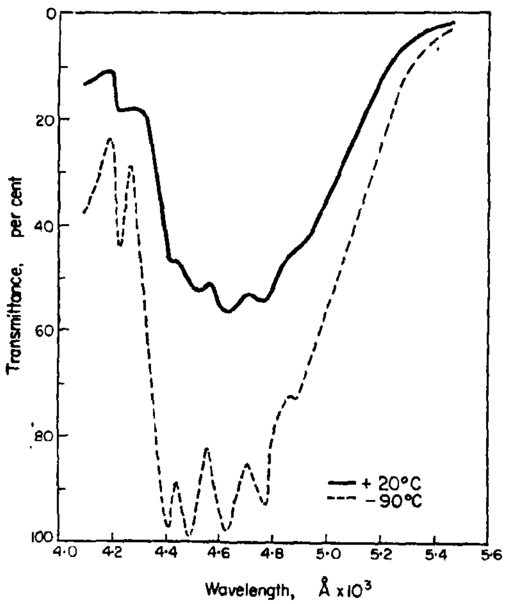

FIG. 8. Absorption spectrum for a single crystal of copper phthalocyanine in the region 4000 Å to 6000 Å. Phonon assisted transitions introduce subsidiary absorption peaks which become sharper as the temperature falls.

copper phthalocyanines can be correlated with sharper peaks observed in the transmission absorption spectra of vapour, solution(1), and sublimed films. If the spectral shifts arising from temperature dependence and the broadening due to crystal field interactions are accounted for there appears to be a one-to-one correspondence between peaks observed in the absorption spectra for molecules in different degrees of association. This makes possible the interpretation of the optical properties in terms of the simple band model. In particular it would appear that a doubly degenerate B_{1u}–E_g transition which has been predicted by BASU(20) in a molecular orbital calculation on phthalocyanine is present in the sublimed film spectrum for this compound. Moreover, this peak, at a wave number of 14720 cm^{-1} (1·82 eV), has a close parallel in the platinum and copper derivatives. There is little evidence of absorption at 21,620 cm^{-1} (2·68 eV), the other peak which was predicted by BASU(20) (Table 1), although there is a slight increase in intensity in this region for the vapour absorption spectrum. Calculations of optical activation energies have been made for copper, platinum and metal-free phthalocyanines on the basis of two arbitrary methods. In the first method (A) the central point on the linear part of the low energy absorption edge was taken as the characteristic wavelength for calculating the single crystal optical activation energy. In the second method (B) that point on the top of the band at which absorption begins to fall was used in the calculations. Such arbitrary methods only yield approximate results but the agreement with values obtained by the Russian authors[3,4] (Table 2) from work with sublimed films is encouraging.

Table 1

Transition	Degeneracy	Calculated Frequency	
		Uncorrected (cm^{-1})	Corrected (cm^{-1})
B_{2u}–E_g	Double	20,470 (89β)	21,620 (94β)
B_{1u}–E_g	Double	13,570 (59β)	14,720 (64β)

The fine structure which is revealed in Fig. 8 for the single crystal absorption spectrum of copper phthalocyanine is to be attributed to the stimulation of lattice vibrations. Energy absorbed from the incident radiation may be used in the energizing of electrons *and* in the creation of phonons. On other occasions the energy for electron excitation derives from both the external radiation and internal lattice vibrations. Phonon-assisted transitions have been observed by other workers in silver cyanamide and in certain of the azides.[21]

Table 2. Phthalocyanines: Optical activation energies

	Metal-free	Copper	Platinum
Single crystal (Method A)	1.55 ± 0·01 eV 2·61 ± 0·03 eV	1·58 ± 0·01 eV 2·81 ± 0·04 eV	1·57 ± 0·02 eV 2·81 ± 0·03 eV
Single crystal (Method B)	1·64 ± 0·03 eV 2·76 ± 0·06 eV	1·67 ± 0·03 eV 3·10 ± 0·15 eV	1·70 ± 0·05 eV 2·95 ± 0·07 eV
Sublimed films (Russian work[3,4])	1·64 eV —	1·64 eV —	— —

There is therefore distinct evidence that the simple band model offers a reasonably good description of the behaviour of crystalline copper, platinum, and metal-free phthalocyanines. The low values of absorption coefficient in the single crystal spectra give cause for some concern, though it is likely that indirect transitions are involved. The energy levels for π-electrons in the isolated molecule are sharp and well-defined, but interactions in the crystal smear out the levels into bands. For the three compounds investigated there appear to be two distinct strong transitions which can be identified in the crystal absorption spectra. The low energy absorption occurs always as a doublet, usually with one branch much more intense than the other.[14] From observations of solution absorption spectra[22] it has been suggested that, for phthalocyanine, two electronic transitions are present with origins at 14,290 cm^{-1} and 15,060 cm^{-1}. There is no evidence, however, that this explanation is more feasible than the suggestion that a 770 cm^{-1} vibrational interval is responsible. First-order calculations of factor group splittings have been made by LYONS[13] who, on the basis of molecular symmetry, suggests tentatively that the 14,290 and 15,060 cm^{-1} bands are components of a single transition which is terminated by a degenerate level. These conclusions are consistent with the prediction by BASU[20] of a doubly degenerate B_{1u}–E_g transition from the ground state to the first excited state of a π-electron on the phthalocyanine ring. The higher energy absorption does not correlate very well with a doubly degenerate B_{2u}–E_g transition at 21,620 cm^{-1} which is also predicted by Basu (Table 1).

The conduction and valence band ideas which apply to inorganic semiconductors must not be extrapolated to organic crystals without careful consideration. It is possible that, for the phthalocyanines,[1] the absorption of light might be accompanied by the formation of excitons which are capable of migrating in the crystal. These excitons, moreover, could be thermally dissociated by absorbing additional energy from the lattice and might disintegrate at impurity centres with the consequent formation of free charges. This would explain the increase of the photosensitivity of copper phthalocyanine crystals in the presence of oxygen and the close similarity of the photoconductive and absorption responses. Similar effects have been observed in anthracene.(23)

CONCLUSION

The transmission absorption spectra of some of the phthalocyanines have been investigated for molecules in different degrees of association. The close similarities which are obtained for vapour, sublimed film, and single crystal spectra suggest that the simple band model offers a reasonably good description of the features observed. In particular, the single crystal copper and platinum phthalocyanine spectra may be explained in terms of two strong π-electron transitions to a metastable excited state. The sharp energy levels of the free molecule evidently transform into broad quasi-continuous bands on crystallization.

Acknowledgements—I thank Dr. F. P. Bowden for his encouragement and Dr. A. D. Yoffe for helpful discussion.

REFERENCES

1. Fielding P. E. and Gutman F., *J. chem. Phys.* **26,** 411 (1957).
2. Vartanyan A. T., *Zh. fiz. khim.* 1028 (1956).
3. Vartanyan A. T. and Karpovich I. A., *Zh. fiz. khim.* 178 (1958).
4. Vartanyan A. T. and Karpovich I. A., *Zh. fiz. khim.* 274 (1958).
5. Terenin A. N., Putzeiko E. and Akimov T., *J. chem. Phys.* **26,** 716 (1957).
6. Tollin G., Kearns D. R. and Calvin M., *J. chem. Phys.* **32,** 1013 (1960).
7. Tollin G., Kearns D. R. and Calvin M., *J. chem. Phys.* **34,** 2022 (1961).
8. Lyons L. E., Walsh J. and White J. W., *J. chem. Soc.* 167 (1960).
9. Eley D. D., *Research* **12,** 293 (1959).
10. Bornmann J. A., *J. chem. Phys.* **27,** 604 (1957).
11. Many A., Harnik E. and Gerlich D., *J. chem. Phys.* **23,** 1733 (1955).
12. Neiman R. and Kivelson D., *J. chem. Phys.* **35,** 162 (1961).
13. Lyons L. E., *J. chem. Soc.* **1347** (1958).
14. Riggleman B. M. and Drickamer H. G., *J. chem, Phys.* **35,** 1343 (1961).
15. Bowden F. P. and Chadderton L. T., *Nature Lond.* **192,** 31 (1961).
16. Bowden F. P. and Chadderton L. T., *Proc. Roy. Soc.* **A269,** 143 (1962).
17. Eley D. D. and Parfitt G. D., *Trans. Faraday Soc.* **51,** 1529 (1955).
18. Davydov A. S., *Zh. eksp. teor. fiz. S.S.S.R.* **18,** 210 (1948).
19. Eley D. D., Parfitt G. O., Parry M. J. and Taysum D. H., *Trans. Faraday Soc.* **49,** 79 (1953).
20. Basu S., *Indian J. Phys.* **37,** 511 (1954).
21. Sole M. J., *Private communication.*
22. Anderson J. S., Bradbrook E. F., Cook A. H. and Linstead R. P. *J. chem. Soc.* 1152 (1938).
23. Carswell D., *J. chem. Phys.* **21,** 1890 (1953).

J. Phys. Chem. Solids Pergamon Press 1963. Vol. 24, pp. 759–769. Printed in Great Britain.

SOME EFFECTS OF CHARGE-COMPENSATING IONS ON CATION SITE PREFERENCES IN COMPLEX OXIDES*

M. ROBBINS,† S. LERNER‡ and E. BANKS

Department of Chemistry, Polytechnic Institute of Brooklyn

(*Received* 3 *October* 1962; *revised* 19 *December* 1962)

Abstract—The influence of anion charge compensation on the site preferences of Ni^{2+} and Co^{2+} in oxides such as spinels and magneto-plumbites is compared with that of cation charge compensation. By means of diffuse reflectance measurements on Co^{2+} and Ni^{2+}-substituted $BaAl_{12}O_{19}$ and $BaGa_{12}O_{19}$, it is concluded that the use of fluoride ion as a charge compensator confers additional stability to bivalent ions in tetrahedral sites. Magnetization data on $BaCo_xFe_{12-x}O_{19-x}F_x$ and $Cu_{1+x}Fe_{2-x}O_{2-x}F_x$ are in accord with this hypothesis. Spectroscopic investigation of Ni^{2+} and Co^{2+} substitution in the garnets $Y_3Al_5O_{12}$ and $Y_3Ga_5O_{12}$ do not show stabilization of the tetrahedral sites, but indicate that some of the bivalent ions appear to have entered yttrium (dodecahedral) sites.

INTRODUCTION

IN TWO previous publications,(1, 2) we have described the occurrence of strong tetrahedral site preference of bivalent cobalt, nickel and copper when these ions were substituted for iron(III) or aluminum in phases with the magnetoplumbite structure, using the replacement of oxide by fluoride as a charge-compensating mechanism.

The ideal formula corresponding to the magnetoplumbite structure is $M\,M'_{12}O_{19}$, where $M = Ba^{2+}, Pb^{2+}, Sr^{2+}$ and $M' = Fe^{3+}, Al^{3+}, Ga^{3+}$. All of the pure end members have been synthesized, at least for the barium compounds. In our previous work, we found that the substitution of bivalent ions could be carried out up to a maximum of about 2·5 g-at. of M^{2+} per formula unit, with an equivalent amount of fluoride added for charge compensation. By replacing part of the barium with lanthanum, bivalent transition metals could be introduced to a much lesser extent than allowed by the formula, at least in the aluminum compound, owing to the formation of the perovskite-like phase, $LaAlO_3$. In the case of the ferrite, complete lanthanum substitution has been achieved(3, 4) for example in $LaFe^{II}Fe^{III}_{11}O_{19}$. In the latter case, the saturation magnetization indicates that the ferrous ions preferentially occupy positions in the dominant magnetic sublattice, and it was suggested that the (12 *k*) sites are most probable inasmuch as they are on the dominant sublattice and lie closer to the barium sites than the other (octahedral) sites on the same sublattice.(3) No direct evidence was obtained that the ferrous ions actually do occupy sites of octahedral symmetry, as the use of spectroscopic techniques is exceedingly difficult in such highly-colored materials.

Our previous work(2) indicated that it was possible to displace Ni^{2+} in $BaAl_{12}O_{19}$ from tetrahedral into octahedral sites by providing a sufficient number of Zn^{2+} ions to fill all the tetrahedral sites, although a quantitative estimate was impossible in the absence of single crystals, which have not yet been successfully grown. Diffuse reflectance data on powdered samples, however, showed a definite displacement of Ni^{2+} by Zn^{2+}. On the other hand, similar experiments showed that Co^{2+} was almost completely bound to tetrahedral sites in the presence of fluoride ion charge compensation, regardless of the amount of zinc added to the preparations. This appears to contradict the previously known behavior of cobalt(II) in spinel type crystals, and was thought to be an effect of the fluoride ion compensation, which is presumably affecting the local symmetry around the cobalt ion.

---

* Abstracted in part from a Ph.D. dissertation and B.S. thesis, Polytechnic Institute of Brooklyn, June 1962. Partially supported by U.S. Signal Corp. Grant No. DA-SIG-36-039-61-G-6 and a grant from the General Chemical Division of Allied Chemical and Dye Corp.

† This work is in partial fulfilment of the requirements for the degree of Doctor of Philosophy in Chemistry from the Polytechnic Institute of Brooklyn.

‡ Undergraduate Research Participant under NSF Grant G-15814 for the Summer of 1961.

The ferrimagnetic behaviors of $BaFe_{12}O_{19}$ and $BaFe^{II}_2Fe^{III}_{16}O_{27}$, in which Cu^{2+}, Ni^{2+} and Co^{2+} were substituted, using charge-compensation by fluoride ions, were all explained by assuming that fluoride-compensated bivalent ion substitution led to tetrahedral site preference, while ions not requiring such compensation (as the Fe^{II} in $BaFe^{II}_2Fe_{16}O_{27}$) could occupy octahedral sites. This assumption can also explain the magnetic moment increase observed by FREI, SCHIEBER and SHTRIKMAN(5) in their pioneering work on the phase $BaFe^{II}_2Fe^{III}_{10}O_{17}F_2$.

This work has now been extended to investigate:

(1) The site preferences of Ni^{2+} and Co^{2+} in $BaGa_{12}O_{19}$, using cationic charge compensation (La^{3+} for Ba^{2+}) as compared to fluoride ion charge compensation.

(2) The site preference of Co^{2+} and Ni^{2+} in $BaFe_{12}O_{19}$ and Co^{2+} in $BaFe^{II}_2Fe_{16}O_{27}$ with F^- charge compensation.

(3) The site preference of Cu^{2+} in the spinel $CuFe_2O_4$.

(4) The site preferences of Ni^{2+} and Co^{2+} in $Y_3Al_5O_{12}$ and $Y_3Ga_5O_{12}$ with F^- charge compensation.

EXPERIMENTAL

The substituted $BaGa_{12}O_{19}$ materials were prepared by firing appropriate mixtures of BaF_2, $BaCO_3$, MO, La_2O_3 and Ga_2O_3 at 1350°C. Excess BaF_2 was used as a flux for the materials which were F^- charge compensated and $BaCl_2$ for materials which were La^{3+} charge compensated (no evidence of chloride in the oxides has been observed). The materials were fired in an anhydrous N_2 atmosphere and cooled at the rate of 15–20°C/hr.

Crystals of the substituted hexagonal ferrites were prepared by firing the appropriate mixtures (using the above mentioned starting materials, but substituting Fe_2O_3 for Ga_2O_3) with a 2·5:1 mole ratio of $NaFeO_2$ flux to ferrite. The mixtures were fired at 1350°C for 4 hr in an atmosphere of anhydrous O_2 and cooled at the rate of 5–10°C/hr. The crystals were separated from the cooled flux by leaching with hot concentrated hydrochloric acid.

Powder samples of $Cu_{1+x}Fe_{2-x}O_{4-x}F_x$ were prepared by prefiring mixtures of CuF_2, CuO, Fe_2O_3 at 800°C for 8 hr, regrinding and firing them at 1300°C for 4 hr and finally cooling at 20°C/hr. Crystals of these materials were prepared by firing the mixtures with the equimolar mixture of $Na_2CO_3 \cdot Fe_2O_3$ (1:1 mole ratio) in the same manner as previously described.

Substituted $Y_3Al_5O_{12}$ and $Y_3Ga_5O_{12}$ were prepared by firing the appropriate mixtures of Y_2O_3, Al_2O_3 or Ga_2O_3, NiO and NiF_2 or $CoCO_3$ and CoF_2 at 1300°C for 24 hr in an atmosphere of dried nitrogen gas, followed by quenching to room temperature.

Chemical analyses were obtained for the bivalent transition metals and for fluoride, on several representative samples of each type, but only for samples whose X-ray diffraction patterns showed only one phase to be present. In all but a few cases, the analyses showed the presence of equal numbers of bivalent (Co^{2+}, Ni^{2+} or Cu^{2+}) ions and of fluoride ions. This was taken to mean that the bivalent ions were substituting for tervalent ions, as Fe^{3+}, Al^{3+}, Ga^{3+} (or Y^{3+} in the garnets). The few exceptions occurred in the case of the $BaFe_{18}O_{27}$ phase. In some Co and Ni-substituted crystals of this structure, the Co^{2+} or Ni^{2+} content exceeded the fluorine content. Here it was assumed that the excess Co^{2+} or Ni^{2+} replaced some of the ferrous ions which are normally present in the structure, and thus did not require charge compensation. This assumption made it possible to account for the magnetic moment of such crystals, with the further assumption that the fluoride-compensated ions occupied tetrahedral sites.(2)

A further conclusion that may be drawn from the equivalence of bivalent transition metal and fluoride ion concentrations is the absence of significant amounts of quadrivalent ions such as

Ti^{4+} and Si^{4+} from these preparations. By compensating for the charge of the bivalent ions, these ions would have caused the ratio of bivalent ion to fluoride to be larger than unity, and also would have confused any attempts to understand the effect of fluoride-compensation on site preferences.

Optical spectra were obtained by the use of a Beckman D.U. Spectrophotometer with a diffuse reflectance attachment.

Magnetic moments were measured using the ponderometer method of RATHENAU and SNOEK.(6) Magnetic measurements were obtained between the Curie temperature and 93°K (liquid nitrogen).

Crystallographic data were obtained by means of a Norelco X-ray diffractometer, using CuK_α radiation for non-magnetic materials and CoK_α radiation for materials of high iron content.

RESULTS

Spectra

As previously shown, when Ni^{2+} and Co^{2+} were substituted for Al^{3+} in $BaAl_{12}O_{19}$ with F^- charge compensation, they exhibited a strong tetrahedral site preference. In order to investigate the effect of the fluoride ion on the site preferences of the bivalent ions, substituted $BaGa_{12}O_{19}$ samples were prepared using both cationic and fluoride charge compensation. The materials prepared were:

	Color	a_0	c_0
$Ba_{0\cdot 8}La_{0\cdot 2}Ni_{0\cdot 2}Ga_{11\cdot 8}O_{19}$	green–blue	5·836	23·08
$BaNi_{0\cdot 5}Ga_{11\cdot 5}O_{18\cdot 5}F_{0\cdot 5}$	deep blue	5·839	23·05
$Ba_{0\cdot 8}La_{0\cdot 2}Co_{0\cdot 2}Ga_{11\cdot 8}O_{19}$	pink	5·838	23·10
$BaCo_{0\cdot 5}Ga_{11\cdot 5}O_{18\cdot 5}F_{0\cdot 5}$	deep blue	5·841	23·05

The spectra of these materials are shown in Figs. 1 and 2. The absorption maxima are compared to the observed spectra of Ni^{2+} and Co^{2+} octahedral and tetrahedral coordinations.(7, 8, 9) The absorption peaks are listed and compared with published values in Tables 1 and 2.

From Fig. 1, it can be seen that in the La^{3+} compensated materials, the tetrahedral absorption peaks at 16,600 and 15,320 cm^{-1} are weak in intensity compared to the one at 25,800 cm^{-1}, which is due to octahedral Ni^{2+}. In the F^- compensated material the absorptions all seem to be of equal intensity. A comparison of these two indicates that the F^- compensated material has a larger amount of tetrahedral nickel, relative to octahedral nickel, than the La^{3+} compensated sample.

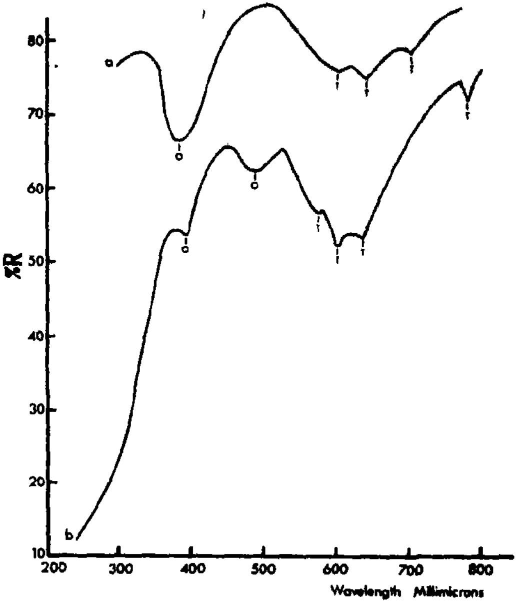

FIG. 1. Diffuse reflectance spectra of nickel-substituted $BaGa_{12}O_{19}$.
Curve (a) $Ba_{0\cdot 8}La_{0\cdot 2}Ni_{0\cdot 2}Ga_{11\cdot 8}O_{19}$;
Curve (b) $BaNi_{0\cdot 5}Ga_{11\cdot 5}O_{18\cdot 5}F_{0\cdot 5}$

In the Co^{2+} substituted materials this difference in tetrahedral site preference is more marked. In this case the spectra of the La^{3+} substituted material (pink in color) indicated that the Co^{2+} ion occupied the octahedral sites preferentially. In the case of the F^- substituted samples, the spectra show that the Co^{2+} ion exhibited a tetrahedral site preference.

After observing the increase in tetrahedral site preference due to fluoride charge compensation it was decided to attempt the same substitutions (Ni^{2+} or Co^{2+} with F^- compensation) in the garnets $Y_3Al_5O_{12}$ and $Y_3Ga_5O_{12}$. Materials with the following formulae were prepared:

	Color	a_0(Å)
1. $Y_3Al_{5-x}Ni_xO_{12-x}F_x$		
$x = 0$	white	12·020
0·2	brown	12·024
0·4	brown	12·026
0·6	brown	12·029
0·8	brown	12·032
0·9	brown (increasing intensity)	12·020
2. $Y_3Ga_{5-x}Ni_xO_{12-x}F_x$		
$x = 0$	white	12·275
0·2	brown	12·302
0·4	brown	13·384
3. $Y_3Al_{5-x}Co_xO_{12-x}F_x$		
$x = 0$	white	12·020
0·2	olive green	12·031
0·6	green	12·033

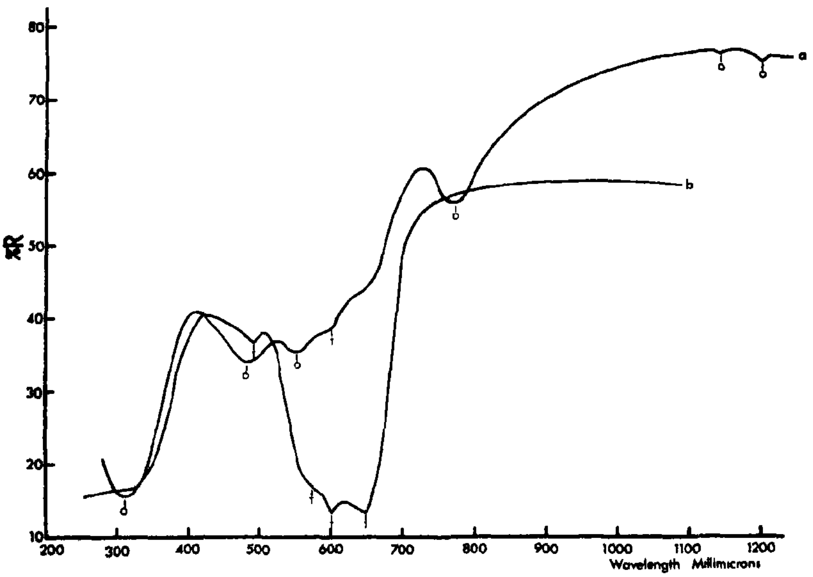

FIG. 2. Diffuse reflectance spectra of cobalt-substituted $BaGa_{12}O_{19}$. Curve (a) $Ba_{0.8}La_{0.2}Co_{0.2}Ga_{11.8}O_{19}$; Curve (b) $BaCo_{0.5}Ga_{11.5}O_{18.5}F_{0.5}$

The brown color of the Ni^{2+} substituted garnets was unexpected, as the color of tetrahedral nickel in oxides is usually blue and that of octahedral nickel is green. The green color of the Co^{2+} was also unusual, as the color of tetrahedral cobalt is normally blue and that of octahedral cobalt is pink.

The diffuse reflectance spectra of some of these materials can be seen in Figs. 3, 4 and 5. From the spectra in Fig. 3 (Ni^{2+} in YAG) absorptions indicative of both octahedral and tetrahedral Ni^{2+} (Table 3) can be identified. There still remain absorptions at ~ 29,000, 22,600 and 21,300 cm^{-1}

Table 1. Observed absorption maxima compared to literature values

Maxima cm^{-1}	Literature value	Site	Peak strength
	$Ba_{0.8}La_{0.2}Ni_{0.2}Ga_{11.8}O_{19}$		
26,320	25,800	Octahedral	VS
16,667	16,600	Tetrahedral	W
15,740	15,320	Tetrahedral	W
14,280	13,600	Tetrahedral	W
	$BaNi_{0.5}Ga_{11.5}O_{18.5}F_{0.5}$		
25,640	25,800	Octahedral	S
21,050	21,550	Octahedral	M
17,400	17,880	Tetrahedral	W
16,667	16,600	Tetrahedral	S
15,740	15,320	Tetrahedral	S
12,790	12,400	Tetrahedral	M

Table 2. Observed absorption maxima compared to literature values

Maxima cm^{-1}	Literature value	Site	Peak strength
	$Ba_{0.8}La_{0.2}Co_{0.2}Ga_{11.8}O_{19}$		
32,260	32,200	Octahedral	VS
20,500	20,500	Octahedral	S
18,180	18,650	Octahedral	S
16,810	16,778	Tetrahedral	W
13,000	13,750	Octahedral	S
8,772	8,756	Octahedral	VW
8,333	8,319	Octahedral	VW
	$BaCo_{0.5}Ga_{11.5}O_{18.5}F_{0.5}$		
20,410	20,964	Tetrahedral	M
17,240	17,241	Tetrahedral	VS
16,667	16,778	Tetrahedral	VS
15,500	16,129	Tetrahedral	VS

which cannot be ascribed either to tetrahedral or octahedral nickel. It was proposed that these absorptions were due to Ni^{2+} in the dodecahedral sites. This hypothesis was substantiated when PAPPALARDO *et al.*(9) observed the spectra of brown colored crystals of Ni^{2+} doped Y.G.G. (two phases were found, one green and one brown). The spectrum of the brown phase was obtained and the remainder of the transitions were calculated using a crystal field approach. The absorption peaks from Fig. 3 are compared to previously observed spectra in Table 3. The spectra of Ni^{2+} (with F^-) in YGG are shown in Fig. 4 with the absorptions listed and compared to literature values in Table 4. The peaks labeled "dodecahedral" are those which do not fit the known tetrahedral or octahedral peaks, but agree with the values suggested by Pappalardo *et al.*

Figure 5 shows the spectra of Co^{2+} and F^- substituted YGG. These showed one strong absorption peak at $\sim 27{,}500$ cm^{-1} (Table 5). This absorption is characteristic neither of tetrahedral nor octahedral cobalt. It was then decided that the strong absorption was due to Co^{2+} in the dodecahedral site as in the case with the Ni^{2+} substituted samples.

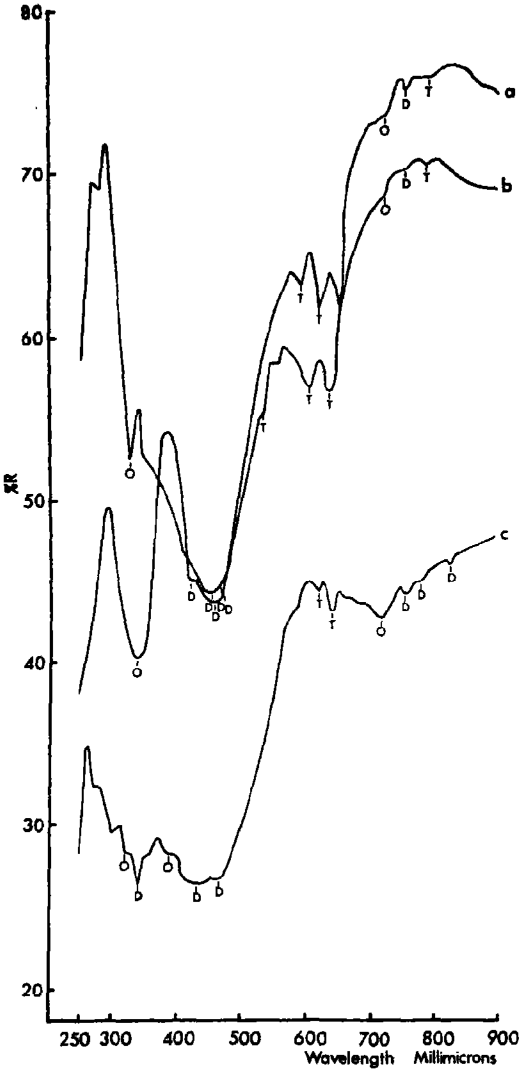

FIG. 3. Diffuse reflectance spectra of nickel-substituted $Y_3Al_5O_{12}$. Starting compositions prepared according to $Y_3Al_{5-x}Ni_xO_{12-x}F_x$.
Curve (a) $x = 0{\cdot}2$; Curve (b) $x = 0{\cdot}6$; Curve (c) $x = 0{\cdot}9$.

It can, therefore, be seen that fluoride compensation does not stabilize the tetrahedral sites in the garnets. However, more work must be done on these phases, including the preparation of materials where the bivalent transition metal ions are deliberately substituted for yttrium.

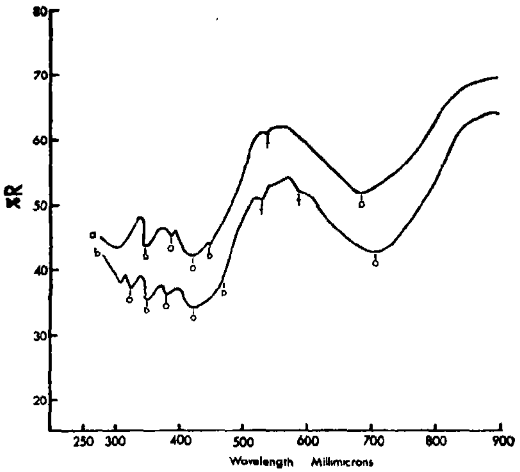

FIG. 4. Diffuse reflectance spectra of nickel-substituted $Y_3Ga_5O_{12}$, prepared according to $Y_3Ga_{5-x}Ni_xO_{12-x}F_x$. Curve (a) $x = 1{\cdot}0$; Curve (b) $x = 1{\cdot}5$.

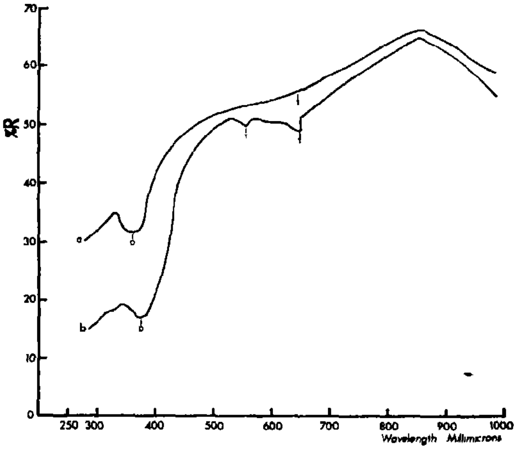

FIG. 5. Diffuse reflectance spectra of cobalt-substituted $Y_3Al_5O_{12}$, prepared according to $Y_3Al_{5-x}Ni_xO_{12-x}F_x$. Curve (a) $x = 0{\cdot}2$; Curve (b) $x = 0{\cdot}6$.

Ferrimagnetic materials

Mixtures intended to give the material, $BaFe_{12-x}Co_xO_{19-x}F_x$ (where $x = 0{\cdot}3, 0{\cdot}4, 0{\cdot}5, 1{\cdot}0$ $2{\cdot}0$) were fired with the Na_2CO_3–Fe_2O_3 flux and cooled slowly in order to grow crystals. X-ray analysis showed that in mixtures where $x < 0{\cdot}5$ the substituted magnetoplumbite was formed but where $x < 0{\cdot}5$ a substituted W-phase

Table 3. ***Absorption maxima compared to literature values of mixtures*** $Y_3Al_{5-x}Ni_xO_{12-x}F_x$

x	Maxima (cm^{-1})	Literature value	Site
0·2	29,400	28,800	Dodecahedral
	23,530	23,810	Octahedral
	22,200	22,600	Dodecahedral
	21,280	21,500	Dodecahedral
	18,500	18,500	Tetrahedral
	16,400	16,286	Tetrahedral
	15,630	15,643	Tetrahedral
	13,600	13,699	Octahedral
	13,000	13,160	Dodecahedral
	12,500	12,670	Tetrahedral
0·6	29,400	28,800	Dodecahedral
	23,530	23,810	Octahedral
	22,200	22,600	Dodecahedral
	16,667	16,280	Tetrahedral
	16,000	15,990	Tetrahedral
	15,100	15,186	Octahedral
	13,600	13,699	Octahedral
	13,000	13,160	Dodecahedral
	12,500	12,670	Tetrahedral
0·9	30,100	30,400	Octahedral
	29,000	28,800	Dodecahedral
	25,600	25,800	Octahedral
	22,740	22,600	Dodecahedral
	21,280	21,500	Dodecahedral
	16,000	15,990	Tetrahedral
	15,630	15,643	Tetrahedral
	14,000	13,927	Octahedral
	13,200	13,160	Dodecahedral
	12,000	12,200	Dodecahedral
	12,800	12,800	Dodecahedral

Table 4. *Absorption maxima compared to literature values of materials* $Y_3Ga_{5-x}Ni_xO_{12-x}F_x$

x	Maxima (cm^{-1})	Literature value	Site
1·0	32,800	32,700	Octahedral
	29,000	28,800	Dodecahedral
	25,600	25,000	Octahedral
	23,800	23,810	Octahedral
	22,500	22,600	Dodecahedral
	18,500	18,500	Tetrahedral
	14,500	14,556	Octahedral
1·5	32,260	32,700	Octahedral
	30,770	30,400	Octahedral
	28,600	28,000	Dodecahedral
	25,600	25,000	Octahedral
	23,800	23,810	Octahedral
	22,500	22,600	Dodecahedral
	18,600	11,500	Tetrahedral
	18,000	17,860	Tetrahedral
	14,400	14,556	Octahedral

Table 5. Absorption maxima of materials $Y_3Al_{5-x}Co_xO_{12-x}F_x$

x	Maxima (cm^{-1})	Literature value	Site
0·2	27,800	—	Dodecahedral?
0·6	27,400	—	Dodecahedral?
	17,700	17,640	Tetrahedral
	15,600	15,674	Tetrahedral

($BaFe^{II}_2Fe_{16}O_{27}$) was obtained. In the former materials the direction of easy magnetization was parallel to the *c*-axis; in the latter materials the easy direction was in the basal plane. When the mixture where $x = 0{\cdot}5$ was fired, a mixture of M and W phases occurred. Chemical analyses were obtained for the single phase materials; the formulae of the various phases can be found in Table 6. With the crystals mounted with the easy direction parallel to the field, measurements of magnetization were made, between liquid nitrogen and room temperature. The Curie temperatures were obtained by making magnetic measurements of the powders. These measurements are shown in Figs. 6 and 7 and the results are compared to values calculated on the basis of a tetrahedral site preference for Co^{2+}, in Table 6. The observed magnetizations are in good agreement with the calculated values, indicating that the Co^{2+} ion exhibited a strong tetrahedral site preference.

As a result of the optical and magnetic results reported herein and in our previous papers,[1, 2] it was decided that the fluoride ion was stabilizing the tetrahedral sites for bivalent ion substitution.

The marked effect of fluoride in enhancing the tetrahedral site preference of nickel and cobalt in spinel-type oxides (the bulk of the magnetoplumbite structure being the same as the spinel

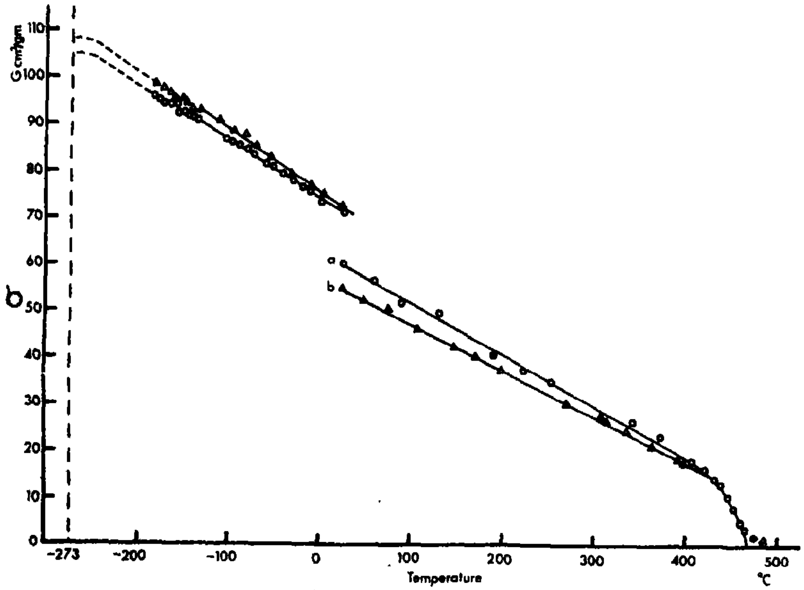

FIG. 6. Specific magnetization vs. temperature for $BaFe_{12-x}Co_xO_{19-x}F_x$. Curve (a) $x = 0{\cdot}3$; Curve (b) $x = 0{\cdot}4$.

Left portion of curves is for single crystals with easy direction parallel to field; right portion on powders for Curie point determination.

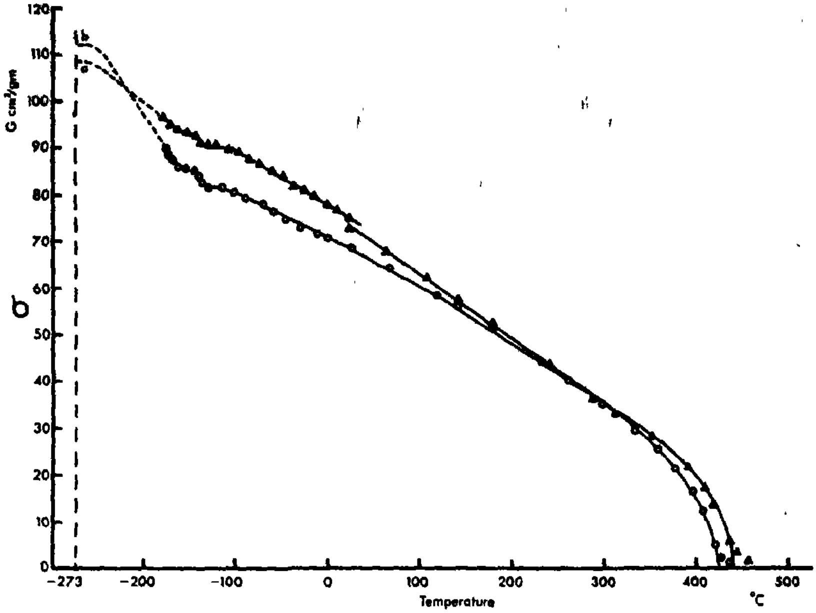

FIG. 7. Specific magnetization vs. temperature for $BaFe^{II}_2Fe_{16-x}Co_xO_{27-x}F_x$ (W-phase). Curve (a) $x = 1\cdot35$; Curve (b) $x = 2\cdot14$.

Table 6. Magnetic properties of Co^{2+} *and* F^- *substituted hexagonal oxides*

Mixt.	Composition			Calculated		Observed		Curie Temp. (°C)
		a_0	c_0	σ_0	M_B	σ_0	M_B	
	$BaFe_{12}O_{19}$			100	20			500
$x = 0\cdot3$	$BaFe_{11\cdot7}Co_{0\cdot3}O_{18\cdot7}F_{0\cdot3}$	5·883	23·13	103	20·6	105	21·0	470
0·4	$BaFe_{11\cdot6}Co_{0\cdot4}O_{18\cdot6}F_{0\cdot3}$	5·886	23·15	104	20·8	108·5	21·7	470
	$BaFe^{II}_2Fe_{16}O_{27}$			98	28			455
$x = 1\cdot0$	$BaFe^{II}_2Fe_{14\cdot7}Co_{1\cdot3}O_{23\cdot7}F_{1\cdot3}$	5·886	32·85	109	30·7	109	30·7	445
5·0	$BaFe^{II}_2Fe_{13\cdot9}Co_{2\cdot1}O_{24\cdot9}F_{2\cdot1}$	5·893	32·87	115	32·3	112	31·5	428

structure) appears to be qualitatively explicable on the basis of the electrostatic attraction of the fluoride ion and the bivalent cation. The latter (at a tervalent ion site) represents a localized negative charge, while the fluoride at an oxygen position has an excess positive charge. If one assumes that the majority of these ion pairs become associated during the crystallization of the phase, they might be expected to locate themselves near tetrahedrally-coordinated cation sites for the following reasons:

1. The cation–anion distances are shorter at tetrahedral sites than at octahedral sites.

2. At a tetrahedral site, the ionic bond strength(10) (z/ν) of the excess charge on the bivalent ion would be $\frac{1}{4}$ of an electronic charge per bond, whereas at an octahedral site, it would be $\frac{1}{6}$. The anion positions in spinels and the spinel blocks of the magnetoplumbite structure are all surrounded in the same way by tetrahedral and octahedral cations. In this discussion, it has been assumed that the bivalent ion in a tervalent ion site behaves like a single excess negative charge, which is compensated by the deficit of one negative charge at a neighboring fluoride ion in an oxygen position.

Explaining the failure of fluoride to stabilize these cations in the tetrahedral sites of the garnet structure requires much more experimental work before even such a crude explanation as the above discussion. The phases we have described here seem to be metastable at ordinary temperatures and there are numerous complications and unanswered questions. For example, all the garnet phases mentioned here seem to be single phases, with no X-ray evidence of a second phase, even though the samples had been formulated on the basis of nickel or cobalt substitution for aluminum or gallium. If the fluoride-compensated ions occupied yttrium sites, one would expect to find Y_2O_3, Al_2O_3, or $YAlO_3$ in the preparation, depending on whether the yttrium could enter the structure by partially occupying aluminum sites. No such phases have been detected. A second complication is that another garnet phase has been found when the nickel and fluoride concentrations are raised to higher levels (similarly for cobalt). These phases seem to contain a larger proportion of octahedral nickel (green) or tetrahedral cobalt (blue), than the lower concentration samples discussed here. A more thorough investigation is now underway.

One possible test of this proposal involves making the same substitutions in the spinels and measuring the magnetic moment. The material chosen for these experiments was the inverse spinel $CuFe_2O_4$. Since $CuFe_2O_4$ is inverse it has a magnetic moment of one Bohr magneton (30 G cm^3/gm).⁽¹¹⁾ Materials represented by the formula $Cu_{1+x}Fe_{2-x}O_{4-x}F_x$ were prepared where $x = 0\cdot4$, $0\cdot65$ and $1\cdot0$. If the proposed mechanism were correct, one would expect an increase in magnetic moment, due to the tetrahedral site preference of the Cu^{2+} ion, with fluoride compensation.

The magnetic moments of these materials were measured between the Curie temperature and liquid nitrogen and are shown in Fig. 8; the results are compared to predicted values in Table 7. There is very good agreement between observed magnetic moments and the values predicted on the basis of tetrahedral site preference for Cu^{2+}.

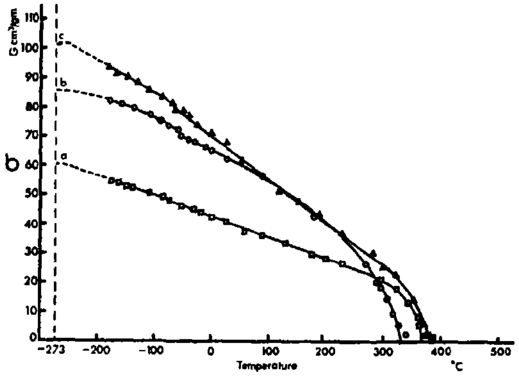

FIG. 8. Specific magnetization vs. temperature for $Cu_{1+x}Fe_{2-x}O_{4-x}F_x$.
Curve (a) $x = 0\cdot40$; Curve (b) $x = 0\cdot65$; Curve (c) $x = 1\cdot0$.

CONCLUSIONS

On the basis of optical spectra of bivalent cobalt and nickel in $BaAl_{12}O_{19}$ and $BaGa_{12}O_{19}$, as well as saturation magnetization of spinel phases and hexagonal phases containing spinel-like regions, it can be concluded that the use of fluoride ion to compensate for the lower charge of the bivalent ions enhances the stability of the tetrahedrally

Table 7. Magnetic measurements of Cu^{2+} *and* F^- *substituted* $CuFe_2O_4$

Composition	a_0(Å)	Calculated σ_0	Calculated M_B	Observed σ_0	Observed M_B	Curie Temp. (°C)
*$Cu_{1\cdot65}Fe_{1\cdot35}O_{3\cdot35}F_{0\cdot65}$	8·412	82·4	3·6	86	3·76	330
*Cu_2FeO_3F	8·418	113·5	5	103	4·54	385
$Cu_{1\cdot4}Fe_{1\cdot6}O_{3\cdot6}F_{0\cdot4}$	8·419	59·5	2·6	61	2·7	370

* Fired with $Na_2CO_3 \cdot Fe_2O_3$ flux, 1/1 mole ratio of flux to spinel, and cooled at 5°C/hr. to grow crystals.

coordinated sites in the structure. It appears that this stabilization is explicable on the basis of the more favorable situation for electrostatic interaction between the bivalent ions and the fluoride when the former are in tetrahedral sites than when they are in octahedral sites.

The situation in garnets is more complex, and does not seem to admit of such a simple explanation. Some absorption spectra of bivalent cobalt and nickel, presumably in sites of dodecahedral coordination, are reported, but no estimate of the concentrations at these sites is possible in the absence of theoretical or empirical evaluations of the oscillator strengths for these transitions. From the limited data presently available, it is not possible to ascertain whether the influence of fluoride ions is similar to that in the spinel-like phases.

REFERENCES

1. Banks E. and Robbins M., *Nature, Lond.* **191,** 1387–1388 (1961).
2. Banks E., Robbins M. and Tauber A., *J. phys. Soc. Japan* **17,** (Suppl. B-1), 196 (1962).
3. Aharoni A. and Schieber M., *Phys. Rev.* **123,** 807 (1961).
4. Morruzi V. L. and Shafer M. W., *J. Amer. ceram. Soc.* **43,** 367 (1960).
5. Frei E. H., Schieber M. and Shtrikman S., *Phys. Rev.* **118,** 657 (1960).
6. Rathenau G. N. and Snoek J. L., *Philips res. Rep.* **1,** 239 (1953).
7. Low W., *Phys. Rev.* **109,** 256 (1958).
8. Pappalardo R., Wood D. L. and Linares R. C. Jr., *J. chem. Phys.* **35,** 1460 (1961).
9. Pappalardo R., Wood D. L. and Linares R. C. Jr., *J. chem. Phys.* **35,** 2041 (1961).
10. Pauling L., *Nature of the Chemical Bond,* 3rd ed., p. 548. Cornell University Press, Ithaca (1960).
11. Smit J. and Wijn H. P. J., *Ferrites,* John Wiley, New York (1959).

J. Phys. Chem. Solids Pergamon Press 1963. Vol. 24, pp. 771–777. Printed in Great Britain.

AN INVESTIGATION OF THE ENERGY LEVELS IN ALKALINE EARTH HYDROXIDES BY INELASTIC SCATTERING OF SLOW NEUTRONS*

GEORGE SAFFORD,† VELKO BRAJOVIC‡ and HENRI BOUTIN

Brookhaven National Laboratory, Upton, New York

(*Received* 22 *October* 1962)

Abstract—The Brookhaven slow chopper was used to study the differential inelastic cross section for 5 meV incident neutrons scattered at 90° from polycrystalline samples of $Mg(OH)_2$ and $Ca(OH)_2$. In the energy interval covered (3–163 meV) corresponding to wave numbers of 25–1300 cm^{-1}, four distinct peaks were observed in both compounds at 293°K. They occur at 633 ± 30 cm^{-1} (*A*), 377 ± 8 cm^{-1} (*B*), 281 ± 9 cm^{-1} (*C*), 135 ± 10 cm^{-1} (*D*), respectively, in $Mg(OH)_2$ and at 540 ± 30 cm^{-1} (*A*), 316 ± 7 cm^{-1} (*B*), 247 ± 15 cm^{-1} (*C*), and 83 ± 7 cm^{-1} (*D*) in $Ca(OH)_2$. A spectrum taken at 103°K for $Mg(OH)_2$ shows that peaks *A*, *B*, and *C* appear unshifted in energy while *D* increases in intensity relative to *A*, *B*, and *C* and appears at 120 ± 7 cm^{-1}. The intensities of the individual peaks in $Mg(OH)_2$ are observed to vary with temperature in accordance with the temperature dependence of one-phonon differential scattering cross section, if $\Theta_{Debye} \gg T$ is assumed. The low energy peaks *D* in both $Mg(OH)_2$ and $Ca(OH)_2$ are too broad to be due to a single transition and have shapes characteristic of an acoustic branch of normal mode. It is shown that the observed spectrum cannot be explained by a highly localized rotational motion of the OH^- ions, as suggested by Hexter and some of the transitions observed are in qualitative agreement with an interpretation in terms of low-frequency lattice modes of the crystal.

INTRODUCTION

THERE has been much interest in both the crystal structures and the infrared spectra of $Mg(OH)_2$ and LiOH,(1–8) BERNAL and MEGAW(1) have pointed out that because of the layer-lattice type structure of these compounds (with tetragonal symmetry for LiOH and trigonal symmetry for $Ca(OH)_2$ and $Mg(OH)_2$) the axis of the OH^- is expected to be perpendicular to the layers with the hydrogen only bound to the oxygen of the hydroxyl group.

Infrared studies have shown that the OH stretching fundamental is bracketed in a nearly symmetric manner by a number of absorption side-bands (up to 16 for $Mg(OH)_2$) whose intensities are less than that of OH fundamental. In order to account for these sidebands, two alternative explanations have been proposed. HEXTER(9, 10) suggested that the sidebands arise from librational or hindered rotational motions of the hydroxide ions which combine with the internal stretching motion of the OH. This highly localized rotational model is based on HEXTER's claims(11) that the spectra of LiOH, $Mg(OH)_2$ and $Ca(OH)_2$ show "great and essential similarity", that in spite of differences in mass and charge of the cations there exist, "near coincidences" in the three spectra, and that the OH ions "undergo all their motions without knowledge of each other's presence". Using a calculation of STERN(12) which gives the energy levels of a hindered rotator in terms of a hindering potential of height V_0 and a rotational constant $B = \hbar^2/2I$. Hexter has attempted a quantitative fit of the sidebands observed in his spectra of these three compounds, in terms of a unique value of the potential V_0.

---

* Work performed under the auspices of the U.S. Atomic Energy Commission.

† Also at Columbia University, Department of Physics.

‡ Guest Scientist, Institute B. Kidric, Beograd, Yugoslavia.

An alternative explanation has been proposed by WICKERSHEIM(13) who assumes that low frequency crystalline lattice modes combine with the internal stretching motion of the OH ion to produce the observed side-bands. At present, this theory does not allow the energy positions, number and intensities of the sidebands to be quantitatively determined. The lack of knowledge of the force constants and of the coupling between the OH stretching fundamental and the low frequency modes prevent such calculations. However, recent infrared measurements on LiOH(14) support certain qualitative features of the lattice frequency model and raise questions as to the validity of the highly localized rotational model. Most of the sidebands of LiOD are observed to shift from those in LiOH in a manner to be expected if the modes that couple to the fundamental were only due to translational motions of the OH^- ions and not to rotational motions. Mixed crystals (LiOH, LiOD) infrared spectra(14) show that weak interactions between the OH ions are influencing the sidebands which contradicts one of the assumptions of the highly localized rotational motion. It is pointed out that the observed irregular variations of the sideband intensities are not consistent with Hexter's rotational model nor are Hexter's claims justified that $Ca(OH)_2$, $Mg(OH)_2$ and LiOH have the same number of sidebands and that "near coincidence" exists among sidebands of the three spectra.

In the present experiment the low energy spectra (900 to 10 cm^{-1}) of polycrystalline $Mg(OH)_2$ and $Ca(OH)_2$ have been investigated by inelastic neutron scattering at a sample temperature of $T = 293$°K. A spectrum was also taken at 113°K for $Mg(OH)_2$. The energy of the incident neutrons (5 meV) is small compared to the thermal energy of the sample and only those neutrons are observed which have gained energy in a single scattering event. Therefore, the observed lines represent transitions from levels populated by thermal excitation. As the neutron scattering cross section of hydrogen (20 barn free atom cross section) is large relative to those of Mg, Ca, O (3–5 barn) and is nearly all incoherent, the spectra observed should directly represent the low frequency motions of the individual OH^- ions that were observed in the infrared spectra coupled to the OH stretching fundamental.

EXPERIMENTAL APPARATUS

The present experiment utilized the cold-neutron facility at the Brookhaven National Laboratory research reactor, which has been described extensively in the literature.(15,16) The neutron beam incident on the scatterer is produced by filtration through 8 in. of refrigerated beryllium. No Bragg (elastic) scattering can occur for the low-energy (0·005 eV) incident neutrons, and the neutrons which are scattered at 90° by the sample are those which have gained energy upon being scattered once by the sample. The energy spectrum of the scattered neutrons was determined by chopper time-of-flight technique.

The polycrystalline $Mg(OH)_2$ and $Ca(OH)_2$ were contained in an aluminum sample holder which was shielded by cadmium so that neutrons could only be scattered off the samples. The effective thickness of the polycrystalline material was sufficiently thin ($\approx 1 \cdot 0$ mm) so that the probability of multiple scattering was negligible. The sample was cooled by a flow of cold nitrogen gas boiled off from liquid nitrogen through coils in contact with the sample holder. It was found that by regulation of the nitrogen flow the sample could be maintained at any desired temperature within 2°K between 294 and 90°K as determined by copper constantan thermocouples in contact with the sample.

RESULTS

The observed spectra (corrected for background, for chopper and counter efficiency, and for air-scattering along the 5 m flight-path) are shown in Fig. 1. The ordinate is the intensity of scattered neutrons in arbitrary units and the abscissa is a time-of-flight or velocity scale (on top of Fig. 1 an energy scale is also represented). The width of one channel is 32 μsec. A peak is observed at channel 154 which corresponds to neutrons elastically scattered from the sample and to the principal Bragg cut-off in Be. In addition, the peak that appears at channel 142 is due to a secondary cut-off in Be at 0·006 eV (and arises from elastic scattering in the sample). The transition energies are obtained by subtracting the incident neutron energy 0·005 eV from energies of the scattered neutrons that correspond to the peaks. Table 1 lists the peak energies with the assigned errors together with the separations from the OH^-

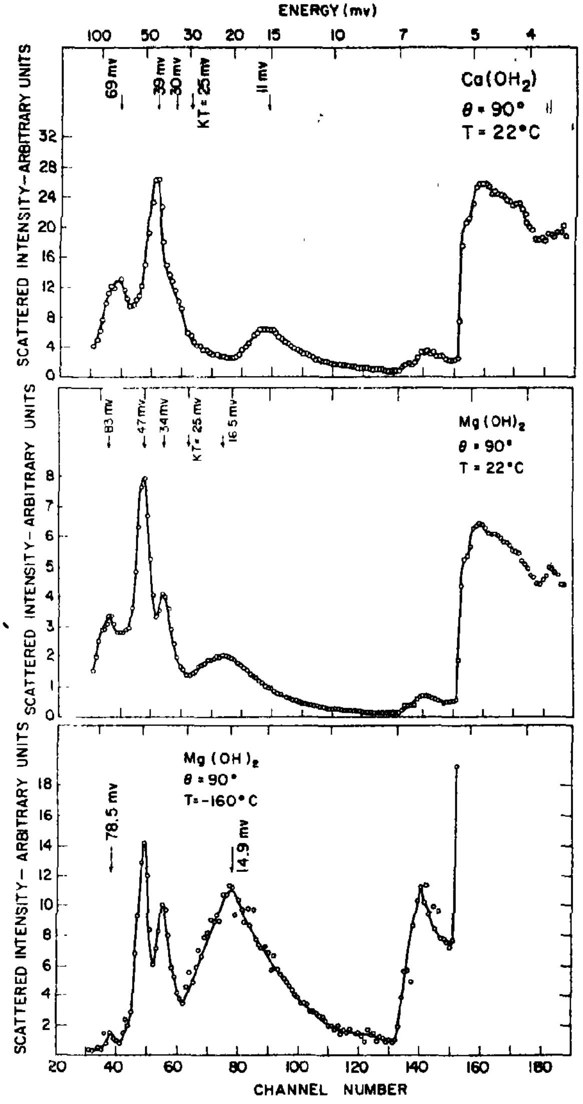

FIG. 1. Inelastic spectra of 5 meV incident neutrons scattered at 90° by polycrystalline sample of $Ca(OH)_2$ at 293°K and $Mg(OH)_2$ at 293 and 173°K. The lower scale in abscissa represents times-of-flight and the upper one is an energy scale. The peak at channel 153 corresponds to the incident neutrons and to the principal Bragg cut-off in the beryllium filter. Another peak around channel 142 is due to a secondary cut-off in Be at 0·006 eV.

Table 1. *Comparison of neutron spectra and infrared sideband spacing*

Compounds	Maxima observed in the neutron spectra (Energies in cm^{-1})			
	A	*B*	*C*	*D*
$Mg(OH)_2$				
$T = 294°K$	633 ± 30	377 ± 8	281 ± 9	135 ± 10
$T = 113°K$	618 ± 30	351 ± 7	267 ± 6	120 ± 7
$Ca(OH)_2$				
$T = 249°K$	540 ± 30	316 ± 7	247 ± 15	83 ± 7
	Infrared sideband separations* (Energies in cm^{-1})			
$Mg(OH)_2$				
$T = 294°K$				
Summation bands +	661 (2)	367 (1) 433	303 (2)	139 (3)
Difference bands −	664 (2)	329 (2) 402	282 (2)	116 (3)
Average of + and −	662·5 (2)	348 418	293 (2)	128 (3)
$Ca(OH)_2$				
$T = 294°K$				
Summation bands +	520	288 255	233	76
Difference bands −	571	350 311	280	121
Average of + and −	545	319 288	256	98·5

The number in parentheses refers to relative intensity of lines—(1) being the most intense line down to (4) being the least intense.

* Calculated from data given by HEXTER. The observed OH^- fundamentals are 3644 cm^{-1} for $Ca(OH)_2$ and 3634 cm^{-1} for $Mg(OH)_2$.

fundamental for each of the sum and difference sidebands of the infrared data and the average of these separations. The energies of the transitions observed in the present experiment are in reasonable agreement with the energy separations of the sidebands. Such an agreement is expected if the motions of the OH^- ions observed directly in this experiment are coupled to the OH^- fundamental and give rise to the sidebands observed in the infrared spectra.

The following features of the spectra obtained with present experiments are noted:

(a) The spectra of $Mg(OH)_2$ and $Ca(OH)_2$ each show four prominent maxima. Proceeding from high to low values of their energies these maxima will be referred to as *A*, *B*, *C*, *D*, respectively. Three of them *A*, *B*, *C* lie at energies above *kT* and a less intense *D* below *kT*.

(b) The energies of *A* and *B* are lower in $Ca(OH)_2$ than in $Mg(OH)_2$. However, peak *C* is closer to peak *B* in $Ca(OH)_2$ (being unresolved) than in $Mg(OH)_2$. Any shift in the energy of peak *C* is within experimental error. Thus, while these two compounds are isomorphous and the over-all features of the scattered neutron spectra are similar, the spectra do show a cation dependence.

(c) The low energy peaks *D* that appear in the vicinity of 120 to 88 cm^{-1} in the spectra of $Mg(OH)_2$ and $Ca(OH)_2$ are too broad in view of the experimental resolution to be due to a transition from a single level. These peaks show a low energy tailing and peak below *kT* in both cases. They have shapes characteristic of an acoustical branch of normal modes.

(d) The three higher energy peaks *A*, *B*, *C* all lie well above the thermal energy of the sample *kT*. They do not show systematic variations in their one-phonon transition probability with increasing energy at a given temperature, as would be expected if they were simply due to successive transitions between levels in a potential common to all four peaks. Indeed as one proceeds to higher energies in the spectra, the relative observed transition probabilities of the peaks vary in an irregular manner.

(e) A comparison of the individual peaks in the spectra of $Mg(OH)_2$ at $T = 296°K$ and $T = 133°K$ show that their intensities decrease as $[\exp(\hbar\omega/kT)-1]^{-1}$ which is the temperature dependence of the differential neutron scattering cross section for one-phonon absorption(17) where $\Theta \gg T$. This behavior is consistent with the observed invariance with temperature of the elastic peak.

(f) The spectrum of $Mg(OH)_2$ at $T = 133°K$ shows that the broad low energy peak has increased in intensity (relative to the three higher energy peaks) as compared with the spectrum at $T = 294°K$.

DISCUSSION

It is of interest to compare the results of the present investigation with the infrared data and its interpretation as given by Hexter. In Table 1 a comparison of the differences in wave number between the sidebands and the OH stretching fundamental, is given for the sum and difference bands together with the results of the present experiment. In order to correlate his observed sideband spacings with a model of hindered rotational motion for the OH ions, Hexter attempted to fit his data with a potential of the form $V = V_0\,(1-\cos 2\theta)^{10}$, a value of $V_0 = 350\ \mathrm{cm}^{-1}$ and a rotational constant $B = 20\ \mathrm{cm}^{-1}$ together with the calculations of Stern. In Table 2 are shown the sum and difference sidebands as given by Hexter's calculations. The designation n and m refers to Stern's specification of the angular momentum quantum numbers. W_1, W_2, W_3 are the successive levels above the ground state as taken from Fig. 1 in STERN's paper.(12) As the actual energy levels and their spacings are quite sensitive to the numerical choice of $2V_0/B$, only the ordering of these levels is considered in Table 2. In a similar manner the present authors attempted to fit the spectra by a calculation including all possible transitions between the different energy levels and dividing all such transitions of energies into four groups. The average energies for the different groups are found to be close to the values of the observed peaks. However, this procedure is not satisfactory for the following reasons:

Table 2. Sideband spectra and corresponding transitions between energy levels of a tortional oscillator with $V_0 = 350\ \mathrm{cm}^{-1}$ and $B = 20\ \mathrm{cm}^{-1}$. The values of the sum and difference lines are taken from Hexter. The OH stretching fundamental is between 3627–3634 cm^{-1}

Summation	Difference	Transition
3770	3494	$W_2 \rightleftharpoons W_1$
3820	3441	$W_3 \rightleftharpoons W_1$
3936	3430	$W_1 \rightleftharpoons W_0$

Ordering of the rotational levels which couple with the OH stretching fundamental

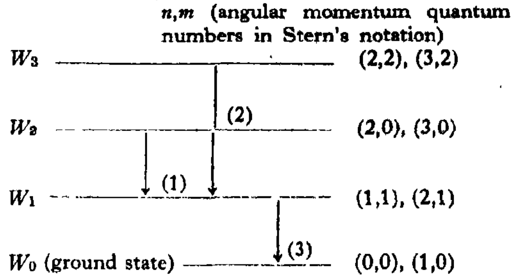

(a) If the peak A at 634 cm^{-1} in $Mg(OH)_2$ is to be explained by such a level scheme it is necessary to assume that at least the first five states above the ground state are strongly populated by the thermal excitation energy kT. Such behavior appears unreasonable; at $T = 294°K$, using a Boltzmann population factor with $kT = 200\ \mathrm{cm}^{-1}$, the relative population of the higher level would be too weak to account for the observed relative transition probability. In addition the energy of peak A must then be explained in terms of a transition from the highest level to the ground state and such a "multilevel transition" would be greatly reduced in intensity compared to transition between neighboring levels. This is due to the rapid decrease in magnitude of a multiphonon cross section for $\Theta \gg T$ as the number of phonons involved increases.(17) It is seen that the energy of peak A is also not explained by Hexter's scheme shown in Table 2.

(b) To explain the width and low energy tail of the observed peak D on the basis of this rotational model, it appears necessary to assume D contains not only one level, as it would if it is associated with the first sideband separation from the fundamental calculated by Hexter (Table 2), but a number of unresolved levels corresponding to small energy transitions. To account for both the number and the small energies of such transitions, it is necessary to assume that they arise from transitions between neighboring high-lying levels.* The intensity of D should then, on the basis of Boltzmann population factor, decrease more rapidly with decreasing temperature than the intensities of B or C which can be ascribed to transitions originating at lower levels than those for D. The reverse of this behavior is observed. The rotational levels represented in Table 2 show that both peak C [$W_3 \rightarrow W_1$ transition] and peak D [$W_2 \rightarrow W_1$ transition] would be expected to decrease in intensity relative to B [$W_1 \rightarrow W_0$ transition] as kT is decreased. Again the present spectra show the reverse behavior.†

CONCLUSION

It thus appears very difficult to explain in a consistent manner all the features of the observed spectra of $Mg(OH)_2$ and $Ca(OH)_2$ on the basis of a single rotational model level scheme of the type used by Hexter.

The lattice vibration model which has been discussed extensively for LiOH(13,14) attributes the observed infrared sidebands to low frequency lattice modes combining with internal stretching modes of OH^- ions. In the present experiment where transitions can be observed as low as 10 cm^{-1}, it is possible to observe directly such low frequency lattice modes. However, without a detailed knowledge of lattice force constants and the coupling interactions, a quantitative prediction of the energies and intensities of the low frequency fundamental modes and the coupled modes cannot be made. Nevertheless this model does predict the following qualitative features for the spectra.(14)

(a) Significant differences in both the fundamental frequencies and the combined frequencies would be caused by changes in the cell dimensions and the masses of the cations.

(b) Irregular spacings of the sidebands with respect to the OH fundamental, due to the independence of the low frequency fundamental modes.

(c) Irregularity of the relative intensities of the sidebands due to differences in both the coupling strength and the intensities of the low frequency modes.

(d) Strong symmetry of the sidebands about the OH fundamental, as a sum and difference sideband is expected for each low frequency mode that couples to the fundamental.

These features have been found in agreement with the infrared sidebands for these compounds and are consistent with the spectra of low energy transitions observed in the present experiment.

The shapes of the lowest energy peaks D in the neutron spectra of $Mg(OH)_2$ and $Ca(OH)_2$ is strongly suggestive of fundamental frequencies of an acoustic branch of normal modes whose propagation vectors vary over the Brillouin zone. The widths and the low energy tailing of peaks D are consistent with this interpretation. In addition, BUCHANAN *et al.*(14) have pointed out that the sideband closest to the OH fundamental in LiOH has a shape suggestive of an acoustic branch of normal modes combining with the OH fundamental.

The types of motions of cations and OH^- ions that correspond to fundamental unit cell lattice modes of $Ca(OH)_2$ and $Mg(OH)_2$ have been diagrammed in detail by HEXTER.(11) These modes can be roughly categorized as follows:

(a) Two modes (γ_3 and γ_2) involving translations in which two neighboring OH^- ions move in opposite directions.

(b) Two modes (γ_{14} and γ_5) involving cooperative rotations of the OH ions.

(c) Two modes (γ_{12} and γ_9) involving translations of the two OH ions and a cation.

However, a unique correlation of such individual low frequency motions, with any of the peaks A, B, or C in the neutron spectra would require a more quantitative knowledge of the frequencies and intensities to be expected for these modes which one does not have at the present time. A measurement of the dispersion curves using a single crystal and the "constant Q" method of Brockhouse would be of great help in that direction.

---

* This results from the fact that the spacing between consecutive levels of a hindered rotor decreases as the energies of the levels increase with regard to the ground state level.

† It should also be noted from Table 2 that in a scheme such as Hexter's the number of possible transitions exceed the number of lines observed in the present experiment.

Acknowledgement—The authors wish to thank Dr. H. Palevsky for permission to use his equipment.

REFERENCES

1. Bernal J. and Megaw H., *Proc. Roy. Soc.* **A151,** 384 (1935).
2. Tsou Ta, *C.R. Acad. Sci. Paris* **211,** 467 (1940).
3. Petch H., *Canad. J. Phys.* **35,** 983 (1957).
4. Petch H. and Megaw H., *J. opt. Soc. Amer.* **44,** 744 (1957).
5. Mara R. T. and Sutherland G. B. B. M., *J. opt. Soc. Amer.* **43,** 400 (1953).
6. Phillips B. E. and Busing W. R., *J. chem. Phys.* **61,** 502 (1957).
7. Busing W. R. and Levy H. A., *J. chem. Phys.* **26,** 563 (1957).
8. Busing W. R. and Morgan H. W., *J. chem. Phys.* **28,** 998 (1958).
9. Hexter R. M. and Dows D. A., *J. chem.. Phys* **25,** 504 (1956).
10. Hexter R. M., *J. opt. Soc. Amer.* **48,** 770 (1958).
11. Hexter R. M., *J. chem. Phys.* **34,** 941 (1961).
12. Stern T. E., *Proc. Roy. Soc.* **A130,** 551 (1930).
13. Wickersheim K. A., *J. chem. Phys.* **31,** 863 (1959).
14. Buchanan R. A., Kinsey E. I. and Caspers H. H., *J. chem. Phys.* **36,** 2665 (1962).
15. Carter R. Palevsky H. and Hughes D. J., *Phys. Rev.* **106,** 1168 (1957).
16. Eisenhauer C., Pelah I., Hughes D. J. and Palevsky H., *Phys. Rev.* **109,** 1046 (1958).
17. Kothari L. S. and Singwi K. S., *Solid State Physics* (edited by Seitz, F. and Turnbull D.) Vol. **8,** p. 109, Academic Press, New York (1959).

LETTERS TO THE EDITOR

X-ray induced particle size changes in thallous azide

(*Received* 28 *December* 1962)

IT HAS been previously reported that various inorganic azides decompose considerably under the influence of X-rays.(1) Some of the X-ray diffraction lines from CuK$_\alpha$ irradiated powder samples change both their position and their shape. In potassium azide type structures(2) (Fig. 1), the line shifts can be attributed to a lattice expansion in direction of the c-axis; the layers perpendicular to the c-axis remain comparatively unchanged. In order to determine the cause of the broadening, the (002) reflection of X-ray irradiated powder samples of thallous azide has been analyzed in terms of Fourier coefficients by WARREN's method.(3, 4) Corrections for instrumental broadening were performed by STOKES(5) method with a computer program by BOYKO and MOHN(6) after adjustments for continuous radiation induced line profile changes during the measurement. (Because of these continuous changes, the accuracy of the method was limited.) The change of the Fourier coefficients with irradiation time is shown in Fig. 2. The results indicate the line broadening (expressed by the deviation of the Fourier coefficients from unity) does not start at the onset of irradiation, but after about 2 hr. The Fourier coefficients then change linearly with the logarithm of the irradiation time between 2 and 30 hr. Within this interval they can be approximated by a family of straight lines:

$$F_n(t) = cn \log \frac{t}{t_0} + y_0 \qquad (1)$$

c —slope of $F_1(t)$
t_0 —abscissa for intersection point
y_0—ordinate of intersection point.

The solid lines in Fig. 2 are drawn to also satisfy the equation

$$F_n(t = \text{const}) = y_0 - \beta n \qquad (2)$$

β = constant.

For $y_0 = 1$, equation (2) becomes the expression derived by Warren for line broadening caused by small particles size. ($1/\beta$ being the average number of unit cells in columns parallel [001]). The deviation of y_0 from 1 is believed to be caused

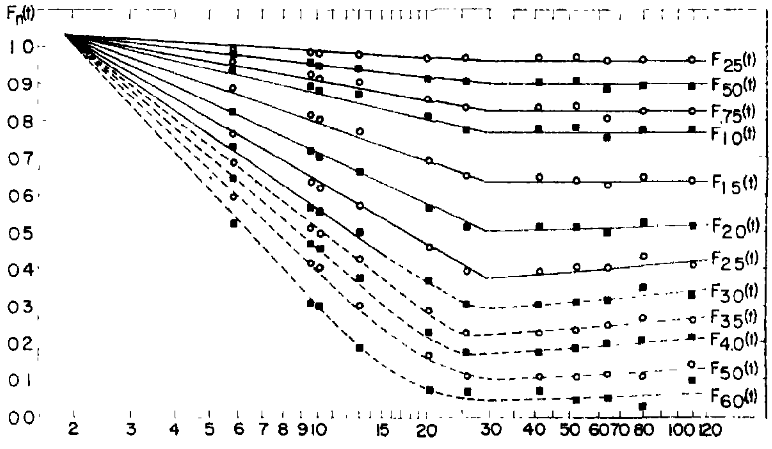

FIG. 2. Change of the Fourier coefficients F_n as function of the irradiation time t. (Irradiation source: Cu-target operated at 35 kV and 39 mA. TlN$_3$ sample on commercial Norelco X-ray wide angle goniometer. 20μ thick Ni–filter between X-ray source and sample.) Unity of parameter (n = 1) corresponds to 56·5 Å.

by experimental errors. From equations (1) and (2) the particle size can be calculated as

$$\bar{x}(t) = -\frac{\delta n}{y_0 - F_n} = \frac{\delta}{c\log(t/t_0)}$$

δ—constant, dependent on the Fourier interval chosen.

For our calculations the angle interval chosen was 1·6 degrees in 2θ corresponding to $1{\cdot}94 < l < 2{\cdot}06$. The particle sizes corresponding to Fig. 2 are shown in Fig. 3. It is likely that part of the line broadening, especially for lines related to other crystallographic directions, is due to crystal distortion. *Accurate* measurements of higher order reflections were not possible, but a brief comparison of the Fourier coefficients for (002) and (004) reflections indicate particle size changes to be the main cause of the line broadening.

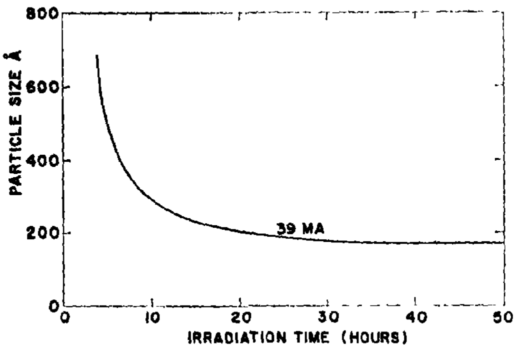

FIG. 3. Change of particle sizes as function of the irradiation time. (Corresponding to Fig. 2.)

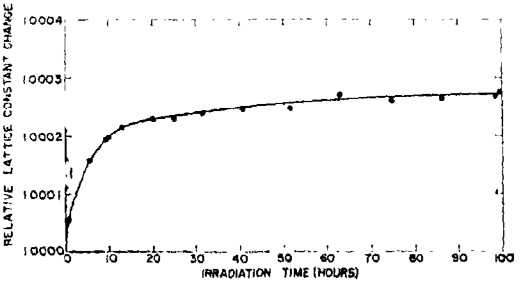

FIG. 4(a). Relative lattice constant change in [001] direction as function of the irradiation time.

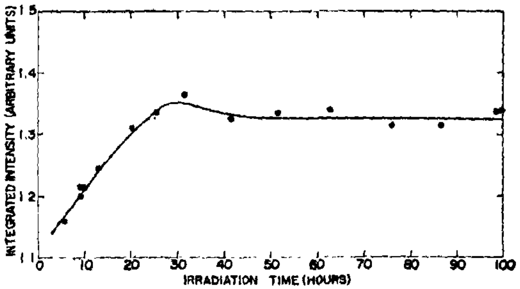

FIG. 4(b). Integrated intensity changes as function of the irradiation times.

Line shifts and line broadening are caused by different processes as can be seen by comparison of Fig. 2 and Fig. 4a. The rate of lattice constant change is highest in the beginning of irradiation when no appreciable line broadening occurs. Neither at 2 hr nor at 30 hr (as in case of the line broadening) is there a marked change in the course of the curve. Changes of the integrated intensities due to extinction probably correspond to those of the line broadening (Fig. 4b) although no statements about the integrated intensities during the first hours of irradiation can be made.

Acknowledgements—I wish to thank Dr. BOYKO for sending the computer program to me, our Computer Section, especially Mrs. B. O. CARROLL and Mr. H. SMITH for programming and extensive data handling, and Mr. H. ROSENWASSER for preparing the thallous azide powder.

Basic Research Group, BRIGITTE H. KRAUSE
U.S. Army Engineer Research
and Development Laboratories,
Fort Belvoir, Virginia

References

1. KRAUSE B. H., *Z. Kristallogr.* **115**, 413 (1961).
2. EVANS B. C., YOFFE A. D. and GRAY P., *Chem. Rev.* **59**, 515 (1959).
3. WARREN B. E. and AVERBACH B. L., *J. appl. Phys.* **21**, 595 (1950).
4. WARREN B. E. and AVERBACH B. L., *J. appl. Phys.* **23**, 497 (1952).
5. STOKES A. R., *Proc. phys. Soc., Lond.* **61**, 382 (1948).
6. BOYKO E. R. and MOHN G. J., private communication.
7. JAMES R. W., *The Optical Principles of the Diffraction of X-rays*, Bell, London (1950).

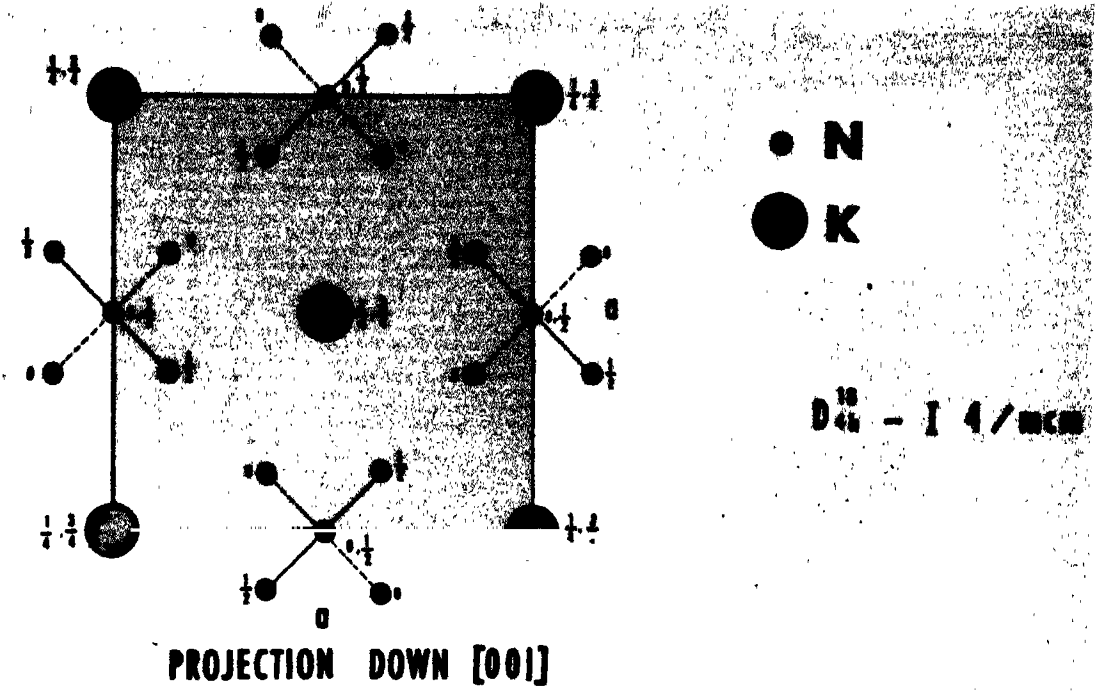

FIG. 1. KN_3—Structure; for TlN_3: a = 6·22 Å, c = 7·37 Å.

A simple model for the Curie temperature of a small ferromagnetic particle

(*Received* 12 *February* 1963)

THE molecular field theory[1] of ferromagnetism predicts that the bulk Curie temperature T_{cB} for a system of spins S is proportional to the exchange integral J times the number of neighbors Z_B (bulk exchange coordination number) participating in this exchange coupling, in accordance with the expression

$$T_{cB} = \frac{2JZ_BS(S+1)}{3k}, \tag{1}$$

where k is Boltzmann's constant. This formula applies to a macroscopic ferromagnet. When the number of surface atoms becomes an appreciable fraction of the total number of atoms and the particle enters the size range where superparamagnetism occurs, then the average exchange coordination number, Z_A, should arise from an average of the atoms' individual coordination numbers, Z_i. The ratio of the Curie temperature, T_c for a small particle to that of an infinitely large particle, T_{cB}, becomes

$$\frac{T_c}{T_{cB}} = \frac{Z_A}{Z_B} = \frac{\sum N_iZ_i}{NZ_B} \tag{2}$$

where N_i is the number of atoms with exchange coordination number Z_i, and N is the total number of atoms,

$$N = \sum N_i. \tag{3}$$

The right-hand side of equation (2) may be determined explicitly for particular lattice structures and particle shapes. In this Letter we will consider only cubic lattices which have the shape of rectangular parallelopipeds. The parameters i, j, and k are used to denote the number of unit cells in the three Cartesian coordinate directions, x, y, and z and the lattice faces are considered to be perpendicular to the x, y, and z-axes. In addition to T_c/T_{cB}, explicit expressions were obtained for the ratio of the number of surface atoms N_s to the total number of atoms N, and these are shown in Table 1. They are valid for all positive integers, i, j, and k.

The reduced Curie temperature, T_c/T_{cB}, is shown in Fig. 1 as a function of the number of atoms in the cluster. A cubic cluster that is approximately 10 Å on a side, contains about 100 atoms (e.g. in f.c.c. nickel there are 0·092 atoms/Å^3). Figure 1 shows that the reduced Curie temperature is not greatly dependent on the lattice type, and cubic clusters with $i = j$ do not greatly depend on the k/j ratio when this varies from 1/10 to 10. Several investigators[2-6] have reported decreases in the Curie temperature for small nickel particles, and a few of their experimental data are included on Fig. 1. Some other

Table 1. *Formulae for* (N_s/N) *and* (T_c/T_{cB}). *The numerators in the second column contain* N_s *and the denominators contain* N *explicitly*

Lattice	$\frac{N_s}{N}$	$\frac{T_c}{T/_{cB}}$
Simple cubic	$\frac{2(ij+jk+ki+1)}{(i+1)(j+1)(k+1)}$	$\frac{ijk+(2/3)(ij+jk+ki)+(1/3)(i+j+k)}{(i+1)(j+1)(k+1)}$
Body-centered cubic	$\frac{2[ij+jk+ki+1]}{ijk+(i+1)(j+1)(k+1)}$	$\frac{2ijk}{ijk+(i+1)(j+1)(k+1)}$
Face-centered cubic	$\frac{4(ij+jk+ki)+2}{4ijk+2(ij+jk+ki)+i+j+k+1}$	$\frac{4ijk+(2/3)(ij+jk+ki)}{4ijk+2(ij+jk+ki)+i+j+k+1}$

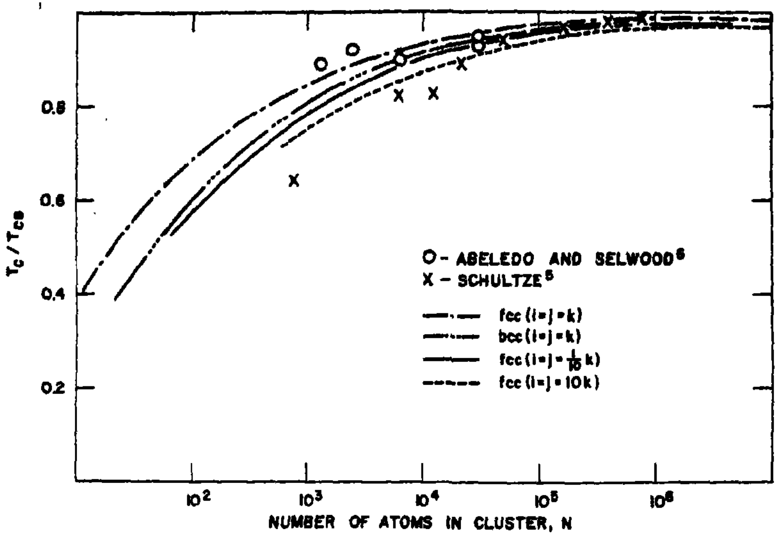

FIG. 1. Variation of reduced Curie temperature T_c/T_{cB} with particle size N for several types and shapes of lattices. The references gave particle diameters D, and these were converted to the number of particles N by using the approximation $N = 0{\cdot}05D^3$, where D is in Ångstrom units.

systems do not exhibit the expected change in Curie temperature with particle size.(7, 8, 9)

The equations in Table 1 may prove useful for correlations with experimental data, although accurate quantum mechanical calculations are expected to produce a much more complex dependence of T_c/T_{cB} on the particle dimensions.

Gulf Research and
Development Company
Pittsburgh 30, *Pa.*

CHARLES P. POOLE, Jr.

References

1. KITTEL C., *Introduction to Solid State Physics*, John Wiley, New York (1956).
2. SELWOOD P. W., ADLER S. and PHILLIPS T. R., *J. Amer. chem. Soc.* **77**, 1462 (1955).
3. KNELLER E., *Z. Phys.* **152**, 574 (1958).
4. RYAN F. M., PUGH E. W. and SMOLUCHOWSKI R., *Phys. Rev.* **116**, 1106 (1959).
5. SCHULTZE D., *Naturwissenschaften* **47**, 128 (1960).
6. ABELEDO C. R. and SELWOOD P. W., *J. appl. Phys.* **32**, 229S (1961).
7. KNAPPWOST A., *Naturwissenschaften* **46**, 65 (1959) and *Z. Elektrochem.* **63**, 965 (1959).
8. NEUGEBAUER C. A., *J. appl. Phys.* **31**, 152S (1960).
9. LUBORSKY F. E. and LAWRENCE P. E., *J. appl. Phys.* **32**, 231S (1961).

Note added in proof: RICHARDSON J. T. and MILLIGAN W. O., *Phys. Rev.* **102**, 1289 (1956), make use of a model similar to the one discussed in this note.

Scattering of cold neutrons in beryllium oxide

(*Received* 16 *October* 1962)

RECENTLY BEGUM *et al.*(1) have experimentally measured the scattering cross section of cold neutrons in the case of polycrystalline beryllium oxide. They used a filtered beam of average wavelength 5·55 Å and the temperature of BeO was varied from 140 to 1100°K. Their experimental results are given by open circles in Fig. 1. These authors have explained their results theoretically by using the formula of "incoherent approximation" as given by KOTHARI and SINGWI(2) (*vide* equation 5.1b) namely, for $\Theta_{D/T} \gg 1$ and $E_1 \ll k_0T$

$$\sigma_{01} = 3\Gamma(7/2)(S+s)\,\frac{m_0}{M}\left(\frac{T}{\Theta_D}\right)^3\left(\frac{k_0T}{E_1}\right)^{1/2} \tag{1}$$

where the symbols have the same meaning as in Ref. 2. By taking a Debye temperature of 1220°K

Begum *et al.* have been able to fit the calculated values with the experimental values in the range 140–325°K. They have calculated only the one phonon cross section.

We, however, find that equation (1) is not valid for cold neutrons for the reason given below. The coherent inelastic scattering cross section for a polycrystalline solid is given in the Debye approximation by (*vide* equation 4.26 of Ref. 2)

$$\sigma_{10} = \sum_{\tau} \frac{S\hbar^2 e^{-2W}}{16\pi\tau M k_1^2}$$

$$\times \int_0^{q_0} \frac{[4\pi^2\tau^2\lambda + 2\pi\tau q\lambda^2 + \frac{1}{3}q^2\lambda^3]_{\lambda_1}^{\lambda_2}}{(\exp[\hbar c q/K_0 T] - 1)} \cdot \frac{q\,\mathrm{d}q}{c\hbar} \tag{2}$$

To arrive at equation (1) it was assumed that the energy of the incident neutron is sufficiently high so that the number of τ-planes is large enough to justify the replacement of summation over τ by an integration (equation 3.13 of Ref. 2). However, for cold neutrons this is not true. We have in the present calculation taken the more rigorous formula namely equation (2) and calculated for neutron wavelengths $\lambda = 5$, 5·5 and 6 Å, the one phonon contribution to scattering by summing over all the reciprocal vectors as allowed by the usual energy and momentum conservation conditions. A simple Debye model has been assumed and the value of Θ_D is chosen as 1200°K as given by the specific heat data. The value of M in equation (2) was taken as 12·5 a.m.u. which is the average mass of beryllium and oxygen nuclei. This average mass was used by Bhandari[(2)] for his calculation of coherent cross section in both cold and thermal range with remarkable success. The choice of average mass was, however, made without theoretical justification. Recently Sharma and Khubchandani[(4)] have considered coherent scattering from a polyatomic cell and shown that the use of average mass for M is fully justified. Four temperatures of BeO were considered, namely 100, 200, 300 and 400°K and the results are given in Table 1.

As the temperature of the crystal is increased, the neutron may exchange more than one phonon with the lattice. Therefore we found it proper to calculate two phonon cross section for temperatures of 300 and 400°K. We find that the two phonon cross section is not negligible at these temperatures.

Table 1. *Calculated coherent one phonon cross sections* (barn) *for cold neutrons in beryllium oxide*

	Temp. of BeO (°K)			
	100	200	300	400
Wavelength of incident neutron (Å)				
$\lambda = 5$	0·013436	0·1218	0·3509	0·6783
$\lambda = 5·5$	0·013425	0·1259	0·3984	0·7229
			(0·1123)	(0·3042)
$\lambda = 6$	0·01356	0·1328	0·4104	0·7856

Quantities in brackets represent contribution of 2-phonon processes which are to be added to the single phonon values to obtain total cross section.

Kothari and Singwi[(5)] have obtained an expression for l phonon exchange in the incoherent approximation using the Debye model. Their expression is given by

$$\sigma_l = \frac{S+s}{2k_1^2 l!}\left(\frac{3}{2M}\right)^l \prod_{j=1}^{l} \int_{-1}^{+1} q_j \left(\coth\frac{q_j}{2T} - 1\right) \mathrm{d}q;$$

$$\times \int_{k_0-k_1}^{k_0+k_1} t^{2l+1} \exp(-6Ft^2/M)\,\mathrm{d}t \tag{3}$$

By putting $l = 2$ in the above expression and on simplification one obtains

$$\sigma_2(E) = \frac{9SM\hbar^4}{512 k_1^2 k_0^6 \Theta_D^6 \alpha^3}$$

$$\times \int_{\max(0, E_1 - 2k_0\Theta_D)}^{E_1 + 8k_0\Theta_D} \left[\left\{1 + \frac{\alpha}{M}(k_1-k_2)^2 + \frac{\alpha^2}{2M^2}\right.\right.$$

$$\left. \times (k_1-k_2)^4 \right\} \exp[-\alpha/M(k_1-k_2)^2]$$

$$- \left\{1 + \frac{\alpha}{M}(k_1+k_2)^2 + \frac{\alpha^2}{2M^2}(k_1+k_2)^4\right\} \tag{4}$$

$$\left. \times \exp[-\alpha/M(k_1+k_2)^2] \right]$$

$$\times \int_{0}^{2k_0\Theta_D-|x|} \left\{\coth\left(\frac{x+\nu}{4k_0T}\right)-1\right\}$$

$$\times \left\{\coth\left(\frac{x-\nu}{4k_0T}\right)-1\right\}(x^2-\nu^2)\,\mathrm{d}\nu\mathrm{d}E_2$$

where

$$x = E_2-E_1 = \frac{\hbar^2}{2m_0}(k_2^2-k_1^2)$$

The integration over ν was easily performed by expanding the coth terms in a power series. The choice of a proper value for S was, however, open to question. In the case of beryllium and oxygen the values of S are 7·54 and 4·24 barn respectively. On the other hand, the total cross sections for thermal neutrons in the range 0·1 to 1 eV are 6·1 and 3·7 barn respectively.(7) As such we have chosen S for BeO as $\approx$ 11 barn against a value of thermal cross section of 9·8 barn. This small uncertainty in S will not contribute appreciable error in the total coherent cross section because contribution of two phonon process is itself not more than 20 per cent of total cross section.

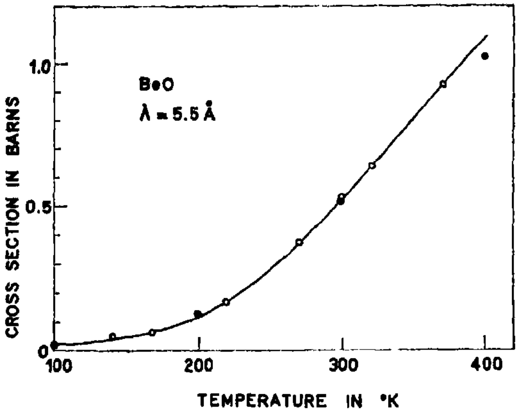

FIG. 1. Comparison of theoretical and experimental values for total cross section of cold neutrons of wavelength λ = 5·5 Å for BeO at different temperatures. The experimental points are given by open circles, while the calculated points by filled circles.

The calculated values are shown in Table 1. The graph in Fig. 1 shows the calculated values in comparison with the experimental results for λ = 5·5 Å neutrons.

Acknowledgements—We are thankful to Dr. R. RAMANNA for his interest in the above work and helpful discussions.

Atomic Energy
Establishment
Trombay,
Bombay, India.

P. G. KHUBCHANDANI
S. SANATANI

References

1. BEGUM R. J., *et al.*, to appear in *J. Phys. Chem. Solids.*
2. KOTHARI L. S. and SINGWI K. S., *Solid State Physics* Vol. 8 (edited by SEITZ F. and TURNBULL D.) p. 109. Academic Press, New York (1959).
3. BHANDARI R. C., Ph.D. Thesis, University of Rajputana (1958).
4. SHARMA R. R. and KHUBCHANDANI P. G., M.Sc. Thesis (SHARMA), University of Bombay (1962).
5. KOTHARI L. S. and SINGWI K. S., *J. Nucl. Energy* **5**, 342 (1957).
6. KOTHARI L. S. and SINGWI K. S., *Proceedings of the 2nd. Geneva Conference on the Peaceful Uses of Atomic Energy* (1958).
7. HUGHES D. J., *Neutron Cross Sections* BNL–325 (1955).

NOTICE

THE Institute of Physics and The Physical Society on behalf of the International Union of Pure and Applied Physics, and the British National Committee for Physics is arranging an International Conference on Magnetism, which will be held at the University of Nottingham on 7–11 September, 1964. The Conference will follow the main lines of earlier conferences at Grenoble and Kyoto and will deal with all fundamental aspects of the magnetism of solids. It is not proposed to arrange for the discussion of the applications of magnetic materials. The main sessions so far proposed will include:

- Theories of magnetism
- Crystal field effects
- Mutual interaction between magnetic carriers (ferromagnetic and anti-ferromagnetic)
- Metals and alloys
- Magnetic resonance and relaxation processes
- Domain structure and magnetization processes
- Magnetic applications of neutron diffraction

It is hoped that each main session will be introduced with an invited review paper. Other sessions to be run in parallel will be arranged. Accommodation will be provided in Halls of Residence.

Registration is necessary. Attendance will be limited and a selection may have to be made by the Organizing Committee. Further information regarding the Conference may be obtained from the *Deputy Secretary, The Institute of Physics and The Physical Society*, 47 *Belgrave Square, London, S.W.*1.

ERRATUM

K. A. GSCHNEIDNER, JR., R. O. ELLIOTT and R. R. MCDONALD: Effects of alloying additions on the $\gamma \rightleftharpoons \alpha$ transformation of cerium —Part I. Pure cerium. *J. Phys. Chem. Solids* **23**, 555 (1962).

p. 565. Column 1, line 5 should read:
α-Ce are the same at 24,800 atm and 695°K, i.e.

NOTICE TO SUBSCRIBERS

Solid State Communications, the new sister journal to *The Journal of Physics and Chemistry of Solids*, will be sent free of charge for the year 1963 to all private subscribers (non institutional). The first issue of the journal will also be sent free of charge to library subscribers. The first issue is expected to be ready for despatch during June 1963. A descriptive brochure with instructions to contributors and details about subscription rates, including airmail charges, is available on request from the Publisher's office.

International Series of Monographs on Semiconductors

General Editor: **H. K. HENISCH**, *Pennsylvania State University*

Volume 1. SEMICONDUCTING III-V COMPOUNDS

C. Hilsum and **A. C. Rose-Innes**, *Services Electronics Research Laboratory, Baldock, Hertfordshire*

It has been known for several years that a variety of semiconducting substances can be formed by combining elements from groups III and V of the Periodic Table. By now, this family of materials has achieved great fundamental and technical importance. This volume gives a concise but comprehensive treatment of theoretical and experimental aspects. It deals with band structure, crystal structure, preparatory techniques, transport processes, optical absorption, photoelectric effects and galvanomagnetic properties, as well as with a number of device applications.

240 pages **Well illustrated** **60s. net**

Volume 2. PHOTO AND THERMOELECTRIC EFFECTS IN SEMICONDUCTORS

J. Tauc, *Czechoslovak Academy of Sciences, Prague*

This volume gives an extensive account of electronic transport processes in semiconductors. It deals specifically with the effect of illumination and with the presence of temperature gradients, magnetic fields and localized variations of impurity content. An introductory chapter is included in which the various practical parameters are discussed in terms of more fundamental relationships. The volume should be of general interest to readers concerned with research, with the design of semiconductor devices and with teaching.

250 pages **Illustrated** **60s. net**

Volume 3. SEMICONDUCTOR STATISTICS

J. S. Blakemore, *Honeywell Research Center, Hopkins, Minnesota*

This monograph provides a comprehensive discussion of the factors which govern the concentration of free charge carriers in semiconductors and thus, to a very important extent, the electrical properties of these materials. It is divided into two parts, dealing respectively with equilibrium and non-equilibrium situations. The book includes an extensive account of carrier recombination under intrinsic and extrinsic conditions and concerns itself with problems arising from magnetic level splitting, multivalent flaws, co-operative impurity phenomena, trapping processes and donor-acceptor compensation.

> "... treats a well defined branch of semiconductor physics in a comprehensive and intelligible manner... presenting to the reader a coherent and significant pattern."
>
> *Solid State Electronics*

390 pages **Numerous illustrations** **84s. net**

Volume 4. THERMAL CONDUCTION IN SEMICONDUCTORS

J. R. Drabble, *Department of Physics, University of Exeter*, and
H. J. Goldsmid, *The General Electric Company, Ltd., Hirst Research Centre, Middlesex*

Recent developments in the field of thermoelectric devices have indicated a great need for a more fundamental understanding of thermal conduction processes in semiconductors, since these processes have a profound influence on all efficiency considerations. Because some of the materials concerned are available in highly pure and well ordered form, they are specially suitable for investigations of this kind. The present volume covers theoretical as well as practical aspects of these problems, including the techniques of measurement.

> "... makes a valuable contribution to the knowledge of thermal conduction ..."
>
> *British Power Engineering*

240 pages **Many illustrations** **60s. net**

Volume 5. ELECTROLUMINESCENCE

H. K. Henisch, *Pennsylvania State University*

The first comprehensive treatment of electroluminescence and related phenomena in book form. It will prove of most value to physicists who are concerned with fundamental processes, and also to engineers and technologists whose interests in the field are essentially practical. The theoretical aspects of the light emitting processes, electroluminescence at crystal boundaries, the properties of single and microcrystalline phosphors and electroluminescent devices are all fully dealt with in this volume.

> "The book is well produced and can be recommended to both the physicist and the electrical engineer."
>
> *Proceedings of the Physical Society*

375 pages **Profusely illustrated** **80s. net**

Any volume sent on 30 days' approval without obligation. Please quote this journal when ordering

PERGAMON PRESS **Headington Hill Hall, Oxford**

Pergamon Press books are distributed in the Western Hemisphere and the Philippines by the Macmillan Company, 60 Fifth Avenue, New York 11, N.Y., and Collier-Macmillan (Canada) Ltd., 132 Water Street South, Galt, Ontario, Canada

Important Services for Your Library from Maxwell Scientific International

- **suppliers of any book or periodical published anywhere in the world**
- **backfile specialists serving the needs of libraries for scholarly and scientific periodicals in any language**
- **originators of a new, free, bibliographic service to provide up-to-date information on new books issued by 1000 publishers throughout the world**

Through its several divisions MAXWELL SCIENTIFIC INTERNATIONAL provides extensive services to libraries everywhere:

I. R. MAXWELL & CO. MAXWELL, MEIER & HOLMES CO.

I. R. Maxwell & Co. and Maxwell, Meier & Holmes Co. provide specialized services to obtain current books and journals as well as back issues of almost every publisher throughout the world! Orders are processed promptly and efficiently . . . collections of duplicates and surplus material in all fields of science, medicine and the humanities are examined and purchased for cash or on exchange—without delay!

MSI DOCUMENTATION AND PROCUREMENT CENTRE

This division provides a *new* bibliographic facility to librarians without charge! It issues current information on the new books of 1000 publishers; simplifies record-keeping by giving new book information on IBM-type cards and provides a fast, reliable and economical channel for ordering books and journals from all publishers throughout the world.

Take advantage now of the highly specialized services offered by the divisions of *MAXWELL SCIENTIFIC INTERNATIONAL!* Write today for complete details—without obligation.

MAXWELL SCIENTIFIC INTERNATIONAL

Headington Hill Hall, Oxford.
Long Island City 1, N.Y.

NOTES FOR CONTRIBUTORS

I. GENERAL

1. Submission of a paper to *The Journal of Physics and Chemistry of Solids* will be taken to imply that it represents original research not previously published (except in the form of an abstract or preliminary report), that it is not being considered for publication elsewhere, and that if accepted it will not be published elsewhere in the same form, in any language, without the consent of the editor-in-chief. It should deal with original research work in the field of the physics and chemistry of solids.

2. Papers should be submitted to the appropriate regional editor (all English-language papers to be sent to the U.S. editor).

3. Papers will be published as quickly as possible after acceptance, and, subject to space being available, should appear in the issue next following, if this is due for publication not earlier than three months after the acceptance date. Short communications under the heading of "Letters to the Editor" will receive priority for publication, and will be published in the issue following receipt, if accepted not later than the beginning of the month preceding publication.

II. SCRIPT REQUIREMENTS

1. Papers submitted should be concise and written in a readily understandable style. Scripts should be typed and double spaced and submitted in duplicate to facilitate refereeing.

It will be appreciated if authors clearly indicate any special characters used. An abstract not exceeding 200 words, should be provided in the language of the paper. French and German papers should be submitted with English abstract and titles, but if this is not possible the abstract will be translated by the publishers. To conserve space, authors are requested to mark less important parts of the paper, such as details of experimental technique, methods, mathematical derivations, etc. for printing in small type. The technical description of methods should be given in detail only when such methods are new. Authors will receive proofs for correction when their papers are first set; further proofs will be sent only when the amount of alteration makes it advisable.

2. **Illustrations** should not be included in the typescript of the paper, and legends should be typed on a separate sheet. Line drawings which require redrawing should include all relevant details and clear instructions for the draughtsman. If figures are already well drawn it may be possible to reproduce them direct from the originals, or from good photo-prints if these can be provided. It is not possible to reproduce from prints with weak lines. Illustrations for reproduction should normally be about twice the final size required. The lettering should be sufficiently large and bold to permit this reduction. Photographs should only be included where they are essential.

3. **Tables and figures** should be so constructed as to be intelligible without reference to the text. Every table and column should be provided with an explanatory heading. Units of measure must always be clearly indicated. The same data should not be published in both tables and figures. The following standard symbols should be used on line drawings since they are easily available to the printers: ○, ●, +, ×, □, ■, △, ▲, ◇, ◆, ▽, ▼.

4. References are indicated in the text by superior numbers in parentheses, and the full reference should be given in a list at the end of the paper in the following form:

1. Hill R., *J. Iron St. Inst.*, **158**, 177 (1948).
2. Pearson C., *The Extrusion of Metals*, p. 137. Chapman and Hall, London (1944).

Abbreviations of journal titles should follow those given for *Physics Abstracts*. It is particularly requested that authors' initials, and appropriate volume and page numbers, should be given in every case.

Footnotes, as distinct from literature references should be indicated by the following symbols—*, †, ‡, ‡‡, commencing anew on each page; they should *not* be included in the numbered reference system.

5. Due to the international character of the journal no rigid rules concerning notation and spelling will be observed, but each paper should be consistent within itself as to symbols and units.

THE JOURNAL OF PHYSICS AND CHEMISTRY OF SOLIDS

VOLUME 24 1963 JANUARY

G. Bemski and B. Szymanski: A new paramagnetic center in electron irradiated silicon . 1

A. Jayaraman, W. Klement Jr., R. C. Newton and G. C. Kennedy: Fusion curves and polymorphic transitions of the group III elements—aluminum, gallium, indium and thallium—at high pressures 7

R. C. Casella: On the possibility of observing a Bose–Einstein condensation of excitons in CdS and CdSe 19

R. F. Brebrick: Deviations from stoichiometry and electrical properties in SnTe . . 27

F. F. Morehead: Luminescence in ZnS, Se:Cu, Cl 37

P. C. Newman: Crystal structures of adamantine compounds 45

R. M. Barrer, R. F. Bartholomew and L. V. C. Rees: Ion exchange in porous crystals Part I. Self- and exchange-diffusion of ions in chabazites 51

Joseph Jach: The thermal decomposition of $NaBrO_3$ Part I—Unirradiated material . 63

Joseph Jach: The thermal decomposition of $NaBrO_3$ Part II—Irradiated material . 75

V. J. Johnson, M. W. Valenta, J. E. Dougherty, R. M. Douglass and J. W. Meadows: $Pb(Sc_{0\cdot5}Nb_{0\cdot5})_x\Phi_{1-x}O_3$, Perovskite-type ferroelectric solid solutions possessing relatively large spontaneous polarizations 85

C. R. Houska: A theoretical treatment of atomic configuration found in some iron–aluminum solid solutions 95

H. J. van Daal, W. F. Knippenberg and J. D. Wasscher: On the electronic conduction of α-SiC crystals between 300 and 1500°K 109

R. Illingworth: Diffusion of thallous ions in single crystals of KBr 129

A. A. Braner and R. Chen: Some optical properties of iodine single crystals . . 135

C. Calvo: The crystal structure and luminescence of γ-zinc orthophosphate . . 141

P. Freymuth und G. Sauerbrey: Ausheilung von Bestrahlungsschäden in Quarz-Schwingkristallen 151

Michael Hoch: Order–disorder reactions in α-Ti(O) and TiO 157

J. R. Drabble: Summary of Conference on the Physics of Semiconductors, Exeter, 1962 161

Letters to the Editor:

Henry M. Otte Faulting in sodium azide 169

J. Beretka: Differential thermal analysis of yttrium iron garnet 169

L. V. Coulter, G. L. Stepakoff and G. C. Roper: The nature of the motion of N_2, CO and CH_4 in their β-quinol clathrates at low temperatures . . . 171

Book Review:

B. Chalmers (Editor): "Progress in Materials Science" (reviewed by A. S. Nowick) 174

PRINTED BY J. W. ARROWSMITH LTD., BRISTOL, ENGLAND